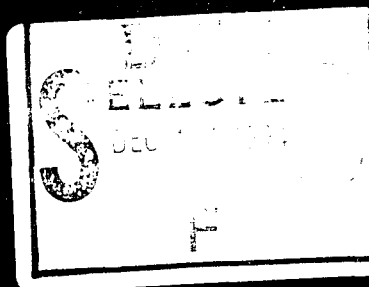The Proceedings

Sixth
International
Conference on

Numerical
Ship Hydrodynamics

2-5 August 1993
Iowa Memorial Union
Iowa City, Iowa, USA

19941207 095

THE UNIVERSITY OF IOWA

30 November 1994

Dr. E.P. Rood
Code 1132F
Scientific Officer, Hydrodynamics
Office of Naval Research
800 North Quincy Street
ARLINGTON, VA 22217-5000

Dear Ed:

<div align="center">

Final Technical Report on ONR Grant N00014-93-1-0038
Sixth International Conference on Numerical Ship Hydrodynamics

</div>

The Sixth International Conference on Numerical Ship Hydrodynamics was held in Iowa City during 2-5 August 1993. The Conference was hosted by the Iowa Institute of Hydraulic Research and co-sponsored by the Institute in collaboration with the David Taylor Research Center, The Office of Naval Research, and the Naval Studies Board of the National Research Council. In keeping with the tradition of the previous conferences, the papers covered a wide range of topics and numerical methods.

Numerical ship hydrodynamics is developing at least as fast as the parent field of computational fluid dynamics, and on some topics it is pioneering new approaches. Such is the case, for example, in the study of the complex flow physics associated with the free surface and related phenomena. The papers presented at the conference reported not only advances made at the fundamental level but also in the application of numerical methods to certain aspects of ship design.

Having the conference in Iowa City provided an opportunity for the research community to celebrate the accomplishments of a distinguished colleague, Professor Louis Landweber. His many contributions to the field of ship hydrodynamics, through research, education and service, were highlighted at the conference. The conference attracted many of his past students and associates to join the celebration.

The conference was judged a great success by all measures. Three copies of the conference Proceeding are being sent to you under separate cover.

Sincerely,

V. C. Patel
Director,
University of Iowa Foundation
Distinguished Professor of Mechanical Engineering

cc: ONR Grant Administrator, Seattle
    DTIS
    UI Sponsored Programs

Proceedings of the

Sixth International Conference on Numerical Ship Hydrodynamics

edited by
V.C. Patel and F. Stern

Accesion For		
NTIS CRA&I	☒	
DTIC TAB	☐	
Unannounced	☐	
Justification		
By		
Distribution /		
Availability Codes		
Dist	Avail and / or Special	
A-1		

SPONSORS

The Executive Committee of the Sixth International Conference on Numerical Ship Hydrodynamics extends its thanks to those organizations whose financial contributions made this conference possible. Because of their generous contributions, copies of the *Proceedings* will be distributed to all member organizations of the International Conference on Numerical Ship Hydrodynamics.

Naval Studies Board of the U.S. National Research Council

Iowa Institute of Hydraulic Research

David Taylor Research Center

Office of Naval Research

PREFACE

The Sixth International Conference on Numerical Ship Hydrodynamics was held in Iowa City on August 2-5, 1993. The conference was hosted by the Iowa Institute of Hydraulic Research and cosponsored by the Institute in collaboration with the David Taylor Research Center, the Office of Naval Research, and the Naval Studies Board of the National Research Council. In keeping with the tradition of the previous conferences, the papers covered a wide range of topics and numerical methods.

Numerical ship hydrodynamics is developing at least as rapidly as the parent field of computational fluid dynamics, and on some topics it is pioneering new approaches. Such is the case, for example, in the study of the complex flow physics associated with the free surface and related phenomena. The papers presented at the conference report advances made not only at the fundamental level but also in the application of numerical methods to certain aspects of ship design.

Having the conference in Iowa City provided an opportunity for the research community to celebrate the accomplishments of a distinguished colleague, Professor Louis Landweber. His many contributions to the field of ship hydrodynamics, through research, education, and service, are highlighted in the accompanying biographical sketch. The conference attracted many of his past students and associates to join the celebration.

The conference was judged a great success by all measures, both technical and social. Organization of such an event demands the time and effort of many individuals. Members of the three conference committees deserve thanks for their effort. In addition, appreciation should be extended to the University of Iowa Center for Conferences and Institutes and to the students and staff of the Institute of Hydraulic Research, who made the arrangements before, during, and after the conference. Special thanks go to Twila Meder and Judy Holland for their help throughout the conference and in timely production of this proceedings volume.

V.C. Patel
Co-Chair

DEDICATION

Louis Landweber was born on January 8, 1912, in New York City. He attended public schools there and received his B.S. degree in mathematics from City College of New York, where he was elected to Phi Beta Kappa. Upon graduation in 1932, he was awarded the Ward Medal for Physics and the Belden Prize for Mathematics and Physics, and he accepted a position as Junior Physicist at the U.S. Experimental Model Basin at the Washington Navy Yard (which became David Taylor Naval Ship Research and Development Center (NSRDC)). He found the subject of his work fascinating and challenging and, though he was a mathematician, he realized that the field required mathematics he had not yet studied. He began work toward his master's degree by attending evening classes at George Washington University. He received a master's degree in physics in 1935. In 1940, Dr. Landweber became head of a small research group when the NSRDC (now David Taylor Model Basin (DTMB)) opened at Carderock, Maryland. This group distinguished itself in vital war-related research, primarily in mine-sweeping problems, which led to his receiving the Navy's Meritorious Civilian Service Award in 1947.

Shortly after World War II, his research group was expanded to become the Hydrodynamics Division. During the years at Carderock, Dr. Landweber completed work on his Ph.D. in physics at the University of Maryland and began teaching some courses for the University at the center. In 1954, he accepted a position at the University of Iowa, where he was Professor in the Department of Mechanics and Hydraulics and Research Engineer in the Iowa Institute of Hydraulic Research. He continued full-time teaching and research, concentrating his efforts in Ship Hydrodynamics, until his retirement in 1982; but he continues to advise students working on new problems.

During his distinguished career, Dr. Landweber has received many awards and citations, the most notable of which include being appointed the David Taylor Lecturer at DTMB and being awarded the Davidson Medal for Ship-Research Accomplishments by the Society of Naval Architects, both in 1978; being honored by a special session at the Third Engineering Mechanics Division Specialty Conference of the American Society of Civil Engineers in 1979; and being named Weinblum Memorial Lecturer for 1981. He was named Fellow both of the Society of Naval Architects and Marine Engineers and the American Academy of Mechanics, and he was elected, in 1980, to the National Academy of Engineering. He has supervised over 50 M.S. and Ph.D. students and has been author, co-author, or editor of approximately 150 technical papers, reports, monographs, and books.

Dr. Landweber's superb research and teaching skills have been enhanced and made even more effective by his very genuine personal qualities. He has been mentor and friend to three generations of students and research associates, all of whom have been influenced by his deep integrity, his warmth and caring, and his wonderful humor. It is indeed appropriate that the Sixth International Conference on Numerical Ship Hydrodynamics was held in his honor and that these *Proceedings* are dedicated to him.

CONTENTS

SESSION 9 VISCOUS FLOW: APPLICATIONS 2

Chair: B. Wooden

SESSION 10 LIFTING-SURFACE FLOW: INVISCID METHODS

Chair: E.O. Tuck

SESSION 11 WAVY/FREE-SURFACE FLOW: SHIP MOTIONS

Chair: I. Tanaka

SESSION 1

WAVY/FREE-SURFACE FLOW: PANEL METHODS 1

Fully Nonlinear Water Wave Computations Using the Desingularized Method

R.F. Beck, Y. Cao, and T.-H. Lee
(University of Michigan, USA)

ABSTRACT

The use of Euler-Lagrange time stepping methods to solve numerically fully nonlinear marine hydrodynamic problems is discussed. The mixed boundary value problem that arises at each time step is solved using a desingularized approach. In this approach the singularities generating the flow field are outside the fluid domain. This allows the singularity distribution to be replaced by simple isolated singularities with a resultant reduction in computational complexity and computer time.

Various examples of the use of the method are presented including two-dimensional water wave problems, the added mass and damping due to sinusoidal oscillations of two-dimensional and axial symmetric bodies, and the wave pattern and wave resistance of a Wigley hull moving at constant forward speed. The results show excellent agreement with other published computations and good agreement with experiments.

INTRODUCTION

In recent years, there has been significant progress in solving marine hydrodynamic problems with fully nonlinear free surface boundary conditions. While some of the work has incorporated fluid viscosity and surface tension, the majority has assumed that the fluid is incompressible and inviscid and that the flow is irrotational. These assumptions lead to a boundary value problem for which the Laplace equation is valid everywhere in the fluid domain. This does not imply that viscous effects are unimportant and in certain situations they may dominate. However, the inviscid problem is an order of magnitude easier to solve and thus has been the basis of much of the research. Throughout this paper it is assumed that the fluid is incompressible and inviscid and that the flow is irrotational.

Fully nonlinear computations can be performed by a variety of methods. For steady forward speed, an iterative procedure can be used to satisfy the nonlinear free surface boundary conditions. In the work of Jensen, et al. (1989), and more recently Kim and Lucas (1990,1992) and Raven (1992), a series of linearized boundary value problems based on the solution to the previous iteration and satisfied on the deformed free surface of that iteration are solved. The iteration is continued until convergence to the complete, nonlinear solution is obtained. Bai et al. (1992) also use an iterative procedure but employ a localized finite-element method to solve the boundary value problem at each iteration. For steady problems the iteration procedure may converge to the fully nonlinear solution faster than a time stepping method.

Longuet-Higgins and Cokelet (1976) first introduced the mixed Euler-Lagrange method for solving two-dimensional fully nonlinear water wave problems. This time stepping procedure requires two major tasks at each time step: the linear field equation is solved in an Eulerian frame; then the fully nonlinear boundary conditions are used to track individual Lagrangian points on the free surface to update their position and potential values. Variations of this method have been applied to a wide variety of two- and three-dimensional problems. Most of the variations involve how the linear field equation is solved at each time step. Among the researchers who applied the method to two-dimensional problems are Faltinsen (1977), Vinje and Brevig (1981), Baker et al. (1982) and more recently Grosenbaugh and Yeung (1988), Cointe et al. (1990) and Saubestre (1990). In three dimensions, the computations become much more difficult because of the large number of unknowns that are required. Results have been obtained by a number of researchers, including Lin et al. (1984), Dommermuth and Yue (1987), Kang and Gong (1990), Zhou and Gu (1990), Cao (1991), Cao et al.

(1990, 1991, 1992), and Lee (1992).

The successful implementation of an Euler-Lagrange method to solve fully nonlinear water wave problems requires a fast and accurate method to solve the mixed boundary value problem that results at each time step and a stable time stepping scheme. In our research, the mixed boundary value problem is solved using a desingularized boundary integral method. Similar to conventional boundary integral methods, it reformulates the boundary value problem into a boundary integral equation. The difference is that the desingularized method separates the integration and control surfaces, resulting in nonsingular integrals. The solution is constructed by integrating a distribution of fundamental singularities over a surface (the integration surface) outside the fluid domain. The integral equation for the unknown distribution is obtained by satisfying the boundary conditions on the surface (the control surface) surrounding the fluid domain.

A variety of problems have been solved by the desingularized approach. Webster (1975) was probably the first to apply the technique to panel methods. He used triangular patches of linearly distributed sources "submerged" within the body surface to study the steady flow past an arbitrary three-dimensional body. Schultz and Hong (1989) showed the effectiveness and accuracy of the desingularized method for two-dimensional potential flow problems. Cao et al. (1991) gave convergence rates and error limits for simple three-dimensional flows including a source-sink pair traveling below a free surface.

The desingularized method has been successfully applied to several free surface problems. Cao et al. (1993a) have investigated the formation of solitons propagating ahead of a disturbance moving in shallow water near the critical Froude number. The wave resistance, lift force and pitch moment acting on a submerged spheroid traveling beneath the free surface were computed by Bertram et al. (1991) and compared to linear theory results. Using an iterative technique, the wave resistance was computed by Jensen et al. (1986, 1989) and Raven (1992). The desingularized method has been applied to ship motion problems by Bertram (1990) and Lee (1992).

There are several computational advantages to the desingularized method. Because of the desingularization, the kernels of the integral equation are no longer singular and special care is not required to evaluate integrals over the panels. Simple numerical quadratures can be used to greatly reduce the computational effort, particularly by avoiding transcendental functions. In fact, for the source distribution method the distributed sources may be replaced by simple isolated sources. Higher order singularities such as dipoles can easily be incorporated. Isolated Rankine sources also allow the direct computation of the induced velocities on the free surface without further numerical integration or differentiation. The resulting code does not require any special logic and is thus easily vectorized. We have not yet installed the code on a parallel machine but the algorithm is straight forward and should not cause any difficulties. At present, the method is $O(N^2)$, but by using multipole expansions it could be reduced to an $O(N \ln N)$ method.

In the next section, the desingularized approach using isolated sources to solve fully nonlinear marine hydrodynamic problems will be discussed. The solution is developed in the time domain starting from rest. Following the theoretical development, some of the details of the numerical methods will be presented. Finally, numerical results will be presented and compared to experimental results where available.

FULLY NONLINEAR PROBLEM FORMULATION

An ideal, incompressible fluid is assumed and surface tension is neglected. The problem is started from rest so that the flow remains irrotational. This implies the existence of a velocity potential such that the fluid velocity is given by its gradient and the governing equation in the fluid domain is the Laplace equation.

A coordinate system Oxyz translating in the negative x direction relative to a space fixed frame is used. The time dependent velocity of translation is given by $U_o(t)$. The Oxyz axis system is chosen such that the $z = 0$ plane corresponds to the calm water level and z is positive upwards. The total velocity potential of the flow can then be expressed as

$$\Phi = U_o(t)x + \phi(x,y,z,t) \qquad (1)$$

where $\phi(x,y,z,t)$ is the perturbation potential. Both Φ and ϕ satisfy the Laplace equation

$$\nabla^2 \Phi = 0 \qquad (2)$$

Boundary conditions must be applied on all surfaces surrounding the fluid domain: the free surface (S_F), the body surface (S_H), the bottom (S_B) and the surrounding surface at infinity (S_∞). A kinematic body boundary condition is applied on the instantaneous position of the body wetted surface:

$$\frac{\partial \phi}{\partial n} = -U_o(t)n_1 + V_H \cdot \mathbf{n} \quad \text{on} \quad S_H \qquad (3)$$

4

where $\mathbf{n} = (n_1, n_2, n_3)$ is the unit normal vector to the surface (out of the fluid domain) and $\mathbf{V}_H$ is the velocity of the body relative to the moving coordinate system. The subscripts 1,2,3 refer to the x, y, and z axis directions respectively. There is also a kinematic condition applied on the bottom:

$$\frac{\partial \phi}{\partial n} = -U_o(t)n_1 + \mathbf{V}_B \cdot \mathbf{n} \quad \text{on} \quad S_B \qquad (4)$$

where $\mathbf{V}_B$ is the velocity of the bottom relative to the Oxyz system. For an infinitely deep ocean equation (4) reduces to

$$\nabla \phi \to 0 \quad \text{as} \quad z \to -\infty \qquad (5)$$

Finite depth will increase the computational time because of the additional unknowns necessary to meet the bottom boundary condition but there is no increase in computational difficulty. In fact, the flatness of the bottom is immaterial. The only overhead relative to a flat bottom is computing the necessary geometrical parameters of a nonflat bottom. This contrasts with the typical Green function approach where a finite depth Green function is significantly harder to compute than an infinite depth Green function and a nonflat bottom can not in general be accommodated.

On the instantaneous free surface both the kinematic and dynamic conditions must be satisfied. The kinematic condition is

$$\frac{\partial \eta}{\partial t} + \nabla \phi \cdot \nabla \eta - \frac{\partial \phi}{\partial z} + U_o(t) \cdot \frac{\partial \eta}{\partial x} = 0 \quad \text{on} \quad S_F \qquad (6)$$

where $z = \eta (x, y, t)$ is the free surface elevation. The dynamic condition requires that the pressure everywhere on the free surface equals the ambient pressure, P_a. The ambient pressure is assumed known and may be a function of space and time. Normally it would be set equal to zero. Using Bernoulli's equation the dynamic condition becomes:

$$\frac{P_a}{\rho} = -\frac{\partial \phi}{\partial t} - g\eta - \frac{1}{2}\nabla \phi \cdot \nabla \phi - U_o(t) \cdot \frac{\partial \phi}{\partial x} \quad \text{on} \quad S_F \qquad (7)$$

where ρ is the fluid density and g the gravitational acceleration.

Because we are solving an initial value problem with no incident waves, the fluid disturbance must vanish at infinity :

$$\nabla \phi \to 0 \quad \text{as} \quad R \to \infty \qquad (8)$$

In addition, the initial values of the potential and free surface elevation must be specified such that

$\phi = 0 \quad t \le 0 \quad$ in fluid domain

$\eta = 0 \quad t \le 0 \qquad\qquad\qquad (9)$

In the Euler-Lagrange method a time stepping procedure is used in which a boundary value problem is solved at each time step. At each step, the value of the potential is given on the free surface (a Dirichlet boundary condition) and the value of the normal derivative of the potential (a Neumann boundary condition) is known on the body surface and bottom surface. The potential and its normal derivative are updated at the end of each time step. The free surface potential and elevation are determined by integrating with respect to time (or time marching) the free surface boundary conditions. In our calculations, a Runge-Kutta-Fehlberg technique is used to do the time stepping. The body and bottom boundary conditions are prescribed for the forced motion problem. In the case of a freely floating body, the equations of motion must be integrated with respect to time in a manner similar to the free surface conditions.

On the free surface, the kinematic condition is used to time step the free surface elevation and the dynamic condition is used to update the potential. Many different approaches are possible to time march the free surface boundary conditions. The most common is a material node approach in which the nodes or collocation points follow the individual fluid particles. Another technique is to prescribe the horizontal movement of the node but allow the node to follow the vertical displacement of the free surface. The prescribed movement may be zero such that the node locations remain fixed in the x-y plane. Depending on the problem, one of the techniques may be easier to apply than the others.

It is convenient to rewrite the free surface boundary conditions, equations (6) and (7), in terms of the time derivative of a point moving with a prescribed velocity $\mathbf{v}$ relative to the Oxyz coordinate system. By adding $\mathbf{v} \cdot \nabla \eta$ to both sides of (6) and $\mathbf{v} \cdot \nabla \phi$ to both sides of (7) and after some algebraic manipulation, the kinematic and dynamic conditions can be put in the form

$$\frac{\delta \eta}{\delta t} = \frac{\partial \phi}{\partial z} - (\nabla \phi - \mathbf{v}) \cdot \nabla \eta - U_o(t)\frac{\partial \eta}{\partial x} \quad \text{on} \quad S_F \qquad (10)$$

and

$$\frac{\delta \phi}{\delta t} = -g\eta - \frac{1}{2}\nabla \phi \cdot \nabla \phi + \mathbf{v} \cdot \nabla \phi - \frac{P_a}{\rho} - U_o(t)\frac{\partial \phi}{\partial x}$$
$$\text{on} \quad S_F \qquad (11)$$

5

where

$$\frac{\delta}{\delta t} \equiv \frac{\partial}{\partial t} + \mathbf{v} \cdot \nabla \qquad (12)$$

is the time derivative following the moving node. This is similar to the usual material derivative of fluid mechanics except the velocity is the given $\mathbf{v}$ rather than the fluid velocity.

If $\mathbf{v}$ is set equal to $\left(U(t), V(t), \frac{\delta \eta}{\delta t} \right)$ the node follows a prescribed path with velocity $(U(t), V(t))$ in the x-y plane and moves vertically with the free surface. Setting $\mathbf{v} = \left(0, 0, \frac{\partial \eta}{\partial t} \right)$ results in the x-y locations of the nodes remaining fixed in the Oxyz coordinate system and equations (10) and (11) reduce to:

$$\frac{\partial \eta}{\partial t} = \frac{\partial \phi}{\partial z} - \nabla \phi \cdot \nabla \eta - U_o(t) \cdot \frac{\partial \eta}{\partial x} \quad \text{on} \quad S_F \qquad (13)$$

and

$$\frac{\delta \phi}{\delta t} = -g\eta - \frac{1}{2} \nabla \phi \cdot \nabla \phi - \frac{P_a}{\rho} + \frac{\partial \eta}{\partial t} \cdot \frac{\partial \phi}{\partial z} - U_o(t) \frac{\partial \phi}{\partial x}$$
$$\text{on} \quad S_F \qquad (14)$$

In the material node approach, the velocity is set equal to the fluid velocity such that $\mathbf{v} = U_o(t)\mathbf{i} + \nabla \phi$, resulting in

$$\frac{D X_F(t)}{Dt} = U_o(t)\mathbf{i} + \nabla \phi \qquad (15)$$

and

$$\frac{D\phi}{Dt} = -g\eta + \frac{1}{2} \nabla \phi \cdot \nabla \phi - \frac{P_a}{\rho} \qquad (16)$$

where $X_F = \left(x_F(t), y_F(t), z_F(t) \right)$ is the position vector of a fluid particle on the free surface and

$$\frac{D}{Dt} = \frac{\partial}{\partial t} + \nabla \Phi \cdot \nabla \qquad (17)$$

is the usual material derivative.

The form of the free surface boundary conditions given by the above equations allows the value of the elevation and potential to be stepped forward in time. The left hand sides of equations (10) - (16) are the derivatives with respect to time of the potential and wave elevation moving with the node. The quantities on the right hand side are all known at each time step; the spatial gradient of the potential can be determined analytically after solving the boundary value problem and the wave elevation is known. The difficulty is the gradient of the free surface elevation ($\nabla \eta$ in equations (10) and (13)) that must be evaluated numerically. This leads to increased computer time and numerical inaccuracies. However, this term is only needed in the prescribed horizontal node movement approach. In the material node approach no extra derivatives need to be evaluated and this probably explains why this is the approach most often used. With material nodes one must always be concerned that the nodes do not penetrate the body surface between time steps since they are unconstrained. In zero forward speed problems, material nodes or fixed nodes seem to be the most appropriate. In problems with forward speed, the material node approach has difficulties near the body because nodes tend to pile up near the bow and stern stagnation regions. The prescribed horizontal node movement approach does not have this difficulty since the node movement is constrained. An appropriate choice of $\mathbf{v}$ is one which parallels the body waterline and is close to $\nabla \Phi$. In this case, the contribution of the $\nabla \eta$ term to the right hand side of (10) will be small and numerical inaccuracies will be minimized. Consequently, fast, simple numerical derivatives can be used to evaluate the $\nabla \eta$ term.

At each time step a mixed boundary value problem must be solved; the potential is given on the free surface and the normal derivative of the potential is known on the body surface and the bottom. In terms of a desingularized source distribution, the potential at any point in the fluid domain is given by

$$\phi(\mathbf{x}) = \iint_\Omega \sigma(\mathbf{x}_s) \frac{1}{|\mathbf{x} - \mathbf{x}_s|} d\Omega \qquad (18)$$

where Ω is the integration surface outside the fluid domain.

Applying the boundary conditions, the integral equations that must be solved to determine the unknown source strengths $\sigma(\mathbf{x}_s)$ are

$$\iint_\Omega \sigma(\mathbf{x}_s) \frac{1}{|\mathbf{x}_c - \mathbf{x}_s|} d\Omega = \phi_o(\mathbf{x}_c) \qquad (19)$$

$$\mathbf{x}_c \in \Gamma_d$$

and

$$\iint_\Omega \sigma(x_s)\frac{\partial}{\partial n}\frac{1}{|x_c - x_s|}\,d\Omega = \chi(x_c) \qquad (20)$$

$$x_c \in \Gamma_n$$

where x_s = a point on the integration surface, Ω

x_c = a point on the real boundary

ϕ_0 = the given potential value at x_c

Γ_d = surface on which ϕ_0 is given

χ = the given normal velocity at x_c

Γ_n = surface on which χ is given

The hydrodynamic forces acting on the body due to a prescribed motion are found by integrating the pressure over the instantaneous wetted surface. The generalized force acting on the body in the jth direction is thus given by:

$$F_j = \iint_{S_H} P n_j \, ds \qquad (21)$$

where n_j is the generalized unit normal into the hull defined as

$$(n_1, n_2, n_3) = \mathbf{n} \qquad (22)$$

$$(n_4, n_5, n_6) = \mathbf{r} \times \mathbf{n}$$

$\mathbf{n}$ = unit normal to body surface (out of fluid)

$\mathbf{r} = (\bar{x}, \bar{y}, \bar{z})$

$O\overline{xyz}$ = body axis system

and $j = 1,2,3$ corresponds to the directions of the $O\overline{xyz}$ axis respectively.

The pressure in the moving coordinate system is given by Bernoulli's equation:

$$\frac{P}{\rho} = -\frac{\delta\phi}{\delta t} - U_o(t)\frac{\partial\phi}{\partial x} - gz - \frac{1}{2}\nabla\phi\cdot\nabla\phi + v\cdot\nabla\phi \qquad (23)$$

where $\frac{\delta\phi}{\delta t}$ is the time derivation of the potential following a moving node on the body and v is the velocity of the node relative to the Oxyz system.

NUMERICAL TECHNIQUES

In the usual manner, the integrals may be discretized to form a system of linear equations to be solved at each time step. In the desingularized method, the source distribution is outside the fluid domain so that the source points never coincide with
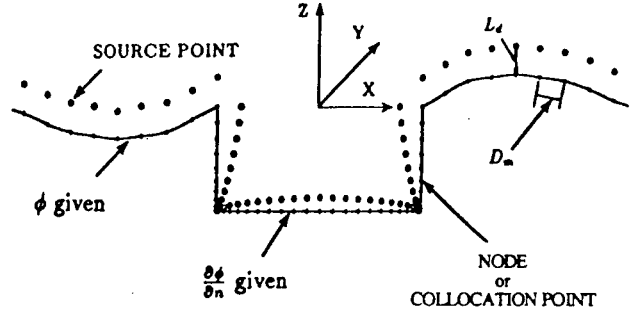
Figure 1: Schematic of source and node locations

the collocation or node points and the integrals are nonsingular. In addition, because of the desingularization we can use simple isolated sources, rather than a distribution and obtain the equivalent accuracy. This greatly reduces the complexity of the form of the influence coefficients that make up the elements of the kernel matrix. As shown in figure 1, nodes (the collocation points) are distributed on the free surface and body surface. The isolated sources are distributed a small distance above each of the nodes. The nondimensional desingularized distance is given by

$$L_d = \ell_d (D_m)^\upsilon \qquad (24)$$

where ℓ_d and υ are constants to be chosen by the user and D_m is a measure of the local mesh size (typically the square root of the panel area in three-dimensional problems). Cao et al. (1991) found values of $\ell_d = 1.0$ and $\upsilon = .5$ to be about optimum. The accuracy and convergence of the solutions are relatively insensitive to the choices of ℓ_d and υ.

At each time step the mixed boundary value problem that must be solved is defined by equations (19) and (20). Using an array of isolated simple sources above the free surface and inside the body surface to construct the velocity potential, equation (18) becomes

$$\phi(x) = \sum_{j=1}^{N_F}\frac{\sigma_j^F}{|x - x_{s_j}^F|} + \sum_{j=1}^{N_B}\frac{\sigma_j^B}{|x - x_{s_j}^B|} \qquad (25)$$

where N_F is the number of the isolated sources above the free surface,

$x_{s_j}^F$ is the location of the jth source and

σ_j^F is the strength of the jth source at $x_{s_j}^F$.

7

Similarly,

N_B, $x_{s_j}^B$ and σ_j^B are the number, location and strength of the sources inside the body surface.

The integral equations (19) and (20) are satisfied at the nodes on the free surface and body surface such that

$$\sum_{j=1}^{N_F} \frac{\sigma_j^F}{\left| x_{c_i}^F - x_{s_j}^F \right|} + \sum_{j=1}^{N_B} \frac{\sigma_j^B}{\left| x_{c_i}^F - x_{s_j}^B \right|} = \phi_0\left(x_{c_i}^F\right)$$

(i=1...N_F)

(26)

$$\sum_{j=1}^{N_F} \sigma_j^F \frac{\partial}{\partial n}\left(\frac{1}{\left| x_{c_i}^B - x_{s_j}^F \right|}\right) + \sum_{j=1}^{N_B} \sigma_j^B \frac{\partial}{\partial n}\left(\frac{1}{\left| x_{c_i}^B - x_{s_j}^B \right|}\right)$$
$$= \chi\left(x_{c_i}^B\right)$$

(i=1...N_B)

with $N = N_F + N_B$ being the total number of unknowns. Equations (26) can also be written in matrix form as

$$A \cdot \Sigma = B \qquad (27)$$

or

$$\begin{pmatrix} A^{(11)} & A^{(12)} \\ A^{(21)} & A^{(22)} \end{pmatrix}\begin{pmatrix} \Sigma^{(1)} \\ \Sigma^{(2)} \end{pmatrix} = \begin{pmatrix} B^{(1)} \\ B^{(2)} \end{pmatrix} \qquad (28)$$

where

$$A_{ij}^{(11)} = \frac{1}{\left| x_{c_i}^F - x_{s_j}^F \right|} \qquad i=1...N_F, \quad j=1...N_F$$

$$A_{ij}^{(12)} = \frac{1}{\left| x_{c_i}^F - x_{s_j}^B \right|} \qquad i=1...N_F, \quad j=(N_F+1)...N$$

$$A_{ij}^{(21)} = \frac{\partial}{\partial n_i}\left(\frac{1}{\left| x_{c_i}^B - x_{s_j}^F \right|}\right) \quad i=(N_F+1)...N, j=1...N_F$$

$$A_{ij}^{(22)} = \frac{\partial}{\partial n_i}\left(\frac{1}{\left| x_{c_i}^B - x_{s_j}^B \right|}\right) \quad i=(N_F+1)...N,$$
$$j=(N_F+1)...N$$

$$\Sigma_i^{(1)} = \sigma_i^F \qquad i=1...N_F$$

$$\Sigma_i^{(2)} = \sigma_i^B \qquad i=(N_F+1)...N$$

$$B_i^{(1)} = \phi_0\left(x_{c_i}^F\right) \qquad i=1...N_F$$

$$B_i^{(2)} = \chi\left(x_{c_i}^B\right) \qquad i=(N_F+1)...N$$

where $x_{c_i}^F$ and $x_{c_i}^B$ are the node points on the free surface and body surface respectively.

Equations (27) are a system of $(N_F + N_B)$ equations for the unknown source strength Σ. Once Σ is known, the velocity potential and fluid velocity can be analytically calculated anywhere in the fluid domain.

Equations (27) can be solved either by a direct or iterative solver depending on the size of the matrix. For most of the two-dimensional problems considered in this paper, we use a LU decomposition solver. For the three-dimensional problems, an iterative solver GMRES is used. For problems where different grid spacings are used on different parts of the domain boundary, solving equation (27) as a whole system may not be efficient. A domain-decomposition technique is often better. In this technique $\Sigma^{(1)}$ and $\Sigma^{(2)}$ are determined separately through an iterative procedure. Rewrite equation (28) as

$$A^{(11)} \cdot \Sigma^{(1)} = B^{(1)} - A^{(12)} \cdot \Sigma^{(2)} \qquad (29)$$

$$A^{(22)} \cdot \Sigma^{(2)} = B^{(2)} - A^{(21)} \cdot \Sigma^{(1)} \qquad (30)$$

$\Sigma^{(1)}$ is determined by solving (29) with $\Sigma^{(2)}$ known (or guessed), then $\Sigma^{(1)}$ is substituted into (30) to determine $\Sigma^{(2)}$. The new $\Sigma^{(2)}$ is then used in (29) to update $\Sigma^{(1)}$. The procedure repeats until both equations are satisfied to the given error tolerance.

After Σ is determined, the fluid velocity on the free surface can be computed so that the right hand sides of the free surface conditions (10) and (11) can be found. The free surface elevation and the potential are then updated by a time stepping procedure. In the free surface updating, if material nodes are used, the spatial derivatives of the free surface elevation, $\nabla\eta$, are not required. The use of generalized nodes moving with prescribed velocity v requires the spatial derivatives of η and central-differencing or cubic splines are used. The time-stepping of the free surface is done by using a fourth-order Runge-Kutta-Fehlberg scheme.

For forced body motion problems, the force acting on the body does not enter the time-stepping procedure. Therefore, the calculation of the forces acting on the body can be post-processed. Bernoulli's equation (23) is used to compute the pressure on the body and the pressure is then integrated over the body surface to determine the forces. The pressure calculation requires the time-derivative of the potential on the body surface which is determined using central-differencing.

NUMERICAL RESULTS

In this section we shall present numerical results for a variety of cases including surface piercing bodies and a two-dimensional wave tank. The wave tank is useful to illustrate several properties of the calculations. Two-dimensional results are presented for a rectangular box in heave. Three-dimensional results are shown for axially symmetric cylinders and a Wigley hull.

Numerical Wave Tank

The two-dimensional wave tank consists of side walls, a wavemaker at one end and an absorbing beach at the other and a bottom at depth h. We have used several types of wavemakers including a paddle, a plunging wedge, and a variable pressure distribution on the free surface. The most effective beaches (cf. Cao, et al. 1993b) seem to be an energy absorbing layer on the free surface proportional to either ϕ or $\partial\phi/\partial n$.

Figure 2 shows the waves generated by a pneumatic sinusoidal wavemaker started from rest. The tank has walls at each end and is .625 wavelengths deep. Two lines are shown: the dash line was computed using the traditional material nodes and the solid line is for fixed horizontal nodes. As can be seen the agreement between the two methods of calculation is excellent.

Figure 3 presents the comparison between two and three dimensional calculations. In this case, the wave tank is 12 units long, 4 units deep and the wavelength is 7.5 units. For the three-dimensional calculations the tank was 6 units wide. For the two-dimensional computations the fundamental singularity is $\ln(r)$ while in the three-dimensional calculations it is $1/r$. As can be seen, the agreement is again very good; it is not perfect because of the panelization of the walls in the three-dimensional calculations. As more panels are used on the walls, the agreement continues to improve. For figure 3, only 8 panels were used at each section to divide the wall from the free surface to the bottom and the tank was less than one wavelength wide. The required number of panels needed to represent the walls is important because for a given total number of panels, the more panels on the walls the less will be available to represent the free surface and the body.

The conservation of energy in the wave tank with a pneumatic wavemaker and a beach proportional to $\partial\phi/\partial n$ is shown in figure 4. The solid line represents the energy build up with respect to time as the waves are made. The pneumatic wavemaker is forced to oscillate through one cycle with a period of $t\sqrt{g/h} = \pi$. Thus, we see that the energy in the tank, E_T, builds up until $t\sqrt{g/h} = \pi$ and then remains constant until the waves start to be absorbed by the beach. E_A represents the energy absorbed by the beach and it starts to build up at approximately $t\sqrt{g/h} = 10$. The sum of $E_T + E_A$ is the energy in the tank plus that absorbed by the beach. As expected the total energy remains constant. At the end of the run some energy remains in the tank because of wave reflection from the beach. The energy in the tank will decrease further if the simulation is allowed to run longer, but it would take a long time for the reflected waves to travel down to the wall at the wavemaker end and return back to the beach. The ratio of the energy remaining in the tank to the total energy is a measure of the reflection from the beach. This particular beach has not been optimized and it appears to absorb about 90% of the energy. One of the problems of fully nonlinear calculations is to find a means of measuring the effectiveness of a beach. The usual reflection coefficient is only valid for linear waves. We have tried several different measures, but none have been very satisfactory.

Dommermuth et al. (1988) showed excellent agreement between their fully nonlinear mixed Euler-Lagrange computations and experimental results. The experiments and numerical calculations were for a piston-type wavemaker programmed to produce wave breaking at mid-tank. To allow comparisons, the Fourier amplitudes and phases of the time history of the wavemaker's velocity are given in their paper. Figure 5 compares the computed wave elevation at five different locations with those presented in Dommermuth et al. (1988, figure 2). To within the accuracy of the graphics, the agreement is excellent. For our computations, the wave tank was 20 units long and 1 unit deep. A absorbing beach is placed at the far end. 501 nodes were placed on the free surface with 26 nodes on the piston wavemaker and 26 nodes on the far wall. The bottom was accounted for by using image sources for each desingularized source. Material nodes were used and the time step size was $\Delta t\sqrt{g/h} = .05$. A fourth-order Runga-Kutta-Fehlberg time stepping scheme is used. The running time on a CRAY-YMP was 1.6 hours.
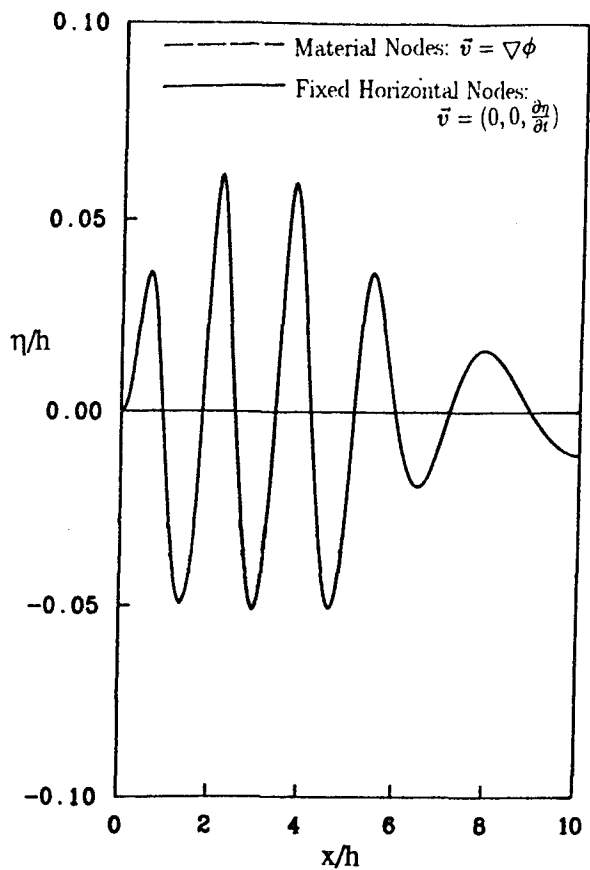
Figure 2: Comparison of fixed horizontal nodes versus material nodes.
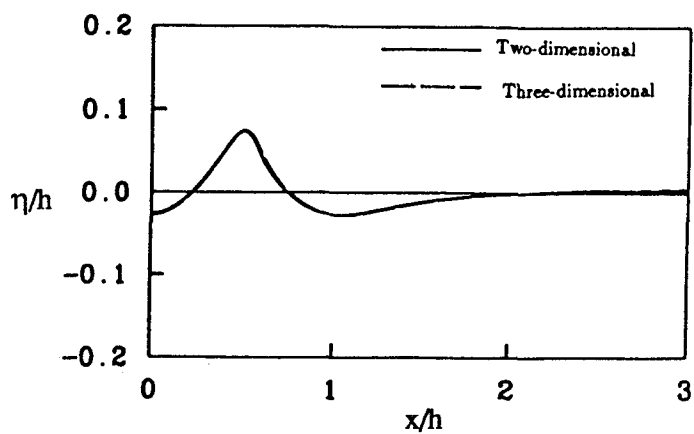
Figure 3: Comparison of two-dimensional versus three-dimensional computations
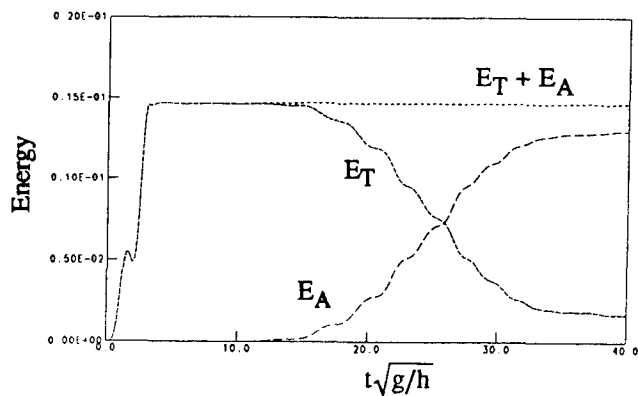
Figure 4: Energy in a wave tank as a function of time
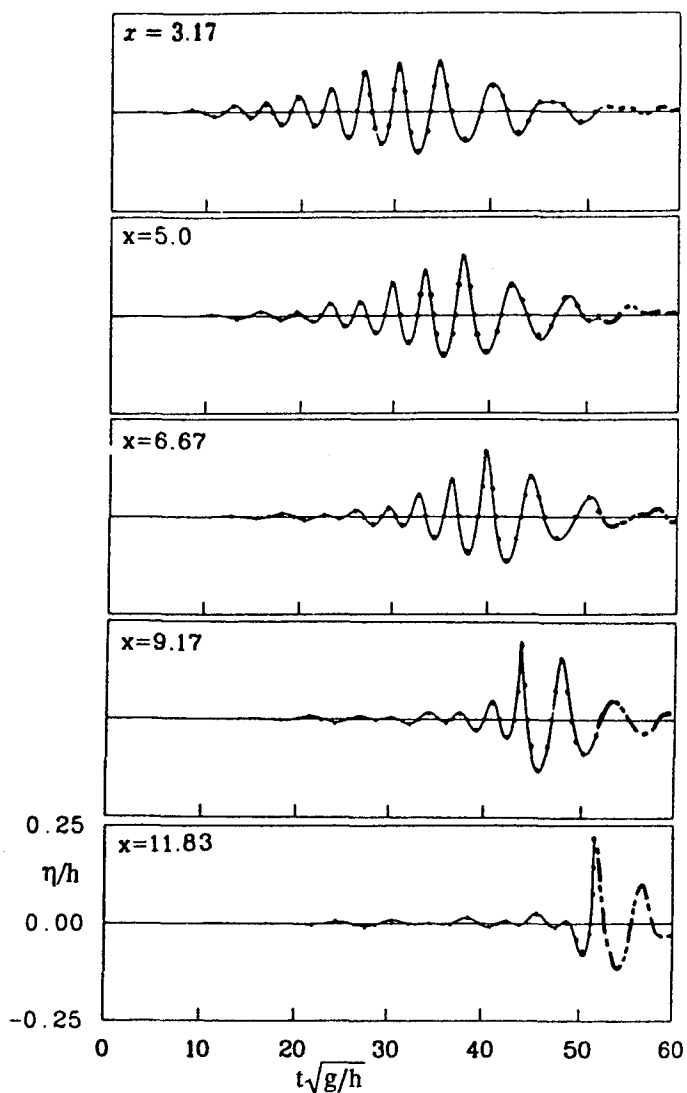
Figure 5: Free surface elevation at various distances from a piston-type wavemaker as a function of time.
Present calculations ———;
Dommermuth et al. (1988)
  experiments- - - ;
  calculations •

10

Heaving two-dimensional rectangle

Two-dimensional computations have been performed on a rectangle in heave and sway; details of the calculations may be found in Lee (1992). The convergence of the numerical results and agreement with experiments are similar for both heave and sway. Because of space limitations only a sampling of the heaving results will be presented here.

Three node spacings on the body have been tried. The first is simple equal spacing between the nodes. The second is a cosine spacing in which the nodes are more closely packed around the sharp corner and the free surface. The third is a semi-cosine spacing that retains the cosine spacing on the bottom but uses only half a cosine on the sides. This keeps the closely packed spacing around the corner but increases the panel size near the free surface. The semi-cosine spacing is useful because for stability reasons the panels on the free surface near the body need to be approximately the same size as the body panels near the waterline. Thus, larger free surface panels can be used for a given number of body panels. Consistent with the findings of Cao et al. (1992) for a Karman-Trefftz airfoil, no node is placed at the corner in any of the spacing schemes in order to avoid a spike in the tangential velocity. Calculations have shown little variation in the numerical results with node spacing schemes.

Figure 6 shows the typical wave profiles generated by a heaving rectangle in infinite water depth. The beam of the rectangle, B, is two and the draft, H, is one. The nondimensional heaving frequency is $\omega\sqrt{H/g} = \pi/3$ and the motion amplitude is 10% of the draft (a/H=.1). Semi-cosine spacing of is used on the body and approximately 30 material nodes per wavelength were used on the free surface. Rather than a beach in the far field, Lee (1992) used an algebraically increasing panel size starting at four wavelengths from the body. The increasing panels are carried out for 80 more wavelengths with the last panel being many wavelengths long. This far field panel arrangement introduces significant numerical damping and greatly delays the significantly attenuated reflected waves from entering the near field of interest. As can be seen in the figure, there is essentially no reflected waves at the edge of the inner region for the time interval shown.

Figure 7 shows the convergence of the numerical calculations to the experimental results of Vughts (1968). Vughts conducted experiments with an oscillating model and compared the results to linear theory calculations using both conformal mapping and Lewis forms. The fully nonlinear calculations converge to a value between Vugts'

experimental and numerical results for a nondimensional frequency of $\pi/3$.

The comparisons between Vughts' results for both the added mass and damping coefficients over the entire frequency range are shown in figures 8 and 9. There figures are for a nondimensional amplitude of .15, the largest amplitude tested. The results for smaller amplitudes are similar. Analogous to the experiments, our results show very little sensitivity to motion amplitude. The variation of the added mass and damping coefficients with amplitude fall approximately within the circles used to plot the fully nonlinear results in figures 8 and 9. As can be seen from the figures, the fully nonlinear computations agree well with the experiments and with linear theory.

Heaving axially-symmetric bodies

The flow due to a heaving three-dimensional cylinder has also been studied, the details may be found in Lee (1992). Axially-symmetric problems can be reduced to a one-dimensional integral equation by employing ring sources such as used by Dommermuth and Yue (1987). Because the desingularized technique is being developed for general body shapes, ring sources were not used in our calculations. Instead, the calculations were performed using multiple planes of symmetry. The first calculations were done using two planes of symmetry so that the unknown sources were distributed over one quarter of the domain. More computational efficiency is gained by increasing the number of planes of symmetry. Figure 10 shows the waves produced at different periods for a circular cylinder (R / H =1.0) in heave. Two sets of results are shown corresponding to using two planes of symmetry and 60 planes of symmetry. The actual panelization of the free surface is very different for the two cases since in the two-plane case the number of nodes is increased as the distance from the origin increases and in the other it is constant. In both cases the number of nodes on the cylinder and at the waterline on the free surface are the same. The results are so close that only one line is apparent in the figure for each period shown.

A more accurate measure of the difference between the predicted wave elevation is given in table I. Table I presents the RMS difference between the wave elevations produced by the two calculations for the different periods. The RMS difference is a measure of the difference in predicted wave profiles at a total of 120 fixed wave probes. The probes were uniformly distributed over the computational domain of interest. Cubic spline interpolation is used to determine the wave elevation at each probe from the values of the wave elevation at the computational

11
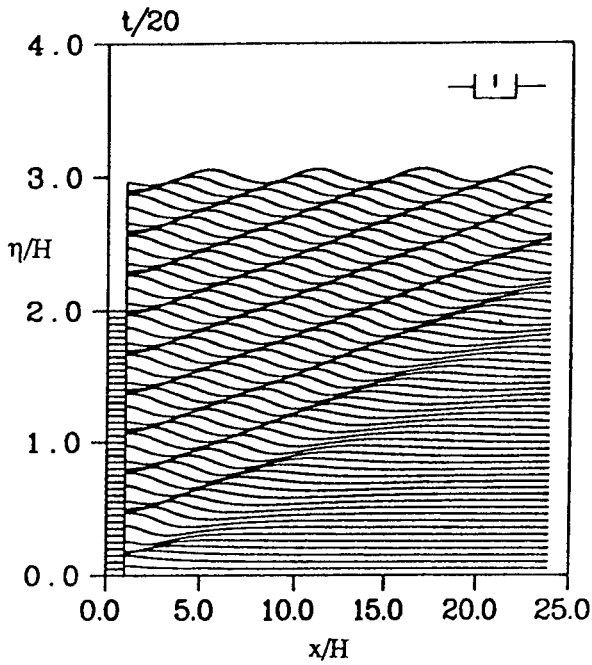
Figure 6: Time history of the free surface profile for a heaving two-dimensional rectangle in infinite water depth, B = 2.0, H = 1.0, a/H = .1, $\omega\sqrt{H/g} = \pi/3$

Figure 8: Added mass coefficient vs frequency for a heaving two-dimensional rectangle in infinite water depth, B = 2.0, H = 1.0, a/H = 0.15, panel size = $\lambda/30$

Figure 7: Added mass coefficient vs number of nodes on the inner domain of the free surface for a heaving two-dimensional rectangle in infinite water depth, B = 2.0, H = 1.0, a/H = .15, $\omega\sqrt{H/g} = \pi/3$
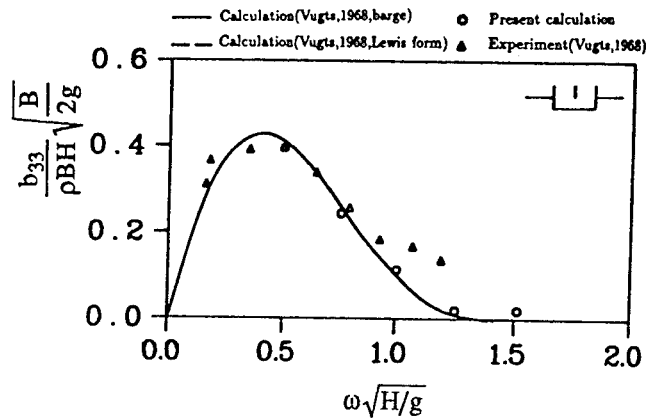
Figure 9: Wave demping coefficient vs frequency for a heaving two-dimensional rectangle in infinite water depth, B = 2.0, H = 1.0, a/H = 0.15, panel size = $\lambda/30$

nodes. The nondimensional RMS difference between wave profiles 1 and 2 is defined as:

$$RMS_{1,2}^2 = \frac{1}{a^2} \sum_{i=1}^{N_{rms}} \frac{(\eta_1(x_i) - \eta_2(x_i))^2}{N_{rms}} \qquad (31)$$

where

x_i = the location of the ith wave probe

N_{rms} = the number of wave probes

$\eta_1(x_i)$ = the wave elevation of the first profile at the ith wave probe

$\eta_2(x_i)$ = the wave elevation of the second profile at the ith wave probe

a = the motion amplitude

As can be seen from table 1, the RMS difference in wave elevation between using two planes of symmetry and multiple planes of symmetry is less than $5. \times 10^{-6}$.

We have also examined the effects of using equal, cosine, or semi-cosine node spacing schemes on the body. The cosine and semi-cosine schemes are the same as described for the two-dimensional rectangle. As expected the equal spacing was the worst. For 90 planes of symmetry and equal numbers of nodes on the body and free surface, the cosine and semi-cosine spacings gave no significant difference between the predicted wave elevations. As previously stated, the semi-cosine spacing leads to a better distribution of panels on the free surface and was therefore used in most of the calculations.

Dommermuth and Yue (1987) considered the case of a cylinder with proportions R/H=2. heaving in shallow water. The draft to water depth ratio, H/h, is .5. The oscillation amplitude, a/H, is .5 and the forcing frequency corresponds to a linear wavelength of 2R. Their calculations were made using ring sources in a Green's theorem formulation to solve the boundary value problem at each time step and material nodes to do the time stepping. Figures 11 and 12 compare our desingularized calculations with the curves presented by Dommermuth and Yue for the time history of the nondimensional heave force $(F_3/\rho g \pi R^2 a)$ and the wave elevation of the free surface at different periods.

The nonlinear forces computed by the desingularized method and Dommermuth and Yue

agree very well considering the two completely different numerical techniques used. As can be seen, the nonlinear forces are significantly different from the linear predictions during the up-stroke but are fairly close on the down-stroke.

Figure 12 shows the comparison of the predicted wave elevations at different periods of motion. Again, the agreement is very good. The desingularized method did not show the slight irregularity near the intersection line experienced by Dommermuth and Yue.

The ability of the desingularized method to handle more complex shapes is illustrated by the results shown in figures 13 and 14. These figures show the nondimensional force and heave displacement of a cylinder (R_{upper}=1.0, H_{upper}=1.0) with an attached larger bottom cylinder (R_{bottom}=1.5, H_{bottom}=.5). In figure 13 the motion amplitude is a/H_{upper}=.25 and in figure 14 it is .5. In both figures the water depth is infinite. In figure 13 the nonlinear effects including the mean shift of the force are small because the amplitude of motion is modest. In figure 14, the amplitude of motion has been doubled; the nonlinear effects are
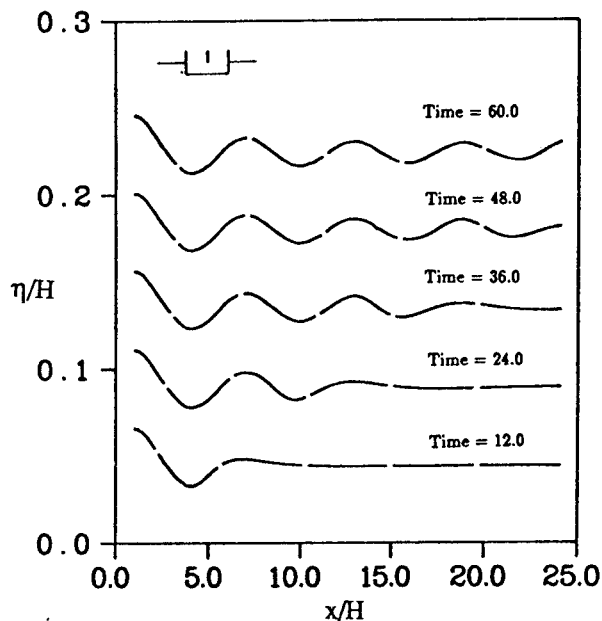
Figure 10: Comparison of the wave profiles using 2 and 60 planes of symmetry at the end of different periods for a heaving three-dimensional cylinder in infinite water depth, R = 1.0, H = 1.0, a/H = 0.1, $\omega\sqrt{H/g} = \pi/3$

13

Table 1: The RMS difference of the free surface elevation at the end of each period using 2 planes of symmetry and 60 planes of symmetry

Time	2T	3T	4T	5T	6T	7T	8T	9T	10T
RMS ($\times 10^6$)	3.93	4.15	4.32	4.73	4.58	4.61	4.70	4.67	4.69
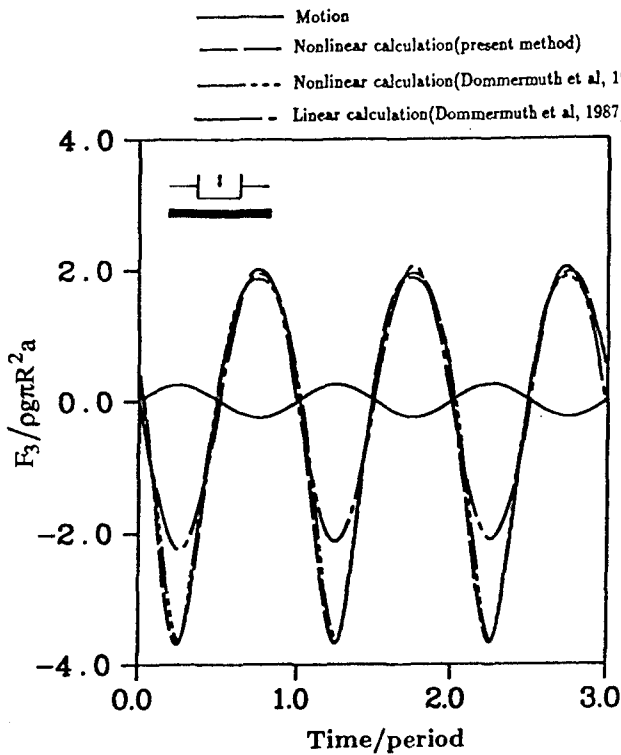
Figure 11: Time history of the vertical force for a heaving three-dimensional cylinder in finite water depth, h/H = 2.0, R = 1.0, H = 0.5, a/H = .5, symmetry plane number = 60

Figure 12: Comparison of instantaneous wave profiles for a heaving cylinder in finite water depth, h/H = 2.0, R = 1.0, H = .5, a/H = .5, symmetry plane number = 60

now obvious and the mean shift is substantial. At the peak of the force curve, the vertical force is well in phase with the motion because the bottom of the cylinder is deeply submerged under the free surface. The force is almost a pure added mass effect. As the cylinder moves upward, however, the bottom is closer to the free surface and a phase difference appears between the curve of the force and the motion as a result of the wave damping.

14
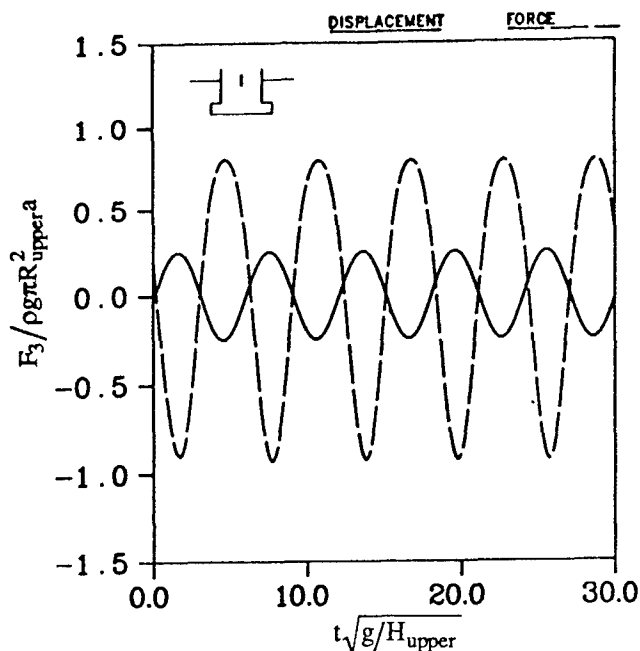
Figure 13: Time history of the heaving amplitude and vertical force on a double cylinder in infinite water depth, $R_{upper} = 1.0$, $H_{upper} = 1.0$, $R_{bottom} = 1.5$, $H_{bottom} = 0.5$, $a/H_{upper} = 0.25$
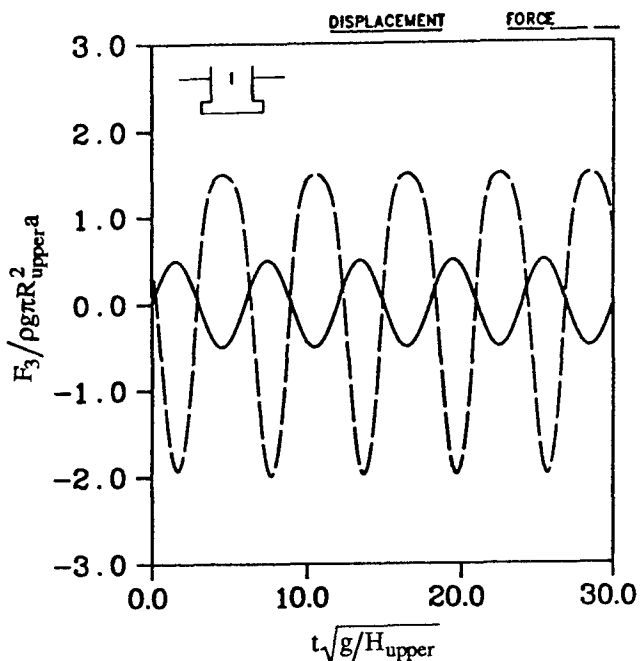
Figure 14: Time history of the heaving amplitude and vertical force on a double cylinder in infinite water depth, $R_{upper} = 1.0$, $H_{upper} = 1.0$, $R_{bottom} = 1.5$, $H_{bottom} = 0.5$, $a/H_{upper} = 0.50$

Wigley Hull Starting from Rest

Results for the free surface waves and wave resistance of a Wigley hull starting from rest have been computed using the desingularized approach. The results we are presenting must be considered as preliminary because all the convergence and other verification tests have not yet been completed. The Wigley hull is a mathematical form having a length-to-beam ratio of 10, a beam-to-draft ratio of 1.6 and the following equation for its hull surface:

$$y = \pm \frac{B}{2} \left(1 - \left(\frac{2x}{L} \right)^2 \right) \left(1 - \left(\frac{z}{H} \right)^2 \right) \quad (32)$$

where L = length
$B/2$ = half-beam
H = draft

The velocity of the model at any time is given by:

$$U_o(t) = U_o \left(1 - e^{-0.05t^2} \right) \quad (33)$$

The computations are made using moving nodes that travel with a velocity in the x-direction of $U_o(t)$. The velocity in the y-direction is set so that the nodes move along prescribed paths around the hull. The prescribed paths and node placement may be seen in figures 15 and 16. Having the nodes move along the prescribed paths eliminates the difficulty that must be overcome of material nodes crossing the hull surface between time steps. To avoid node pile up at the stagnation points, no nodes are distributed on the plane of symmetry. To allow unequal spacing in the x-direction, regridding is used after each time step. Regridding is also used on the body surface to reposition the nodes as the waterline moves vertically during the unsteady start-up phase. In the calculations to date, the model has been fixed in position. Since the program is in the time domain, allowing sinkage and trim is a simple addition but it has not yet been made.

On the upstream boundary it is assumed that both the potential and wave elevation are zero. The nodes are convected downstream so that no downstream boundary condition appears necessary. On the side boundaries no special conditions are imposed. This has been observed to lead to wave reflection at the side boundaries when the boundaries are too close to the vessel, but normally the reflected waves are outside the domain of interest.

Figures 15 and 16 present the wave elevation contours for a Froude number .25 at time step $t\sqrt{g/L} = 14$ for two different numbers of nodes.
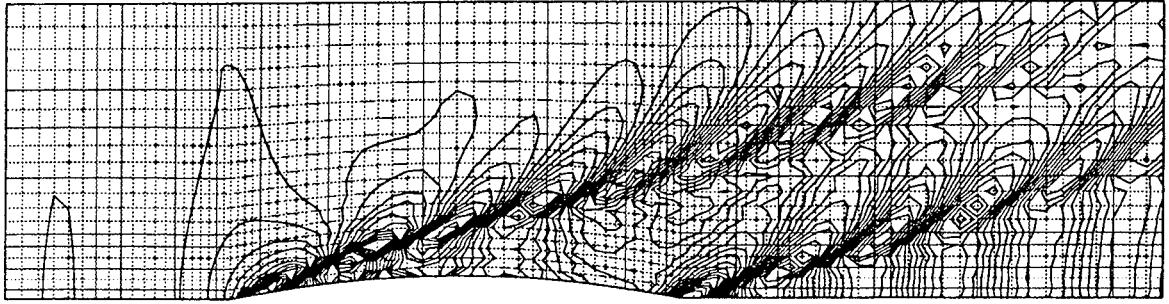
Figure 15: Wave contours for the Wigley Hull, Froude number = .25, coarse grid, $N_F = 1920$, $N_B = 369$, $t\sqrt{g/L} = 14$
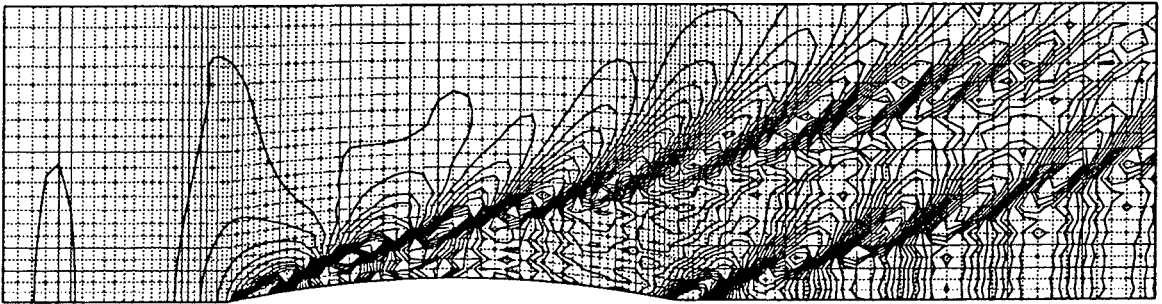
Figure 16: Wave contours for the Wigley Hull, Froude number = .25, fine grid, $N_F = 2478$, $N_B = 510$, $t\sqrt{g/L} = 14$
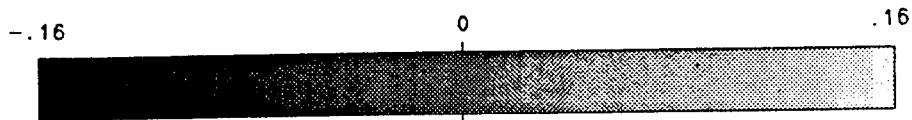
Figure 17: Shaded rendering of the waves generated by the Wigley Hull, Froude number = .25, fine grid, $t\sqrt{g/L} = 14$

The coarse spacing used in figure 15 has 1920 nodes on the free surface and 369 nodes on the body. The fine spacing used for figure 16 has 2478 nodes on the free surface and 510 nodes on the body surface. As can be seen, the finer grid spacing yields more detail around the hull but basically the waves are quite similar. Note that there does not appear to be any visible wave reflection from the side boundaries. A shaded rendering of the contour plot in figure 16 is shown in figure 17.

The development of the wave system along the plane of symmetry and around the hull is seen in figure 18 for the fine grid. An expanded scale of the wave profile along the hull for the last time step is given in figure 19. Also plotted in figure 19 is the wave profile along Wigley hull as experimentally measured by the University of Tokyo (see Noblesse and McCarthy 1983 or Noblesse et al. 1991). It should be noted that the experimental measurements show a great deal of variation depending on model size. While the waves shown in figure 18 have not completely reached steady state (in particular the transverse wave system behind the model), the wave profile long the hull appears close to steady. The comparisons with the experimental results in figure 19 indicate that the bow wave height is underpredicted and that there is higher frequency noise around midship. However, in general the comparison is good. We are presently investigating the reasons for the bow wave discrepancy and methods to eliminate the noise around midship. No smoothing or low pass filtering has been done on the data in figures 15-19.

The wave resistance acting on the hull is shown in figures 20 and 21 for the course and fine grid spacings respectively. The contributions of the five individual components identified from equation (23) are also plotted in the figures. The resistance force components are nondimensionalized as $F/\frac{1}{2}\rho U_o^2 S_o$ where U_o is the final velocity and S_o is the nominal wetted surface ($S_o = 0.1487L^2$) The first component and largest during the initial start-up, is due to the time derivative of the potential following each individual node. The second term is the linear pressure due to the forward speed. This is the usual linear pressure component in steady forward motion problems. It is large and positive and dominates at large times. The remaining components are all nonlinear. The third is the gravity term due to the change in the integration of ρgz over the wetted surface. This term is proportional to the wave elevation squared and is small and negative. The forth component is the velocity squared term which is also small and negative. The final component is the correction for the moving nodes. The node movement is due to the changing wave elevation along the hull and is

consequently small, eventually going to zero. The net result is that this component is very small. For unsteady ship motion problems it could conceivably become much larger.
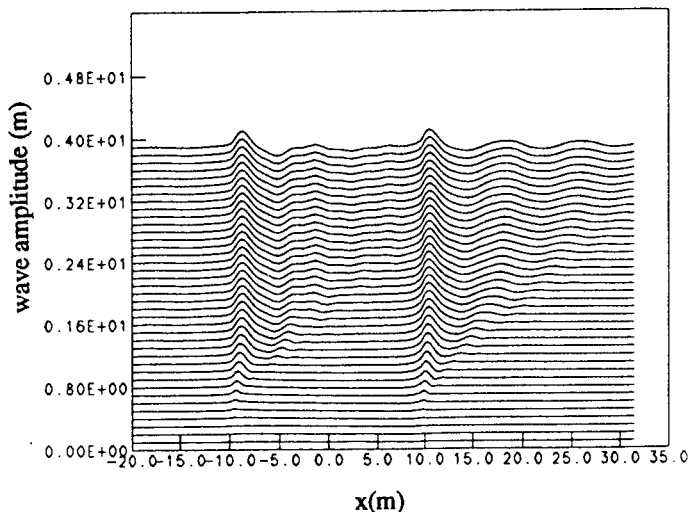
Figure 18: Development of wave system along Wigley Hull surface, Froude number = .25, fine grid
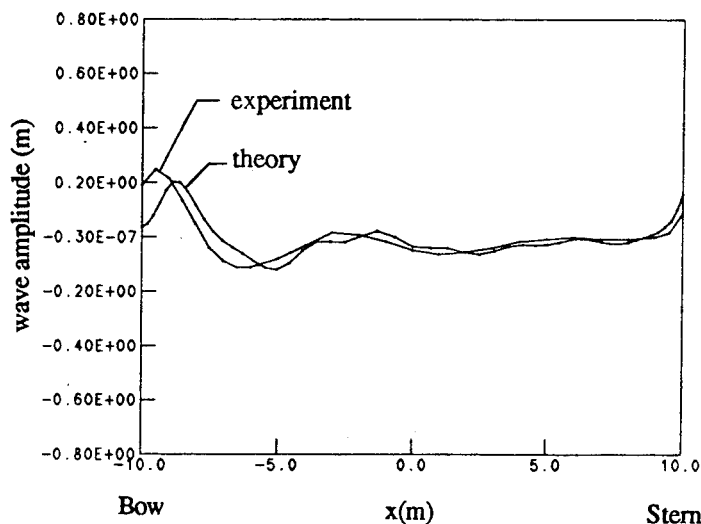
Figure 19: Wave amplitude along Wigley Hull, Froude number = .25, $t\sqrt{g/H} = 20$

17
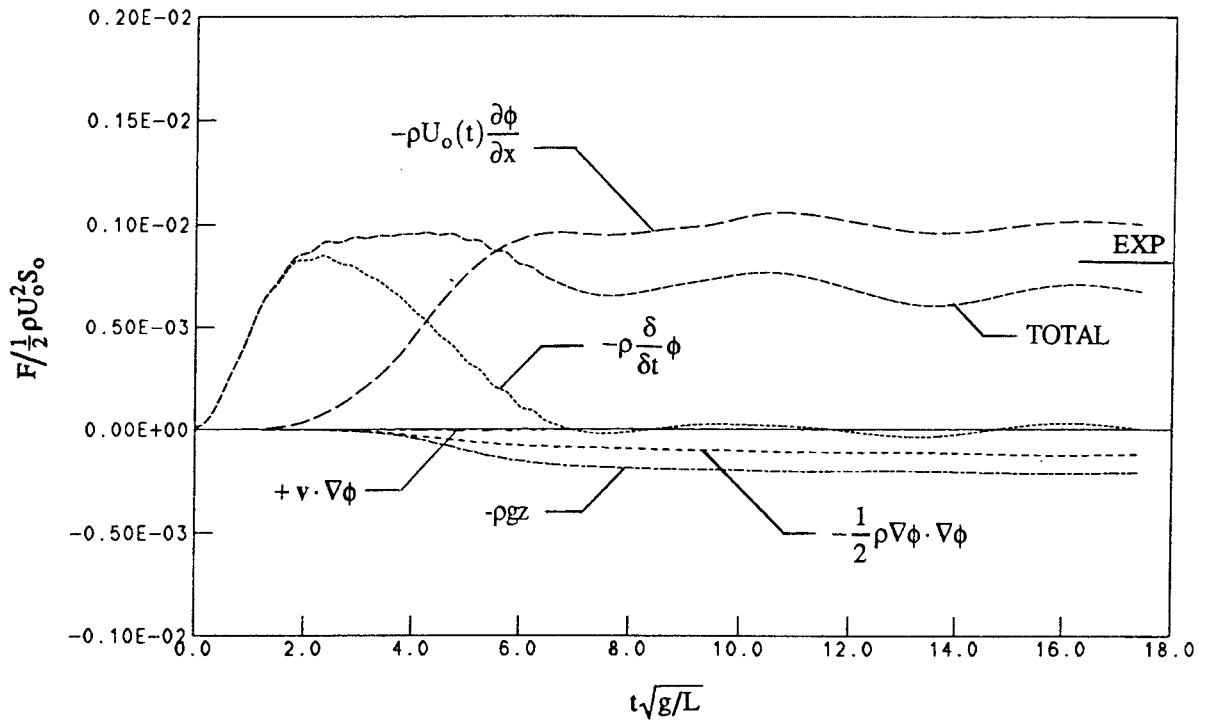
Figure 20: Wave resistance components for Wigley Hull, Froude number = .25, coarse grid
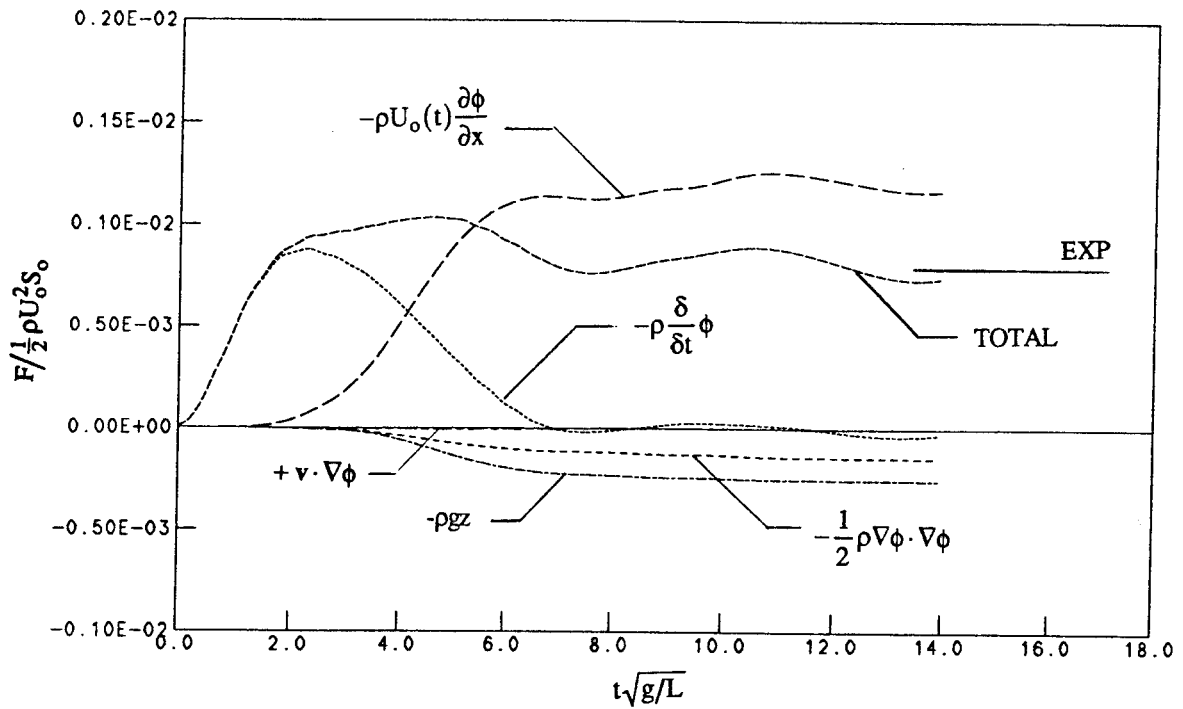
Figure 21: Wave resistance components for Wigley Hull, Froude number = .25, fine grid

The fine grid calculations shown in figure 21 have not been carried out further because of the unavailability of CRAY time. The horizontal line in both figures is the experimental wave resistance as measured by the University of Tokyo on the 2.5m model (cf. Noblesse and McCarthy 1983). Using different model scales or the wave pattern resistance would result in a slightly different experimental line. The oscillations in the total force curve are the $\tau=1/4$ oscillations that occur in the wave resistance when starting from rest and their decay rate is proportional to $1/t$.

The total wave resistance of the fine grid results (figure 21) is approaching the experimental value while the coarse grid is approximately 12 to 15% low. The reason the fine grid has higher wave resistance is due to a slightly higher bow wave and a small trough near the stern. Further computations are necessary to confirm the convergence.

Another difference between the coarse and fine grid results is the high frequency oscillations occurring in the coarse grid results during the nondimensional time range 3-4 and again in the range of 7-9. The oscillations seem to almost have disappeared in the fine grid calculations. Apparently, they are related to the lack of resolution in the coarse grid. The time step size was $\Delta t \sqrt{g/L} = .07$ for both calculations.

CONCLUSIONS

The desingularized method is a viable alternative for solving fully nonlinear water wave problems. The desingularization allows the use of simple isolated sources with little loss in accuracy. The resulting code is straight forward and easily vectorized. The use of generalized nodes on the free surface rather than always using material nodes can have computational advantages. For a given problem, it might be more beneficial to use material nodes, nodes fixed in a horizontal position relative to the body, or nodes following a prescribed path.

The method has been applied to a variety of problems in two and three dimensions. Comparisons with other numerical computations and with experimental results have shown very good to excellent agreement.

The results for the Wigley hull at a Froude number of .25 are promising but much more research needs to be done. Verificaton and convergence checks need to be completed and a complete range of Froude numbers investigated. The wave resitance is acccurately predicted when compared with experiments. The wave profile along the hull is generally well predicted, but the bow wave is slightly under predicted and there are small higher frequency waves near midship.

REFERENCES

Bai, K., J. Kim and H. Lee (1992), "A Localized Finite-Element Method for Nonlinear Free-Surface Wave Problems," *Proceedings* 19th Symposium on Naval Hydrodynamics, Seoul, Korea, pp. 90-114.

Baker, G.R., D.I. Meiron, and S.A. Orszag (1982), "Generalized Vortex Methods for Free-Surface Flow Problems," *J. Fluid Mech.*, 123, pp. 477-501.

Bertram, V. (1990), "Ship Motions by Rankine Source Method," *Ship Technology Research*, Vol. 37, No. 4, pp. 143-152.

Bertram, V., W.W. Schultz, Y. Cao, and R.F. Beck (1991), "Nonlinear Computations for Wave Drag, Lift and Moment of a Submerged Spheroid," *Ship Technology Research*, Vol. 38, No. 1, pp. 3-5.

Cao, Y., W.W. Schultz and R.F. Beck (1990), "Three-Dimensional, Unsteady Computations of Nonlinear Waves Caused by Underwater Disturbances," *Proceedings* 18th Symposium on Naval Hydrodynamics, Ann Arbor, Michigan, pp. 417-427.

Cao, Y. (1991), "Computations of Nonlinear Gravity Waves by a Desingularized Boundary Integral Method," Ph.D. Thesis, Technical Report No. 91-3, Department of Naval Architecture and Marine Engineering, The University of Michigan, Ann Arbor, Michigan, USA.

Cao, Y., W.W. Schultz and R.F. Beck (1991), "A Three-Dimensional Desingularized Boundary Integral Method for Potential Problems," *International Journal of Numerical Methods in Fluids*, Vol. 11, pp. 785-803.

Cao, Y., T. Lee and R.F. Beck (1992), "Computation of Nonlinear Waves Generated by Floating Bodies," 7th International Workshop on Water Waves and Floating Bodies, Val de Reuil, France, pp. 47-52.

Cao, Y., R.F. Beck and W.W. Schultz (1993a), "Numerical Computations of Two-Dimensional Solitary Waves Generated by Moving Disturbances," accepted for publication in the *International Journal for Numerical Methods in Fluids*.

Cao, Y., R.F. Beck and W.W. Schultz (1993b), "An Absorbing Beach for Numerical Simulations of Nonlinear Waves in a Wave Tank," 8th International Workshop on Water Waves and Floating Bodies, St. Johns, Newfoundland, Canada.

Cointe, R., P. Geyer, B. King, B. Motin, and M. Tramoni (1990), "Nonlinear and Linear Motions of a Rectangular Barge in a Perfect Fluid," *Proceedings* 18th Symposium on Naval Hydrodynamics, Ann Arbor, MI, pp. 85-99.

Dommermuth, D.G. and D.K.P. Yue (1987), "Numerical Simulations of Nonlinear Axisymmetric Flows With a Free Surface," *Journal of Fluid Mechanics*, Vol. 178, pp. 195-219.

Dommermuth, D.G., D.K.P, Yue, W.M. Lin, R.J. Rapp, E.S. Chan, and W.K. Melville, (1988), "Deep-Water Plunging Breakers: A Comparison Between Potential Theory and Experiments," *J. Fluid Mechanics*, Vol. 189, pp. 423-442.

Faltinsen, O.M. (1977), "Numerical Solution of Transient Nonlinear Free-Surface Motion Outside or Inside Moving Bodies, *Proceedings 2nd Conf. on Num. Ship. Hydro.*, U.C. Berkeley, (ed. J.V. Wehausen and N. Salvesen), pp. 347-357, University Extension Publications.

Grosenbaugh, M.A. and R.W. Yeung (1988), "Nonlinear Bow Flows - An Experimental and Theoretical Investigation," *Proceedings* 17th Symposium on Naval Hydrodynamics, The Hague, Netherlands, pp. 195-214.

Jensen, G., H. Söding and Z.-X. Mi (1986), "Rankine Source Methods for Numerical Solution of the Steady Wave Resistance Problem," *Proceedings* 16th Symposium on Naval Hydrodynamics, University of California, Berkeley, pp. 575-582.

Jensen, G., V. Bertram and H. Söding (1989), "Ship Wave-Resistance Computations," *Proceedings* 5th International Conference on Numerical Ship Hydrodynamics, Hiroshima, Japan, pp. 593-606.

Kang, C.-G. and I.Y. Gong (1990), "A Numerical Solution Method for Three-Dimensional Nonlinear Free Surface Problems," *Proceedings* 18th Symposium on Naval Hydrodynamics, Ann Arbor, Michigan, pp. 427-438

Kim, Y.-H. and T. Lucas (1990), "Nonlinear Ship Waves," *Proceedings* 18th Symposium on Naval Hydrodynamics, Ann Arbor, Michigan, pp. 439-452.

Kim, Y.-H. and T. Lucas (1992), "Nonlinear Effects on High Block Ship at Low and Moderate Speed, *Proceedings* 19th Symposium on Naval Hydrodynamics, Seoul, Korea, pp. 43-52.

Lee, T.-H (1992), "Nonlinear Radiation Problems for a Surface-Piercing Body," Ph.D. Thesis, Report No. 323, Department of Naval Architecture and Marine Engineering, University of Michigan, Ann Arbor, Michigan.

Lin, W.M., J.M. Newman and D.K. Yue (1984), "Nonlinear Forced Motions of Floating Bodies," *Proceedings* 15th Symposium on Naval Hydrodynamics, Hamburg, pp. 33-49, Washington: National Academy Press.

Longuet-Higgins, M.S. and E.D. Cokelet (1976), "The Deformation of Steep Surface Waves on Water: I. A Numerical Method of Computation," *Proc. R. Soc. Lond.*, A350, pp. 1-26.

Noblesse, F., and J.H. McCarthy (1983), editors, "Ship Wave-Resistance Computations," *Proceedings* of the Second DTNSRDC Workshop.

Noblesse, F., D.M. Hendrix and L. Kahn (1991), "Nonlinear Local Analysis of Steady Flow About a Ship," *Journal of Ship Research*, Vol. 35, No. 4, pp. 288-294.

Raven, H.C. (1992), "A Practical Nonlinear Method for Calculating Ship Wavemaking and Wave Resistance," *Proceedings* 19th Symposium on Naval Hydrodynamics, Seoul, Korea.

Saubestre, V. (1990), "Numerical Simulation of Transient Nonlinear Free-Surface Flows with Body Interaction," Technical Report 90-52, Department of Mechanical and Environmental Engineering, University of California, Santa Barbara.

Schultz, W.W. and S.W. Hong (1989), "Solution of Potential Problems Using an Overdetermined Complex Boundary Integral Method," *J. Comput. Phys.*, No. 84, pp. 414-440.

Vinje, T. and P. Brevig (1981), "Nonlinear Ship Motions," *Proceedings* 3rd International Symp. Num. Ship Hydro., Paris, pp. 257-268, Bassin d'Essais des Carenes, France.

Vughts, J.H. (1968), "The Hydrodynamic Coefficients for Swaying, Heaving and Rolling Cylinders in a Free Surface," International Shipbuilding Progress, Vol. 15, pp. 251-276.

Webster, W.C. (1975), "The Flow About Arbitrary, Three-Dimensional Smooth Bodies," *J. Ship Research*, No. 19, pp. 206-218.

Zhou, Z. and M. Gu (1990), "A Numerical Research of Nonlinear Body-Wave Interactions," *Proceedings* 18th Symposium on Naval Hydrodynamics, Ann Arbor, MI., pp. 103-118.

Rankine Source Method in High Speed Range

K. Kataoka, J. Ando, K. Nakatake, and K. Oda
(Kyushu University, Japan)

ABSTRACT

The conventional Rankine source method (Low Speed Approximation, LSA) uses the double body flow as the basic flow. We propose a new Rankine source method (High Speed Approximation, HSA) which uses the inverse image above the still water surface in the high speed range. In order to show the availability of HSA, computations for 2-D point doublet are carried out and then the numerical results are compared with the analytical ones. And we introduce a new panel method named SQCM (Source panel with Quasi-Continuous Vortex Lattice Method), which represents the flow around a wing.

Next, applying LSA and HSA together with SQCM to the flows around circular cylinder, 2-D, 3-D mono and tandem hydrofoils in a wide range of speeds, the wave profiles, lifts and wavemaking resistances are obtained and compared with the analytical solutions or the experimental results.

According to these results, we show that HSA is more easily applicable to the tandem hydrofoil system in the high speed range.

NOMENCLATURE

$\phi/\mathbf{q}$: velocity potential/vector around hydrofoil

$\phi_0/\mathbf{q}_0$: velocity potential/vector due to basic flow

$\phi_1/\mathbf{q}_1$: velocity potential/vector due to wave flow

$\phi_F/\mathbf{q}_F$: velocity potential/vector due to σ_F

$\phi_S/\mathbf{q}_S$: velocity potential/vector due to source m

$\phi_V/\mathbf{q}_V$: velocity potential/vector due to vortex γ

$\mathbf{q}_U$: velocity vector of uniform flow

C_p : pressure coef.

D : drag

D_1 : drag of fore/first foil

D_2 : drag of aft/second foil

F_n : Froude number $(= V/\sqrt{gc})$

L : lift

L_1 : lift of fore/first foil

L_2 : lift of aft/second foil

L_∞ : lift of mono foil in unbounded flow

R_w : wavemaking resistance

S_F : still water surface

S_c : surface of circular cylinder

S_w : hydrofoil surface

V : uniform flow velocity at infinity

c : hydrofoil chord length

f : submergence of leading edge(fore foil)

g : acceleration of gravity

k_0 : number of wave $(= g/V^2)$

m : source strength on body surface

n_x, n_y : x and y components of external unit normal vector

p : pressure in fluid

p_0 : pressure at upstream infinity

s : stagger (distance of leading edges)

s : hydrofoil span

x, y, z : rectangular coordinate

α : geometric angle of attack

γ : vortex strength

η : wave height

μ : strength of point doublet

ρ : fluid density

σ_F : source strength on still water surface

ϕ_c, ϕ_μ : velocity potential due to circular cylinder

ϕ_w : velocity potential due to hydrofoil

$\overline{\text{(overline)}}$: basic flow effect component

Δ : free surface effect component

suffix j : value for j-th hydrofoil

INTRODUCTION

Rankine source method presented by Dawson [1] has been applied widely as a practical method for calculating wave resistance and many improvements have been made. Most of Rankine source method uses double model flow as the basic flow in the limiting case of zero Froude number (Low Speed Approximation, LSA). It is considered that LSA is successful in case of ship wave calculation because Froude number based on the ship length in general is relatively small. However, when we try to solve the wave resistance problem in the high speed range by Rankine source method, it is doubtful whether we can use LSA to represent the basic flow in the same way as the low speed range [2] or not.

By the way, it is well known that the research and development of high speed marine vehicles have been performed all over the world. Among them, we can find many crafts which have hydrofoils to lift up the hulls [3]. A review of hydrofoils and hydrofoil craft was given by Acosta [4]. In recent studies of the hydrofoil problems, Lee et al. [5] treated the 2-D cavitating hydrofoil advancing under the free surface. Bai et al.[6] presented a localized finite-element method for nonlinear 3-D free surface ploblems.

It is clear that the free surface effect on the lift and drag of hydrofoil is not negligible. In case of hydrofoil, Froude number based on the chord length is much higher than Froude number of ship. So, if we use the conventional Rankine Source method for the free surface problem in high speed range, a question will arise whether we can use LSA or not. To clear this question, we present a new Rankine source method which uses inverse image above the still water surface to represent the basic flow (High Speed Approximation, HSA). At first, we discuss the free surface problem of 2-D point doublet in high speed range. Next, we show the calculated results of 2-D hydrofoil. And we describe a new panel method named SQCM, which represents the flow around a wing.

Hydrofoil craft has usually tandem foil system, that is, one foil is located at the front and the other is at the rear. The lift and drag of the tandem foil system advancing under the free surface may be affected by the advancing speed, the depth of immersion, the vertical and horizontal distance between two foils and so on. However, we can not find the papers which show the effects of these parameters on the performance of the tandem foil system. In this paper, we show the calculated results of the lift and drag of 2-D and 3-D tandem foil system by using of a numerical method which combines SQCM and the new Rankine source method. In addition, we compare these results with the experimental ones of 3-D tandem foil system, which was performed at Kyushu University.

FORMULATION OF TWO KINDS OF RANKINE SOURCE METHODS

2-D circular cylinder

At first, we derive the formulation of HSA and LSA for a circular cylinder located under the still water surface, and then we give some additional explanations to the case of a 2-D point doublet.

We take the x-axis in the direction of uniform flow with speed V and the y-axis in the vertically upward direction as shown in Fig. 1.

Let us consider a circular cylinder of diameter $D(= 2a)$ located at $y = -f$ in a uniform flow (see Fig. 1). Here we distribute the source m on the surface of the circular cylinder S_c and the source σ_F on the still water surface S_F. Then the velocity potential to express the flow field around the circular cylinder ϕ is given as

$$\phi = \phi_0 + \phi_1. \tag{1}$$

In Eq.(1), ϕ_0 and ϕ_1 are the velocity potentials to express the basic flow and the effect of the free surface disturbance, respectively, and are given as

$$\phi_0 = Vx + \overline{\phi}_c, \quad \phi_1 = \Delta\phi_c + \phi_F. \tag{2}$$

In Eq.(2), $\overline{\phi}_c$ and $\Delta\phi_c$ are the disturbed velocity potentials to express the basic disturbance due to the double model or the inverse image and the effect of the free surface on the cylinder, respectively. Denoting the combined disturbed velocity potential due to $\overline{\phi}_c$ and $\Delta\phi_c$ by ϕ_c, ϕ_c is represented by the following equation

$$\begin{aligned}\phi_c &= \overline{\phi}_c + \Delta\phi_c \\ &= \int_{S_c} m(x', y') \left\{ \log\sqrt{(x-x')^2 + (y-y')^2} \right. \\ &\quad \left. \pm \log\sqrt{(x-x')^2 + (y+y')^2} \right\} dS_c. \end{aligned} \tag{3}$$

In the above equation, the sign $+$ means the double model and the sign $-$ does the inverse image. The source strength m is divided into $\overline{m}$ used for the basic flow and Δm used for the free surface effect as

$$m = \overline{m} + \Delta m. \qquad (4)$$

In Eq. (2), the disturbed velocity potential due to the free surface wave ϕ_F is represented by

$$\phi_F = \int_{S_F} \sigma_F(x') \log \sqrt{(x-x')^2 + y^2} dS_F \qquad (5)$$

As described above, we obtained two kinds of velocity potentials for the flow field around the circular cylinder. Considering the facts that $\phi_{0y} = 0$ at $y = 0$ in case of the double model flow and $\phi_{0x} = 0$ at $y = 0$ in case of the inverse image flow, the linearized free surface condition is expressed as

$$\phi_{1xx} + k_0 \phi_{1y} = -(\phi_{0xx} + k_0 \phi_{0y}) \qquad (6)$$

where $k_0 = g/V^2$ and g is the gravitational acceleration. Then the velocity potential ϕ must satisfy the boundary condition on the surface of the circular cylinder as

$$\frac{\partial \phi}{\partial n} = 0 \qquad (7)$$

Solving Eqs.(6) and (7) simultaneously, we can obtain m on the cylinder surface and σ_F on the still water surface. As to the radiation condition, we satisfy it by Kyushu University method [7] which shifts downwards the source loading mesh from the control point mesh by one mesh length.

Using the obtained m and σ_F, we calculate the wave height η and the wavemaking resistance R_w by the following equations,

$$\eta = -\frac{V}{g}(\phi_{0x} + \phi_{1x})_{y=0} \qquad (8)$$

$$R_w = \int_{S_c} (p - p_0) n_x dS_c , \qquad (9)$$

where $\qquad p - p_0 = \frac{1}{2}\rho(V^2 - \phi_x^2 - \phi_y^2)$

Next, we give some additional explanations to the case of a point doublet to express the circular cylinder. Denoting the strength of a point doublet with the axis in the $-x$ direction, the disturbed velocity potential $\overline{\phi}_\mu$ is expressed as

$$\overline{\phi}_\mu = \mu \left\{ \frac{x}{x^2 + (y+f)^2} \pm \frac{x}{x^2 + (y-f)^2} \right\} , \qquad (10)$$

where $\qquad \mu = Va^2$

In this case, ϕ_0 and ϕ_1 become

$$\phi_0 = Vx + \overline{\phi}_\mu , \quad \phi_1 = \phi_F \qquad (11)$$

In this formulation, only σ_F is unknown and is obtained by solving Eq.(6) making use of Kyushu University method. Then the wave profile is calculated by Eq.(8) and the wavemaking resistance R_w is obtained by Lagally's theorem, i.e.

$$R_w = 2\pi\rho\mu(\phi_{xx})_{x=0,y=-f} \qquad (12)$$

The analytical wave height and wavemaking resistance are given by Havelock [8] as,

$$\eta = \frac{2a^2 f}{x^2 + f^2} + 2a^2 k_0 P \qquad (x < 0)$$
$$\eta = \frac{2a^2 f}{x^2 + f^2} + 2a^2 k_0 P$$
$$\quad - 4\pi k_0 a^2 e^{-k_0 f} \sin k_0 x \quad (x > 0) \qquad (13)$$

where

$$P = \text{Real Part of} \int_0^\infty \frac{e^{-(|x|+if)m}}{m + ik_0} dm$$

$$R_w = 4\pi^2 g\rho a^4 k_0^2 e^{-2k_0 f} \qquad (14)$$

Hydrofoils

Here, we derive the formulation of HSA and LSA for the three cases, i.e. 2-D mono hydrofoil, 2-D and 3-D tandem hydrofoil-system problems, together. We call the fore foil the first one ($j = 1$) and do the aft foil the second one ($j = 2$) in tandem systems. But when the mono foil problem is considered, we use only the first/fore foil neglecting the terms of the second/aft one.

Let us consider a hydrofoil-system whose chord length is c and the leading edge of the first foil is located at $y = -f$ in the inviscid incompressible and irrotational uniform flow (see Fig. 2). In our usual calculation method [9] for the 3-D wing section, we used the source distributing panels on wing surface and the vortex surface on which vortices distribute constantly in the chordwise direction. In the 3-D problem, we must solve the nonlinear simultaneous equations derived from the Kutta's condition. In order to avoid this numerical difficulty, we use source distributions m_1, m_2 on the surface panels of both foils S_{w1}, S_{w2} together with the vortices γ_1, γ_2 distributing discretely on the camber surfaces C according to the Lan's QCM [10] which expresses thin wing approximately. Then the number of the equations is increased but we can solve linear simultaneous equations at a time and reduce the computational time. We call this new QCM combined with the source panels SQCM (Source panels with QCM) briefly [11].

23

In the 3-D problem, free vortices flow along the camber surface and to the rear infinity parallel to the nose-tail line through the trailing edges. In addition to the sources $m(m_1, m_2)$ on the hydrofoil surfaces and vortices $\gamma(\gamma_1, \gamma_2)$ on the camber, the source σ_F is distributed on the still water surface S_F, which expresses wave flow. These singularities induce the velocity vectors $\mathbf{q}_S$, $\mathbf{q}_V$ and $\mathbf{q}_F$ (cf. Appendix).

The source and vortex strength m, γ are divided into $\overline{m}$, $\overline{\gamma}$ used for the basic flow and Δm, $\Delta\gamma$ used for the free surface effect as

$$\begin{aligned} m_j &= \overline{m}_j + \Delta m_j \\ \gamma_j &= \overline{\gamma}_j + \Delta\gamma_j \quad (j = 1, 2) \end{aligned} \tag{15}$$

Then the velocity vector $\mathbf{q}$ around hydrofoil-system can be also expressed by the sum of the basic flow velocity vector $\mathbf{q}_0$ and the wave flow velocity vector $\mathbf{q}_1$ as

$$\mathbf{q} = \mathbf{q}_0 + \mathbf{q}_1, \tag{16}$$

where $\mathbf{q}_0$ is expressed by HSA in case of high speed and by LSA in case of low speed. Here $\mathbf{q}_0$ and $\mathbf{q}_1$ are shown as follows [2].

$$\begin{aligned} \mathbf{q}_0 &= \mathbf{q}_U + \sum_{j=1,2}(\overline{\mathbf{q}}_{Sj} + \overline{\mathbf{q}}_{Vj}) \\ \mathbf{q}_1 &= \mathbf{q}_F + \sum_{j=1,2}(\Delta\mathbf{q}_{Sj} + \Delta\mathbf{q}_{Vj}) \end{aligned} \tag{17}$$

where $\mathbf{q}_U$ is velocity vector of the uniform flow and $\overline{\mathbf{q}}_{Sj}$, $\overline{\mathbf{q}}_{Vj}$ are the disturbed velocity vectors to express the basic flow, i.e. the double model or the inverse image and $\Delta\mathbf{q}_{Sj}$, $\Delta\mathbf{q}_{Vj}$ are the effects of the free surface on the flow field around each foil surface, respectively.

To express $\mathbf{q}_V$ by N vortex lattices, the loading point x_k and the control point x_i are selected as follows according to QCM.

$$\begin{aligned} &\text{(loading points)} \\ &x_k = \frac{1}{2}\left(1 - \cos\frac{2k-1}{2N}\pi\right) \quad k = 1, 2, \dots, N \\ &\text{(control points)} \\ &x_i = \frac{1}{2}\left(1 - \cos\frac{i\pi}{N}\right) \qquad i = 1, 2, \dots, N \end{aligned} \tag{18}$$

where chord length equals 1.

We can obtain vortices $\overline{\gamma}_1, \overline{\gamma}_2$ and sources $\overline{m}_1, \overline{m}_2$ simultaneously solving the boundary conditions, that is, there does not exist normal component of the velocity vector both at the camber surface elements and on the hydrofoil surfaces. At this time, the Kutta's condition is satisfied sufficiently according to QCM of itself.

Making use of HSA (inverse image) or LSA (normal image), the linearized free surface condition (A-15) is solved and σ_F is obtained. And then γ_1, γ_2 and m_1, m_2 influenced by σ_F are calculated and σ_F is obtained by solving the linearized free surface condition again. These procedures are repeated three or four times.

Wave profiles which hydrofoil system makes are calculated using these singularities $\gamma_1, \gamma_2, m_1, m_2$ and σ_F by Eq.(A-16), which satisfies the linearized free surface condition (A-15) and the radiation condition. As to the radiation condition, we satisfy it by Kyushu University method [7] as well as the circular cylinder problems.

Lift and drag are obtained by summing up of horizontal and vertical components of the pressure around hydrofoil surfaces. They are expressed for $j = 1, 2$ as follows

$$\begin{aligned} L_j &= \frac{1}{2}\rho\int_{S_{wj}}(V^2 - \mathbf{q}^2)n_y\, dS_{wj} \\ D_j &= \frac{1}{2}\rho\int_{S_{wj}}(V^2 - \mathbf{q}^2)n_x\, dS_{wj}, \end{aligned} \tag{19}$$

where n_x, n_y show the x, y components of the external unit normal vectors on the foil surface, respectively. Then lift L and wavemaking drag D of the tandem hydrofoil system are

$$L = L_1 + L_2 \quad , \qquad D = D_1 + D_2. \tag{20}$$

RESULTS AND DISCUSSION

Results of 2-D circular cylinders

We consider the wavemaking problem due to a circular cylinder ($D = 1.0$m) located at a depth ($f = 1.0$m).

Point Doublet

At first, we show some results of the case to use a point doublet for the circular cylinder. Calculation region on the still water surface and the panel size are almost $-15.0 \leq x \leq 15.0$ and 0.20m, respectively, though they change a little with Froude number $F_n(= V/\sqrt{gD})$.

Figs. 3(a), (b) show comparisons of source distributions on still water surface due to the circular cylinder obtained by LSA and HSA at $F_n = 0.85, 10.0$. At $F_n = 0.85$, both numerical results by LSA and HSA are very similar to each other except right above the cylinder, however, at $F_n = 10.0$ results of LSA are quite different from ones of HSA.

Figs. 4(a), (b) show comparisons of wave profiles obtained by LSA, HSA and analytical

24

method at $F_n = 0.85, 10.0$. At $F_n = 0.85$, both numerical results by LSA and HSA agree well with the analytical ones, however, at $F_n = 10.0$ LSA gives quite different wave profile from results of HSA and analytical method. In Fig. 5, the wavemaking resistance coefficient $C_w (= 2R_w/\rho V^2 D)$ of a point doublet is shown in the speed range $F_n = 0.2 \sim 10.0$. Though the wave profiles differ in case of LSA at high speed, we can not recognize the difference of C_w in the wide range of Froude number. We think that HSA gives more correct wave profiles at high speed than LSA compared with the analytical method.

Surface Source Distribution

Next, we show some results of the case to use the surface source distribution for the circular cylinder. We divide the cylinder surface into 90 segments and do the still water surface as stated before. Figs. 6(a), (b) show comparisons of wave profiles obtained by LSA and HSA compared with the analytical method. At $F_n = 0.85$ and 10.0, the wave profiles show nearly the same tendencies as Figs. 4(a), (b). Little difference may be due to the consideration of the boundary condition on the circular cylinder. In Fig. 7, C_w of the circular cylinder is shown. At $F_n \approx 1.0$, numerical results differ from the analytical ones, however, the values themselves do not differ so much. These tendencies are also same as the case of a point doublet. In order to confirm these behavior, we calculate the pressure coefficient $C_p (= 2(p - p_0)/\rho V^2)$ and show them in Figs. 8(a), (b), (c) which indicate C_p around the circular cylinder at $F_n = 0.20$, 0.85, 10.0. We know that the pressure distributions becomes similar after satisfying the boundary conditions correctly even if the basic flows are different.

Results of Hydrofoils

In order to confirm the program codes, using a 2-D wing NACA0012 in the unbounded flow, we calculate the pressure coefficient over the wing surface and compare the results by SQCM with one of the panel method in Fig.9. We divide the wing surface into 50 segments and the camber surface into 25 segments in the case of SQCM. The pressure distributions agree very well with each other and we confirm the availability of SQCM.

2-D Mono Hydrofoil

In the following calculations, NACA0005 symmetric wing section is used and chord length

$c = 1m$ and angle of attack $\alpha = 5°$. We divide the hydrofoil surface into 90 segments around the wing section and the camber line into 45 segments and the division of the still water surface is similar to the case of circular cylinder.

Fig.10 shows wave profiles η varying with $F_n (= V/\sqrt{gc})$. At $F_n = 1.0$ there is little difference between LSA and HSA, but above $F_n = 3.0$ wave profiles by LSA show the depression above the foil and entire profiles are risen up unnaturally. On the other hand, HSA shows calm variation and seems to converge to a natural profile. This profile is very similar to the result of the experimental investigation [12]. In the case $F_n = 10.0$, it is also shown the wave profiles in the high speed limit which is derived from Eq.(A-18) when the upstream end $\eta = 0$. It looks like the result of HSA.

In Figs.11(a)~(c) lift L and drag D are shown for various F_n, as the ratios of them to the lift in unbounded flow (L/L_∞, D/L_∞). Additionally, the analytical solutions are shown for the lift and wavemaking resistance of 2-D flat plate obtained by Nishiyama [13]. Fig.11(a) shows the results in case of the depth $f/c = 0.956$. It is seen that the values obtained by LSA are going to converge to each constant value, but both lift and drag by HSA are converging to the analytical solutions in high speed range ($F_n > 5.0$). However, the results by both LSA and HSA are different from the analytical solution in relatively low speed range. This means that the effect of the free surface is large at the depth of the chord length level and the effect of the wing thickness 5% is clear, which is the difference between wing section and the flat plate. Then in the deeper cases, $f/c = 1.956$ and 3.956 as Figs.11(b) and (c), the difference becomes small and they agree to the analytical solutions.

Figs.12(a)~(c) show in case of $f/c = 0.956$ the pressure coefficients around the hydrofoil surface, comparing the results of LSA and HSA as well as the case of the circular cylinder (Figs. 8(a)~(c)). These broken and full lines mean the pressure distributions in the basic flow field and the wave flow field, respectively. It is not similar to the case of the circular cylinder. There exists remarkable difference in the wave flow between LSA and HSA and this can explain the difference of the lifts and drags in Fig.11(a). Especially in LSA, it does not change the pressure distribution around the hydrofoil surface in the high speed range ($F_n > 4.0$).

25

2-D Tandem Hydrofoil-System

In the following calculations, the wing parameters are the same for the fore and aft foils, that is, NACA0012 symmetric wing sections is used, chord length $c = 1m$ and angle of attack $\alpha = 5°$. We divide the hydrofoil surface into 90 segments around the wing section and do the camber line into 45 segments and the division of the still water surface is similar to the case of the mono hydrofoil.

First we show the source distribution σ_F on the still water surface comparing HSA with LSA at the low speed ($F_n = 0.88$), and at the high speed ($F_n = 5.0$) in Figs.13(a),(b), where the two arrows mean the horizontal positions of the fore and aft foils. In this case $s/c = 10.0$ and it is same in the following figures.

There is little difference of σ_F between HSA (thick line) and LSA (thin line) at the low speed ($F_n = 0.88$), but at the high speed ($F_n = 5.0$) there is a big difference. These σ_F create the wave profiles as Figs.14(a),(b). HSA and LSA make similar wave profiles to each other at the low speed ($F_n = 0.88$), but very different at the high speed ($F_n = 5.0$). It is seen that the wave profile by HSA rises up and the one by LSA shows the unnatural depressions just above each hydrofoil in the high speed range.

Figs.15(a),(b) show the lift and drag interference factors for the fore, the aft and combined system according to the distance between two foils. Here we define the interference factor as the ratio of forces to the value of mono foil in the unbounded flow. From Fig.15(a), in case of high speed ($F_n = 5.0$) and the stagger ($s/c > 5.0$) it is seen that both lift L and drag D of tandem-system are almost invariant to the stagger s. But, these factors decrease due to the effect of the free surface in case of s/c less than 5.0. In Fig.15(b) we show the lift and drag interference factors for the fore, the aft and combined system in case of the low speed ($F_n = 0.88$). Lift and drag of the aft foil are affected very much by the wave which is created by the fore foil, but those changes of the fore foil are not affected in case of s/c above 3.0. Then wave profile at the high speed ($F_n = 5.0$) varies as Fig.16 and there is a convex part of the free surface above the aft foil. In Fig.16(b) we show the wave profiles in the low speed ($F_n = 0.88$). Here these values of s/c are chosen so that they are corresponding to the maximal or minimal position of lift and drag in Fig.15(b). It is seen that the amplitudes of wave profiles in the downstream are correspond-

ing to the maximal or minimal position of drag, and this tendency agrees well to the linear analytical solution of hydrofoil problem in stationary wave [14], in which the phase of wave is discussed corresponding to change of lift and drag. However, in case of lift, the position of lift maximal is different from the analytical solution. Though there is a possibility that the aft foil may vary the wave profile near itself, we do not know the true reason.

Figs.17(a)~(b) show the lift and drag interference factors for the fore and aft foils comparing the results of HSA and LSA against F_n. In case of the fore foil those are similar to the results of mono hydrofoil in Fig.11 and minus value of drag is shown in the high speed range. In case of the aft foil, it is seen that the wave effect is large, which is created by the fore foil. Here minus value of drag is also shown in low speed range, but in the tandem-system total drag never become minus value. We notice that the lift and the drag by LSA have a tendency to converge to each constant value and on the contrary by HSA, lift approaches the value in the unbounded flow and drag does zero in high speed range ($F_n > 5.0$). In Fig.18 wave profiles are shown in the relatively high speed range ($F_n > 1.0$) and it is seen that strange depressions above each hydrofoil by LSA in the high speed range ($F_n > 3.0$). On the other hand, wave height by HSA is different but it is a common phenomenon that long, convex and smooth wave profiles are created in the high speed range. Then it can be understood that from these variations of wave profiles in the high speed range lifts and drags are not affected very much by the position of the aft foil as Fig.15(a).

3-D Tandem Hydrofoil-System

In order to confirm SQCM in 3-D problem, we compare the numerical result with experiment [15]. Fig.19 shows the pressure distributions on the mono hydrofoil surface along the midspan chord in the 3-D unbounded flow. We divide the hydrofoil surface into 50×7 segments around the wing section and along the half-span and do the camber surface into 25×7 segments along the chord and the half-span. Since the foil is symmetric to the midspan, we calculate the one side using the image. The smooth pressure distribution on the 3-D hydrofoil is obtained and the tendency agrees well with an experiment. Especially around the trailing edge it is seen that the Kutta's condition is satisfied well by SQCM.

In the following calculations and exper-

iments, both the fore and aft foils have the same principal dimensions, that is, they have NACA0012 symmetric wing sections, chord length $c(= 0.06m)$, span length $s(= 0.3m)$ and angle of attack $\alpha(= 5°)$.

Fig.20 shows the pressure distributions around the tandem hydrofoil surfaces in unbounded flow. The distance between the trailing edge of the fore foil and the leading edge of the aft foil equals one chord length, that is $s/c = 2.0$. Mesh sizes around the hydrofoil surfaces and on the camber surface are same as Fig.19. It is seen that the pressure distributions of both foils are smooth and the Kutta's condition is satisfied enough.

Fig.21 shows the lift coef. C_L and the drag coef. C_D for various stagger s/c and shows the interference between the fore and aft foils. When s/c is small, the ratios of interference are large, and drags of each foil are changed according to s/c but average drag for tandem system is almost constant. This phenomenon is known as the Munk's theorem [16].

Using HSA and LSA, we obtain the wave profiles and the pattern contours per 1.0mm for mono hydrofoil whose depth is just chord length ($f/c = 1.0$). Typical examples are shown in Figs.22(a)~(b), and the relation between wave profiles and wave patterns is one of the elevation and the plane figure. We divide still water surface area ($-6.0 \leq x/c \leq 10.0$ and $0 \leq z/(s/2) \leq 2.72$) into 30×10 segments (coarse or single mesh). The mesh division and hydrofoil plane are also projected in the figure where thick line means still water level, and full and broken lines do crest and trough side, respectively. There is no extreme difference between LSA and HSA in the case of relatively low speed ($F_n = 0.8$). But when $F_n = 4.0$, it is seen that smooth wave profiles are obtained by HSA and sharp trench appears right above the hydrofoil by LSA as well as the 2-D problems. Then in order to confirm the effect of the division of still water surfaces we carry out the calculation on the same condition as Fig.22(b) using 60×20 double segments (fine or double mesh) and show the results in Fig.23. When $F_n = 4.0$ in case of high speed, there are little differences in the results of HSA using the coarse mesh. On the contrary, it is shown the depression is reduced if we use fine mesh in LSA. Moreover, more fine mesh may erase the depression obtained by LSA. The trouble is that it appears the tremendous concave area afterwards the hydrofoil and the computational time increases rapidly. For example single

mesh in Fig.22 needs 4 minutes and triple mesh does about 4 hours. Furthermore we calculate the 2-D doublet problem by LSA using very fine mesh of 250 times, it is confirmed that the depression becomes very small but never agree to the analytical solution.

Next, we compare the lift coef. C_L and the drag coef. C_D with the experimental results and show them in Fig.24 for various F_n with broken line (coarse mesh, Fig.22) and full line (fine mesh, Fig.23). The difference of the results between the mesh size (full and broken lines) is very small, but the difference of C_L between HSA and LSA (thick and thin lines) is large. And the results of HSA are very similar to the experiments. Here we can not make a quantitative comparison directly, because these experimental values involve the effect of viscous drag of two struts, and it seems this effect also affects qualitatively the drag coef. C_D.

From the above discussions it may be clear that HSA is more useful to reduce the number of mesh and CPU time than the conventional method LSA. Then in the following calculations, we use coarse mesh and compare the calculated results between HSA and LSA.

In Figs.25(a)~(c) we show the wave profiles and the wave patterns of the tandem foil system comparing HSA with LSA. The conditions of tandem system are that the stagger $s/c = 6.0$, the gap $h/c = 0$ and the depth $f/c = 1.0$, too. Calculation area and mesh on the still water surface are almost same as the case of mono hydrofoil, but we add another meshes afterwards corresponding to the stagger of each foils s/c.

In Figs.25(a)~(c), there is no extreme difference between LSA and HSA in the case of $F_n = 1.2$, but in the cases of $F_n = 2.0$ and 4.0, we notice that smooth wave profiles are obtained by HSA and sharp depressions appear right above each hydrofoil by LSA. On the other hand, we notice a little rise right above each hydrofoils by HSA. These are very similar results to those of the 2-D problems [17]and we think that HSA is also useful in the 3-D hydrofoil problems in the high speed range.

At last we show the variation of the lift coef. C_L and the drag coef. C_D for the fore, the aft foils and the combined hydrofoil system in the case of $s/c = 2.5, 6.0, 10.0$ comparing the results of HSA and LSA with the experiments.

Figs.26(a) and (b) show the lift coef. C_L of the fore and the aft foils, respectively. The results of the fore foil are very similar to ones of the mono hydrofoil and there is no difference

due to s/c. But the difference due to s/c is clear for the aft foil in high speed range ($F_n > 2.0$). However, in relatively low speed range, it varies extremely according to the wave profiles created by the fore foil. And the numerical results agree well with the experiments.

Figs.27(a) and (b) show the drag coef. C_D of the fore and the aft foils, respectively. Both results of HSA and LSA agree well with each other, but are different from the experiments. However, since the experimental results involve the effects of struts, it is difficult to compare them directly with the numerical one.

Figs.28(a) and (b) show the lift coef. C_L and the drag coef. C_D of the combined tandem hydrofoil system. That is an average of the values of the fore and the aft foils. We understand the effect of the aft foil is predominant and the lifts coincide with the results of experiments but the tendency of the calculated drags for s/c is contrary to the experiments.

Through Fig.26 to Fig.28 there exists a difference between HSA and LSA, but as to the force they are not so different as in case of wave profiles in the high speed range. These are similar to 2-D problem.

CONCLUSION

We introduced a new calculation method SQCM which combines the source distributing surfaces panels with QCM and satisfies well the Kutta's condition. Since there needs no iteration, it is very effective calculation method of characteristics of 3-D wings.

We proposed a new Rankine source method named HSA which uses the inverse image above the still water surface in the high speed range. We carried out the numerical calculations for a circular cylinder and 2-D thin hydrofoil in the high speed range and confirm that both forces and wave profiles agree very well to the analytical ones. The wave profile obtained by HSA is smooth and shows a little rise above the hydrofoil.

On the contrary, wave profile calculated by LSA shows so big depression right above the hydrofoil, using usual mesh size of still water surface. In addition, the depression increases with Froude number and it seems to be very strange.

Next, applying LSA and HSA to the flows around 2-D and 3-D mono and tandem hydrofoils in a wide range of speeds, we obtain the wave profiles, lifts and wavemaking resistances and compare them with the experimental results.

According to these results, HSA seems more applicable than LSA in the high speed range, and is expected to be a useful tool to predict the wave flow around the high speed ship with hydrofoils.

Acknowledgment

REFERENCES

1. Dawson C. W., "A Practical Computer Method for solving Ship Wave Problems", Second International Conference on Numerical Ship Hydrodynamics, Berkeley, 1977

2. Ando J., Kataoka K., Nakatake K., "Rankine Source Method in High Speed Range" (in Japanese), Transactions of the West-Japan Society of Naval Architects, , No.84 . 1992, pp. 1-10

3. "First International Conference on Fast Sea Transportation", Norwegian Institute of Technology , Trondheim, Norway, 1991

4. Acosta A. J., "Hydrofoils and Hydrofoil Craft", Annual Review of Fluid Mechanics, Vol.5 ,1973

5. Lee C. S., Lew J. M. and Kim Y.G., "Analysis of a Two-Dimensional Partially- or Supercavitating Hydrofoil Advancing under a Free Surface with a Finite Froude Number", Nineteenth Symposium on Naval Hydrodynamics, Seoul, 1992

6. Bai K. J. Kim J. and Lee H., "A localized Finite-Element Method Froude Number", Nineteenth Symposium on Naval Hydrodynamics, Seoul, 1992

7. Ando, J. and Nakatake, K., "A Method to Calculate Wave Flow by Rankine Source" (in Japanese), Transactions of the West-

Japan Society of Naval Architects, No.75 . 1988, pp. 1-12

8. Havelock, T. H., "Some Cases of Wave Motion due to a Submerged Obstacles", Proc. Roy. Soc. London, vol. 93, 1917

9. Nakatake K., Komura A., Ando J., Kataoka K., "On the Flow Field and the hydrodynamic Forces of an Obliquing Ship" (in Japanese), Transactions of the West-Japan Society of Naval Architects, No.80 . 1990, pp. 1-12

10. Lan, C.E., "A Quasi-Vortex-Lattice Method in Thin Wing Theory", Journal of Aircraft, Vol.11, No.9 ,1974, pp. 518-527

11. Kataoka K., Ando J., Nakatake K., "On Characteristics of Three-Dimensional tandem hydrofoils" (in Japanese), Transactions of the West-Japan Society of Naval Architects, No.86 . 1993, pp. 1-14

12. Parkin B., Perry B., Wu T., "Pressure Distribution on a hydrofoil near the Water Surface", Journal of Applied Physics, Vol. 27, No. 3 , 1956, pp. 232-240

13. Nishiyama T., " Linearized Steady Theory of Fully Wetted hydrofoils ", Advances in Hydroscience, Vol. 3, pp. 237 - 342, 1966

14. Nishiyama, "Characteristics of the submerged hydrofoil among stationary waves.", J.Soc.Naval Arch.Japan,No.97,1955,pp.1-8

15. Pinkerton, R. M.,"Calculated and Measured Pressure Distributions over the Midspan Section of the N.A.C.A. 4412 Airfoil", NACA Report No. 563 ,1936

16. Moriya T.,"An Introduction to Aerodynamics", Baifukan Book Co., Tokyo, 1959

17. Kataoka K., Ando J., Nakatake K., "On Characteristics of Two-Dimensional tandem hydrofoils" (in Japanese), Transactions of the West-Japan Society of Naval Architects, No.85 . 1993, pp. 1-14

APPENDICES

Expression of Hydrofoil Using Potential

When we consider a hydrofoil-system in the inviscid incompressible and irrotational uniform flow, the flow field can be expressed by the velocity potential ϕ. Then ϕ satisfies the equation of continuity

$$\nabla^2 \phi = 0, \qquad (A\text{-}1)$$

and body surface condition

$$\frac{\partial \phi}{\partial n} = 0. \qquad (A\text{-}2)$$

And ϕ is expressed by the sum of the potential ϕ_0 expressing basic flow and the potential ϕ_1 expressing free surface effects as

$$\phi = \phi_0 + \phi_1. \qquad (A\text{-}3)$$

where ϕ_0 is expressed by HSA in case of high speed or by LSA in case of low speed and ϕ_0 and ϕ_1 are shown as follows

$$\left. \begin{array}{l} \phi_0 = Vx + \displaystyle\sum_{j=1,2} \overline{\phi}_{wj} \\ \phi_1 = \displaystyle\sum_{j=1,2} \Delta\phi_{wj} + \phi_F \end{array} \right\} \qquad (A\text{-}4)$$

respectively. where $\overline{\phi}_{wj}$ is the disturbed velocity potentials to express the basic disturbance to use the double model or the inverse image and $\Delta\phi_{wj}$ expresses the effect of the free surface on the each foil surface, respectively. Then the disturbed velocity potential of the hydrofoil system ϕ_w is divided into the term ϕ_S due to the source on the hydrofoil surface and ϕ_V due to the vortex on the camber surface

$$\phi_w = \phi_S + \phi_V. \qquad (A\text{-}5)$$

We express these ϕ_S, ϕ_V, ϕ_F and the induced velocity in the following sections.

Expression of q_S and ϕ_S

Flow velocity vectors $\mathbf{q}_S$ induced by the source distributions around the hydrofoil surfaces are given as

$$\mathbf{q}_S = \text{grad } \phi_S \qquad (A\text{-}6)$$

where ϕ_S is the disturbed velocity potential due to the source and in the 2-D problem

$$\begin{aligned} \phi_S &= \sum_{j=1,2} \left(\overline{\phi}_{Sj} + \Delta\phi_{Sj} \right) \\ &= \sum_{j=1,2} \int_{S_{wj}} m_j(x', y') \\ &\quad \times \left\{ \log \sqrt{(x-x')^2 + (y-y')^2} \right. \\ &\quad \left. \pm \log \sqrt{(x-x')^2 + (y+y')^2} \right\} dS_{wj} \qquad (A\text{-}7) \end{aligned}$$

and in the 3-D problem

$$\phi_S(x, y, z) = -\sum_{j=1,2} \left(\overline{\phi}_{Sj} + \Delta\phi_{Sj}\right)$$

$$= -\sum_{j=1,2} \int_{S_{wj}} m_j(x', y', z') \times$$

$$\left\{ \frac{1}{\sqrt{(x-x')^2 + (y-y')^2 + (z-z')^2}} \right.$$

$$\left. \pm \frac{1}{\sqrt{(x-x')^2 + (y+y')^2 + (z-z')^2}} \right\} dS_{wj},$$

$$(A\text{-}8)$$

where the sign $+$ means LSA and the sign $-$ does HSA.

Expression of q_V and ϕ_V

The velocity vector $\mathbf{q}_V$ induced by the vortex γ_j distributing on the camber surface is shown as

$$\mathbf{q}_V = \mathrm{grad}\ \phi_V, \qquad (A\text{-}9)$$

where ϕ_V is in the 2-D problem

$$\phi_V = \sum_{j=1,2} \left(\overline{\phi}_{Vj} + \Delta\phi_{Vj}\right)$$

$$= \sum_{j=1,2} \gamma_j \int_{C_j} \left\{ \tan^{-1}\left(\frac{y-y'}{x-x'}\right) \right.$$

$$\left. \mp \tan^{-1}\left(\frac{y+y'}{x-x'}\right) \right\} dC_j \quad, \qquad (A\text{-}10)$$

and in the 3-D problem $\mathbf{q}_V$ is shown directly as

$$\mathbf{q}_V = \sum_{j=1}^{2} \sum_{k=1}^{N} \gamma_j(x_k, y_k) \sqrt{x_k(1-x_k)} \times$$

$$\left\{ \int_{C_k} \frac{\mathbf{r}(x,y,z) - \mathbf{r}(x',y',z')}{|\mathbf{r}(x,y,z) - \mathbf{r}(x',y',z')|^3} d\mathbf{c}(x', y', z') \right.$$

$$\left. \mp \int_{C_k} \frac{\mathbf{r}(x,y,z) - \mathbf{r}(x',-y',z')}{|\mathbf{r}(x,y,z) - \mathbf{r}(x',-y',z')|^3} d\mathbf{c}(x', -y', z') \right\},$$

$$(A\text{-}11)$$

where $\mathbf{r}(x, y, z)$ means the position vector.

In the above equation, the sign $+$ means HSA and the sign $-$ does LSA. The $d\mathbf{c}(x,y,z)$ means a line element vector of the k-th vortex line which is located discretely at (x_k, y_k) on the camber surface following QCM. The contour C_k is made of the three vortex lines, one is spanwise on the camber surface and the others start chordwise from both ends to the rear infinity through the trailing edges.

Expression of q_F and ϕ_F

The velocity vector $\mathbf{q}_F$ induced by source σ_F distributing on the still water surface is shown by the disturbed velocity potential ϕ_F as follows

$$\mathbf{q}_F = \mathrm{grad}\ \phi_F. \qquad (A\text{-}12)$$

where ϕ_F is

$$\phi_F(x, y) = \int_{S_F} \sigma_F(x') \log \sqrt{(x-x')^2 + y^2} dS_F$$

$$(A\text{-}13)$$

in the 2-D problem, and

$$\phi_F(x, y, z) = -\int_{S_F} \sigma_F(x', z')$$

$$\times \frac{1}{\sqrt{(x-x')^2 + y^2 + (z-z')^2}} dS_F \quad (A\text{-}14)$$

in the 3-D one.

Expression of Linearized Free Surface Condition and Wave Profile

As above mentioned, two types of disturbed velocity potential are available. In the case of LSA (Normal Image) is used, $\phi_{0y} = 0$, at $y = 0$ and in the case of HSA (Inverse Image), $\phi_{0x} = 0$ at $y = 0$. Involving both cases, the linearized free surface condition and corresponding wave profile η are given as follows.

$$\phi_{1xx} + k_0\phi_{1y} = -(\phi_{0xx} + k_0\phi_{0y}) \qquad (A\text{-}15)$$

$$\eta = -\frac{V}{g}(\phi_{0x} + \phi_{1x}) \qquad (A\text{-}16)$$

where g is acceleration of gravity, $k_0 = g/V^2$ is the number of wave.

Using HSA, since there is no analytical solution for hydrofoils, we define the wave profiles in the limit of high speed analytically from the linearized free surface condition,

$$V\eta_x - (\overline{\phi}_{Sy})_{y=0} = 0. \qquad (A\text{-}17)$$

It is shown as

$$\eta = \frac{1}{V} \int (\overline{\phi}_{Sy})_{y=0} dx + \mathrm{const.}. \qquad (A\text{-}18)$$
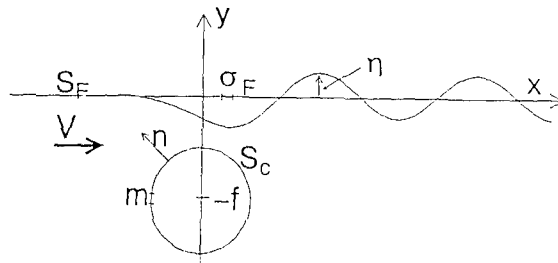
Fig.1 Coordinate system of circular cylinders
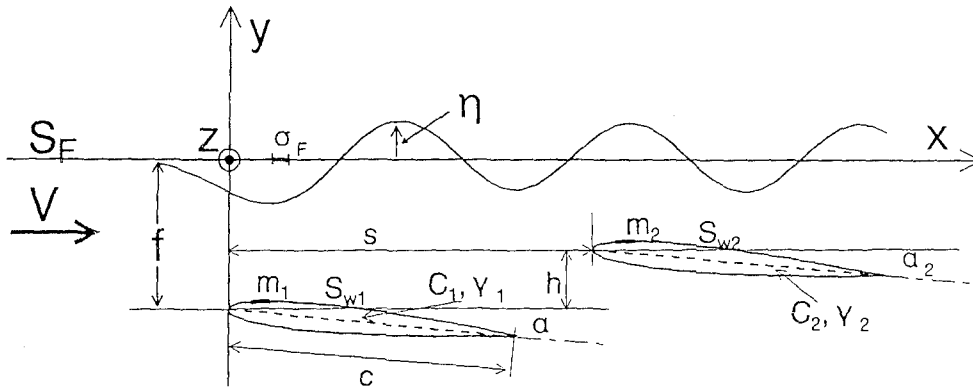
Fig.2 Coordinate system of hydrofoils
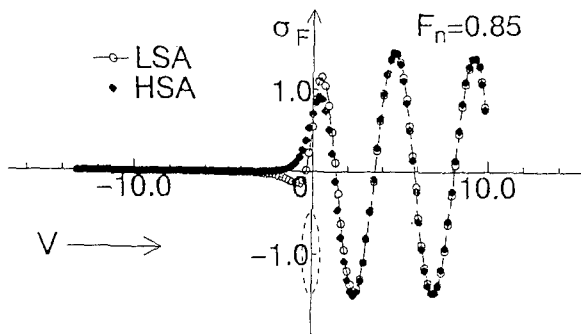
Fig.3(a) Source distribution on still water surface due to circular cylinder
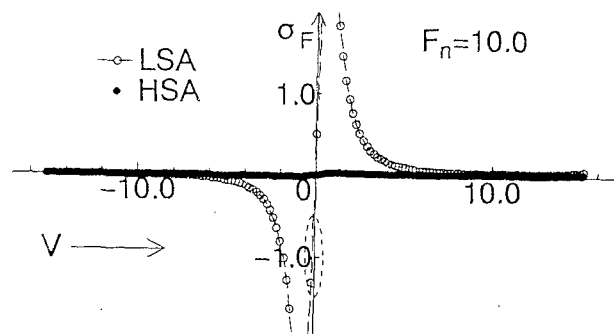
Fig.3(b) Source distribution on still water surface due to circular cylinder
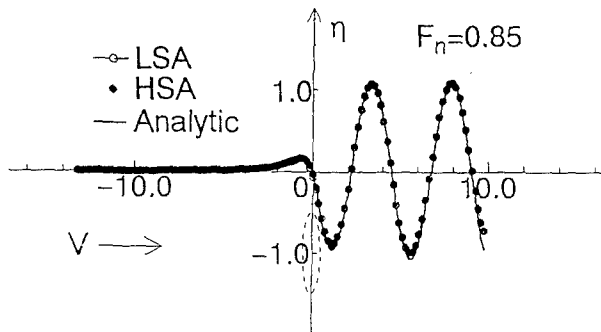
Fig.4(a) Wave profiles due to point doublet
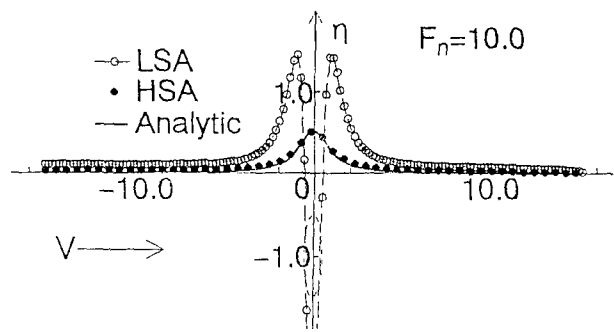
Fig.4(b) Wave profiles due to point doublet

31
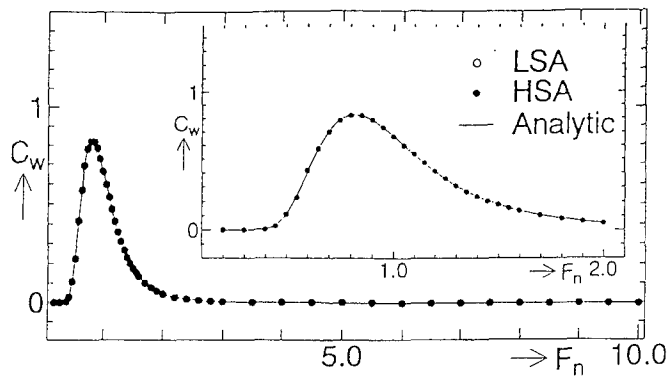
Fig.5 Wave making resistance coeffi-
cient C_w of point doublet
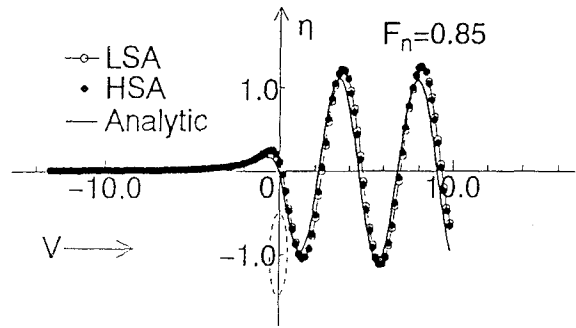
Fig.6(a) Wave profiles due to circular
cylinder
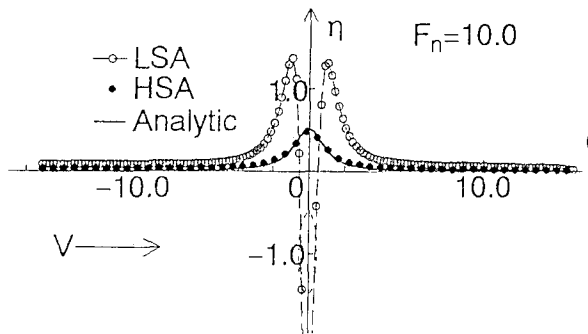
Fig.6(b) Wave profiles due to circular
cylinder
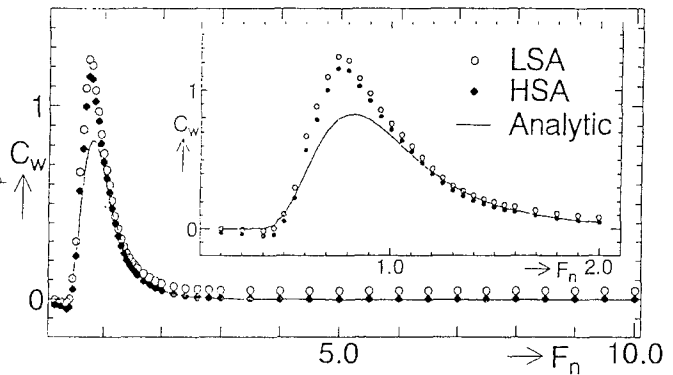
Fig.7 Wave making resistance coeffi-
cient C_w of circular cylinder

(a)   (b)   (c)
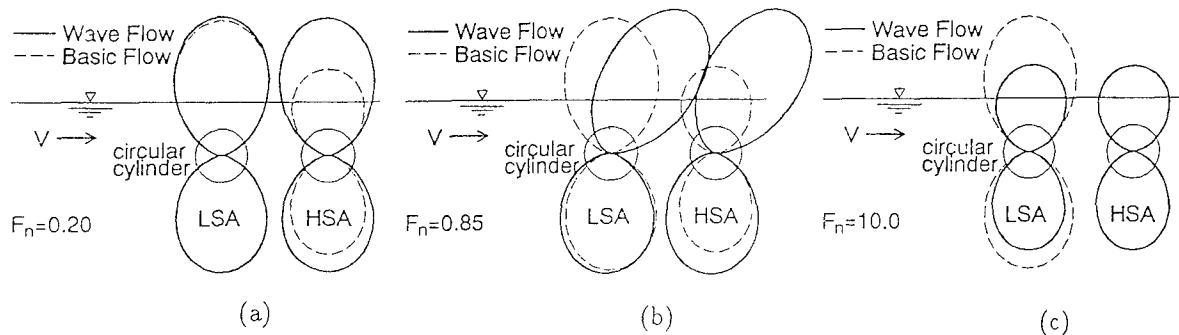
Fig.8 Pressure distribution on circular cylinder surface
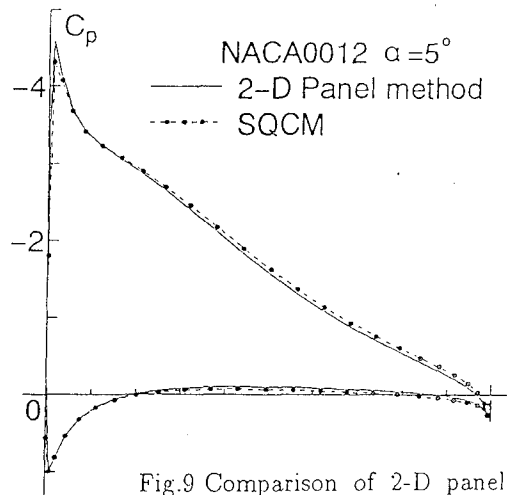
Fig.9 Comparison of 2-D panel method
and SQCM

$F_n= 0.70$ $F_n= 4.00$

$F_n= 1.00$ $F_n= 5.00$

$F_n= 1.50$ $F_n= 6.00$

$F_n= 2.00$ $F_n= 8.00$

$F_n= 3.00$ $F_n=10.00$

○ LSA
• HSA
— Analytic

(NACA0005 , $\alpha = 5°$, f/c=0.956)
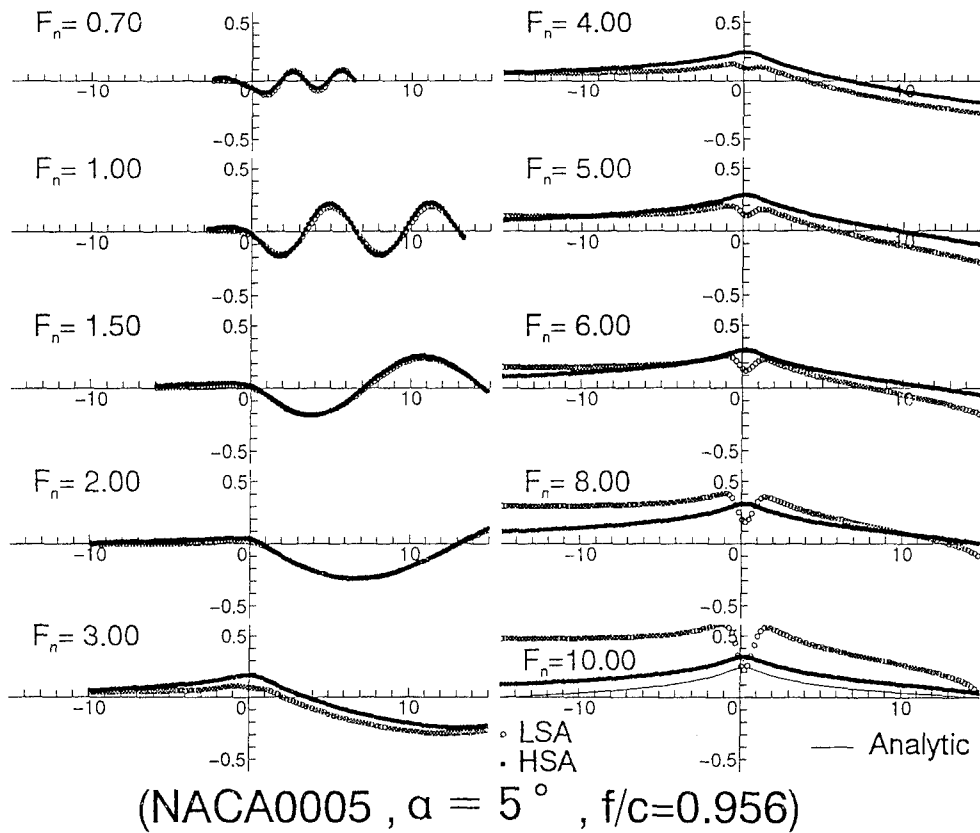
Fig.10 Wave profiles due to hydrofoil (NACA0005, $h/c = 0.956, \alpha = 5°$)

(a)	(b)	(c)
(NACA0005 , $\alpha = 5°$, f/c=0.956)	(NACA0005 , $\alpha = 5°$, f/c=1.956)	(NACA0005 , $\alpha = 5°$, f/c=3.956)
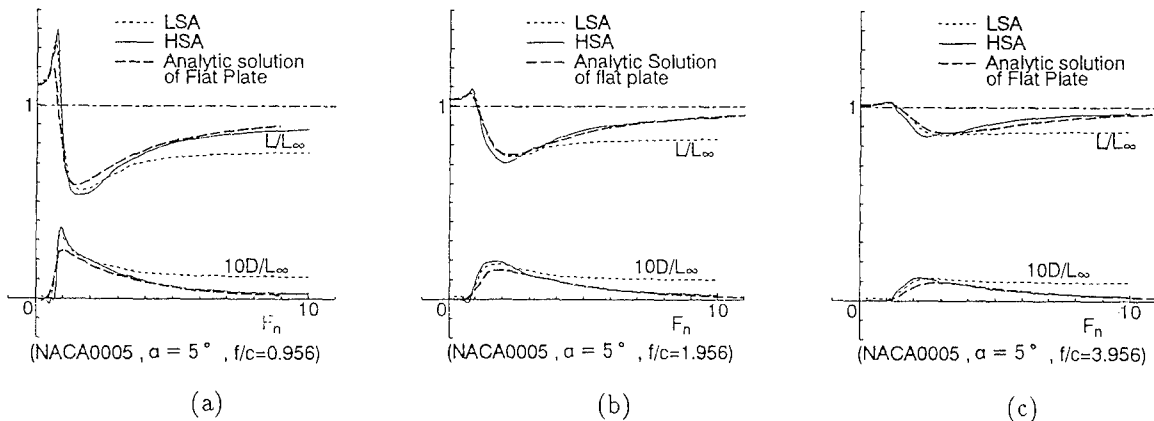
Fig.11 Lift and drag with analytical solution

(a)	(b)	(c)
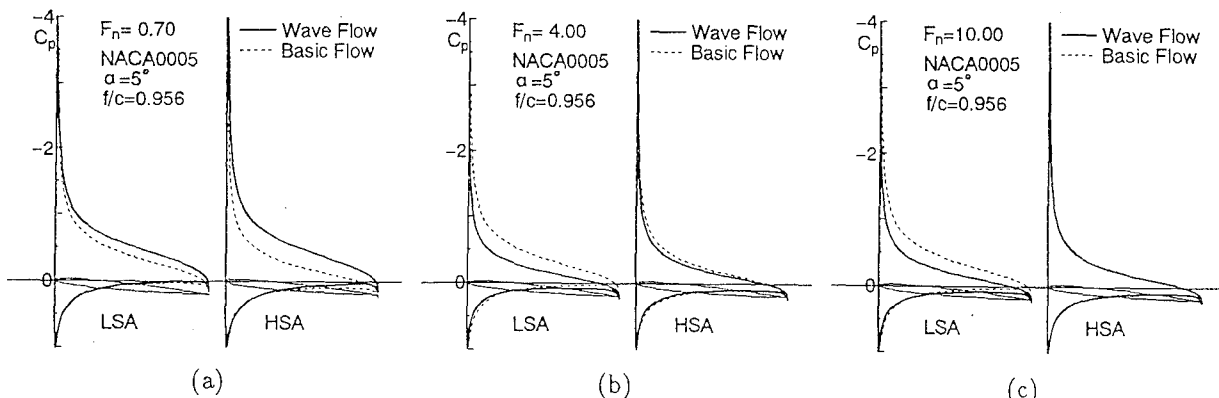
Fig.12 Pressure distribution on hydrofoil surface

33
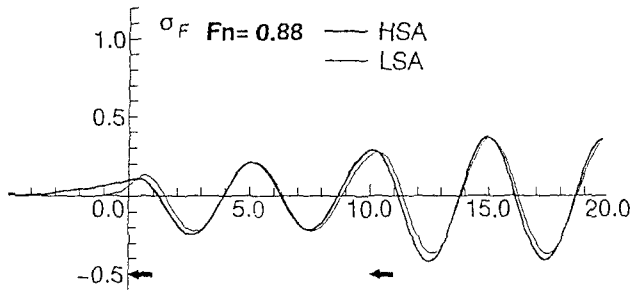
Fig.13(a) Comparison of source distribution between HSA and LSA
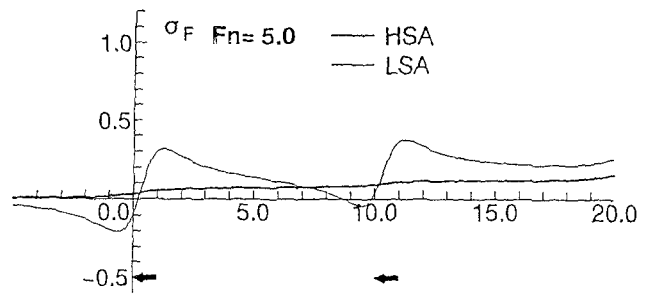
Fig.13(b) Comparison of source distribution between HSA and LSA
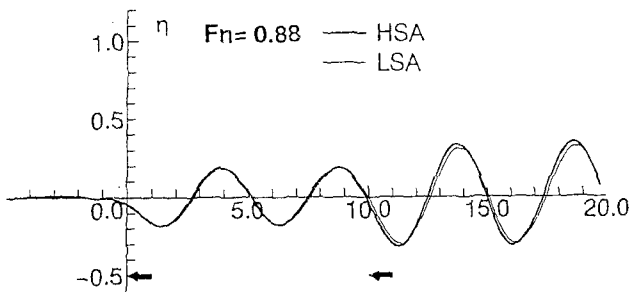
Fig.14(a) Comparison of wave profiles between HSA and LSA
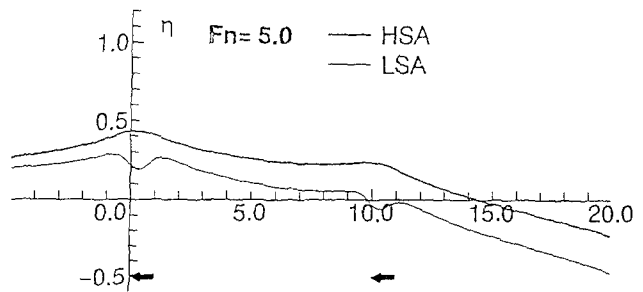
Fig.14(b) Comparison of wave profiles between HSA and LSA
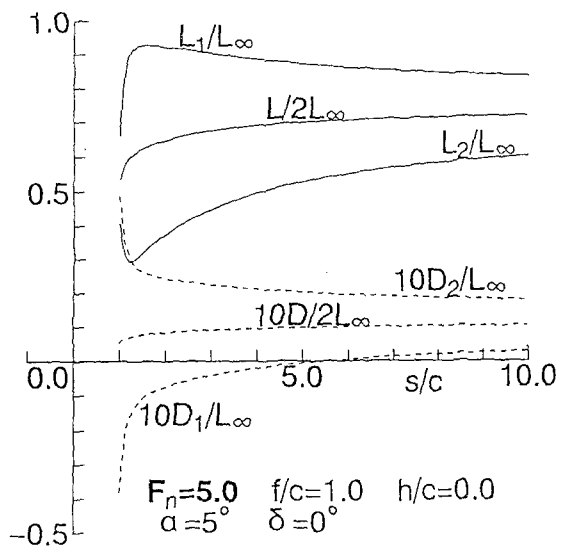
Fig.15(a) Change of interference factor versus stagger
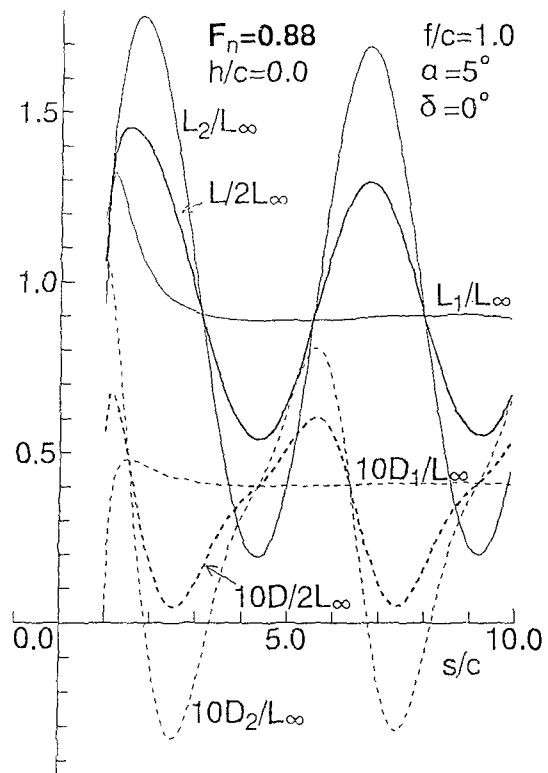
Fig.15(b) Change of interference factor versus stagger

34
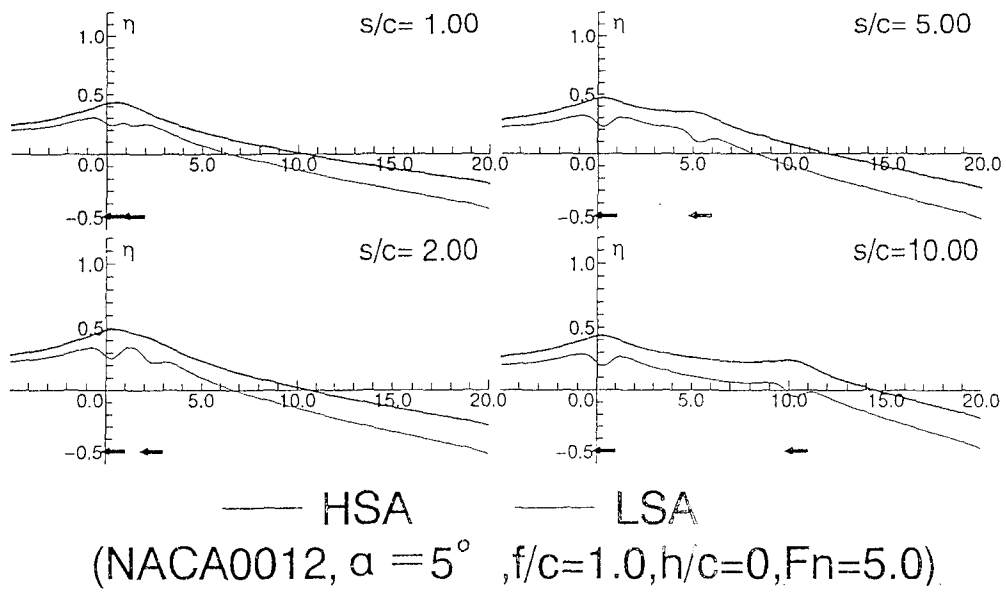
Fig.16(a) Wave profiles versus stagger
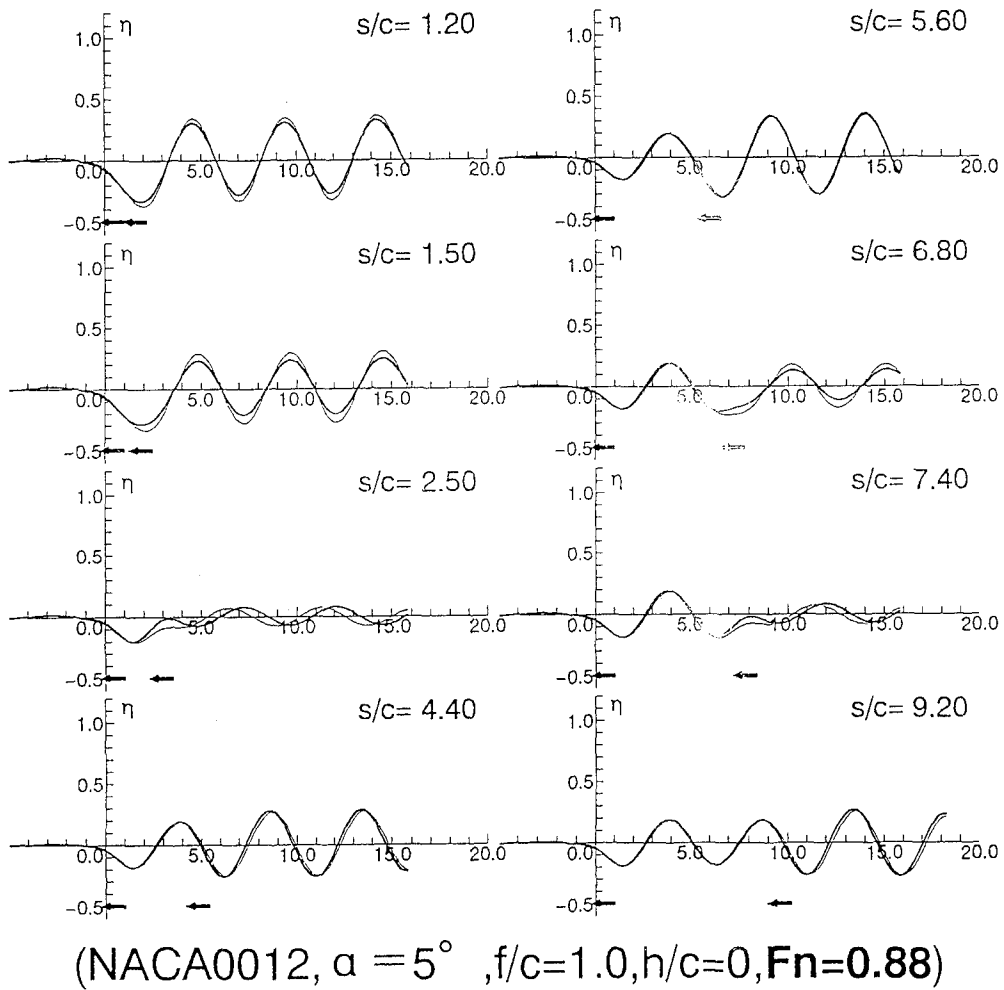
Fig.16(b) Wave profiles versus stagger

Fore Foil

f/c=1.0 s/c=10.0 h/c=0.0
α=5°   δ=0°

L_1/L_∞

- ---- HSA
- ---- LSA

$10D_1/L_\infty$

F_n

Fig.17(a) Change of interference factor versus F_n

Aft Foil

f/c=1.0 s/c=10.0 h/c=0.0
α=5°   δ=0°

L_2/L_∞

- ---- HSA
$10D_2/L_\infty$ - ---- LSA
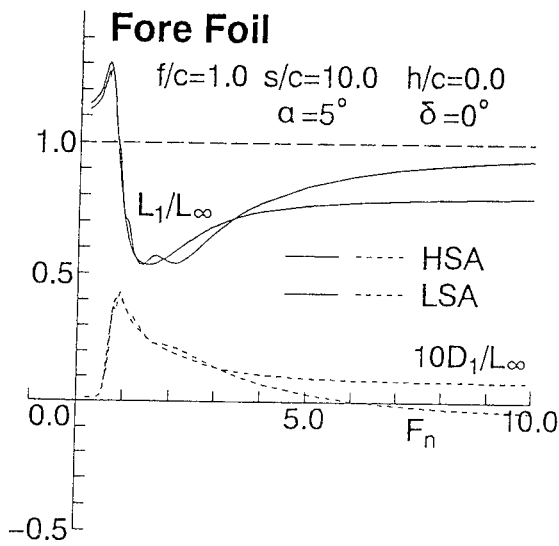
F_n

Fig.17(b) Change of interference factor versus F_n

η Fn= 1.00

η Fn= 4.00

η Fn= 1.50

η Fn= 5.00

η Fn= 2.00

η Fn= 7.00

η Fn= 3.00

η Fn=10.00

—— HSA —— LSA

(NACA0012, α=5° ,f/c=1.0,h/c=0.0,s/c=10.0)
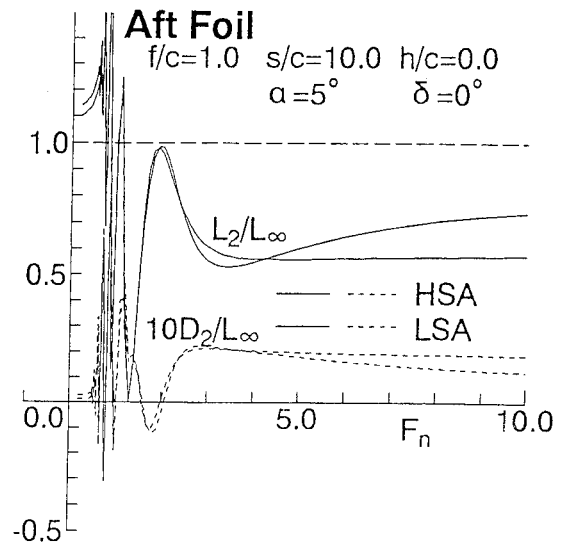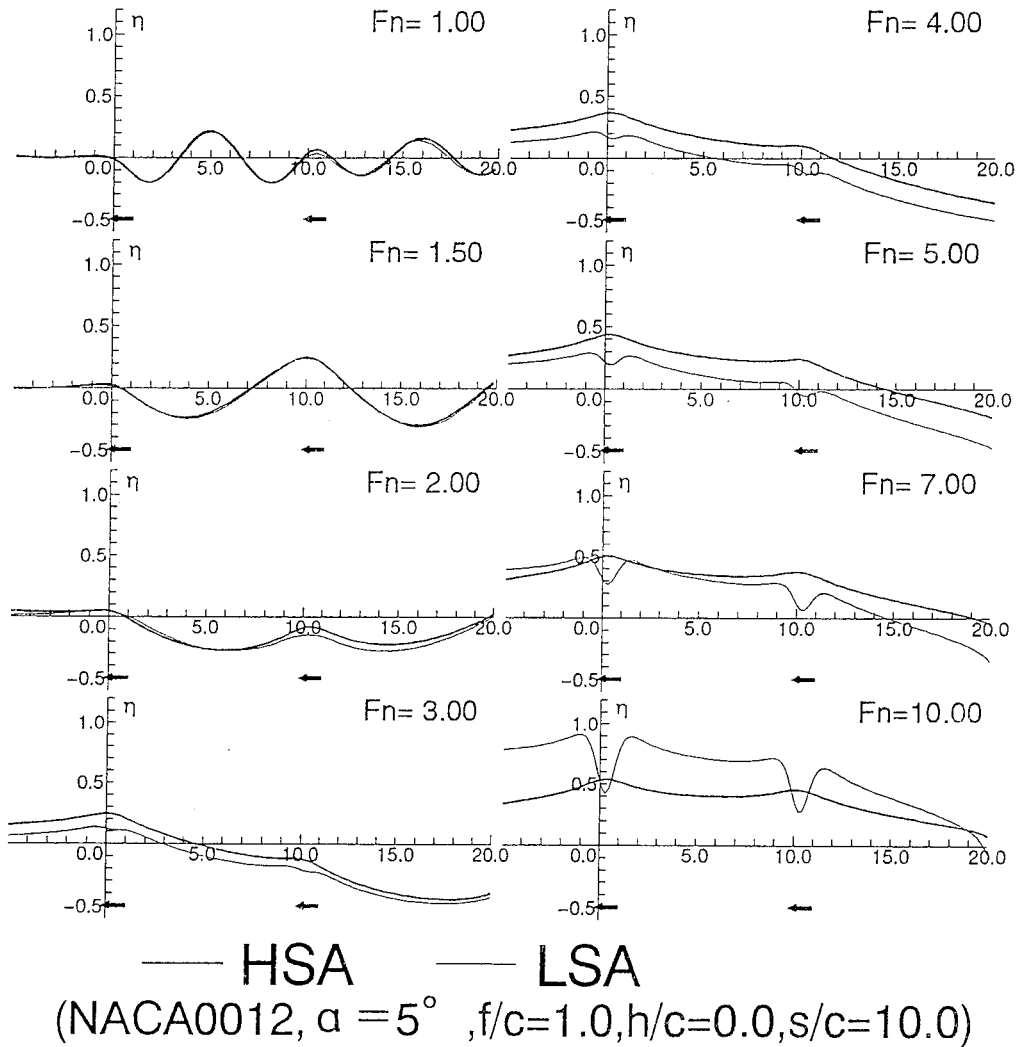
Fig.18 Wave profiles versus F_n

36
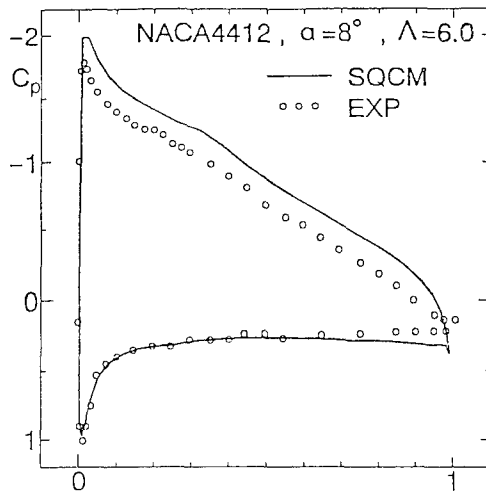
Fig.19 Pressure coef. on 3-D mono-
foil surface in unbounded flow
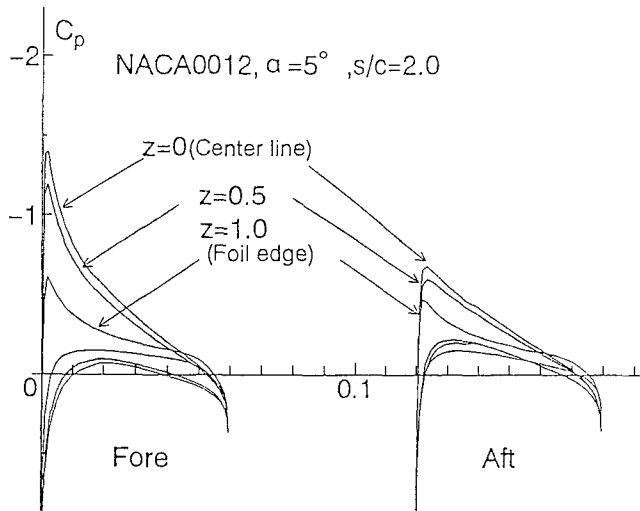
Fig.20 Pressure coef. on 3-D tandem-foil
surfaces in unbounded flow
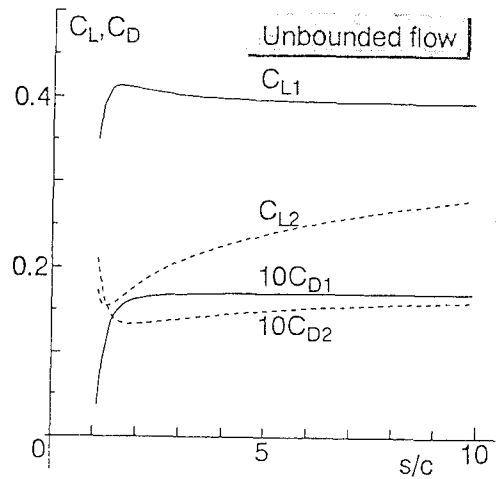
Fig.21 interference factor of lift and
drag against stagger
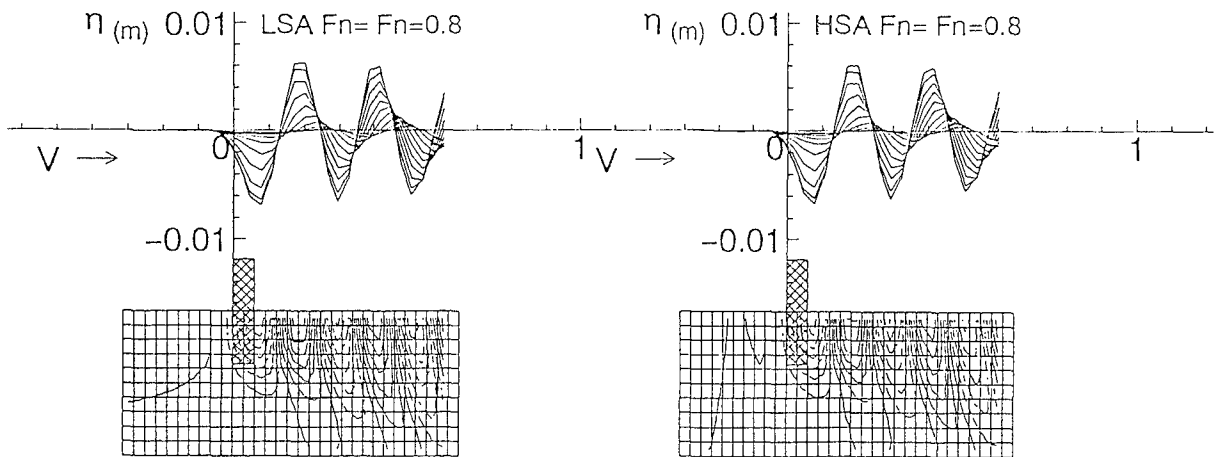
Fig.22(a) Comparison of wave profiles and patterns between LSA and HSA (Coarse mesh)
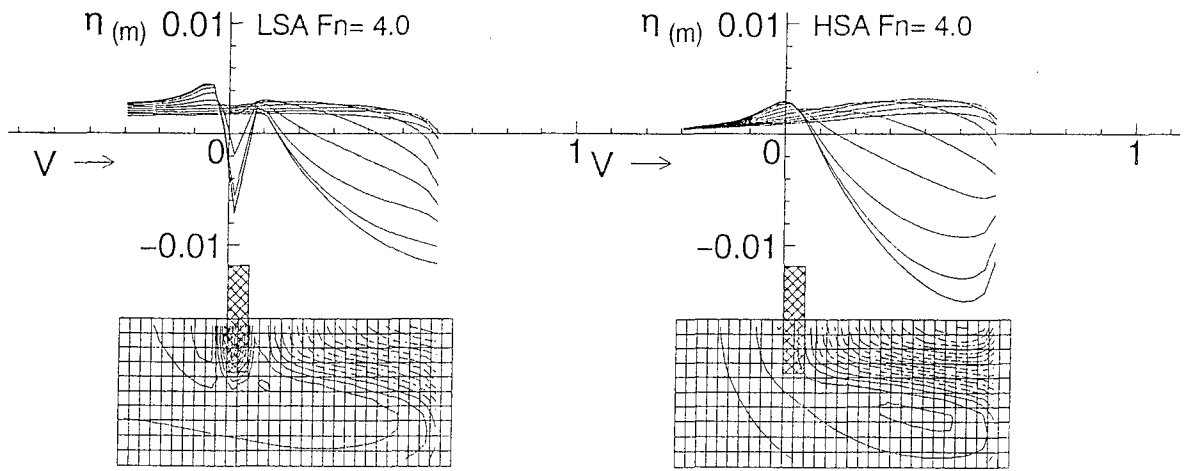
Fig.22(b) Comparison of wave profiles and patterns between LSA and HSA (Coarse mesh)
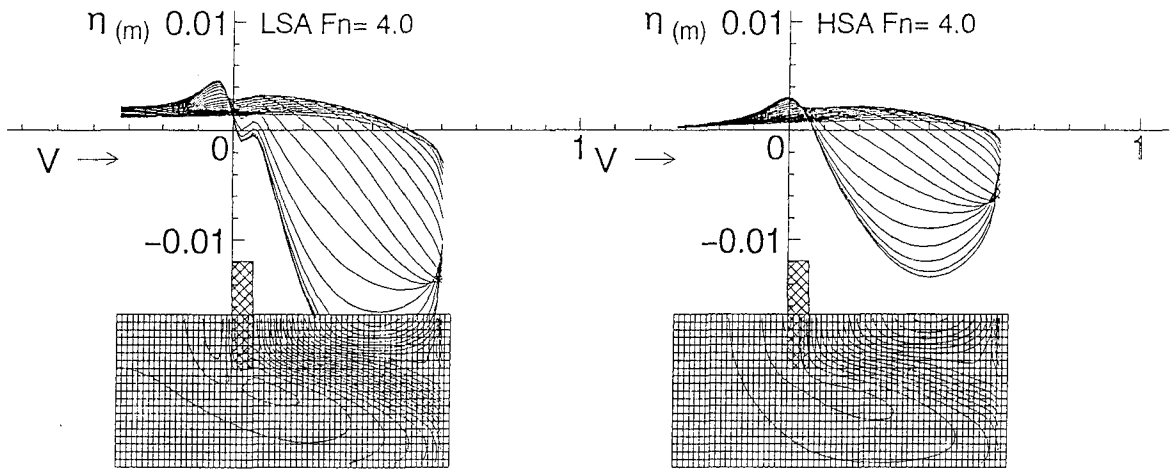
Fig.23 Comparison of wave profiles and patterns between LSA and HSA (Fine mesh)
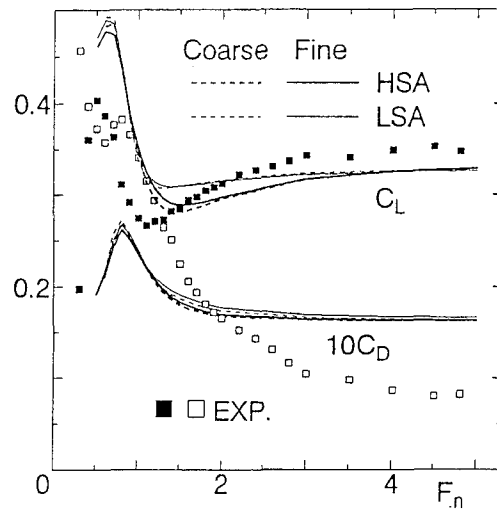
Fig.24 Lift coef. and drag coef. of
mono-hydrofoil
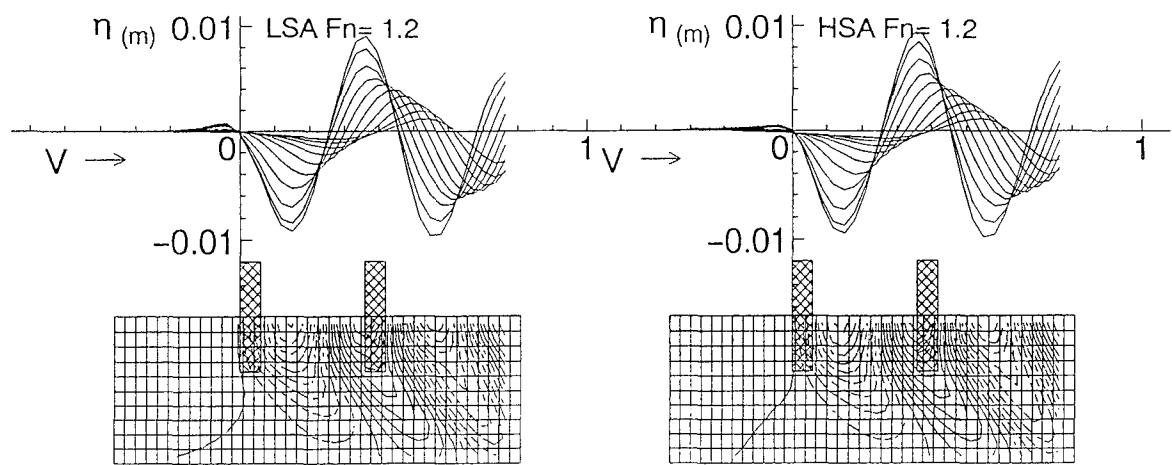
Fig.25(a) Comparison of wave profiles and patterns between LSA and HSA (tandem foil, $s/c = 6.0$)
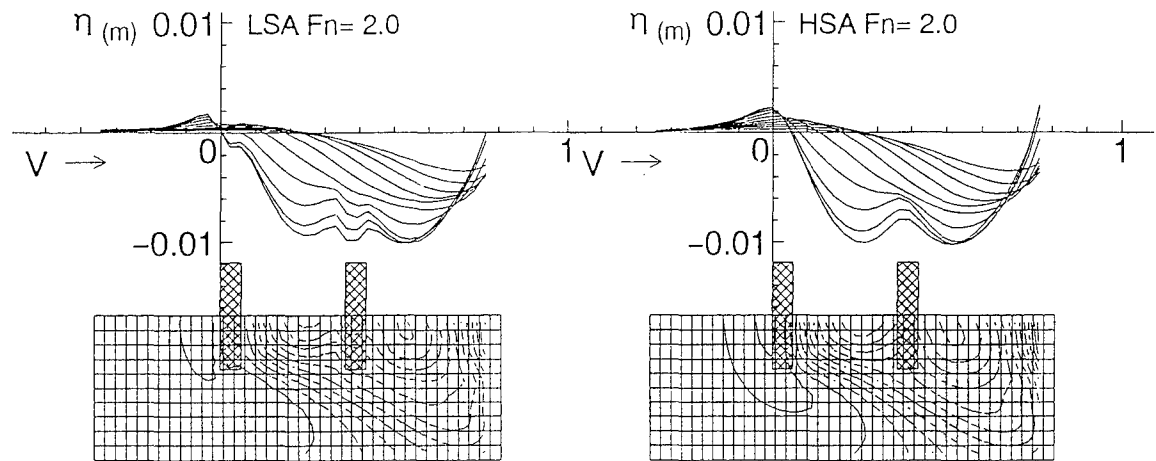
Fig.25(b) Comparison of wave profiles and patterns between LSA and HSA (tandem foil, $s/c = 6.0$)
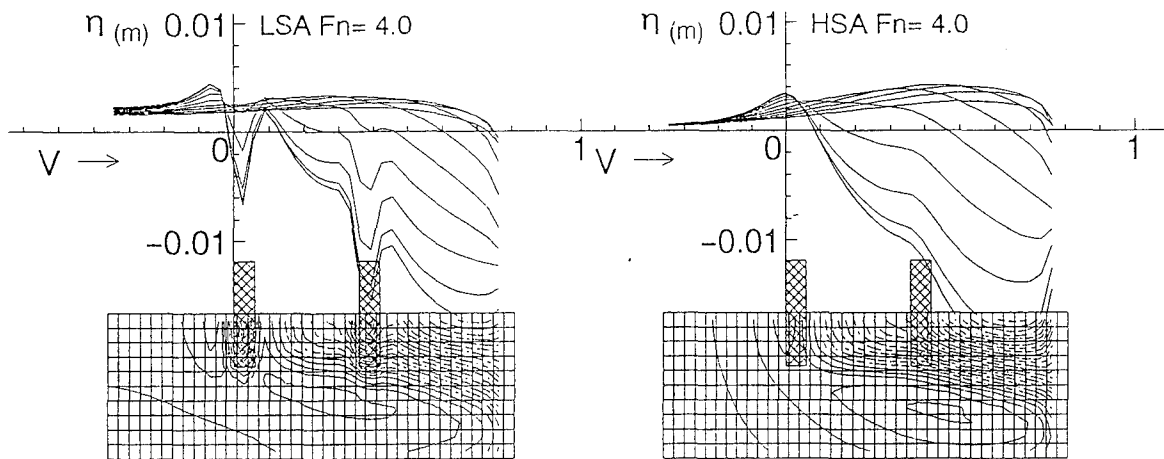
Fig.25(c) Comparison of wave profiles and patterns between LSA and HSA (tandem foil, $s/c = 6.0$)
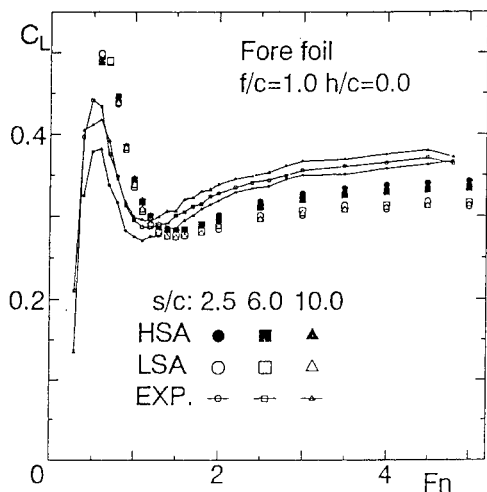
Fig.26(a) Comparison of C_L (fore foil)
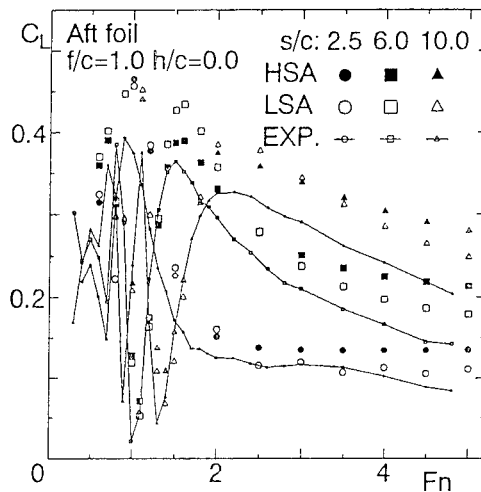
Fig.26(b) Comparison of C_L (aft foil)
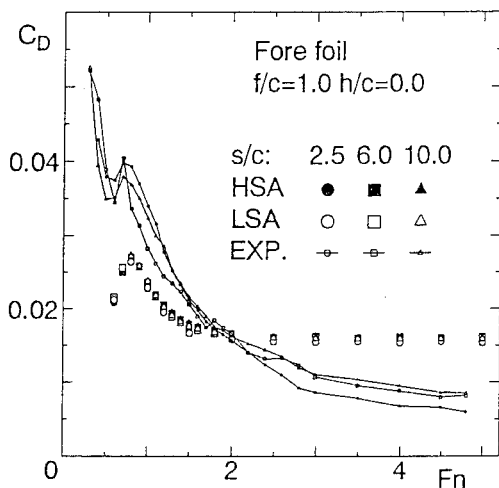
Fig.27(a) Comparison of C_D (fore foil)
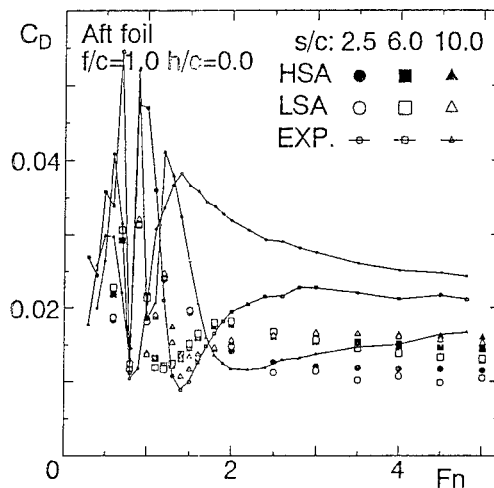
Fig.27(b) Comparison of C_D (aft foil)
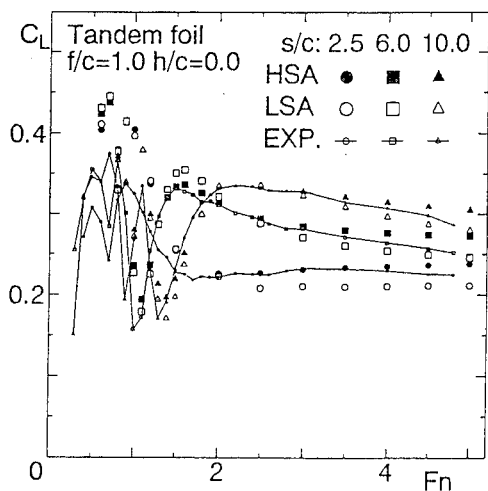
Fig.28(a) Comparison of C_L (tandem foil)
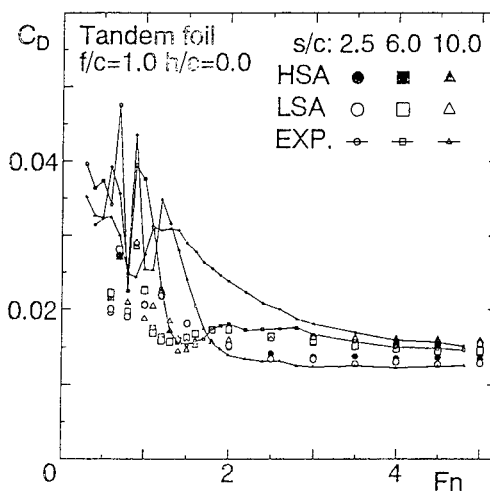
Fig.28(b) Comparison of C_D (tandem foil)

DISCUSSION
by Dr. Spyros Kinnas, MIT

The authors should be congratulated for their extensive study of the Rankine Source Method. I have two questions concerning the so-called SQCM:

1. What is the theoretical basis of combining a QCM (an inherently linearized formulation) to a source method with the sources distributed on the exact hydrofoil surface? Is this a consistent formulation?

2. Can their method predict the correct effect of thickness on the hydrofoil loading? (See for example JSR paper on "A General Theory for the Coupling Between Thickness and Loading," S. Kinnas, 1992). In other words, is their method predicting the correct value of the derivative of the lift L with respect to the τ_{max} ($dL/d\tau_{max}$) while the camber and angle of attack remains the same?

Author's Reply
1. We can select an arbitrary form and location of distributing vortices around the foil. Then we use those of the QCM formally and satisfy the Kutta's condition. Though there is no assumption of a thin wing, we think this is consistent.

2. In Figure A1 we show the SQCM results of the lift variation due to thickness comparing with our panel method and the QCM for the 2-D NACA symmetric wing sections. We can see the thickness increases lift as well as the panel method and the discusser's method.

DISCUSSION
by Kazu-hiro Mori, Hiroshima University

Can we not expect to have the same results even if the expressions of the basic solution are not the same? This can be supported by the results of C_w shown in Fig. 7. The differences in wave elevation shown in Fig. 4 are suspected to have appeared from numerical reasons; the elevation is obtained by the finite difference of the velocity potential with respect to x.

Author's Reply
Thank you for your discussion.

We agree with the discusser in thinking that both results should agree with each other on an ideal numerical calculation. However, we have tried to use finer mesh on still water surface using 2-D circular cylinder problem and have also checked them using double precision (REAL$\$$*8) and four times precision (REAL$\$$*16) options, but it is confirmed that the depression becomes smaller but never agree with the HSA solution. We may say that both results never agree at high speed.

In order to understand this phenomenon we show calculated results in Figure A2. The condition is corresponding to Figure 4(b) of the text, that is, one of the 2-D circular cylinder problem with a point doublet. We inversely obtained the source distribution on the still water surface from the wave profile which is obtained by the HSA. This source distribution differs only near the steep peaks from results of the LSA. This difference causes the peculiar depression above the doublet.

We also show other two results by the ordinary LSA; one is the usual case in which calculated region on the still water surface(-15.0< x <15.0) is divided into about 150 pieces and the other is the 25 times finer mesh case. Even if we use very fine mesh, we can not follow the steep peaks obtained above.

Then, we think the HSA is very effective in order to avoid this numerical difficulty in the high speed range.

DISCUSSION
by Dr. H. Raven, MARIN

Your paper suggests that you have tested two different linearizatons : LSA, with the basic flow being a double body flow, and HSA, with the basic flow being an 'inverse image flow.' You then conclude that HSA is better because it more closely agrees with analytic solutions. But these analytic solutions are linearized with respect to uniform flow, and will never tell you which linearization is better. To get the best

41

agreement with these analytic solutions you should impose a Kelvin condition.

On the other hand, (6) is not a useful double-body linearization but is equivalent to a Kelvin condition, could you clarify this?

Author's Reply

Thank you for your discussion.

The Eq. (6) $\phi_{1xx} + k_0\phi_{1y} =$ $-(\phi_{0xx} + k_0\phi_{0y})$ is exactly the Kelvin condition which is derived substituting $\phi = \phi_0 + \phi_1$ to the linearized free surface condition $\phi_{xx} + k_0\phi_y = 0$, but is not double-body linearization, i.e.,

$$\phi_{0x}^2 \phi_{1xx} + 2\phi_{0x}\phi_{0xx}\phi_{1x} + g\phi_{1y} = -\phi_{0x}^2 \phi_{0xx}$$

in case of normal image.

However, the difference between the LSA and the HSA is not one of linearization but one of the equation expressed in the text. That is, in the case of the LSA, Eq. (6) becomes from $\phi_{0y} = 0$ and it becomes also $\phi_{1xx} + k_0\phi_{1y} = -k_0\phi_{0y}$ from $\phi_{0xx} = 0$ in the case of the HSA.

DISCUSSION
by Dr. Henry T. Wang, Naval Research Laboratory

The authors are to be commended for bringing out the High Speed Approximation (HSA) as an alternative to the Low Speed Approximation (LSA), which is usually used in ship hydrodynamics. The authors' figures indicate that the wave profile and force coefficient results for LSA and HSA are similar at low *Fn* and diverge at high *Fn*. Have the authors considered other criteria, which may indicate *a priori* the approximate point of divergence of the two theories? For example, could one such criterion be related to the vertical velocity at the free surface (which is identically zero for LSA) reaching a certain fraction of the hydrofoil velocity? Also, can the authors comment on the conditions in which HSA, rather than the presently used LSA, would be more appropriate as the basic flow for surface ship problems?

Author's Reply

Thank you for your discussion.

It seems to be very useful to use such an index. In fact we have tried to search for a criteria, but we have found nothing indicating those matters generally. As the LSA is effective at a somewhat high speed and the HSA is also useful in a low speed problem to a degree, it is relative to use the LSA or the HSA. The point is that the speed range should be respected in which both results agree, and when they begin to diverge numerically, we should choose the HSA or the LSA.

We wish to consider the surface ship problem in the near future.

SESSION 2

WAVY/FREE-SURFACE FLOW: PANEL METHODS 2

Numerical Analysis of Nonlinear Ship Wavemaking Problem by the Coupled Element Method

X.W. Yu,[1] S.M. Li,[2] and C.C. Hsiung[1]
([1]Technical University of Nova Scotia, Canada,
[2]Wuhan University of Water Transportation Engineering, PRC)

Abstract

In this paper, the free surface condition for the ship wavemaking problem is analyzed and simplified with a new order analysis for the ship wavemaking potential based on the slow–ship theory. The total velocity potential is expressed as $\Phi = x + \varphi_r + \varphi$, where φ is the wave disturbance potential, and φ_r is the double–body disturbance potential with the order $O(F_n^k)$ and $k > 1$, so that the nonlinear free surface condition can be simplified and calculated on $z = 0$. In the numerical calculation, the coupled element method is applied. The flow domain is divided into inner and outer regions. The finite element method is used with the simplified nonlinear free surface condition for the inner region and the Green function method is employed with the linear free surface condition for the outer region. In the outer region, the Kelvin source function is used as the Green function, so that no numerical treatment of the radiation condition is needed. Numerical calculations were carried out for a cylinder, a sphere, a Wigly model and a Series 60 Block 60 ship model. The computed results agree well with the experimental results.

Nomenclature

a	:	radius of a cylinder or a sphere
A,B,C,D,E,F,H, P,Q,R,S,U,V,W	:	order groups or coefficient matrices
C_B	:	block coefficient
C_L	:	lift coefficient
C_w	:	wave resistance coefficient
C_x	:	midship section coefficient
C_s	:	wetted surface area coefficient
D	:	flow domain
D_1	:	inner region of the flow domain
D_2	:	outer region of the flow domain
F_n	:	Froude number
g	:	gravitational acceleration
G	:	Green's function
L,B,T	:	ship length, beam, and draft, respectively
L_B	:	intersection of ship hull and free surface
L_1, L_2, L_3	:	path of the line integral
$\vec{n}(n_x, n_y, n_z)$	:	unit outer normal vector
N	:	total number of nodes
N_i	:	shape function
p	:	pressure
R_w,L	:	wave resistance and lift on a body, respectively
S_B	:	wetted surface of ship
S_1	:	boundary of the inner region
S_2	:	boundary of the outer region
S_{F_1}	:	free surface of the inner region
S_{F_2}	:	free surface of the outer region
S_j	:	interface of the inner and outer regions
S_∞	:	boundary surface at infinity
U	:	ship speed
x,y,z	:	Cartesian coordinate system
α	:	solid angle at a control point
η	:	wave elevation
Φ	:	total velocity potential
ϕ	:	disturbance potential
φ	:	wave disturbance potential
φ_r	:	double–body disturbance potential
ρ	:	fluid density

1 Introduction

Normally, ship wavemaking is a highly non-linear problem. The major difficulty in this problem lies in the nonlinear boundary condition at the unknown location of the free surface. A basic approach to deal with this nonlinear problem is to employ the perturbation analysis. Almost exclusively a linearized condition is applied at the free surface, and in most cases the solution is described by a superposition of complicated singularities that satisfy this linearized free surface condition. Based on the assumption of small Froude number the low–speed ship theory, which takes account of the nonlinear effect on the free surface condition, has been developed. The perturbation process was applied to the zero–Froude number flow field instead of the free stream. The series expansion with respect to the wave elevation was carried out. The small parameter of Froude number was introduced to simplify the nonlinear free surface condition. This perturbation analysis with a quasi–analytic method, which was developed by Baba[1] for the low–speed flow past a blunt ship bow, gave a good agreement of computed and experimental results of wave–resistance coefficient over a range of low Froude numbers. Based on the same perturbation method, in 1977, Dawson[2] developed a numerical method by distributing the Rankine sources on the body surface and on the local free surface around the body. A wave field was superimposed on the double–body flow. The source strength distribution on the body surface and on the local free surface was obtained by satisfying the body boundary condition and the free surface condition. The radiation condition, which states that the ship waves occur only behind the ship, was replaced by a one–side finite difference operator for the second derivative of the potential in the direction of the double–body streamlines appearing in Dawson's free surface boundary condition. Good numerical results were obtained by Dawson's method despite the fact that the numerical treatment of the radiation condition has no theoretical support.

The finite element method is known to be flexible for the nonlinear problem and for the boundary value problem with a complicated boundary. Therefore many researchers have developed numerical methods based on the finite element method to solve the free surface flow problems. Bai[3] developed the localized finite element method for calculating wave resistance of a body moving in a channel. Recently Bai and others[4] successfully used the finite element method to solve the nonlinear wavemaking problem in shallow water, but his method was not applied to the infinite domain. Eatok–Taylor and Wu[5] used the coupled element method to calculate wave resistance and lift on 2–D submerged cylinders, but did not cover the 3–D ship wavemaking problem.

In this work, a new order analysis of the wavemaking potential is developed. As a result, a simplified free surface condition, which takes account of the effect of nonlinearity but is different from Dawson's free surface condition, is obtained. The coupled element method is employed to solve the 3–D ship wavemaking problem. In the numerical computation, the flow domain is divided into two regions as shown in Fig.1: the inner region originates around the ship hull and is bounded by surfaces $S_j + S_B + S_{F_1}$; the outer region is outside the interface S_j and is bounded by surfaces $S_j + S_{F_2} + S_\infty$. In the inner region the effect of nonlinearity of the free surface is very important, so that the finite element method is used together with the simplified nonlinear free surface condition. The effect of nonlinearity is negligible in the outer region far from the ship hull, where the Green function method is employed with the linear free surface condition. The Kelvin source function is adopted as the Green function, consequently, the radiation condition is satisfied exactly. By matching the solutions of the inner and outer regions at the interface of two regions, the solution for the entire flow field can be found. Numerical computations have been carried out for a submerged cylinder, a submerged sphere, a Wigly model and also a Series 60 Block 60 ship model. The computed results agree well with the experimental results.

2 The Free Surface Condition

2.1 Exact Mathematical Expression for the Wavemaking Potential

The coordinate system and flow domain are shown in Fig. 1. It is assumed that the fluid is ideal and incompressible, and the flow is irrotational and steady. The Froude number is defined by $F_n = \frac{U}{\sqrt{gL}}$, where U is the ship speed, g the gravitational constant and L the ship length. The

total velocity potential is written as

$$\Phi = x + \phi \qquad (1)$$

in which ϕ must satisfy the Laplace equation

$$\nabla^2 \phi = 0 \quad in \ domain \ D \qquad (2)$$

subject to the following boundary conditions:

$$\eta + F_n^2\left(\frac{\partial \phi}{\partial x} + \frac{1}{2}\nabla\phi \cdot \nabla\phi\right) = 0$$
$$on \ the \ free \ surface \ \eta(x,y) \qquad (3)$$

$$\frac{\partial \eta}{\partial x} + \frac{\partial \phi}{\partial x}\frac{\partial \eta}{\partial x} + \frac{\partial \phi}{\partial y}\frac{\partial \eta}{\partial y} - \frac{\partial \phi}{\partial z} = 0$$
$$on \ the \ free \ surface \ \eta(x,y) \qquad (4)$$

$$\frac{\partial \phi}{\partial n} = -n_x$$
$$on \ the \ body \ surface \ S_B \qquad (5)$$

$$\phi = \begin{cases} O\left(\frac{1}{\sqrt{x^2+y^2}}\right) & x < 0 \\ O(1) & x > 0 \end{cases}$$
$$for \ x^2 + y^2 \to \infty \qquad (6)$$

The problem described by $(2) - (6)$ is the exact mathematical representation of the boundary value problem of the ship wavemaking potential.

2.2 Simplification of the Free Surface Condition

The ship wavemaking problem described by $(2) - (6)$ is a highly nonlinear problem. As well-known, the difficulty lies in that the free surface condition is nonlinear and must be satisfied on the unknown surface. Before trying to solve the nonlinear problem, we have to simplify the free surface condition. It is assumed that the Froude number, F_n, is sufficiently small.

By substituting (3) into (4) and keeping the terms of the products of derivatives of ϕ

$$\frac{\partial \phi}{\partial z} + F_n^2\frac{\partial^2 \phi}{\partial x^2} + 2F_n^2\nabla\phi_x \cdot \nabla\phi = 0$$
$$on \ z = \eta(x,y) \qquad (7)$$

after applying Taylor's expansion to the wave elevation and again keeping the products of derivatives of ϕ, we obtain

$$\frac{\partial \phi}{\partial z} - F_n^2\frac{\partial \phi}{\partial x}\frac{\partial^2 \phi}{\partial z^2} + F_n^2\frac{\partial^2 \phi}{\partial x^2} - F_n^4\frac{\partial \phi}{\partial x}\frac{\partial^3 \phi}{\partial x^2 \partial z}$$

$$+2F_n^2\nabla\phi_x \cdot \nabla\phi = 0 \qquad on \ z = 0 \qquad (8)$$

The disturbance potential ϕ can be further decomposed into two parts,

$$\phi = \varphi_r + \varphi \qquad (9)$$

where φ_r denotes the double body disturbance potential and φ the wave disturbance potential.

If we assume that:

$$(1) \qquad |\frac{\partial \varphi_r}{\partial x_i}| = O(F_n^k), \quad \frac{\partial}{\partial x_i} = O(1)$$
$$for \ \varphi_r, \quad i = 1,2,3$$

$$(2) \qquad \varphi = O(F_n^n), \quad \frac{\partial}{\partial x_i} = O(F_n^{-2}),$$
$$for \ \varphi, \quad i = 1,2,3$$

Substituting (9) into (8), we obtain

$$\frac{\partial \varphi}{\partial z} - F_n^2\frac{\partial \varphi}{\partial x}\frac{\partial^2 \varphi}{\partial z^2} - F_n^2\frac{\partial \varphi}{\partial x}\frac{\partial^2 \varphi_r}{\partial z^2}$$

$$-F_n^2\frac{\partial \varphi_r}{\partial x}\frac{\partial^2 \varphi}{\partial z^2} - F_n^2\frac{\partial \varphi_r}{\partial x}\frac{\partial^2 \varphi_r}{\partial z^2}$$

$$+F_n^2\frac{\partial^2 \varphi}{\partial x^2} + F_n^2\frac{\partial^2 \varphi_r}{\partial x^2} - F_n^4\frac{\partial \varphi}{\partial x}\frac{\partial^3 \varphi}{\partial x^2 \partial z}$$

$$-F_n^4\frac{\partial \varphi_r}{\partial x}\frac{\partial^3 \varphi}{\partial x^2 \partial z} + 2F_n^2\frac{\partial \varphi}{\partial x}\frac{\partial^2 \varphi}{\partial x^2}$$

$$+2F_n^2\frac{\partial \varphi}{\partial x}\frac{\partial^2 \varphi_r}{\partial x^2} + 2F_n^2\frac{\partial \varphi_r}{\partial x}\frac{\partial^2 \varphi}{\partial x^2}$$

$$+2F_n^2\frac{\partial \varphi_r}{\partial x}\frac{\partial^2 \varphi_r}{\partial x^2} + 2F_n^2\frac{\partial \varphi}{\partial y}\frac{\partial^2 \varphi}{\partial x \partial y}$$

$$+2F_n^2\frac{\partial \varphi}{\partial y}\frac{\partial^2 \varphi_r}{\partial x \partial y} + 2F_n^2\frac{\partial \varphi_r}{\partial y}\frac{\partial^2 \varphi}{\partial x \partial y}$$

$$+2F_n^2\frac{\partial \varphi_r}{\partial y}\frac{\partial^2 \varphi_r}{\partial x \partial y} + 2F_n^2\frac{\partial \varphi}{\partial z}\frac{\partial^2 \varphi}{\partial x \partial z} = 0$$
$$on \ z = 0 \qquad (10)$$

If (10) is classified according to the following orders

$$A: \quad O(F_n^{n-2}), \quad \frac{\partial \varphi}{\partial z} + F_n^2\frac{\partial^2 \varphi}{\partial x^2}$$

$$B: \quad O(F_n^{k+2}), \quad +F_n^2\frac{\partial^2 \varphi_r}{\partial x^2}$$

$C:$ $O(F_n^{2k+2})$, $-F_n^2 \dfrac{\partial \varphi_r}{\partial x} \dfrac{\partial^2 \varphi_r}{\partial z^2}$

$$+2F_n^2 \frac{\partial \varphi_r}{\partial x} \frac{\partial^2 \varphi_r}{\partial x^2}$$

$$+2F_n^2 \frac{\partial \varphi_r}{\partial y} \frac{\partial^2 \varphi_r}{\partial x \partial y}$$

$D:$ $O(F_n^{n+k-2})$, $-F_n^2 \dfrac{\partial \varphi_r}{\partial x} \dfrac{\partial^2 \varphi}{\partial z^2}$

$$-F_n^4 \frac{\partial \varphi_r}{\partial x} \frac{\partial^3 \varphi}{\partial x^2 \partial z}$$

$$+2F_n^2 \frac{\partial \varphi_r}{\partial y} \frac{\partial^2 \varphi}{\partial x \partial y}$$

$$+2F_n^2 \frac{\partial \varphi_r}{\partial x} \frac{\partial^2 \varphi}{\partial x^2}$$

$E:$ $O(F_n^{n+k})$, $-F_n^2 \dfrac{\partial \varphi}{\partial x} \dfrac{\partial^2 \varphi_r}{\partial z^2}$

$$+2F_n^2 \frac{\partial \varphi}{\partial x} \frac{\partial^2 \varphi_r}{\partial x^2}$$

$$+2F_n^2 \frac{\partial \varphi}{\partial y} \frac{\partial^2 \varphi_r}{\partial x \partial y}$$

$F:$ $O(F_n^{2n-4})$, $-F_n^2 \dfrac{\partial \varphi}{\partial x} \dfrac{\partial^2 \varphi}{\partial z^2}$

$$-F_n^4 \frac{\partial \varphi}{\partial x} \frac{\partial^3 \varphi}{\partial x^2 \partial z}$$

$$+2F_n^2 \frac{\partial \varphi}{\partial x} \frac{\partial^2 \varphi}{\partial x^2}$$

$$+2F_n^2 \frac{\partial \varphi}{\partial y} \frac{\partial^2 \varphi}{\partial x \partial y}$$

$$+2F_n^2 \frac{\partial \varphi}{\partial z} \frac{\partial^2 \varphi}{\partial x \partial z}$$

From above, these different groups generally differ from one another with their orders of magnitude. It is clear that:

1. for the terms with the wave potential φ, no matter what value n is, the following is always true:

$$n - 2 < n + k - 2 < n + k$$

which means that group D is smaller than group A by $O(F_n^k)$, and group E is smaller than group D by $O(F_n^2)$.

2. for the terms only including the double-body disturbance potential, no matter what value k is, the following always exists

$$k + 2 < 2k + 2$$

which means that group C is smaller than group B by $O(F_n^k)$.

The order of magnitude of each group with the difference between n and k is shown in Table 1.

Table 1   The order of magnitude
with the difference between n and k

GROUP	ORDER	n=k+5	n=k+4	n=k+3	n=k+2
A	n-2	k+3	k+2	k+1	k
B	k+2	k+2	k+2	k+2	k+2
C	2k+2	2k+2	2k+2	2k+2	2k+2
D	n+k-2	2k+3	2k+2	2k+1	2k
E	n+k	2k+5	2k+4	2k+3	2k+2
F	2n-4	2k+6	2k+4	2k+2	2k

From Table 1, it can be seen that:

1. Group E is the first one to be neglected.

2. With a decrease of the difference between n and k, group F becomes more influential and group C becomes less influential.

3. In addition to groups A and B, the first group to be considered is group D.

4. The value of k has no effect on the choice of the terms in the free surface condition.

The difference between n and k represents the magnitude of the wave potential. The large difference shows the small effect of wave potential, and the small difference means that large wave has been made by the ship at high speed. Since we assume that the ship speed is low, the small difference will lead to invalidation of the assumption, therefore in the numerical calculation we only keep groups A, B, C and D in the free surface condition:

$$\frac{\partial \varphi}{\partial z} + F_n^2 \frac{\partial^2 \varphi}{\partial x^2} + 3F_n^2 \frac{\partial \varphi_r}{\partial x} \frac{\partial^2 \varphi}{\partial x^2}$$

$$+2F_n^2 \frac{\partial \varphi_r}{\partial y} \frac{\partial^2 \varphi}{\partial x \partial y} + F_n^2 \frac{\partial \varphi_r}{\partial x} \frac{\partial^2 \varphi}{\partial y^2}$$

$$-F_n^4 \frac{\partial \varphi_r}{\partial x} \frac{\partial^3 \varphi}{\partial x^2 \partial z} + F_n^2 \frac{\partial^2 \varphi_r}{\partial x^2}$$

$$+3F_n^2 \frac{\partial \varphi_r}{\partial x} \frac{\partial^2 \varphi_r}{\partial x^2} + 2F_n^2 \frac{\partial \varphi_r}{\partial y} \frac{\partial^2 \varphi_r}{\partial x \partial y}$$

$$+F_n^2 \frac{\partial \varphi_r}{\partial x} \frac{\partial^2 \varphi_r}{\partial y^2} = 0$$

$$z = 0 \qquad\qquad (11)$$

48

If only the group A is kept in the free surface condition, the well–known linear free surface condition is obtained:

$$\frac{\partial \varphi}{\partial z} + F_n^2 \frac{\partial \varphi}{\partial x^2} = 0$$
$$z = 0 \qquad (12)$$

3   The Coupled Element Method for the Ship Wavemaking Problem

In the boundary value problem of ship wavemaking, the wave disturbance potential should satisfy:

$$\nabla^2 \varphi = 0 \qquad\qquad z \leq 0 \qquad (13)$$

$$\frac{\partial \varphi}{\partial z} = f_1(x, y) \qquad z = 0 \qquad (14)$$

$$\frac{\partial \varphi}{\partial n} = f_2(x, y, z) \qquad on \ S_B \qquad (15)$$

$$\varphi = \begin{cases} O\left(\frac{1}{\sqrt{x^2+y^2}}\right) & x < 0 \\ O(1) & x > 0 \end{cases}$$
$$for \ x^2 + y^2 \to \infty \qquad (16)$$

where for the linear ship wavemaking problem, $f_1(x, y) = -F_n^2 \frac{\partial^2 \varphi}{\partial x^2}$, $f_2(x, y, z) = -n_x$; and for the nonlinear problem, it is easy to obtain $f_1(x, y)$ from (11), and $f_2(x, y, z) = 0$.

As mentioned before, for numerical calculation, the flow domain is divided into two regions. In the inner region around the ship hull, the finite element method is used to solve the nonlinear problem; whereas, the effect of nonlinearity is negligible in the outer region far from the ship hull, thus the Green function method is adopted to solve the linear problem. By matching the solutions of inner and outer regions at their interface, the solution for the entire flow field can be obtained.

The flow domain is shown in Fig. 1. D_1, with the boundary $S_1 = S_B + S_{F_1} + S_j$, represents the inner region where the wave potential is defined by φ_1. D_2, with the boundary $S_2 = S_j + S_{F_2} + S_\infty$, represents the outer region where the wave potential is defined by φ_2. On S_j, the interface of two regions, φ_1 and φ_2 should satisfy the matching conditions:

$$\varphi_1 = \varphi_2 \qquad on \ S_j \qquad (17)$$

$$\frac{\partial \varphi_1}{\partial n} = -\frac{\partial \varphi_2}{\partial n} \qquad on \ S_j \qquad (18)$$

3.1   The Green Function Method for φ_2 in the Outer Region

In the outer region D_2, the linear free surface condition (12) is used. Applying the Green function method to the potential φ_2 in D_2 gives

$$\varphi_2(p) = \int\int_{S_2} \left[\frac{\partial G}{\partial n}\varphi_2 - \frac{\partial \varphi_2}{\partial n}G\right] dS$$
$$= \int\int_{S_j+S_{F_2}+S_\infty} \left[\frac{\partial G}{\partial n}\varphi_2 - \frac{\partial \varphi_2}{\partial n}G\right] dS$$
$$for \ p \in D_2 \qquad (19)$$

Using the matching conditions (17) and (18), on the surface S_j, we obtain

$$\frac{\alpha \varphi_1(p)}{4\pi} + \int\int_{S_j} \frac{\partial G}{\partial n}\varphi_1 dS$$
$$-F_n^2 \int_{L_1+L_2} \frac{\partial G}{\partial n}\varphi_1 dy$$
$$= \int\int_{S_j} G\frac{\partial \varphi_1}{\partial n}dS - F_n^2 \int_{L_1+L_2} G\frac{\partial \varphi_1}{\partial n}dy$$
$$for \ p \in S_j \qquad (20)$$

where α is the solid angle at the control point p on S_j and G is the Kelvin source function[8]

$$G = \frac{1}{4\pi}\Bigg\{ -\frac{1}{r} + \frac{1}{r_1}$$
$$+\frac{F_n^{-2}}{\pi} \cdot Re \int_0^{2\pi}\int_0^\infty \frac{\sec^2\theta}{k - \sec^2\theta}$$
$$\cdot exp\Big[kF_n^{-2}[(z + z_0) + i(x - x_0)\cos\theta$$
$$+i(y - y_0)\sin\theta]\Big]dkd\theta$$
$$-Re2i \int_{-\frac{\pi}{2}}^{\frac{\pi}{2}} F_n^{-2}\sec^2\theta$$
$$\cdot exp\Big[F_n^{-2}\sec^2\theta \cdot [(z + z_0) + i(x - x_0)\cos\theta$$
$$+i(y - y_0)\sin\theta]\Big]d\theta \Bigg\} \qquad (21)$$

$$r = \sqrt{(x - x_0)^2 + (y - y_0)^2 + (z - z_0)^2}$$
$$r_1 = \sqrt{(x - x_0)^2 + (y - y_0)^2 + (z + z_0)^2}$$

If φ_1 and $\frac{\partial \varphi_1}{\partial n}$ in D_1 are now approximated by

$$\varphi_1 = \sum_{i=1} \varphi_{1i}N_i \qquad (22)$$

$$\frac{\partial \varphi_1}{\partial n} = \sum_{i=1} \left(\frac{\partial \varphi_1}{\partial n}\right)_i N_i \qquad (23)$$

where N_i is the so-called shape function. If the problem we deal with is a Neumann–Kelvin problem of a submerged body, we can choose the inner region under the free surface, then the line integral on the line $L_1 + L_2$ will disappear. Eq. (20) can be simply rewritten in a discretized form

$$[A][\varphi_1] = [B]\left[\frac{\partial \varphi_1}{\partial n}\right] \qquad (24)$$

or, identically,

$$\left[\frac{\partial \varphi_1}{\partial n}\right] = [C][\varphi_1] = [B]^{-1}[A][\varphi_1] \qquad (25)$$

where the element of [A] is

$$a_{ij} = \frac{\alpha \delta_{ij}}{4\pi} + \int\int_{S_j} \frac{\partial G(P_j)}{\partial n} \cdot N_i dS \qquad (26)$$

the element of [B] is

$$b_{ij} = \int\int_{S_j} G(P_j) \cdot N_i dS \qquad (27)$$

In a general case, the line integral on $L_1 + L_2$ exists, then Eq.(20) can not be written as (24). We have to pay special attention to the treatment of the line integral.

3.2 Auxiliary Equations for Computing the Line Integral on the Free Surface

When the boundary of the inner region D_1 includes the free surface S_{F_1}, the line integral on $L_1 + L_2$ exists(please see Fig. 1). Since the Kelvin source function is not defined on the free surface when control points are the nodes on the $L_1 + L_2$, the Kelvin sources cannot be distributed on these points. After discretization, the number of equations is not equal to the number of nodes on the interface S_j, then the linear equation system is not in a closed form. It can be expressed by the following matrix form

$$[D][\varphi_1] + [E][\varphi_{10}] = [F][\frac{\partial \varphi_1}{\partial n}] + [H][\frac{\partial \varphi_{10}}{\partial n}] \quad (28)$$

where $[\varphi_1]$ is the unknown potential vector at the nodes on the surface S_j under the free surface, and $[\varphi_{10}]$ is the unknown potential vector at the nodes on the path of the line integral. [D] and [F]

are the coefficient matrices including the contribution from both surface integrals and line integrals on the interface elements, [E] and [H] are the coefficient matrices only related to line integrals on $L_1 + L_2$.

Since the system equation expressed by Eq.(28) is not in a closed form, we have to establish auxiliary equations from the relationship between φ_1 and $\frac{\partial \varphi_1}{\partial n}$ on $L_1 + L_2$. The potential φ_1 has to satisfy the following conditions: φ_1 is continuous in D_1, and the continuity is extended to the boundary of D_1; in addition, φ_1 has to satisfy the Laplace equation and the free surface condition.

By the finite element approach, we can write

$$\varphi_1 = \sum_{i=1} \varphi_{1i} \cdot N_i(\xi, \eta, \zeta) \qquad (29)$$

$$\frac{\partial \varphi_1}{\partial n} = \sum_{i=1} (\frac{\partial \varphi_1}{\partial n})_i \cdot N_i(\xi, \eta, \zeta) \quad (30)$$

then we have

$$\frac{\partial \varphi_1}{\partial z} = \frac{\partial \varphi_1}{\partial \xi} \cdot \frac{\partial \xi}{\partial z} + \frac{\partial \varphi_1}{\partial \eta} \cdot \frac{\partial \eta}{\partial z} + \frac{\partial \varphi_1}{\partial \zeta} \cdot \frac{\partial \zeta}{\partial z} \quad (31)$$

For example, on L_2, we have

$$\frac{\partial \varphi_1}{\partial n} = \frac{\partial \varphi_1}{\partial x} \qquad (32)$$

$$\frac{\partial^2 \varphi_1}{\partial x^2} = \frac{\partial(\frac{\partial \varphi_1}{\partial x})}{\partial x} = \frac{\partial(\frac{\partial \varphi_1}{\partial n})}{\partial x}$$
$$= \frac{\partial(\frac{\partial \varphi_1}{\partial n})}{\partial \xi} \cdot \frac{\partial \xi}{\partial x} + \frac{\partial(\frac{\partial \varphi_1}{\partial n})}{\partial \eta} \cdot \frac{\partial \eta}{\partial x}$$
$$+ \frac{\partial(\frac{\partial \varphi_1}{\partial n})}{\partial \zeta} \cdot \frac{\partial \zeta}{\partial x} \qquad (33)$$

In the outer region D_2, we have the linear free surface condition:

$$\frac{\partial \varphi}{\partial z} + F_n^2 \frac{\partial^2 \varphi}{\partial x^2} = 0$$

After discretization, we can write the matrix form

$$[P][\varphi_1] + [Q][\varphi_{10}] = [R][\frac{\partial \varphi_1}{\partial n}] + [S][\frac{\partial \varphi_{10}}{\partial n}] \quad (34)$$

combining (28) and (34), we get

$$\begin{bmatrix} D & E \\ P & Q \end{bmatrix} \begin{bmatrix} \varphi_1 \\ \varphi_{10} \end{bmatrix} = \begin{bmatrix} F & H \\ R & S \end{bmatrix} \begin{bmatrix} \frac{\partial \varphi_1}{\partial n} \\ \frac{\partial \varphi_{10}}{\partial n} \end{bmatrix}$$
$$(35)$$

50

we can also write (35) as

$$[\frac{\partial \varphi_1}{\partial n}] = [C][\varphi_1] = [B]^{-1}[A][\varphi_1] \qquad (36)$$

where

$$[A] = \begin{bmatrix} D & E \\ P & Q \end{bmatrix}_{N \times M}$$

$$[B] = \begin{bmatrix} F & H \\ R & S \end{bmatrix}_{N \times N}$$

where N is the total number of nodes on the S_j, and M is the total number of nodes on the elements only along the line integral path plus the total number of nodes on the S_j.

3.3 The Finite Element Method for φ_1 in D_1

According to the Galerkin method, for every N_i, $\varphi_1(x, y, z)$ has to satisfy

$$\int\int\int_{D_1} \nabla^2 \varphi_1 \cdot N_i dV = 0 \qquad (37)$$

By the Green thoerom, it is clear that

$$\int\int\int_{D_1} \nabla \varphi_1 \cdot \nabla N_i dV - \int\int_{S_1} \frac{\partial \varphi_1}{\partial n} \cdot N_i dS = 0 \qquad (38)$$

where $S_1 = S_j + S_B + S_{F_1}$.

(38) becomes

$$\int\int\int_{D_1} \nabla \varphi_1 \cdot \nabla N_i dV - \int\int_{S_1} \frac{\partial \varphi_1}{\partial n} \cdot N_i dS$$

$$= \int\int\int_{D_1} \nabla \varphi_1 \cdot \nabla N_i dV - \int\int_{S_j} \frac{\partial \varphi_1}{\partial n} \cdot N_i dS$$

$$- \int\int_{S_B} f_2(x, y, z) \cdot N_i dS$$

$$- \int\int_{S_{F_1}} f_1(x, y) \cdot N_i dx dy = 0 \qquad (39)$$

a. the Neumann–Kelvin problem

For the Neumann–Kelvin problem

$$f_1(x, y) = \frac{\partial \varphi_1}{\partial z} = -F_n^2 \frac{\partial^2 \varphi_1}{\partial x^2} \qquad (40)$$

$$f_2(x, y, z) = -n_x \qquad (41)$$

(39) becomes

$$\int\int\int_{D_1} \nabla \varphi_1 \cdot \nabla N_i dV - \int\int_{S_j} \frac{\partial \varphi_1}{\partial n} \cdot N_i dS$$

$$- F_n^2 \int\int_{S_{F_1}} \frac{\partial \varphi_1}{\partial x} \cdot \frac{\partial N_i}{\partial x} dx dy$$

$$+ F_n^2 \int_{L_B} \frac{\partial \varphi_1}{\partial x} \cdot N_i dy$$

$$+ F_n^2 \int_{L_1+L_2} \frac{\partial \varphi_1}{\partial n} \cdot N_i dy$$

$$= - \int\int_{S_B} n_x \cdot N_i dS \qquad (42)$$

From (36),

$$(\frac{\partial \varphi_1}{\partial n})_j = \sum_{k=1} c_{jk} \cdot \varphi_{1k} \qquad (43)$$

$$\frac{\partial \varphi_1}{\partial n} = \sum_{j=1} \sum_{k=1} c_{jk} \cdot \varphi_{1k} \cdot N_j \qquad (44)$$

Substituting (43) and (44) into (42), we write (42) as a matrix form

$$[U + V][\varphi_1] = [W] \qquad (45)$$

where the elements of [U] are

$$u_{ij} = \int\int\int_{D_1} \nabla N_i \cdot \nabla N_j dV$$

$$- F_n^2 \int\int_{S_{F_1}} \frac{\partial N_i}{\partial x} \cdot \frac{\partial N_j}{\partial x} dx dy$$

$$+ F_n^2 \int_{L_B} N_i \cdot \frac{\partial N_j}{\partial x} dy \qquad (46)$$

The matrix [V] expresses the matching conditions. Its elements are

$$v_{ij} = - \int\int_{S_j} N_i \cdot \sum_{k=1} N_k \cdot c_{jk} dS$$

$$+ F_n^2 \int_{L_1+L_2} N_i \cdot \sum_{k=1} N_k \cdot c_{jk} dy$$

$$\qquad (47)$$

[W] is the known vector,

$$w_i = - \int\int_{S_B} n_x \cdot N_i dS \qquad (48)$$

51

b. the nonlinear problem

For the nonlinear problem, refer to Eq.(11) and Eq.(14)

$$
\begin{aligned}
f_1(x,y) &= -F_n^2 \Big(\frac{\partial^2 \varphi_1}{\partial x^2} + 3 \frac{\partial \varphi_r}{\partial x} \cdot \frac{\partial^2 \varphi_1}{\partial x^2} \\
& \frac{\partial \varphi_r}{\partial y} \cdot \frac{\partial^2 \varphi_1}{\partial x \partial y} + \frac{\partial \varphi_r}{\partial x} \cdot \frac{\partial^2 \varphi_1}{\partial y^2} \\
& -F_n^2 \frac{\partial \varphi_r}{\partial x} \cdot \frac{\partial^3 \varphi_1}{\partial x^2 \partial z} \Big) \\
& -F_n^2 \Big(\frac{\partial^2 \varphi_r}{\partial x^2} + 3 \frac{\partial \varphi_r}{\partial x} \cdot \frac{\partial^2 \varphi_r}{\partial x^2} \\
& +2 \frac{\partial \varphi_r}{\partial y} \cdot \frac{\partial^2 \varphi_r}{\partial x \partial y} + \frac{\partial \varphi_r}{\partial x} \cdot \frac{\partial^2 \varphi_r}{\partial y^2} \Big)
\end{aligned} \tag{49}
$$

For Eq.(15)

$$ f_2(x,y,z) = 0 \tag{50} $$

Similarly as (45), for the nonlinear problem we can also obtain

$$ [U + V][\varphi_1] = [W] \tag{51} $$

where

$$
\begin{aligned}
u_{ij} &= \iiint_{D_1} \nabla N_i \cdot \nabla N_j dV \\
& +F_n^2 \iint_{S_{F_1}} \Big[- \frac{\partial N_i}{\partial x} \cdot \frac{\partial N_j}{\partial x} \\
& -3 \frac{\partial N_j}{\partial x} \cdot \Big(\frac{\partial^2 \varphi_r}{\partial x^2} \cdot N_i + \frac{\partial \varphi_r}{\partial x} \cdot \frac{\partial N_i}{\partial x} \Big) \\
& -2 \frac{\partial N_j}{\partial y} \cdot \Big(\frac{\partial^2 \varphi_r}{\partial x \partial y} \cdot N_i + \frac{\partial \varphi_r}{\partial y} \cdot \frac{\partial N_i}{\partial x} \Big) \\
& - \frac{\partial N_j}{\partial y} \cdot \Big(\frac{\partial^2 \varphi_r}{\partial x \partial y} \cdot N_i + \frac{\partial \varphi_r}{\partial y} \cdot \frac{\partial N_i}{\partial y} \Big) \\
& +F_n^2 \frac{\partial^2 N_j}{\partial x \partial z} \cdot \Big(\frac{\partial^2 \varphi_r}{\partial x^2} \cdot N_i \\
& + \frac{\partial \varphi_r}{\partial x} \cdot \frac{\partial N_i}{\partial x} \Big) \Big] dx dy \\
& +F_n^2 \int_{L_B} \Big[\frac{\partial N_j}{\partial x} \cdot N_i \big(1 + 3 \frac{\partial \varphi_r}{\partial x} \big) \\
& +2 \frac{\partial \varphi_r}{\partial y} \cdot \frac{\partial N_j}{\partial y} \cdot N_i \\
& -F_n^2 \frac{\partial \varphi_r}{\partial x} \cdot \frac{\partial^2 N_j}{\partial x \partial z} \cdot N_i \Big] dy \\
& +F_n^2 \int_{L_B} \frac{\partial \varphi_r}{\partial x} \cdot \frac{\partial N_j}{\partial y} \cdot N_i dx
\end{aligned}
$$

$$
\begin{aligned}
& +F_n^2 \int_{L_2} \Big[2 \frac{\partial \varphi_r}{\partial y} \cdot \frac{\partial N_j}{\partial y} \cdot N_i \\
& -F_n^2 \frac{\partial \varphi_r}{\partial x} \cdot \frac{\partial^2 N_j}{\partial x \partial z} \cdot N_i \Big] dy \\
& +F_n^2 \int_{L_1} \Big[-2 \frac{\partial \varphi_r}{\partial y} \cdot \frac{\partial N_j}{\partial y} \cdot N_i \\
& +F_n^2 \frac{\partial \varphi_r}{\partial x} \cdot \frac{\partial^2 N_j}{\partial x \partial z} \cdot N_i \Big] dy
\end{aligned} \tag{52}
$$

$$
\begin{aligned}
v_{ij} &= - \iint_{S_j} N_i \cdot \sum_{k=1} N_k \cdot c_{kj} dS \\
& +F_n^2 \int_{L_1+L_2} N_i \cdot \sum_{k=1} N_k \cdot c_{kj} dy \\
& +3F_n^2 \int_{L_1+L_2} \frac{\partial \varphi_r}{\partial x} \cdot N_i \cdot \sum_{k=1} N_k \cdot c_{kj} dy \\
& +F_n^2 \int_{L_3} \frac{\partial \varphi_r}{\partial y} \cdot N_i \cdot \sum_{k=1} N_k \cdot c_{kj} dx
\end{aligned} \tag{53}
$$

$$
\begin{aligned}
w_i &= -F_n^2 \iint_{S_{F_1}} \Big[\frac{\partial^2 \varphi_r}{\partial x^2} \\
& +3 \frac{\partial \varphi_r}{\partial x} \cdot \frac{\partial^2 \varphi_r}{\partial x^2} + 2 \frac{\partial \varphi_r}{\partial y} \cdot \frac{\partial^2 \varphi_r}{\partial x \partial y} \\
& + \frac{\partial \varphi_r}{\partial x} \cdot \frac{\partial^2 \varphi_r}{\partial y^2} \Big] \cdot N_i dx dy
\end{aligned} \tag{54}
$$

By solving (51) we can obtain φ_1 for the inner region.

4   Numerical Results

The numerical calculations have been carried out for wave resistance of a 2–D submerged cylinder, a 3–D submerged sphere, a Wigly model and a Series 60 Block 60 model.

From the Bernoulli integral

$$ p = \rho F_n^2 \Big[\frac{\partial \phi}{\partial x} + \frac{(\nabla \phi)^2}{2} \Big] \tag{55} $$

for the nonlinear problem, $\phi = \varphi_r + \varphi_1$.

The wave resistance and lift are calculated by integrating pressure over the wetted body surface.

$$ R_w = \iint_{S_B} p \cdot n_x dS \tag{56} $$

$$ L = \iint_{S_B} p \cdot n_z dS \tag{57} $$

52

4.1 The Submerged Cylinder

For a submerged cylinder the wave resistance and lift have been calculated by the coupled element method. The inner region D_1 was discretized with 8–node isoparameter quadrilateral elements. The nonlinear free surface condition is

$$\frac{\partial \varphi}{\partial z} + F_n^2 \frac{\partial^2 \varphi}{\partial x^2} + 3F_n^2 \frac{\partial \varphi_r}{\partial x} \frac{\partial^2 \varphi}{\partial x^2}$$
$$-F_n^4 \frac{\partial \varphi_r}{\partial x} \frac{\partial^3 \varphi}{\partial x^2 \partial z} + F_n^2 \frac{\partial^2 \varphi_r}{\partial x^2}$$
$$+3F_n^2 \frac{\partial \varphi_r}{\partial x} \frac{\partial^2 \varphi_r}{\partial x^2} = 0$$
$$z = 0 \tag{58}$$

and the 2–D Green function[8] for the outer region is

$$G = \frac{1}{2\pi} \Bigg\{ \ln r + \ln r_1$$
$$+2pv \cdot F_n^{-2} \int_0^\infty \frac{1}{k-1}$$
$$exp\left[kF_n^{-2}(z+z_0)\right] \cdot \cos\left[kF_n^{-2}(x-x_0)\right]$$
$$+2\pi exp\left[F_n^{-2}(z+z_0)\right] \cdot \sin\left[F_n^{-2}(x-x_0)\right] \Bigg\}$$
$$\tag{59}$$

where

$$r = \left[(x-x_0)^2 + (z-z_0)^2\right]^{\frac{1}{2}}$$
$$r_1 = \left[(x-x_0)^2 + (z+z_0)^2\right]^{\frac{1}{2}}$$

The computed results are compared with results from Havelock's analytical solution and Eatock–Taylor and Wu's numerical results as shown in Fig.3. For the Neumann–Kelvin problem, our numerical results agree very well with the referred results. The solution with the non-linear free surface condition is not too different from the solution with the linear free surface condition.

4.2 The Submerged Sphere

Using the coupled element method, the Neumann–Kelvin problem has been solved for a submerged sphere. The inner region D_1 was under the free surface. 20–node isoparameter hexagon elements were used to discretize the inner region. The comparison between the numerical result and Havelock's analytical solution is shown in Fig. 4. They agree very well.

4.3 Wigly Ship Model

The Wigly ship hull of mathematical form is expressed by

$$y = \pm \frac{B}{2} \cdot \left[1 - (\frac{x}{L})^2\right] \cdot \left[1 - (\frac{z}{T})^2\right] \tag{60}$$

where

$$\frac{B}{L} = 0.10000 \qquad \frac{T}{L} = 0.0625$$

with

$$C_B = 0.444 \qquad C_P = 0.667$$
$$C_x = 0.667 \qquad C_s = 0.661$$
$$\frac{S}{L^2} = 0.1487$$

The numerical results for the wave resistance coefficient are compared with the experimental results, shown in Fig. 5. Comparing with the solution with the linear free surface condition, the numerical solution with the simplified nonlinear free surface condition is more agreeable with the experimental results.

4.4 Series 60 Block 60 Ship Model

In the numerical calculation, the inner region D_1 is chosen as $-1.25L \leq x \leq 1.25L$, $0 \leq y \leq 0.5L$ and $-0.06L \leq z \leq 0$. We discretized D_1 into 120 quadratic isoparameter hexahedron elements with 819 nodes. The computed wave resistance coefficient curves are compared with other known results, shown in Fig. 6.

5 Discussion and Concluding Remarks

In the present study, based on the low–speed ship theory, an investigation has been made into the free surface conditions. Through a new approach of the order analysis, a simplified nonlinear free surface condition, which is different from Baba's and Dawson's, has been obtained.

The coupled element method has been introduced for numerical calculation. Efforts have been made for the treatment of the line integral along L_1+L_2 (Fig. 1). Auxiliary equations on the path $L_1 + L_2$ of the line integral were established by using the free surface and continuity conditions to overcome the difficulty arisen in computing the line integral. Also, by using the Kelvin source function as the Green function in the outer

region, no numerical treatment of the radiation condition is needed.

In the finite element method, the form of the shape function and the element dimension have an important effect on the numerical result. The quadratic isoparameter hexahedron elements were used to discretize the inner region in order to match the ship hull geometry. The element dimension has a direct effect on the computer time, storage of data and solution accuracy. Before using the coupled element method to the ship wave-making problem, a special investigation was carried out to find the effect of the element dimension on the numerical results. Wave resistance and lift coefficients of a submerged sphere have been computed for different values of maximum element dimension $L_m/(U^2/g)$. They are shown in Table 2.

Table 2

$L_m/(U^2/g)$	C_w	C_L
0.5	0.06210	-0.02910
1.0	0.06190	-0.02915
1.5	0.06195	-0.02920
2.5	0.06220	-0.02930
3.0	0.06230	-0.02950
3.5	0.06450	-0.03130

From Table 2, it is suggested to keep $L_m/(U^2/g)$ within the limit of 1.0 ~ 3.0 for calculations.

Computations were carried out on Silicon Graphics IRIS 4D/120SX. The CPU time for computing the wave resistance coefficient for one Froude number on the Series 60 Block 60 model is about 28 minutes. For this numerical calculation, the inner region D_1 was discretized into 120 quadratic isoparameter hexahedron elements with 819 nodes, and the interface S_j was represented by 96 quadratic isoparameter quadrilateral elements with 329 nodes. Most of the computer time was consumed on computation of coefficient matrices A and B in Eq.(36) which is related to integrals of the Kelvin source function and its derivatives on quadrilateral elements. The calculation method was mainly based on Shen and Farell's work[9]. The four-point Gaussian quadrature was employed for computing the surface integrals. The nine-point Gaussian quadrature was also applied. It increased the computing time by almost twice for one Froude number but did not

improve the computing results significantly, only varied about 3 to 4%. The computed results of the Series 60 Block 60 model agree well with the experimental results.

Acknowledgements

References

1. Baba, E., and Hara, M., "Numerical Evaluation of Wave–Resistance Theory for Slow Ships," Second International Conference on Numerical Ship Hydrodynamics, Sept. 1977, PP. 17-29.

2. Dawson, C.W., "A Practical Computer Method for Solving Ship Wave Problem," Second International Conference on Numerical Ship Hydrodynamics, Sept. 1977, pp. 30-38.

3. Bai, K.J., "A localized Finite Element Method for Steady Three-Dimensional Free–Surface Flow Problem," Second International Conference on Numerical Ship Hydrodynamics, Sept. 1977, pp. 78-87.

4. Choi, H.S., Bai, K.J., Kim, J.W., and Cho, I.H., "Nonlinear Free Surface Waves Due to a Ship Moving Near the Critical Speed in a Shallow Water," Eighteenth Symposium on Naval Hydrodynamics, 1991, pp. 173-190.

5. Eatock–Taylor, R., and Wu, G.X., "Wave Resistance and Lift on Cylinders By Coupled Element Technique," International Ship Progress, Vol.33, 1986

6. Raven, H., "Adequacy of Free Surface Conditions for the Wave Resistance Problem," Eighteenth Symposium on Naval Hydrodynamics, 1991, pp. 375-396.

7. Aanesland, V., "A Hybrid Model for Calculating Wave–Making Resistance," Fifth International Conference on Numerical Ship Hydrodynamics, Sept. 1989, pp. 657-666.

8. Wehausen, J.V., and Laitone, E.V., "Surface Waves," Handbuch der Physik, Vol.9, 1960

9. Shen, H.T., and Farell, C., "Numerical Calculation of the Wave Integrals in the Linearized Theory of Water Waves," Journal of Ship Research, Vol.21, No.1, 1977, pp. 1-10.
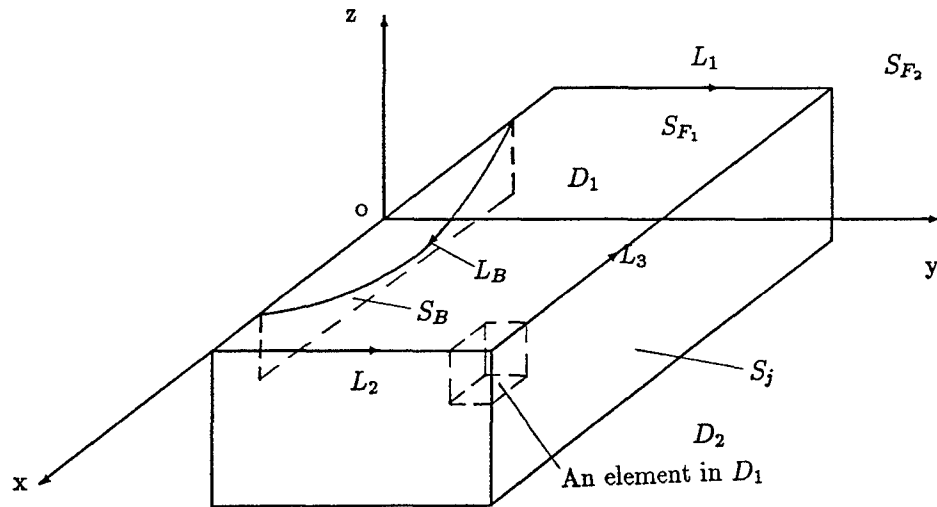
Fig. 1 Coordinate System and Flow Domain
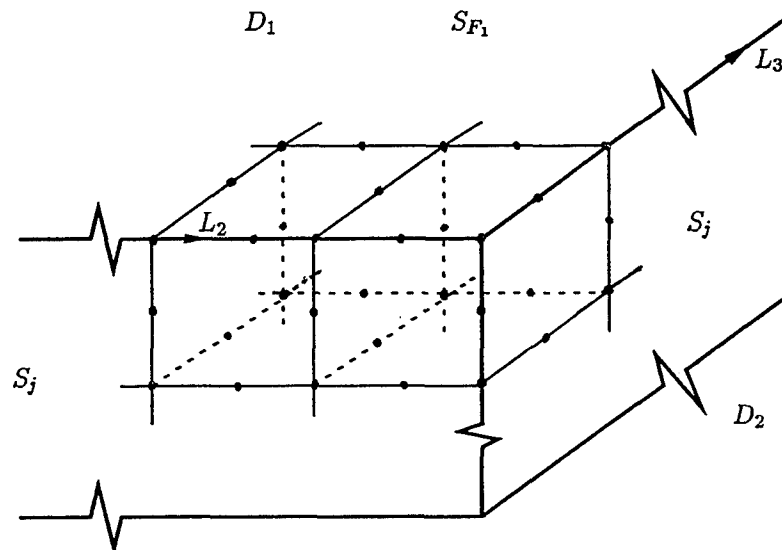
Fig. 2 Finite Elements in D_1

$C_w, C_L * 10$
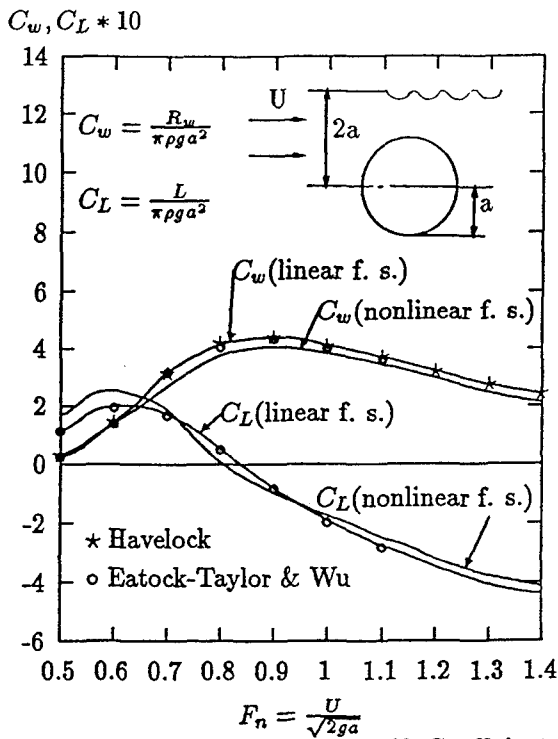
Fig. 3 Wave Resistance and Lift Coefficients
of a Submerged Cylinder

$C_w, C_L * 100$
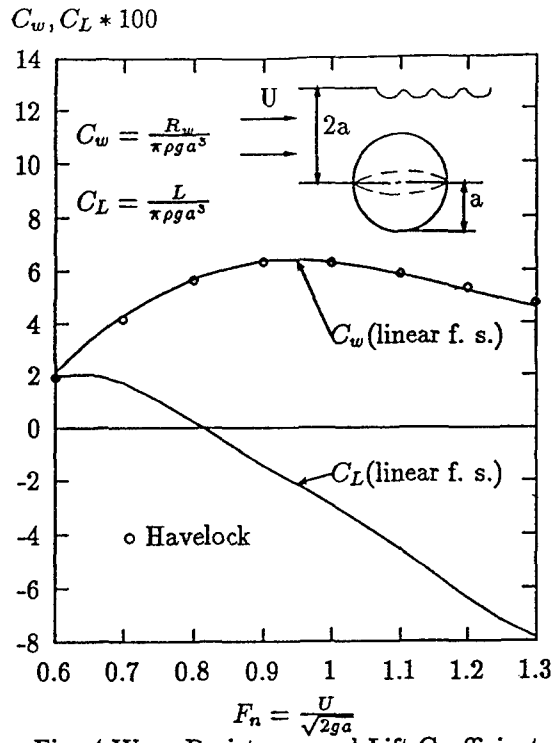
Fig. 4 Wave Resistance and Lift Coefficients
of a Submerged Sphere

$C_w * 10^3$
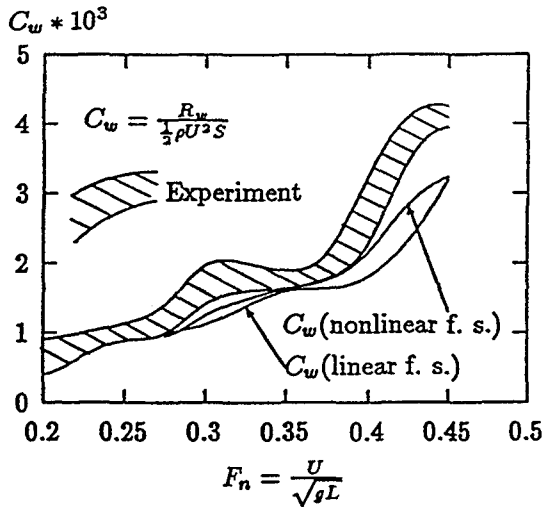
Fig. 5 Wave Resistance Coefficient
of a Wigly Model

$C_w * 10^3$
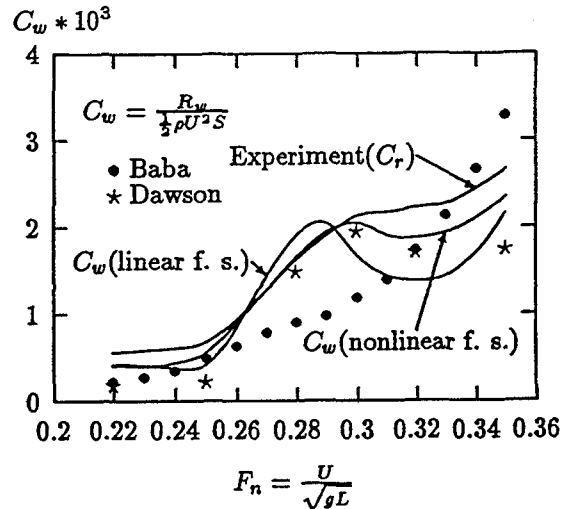
Fig. 6 Wave Resistance Coefficient
of a Series 60 Block 60 Model

Seakeeping and Wave Induced Loads on Ships with Flare by a Rankine Panel Method

P.D. Sclavounos, D.E. Nakos, and Y. Huang
(Massachusetts Institute of Technology, USA)

ABSTRACT

A Rankine Panel Method developed for the prediction of the seakeeping of ships advancing with forward velocity in regular waves is in this paper extended to treat realistic hull forms with flare at their bow and stern. The method is based on the distribution of panels over the ship hull and the free surface with a bi-quadratic spline variation of the velocity potential over their surface. For ships with significant flare or a transom stern a strip of panels forming a 'wake' trailing the ship is introduced and Kutta-type conditions of smooth detachment of the steady and unsteady flow at the stern are enforced.

In steady flow, computations are presented of the Kelvin wake of a transom stern ship and in time-harmonic flow of the hydrodynamic coefficients, heave and pitch motions and wave induced structural loads for the SL7, S-175 hulls and an IACC yacht in head, beam and quartering waves. They are found to be in very good agreement with experimental measurements and point to the importance of effects of flare and the coupling between the steady and unsteady flow components at the bow and stern.

1. INTRODUCTION

The advent of powerful computational environments over the past decade has encouraged the development of numerous three-dimensional panel methods for the solution of the steady, time-harmonic and transient potential flow around ships advancing with forward velocity. The Rankine Panel Method (RPM) has in particular enjoyed thorough study, following the pioneering numerical studies of Dawson(1977) and Gadd(1976). The success of the RPM may be attributed to the property of most forward-speed ship flows that the condition of no waves upstream is sufficient to ensure the proper physical behaviour of the wave patterns trailing a ship in steady and time-harmonic flow and to the simplicity of the Rankine source used as the Green function in the integral equation governing the velocity potential.

Several studies have reported success with the Rankine Panel Method (RPM) for the linear and nonlinear steady potential flow past ships, including Xia(1986), Jensen and Soding (1989), Raven (1992), Kim and Lucas (1990), Reed, Telste and Scragg (1990), and Rosen et. al. (1993). Extensions of the RPM have appeared recently for the solution of forward speed ship flows in the time domain by Cao, Schultz and Beck(1990), Maskew (1992) and the companion paper by Nakos, Kring and Sclavounos (1993), which extends the RPM method of the present study in the time domain.

The present paper reports on the continued development of the RPM developed at MIT over the past several years for the solution of the steady and time-harmonic ship flows [cf. Sclavounos and Nakos (1988), Nakos and Sclavounos (1990a,b)]. To date most RPM's

---

have considered the solution of free surface flows past ships with mathematical shape and wall sided geometries, like the Wigley and the Series 60 (Cb=0.6) hulls. This study reports upon the extension of the MIT RPM method, hereafter referred to as SWAN (ShipWaveANalysis), to the treatment of forward-speed free surface flows past realistic ship forms with significant flare at the bow or stern, including transoms. Both steady and time-harmonic flows are considered, since the accurate solution of the latter is found to hinge upon the proper treatment of the former.

The physics and numerical treatment by RPM methods of the flow past wall sided and flared hulls will next be briefly discussed for the steady flow. Similar conclusions will apply to time-harmonic flow. The most evident difference in the flow around wall-sided versus flared ships is the extent and intensity of the spray formation in the bow region, which is more pronounced for ships with flare. Most RPM's developed to date, including SWAN, are based on the linearization of the free surface condition, and as such they cannot model the formation of spray. Yet the numerical solution in the vicinity of the bow obtained by SWAN is robust and for flared bows tends to predict a significant wave elevation which is typically smaller than measured values.

The properties of the flow near the stern are more subtle. Experiments often suggest that the steady flow in the vicinity of the stern of well designed ships, wall sided, flared or transom, does not display the nonlinearity observed in the bow region. Viscosity is largely responsible for this behaviour, yet unlike the bow region, this regularity is seen to persist both for wall-sided and flared ship forms. As with the unseparated flow at the trailing edge of lifting surfaces, viscosity exerts a regularizing influence upon the potential flow which is a valid model outside the ship boundary layer. Therefore, the proper statement of the boundary value problem governing the potential flow must include a Kutta-type condition in the vicinity of the stern which serves to ensure that the free surface detaches smoothly from the ship hull.

The difference in the local stern flow physics for flared and wall sided hull shapes is significant. It can be best illustrated by considering two ex-

treme hull forms, a thin vertical strut and a flat vessel with a transom stern. For the thin vessel the flow locally resembles a thickness flow symmetric about the stem of the stern, for which a Kutta condition is unnecessary. For the flat vessel the stern flow may be locally approximated by a one-sided lifting flow, with the transom stern playing the role of the trailing edge where a smooth detachment condition must be enforced.

The panel method implemented in SWAN has been extended to account for ship forms with flat sterns. A strip of panels trailing the stern is added forming a free-surface wake equipped with two smooth detachment conditions, namely a specified wave elevation equal to the transom draft and a continuous free surface slope at the stern. Computations of the Kelvin wave pattern of a transom stern destroyer hull demonstrate the effectiveness of these conditions and the convergence of the numerical solution. More details on the steady flow may be found in Nakos and Sclavounos (1993) where the computation of the wave resistance and the Kelvin wave patterns trailing transom stern vessels are discussed.

In the linearized time-harmonic problem, the enforcement of the smooth detachment condition at the transom is similar and equally important for the convergence of the numerical solution, in analogy to the unsteady Kutta condition of finite velocity in lifting flows. Otherwise the time-harmonic forward-speed free surface problem is linearized about the double-body flow, leading to a free surface condition with variable coefficients and a ship hull condition which includes the familiar m-terms. The statement of both boundary value problems is summarized in Sections 2-6.

Computations have been carried out of the heave and pitch added-mass, damping coefficients and exciting forces on three hull forms with significant flare at their bow and stern, namely the S-175 and SL7 hulls and an IACC yacht. Systematic convergence studies were conducted aiming to establish the sensitivity of the numerical solution upon on the number of panels, their aspect ratio and the truncation distance of the free surface mesh upstream, sideways and downstream of the ship.

Ship motion computations with SWAN for wall

58

sided ships like the Wigley and the Series 60 (Cb=0.6), hull have been found to be in very good agreement with experimental measurements in Nakos and Sclavounos (1990). Similar computations for flared ship forms however reveal an overprediction by SWAN of the measured heave and pitch RAO's. Systematic numerical tests suggest a strong sensitivity of the hydrostatic coefficients upon the interaction of the steady wave profile with flared sterns. Especially in the case of the SL7 hull which has a rather long countertop stern, the steady wave profile wets a significant portion of the stern thus altering significantly the restoring coefficients which enter the heave and pitch equations of motion. Computations have been carried out with SWAN of the steady wave profile and its effect upon the heave and pitch hydrostatic coefficients. The resulting motion amplitudes were reduced significantly and were found to be in very good agreement with experiments, unlike their linear counterparts. These computations, including the SWAN heave and pitch motion predictions for a generic IACC yacht hull, are presented in Section 7.

The vertical shear force and bending moment distribution, on the SL-7 and S-175 hulls translating in head, beam and quartering waves are discussed in Sections 6 and 8. Definitions of the wave induced loads in the general three-dimensional case are derived, consistent with the assumptions underlying linear theory. The structural load expressions include surface as well as waterline contributions, the latter found to be significant for ships with flare where the steady wave elevation has a significant value. Computations of the vertical bending moment and shear force for the SL-7 and S-175 hulls were carried out using the linear heave and pitch motion predictions as well as their 'nonlinear' values based on the corrected values of the hydrostatic coefficients derived from the steady wave profile build-up on the stern. Comparison with experimental measurements presented in Dalzell(1992) is found to be very satisfactory in all wave headings. Of particular interest is the contribution of the waterline integrals to the wave loads which may be shown to vanish for wall sided vessels. Their contribution is found to be significant and of comparable magnitude to the integrals over the hull surface, pointing to the importance of flare effects.
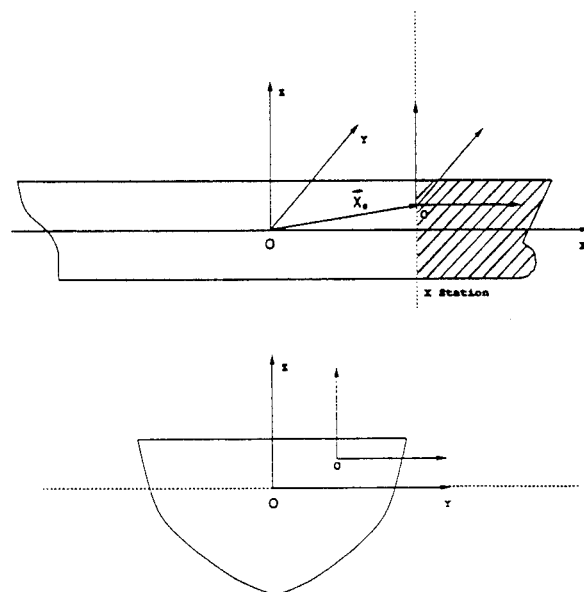
Figure 1 :   Coordinate System.

2. PROBLEM FORMULATION

Figure 1 illustrates a Cartesian coordinate system $\vec{x} = (x, y, z)$ fixed on the mean translating position of the ship which advances in the positive x—direction with a constant velocity U. The positive z—axis points upwards and the origin of the coordinate system is located on the calm water plane. The second coordinate system centered at $\vec{X}_0$ will be used for the derivation of the wave induced structural loads, carried out in Section 6.

Potential flow is assumed, governed by the velocity potential $\Psi(\vec{x})$ which is subject to the Laplace equation in the fluid domain. The nonlinear free surface condition is linearized on the assumption that either the ship hull form is slender or that the ship speed is low. Both these linearization assumptions may be accommodated by the double-body linearization of the free-surface condition, which assumes the decomposition of Ψ into the double-body potential, Φ, the steady wave potential, ϕ , and

the unsteady potential ψ, or

$$\Psi = \Phi + \phi + \psi \ . \qquad (2.1)$$

The flow velocities due to the last two components in (2.1) are assumed small relative to the double-body flow velocity $\nabla\Phi$ which far from the ship tends to a uniform flow with velocity $(-U, 0, 0)$.

The linearized free surface conditions governing the steady and unsteady wave disturbances have been derived and discussed in Nakos and Sclavounos (1990). They take the form:

$$\nabla\Phi \cdot \nabla(\nabla\Phi \cdot \nabla\phi) + \frac{1}{2}\nabla(\nabla\Phi \cdot \nabla\Phi) \cdot \nabla\phi +$$

$$g\phi_z - \Phi_{zz}(\nabla\Phi \cdot \nabla\phi) = -\frac{1}{2}\nabla(\nabla\Phi \cdot \nabla\Phi) \cdot \nabla\Phi$$

$$-\frac{1}{2}(U^2 - \nabla\Phi \cdot \nabla\Phi)\Phi_{zz} \ , \qquad \text{on } z = 0$$

$$\zeta(x, y) = -\frac{1}{g}\left(\frac{1}{2}\nabla\Phi \cdot \nabla\Phi - \frac{1}{2}U^2 + \nabla\Phi \cdot \nabla\phi\right)_{z=0}$$
$$(2.2)$$

for the steady flow, and

$$\psi_{tt} + 2\nabla\Phi \cdot \nabla\psi_t + \nabla\Phi \cdot \nabla(\nabla\Phi \cdot \nabla\psi) +$$

$$\frac{1}{2}\nabla(\nabla\Phi \cdot \nabla\Phi) \cdot \nabla\psi + g\psi_z -$$

$$\Phi_{zz}(\psi_t + \nabla\Phi \cdot \nabla\psi) = 0 \ , \qquad \text{on } z = 0$$

$$\zeta(x, y, t) = -\frac{1}{g}(\psi_t + \nabla\Phi \cdot \nabla\psi)_{z=0} \qquad (2.3)$$

for the unsteady flow.

The linearized the ship hull condition takes the familiar form

$$\frac{\partial \Phi}{\partial n} = 0 \ , \quad \text{on } (\overline{B}) \qquad (2.4)$$

for the double-body flow,

$$\frac{\partial \phi}{\partial n} = 0 \ , \quad \text{on } (\overline{B}) \qquad (2.5)$$

for the steady flow, and

$$\frac{\partial \psi}{\partial n} = \sum_{j=1}^{6}\left(\frac{\partial \xi_j}{\partial t}n_j + \xi_j m_j\right) \ , \quad \text{on } (\overline{B}) \qquad (2.6)$$

for the unsteady flow, all applying on the mean position of the ship hull $\overline{B}$. In equation (2.6)

the summation is carried out over all six rigid-body modes, namely the surge, sway, heave displacements (ξ_1, ξ_2, ξ_3) and the roll, pitch and yaw rotations (ξ_4, ξ_5, ξ_6). The normal vector components n_j are defined as follows, $\vec{n} = (n_1, n_2, n_3)$ and $\vec{x} \times \vec{n} = (n_4, n_5, n_6)$, while the so-called m-terms are defined as in Ogilvie and Tuck (1969) in terms of the double gradients of the double body velocity potential Φ.

Frequency Domain Formulation

It is customary in linear seakeeping theory and computation to solve the boundary value problem for the unsteady flow in the frequency domain. Denote by ϕ_0 the velocity potential of a regular surface wave of amplitude A, absolute frequency ω_0, heading β, relative to the positive x-axis and wavenumber in deep water, $\nu = \omega_0^2/g$. Relative to the translating coordinate system, it is defined as follows:

$$\phi_0(\vec{x}, t) = Re\left(A\varphi_0 e^{i\omega t}\right) , \qquad (2.7)$$

where the complex velocity potential φ_0 is given by

$$\varphi_0(\vec{x}, t) = i\frac{g}{\omega_0}e^{\frac{\omega_0^2}{g}(z - ix\cos\beta - iy\sin\beta)}e^{i\omega t} ,$$
$$(2.8)$$

with the *encounter frequency* ω defined as follows

$$\omega = \mid \omega_0 - U\frac{\omega_0^2}{g}\cos\beta \mid. \qquad (2.9)$$

Decomposing the unsteady wave disturbance into incident, diffraction and radiation components and adopting the complex notation (2.7), the unsteady potential may be cast in the form

$$\psi(\vec{x}, t) = \Re\{e^{i\omega t}[A(\varphi_o + \varphi_7) + i\omega \sum_{j=1}^{6}\xi_j \varphi_i]\} , \qquad (2.10)$$

where φ_7 is the complex diffraction potential and φ_j are the complex radiation potentials due to the harmonic oscillation of the ship in each rigid body mode with unit velocity at the frequency of encounter ω.

60

3. THE HYDRODYNAMIC FORCES AND EQUATIONS OF MOTION

The linearized unsteady hydrodynamic pressure on the mean position of the ship hull follows from Bernoulli's equation,

$$p = -\rho \ (\psi_t + \nabla\Phi \cdot \nabla\psi)_{\vec{x}\in(\overline{B})}$$

$$-\rho \ [(\vec{a} \cdot \nabla)(\frac{1}{2}\nabla\Phi \cdot \nabla\Phi + gz)]_{\vec{x}\in(\overline{B})} \tag{3.1}$$

where $\vec{a}$ denotes the vector oscillatory displacement of the ship surface due to a six-degree-of-freedom oscillatory motion. The second component of (3.1) consists of two terms. The last term contributes the hydrostatic restoring force and moments, while the first term supplies a dynamic correction to the hydrostatic effect which arises from the oscillatory displacement of the ship in the non-uniform steady flow created by the ship forward translation. For the Froude numbers considered in this paper this dynamic contribution to the restoring coefficients was found to be small and was neglected. Yet, at higher Froude numbers this effect may be significant.

The linear equations of motion governing the time-harmonic responses of the ship follow from Newton's law. In complex notation, they accept the familiar form

$$\sum_{j=1}^{6} \ [-\omega^2(m_{ij} + a_{ij}) + i\omega b_{ij} + c_{ij}]\xi_j = X_i \ ,$$

$$i = 1, ..., 6 \ , \tag{3.2}$$

where m_{ij} is the ship inertia matrix, ξ_j the complex amplitude of the ship oscillatory displacement and c_{ij} the matrix which which accounts for hydrostatic and inertia restoring effects. The hydrodynamic added-mass and damping coefficients, a_{ij} and b_{ij} respectively and the exciting forces and moments X_j, are defined as follows

$$X_i = -\rho \ \Re \ \{ \iint_{(\overline{B})} [i\omega(\varphi_0 + \varphi_7) +$$

$$\nabla\Phi \cdot \nabla(\varphi_0 + \varphi_7)] \ n_i ds\}$$

$$a_{ij} = -\frac{\rho}{\omega^2} \ \Re \ \{\iint_{(\overline{B})} (i\omega\varphi_j + \nabla\Phi \cdot \nabla\varphi_j)n_i ds\}$$

$$b_{ij} = \frac{\rho}{\omega} \ \Im \ \{\iint_{(\overline{B})} (i\omega\varphi_j + \nabla\Phi \cdot \nabla\varphi_j)n_i ds\} \tag{3.3}$$

As indicated by (3.1) and (3.3) all hydrodynamic forces are evaluated by direct integration of the hydrodynamic pressure over the mean position of the ship hull. The numerical algorithm implemented in SWAN determines the flow velocity on the panels as part of the solution, therefore, it is unnecessary to apply Stokes' theorem for the evaluation of (3.3) as suggested in Ogilvie and Tuck (1969).

4. THE RANKINE PANEL METHOD

In this section the principal attributes of the Rankine Panel Method developed for the solution of the steady and unsteady free surface problems will be described. Further details may be found in Sclavounos and Nakos (1988) and Nakos and Sclavounos (1990a,b).

Plane quadrilateral panels are distributed over the ship hull and part of the free surface, as illustrated in Figure 3 for the S-175 hull. The potential flow in the fluid domain is solved by an application of Green's second identity for the unknown potentials ϕ, φ using the Rankine unit source as the Green function. The result is an integro-differential equation for the unknown steady and unsteady potentials and their gradients over the mesh illustrated in the Figure. Four aspects of the Rankine Panel Method implemented in SWAN deserve special mention. They are discussed below:

1. Bi-Quadratic Spline Scheme
     — Stability Analysis

A bi-quadratic spline basis function has been introduced for the approximation of the velocity potential over the ship hull and the free surface. The numerical properties of this representation for forward speed free surface flows were studied in Nakos and Sclavounos (1990b). The method was found to be free of numerical damping or amplification, a very desirable property in the computation of ship wave patterns. A stability criterion was developed restricting the selection of the panel aspect ratio relative to the Froude number and frequency rendered non-dimensional by the panel size h. The numerical dispersion of

61

the method was determined to be of $O(h^3)$ which was found to introduce negligible numerical error.

2. Radiation Condition

With Rankine Panel Methods, the proper enforcement of the radiation condition at infinity is essential for their successful use. In SWAN the condition of no waves upstream of the ship has been satisfied by requiring that both the wave elevation and its slope vanish at the upstream boundary of the free surface discretization. The formal derivation of this radiation condition in steady flow is presented in Sclavounos and Nakos (1988), were its preformance for a range of 2D and 3D steady and unsteady flows has been tested and found to be very satisfactory. The transverse and downstream ends of the free surface mesh are successfully treated as free boundaries. For values of the reduced frequency $\tau = \omega U/g$ less than 1/4, a component of the unsteady wave disturbance generated by the ship is known to propagate upstream. In such cases the same upstream radiation condition was found to generate convergent computations of the unsteady flow past the ship for Froude numbers typically larger than 0.15. Seakeeping experiments in the vicinity of $\tau = 1/4$ are unfortunately scarce, therefore the fidelity of the SWAN computations in such cases is to be determined.
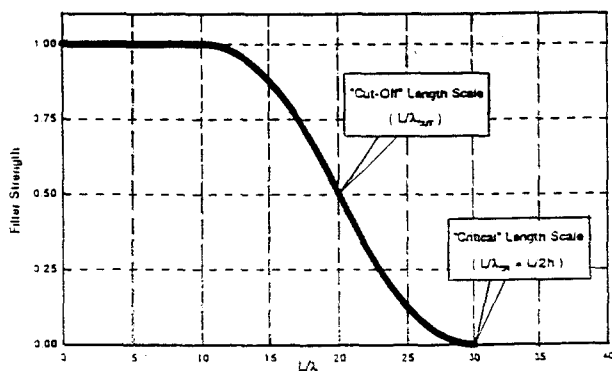
Figure 3 : The Low-pass Filter Used for Smoothing the Basis Flow.

3. Filtering Algorithm

The steady and time-harmonic free surface flows past elementary wave singularities have shown

that the linearized free surface condition allows for wave disturbances with very small length scales associated with divergent wave systems. The presence of such short scales in ship flows modelled by linearized free surface conditions cannot therefore be ruled out. Moreover, experimental evidence may be misleading when it comes to the existence of short scales in the solution of linearized forward-speed ship flows because of the prevalence in the physical flow of nonlinearity at the bow and viscosity at the stern.

In early computations with SWAN attempts to generate convergent wave pattern predictions in the steady and time-harmonic problems revealed either lack of convergence and the manifestation of short scale spatial oscillations in the numerical solution. Unable to determine the degree to which they are to be attributed to a short scale analytical behaviour in the wave pattern or to numerical error, the decision was taken to filter such short scales out of the numerical solution.

There exist several ways to carry out such a filtering. In the SWAN formulation, as in most double-body linearizations of the free surface condition, short scales are likely to be generated by the sharp gradients of the double-body flow near the ship ends. The low-pass filter shown in Figure 3 is applied to the *second-gradients* of the double-body flow by discrete convolution in the $x-$ and $y-$directions. The remaining gradients of Φ which enter in the free-surface conditions (2.2) and (2.3) are not filtered. In Figure 3 two characteristic length scales are defined. The scale λ_{CR} denotes the shortest wavelength which can be resolved by the numerical scheme, and equals $2h$, where h is the typical grid size in the streamwise direction. In Figure 3 this scale is selected to be 30 times smaller that the ship length. The second length scale λ_{CUT} is a parameter of the filter function and denotes the upper bound of the length scales which are to be trusted as accurate in the numerical solution. Numerical experiments suggest that numerical error may be significant for length scales between λ_{CR} and λ_{CUT}. The former is essentially the Nyquist length scale $2h$ and is controlled by the selection of the number of panels. The latter is a parameter of the filter which may be selected independently of the number of panels.

In the SWAN computations reported in the present paper λ_{CUT} was selected equal to $L/15$, where L is the ship length. The SWAN computations of the wave pattern have been found to be convergent for such a cutoff lengthscale, therefore the numerical solution of the linear boundary-value problem should be trusted for wavelengths larger than λ_{CUT}. Such a claim cannot be made for shorter scales, regardless of their analytical or physical relevance. Further properties of this filtering algorithm in the computation of Kelvin wave patterns and wave resistance are discussed in Nakos and Sclavounos (1993).

4. Iterative Solution of Linear System

The efficient solution of the real or complex linear system obtained from RPM formulations is essential for the utility of such methods in practice. The associated matrices are full, asymmetric and generally poorly conditioned, therefore robust and efficient solution algorithms must be available for their solution.

The linear systems in SWAN are presently solved by block Gauss-Siedel iteration, equipped with a minimum-residual acceleration scheme. The block size is typically selected to be a quarter of the matrix size, leading to convergence in about 20-30 iterations for the unsteady problem. This rate of convergence is found to be insensitive to the number of panels used as long as the block/matrix ratio is kept equal to $1/4$.

A preconditioner is currently under development for the SWAN sub-matrix which is associated with the free surface grid. Preliminary results indicate that the rate of convergence of basic iterative methods on the preconditioned matrix are increased and the need for block iteration is eliminated. The objective is the development of a rapidly convergent preconditioned iterative method based on the efficient access and computation of large matrix-vector products.

5. THE FREE SURFACE WAKE

As outlined in the Introduction, for ships with transom or flared sterns, the proper treatment of the local free surface flow physics calls for the introduction of a free surface wake, consisting of a strip of panels trailing the ship as illustrated in

Figure 2. Denoting by $h(x, y)$ the vertical offset of the ship hull near the stern and by $\zeta(x, y)$ the free surface elevation just downstream of it as defined by equation (2.2), the following smooth detachment conditions are enforced at the stern in the case of steady flow:

$$\zeta(x_T, y) = h(x_T, y) \qquad (5.1)$$

$$\frac{\partial \zeta(x_T, y)}{\partial x} = \frac{\partial h(x_T, y)}{\partial x}. \qquad (5.2)$$

These conditions state that the free surface elevation at the upstream end of the free surface wake leaves the stern smoothly, preserving the continuity of the steady flow streamlines.

The same conditions are enforced in the time-harmonic problem with the unsteady free surface elevation now defined by expression (2.3). In both steady and unsteady problems the smooth detachment conditions (5.1) and (5.2) merely enforce a finite velocity over the portion of the stern which sheds a wake. The analogy with the linearized Kutta conditions in lifting surface theory is evident.

Expressions (5.1)-(5.2) are expected to properly model stern flows past transom sterns of small or zero draft. In either case the two conditions are transferred on the $z = 0$ plane and enforced on the upstream side of the wake. In the numerical implementation of (5.1) and (5.2) it was found that the most essential condition to enforce is the continuity of the velocity potential. This finding is consistent with similar implementations of the linearized Kutta condition, also known as Morino condition, in potential based steady and unsteady lifting flows.

6. STRUCTURAL LOADS

Figure 1 illustrates two Cartesian coordinate systems, fixed relative to the ship hull and translating with its forward speed. The *reference* coordinate system (x, y, z) has been defined above in connection with the formulation of the free surface boundary value problems. The second coordinate system, is obtained by parallel shift of the axes of the reference frame by the vector $\vec{X}_0$. It is centered at an arbitrary point O with

respect to which all components of the structural loads exerted by inertia and fluid forces on the shaded portion of the ship hull will be determined.

All forces will be linearized about the mean position of the ship hull, therefore use will be made of the linear version of the skew symmetric rotation matrix T,

$$T = \begin{pmatrix} 1 & -\xi_6 & \xi_5 \\ \xi_6 & 1 & -\xi_4 \\ -\xi_5 & \xi_4 & 1 \end{pmatrix} \qquad (6.1)$$

where (ξ_4, ξ_5, ξ_6) are the linear roll, pitch and yaw ship displacements. It follows that the linear displacement of a point on or inside the ship hull, fixed relative to the reference frame (x, y, z), is defined by

$$\vec{r} = \vec{\xi} + T\vec{x} \qquad (6.2)$$

where $\vec{\xi} = (\xi_1, \xi_2, \xi_3)$ denotes the vector of linear ship displacements and the vector $\vec{x}$ is to be regarded as a quantity independent of time.

The fluid pressure acting on the wetted part of the shaded portion of the ship hull is determined from the solution of the steady and time harmonic free surface flows described above. The resultant forces and moments follow by direct integration over the ship hull of the hydrodynamic pressure as defined by (3.1). For the Froude numbers considered in the present study, the contribution to the structural loads by the steady pressure was found to be small and was ignored.

Denoting by S the mean wetted surface of the shaded portion of the ship hull, by C the mean position of its waterline and V the volume over which mass elements are distributed, the unsteady force vector acting over (S, V) by fluid and inertia forces follows in the form

$$\vec{F} = \iiint_V \frac{d^2\vec{r}}{dt^2} dm - \iint_S p\vec{n}ds +$$

$$\oint_C \eta_s(\rho g\eta_r - p)\vec{n}ds - \iiint_V (T^T - I)\vec{g}dm \qquad (6.3)$$

where p is the unsteady pressure, η_s is the steady and η_r the relative wave elevations along the ship

waterline, the latter defined as the difference between the total unsteady wave elevation and the vertical ship displacement. The corresponding moment vector acting over the same portion of the ship hull, about the axes of the coordinate system centered at the point O, is defined as follows

$$\vec{M} = \iiint_V (\vec{x} - \vec{x}_0) \times \frac{d^2\vec{r}}{dt^2} dm -$$

$$\iint_S p[(\vec{x} - \vec{x}_0) \times \vec{n}]ds +$$

$$\oint_C \eta_s(\rho g\eta_r - p)[(\vec{x} - \vec{x}_0) \times \vec{n}]ds -$$

$$\iiint_V (\vec{x} - \vec{x}_0) \times [(T^T - I)\vec{g}]dm \qquad (6.4)$$

In (6.3) and (6.4), the second terms arise from the fluid pressure forces which include the hydrostatic contribution by virtue of the last term in the definition (3.1) of the pressure. The leading terms account for the inertia effect contributed by the acceleration of the differential mass dm and the last terms represent the restoring force and moment, respectively, contributed by the mass of the shaded part of the ship as it undergoes rotational oscillations. A more detailed derivation of (6.3) and (6.4) is carried out by Helmers (1992)(private communication).

The waterline integrals may be seen to depend on the steady wave elevation along the waterline which is assumed to be large for flared geometries. For the vertical loads, the normal vector component n_3 may be seen to be equal to the sine of the the flare angle which vanishes for wall sided ships. The magnitude of the waterline integral contribution to the vertical wave loads will be studied in Section 8. Expressions (6.3) and (6.4) represent the unsteady contribution to the structural loads which must be added to the static loads acting upon a ship in calm water.

By virtue of the three dimensional nature of the hydrodynamic solution determined by SWAN, the force and moment vectors defined by (6.3) and (6.4) may be evaluated at any arbitrary point O over the ship surface or its interior, as the structural analysis may require. The evaluation of the volume integrals accounting for the

dynamic and restoring inertial effects may be easily evaluated by a summation over as many mass points as are necessary to distribute over the ship interior in order to represent its inertia properties. This is the method adopted in SWAN.

7. NUMERICAL RESULTS

7.1 Kelvin Wave Patterns Past Transom Stern Ships

Figure 4 illustrates the hull discretization of the transom stern DTMB model 5415 consisting of 80 panels along the ship length and 10 panels along its half section. A strip of panels trailing its transom is added with the smooth detachment conditions (5.1) and (5.2) enforced at its upstream end. Computations of the Kelvin pattern at a Froude number 0.25 are presented, where their convergence is studied as a function of the number of panels along the ship length. A comparison is also carried out of the computed Kelvin wake spectrum with the measurements carried out in the 'wakeoff' comparative study of Lindenmuth, Ratcliffe, and Reed (1991) with good agreement. In all computations the panel aspect ratio α was taken equal to 1 on the free surface and near the ship hull. This selection of the aspect ratio typically requires a large number of panels on the free surface but has been found to lead to convergent computations.

7.2 Hydrodynamic Forces and Motions of the SL7 and S-175 Hulls

Computations have been carried out of the heave and pitch damping coefficients of the SL7 and S-175 hulls. Both hulls have flared geometries at the stern which must be taken into account properly for the accurate computation of their seakeeping properties.

The steady problem is solved first about the calm water position of the hull and its sinkage, trim and steady wave profile are evaluated along the waterline and downstream of the stern. Based on this information, the new position of the ship waterline relative to the ship hull is determined and the extent of the ship stern that gets wet is determined by intersecting the steady wave profile with the stern profile, including effects of sinkage and trim. The SL7 stern possesses a long

countertop, a significant portion of which gets wet as a result of the sinkage, trim and steady elevation downstream of the stern. A similar but less pronounced effect may be observed for the S-175 hull and generally for hull shapes with significant flare at their stern. The corresponding effect at the bow is less pronounced for nearly vertical bow stems.

Computations of the hydrostatic, impedance forces and ship motions for the linear and 'nonlinear' wetted surface of the ship hull revealed a strong sensitivity of the motions on the steady wave profile effect on the hydrostatic coefficients. The hydrodynamic coefficients were found not to be appreciably different in the two cases and they have thus been computed about the linear wetted surface, for the sake of simplicity.

The proper discretization of the free surface in the vicinity of the stern of a flared hull is essential for the robustness and convergence of the numerical solution. An attempt to distribute panels around flared sterns without the introduction of a wake revealed a strong sensitivity of the numerical solution on the number and arrangement of panels. The introduction of a wake strip of panels trailing the stern was found to cure this problem and lead to convergent computations. The panel arrangement in the vicinity of the stern of the S-175 is illustrated in Figure 2 where the shallow portion of the stern has been removed and an equivalent transom was introduced as indicated in the Figure.

Convergence tests were carried out using the grid arrangement shown in Figure 2. The parameters varied included the panel aspect ratio and the total number of panels. For both ship hulls and for all frequencies and Froude numbers tested, convergence to within graphical accuracy was achieved, using up to about 5,000 panels on half the ship hull, free surface and wake with the panel aspect ratio varying from 1.5 to 2.0, defined at the ratio of the streamwise to the transverse dimensions of a typical panel in the vicinity of the ship waterline. The aspect ratio of 1.5 was selected in the final computations. The extent of the free surface grid relative to the ship dimension is illustrated in Figure 2.

The heave and pitch added mass and damping coefficients of the SL7 hull advancing at a Froude

number 0.3 are illustrated in Figure 5. The computations by SWAN are compared to the experimental measurements by O'Dea and Jones (1983). The corresponding computations for the S-175 advancing at a Froude number 0.275 are plotted in Figure 7. Computations by SWAN of the heave and pitch exciting forces for the SL7 advancing in head waves are compared to experiments in Figure 6. The agreement is very satisfactory, as is usually the case with the exciting forces.

Heave and pitch motion amplitude and phase computations by SWAN for the SL7 are compared to experiments in Figure 8 in head waves and a Froude number $Fr = 0.3$. The SWAN predictions marked as 'nonlinear' have accounted for the effect of the hull sinkage, trim and steady wave profile upon the restoring coefficients. The corresponding head wave heave and pitch motion computations for the S-175 hull at a Froude number 0.275, are illustrated in Figure 10. The experimental measurements for the S-175 hull have been reported by the ITTC and are discussed in more detail by Dalzell (1992).

A clear trend emerges from these computations. The account of the nonlinear effect described above reduces the amplitude of the heave and pitch motions at resonance by an appreciable amount, leading to a good agreement with experimental measurements. Both the linear SWAN computations and strip theory tend to overpredict the heave and pitch motions at resonance, a trend which is not evident for wall sided geometries like the Wigley and the Series 60 hull, studied in Nakos and Sclavounos (1990).

Heave and pitch motions of the S-175 advancing at Fr = 0.275 in beam (β = 90 deg) and quartering (β = 60 deg) waves are plotted in Figure 10 and compared with good agreement to the experimental measurements reported by the ITTC. All hydrodynamic force and motion computations reported in this study correspond to Froude number and frequency combinations such that the values of the reduced frequency $\tau = \omega U/g$ are greater than 1/4.

7.3 Heave and Pitch Motions of an IACC Yacht Hull

Figure 11 illustrates the body plan and free

surface discretization of an International America's Cup Class generic yacht hull, code named PACT (Partnership for America's Cup Technology) baseline geometry, characterized by its small draft and significant flare along its entire length. The robust solution of the steady and unsteady flows around such hulls necessitates the introduction of a free surface wake which may be seen trailing the yacht stern in Figure 11. The wake panels are distributed around the flared portion of the stern, since in this case the definition of an equivalent transom is not as evident as for the SL7 and S-175 hulls.

Computations of the heave and pitch motion amplitudes including the nonlinear steady state effect discussed above are compared in Figure 11 with experimental measurements by Cohen and Beck (1992). Consistently with the SL7 and S-175 computations, the heave and pitch motion amplitudes are found not to display a resonant peak, which is clearly visible in the linear SWAN computations not shown in the figure. Further seakeeping and added resistance computations for the PACT and other yacht hull geometries are presented in Sclavounos and Nakos (1993).

8. WAVE INDUCED STRUCTRURAL LOADS ON THE SL-7 and S-175 HULLS

Computations were carried out of the vertical shear force and bending moment induced at the midship section and about a transverse axis coinciding with the $z = 0$ plane. Expressions (6.3) and (6.4) were used with all integrations carried out over the fore half of the ship hull. The wave induced loads have been determined using both the linear and nonlinear heave and pitch motion amplitudes evaluated in the manner described in Section 7. Furthermore the contribution to the loads from the waterline integrals in (6.3) and (6.4) which account for the effect of flare has been isolated and compared to the surface and volume integrals in the same expressions.

The vertical shear force and bending moment induced by head waves on the SL7 hull are presented in Figure 9. SWAN computations using the linear and nonlinear heave and pitch motion amplitude predictions are shown and the latter are found to be in very good agreement

with the measured values. It is noteworthy that the account of the nonlinear effect in the motion amplitude tends to decrease the peak value of the shear force modulus and increase the corresponding modulus of the bending moment, consistently with the experimental trend.

The corresponding head wave shear force and bending moment computations for the S-175 hull are presented in Figure 12. Again the wave load predictions based on the 'nonlinear' heave and pitch motions are in better agreement with the experimental measurements and as for the S-175 hull are found to differ appreciably from their linear counterparts. The SWAN wave load predictions in beam and quartering waves are also illustrated in Figure 11 using the 'nonlinear' heave and pitch motions amplitudes. The agreement with experiments, where available, is again seen to be satisfactory.

The importance of the waterline contribution to the wave loads is demonstrated in Figure 12 where the S-175 head wave midship bending moment defined by expression (6.4) is plotted with and without the waterline terms. It is evident that ignoring the waterline integral, may lead to a marked underprediction of the bending moment. This trend is also evident in the shear force predictions and for other wave headings. Recalling that the waterline-integral contributions are absent for wall-sided hull geometries, it is concluded that the effect of flare near the fore end of a ship hull is responsible for a significant component of the vertical wave induced loads, as intuition alone might suggest.

9. SUMMARY

Seakeeping and wave induced structural load computations have been presented for the SL7, S-175 hulls and an IACC yacht with the Rankine Panel Method SWAN. All three hulls are characterized by the presence of significant flare near their bow and stern regions. Extensions of SWAN are developed which account for the effects of flare, driven by the flow physics and aiming to generate robust and accurate numerical predictions for the ship motions and wave loads. They include; a) the introduction of a wake of panels trailing transom and flared sterns, equipped with Kutta type conditions of finite velocity, b) the account of the effect of the ship

sinkage, trim and steady wave profile interaction with the stern upon the hydrostatic coefficients and c) the derivation of waterline corrections to the linearized wave load definitions, which account for effects of flare.

Heave and pitch motion computations, corrected for the effects of flare as outlined above, are found to be in very good agreement with experiments, particularly near resonance where flare effects appear to introduce a detuning to the heave/pitch oscillation and a reduction of their respective amplitudes. Computations of the vertical shear force and bending moments in head and oblique waves for the SL7 and the S-175 hulls show a strong dependence upon, a) the use of the 'nonlinear' heave and pitch motion amplitudes, corrected for the effects of flare at the stern, and b) the account of waterline terms in the definition of the loads, which arise only when flare is present near the ship bow.

10. Acknowledgements

References

Cao, Y., Schultz, W.W. and Beck, R.F. 1992, "Three Dimensional Unsteady Computations of Nonlinear Waves Caused by Underwater Disturbances". Proceedings 18th Symposium on Naval Hydrodynamics, Ann Arbor, Michigan.

Dalzell, J.F., Thomas, W.L., III and Lee, W.T., 1992, "Correlations of Model Data with Analytical Load Predictions for Three High Speed Ships", Report SHD-1374-02, Naval Surface Warfare Center.

Dawson, C.W., 1977, "A practical computer method for solving ship-wave problem", 2nd International Conference on Numerical Ship Hydrodynamics, USA.

Gadd, G.E., 1976, " A method for computing the flow and surface wave pattern around full forms", Trans. Roy. Asst. Nav. Archit., Vol 113, pg. 207.

Jensen, G., and Soding, H., 1989, "Ship Wave Resistance Computations", Finite Approximations in Fluid Mechanics II, Vol 25.

Kim, Y.H., and Lucas, T., 1990, "Nonlinear Ship Waves", Proceedings of the 18th Symposium on Naval Hydrodynamics, Ann Arbor, MI, USA.

Lindenmuth, W. T., ratcliffe, T. J. and Reed, A. M., 1991, "Comparative Accuracy of Numerical Kelvin Code Predictions - Wake-Off". DTMB Report 91/004, Bethesda, Maryland.

Maskew, B., 1992, "Prediction of Nonlinear Wave/Hull Interactions on Complex Vessels", Proceedings of the 19th Symposium on Naval Hydrodynamics, Seoul, Korea.

Nakos, D.E. and Sclavounos P.D., 1990b, "On steady and unsteady ship wave patterns", Journal of Fluid Mechanics, Vol. 215, pp. 256-288.

Nakos, D.E. and Sclavounos P.D., 1990a, "Ship Motions by a Three Dimensional Ranking Panel Method", Proceedings of the 18th Symposium on Naval Hydrodynamics, Ann Arbor, MI, USA.

Nakos, D.E. and Sclavounos, P.D. 1993, "Kelvin Wakes and Wave Resistance of Cruiser and Transom Stern Ships". To appear in *Journal of Ship Research.*

Nakos, D.E., Kring, D.C. and Sclavounos, P.D., 1993, "Ranking Panel Methods for Time-Domain Free Surface Flows" 5th International Conference on Numerical Ship Hydrodynamics, USA.

O'Dea, J.F. and Jones, H.D., 1983, "Absolute and Relative Motion Measurements on a Model of a High-speed Containership", Proceedings of the 20th American Towing Tank Conference, Hobeken, NJ, USA, Vol. II.

Raven, H., 1992, "A Practical Nonlinear Method for Calculating Ship Wavemaking and Wave Resistance", Proceedings of the 19th Symposium on Naval Hydrodynamics, Seoul, Korea.

Reed, A.M., Telste, J.G., Scragg, C.A. and Liepmann, D., 1990, "Analysis of Transom Stern Flows", Proceedings of the 18th Symposium on Naval Hydrodynamics, Ann Arbor, MI, USA.

Rosen, B.S., Laiosa, J. P., Davis, W. H. and Stavetski, D., 1993, "SPLASH Free-Surface Flow Code Methodology for Hydrodynamic Design and Analysis of IACC Yachts". Proceedings of 11th Chesapeake Sailing Yacht Symposium, Annapolis, Marland.

Sclavounos, P.D. and Nakos, D.E., 1988, "Stability Analysis of Panel Methods for Free-Surface Flows with Forward Speed", Proceedings of the 17th Symposium on Naval Hydrodynamics, The Hague, The Netherlands.

Sclavounos, P.D. and Nakos, D.E., 1993, "Seekeeping and Added Resistance of IACC Yachts by a Three Dimensional Panel Method", 11th Chesapeake Sailing Yacht Symposium, Annapolis, IN, USA.

Xia, F., 1986, "Numerical Calculations of Ship Flows with Special Emphasis on the Free Surface Potential Flow", Doctoral Thesis, Chalmers University of Technology, Sweden.

4290 Panels
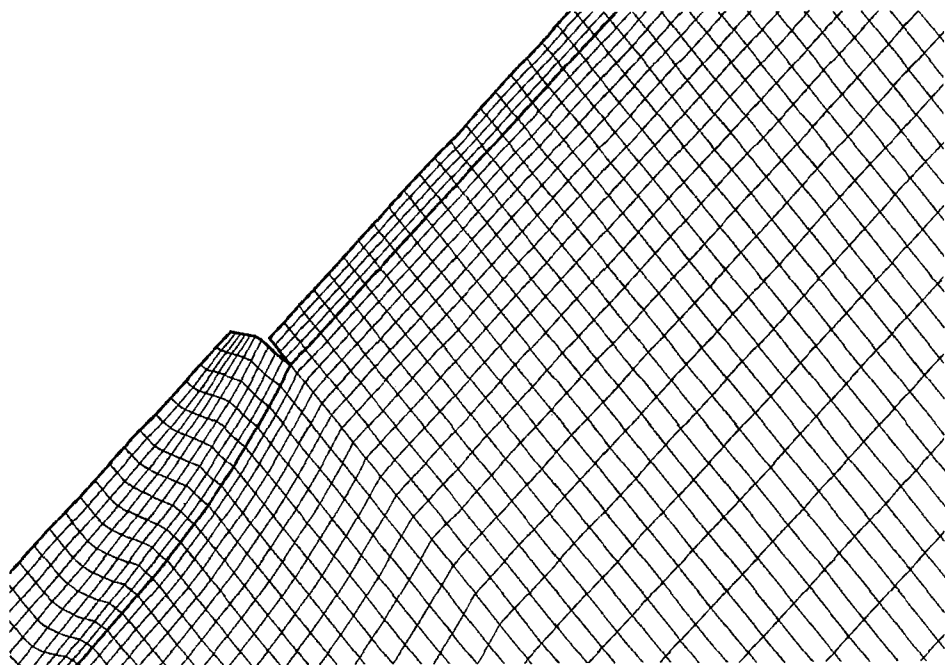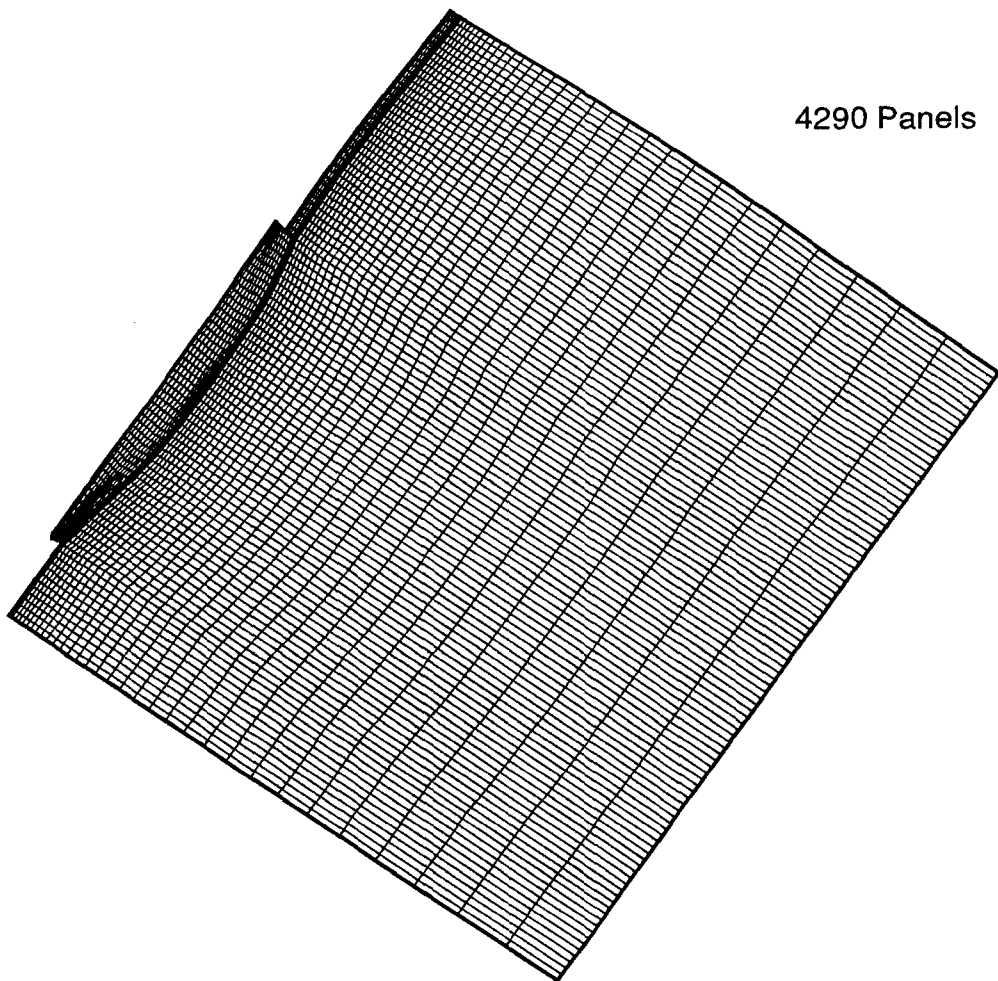
Figure 2 : Hull and Free Surface Discretization for S-175 Hull.
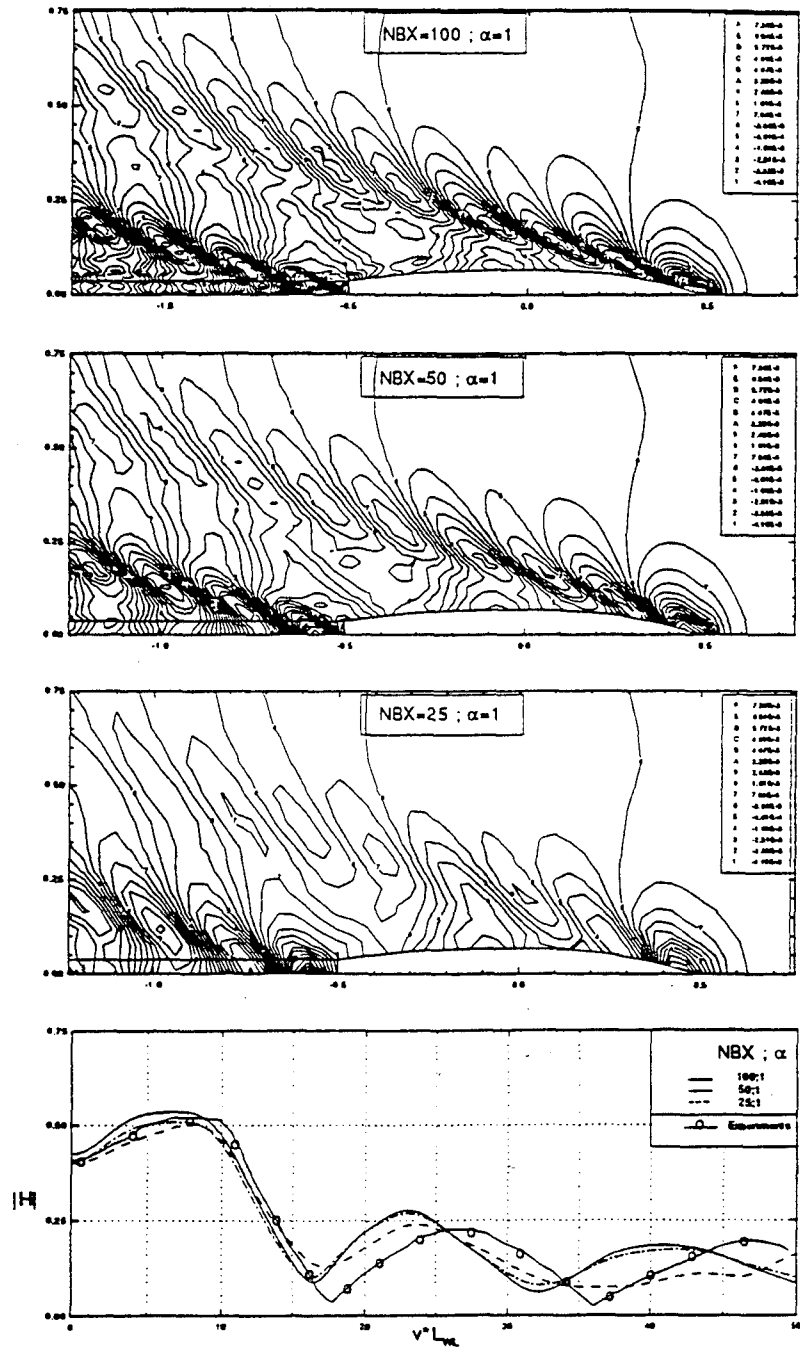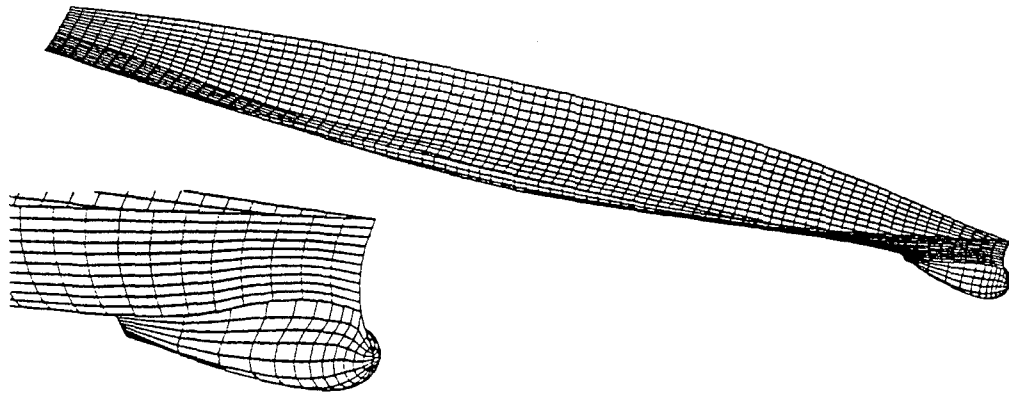
Figure 4 : Wave Pattern and Spectrum for the Model 5415 at Fr = 0.25.
Computations Using Systematically Refined Grids.

70
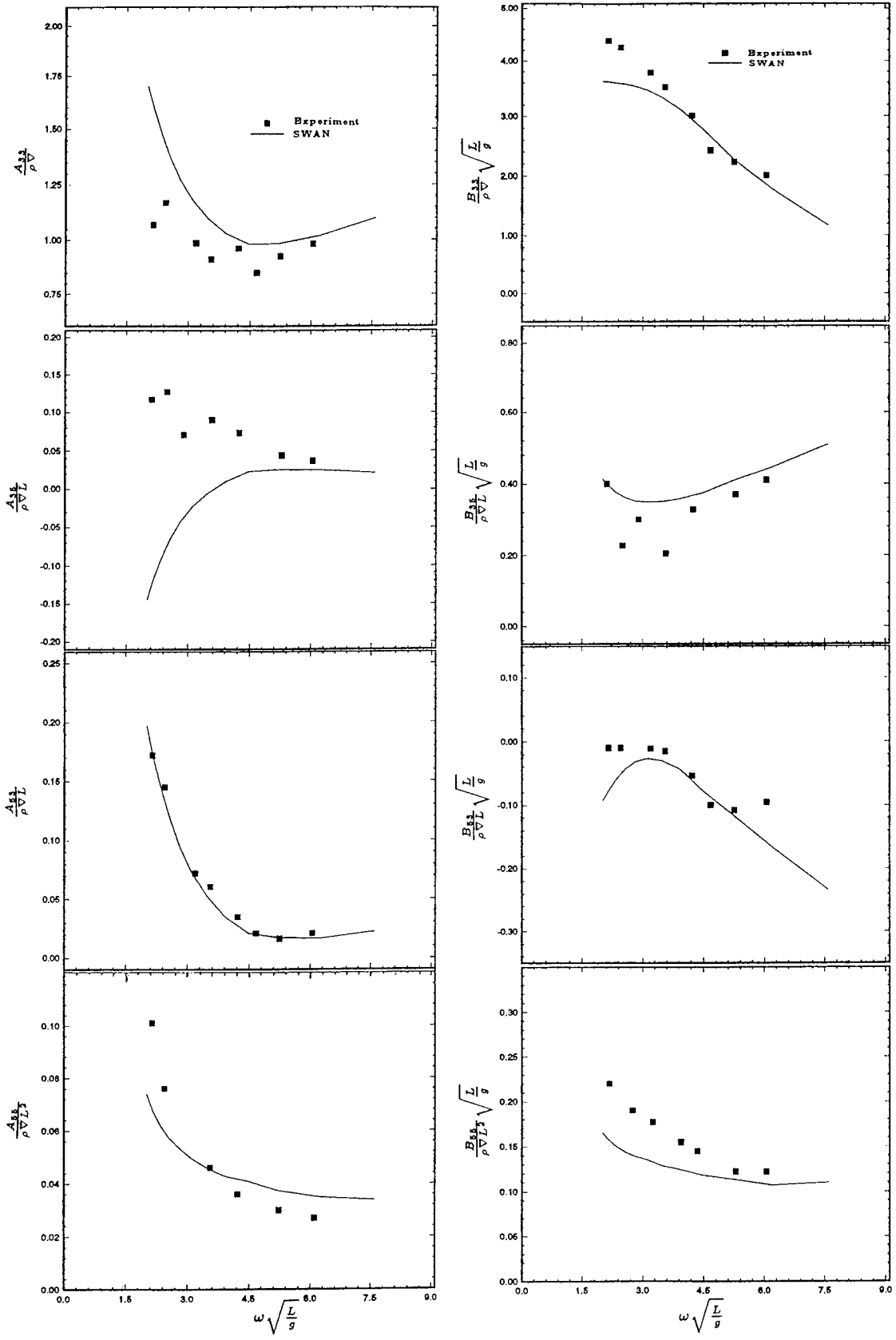
Figure 5 : Heave and Pitch Hydrodynamic Coefficients for the SL-7 Hull at Fr = 0.3.
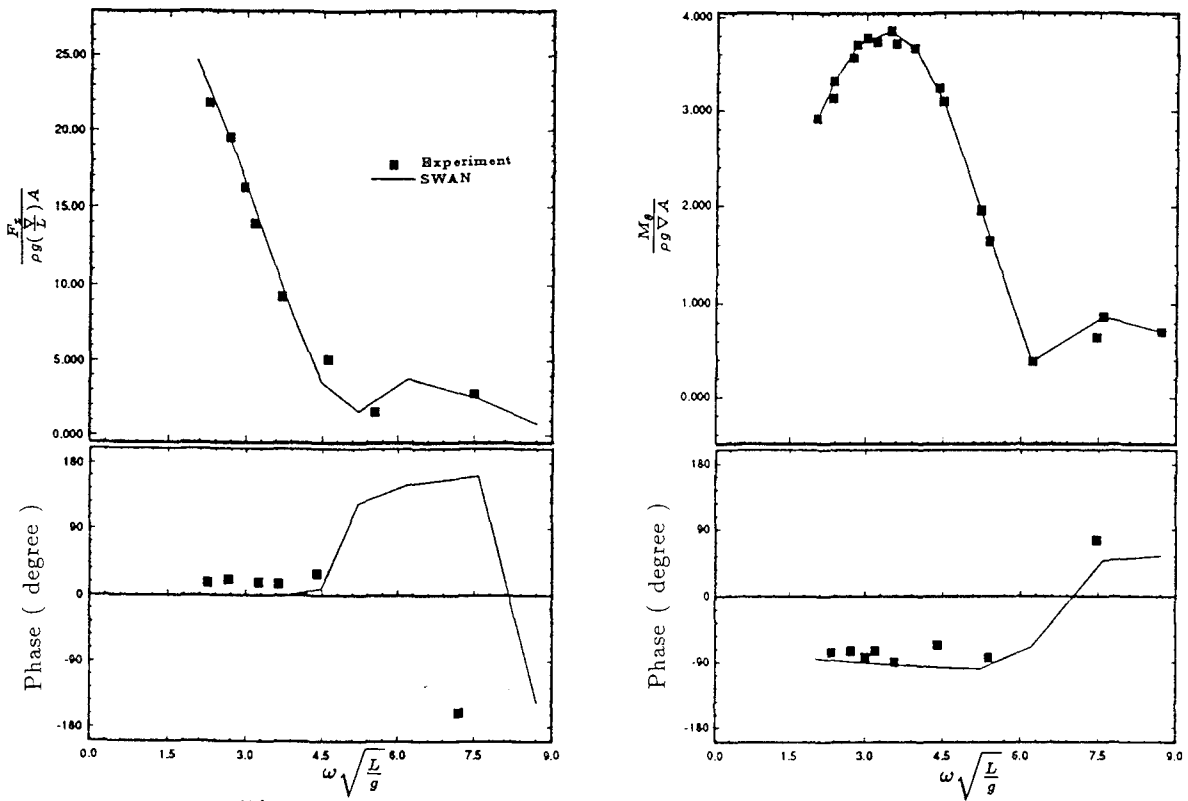
Figure 6 : Heave and Pitch Excitation Forces on the SL-7 Hull
in Head Waves at Fr = 0.3.
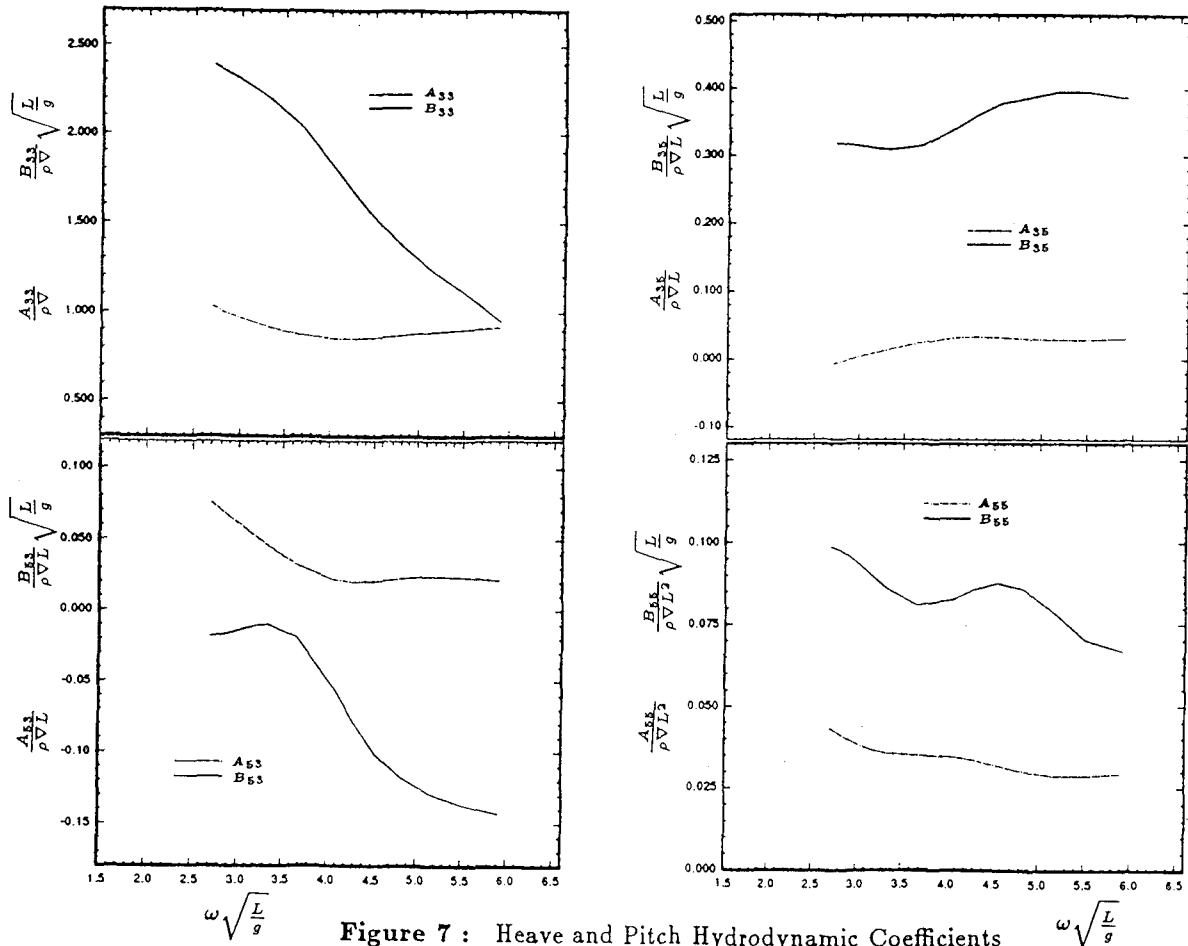
Figure 7 : Heave and Pitch Hydrodynamic Coefficients
for the S-175 Hull at Fr = 0.275.
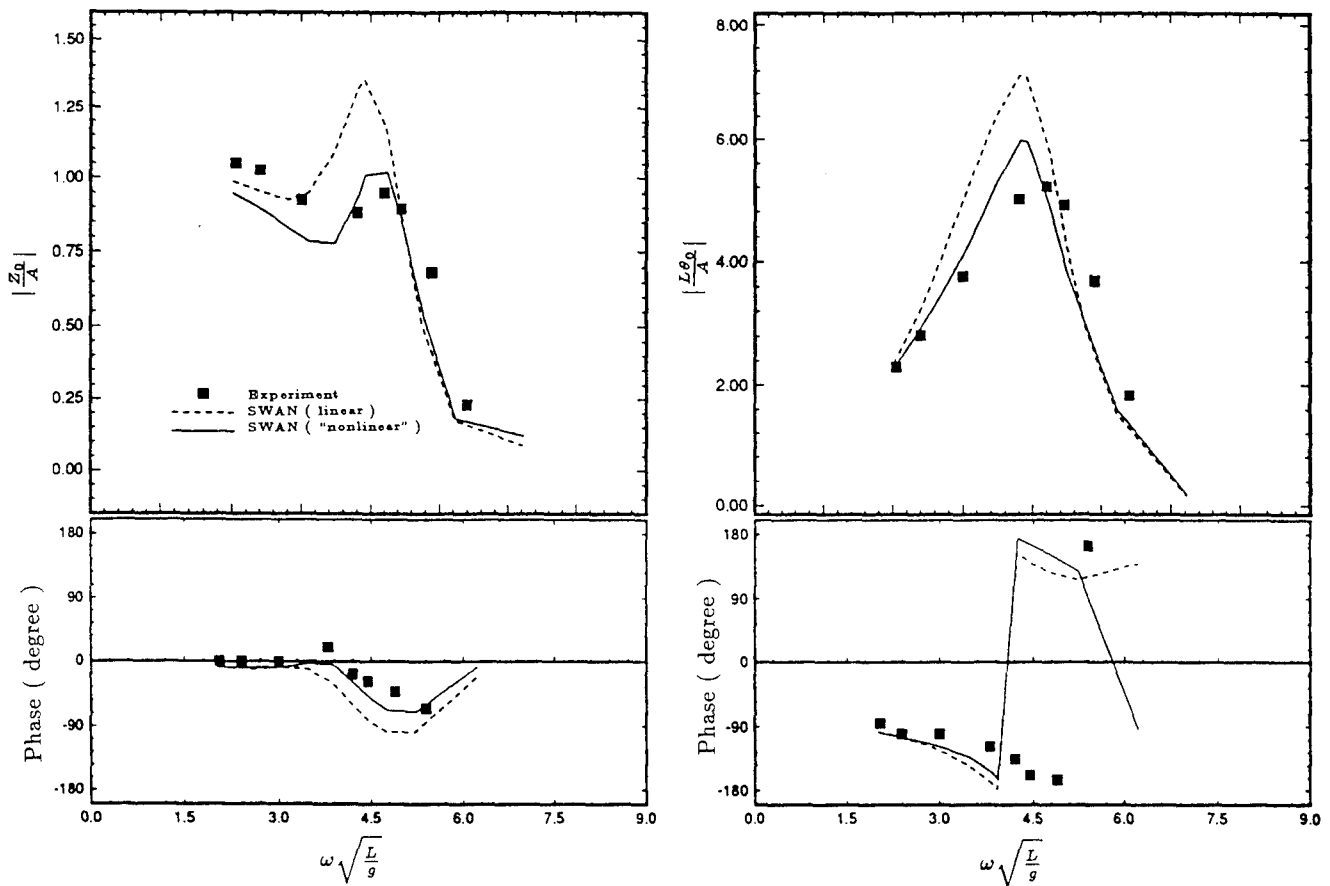
Figure 8 : Heave and Pitch Motions for the SL-7 Hull in Head Waves at Fr = 0.3.
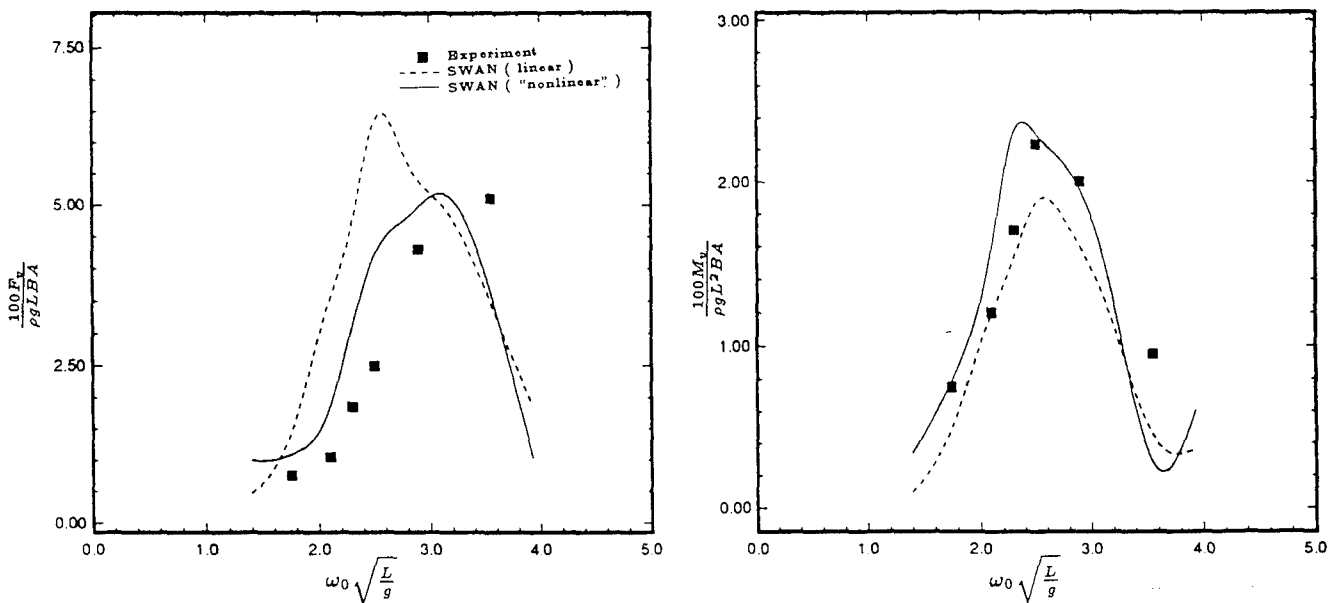
Figure 9 : Vertical Shear Force and Bending Moment at Midship Section of the SL-7
Hull in Head Waves at Fr = 0.3.
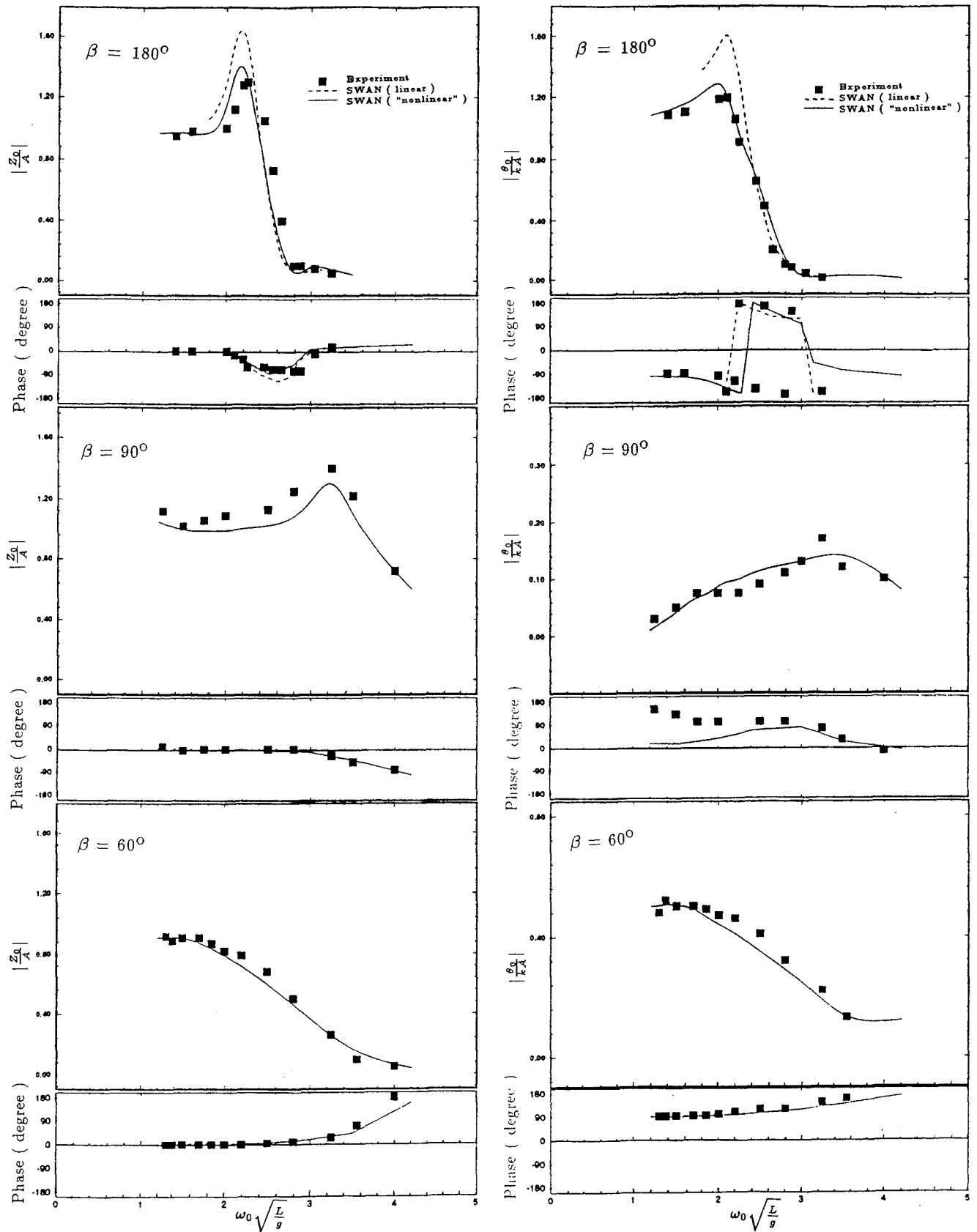
Figure 10 : Heave and Pitch Motions for the S-175 Hull in Head, Beam and Quartering Waves at Fr = 0.275.
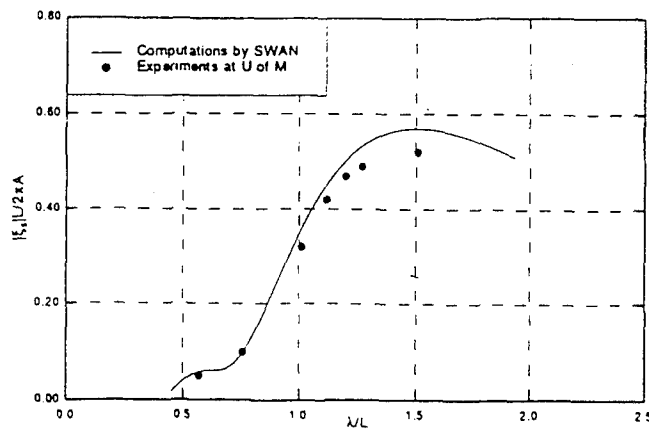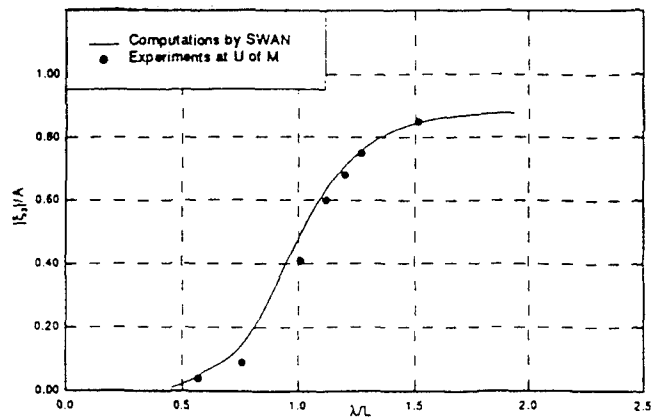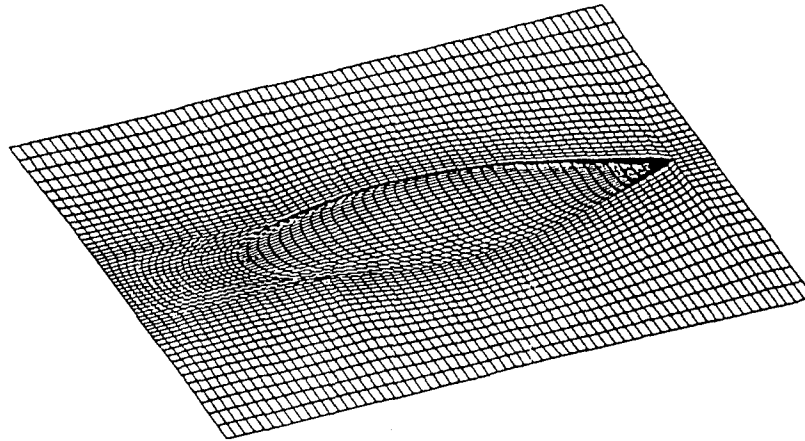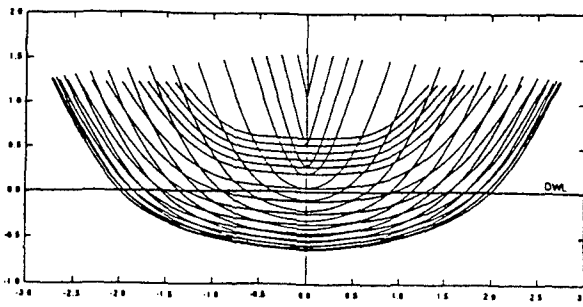
Figure 11 : IACC Hull.
Body Plan, Discretization and Heave & Pitch Motions
for PACT IACC Yacht Hull in Head Waves at Fr = 0.33.
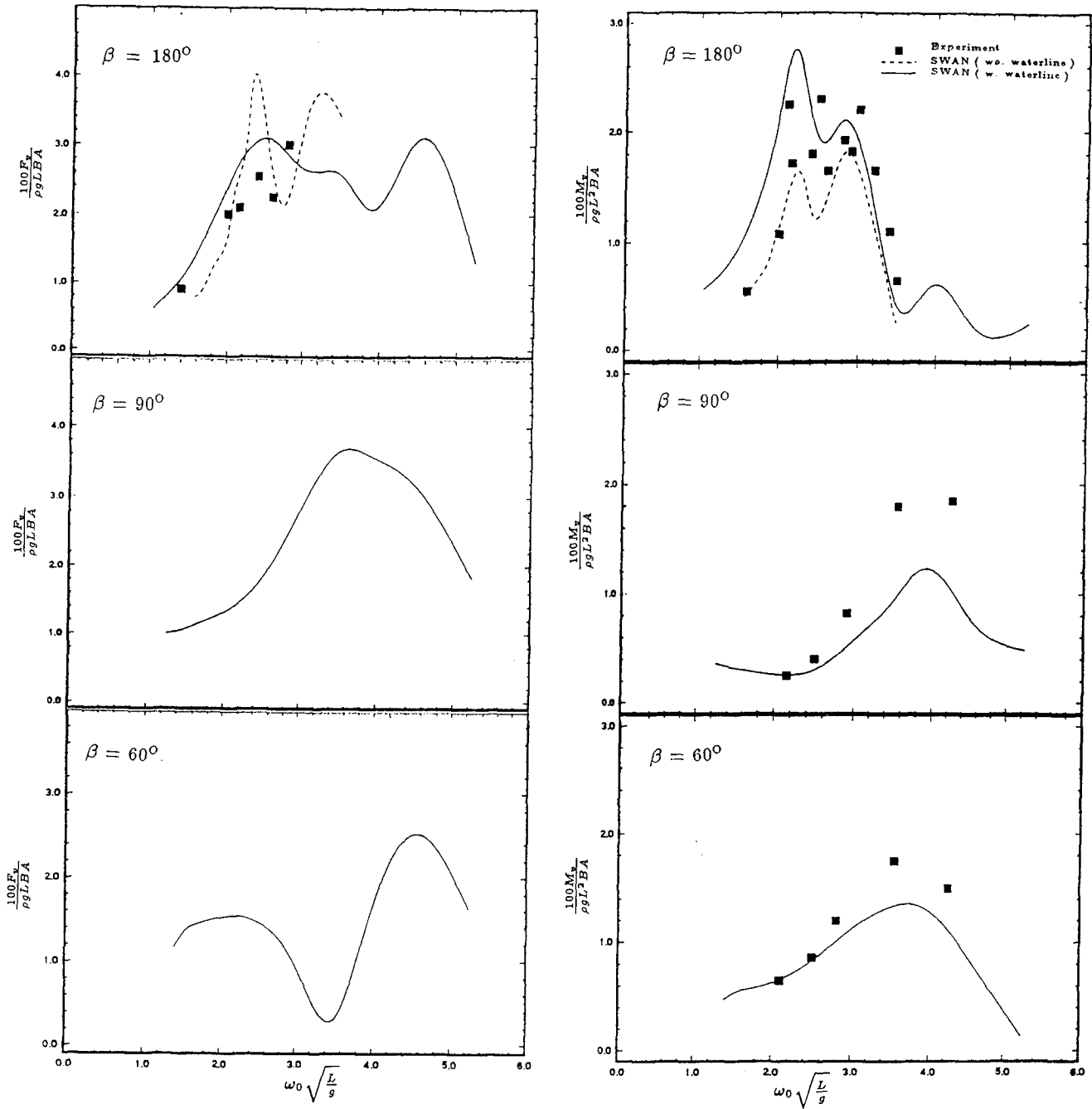
Figure 12 : Vertical Shear Force and Bending Moment at Midship Section of the S-175 Hull in Head, Beam and Quartering Waves at Fr = 0.275.

DISCUSSION

by Professor Robert Beck, University of Michigan, Ann Arbor

Do you have an explanation to the hump that appears in the bending moment curve at high frequencies?

Author's Reply

I would attribute the mid-ship bending moment hump at high frequencies to constructive/destructive interference effects caused for wavelengths shorter than the ship length of nature similar to that encountered in the high-frequency behavior of the heave and pitch exciting forces. The amplitude of these effects is magnified in the mid-ship bending moment and shear force integrations which are carried out over half the ship surface. Similar interference effects in the exciting force evaluation are less pronounced due to cancellation in the respective integration which is carried out along the entire ship length.

DISCUSSION

by Emilio Campana, INSEAN, Italian Ship Model Basin

In your paper you say that for the solution of the large linear system a wave preconditioner, based on the free surface grid, has been used. Can you give some more details?

Author's Reply

We have developed a reconditioner which is custom designed for real and complex matrix equations arising in Rankine panel methods. The preconditioner is based on the approximate inversion of the sub-matrix associated with the free-surface mesh by a discrete FFT technique. The resulting preconditioned matrix (real for the steady and complex for the unsteady problem) becomes diagonally dominant and its inversion becomes possible by point, as opposed to block, minimum residual accelerated Jacobi and Gauss-Siedel iteration. The rate of convergence of this new iterative scheme was found to be uniformly faster than the original block iteration method over a broad range of frequencies and speeds.

Calculation of Transom Stern Flows

J.G. Telste and A.M. Reed

(David Taylor Model Basin, USA)

ABSTRACT

This paper presents a method of calculating the flow near a transom stern ship moving forward at a moderate to high steady speed into otherwise undisturbed water. The speed is assumed to be sufficient to guarantee smooth flow separation at the stern and a dry transom. In addition, conditions necessary to justify the assumption of potential flow are assumed. Modified free-stream linearization is used to obtain a Neumann–Kelvin boundary value problem in which the usual linearization about the mean free-surface level is replaced in the area behind the transom stern by linearization about a surface originating at the hull–transom intersection. A Rankine singularity integral equation is presented for obtaining the solution of the resulting mathematical boundary–value problem. The integral equation involves line integrals around the hull and has been designed so that it greatly reduces the requirement of using forward finite differences to enforce the radiation boundary condition. The approach permits the presence of free-surface dipoles and provides a mechanism for carrying lift downstream from a transom stern in accordance with the work of various researchers who, in recent years, had suggested that lift effects are an important component of wave resistance under certain conditions. Computational results are presented for two transom-stern ships.

NOMENCLATURE

C_{WP} wave resistance coefficient computed from wave spectral energy ($= 2R_W/\varrho SU^2$)

$E(x,y)$ surface behind a transom stern on which linearized free-surface boundary conditions are applied ($= S_E$)

F Froude number ($= U/\sqrt{gL}$)

$\mathcal{F}(u)$ sine component of the free-wave spectrum

g gravitational acceleration

$\mathcal{G}(u)$ cosine component of the free-wave spectrum

k_0 fundamental wave number ($= g/U^2$)

L ship length

$\vec{n}$ unit normal directed into the fluid

(n_x, n_y, n_z) components of the normal vector $\vec{n}$ in the x-, y-, and z-directions

r distance from the singular point $\vec{\xi}$ to the field point $\vec{x}$

R_W wave resistance

S wetted surface area of the hull

S_B hull surface (zero sinkage and trim)

S_E surface behind a transom stern on which linearized free-surface boundary conditions are applied ($= E(x,y)$)

S_E' projection of S_E onto the mean free-surface level

S_F mean free-surface level

U ship speed

u transverse wave number ($= \sec\theta\tan\theta$)

v longitudinal wave number ($= \sec\theta$)

$\vec{x}$ vector notation of the field point (x,y,z)

(x,y,z) coordinates of the field point $\vec{x}$ in a right-handed ship-fixed coordinate system, x positive downstream, y positive to starboard, and z positive upward

$\vec{x}_T$ point on the hull–transom intersection

$Z(x,y)$ wave elevation

$\vec{\xi}$ vector notation for a singular point (ξ, η, ζ)

(ξ, η, ζ) coordinates of the singular point $\vec{\xi}$

ϱ density of water

Φ velocity potential

ϕ perturbation potential

θ angle from which the transverse wave number is computed

INTRODUCTION

Before the appearance of high–speed computers, ship designers had to rely solely on systematic-series experiments for designing criteria. With the great improvement in the capability of computing quantities such as wave resistance, trim moment, and the Kelvin wave pattern that has occurred especially since the 1970's, designers now frequently rely on a complementary combination of experiments and computer simulations. The increased computational capability has come about because of the effort that has been expended through the years in the development of computer codes to simulate flow near ships moving steadily into otherwise undisturbed water — the wave resistance problem. Computational results for several of these codes can be seen in the "Wake-Off" report of Lindenmuth *et al.* (1). One of the conclusions of that report was that the predictions of Kelvin wave pattern for ships with transom sterns were poor.

Since the "Wake-Off," additional effort has been expended in trying to properly model flow in the neighborhood of the transom stern of a translating ship. Results of such work are presented in the papers of Cheng (2), Reed *et al.* (3), and Nakos and Sclavounos (4). In their paper, Nakos and Sclavounos present computational results in which a lifting surface originating at the stern is present. Kutta–like conditions are enforced at the stern. For shallow transom sterns the wake is collapsed onto the mean free–surface level. Reed *et al.* present various arguments to show that it is reasonable and even necessary to include a lift model for flows in the vicinity of a moderate to high-speed transom stern ship, as is done to model the flow about three–dimensional wings. The arguments were based on analogies with high-speed planing craft and ventilated hydrofoils at moderate speeds, as well as the theoretical work and analysis of experimental work of Tulin and Hsu (5). The point of the argumentation was that under certain conditions effects due to lift form a significant component of the wave resistance. Reed *et al.* present the effects of including a lift model in Rankine and Havelock singularity codes. The effects of lift could be more easily separated in the computational results from the Havelock singularity code, where it was shown that lift modifies the diverging waves of the Kelvin wave pattern originating at the stern. Additionally, it was shown that the strength of the dipole distribution along the transom has a shape similar to that of an elliptic loading on a three–dimensional lifting surface. The effect of lift in the Rankine singularity code could not be distinguished so easily.

This paper presents a method of calculating the flow near a transom stern ship moving forward at a moderate to high steady speed into otherwise undisturbed water. This is a Rankine singularity method in which several enhancements have been made so that the effect of including lift can be seen more clearly in the computational results. The speed is assumed to be sufficiently high to guarantee smooth flow separation at the stern and a dry transom. In addition, conditions necessary to justify the assumption of potential flow are assumed. A modified free–stream linearization is used to obtain a Neumann–Kelvin boundary value problem. In this linearization scheme, for most of the free surface, the usual linearization is used. However, behind the transom, the usual linearization about the mean free–surface level is replaced by linearization about a surface originating at the hull–transom intersection. A Rankine singularity integral equation is presented for obtaining the solution of the resulting mathematical boundary value problem. The integral equation involves line integrals around the hull and has been designed so that it greatly reduces the requirement of using forward finite differences to enforce the radiation boundary condition. The approach permits the presence of free–surface dipoles and provides a mechanism for carrying lift downstream from a transom stern.

MATHEMATICAL FORMULATION

A coordinate system is fixed to the ship with the origin inside the hull on the mean free–surface level so that x is positive downstream, z is positive above the mean free–surface level, and y is positive on the starboard side. In this coordinate system a uniform stream of speed U is flowing past the hull in the positive x-direction.

Boundary Value Problem

Conditions necessary for potential flow are assumed. For now, a cruiser stern is assumed and free–stream linearization about the mean free–surface level is used. The total potential Φ is written as the sum of the free–stream potential Ux and a disturbance potential ϕ:

$$\Phi = Ux + \phi \qquad (1)$$

Then the following dimensional equations characterize the boundary value problem:

$$\nabla^2 \Phi = \nabla^2 \phi = 0 \qquad (2)$$

$$UZ_x - \phi_z = 0 \quad on \ S_F \qquad (3)$$

$$U\phi_x + gZ = 0 \quad on \ S_F \qquad (4)$$

$$\frac{\partial \phi}{\partial n} = -Un_x \quad on \ S_B \qquad (5)$$

where S_F is the mean free-surface level, S_B is the hull surface below the mean free-surface level, Z is the free-surface height, and $\vec{n}$ is the unit normal directed into the fluid. Eqs. (3) and (4) are the kinematic and dynamic free-surface boundary conditions, which are to be satisfied on the mean free-surface level. To ensure a unique solution, a radiation condition that no waves propagate upstream of the hull must also be satisfied.

After normalizing lengths by the length L of the ship and velocities by the speed U, the equations take the form

$$\Phi = x + \phi \tag{6}$$

$$\nabla^2 \Phi = \nabla^2 \phi = 0 \tag{7}$$

$$Z_x - \phi_z = 0 \quad on \quad S_F \tag{8}$$

$$\phi_x + Z/F^2 = 0 \quad on \quad S_F \tag{9}$$

$$\frac{\partial \phi}{\partial n} = -n_x \quad on \quad S_B \tag{10}$$

where F is the Froude number given by $F = U/\sqrt{gL}$. The nondimensional kinematic and dynamic boundary conditions, eqs. (8) and (9), can be combined into the single boundary condition

$$F^2 \phi_{xx} + \phi_z = 0 \tag{11}$$

which is to be applied on the mean free-surface level.

Integral Equation

Green's second identity can be used to obtain an integral equation for the solution of eqs. (7)–(10). If the integral over a hemispherical surface beneath the mean free-surface level vanishes as that surface is expanded to infinity, then the integral equation

$$2\pi\phi(\vec{x}) = \int_{S_B} \phi(\vec{\xi})\frac{\partial}{\partial n_\xi}\frac{1}{r}dS(\vec{\xi}) - \int_{S_B} \frac{\partial\phi}{\partial n_\xi}(\vec{\xi})\frac{1}{r}dS(\vec{\xi})$$

$$+ \int_{S_F} \phi(\vec{\xi})\frac{\partial}{\partial n_\xi}\frac{1}{r}dS(\vec{\xi}) - F^2\int_{S_F} \frac{\phi_{\xi\xi}(\vec{\xi})}{r}dS(\vec{\xi}) \tag{12}$$

holds for $\vec{x} \in S_B \bigcup S_F$. All integrals other than the first or third one are regular. If $\vec{x} \in S_B$, then the first integral is a principal-value integral; otherwise $\vec{x} \in S_F$ and the third integral is a principal-value integral. Eq. (11), the combined free-surface boundary

condition, was used to obtain the last term in its present form.

It is intended to solve the boundary value problem with a low-order Rankine singularity panel code in which the source and dipole distributions over each panel are uniform. Such codes often use finite differences to approximate the derivative of the potential in the last term of the integral equation. However, as is stated in the recent paper by Lechter (6), there is really no satisfactory finite difference scheme for Rankine singularity methods. The situation is worsened by the appearance of the second derivative $\phi_{\xi\xi}$ rather than a first derivative. In this case, however, the need for finite differencing can be greatly reduced by applying Stokes' theorem to the last term of eq. (12). Then a collocation point shifting scheme together with analytic differentiation can be used over most of the free surface. This scheme is similar to the scheme used by Jensen (7). As is pointed out in (6), there are difficulties associated with Jensen's method, especially at low speeds; even so, at the moderate to high speed flows with which this paper deals, the method is an improvement over one in which $\phi_{\xi\xi}$ is approximated by forward finite differences. The first application of Stokes' theorem follows a simple use of the chain rule for differentiation. The result is

$$\int_{S_F} \frac{\phi_{\xi\xi}(\vec{\xi})}{r}dS(\vec{\xi}) = \int_{S_F} \left(\frac{\phi_\xi}{r}\right)_\xi d\xi d\eta - \int_{S_F} \phi_\xi\left(\frac{1}{r}\right)_\xi d\xi d\eta$$

$$= \frac{\partial}{\partial x}\int_{S_F} \frac{\phi_\xi}{r}dS(\vec{\xi}) + \oint \frac{\phi_\xi}{r}d\eta \tag{13}$$

in which the line integral is counterclockwise around the outer edges of the computational region and clockwise around the hull. The x-derivative in front of the surface integral was obtained from the symmetry of r with respect to $\vec{x}$ and $\vec{\xi}$ and from the fact that the integration variable is independent of x. The range of integration for the surface integrals is taken to be the finite portion of the mean free-surface level which is to be paneled later. If the computational domain has sides parallel to the x-z plane, then the line integral has nonvanishing contributions only from around the hull, along the upstream boundary, and along the downstream boundary. The technique can be used again to remove the remaining derivative from inside the surface integral. The result is

$$\int_{S_F} \frac{\phi_{\xi\xi}(\vec{\xi})}{r}dS(\vec{\xi}) = \frac{\partial^2}{\partial x^2}\int_{S_F} \frac{\phi}{r}d\xi d\eta$$

81
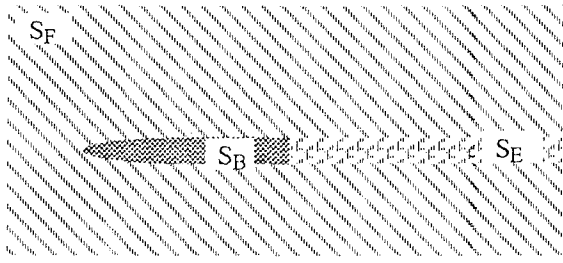
Fig. 1 — Top view of surfaces defined for a transom-stern ship.

$$+ \frac{\partial}{\partial x} \oint \frac{\phi}{r} d\eta + \oint \frac{\phi_\xi}{r} d\eta. \qquad (14)$$

Therefore, the final form of the integral equation is

$$2\pi\phi(\vec{x}) = \int_{S_B} \phi(\vec{\xi}) \frac{\partial}{\partial n_\xi} \frac{1}{r} dS(\vec{\xi}) - \int_{S_B} \frac{\partial\phi}{\partial n_\xi}(\vec{\xi}) \frac{1}{r} dS(\vec{\xi})$$

$$+ \int_{S_F} \phi(\vec{\xi}) \frac{\partial}{\partial n_\xi} \frac{1}{r} dS(\vec{\xi}) - F^2 \frac{\partial^2}{\partial x^2} \int_{S_F} \frac{\phi}{r} dS(\vec{\xi})$$

$$- F^2 \frac{\partial}{\partial x} \oint \frac{\phi}{r} d\eta - F^2 \oint \frac{\phi_\xi}{r} d\eta. \qquad (15)$$

Transom Stern

Flow past a ship with a transom stern is now considered. The flow is assumed to separate smoothly at the hull–transom intersection. As before S_B denotes the hull surface beneath the mean free-surface level. In this case, however, S_F denotes the mean free-surface level only for that portion which is not directly behind the stern. There is an additional surface S_E which extends from the separation line at the hull–transom intersection to downstream infinity. Eventually, it would be desirable for S_E to vary with respect to distance downstream from the hull so that the surface approaches the mean free-surface level downstream of the stern. In this paper, however, S_E does not vary in x and so forms a cylindrical surface downstream of the transom stern. It is assumed that $S_F \bigcup S_E$ is a smooth surface. The surfaces, viewed from above, are depicted in Fig. 1.

Under the same conditions that were required in the case of a cruiser stern, Green's second identity can be used to obtain the integral equation

$$2\pi\phi(\vec{x}) = \int_{S_B} \phi(\vec{\xi}) \frac{\partial}{\partial n_\xi} \frac{1}{r} dS(\vec{\xi}) - \int_{S_B} \frac{\partial\phi}{\partial n_\xi}(\vec{\xi}) \frac{1}{r} dS(\vec{\xi})$$

$$+ \int_{S_F \bigcup S_E} \phi(\vec{\xi}) \frac{\partial}{\partial n_\xi} \frac{1}{r} dS(\vec{\xi}) - \int_{S_F \bigcup S_E} \frac{\partial\phi}{\partial n_\xi}(\vec{\xi}) \frac{1}{r} dS(\vec{\xi}), \qquad (16)$$

which is valid for $\vec{x} \in S_B \bigcup S_F \bigcup S_E$. For $\vec{x} \in S_B$, the first integral is a principal–value integral; for $\vec{x} \in S_F \bigcup S_E$, the third integral is a principal-value integral; otherwise, the integrals are regular. To continue as before, the normal derivative in the last integral must be expressed in terms of the potential and its tangential derivatives on the boundary. If the surface $S_F \bigcup S_E$ is given by the equation

$$z - E(x, y) \equiv 0, \qquad (17)$$

then the unit normal directed into the fluid is given by

$$\vec{n} = (E_x, E_y, -1) / \sqrt{1 + E_x^2 + E_y^2} \qquad (18)$$

and the last term of the integral equation can be rewritten as

$$\int_{S_F \bigcup S_E} \frac{\partial\phi}{\partial n_\xi}(\vec{\xi}) \frac{1}{r} dS(\vec{\xi})$$

$$= \int_{S_F \bigcup S'_E} \left[\frac{\phi_\xi E_\xi + \phi_\eta E_\eta - \phi_\zeta}{r} \right]_{\zeta = E(\xi, \eta)} d\xi d\eta. \qquad (19)$$

Here S'_E refers to the projection of S_E onto the mean free-surface level.

On the actual free surface $z = Z(x, y)$, which is to be distinguished from the surface $z = E(x, y)$, the nonlinear kinematic and dynamic free-surface boundary conditions are given by

$$\phi_z - Z_x(1 + \phi_x) - Z_y \phi_y = 0 \qquad (20)$$

and

$$\phi_x + \frac{Z}{F^2} + \frac{1}{2}(\phi_x^2 + \phi_y^2 + \phi_z^2) = 0, \qquad (21)$$

respectively. It is assumed that $\phi_x^2 + \phi_y^2 + \phi_z^2 \ll 1$, although it might be argued that ϕ_y is not negligible in the vicinity of deep transoms with steep side walls.

After discarding these terms, the dynamic free–surface boundary condition becomes

$$\phi_x + Z/F^2 = 0 \quad on \quad z = Z(x,y). \tag{22}$$

Expanding the factors involving the potential in eqs. (20) and (22) in Taylor series about $z = E(x, y)$ and dropping all terms of the series expansions except the lowest order terms, we obtain

$$\phi_z - Z_x - Z_x\phi_x - Z_y\phi_y = 0 \tag{23}$$

and

$$\phi_x(x, y, E(x, y)) + \frac{Z(x, y)}{F^2} \equiv \phi_x + \frac{Z}{F^2} = 0 \tag{24}$$

on $z = E(x, y)$. Eq. (24) can be differentiated with respect to x and combined with eq. (23) to obtain

$$\phi_z - Z_x\phi_x - Z_y\phi_y + F^2(\phi_{xx} + \phi_{xz}E_x) = 0 \tag{25}$$

on $z = E(x, y)$ which, if we assume $|\phi_{xz}E_x| \ll 1$, becomes

$$\phi_z - Z_x\phi_x - Z_y\phi_y + F^2\phi_{xx} = 0 \tag{26}$$

on $z = E(x, y)$. This equation is used to eliminate ϕ_z from the the right hand side of eq. (19):

$$\int_{s_F \cup s_E} \frac{\partial \phi}{\partial n_\xi}(\vec{\xi})\frac{1}{r}dS(\vec{\xi}) = \int_{s_F \cup s_E} d\xi d\eta \ \cdot$$

$$\cdot \left[\frac{(E - Z)_\xi\phi_\xi + (E - Z)_\eta\phi_\eta + F^2\phi_{\xi\xi}}{r}\right]_{\zeta = E(\xi, \eta)} \tag{27}$$

If $|(E_\xi - Z_\xi)\phi_\xi| \ll 1$ and $|(E_\eta - Z_\eta)\phi_\eta| \ll 1$, then eq. (27) becomes

$$\int_{s_F \cup s_E} \frac{\partial \phi}{\partial n_\xi}(\vec{\xi})\frac{1}{r}dS(\vec{\xi}) = F^2\int_{s_F \cup s_E} \frac{\phi_{\xi\xi}}{r}d\xi d\eta. \tag{28}$$

and eq. (16) becomes

$$2\pi\phi(\vec{x}) = \int_{s_B} \phi(\vec{\xi})\frac{\partial}{\partial n_\xi}\frac{1}{r}dS(\vec{\xi}) - \int_{s_B} \frac{\partial \phi}{\partial n_\xi}(\vec{\xi})\frac{1}{r}dS(\vec{\xi})$$

$$+ \int_{s_F \cup s_E} \phi(\vec{\xi})\frac{\partial}{\partial n_\xi}\frac{1}{r}dS(\vec{\xi}) - F^2\int_{s_F \cup s_E'} \frac{\phi_{\xi\xi}(\vec{\xi})}{r}d\xi d\eta, \tag{29}$$

which is almost the same as eq. (12). The application of Stokes' theorem proceeds as it does for the case of a cruiser stern and we obtain the integral equation

$$2\pi\phi(\vec{x}) = \int_{s_B} \phi(\vec{\xi})\frac{\partial}{\partial n_\xi}\frac{1}{r}dS(\vec{\xi}) - \int_{s_B} \frac{\partial \phi}{\partial n_\xi}(\vec{\xi})\frac{1}{r}dS(\vec{\xi})$$

$$+ \int_{s_F \cup s_E} \phi(\vec{\xi})\frac{\partial}{\partial n_\xi}\frac{1}{r}dS(\vec{\xi})$$

$$- F^2\frac{\partial^2}{\partial x^2}\int_{s_F \cup s_E} \frac{\phi}{r\sqrt{1 + E_\xi^2 + E_\eta^2}}dS(\vec{\xi})$$

$$- F^2\frac{\partial}{\partial x}\oint \frac{\phi}{r}d\eta - F^2\oint \frac{\phi_\xi}{r}d\eta. \tag{30}$$

This equation is the final form of the integral equation for the case of a transom stern hull.

Free–Wave Spectrum and Wave–Pattern Resistance

We wish to compute the magnitude of the free–wave spectrum whose sine and cosine components $\mathcal{F}(u)$ and $\mathcal{G}(u)$ are defined in eq. (35) of Eggers et al. (8). The definitions assume that all lengths have been normalized by the inverse of the fundamental wave number k_0. The same normalization applies to $\mathcal{F}$, $\mathcal{G}$, and the magnitude of the spectrum. The transverse wave number u has been normalized by k_0.

The free–wave spectrum is calculated from a pair of transverse wave cuts by a method derived by Sharma (9). Sharma, in contrast to Eggers et al., retained dimensions. Taking into account this difference, $\mathcal{F}$ and $\mathcal{G}$ are reproduced here in terms of the non-dimensional variables of this paper. If the two transverse wave cuts are $Z_1(y) \equiv Z(x_1, y)$ and $Z_2(y) \equiv Z(x_2, y)$, then

$$\mathcal{F}(u) = \frac{1}{F^4}\left[\frac{\sin \overline{X}}{\cos \delta X}(C_1 + C_2) + \frac{\cos \overline{X}}{\sin \delta X}(C_1 - C_2)\right] \tag{31}$$

and

83

$$g(u) = \frac{1}{F^4}\left[\frac{\sin \bar{X}}{\sin \delta X}(C_1 - C_2) - \frac{\cos \bar{X}}{\cos \delta X}(C_1 + C_2)\right] \tag{32}$$

where

$$\bar{X} = \sec^2\theta\cos\theta\frac{x_1 + x_2}{2F^2}, \tag{33}$$

$$\delta X = \sec^2\theta\cos\theta\frac{x_1 - x_2}{2F^2}, \tag{34}$$

and

$$C_k = 2\int_0^\infty Z_k\cos\left(\frac{y}{F^2}\sec^2\theta\sin\theta\right)dy \tag{35}$$

for $k = 1,2$.

Using eq. (2.49) of Sharma, the wave resistance R_W can be written in terms of $\mathcal{F}$ and g. The corresponding nondimensional wave–pattern resistance C_{WP} is given by

$$C_{WP} = \frac{F^4}{8\pi(S/L^2)}\int_0^{\pi/2}\left\{[\mathcal{F}(u(\theta))]^2 + [g(u(\theta))]^2\right\}\cdot$$

$$\cdot (1 + \sin^2\theta)^2\sec^3\theta d\theta \tag{36}$$

where S is the wetted area and L is the length of the hull.

NUMERICAL IMPLEMENTATION

The hull surface and the finite portion of $S_F \bigcup S_E$ within the finite computational domain are approximated by strips of flat rectangular panels. Strips on S_E originate at the hull–transom intersection; strips on S_F originate at the computational boundary upstream of the hull. For the time being, the upstream panel in each strip of S_F is assumed to have approximately twice the longitudinal dimension of those panels immediately downstream from it.

On each panel, the perturbation potential ϕ and its derivative $\partial\phi/\partial n_\xi$ in the surface integrals of integral eq. (30) are assumed to be uniform and equal to their values at the centroid of the panel. Surface integrals over panels are then evaluated analytically.

On the most forward panel of each longitudinal strip of S_F, the surface integral and the line integrals along the upstream edge of the strip in the last three

terms of the integral equation are combined. On and around this panel ϕ_ξ is set to zero. Then, when the range of integration for the integrals is restricted to this panel and its edges, the sum of the last three terms in the integral equation on this panel becomes

$$\frac{\partial^2}{\partial x^2}\int\frac{\phi}{r}d\xi d\eta + \frac{\partial}{\partial x}\int^4\frac{\phi}{r}d\eta + \int^4\frac{\phi_\xi}{r}d\eta$$

$$= -\frac{\partial}{\partial x}\oint\frac{\phi}{r}d\eta + \frac{\partial}{\partial x}\int^4\frac{\phi}{r}d\eta$$

$$= \frac{\partial}{\partial x}\left\{\int_1^4 - \int_1^4 - \int_4^3 - \int_3^2 - \int_2^1\frac{\phi}{r}d\eta\right\}$$

$$= \frac{\partial}{\partial x}\left\{\int_1^2 + \int_2^3 + \int_3^4\frac{\phi}{r}d\eta\right\}.$$

Here the common multiplicative factor of F^2 has been deleted. The numbers 1 through 4 refer to the vertices in clockwise order around the panel when the panel is viewed from above. The side joining vertices 1 and 4 is at the upstream edge of the computational region. The first and third integrals are zero when the edges joining vertices 1 and 2 and vertices 3 and 4 are parallel to the x-z plane.

Similar treatment of the line and surface integrals at the downstream boundaries of the computational domain is employed except that ϕ_ξ in the second line integral is discarded. Since disturbances propagate downstream, this treatment of ϕ_ξ at the downstream boundary should not affect the flow near the ship if the downstream boundary is far enough downstream.

Hull–waterline integrals are split into a part along the hull–transom intersection and a part along the sides of the hull. The numerical treatment of the two parts differs. Along the sides of the hull in the first line integral of eq. (30), ϕ is assumed to be uniform over the edge of a panel where its value is extrapolated from function values at the centroids of two nearby free–surface panels. The derivative of the potential in the second line integral is approximated by finite differences as is shown in Fig. 2 and is assumed to be uniform over the edge of a panel. In particular, the derivative ϕ_ξ at the waterline point $\mathbf{a}$ is approximated by a linear combination of the potential at $\mathbf{a}$ and at three points upstream of $\mathbf{a}$; this differencing scheme is the same one as was used by Dawson (10). The potential at each of the points $\mathbf{a}$ through $\mathbf{d}$ is in
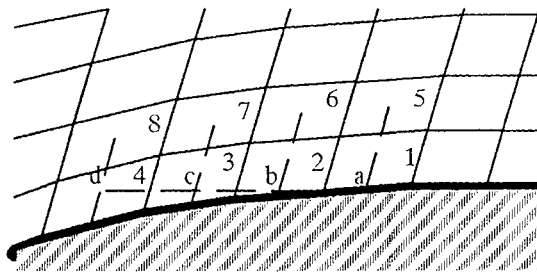
Fig. 2 — Top view of free-surface panels adjacent to the hull. The x-derivative of the potential at a is a linear combination of the potential at the points **a**, **b**, **c**, and **d**. The potential at **a** is in turn a linear combination of the potential at the centroids of panels 1 and 5. Similarly, the potential at each of the points **b**, **c**, and **d** is a linear combination of the potential at the centroids of two numbered panels. Thus the derivative of the potential at **a** is a linear combination of the potential at the centroids of the panels numbered 1 through 8.

Fig. 3 — Top view of some of the panels in the neighborhood of a transom stern. Panels to the left of the heavy line are on the hull surface; panels to the right are on the surface about which the free-surface boundary conditions are linearized.

turn expressed as a linear combination of the potential at the centroids of two free-surface panels. Thus the derivative at each waterline point is approximated by a linear combination of the potential at the centroids of eight free-surface panels.

At the hull-transom intersection along the assumed separation line which corresponds to the upstream edge of S_E, an approximation to ϕ_ξ based on hull geometry and a linearized form of Bernoulli's equation is available since it is known that the pressure there is atmospheric pressure. With this approximation, the last line integral of eq. (30) is evaluated analytically along the intersection. The potential ϕ along the separation line in the other line integral is set to the potential at the centroid of the free-surface panel directly behind the stern.

On the hull surface S_B, collocation points are placed at the centroids of panels. For each panel on $S_F \bigcup S_E$, there is associated a collocation point located at the centroid of the panel just upstream of it. This collocation point shifting is a convenient way of enforcing the radiation condition without the use of upstream finite differences.

At the upstream end of S_F, where there are no upstream panels, the collocation point is shifted forward a distance approximately equal to the longitudinal dimension nearby free-surface panels. The upstream panel has two collocation points on it because it has twice the longitudinal dimension of the free-surface panels immediately downstream from it. All collocation points associated with S_F thus lie on S_F.

At the upstream end of strips of panels originating at the hull-transom intersection, collocation points are not associated with panels closest to the
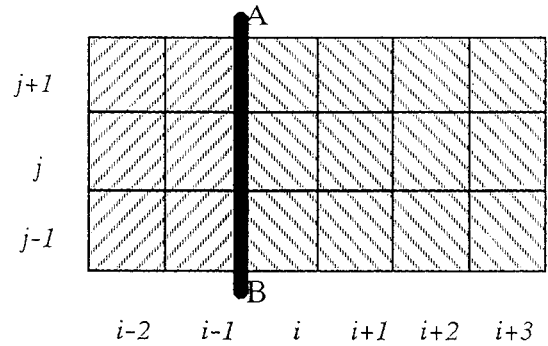
transom. Instead, equations that would be associated with these collocation points are replaced with equations specifying free-surface depth and slope in terms of the hull geometry at the transom stern. This treatment is based on the work of Sclavounos and Nakos (11) which showed that wave height and slope must be specified at the forward edge of a truncated computational free-surface domain. The specified free-surface elevation and slope ensure that the free-surface elevation and slope at the transom match the hull depth and hull shape. For a linearized problem, these are conditions on ϕ_x and ϕ_{xx} at the transom. After numerical experimentation, it was decided to enforce conditions on ϕ_x at two successive panels immediately behind the stern rather than to use the direct approach of setting ϕ_x at the centroid of one panel and ϕ_{xx} at the centroid of a second panel. At the centroids of the two successive panels, ϕ_x is set by means of finite difference equations to values obtained from truncated Taylor series expansions involving ϕ_x and ϕ_{xx} at the transom. An example of such a difference equation for strip j in Fig. 3 is

$$\phi_{i,j} - \phi_{i-1,j} = (x_{ij} - x_{i-1,j}) \cdot$$
$$\cdot \left[\phi_x(\vec{x}_T) + \left(\frac{x_{ij} + x_{i-1,j}}{2} - x_T \right) \phi_{xx}(\vec{x}_T) \right]$$

where $\vec{x}_T$ is the midpoint of the forward edge of the j-th strip on S_E and the other, subscripted x-values refer to the centroids of panels immediately downstream from the hull-transom intersection.

For free-surface paneling behind a transom stern, where smaller paneling is usually used, there is a lot of noise in the solution. An examination of columns of the final matrix showed that there was much more upstream-downstream symmetry in the matrix near diagonal elements corresponding to panels be-

hind the stern than elsewhere on the free surface. To produce more upstream-downstream asymmetry near these diagonal elements, a small additional shift downstream was used for the collocation points in the strips of panels behind the transom stern. The additional downstream shift succeeded in damping the numerical noise. For all the results presented in this paper, the additional shift downstream was applied only in strips directly behind the transom stern and it amounted to $0.0002L$ where L is the length of the hull. This value was determined by numerical experimentation so as to minimize the additional downstream shift of the collocation points and at the same time provide enough numerical damping to produce the desired effects.

A full, nonsymmetric system of linear equations is obtained. To solve it, the system is first row scaled; then an accelerated block Gauss-Seidel solver is used to obtain a solution. Smaller Froude numbers and smaller panel sizes tend to increase the number of iterations required in the solver, but convergence is almost always obtained. If not, a change in paneling seems to help convergence.

PREDICTIONS

Athena Hull

Plots of the computed Kelvin wave pattern and the amplitude of the free-wave spectrum obtained from the computed wave pattern are presented for speeds corresponding to the Froude numbers 0.48 and 0.4. The first speed is especially interesting because the wave elevation immediately aft of the transom stern can be compared with published measurements.

The body plan of the Athena hull and the paneling on and near the hull are depicted in Fig. 4 and Fig. 5. Since the flow configuration is symmetric about the center plane, only the starboard half is paneled. In this case, the starboard half of the hull is paneled with 8 longitudinal strips of 50 panels whose longitudinal dimensions are nearly uniform ($\Delta x \approx 0.02$). The widths of these strips at each longitudinal station along the hull are nearly uniform. Free-surface paneling covers a region extending from one ship length upstream to nearly one and a half ship lengths downstream from the hull, extends laterally from the center plane to one ship length away, and is swept back at a $45°$ angle from the center plane. Except upstream of the hull where the longitudinal dimension of free-surface panels is gradually increased, free-surface panels have approximately the same longitudinal dimension ($\Delta x = 0.02$) as that of the hull panels. Adjacent to the hull, free-surface panels have aspect ratios nearly equal to unity and match the hull panels at the waterline; the widths of the strips gradually increase

with increasing distance from the center plane. Behind the transom, eight strips of panels lying on a cylindrical surface originating at the stern and extending downstream are used. There is no variation in the depth of these strips with respect to distance downstream from the transom. At the stern the forward edges of these strips match the downstream edges of the strips of panels on the hull. Due to the narrowness of the strips behind the stern, the longitudinal dimension of the panels is halved to avoid numerical problems that occur with panels of aspect ratio greater than two. In this paneling arrangement, the total number of panels used on the starboard half of the configuration is 3880.

Fig. 6 presents a contour plot of the computed Kelvin wave pattern in a neighborhood of the high-speed Athena hull at Froude number 0.48. Figs. 7a and 7b present the same data in close-up contour plots of the computed and measured wave elevation near the transom stern. The computed elevation behind of the stern is slightly deeper and rises more quickly toward the mean free-surface level than is indicated by the measured results of Fig. 7b. However, the fact that the two contour plots agree as well as they do is encouraging. Fig. 8 shows the amplitude of the free-wave spectrum for this flow configuration. The wave resistance computed from this spectrum is 0.0015, higher than the experimental result of 0.0013 reported in (12) for the slightly higher Froude number 0.484.

A contour plot of the computed wave elevation and a plot of the computed amplitude of the free-wave spectrum for Froude number 0.4 appear in Fig. 9 and Fig. 10. The corresponding computed wave resistance is 0.0012.

Model 5415

The body plan for Model 5415 is shown in Fig. 11. Comparison with Fig. 4 shows that with respect to the midship section, the transom stern on the Athena hull is larger and more rectangular than on Model 5415. The two hulls differ mainly in that Model 5415 has a bow dome. This difference, however, is irrelevant to the content of this paper. Paneling for the hull and the surrounding free surface is depicted in Fig. 12. The paneling is similar to the paneling used for the Athena hull. Experimental data measurements for this model at several speeds are available in a report by Ratcliffe and Lindenmuth (13). The measurements are presented in the form of plots of the wave spectrum and contour plots of the measured wave elevation. Two speeds corresponding to Froude numbers 0.414 and 0.25 are considered here. For the slower speed, measured free-surface height is available in the region immediately behind the transom stern.

Contours of the computed wave elevation near the stern of this hull for a speed corresponding to

Fig. 4 — Body plan of the Athena hull.

(a) Computed

(b) Measured

Fig. 7 — Contours of the Kelvin wave pattern near the transom stern of the Athena hull at F = 0.48. (a) Contours of the computed wave elevation. (b) Contours of the measured wave elevation. [Measured data from (12).] The contour levels are the same as in Fig. 6.
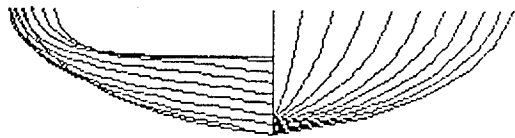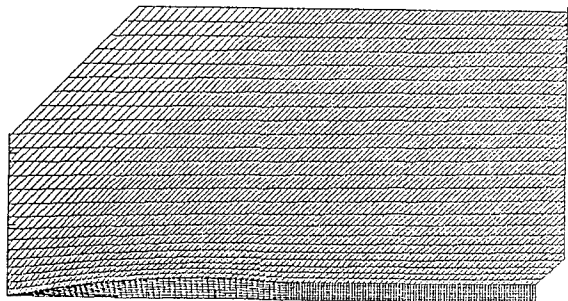
Fig. 5 — Top view of the paneling of the Athena hull and the free surface near the hull.
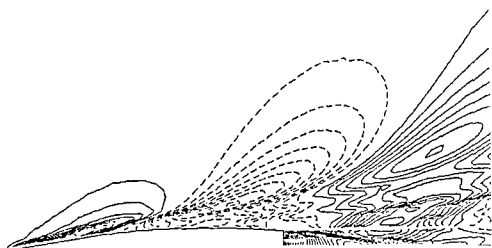
Fig. 6 — Contours of the computed free-surface elevation for the Athena hull at F = 0.48. Solid lines indicate positive nondimensional wave elevation $Z/F^2 = 0.005j$ for j = 1, 2, etc. Dashed lines indicate negative wave elevation $Z/F^2 = -0.005j$ for j = 1, 2, etc. The zero contour level is not drawn.

Transverse Wave Number, u

Fig. 8 — Amplitude of the free-wave spectrum from a pair of transverse wave cuts at 1.15 and 1.20 ship lengths aft of the midship section of the Athena hull for F = 0.48.

87
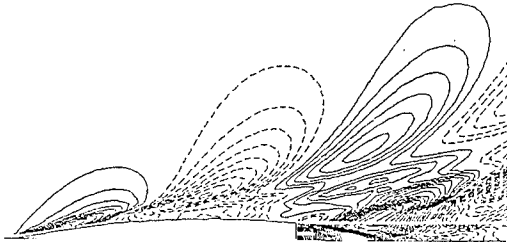
Fig. 9 — Contours of the computed free-surface elevation for the Athena hull at $F = 0.4$. Solid lines indicate positive nondimensional wave elevation $Z/F^2 = 0.005j$ for $j = 1, 2$, etc. Dashed lines indicate negative wave elevation $Z/F^2 = -0.005j$ for $j = 1, 2$, etc. The zero contour is not drawn.

Fig. 10 — Amplitude of the free-wave spectrum obtained from a pair of transverse wave cuts at 1.15 and 1.20 ship lengths aft of the midship section of the Athena hull for $F = 0.4$.

Froude number 0.414 are shown in Fig. 13 and Fig. 14a. The computed contours near the transom are compared with the corresponding contours obtained from measurements in Fig. 14. (In Fig. 14b, the contours immediately behind the transom are computed, not measured, since no measurements were obtained in this region.) From Fig. 14b it appears that the peak behind the stern is nearly in the correct position. The measured contours of the wave elevation in Fig 14b show a sharp gradient of the wave elevation that starts approximately 0.1 ship length aft of the stern and lies along a ray at about the Kelvin angle away from the center plane. In the computed contours of Fig. 14a there is a corresponding surface height gradient, but is not as sharp. The peak of the computed free-surface elevation here corresponds to level $0.08F^2$ whereas the measured wave height corresponds to level $0.085F^2$. A comparison of the amplitude of the free-wave spectrum obtained from computed wave elevations along transverse wave cuts and from measured wave elevations is presented in Fig. 15. The wave resistance computed from the amplitude of the wave spectrum shown in this figure is 0.0018, which is lower than the value of 0.0024 obtained from experimental data.

For Froude number 0.25 contours of the computed free-surface height are shown in Figs. 16 and 17a. The corresponding amplitude of the free-wave spectrum is plotted in Fig. 18. A close-up comparison of the contours of computed and measured wave elevation near the stern of Model 5415 at Froude number 0.25 is provided in Fig. 17. For this speed, measurements are available in the region immediately behind the stern. The positions of the computed and measured peaks behind the stern agree fairly well. Outside the area immediately behind the stern, as is the case for the higher speed, there is a sharp gradient in the measured wave elevation along a line starting
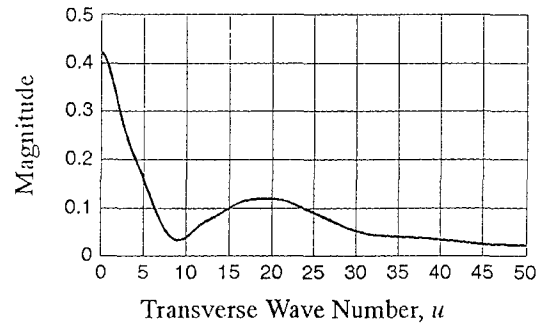
at the stern and radiating downstream from the hull at approximately the Kelvin angle. The large gradient is also present in the computed results, but it is not as sharp. At the peak elevation near the sharp gradient, the computed nondimensional free-surface height is $0.08F^2$. Except for a very small area where the measured elevation is higher, this is the nondimensional wave height of the highest measured contour level plotted. The wave resistance computed from the magnitude of the wave spectrum is 0.00042, which is higher than the value of 0.00037 obtained from experimental data.

If paneling behind the stern is placed on the mean free-surface level rather than on the cylindrical surface surface extending downstream from the hull-transom intersection and if no strips of wake panels originating at the transom are used, then a different solution is obtained. In this case finite differencing to set the free-surface depth and slope immediately behind the stern is based on the potential solely at the centroids of free-surface panels and thus excludes the potential on the hull. Contours of the wave elevation near the stern for Froude numbers 0.25 and 0.414 are shown in Figs. 19 and 20. These are to be compared with the previous results depicted in Figs 17a and 14a, respectively. There is a visible difference in the contours. There is less of the sharp gradient that is seen in the contours of the experimental measurements. This difference is more obvious for the lower speed. Corresponding plots of the amplitude of the free-wave spectrum are given in Figs. 21 and 22. There is not much difference at Froude number 0.414.

CONCLUSION

It has been shown that it is possible to linearize the wave resistance problem about a surface that originates at the intersection of the hull and a transom

88
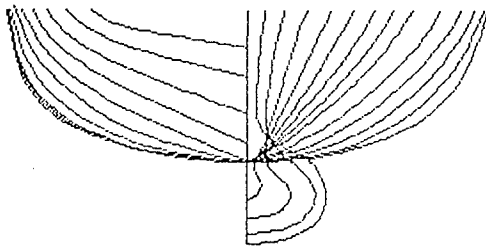
Fig. 11 — Body plan of Model 5415.
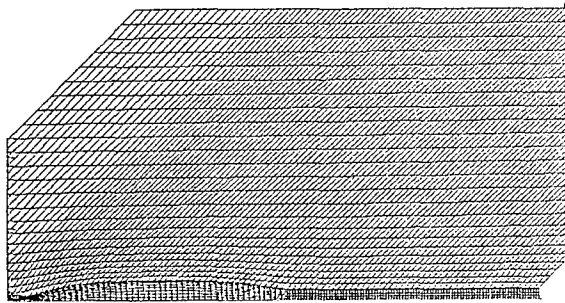
Fig. 12 — Top view of the paneling on Model 5415 and on the surrounding free surface.

(a) Computed

(b) Measured, except behind the stern

Fig. 14 — Contours of the free–surface elevation near the transom stern of Model 5415 at $F = 0.414$. (a) Contours of computed wave elevation. (b) Contours of measured wave elevation except aft of the transom where contours of computed wave elevation are presented (and are identical to the corresponding contours in (a)). Contour levels are the same as in Fig. 13

Fig. 13 — Contours of the computed Kelvin wave pattern for Model 5415 at $F = 0.414$. Solid lines indicate positive nondimensional wave elevation $Z/F^2 = 0.005j$ for $j = 1, 2$, etc. Dashed lines indicate negative wave elevation $Z/F^2 = -0.005j$ for $j = 1, 2$, etc. The zero contour level is not drawn.
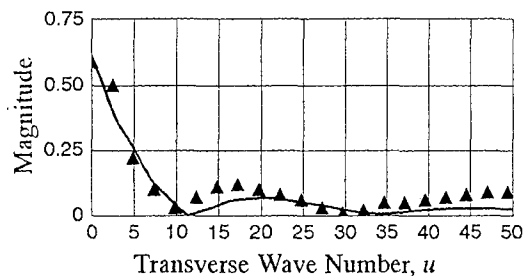
Fig. 15 — Comparison of the amplitude of the free–wave spectrum for Model 5415 at $F = 0.414$ obtained from a pair of computed transverse wave cuts (—) and from experiments (▲).

89

Fig. 16 — Contours of the computed free-surface elevation for Model 5415 at $F = 0.25$. Solid lines indicate positive wave elevation $Z/F^2 = 0.005j$ for $j = 1, 2$, etc., and dashed lines, negative wave elevation $Z/F^2 = -0.005j$ for $j = 1, 2$, etc. The zero contour is not drawn.

(a) Computed
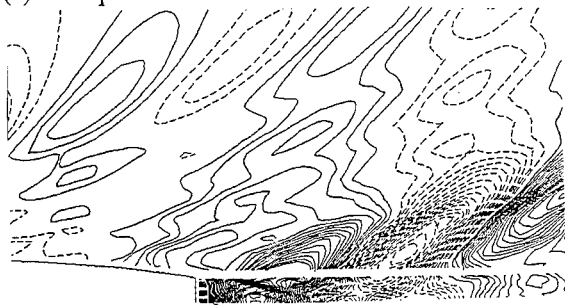
(b) Measured

Fig. 17 — Contours of the free-surface elevation near the stern of Model 5415 at $F = 0.25$. (a) Contours of computed wave elevation. (b) Contours of measured wave elevation. Contour levels are the same as in Fig. 16.
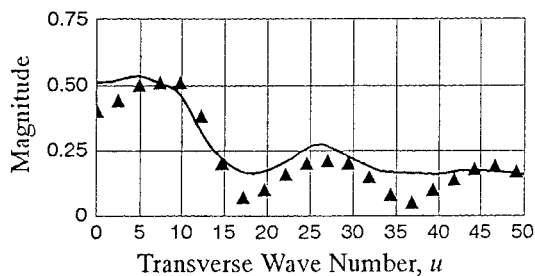
Fig. 18 —Amplitude of the free-wave spectrum for Model 5415 at $F = 0.25$ obtained from a pair of computed transverse wave cuts (——) and from experiments (▲).

stern and which extends downstream from this intersection. The computed wave height is different from the wave height obtained using a model in which panels behind a transom stern are placed on the mean free-surface level and the transom is left open. For the few results presented here, some features present in experimental results show up more clearly when panels behind the stern are placed on the surface originating at the hull-transom intersection.

To compute the solution of the wave resistance problem, we have modified an existing Rankine singularity code that had been based on the use of distributions of sources and dipoles on the mean free-surface level. The finite-differencing scheme in the code was replaced by one in which analytic differentiation and collocation point shifting are used to enforce the radiation boundary condition. In so doing free-surface integrals have been replaced by a combination of free-surface and hull-waterline integrals. The hull-waterline integrals are analogous to those customarily seen in Havelock singularity methods only in that similar mechanisms are used to arrive at them; they are otherwise completely different. The wave height appears to be calculated more accurately by using this scheme than by using the scheme in the original code.

Difficulties can be expected in this method when the wave slope is enforced at a transom stern. Several causes can be singled out. First, obtaining the hull slope is problematic since there is typically a rapid variation in the hull shape at the stern. Second, developing an accurate numerical scheme that enforces the slope on a curved surface is complicated. Here part of the latter problem has been eliminated by using a cylindrical surface beneath the mean free-surface level without longitudinal variation in depth downstream of the hull-transom intersection.

Further developments might be made. The first involves putting panels behind a hull-transom intersection on a curved surface that rises toward the mean free-surface level. This was tried, but anomalies in the contours of the computed wave elevation directly behind the transom led to the simpler approach of putting panels on a cylindrical surface originating at the intersection. Perhaps the linearization scheme should be reexamined, or perhaps the accuracy to which higher derivatives of the potential due to source and dipole distributions on curved surfaces can be computed should be reevaluated. As a second refinement, the nonlinear zero-pressure Kutta condition, Bernoulli's equation with the pressure set to atmospheric pressure, could be satisfied at the transom stern. This nonlinear Kutta condition should be used in conjunction with a varying depth in the surface originating at the hull-transom intersection about which the free-surface boundary conditions are linea-

90

Fig. 19 — Contours of computed free-surface elevation for Model 5415 hull at $F = 0.25$. Paneling behind the transom stern has been placed on the mean free-surface level. Finite differencing at the upstream end of strips of panels originating at the stern involves the disturbance potential only at the centroids of free-surface panels instead of at the centroids of neighboring free surface and hull panels. Solid lines indicate positive wave elevation $Z/F^2 = 0.005j$ for $j = 1, 2$, etc. and dashed lines, negative elevation $Z/F^2 = -0.005j$ for $j = 1, 2$, etc. The zero contour level has not been drawn.

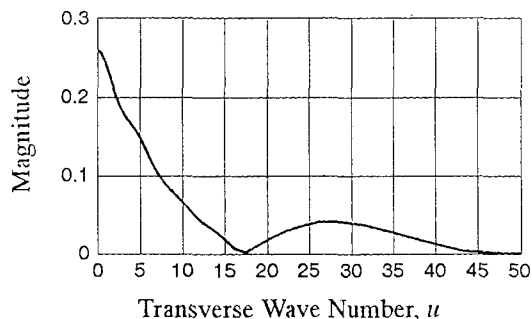**Fig. 21** — Amplitude of the free-wave spectrum obtained from a pair of computed transverse wave cuts at 1.15 and 1.20 ship lengths aft of the midship of Model 5415 Froude number 0.25 (—) and the corresponding spectrum obtained from experimental data (▲). Paneling aft of the transom stern has been placed on the mean free-surface level. Finite differencing at the upstream end of strips of panels originating at the stern involves the disturbance potential only at the centroids of free-surface panels instead of at the centroids of neighboring free-surface and hull panels.

Fig. 20 — Contours of computed free-surface elevation for Model 5415 hull at $F = 0.414$. Paneling aft of the transom stern has been placed on the mean free-surface level. Finite differencing at the upstream end of strips of panels originating at the stern involves the disturbance potential only at the centroids of free-surface panels instead of at the centroids of neighboring free-surface and hull panels. The contour levels are the same as in Fig. 19.
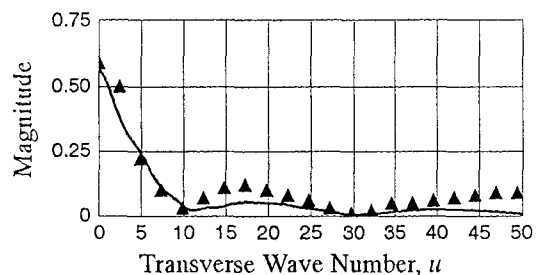
Fig. 22 — Amplitude of the free-wave spectrum obtained from a pair of computed transverse wave cuts at 1.15 and 1.20 ship lengths aft of the midship section of Model 5415 at $F = 0.414$ (—) and the corresponding spectrum obtained from experimental data (▲). Paneling aft of the transom stern has been placed on the mean free-surface level. Finite differencing at the upstream end of strips of panels originating at the stern involves the disturbance potential only at the centroids of free-surface panels instead of at the centroids of neighboring free surface and hull panels.

91

rized. The combination may be especially important for deep transoms.

Although, according to Lechter (6), the method of collocation point shifting and analytic differentiation may break down at low Froude numbers, several enhancements might be made to the Rankine singularity method that was used to obtain numerical approximations to free-surface potential flows. They are related to the more general problem of calculating the linearized free-surface potential flow near arbitrarily shaped ships advancing into calm water. The first would be to eliminate the finite differencing at the hull waterline. This would eliminate all finite differences except those at the hull-transom intersection. Second, the relationship between free-surface paneling and collocation point shifting should be clarified. When a second small longitudinal shift downstream is used, damping is introduced into the wave pattern. Further, a more or less rectangular grid of panels on the free surface damps the waves in the Kelvin wave pattern more than the arrangement used in this paper, in which the computational free-surface domain is swept back at a 45-degree angle. The effect is most noticeable in the diverging waves seen in contour plots. Finally, it might be useful to consider whether something similar to the DtN exact boundary condition of Keller and Givoli (14) could be used for the outer boundaries of the computational domain to handle the boundary conditions there more accurately and to reduce the size of the computational domain.

ACKNOWLEDGMENT

REFERENCES

1. Lindenmuth, W. T., Ratcliffe, T. J., and Reed, A. M., "Comparative Accuracy of Numerical Kelvin Wake Code Predictions — 'Wake-Off'". DTRC Ship Hydromechanics Dept. R & D Report DTRC-91/004, 1991, 257+xiv p.

2. Cheng, B. H., "Computations of 3D Transom Stern Flows," Proc. Fifth International Conference on Numerical Ship Hydrodynamics, National Academy Press: Washington, DC, 1989, pp. 581-592.

3. Reed, A., Telste, J., and Scragg, C., "Analysis of Transom Stern Flows," Proc. Eighteenth Symposium on Naval Hydrodynamics, National Academy Press: Washington, DC, 1990, pp. 207-220.

4. Nakos, D. E. and Sclavounos, P. D. "Kelvin Wakes and Wave Resistance of Cruiser and Transom Stern Ships," Journal of Ship Research, to appear.

5. Tulin, M. P. and Hsu, C. C., "Theory of High-Speed Displacement Ships with Transom Sterns," Journal of Ship Research, Vol. 30, No. 3, 1986, pp. 186-193.

6. Lechter, J. S., "Properties of Finite-Difference Operators for the Steady-Wave Problem," Journal of Ship Research, Vol. 37, No. 1, March 1993, pp. 1-7.

7. Jensen, P. S., "On the numerical radiation condition in the steady-state ship wave problem," Journal of Ship Research, Vol. 31, No. 1, March, 1987, pp. 14-22.

8. Eggers, K., Sharma, S. D., and Ward, L. W., "An Assessment of Some Experimental Methods for Determining the Wavemaking Characteristics of a Ship Form," SNAME Transactions, Vol. 75, 1967, pp. 112-57.

9. Sharma, S. D., "A Comparison of the Calculated and Measured Free-Wave Spectrum of an Inuid in Steady Motion," Proc. Int'l Seminar on Theoretical Wave-Resistance, Vol 1, University of Michigan, Ann Arbor, 1963, pp. 203-272.

10. Dawson, C. W., "A Practical Computer Method for Solving Ship-Wave Problems," Proc. Second International Conference on Numerical Ship Hydrodynamics, Univ. of California: Berkeley, California, CA, 1977, pp. 30-38.

11. Sclavounos, P. D. and Nakos, D E., "Stability of Panel Methods for Free-Surface Flows with Forward Speed," Proc. Seventeenth Symposium on Naval Hydrodynamics, National Academy Press: Washington, DC, 1988, pp. 173-93.

12. Jenkins, D. S., "Resistance Characteristics of the High Speed Transom Stern Ship R/V Athena in the Bare Hull Condition, Represented by DTNSRDC Model 5365," Ship Performance Dept. R & D Report DTNSRDC-84/024, 1984, 59+ix p.

13. Ratcliffe, T. J. and Lindenmuth, W. T., "Kelvin Wake Measurements Obtained on Five Surface Ship Models," DTRC Ship Hydromechanics Dept. R & D Report DTRC-89/038, 1990, 88+x p.

14. Keller, J. B. and Givoli, D., "Exact Non-reflecting Boundary Conditions," Journal of Computational Physics, Vol. 82, 1989, pp. 172-192.

SESSION 3

WAVY/FREE-SURFACE FLOW: PANEL METHODS 3

Nonlinear Ship Wave Calculations Using the RAPID Method

H.C. Raven (MARIN, The Netherlands)

ABSTRACT

The RAPID (RAised-Panel Iterative Dawson) approach for solving the fully nonlinear wave-resistance problem is described. This method, developed at MARIN, uses an iterative procedure based on a Rankine panel method similar to that of Dawson. No convergence problems are usually met in the speed and fullness range of practical ships, and even for cases showing extensive wave breaking in reality. The validity of the method regarding the occurrence of wave breaking and steep wave slopes is discussed. The modeling of the flow off a transom stern and its implementation in RAPID and in the corresponding linearized problem is studied. The nonlinear solution is found to be realistic and very accurate numerically. A number of validation studies shows that the RAPID results are very good in most respects, and often mean a surprisingly large improvement compared to linearized solutions. The principal remaining problems are resolution of short wave components, certain geometric complications, and the absence of a 3D model for wave breaking.

1. INTRODUCTION

Wave resistance is one of the most important resistance components of a ship, generally contributing 20 to 80 % of the total resistance of a ship sailing in still water. Experience has shown that this resistance component is quite sensitive to modifications in the design, and large reductions of the wave resistance can often be obtained without any important sacrifice in deadweight or cargo capacity. The effect of a bulbous bow is a well-known example. A capability to predict and minimize wave resistance in the design stage of a ship is, therefore, very desirable. Theoretical studies of the wave resistance

problem have been carried out already for a century. Since Michell's paper of 1898, many studies of the linearized free-surface potential flow problem have been made, and several alternative solution methods and linearizations have been proposed; some of them very useful for a certain range of applications. Particularly in the early seventies much work has been done on this problem. In 1977, Dawson [1] proposed his well-known method, which in a number of comparative studies turned out to give realistic predictions, and to be more practical than most other proposals.

Much work has been done since on validation and improvement of Dawson's method. There is a large body of literature on this method, and the mathematical background of the "engineering approach" has been more and more clarified. A code for Dawson's method is available at many institutes all over the world. Still, the actual use in commercial ship design work is quite limited. While at MARIN the code DAWSON [2] is being applied to 70 to 100 hull forms per year in commercial work and important successes have been obtained, most other versions of the method seem to be rarely applied.

As a matter of fact, the routine use at MARIN has made us aware of several shortcomings that make application more difficult. In particular, the resistance predicted by the code is not very reliable; for slender ships the estimate is usually fair, but for full hull forms the wave resistance is underestimated or even negative (a phenomenon explained in [3]). It is, therefore, not safe to optimize a hull form on the basis of the predicted wave resistance alone, as this sometimes even incorrectly indicates the order of merit of design variations. But at the same time the wave pattern and profile, the hull pressure distribution and flow direction have turned out to be realistic enough to be used for improving the design. Hull

form optimization using DAWSON is thus an art that requires insight in the assumptions made in the theory, knowledge of fluid dynamics and wave making, and much experience. Only few have collected enough experience to fruitfully use Dawson's method.

Although, therefore, the shortcomings of Dawson's method do not prohibit its very effective use, a next step has to be made. Not only a greater accuracy of the predictions is desired, but also we should like to include several aspects of the flow that cannot be taken into account in DAWSON. Specifically:

- the neglect of nonlinear terms and transfer terms in the free surface boundary condition introduces inaccuracies;
- the hull form above the undisturbed waterline cannot be taken into account in a linearized method; this eliminates the effects of bow flare, flat sterns, surface-piercing bulbous bows and so on;
- doubts exist on the modeling of the flow off an immersed transom stern .

All these inaccuracies and limitations can in principle be removed by solving the fully nonlinear problem, rather than applying the slow-ship linearization underlying Dawson's method. At several institutes the development of a method for solving the fully nonlinear free surface flow problem is now in progress. Both panel or boundary integral methods, and field equation methods are used. The latter usually deal with viscous flows and almost invariably unsteady problems (or, at least, transient solution methods), and will not be discussed here.

The majority of methods for free surface flows around ships assumes a potential flow. Using Green's identity the problem is conventionally recast in a boundary integral form. There are many boundary integral methods addressing *unsteady* problems, e.g. [4,5]. Although in most cases the main purpose of the developments is to solve seakeeping or other actually unsteady problems, they may be applied to steady problems as well. One particular method to be mentioned here is that of Cao, Beck and Schultz [6] with its unconventional but very successful use of point sources at a distance above the free surface.

The most direct way to address the wave resistance problem is the solution of the *steady* free surface potential flow problem, which has been given much less attention. Most methods in this class are based on an approach similar to the linearized method of Dawson. This means that a distribution of Rankine sources or other simple singularities is used both on the hull and on a part of the free surface around it. For solving the nonlinear problem an

iterative procedure is needed. Among the first to study such a method was Ni [7]. His method was Dawson-like, with panels on the free surface that were moved in every iteration. Although convergence was problematic, he succeeded to get converged solutions for a range of cases, subject to several restrictions on the use of particular difference schemes and so on. His method was later extended and improved in Larssons group [8]. Later Kim and Lucas [9] came up with a very similar approach, but found it necessary to apply artificial numerical damping in order to obtain convergence. In [10] they proposed a modified double iteration scheme which was claimed to improve the convergence. Another method was proposed by Delhommeau [11], also using panels on the free surface. Convergence again turned out to be problematic.

At the same time, some other developments were based on the use of singularity distributions not on but *above* the free surface. This choice was inspired by obvious practical advantages for the problem considered. One of the first efforts was due to Xia [12], who describes some initial attempts to solve the nonlinear problem. However, a too large sensitivity to the distance from the panels to the water surface made him give up. Much more successful were Jensen et al [13,14] with their method using point sources above the wave surface, analytical second derivatives and a special way of satisfying the radiation condition. In several further publications the method has been extended to shallow water, channel flows, unsteady cases in the frequency domain etc. At the same time, convergence of the method still can provide severe problems as soon as e.g. different panel distributions are used.

In [15, 16], the present author proposed the so--called RAPID approach (RAised Panel Iterative Dawson). The use of free surface source panels raised above the free surface is largely similar to Jensen's method; but most details are different. The iterative procedure, selected on the basis of previous numerical estimates of the different nonlinear contributions [3], has appeared to be unusually stable and robust: Contrary to almost all previous methods for the same problem, no convergence problems are generally met. It thus seems to be one of the most practical methods, and, together with Jensen's method, it seems to be the only code for the nonlinear problem that is already actually applied in ship design work.

This paper describes recent progress in the further development and validation of the RAPID code. In [16], the essence of the method was explained and the results of several numerical experi-

ments were discussed. This will briefly be summarized in the next section, paying some more attention to the convergence properties and to the importance of nonlinear effects. Section 3 is devoted to a discussion of the flow off an immersed transom stern. The various flow regimes are studied, and the implementation of the transom flow model in both the linearized (DAWSON) and the nonlinear (RAPID) code are described and compared. Section 4 then discusses a number of detailed validation studies.

2. R A P I D

2.1 The mathematical model

We consider the flow around a ship hull in a uniform flow from ahead. The origin of our coordinate system is located amidships at the level of the undisturbed free surface. The x-coordinate is positive astern, and y is positive in upward direction. The coordinate system does not move with the dynamic trim and sinkage of the ship. All quantities are nondimensionalized with the ship speed and length.

The potential flow assumption is made, and a velocity potential ϕ is introduced such that:

$$\vec{V} = \nabla\varphi \qquad (1)$$

The field equation to be satisfied is the Laplace equation. The flow is undisturbed far ahead and at large lateral distances, while a wave pattern with a known rate of decay is present downstream.
On the wetted part of the hull the flow must be tangential to the hull, as represented by a Neumann boundary condition for the potential:

$$\varphi_n = 0 \qquad (2)$$

On the free surface a kinematic boundary condition is to be satisfied, requiring that the flow is tangential to the wave surface:

$$\varphi_x\eta_x + \varphi_y\eta_y - \varphi_y = 0 \ on \ y=\eta \qquad (3)$$

and a dynamic boundary condition that the pressure in the flow at the free surface must equal the atmospheric pressure (4):

$$\frac{1}{2}F_n^2(1-\varphi_x^2-\varphi_y^2-\varphi_z^2) - \eta = 0 \qquad on \ y = \eta \qquad (4)$$

2.2 Iterative solution

Contrary to what is done in linearized methods, these boundary conditions will be applied on the correct surfaces; i.e. the hull condition on the part of the hull that is actually wetted, and the free surface

conditions on the actual wave surface. No simplifications are thus made. Solving this fully nonlinear free surface problem requires iteration. The iteration procedure is set up as follows.

While in a linearized method such as DAWSON the flow field and free surface are decomposed into a known base flow and a small perturbation, and linearization in terms of this perturbation is performed, we now make a similar assumption that the solution of a certain iteration differs only by a small amount from the flow field and free surface shape found in the previous iteration. Again we linearize in terms of this perturbation and impose the boundary condition at the previous free surface. Thus we obtain a linear fixed-domain problem to be solved in the current iteration. Having found the solution we update the base flow field and free surface, and start the next iteration.

Specifically, defining

$$\eta = H + \eta' \qquad (5)$$

$$\nabla\varphi = \nabla\phi + \nabla\varphi' \qquad (6)$$

and substituting this into the dynamic and kinematic boundary conditions, we obtain linearized kinematic and dynamic conditions:

$$\phi_x\eta_x + \phi_z\eta_z + \varphi_x'H_x + \varphi_z'H_z - \phi_y - \varphi_y' = 0 \qquad (7)$$

$$\eta = \frac{1}{2}F_n^2(1-\phi_x^2-\phi_y^2-\phi_z^2 -2\phi_x\varphi_x'$$
$$-2\phi_y\varphi_y'-2\phi_z\varphi_z') \qquad on \ y=H \qquad (8)$$

These two conditions are combined in exactly the same way as in Dawson's method by eliminating the wave height perturbation, and we obtain the linearized free surface condition (FSC) to be imposed on the wave surface found in the previous iteration:

$$-\frac{1}{2}F_n^2(\phi_x\frac{\partial}{\partial x}+\phi_z\frac{\partial}{\partial z})(\phi_x^2+\phi_y^2+\phi_z^2 +2\phi_x\varphi_x' +2\phi_y\varphi_y'$$
$$+2\phi_z\varphi_z') +\varphi_x'H_x+\varphi_z'H_z-\phi_y-\varphi_y' = 0 \qquad on \ y=H \qquad (9)$$

It is noted in passing that actually a consistent linearization would add certain terms representing the transfer of the boundary condition from the free surface to be calculated, towards the free surface found in the previous iteration. These terms are intentionally disregarded here, as they have been found to be rather irregular for the source distribution employed here and might lead to divergence of the iteration. To the converged solution these terms

make no contribution of course, since η' then vanishes and the FSC is imposed on the actual free surface.

Once the linear problem of the current iteration has been solved, the velocities found are substituted in the original dynamic condition (4), and a new free surface is found. This, together with the new velocity field, is the basis for the linearization of the next iteration.

This iterative process is started from any initial guess. As no assumptions have been made on the relation between the base flow field and the base free surface, this initial guess can be selected on the basis of convenience only. In most cases we start simply from a uniform flow and flat free surface; the first iteration thus becomes the Neumann-Kelvin problem. The iteration is repeated until the residual errors in both the dynamic and the kinematic boundary conditions are below a predefined tolerance in all free surface points (i.e. a maximum norm is used). In most cases, we impose tolerances of 0.1 % of the ship speed for the kinematic condition, and 0.2 % of the stagnation pressure for the dynamic condition. It is important to note that checking these residuals is the only safe procedure; visual inspection of the changes in a hull wave profile, as is often done, does not guarantee that the solution has converged !

2.3 Implementation

To implement the mathematical model outlined above, singularity distributions are specified for all boundaries where non-trivial boundary conditions are to be imposed, i.e. the wetted part of the hull and the surrounding part of the wave surface. On the hull the familiar distribution of quadrilateral constant-strength source panels is used, with collocation points in the panel centroids. For the free surface however, a less conventional choice has been made: quadrilateral constant-strength source panels are located at a certain distance above the wave surface, while the collocation points are on the wave surface itself. Within certain limits for the distance of the panel to the free surface this is permitted theoretically, and it has several practical advantages:
• as there is freedom in the distance from a panel to the corresponding collocation point, the panels need not be repositioned in each iteration; only the collocation points are moved towards the new free surface position. This saves some work and avoids potentially destabilizing geometric manipulations;
• the velocity field in the fluid domain is smoother than with constant-strength source panels on the boundary itself;

• the numerical dispersion (i.e. the error in the wave length due to the discretization of the continuous velocity field and boundary condition) is far smaller than with the usual implementation;
• the outer boundaries of the free surface domain are less reflective.
• the implementation is simplified on several points.

There are, however, some disadvantages as well:
• the conditioning of the system of equations is slightly worse; by a proper selection of the panel elevation this can, however, be minimized.
• if the section shape has a large slope above the waterline, the collocation points right under the centers of the free surface panels adjacent to the hull are at a rather large distance from the waterline, with resulting inaccuracy. If the collocation points are kept at a constant distance from the actual waterline, the free-surface boundary condition is better resolved, but the conditioning is worse. This trade-off can present some problems, in particular for flat sterns. fter all, the use of raised panels has turned out to be extremely effective for this class of problems.

The limits of the distance from the panels to the free surface are, as shown in [16], roughly between 0.5 and 1.5 panel dimension. Here the panel length is more important than the transverse size. It will be obvious that the distance cannot be kept inside these limits if the panels are not adjusted to the free surface shape. E.g. the stagnation height at a ship speed U is $U^2/2g$, and for a usual panel density of 20 panels per transverse wave length this is 1.6 times the panel length. Therefore, as described in [16], the free surface panel distribution must be adapted to the wave surface such as to stay at a more or less constant distance. But there is no need to do this very accurately, as the distance only has to be kept inside the limits mentioned before. Therefore, the calculation is made in separate jobs of 2 to 6 iterations, each time followed by an automatic adaptation of the free surface paneling to the last calculated wave shape, and of the hull paneling to the modified intersection with the free surface panels. If desired, the position of the hull is adapted to the new estimate of the trim and sinkage. Then the process is restarted from the results of the previous iteration. In this way, the efficiency and stability of the process is kept while a good conditioning and accuracy can be guaranteed.

Another detail of the implementation to be mentioned is the use of an upstream difference scheme for the derivatives of velocities in the free surface condition. This is exactly similar to the use in Dawson's method, and helps the satisfaction of the radiation condition at the expense of a small

numerical damping. The detrimental effect of this damping can be minimized by choosing a sufficient panel density. On the other hand, in order to increase the numerical accuracy at a given panel number, the use of a difference scheme might be dispensed with in the future.

The complete iterative procedure can be summarized as follows:

1. Define the initial hull and free surface panel distribution; choose the distance of the panels above the free surface.
2. Choose an initial free surface velocity distribution and wave elevation.
3. Impose the combined FSC, linearized with respect to the last free surface shape and velocity field, in the free surface collocation points; and the hull boundary condition in the hull points;
4. Solve the linear problem. Calculate the new free surface and velocity field;
5. Move the free surface collocation points to the new wave elevation, applying underrelaxation if desired;
6. If needed, adapt the free surface paneling to the new wave surface; adjust the hull paneling; adjust trim and sinkage of the hull.
7. Calculate the residual errors in all points, and decide to stop or to return to step 3.

2.4 Convergence and calculation time

As described in [16] , the method displays
• a good convergence with respect to increasing panel density;
• only very little effect of the distance of the panels to the free surface;
• a robust and easy convergence of the iterative procedure, without any tuning, smoothing or filtering.
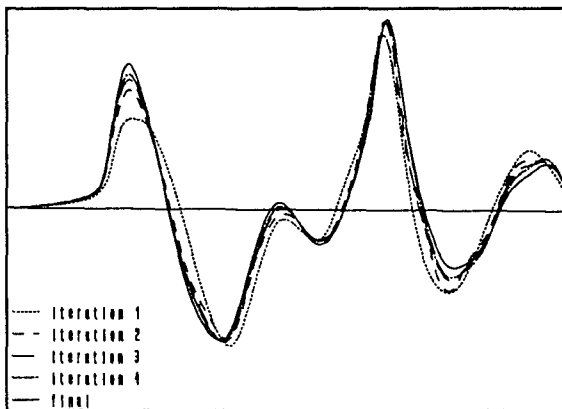
Figure 1. Convergence of hull wave profile

Fig. 1 illustrates the convergence of the hull wave profile for a Series 60 Cb = 0.60 hull at Fn=0.316, with a very dense paneling. 12 iterations were required to reduce the residuals to the desired level, but already after 4 iterations the hull wave profile is very close to the final solution.

An example of the convergence history is shown in Fig. 2, in which the logarithms of the maximum residual errors in the kinematic and dynamic boundary conditions are plotted against the iteration level.
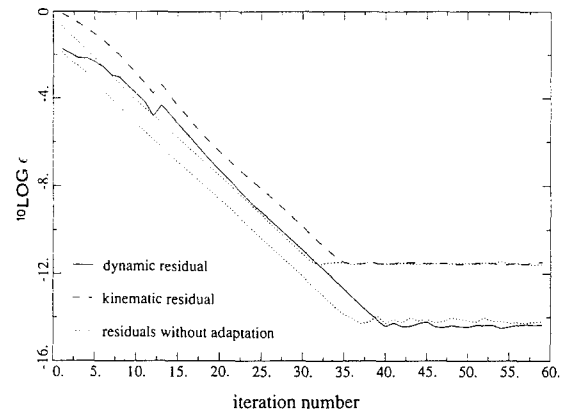
Figure 2. Convergence history with and without free surface panel adaption

The convergence rate is constant after the initial iterations, and the residuals are reduced until a minimum level determined by the machine accuracy is reached. For the kinematic residual this level is higher than for the dynamic residual as can be understood from its more complicated expression.

The same case was run with the method without any free surface panel adaptation. From Fig. 2 the convergence appears to be slightly faster; the free surface panel adaptations in the original method at iterations 4, 8 and 13 slightly delay the error decrease as a result of e.g. the geometric changes. On the other hand, adaptation from time to time is unavoidable if one wants to use a fine paneling for steep waves and still have convergence. It is noted that methods using panels on the free surface itself are forced to apply such panel adaptations in *every* iteration. That a raised-panel method makes it unnecessary to do so may be one of the explanations for its robustness.

The code currently runs on a CRAY-YMP supercomputer. Calculation times vary widely according to the number of panels. To give some examples:

# hull panels	# FS panels	CP sec/iteration
340	540	2.7
680	1056	17
624	2312	100

These calculation times can probably be reduced substantially, but this has not been given priority up to now.

The number of iterations to reach the prescribed level of residual errors usually varies between 5 and 15, dependent on the difficulty of the case. On the basis of a visual inspection of the results, the calculations would probably be terminated after 5 iterations in most cases.

2.5 Nonlinearities and wave breaking

At the 1992 Symposium on Naval Hydrodynamics, discussers of [16] indicated some restrictions of this class of nonlinear solution methods. In the first place, methods that describe the free surface as a single-valued function of the two horizontal coordinates cannot cope with extreme wave slopes, which was stated to be an important drawback in practice. Thus such methods could impossibly converge in cases in which wave breaking occurs in reality, according to these discussers. And even, because of the above, this class of solution methods would be limited to so-called "weak singularities". Similar statements can be found in [17].

As not all of these statements seem equally true, it may be useful to pay some more attention to the validity of the present method. Let us consider the physical phenomena that occur for steep waves. Most steady breakers are similar to spilling breakers: a region of turbulent flow with air entrainment, riding steadily on top of the wave pattern that otherwise remains relatively smooth. There are several experimental indications that this steady breaking occurs already at a smaller wave steepness than the Stokes limiting wave; but even the latter is described as a single-valued function of the horizontal coordinate. According to Duncan [18], wave breaking induced by a submerged hydrofoil occurs for wave slopes exceeding 16 to 24 degrees. That perhaps the spilling breaker itself has a very large local surface slope is a different issue, as the breaking will require another modeling anyway. But we can conclude that the potential flows giving rise to this kind of wave breaking and underlying the breaking zone can be easily *described* using a single-valued free surface; and that excessive wave slopes that cannot be described will rarely occur in reality because wave breaking eliminates them.

The next question is then: is it possible to *compute* waves so steep that breaking occurs? As mentioned above, some discussers expected that divergence would prohibit such calculations. In

principle, I see three possibilities:
- the iteration does not converge;
- it converges, but a grid-independent solution cannot be obtained;
- it converges, but to a non-breaking solution that is not physically realizable.
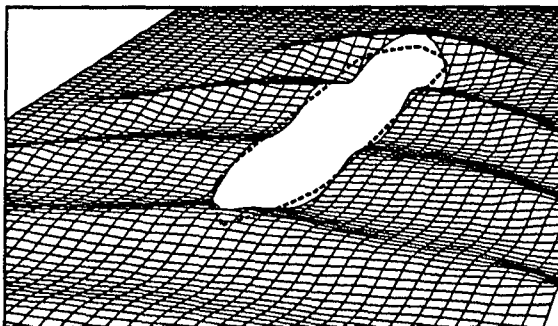
Figure 3 Calculated wave pattern for a tanker at Fn=0.25

Based on results obtained up to now the third option seems most likely, and we can at least reject the first possibility. As an example, Fig. 3 shows the wave pattern found for a tanker with a block coefficient of 0.83, at the unrealistic Froude number of 0.25. A converged solution was fairly easily obtained, although there is no doubt that extensive wave breaking will be present, e.g. in the wave trough behind the bow wave: The calculated local wave slope is almost 30 degrees, and the ratio of peak-to-trough wave height to wave length is 0.16. Both exceed known threshold values for inception of breaking. The panel length was 0.04 transverse wave length here, but grid independence has not been checked thoroughly for this case.

Similarly, in [10] a converged solution was obtained for a Series 60 C_B=0.80 model at Fn=0.30, although on a rather coarse free surface grid.

Therefore wave breaking does not necessarily lead to divergence of the iteration process, and nonlinear methods like the one presented here can be a useful tool also in cases with wave breaking. But for completing the flow picture a separate criterion is required to determine whether a potential flow solution in practice will give rise to wave breaking, and some model of the breaking should eventually be incorporated. A proposal for such a model in 2D is [19].

The above example also illustrates that RAPID is stable enough to solve the nonlinear potential flow problem for all realistic speeds. At the same time it refutes the statement that these methods can only deal with "weak nonlinearities". I am not aware of the existence of a clear definition of the latter, but I would not call the nonlinearities in this example

weak. The calculated peak-to-trough wave height is as large as the draft of the vessel and vertical velocities exceed 45 % of the ship speed.

Of course, other types of wave breaking occur. A sharp ship bow may act as a sort of ploughshare and induce a flow similar to a plunging breaker. This behaviour is definitely outside the reach of RAPID and all similar methods. Other methods, usually time-dependent, with a more general free surface description, have been applied to plunging breakers and do give a picture of the flow up to the moment of impact of the jet on the free surface. But then they stop ! Consequently also those methods have to be supplemented by some kind of local model for the plunging-type wave breaking and its effect on the flow field. In that respect they may have only a small advantage compared to the present approach.

An interesting related point of discussion is the question what happens if the discretization is further and further refined towards the bow. Again the same three pitfalls seem possible: divergence, unresolvable grid-dependence or an unphysical solution. The problem can be studied a little bit further by invoking the similarity between the steady flow at a sharp ship bow and a time-dependent 2D flow in cross planes. For a bow with a finite entrance angle the corresponding 2D case is that of an impulsively started wavemaker. From small-time expansions a logarithmic singularity in the wave elevation has been shown to exist in that case, representing a jet shooting up along the wavemaker. Numerical studies using time-dependent fully nonlinear boundary integral methods, e.g. [20,21] actually reproduced this behaviour. The finer the paneling, the higher the jet, and no grid-independence could be reached. But this is extremely localized, and the result at very small distances away from the wavemaker and everywhere else is totally unaffected by the grid dependence at the intersection. Analogously, and keeping in mind that in 3D steady flows singularities are likely to be weaker than in 2D time-dependent flows, I expect that for sharp bows in fact eventually no convergence will be obtained in RAPID if the discretization is refined towards the waterline; that locally no grid-independent solution or even no physically correct solution may thus be reached; but that the resulting error will be extremely localized and unimportant from the point of view of the global flow field. For almost all practical applications this theoretical drawback is then of no interest. Although there is some speculation in these statements, current experience with the method actually points in this direction. Further study is desired.

All this does not mean that the method proposed here is the final answer; but, subject to certain improvements in resolution and in numerical details, it may be the answer to most of the practical questions that can be dealt with using potential flow assumptions.

3. THE FLOW OFF A TRANSOM STERN

3.1 Physical Phenomena

As most current ship forms have a transom stern, the capability of a method to handle transom flows is of primary importance. In linearized methods the hull form above the undisturbed waterline has no effect, and transom sterns above the design waterline are usually not treated as transom sterns. But in a nonlinear method transom flow modeling is also required for all those cases in which a transom becomes immersed only at speed.

For ships having a transom stern, three flow regimes may be distinguished:
• the "regular" type of flow, which is similar to the flow past a cruiser stern. This type of flow will occur if the transom is at a sufficient distance above the undisturbed free surface. Dependent on the hull form the last part of the actual waterline in potential flow may be either a streamline or an envelope of streamlines that leave the hull tangentially and continue on the free surface. At the smooth detachment of the free surface from the hull surface, both the hull boundary condition and the two free surface boundary conditions must be satisfied. Unless the detachment is in a stagnation point, this means that the flow leaves the hull tangentially.
• the "transom flow", occurring for immersed transoms at a sufficiently high speed. At the transom edge the hull streamlines leave the hull and continue on the free surface. The negative hydrodynamic pressure needed to make the pressure at the transom edge atmospheric is achieved by an upward curvature of the flow immediately aft of the transom edge, resulting in a more or less marked "rooster tail".
• The flow around a deeply immersed transom at low speed. At the sharp convex corner of the transom edge, viscous flow separation occurs and a dead-water region aft of the transom is formed.

The transitions between the various flow regimes are practically relevant, as a dead-water region is to be avoided, and a transom that is at a too high position as well. Let us further consider what phenomena determine these transitions. Suppose a regular flow type occurs, with the transom above the

water surface, and we increase the draft of the vessel. The detachment position is likely to move aft and at some moment reaches the transom edge. The streamline shape then further adjust so as to maintain a zero pressure at the edge. While in regular flow the curvature is bounded at detachment, this need not be true in the transom flow.

For a further increasing transom depth or for decreasing speed the hydrodynamic pressure coefficient required to balance the hydrostatic pressure at the transom edge increases in absolute value, and the upward curvature of the streamlines must increase. A very steep forward face of the wave aft of the transom results, eventually giving rise to a spilling breaker following the transom at a short distance. At still lower speed or greater draught this closes upon the transom and forms a dead-water zone.

From these preliminary considerations, we can list the requirements of the "ultimate" nonlinear potential flow model:

I.   it should contain a model for at least the regular and the transom flow;

II. it should indicate the transition from a regular to a transom flow and reversely;

III. it should preferably indicate the transition from transom flow to dead-water flow.

If not all transitions can be incorporated in the code, one may try both flow regimes and check for anomalies. We can immediately note that point III will perhaps still be impossible to realize. If it is true that wave breaking determines this transition, a proper breaking criterion will be indispensable. Furthermore one should be aware of possibly large viscous effects on this transition. Moreover, point II requires the ability to compute the regular flow for extremely flat afterbodies; this is a very high demand for any iterative nonlinear method, as a small change of the wave elevation then results in a very large (and destabilizing) shift of the waterline.

Below, we shall consider the modeling of the transom flow in linearized and nonlinear models, and discuss the question of the transitions.

3.2 Mathematical Modeling

There seems to be some confusion about the type of modeling appropriate for transom flows. The boundary conditions to be imposed are fairly evident: on the hull the flow again must be tangential, and on the entire free surface it must be tangential and have a zero pressure. That there are two boundary conditions on the free surface corresponds with the additional degree of freedom there, the elevation of

the free surface. At the transom edge however, the confluence of boundary conditions poses some problems. The two kinematic conditions can be reconciled if the flow leaves the hull tangentially. But as the edge location is fixed, the degree of freedom due to the wave elevation seems to be lost. How to impose the dynamic boundary condition ?

This apparent overspecification of the problem reminds of the flow around a lifting body, in which circulation provides the additional degree of freedom. The analogy with a Kutta condition, which also imposes an extra condition on the flow at a sharp corner, has sometimes been invoked. Consequently, trailing vortex wakes or dipole sheets are introduced, e.g. in [22]. But the success of such an implementation could not be shown convincingly; in [22] the use of source panels on the transom instead of a trailing vortex wake led to almost identical results.

Another proposal for modeling transom flows is [23], which deals with slender hulls at very high speeds. Also here the necessity of introducing trailing longitudinal vorticity on the free surface is advocated. However, this vorticity appears not to result from the presence of a transom but from the use of a reverse image of the flow above the still water surface, as is appropriate in the infinite-Froude-number limit. The same trailing vorticity would in this model be required for hulls without transom. The slender-body formulation adopted causes this boundary vorticity to extend to downstream infinity with constant strength.

To study the meaning of trailing vorticity for transom flows, let us first consider the flow around a two-dimensional body with a transom stern. The flow domain is bounded by the hull and the free surface which originates from the transom edge. Therefore the domain is singly connected, and there cannot be any unknown circulation around the body.

In a three-dimensional case the situation is similar. Is there any reason why the three-dimensionality would suddenly introduce spanwise vorticity? If it would, trailing longitudinal vorticity would in fact also be present. However, this vorticity would start at the transom edge, i.e. on the free surface, so it would remain on the free surface; on the boundary of the fluid domain therefore. There is no cut in the domain, no additional degree of freedom, and the boundary vorticity has no physical effect on the flow field in the domain at all; it just affects the form of the Fredholm equation to be solved.

Therefore, in my opinion the use of a trailing vortex wake for transom flows, although perhaps

numerically helpful in some models, cannot be given any *physical* meaning. Rather than pointing out the analogy with the Kutta condition we might consider free streamline theory, as applied to e.g. the cavity or wake flow behind a flat plate at large incidence. Although the neglect of gravity may well affect some of the conclusions, free-streamline theory tells that the flow leaves the transom edge tangentially, but with infinite curvature. Even more illuminating is [24], in which for a flat-ship linearization in a 2D free-surface potential flow around a semi-infinite body the behaviour at the transom edge is derived. Again, the conclusion is that the slope of the streamline is continuous (tangential flow), but that the curvature tends to infinity at the edge. Specifically, the free surface shape aft of the transom is described as follows:

$$\eta(x) = \eta_{tr} + \eta'(x_{tr})(x-x_{tr}) + \frac{2}{3}C_2(x-x_{tr})^{3/2}$$
$$+ O(x-x_{tr})^2 \tag{10}$$

where η_{tr} is the height of the transom edge and the coefficient C_2, which can be expressed in the hull geometry, is the degree of freedom required to satisfy the dynamic condition. Although the details of this result may be a consequence of the necessary simplifications and linearization, this study suggests that all transom conditions can be satisfied without any physical vorticity; that the additional degree of freedom is the streamline shape at the transom edge; and that a more or less singular behaviour at the edge may result.

3.3 Implementation

We shall now discuss the implementation of transom conditions. Because of the mentioned lack of general agreement on the proper modeling it seems useful to study the implementation in a linearized method as well. This has been used already for several years in the DAWSON code and provided good guidelines for the nonlinear implementation which we shall consider subsequently.

It is interesting to note that implementing transom conditions in a linearized method is basically inconsistent. Linearization assumes that the variation of the hull shape near the undisturbed waterline is small; i.e. a small curvature, and in slow-ship theory also a small slope of the sections and buttocks. Only then the exact position of the hull - free surface intersection has a negligible effect on the flow and linearization is permitted. However, at a transom edge the hull curvature is infinite, and we want to

have a particular hull - free surface intersection. Nevertheless a quite reasonable representation of transom flows appears to be possible in linearized methods as well.

In the hull paneling the transom is left open. The free surface panel distribution is adapted to the transom by the addition of a few extra strips of panels aft of the transom. One might think of imposing transom conditions in points right at the transom edge; but with the usual constant-strength source panels on the hull the velocity field is singular here in the discretized formulation. Therefore transom conditions are to be imposed in the first collocation points aft of the transom.

In the *linearized* problem we can only impose one single FSC, a combination of the kinematic and dynamic FSC. The usual FSC is derived by expressing the term η_x in the kinematic condition in the wave elevations η in the point considered and a few upstream points using a difference scheme; and expressing these η's in the velocities through the dynamic condition. In this process any arbitrary pressure added to the dynamic condition drops out; in other words, the combined form actually means that in the free surface collocation points the velocity must be parallel to the *isobar surface* passing through that point, but the pressure corresponding to that isobar surface is eliminated. The wave elevation is only retrieved afterwards from the dynamic FSC. Thus the ordinary form of the FSC makes it impossible to impose any condition on the wave elevation at or near the transom itself, and the free surface will most likely start somewhere at the transom face.

The solution of this difficulty is well known: the FSC must be modified so as to avoid elimination of the pressure level. This is easily achieved by imposing in the first collocation points the condition that the velocity must be directed parallel to a line from the transom edge to the wave elevation at the point, e.g.

$$\eta_x = \frac{\eta - \eta_{tr}}{x-x_{tr}} \tag{11}$$

The same transom condition can be derived by substituting into the usual FSC the velocity required for zero pressure at the transom edge.

Instead of the two-point formula for η_x, higher-order expressions may be used. These require that an assumption is made on the local behaviour at the edge. Two alternatives have been tried:
- the behaviour according to Schmidt [24], (10)
- a simple Taylor expansion in the transom edge

point

The former has been derived from a flat-ship linearization and is, therefore, not necessarily appropriate here; but it allows an infinite curvature at the edge. The second formulation is generally applicable to regular behaviour aft of the transom edge.

With this simple modification the transom conditions to be imposed in the first points of the free surface strips aft of the transom are in principle complete for a linearized method. For the second points, in the FSC the same three-point difference scheme is used as everywhere else. This involves again the transom edge height. For all downstream points no modification is needed.

One should notice that in principle this treatment of the transom conditions does not guarantee that the solution satisfies the zero-pressure condition at the transom edge; and if not, it does not satisfy the kinematic condition in the first free surface point either. However, a mechanism that physically governs the transom flow is incorporated. The inherent continuity of solutions of the Laplace equation will make the flow leave the transom more or less tangentially. If the wave elevation in the first free surface points aft of the transom deviates from this tangent, a large streamline curvature at the transom edge results, inversely proportional to the square of the distance from the transom to the first points. This curvature adjusts the pressure at the edge and the wave elevation. Thus upon panel refinement the wave height at the first free surface collocation points will be forced to approach the transom edge. How appropriate this FSC is for finite panel sizes can only be deduced by numerical experimentation. The quality of the linearized predictions will be studied in Section 3.4

The implementation of the transom edge conditions in the *nonlinear* method is actually quite similar to that outlined above. As again no collocation point can be located at the transom edge itself, the free surface conditions are imposed at a small distance aft of the transom. Again, the free surface slope to be substituted in the FSC is expressed in the difference between the transom edge height and the Bernoulli expression for the collocation point, through one of the alternative expressions. The free-surface boundary conditions are now linearized with respect to the previous iteration; and the iterative procedure will converge to the fully nonlinear solution.

It was found that the convergence of the iterative procedure is excellent. As the transom edge is a fixed point in the result, extremely large errors in the

dynamic and kinematic boundary conditions are found initially if one starts from a flat free surface. But the fact that this point is fixed also appears to stabilize the results locally, and convergence presents no problem at all.

Although basically the linearized and nonlinear treatment of the transom conditions is similar, it is a significant advantage of the latter that the nonlinear terms and transfer terms are fully included. These can be very large, in particular for low transom depth Froude numbers, when large vertical velocities and large free surface curvature occur near the transom. Moreover, since the nonlinear method imposes the exact free surface boundary conditions, we can be more confident that the physical mechanisms governing the transom flow are fully included.

3.4 Results

As the actual behaviour at the transom edge in a 3D nonlinear case is not known, I have chosen the following path for verifying the method. I see two possible causes why it might give erroneous results. The first is discretization; therefore careful grid refinement studies have been carried out. The second would be an incorrect modeling of some kind of singularity at the transom edge. The importance of this will be studied by comparing the results found with different assumptions on the flow behaviour at the edge.

For the panel refinement study, the test case (Fig. 4) is a mathematical hull form with rectangular sections with a rounded bilge; parabolic waterlines in the forebody; an afterbody that is prismatic up to x = 0.25 L, and has a bottom slope of 1 : 0.16 aft of this point.
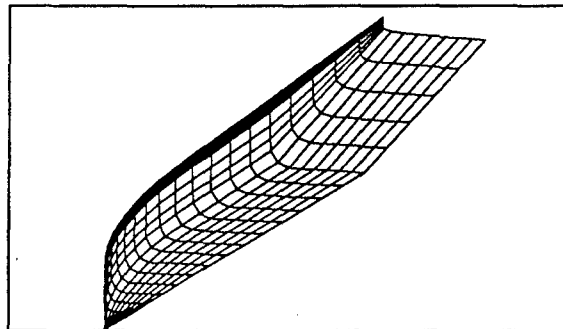
Figure 4. Mathematical hull form with transom

The panel refinement study discussed here addressed a case with a Froude number of 0.40 and a transom immersion of 0.01 L. The Froude number based on transom depth is 4.0, which may be just sufficient to make the flow clear the transom.

Let us first look at the results of the linearized

104
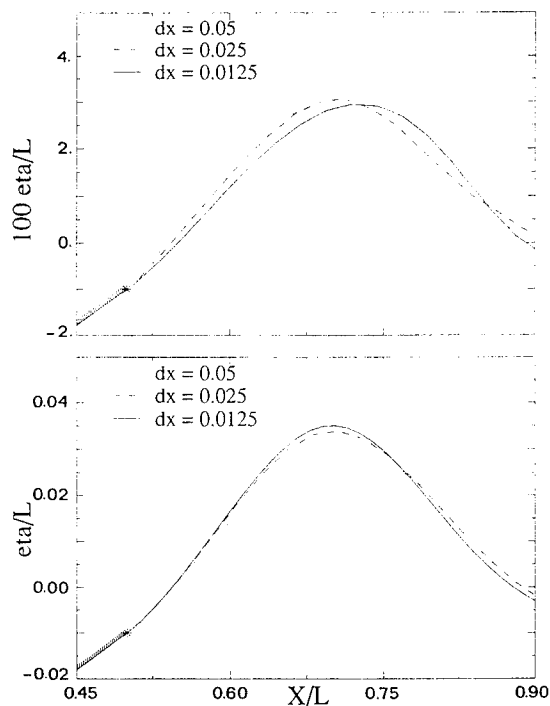
Figure 5. Wave profile behind transom, for 3 panel densities; linearized (top) and nonlinear (bottom)
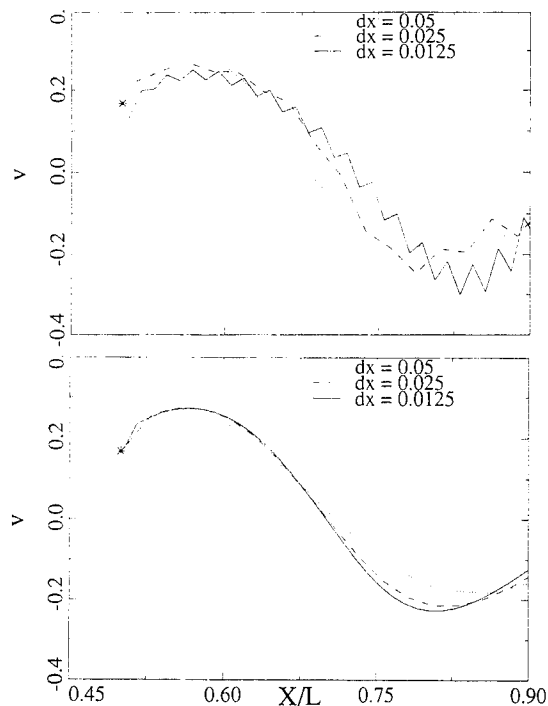
Figure 6. Vertical velocity behind transom, for 3 panel densities; linearized (top) and nonlinear (bottom)
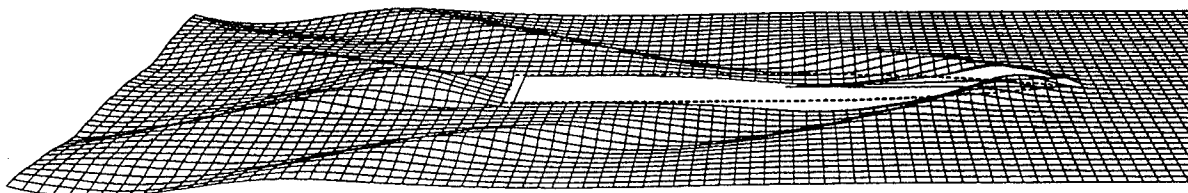
Figure 7. Calculated wave pattern for transom stern hull; nonlinear method
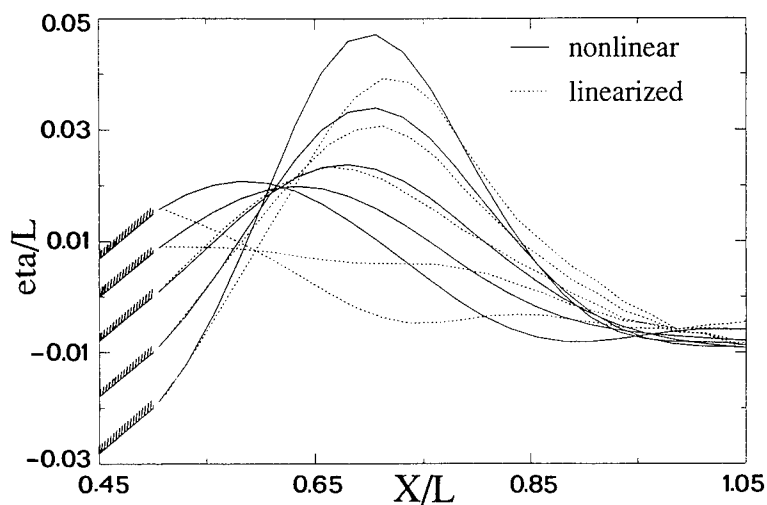
Figure 8. Wave profile for varying transom edge height; linearized and nonlinear method
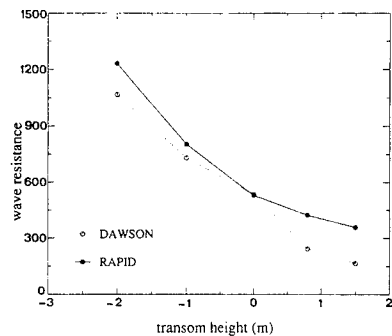
Figure 9. Wave resistance against transom edge height; linearized and nonlinear method

105

(DAWSON) code. Fig. 5 (top) shows the predicted free surface shape aft of the transom on the line of collocation points closest to the centerline, for hull and free surface panel lengths of 0.05 L, 0.025 L and 0.0125 L respectively. Some grid dependence appears to be there, with a downstream shift of the wave crest but not too much change in amplitude. Fig. 6 (top) shows the vertical velocity on this same line. The marker indicates the value at the transom edge, deduced from the dynamic condition and the transom slope. The value found on the free surface aft of the transom is too high for the coarser panelings, and too low for the finest distribution. The latter result may be due to the large oscillations in the vertical velocity that are typical for the Dawson-type of discretization at small panel sizes. 80 panels per wavelength is, by the way, not a density one would use in practice. Anyhow, the linearized transom modeling seems to give a qualitatively correct behaviour, but its accuracy is not quite convincing.

For the corresponding nonlinear (RAPID) calculations, the results are shown in Figs. 5 and 6, and Fig. 7. The calculated flow is absolutely smooth and satisfies both transom conditions accurately: no deviation is visible on the scale of the paneling. The convergence of the wave profile for decreasing panel size is very good, and there is hardly any difference between the two finer panelings. In particular the behaviour just aft of the transom is perfect. The vertical velocity converges well and consistently matches the transom edge value indicated.

We thus find that, as panel refinement has very little effect on the solution, we can be confident that the exact FSC's are accurately satisfied in all points on the free surface (not only the collocation points) in the converged nonlinear solution. But an exception must be made for the point right at the transom edge: no collocation point is present here, and if some sort of singular behaviour occurs, panel refinement could in principle give convergence towards an erroneous solution. Therefore the effect of the choice of the flow model at the edge has been considered. But the difference between the results obtained with the Schmidt- and the Taylor expression was only quite local and too small to be distinguished on the scale of the plots. In both cases the calculated vertical velocity was continuous (tangential flow) , but with a discontinuous $\partial v/\partial x$ and a discontinuous but finite curvature of the free surface streamlines. This does not exactly correspond with the Schmidt theory, but does allow a Taylor expansion.

Since, therefore, the particular assumptions on the behaviour here have only a very small and

localized effect, we may conclude that this detail of the modeling is not too important and is very unlikely to lead to an erroneous solution globally. Thus the method proposed is adequate.

Next, we study the effect of the transom depth on the predictions. The draft of the ship is varied to obtain the transom heights - 0.02 L, -0.01 L, 0., 0.008 L and 0.015 L (positive is above the still water level). Fig. 8 shows the wave profile on the centerline behind the transom predicted by DAWSON and RAPID. In all cases the free surface correctly starts at the edge. The wave profiles predicted by DAWSON and by RAPID are remarkably close for all immersed transoms. The nonlinear predictions have a somewhat higher and steeper stern wave, with a difference of up to 20 %. The greater the transom immersion, the stronger the nonlinearity. But, fortuitously or not, the several nonlinear contributions, each very large for the large vertical velocities occurring (up to 40 % of the ship speed), appear to cancel to a substantial extent; the difference between DAWSON and RAPID is therefore relatively moderate.

For the cases with the transom *above* the still water level however, the difference between DAWSON and RAPID is much larger. The rooster tail suddenly disappears in DAWSON as soon as the transom edge comes above the still water line. As the still water level is of little meaning for the local flow, there is no physical explanation for this drastic change. As opposed to this, in RAPID the height of the rooster tail continuously decreases, which must be the proper behaviour.

Similarly, all RAPID calculations display the correct free surface slope at the edge, corresponding to a tangential flow off the hull; while in the DAWSON predictions only the cases with the transom edge on or below the still water level have the correct slope. The same tendencies are found in the predicted wave resistance (Fig. 9). For DAWSON, a contribution

$$F_{stat} = \frac{1}{2} \rho g \int \eta_{tr}^2 \, d z$$

has been added, which in an ad hoc fashion accounts for the absence of hydrostatic pressure on the transom. Although entirely inconsistent, this correction appears to bring the resistance fairly close to the nonlinear result (which does not require such a correction because the total pressure is integrated over the hull). At zero transom immersion the two predictions are almost equal. The cases with transom above the still water surface again show a deviation in the DAWSON results.

106

The explanation of the bad linearized predictions for transoms above the still water level is of course that the hull must be cut off at the undisturbed water level in a linearized method. The hull paneling then ends at some point ahead of the transom. While the transom conditions in the first free surface collocation points can be imposed just as well if the transom height is positive, no boundary condition can be imposed on the part of the hull bottom above the still water level. But, because of the double-body linearization and the symmetry with respect to the still water level, imposing no boundary condition is the same as imposing a zero vertical velocity on this part of the water surface! This may be an acceptable approximation for cases with small buttock angle near the transom, but not for the present case where the vertical velocity should be around 0.16.

Summarizing, for the cases studied the results with the linearized method appear to be quite reasonable for all immersed transoms, with a moderate deviation due to nonlinear effects; but for transoms above the still water level the representation of the flow off the transom edge is relatively poor.

The RAPID solutions however are very accurate and satisfy all boundary conditions to the degree to be expected. Even for transoms above the still water level the hull shape near the transom is completely taken into account. Optimization of the transom immersion and stern shape seems to be possible now throughout the practical range.

Remains the question to what extent the transitions to the other flow regimes (dead water and early detachment) are indicated by the nonlinear calculations. As expected, the transition to a dead-water zone is not indicated as no criterion for the inception of wave breaking is included. In [25], the nonlinear stern waves behind a flat bottomed semi-infinite two-dimensional body have been studied theoretically, and it was derived that a solution with the free surface detaching from the transom edge exists only for a transom depth Froude number exceeding 2.23; and that breaking occurs for all Froude numbers below 2.26. Hoping to find anything particular I made calculations for a flat-bottomed finite-length 3D ship with a transom depth Froude number of 2.0. But again a converged solution was obtained, and no particular indication of non-existence was found. However, the result (Fig. 10) was markedly three-dimensional, so the theory of [25] does not apply and probably nothing more could be expected.
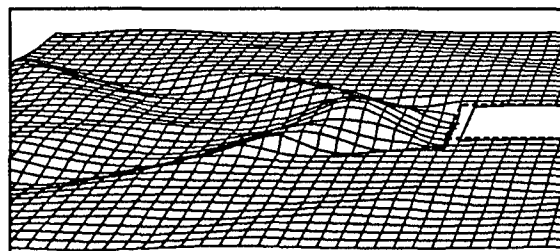
Figure 10. Calculated wave pattern for a flat-bottomed hull at transom depth Froude number 2.0

The transition to a detachment ahead of the transom is indicated by the calculations, although rather indirectly. For the highest position of the transom edge considered here, the pressure along the bottom of the hull falls below zero before the transom is reached. But on that part of the boundary only a hull condition is imposed, and passing the zero pressure level has no effect. One has to watch the pressure distribution on the hull, and as soon as this falls below zero the regular flow type is to be attempted. Geometric complications currently prevent the RAPID code to make this switch without any user intervention; and at this moment the degree of generality of the code is still insufficient to deal with regular flow around flat sterns with extremely blunt waterlines. These restrictions will hopefully be eliminated in the near future.

4. VALIDATION STUDIES

While [16] focused on the theoretical background of the RAPID-approach and discussed several studies of the numerical accuracy, grid independence and so on, in the meantime a number of validation studies has been carried out in which the predictions were compared with experimental data. Because of the availability of very detailed and accurate measurements, we first consider two standard test cases.

4.1 Wigley hull at Fn = 0.316

For this case, data from the ITTC Cooperative Experimental Program are available. A comparison has been made of the wave profiles with zero trim and sinkage. Calculations were made with 624 panels on the port half of the hull and two different free surface panelings, with 1148 and 2312 panels, respectively, in an attempt to elucidate the cause of the general underprediction of the bow wave height in all published results for this particular case. Fig. 11 shows that for both panelings the agreement of the calculated and experimental hull wave profile

is almost perfect, and far better than in most calculations published before. Grid dependence is only visible in the immediate vicinity of the bow, were the wave height is again slightly underpredicted. Further study, preferably for a simplified test case, must show whether this local effect is a consequence of incomplete resolution or of the possible bow singularity discussed before.
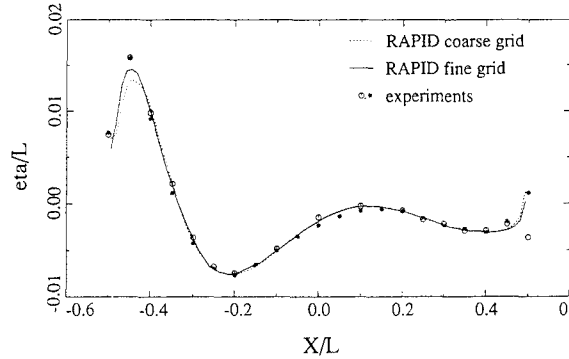
Figure 11. Hull wave profile; Wigley hull, Fn = 0.316

Fig. 12 compares the wave profiles on the line of collocation points adjacent to the hull and centerline as predicted by DAWSON, RAPID, and the first RAPID-iteration which is a Neumann-Kelvin linearization. Substantial differences are observed. Notwithstanding the slenderness of the vessel, the nonlinear method brings about a distinct improvement.
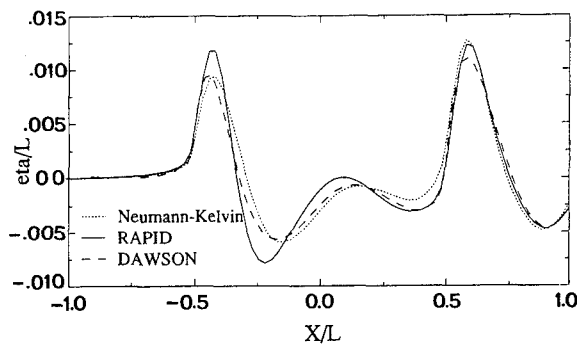
Figure 12. Wave profile, Wigley hull, Fn = 0.316

4.2 Series 60 Cb = 0.60 at Fn = 0.316

For this case a very extensive set of measurements is available, which have been carried out at IIHR [26]. A large number of longitudinal and transverse cuts has been measured. A disadvantage of these data is that they apply to a very small model of 3 m length, in a narrow towing tank (Rn ≈ 4 . 10^6). Initial calculations were made using 24 * 25 hull panels. Three free surface panelings have been tested: Grid I with 10 strips on each side of the hull and a panel length of 5 % of the transverse wave length; Grid II with 20 strips of 5% panels; Grid III with 10 strips of panels with a 2.5% length.

Fig. 13 compares the Neumann-Kelvin, Dawson and Rapid predictions for 2 longitudinal cuts. They all reasonably well correspond with the data, the Neumann-Kelvin results (in the present implementation) giving the worst agreement, with some phase shift in particular. While the nonlinear effects are not too large here, RAPID consistently gives the best agreement. An exception is the flow aft of the stern. The bad correlation in this region can safely be attributed to viscous effects; calculations for a displacement body in [25] in fact indicate a very important effect on stern wave amplitude.

The comparison of the nonlinear results on the 3 free surface grids showed that the first grid was somewhat less accurate, and slightly reduced the bow wave height due to an insufficient resolution. Grid II and III gave largely equivalent results, but at greater distances from the hull Grid III was marginally better due to the slightly smaller numerical damping. As the main difference between the data and the nonlinear calculation, a small, very short wave component was observed, generated at the bow and riding on top of the pattern of longer wave components. The length of this diverging wave was about 0.2 L, and the corresponding angle of the wave is 71 degrees. Although such a component is usually meaningless from the resistance point of view, the question was posed whether this deficiency was due to wave breaking, an unresolved strongly nonlinear effect or simply a lack of resolution.

Therefore grid IV has been generated, having 17 strips on the free surface and 56 panels per transverse wavelength. Besides, the hull paneling was refined to 56 * 15 panels. As Fig. 14 illustrates, the short wave component now actually enters (most clearly at x = 0.6 - 0.9), and has an approximately correct phase and position, but not an entirely correct amplitude. While it apparently still is distorted by the poor resolution, this result definitely suggests that even this detail is fully contained in the mathematical model, and just requires a very fine discretization to turn up in the prediction. This short wave is, however, something of theoretical interest only.

108
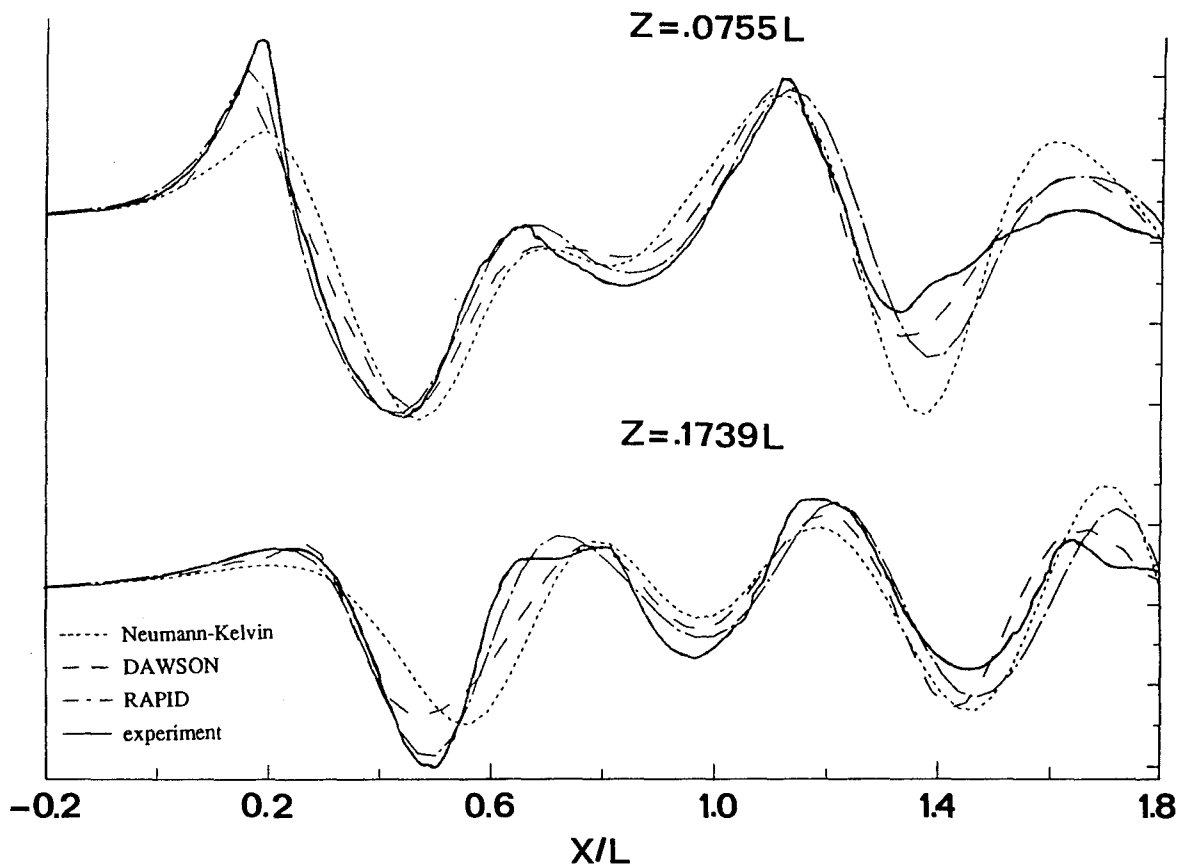
Figure 13. Longitudinal cuts, linearized and nonlinear; series 60 Cb = 0.60, Fn = 0.316
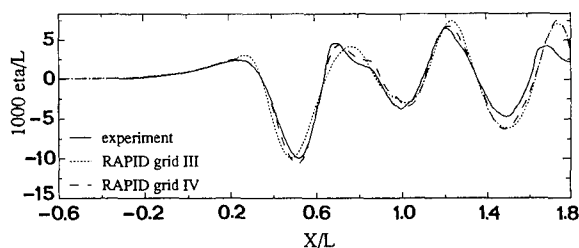
Figure 14. Grid dependence of short wave component; series 60 Cb = 0.60, Fn = 0.316

Fig. 15 shows the comparison of the calculation on the finest grid and the experiment, for 9 longitudinal cuts. It is noted that at the outer longitudinal cuts the agreement is not quite as good. However, these cuts are located around z = 0.30L, which may have been too close to the wave absorber

(at z = 0.40L) and the tank wall (z=0.50L). Everywhere else the agreement is, in my opinion, extremely good and these are probably the best results for this case ever published up to now.

Also the hull wave profile (Fig. 16) corresponds quite well with the data. Grid IV represents some improvement compared to grid III; this is likely to be primarily a result of the finer hull paneling. The maximum bow wave height is accurately predicted on both grids, but the high wave elevation right at the fore perpendicular is not reproduced. As this appears to have no effect in the nearby longitudinal cut, this probably has been a very thin fluid or spray sheet in the experiment.

Summarizing, in general an excellent agreement has been obtained for this case. Panel refinement makes the results converge towards the experimental data, even for details such as the short diverging waves. There is no trace of any unresolved "strong nonlinearities" in the near field having an effect at greater distances from the hull.

109
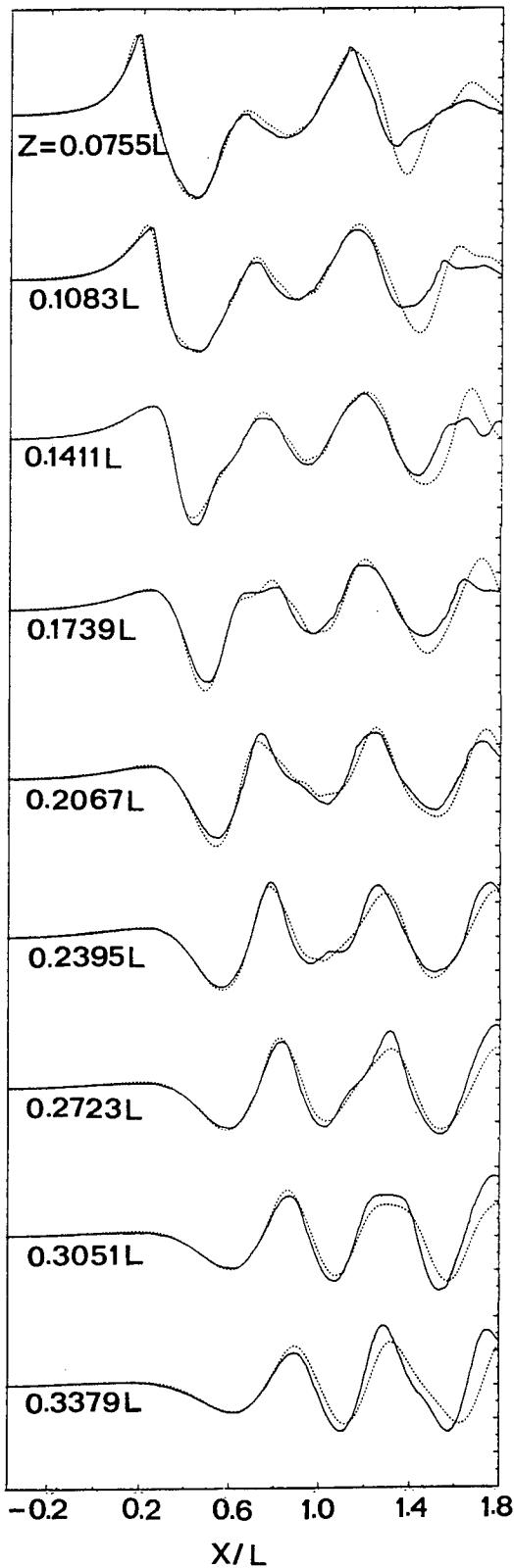
Figure 15. Longitudinal cuts, calculated (Grid IV) and experimental; series 60 Cb = 60, Fn = 0.316
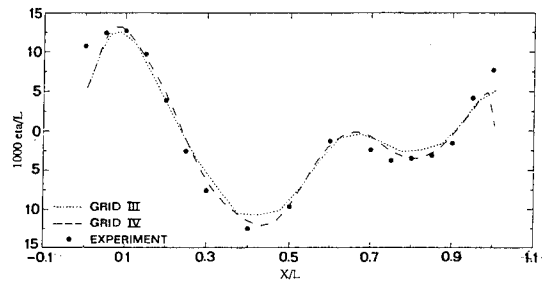
Figure 16 Hull wave profile, series 60 CB = 0.60, Fn = 0.316

4.3 Container ship

Of course further validations for more up-to-date hull forms are desired and will be carried out. Also, it is useful to compare linearized and nonlinear pedictions for ships exciting more diverging waves, as experience has shown that these tend to be rather poorly represented in linearized methods. Whether this is caused by numerical dispersion or damping or by the linearization was not quite clear until recently.

Our test case is a container ship with a bulbous bow, running at Fn = 0.24. Two longitudinal cuts were measured during the towing tests at MARIN. DAWSON and RAPID calculations have been carried out. However, as the ship has a transom stern above the still waterline and stern sections with a very large slope, at the moment of making these calculations we were forced to modify the afterbody in the RAPID calculations. As the primary interest was in the forebody design, this was an acceptable change; but consequently the RAPID stern wave predictions cannot be compared with the data and have not been plotted. In DAWSON the transom flow model has been applied with a positive transom edge height.

Fig. 17 shows the predicted and measured longitudinal cuts for the full-draught case. At z = 0.10 L , RAPID obviously gives a far better prediction of the amplitude of the diverging bow wave system, which is severely underestimated by DAWSON. Further downstream, RAPID consistently improves upon the DAWSON results. But DAWSON is doing well for the rather transverse waves generated at the stern, notwithstanding the deficiencies in the modeling. In the second longitudinal cut, at a distance of 0.30 L from the centerplane, the agreement is slightly worse, and the bow wave system soon mixes up with the stern waves that prohibit further comparisons. But again here, RAPID is substantially closer to the data.

110
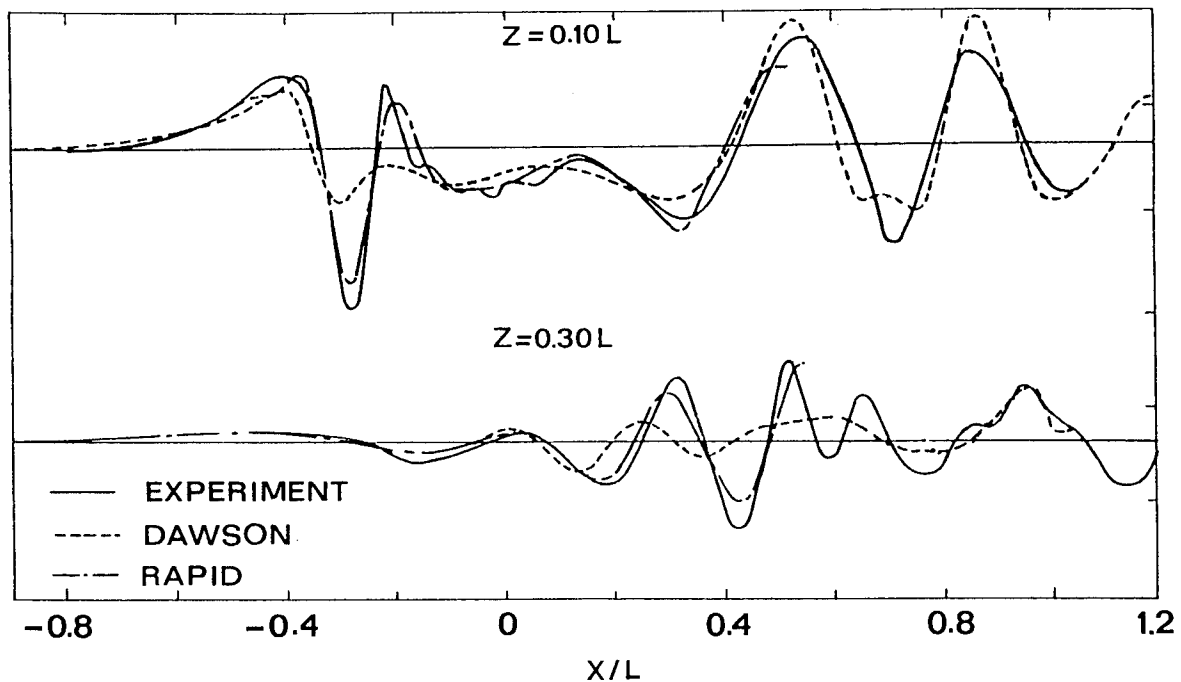
Figure 17. Longitudinal cuts for container ship, full draught

The first iteration of RAPID (a Neumann-Kelvin approximation) was quite similar to the DAWSON results, which proved that the underprediction of diverging waves is caused by neglecting nonlinear effects and not by numerical dispersion or insufficient resolution in the DAWSON results. The same has been found for other cases. It appears that the short diverging waves have a stronger tendency to steepen than the long transverse waves, and thus display stronger nonlinear effects.

For the same vessel in ballast condition the top of the bulbous bow is at 1.2 m above the still waterline (which is 15 % of the stagnation height). An important practical question is then, whether it still becomes completely immersed at the service speed; if not, a significant resistance penalty can be incurred.

This cannot be studied using a linearized method. Inherent to the linearization is the transfer of the boundary condition towards the undisturbed free surface. The greater part of the bulbous bow is above that surface and plays no role in the calculation. Therefore the predicted bow wave form is unrealistic. The same is true if the top of the bulbous bow is extremely close to the undisturbed waterplane [16]. In RAPID however, the free surface boundary conditions are applied at the actual wave surface. If the bow becomes completely submerged due to the bow wave elevation, its effect is fully included in the

mathematical model. The only precaution needed is to start with an increased draught to make the bow fully submerged, and to gradually reduce this draught in the course of the iteration until the equilibrium position is reached.

RAPID here predicted that the bulbous bow would just emerge above the wave surface, by some 0.20 m. But as the free surface panel size was fairly large compared to the dimensions of the bulbous bow there was a risk of insufficient resolution of the large gradients that can occur above such bows. In fact, the towing test showed that an extremely thin sheet of water just wetted the upper side of the bulb. Immediately downstream a deep wave trough next to the hull was formed, and breaking phenomena affected the wave pattern. The less accurate prediction (Fig. 18) therefore comes as no surprise, although the major aspects of the wave pattern are captured.

The calculations for this container ship thus show that also for fairly slender vessels at moderate speed, nonlinear effects can be surprisingly large in some respects, and for diverging waves in particular. The nonlinear code gives a much better agreement with the experimental data, and additionally it permits to make calculations for surface-piercing bows; but resolution of the rather violent flow features here requires care.

111
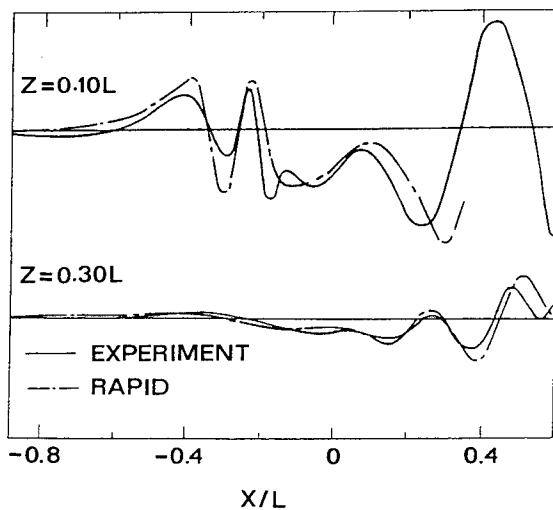
Figure 18. Longitudinal cuts for container ship, ballast draught

4.4 Frigate

In order to specifically test the transom flow modeling, linearized and nonlinear calculations have been carried out for a frigate-type hull with a wide transom, for which older experimental data were available. However, the Froude number based on the transom immersion was only 2.65, and this may well have been a case with a dead-water zone. Moreover, wave breaking near the corners of the transom was observed in corresponding wake survey data. A good agreement could therefore not be expected. As a matter of fact, both the DAWSON- and the RAPID-predictions showed a largely sinusoidal wave aft of the transom, while in the experiment a rather disturbed free surface with modest wave amplitude was observed. Accordingly, the magnitude of the diverging wave from the transom edge was substantially overestimated by both codes, and by RAPID in particular. On the other hand the diverging waves from the bow were again much better represented in RAPID. This case, therefore, turned out to be less appropriate for testing an inviscid potential flow model. Further validations will be carried out in the near future.

5. CONCLUSIONS

This paper has described part of the recent progress in the development of the RAPID-method towards a generally applicable ship design tool. In particular, attention was paid to the convergence of the iterative procedure and the applicability to flows with wave breaking; to the modeling of the flow off an immersed transom stern; and to some of the

validation studies. Main conclusions are:

• The method does not require any smoothing, filtering or damping and usually converges reliably to machine accuracy. The convergence problems typical of most steady nonlinear free surface flow solvers do not occur unless in exceptional cases.

• A converged solution is also obtained for cases in which extensive wave breaking will occur in real flows, such as full hull forms at high speed. A separate criterion for the inception of wave breaking and a model for its effect on the flow field would be required to complete the flow picture in such cases.

• It is argued that vorticity physically plays no role in the flow off a transom stern. The implementation of transom conditions in linearized and nonlinear methods is discussed an studied numerically. The linearized form appears to give reasonable results; the nonlinear method satisfies the transom conditions most accurately and shows very little grid-dependence. Optimization of the transom stern shape now seems possible, even for transoms above the still water line.

• Comparisons with experimental data show that even for slender ships nonlinear effects are larger than was expected before. Diverging waves in particular are much better predicted by RAPID. Including nonlinear terms consistently improves the results. With sufficiently dense panelings very good agreement with experiments can be achieved, even for short wave components. For bulbous bows very close to the wave surface, resolution of small-scale flow phenomena requires care.

• Future work will be directed to further experimental validation, improving the numerical and computational efficiency, and extensions to more complicated stern shapes.

REFERENCES

[1] Dawson,C.W., " A Practical Computer Method for Solving Ship-Wave Problems", <u>Proc. 2nd Int. Conf. Num. Ship Hydrodynamics</u>, Berkeley, USA, 1977.

[2] Raven, H.C., "Variations on a Theme by Dawson", Proc.17th Symp. Naval Hydrodynamics, The Hague, Netherlands, 1988.

[3] Raven, H.C., "Adequacy of Free-Surface Conditions for the Wave-Resistance Problem", Proc.18th Symp. Naval Hydrodynamics, Ann Arbor, USA, 1990.

[4] Zandbergen, P.J., Broeze,J., and Van Daalen, E.F.G., "A Panel Method for the Simulation of Nonlinear Gravity Waves and Ship Motions", in: Advances in Boundary Element Techniques, Springer Verlag, 1992.

[5] Xü, H., and Yue, D., "Computations of Fully Nonlinear Three-Dimensional Water Waves", 19th Symp. Naval Hydrodynamics, Seoul, South-Korea, 1992.

[6] Cao, Y., "Computations of Nonlinear Gravity Waves by a Desingularized Boundary Integral Method," Ph.D.Thesis, Univ. of Michigan, Ann Arbor, 1991.

[7] Ni, S.-Y., "A Method for Calculating Nonlinear Free Surface Potential Flows using Higher-Order Panels", in: Ph.D.Thesis, Chalmers Univ., Gothenburg, Sweden, 1987.

[8] Larsson, L., Kim, K.J., and Zhang, D.H., "New Viscous and Inviscid CFD-Techniques for Ship Flows", Proc. 5th Int. Conf. Numerical Ship Hydrodynamics, Hiroshima, Japan, 1988.

[9] Kim, Y.-H., and Lucas, T., "Nonlinear Ship Waves", Proc. 18th Symp. Naval Hydrodynamics, Ann Arbor, USA, 1990.

[10] Kim, Y.-H., and Lucas, T., "Nonlinear Effects on High Block Ship at Low and Moderate Speed", 19th Symp. Naval Hydrodynamics, Seoul, South-Korea, 1992.

[11] Delhommeau, G.," Computation of Nonlinear Wave and Wave Resistance", Proc. 7th Int. Workshop on Water Waves and Floating Bodies", Val de Reuil, France, 1992.

[12] Xia, F., "A Study on the Numerical Solution of Fully Nonlinear Ship Wave Problems", in :Ph.D.Thesis, Chalmers Univ., Gothenburg, Sweden, 1986.

[13] Jensen, G., "Berechnung der Stationären Potentialströmung um ein Schiff unter Berücksichtigung der nichtlinearen Randbedingung an der Wasseroberfläche", Ph.D.Thesis, IfS Bericht 484, Hamburg, 1988.

[14] Jensen,G., Bertram,V., and Soding, H., "Ship Wave-Resistance Computations", Proc. 5th Int. Conf. Numerical Ship Hydrodynamics, Hiroshima, Japan, 1988.

[15] Raven, H.C., "The RAPID Solution of Steady Nonlinear Free Surface Problems", Proc. 7th Int. Workshop on Water Waves and Floating Bodies, Val de Reuil, France, 1992.

[16] Raven, H.C., "A Practical Nonlinear Method for Calculating Ship Wavemaking and Wave Resistance", 19th Symp. Naval Hydrodynamics, Seoul, South-Korea, 1992.

[17] Bertram,V., Laudan,J., and Jensen,G., "Validation Gives New Insights into Nonlinear Inviscid Flow Computations", 8th Int. Workshop on Water Waves and Floating Bodies, St John's, Canada, 1993.

[18] Duncan, J.H., "The Breaking and Non-Breaking Resistance of a Two-Dimensional Hydrofoil", Jnl. Fluid Mechanics, Vol.126,1983, pp.507-520.

[19] Tulin,M.P., and Cointe, R., "A Theory of Spilling Breakers", Proc. 16th Symp. Naval Hydrodynamics, Berkeley, 1986.

[20] Lin,W.M., Newman,J.N., and Yue, D.K.P, "Nonlinear Forced Motions of Floating Bodies", Proc. 15th Symp. Naval Hydrodynamics, Hamburg, Germany, 1984.

[21] Van Daalen, E.F.G., "Numerical and Theoretical Studies of water Waves and Floating Bodies", Ph.D.Thesis, Twente University, Netherlands, 1993.

[22] Reed, A., Telste, J., Scragg, C., "Analysis of Transom Stern Flows", Proc. 18th Symp. Naval Hydrodynamics, Ann Arbor, USA, 1990.

[23] Tulin, M.P., and Hsu,C.C., "Theory of High-Speed Displacement Ships with Transom Sterns", Jnl. Ship Research, Vol.30-3, 1986, pp. 186-193.

[24] Schmidt, G.H., "Linearized Stern Flow of a Two-Dimensional Shallow-Draft Ship", Jnl. Ship Research, Vol.25-4, dec. 1981, pp. 236-242.

[25] Vanden-Broeck, J.-M., "Nonlinear Stern Waves" Jnl. Fluid Mech., Vol.96, part 3, pp.603-611.

[26] Toda,Y., Stern,F., and Longo, J., "Mean-Flow Measurements in the Boundary Layer and Wake and Wave Field of a Series 60 Cb=.6 Ship Model for Froude Number .16 and .316 ", IIHR Report no. 352, Iowa, USA, 1991.

DISCUSSION
by Professor P. D. Sclavounos, MIT

1. Schmidt (1980) proves in his paper that for overhanging sterns, the coefficient C_2 in the local expansion near the stern vanishes, thus establishing that the curvature of the wave profile is preserved in this case.

Author's Reply:

See common response for the above at the end of this section.

2. My question pertains to your experience with regard to the prediction of the wave resistance with your nonlinear method. Have you experienced improved predictions in the wave resistance which result from improved wave profile calculations?

Author's Reply

It has been found that slow-ship linearized methods:

- generally predict the resistance reasonably well for relatively slender vessels at fairly high speed, with substantial wave making, but often underestimate the resistance otherwise;

- generally predict a negative wave resistance for full hull forms at low Froude numbers. As shown in [3] this may be a result of a spurious momentum flux through the calculated free surface owing to the slow-ship linearization of the free surface boundary condition. One thus expects an improvement for a nonlinear method.

Current experience with RAPID indicates that:- for slender ships at high speed, the resistance prediction is good but not much different from that of a linearized method; - in some cases dominated by diverging waves, the resistance predicted by RAPID was much closer to experimental values;- for slow ships at low speed, the resistance is not consistently negative anymore, but it is hard to obtain an accurate prediction from pressure integration over the hull. This is due to the fact that, contrary to a linearized method, a nonlinear method requires the hydrostatic + hydrodynamic pressure to be integrated

over the hull, which at low Froude numbers is a badly conditioned calculation.

More validations are, however, required. The accuracy of the resistance predictions, and possible alternative expressions for it, will be studied in the near future.

DISCUSSION
by Dr. D. Nakos, Intec Software & Consulting

In case that one of your iterations (towards the nonlinear solution) indicates that the flow separates at the stern before the ship transom, do you correct the assumed separation line?

Author's Reply:

See common response for the above at the end of this section.

DISCUSSION
by Dr. S. Kinnas, MIT

I would like to congratulate Dr. Raven for his impressive work. It appears to me that the detachment of the transom stream-surface is similar to the smooth detachment condition (Villat-Brillouin condition) for cavity flows, in which the cavity detaches at a point where the slope as well as the curvature are continuous. What are the author's comments to this? Is this an adequate condition or we must consider the viscous flow in front of the detachment point similar to what is done for cavity flows by Arakeri, Frank, & Michel?

Author's Reply:

See common response for the above at the end of this section.

DISCUSSION
by Professor E. O. Tuck, University of Adelaide, Australia

I compliment the author on an excellent paper. My comment relates only to the minor matter raised at the end of it concerning transom sterns which are well above the undisturbed water level. This causes no extra difficulty with RAPID, apparently, which is as it should be. The only problem with this case is that the con-

114

verged results from RAPID passes a physically-unacceptable region of pressure less than atmospheric, just ahead of the transom. In practice, the flow would have detached prior to reaching the transom, perhaps quite next to the station where in the non-physical case studied, the pressure first goes negative (relative to atmospheric). In a similar planning context, I have had success in finding the actual detachment contour by iteration, the aim being to converge towards a final detachment contour or artificial transom on which not only the pressure but also the pressure gradient is zero. This is equivalent to requiring continuity of curvature, as well as slope, at detachment.

Author's Reply:

See common response for the above at the end of this section.

Author's Reply to Professors Sclavounos, Nakos, Kinnas, and Tuck

All above discussers address the problem of modeling the detachment of the free surface from a smooth surface, the bottom of a flat hull with the transom far above the undisturbed water level. If in a numerical solution the pressure on the hull falls below atmospheric pressure, this early detachment of the free surface may be supposed to occur physically. To model this, one should modify both the location of the detachment line and the assumed free surface behavior there. As mentioned in my paper this is not being done yet, and I had not yet given much thought to the details of this problem. The comments of the discussers are, therefore, welcomed.

As stated in Section 3.1 of the paper, in such a 'regular flow' the curvature of the streamline at detachment is bounded. It can then be shown, at least in a 2D case, that the curvature must be equal to that of the wall, and that the pressure gradient along the wall must be zero at detachment. As Prof. Sclavounos rightly points out, this same conclusion follows from Schmidt's 2D flatship analysis, where the coefficient C2 in eq. (10) vanishes for a smooth detachment. Prof. Tuck points out that these conditions of zero pressure and zero pressure gradient at the wall permit to determine the detachment point by iteration. One could assume a detachment position and solve the problem in a way similar to the

transom flow solution in RAPID (but with different local behavior at detachment). If the guessed detachment point is too far forward, there will be an infinite upward curvature of the streamline at this point, and the free surface penetrates the hull. If it is too far aft, there will be an infinite downward curvature, and the pressure along the hull ahead of the detachment point becomes negative. The correct position can thus be found, and has been found in earlier work by others.

Dr. Kinnas notes the analogy with the detachment of wall streamlines at the leading edge of a sheet cavity, where the inviscid-flow problem has almost the same properties. The conditions of continuous slope and curvature, called Villat-Brillouin condition in this field, have been imposed by e.g. Pellone and Rowe [D1], who iteratively located the detachment point from the condition of zero pressure gradient in a discretized form.

Including such an iteration in the method presented here would require much care because of the fine discretizations required and the repeated rediscretization of hull and free surface to fit the shifting intersection. But a complete description of inviscid flow off a ship afterbody may eventually require this addition.

Dr. Kinnas additionally raises the question of the importance of viscous effects. To what extent these will affect the location of smooth detachment, and the flow off an immersed transom stern as well, will depend on the hull form and the thickness of the boundary layer or wake. One expects little effect for slender high-speed vessels, but much more for slower, fuller hull forms. Some validations to be carried out now at MARIN may shed some light on this issue. If viscous effects are found to be important, I am afraid that the methods of Arakeri or Franc & Michel will be of little help, since they seem to exclusively apply to laminar separation in thin boundary layers upstream of cavity detachment on headforms and foils. But Dr. Kinnas's remark is of course entirely justified.

References for the Replies:

[D1] Pellone, C., and Rowe, A., "Supercavitating Hydrofoils in Nonlinear

Theory", 3rd Int. Conf. Numerical Ship Hydrodynamics, Paris, France, June 1991.

[D2] Van den Berg, W., Raven, H.C., and Valkhof, H.H., "Free-Surface Potential Flow Calculations for Merchant Vessels", Int. Symp. on CFD and CAD in Ship Design, Wageningen, Netherlands, Sept. 1990.

[D3] Ligtelijn, J.Th, Raven, H.C., and Valkhof, H.H., "Ship Design Today: Practical Applications of Computational Fluid Dynamics", HADMAR '91 Symposium, Varna, Bulgaria, Oct. 1991.

[D4] Sclavounos, P.D., and Nakos, D.E., "Stability Analysis of Panel Methods for Free-Surface Flows with Forward Speed", 17th Symp. Naval Hydrodynamics, The Hague, Netherlands, 1988.

DISCUSSION
by Bill H. Cheng, David Taylor Model Basin

The author is commended for his contributions to nonlinear ship wave computations. MARIN's track record in applying a Dawson code to some 100 hull forms per year is impressive. I would be interested in learning more about this experience. In particular, typical examples of slender ships and full hull forms, for which Dawson codes work well and not so well, are of great interest to me.

At DTMB, the XYZFS program based on Charles Dawson's original code continues to be enhanced for use in ship design. I develop a dry transom algorithm [1] which has been successfully applied to transom-stern ships with and without bow domes [2, 3, 4, 5]. The wave resistance predictions are reasonable for moderate speeds corresponding to Froude numbers between 0.35 to 0.45. However, the predictions are less accurate outside this Froude number range since the dry transom assumption is no longer valid at lower Froude numbers and the stability and convergence become a problem at higher Froude numbers.

I am currently working on improving the stability and convergence of the Dawson method. Our outlook is more optimistic than Letcher's

assessment [6]. Our approach which uses finite difference methods to satisfy the radiation conditions is described in [7]. A new five-point upstream operator has been found to work well for fine grids corresponding to high speeds. This operator improves the stability and convergence by eliminating the spurious mode introduced by the numerics. Our latest approach is to use a family of difference operators to control the stability and convergence. A 2-D submerged source has been used as the first test case and the results show significant improvement for a wide range of Froude numbers. This finite difference method is being extended to 3-D linear problems and our results will be compared with the corresponding RAPID predictions.

References
1. Cheng, B.H., 5th Int. Conf. on Numerical Ship Hydrodynamics, Hiroshima, Japan, Sept. 1989.
2. Cheng, B. H., Dean, J.S., and Jayne, J.L., 2nd Workshop on Ship Wave Resistance Computations, DTNSRDC, Bethesda, Maryland, Nov. 1983.
3. Cheng, B.H. et al., Int. Conf. on Computer Aided Design, Manufacture and Operation in Marine and Offshore Industries, Springer-Verlag, Sept. 1986.
4. Hoyle, J.W. et. al., SNAME, Vol. 94, Nov. 1986.
5. Cheng, B.H. et al., Naval Engineers Journal, Vol. 101, No. 3, May 1989.
6. Letcher, J.S., Journal of Ship Research, Vol. 37, No. 1, Mar. 1993.
7. Strobel, K.H. and Cheng, B.H., 11th Int. Conf. on Offshore Mechanics and Arctic Engineering, Calgary, Canada, June 1992.

Author's Reply
Thanks for your comment. For some of our experience on practical applications of Dawson's method, see Refs. [D2] and [D3]. Concerning the use of linearized methods I would like to add that, although as a matter of fact the predicted wave resistance is not useful for full ships at low Froude numbers, the wave pattern predicted by our DAWSON code is qualitatively correct, as comparison with RAPID predictions has shown. In my opinion, a proper use of these linearized methods in ship design does not rely on the predicted resistance but on careful analysis of the entire flow field, pressure distribution and flow

direction. Thus handled, linearized methods are equally useful at lower Froude numbers.

I am interested in your progress in optimizing the choice of difference operators for the free surface condition. Of course, for studying the stability and accuracy of discretizations one should consider not only the effects of the difference operators, but simultaneously those due to the discretization of the singularity distribution. Note the difference in both numerical dispersion and stability of the DAWSON and RAPID implementations (see Figs 5 and 6 for example), which use identical difference schemes but different discretizations. This is one of the reasons that, like you, I do not share Letcher's conclusions. The most complete analysis is that proposed by Sclavounos and Nakos [D4], which allows to clearly identify the most promising implementations and discretizations. It will be interesting to compare the results of a linear method, optimized in this respect, with those of the nonlinear RAPID method, which has very good stability, virtually zero numerical dispersion but a numerical damping similar to that of Dawson's original method. But remember that nonlinear effects have been found to be substantial in several, sometimes unexpected, cases.

DISCUSSION
by Dr. Henry J. Haussling, David Taylor Model Basin

The author is to be commended on the development of a powerful method for the prediction of the flow about general hull geometries including nonlinear free-surface effects. I found the treatment of transom sterns interesting, as apparently did much of the audience, judging by the discussion that followed the talk. I therefore take this opportunity to recall the attention of the interested community to pertinent work, carried out some years ago at David Taylor Model Basin, that resulted in a series of publications [1-4] on stern flows. The approach taken in that work seems to be much the same as that taken by Dr. Raven in the present paper.

The earlier work covered both the "regular" and "transom" types of flow defined in the current paper. It started with two-dimensional linearized stern flows [1] and progressed to the three-dimensional nonlinear regime [4]. It cul-

minated in [4] with the development of a method for the computation of the wetted hull area in the vicinity of a transom or cruiser stern in such a way as to eliminate the possibility of negative pressures on the hull.

I would also like to point out that the earlier work included a careful comparison of computations of steep waves behind a two-dimensional flat-bottomed transom stern with the analytical work of Vanden-Broeck (reference [25] of the current paper). In particular, Figure 9 of [3] showed a remarkably close relationship between numerical solution behavior and Vanden-Broeck's analytic predictions in the Froude number range in which transition from non-breaking to breaking waves occurs. It was concluded that the numerical methods were accurate in the sense that they predicted the waves accurately up to the limit of breaking and that for breaking waves, where presumably a nonlinear free-surface potential flow does not exist, the numerical scheme diverged. However, Dr. Raven obtains a solution with his method even for cases in which the waves would break in reality. It is my understanding that he attributes this difference in results to his iterative scheme which is different from the time-accurate unsteady approach of the earlier work. Presumably his scheme finds a solution which is not found by the unsteady approach. If true, this would be a significant finding with important implications for nonlinear wave computations. Because of this importance, I would urge Dr. Raven to carry out careful grid refinement studies to determine the validity of his non-breaking solutions. Also, he should monitor energy conservation in his computations to make sure that he is not losing energy somewhere. Energy was carefully monitored in the earlier work. Could he repeat the two-dimensional computations of [3] with his method?

References
1. Haussling, H.J., "Two-dimensional Linear and Nonlinear Stern Waves," Journal of Fluid Mechanics, Vol. 97, Part 4, Page 759 (1980).
2. Van Eseltine, R.T. and Haussling, H.J., "Flow About Transom Sterns," Proc. of the Third Int. Conf. on Numerical Ship Hydrodynamics, Paris, Page 121 (1981).
3. Coleman, R.M. and Haussling, H.J. "Nonlinear Waves Behind an Accelerated Transom Stern," Proc. of the Third Int. Conf.

117

on Numerical ship Hydrodynamics, Paris, Page 111 (1981).

4. Coleman, R.M., "Nonlinear Flow About a Three-Dimensional Transom Stern," Proc. of the Fourth Int. Conf. on Numerical Ship Hydrodynamics, Washington, Page 234 (1985).

Author's Reply

Since the statements in the paper on wave breaking and its relevance for potential flow solutions are meant to stimulate a discussion on these apparently unsettled issues, I am most pleased with Dr. Haussling's discussion.

According to Vanden-Broeck's theory the steepness of the waves behind a 2D transom increases for decreasing transom Froude number. At a Froude number of 2.26, the limiting steepness of a Stokes wave is reached. The wave crests then attain stagnation height. For even lower transom Froude numbers, a steady potential flow solution does not exist.

The impressive work done by Dr. Haussling and coworkers already several years ago reproduced this. Nonlinear time-dependent calculations for 2D semi-infinite flat-bottomed transom stern hulls (his ref. [3]) at a Froude number of 2.3 and below broke down, at higher Fn they converged to a steady state. It seems obvious in this case (in absence of viscosity) that if a steady potential flow solution does not exist, wave breaking must occur . However, the converse is not true: Even while a steady potential flow exists theoretically, wave breaking may occur in reality. E.g. in Duncan's experiments and several others, wave breaking inception occurred before the limiting steepness was reached. Similarly, in this case the stern waves most likely will break already at transom Froude numbers higher than 2.26. Therefore, also in Dr. Hausslings calculations a solution was obtained in cases that wave breaking occurs in reality. In this sense, his results confirm my statement that a separate wave breaking criterion is required.

Remains the question why the result of Fig. 10 could be obtained, for a transom Froude number of 2.0. But the maximum wave height found was 80 % of the stagnation height, so the theoretical limit, which in 2D is reached at Fn = 2.26, had not yet been reached here. In my opinion this is due to the three-dimensionality and not to the

difference in solution methods. Most recently I triedto further increase the transom draft for the same 3D case, and did not succeed to obtain convergence below Fntr = 1.77. The wave crest height then amounted to 94% of the stagnation height. This suggests that the same behaviour is found, but in 3D cases the limiting Froude number is somewhat different. Grid refinement studies and energy checks would as a matter of fact be requiredto establish the precise limits, but it seems that Vanden Broeck's theory and Dr. Haussling's and my calculations confirm rather than contradict each other. This could in fact better be studied by carrying out 2D calculations with the RAPID method, which, however, would require a substantial adaptation of the code. Similarly it is unfortunate that the results in your ref. [4] do not apply to lower transom Froude numbers in 3D flows.

In the discussion in Section 2.5 on wave breaking in more general 3D cases, wave breaking is again not defined as the nonexistence of a potential flow solution, but as the physical phenomenon. The wave pattern in Fig. 3 most likely will give rise to extensive breaking at the forward shoulder, but a steady potential flow solution may well exist (note that these are not far field waves). This calculation served to demonstrate that the convergence of the method is good enough to cover the range of wave steepnesses where wave breaking is not dominant in real flows.

118

Panel-Convergence of Steady Free-Surface Flow Calculations

D. Hendrix and F. Noblesse
(David Taylor Model Basin, USA)

ABSTRACT

Steady free-surface potential flow about a mathematically-defined hull form is considered. The flow is defined using the slender-ship approximation. The hull form is approximated by means of flat triangular panels within which the source strength is assumed piecewise constant. Convergence of the computed velocity potential, wave profile, and lift, moment and drag with respect to the number of panels is evaluated.

INTRODUCTION

Numerical methods for computing free-surface flows about ship forms are increasingly utilized for practical design studies. These methods are typically validated by comparisons between numerical predictions and experimental measurements. Although experimental validation of any numerical method is obviously necessary, it is not sufficient to demonstrate the reliability of the method. Indeed, experimental validation cannot be convincing unless the reliability and the accuracy of the method are established independently of comparison with experimental data. For instance, favorable comparisons between numerical predictions and experimental measurements are not meaningful if the numerical predictions depend appreciably upon some parameters such as the number and the arrangement of the panels used for representing the ship hull.

Efforts aimed at establishing the reliability and the accuracy of numerical methods are increasingly reported in the literature on numerical free-surface hydrodynamics. These efforts include studies of convergence with respect to the number of panels. As numerical methods are increasingly utilized for design studies, there is indeed a need for guidelines with respect to the number of panels that should be employed to achieve a desired accuracy.

Systematic panel-convergence studies for realistic ship forms are rendered difficult by practical limitations in computing time and computer memory, as well as by more fundamental limitations stemming from numerical uncertainties related to causes other than hull-discretization. For instance, if a numerical method relies on a solution procedure having uncertain robustness (as may be the case for the Neumann-Kelvin integral-equation) or if the required numerical calculations (such as the evaluation and panel-integration of a Green function) are performed with insufficient accuracy, it may not be meaningful to perform a panel-convergence study in which the number of panels is increased beyond a modest number.

A limited step toward the goal of developing guidelines with respect to the number of panels that must be employed to achieve a desired accuracy is made here. The present panel-convergence study is restricted to steady free-surface flow calculations based on flat triangular panels and the Green function associated with the linearized free-surface boundary condition.

FRAMEWORK OF STUDY

Specifically, the velocity potential due to a distribution of Kelvin sources on a ship's mean wetted hull surface is considered. The source strength is taken equal to the component n_x of the unit vector $\vec{n}$ normal to the hull along the direction of motion of the ship, according to the slender-ship approximation. The source strength thus is defined explicitly in terms of the hull geometry. Difficulties and uncertainties as-

119

sociated with the numerical solution of an integral equation therefore are avoided in the present panel-convergence study. The present study is in this respect simpler and less ambitious than the convergence studies reported by Doctors and Beck (1987) and others. However, the simplified approach based on the slender-ship approximation adopted here makes it possible to perform a panel-convergence analysis in which a large number of panels is employed.

Recipes for computing the velocity potential due to a piecewise-constant source distribution on a set of flat triangles within 0.1% accuracy are given in Hendrix and Noblesse (1992). This calculation method is used here. The slender-ship potential, denoted ψ, is expressed as the sum of a nonoscillatory near-field potential ψ_{SN} and a wave potential ψ_W corresponding to the wave field generated by the ship. We thus have

$$\psi = \psi_{SN} + \psi_W \,.$$

The potential ψ_{SN} is evaluated using a "direct" approach in which the nonoscillatory component of the Green function is computed and integrated over a panel (by means of Gauss integration rules or analytical formulas). The wave potential ψ_W is evaluated using an "indirect" approach based on the Fourier-Kochin representation.

All calculations are performed using Silicon Graphics (SGI) computers with 32 bit floating point arithmetic and SGI's Fortran compiler.

HULL FORM

A mathematically-defined hull form is considered for the sake of simplicity and accuracy. The hull form is depicted in Figure 1. Coordinates (x, y, z) rendered nondimensional with respect to the ship length are defined. The undisturbed waterplane is taken as the plane $z = 0$, the ship centerplane is chosen as the plane $y = 0$, and the ship bow and stern are located at $x = 1/2$ and $x = -1/2$, respectively. The nondimensional beam and draft are denoted b and d, respectively, and are taken equal to $b = 0.1$ and $d = 0.035$.

The hull form is defined by means of parametric equations. The parameters, denoted λ and μ, vary within the unit square $0 \leq \lambda \leq 1$ and $0 \leq \mu \leq 1$. The parameter λ is equal to 0 along the stem profile and 1 along the stern profile, and the parameter μ is equal to 0 at the static waterline and 1 at the keel. The hull form is divided into three regions, which are defined by means of different sets of parametric equations. The forebody $1/2 - L_b \leq x \leq 1/2$ corresponds to

$0 \leq \lambda \leq L_b$. The aftbody $-1/2 \leq x \leq -1/2 + L_s$ corresponds to $1 - L_s \leq \lambda \leq 1$. Finally, the parallel midbody $-1/2 + L_s \leq x \leq 1/2 - L_b$ corresponds to $L_b \leq \lambda \leq 1 - L_s$. The lengths of the forebody and aftbody are taken equal to $L_b = 0.45$ and $L_s = 0.45$.

The notation $\lambda_b \equiv \lambda/L_b$ is used in the parametric equations defining the forebody $0 \leq \lambda \leq L_b$. These equations are

$$x = 1/2 - \lambda$$
$$2y/b = \lambda_b(2 - \lambda_b)\sqrt{\cos(\pi\mu/2)} - \beta_b \lambda_b(1 - \lambda_b)^2 \mu(1 - \mu)^2$$
$$z/d = -\sin(\pi\mu/2)$$

where the constant β_b, which controls the fullness of the bow sections, is taken equal to 1.

The parallel midbody $L_b \leq \lambda \leq 1 - L_s$ is defined by the parametric equations

$$x = 1/2 - \lambda$$
$$2y/b = \sqrt{\cos(\pi\mu/2)}$$
$$z/d = -\sin(\pi\mu/2)\,.$$

The aftbody $1 - L_s \leq \lambda \leq 1$ is defined by the parametric equations

$$x = 1/2 - \lambda + t^2 x_s$$
$$2y/b = \sqrt{1 - t^2}\left[\sqrt{\cos(\pi\mu/2)} - \beta_s t^2 \mu \cos(\pi\mu/2)\right]$$
$$z/d = -\sin(\pi\mu/2)$$

where t and x_s are given by

$$t = 1 + (\lambda - 1)/L_s$$
$$x_s = \ell_s\left[1 - \cos(\pi\mu/2)\right] + \gamma_s \mu^2(1 - \mu)^2$$

and the constants ℓ_s, β_s, and γ_s are taken equal to $\ell_s = 0.15$, $\beta_s = 1.4$, and $\gamma_s = 1.1$. The constant ℓ_s determines the point at which the keel rises from the baseline toward the stern. The constants β_s and γ_s control the fullness of the stern sections and the shape of the stern profile, respectively.

Finally, the x coordinate in the foregoing parametric equations is stretched via the linear transformation

$$\xi = (x - 0.005)/0.99\,,$$

which yields $\xi = 1/2$ for $x = 1/2$ and $\xi \simeq -0.51$ for $x = -1/2$. This stretching of the longitudinal coordinate x thus does not alter the location of the bow but slightly displaces the stern from $x = -0.5$ to $\xi \simeq -0.51$. A hull form having a small transom is defined by truncating the portion of the stretched hull extending beyond the station $\xi = -0.5$. The resulting truncated hull form is depicted in Figure 1 and used for the calculations.

120
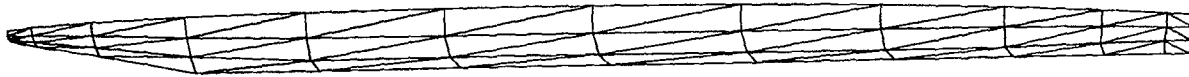
Figure 1: Hull form and panel refinement scheme used in study.

PANEL ARRANGEMENT

Flat triangular panels are used to approximate the hull, as was already noted. The panels are defined so that the vertices of the panels corresponding to the coarsest panel distribution are also panel vertices of all finer distributions. The hull is divided longitudinally by constant-x stations (as is required by the theoretical formulation) and transversely by dividing each station into the same number of equal-length segments. The stations are "cosine" spaced with the minimum spacing at the bow and the stern chosen so that the aspect ratio of the panels approaches 1 at the bow for the finest panel arrangements considered in the study.

The coarsest panel arrangement used in the study, shown in the upper part of Figure 1, consists of 72 panels on one half of the hull. The lower part of Figure 1 depicts an example of a finer panel arrangement corresponding to 1152 panels. This panel arrangement is defined by subdividing each of the panels obtained in the 72-panel coarsest panel arrangement into 16 panels.

The panel distributions used in the study are listed in Table 1. In this table N_x represents the number of segments between constant-x stations and N_{yz} is the number of segments defining a station. The total number of triangular panels on one half of the hull is then equal to

$$N = 2\,N_x\,N_{yz}\,.$$

The ratio N_x/N_{yz} was selected so that the aspect ratio of most panels is roughly equal to five, as is apparent from Figure 1. This ratio was adjusted when necessary in order to limit the maximum aspect ratio to ten, in accordance with the restriction recommended in Hendrix and Noblesse (1992). The aspect ratio of a panel is defined here as the length of the longest side of a panel divided by the distance to the correspond-

N_x	N_{yz}	N
12	3	72
24	6	288
36	9	648
48	12	1152
60	15	1800
72	18	2592
84	21	3528
96	24	4608
108	27	5832
120	30	7200
132	33	8712
144	36	10368
168	42	14112
192	48	18432
216	54	23328
240	60	28800
300	75	45000
360	87	62640
420	90	75600
480	102	97920
540	120	129600
684	144	196992
1056	189	399168
1536	258	792576

Table 1: Panel arrangements used in study.

ing opposite vertex. The panel configurations listed in Table 1 were not all used in all the convergence studies. These panel arrangements represent a reasonable, although not optimal, panel distribution.

SURFACE AREA

Figure 2 presents the percent relative error in the computed surface area of the hull. Five curves are shown in this figure. The curves cor-

121
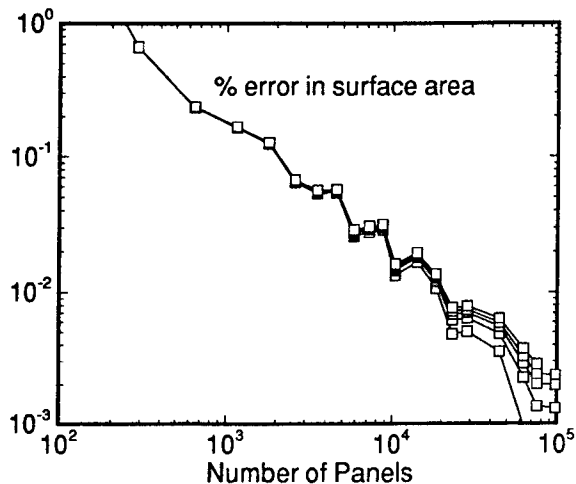
Figure 2: Relative error in surface area.

respond to the errors determined using different assumed "exact" values of the surface area.

Specifically, the lowest curve corresponds to the assumption that the surface area computed using (approximately) 100,000 panels is exact. The next three curves were similarly determined by taking the "exact" value of the surface area as that computed using (approximately) 200,000, 400,000, and 800,000 panels. The uppermost curve was determined by means of an extrapolation based on the other four curves to obtain an estimate of the true error ϵ_∞ corresponding to an infinite number of panels $N_{exact} = \infty$. The extrapolation is based on a least-squares fit to the equation

$$\epsilon = \epsilon_\infty + C_1/\sqrt{N_{exact}} + C_2/N_{exact}.$$

Figure 2 shows that approximations to the surface area accurate within 1% and 0.1% are obtained using about 250 and 2000 panels, respectively. This figure also shows that the error ϵ decreases approximately in proportion to $1/N$ in the limit $N \to \infty$.

VELOCITY POTENTIAL

The vertices of the 72 panels corresponding to the coarsest panel arrangement shown in the upper part of Figure 1 define 52 points. The velocity potential is evaluated at these 52 calculation points, which are panel vertices for all the panel arrangements considered in the study as was already noted.

Potentials ψ_0 and ψ_∞

The velocity potentials ψ_0 and ψ_∞ corresponding to the "zero" and "infinite" Froude-

number limits are considered first. The upper part of Figure 3 depicts the RMS (root-mean-square) of the errors

$$\psi_i(N) - \psi_i^{exact}$$

at the 52 calculation points. Here, $\psi_i(N)$ represents the value of the potential ψ, which stands for ψ_0 or ψ_∞, at the "calculation point" number i (with $1 \leq i \leq 52$) obtained using N panels, and ψ_i^{exact} is the corresponding "exact" value of the potential.

In Figure 3 the RMS of the errors at the 52 calculation points is normalized by the RMS of the "exact" values ψ_i^{exact} of the potential at the 52 points. Figure 3 therefore depicts

$$\sqrt{\Sigma_{i=1}^{52}[\psi_i(N) - \psi_i^{exact}]^2} / \sqrt{\Sigma_{i=1}^{52}(\psi_i^{exact})^2}$$

as a function of the number N of panels. The five curves shown in the figure were determined in the manner explained previously in connection with Figure 2. Thus, ψ_i^{exact} in the foregoing expressions is taken as $\psi_i(N)$ with N (approximately) equal to 100,000, 200,000, 400,000, and 800,000 for the four lowest curves, and the uppermost curve is obtained by means of a least-squares extrapolation based on the four lower curves.

The upper part of Figure 3 shows that approximately 500 and 1000 panels are required to compute the potentials ψ_0 and ψ_∞, respectively, within a RMS accuracy of 1%, and that approximately 6,000 and 50,000 panels are required to obtain 0.1% accuracy. Thus, considerably more panels are required to compute, within the same accuracy, the potential ψ_∞ than the potential ψ_0.

The lower part of Figure 3 depicts the error

$$[\psi_i(N) - \psi_i^{exact}] / \sqrt{\Sigma_{i=1}^{52}(\psi_i^{exact})^2/52},$$

which is normalized by the RMS value of the potential, for each of the 52 calculation points. Here the "exact" value ψ_i^{exact} of the potential ψ is taken as the value $\psi_i(N)$ of the potential obtained using $N \approx 800,000$ panels.

Considerable variation exists among the 52 curves corresponding to the various calculation points, although these curves generally follow a similar trend. A notable exception is the uppermost curve. This curve corresponds to the intersection between the stemline and the keel, where the geometry is changing rapidly and a locally more refined panel arrangement would be required. If this point is ignored, the lower part of Figure 3 shows that approximately 10,000 and
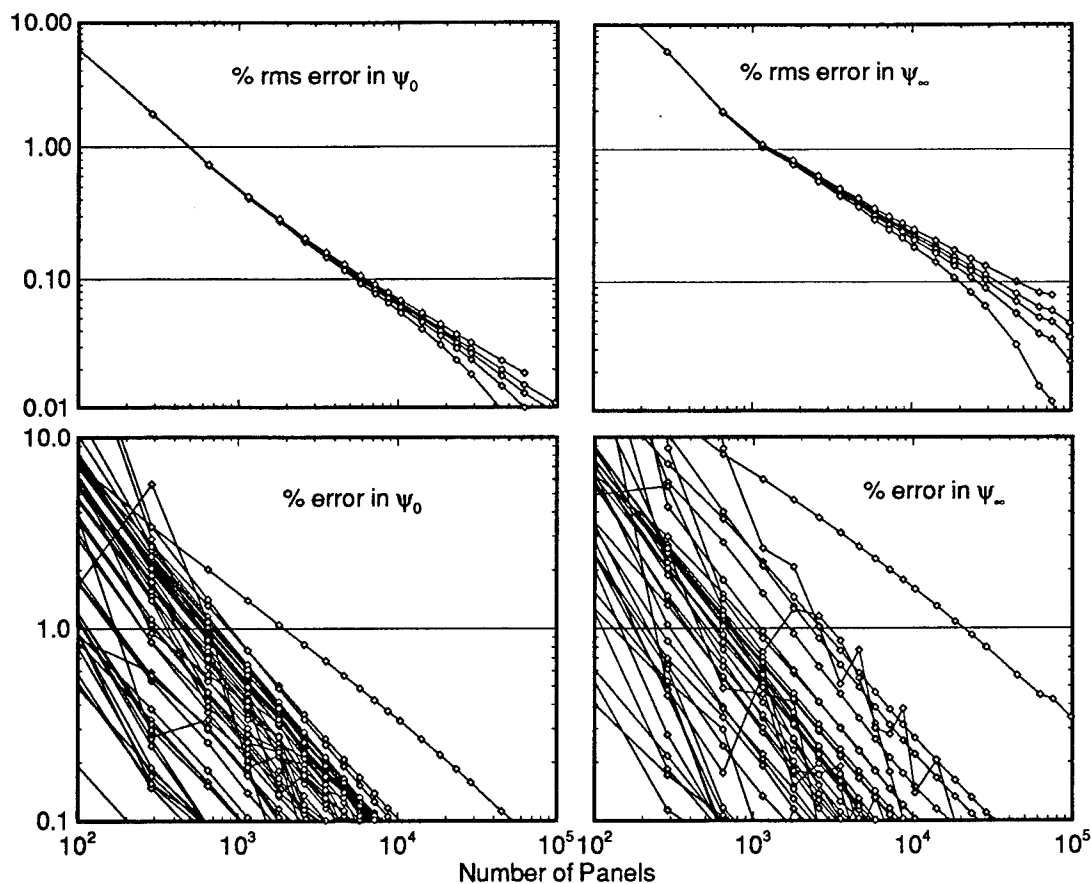
Figure 3: Relative error in velocity potential at zero and infinite Froude numbers.

30,000 panels are required to compute the potentials ψ_0 and ψ_∞, respectively, within a relative error of 0.1%. The upper and lower parts of Figure 3 show that errors in the calculation of the potentials ψ_0 and ψ_∞ decrease approximately in proportion to $1/N$ as the panel-number N increases.

Potentials ψ, ψ_W and ψ_{SN}

The velocity potential ψ is considered in Figures 4 and 5 for three values of the Froude number F equal to 0.1, 0.25, and 0.5, which correspond to the top, center, and bottom rows of these two figures. The potential ψ is considered in the right columns of Figures 4 and 5 and the "nonoscillatory near-field component" ψ_{SN} and "wave component" ψ_W of the potential ψ are considered in the left and center columns, respectively. Figure 4 presents the RMS error, defined as in the upper part of Figure 3, in the potentials ψ, ψ_W and ψ_{SN}.

The left column of Figure 4 shows that approximately 500, 600 and 2,500 panels are required to compute the component ψ_{SN} at values of the Froude number F equal to 0.1, 0.25, and 0.5, respectively, within 1%, and that a greater accuracy of 0.1% requires 6,000, 30,000 and more than 100,000 panels. The number of panels required for computing the near-field potential ψ_{SN} within a specified accuracy therefore increases appreciably with the Froude number.

The center column of Figure 4 shows that approximately 1000, 500 and 300 panels are required to compute the wave component ψ_W within 1% for values of F equal to 0.1, 0.25, and 0.5, respectively, and that an accuracy of 0.1% requires approximately 50,000, 30,000 and 3,000 panels. The number of panels required for computing the wave potential ψ_W within a specified accuracy thus increases appreciably as the Froude number decreases, whereas the opposite was just found to hold for the near-field potential ψ_{SN}.

123
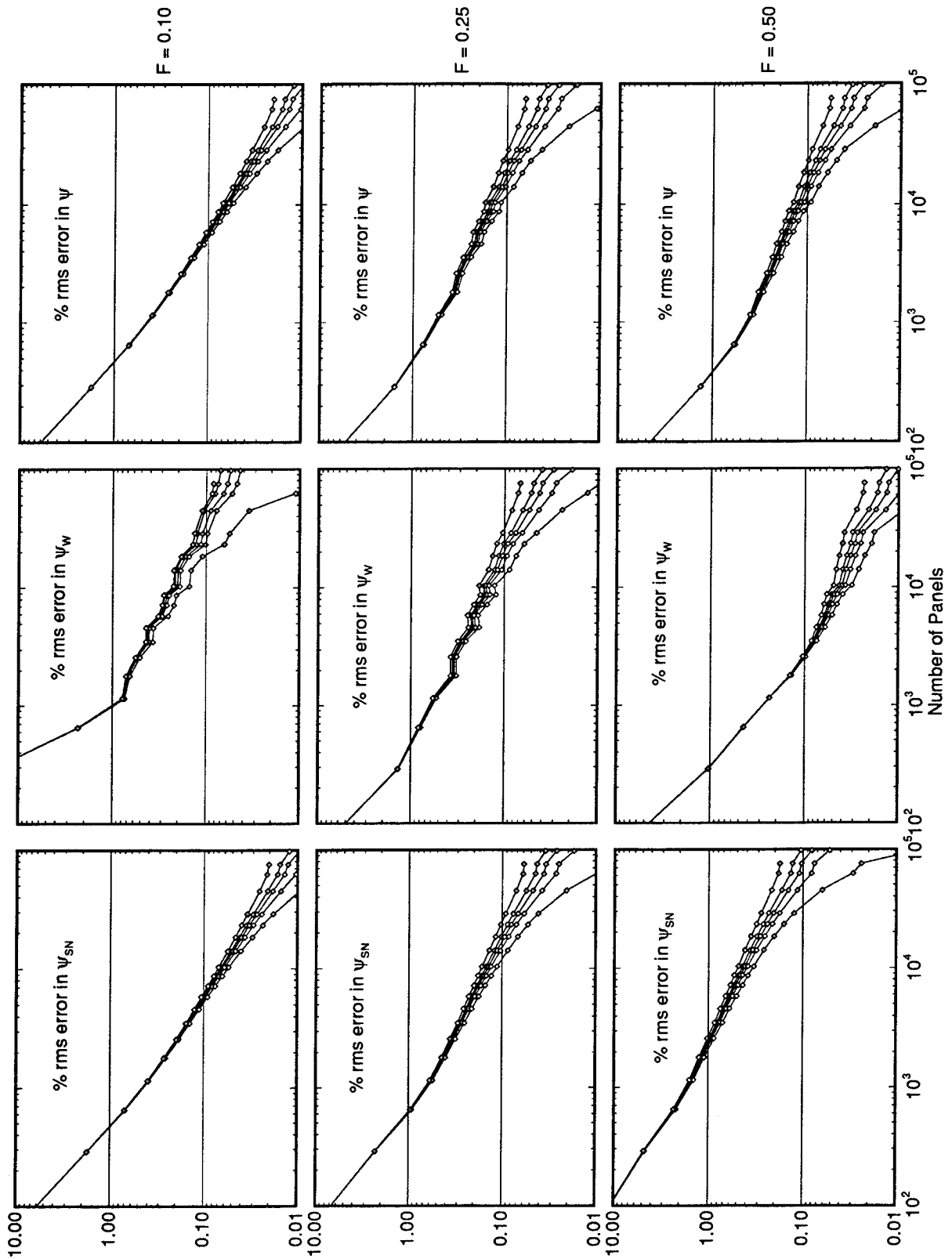
Figure 4: Root-mean-square error in nonoscillatory and wave potentials at three Froude numbers.

124
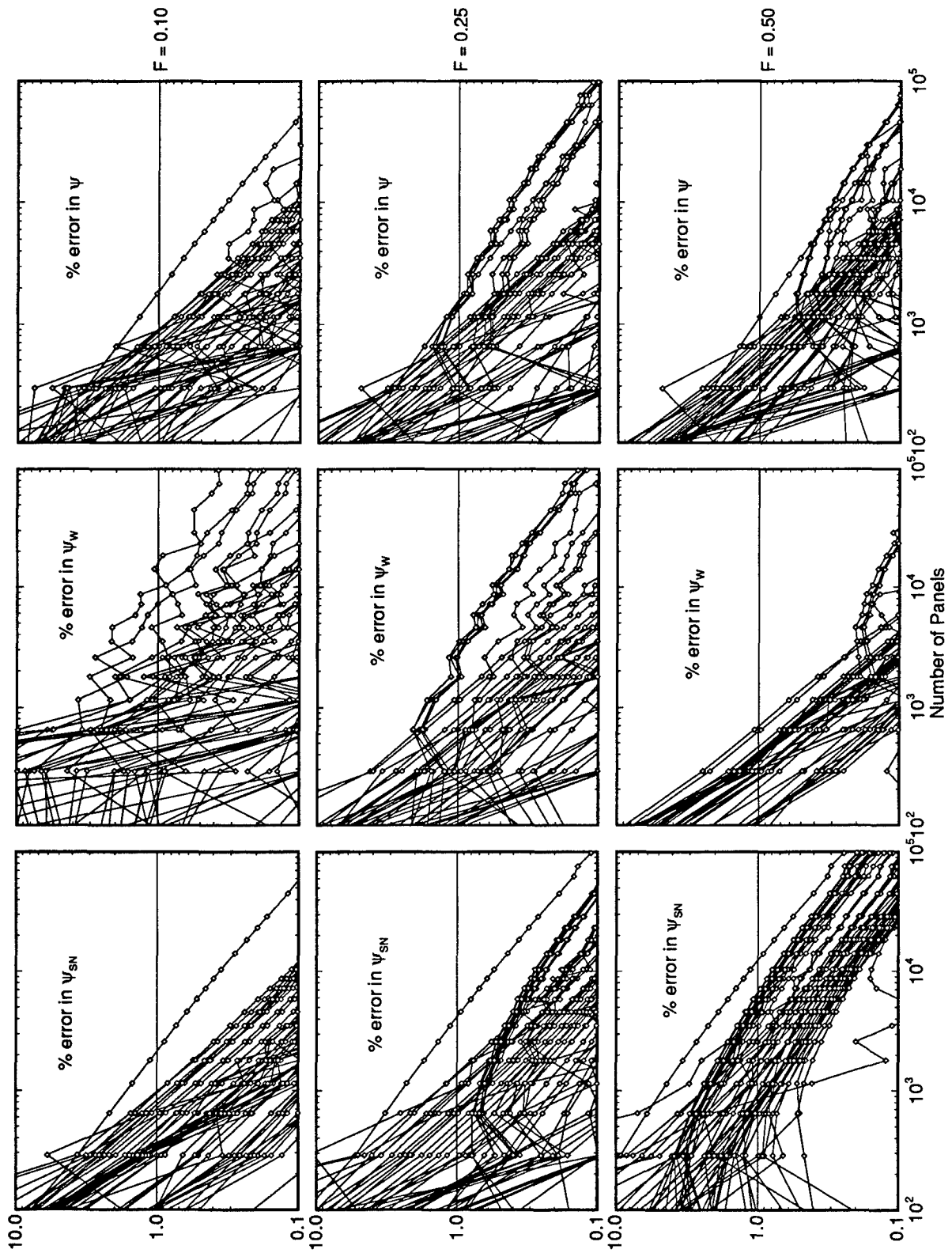
Figure 5: Relative error in nonoscillatory and wave potentials at three Froude numbers.

The right column of Figure 4 shows that approximately 500, 500, and 400 panels are required to compute the total potential

$$\psi \equiv \psi_{SN} + \psi_W$$

within 1% at $F = 0.1$, 0.25, and 0.5, respectively, and that an accuracy of 0.1% requires approximately 6,000, 30,000 and 20,000 panels. The number of panels required for computing the total potential ψ within a specified accuracy is then much less affected by the Froude number than the components ψ_W and ψ_{SN}.

Figure 5 corresponds to the lower part of Figure 3, and depicts the error at each of the 52 calculation points. Considerable variation exists among the 52 curves, although these curves generally follow roughly a similar trend. The largest error in the left column, corresponding to the nonoscillatory potential ψ_{SN}, occurs for the point at the intersection between the stemline and the keel, as was found earlier in Figure 3. For most panel arrangements, the largest errors for the wave potential ψ_W considered in the center column occur at the transom. The right column of Figure 5 shows that 100,000 panels provide 3 digits of accuracy for all the 52 points and the 3 Froude numbers considered. The errors for 10,000 panels are smaller than 0.1% for most points and are no larger than 0.5%.

Figure 4 shows that errors in the calculation of the potentials ψ, ψ_W, and ψ_{SN} decrease roughly in proportion to $1/N$. However, the RMS errors presented in Figure 4 decrease at a slower rate for large values of the panel-number N. This slow-down of the rate of convergence with increasing values of N appears to be more pronounced for larger values of the Froude number, and is also more pronounced in the center column corresponding to the wave potential ψ_W. The variation in the rate of decay of the RMS error may be due to the fact that the errors in Figure 5 decay at the rate $1/N$ at some points and at a slower rate for other calculation points. In particular, errors for most calculation points decay approximately in proportion to $1/N$ in the upper left corner of Figure 5, corresponding to the potential ψ_{SN} at $F = 0.1$, while errors for most calculation points decay approximately in proportion to $1/\sqrt{N}$ in the lower left grid, corresponding to ψ_{SN} at $F = 0.5$.

WAVE PROFILE

The wave profile is now considered. The nondimensional wave elevation for linearized po-

tential flow is given by $E/L = F^2 \partial\psi/\partial x$, where E is the free-surface elevation, L is the ship length, and F is the Froude number based on the ship length.

The velocity component $\partial\psi/\partial x$ along the x-axis can be expressed in terms of the components (ψ^n, ψ^s, ψ^t) of the fluid velocity

$$\nabla\psi = \vec{n}\,\psi^n + \vec{s}\,\psi^s + \vec{t}\,\psi^t$$

along the unit vectors

$$\vec{n} = (n_x, n_y, n_z) \quad \vec{s} = (s_x, s_y, s_z) \quad \vec{t} = (t_x, t_y, t_z)$$

as

$$\partial\psi/\partial x = n_x\,\psi^n + s_x\,\psi^s + t_x\,\psi^t .$$

The vector $\vec{n}$ is normal to the hull. The vectors $\vec{s}$ and $\vec{t}$ are tangent to the hull, and approximately aligned with framelines and waterlines, respectively. At the plane $z = 0$ the vector $\vec{t}$ is tangent to the static waterline (we then have $t_z = 0$). The components (ψ^n, ψ^s, ψ^t) of the velocity vector $\nabla\psi$ can be expressed in terms of the fluid velocities $(\partial\psi/\partial n, \partial\psi/\partial s, \partial\psi/\partial t)$ in the directions of the vectors $(\vec{n}, \vec{s}, \vec{t})$ by means of the relations $\psi^n = \partial\psi/\partial n$ and

$$\psi^s = (\partial\psi/\partial s - \kappa\,\partial\psi/\partial t)/(1-\kappa^2)$$

$$\psi^t = (\partial\psi/\partial t - \kappa\,\partial\psi/\partial s)/(1-\kappa^2)$$

where κ is defined as $\kappa = \vec{s}\cdot\vec{t}$. The normal derivative $\partial\psi/\partial n$ is taken equal to n_x by virtue of the hull boundary condition. The free-surface elevation $F^2\partial\psi/\partial x$ is then determined in terms of the tangential derivatives $\partial\psi/\partial s$ and $\partial\psi/\partial t$.

The free-surface elevation at the waterline is evaluated at the center of every straight waterline segment via numerical differentiation of the velocity potential. Specifically, the derivative $\partial\psi/\partial t$ is determined at the center of a waterline segment using two-point central differencing of the potential at the end-points of the waterline segment. The derivative $\partial\psi/\partial s$ at the center of a waterline segment is taken as the average of the values of the derivative $\partial\psi/\partial s$ at the end-points of the waterline segment. The derivative $\partial\psi/\partial s$ at an end-point of a waterline segment is determined using two-point one-sided differencing of the potential at the end-point of the segment and at the panel-vertex immediately below.

For a given panel distribution, the wave profile is determined using linear interpolation between the values of the free-surface elevation computed at the centers of the waterline segments. Linear extrapolation is used to determine the

wave profile at the bow and the stern. The RMS error in the wave profile is depicted in Figure 6 for three values of the Froude number F equal to 0.1, 0.25, and 0.5. The RMS error in this figure is defined as

$$\sqrt{\int_{-1/2}^{1/2} [\psi_x(N) - \psi_x^{exact}]^2 dx} / \sqrt{\int_{-1/2}^{1/2} (\psi_x^{exact})^2 dx}$$

where $\psi_x \equiv \partial\psi/\partial x$, $\psi_x(N)$ is the wave-elevation obtained using N panels to approximate the hull, and ψ_x^{exact} represents the "exact" wave profile.

A modification of the recipes given in Hendrix and Noblesse (1992) was made for the calculations of the wave profile using a large number of panels. Specifically, the upper limit of integration t_{max} in the wave integral (66) in Hendrix and Noblesse (1992) was increased in order to obtain a smooth wave profile in the immediate vicinity of the bow and stern. The upper limit of integration t_{max} has been multiplied by a factor taken equal to 3.5 for wave-profile calculations performed using 100,000 panels. A smaller multiplicative factor is required for a smaller number of panels.

Figure 6 corresponds to Figure 4 and the upper part of Figure 3, and likewise depicts 5 curves. The four lower curves were determined by taking the "exact" wave profile as that computed using N equal to (approximately) 10,000, 23,000, 45,000, and 100,000 panels. The uppermost curve was obtained via extrapolation of the 4 lower curves, in the manner explained previously in connection with Figure 2.

Figure 6 shows that approximately 7,000, 700, and 800 panels are required to compute the wave profile with a RMS error of 10% for values of F equal to 0.1, 0.25, and 0.5, respectively. It can also be estimated from Figure 6 that a greater accuracy of 3% requires roughly 40,000, 10,000, and 40,000 panels for F equal to 0.1, 0.25, and 0.5, respectively.

LIFT, DRAG, AND MOMENT

The hydrodynamic lift, drag, and trimming moment determined via integration of the pressure at the hull are finally considered. The pressure is taken as the linearized potential-flow approximation $\rho\, \mathcal{U}^2\psi_x$, where ρ is the water density and $\mathcal{U}$ is the speed of the ship. The fluid velocity ψ_x is determined, using the relations given previously for the wave profile, at the centroid of every hull panel and regarded as piecewise constant within the corresponding panel. The derivatives $\partial\psi/\partial s$ and $\partial\psi/\partial t$ for a given panel are evaluated at the centers of the two shortest sides of the panel
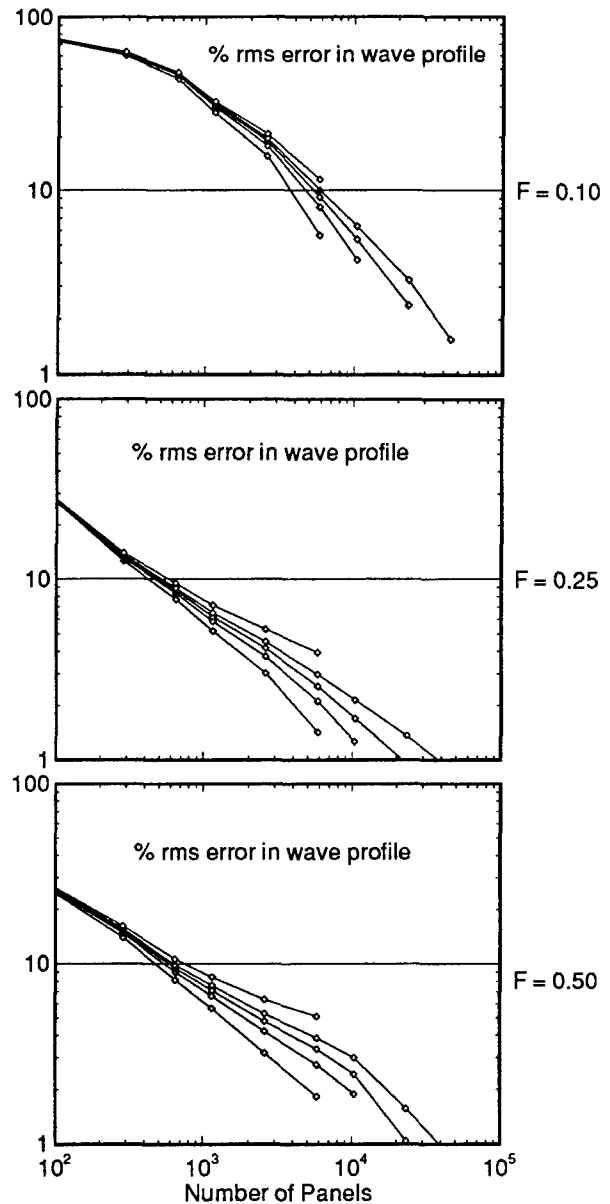
Figure 6: Root-mean-square error in the wave profile at three Froude numbers.

using two-point central differencing of the potential computed at the corresponding vertices of the panel.

The lift, drag, and moment have been computed for 5 values of the Froude number F equal to 0.1, 0.2, 0.25, 0.3, and 0.5. "Exact" values of the lift, drag, and moment are determined by means of extrapolation of the corresponding values computed using 2,592, 5,832, 10,368, and 23,328 panels. The extrapolated "exact" values are obtained using a least-squares fit to the equa-

127
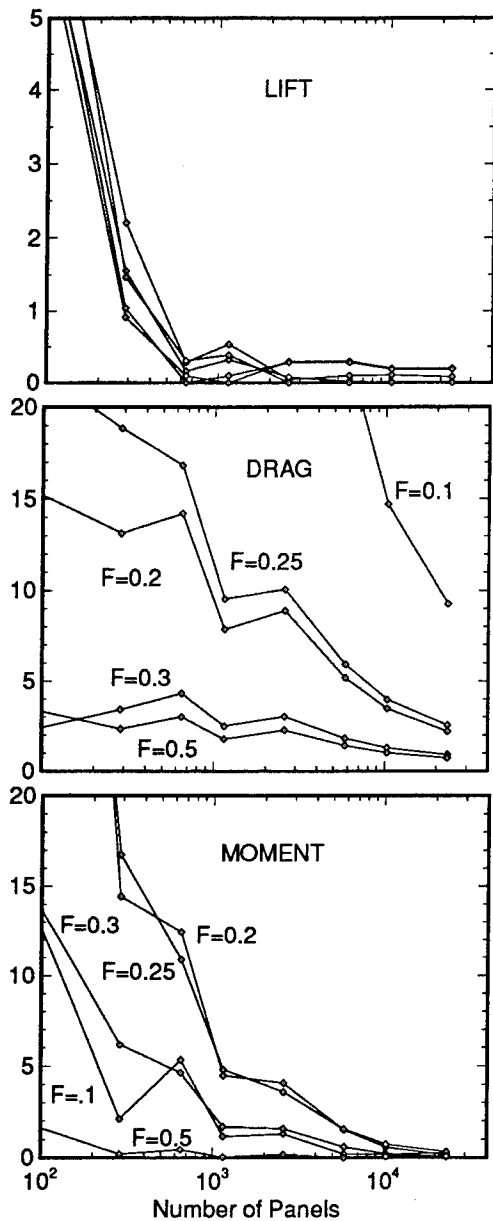
Figure 7: Percent relative error in lift, drag, and moment.

Figure 8: Percent relative error in lift, drag, and moment defined in terms of values at moderate Froude numbers.

tion

$$f = f_{exact} + C_1/\sqrt{N} + C_2/N$$

where the variable f stands for the lift, drag, or moment.

The percent relative error, defined as

$$|\,[\,f(N) - f_{exact}\,]\,/f_{exact}\,|\,,$$

corresponding to the lift, drag, and moment are depicted in the top, center, and bottom grids of

Figure 7. This figure shows considerable variation in the errors corresponding to the drag, and to a lesser extent the moment. These variations in the errors stem largely from the large variations of the drag, and to a lesser extent the moment, with respect to the Froude number. The variation in the errors presented in Figure 7 makes it difficult to draw any conclusion with respect to the number of panels which is required for obtaining

	Froude Number				
	0	0.1	0.25	0.5	∞
Hull area 1%	250 panels				
Hull area 0.1%	2,000				
Potential 1% RMS	500	500	500	400	1,000
Potential 0.1% RMS	6,000	6,000	30,000	20,000	50,000
Wave profile 10% RMS	–	8,000	700	800	–
Wave profile 3% RMS	–	> 40,000	10,000	40,000	–
Lift (rel. to avg.) 1%	–	500			–
Moment (rel. to avg.) 1%	–	8,000			–
Drag (rel. to avg.) 2%	–	20,000			–

Table 2: Number of panels required for computing various characteristics.

a specified accuracy.

Figure 8 depicts the modified relative error

$$| [f(N) - f_{exact}] / \widehat{f}_{exact} | ,$$

where $\widehat{f}_{exact}$ is defined as the average of the values of f_{exact} at the moderate Froude numbers $F = 0.2, 0.25, 0.3$. We thus have

$$\widehat{f}_{exact} = (f_{exact}^{F=0.2} + f_{exact}^{F=0.25} + f_{exact}^{F=0.3})/3 .$$

The large variations in the errors for the wave drag presented in Figure 7 are greatly reduced in Figure 8. This result indicates that although the lift, drag, and moment vary considerably with Froude number the absolute errors in these quantities do not vary appreciably with Froude number.

Figure 8 shows that 500 panels are sufficient to compute the lift within 1%. However, about 8,000 panels are required to compute the moment with the same accuracy, and the wave drag can be computed within about 2% using 20,000 panels.

CONCLUSION

The panel-convergence study presented in the foregoing is summarized in Table 2, which provides guidelines about the number of (flat triangular) panels that is required for predicting various flow characteristics. Table 2 shows that prediction of different flow characteristics, such as the wave drag and the hydrodynamic lift, may require widely-different numbers of panels. For instance, 500 panels are sufficient to compute the lift within 1%, but 20,000 panels are required to predict the drag within 2%.

The results summarized in Table 2 were obtained using the slender-ship approximation, in which the source density is defined explicitly in terms of the hull geometry. A greater number of panels may be required if an integral equation is solved since the variation of the source/doublet density depends on the Froude number as well as the hull geometry, and may therefore vary more rapidly than the x component n_x of the unit normal vector $\vec{n}$ to the hull used in the slender-ship approximation.

The number of panels indicated in Table 2 is in most cases fairly large. Higher-order boundary element methods may therefore offer significant advantages in comparison to constant-panel methods. Table 2 also suggests that conclusions with respect to the benefits of nonlinear, or otherwise more refined, mathematical models could be questionable unless a sufficiently large number of panels is used.

ACKNOWLEDGMENTS

REFERENCES

Doctors, Lawrence, and Beck, Robert, "Numerical Aspects of the Neumann-Kelvin Problem," Journal of Ship Research, Vol. 31, No. 1, March 1987, pp. 1–13.

Hendrix, Dane, and Noblesse, Francis, "Recipes for Computing the Steady Free-Surface Flow Due to a Source Distribution," Journal of Ship Research, Vol. 36, No. 4, Dec. 1992, pp. 346–359.

by Professor Dr. Ing. S. D. Sharma, University of Duisburg

The authors deserve praise for a thorough and systematic study of the computational effort required to attain prescribed error margins for integral quantities of primary interest, e.g., lift, drag, and moment. This is the kind of paper one expects to see at a conference on <u>numerical</u> ship hydrodynamics. I would like to comment on the tremendous discrepancy in the effort required for calculating lift (500 panels for 1% error) and drag (20,000 panels for 2% error). This phenomenon is well known from all previous work, both computational and experimental, and is related to the fact that pressure drag on a ship arises from the small difference between large contributions of opposite sign from the bow and the stern. An efficient determination of pressure drag would require a uniform distribution of panels in the body plan rather than on the hull surface as seems to be the case in authors' Figure 1. (Previous workers have even obtained a negative pressure drag as a consequence of an improper distribution of panels!) A possible solution to this problem may be to use Lagally's theorem rather than pressure integration for computing drag. Since all necessary source strengths and perturbation velocities are already generated by the authors' algorithm, this should be easily feasible. Would the authors care to give it a try?

<u>Author's Reply</u>

We thank Professor Sharma for his encouraging words on our efforts to quantify some of the numerical errors associated with free-surface flow calculations. We agree that it has long been recognized that wave-drag calculations by pressure integration are much more demanding than calculations of lift and moment. The magnitude of the errors associated with the prediction of wave drag using pressure integration however is not always fully appreciated. As we already noted in reply to Professor Landweber's comments, the primary aim of our study is to investigate panel convergence for conditions representing typical computational methods. Prediction of wave drag by pressure integration is commonly used, notably in Rankine source methods. Thus, pressure integration is also used in our study to estimate the corresponding errors (and for consistency with lift and moment calculations). As is

emphasized by Professor Sharma, it is found that a very large number of panels must be used to obtain minimally-acceptable accuracy in wave drag by pressure integration (even though we use smaller panels near the bow and stern). Two conclusions can be drawn from this finding. One conclusion is that validation of numerical methods based on favorable comparisons between experimental data and wave-drag predictions obtained using pressure integration are in many instances questionable. Conclusions about the benefits of nonlinear, or otherwise refined, mathematical models can also be questioned, as is noted in our paper.

The other conclusion is that pressure integration is not a satisfactory method for practical wave drag calculations, and we certainly do not advocate using this method. The method based on Lagally's theorem mentioned by Professor Sharma is an alternative approach which can be expected to provide better accuracy. This method could probably be implemented fairly easily as Professor Sharma suggests, but has not been tried. Another alternative approach is the Havelock formula based on energy-flux integration. This well-known formula, made popular by the classical paper of Eggers, Sharma, and Ward (1967, *Trans.* SNAME, pp. 112-144), appears to offer the most general practical way of calculating wave drag. That this formula offers a means of determining wave drag more accurately than pressure integration is demonstrated by the "zeroeth-order" slender-ship approximation for the wave drag given in Noblesse (1983) *J. Ship Research*, pp. 13-33. In this formula the velocity potential of the flow due to the ship is simply taken equal to zero, which yields zero drag by pressure integration (a result that is better than negative drag). Nevertheless, this crudest possible approximation of the near-field flow provides a reasonable approximation to the wave drag using the Havelock formula.

by Dr. Henry T. Wang, Naval Research Laboratory

I am particularly interested in the reasons for the differences in the convergence behavior of slender ship, zero Froude number, and infinite Froude number theories. Each has been used as the starting, or basic, flow in calculating the

potential flow around surface ships. Thus, each of these flows is of special interest in its own right. Did you study the detailed variation of the potential or source strength on the hull to determine the reasons for the differences in accuracy?

Author's Reply

As Dr. Wang observes, Figure 3 in the paper shows that there are significant differences between the errors corresponding to the "zero" and "infinite" Froude-number limits, and that the errors shown in Figures 4 and 5 for free-surface flows vary between these two limiting cases. The source density in these calculations is in all cases taken equal to n_x which corresponds to the slender-ship approximation. The behavior of the near-field and wave components of the velocity potential at the hull surface is significantly different. There are also significant differences in the behavior of the near-field component of the free-surface potential and its zero and infinite Froude-number limits, notable at the waterline. These differences stem from the differences in the Green functions for these cases. In particular, the Green functions for the zero and infinite Froude-number limits, given by a source and a free-surface image source or sink, result in large differences in the behavior of the corresponding potentials near the waterline. A study of the variation of these potentials at the hull surface will be presented elsewhere.

DISCUSSION
by Professor Emeritus Louis Landweber, The University of Iowa

I suggested that convergence might have been obtained with fewer panels if the authors had introduced a correction for the curvatures of the hull. This was illustrated for the case of a sphere immersed in a uniform stream. It was found, using N flat rectangular panels, that the error varied inversely as $\sqrt{N}$. This was presented at a symposium in honor of Ted Wu and published by World Scientific Publishing Company in 1990 on pages 415-428 of a book entitled Engineering Science, Fluid Dynamics. The title of the paper is "Properties of the Neumann Kernel and Interior Irrotational Flow for a Nearly Closed Surface," a copy of which is being sent to the authors.

Author's Reply

The primary aim of our study is to investigate panel convergence for conditions representing typical computational methods. Flat panels are most commonly employed in current calculation methods and therefore are also used in our study. A main finding of this study is that convergence for flat panels is quite slow, as was also shown by Professor Landweber, and that a very large number of panels is required for accurate calculations. We agree with Professor Landweber that a correction for curvature, or the use of a higher order boundary-element method, would significantly reduce the required number of panels and represents a desirable improvement over existing constant-panel methods, as is noted in our conclusion.

A Higher-Order Panel Method Based on B-Splines

C.Y. Hsin, J.E. Kerwin, and J.N. Newman
(Massachusetts Institute of Technology, USA)

Abstract

A two-dimensional higher order panel method using B-splines has been developed, and the results of this method show that it is not only accurate, but also robust and efficient. In this method, both the panel geometry and singularity distributions are defined by B-splines, and Green's theorem is then applied at selected collocation points. The integrals of the influence functions are expressed in terms of polynomials of a parametric coordinate, and calculated analytically. Both the collocation method and the Galerkin method are presented to solve the system of equations.

Nomenclature

L	number of panels; number of intervals between knots
K	order of polynomials
N_v	number of B-spline vertices
N_c	number of collocation points on each panel
N	degree of polynomials, $N = K - 1$
M	maximum number of degrees of the polynomials expansions
$\vec{U}_\infty$	inflow velocity
x, y	coordinates of the geometry
z	$= x + iy$
ϕ	velocity potential
x_v, y_v	B-spline control polygon vertices of the geometry
ϕ_v	B-spline control polygon vertices of the potential
$\mathcal{N}^K$	B-spline basis function of order K
ψ_n, ϕ_n	n^{th} degree influence functions of the source and dipole distributions.

1 Introduction

Panel methods have been used for aerodynamics, solid mechanics and hydrodynamics applications for decades. The principal reason for developing higher-order panel methods is to increase accuracy. However, the efficiency and robustness of higher-order methods is still debatable. In this paper, a two-dimensional higher order panel method using B-splines is presented. The results of this method show that it is not only accurate, but also robust and efficient.

The reasons for developing a higher-order panel method based on B-splines are: First, geometries can be directly passed to and from standard CAD/CAM systems, since geometries in these systems are commonly defined by B-splines. Secondly, the orders of panel geometries and singularity distributions can be arbitrary — not limited to linear, quadratic, or cubic. Also, the derivatives of the potential on the body can be directly calculated without using a numerical differencing scheme. Finally, because B-splines are naturally continuous, there is no need to impose continuity conditions at the panel boundaries.

Okan and Umpleby [6] have developed a B-spline based panel method, with similar objectives to the present work. The solution is based on the source formulation, with the velocity potential represented by a distribution of sources of unknown strength on the body surface. No details are given regarding the numerical analysis, and it is not clear how the influence functions are evaluated. The principal test computations, for the pressure distributions on two NACA foils, show significant errors near the trailing edge.

In the present work, both the panel geometry and singularity distributions are defined by B-splines, and Green's theorem is then applied. The

integrals of the influence functions are expressed in terms of polynomials of a parametric coordinate, and the polynomial coefficients are derived from the B-spline basis function. Source and normal dipole influence functions are calculated analytically so that their evaluation is both accurate and efficient.

We first present a collocation method, in which an overdetermined linear system is solved by least squares for the unknown potentials. A Galerkin method is then presented which uses the B-spline basis functions as the test functions. This method results in a square linear system for the unknown potentials. The unknowns in both methods are the polygon vertices of the B-splines representing the perturbation potentials, not the perturbation potentials themselves. The perturbation potentials and their derivatives can then be obtained from the resulting B-spline.

Two examples of uniform flow past a body have been selected to demonstrate the accuracy and efficiency of this method. The first is that of a square body section, intended to test the applicability to bodies with sharp corners, as are common with some offshore platforms. The second example is the flow past a Karman-Treftz foil, at an angle of attack, intended to test the method for use in lifting problems. In both cases comparisons are made with exact analytic results, to determine the accuracy of the numerical solutions. For a given accuracy, the computational time and storage requirements of the present method are far less than for a low order panel method.

2 B-Spline Basics

In order to show how B-splines can be applied to the solution of two-dimensional potential flow problems, we must first introduce the essential elements of B-spline curves. Rather than presenting the theory of B-splines in its most complete and general form, we will take a very simplistic approach here, and introduce only those bare essentials needed for our present purpose. More complete accounts can be found in recent texts such as [7].

Consider a two-dimensional curve expressed in parametric form

$$
\begin{aligned}
x &= x(t) \\
y &= y(t)
\end{aligned}
\tag{1}
$$

where t is a parameter which is a monotonically increasing function of arc length along the curve,
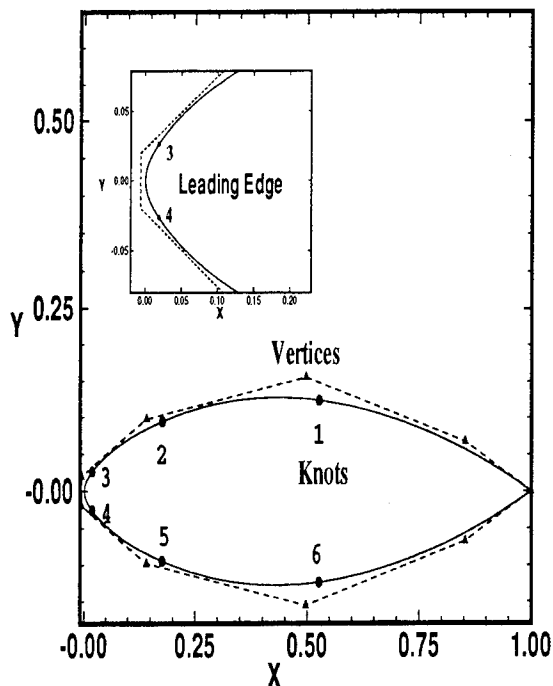
Figure 1: Notation for B-spline representation of a two-dimensional curve

starting with a value of zero at one end and ending with a value t_{max}. The curve will be required to be continuously differentiable except at a set of $L-1$ discrete values of t which are designated as *knots*. In the present application, the maximum value of t will be L and the knots will be located at integral values of t,

$$
t = 1, 2, 3, \ldots, L - 1
\tag{2}
$$

The number of intervals between knots will therefore be L. This notation is illustrated in figure 1.

Within each interval between knots, the curve $x(t), y(t)$ will be represented as a weighted sum of N_v polynomials of order K, (degree $N = K - 1$).

$$
\begin{aligned}
x(t) &= \sum_{i=1}^{N_v} x_{v,i} \mathcal{N}_i^K(t) \\
y(t) &= \sum_{i=1}^{N_v} y_{v,i} \mathcal{N}_i^K(t)
\end{aligned}
\tag{3}
$$

where $x_{v,i}, y_{v,i}$ are the $i'th$ weights, and $\mathcal{N}_i^K$ is a polynomial basis function of degree $K - 1$ associated with that weight.

B-spline curves, by definition, are generated by a particular set of basis functions. In their

134

most general form, the B-spline basis functions are rational functions of the parameter t, and the resulting curves are termed *rational B-spline curves*. In the special case when the denominators of the basis functions are constants, the basis functions become polynomials and the resulting curves are termed *integral B-spline curves*. In the present application, we will consider only polynomial basis functions.

While the basis functions in each interval between knots will always be required to be polynomials of the same degree, they will not generally be the same polynomials. Hence, the resulting curve will be a piecewise polynomial of specified degree in the parameter t. The degree of continuity of the basis functions at each knot boundary may be readily specified. Most frequently, one wishes the smoothest possible curve, in which case the basis functions of degree $K - 1$ can be specified to have $K - 2$ continuous derivatives at each knot. A B-spline curve with uniformly spaced knots, and with $K - 2$ continuous derivatives at each knot is termed a uniform B-spline curve.

On the other hand, for shapes with sharp corners, as will be presented later in this paper, basis functions with discontinuous first derivatives at specified points can be generated. These can be generated by specifying that two or more knots have the same parameter value, t. Each additional knot at the same value of t reduces the number of continuous derivatives there by one. In that case, the knot spacing is no longer uniform, and the resulting curves are called *non-uniform B-splines*.

Finally, B-spline curves may either be closed and continuous, or open. The former are identified as *periodic B-splines* while the latter are *open B-splines*. Open B-splines can still form closed curves, as in the example shown in figure 1, but they are logically open in the sense that no conditions of continuity are imposed at the point of closure.

A recursive formula for generating B-spline basis functions of any order and degree of continuity was developed by Cox and de Boor, and may be found in [7]. Figure 2 shows a set of *open, uniform, integral B-spline basis functions* of order $K = 4$. In this example, $L = 7$ and $N_v = 10$. For a given choice of K and L, N_v is not arbitrary, but must have the unique value

$$N_v = K + L - 1 \qquad (4)$$

in order that all of the required conditions im-

Parameter t
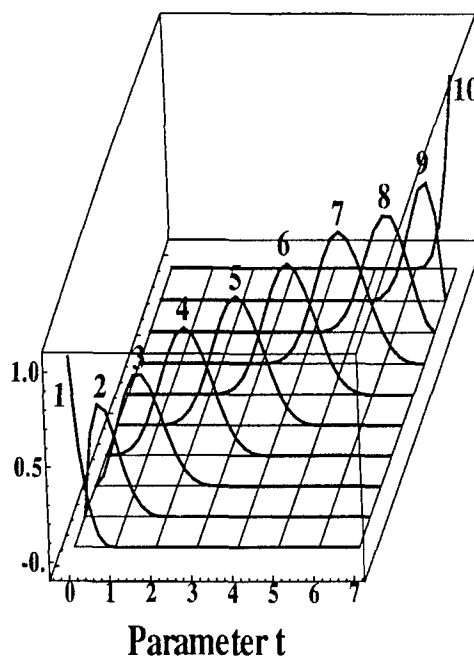
Figure 2: Basis functions for an open, uniform, integral B-spline curve with $K = 4$, $L = 7$, $N_v = 10$.

posed on the basis functions be met.

A major reason for the popularity of B-splines for CAD applications may be found in the geometric interpretation of the weights, x_v, y_v. If one connects the weights with straight lines, one generates a polygon which can be seen, in a sense, to approximate the resulting B-spline curve, as shown in figure 1. This is in contrast to most polynomial representations of curves, where the order of magnitude of the coefficients may vary widely and where the effect of changing one or more of the coefficients is far from intuitive.

In view of this geometrical interpretation, the term *weights* will be replaced by *control polygon vertices*, or simply *vertices*. These are sometimes referred to in the literature as *control points*, but this terminology will be avoided here since this term is commonly used to designate points on a body where boundary conditions of the hydrodynamic problem are to be satisfied.

While we started the discussion of B-spline curves by introducing the concept of knots, in most cases one generates a curve by selecting a set of vertices. In this case, equation (3) can be used to evaluate the curve. The position of the knots therefore follows by setting the parameter t to $0, 1, \ldots, L$. One can, in principle, start by specifying a set of knot coordinates at which point

equation (3) becomes a set of linear equations which can be readily solved for the vertex positions. However, the relationship between knot positions and the shape of the curve between knots is not intuitive, and great care must be taken in following this approach.

In any event, once one has selected the order of the B-spline, the degree of continuity at the knots and the vertex positions, all quantities on the right hand side of equation (3) are known. One can therefore carry out the summation and represent the curve in the $I'th$ interval between knots as a single polynomial of degree $K - 1$,

$$x(t) = \sum_{k=0}^{K-1} x_{I,k} t^k$$

$$y(t) = \sum_{k=0}^{K-1} y_{I,k} t^k \tag{5}$$

where $x_{I,k}, y_{I,k}$ are constants generated by carrying out the summation in equation (3). When expressed in the form of equation (5), auxiliary geometric properties such as arc length and unit normal vectors may be readily determined. The fact that the curve was originally generated by B-spline basis functions is immaterial at this stage.

3 B-splines and Surface Potential Distributions

So far we have only discussed geometry. Our real objective, of course, is to solve for the potential flow around arbitrary two-dimensional bodies. This can be reduced to the problem of finding the distribution of velocity potential, $\phi(s)$ along the surface of the body. With the widespread use of potential based panel methods for both two and three dimensional flow problems, it is well known that the potential at a point on the body surface can be expressed in the form of integrals of source and dipole distributions over the body surface.

This approach will be followed in the present paper. However, instead of solving directly for the potential at a discrete set of points on the body, the potential is represented in the same form as the geometry itself. Hence, equation (1) becomes

$$x = x(t)$$

$$y = y(t) \tag{6}$$
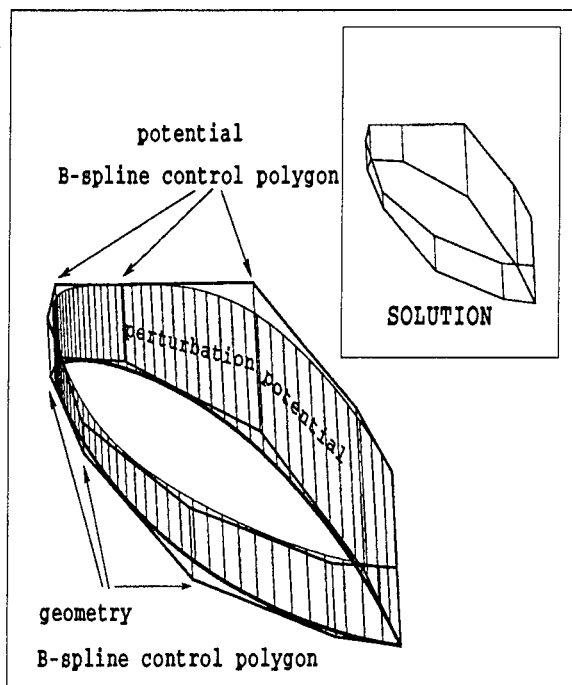
Figure 3: B-spline representation of a two-dimensional foil, together with the potential distribution over its surface.

$$\phi = \phi(t)$$

and equation (3) becomes

$$x(t) = \sum_{i=1}^{N} x_{v,i} N_i^K(t)$$

$$y(t) = \sum_{i=1}^{N} y_{v,i} N_i^K(t) \tag{7}$$

$$\phi(t) = \sum_{i=1}^{N} \phi_{v,i} N_i^K(t)$$

The unknowns in the hydrodynamic problem are therefore the values of the *potential vertices*, $\phi_{v,i}$, which are not potentials in the physical sense. However, a given set of potential vertices, together with the appropriate B-spline basis functions, generates a continuous distribution of the physical velocity potential along the surface of the body. Discontinuities in higher derivatives of the potential will occur at the knots, in the same way as for the geometry. However, so long as at least first derivative continuity is maintained, the surface derivative of the potential, and hence velocity, is defined at all points on the body. This representation of the geometry and surface potential is shown in figure 3.

136

4 Discretized Green's Formula

The common basis of all panel methods is Green's theorem [4]. For a two dimensional problem, the potential based formulation can be derived from the Green's theorem as follows:

$$
\begin{aligned}
-\pi\phi_p \;=\; & \int_{l_B} [\phi_q \frac{\partial}{\partial n_q} \ln r_{p,q} - \frac{\partial \phi_q}{\partial n_q} \ln r_{p,q}] dl \\
& + \int_{l_W} \Delta\phi \frac{\partial}{\partial n} \ln r \, dl \qquad (8)
\end{aligned}
$$

where l_B is the boundary of the body, and l_W is the wake surface of a lifting body. ϕ is the perturbation potential, and $r_{p,q}$ is the distance between point p and point q. In applications with Neumann boundary condition, the normal derivative of ϕ is specified on l_B, for example in the form,

$$
\frac{\partial \phi_q}{\partial n_q} \;=\; -\vec{n}_q \cdot \vec{U}_\infty \qquad (9)
$$

for streaming flow with velocity $\vec{U}_\infty$ past a fixed body.

The discretized form of equation (8) can then be expressed as

$$
\begin{aligned}
\sum_{j=1}^{j=L} & \int_{l_B} \phi_j(t) \frac{\partial}{\partial n_j} \ln r_{i,j} + \int_{l_W} \Delta\phi \frac{\partial}{\partial n} \ln r \, dl \\
& = \sum_{j=1}^{j=L} \frac{\partial \phi_j}{\partial n_j} \ln r_{i,j} dl \qquad (10)
\end{aligned}
$$

where i and j are the discretized panel indices, and L is the total number of panels.

Our purpose is to define both the geometry, l_B, and the singularity strengths, ϕ, $\frac{\partial \phi}{\partial n}$, by B-splines. We already described the way to define the geometry by B-splines in the last section, and we are going to describe the way to define singularity strengths by using the B-splines.

In equations (8), (9) and (10), the term $\frac{\partial}{\partial n} \ln r$ is the expression of the influence function of a two-dimensional dipole, and the term $\ln r$ is the expression of the influence function of a two-dimensional source (or, Green's function). Therefore, $\frac{\partial \phi}{\partial n}$ in the Neumann boundary condition (equation (9)), can be thought of as the source strength, and the unknown perturbation potentials, ϕ, can be thought of as the dipole moment. In equation (9), the normal vector $\vec{n}$ can be written as

$$
\vec{n} = \left(-\frac{dy}{dt} \Big/ \frac{dl}{dt}, \ \frac{dx}{dt} \Big/ \frac{dl}{dt} \right) \qquad (11)
$$

where l is the arc length of the curve. Since we have expressed x and y as polynomials in the local parameter t, the normal vector can be also written as a polynomial of t by taking the derivatives of x and y (equation (5)). For panel j, the normal vectors can be expressed as follows:

$$
\vec{n}_j(t) = \sum_{k=0}^{M} \vec{n}_{j,k} t^k \qquad (12)
$$

The source strength, σ, is specified by the boundary condition that $\sigma = -\vec{n} \cdot \vec{U}_\infty$. Thus, the source strength on panel j, σ_j, can be written as

$$
\sigma_j(t) = \sum_{k=0}^{M} \sigma_{j,k} t^k \qquad (13)
$$

where $\sigma_{j,k}$ is the B-spline coefficient of the source strength. M is the maximum degree of the polynomial expansions, which will be discussed in the next section. Similarly, the unknown perturbation potential strength, ϕ, on panel j can be written as

$$
\phi_j(t) = \sum_{k=0}^{n} \phi_{j,k} t^k \qquad (14)
$$

By inserting the equations (13) and (14) into equation (10), we have the following discretized formula:

$$
\begin{aligned}
& \sum_{j=1}^{L} \sum_{k=0}^{n} \phi_{j,k} \int_{l_B(j)} t^k \frac{\partial}{\partial n_j} \ln r_{i,j} dl \\
& + \int_{l_W} \Delta\phi \frac{\partial}{\partial n} \ln r \, dl \\
& = \sum_{j=1}^{L} \sum_{k=0}^{n} \sigma_{j,k} \int_{l_B(j)} t^k \ln r_{i,j} dl \qquad (15)
\end{aligned}
$$

The source strength B-spline coefficients, $\sigma_{j,k}$, are known from the boundary condition, and the dipole moments are unknowns to be solved. These B-spline coefficients are functions of the B-spline polygon vertices. Therefore, the unknowns can be reduced to the B-spline polygon vertices defining the dipole moment instead of the B-spline coefficients. The terms $\int t^k \frac{\partial}{\partial n} \ln r \, dl$ and

137

$\int t^k \ln r\, dl$ are the moments of the influence functions, and their evaluations are described in the next section.

5 Calculations of the influence functions

5.1 Introduction

Both the panel geometry and the basis functions for the singularity distributions are defined by polynomials of the general form

$$f(t) = \sum_{n=0}^{N} f_n t^n \qquad (16)$$

where the parametric coordinate t is in the range $t_1 \leq t \leq t_2$. As t varies in this range, the coordinates of the panel are generated in the complex plane $z = x + iy$, in accordance with the representation

$$z(t) = \sum_{n=0}^{M} z_n t^n \qquad (17)$$

The end points of the panel are defined by the coordinates $Z_1 = z(t_1)$ and $Z_2 = z(t_2)$.

The required influence functions are defined in the forms

$$\begin{aligned}
\psi_n &= \int_{Z_1}^{Z_2} t^n \log(z - w) d\ell \\
&= \int_{t_1}^{t_2} t^n \log(z(t) - w) \frac{d\ell}{dt} dt \qquad (18)
\end{aligned}$$

for the source distribution, and

$$\phi_n = \int_{Z_1}^{Z_2} t^n \frac{\partial}{\partial n} \log(z - w) d\ell \qquad (19)$$

for the normal dipole distribution. In both integrals the field point w is arbitrary, with special provisions in the limiting case where it is on the panel. Only the real parts of (18)-(19) are required in applications. The normal derivative in (19) is defined with respect to the source coordinate z along the panel contour.

By assumption the range (t_1, t_2) is sufficiently small that the polynomials are accurate to some useful tolerance. To be as general as possible M will be unrestricted here, and recursion formulae will be used to permit the results to be derived for arbitrary values of M. It will turn out that higher-order polynomials of degree $N > M$

are required in the intermediate analysis to follow, to give controlled accuracy of the influence functions. Thus two independent parameters M and N are retained in (16)-(17), with the understanding that M corresponds to the specified geometrical representation, and N corresponds to the series expansions which are required for the analysis. The maximum degree n of the integrals (18)-(19) is expected to be between M (or possibly $M - 1$), and N, and is not restricted in the analysis.

Two distinct regimes are dealt with in the following analysis. Most straightforward is the regime where the field point w is sufficiently far from the panel so that multipole expansions can be utilized. These are equivalent to expansions of (18)-(19) in descending negative powers of w, with coefficients which depend on the panel geometry and can be pre-evaluated. (The source integral (18) must also include one term proportional to the logarithm of w.) Numerical experiments indicate that these multipole expansions are effective outside a circle, centered on the mid-point of the panel, with a radius on the order of 1.5 times the length of the panel. Thus for a succession of panels of approximately equal length, along a slowly varying arc, with collocation points in the interior of each panel, the only evaluations where the multipole expansion is not effective are for the panel itself and its two contiguous neighbors.

For the contiguous neighbors, and more generally for any field point which is not on the panel, the same multipole expansions can be used provided the panel is sub-divided into a set of sub-panels, with the maximum length of each sub-panel chosen to satisfy the minimum radius requirement above, i.e. its length is less than or equal to two-thirds of the distance from its center to the field point. In this manner the utility of the multipole expansions is extended to apply in all cases except that where the field point is on the panel itself.

A separate analysis is required when the field point is on the panel. In this case it is possible to use the same polynomial representation (17) for both the source and field points, and to write the difference $(z - w)$ as a polynomial with a prescribed zero, say at the point $t = t_0$, which can be factored and treated analytically. The remaining factor is non-zero on the panel, and thus its logarithm or inverse can be expanded in polynomials. This leads to the desired relations for the special case where the field point is on the panel,

and complements the multipole expansions.

The analysis is based on a sequence of recursion formulae which are outlined in the following section.

5.2 Recursion Formulae

Given a truncated series of the form (16), the square of this series can be expanded in the form

$$f^2 \simeq \sum_{n=0}^{N} f_n^{(2)} t^n \qquad (20)$$

where

$$f_n^{(2)} = \sum_{\nu=0}^{n} f_\nu f_{n-\nu} \qquad (21)$$

More generally, for any integer power m,

$$f^m \simeq \sum_{n=0}^{N} f_n^{(m)} t^n \qquad (22)$$

where

$$f_n^{(m)} = \sum_{\nu=0}^{n} f_\nu^{(1)} f_{n-\nu}^{(m-1)} \qquad (23)$$

and $f_\nu^{(1)} \equiv f_\nu$.

In the derivations of the multipole expansions (22)-(23) will be used to evaluate higher powers of the polynomial

$$z - z_0 = \sum_{n=1}^{N} z_n t^n \qquad (24)$$

in the form

$$(z - z_0)^m \simeq \sum_{n=m}^{N} z_n^{(m)} t^n \qquad (25)$$

where, from (23),

$$z_n^{(m)} = \sum_{\nu=1}^{n-m+1} z_\nu^{(1)} z_{n-\nu}^{(m-1)} \qquad (26)$$

The coefficients $z_n^{(m)}$ are non-zero only within the triangular matrix $(m \leq n)$.

If $m = 0$, (22) remains valid with the convention that $f_n^{(0)} = \delta_{n0}$. (Here the Kroenecker delta function is defined such that $\delta_{nn} = 1$ and $\delta_{mn} = 0$ if $m \neq n$.)

Equation (23) can be used with $m = 0$ to find the coefficients $f_n^{(-1)}$ for the inverse $1/f$ of the original polynomial (16). The required coefficients are found recursively, from the first term in the sum of (23):

$$f_0^{(-1)} = 1/f_0 \qquad (27)$$

$$f_n^{(-1)} = \left(\sum_{\nu=1}^{n} f_\nu^{(1)} f_{n-\nu}^{(-1)} \right) / f_0 \qquad (28)$$

The square-root of a truncated series can be expanded in a similar form, using (21) to find the coefficients f_n from given values of $f_n^{(2)}$. Thus if the given series is of the form (20), successive coefficients of its square-root (16) can be found from the relations

$$f_0 = \sqrt{f_0^{(2)}} \qquad (29)$$

$$f_n = \left(f_n^{(2)} - \sum_{\nu=1}^{n-1} f_\nu f_{n-\nu} \right) / (2f_0) \qquad (30)$$

5.3 The Source Integral

The objective is to evaluate the real part of the integral

$$\begin{aligned} \psi_n &= \int_{Z_1}^{Z_2} t^n \log(z - w) d\ell \\ &= \int_{t_1}^{t_2} t^n \log(z(t) - w) \frac{d\ell}{dt} dt \qquad (31) \end{aligned}$$

Here $d\ell$ is the differential element of arc length along the contour:

$$d\ell = \sqrt{(dx)^2 + (dy)^2} \qquad (32)$$

Thus

$$d\ell/dt = \sqrt{(dx/dt)^2 + (dy/dt)^2} \simeq \sum_{n=0}^{N} d_n t^n \qquad (33)$$

The separate derivatives dx/dt, dy/dt are obtained directly from (17). The sum of their squares is then given in the form

$$(dx/dt)^2 + (dy/dt)^2 \simeq \sum_{n=0}^{N} s_n t^n \qquad (34)$$

where

$$\begin{aligned} s_n &= \sum_{\nu} (\nu+1)(n-\nu+1) \\ &\quad \cdot (x_{\nu+1} x_{n-\nu+1} + y_{\nu+1} y_{n-\nu+1}) \qquad (35) \end{aligned}$$

$$(n = 0, 1, 2, ..., 2M - 2)$$

The only non-zero terms in (35) are in the range $\max(0, n-2) \leq \nu \leq \min(2, n)$.

139

Forming the square-root of (34) as indicated in (29)-(30), the coefficients of (33) are given by

$$d_0 = \sqrt{x_1^2 + y_1^2} \qquad (36)$$

$$d_n = \left(s_n - \sum_{\nu=1}^{n-1} d_\nu d_{n-\nu}\right)/2d_0$$
$$(n = 1, 2, ..., N) \qquad (37)$$

Thus the source integral (18) is transformed in the form

$$\psi_n = \sum_{m=0}^{N} d_m \int_{t_1}^{t_2} t^{m+n} \log(z - w) dt \qquad (38)$$

5.4 The Dipole Integral

Next consider the normal-dipole integrals (19). The normal derivative can be written as

$$\mathbf{n_Z} \cdot \nabla_z = -\mathbf{n_Z} \cdot \nabla_w = -(n_x + in_y)\frac{\partial}{\partial w} \qquad (39)$$

where the normal vector has been defined in equation (11), and

$$n_x + in_y = i\frac{dz}{dt} / \left|\frac{dz}{dt}\right| = i\frac{dz}{dt} / \frac{d\ell}{dt} \qquad (40)$$

From these relations it follows that the dipole integral can be evaluated in the form

$$\phi_n = -i\frac{\partial}{\partial w} \int_{t_1}^{t_2} t^m \log(z - w) dz$$
$$= -i\frac{\partial}{\partial w} \int_{t_1}^{t_2} t^n \log(z - w)\frac{dz}{dt} dt$$
$$= -i\sum_{m=0}^{M-1} (m+1)z_{m+1}$$
$$\frac{\partial}{\partial w} \int_{t_1}^{t_2} t^{m+n} \log(z - w) dt \qquad (41)$$

5.5 Multipole expansions

For sufficiently large values of $|w - z_0|$ the logarithmic function in (38) and (41) can be expanded in Taylor series, about the point $z = z_0$, and integrated term-by-term:

$$\int_{t_1}^{t_2} t^\mu \log(z - w) dt$$

$$= \log(z_0 - w) \int_{t_1}^{t_2} t^\mu dt$$
$$- \sum_{k=1}^{\infty} \frac{1}{k}(w - z_0)^{-k} \int_{t_1}^{t_2} t^\mu (z - z_0)^k dt \qquad (42)$$

Using (25),

$$\int_{t_1}^{t_2} t^\mu \log(z - w) dt$$

$$= \log(z_0 - w) \int_{t_1}^{t_2} t^\mu dt$$
$$- \sum_{k=1}^{\infty} \frac{1}{k}(w - z_0)^{-k} \sum_{\nu=k}^{N} z_\nu^{(k)} \int_{t_1}^{t_2} t^{\mu+\nu} dt \qquad (43)$$

The integrals which remain in (43) are elementary:

$$I_\mu = \int_{t_1}^{t_2} t^\mu dt = \frac{1}{\mu+1}\left(t_2^{\mu+1} - t_1^{\mu+1}\right) \qquad (44)$$

With this definition (43) can be evaluated in the form

$$\int_{t_1}^{t_2} t^\mu \log(z - w) dt$$
$$= \log(z_0 - w) I_\mu$$
$$- \sum_{k=1}^{\infty} \frac{1}{k}(w - z_0)^{-k} \sum_{\nu=k}^{N} z_\nu^{(k)} I_{\mu+\nu} \qquad (45)$$

To simplify these evaluations, define the following coefficients

$$\delta_n = \sum_{m=0}^{N} d_m I_{m+n} \qquad (n = 0, 1, 2, ...) \qquad (46)$$

$$\zeta_n = \sum_{m=0}^{M-1} z_{m+1}(m+1) I_{m+n-1}$$
$$(n = 1, 2, ...) \qquad (47)$$

$$a_k^{(n)} = \frac{1}{k}\sum_{\nu=k}^{N} z_\nu^{(k)} \delta_{n+\nu} \qquad (48)$$

$$b_k^{(n)} = -i\sum_{\nu=k}^{N} z_\nu^{(k)} \zeta_{n+\nu+1} \qquad (49)$$

Interchanging the order of summation in (43) and truncating the Taylor series, it follows that

140

$$\psi_n = \log(z_0 - w)\delta_n - \sum_{k=1}^{N} a_k^{(n)}(w - z_0)^{-k} \quad (50)$$

$$\phi_n = -i(w - z_0)^{-1}\zeta_{n+1}$$
$$- i\sum_{k=1}^{N} b_k^{(n)}(w - z_0)^{-k-1} \quad (51)$$

The coefficients (48 - 49), which depend only on the geometric properties of each panel, can be pre-evaluated and stored for subsequent use. Thus the evaluation of equations (50-51) for multiple field points can be affected with relatively small computational cost.

When the field point is too close to the panel for the direct use of these expansions, sub-division is necessary. The limits (t_1, t_2) of each sub-divided panel are within the domain of the original panel, and the only change required is to evaluate the Taylor expansion about a shifted reference $\tilde{z}_0$, situated at an arbitrary point in the panel. There are various ways to make this generalization using the binomial theorem. The following appears to be relatively robust.

With the definition $\tilde{z}_0 = z(t_0)$ of the parametric point t_0 corresponding to the shifted origin, shifted coefficients $\tilde{z}_n^{(m)}$ are defined for the expansion of $(z - \tilde{z}_0)^m$ in powers of the shifted parameter $\tilde{t} = t - t_0$. Equations (42 - 43) then can be replaced by

$$\int_{t_1}^{t_2} t^\mu \log(z - w)dt$$
$$= \log(\tilde{z}_0 - w)\int_{t_1}^{t_2} t^\mu dt$$
$$- \sum_{k=1}^{\infty} \frac{1}{k}(w - \tilde{z}_0)^{-k}\int_{t_1}^{t_2} t^\mu (z - \tilde{z}_0)^k dt$$
$$= \log(\tilde{z}_0 - w)I_\mu$$
$$- \sum_{k=1}^{\infty} \frac{1}{k}(w - \tilde{z}_0)^{-k}\sum_{\nu=k}^{N} z_\nu^{(k)}\int_{t_1}^{t_2} t^{m+n}\tilde{t}^\nu dt$$
$$= \log(\tilde{z}_0 - w)I_\mu$$
$$- \sum_{k=1}^{\infty} \frac{1}{k}(w - \tilde{z}_0)^{-k}\sum_{\nu=k}^{N} z_\nu^{(k)} I_{m+n}^{(\nu)} \quad (52)$$

where, from the binomial theorem,

$$I_\mu^{(\nu)} = \int_{t_1}^{t_2} t^\mu \tilde{t}^\nu dt$$

$$= \sum_{j=0}^{\mu} \binom{\mu}{j} t_0^{\mu-j} \frac{\tilde{t}_2^{j+\nu+1} - \tilde{t}_1^{j+\nu+1}}{j + \nu + 1} \quad (53)$$

The integrals (53) can be evaluated from the recursion relations

$$I_0^{(\nu)} = \int_{t_1}^{t_2} \tilde{t}^\nu dt = \frac{1}{\nu+1}\left(\tilde{t}_2^{\nu+1} - \tilde{t}_1^{\nu+1}\right) \quad (54)$$

and

$$I_{\mu+1}^{(\nu)} = t_0 I_\mu^{(\nu)} + I_\mu^{(\nu+1)} \quad (55)$$

If t_0 is situated at the mid-point between t_1 and t_2 on the sub-divided panel, the only non-zero terms in (54) are those where ν is even.

From (38) it follows that

$$\psi_n = \log(\tilde{z}_0 - w)\delta_n$$
$$- \sum_{m=0}^{N} d_m \sum_{k=1}^{\infty} \frac{1}{k}(w - \tilde{z}_0)^{-k}$$
$$\sum_{\nu=k}^{N} z_\nu^{(k)} I_{m+n}^{(\nu)} \quad (56)$$

Similarly, from (41),

$$\phi_n = -i(w - \tilde{z}_0)^{-1}\zeta_{n+1} - i\sum_{m=0}^{N-1} (m+1)z_{m+1}$$
$$\sum_{k=1}^{\infty} (w - \tilde{z}_0)^{-k-1}\sum_{\nu=k}^{N} z_\nu^{(k)} I_{m+n}^{(\nu)} \quad (57)$$

To facilitate the evaluation of (56)-(57) it is useful to define the sums

$$\Psi_\nu = \sum_{k=1}^{\nu} \frac{1}{k}(w - \tilde{z}_0)^{-k} z_\nu^{(k)}$$
$$(\nu = 1, 2, ..., N) \quad (58)$$

and

$$\Phi_\nu = \sum_{k=1}^{\nu} (w - \tilde{z}_0)^{-k-1} z_\nu^{(k)}$$
$$(\nu = 1, 2, ..., N) \quad (59)$$

The local multipole expansions for the sub-divided panel are then evaluated in the forms

$$\psi_n = \log(\tilde{z}_0 - w)\delta_n - \sum_{\nu=1}^{N} \Psi_\nu \sum_{m=0}^{N} d_m I_{m+n}^{(\nu)} \quad (60)$$

141

$$\phi_n = -i(w - \tilde{z}_0)^{-1}\zeta_{n+1}$$

$$- i\sum_{\nu=1}^{N}\Phi_\nu \sum_{m=0}^{N}(m+1)z_{m+1}I_{m+n}^{(\nu)} \quad (61)$$

The latter forms reduce the number of nested loops, with a resulting improvement in computational efficiency.

5.6 Field point on the panel

Consider first the case where the field point is at $w = z_0$ in physical coordinates, corresponding to $t = 0$ in parametric coordinates. In this case

$$z - w = t\sum_{n=1}^{M} z_n t^{n-1} \quad (62)$$

and the logarithm can be decomposed in the form

$$
\begin{aligned}
\log(z - w) &= \log t \\
&+ \log\left(\sum_{n=1}^{M} z_n t^{n-1}\right) \quad (63)
\end{aligned}
$$

If the last term is expanded in a Taylor series the formal result is

$$
\begin{aligned}
\log\left(\sum_{n=1} z_n t^{n-1}\right) &= \log z_1 \\
&+ \sum_{k=1}^{\infty}\frac{(-1)^{k-1}}{k}p^k \quad (64)
\end{aligned}
$$

where

$$p = \sum_{n=1}^{M-1}(z_{n+1}/z_1)t^n \quad (65)$$

With the coefficients of (65) denoted by p_n, successive powers of p can be expanded using the algorithm (25 - 26). Thus

$$p^k = \sum_{j=k}^{N} p_j^{(k)} t^j \quad (66)$$

where

$$p_j^{(k)} = \sum_{\nu=1}^{j-k+1} p_\nu^{(1)} p_{j-\nu}^{(k-1)}$$

$$(k = 2, 3, ..., N; \ j = k, ..., N) \quad (67)$$

and

$$p_n^{(1)} = z_{n+1}/z_1 \quad (n = 1, 2, ..., N-1) \quad (68)$$

Substituting (66) for each term in the series of (64), and collecting the homogeneous coefficients, gives the desired result

$$\log(z - w) = \log t + \sum_{j=0}^{N} q_j t^j \quad (69)$$

where

$$q_0 = \log z_1 \quad (70)$$

and

$$q_j = \sum_{k=1}^{j}\frac{(-1)^{k-1}}{k}p_j^{(k)} \quad (j = 1, 2, ..., N) \quad (71)$$

The source integral can be evaluated using (69), with the result

$$
\begin{aligned}
\psi_n &= \sum_{m=0}^{N} d_m \left[\frac{1}{m+n+1}\left(t^{m+n+1}\log t\right.\right. \\
&- \left.\frac{t^{m+n+1}}{m+n+1}\right) \\
&+ \left.\sum_{j=0}^{N} q_j \frac{t^{m+n+j+1}}{m+n+j+1}\right]_{t_1}^{t_2} \\
&= \sum_{m=0}^{N}\frac{d_m}{m+n+1}\left[t^{m+n+1}\log t\right. \\
&- \left.\frac{t^{m+n+1}}{m+n+1}\right]_{t_1}^{t_2} + \sum_{j=0}^{N} q_j \delta_{n+j} \quad (72)
\end{aligned}
$$

The normal dipole integral requires a separate analysis. Evaluating the indicated derivative in (44), and using (66),

$$\phi_n = i\sum_{m=0}^{M-1}(m+1)z_{m+1}$$

$$\int_{t_1}^{t_2} t^{m+n-1}\left(\sum_{\nu=0}^{M-1} z_{\nu+1} t^\nu\right)^{-1} dt \quad (73)$$

To evaluate the inverse of the series in (73), (27 - 28) are used to find the coefficients $f_n^{(-1)}$, with $f_n^{(0)} = \delta_{n0}$, and $f_n^{(1)} = z_{n+1}$. The resulting coefficients are

$$f_0^{(-1)} = \frac{1}{z_1} \quad (74)$$

and

$$f_n^{(-1)} = -\frac{1}{z_1}\sum_{\nu=1}^{n} z_{\nu+1} f_{n-\nu}^{(-1)} = -\sum_{\nu=1}^{n} p_\nu^{(1)} f_{n-\nu}^{(-1)}$$

$$(n = 1, 2, ..., N) \quad (75)$$

The normal dipole integral is then given as

$$\phi_n = i \sum_{m=0}^{M-1} (m+1) z_{m+1}$$

$$\sum_{j=0}^{N} f_j^{(-1)} \int_{t_1}^{t_2} t^{j+m+n-1} dt \qquad (76)$$

Except for the singular case $j + m + n = 0$ the integrals are elementary, with the result

$$\phi_n = i \sum_{m=0}^{M-1} (m+1) z_{m+1} \sum_{j=0}^{N} f_j^{(-1)} I_{m+m+j-1}$$

$$= i \sum_{j=0}^{N} f_j^{(-1)} \zeta_{j+n} \qquad (77)$$

where the integrals I_μ are defined by (44). The singular case occurs only for $n = 0$, where the contribution from the term where $m = 0$ and $j = 0$ is given by

$$i z_1 f_0^{(-1)} \int_{t_1}^{t_2} t^{-1} dt = i \int_{t_1}^{t_2} t^{-1} dt \qquad (78)$$

Thus, when $n = 0$, (77) applies in the modified form

$$\phi_0 = i \int_{t_1}^{t_2} t^{-1} dt + i f_0^{(-1)}$$

$$\sum_{m=1}^{N-1} (m+1) z_{m+1} I_{m+n-1}$$

$$+ i \sum_{j=1}^{N} f_j^{(-1)} \zeta_j \qquad (79)$$

Depending on the definition of ϕ_0 (as a principal-value integral or as the limit where $w \to z_0$ on a specified side of the panel), the integral in (79) is either real, or differs from a real quantity by $\pm \pi i$. The only contribution to the real part of (79) is in the latter case.

For the more general case where the field point is on the panel at $w = z(t_0)$, with t_0 an arbitrary point in parametric space in the open interval (t_1, t_2), the results above can be extended using the binomial theorem. Hereafter a tilde is used to denote the shifted variable $\tilde{t} = t - t_0$, or the coefficients in a series involving this variable. Thus the panel is defined in physical space by analogy with (17), in the form

$$w = z(t) = \sum_{n=0}^{N} z_n t^n = \sum_{n=0}^{N} \tilde{z}_n \tilde{t}^n \qquad (80)$$

where

$$\tilde{z}_n = \sum_{\nu=n}^{M} \binom{\nu}{n} z_\nu t_0^{\nu-n}$$

$$(n = 0, 1, 2, ..., M) \qquad (81)$$

In place of (69) we write

$$\log(z - w) = \log(t - t_0) + \sum_{j=0}^{N} \tilde{q}_j \tilde{t}^j \qquad (82)$$

where the coefficients $\tilde{q}_n$ are evaluated from the relations

$$\tilde{p}_n^{(1)} = \tilde{z}_{n+1} / \tilde{z}_1 \qquad (n = 1, 2, ..., M-1) \qquad (83)$$

$$\tilde{p}_j^{(k)} = \sum_{\nu=1}^{j-k+1} \tilde{p}_\nu^{(1)} \tilde{p}_{j-\nu}^{(k-1)}$$

$$(k = 2, 3, ..., N; \; j = k, ..., N) \qquad (84)$$

$$\tilde{q}_0 = \log \tilde{z}_1 \qquad (85)$$

$$\tilde{q}_j = \sum_{k=1}^{j} \frac{(-1)^{k-1}}{k} \tilde{p}_j^{(k)} \qquad (j = 1, 2, ..., N) \qquad (86)$$

The contribution to the source integral from the logarithmic singularity in (82) is

$$\int_{t_1}^{t_2} t^\mu \log(t - t_0) dt$$

$$= \frac{1}{\mu+1} \left[(t^{\mu+1} - t_0^{\mu+1}) \log(t - t_0) \right.$$

$$\left. - \sum_{\nu=0}^{\mu} \frac{t_0^{\mu-\nu}}{\nu+1} t^{\nu+1} \right]_{t_1}^{t_2} \qquad (87)$$

The contribution from the remaining terms in (82) is

$$\int_{t_1}^{t_2} t^\mu \sum_{j=0}^{N} \tilde{q}_j \tilde{t}^j dt = \sum_{j=0}^{N} \tilde{q}_j \sum_{k=0}^{j} \binom{j}{k} (-t_0)^{j-k} I_{\mu+k}$$

$$= \sum_{k=0}^{N} \hat{q}_k I_{\mu+k} \qquad (88)$$

143

where

$$\hat{q}_k = \sum_{j=k}^{N} \tilde{q}_j \binom{j}{k} (-t_0)^{j-k}$$

$$(k = 0, 1, 2, ..., N) \qquad (89)$$

Thus the source integral is evaluated in the more general form

$$\psi_n = \sum_{m=0}^{N} d_m \left[\frac{1}{m+n+1} \left((t^{m+n+1} - t_0^{m+n+1}) \right. \right.$$
$$\left. \log(t - t_0) - \sum_{\nu=0}^{m+n} \frac{t_0^{m+n-\nu}}{\nu+1} t^{\nu+1} \right)$$
$$+ \sum_{j=0}^{N} \hat{q}_j \frac{t^{m+n+j+1}}{m+n+j+1} \Big]_{t_1}^{t_2}$$

$$= \sum_{m=0}^{N} \frac{d_m}{m+n+1} \left[(t^{m+n+1} - t_0^{m+n+1}) \right.$$
$$\left. \log(t - t_0) - \sum_{\nu=0}^{m+n} \frac{t_0^{m+n-\nu}}{\nu+1} t^{\nu+1} \right]_{t_1}^{t_2}$$

$$+ \sum_{j=0}^{N} \hat{q}_j \delta_{n+j} \qquad (90)$$

Following a similar generalization for the normal dipole integral, (73)-(76) are replaced by

$$\phi_n = i \sum_{m=0}^{M-1} (m+1) z_{m+1}$$
$$\int_{t_1}^{t_2} t^{m+n} \left(\sum_{\nu=0}^{N} \tilde{z}_{\nu+1} \tilde{t}^{\nu+1} \right)^{-1} dt$$

$$= i \sum_{m=0}^{M-1} (m+1) z_{m+1}$$
$$\sum_{j=0}^{N} \tilde{f}_j^{(-1)} \int_{t_1}^{t_2} t^{m+n} \tilde{t}^{j-1} dt \qquad (91)$$

where

$$\tilde{f}_0^{(-1)} = \frac{1}{\tilde{z}_1} \qquad (92)$$

$$\tilde{f}_n^{(-1)} = -\frac{1}{\tilde{z}_1} \sum_{\nu=1}^{n} \tilde{z}_{\nu+1} \tilde{f}_{n-\nu}^{(-1)} = -\sum_{\nu=1}^{n} \tilde{p}_\nu^{(1)} \tilde{f}_{n-\nu}^{(-1)}$$

$$(n = 1, 2, ..., M - 1) \qquad (93)$$

The singular case $j = 0$ simplifies again, as a result of the identity

$$\sum_{m=0}^{M-1} (m+1) z_{m+1} t_0^m = \tilde{z}_1 \qquad (94)$$

Thus

$$\phi_n = i t_0^n \left[\int_{t_1}^{t_2} \frac{dt}{t - t_0} \right]_{t_1}^{t_2}$$
$$+ i \tilde{f}_0^{(-1)} \sum_{m=0}^{M-1} (m+1) z_{m+1} \sum_{\nu=1}^{m+n} t_0^{m+n-\nu} I_{\nu-1}$$
$$+ i \sum_{m=0}^{N-1} (m+1) z_{m+1} \sum_{j=1}^{N} \tilde{f}_j^{(-1)}$$
$$\sum_{k=1}^{j} \binom{j-1}{k-1} (-t_0)^{j-k} I_{m+n+k-1} \qquad (95)$$

This equation can be simplified by extending the definition (46) of the coefficients ζ_n, with the final result

$$\phi_n = i t_0^n \left[\int_{t_1}^{t_2} \frac{dt}{t - t_0} \right]_{t_1}^{t_2} + i \tilde{f}_0^{(-1)}$$
$$\sum_{m=0}^{3+n-2} t_0^m \zeta_{n-m} + i \sum_{k=1}^{N} \zeta_{n+k} \hat{f}_k \qquad (96)$$

where

$$\hat{f}_k = \sum_{j=k}^{N} \tilde{f}_j \binom{j-1}{k-1} (-t_0)^{j-k}$$

$$(k = 1, 2, ..., N) \qquad (97)$$

Here the coefficients ζ_n are defined for $n = 0, -1, -2, ...$ as in (46), but with the lower limit of the sum $m = 1 - n$.

As in the discussion following (79), the only contribution to the real part of the dipole potential from the singular integral which in (95 - 96) is from the residue.

6 System of Equations

We have discussed the B-spline defined singularity strengths and calculations of the influence functions in the above sections. In this section, we are going to discuss the implementations of the system of equations. The collocation method will be discussed first, and then the Galerkin method.

6.1 The Collocation Method

In this system of equations, the boundary condition is satisfied at collocation points, and the unknowns to be solved are the B-spline polygon vertices of the dipole moments. The number of

144

collocation points on each panel can be arbitrary subject to the condition that the system is not underdetermined.

Consider the discretized Green's formula (15). The influence of the dipole singularities on the collocation point i is

$$\sum_{j=1}^{L}\sum_{k=0}^{N}\phi_{j,k}\int_{l_B(j)} t^k \frac{\partial}{\partial n_j}\ln r_{i,j}\,dl \qquad (98)$$

where $\phi_{j,k}$ is the kth degree B-spline coefficient of the dipole moment on the jth panel. The moments of the influence functions can be evaluated as described in the last section, and we will define $\tilde{a}_{i,j}^k$ as the kth moment of the dipole influence function on collocation point i by panel j. Therefore, the dipole influence of panel j on collocation point i can be written as,

$$\int \phi_j(t)\frac{\partial}{\partial n_j}\ln r_{i,j}\,dl = \sum_{k=0}^{N}\phi_{j,k}\tilde{a}_{i,j}^k \qquad (99)$$

From section 3, $\phi_{j,k}$ is a function of the B-spline polygon vertices, therefore, (99) can be further expanded as follows:

$$\int \phi_j(t)\frac{\partial}{\partial n_j}\ln r_{i,j}\,dl$$
$$= \sum_{k=0}^{N}\{\sum_{m=j}^{j+N}\beta_m^k\phi_{v,m}\}\tilde{a}_{i,j}^k \qquad (100)$$
$$= \sum_{m=j}^{j+N}\{\sum_{k=0}^{N}\beta_m^k\tilde{a}_{i,j}^k\}\phi_{v,m}$$

where $\phi_{v,m}$ is the mth B-spline vertex of the dipole moment, and the coefficients β_m^k can be obtained by expanding the basis functions

$$\mathcal{N}_m^K(t) = \sum_{k=0}^{N}\beta_m^k t^k \qquad (101)$$

Now the left-hand-side of the discretized Green's formula (10) can be rewritten as follows:

$$\sum_{j=1}^{j=L}\int_{l_B(j)}\phi_j(t)\frac{\partial}{\partial n_j}\ln r_{i,j}$$
$$= \sum_{j=1}^{L}\sum_{m=j}^{j+N}\{\sum_{k=0}^{N}\beta_m^k\tilde{a}_{i,j}^k\}\phi_{v,m} \qquad (102)$$
$$= \sum_{m=1}^{L+N}[\sum_{j=m-N}^{m}\{\sum_{k=0}^{N}\beta_m^k\tilde{a}_{i,j}^k\}]\phi_{v,m}$$

Hence, the left-hand-side of the system of equations has been established.

We can calculate the influence of the sources, the right-hand-side of the system of equations, in a similar way. Since the strengths of the sources are known, the calculations are relatively simple.

Starting with equation (13), the source strength of panel j, σ_j, can be expressed as $\sigma_j(t) = \sum_{k=0}^{M}\sigma_{j,k}t^k$. We next define the source influence function $\tilde{b}_{i,j}^k$ such that $\tilde{b}_{i,j}^k = \int t^k \ln r_{i,j}$, where $\tilde{b}_{i,j}^k$ is the kth moment of the source influence function on the collocation point i by the panel j. Then the total source influence on the collocation point i will be,

$$\sum_{j=1}^{j=L}\sum_{k=0}^{N}\sigma_{j,k}\tilde{b}_{i,j}^k \qquad (103)$$

Equation (103) gives the right-hand-side of the system of equations.

Therefore, the discretized Green's formula becomes,

$$\sum_{m=1}^{L+N}\sum_{j=m-N}^{m}\sum_{k=0}^{N}\beta_m^k\tilde{a}_{i,j}^k\phi_{v,m}$$
$$= \sum_{j=1}^{j=L}\sum_{k=0}^{N}\sigma_{j,k}\tilde{b}_{i,j}^k \qquad (104)$$

Equation (104) is the complete formulation for non-lifting problems. The effect of the wake and the Kutta condition on the formulation of the lifting problem will be discussed later in this section.

Defining $a_{i,m} = \sum_{j=m-N}^{m}\sum_{k=0}^{N}\beta_m^k\tilde{a}_{i,j}^k$, and $RHS_i = \sum_{j=1}^{j=L}\sum_{k=0}^{N}\sigma_{j,k}\tilde{b}_{i,j}^k$, we obtain the system of equations in the matrix form $[A][\Phi_v] = [RHS]$. In this system, there are $L+N$ unknowns, and $L*N_c$ equations (N_c is number of collocation points per panel). Therefore, we need more than one collocation point per panel to avoid an underdetermined system. Increasing the number of collocation points per panel, N_c, increases the computational time but also improves the stability of the solution. Based on numerical experiments we have selected $N_c = 3$. Using a cubic B-spline with three collocation points on each panel, the left-hand-side matrix $[A]$ is,

145

$$[A] = \begin{bmatrix} a_{1,1} & a_{1,2} & \cdot & \cdot & \cdot & a_{1,L+3} \\ a_{2,1} & a_{2,2} & \cdot & \cdot & \cdot & a_{2,L+3} \\ \cdot & \cdot & \cdot & \cdot & \cdot & \cdot \\ \cdot & \cdot & \cdot & \cdot & \cdot & \cdot \\ \cdot & \cdot & \cdot & \cdot & \cdot & \cdot \\ a_{L*3,1} & a_{L*3,2} & \cdot & \cdot & \cdot & a_{L*2,L+3} \end{bmatrix} \tag{105}$$

and the unknowns are

$$[\Phi_v] = \begin{bmatrix} \phi_{v,1} \\ \phi_{v,2} \\ \cdot \\ \cdot \\ \cdot \\ \phi_{v,L+3} \end{bmatrix} \tag{106}$$

This is an overdetermined system, which can be solved by a least squares approach. The solution of this least squares system initially was carried out by both the Householder method and the normal equation approach [2], and both methods gave the same solution. In the present method, the Householder method is used.

To solve a lifting problem, the influence of the wake must also be included. For a two-dimensional, steady lifting problem, the strength of the wake sheet dipole is equivalent to a point vortex at the trailing edge, and the strength of this vortex should satisfy the Kutta condition. As shown by Morino [5], the strength of this vortex Γ is equal to the the potential jump at the trailing edge,

$$\Gamma = \phi^+ - \phi^- \tag{107}$$

where ϕ^+ is the dipole moment at the trailing edge of upper side (suction side), and ϕ^- is the dipole moment at the trailing edge of lower side (pressure side). The system of equations thus becomes,

$$\sum_{m=1}^{L+N} \{ \sum_{j=m-N}^{m} \{ \sum_{k=0}^{N} \beta_m^k \tilde{a}_{i,j}^k \} \phi_{v,m}$$
$$= \sum_{j=1}^{j=L} \sum_{k=0}^{N} \sigma_{j,k} \tilde{b}_{i,j}^k + \Gamma w_i \tag{108}$$

where w_i is the wake influence function, *i.e.* the contribution from the last term of equation (8) to the ith panel on the foil.

When applying B-splines to define the dipole moment, these two values are the dipole moments at the "end points" of the B-spline, and are therefore equal to the first and the last of the B-spline polygon vertices.

$$\Gamma = \phi_{v,L+N} - \phi_{v,1} \tag{109}$$

Therefore, the wake influence functions can be coupled into the left-hand-side of the least squares system. However, this will cause the system of equations to become more ill-conditioned, and will therefore increase the numerical error in the solution. In the present method, we first guess the initial solution Γ_0, and then impose a pressure Kutta condition to get the final solution iteratively. The pressure Kutta condition used here was first introduced by Kerwin, et al. [3] for three-dimensional propeller problems, and it requires the equality of the pressures on the upper and lower sides of the trailing edge. This non-linear pressure Kutta condition has been described in [3], and it can be simplified for two-dimensional problems. It is found that by using this approach, the solution procedure is more stable and more accurate. In the present paper, we used the two-dimensional flat plate solution ($2\pi\alpha$, where α is the angle of attack) to be our initial solution, however, the selection of the initial solution (including zero) will not affect the final solution since the satisfaction of the Kutta condition should provide a unique solution.

For non-lifting problems, the accuracy is improved by imposing a continuity condition at the two ends of the B-splines. That is,

$$\phi_{v,1} = \phi_{v,L+N} \tag{110}$$

Although solving a least squares system sometimes is less accurate and robust than solving a square linear system, it provides more freedom to set up the system of equations. The selection of the number of collocation points on each panel is one example, and the applications of the Kutta condition and the continuity condition described above further demonstrate the flexibility of the present method. However, the size of the matrix is increased by the number of collocation points. This issue will be discussed later.

6.2 The Galerkin Method

The Galerkin method used here is the Bubnow-Galerkin method, in which the test functions are selected to be the same as the interpolation functions.

Applying the Galerkin method to the integral equation expressed in equations (8) and (9), we will have,

$$\int \left[\int \phi(t) \frac{\partial}{\partial n} \ln r \frac{dl}{dt} dt \right] \mathcal{N}_i(\tilde{t}) d\tilde{t}$$

$$= \int \left[\int -\vec{n}(t) \cdot \vec{U}_\infty \frac{dl}{dt} dt \right] \mathcal{N}_i(\tilde{t}) d\tilde{t}$$

$$+ \int \left[\int \Gamma \frac{\partial}{\partial n} \ln r \frac{dl}{dt} dt \right] \mathcal{N}_i(\tilde{t}) d\tilde{t} \quad (111)$$

where the dipole moment, $\phi(t)$, can be expressed in terms of the B-spline basis functions as equation (7).

The inner integrals in the equation (111) are exactly the same as the collocation method described in the last section, therefore, the discretized form of equation (111) can be derived similarly. Let us define functions $f(\tilde{t}_{l_i})$, and $g(\tilde{t}_{l_i})$ as the discretized forms of the inner integrals of the left-hand-side and the right-hand-side of the equation (111), where l_i stands for the lth collocation point of panel i. Therefore, they represent the total influence on the collocation point l of the panel i of the dipole and source (plus the wake effect for the lifting problems) separately. From equation (108), we have,

$$f(\tilde{t}_{l_i}, t_j) = \sum_{m=0}^{L+N} \left[\sum_{j=m-N}^{m} \left\{ \sum_{k=0}^{N} \beta_m^k \tilde{a}_{l_i,j}^k \right\} \right]$$
$$\cdot (\phi_v)_m$$

$$g(\tilde{t}_{l_i}, t_j) = \sum_{j=1}^{j=L} \sum_{k=0}^{N} \sigma_{j,k} \tilde{b}_{l_i,j}^k + \Gamma \omega_{l_i} \quad (112)$$

Equation (111) becomes the following equation by replacing these two functions with the inner integrals:

$$\int f(\tilde{t}_{l_i}) \mathcal{N}(\tilde{t}_{l_i}) d\tilde{t} = \int g(\tilde{t}_{l_i}) d\tilde{t} \quad (113)$$

By applying a quadrature rule to this equation, we then have,

$$\sum_{i=1}^{L} \sum_l f(\tilde{t}_{l_i}) \mathcal{N}(\tilde{t}_{l_i}) \omega_l \Delta \tilde{t}$$

$$= \sum_{i=1}^{L} \sum_l g(\tilde{t}_{l_i}) N(\tilde{t}_{l_i}) \omega_l \Delta \tilde{t} \quad (114)$$

where ω_l is the weighting function of the numerical integration. The resultant system of equations

is an $L+N$ by $L+N$ linear system for a degree N higher order panel method. If we expressed the matrix system as equation (105 - 106), the matrix system of the Galerkin method will then be $[Q][A][\Phi_v] = [Q][B]$, and the matrix $[Q]$ is,

$$\begin{bmatrix} \omega_1 \mathcal{N}_1(\tilde{t}_{1_1}) & \omega_2 \mathcal{N}_1(\tilde{t}_{2_1}) & \cdot & \omega_3 \mathcal{N}_1(\tilde{t}_{3_L}) \\ \omega_1 \mathcal{N}_2(\tilde{t}_{1_1}) & \omega_2 \mathcal{N}_2(\tilde{t}_{2_1}) & \cdot & \omega_3 \mathcal{N}_2(\tilde{t}_{3_L}) \\ \cdot & \cdot & \cdot & \cdot \\ \cdot & \cdot & \cdot & \cdot \\ \cdot & \cdot & \cdot & \cdot \\ \omega_1 \mathcal{N}_{L+N}(\tilde{t}_{1_1}) & \omega_2 \mathcal{N}_{L+N}(\tilde{t}_{2_1}) & \cdot & \omega_3 \mathcal{N}_{L+N}(\tilde{t}_{3_L}) \end{bmatrix}$$
$$(115)$$

if the number of collocation points is selected as 3.

The Galerkin method utilized here uses the exact form for the inner integrals, and a numerical integration for the outer integrals. Chandler and Sloan [1] called this a "qualocation" method.

The numerical examples shown later show that the Galerkin method has almost the same accuracy and efficiency as the collocation method. However, the left-hand-side matrix size of the Galerkin method will be smaller than that of the collocation method. For a cubic higher order panel method, with L panels and N_c collocation points, the collocation methods will give an $L * N_c$ by $L + 3$ left-hand-side matrix, and the Galerkin method will give an $L + 3$ by $L + 3$ left-hand-side matrix. If we used a Householder least squares solution for the collocation method, then it needs $2(L+3)^2(L * N_c - (L+3)/3)$ flops. On the other hand, the Galerkin method needs $2(L+3)^3/3$ flops to solve the matrix system by using Gaussian elimination. The collocation method needs about $3(N_c - 1)$ times more computational time than the Galerkin method. This factor is not important for two-dimensional problems because only a small portion of the computational time is spent on solving the matrix (less than 10%).

In the next section, we will show results for both the non-lifting and lifting problems by applying the present method.

7 Computational Results

In this section, several numerical examples will be shown for the present method. We will first show results of the collocation method for all the cases, and then compare the solutions of the Galerkin method to the solutions of the collocation method.
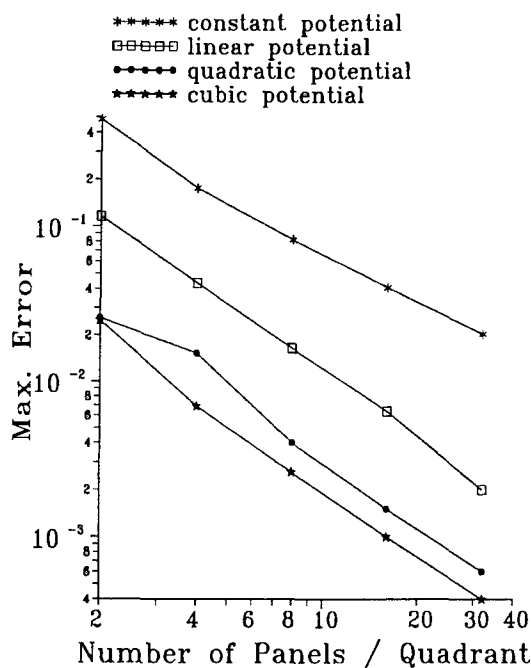
Figure 4: The number of panels used on one quadrant *vs.* the maximum error of the solutions of different order panel methods for the case of a uniform inflow past a square.
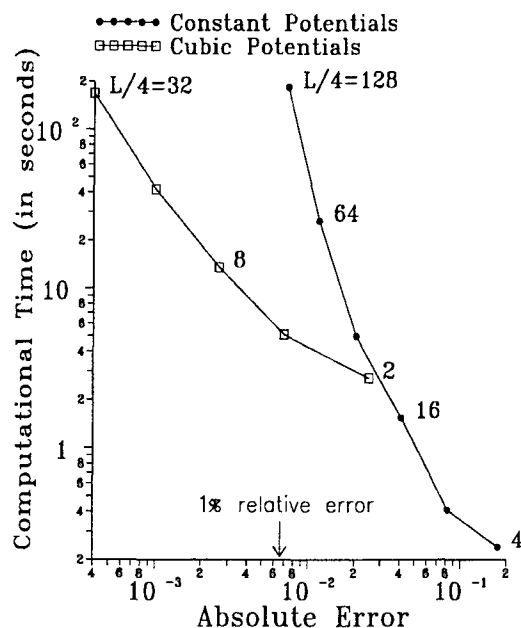
Figure 5: The absolute error (maximum error of the solutions) of the case a uniform inflow past a square, *vs.* the computational time of different order panel methods. The computational time is measured on a SiliconGraphics Iris 4D25 machine.

The first case we tested is that of uniform flow past a square. Since the present method is a general higher order method, we will present the results of linear potentials, quadratic potentials, and cubic potentials, and compare these results to the analytical results and results of a low order panel method.

Due to the sharp corners of the square, a non-uniform B-spline curve is used to define the geometry. An end condition is applied for the continuity as described in (110), such that the first B-spline control point coincides with the last B-spline control point. The error of this test case is defined as the maximum difference between the computational results and the analytical solution. Figure 4 shows the results of linear potential, quadratic potential, and cubic potential from the present method, along with the results from a two-dimensional constant potential panel method. The accuracy of the higher order panel method is much better than that of the low order panel method. Figure 5 shows the errors vs. the computational time (run on a SiliconGraphics Iris 4D25 machine) by using the cubic potentials and constant potentials. For a 1% error, the computational time of the constant potential method is about 36 times longer than that of the cubic potential method. This means that the present method is not only accurate, but also efficient.

The second case we tested is a symmetrical Karman-Treftz foil with a thickness/chord ratio of 25% and a tail angle of 45° (as shown in figure 1). The angle of attack is selected as 5 degrees. The error in this case is defined as the difference between the computational circulation and the analytical solution. Figure 6 shows the errors by using the different order of panel methods. It shows the similar trend as the square case. One of the advantages of applying the B-splines to define the solutions is that the derivatives of solutions can be directly calculated from the B-spline basis functions and solved B-spline polygon vertices. That is, the velocities can be computed directly without using finite differencing schemes. Figure 7 shows the calculated pressure distribution of this foil by using cubic potentials compared to the analytical results. It shows that even 10 panels gives a very good result for the pressure distribution. Notice that although we only show the pressure coefficients on the panel boundaries, in fact the solutions are continuous because they are defined by B-splines. Figure 8 again shows the error vs. the computational time of this case, and for the 1% error, the computational time of
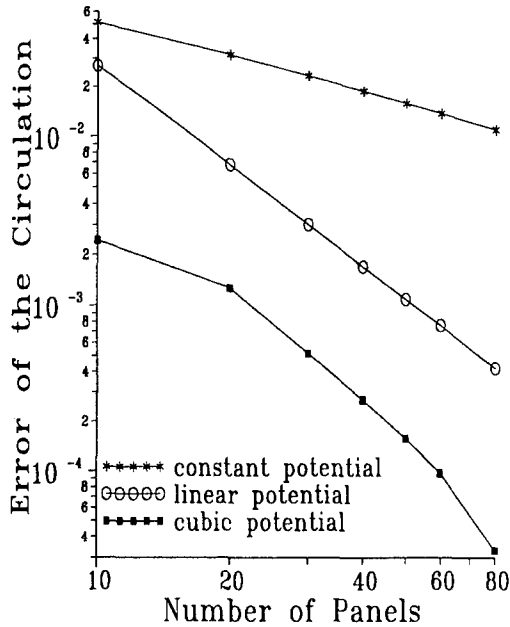
Figure 6: The number of panels used *vs.* the error of the solutions of different order panel methods for the Karman-Treftz foil case.

Figure 8: The absolute error (error of the calculated circulation) *vs.* the computational time of different order panel methods for the hydrofoil case. The exact solution is 0.33. The computational time is measured on a SiliconGraphics Iris 4D25 machine.

Figure 7: The pressure distribution of calculated results and analytical solutions of the Karman-Treftz foil case.

the constant panel method is 41 times that of the cubic potential method. Notice that the constant potential method needs 480 panels to get a result within 1% error, and the cubic potential method only needs 10 panels.

To explore alternative solution techniques we have compared the results based on the collocation and Galerkin methods. Three collocation points are used on each panel, which were selected initially to provide uniform spacing in the parametric coordinate t, at the points $1/6, 1/2, 5/6$ of the distance between each pair of vertices. The Galerkin scheme was implemented using the same integration nodes with equal weights. Subsequently, to refine the Galerkin integration, Gauss nodes were substituted in both methods. As shown in Figure 9, the improved accuracy of the Galerkin method is practically insignificant, while the use of Gauss nodes reduces the error in both methods by a factor of order two.

Figure 10 demonstrates the error em vs. the number of elements in the LHS matrix (hereafter refer to as the "matrix size") of the constant potential method, and higher order (cubic) collocation method and higher order Galerkin method.

149
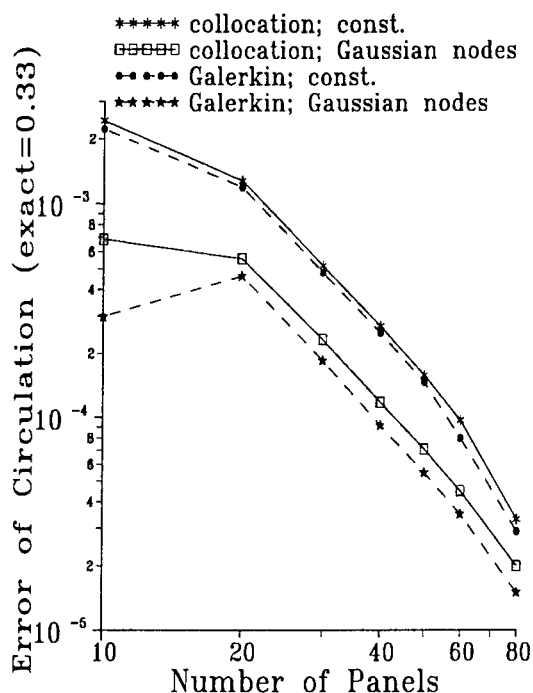
Figure 9: The error of computational results from the collocation method and the Galerkin method. The test case is the Karman-Treftz foil
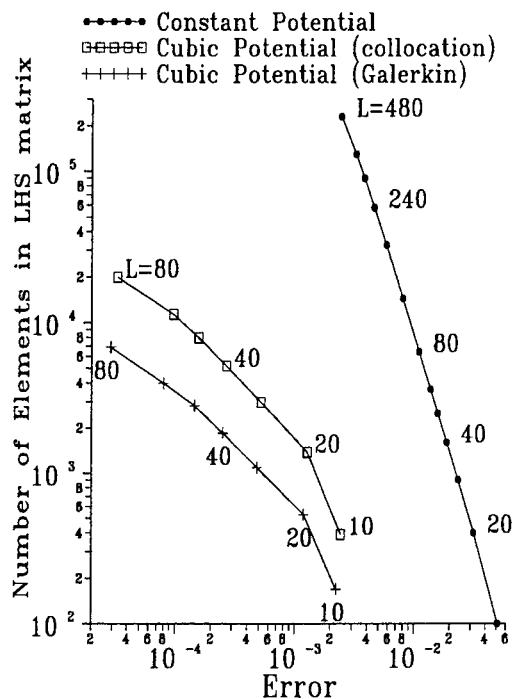
Figure 10: The error vs. the matrix size of different order panel methods for the Karman-Treftz foil case.

The matrix size of the constant potential method is the square of the number of panels, L, the matrix size of the higher order collocation method is $3 * L$ (for three collocation points each panel), multiplied by $L + 3$, and the matrix size of the higher order Galerkin method is the square of $L+3$. From figure 10, one can see that 480 panels of the constant potential, 10 panels of the collocation and Galerkin higher order methods have similar errors (about 0.7% of the exact value). However, the number of elements in the matrix of these methods are 230400, 390 and 169 separately. That is, for the same error, the matrix size that the constant potential method needs is about 600 times larger than that of the higher order collocation method, and 1400 times larger than that of the higher order Galerkin method! Therefore, the presented method also has the advantage of using less computer resources.

8 Conclusion

We have presented a higher order panel method by using B-splines to define both the geometry and solutions. The test solutions show that for a given number of panels, the present method is more accurate than the low order method, and for a given accuracy, the computational time is far less than that of a low order panel method. The solutions are naturally continuous, and the derivatives of potentials can be directly calculated from the B-spline polygon vertices and B-spline basis functions. Also this method needs far less computer storage space or memory than the low order method, which will be significant advantage when solving three dimensional problems.

This method has been implemented by both the collocation method and the Galerkin method. The accuracies of both methods are equally good. The left-hand-side matrix of the Galerkin method is smaller than the collocation method. The resulting savings of the computational time, memory, and storage space are relative minor in solving two-dimensional problems; however, these savings are expected to be substantial in solving three-dimensional problems.

The extension of this method to solve three dimensional problems is under research. The problems of three-dimensional geometries are much more complicated, such as the connection of two surfaces, or the intersection of two surfaces. These complexities have to be well defined, and carefully incorporated into the solution

150

matrix system. The calculations of the influence functions are also much more difficult than the two-dimensional problems. It is hoped that this method will not only be able to provide more accurate solutions than the low order panel method, but also be more effective of solving problems such as wave body interactions, and lifting problems.

Acknowledgements

References

[1] G.A. Chandler and I.H. Sloan. Spline qualocation methods for boundary integral equations. *Numer. Math.*, 58, pp. 537–567, 1990.

[2] G.H. Golub and C.F. Van Loan. *Matrix Computations*. The Johns Hopkins University Press, Baltimore, Maryland, 1989.

[3] J.E. Kerwin, S.A. Kinnas, J-T Lee, and W-Z Shih. A surface panel method for the hydrodynamic analysis of ducted propellers. *Trans. SNAME*, 95, 1987.

[4] Sir Horace Lamb. *Hydrodynamics*. Cambridge University Press, sixth edition, 1932.

[5] Luigi Morino and Ching-Chiang Kuo. Subsonic potential aerodynamic for complex configurations : a general theory. *AIAA Journal*, vol 12, no 2, pp. 191–197, February 1974.

[6] M.B. Okan and S.M. Umpleby. The use of B-splines for the calculation of two-dimensional potential around arbitrary bodies. *Int. Shipbuilding Progress*, 32, June 1985.

[7] D.F. Rogers and J. A. Adams. *Mathematical Elements for Computer Graphics*. McGraw-Hill, Inc., New York, 1990.

SESSION 4

WAVY/FREE-SURFACE FLOW: FIELD-EQUATION METHODS

A Fast Multigrid Method for Solving the Nonlinear Ship Wave Problem with a Free Surface

J. Farmer, L. Martinelli, and A. Jameson

(Princeton University, USA)

Abstract

This paper presents a finite volume method for the solution of the three dimensional, nonlinear ship wave problem. The method can be used to obtain both Euler and Navier-Stokes solutions of the flow field and the *a priori* unknown free surface location by coupling the free surface kinematic and dynamic equations with the equations of motion for the bulk flow. The evolution of the free surface boundary condition is linked to the evolution of the bulk flow via a novel iteration strategy that allows temporary leakage of mass through the surface before the solution is converged. The method of artificial compressibility is used to enforce the incompressibility constraint for the bulk flow. A multigrid algorithm is used to accelerate convergence to a steady state. The two-layer eddy viscosity formulation of Baldwin and Lomax is used to model turbulence. The scheme is validated by comparing the numerical results with experimental results for the Wigley parabolic hull and the Series 60, $C_b = 0.6$ hull. Waterline profiles from bow to stern are in excellent agreement with experiment. The computed wave drag compares favorably with experiment. Overall, the present method proves to be accurate and efficient.

1 Introduction

It is well established that a complex interaction exists between the viscous boundary layer and wake of a ship hull and the resulting wave pattern [1, 2]. The existence of two similarity parameters, the Froude number (Fr) and the Reynolds number (Re), which do not scale identically between model and full scale hulls, make it difficult to predict the viscous effect on the wave and total drag through model testing. The ship designer may thus resort to numerical simulation, and a great deal of effort has been devoted toward developing numerical tools capable of simulating the flow field about a translating ship. Some of these tools have met with success in capturing the salient features of the flow field, including the difficult-to-model stern region of ship hulls. However, many of the computational methods developed to date, especially those that include viscous effects and a moving free surface, tend to be very complicated and expensive. Thus, the focus of this work is the development of a fast and robust means to compute either viscous or inviscid flow fields about surface piercing ship hulls, and to make comparisons with experimental data.

The method of Hino [3] is a widely used approach for solving incompressible flow problems. This method takes the divergence of the momentum equation and solves implicit equations at each time step for the pressure and velocity fields such that continuity is satisfied. The method is expensive both because of the need to solve implicit equations by an iterative method and because of the cost of calculating the divergence of the momentum equations in a curvilinear coordinate system. Hino uses a finite difference scheme expressed in body-fitted curvilinear coordinates to discretize the solution domain on and below the free surface. The computational grid is not allowed to move with the free surface so an approximation must be employed to model the free surface boundary conditions. A Baldwin-Lomax turbulence model is used in conjunction with the wall function to model the viscous boundary layer. The scheme is first-order accurate in time and requires 10^4-plus global iterations to reach steady state for simple hull shapes.

The method of Miyata *et al.* (1987) [4] uses a similar velocity and pressure coupling procedure but now the grid is allowed to move with the free surface, providing a more exact treatment of the free surface boundary conditions. A sub-grid-scale turbulence model is employed and computations performed for Reynolds numbers up to 10^5. As with Hino's method, the time-accurate formulation necessitates several thousand time steps to reach steady state solutions. In a later paper, Miyata *et al.* (1992) [5] present a finite volume approach that substantially improves the computed results over those obtained using the finite difference approach. Simulations using Reynolds numbers up to 10^6 were made and more complicated hull shapes examined. The method still requires many thousands of time steps to achieve steady state solutions.

The interactive approach of Tahara *et al.* [6] uses a field method based on the finite-analytic method used by Chen *et al.* [7] for the viscous region, and a surface singularity method based on the "SPLASH" panel method of Rosen [8] for the inviscid outer domain. The method iterates between the inviscid and viscous regions by adjusting the small-domain panel distribution to allow for the boundary layer displacement thickness determined from the large-domain solution. The free surface boundary conditions are linearized and applied at the mean water elevation surface. Results of this approach appear to be quite promising for the Wigley hull, and a substantial savings in required computational cost is realized over the large-domain approaches of Hino and Miyata.

In this work, a field method is adopted for the entire flow domain like Hino and Miyata. However, the incompressibility constraint is enforced through the method of *artificial compressibility*, rather than the velocity-pressure coupling method. The method of artificial compressibility was originally proposed by Chorin [9] in 1967 to solve viscous flows. Since then, Rizzi and Eriksson [10] have applied it to rotational inviscid flow, Dreyer [11] has applied it to low speed two dimensional airfoils and Kodama [12] has applied it to ship hull forms with a symmetric free surface. In addition, Turkel [13] has investigated more sophisticated preconditioners than those originally proposed by Chorin. The basic idea behind artificial compressibility is to introduce a pseudotemporal equation for the pressure through the continuity equation. Use of this pressure equation, rather than the

velocity-pressure coupling procedure described in references [3] - [7], renders the new set of equations well conditioned for numerical computation along the same lines as those used to calculate compressible flow about complete aircraft [14, 15]. When combined with multigrid acceleration procedures [16, 17, 18] it proves to be particularly effective. Converged solutions of incompressible flows over three dimensional isolated wings are obtained in 25-50 cycles.

The general objective of this work is to build on these ideas to develop a more efficient method to predict free surface wave phenomena, for both inviscid and viscous flows. The viscous solution method introduced in this work is an extension of the inviscid method presented in reference [19, 20]. The nonlinear free surface boundary condition is satisfied by an iterative procedure in which the grid is moved with the free surface. Comparisons of numerical predictions with experimental data, for the Wigley hull and Series 60, $C_b = 0.6$ ship hull, show encouraging results for both waterline profiles and wave drag. Furthermore, it appears that this approach yields a substantial savings in the computational resources required for the simulations.

2 Mathematical Model

Figure 1 shows the reference frame and ship location used in this work. A right-handed coordinate system $Oxyz$, with the origin fixed at midship on the mean free surface is established. The z direction is positive upwards, y is positive towards the starboard side and x is positive in the aft direction. The free stream velocity vector is parallel to the x axis and points in the same direction. The ship hull pierces the uniform flow and is held fixed in place, ie. the ship is not allowed to sink (translate in z direction) or trim (rotate in $x - z$ plane).

2.1 Bulk Flow

For a viscous incompressible fluid moving under the influence of gravity, the continuity equation and the Reynolds averaged Navier-Stokes equations may be put in the form [3],

$$u_x + v_y + w_z = 0 \qquad (1)$$

$$u_t + uu_x + vu_y + wu_z = $$
$$-\psi_x + \left(Re^{-1} + \nu_t\right)\left(\nabla^2 u\right)$$
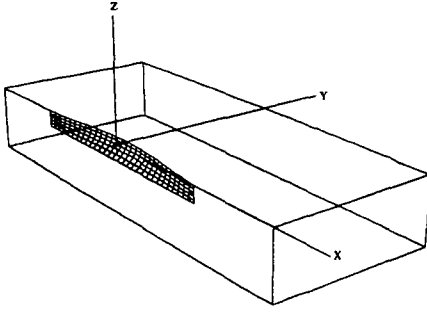
Figure 1: Reference Frame and Ship Location

$$v_t + uv_x + vv_y + wv_z =$$
$$-\psi_y + \left(Re^{-1} + \nu_t\right)\left(\nabla^2 v\right) \qquad (2)$$

$$w_t + uw_x + vw_y + ww_z =$$
$$-\psi_z + \left(Re^{-1} + \nu_t\right)\left(\nabla^2 w\right).$$

Here, $u = u(x,y,z,t)$, $v = v(x,y,z,t)$ and $w = w(x,y,z,t)$ are the mean total velocity components in the x, y and z directions. All lengths and velocities are nondimensionalized by the ship length L and the free stream velocity U, respectively. The pressure ψ is the static pressure p minus the hydrostatic component $-zFr^{-2}$ and may be expressed as $\psi = p + zFr^{-2}$, where $Fr = \frac{U}{\sqrt{gL}}$ is the Froude number. The pressure variable ψ is nondimensionalized by ρU^2. The Reynolds number Re is defined by $Re = \frac{UL}{\nu}$ where ν is the kinematic viscosity of water and is constant. ν_t is the dimensionless turbulent eddy viscosity, computed locally using the Baldwin-Lomax turbulence model. This set of equations shall be solved subject to the following boundary conditions.

2.2 Boundary Conditions

2.2.1 Free Surface

When the effects of surface tension and viscosity are neglected, the boundary condition on the free surface consists of two equations. The first, the dynamic condition, states that the pressure acting on the free surface is constant. The second, the kinematic condition, states that the free surface is a material surface: once a fluid particle is on the free surface, it forever remains on the surface. The dynamic and kinematic boundary conditions may be expressed as

$$p = constant$$

$$\frac{d\beta}{dt} = w = \beta_t + u\beta_x + v\beta_y \qquad (3)$$

where $z = \beta(x,y,t)$ is the free surface location. Equation 3 only permits solutions where β is single valued. Consequently, it does not allow for the breaking of bow waves which can often be observed with cruiser type hulls. Breaking waves are difficult to treat numerically and are not considered in this work.

2.2.2 Hull and Farfield

The remaining boundaries consist of the ship hull, the boundaries which comprise the symmetry portions of the meridian plane and the far field of the computational domain. On the ship hull, the condition is that of no-slip and is stated simply by

$$u = v = w = 0.$$

On the symmetry plane (that portion of the (x,z) plane excluding the ship hull) derivatives in the y direction as well as the v component of velocity are set to zero. The upstream plane has $u = U$ and $\psi = 0$ ($p = -zFr^{-2}$) with the v and w velocity components set to zero. Similar conditions hold on the bottom plane which is assumed to represent infinitely deep water where no disturbances are felt. One-sided differences are used to update the flow variables on the starboard plane. A radiation condition should be imposed on the outflow domain to allow the wave disturbance to pass out of the computational domain. Although fairly sophisticated formulations may be devised to represent the radiation condition, simple extrapolations proved to be sufficient in this work.

2.3 Turbulence Model

To model turbulence in the flow field the laminar viscosity is replaced by

$$\mu = \mu_l + \mu_t$$

where the turbulent viscosity μ_t is computed using the algebraic model of Baldwin and Lomax [22]. The Baldwin-Lomax model is an algebraic scheme that makes use of a two-layer, isotropic eddy viscosity formulation. In this model the turbulent viscosity is evaluated using

$$\mu_t = \begin{cases} (\mu_t)_{inner} & y \le y_{crossover} \\ (\mu_t)_{outer} & y > y_{crossover} \end{cases}$$

157

where y is the distance measured normal to the body surface and $y_{crossover}$ is the minimum value of y where both the inner and outer viscosities match. The inner viscosity follows the Prandtl-Van Driest formula,

$$(\mu_t)_{inner} = l^2 |\omega|$$

where

$$l = ky \left[1 - exp(-y^+/A^+)\right]$$

is the turbulent length scale for the inner region, k and A^+ are model constants, $|\omega|$ is the vorticity magnitude and $y^+ = (\tau_w/\mu_w)y$ is the dimensionless distance to the wall in wall units.

In the outer region of the boundary layer, the turbulent viscosity is given by

$$(\mu_t)_{outer} = KC_{cp}F_{wake}F_{Kleb}$$

where K and C_{cp} are model constants, the function F_{wake} is

$$F_{wake} = min\left(y_{max}F_{max}, C_{wk}y_{max}U_{dif}^2/F_{max}\right)$$

and the function F_{Kleb} is

$$F_{Kleb} = \left[1 + 5.5\left(\frac{C_{Kleb}y}{y_{max}}\right)^6\right]^{-1}.$$

The quantities F_{max} and y_{max} are determined by the value and corresponding location, respectively, of the maximum of the function

$$F = y|\omega|\left[1 - exp(-y^+/A^+)\right].$$

The quantity U_{dif} is the difference between maximum and minimum velocity magnitudes in the profile and is expressed as

$$U_{dif} = (u^2 + v^2 + w^2)_{max}^{1/2} - (u^2 + v^2 + w^2)_{min}^{1/2}$$

C_{Kleb} and C_{wk} are additional model constants. Numerical values for the model constants used in the computations are listed here:

$$A^+ = 26,\ k = 0.4,\ K = 0.0168,$$

and

$$C_{cp} = 1.6,\ C_{wk} = 1.0,\ C_{Kleb} = 0.3.$$

3 Numerical Solution

The formulation of the numerical solution procedure is based on a finite volume method (FVM) for the bulk flow variables (u, v, w and ψ), coupled to a finite difference method for the free surface evolution variables (β and ψ). Alternative cell-centered and cell-vertex formulations may be used in finite volume schemes [16]. A cell-vertex formulation was preferred in this work because values of the flow variables are needed on the boundary to implement the free surface boundary condition. The bulk flow is solved subject to Dirichlet conditions for the free surface pressure, followed by a free surface update via the bulk flow solution (ie. constant values for the velocities in equation 3). Each formulation is explicit and uses local time stepping. Both multigrid and residual averaging techniques are used in the bulk flow to accelerate convergence.

3.1 Bulk Flow Solution

Following Chorin [9] and more recently Yang et al. [23], the governing set of incompressible flow equations may be written in vector form as

$$\mathbf{w}_{t^*} + (\mathbf{f} - \mathbf{f_v})_x + (\mathbf{g} - \mathbf{g_v})_y + (\mathbf{h} - \mathbf{h_v})_z = 0 \quad (4)$$

where the vector of dependent variables $\mathbf{w}$ and inviscid flux vectors $\mathbf{f}$, $\mathbf{g}$ and $\mathbf{h}$ are given by

$$\begin{aligned}
\mathbf{w} &= [\psi,\ u,\ v,\ w]^T \\
\mathbf{f} &= [\Gamma^2 u,\ u^2 + \psi,\ uv,\ uw]^T \\
\mathbf{g} &= [\Gamma^2 v,\ vu,\ v^2 + \psi,\ vw]^T \\
\mathbf{h} &= [\Gamma^2 w,\ wu,\ wv,\ w^2 + \psi]^T.
\end{aligned}$$

The viscous flux vectors $\mathbf{f_v}$, $\mathbf{g_v}$ and $\mathbf{h_v}$ are given by

$$\begin{aligned}
\mathbf{f_v} &= [0,\ \tau_{xx},\ \tau_{xy},\ \tau_{xz}]^T \\
\mathbf{g_v} &= [0,\ \tau_{yx},\ \tau_{yy},\ \tau_{yz}]^T \\
\mathbf{h_v} &= [0,\ \tau_{zx},\ \tau_{zy},\ \tau_{zz}]^T
\end{aligned}$$

where the viscous stress components are defined as

$$\begin{aligned}
\tau_{xx} &= (Re^{-1} + \nu_t)(2u_x - 2/3(u_x + v_y + w_z)) \\
\tau_{yy} &= (Re^{-1} + \nu_t)(2v_y - 2/3(u_x + v_y + w_z)) \\
\tau_{zz} &= (Re^{-1} + \nu_t)(2w_z - 2/3(u_x + v_y + w_z)) \\
\tau_{xy} &= (Re^{-1} + \nu_t)(u_y + v_x) \\
\tau_{yz} &= (Re^{-1} + \nu_t)(v_z + w_y) \\
\tau_{zx} &= (Re^{-1} + \nu_t)(w_x + u_z).
\end{aligned}$$

Γ is called the "artificial compressibility" parameter due to the analogy that may be drawn between the above equations and the equations of

motion for a compressible fluid whose equation of state is given by [9]

$$\psi = \Gamma^2 \rho.$$

Thus, ρ is an artificial density and Γ may be referred to as an artificial sound speed. When the temporal derivatives tend to zero, the set of equations satisfy precisely the incompressible equations 2, with the consequence that the correct pressure may be established using the artificial compressibility formulation. The artificial compressibility parameter may be viewed as a device to create a well posed system of hyperbolic equations that are to be integrated to steady state along lines similar to the well established compressible flow FVM formulation [18]. In addition, the artificial compressibility parameter may be viewed as a relaxation parameter for the pressure iteration. Note that temporal derivatives are now denoted by t^* to indicate pseudo time; the artificial compressibility, as formulated in the present work, destroys time accuracy.

To demonstrate the effect of Γ on the above set of equations and to establish the hyperbolicity of the set, the convective part of equation 4 may be written in quasi-linear form to determine the eigenvalues [10]. The eigenvalues are found to be

$$\lambda_1 = U, \quad \lambda_2 = U, \quad \lambda_3 = U + a, \quad \lambda_4 = U - a,$$

where

$$U = u\omega_x + v\omega_y + w\omega_z$$

and

$$a^2 = U^2 + \Gamma^2(\omega_x^2 + \omega_y^2 + \omega_z^2).$$

The wave number components ω_x, ω_y and ω_z are defined on $-\infty \le \omega_x, \omega_y, \omega_z \le +\infty$. Since the eigenvalues are clearly real for any value of ω_x, ω_y and ω_z, the system of equations 4 is hyperbolic.

The choice of Γ is crucial in determining convergence and stability properties of the numerical scheme. Typically, the convergence rate of the scheme is dictated by the slowest system waves and the stability of the scheme by the fastest. In the limit of large Γ the difference in wave speeds can be large. Although this situation would presumably lead to a more accurate solution through the "penalty effect" in the pressure equation, very small time steps would be required to ensure stability. Conversely, for small Γ, the difference in the maximum and minimum wave speeds may be significantly reduced, but

at the expense of accuracy. Thus a compromise between the two extremes is required. Following the work of Dreyer [11], the choice for Γ is taken to be

$$\Gamma^2 = \gamma(u^2 + v^2 + w^2),$$

where γ is a constant of order unity. In regions of high velocity and low pressure where suction occurs, Γ is large to improve accuracy, and in regions of lower velocity, Γ is correspondingly reduced.

The choice of Γ also influences the outflow boundary condition, or radiation condition. If it can be demonstrated that all system eigenvalues are both real and positive, then downstream or outflow boundary points may be extrapolated from the interior upstream flow. Even though an examination of the eigenvalues reveals that this can never be the case, the condition can be approached by a judicious choice of Γ. If Γ is large, extrapolation fails because the flow has both downstream and upstream dependence. As Γ is reduced, the upstream dependence becomes more pronounced and the downstream is reduced. Eventually, the upstream dependence is sufficiently dominant to allow extrapolation. Hence, all outflow variables are updated using zero gradient extrapolation.

Following the general procedures for FVM, the governing equations may be integrated over an arbitrary volume Λ. Application of the divergence theorem on the convective and viscous flux term integrals yields

$$\frac{\partial}{\partial t^*} \int_\Lambda \mathbf{w}\, d\Lambda +$$

$$\int_{\partial\Lambda} (\mathbf{f}\, dS_x + \mathbf{g}\, dS_y + \mathbf{h}\, dS_z) -$$

$$\int_{\partial\Lambda} (\mathbf{f_v}\, dS_x + \mathbf{g_v}\, dS_y + \mathbf{h_v}\, dS_z) = 0 \quad (5)$$

where S_x, S_y and S_z are the projected areas in the x, y and z directions, respectively. The computational domain is divided into hexahedral cells. Application of FVM to each of the computational cells results in the following system of ordinary differential equations,

$$\frac{d}{dt^*} (\Lambda_{ijk}\mathbf{w}) + C_{ijk} - V_{ijk} = 0.$$

The volume Λ_{ijk} is given by the summation of the eight cells surrounding node i,j,k. The convective flux $C_{ijk}(\mathbf{w})$ is defined as

$$C_{ijk}(\mathbf{w}) = \sum_{k=1}^{n} (\mathbf{f}S_x + \mathbf{g}S_y + \mathbf{h}S_z)_k \quad (6)$$

159

and the viscous flux $V_{ijk}(\mathbf{w})$ is defined as

$$V_{ijk}(\mathbf{w}) = \sum_{k=1}^{n} (\mathbf{f_V} S_x + \mathbf{g_V} S_y + \mathbf{h_V} S_z)_k \quad (7)$$

where the summation is over the n faces surrounding Λ_{ijk}.

The projected areas may be computed by taking the cross product of the two vectors joining opposite corners of each cell face in the physical coordinate system. They correspond to the grid metrics $J\xi_x$, $J\xi_y$, $J\xi_z$, etc. appearing in a transformation to a curvilinear coordinate system $\xi = \xi(x,y,z)$, $\eta = \eta(x,y,z)$ and $\zeta = \zeta(x,y,z)$ where J is the Jacobian of the transformation. The flow variables required in the flux evaluation may be averaged on each cell face through the four nodal values associated with each face. Evaluation of the flux terms in equations 6 and 7 may be performed directly, without direct differentiation and without the need to handle grid singularities in a special fashion.

3.1.1 Artificial Dissipation

This scheme reduces to a second order accurate, nondissipative central difference approximation to the bulk flow equations on sufficiently smooth grids. A central difference scheme permits odd-even decoupling at adjacent nodes which may lead to oscillatory solutions. To prevent this "unphysical" phenomena from occurring, a dissipation term is added to the system of equations such that the system now becomes

$$\frac{d}{dt^*}(\Lambda_{ijk}\mathbf{w})+$$
$$[C_{ijk}(\mathbf{w}) - V_{ijk}(\mathbf{w}) - D_{ijk}(\mathbf{w})] = 0. \quad (8)$$

For the present problem a third order background dissipation term is added. The dissipative term is constructed in such a manner that the conservation form of the system of equations is preserved. The dissipation has the form

$$D_{ijk}(\mathbf{w}) = D_\xi + D_\eta + D_\zeta \quad (9)$$

where

$$D_{\xi_{ijk}} = d_{\xi_{i+1,j,k}} - d_{\xi_{i,j,k}}$$

and

$$d_{\xi_{i,j,k}} = \alpha \delta_\xi^2 (\mathbf{w}_{i+1,j,k} - \mathbf{w}_{i,j,k}). \quad (10)$$

Similar expressions may be written for the η and ζ directions with δ_ξ^2, δ_η^2 and δ_ζ^2 representing second difference central operators.

In equation 10, the dissipation coefficient α is a scaling factor proportional to the local wave speed, and renders equation 9 third order in truncation terms so as not to detract from the second order accuracy of the flux discretization. The actual form for the coefficient is based on the spectral radius of the system and is given in the ζ direction as

$$\alpha = \epsilon(J|\tilde{u}| + \Gamma(S_x^2 + S_y^2 + S_z^2)^{1/2})$$

where $\tilde{u}$ is the contravariant velocity component

$$\tilde{u} = u\xi_x + v\xi_y + w\xi_z.$$

Similar dissipation coefficients are used for the η and ζ components in equation 9. The ϵ term is used to manually adjust the amount of dissipation.

3.1.2 Viscous Discretization

The discretization for the viscous fluxes follows the guidelines originally proposed in [24, 25] for the simulation of two dimensional viscous flows. The components of the stress tensor are computed at the cell centers with the aid of Gauss' formula. The viscous fluxes are then computed by making use of an auxiliary cell bounded by the faces lying on the planes containing the centers of the cells surrounding a given vertex and the mid-lines of the cell faces. For example, the u_x term in τ_{xx} may be computed from

$$u_x \Lambda = \int_\Lambda u_x d\Lambda = \int_{\partial\Lambda} u\,d\partial\Lambda_x \approx \sum_{k=1}^{6} u_k S_{x_k}$$

where $k = 1,6$ are the six faces surrounding a particular cell, u_k is an average of the velocities from the nodes that define the kth face and S_{x_k} are the projected areas in the x direction corresponding to each face. Once the components of the complete stress tensor are computed at the centroids of the cells then the same method of evaluation may be used to compute the viscous fluxes at the vertex through use of equation 7. For this purpose the control volume is now constructed by assembling $\frac{1}{8}$ fractions of each of the eight cells surrounding a particular vertex. The equivalent two dimensional control volume is sketched in the figure below. This discretization procedure is designed to minimize the error induced by a kink in the grid. It has proved to be accurate and efficient in applications to the solution of three dimensional compressible viscous flows [26, 27].

160
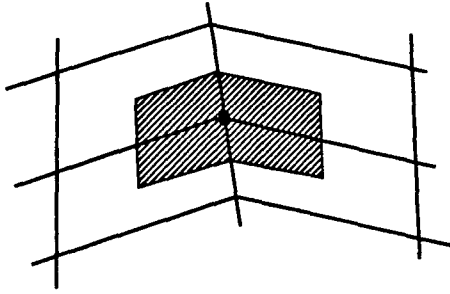
3.1.3 Time Integration

Equation 8 is integrated in time by an explicit multistage scheme. For each bulk flow time step, the grid, and thus Λ_{ijk}, is independent of time. Hence equation 8 can be written as

$$\frac{d\mathbf{w}_{ijk}}{dt^*} + R_{ijk}(\mathbf{w}) = 0, \qquad (11)$$

where the residual is defined as

$$R_{ijk}(\mathbf{w}) = C_{ijk}(\mathbf{w}) - V_{ijk}(\mathbf{w}) - D_{ijk}(\mathbf{w}),$$

and the cell volume Λ_{ijk} absorbed into the residual for clarity. If one analyzes a linear model problem corresponding to (11) by substituting a Fourier mode $\hat{w} = e^{ipx_j}$, the resulting Fourier symbol has an imaginary part proportional to the wave speed, and a negative real part proportional to the diffusion. Thus the time stepping scheme should have a stability region which contains a substantial interval of the negative real axis, as well as an interval along the imaginary axis. To achieve this it pays to treat the convective and dissipative terms in a distinct fashion. Thus the residual is split as

$$R_{ijk}(\mathbf{w}) = C_{ijk}(\mathbf{w}) + \mathcal{D}_{ijk}(\mathbf{w})$$

where $C_{ijk}(\mathbf{w})$ is the convective part and $\mathcal{D}_{ijk}(\mathbf{w}) = -(V_{ijk} + D_{ijk})$ the dissipative part. Denote the time level $n\Delta t$ by a superscript n, and drop the subscript for clarity. Then the multistage time stepping scheme is formulated as

$$\mathbf{w}^{(n+1,0)} = \mathbf{w}^n$$
$$\dots$$
$$\mathbf{w}^{(n+1,k)} = \mathbf{w}^n - \alpha_k \Delta t \left(C^{(k-1)} + \mathcal{D}^{(k-1)} \right)$$
$$\dots$$
$$\mathbf{w}^{n+1} = \mathbf{w}^{(n+1,m)}$$

where the superscript k denotes the k-th stage, $\alpha_m = 1$, and

$$C^{(0)} = C(\mathbf{w}^n), \quad \mathcal{D}^{(0)} = \mathcal{D}(\mathbf{w}^n)$$
$$\dots$$
$$C^{(k)} = C\left(\mathbf{w}^{(n+1,k)}\right)$$
$$\mathcal{D}^{(k)} = \beta_k \mathcal{D}\left(\mathbf{w}^{(n+1,k)}\right) + (1 - \beta_k)\mathcal{D}^{(k-1)}$$

The coefficients α_k are chosen to maximize the stability interval along the imaginary axis, and the coefficients β_k are chosen to increase the stability interval along the negative real axis.

A five-stage scheme with three evaluations of dissipation has been found to be particularly effective. Its coefficients are

$$
\begin{aligned}
\alpha_1 &= 1/4 & \beta_1 &= 1 \\
\alpha_2 &= 1/6 & \beta_2 &= 0 \\
\alpha_3 &= 3/8 & \beta_3 &= 0.56 \\
\alpha_4 &= 1/2 & \beta_4 &= 0 \\
\alpha_5 &= 1 & \beta_5 &= 0.44
\end{aligned}
$$

The actual time step Δt is limited by the Courant number (CFL), which states that the fastest waves in the system may not be allowed to propagate farther than the smallest grid spacing over the course of a time step. In this work, local time stepping is used such that regions of large grid spacing are permitted to have relatively larger time steps than regions of small grid spacing. Of course the system wave speeds vary locally and must be taken into account as well. The final local time step is thus computed as,

$$\Delta t^*_{ijk} = \frac{(CFL)\Lambda_{ijk}}{\lambda_{ijk}}$$

where λ_{ijk} is the sum of the spectral radii of both the convective and viscous flux Jacobian matrices in the x, y and z directions. In regions of small grid spacing and/or regions of high characteristic wave speeds, the time step will be smaller than elsewhere.

3.1.4 Residual Averaging

The allowable Courant number may be increased by smoothing the residuals at each stage using the following product form in three dimensions [18]

$$(1 - \epsilon_\xi \delta_\xi^2)(1 - \epsilon_\eta \delta_\eta^2)(1 - \epsilon_\zeta \delta_\zeta^2)\bar{R} = R$$

where ϵ_ξ, ϵ_η and ϵ_ζ are smoothing coefficients and the $\delta_{\xi,\eta,\zeta}^2$ are central difference operators in computational coordinates. Each residual R_{ijk} is thus replaced by an average of itself and the neighboring residuals.

161

3.1.5 Multigrid Scheme

Very rapid convergence to a steady state is achieved with the aid of a multigrid procedure. The idea behind the multigrid strategy is to accelerate evolution of the system of equations on the fine grid by introducing auxiliary calculations on a series of coarser grids. The coarser grid calculations introduce larger scales and larger time steps with the result that low-frequency error components may be efficiently and rapidly damped out. Auxiliary grids are introduced by doubling the grid spacing, and values of the flow variables are transferred to a coarser grid by the rule

$$\mathbf{w}_{2h}^{(0)} = T_{2h,h}\mathbf{w}_h,$$

where the subscripts denote values of the grid spacing parameter (ie. h is the finest grid, $2h$, $4h$, ... are successively coarser grids) and $T_{2h,h}$ is a transfer operator from a fine grid to a coarse grid. The transfer operator picks flow variable data at alternate points to define coarser grid data as well as the coarser grid itself. A forcing term is then defined as

$$\mathbf{P}_{2h} = \sum R_h(\mathbf{w}_h) - R_{2h}(\mathbf{w}_{2h}^{(0)}),$$

where R is the residual of the difference scheme. To update the solution on the coarse grid, the multistage scheme is reformulated as

$$\mathbf{w}_{2h}^{(1)} = \mathbf{w}_{2h}^{(0)} - \alpha_1 \Delta t^*(R_{2h}^{(0)} + P_{2h})$$
$$\cdots$$
$$\mathbf{w}_{2h}^{(q+1)} = \mathbf{w}_{2h}^{(0)} - \alpha_q \Delta t^*(R_{2h}^{(q)} + P_{2h})$$
$$\cdots$$

where $R^{(q)}$ is the residual of the qth stage. In the first stage, the addition of P_{2h} cancels $R_{2h}(\mathbf{w}^{(0)})$ and replaces it by $\sum R_h(\mathbf{w}_h)$, with the result that the evolution on the coarse grid is driven by the residual on the fine grid. The result $\mathbf{w}_{2h}^{(m)}$ now provides the initial data for the next grid $\mathbf{w}_{4h}^{(0)}$ and so on. Once the last grid has has been reached, the accumulated correction must be passed back through successively finer grids. Assuming a three grid scheme, let $\mathbf{w}_{4h}^{(+)}$ represent the final value of $\mathbf{w}_{4h}$. Then the correction for the next finer grid will be

$$\mathbf{w}_{2h}^{(+)} = \mathbf{w}_{2h}^{(m)} + I_{2h,4h}(\mathbf{w}_{4h}^{(+)} - \mathbf{w}_{4h}^{(0)}),$$

where $I_{a,b}$ is an interpolation operator from the coarse grid to the next finer grid. The final result on the fine grid is obtained in the same manner:

$$\mathbf{w}_h^{(+)} = \mathbf{w}_h^{(m)} + I_{h,2h}(\mathbf{w}_{2h}^{(+)} - \mathbf{w}_{2h}^{(0)}).$$

The process may be performed on any number of successively coarser grids. The only restriction in the present work being use of a structured grid whereby elements of the coarsest grid do not overlap the ship hull. A 4-level "W-cycle" is used in the present work for each time step on the fine grid [18].

3.1.6 Grid Refinement

The multigrid acceleration procedure is embedded in a grid refinement procedure to further reduce the computer time required to achieve steady state solutions on finely resolved grids. In the grid refinement procedure the flow equations are solved on coarse grids in the early stages of the simulation. The coarse grids permit large time steps, and the flow field and the wave pattern evolve quite rapidly. When the wave pattern approaches a steady state, the grid is refined by doubling the number of grid points in all directions and the flow variables and free surface location are interpolated onto the new grid. Computations then continue using the finer grid with smaller time steps. The multigrid procedure is applied at all stages of the grid refinement to accelerate the calculations on each grid in the sequence, producing a composite "full multigrid" scheme which is extremely efficient.

3.2 Free Surface Solution

Both a kinematic and dynamic boundary condition must be imposed at the free surface. For the fully nonlinear condition, the free surface must move with the flow (ie. up or down corresponding to the wave height and location) and the boundary conditions applied on the distorted free surface. Equation 3 can be cast in a form more amenable to numerical computations by introducing a curvilinear coordinate system that transforms the curved free surface $\beta(x,y)$ into computational coordinates $\beta(\xi,\eta)$. This results in the following transformed kinematic condition

$$\beta_{t^*} + \tilde{u}\beta_\xi + \tilde{v}\beta_\eta = w, \qquad (12)$$

where $\tilde{u}$ and $\tilde{v}$ are contravariant velocity components given by

$$\tilde{u} = u\xi_x + v\xi_y$$

$$\tilde{v} = u\eta_x + v\eta_y.$$

162

The free surface kinematic equation may now be expressed as

$$\frac{d\beta_{ij}}{dt^*} + Q_{ij}(\beta) = 0$$

where $Q_{ij}(\beta)$ consists of the collection of velocity and spacial gradient terms which result from the discretization of equation 12. Note that this is not the result of a volume integration and thus the volume (or actually area) term does not appear in the residual as in the FVM formulation. Throughout the interior of the (x, y) plane, all derivatives are computed using the second order centered difference stencil in computational coordinates ξ and η. On the boundaries a second order centered stencil is used along the boundary tangent and a first order one sided difference stencil is used in the boundary normal direction.

As was necessary in the FVM formulation for the bulk flow, background dissipation must be added to prevent decoupling of the solution. The method used to compute the dissipative terms borrows from a two dimensional FVM formulation and appears as follows:

$$D_{ij} = D_\xi + D_\eta$$

where

$$D_{\xi_{ij}} = d_{\xi_{i+1,j}} - d_{\xi_{i,j}}$$

and

$$d_{\xi_{i,j}} = \alpha \delta_\xi^2 (\beta_{i+1,j} - \beta_{i,j}).$$

The expression for α may be written as

$$\alpha = \epsilon(|\tilde{u}_{i+1,j}| + |\tilde{u}_{i,j}|)J$$

where J is the sum of the cell Jacobians and ϵ is used to manually adjust the amount of dissipation. Hence the system of equations for the free surface is expressed as

$$\frac{d\beta_{ij}}{dt^*} + R_{ij}(\beta) = 0$$

where

$$R_{ij} = Q_{ij} - D_{ij}.$$

The same scheme used to integrate equation 11 is also used here. Once the free surface update is accomplished the pressure is adjusted on the free surface such that

$$\psi^{(n+1)} = \beta^{(n+1)} Fr^{-2}.$$

The free surface and the bulk flow solutions are coupled by first computing the bulk flow at each time step, and then using the bulk flow velocities to calculate the movement of the free surface. After the free surface is updated, its new values are used as a boundary condition for the pressure on the bulk flow for the next time step. The entire iterative process, in which both the bulk flow and the free surface are updated at each time step, is repeated until some measure of convergence is attained; usually steady state wave profile and wave resistance coefficient.

Since the free surface is a material surface, the flow must be tangent to it in the final steady state. During the iterations, however, the flow is allowed to *leak* through the surface as the solution evolves towards the steady state. This leakage, in effect, drives the evolution equation. Suppose that at some stage, the vertical velocity component w is positive (cf. equation 3 or 12). Provided that the other terms are small, this will force β^{n+1} to be greater than β^n. When the time step is complete, ψ is adjusted such that $\psi^{n+1} > \psi^n$. Since the free surface has moved farther away from the original undisturbed upstream elevation and the pressure correspondingly increased, the velocity component w (or better still $\mathbf{q} \cdot \mathbf{n}$ where $\mathbf{n} = \frac{\nabla F}{|\nabla F|}$ and $F = z - \beta(x, y)$) will then be reduced. This results in a smaller $\Delta\beta$ for the next time step. The same is true for negative vertical velocity, in which case there is mass leakage into the system rather than out. Only when steady state has been reached is the mass flux through the surface zero and tangency enforced. In fact, the residual flux leakage could be used in addition to drag components and pressure residuals as a measure of convergence to the steady state.

This method of updating the free surface works well for the Euler equations since tangency along the hull can be easily enforced. However, for the Navier-Stokes equations the no-slip boundary condition is inconsistent with the free surface boundary condition at the hull/waterline intersection. To circumvent this difficulty the computed elevation for the second row of grid points away from the hull is extrapolated to the hull. Since the minimum spacing normal to the hull is small, the error due to this should be correspondingly small, comparable with other discretization errors. The treatment of this intersection for the Navier-Stokes calculations, should be the subject of future research to find the most accurate possible procedure.

163

4 Results

4.1 Computational Conditions

Figures 2 and 3 show portions of the fine grids used for the Navier-Stokes calculations. The number of grid points is 193, 65 and 49 in the x, y and z-directions respectively, and the $H-H$ type grid is used. Grid points are clustered near the bow and stern with a minimum spacing of 0.005 dimensionless units based on the hull length. The grid extends $\frac{1}{2}$ ship length upstream from the bow, $1\frac{1}{2}$ ship lengths downstream from the stern, $1\frac{1}{2}$ ship lengths to starboard, and 1 ship length down below the undisturbed free surface. The minimum spacing in the y-direction, normal to the hull surface, is 0.0001 for the Navier-Stokes computations and 0.0025 for the Euler computations. The resolution on the hull surface is 97 by 17 for the Wigley hull and 97 by 25 for the Series 60. Only the number of grid points in the y-direction is changed for the Euler calculations; rather than 65 the number is 49.

The following subsections present the computational results for the Wigley hull and the Series 60, $C_b = 0.6$ hull.

4.2 Wigley Hull

Figures 4 through 9 display computed and experimental results for the Wigley hull at Froude numbers 0.250 and 0.289. Both the Euler and the Navier-Stokes results for the waterline profile along the hull show good agreement with the experimental data [28]. Discrepancies are noted in the stern region where the Navier-Stokes model produces a slight flattening of the wave profile but correctly captures the aft-most waterline elevation, whereas the Euler model shows no tendency to flatten the wave profile but incorrectly predicts the aft-most waterline elevation. The computed wave drag (cf. fig. 5), obtained by integrating the longitudinal component of pressure on the wetted hull surface, shows favorable agreement with the experimentally determined value, $C_{w(exp)} = 0.821$. The experimental wave drag is inferred by subtracting an estimate of the friction drag from the total drag or by wave analysis. Note that the computed wave drag is evaluated after each multigrid cycle and hence the evolution of the drag is plotted vs. the steady state drag (marked by the x's) determined experimentally. The capital letters C, M and F refer to coarse, medium and fine grids respectively in the grid refinement procedure. The comparisons

between computed overhead profiles show agreement between the two methods, except in the stern region and aft where viscous effects cause separation of the flow and a reduction in the amplitudes of the downstream waves (cf. fig. 6).

Essentially the same behavior is noted for the Fr = 0.289 case in the next set of figures. The waterline profile is predicted almost exactly for the Navier-Stokes simulation whereas the Euler case predicts a lower waterline level at the stern region. The computed values of the wave drag are in good agreement with the experimentally determined value $C_{w,exp} = 1.18$.

Figures 11 and 10 are included to show the computed velocity profile at the hull/waterline intersection. The prediction of separation is clearly evident in the stern region of the hull.

4.3 Series 60, $C_b = 0.6$ Hull

In contrast to the Wigley hull, which is an idealized shape, the Series 60 hull is a practical geometry for an actual ship hull. The only major difference in the method of computing the flow about this hull and the Wigley model is the effort required to maintain the proper hull shape as the grid is distorted by the moving free surface. To accomplish this, a grid is produced for the entire hull, both above and below the undisturbed free surface. Spline coefficients are then determined for the entire grid and stored. A new grid is then produced with the uppermost plane of points residing in the plane of the undisturbed waterline at $z = 0$. With the stored spline data the grid is now easily updated as the free surface evolves by redistributing points at intervals of equally spaced arc length. It was found that this method prevents the grid lines from crossing at the close tolerances required for the viscous computations.

The waterline contours shown in figure 12 are in reasonably good agreement for both the Euler and Navier-Stokes simulations. Except for the bow region, it appears that the Euler method does an equally good job, if not better, than the Navier-Stokes method. There is some discrepancy amidship in the Navier-Stokes computation which is possibly due to the method used to update points on the hull/waterline intersection set of points. However, as in the Wigley cases, the drag calculation is in good agreement with experiment ($C_{w,exp} = 2.6$) [29] and the overhead profiles show good agreement with each other.

164

5 Conclusions

The objective of the present work was to develop an efficient method to compute Euler and Navier-Stokes solutions for the nonlinear ship wave problem. The results for the Wigley hull and Series 60 hull suggest that the objective has been reached and the resulting computer code has been validated, at least for the range of test cases examined. The wave elevations predicted by the numerical simulations are in excellent agreement with the experimental measurements. In addition, the computed wave drag is in good agreement with the wave drag inferred from the experiments.

The Euler method, which requires significantly less computational resources than the Navier-Stokes method, produces results that appear to be within a reasonable degree of accuracy for engineering design work. As the present method is refined and improved, and applied to other geometries (such as submarines, sailing yachts and more practical stern flows), it is planned to continue the comparison between the two methods in order to establish the conditions under which the Euler method can be expected to give accurate results.

The computational times for the simulations are approximately 10 and 12 hours for the Euler calculations on the Wigley and Series 60 hulls, respectively, and approximately 18 hours for the Navier-Stokes calculations for both hulls. The Euler simulations consist of 100 steps on a $49 \times 13 \times 13$ grid, 200 steps on a $97 \times 25 \times 25$ grid and 200 steps on a $193 \times 49 \times 49$ grid. The Navier-Stokes simulations consist of 100 steps on a $49 \times 17 \times 13$ grid, 200 steps on a $97 \times 33 \times 25$ grid and 200 steps on a $193 \times 65 \times 49$ grid. These times were recorded in calculations using a single processor Convex 3400 computer with 64-bit arithmetic. For the given resolution they appear to represent about a ten-fold decrease in the CPU times reported in the earlier literature, which have usually been presented for coarser grids. The CPU time required for the free surface update and regriding procedures is approximately seven percent that required for the bulk flow calculations.

Acknowledgment

References

[1] Toda,Y., Stern,F., and Longo,J., "Mean-Flow Measurements in the Boundary Layer and Wake and Wave Field of a Series 60 $C_B = 0.6$ Ship Model–Part1: Froude Numbers 0.16 and 0.316," *Journal of Ship Research*, v. 36, n. 4, pp. 360-377, 1992.

[2] Longo,J., Stern,F., and Toda,Y., "Mean-Flow Measurements in the Boundary Layer and Wake and Wave Field of a Series 60 $C_B = 0.6$ Ship Model–Part2: Effects on Near-Field Wave Patterns and Comparisons with Inviscid Theory", *Journal of Ship Research*, v. 37, n. 1, pp. 16-24, 1993.

[3] Hino,T., "Computation of Free Surface Flow Around an Advancing Ship by the Navier-Stokes Equations", *Proceedings, Fifth International Conference on Numerical Ship Hydrodynamics*, pp. 103-117, 1989.

[4] Miyata,H., Toru,S., and Baba,N., "Difference Solution of a Viscous Flow with Free-Surface Wave about an Advancing Ship", *Journal of Computational Physics*, v. 72, pp. 393-421, 1987.

[5] Miyata,H., Zhu,M., and Wantanabe,O., "Numerical Study on a Viscous Flow with Free-Surface Waves About a Ship in Steady Straight Course by a Finite-Volume Method", *Journal of Ship Research*, v. 36, n. 4, pp. 332-345, 1992.

[6] Tahara,Y., Stern,F., and Rosen,B., "An Interactive Approach for Calculating Ship Boundary Layers and Wakes for Nonzero Froude Number", *Journal of Computational Physics*, v. 98, pp. 33-53, 1992.

[7] Chen,H.C., Patel,V.C., and Ju,S., "Solution of Reynolds-Averaged Navier-Stokes Equations for Three-Dimensional Incompressible Flows", *Journal of Computational Physics*, v. 88, pp. 305-336, 1990.

[8] Rosen,B.S., Laiosa,J.P., Davis,W.H., and Stavetski,D., "SPLASH Free-Surface Flow Code Methodology for Hydrodynamic Design and Analysis of IACC Yachts", *The Eleventh*

Chesapeake Sailing Yacht Symposium, Annapolis, MD, 1993.

[9] Chorin,A., "A Numerical Method for Solving Incompressible Viscous Flow Problems", *Journal of Computational Physics*, v. 2, pp. 12-26, 1967.

[10] Rizzi,A., and Eriksson,L., "Computation of Inviscid Incompressible Flow with Rotation", *Journal of Fluid Mechanics*, v. 153, pp. 275-312, 1985.

[11] Dreyer,J., "Finite Volume Solutions to the Unsteady Incompressible Euler Equations on Unstructured Triangular Meshes", M.S. Thesis, MAE Dept., Princeton University, 1990.

[12] Kodama,Y., "Grid Generation and Flow Computation for Practical Ship Hull Forms and Propellers Using the Geometrical Method and the IAF Scheme", *Proceedings, Fifth International Conference on Numerical Ship Hydrodynamics*, pp. 71-85, 1989.

[13] Turkel,E., "Preconditioned Methods for Solving the Incompressible and Low Speed Compressible Equations", ICASE Report 86-14, 1986.

[14] Jameson,A., Baker,T., and Weatherill,N., "Calculation of Inviscid Transonic Flow Over a Complete Aircraft", *AIAA Paper 86-0103, AIAA 24th Aerospace Sciences Meeting*, Reno, NV, January 1986.

[15] Jameson,A., "Computational Aerodynamics for Aircraft Design", *Science*, v. 245, pp. 361-371, 1989.

[16] Jameson,A., "Solution of the Euler Equations for Two Dimensional Transonic Flow by a Multigrid Method", *Applied Math. and Computation*, v. 13, pp. 327-356, 1983.

[17] Jameson, A., "Computational Transonics", *Comm. Pure Appl. Math.*, v. 41, pp. 507-549, 1988.

[18] Jameson,A., "A Vertex Based Multigrid Algorithm For Three Dimensional Compressible Flow Calculations", *ASME Symposium on Numerical Methods for Compressible Flows*, Anaheim, December 1986.

[19] Farmer,J., "A Finite Volume Multigrid Solution to the Three Dimensional Nonlinear Ship Wave Problem", Ph.D. Thesis, MAE 1949-T, Princeton University, January 1993.

[20] Farmer,J., Martinelli,L., and Jameson,A., "A Fast Multigrid Method for Solving Incompressible Hydrodynamic Problems with Free Surfaces", Accepted for publication in the AIAA Journal, 1993.

[21] Orlanski,I., "A Simple Boundary Condition for Unbounded Hyperbolic Flows", *Journal of Computational Physics*, v. 21, 1976.

[22] Baldwin,B.S., and Lomax,H., "Thin Layer Approximation and Algebraic Model for Separated Turbulent Flows", *AIAA Paper 78-257, AIAA 16th Aerospace Sciences Meeting*, Reno, NV, January 1978.

[23] Yang,C-I., Hartwich,P-M., and Sundaram,P., "Numerical Simulation of Three-Dimensional Viscous Flow around a Submersible Body", *Proceedings, Fifth International Conference on Numerical Ship Hydrodynamics*, pp. 59-69, 1989.

[24] Martinelli,L., "Calculations of Viscous Flows with a Multigrid Method", Ph.D. Thesis, MAE 1754-T, Princeton University, 1987.

[25] Martinelli,L. and Jameson,A., "Validation of a Multigrid Method for the Reynolds Averaged Equations", *AIAA Paper 88-0414, AIAA 26st Aerospace Sciences Meeting*, Reno, NV, January 1988.

[26] Liu,F. and Jameson,A., "Multigrid Navier-Stokes Calculations For Three-Dimensional Cascades", *AIAA Paper 92-0190, AIAA 30th Aerospace Sciences Meeting*, Reno, NV, January 1990.

[27] Martinelli,L., Jameson,A., and Malfa,E., "Numerical Simulation of Three-Dimensional Vortex Flows Over Delta Wing Configurations", *Lecture Notes in Physics, Volume 414. Thirteenth International Conference on Numerical Methods in Fluid Dynamics,*. M. Napolitano and F. Sabetta (Eds.), Rome, Italy, 1992.

[28] "Cooperative Experiments on Wigley Parabolic Models in Japan", *17th ITTC Resistance Committee Report*, 2nd ed., 1983.

[29] Toda,Y., Stern,F., and Longo,J., "Mean-Flow Measurements in the Boundary Layer and Wake and Wave Field of a Series 60 $C_B = 0.6$ Ship Model for Froude Numbers .16 and .316", IIHR Report No. 352, Iowa Institute of Hydraulic Research, The University of Iowa, Iowa City, Iowa, 1991.
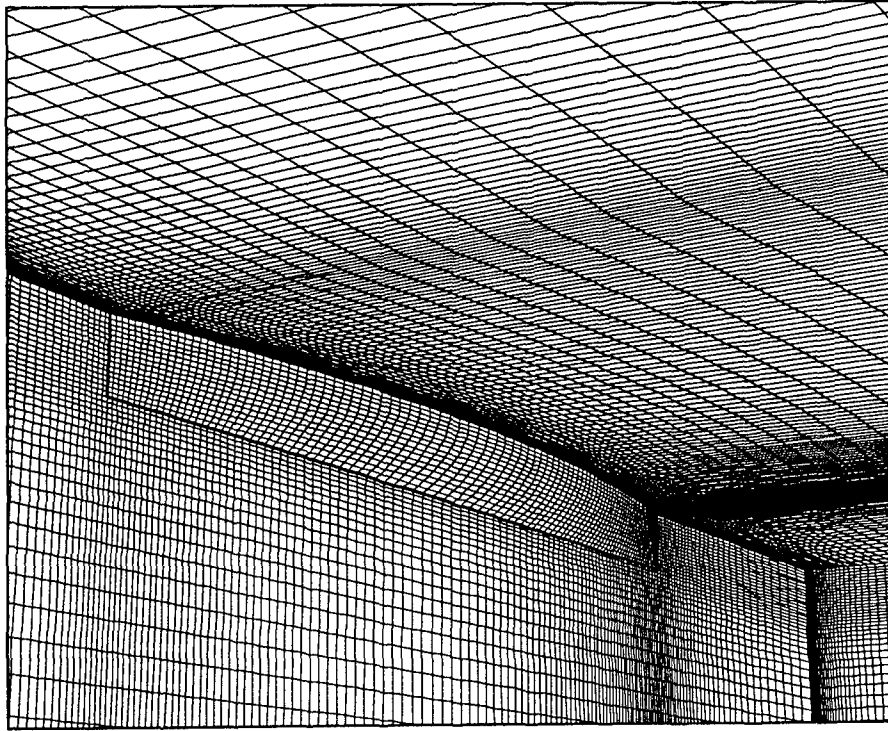
Figure 2: Fine Grid for Wigley Hull Navier-Stokes Computations ($193 \times 65 \times 49$)
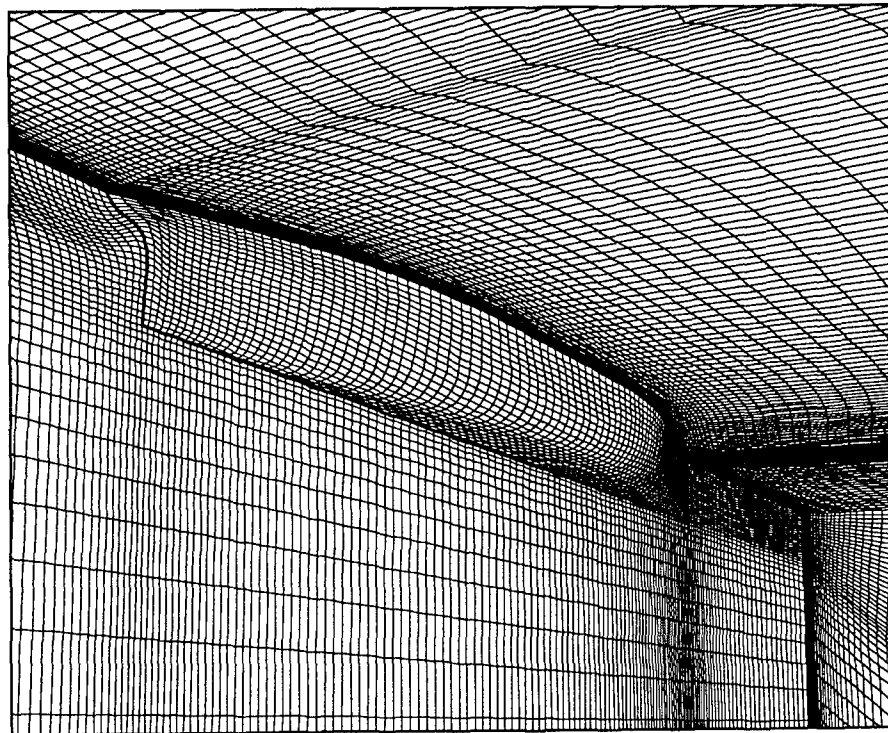
Figure 3: Fine Grid for Series 60, $C_b = 0.6$ Navier-Stokes Computations ($193 \times 65 \times 49$)

167
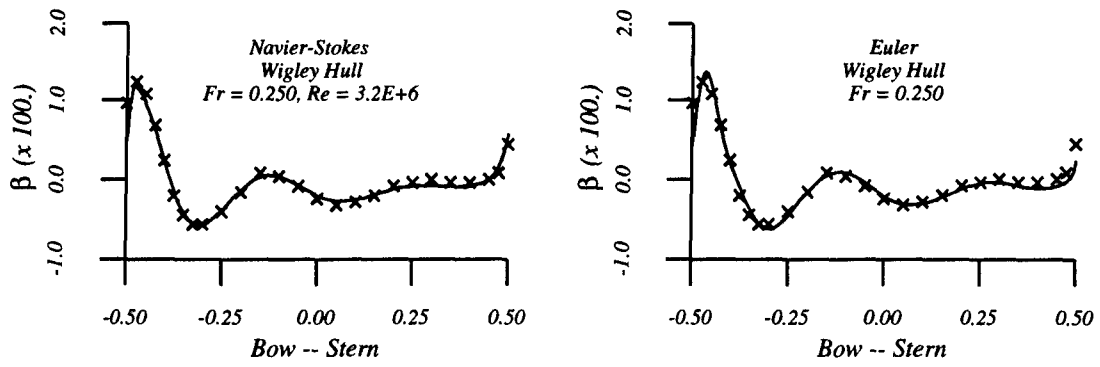
Figure 4: Computed vs. Experimental Wave Elevation
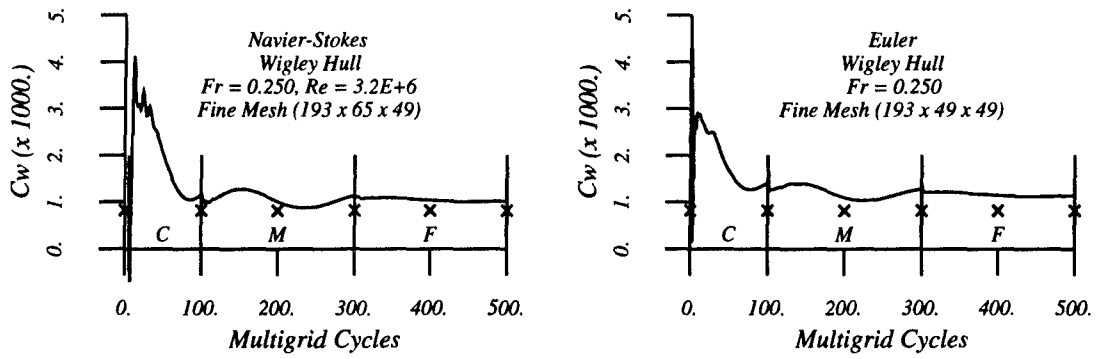
Figure 5: Computed vs. Experimental Wave Drag
C = Coarse Mesh, M = Medium Mesh, F = Fine Mesh
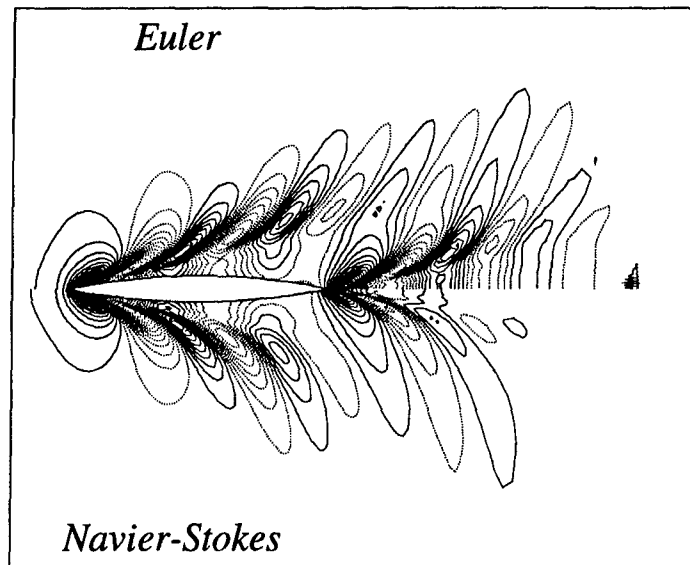
Figure 6: Comparison of Computed Overhead Wave Profiles, Wigley Hull, Fr = 0.250
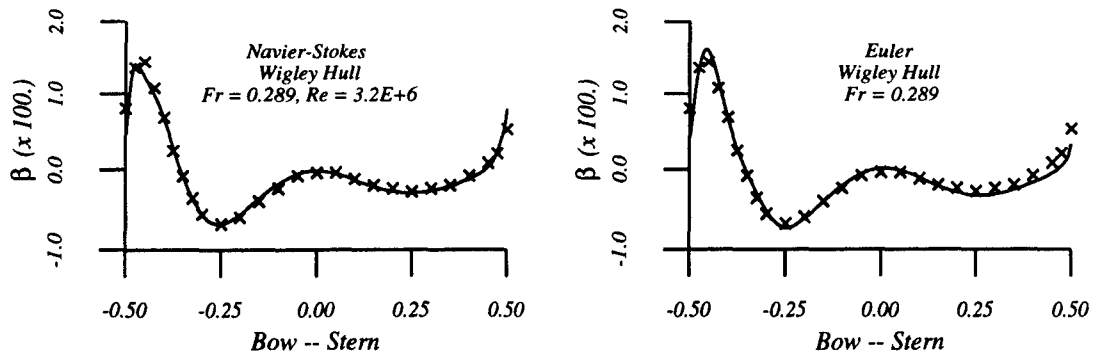
Figure 7: Computed vs. Experimental Wave Elevation
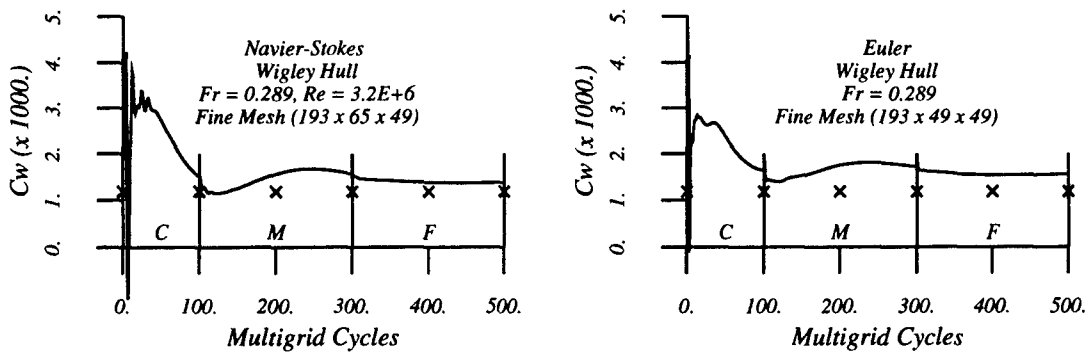
Figure 8: Computed vs. Experimental Wave Drag
C = Coarse Mesh, M = Medium Mesh, F = Fine Mesh
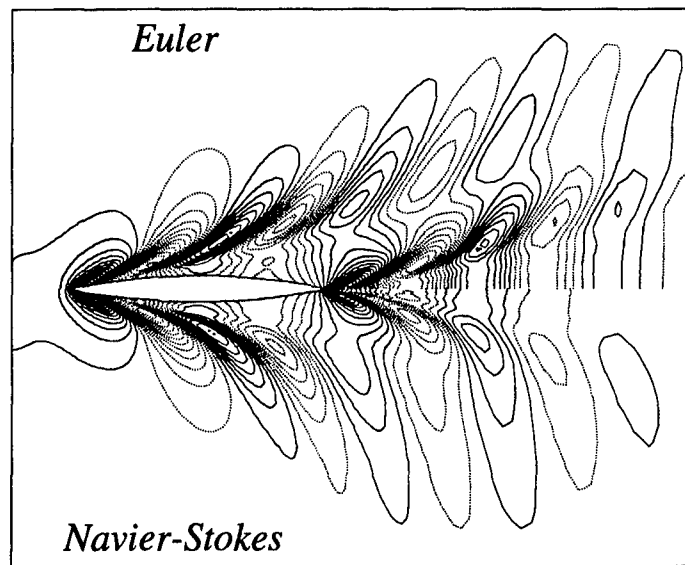
Figure 9: Comparison of Computed Overhead Wave Profiles, Wigley Hull, Fr = 0.289

169
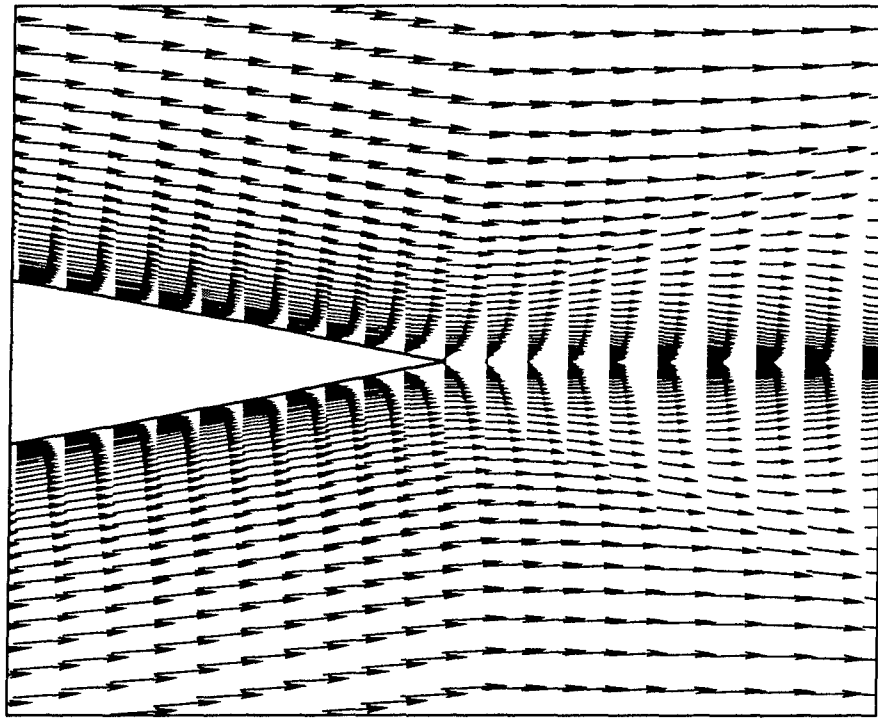
Figure 10: Velocity Vectors, Wigley Hull Stern Region, Fr = 0.289, Re = 3.2E+06
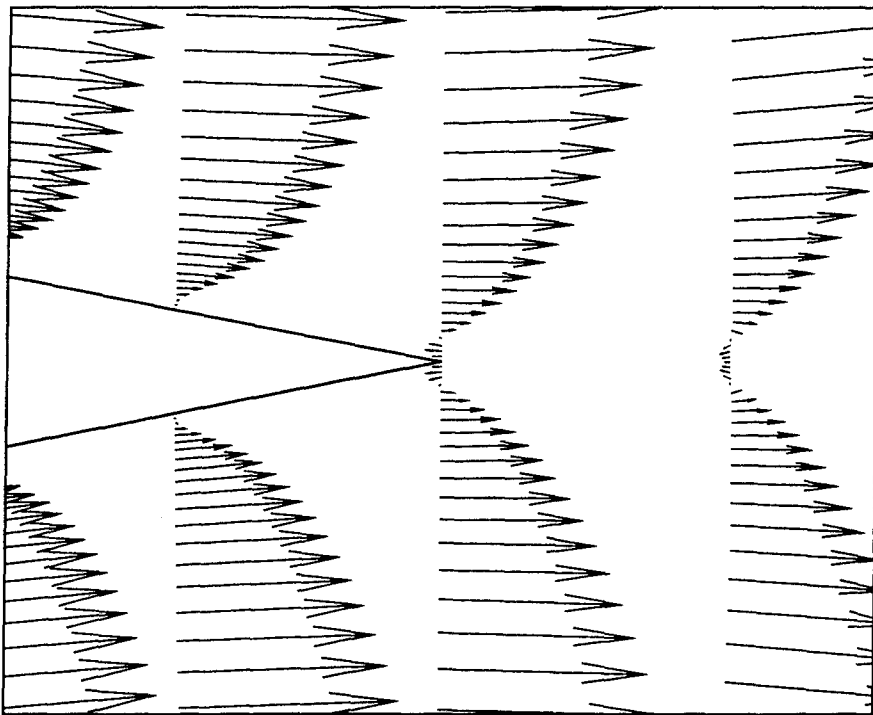
Figure 11: Velocity Vectors, Wigley Hull Stern Region, Fr = 0.289, Re = 3.2E+06
(close up view)
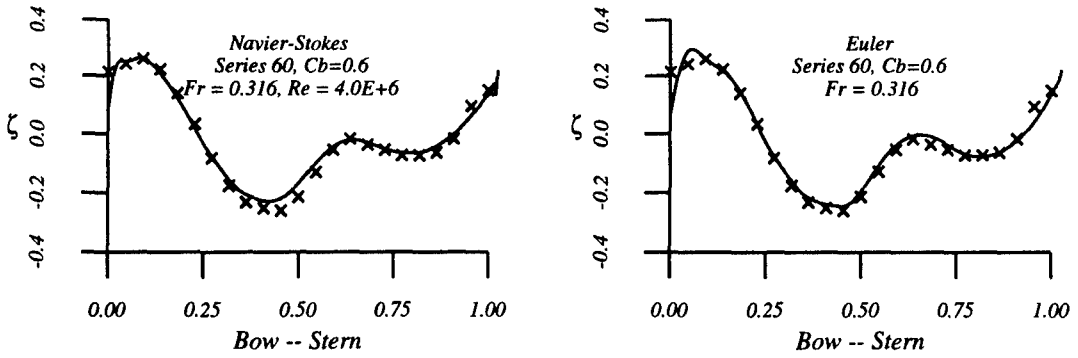
Figure 12: Computed vs. Experimental Wave Elevation, $(\zeta = 2\beta Fr^{-2})$
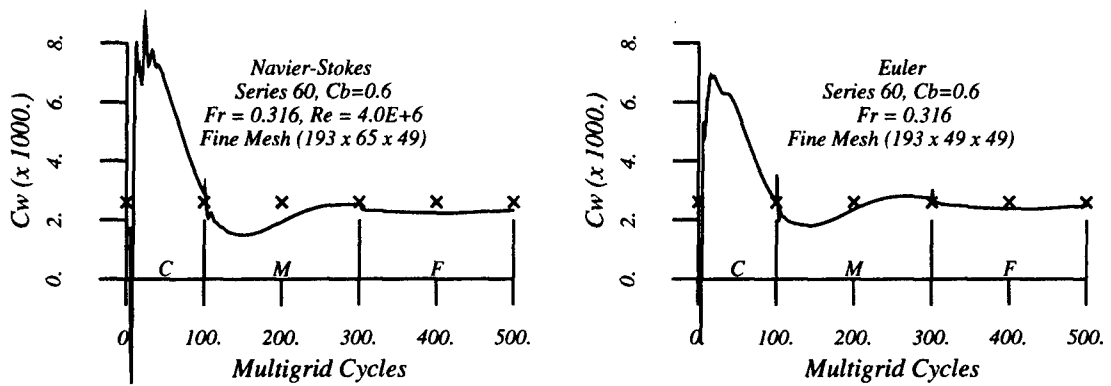
Figure 13: Computed vs. Experimental Wave Drag
C = Coarse Mesh, M = Medium Mesh, F = Fine Mesh
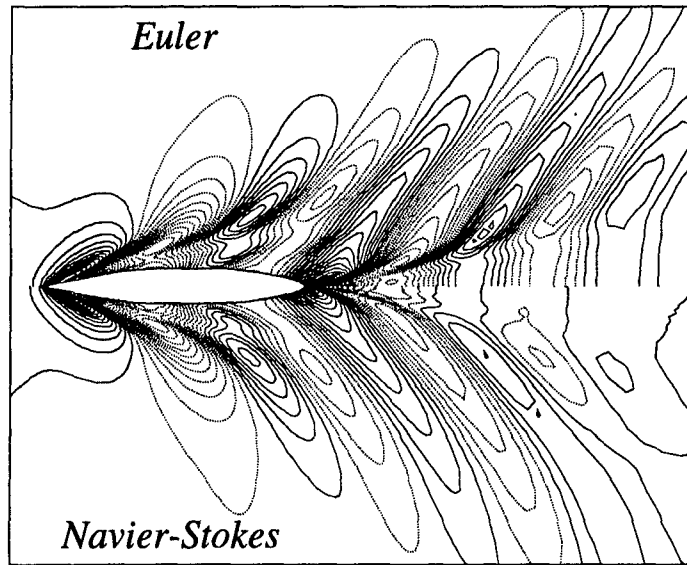
Figure 14: Comparison of Computed Overhead Wave Profiles, Series 60, $C_b = 0.6$, Fr $= 0.316$

by Professor J. Feng, Penn State University

(1) The definition of Γ, the artificial sound speed, given by the authors works well for Euler solvers, but needs further attention in viscous region where the size of time is controlled by restrictions from viscous terms in a N-S solver. Did the authors rescale the Γ in the viscous region for their calculations, or probably, for the problem concerned, it is not important (high Reynolds number/thin boundary layer).

(2) The coefficients α_κ, β_κ, ($\kappa = 1,2,5$) look very interesting. Could the authors explain briefly on the principles and procedures in deriving these coefficients?

Author's Reply

(1) In the viscous boundary layer the velocity will tend toward zero due to the no-slip boundary condition s the normal distance to the ship hull tends to zero. When the velocity becomes low in this region Γ becomes small as can be seen from the definition in the text. To prevent Γ from tending toward zero a cut-off value is introduced such that Γ never becomes less than 0.25. Note that the same cut-off value must be used in a stagnation region as well. There is no other special treatment for the artificial compressibility parameter.

(2) The coefficients α_κ are chosen to maximize the stability limit along the imaginary axis and the β_κ are chosen to maximize the stability limit along the negative real axis. The coefficients are typically chosen through analysis of a model one-dimensional convection/diffusion equation. For information regarding the selection of the coefficients which maximize the stability region refer to the following reference; Jameson, A., "Transonic Flow Calculations," MAE Report #1651, Princeton University, 1984. This reference is also included in Lecture Notes in Mathematics, 1127, edited by F. Brezzi, Springer Verlag, 1985, pp. 156-242.

DISCUSSION
by Dr. David Hally, DREA, Dartmouth

Could you please describe how you generated your grids and what calculations must be done to make them conform dynamically to the free surface?

Author's Reply

The grid for the Wigley hull was constructed analytically using straight lines projecting away from the hull. The grid for the Series 60 was constructed using the GRIDGEN grid generator. Both grids are initially constructed using the entire hull surface, including that portion above the waterline. The grid lines running in the vertical direction are then splined and the coefficients stored. All the grid points above the waterline are then shifted below the waterline with the uppermost plane of points residing on the undisturbed waterline. At this point the flow calculations commence and distortion of the mesh is accomplished by redistributing the grid points, above and below the waterline, according to the current free surface value of β and the stored spline information. It is important to note that the grid is only "generated" once, before the calculations commence. The spline data from the original grid is used to update the grid points by the flow solver as the simulation proceeds.

A Finite-Volume Method with Unstructured Grid for Free Surface Flow Simulations

T. Hino (Ship Research Institute, Japan)
L. Martinelli and A. Jameson (Princeton University, USA)

ABSTRACT

An unstructured grid method developed initially for the transonic inviscid flow is applied to free surface problems around submerged hydrofoils. The flow domain around a submerged body is divided into triangular cells, which makes up the unstructured grid system fitted to a free surface boundary. The incompressible Euler equations and the continuity equation with artificial compressibility are discretized by the finite-volume method in the unstructured grid. Time integration is made by the Runge-Kutta method. Nonlinear free surface conditions are implemented in the scheme. Several techniques for convergence acceleration are used, including the local time steeping, the residual smoothing and the unstructured multigrid. The outline of numerical procedure is presented together with the results of applications. Comparisons of the results with experimental data prove accuracy and efficiency of the present method.

NOMENCLATURE

CFL	Courant number
D	dissipation term
F	Froude number
f	flux in x-direction
g	gravitational constant
g	flux in y-direction
h	wave height
I_k^{k+1}	interpolation operator in multigrid scheme
L	chord length of hydrofoil
P	pre-conditioning matrix
P_k	forcing function in multigrid scheme
p	pressure without hydrostatic component
$\hat{p}$	pressure
Q_k^{k+1}	residual transfer operator in multigrid scheme
Q	convective term
R	residual
s	submergence of hydrofoil
T_k^{k+1}	solution transfer operator in multigrid scheme
t	time
u	velocity in x-direction
v	velocity in y-direction
w	solution vector
x	horizontal Cartesian coordinate
y	vertical Cartesian coordinate
α_m	parameters in Runge-Kutta scheme
β^2	artificial compressibilty parameter
β_{qr}	parameter of Runge-Kutta scheme
$\gamma(x)$	damping term of wave height equation
γ_{qr}	parameter of Runge-Kutta scheme
ϵ	parameter of residual smoothing
λ	wave speed

INTRODUCTION

Free surface flows have significant importance in ship hydrodynamics. Wave resistance is the major part of the resistance that determines the

173

propulsive performance of ships. Also, waves generated by a ship interact with the boundary layer along a ship hull and affect stern flows which are important for a propeller design. Motions of ships or floating marine structures in ocean waves are of practical importance. Impact loads due to the large ocean waves sometimes damage ships or marine structures. A number of methods have been developed to solve these free surface problems. However, the nonlinearity of the problems makes it difficult to predict the properties of free surface flows accurately and efficiently.

Rapid development of computer hardwares and softwares in recent years enables the large-scale computation. Thus, Computational Fluid Dynamics (CFD) becomes another way to analyze flow properties. CFD activities in ship hydrodynamics have been mainly for the prediction of viscous flows around a ship stern[1,2] in which free surface is treated as a symmetric boundary. Free surface flows have been treated by a kind of a panel method assuming inviscid flows[3]. However, because there are interactions between viscous flows and free surface waves, it is desirable to solve viscous flow problems under free surface effects. Attempts to this direction are Hino[4], Miyata et al.[5], Tahara et al.[6] and so on.

When one solves nonlinear free surface flows around a ship with a boundary-fitted grid, which is common in the recent CFD method, a grid must be generated at each time step, because free surface is dynamic in time. The grid generation is not an easy task even without a free surface movement when the body geometry becomes complex. Free surface deformations which are large particularly near the body gives additional complexity to the grid generation.

CFD in aerodynamics is much older than its counterpart in ship hydrodynamics. Various new technologies have been invented in the CFD for aerodynamics. Among them, Jameson et al.[7] developed unstructured grid method for transonic flow computations which uses the triangular grid rather than rectilinear grid in the structured grid case. Later, this method is applied to incompressible flow problems by introducing the artificial compressibility[8]. This unstructured grid method has capability to cope with the geometrical complexity and therefore suitable for free surface flow problems.

In this paper, an unstructured grid method is applied to free surface problems. The problems concerned are flows around a submerged hydrofoils. This is chosen partly because the

problem is much simpler compared with flows around a surface-piercing body and partly because the original method is for transonic aerofoils and can be naturally extended to hydrofoil problems.

The governing equations are incompressible Euler equations. Though the final goal of the study is the viscous flow computations, the Euler equations are selected as the governing equation for its simplicity. Artificial compressibility is introduced in the continuity equation. This makes the system of equations hyperbolic and the well-developed efficient techniques to solve hyperbolic equations can be used.

NUMERICAL PROCEDURES

Governing Equations

Governing equations are two-dimensional incompressible Euler equations and are expressed in the form non-dimensionalized by the chord length of a hydrofoil L, the uniform flow velocity U and the fluid density ρ as follows:

$$\frac{\partial u}{\partial x} + \frac{\partial v}{\partial y} = 0 \qquad (1)$$

$$\frac{\partial u}{\partial t} + \frac{\partial(u^2 + \hat{p})}{\partial x} + \frac{\partial(uv)}{\partial y} = 0 \qquad (2)$$

$$\frac{\partial v}{\partial t} + \frac{\partial(uv)}{\partial x} + \frac{\partial(v^2 + \hat{p})}{\partial y} + \frac{1}{F^2} = 0 \qquad (3)$$

where (x, y) are Cartesian coordinates (y is upward positive) and (u, v) are the velocity components in (x, y) directions, respectively. $\hat{p}$ is the static pressure and t is time. F is Froude number defined using the gravitational constant g as

$$F = \frac{U}{\sqrt{gL}} \qquad (4)$$

Since there is no term associated with the time derivative of pressure in the governing equations (1)-(3), difficulties come out when one solves these equations in the time-marching manner. Usually pressure field is computed by the Poisson equation which is derived from the divergence of the momentum equations (2)-(3) and the continuity equation (1) in such a way that the velocity field satisfies the continuity condition at each time step [9].

When only the steady state solution is required, the alternative approach called the artificial compressibility method can be used. In this

method first proposed by Chorin [10], the continuity equation is modified by introducing the pseudo-compressibility as follows:

$$\frac{\partial p}{\partial t} + \beta^2 \left(\frac{\partial u}{\partial x} + \frac{\partial v}{\partial y} \right) = 0 \qquad (5)$$

where β^2 is the artificial compressibility parameter. When the solution becomes steady, the equation (5) recovers the original form (3). Since the system of equations (5), (2) and (3) is hyperbolic, efficient numerical solution methods for the hyperbolic equations can be applied.

The parameter β^2 is determined by using the local velocity magnitude as

$$\beta^2 = r_b * \min(u^2 + v^2, \beta^2_{\min}) \qquad (6)$$

where r_b is a global constant and the parameter $\beta^2_{\min}$ is used to prevent β^2 from approaching zero near the stagnation point. $r_b = 5$ and $\beta^2_{\min} = 0.3$ are typical values in the present study.

Eqs.(5), (2) and (3) can be rewritten in the vector form as

$$\frac{\partial \boldsymbol{w}}{\partial t} + \boldsymbol{P} \left(\frac{\partial \boldsymbol{f}}{\partial x} + \frac{\partial \boldsymbol{g}}{\partial y} \right) = 0 \qquad (7)$$

where

$$\boldsymbol{w} = \begin{bmatrix} p \\ u \\ v \end{bmatrix}, \; \boldsymbol{f} = \begin{bmatrix} u \\ u^2 + p \\ uv \end{bmatrix}, \; \boldsymbol{g} = \begin{bmatrix} v \\ uv \\ v^2 + p \end{bmatrix} \qquad (8)$$

and p is the pressure without the hydrostatic component, i.e.,

$$p = \hat{p} + \frac{y}{F^2} \qquad (9)$$

$\boldsymbol{P}$ is a matrix defined as

$$\boldsymbol{P} = \begin{bmatrix} \beta^2 & 0 & 0 \\ 0 & 1 & 0 \\ 0 & 0 & 1 \end{bmatrix} \qquad (10)$$

Boundary conditions needed for free surface flow problems are a body surface condition, a free surface condition and a far field condition. The first one is the free-slip condition in case of the inviscid flow, that is,

$$u \, n_x + v \, n_y = 0 \qquad (11)$$

where (n_x, n_y) are the unit vector outward normal to the body surface.

The second one, the free surface condition consists of two conditions. One is the dynamic condition that states the continuity of stresses on the air-liquid interface. For the inviscid case this is expressed as

$$\hat{p} = p_0 \quad \text{on} \quad y = h \qquad (12)$$

or, equivalently,

$$p = p_0 + \frac{h}{F^2} \quad \text{on} \quad y = h \qquad (13)$$

where p_0 is atmospheric pressure (assumed to be constant) and $y = h(x; t)$ is the free surface location. The other free surface condition is called the kinematic condition that means the fluid particles on the free surface keep remaining on it. This is written as

$$\frac{\partial h}{\partial t} + u \frac{\partial h}{\partial x} - v = 0 \qquad (14)$$

The free surface shape can be updated by Eq.(14) in the time-marching manner.

The far field conditions are as follows. At far upstream, flow is uniform and free surface is undisturbed. On the other hand, the waves generated by a hydrofoil propagate to far down stream. Water depth is assumed infinite.

Spatial Discretization

Finite-Volume Method

In a finite-volume formulation a solution domain is divided into small cells. The present method employs unstructured grid in which every cell is triangular. One of the superiorities of unstructured grids over structured ones is its flexibility to deal with complex geometry. Therefore, unstructured grids are particularly suitable to free surface flow problems in which the deformation of free surface boundary causes further geometrical complexity in addition to that of body configuration.

The flow variables (u, v) and p are defined at the vertices of each triangle. The control volume for a given node i is taken as the union of all the triangles which share that node as a vertex as shown in Fig.1. The integration of the governing equation (7) over this control volume yields

$$\frac{\partial}{\partial t} \iint_\Omega \boldsymbol{w} \, dx \, dy = -\iint_\Omega \boldsymbol{P} \left(\frac{\partial \boldsymbol{f}}{\partial x} + \frac{\partial \boldsymbol{g}}{\partial y} \right) dx \, dy$$

$$= -\oint_{\partial \Omega} \boldsymbol{P}(\boldsymbol{f} \, dy - \boldsymbol{g} \, dx) \quad (15)$$

where Ω means the control volume and $\partial\Omega$ is its boundary. Since the grid is aligned to the free
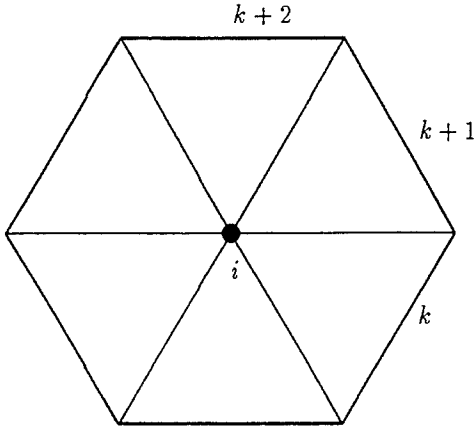
Figure 1: Control volume around the node i

surface boundary which moves in time, the grid is time-dependent and the effects of grid movement must be taken into account for the time-accurate computation. However, since the present method employs the steady state formulation and the transient solution does not have physical meaning, one can make approximation to drop all the terms associated with the grid movement. Thus, f and g in Eq.(15) have the same form as in Eq.(8). In the discrete form, Eq.(15) becomes

$$\frac{d}{dt}(S_i\,w_i) + \sum_{k=1}^{n_e} P(f_k\Delta y_k - g_k\Delta x_k) = 0 \quad (16)$$

where S_i is the area of the control volume around the node i which is computed by the summation of the area of each triangle in the control volume. The summation in Eq.(16) is taken over all the edges surrounding the control volume and n_e is the number of the edges. Also, $(\Delta y_k, -\Delta x_k)$ gives the unscaled outward normal vector of the k-th edge. f_k and g_k are the flux vectors evaluated by taking average of the values at both ends of the edge. This discretization corresponds to the central difference scheme in the structured grid case. The time integration scheme for Eq.(16) is described in the subsequent section.

Artificial Dissipation

Since the evaluation of Eq.(16) described above is the scheme equivalent to the central difference scheme for the Euler equations, this scheme is not stable due to the decoupling of neighboring node unless one adds the artificial dissipation terms to the equations. To keep the second order accuracy of the scheme, the fourth-order dissipation models are used in the scheme, while the second-order dissipation terms used in the compressible flow code [11] to prevent oscillation near shocks are not used.

By adding the artificial dissipation terms, Eq.(16) is rewritten as

$$\frac{d}{dt}(S_i\,w_i) + Q_i(w) - D_i(w) = 0 \quad (17)$$

where

$$Q_i(w) = \sum_{k=1}^{n_e} P(f_k\Delta y_k - g_k\Delta x_k) \quad (18)$$

and $D_i(w)$ is the dissipation terms. The dissipation terms are evaluated as follows. First, the undivided Laplacian in the computational space is approximated as,

$$\nabla^2 w_i = \sum_{j=1}^{n_n}(w_j - w_i) \quad (19)$$

The dissipation terms are constructed by using this $\nabla^2 w$ as

$$D(w)_i = \sum_{j=1}^{n_n} \epsilon\lambda_{ij}(\nabla^2 w_j - \nabla^2 w_i) \quad (20)$$

where ϵ is a global constant which controls the amount of dissipation and λ_{ij} is a scale factor. The summation is taken over all the nodes on the boundary of the control volume around the node i and n_n is the number of the nodes.

From the analogy to upwind differencing, the scale factor λ_{ij} is determined as follows. First, the maximum wave speed is determined by the spectral radii of the flux Jacobian matrices as

$$\lambda = \rho(A\Delta y - B\Delta x) \quad (21)$$

where

$$A = P\frac{\partial f}{\partial w} = \begin{bmatrix} 0 & \beta^2 & 0 \\ 1 & 2u & 0 \\ 0 & v & u \end{bmatrix},$$

$$B = P\frac{\partial g}{\partial w} = \begin{bmatrix} 0 & 0 & \beta^2 \\ 0 & v & u \\ 1 & 0 & 2v \end{bmatrix} \quad (22)$$

This yields

$$\lambda = |(u\,\Delta y - v\,\Delta x)| + \sqrt{(u\,\Delta y - v\,\Delta x)^2 + \beta^2(\Delta x^2 + \Delta y^2)} \quad (23)$$

176

Thus, a scale factor λ_{ij} which is λ associated with the edge consists of the nodes i and j is defined as

$$\lambda_{ij} = \max(|q_i|, |q_j|) + \sqrt{\max(c_i, c_j)} \qquad (24)$$

where

$$q_i = u_i \Delta y_{ij} - v_i \Delta x_{ij} \qquad (25)$$

$$c_i = q_i^2 + \beta_i^2 \sqrt{\Delta x_{ij}^2 + \Delta y_{ij}^2} \qquad (26)$$

and $(\Delta x_{ij}, \Delta y_{ij})$ is the vector from the node i to the node j. q_j and c_j can be evaluated by replacing u_i, v_i and β_i^2 in the above equations by u_j, v_j and β_j^2, respectively.

Boundary Conditions

Body Boundary Condition

Free-slip condition on the body (11) is implemented in the following way. To determine two velocity components (u, v) on the boundary, two conditions are required. One condition is apparently the free slip condition (11). The other condition is that the tangential velocity does not have gradient in the normal direction, that is,

$$\frac{\partial q_t}{\partial n} = 0 \qquad (27)$$

where n is the normal direction and q_t is the tangential velocity defined by using the unit outward vector on the body (n_x, n_y) as

$$q_t = u\, n_y - v\, n_x \qquad (28)$$

For the node which lies on the body boundary, the tangential velocity is extrapolated from the inside in such a way that Eq. (27) is satisfied. First, for each node on the body boundary, the edge from which velocity is extrapolated is searched. Searching procedure is 1) search the triangle that consists of the boundary node under consideration and two internal nodes, 2) the edge formed by the two internal nodes is registered as a candidate edge, 3) from the candidates select the edge in such a way that the angle between the vector from the boundary node to the mid-point of the edge and the outward normal vector of the boundary node is minimum. Thus, the velocity can be extrapolated from the direction approximately normal to the body surface. Suppose that the boundary node is denoted as O and that the end points of the corresponding edge are A and B as shown in Fig. 2, the extrapolation formula is

$$(q_t)_o = (1 - \kappa)(q_t)_A + \kappa(q_t)_B \qquad (29)$$
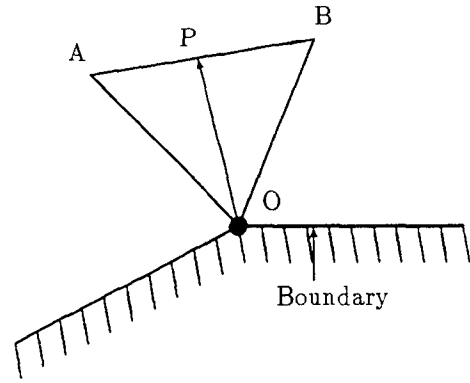
Figure 2: Velocity extrapolation of the boundary node
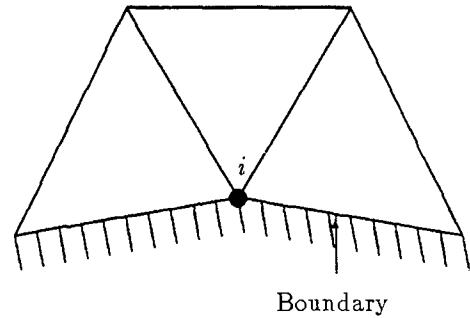
Figure 3: Control volume for the boundary node

where

$$\kappa = \frac{\overline{AP}}{\overline{AB}} \qquad (30)$$

where P is the intersection point between $\overline{AB}$ and the vector normal to the boundary (see Fig. 2). From Eqs.(29) and (11), the velocity component on the body is computed as

$$u = (q_t)_o\, n_y, \quad v = -(q_t)_o\, n_x \qquad (31)$$

The pressure on the body is computed by the modified continuity equation (5). The control volume is taken as shown in Fig. 3. Mass fluxes across the boundary edges are set zero because of the free-slip condition. The discretization is carried out in the usual way except that the node is on the perimeter of the control volume.

177
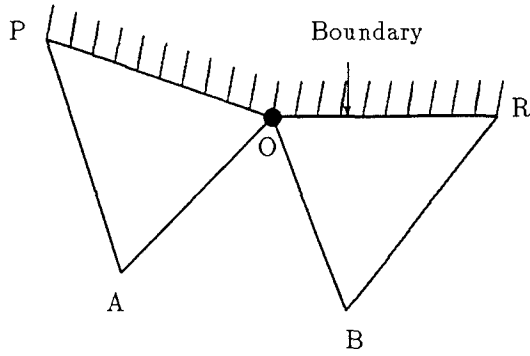
Figure 4: Velocity extrapolation on the free surface

Free Surface Condition

Since the the grid is aligned to the free surface boundary, the free surface dynamic condition (13) is satisfied by simply setting pressure value on the free surface to $p_0 + h/F^2$.

The velocity on the free surface is extrapolated from inside in such a way that the velocity gradient in the normal direction is zero. Though this can be approximated in the same way as for the body boundary, the simpler extrapolation scheme is preferable because re-calculation of extrapolation coefficient κ at each time-step due to the grid movement is time-consuming. (Note that the grid points close to the body boundary do not move in time as described in the subsequent section.) Suppose that the free surface node O is the common node for the boundary edge $\overline{PO}$ and $\overline{OR}$ and these edges are the part of the triangles $\triangle POA$ and $\triangle OBR$, respectively as depicted in Fig.4 (Note that node O, A and B do not necessarily form a triangle), then velocity at node O is computed by

$$u_O = \frac{1}{2}(u_A + u_B), \; v_O = \frac{1}{2}(v_A + v_B) \qquad (32)$$

In the above approximation, the mid-point of $\overline{AB}$ is assumed to be in the normal direction from the node O.

The kinematic condition (14) is used to update the free surface shape. The spatial discretization is based on the third-order upwind finite-differencing scheme and the equation for the node i becomes

$$\frac{dh_i}{dt} + u_i \frac{2h_{i+1} + 3h_i - 6h_{i-1} + h_{i-2}}{2x_{i+1} + 3x_i - 6x_{i-1} + x_{i-2}} - v_i = 0 \qquad (33)$$

where the node numbering is sequential from upstream to downstream and (u_i, v_i) is the velocity at the node i whose coordinate is given by (x_i, h_i).

Far Field Conditions

At inflow, flow is uniform, that is,

$$u = 1, \, v = 0, \, p = 0, \, h = 0 \qquad (34)$$

are given.

At outflow, since waves generated by a hydrofoil propagate to infinite downstream, flow is not uniform. To prevent the reflection of waves to the solution domain, the outflow conditions must be carefully implemented. The open boundary conditions for free surface problems are treated by the various methods [12]. Among them, the procedure used here is the artificial damping method, in which waves going through the outflow boundary is dissipated by adding artificial damping terms in the flow equation.

The free surface kinematic condition is modified as

$$\frac{\partial h}{\partial t} + u \frac{\partial h}{\partial x} - v + \gamma(x) = 0 \qquad (35)$$

where γ is the artificial damping terms defined as

$$\gamma(x) = \begin{cases} A\left(\dfrac{x - x_d}{x_o - x_d}\right)^2 h(x) & \text{if } x_d \le x \le x_o \\ 0 & \text{otherwise} \end{cases} \qquad (36)$$

where A is a constant that controls the amount of damping and x_o is the x-coodinate of the outflow boundary. x_d is defined as

$$x_d = x_o - 2\pi F^2 \qquad (37)$$

That is, the damping zone is set one wavelength computed by the linear theory from the outflow boundary. The quadratic form of the damping term in Eq.(36) gives the gradual increase of dissipation, which prevents the reflection of waves at the edge of the damping zone.

Velocity and pressure on the outflow boundary is computed by the control volume of Fig.3, which is equivalent to rhe one-sided differencing.

At the bottom boundary, pressure p is assumed to zero, which corresponds to the hydrostatic value and velocity is computed from momentum equations with the one-sided differencing using the control volume of Fig.3.

178

Time Stepping

As the time integration scheme, the explicit multi-stage Runge-Kutta scheme originally developed for compressible flows [11] is used here.

As stated earlier, the grid is time-dependent in the present case, therefore, the control volume is also time-dependent. However, when only steady state solutions are of interest, one can simplify the solution procedure by dropping the terms associated with the grid movement. Suppose that one has the grid and the solution at time step (n), the procedure to proceed one time step is as follows. The flow equations (17) are solved assuming that the grid does not move in time, that is, S_i, Δx and Δy appeared in Eq.(17) are evaluated using the grid at time step (n) and are kept constant in time. Thus, Eq.(17) can be rewritten as

$$\frac{dw_i}{dt} + \frac{1}{S_i}(Q_i(w) - D_i(w)) = 0 \quad (38)$$

This equation gives an approximated solution at time step $(n+1)$. Then, the free surface kinematic condition (14) is solved in the same manner as the flow equations and the wave height at time step $(n+1)$ is obtained. Next, the grid points are redistributed in such a way that the grid is conformed to the newly computed free surface configuration. During this redistribution process, the number of grid points and the edge connectivity are not changed so as to avoid the re-triangulation at each time step. The flow variables at time step $(n+1)$ are set equal to the values computed under the approximation that the grid is fixed. The geometric quantities S_i, Δx and Δy are recomputed by using the new coordinates and the computation proceeds to the next time-step.

Since the grid points do not move in time when a solution becomes steady, this approximated procedure must give the same steady state solutions as the time-accurate scheme does.

Time integration scheme for the flow equation (38) and the wave height equation (14) is the Runge-Kutta method which is a class of one-step multi-stage explicit schemes. The general m-stage solution procedure for Eq.(38) from the time step (p) to $(p+1)$ can be written as follows:

$$w^{(0)} = w^p \quad (39)$$

$$w^{(1)} = w^{(0)} - \alpha_1 \frac{\Delta t}{S} R^{(0)}(w) \quad (40)$$

$$w^{(2)} = w^{(0)} - \alpha_2 \frac{\Delta t}{S} R^{(1)}(w) \quad (41)$$

$$\cdots$$

$$w^{(m)} = w^{(0)} - \alpha_m \frac{\Delta t}{S} R^{(m-1)}(w) \quad (42)$$

$$w^{p+1} = w^{(m)} \quad (43)$$

where $R^{(q)}(w)$ is the residual evaluated at q-th stage and is defined by the weighted average of the residuals computed by the flow variables of previous stages, i.e.,

$$R^{(q)}(w) = \sum_{r=0}^{q}\{\beta_{qr}Q(w^{(r)}) - \gamma_{qr}D(w^{(r)})\} \quad (44)$$

α_m, β_{qr} and γ_{qr} define the particular scheme. The values of these coefficients for the 4-stage scheme used in this study are as follows.

$$\alpha_1 = 1/3, \ \alpha_2 = 4/15, \ \alpha_3 = 5/9, \ \alpha_4 = 1 \quad (45)$$

$$\beta_{qr} = \begin{cases} 1 & \text{if } q = r \\ 0 & \text{otherwise} \end{cases} \quad (46)$$

$$\begin{aligned} &\gamma_{00} = 1 \\ &\gamma_{10} = 0.5, \ \gamma_{11} = 0.5 \\ &\gamma_{20} = 0.5, \ \gamma_{21} = 0.5, \ \gamma_{22} = 0 \\ &\gamma_{30} = 0.5, \ \gamma_{31} = 0.5, \ \gamma_{32} = 0, \ \gamma_{33} = 0 \end{aligned}$$
$$(47)$$

Thus, the dissipation terms are evaluated twice in one time-step.

The free surface kinematic condition (14) is solved in the same manner except that there are no dissipation terms due to the use of upwind differencing.

Grid Generation and Grid Movement

The generation of unstructured triangular grid around a body can be achieved by various ways. Among them, the Delaunay triangulation method [14] and the advancing front method [13] are commonly used in the CFD field. The former is the procedure to establish unique triangulation of given grid points covering solution domain, while the latter is the method to generate points and connect them simultaneously.

The unstructured grid around the submerged hydrofoil used here is generated by the Delaunay triangulation. The set of points are generated by the combination of the conformal mapping around the region close to a foil and the algebraic method in the other region. The conformal mapping is an established way to generate O-grid around a foil of an arbitrary shape. The algebraic method is required since the outer

boundary is rectangular and since the grid spacing control is needed for the better resolution of the free suface region. The points are clustered in the region above and behind the body and near the free surface where the free surface deformation is expected to be large.

The grid movement is carried out in the following way. The initial grid is generated by assuming the flat free surface. On this stage y-coordinate of the uppermost point generated by the conformal mapping is searched and stored as y_u. y_u is the uppermost extent of the 'inner grid' that is generated in the region close to the body and only the grid point above y_u are allowed to move following free surface movement. Assume that the wave height at time step n is given by $h^n(x)$, then the grid movement of the node i is defined as

$$x_i^{n+1} = x_i^n \qquad (48)$$

$$y_i^{n+1} = \begin{cases} y_u + \dfrac{(h^{n+1}(x_i) - y_u)}{(h^n(x_i) - y_u)}(y_i^n - y_u) \\ \qquad\qquad\qquad \text{if } y_i^n > y_u \\ y_i^n \qquad\qquad\quad \text{otherwise} \end{cases}$$

$$\qquad (49)$$

where $h(x_i)$ is the wave height at $x = x_i$ and is computed by the linear interpolation because x_i does not necessarily coincide with the x-coordinate of the free surface nodes. Thus, all the points above y_u move vertically due to the free surface movement. The moving distance is linearly distributed between h^{n+1} and y_u. By this procedure the grid points near the body do not move and the complicated re-distribution procedure for points near the body is avoided.

Convergence Acceleration Techniques

Three techniques are used to accelerate the convergence of solutions to the steady state in the present scheme. A local time stepping is the method in which the solution at each point proceeds in time with the time step defined locally from the local stability limit, while a residual smoothing is used to increase the bound of the stability limit of the time stepping scheme itself. A multigrid method is an efficient way to accelerate the convergence, where the time stepping is carried out by using successively coarser grids as well as the original finest grid.

Local Time Step

For explicit schemes the maximum permissible time step is limited by the Courant-Friedrichs-

Lewy (CFL) condition. In one dimensional case, this is written as

$$\Delta t \leq CFL\frac{\Delta x}{c} \qquad (50)$$

where CFL is the maximum Courant number permitted by the scheme, Δx is the grid size, and c is the maximum wave speed. When one uses the globally constant time step, Δt must be smaller than the minimum value of $CFL\Delta x/c$.

In practice, the grid spacing is not uniform due to the clustering of points. Therefore the time step is determined based on the minimum grid spacing. This yields the small time step and causes slow convergence.

If only steady state solutions are of interest, one can use the locally varying time step at the expense of time-accuracy. The local time step Δt_i is taken as its maximum permissible value, i.e.,

$$\Delta t_i = CFL\frac{\Delta x_i}{c_i} \qquad (51)$$

In case of unstructured grid employed here, the above equation is modified as

$$\Delta t_i = CFL\frac{S_i}{\lambda_i} \qquad (52)$$

where S_i is the area of the control volume around the node i.

Residual Smoothing

As stated earlier, explicit schemes have the CFL limit of stability. Residual smoothing procedure described below is the way to increase the stability bound of a time stepping scheme. Thus, larger time step can be taken and the fast convergence is achieved. In the method, the residual at the node i, $R_i(w)$ is replaced by implicitly averaged value $\tilde{R}_i(w)$, where

$$\tilde{R}_i = R_i + \epsilon\nabla^2\tilde{R}_i \qquad (53)$$

where ϵ is a constant and the operator ∇^2 is the undivided Laplacian in the computational space defined in Eq.(19). The resulting linear equation

$$(1 - \epsilon\nabla^2)\tilde{R}_i = R_i \qquad (54)$$

is solved iteratively by the Jacobi method. This gives the implicit property to the scheme and the CFL limit can be larger than the unsmoothed case. One dimensional analysis shows that one can take arbitrary large time step as far as ϵ is taken correspondingly large [11]. In this study ϵ is taken 0.5.

180

Unstructured Multigrid

Multigrid method is known as the efficient way to get fast convergence. The concept of the multigrid time stepping applied to the solution of hyperbolic equations by Jameson [11] is to compute corrections to the solution on a fine grid by the time-stepping on a coarser grid.

The general procedure of the multigrid method is as follows. Equations to be solved is written as

$$\frac{dw}{dt} = -R(w) \tag{55}$$

and the subscript k refers as the grid index.

First, the solution w_k is obtained in the fine grid (k) by solving

$$\frac{dw_k}{dt} = R_k(w_k) \tag{56}$$

by the Runge-Kutta scheme described above. Then, the solution is transferred from the fine grid (k) to the next coarser grid $(k+1)$ by

$$w_{k+1}^{(0)} = T_k^{k+1} w_k \tag{57}$$

where T_k^{k+1} is a transfer operator. The solution in the coarse grid is updated by solving the equation

$$\frac{dw_{k+1}}{dt} = -R_{k+1}(w_{k+1}) - P_{k+1} \tag{58}$$

with the Runge-Kutta scheme and w_{k+1}^+ is obtained. P_{k+1} in the above equation is the forcing function in the coarse grid $(k+1)$ defined as

$$P_{k+1} = Q_k^{k+1} R_k(w_k) - R_{k+1}(w_{k+1}^{(0)}) \tag{59}$$

where Q_k^{k+1} is another transfer operator. The first term of the right-hand-side of Eq.([?]) is the residual transferred from the finer grid and the second term is the residual evaluated by the transferred solution. This second term cancels the residuals in the coarse grid only and the driving force comes from only the residual transfered from the finer grid.

$w_{k+1}^+ - w_{k+1}^{(0)}$ gives the correction of the solution at the grid $(k+1)$. This procedure is repeated on successively coarser grid. Finally, after the computation of the correction at the coarsest gird, the correction is transferred back from the coarse grid $(k+1)$ to the fine grid (k) by

$$w_k^+ = w_k + I_{k+1}^k(w_{k+1}^+ - w_{k+1}^{(0)}) \tag{60}$$

where I_{k+1}^k is an interpolation operator. The multigrid cycle employed here is V-cycle in which
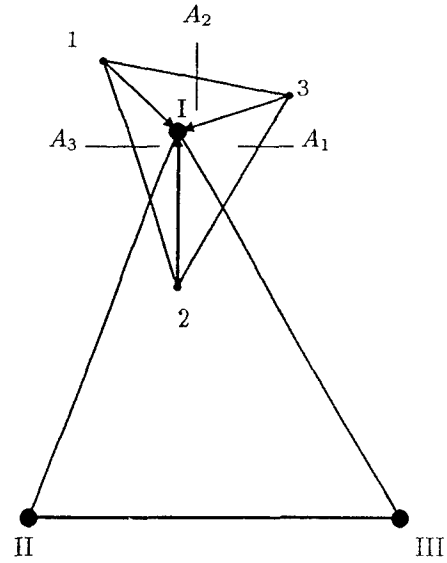
Figure 5: Transfer of solution

the equations are solved only when the solution moves from the fine grid to the coarse one and the interpolation is used in the transfer of correction from the coarse grid to the fine one.

In case of the structured grids, the generation of successively coarser grids can be done simply by deleting the alternate points along each grid line. This also makes it easy to define the operators described above. In the unstructured grids, however, neither the grid generation nor the definition of the operators is straightforward.

In the present study, the multigrid strategy of Mavriplis [14] is employed. That is, to keep flexibility of unstructured grids as much as possible, the series of coarser grids are generated independently. The grid generation procedure is repeated fo each grid with changing the grid density parameters.

The operators for the transfers are defined as follows. T_k^{k+1} is the operator with which the solution w transfers from the fine grid to the coarse one. This is defined as

$$w_I = \frac{(A_1 w_1 + A_2 w_2 + A_3 w_3)}{A_1 + A_2 + A_3} \tag{61}$$

where I is the node in the coarse grid under concideraton and 1, 2 and 3 are the nodes forming the triangle in the fine grid which contain the node I. A_1 is the area of the triangle consists of I, 2 and 3 as shown in Fig.5. A_2 and A_3 are defined similarly.

Q_k^{k+1} is the transfer operator of the residuals. The residual at the node I in the coarse grid

181
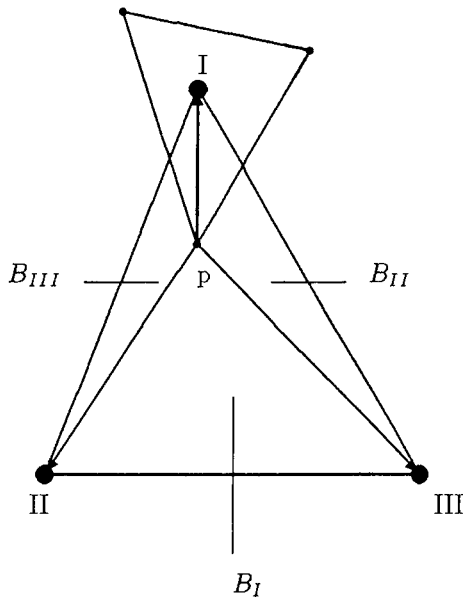
Figure 6: Transfer of residuals

Figure 7: Transfer of correction

is computed by

$$R_I = \sum_\Delta (\sum_p \frac{B_I R_p}{B_I + B_{II} + B_{III}}) \qquad (62)$$

The first summation is over the triangles of coarse grid that share the node I as a common vertex. The second summation is taken over all the nodes in the fine grid that lie inside the triangles determined in the first summation. B_I is the area of the triangle consists of the nodes p, II and III as shown in Fig.6. B_{II} and B_{III} are defined similarly. Thus, the residuals in the coarse grid are linearly distributed to the nodes in the fine grid. Note that this procedure is conservative, that means the grand sum of the residuals in the coarse grid is equal to the grand sum of the residuals in the fine grid. This feature is important, because the the driving force in the coarse grid comes only from the fine grid residuals due to the forcing function (59).

Finally, I_k^{k+1} is for the interpolation of the corrections in the coarse grid to the fine grid. From Eq.(60) the correction dw is defined by

$$dw = w^+ - w^{(0)} \qquad (63)$$

The transfer of the correction from the coarse grid to the fine grid is done as follows.

$$dw_1 = \frac{B_I dw_I + B_{II} dw_{II} + B_{III} dw_{III}}{B_I + B_{II} + B_{III}} \qquad (64)$$

where the node 1 is the node of the fine grid and it lies inside the triangle of the nodes I, II and III in the coarse grid as shown in Fig.7. B_I is the area of the triangle of 1, II and III. B_{II} and B_{III} are defined similarly

Since the grid is dynamic in time for the present case, the above operators must be re-computed at each time step using new coordinates of the grid. The most time-consuming part of this re-computation is the search of the triangle in which the certain point lies. The procedure taken here is based on the tree-search algorithm similar to the one used by Mavriplis[14]. First, every triangle has a list of three neighbour triangles. This list does not change by the grid movement because the point connectivity is fixed. At the beginning, the search of the triangle is carried out by the simple search consists of the loop over all the triangles.

The search of triangles after the grid movement are achieved by the following procedure. The search starts with the triangle in which the point under consideration lies before the grid movement. If the point still lies in this triangle, the search ends. If not, the three triangles which are the neighbours of the first triangle are searched next. The search region is extended successively to the neigbours of the neigbours until the desired triangle is found. Since the moving distance of grid points are not large, this search converges usually in a few extensions. The computational time required is much less than that

182

of the loop over all the triangles.

RESULTS

The numerical procedure described above is applied to free surface flow simulations around a submerged hydrofoil. A hydrofoil section used here is NACA0012 and the angle of attack is set 5 degrees. The depth of submergence s measured at the mid-chord and nondimensionalized by the chord length varies from 1.034 to 0.911. Froude number $F = 0.5672$ and water depth is assumed to be infinite. These conditions correspond with the experiments by Duncan [15] except that the experiments were carried out in the tank of a finite water depth (varies from 1.90 to 1.77, nondimensionalized by a chord length).

For all the computation, the initial computational domain is taken as

$$-7 \leq x \leq 6.25, \ -7 \leq y \leq 0 \qquad (65)$$

unless otherwise noted. $x = 0$ is the 1/4 chord aft from the leading edge of the hydrofoil and $y = 0$ is the undisturbed water level.

Three levels of multigrids used for the computation with the submergence $s = 1.034$ are shown in Fig.8. The finest grid consists of 6,587 nodes and 12,854 triangles. Among them, 64 nodes are distributed on the body. The medium grid has 1,642 nodes and 3,130 triangles while the coarsest one has 409 nodes and 745 triangles. Since these grids are for the converged solution, the free surface configurations correspond to the developed wave field, though the initial grids are generated under the undisturbed free surface. Maginified view of the finest grid is depicted in Fig.9.

The computed pressure distributions with the multi- and single- grid cases are shown in Figs.10 and 11. Both are the results at 400 time cycles with the Courant number CFL being 5.0.

The single grid case shows the undeveloped wave field in which the waves generated by the hydofoil do not yet reach the outflow boundary, while in the multigrid case the converged solution with developed wave field (except for the region close to the outflow boundary where numerical damping is added) is obtained. This is due to the fact that time advancement in one multigrid cycle in the three-level mutigrid is approximately $\Delta t + 2\Delta t + 4\Delta t = 7\Delta t$, where Δt is the time step in the finest grid, because the local time stepping is taken proportional to the cell area. On the other hand, time advancement in the single-grid case in one cycle is just Δt.

For the practical computations shown hereafter the full multigrid scheme is employed, in which the initial solution is obtained with only the coarsest grid, then the solution is transferred to the next finer grid and the solution is updated by the multigrid method using the coarsest grid and the next finer grid. The procedure is repeated with adding one level of multigrid at a time until the finest grid is reached. The cycles for each stage are 1,000 cycles with the single coarsest grid, 500 cycles with the double grid (the medium and the coarsest) and 400 cycles with triple grid (the finest, the medium and the coarsest grids). With this scheme, the residual in the final stage is $O(10^{-4})$.

The effect of numerical damping expressed by Eq.(36) is verified next. Fig.12 compares two computed wave configurations. One has the solution domain of $-7 \leq x \leq 6.25$, and the other has the longer domain of $-7 \leq x \leq 8.25$. The number of grid points in the longer domain case increases in such a way that the grid density is approximately the same in both cases. Since Froude number is 0.5672, the length of the damping zone defined in Eq.(37) is about 2.02. Waves going through the outflow boundary are damped effectively in the damping zone and the reflection of waves on the outflow boundary cannot be observed. Also, the comparison of the long-domain solution and the short-domain one shows that the artificial damping does not affect the flow field upstream of the damping zone.

In Fig.13 the computed wave height is compared with the experimental data by Duncan [15]. The present result is in good agreement with the experimental data. Fig.14 and 15 show the pressure distribution and the velocity vectors in the vicinity of the hydrofoil, respectively. Fig.16 shows the computed Cp distribution on the body.

Fig.17 is the result with $s = 0.951$. Again, the computed wave profile shows good agreement with experimental data [15]. When the submergence of the hydrofoil decreases, the wave amplitude becomes larger and wave length becomes shorter than the deep submergence case. These nonlinear features of wave formations in the experiment are clearly captured by the present method. Note that in the experiment with $s = 0.951$, two types of wave profiles, one is breaking and the other is non-breaking, are obtained depending on the experimental condition. However, the present computation predicts only the non-breaking waves.

When the submergence decreases further

to $s = 0.911$, only the breaking waves exist in the experiment. However, the present method predicts the very steep but non-breaking wave as shown in Fig.18. In the implementation of the kinematic free surface condition, the wave height is assumed to be expressed by the single-valued function of x. Thus, breaking waves or overturning waves cannot be simulated by the present scheme. However, more flexible treatment of the free surface movement such as the Lagrangian method can be adopted without difficulties. The nature of unstructured grid methods enables the spatial discretization in such a highly deformed region. This improvement together with development of the time-accurate scheme makes it possible to simulate transient breaking or overturning waves in the near future.

CONCLUSIONS

In the present study, a finite-volume method with an unstructured grid method which has been originally developed for transonic flow computations is successfully applied to incompressible flows with a free surface. The computed results for a submerged hydrofoil show good agreement with the experimental data.

Further extensions of this method are the inclusion of viscous effects, transient flow computation using time-accurate scheme, breaking or overturning waves simulation and so on. Also, the three-dimensional version of the present method, already exists for transonic flow computations[16], must be a useful tool for ship hydrodynamics or marine engineering.

ACKNOWLEDGEMENT

REFERENCES

[1] Kodama, Y.:"Grid Generation and Flow Computation for Practical Ship Hull Forms and Propellers Using the Geometrical Method and the IAF Scheme.", Proc. 5th Intern. Conf. Numerical Ship Hydrodynamics , Hiroshima, (1989).

[2] Chen, H.C.:"Solution of Reynolds-Averaged Navier-Stokes Equations for Three-Dimensional Incompressible Flows.", J. Comput. Phys., Vol.88, (1990).

[3] Dawson, C.W.:"A Practical Computer Method for Solving Ship Wave Problems.", Proc. 2nd Intern. Conf. Numerical Ship Hydrodynamics, Berkeley, (1977).

[4] Hino, T.:"Computation of a Free Surface Flow around an Advancing Ship by the Navier-Stokes Equations.", Proc. 5th Intern. Conf. Numerical Ship Hydrodynamics, Hiroshima, (1989).

[5] Miyata, H. et al.:"Difference Solution of a Viscous Flow with Free-Surface Wave about an Advancing Ship.", J. Comput. Phys., Vol.72, (1987).

[6] Tahara, Y. et al.:"An Interactive Approach for Calculating Ship Boundary Layers and Wakes for Nonzero Froude Number.", J. Comput. Phys., Vol.98, (1992).

[7] Jameson, A. et al.:"Finite Volume Solution of the Two-Dimensional Euler Equations on a Regular Triangular Mesh.", AIAA J., Vol.24, No.4, (1986).

[8] Dreyer, J.D.:"Finite Volume Solutions to the Steady Incompressible Euler Equations on Unstructured Triangular Meshes.", MSE Thesis, Dept. Mechanical and Aerospace Engineering, Princeton University, (1990).

[9] Harlow F.H. et al.:"Numerical Calculation of Time-Dependent Viscous Flow of Fluid with Free Surface.", Physics of Fluids, Vol.8, (1965).

[10] Chorin, A,J.:"A Numerical Method for Solving Incompressible Viscous Flow Problems.", J. Comput. Phys., Vol.2, (1967).

[11] Jameson, A:"Computaional Transonics", Comm. Pure Appl. Math., Vol.XLI, (1988).

[12] Romante, J.E.:"Absorbing Boundary Conditions for Free Surface Waves.", J. Comput. Phys., Vol.99, (1992).

[13] Peraire, J. et al.:"Adaptive Remeshing for Compressible Flow Computations.", J. Comput. Phys., Vol.72, (1987).

[14] Mavriplis, D.:"Solution of the Two-Dimensional Euler Equations on Unstructured Triangular Meshes", PhD Thesis, Dept. Mechanical and Aerospace Engineering, Princeton University, (1987).

[15] Duncan, J.H.:"The Breaking and Non-Breaking Wave Resistance of a Two-Dimensional Hydrofoil.", J. Fluid Mech., Vol.126, (1983).

[16] Jameson, A. et al.:"Calculation of Inviscid Transonic Flow over a Complete Aircraft.", AIAA paper 86-0103, (1986).
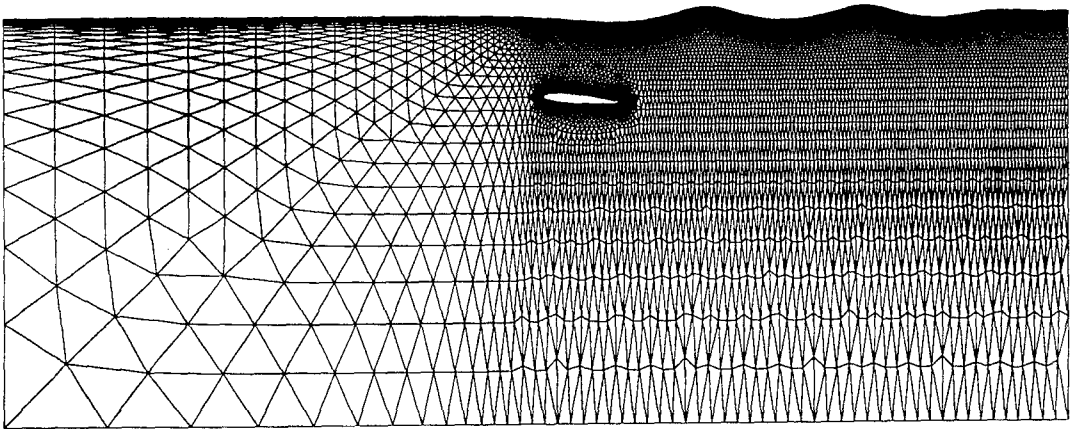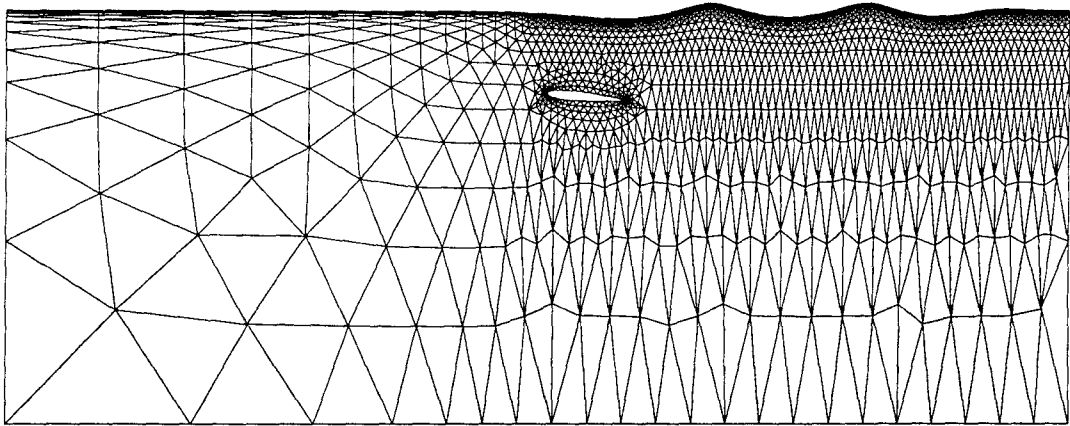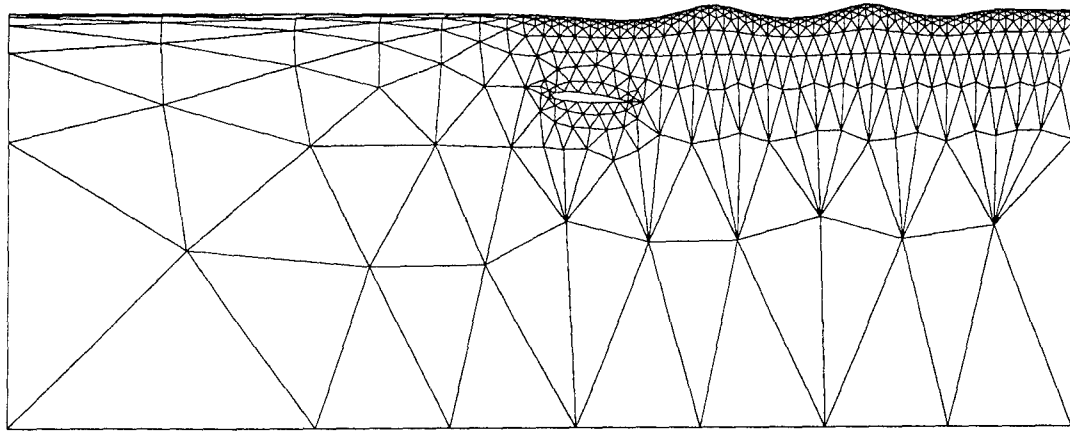
Figure 8: Sequence of multigrids around NACA0012.
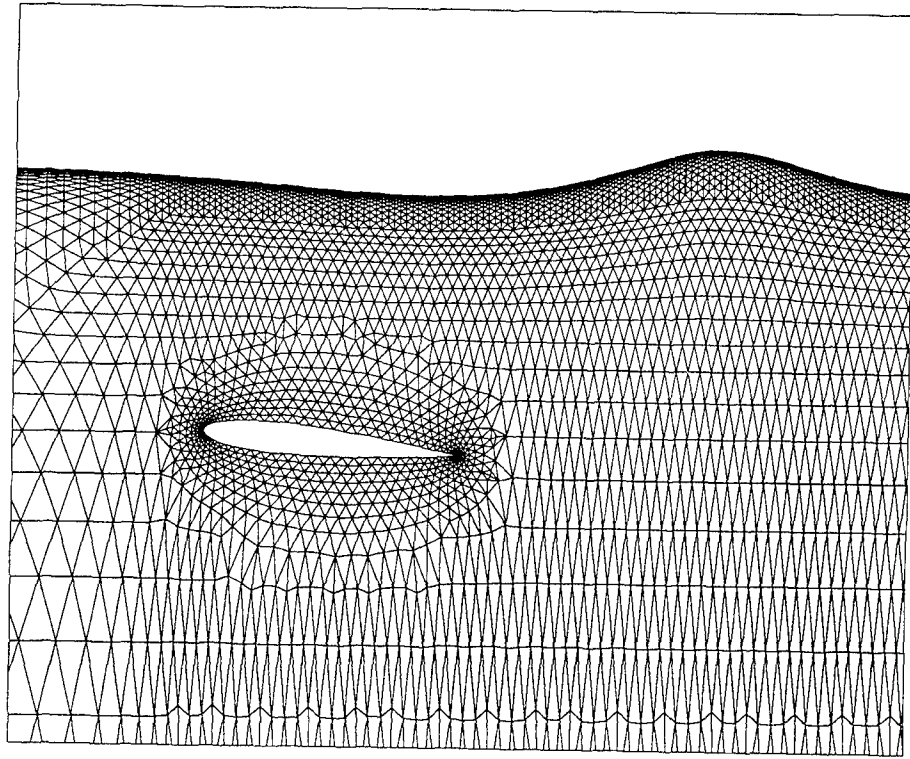
Figure 9: Magnified view of the finest grid around NACA0012.
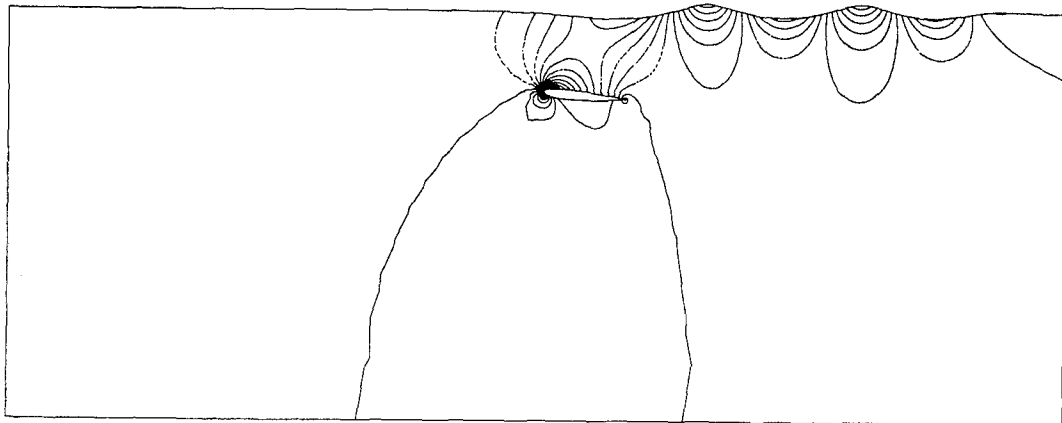
Figure 10: Computed pressure distribution with the multigrid case.

187
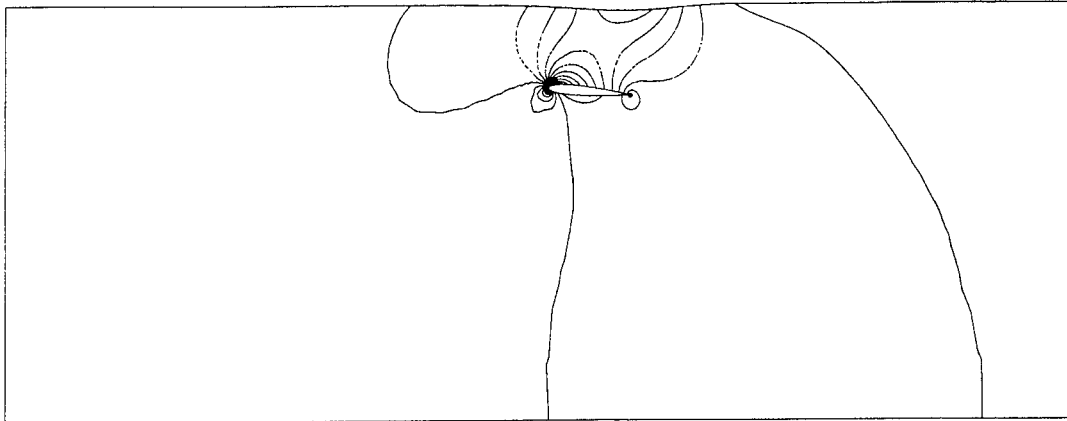
Figure 11: Computed pressure distribution with the single grid case.
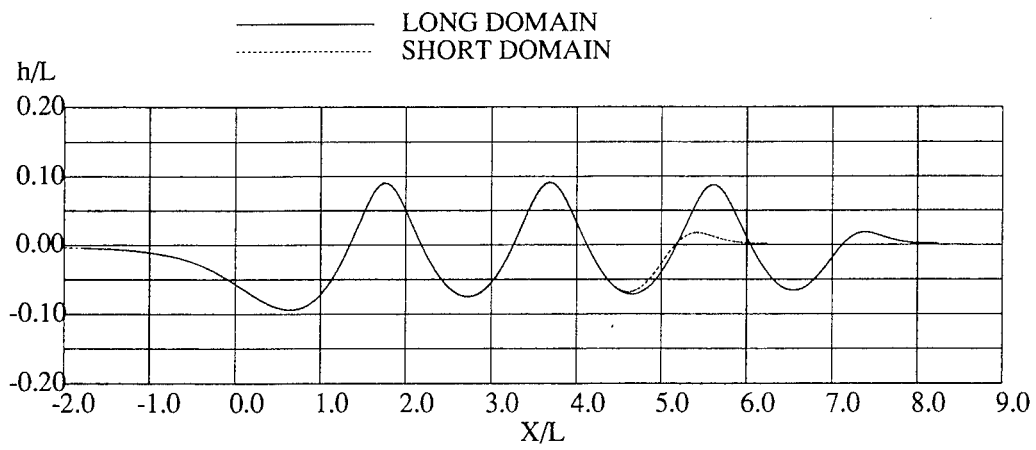
Figure 12: Comparison of wave profiles with the long and the short domains.
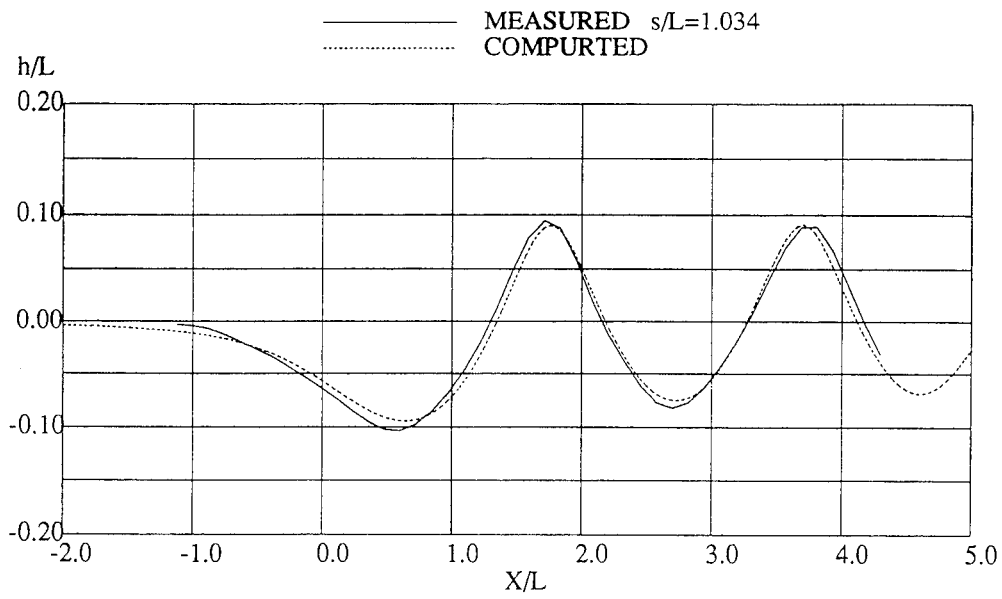
Figure 13: Comparison of wave profiles at $s = 1.034$
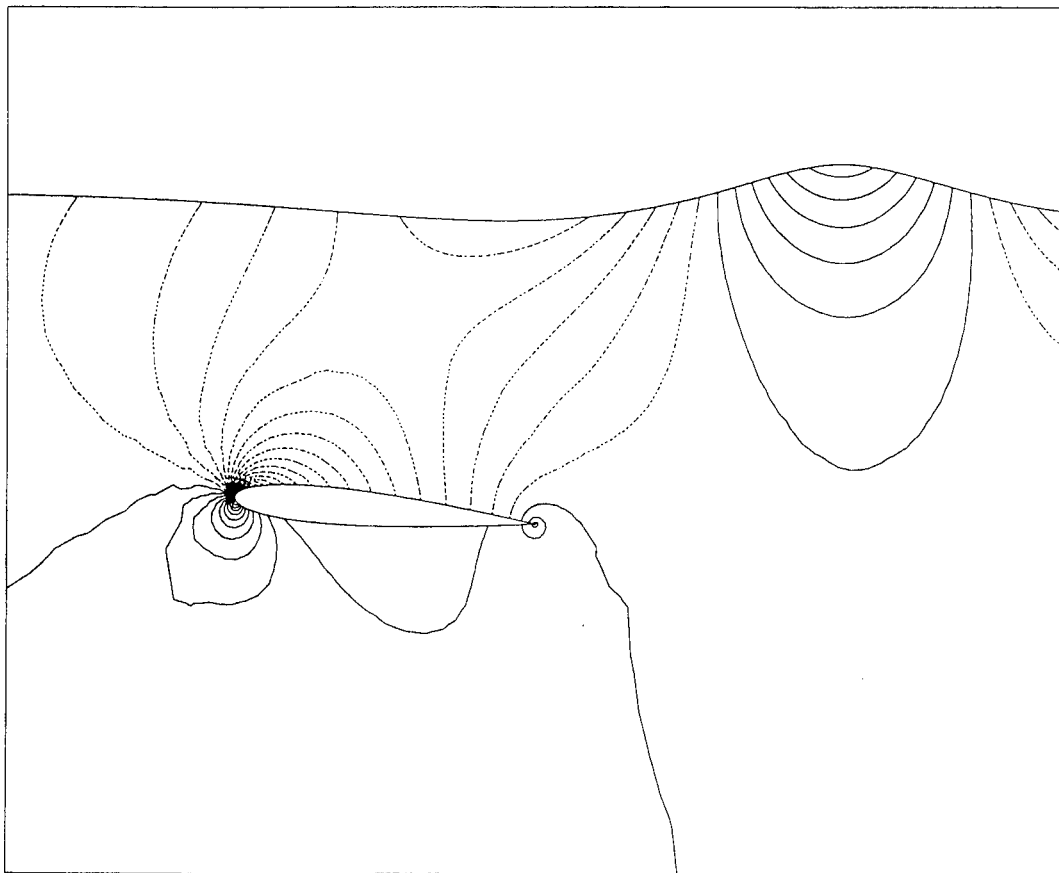
Figure 14: Computed pressure distribution.

189
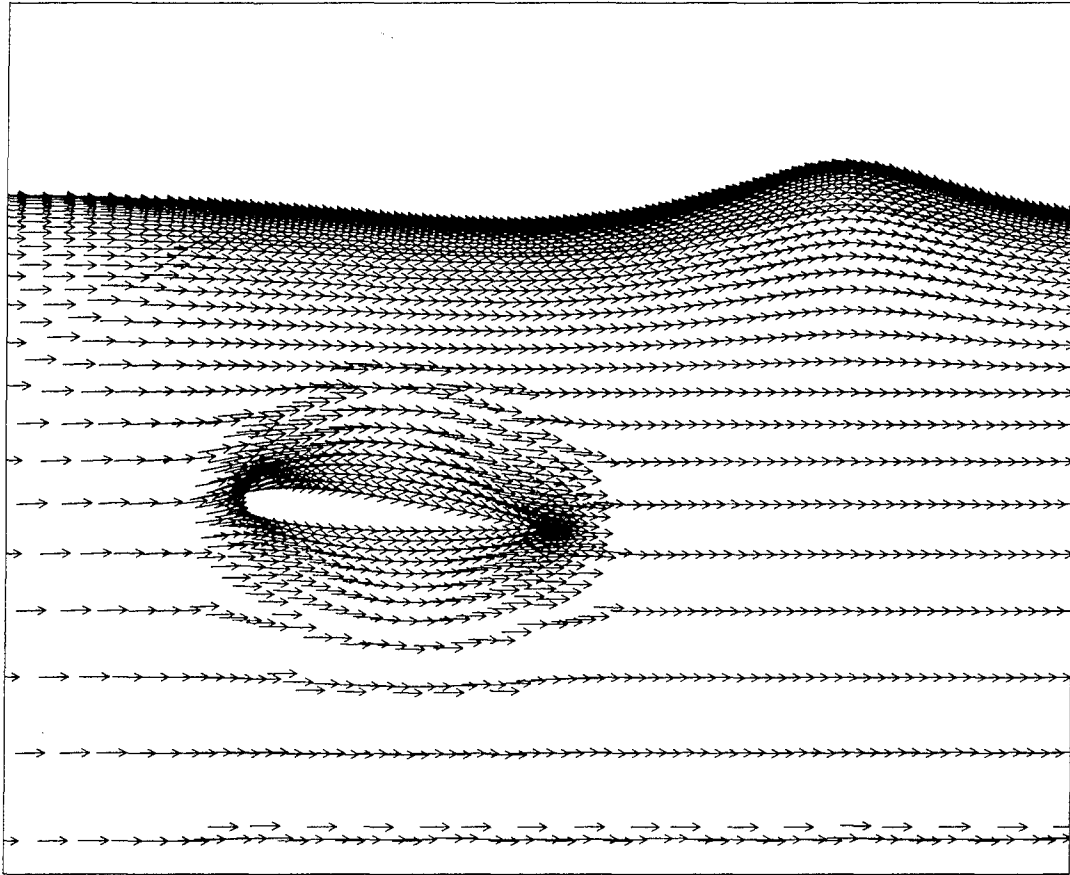
Figure 15: Computed velocity vectors.
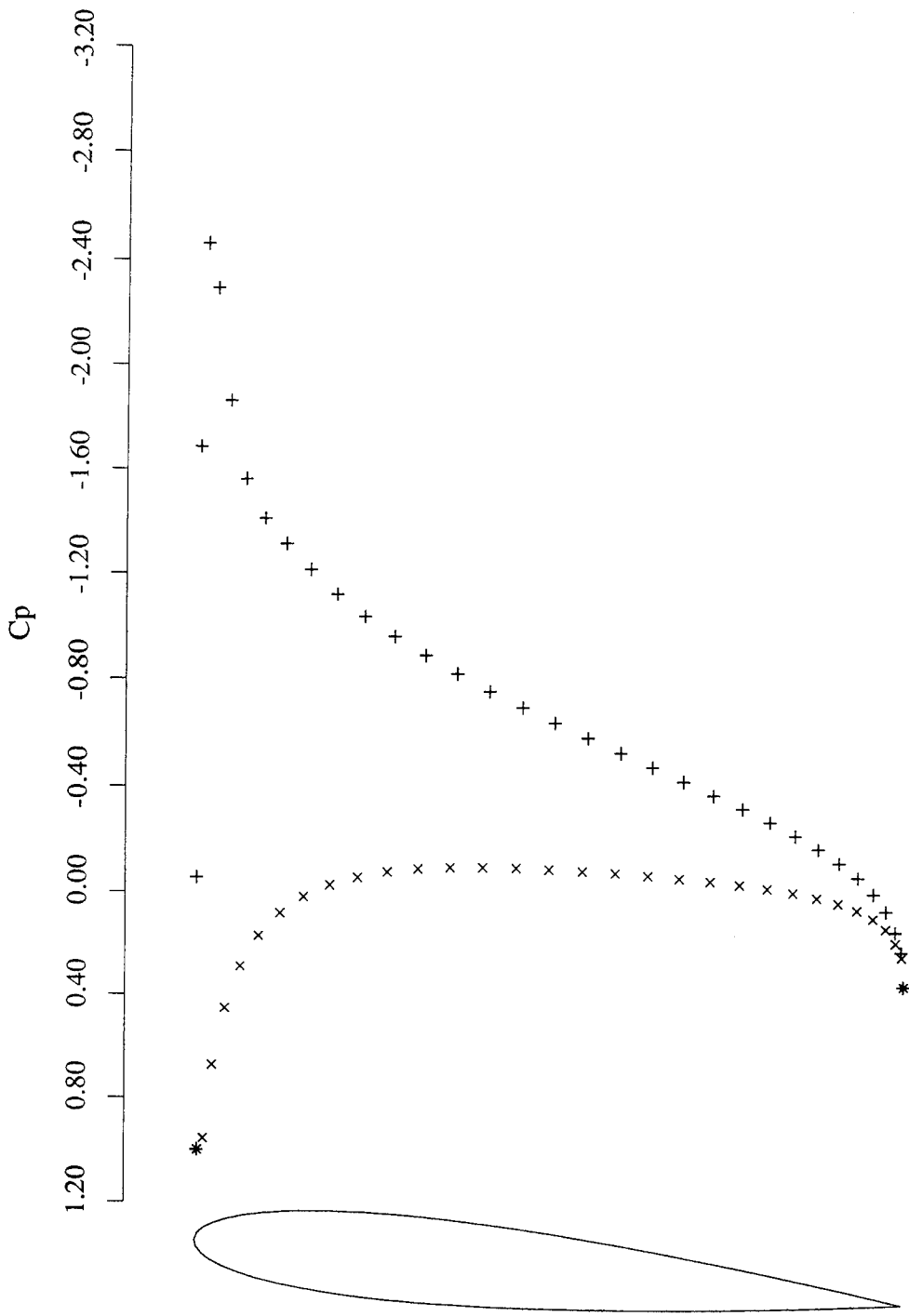
NACA0012   s/L=1.034
Froude no.   0.567   alpha 5.000

Figure 16: Computed Cp distribution.

191
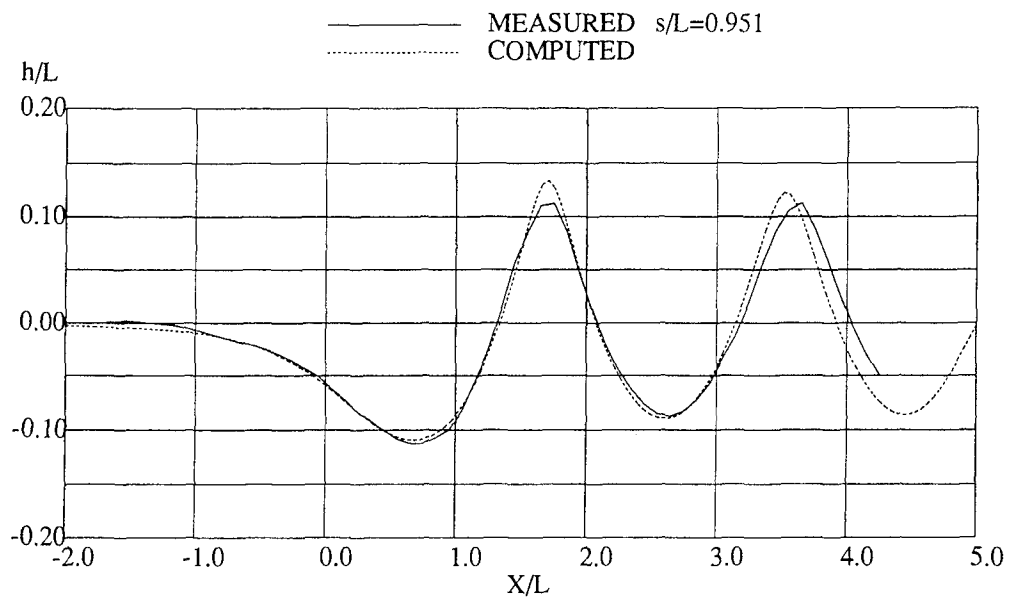
Figure 17: Comparison of wave profiles at $s = 0.951$
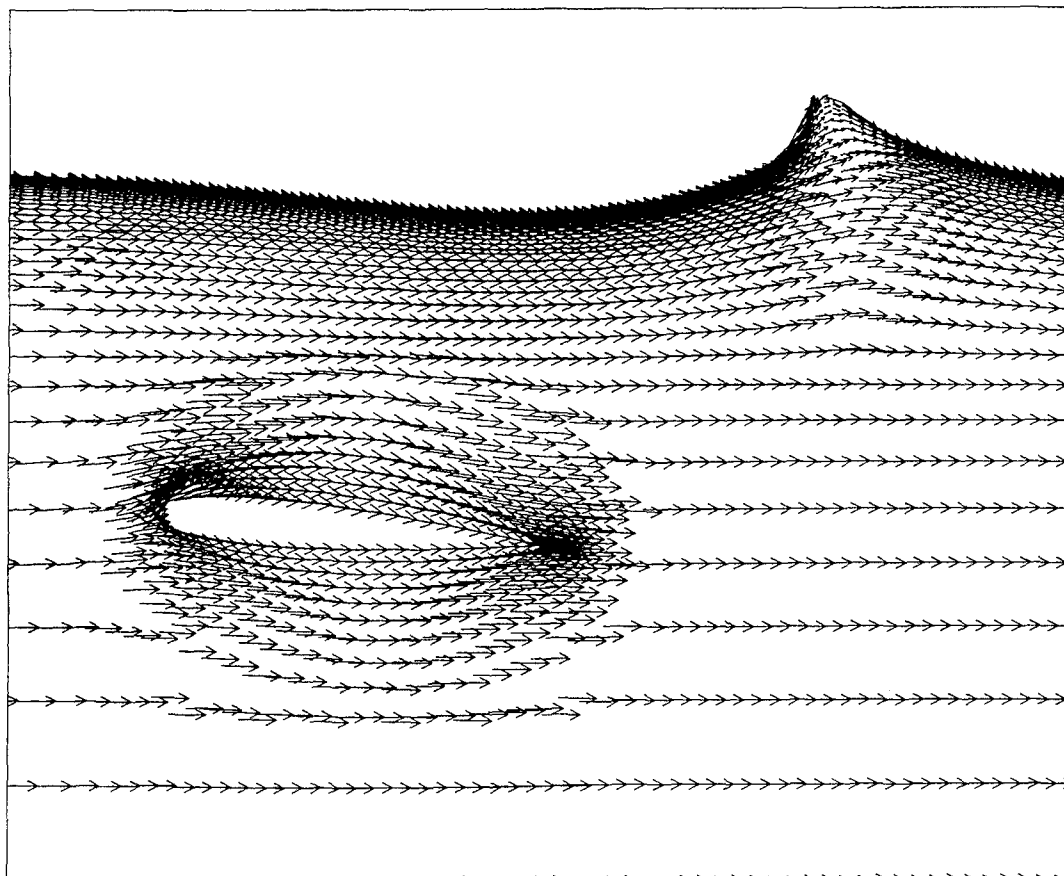
Figure 18: Computed wave profile and velocity distributions at $s = 0.911$

DISCUSSION
by Dr. Antony J. Musker, DRA Haslar, England.

A very sophisticated algorithm has been presented for solving the 2D Euler equations for the free-surface wave-making problem. There is little doubt that an Euler approach will perform better in the near wave-breaking region compared with Rankine source density methods since these fail completely for extreme non-linear cases. It is not clear, though, how the methodology described in your paper can be expanded to deal with actual wave-breaking. Does your suggestion of adopting a Lagrancian approach imply that one has to start again from first principles or that some modification can be made to the existing approach?

The grid is composed of triangles constructed according to Delaunay criterion. I believe it is a property of this technique that the resulting triangles tend to be not far from equilateral. Although this may work for Euler solvers, it is doubtful that it will work for Navier-Stokes solvers because of the need to resolve the very high velocity gradients close to solid boundaries. Perhaps the authors could comment on this?

Author's Reply

In order to simulate breaking waves, the free surface conditions, both kinematic and dynamic conditions, should be satisfied as accurately as possible. The unstructured grid method shown here can cope with the dynamic condition in case of the complex geometry which may occur in the wave breaking process.

The implementation of the kinematic free surface condition is crucial for breaking wave simulations. The Lagrangean approach may be the most promising way to deal with large deformation such as overturning waves. In the present flow solver, any algorithm for free surface tracking can be used with the proper triangulation procedure of flow domain. The modifications are needed only in the free surface tracking and re-girding routines.

The unstructured grids for the Navier-Stokes solutions require high-aspect-ratio triangles near the solid boundary. The simple Delaunay triangulation does not work well in such cases. However, by using the local mapping, the stretching grid for the viscous computations can be generated by the Delaunay algorithm, see the following reference.

Reference

Mavriplis, D.J., "Adaptive Mesh Generation for Viscous Flows Using Delaunay Triangulation," Journal of Computational Physics, Vol. 90, No. 2, 1990.

193

A Semi-Implicit Semi-Lagrangian Finite Element Model for Nonlinear Free Surface Flow

A. Allievi and S. Calisal

(University of British Columbia, Canada)

ABSTRACT

Potential flow initial-boundary value problems describing fluid structure interaction with fully nonlinear free surface boundary conditions have been studied using a mixed Lagrangian Eulerian formulation. The two dimensional boundary value problem has been solved in the physical domain by means of a Bubnov-Galerkin formulation of the Laplace equation. The initial-value problem related to the behavior of some of the moving boundaries has been discretized using a semi-implicit semi-Lagrangian two time level iterative scheme that is *almost* free from smoothing.

Fluid responses to periodic excitation of surface piercing and submerged bodies have been calculated. The impulsive response of tanks of various shapes has also been simulated. Resulting natural frequencies show good agreement with available data.

A slender body representation of the flow around a hull advancing with forward speed in otherwise calm water has also been simulated. Numerical calculations of a number of quantities of engineering interest are presented for different length Froude numbers. Results compare favorably with experimental data.

NOMENCLATURE

A: Body motion amplitude
$B(x,y)$: Body offset
C_B: Block coefficient
C_P: Prismatic coefficient
C_w: Wave resistance coefficient
C_{WP}: Waterplane coefficient
D: Ship draft
f: Distortion function for mesh generation
F_n: Length Froude number, $F_n = \frac{U}{\sqrt{gL}}$
g: Acceleration of gravity
J: Jacobian of the transformation from (x,y) to (ξ, η) coordinates
J^*: Jacobian of the transformation from (ε, ϱ) to (ξ, η) coordinates
L: Ship length
$\vec{n}$: Unit normal vector
t: Time
U: Ship forward speed
x, y, z: Cartesian coordinates
α: Parameter for modified Lax method
ξ, η: Isoparametric coordinates
ε, ϱ: Boundary fitted curvilinear coordinates
Γ: Boundary of domain of integration Ω
ω: Body motion frequency
Ω: Domain of integration
ϕ: Velocity potential
Φ_j: Linearly independent functions
$\varsigma(z, t)$: Free surface elevation
$\varsigma_0(t)$: Unsteady Bernoulli constant
ρ: Water density

1. INTRODUCTION

In ship design, it is important to determine the behavior of a vessel at sea as a function of its form and dimensions. From this information, the designer is able

- to select an optimal hull form that will satisfy predefined criteria such as type of cargo, speed, displacement and route of operation

- to predict the behavior of the chosen configuration and to ascertain the consequences of this behavior on various effects such as safety, structural dimensioning, resistance and propulsion.

At the preliminary design stage, many ship parameters remain to be varied. Principal dimensions, line plans, and various hull coefficients are some of the variables involved in the primary selection of a ship hull. Testing of this initially large number of concepts is more easily executed by mathematical simulations than by physical model tests. Test facilities and costs may also be restrictive factors in the use of the latter models.

In order to have reliability of the numerical simulation results, all possible phenomena that are related to the type of problem to be solved should be incorporated in the development of the computer code. The variables related to these phenomena can be considered as part of a three dimensional nonlinear problem. This requires the solution of very large systems of algebraic equations at each of a large number of time steps. In this case, excessive memory and CPU requirements may pose restrictions on the viability of the calculations. In order to make this problem more tractable in a numerical sense, certain simplifications in ship dimensions may be introduced to reduce the computational demands required for the solution of the problem. Simplifying steps can be taken in limiting the ratio of the transverse to longitudinal physical dimensions of the ship. This is known as a *slender body approximation*[1].

For a slender body, the underlying physical idea is that flow variations in the longitudinal direction are much smaller than those occurring in other directions in the local vicinity of the body. The cross-flow at each cross-section is considered to be independent of the flow downstream of that section. The fluid flow at each cross-section is only determined by information conveyed from upstream conditions. The connection of these series of two dimen-

sional flows with the actual three-dimensional flow is achieved through the body boundary condition that contains the longitudinal x-variable. One of the first attempts to use slender body theory for surface ships was made by Cummins[2] in the solution of the wave resistance problem. Later, Kaplan[3] studied the vertical force and pitching moment on a slender body moving normal to the crests of regular waves.

As a result of these investigations, a considerable number of researchers made use of slender body theory in works related to the marine environment. Lighthill[4] studied the thrust efficiency of a slender fish and concluded that this parameter would depend strongly on the wave like motion of the fish and its propagation speed along the spinal cord. Vossers[5] and Maruo[6] studied wave resistance of a ship with uniform forward speed. Ursell[7] approximated the flow around a stationary ship by an axial line distribution of known point singularities and the harmonic small motions by wave sources satisfying the free surface condition. Tuck[8] extended this work to the steady translation of a slender ship. Newman and Tuck[9] described a complete systematic linear theory of the motions of a slender ship in a seaway. Newman[10] generalized the Haskind relations[11] for the six exciting forces and moments in waves to include the effect of forward speed as a function of the wave length, heading angle and forward speed. Tuck[12] solved the problem of the disturbance produced to a shallow water stream by an immersed slender body.

Much of the progress in slender body theory as applied to submerged and floating marine vehicles was carried out in the 1960's. Newman[13] summarized the advances made during this period. Research until then had focused on analytical techniques for steady state problems. Numerical results related to slender-ship motions were then published. These results compared analytical and numerical calculations within the realm of linear boundary conditions compatible with small departures of the body from an equilibrium position and with infinitesimal deviations of the free surface from undisturbed conditions. Some of these works are by Chapman[14] and Jensen and Pedersen[15]. Troesch[16,17] ob-

tained sway, roll and yaw motion coefficients for a slender ship with uniform forward speed. A simplified boundary value problem was later introduced by Maruo[18] in a new slender body approach to calculate resistance of a ship with uniform forward speed. Other slender-ship approximations were presented by Noblesse[19] for the calculation of linear wave resistance problems using a new integro-differential equation for the velocity potential of the flow caused by the ship. Faltinsen[20] studied the flow around a ship bow at high Froude numbers and regular incident head sea waves with complete linear boundary conditions. Chen and Noblesse[21,22] presented numerical results for wave resistance at a relatively wide range of Froude numbers for the theory developed by Noblesse in[19]. Diffraction of free surface waves using linear theory was presented by Sclavounos[23] using matched asymptotic expansions to match a two dimensional inner field with the three dimensional solution of the far field. Sclavounos[24] extended this work to address linear diffraction and radiation problems for heave and pitch motions of a ship with forward speed in waves. Breit and Sclavounos[25] used a linear approximation for surface wave radiation by two adjacent slender bodies. Maruo's approach[18] was numerically studied by Song et. al.[26] in the calculation of wave patterns and wave resistance of a Wigley hull. Various computational procedures making use of slender body approximations with different degrees of nonlinearities included in their schemes were also tackled by Choi and Mei[27], Kashiwagi[28], Kashiwagi and Ohkusu[29], Calisal and Chan[30] and Ando[31]. Further progress of the theory presented by Maruo [18] were later reported by this author[32].

Slender body theory assumes the validity of a two-dimensional cross-sectional flow that is carried along the remaining third dimension through appropriate boundary conditions. In this case it seems advisable to initially develop a robust model that can describe two-dimensional flow with a nonlinear free surface in a reliable and accurate form. As a consequence of intensified research in relatively recent years, the importance of two-dimensional nonlinear free surface hydrodynamic problems has become appar-

ent. A compilation of some of the methodologies used to solve these types of problems during preliminary years has been outlined by Yeung[33]. The pioneer work by Longuet-Higgins and Cokelet [34] used an integral equation formulation to simulate large amplitude steep waves and wave breaking. Later investigations by Vinje and Brevig [35] and Lin, Newman and Yue[36] added the presence of a moving body. A number of contributions in the area of integral-equation methods were also made by Baker, Meiron and Orzag[37], Dold and Peregrine[38] and Suzuki[39]. Sen et.al. [40] studied the propagation of steep two dimensional periodic waves and the large motions induced by these waves on free floating bodies. Cointe[41] studied the nonlinear forced motion of surface piercing bodies and the nonlinear motion of a rectangular barge in beam seas[42].

Finite difference techniques have also been employed in nonlinear wave-body problems by numerically mapping the physical domain onto a regular computational domain. Ghia, Shin and Ghia[43] and Haussling[44] used this approach to study the formation of breaking waves. Telste[45] and Yeung and Wu[46,47] solved nonlinear free surface problems associated with forced periodic motion in a tank.

Finite element techniques were introduced in the context of free surface flows by Luke[48]. A modified form of Luke's formulation was used by Whitman[49,50] to study wave dispersion. Bai and Yeung[51] studied linear forced motion problems using the conventional variational formulation and a more efficient modified variational method in order to truncate the original infinite domain of solution. The first procedure presented by Bai and Yeung[51] was used by Bai[52] to study diffraction of oblique waves by an infinite cylinder with linear boundary conditions. Yim[53] addressed the problem of nonlinear steady ship waves using an approach with linear theory in the outer region. Bai[54,55] calculated flow about two dimensional bodies under a linear free surface using weak and variational formulations. Bai[56] also derived an approximate formula for blockage effects affecting the flow past ship models moving in a towing tank with a free surface. Wellford and Ganaba[57] implemented a pseudo-variational approach for

unsteady water wave problems. Further contributions using finite element techniques in ship hydrodynamics using free surface potential flow were presented at the 3rd International Conference on Numerical Ship Hydrodynamics. Oomen [58] used perturbation analysis of the velocity potential and free surface elevation. This technique produced a series of linearized two dimensional problems that were used to study the steady translation of a Series 60 model in calm water. Jami[59] solved the linearized flow past a submerged body with arbitrary transient motion of small amplitude. Numerical results were presented for two-dimensional transient forces acting on the body. Euvard et. al.[60] coupled finite element and singularity distribution procedures.

In this work, consideration has been given to produce a simplified model that can reliably predict quantities required in ship design with affordable computer hardware. A Bubnov-Galerkin formulation of the boundary value problem describing two-dimensional potential flow was developed for the spatial estimation of the velocity potential. It was foreseen that this formulation would require an efficient mesh generation system capable of adapting to the changes of the nonlinear moving boundaries. Again, a Bubnov-Galerkin formulation of the grid generation equations was performed. Significant computational advantages over previous methods of solution have been realized [61,62]. Linear and quadratic isoparametric elements were used and their relative merits analyzed.

The time derivatives describing the nonlinear boundary conditions were initially discretized using various orders of explicit-implicit predictor-corrector methods. These methods exhibited excellent stability characteristics and improved accuracy for linear free surface applications. However, for nonlinear free surface flow calculations these procedures displayed unstable behaviour. Numerical dissipation of the velocity potential and the free surface elevation then had to be introduced. The resulting motion of the free surface fluid particles exhibited inaccuracies that negatively affected the calculation of quantities of engineering interest. In order to avoid erroneous estimations due to smoothing, efforts were directed towards devising a numerical scheme that would be stable with minimum numerical dissipation. A two time level semi-implicit semi-Lagrangian iterative integration scheme was then conceived[63]. The method is *almost* free from so called smoothing. Iterative schemes of a similar nature were used by Robert[64,65], Staniforth and Temperton[66,67] and Bermejo[68]. These works were concerned with meshes whose boundaries remained unchanged as the solution progressed in time. In this work, an iterative semi-implicit semi-Lagrangian scheme is used to locate the fluid particles in contact with the moving boundaries. In addition, values of the dependent variable are obtained on these material points.

In order to validate the methodologies previously mentioned, a number of two-dimensional problems have been solved. Results are given for fluid response due to forced oscillations of surface piercing and submerged bodies in a closed domain. Fluid response in tanks of different shapes due to impulsive loading is also studied. The two dimensional results are subsequently extended to study a mathematically defined slender body, the Wigley hull, advancing with forward speed in otherwise calm water. All concepts and results reported in this paper can be found in greater detail in[63].

2. GOVERNING EQUATIONS

We consider the two-dimensional motion of an inviscid, incompressible and homogeneous fluid undergoing irrotational motion in a tank. A Cartesian coordinate system (y, z) fixed in space is adopted. Acceleration of gravity g acts in the negative y-direction and $y = 0$ is the plane of the undisturbed free surface. The fluid velocity vector $\vec{V}(y, z, t)$, where t denotes time, can then be represented by the gradient of a scalar potential $\phi(y, z, t)$ which satisfies the Laplace equation. Denoting $B(y, t)$ the moving body surface, $\varsigma(z, t)$ the free surface elevation and S_w, S_b the tank's bottom and side walls respectively, we can write the initial-boundary value problem in a two-dimensional tank as

$$\frac{\partial^2 \phi}{\partial y^2} + \frac{\partial^2 \phi}{\partial z^2} = 0 \qquad (1)$$

$$\frac{dy}{dt} - \frac{\partial\phi}{\partial y} = 0 \qquad (2)$$

$$\frac{dz}{dt} - \frac{\partial\phi}{\partial z} = 0 \qquad (3)$$

$$\frac{d\phi}{dt} + g(\varsigma - \varsigma_0(t)) - \frac{1}{2}\nabla\phi\nabla\phi = 0 \qquad (4)$$

$$\frac{\partial\phi}{\partial n} - n_i q_i = 0 \qquad on \ z = B(y,t) \qquad (5)$$

$$\frac{\partial\phi}{\partial n} = 0 \qquad on \ S_w \ , \ S_b \qquad (6)$$

Equation (1) describes a boundary value problem which is solved subject to the moving boundary conditions (2) to (5) and (6). Details on the calculation of Bernoulli's constant $\varsigma_0(t)$ were reported by Yeung and Wu[46].

3. GALERKIN FORMULATION IN SPACE

The boundary value problem has been solved using a Galerkin formulation of the Laplace equation. The basic idea of this method is to obtain the solution of a partial differential equation by introducing an approximate solution $\hat{\Phi}$ which is in turn equal to the summation of n linearly independent functions Φ_i times the nodal values $\bar{\phi}_j$ of the dependent variable. Minimization of the resulting residual leads to

$$\int_{-1}^{+1}\int_{-1}^{+1}\sum_{j=1}^{m}\bar{\phi}_j\left\{\left[\bar{J}_{11}\frac{\partial\Phi_j}{\partial\xi} + \bar{J}_{12}\frac{\partial\Phi_j}{\partial\eta}\right]\right.$$

$$\left[\bar{J}_{11}\frac{\partial\Phi_i}{\partial\xi} + \bar{J}_{12}\frac{\partial\Phi_i}{\partial\eta}\right] +$$

$$+ \left[\bar{J}_{21}\frac{\partial\Phi_j}{\partial\xi} + \bar{J}_{22}\frac{\partial\Phi_j}{\partial\eta}\right] \qquad (7)$$

$$\left.\left[\bar{J}_{21}\frac{\partial\Phi_i}{\partial\xi} + \bar{J}_{22}\frac{\partial\Phi_i}{\partial\eta}\right]\right\}det[J]d\xi d\eta =$$

$$= \int_{\Gamma_l}\Phi_i\frac{\partial\hat{\Phi}}{\partial n}d\Gamma_l$$

where J_{km} are the components of the Jacobian of the transformation from Cartesian coordinates to isoparametric coordinates. Equation (7) is solved subject to equations (2) to (5) at the exact instantaneous position of the moving boundaries. Dirichlet-type boundary conditions have been used for the free surface. Neumann boundary conditions are used on all fixed and moving solid boundaries by calculating the right side of (7).

4. DISCRETIZATION OF THE FREE SURFACE IN TIME

Equations (2) and (3) are used to obtain the trajectories followed by fluid particles located on the fluid-air interface . In order to integrate these equations, an iterative scheme was developed by Allievi[63] to obtain vectorial position and value of the velocity potential at each fluid particle on this boundary. We write the expressions for the *first increment* of each Lagrangian derivative (2), (3) and (4) on the free surface in the following second-order extrapolative form

$$\alpha_i^{(0),t+\frac{\Delta t}{2}} = \Delta t\left\{\frac{3}{2}\left[\frac{\partial\phi}{\partial y}\right]_i^t - \frac{1}{2}\left[\frac{\partial\phi}{\partial y}\right]_i^{t-1}\right\} \qquad (8)$$

$$\beta_i^{(0),t+\frac{\Delta t}{2}} = \Delta t\left\{\frac{3}{2}\left[\frac{\partial\phi}{\partial z}\right]_i^t - \frac{1}{2}\left[\frac{\partial\phi}{\partial z}\right]_i^{t-1}\right\} \qquad (9)$$

$$\gamma_i^{(0),t+\frac{\Delta t}{2}} = \Delta t\left\{\frac{3}{2}\left[\frac{d\phi}{dt}\right]_i^t - \frac{1}{2}\left[\frac{d\phi}{dt}\right]_i^{t-1}\right\} \qquad (10)$$

where the subindex i refers to a fluid particle on the free surface. Now, with an initial value given by the equations above we iterate the following scheme

$$k = 1, ..., m$$
$$z_i^{(k),t+\frac{\Delta t}{2}} = z_i^t + \frac{1}{2}\alpha_i^{(k-1),t+\Delta t}$$
$$y_i^{(k),t+\frac{\Delta t}{2}} = y_i^t + \frac{1}{2}\beta_i^{(k-1),t+\Delta t} \qquad (11)$$
$$\phi_i^{(k),t+\frac{\Delta t}{2}} = \phi_i^t + \frac{1}{2}\gamma_i^{(k-1),t+\Delta t}$$

$$\alpha_i^{(k),t+\Delta t} =$$
$$\Delta t\frac{\partial\phi}{\partial y}(z_i^{(k),t+\frac{\Delta t}{2}}, y_i^{(k),t+\frac{\Delta t}{2}}, \phi_i^{(k),t+\frac{\Delta t}{2}}) \qquad (12)$$

$$\beta_i^{(k),t+\Delta t} =$$
$$\Delta t\frac{\partial\phi}{\partial z}(z_i^{(k),t+\frac{\Delta t}{2}}, y_i^{(k),t+\frac{\Delta t}{2}}, \phi_i^{(k),t+\frac{\Delta t}{2}}) \qquad (13)$$

$$\gamma_i^{(k),t+\Delta t} =$$
$$\Delta t\frac{d\phi}{dt}(z_i^{(k),t+\frac{\Delta t}{2}}, y_i^{(k),t+\frac{\Delta t}{2}}, \phi_i^{(k),t+\frac{\Delta t}{2}}) \qquad (14)$$

The iteration is continued until

199

$$\alpha_i^{(k),t+\Delta t} - \alpha_i^{(k-1),t+\Delta t} < \epsilon_\alpha$$

$$\beta_i^{(k),t+\Delta t} - \beta_i^{(k-1),t+\Delta t} < \epsilon_\beta$$

$$\gamma_i^{(k),t+\Delta t} - \gamma_i^{(k-1),t+\Delta t} < \epsilon_\gamma$$

where $\epsilon_\alpha, \epsilon_\beta$ and ϵ_γ are tolerances to be specified. When convergence has been achieved at the m iteration, the free surface is updated as

$$z_i^{t+\Delta t} = z_i^t + \alpha_i^{(m),t+\Delta t}$$
$$y_i^{t+\Delta t} = y_i^t + \beta_i^{(m),t+\Delta t} \qquad (15)$$
$$\phi_i^{t+\Delta t} = \phi_i^t + \gamma_i^{(m),t+\Delta t}$$

In some instances numerical dissipation was applied to maintain stability of the numerical scheme. This was performed only on the velocity potential $\phi_i^{t+\Delta t}$ using a modified Lax method as

$$\phi_i^{t+\Delta t} = \frac{1}{2}\alpha(\phi_{i+1}^{t+\Delta t}+\phi_{i-1}^{t+\Delta t})+(1-\alpha)\phi_i^{t+\Delta t} \quad (16)$$

with α specified as the minimum value that would result in a stable run. Note that for $\alpha = 0$ no dissipation is introduced and for $\alpha = 1$ we have the traditional Lax method.

5. MESH GENERATION

The mesh generation system used here was developed by Ryskin and Leal[69]. It has been solved using a Bubnov-Galerkin formulation. For the z-coordinate, we then have

$$\int_{-1}^{+1}\int_{-1}^{+1}\sum_{j=1}^{n} z_j \left\{ f_j \left[\bar{J}_{11}^* \frac{\partial\Phi_j}{\partial\xi} + \bar{J}_{12}^* \frac{\partial\Phi_j}{\partial\eta} \right] \right.$$
$$\left[\bar{J}_{11}^* \frac{\partial\Phi_i}{\partial\xi} + \bar{J}_{12}^* \frac{\partial\Phi_i}{\partial\eta} \right] +$$
$$+ \frac{1}{f_j} \left[\bar{J}_{21}^* \frac{\partial\Phi_j}{\partial\xi} + \bar{J}_{22}^* \frac{\partial\Phi_j}{\partial\eta} \right]$$
$$\left. \left[\bar{J}_{21}^* \frac{\partial\Phi_i}{\partial\xi} + \bar{J}_{22}^* \frac{\partial\Phi_i}{\partial\eta} \right] \right\} det[J] d\xi d\eta =$$
$$= \int_{\Gamma_l} \Phi_i \left\{ \left(f_{\Gamma_l} \frac{\partial z}{\partial \varepsilon} \right) \vec{n}_\varepsilon + \left(\frac{1}{f_{\Gamma_l}} \frac{\partial z}{\partial \varrho} \right) \vec{n}_\varrho \right\} d\Gamma_l$$
$$(17)$$

Similarly, for the y-coordinate we have

$$\int_{-1}^{+1}\int_{-1}^{+1}\sum_{j=1}^{n} y_j \left\{ f_j \left[\bar{J}_{11}^* \frac{\partial\Phi_j}{\partial\xi} + \bar{J}_{12}^* \frac{\partial\Phi_j}{\partial\eta} \right] \right.$$
$$\left[\bar{J}_{11}^* \frac{\partial\Phi_i}{\partial\xi} + \bar{J}_{12}^* \frac{\partial\Phi_i}{\partial\eta} \right] +$$
$$+ \frac{1}{f_j} \left[\bar{J}_{21}^* \frac{\partial\Phi_j}{\partial\xi} + \bar{J}_{22}^* \frac{\partial\Phi_j}{\partial\eta} \right]$$
$$\left. \left[\bar{J}_{21}^* \frac{\partial\Phi_i}{\partial\xi} + \bar{J}_{22}^* \frac{\partial\Phi_i}{\partial\eta} \right] \right\} det[J] d\xi d\eta =$$
$$= \int_{\Gamma_l} \Phi_i \left\{ \left(f_{\Gamma_l} \frac{\partial y}{\partial \varepsilon} \right) \vec{n}_\varepsilon + \left(\frac{1}{f_{\Gamma_l}} \frac{\partial y}{\partial \varrho} \right) \vec{n}_\varrho \right\} d\Gamma_l$$
$$(18)$$

Details on the derivation and application of these equations to various geometries were reported by Allievi and Calisal[61,62].

6. NUMERICAL RESULTS

6.1 Heave of surface-piercing cylinder in a tank

In this section, we present results corresponding to vertical sinusoidal forced motion of the composite surface piercing cylinder shown in Figure 1. This case was studied by Yeung and Wu[46] using a computational domain finite difference discretization. Where appropriate, comparison is made with this publication. All results are non-dimensionalized using acceleration of gravity g, density ρ and radius of the circular section. The variable NI appearing in this section corresponds to the number of divisions used to discretize the free surface and *half* of the body surface. Nonlinear results in this section have been obtained using $\alpha = 0.01$.

Figures 2 and 3 show time histories of the free surface elevation produced by vertical forced excitation of the composite cylinder shown in Figure 1 with $A = 0.5$ and $\omega = 1.25$. Vertical dimensions have been magnified 10 times. As noted by Yeung and Wu[46] the free surface remains regular for linear free surface boundary conditions. However, there is qualitative differences in the free surface profiles. This is particularly noticeable towards the end of the run. While quadratic elements tend to predict a smoother $y - z$ contour of the free surface, linear elements show the appearance of a hump.

Figures 4 and 5 show linear and nonlin-
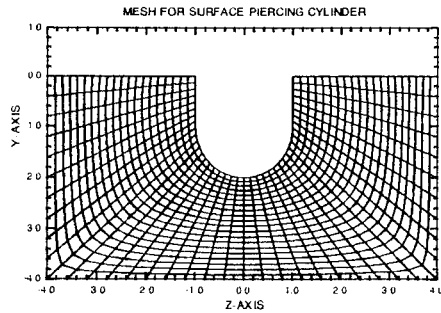
Figure 1: Typical mesh for surface-piercing cylinder.

Figure 2: Linear free surface time record for surface-piercing cylinder $(NI = 30, \Delta t = 0.1)$.

Figure 3: Linear free surface time record for surface-piercing cylinder $(NI = 20, \Delta t = 0.1)$.

Figure 4: Linear free surface evolution up to 20 cycles, NI=10, Δt=0.1.

Figure 5: Nonlinear free surface evolution up to 20 cycles, NI=10, Δt=0.1.

ear free surface profiles corresponding to $\omega = 1.25$ and $A = 0.5$ through 20 cycles of oscillation. The nonlinear free surface tends to be more irregular than that predicted by linear the-ory. However, irregularities are not as pronounced as those reported by Yeung and Wu[46]. This is more easily seen in Figure 6 where grids at approximately 8.25, 8.5, 8.75 and 9th cycles are shown. Figure 7 shows velocity vector plots for the mesh points shown in Figure 6. It can be seen that good quality meshes and smooth velocity field distributions are obtained.

Figure 8 shows hydrodynamic heave forces for the conditions used in Figure 6. As pointed out by Yeung and Wu[46], for large oscillations, nonlinear theory predicts a larger negative peak and a smaller positive one with respect to the sinusoidal prediction of linear theory. This effect is essentially a consequence of the relative dimensions of the tank and the moving body. Figure 9 shows the effect of increasing the tank dimensions by 2 and 3 times while keeping the body dimensions constant. The resulting effect

201
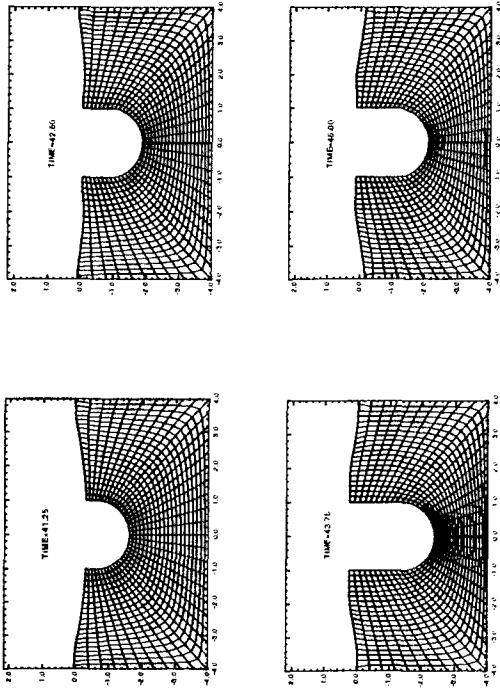
Figure 6: Mesh deformation at 8.25, 8.5, 8.75 and 9th cycles.
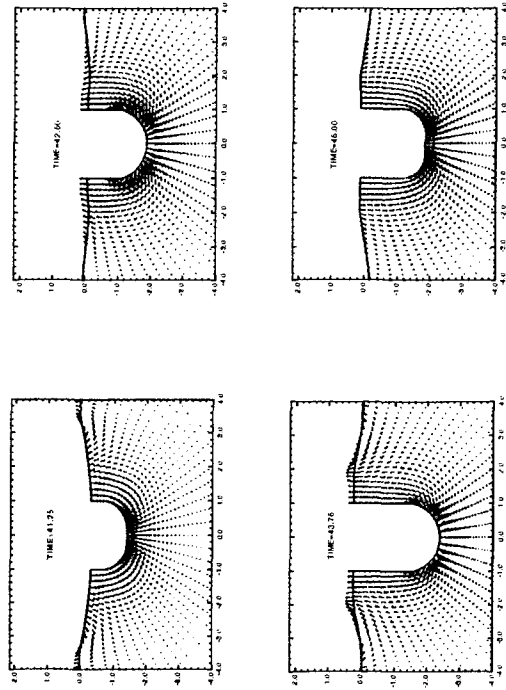
Figure 7: Velocity vector plots at 8.25, 8.5, 8.75 and 9th cycles.

is two-folded. First, a significant reduction of the amplitude of the hydrodynamic force is observed. Also, a decrease in the difference between positive and negative peaks of this force occurs.

6.2 Heave of submerged cylinder in a tank

Figure 10 shows a typical configuration for the mesh corresponding to the submerged cylinder. For this case, the cylinder radius is unity. The variable NI appearing in this section corresponds to the number of divisions used to discretize the free surface and *a quarter* of the body surface. Based on the experience gained in the case of the surface-piercing cylinder, in this section we have opted to use quadratic elements only. No smoothing was required for this case.

Figures 11 and 12 respectively show linear and nonlinear free surface time histories for $A = 0.5$. Vertical dimensions have also been magnified by 10 times. Steeper peaks were ob-
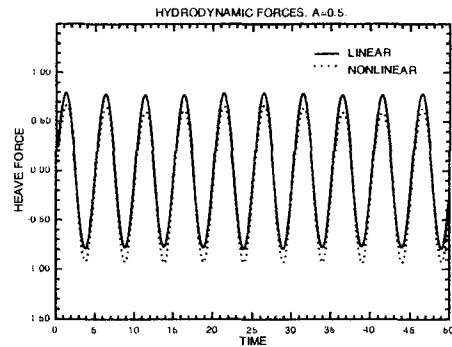
Figure 8: Hydrodynamic forces for surface-piercing cylinder.

served to develop in the regions next to the tank walls for nonlinear results. Linear results predicted an almost sinusoidal behavior of the free surface across the width of the tank. As expected, vertical elevations remained lower than that obtained for the case of the surface-piercing cylinder.

Figure 13 shows mesh deformation corre-

202
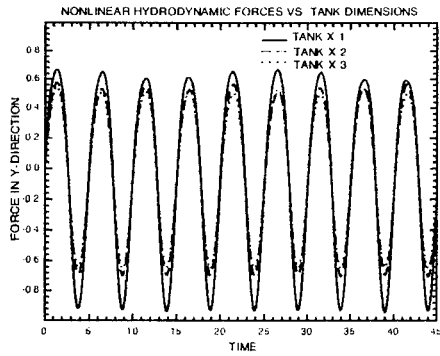
Figure 9: Hydrodynamic forces for surface-piercing cylinder versus tank dimensions.
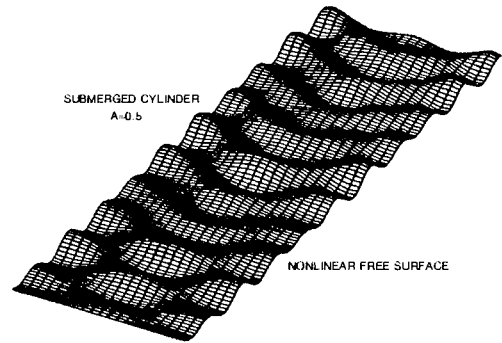
Figure 12: Nonlinear free surface time record for submerged cylinder ($NI = 10, \Delta t = 0.05$).
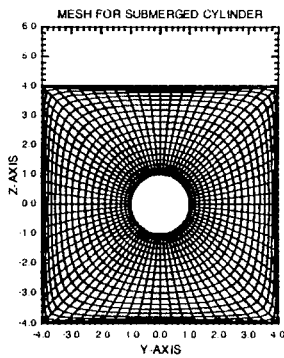
Figure 10: Typical mesh for submerged cylinder.

Figure 13: Mesh deformation at 9.25, 9.5, 9.75 and 10th cycles.

Figure 11: Linear free surface for submerged cylinder ($NI = 20, \Delta t = 0.1$).

sponding to the 9.25, 9.5, 9.75 and 10th cycles of oscillation. Figure 14 shows corresponding velocity vector plots. Again, velocity fields behaved in a physically acceptable manner with

very small differences between specified and calculated values.

For $A = 0.5$, linear and nonlinear prediction of the hydrodynamic forces resulting from vertical motion of the circular cylinder displayed similar trends. Figure 15 shows linear and nonlinear hydrodynamic forces corresponding to an amplitude of motion $A = 1.5$. Even for this extremely large amplitude of motion, both formulations gave similar results. Some differences

203
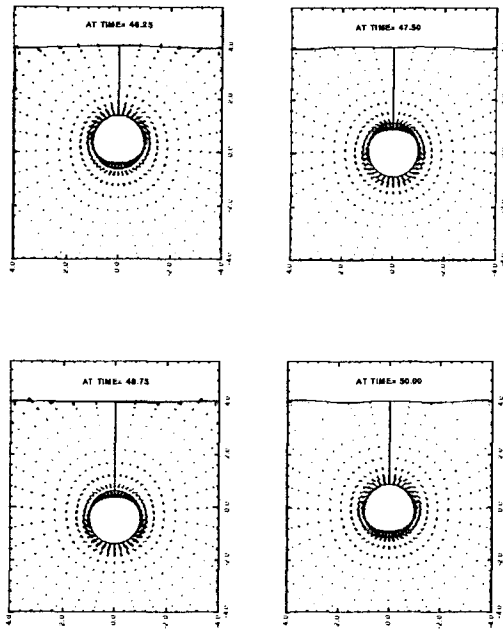
Figure 14: Velocity vector plots at 9.25, 9.5, 9.75 and 10th cycles.
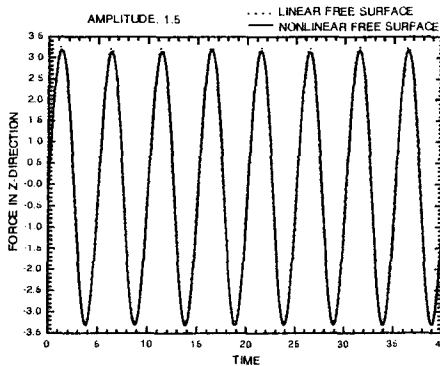
Figure 15: Hydrodynamic force due to sinusoidal excitation, A=1.5.

can again be seen in the force peaks, but these are significantly less noticeable than for the surface piercing case.

6.3 Impulsive motion in a tank

In this section, we present results corresponding to free surface response due to impulsive excitation of tanks of different shapes. Excitation is prescribed as a step velocity at $t = 0$. We have opted to match the types of excita-
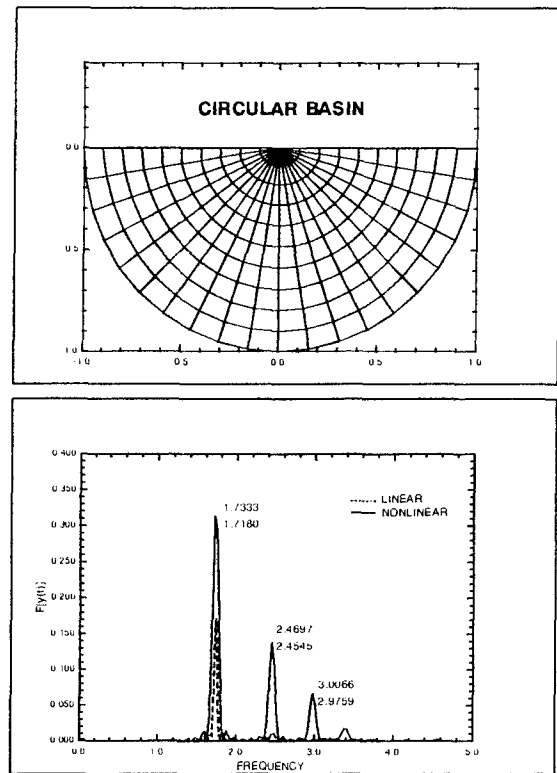
Figure 16: Free surface frequency spectra due to impulsive motion for circular basin.

tions given by Yeung and Wu[47]. Application of Fast Fourier Transform to the time record of the free surface elevation measured at a fixed point yields the frequency spectrum. Nondimensional frequencies for linear and nonlinear free surface boundary conditions are presented. Smoothing in the worst of these cases was applied using $\alpha = 1$ every 10th time step.

Figure 16 shows linear and nonlinear frequency spectra results for a circular tank. In this case, frequencies predicted by linear theory tend to be slightly higher than those given by nonlinear theory. Table 1 shows comparison with results given by Chang and Wu[70] (CW) using an integral equation formulation with linear boundary conditions. Their results also exhibit higher values than those predicted by nonlinear theory.

Corresponding results for a parabolic basin are given in Figure 17. For this particular configuration, results tend to show no difference be-

tween linear and nonlinear predictions. Table 2 compares our results with those given by Yeung and Wu[47]. In general, good agreement is achieved.

CIRCULAR TANK			
Freq.	Lin.	Nonl.	CW
1st	1.7330	1.7180	1.7492
2nd	2.4697	2.4545	2.5632
3rd	3.0066	2.9759	——

Table 1   Nondimensional frequencies for circular tank

PARABOLIC TANK				
Freq.	Lin.	Nonl.	YW. Lin.	YW. Nonl
1st	1.6720	1.6720	1.6846	1.6846
2nd	2.4390	2.4390	2.4170	2.4170
3rd	3.0066	3.0066	3.0029	3.0029

Table 2   Nondimensional frequencies for parabolic tank

Figure 18 shows results for a triangular basin. For this case, no definite trend is shown between linear and nonlinear results. As noted in Table 3, this effect is also shown in the results of Yeung and Wu[47]. Results by Lamb[71] are also presented.

TRIANGULAR TANK					
Freq.	Lin.	Nonl.	YW. Lin.	YW. Nonl	Lamb
1st	1.5339	1.5646	1.5381	1.5381	1.5244
2nd	2.3930	2.3930	2.3439	2.3438	2.3447
3rd	3.0066	2.9912	2.9297	3.0029	2.9393

Table 3   Nondimensional frequencies for triangular tank
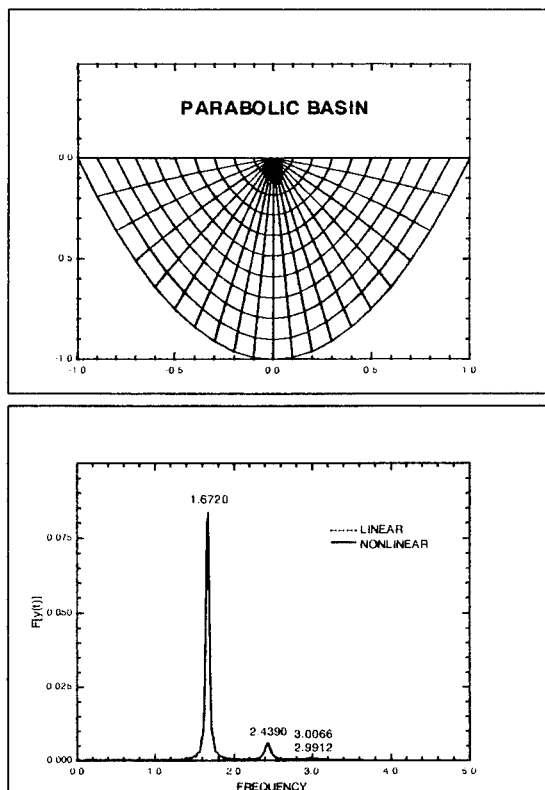
Figure 17: Free surface frequency spectra due to impulsive motion for parabolic basin.

6.4 Slender body calculations

In this section we present results corresponding to the forward motion of a mathematically defined ship hull advancing at zero angle of attack in otherwise calm water. The Wigley parabolic hull, whose main parameters are given in Table 4, is defined as

$$z(x,y) = \frac{B}{2}\left\{1 - \left(\frac{2x}{L}\right)^2\right\}\left\{1 - \left(\frac{y}{D}\right)^2\right\} \quad (19)$$

WIGLEY PARABOLIC HULL[m]					
Length L	Beam B	Draft D	C_B	C_{WP}	C_P
2	0.2	0.125	0.444	0.667	0.667

Table 4   Wigley hull dimensions

Coordinates z and y remained as defined in pre-
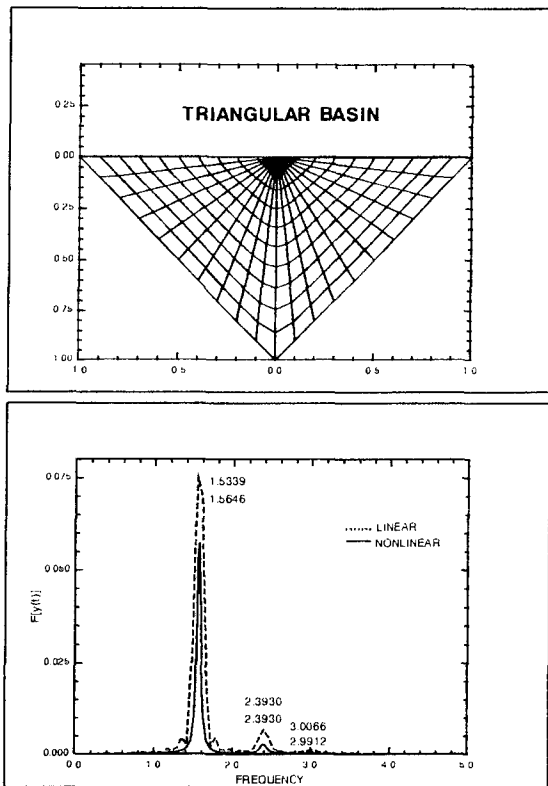
Figure 18: Free surface frequency spectra due to impulsive motion for triangular basin.

vious sections for surface-piercing cases. The coordinate x is directed along the length of the hull and considered positive towards the stern.

Results presented for trim, sinkage and wave-resistance coefficients have been obtained for the conditions shown in Table 5. The tank width is in metres. The variable Δx refers to the spatial increment used along the x-coordinate in metres. For the length of the Wigley hull used in this study, this increment resulted in 2000 stations. CPU time estimates are presented in Table 6. Smoothing in the worst of these cases was also applied using $\alpha = 1$ every 10th time step.

COMPUTATIONAL CONDITIONS			
Δx	Tank Width	No of elements	No of Nodes
0.001	3.0	1200	3741

Table 5 Computational conditions for Wigley hull calculations

COMPUTATIONAL DEMANDS		
Machine Type	Mflops	CPU [min/Δx]
SUN MP/670	4.0	5.0
IBM RS/6000	31.0	0.75

Table 6 Computational demand for Wigley hull calculations

Figures 19 and 20 show linear and nonlinear three dimensional views of the free surface elevation for the Wigley hull advancing with a forward speed of $1.182 \frac{m}{sec}$. This corresponds with a length Froude number of 0.267. It is clear that nonlinear theory predicts a more realistic shape of the free surface. This is evident in the aft-half of the hull where linear theory is not able to produce the recovery from the second crest of the wave next to the hull. This is more easily seen in Figure 21 where comparison has been made with results presented by Maruo and Song[32]. Nonlinear results show good agreement with experimental values for the wave past the midship section. However, there is a shift of the first crest and trough of the fore-half of the wave. It is conjectured that one possible reason for this shift is due to the at rest (zero-valued) initial conditions used in this work. Figure 21 shows numerical results given by Maruo and Song[32] which clearly display non-homogeneous initial conditions. Free surface elevation contours are also shown in Figure 22 and Figure 23 for linear and nonlinear boundary conditions respectively. Nonlinear results show a 'jagged' nature due to small wiggles appearing on the free surface. These wiggles were typical of nonlinear free surface profiles and occasionally were the origin of unstable behavior. In order to maintain the size of these wiggles bounded, small time steps (Δx) were used.

Figure 24 shows the wave resistance coefficient as a function of the Froude number F_n for linear and nonlinear formulations. Data given by Aanesland[72] and mean values of experimental data from the 1st and 2nd Workshops on Wave Resistance Computations are presented [73,74]. At low values of F_n nonlinear prediction shows significant improvement over results

206
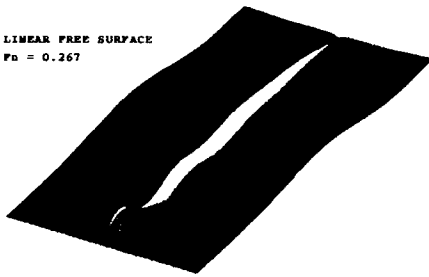
Figure 19: Linear free surface elevation for Wigley hull with forward speed, $F_n = 0.267$.

Figure 20: Nonlinear free surface elevation for Wigley hull with forward speed, $F_n = 0.267$.

obtained using linear theory. In fact, linear theory gives very poor agreement with experimental results for this F_n-range. For this set of experimental data, nonlinear results show superior performance throughout the F_n interval. Figure 25 shows the wave resistance coefficient compared with Maruo and Song[32]. Again, at low values of the Froude number nonlinear results give a better prediction than linear ones. However, as the Froude number increases, linear results show improvement over their nonlinear counterpart. This is a clear example of the scatter encountered in experimental data for these type of physical problems.

Figures 26 and 27 show sinkage and trim of the Wigley hull as a function of F_n. Improved predictions at the lower end of the Froude number interval used in this work are again realized for nonlinear results. This improvement is more clearly seen in the results for sinkage. These results suggest that nonlinear theory predicts a more accurate magnitude of the forces. This is consistent with results obtained for wave resistance as shown in Figure 24. Trim calculations show little discrepancy between linear and nonlinear results. In turn, this suggests that the distribution of forces is predicted with similar accuracy in both formulations.

CONCLUSIONS

The boundary value problem defined by the

Figure 21: Wave profile at side of Wigley hull with forward speed, $F_n = 0.267$.
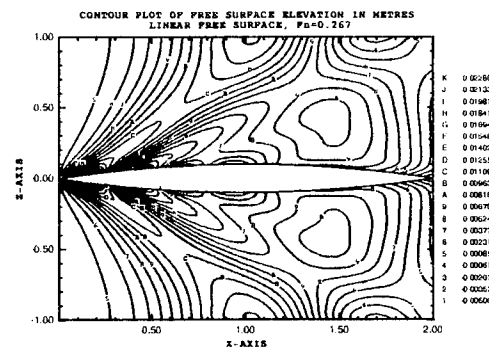
Figure 22: Linear free surface elevation contours of Wigley hull with forward speed, $F_n = 0.267$.

Laplace equation for the solution of potential
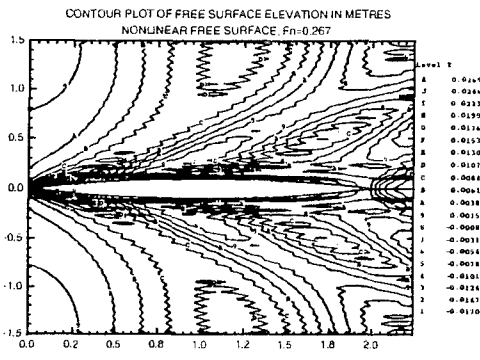
Figure 23: Nonlinear free surface elevation contours of Wigley hull with forward speed, $F_n = 0.267$.
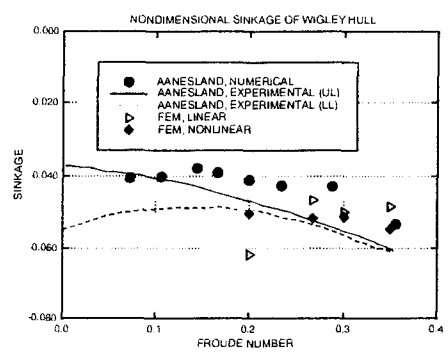
Figure 26: Sinkage of Wigley hull versus F_n.
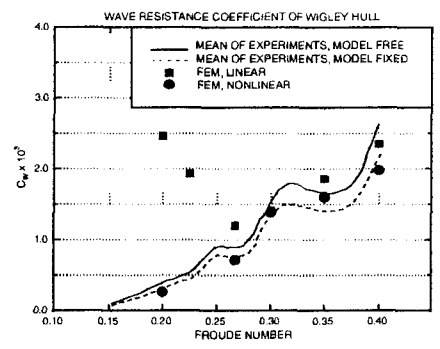
Figure 24: Wave resistance coefficient of Wigley hull versus F_n.
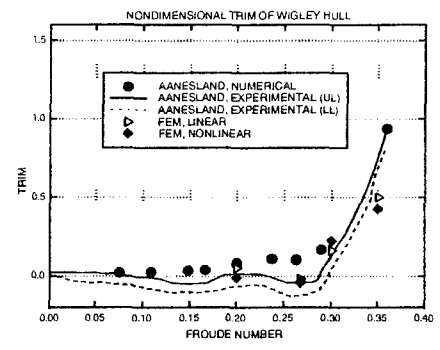
Figure 27: Trim of Wigley hull versus F_n.
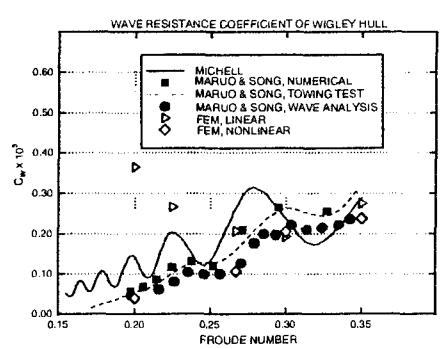
Figure 25: Wave resistance coefficient of Wigley hull versus F_n.

flow in two dimensions has been formulated using a Bubnov-Galerkin weighted residual method to obtain the spatial variation of the velocity potential. The moving boundary problem corresponding to the a-priori unknown dependent and independent spatial variables in the nonlinear boundary conditions has been treated using a semi-Lagrangian semi-implicit scheme. This method proved to be more accurate and stable than predictor-corrector methods. When necessary, dissipation was applied only to the velocity potential.

ACKNOWLEDGEMENT

REFERENCES

[1] Van Dyke M.D., 'Perturbation Methods in Fluid Mechanics', Academic Press, 1964.

[2] Cummins W.E., 'The Wave Resistance of a Floating Slender Body', Unpublished Thesis, American University, 1956.

[3] Kaplan P., 'Application of Slender Body Theory to Forces Acting on Submerged Bodies and Surface Ships in Regular Waves', Journal of Ship Research, vol. 1, 1957.

[4] Lighthill M.J., 'Note on the Swimming of Slender Fish', Journal of Fluid Mechanics, vol. 9, 1960.

[5] Vossers G., 'Wave Resistance of a Slender Ship', Schiffstechnik, vol. 9, 1962.

[6] Maruo H., 'Calculation of the Wave Resistance of Ships, the draft of which is as small as the beam', Journal of the Society of Naval Architects of Japan, vol. 112, 1962.

[7] Ursell F., 'Slender Oscillating Ships At Zero Forward Speed', Journal of Fluid Mechanics, vol. 14, 1962.

[8] Tuck E.O., 'A Systematic Asymptotic Expansion Procedure for Slender Ships', Journal of Ship Research, vol. 8, 1964.

[9] Newman J.N. and Tuck E.O., 'Current Progress in the Slender Body Theory for Ship Motions', Procceedings of the 5th Symposium on Naval Hydrodyanmics, 1964.

[10] Newman J.N., 'The exciting Forces on a Moving Body in Waves', Journal of Ship Research, vol. 9, 1965.

[11] Haskind M.D., 'The exciting Forces and Wetting of a Ship in Waves', Izvestia Akademii Nauk SSSR, 1957 (in russian). DTMB translation No 307, 1962.

[12] Tuck E.O., 'Shallow-Water Flows Past Slender Bodies', Journal of Fluid Mechanics, vol. 26, 1966.

[13] Newman J.N., 'Applications of Slender Body Theory in Ship Hydrodynamics', Annual Review of Fluid Mechanics, vol. 2, 1970.

[14] Chapman R.B., 'Free Surface Effects for Yawed Surface Piercing Plates', Journal of Ship Research, vol. 20, 1976.

[15] Jensen J.J. and Pedersen P.T., 'Wave-Induced Bending Moments in Ships', Transactions of the Royal Institute of Naval Architects, vol. 121, 1979.

[16] Troesch A.W., 'Sway, Roll and Yaw Motion Coefficients Based on a Forward Speed Slender Body Theory: Part 1', Journal of Ship Research, vol. 25, 1981.

[17] Troesch A.W., 'Sway, Roll and Yaw Motion Coefficients Based on a Forward Speed Slender Body Theory: Part 2', Journal of Ship Research, vol. 25, 1981.

[18] Maruo H., 'New Approach to the Theory of Slender Ships with Forward Speed', Bulletin of the Faculty of Engineering, Yokohama University, vol. 31, 1982.

[19] Noblesse F., 'A Slender Ship Theory of Wave Resistance', Journal of Ship Research, vol. 27, 1983.

[20] Faltinsen O.M., 'Bow Flow and Added Resistance of Slender Ships at High Froude Numbers and Low Wave Lengths', Journal of Ship Research, vol. 27, 1983.

[21] Chen C.Y. and Noblesse F., 'Preliminary Numerical Study of a New Slender Ship Theory of Wave Resistance', Journal of Ship Research, vol. 27, 1983.

[22] Chen C.Y. and Noblesse F., 'Comparison Between Theoretical Predictions of Wave Resistance and Experimental Data for the Wigley Hull', Journal of Ship Research, vol. 27, 1983.

[23] Sclavounos P.D., 'The Diffraction of Free Surface Waves by a Slender Ship', Journal of Ship Research, vol. 28, 1984.

[24] Sclavounos P.D., 'The Unified Slender Body Theory: Ship Motions in Waves', Proceedings of the 15th Symposium on Naval Hydrodynamics, 1984.

[25] Breit S.R. and Sclavounos P.D., 'Wave Interactions Between Adjacent Slender Bodies', Journal of Fluid Mechanics, vol. 165, 1986.

[26] Song W., Ikehata M. and Suzuki K., 'Computation of Wave Resistance and Ship Wave Pattern by the Slender Body Approximation', Journal of the Kamsai Society of Naval Architects of Japan, vol. 209, 1988, in japanese.

[27] Choi H.S. and Mei C.C., 'Wave Resistance

and Squat of a Slender Ship Moving Near the Critical Speed in Restricted Waters', Proceedings of the 5th International Conference on Numerical Ship Hydrodynamics, 1989.

[28] Kashiwagi M., 'Theoretical prediction of Tank Wall Effects on Hydrodynamic Forces Acting on an Oscillating and Translating Slender Ship', Extended Abstracts of the 4th International Workshop on Water Waves and Floating Bodies, 1989.

[29] Kashiwagi M., 'Side Wall Effects on Hydrodynamic Forces Acting on a Ship with Forward and Oscillating Motions', Proceedings of the 5th International Conference on Numerical Ship Hydrodynamics, 1989.

[30] Calisal S.M. and Chan J.L.K., 'A Numerical Model of Ship Bow Waves', Journal of Ship Research, vol. 33, 1989.

[31] Ando S., 'Forward Speed Effect in Head Wave Diffraction over the Forebody of A Slender Hull', Extended Abstracts of the 4th International Workshop on Water Waves and Floating Bodies, 1989.

[32] Maruo H. and Song W., 'A Numerical Appraisal of the New Slender Ship Formulation in Steady Motion', Proceedings of the 18th Symposium on Naval Hydrodynamics, 1990.

[33] Yeung R. W., 'Numerical Methods in Free Surface Flows', Annual Review of Fluid Mechanics, vol. 14, 1982.

[34] Longuet-Higgins M.S. and Cokelet E.D., 'The Deformation of Steep Surface Waves on Water I: A Numerical Method of Computation'. Proceedings of the Royal Society of London, Series A 350, 1976.

[35] Vinje T. and Brevig P., 'Nonlinear Ship Motion', Proceedings of the 3rd International Conference on Numerical Ship Hydrodynamics, 1981.

[36] Lin W.M, Newman J.N. and Yue D.K., 'Nonlinear Forced Motions of Floating Bodies', Proceedings of the 15th International Symposium on Naval Hydrodynamics, 1985.

[37] Baker G.R., Meiron D.J. and Orzag S.A., 'Generalized Vortex Methods for Free-Surface Flow Problems', Journal of Fluid Mechanics, vol. 123, 1982.

[38] Dold J.W. and Peregrine D.H., 'Steep Unsteady Water Waves: An Efficient Computational Scheme', Proceedings of the 19th International Conference on Coastal Engineering, ASCE, 1984.

[39] Suzuki K., 'Calculation of Nonlinear Water Waves Around a Two-Dimensional Body in Uniform Flow by Means of a Boundary Element Method', Proceedings of the 5th International Conference on Numerical Ship Hydrodynamics, 1989.

[40] Sen, D., Pawlowsky J.S., Lever J. and Hinchey M.J., 'Two-Dimensional Numerical Modelling of Large Motions of Floating Bodies in Waves', Proceedings of the 5th International Conference on Numerical Ship Hydrodynamics, 1989.

[41] Cointe R., 'Nonlinear Simulation of Transient Free Surface Flows', Proceedings of the 5th International Conference on Numerical Ship Hydrodynamics, 1989.

[42] Cointe R., Geyer P., King B., Molin B. and Tramoni M., 'Nonlinear and Linear Motions of a Rectangular Barge in a Perfect Fluid', Proceedings of the 18th International Symposium on Naval Hydrodynamics, 1990.

[43] Ghia U., Shin C.T. and Ghia K.N., 'Analysis of a Breaking Free Surface Wave Using Boundary Fitted Coordinates for Regions Including Reentrant Boundaries', Proceedings of the 3rd International Conference on Numerical Ship Hydrodynamics, 1981.

[44] Haussling A.J., 'Solution of Nonlinear Water Wave Problems Using Boundary Fitted Coordinate Systems', Numerical Grid Generation: J. Thompson, editor, 1982.

[45] Telste J.G., 'Calculation of Fluid Motion from Large-Amplitude Forced Heave Motion of a Two-Dimensional Cylinder in a Free Surface', Proceedings of the 4th International Conference on Numerical Ship Hydrodynamics, 1985.

[46] Yeung R.W. and Wu C., 'Nonlinear Wave-Body Motion in a Closed Domain', Computers & Fluids, vol. 17, 1989.

[47] Yeung R.W. and Wu C. , 'On Nonlinear Wave Motion in a Closed Domain', Jahrbuch

der Schiffbautechnischen Gesellschaft, vol. 83, 1989.

[48] Luke J.C., 'A Variational Principle for a Fluid with a Free Surface', Journal of Fluid Mechanics, vol. 27, 1967.

[49] Whitman G.B., 'Nonlinear Dispersion of Water Waves', Journal of Fluid Mechanics, vol. 27, 1967.

[50] Whitman G.B., 'Two-timing, Variational Principles and Waves', Journal of Fluid Mechanics, vol. 44, 1970.

[51] K.J. Bai and R.W. Yeung, 'Numerical Solutions to Free Surface Flow Problems', Proceedings of the 10th Symposium on Naval Hydrodynamics, 1974.

[52] Bai K.J., 'Diffraction of Oblique Waves by an Infinite Cylinder', Journal of Fluid Mechanics, vol. 68, 1975.

[53] Yim B., 'A Variational Principle Associated with a Localized Finite Element Technique for Steady Ship-Wave and Cavity Problems', Proceedings of the 1st International Conference on Numerical Ship Hydrodynamics, 1975.

[54] Bai K.J., 'A Localized Finite Element Method for Steady, Two Dimensional Free Surface Flow Problems', Proceedings of the 1st International Conference on Numerical Ship Hydrodynamics, 1975.

[55] Bai K.J., 'A Localized Finite Element Method for Two-Dimensional Steady Potential Flows with a Free Surface', Journal of Ship Research, vol. 22, 1978.

[56] Bai K.J., 'Blockage Correction with a Free Surface', Journal of Fluid Mechanics, vol. 94, 1979.

[57] Wellford C.L. and Ganaba T., 'Finite Element Procedures for Fluid Mechanics Problems Involving Large Free Surface Motion', Proceedings of the 3rd International Conference in Finite Elements in Flow Problems, 1980.

[58] Oomen A., 'Free Surface Potential Flow Computation Using a Finite Element Method', Proceedings of the 3rd International Conference on Numerical Ship Hydrodynamics, 1981.

[59] Jami A., 'Numerical Solving of Transient Linear Hydrodynamics Problems by Coupling Finite Elements and Integral Representation', Proceedings of the 3rd International Conference on Numerical Ship Hydrodynamics, 1981.

[60] Euvard D., Jami A., Lenoir M. and Martin D., 'Recent Progress Towards an Optimal Coupling between Finite Elements and Singularity Distribution Procedures', Proceedings of the 3rd International Conference on Numerical Ship Hydrodynamics, 1981.

[61] Allievi A. and Calisal S.M., 'Finite Element Application to Grid Generation for Submerged and Floating Bodies', International Symposium on Hydro & Aero Dynamics In Marine Engineering, 1991.

[62] Allievi A. and Calisal S. M., 'A Bubnov-Galerkin Formulation For Orthogonal Grid Generation', Journal of Computational Physics, vol. 98, 1992.

[63] Allievi A., 'On Nonlinear Free Surface Potential Flow by a Bubnov-Galerkin Formulation in Space and a Semi-Lagrangian Semi-implicit scheme in Time', Ph.D. thesis, University of British Columbia, in preparation.

[64] Robert A.J., 'A Stable Numerical Integration Scheme for the Primitive Meteorological Equations', Atmosphere-Ocean, vol. 19, 1981.

[65] Robert A.J., 'A Semi-Lagrangian and Semi-Implicit Numerical Integration Scheme for the Primitive Meteorological Equations', Journal of the Meteorological Society of Japan, vol. 60, 1982.

[66] Staniforth A. and Temperton C., 'Semi-Implicit Semi-Lagrangian Integration Schemes for a Barotropic Finite-Element Regional Model', Monthly Weather Review, vol. 114, 1986.

[67] Staniforth A. and Temperton C., 'An Efficient Two-Time-Level Semi-Lagrangian Semi-Implicit Integration Scheme', Quarterly Journal of the Royal Meteorological Society, vol. 113, 1987.

[68] Bermejo R., 'An Analysis of an Algorithm for the Galerkin-Characteristic Method', Numerische Mathematik, vol. 60, 1991.

[69] Ryskin G. and Leal L.G., 'Orthogonal Map-

ping', Journal of Computational Physics, vol. 50, 1983.

[70] Chang S.C. and Wu S.T., 'On the Natural Frequencies of Standing Waves in a Canal of Arbitrary Shape', Journal of Applied Mathematics and Physics, vol. 23, 1972.

[71] Lamb H., 'Hydrodynamics', Cambridge University Press, 1932.

[72] Aanesland V., 'A Hybrid Model for Calculating Wave Making Resistance', Proceedings of the 5th International Conference on Numerical Ship Hydrodynamics, 1989.

[73] 'Proceedings of the First Workshop on Ship Wave Resistance Computations', David Taylor Naval Ship Research and Development Center, 1979.

[74] 'Proceedings of the Second Workshop on Ship Wave Resistance Computations',David Taylor Naval Ship Research and Development Center, 1983.

SESSION 5

WAVY/FREE-SURFACE FLOW:
VISCOUS FLOW AND INTERNAL WAVES

Solid-Fluid Juncture Boundary Layer and Wake with Waves

J.E. Choi and F. Stern

(University of Iowa, USA)

ABSTRACT

Laminar and turbulent solutions are presented for the Stokes-wave/flat-plate boundary-layer and wake for small-large wave steepness, including exact and approximate treatments of the free-surface boundary conditions. The macro-scale flow exhibits the wave-induced pressure-gradient effects described in precursory work. For laminar flow, the micro-scale flow indicates that the free-surface boundary conditions have a profound influence over the boundary layer and near and intermediate wake: the wave elevation and slopes correlate with the depthwise velocity; the streamwise and transverse velocities and vorticity display large variations, including islands of maximum/minimum values, whereas the depthwise velocity and pressure indicate small variations; significant free-surface vorticity flux and complex vorticity transport are displayed; wave-induced effects normalized by wave steepness are larger for small steepness with the exception of wave-induced separation; order-of-magnitude estimates are confirmed; and appreciable errors are introduced through approximations to the free-surface boundary conditions. For turbulent flow, the results are similar, but preliminary due to the present uncertainty in appropriate treatment of the turbulence free-surface boundary conditions and meniscus boundary layer.

NOMENCLATURE

A = wave amplitude
Ak = wave steepness
Fr = Froude number (= $U_0/\sqrt{gL}$)
g = gravitational acceleration
k = turbulent kinetic energy
  = wave number
L = body characteristic length
n = unit normal vector
o( ),( ) = order of magnitude
p = piezometric pressure

p* = static pressure
q = free-surface vorticity flux (= q_x,q_y,q_z)
q_w = wall vorticity flux (= q_{wx},q_{wy},q_{wz})
Re = Reynolds number (= U_0L/ν)
u,v,w = fluctuating velocities
U_0 = reference velocity
$-u_iu_j$ = Reynolds shear stresses
V = mean-velocity vector (= U,V,W)
x,y,z = Cartesian coordinates
δ = body (δ_b) or free-surface (δ_{fs}) boundary-layer or wake (δ_w) thickness
δ^* = streamwise displacement thickness
Δφ = difference between zero and nonzero wave-steepness values of φ
ε = rate of turbulent energy dissipation
  = boundary-layer and wake thickness
φ = transport quantities (= U,V,W,k,ε)
  = relevant variable or equation
η = wave elevation
λ = wave length
μ = viscosity
ν = kinematic viscosity (= μ/ρ)
ρ = density
τ_w = wall-shear stress
τ_{ij} = fluid stress tensor
τ_{ij}^* = external stress tensor
ξ,η,ζ = nonorthogonal curvilinear coordinates
ω = mean vorticity vector (= $\omega_x,\omega_y,\omega_z$)

INTRODUCTION

Ship boundary layers and wakes (blw's) are unique in that they are influenced by the presence of the free-surface and gravity waves. The wave pattern, breaking, and -induced separations along with turbulence/vortex/free-surface interaction, bubble entrainment, etc. are key issues with regard to performance prediction, signature reduction, and propeller-hull interaction.

In spite of this, until fairly recently, very little detailed experimental or rigorous theoretical work has been done on this problem. In

particular, over the past ten years, the Iowa Institute of Hydraulic Research (IIHR) has carried out an extensive experimental and theoretical program of research concerning free-surface effects on ship blw's: problem formulation and model problem identification [Stokes-wave/flat-plate (Sw/fp) flow field] and calculations [1]; towing-tank experiments for idealized (foil-plate model which simulates the Sw/fp flow field) and practical hull form (Series 60 C_B = .6) geometries [2-5]; and the development of computational fluid dynamics (cfd) methods, including validation studies for the foil-plate model [3] and Wigley [6] and Series 60 C_B = .6 [7] hull forms. Through this work, significant progress has been made in explicating certain features of the flow physics (e.g., wave/blw interaction, including the role of wave-induced pressure gradients, wave-induced separation, and scale-effects on near-field wave patterns) and identifying issues for further study (e.g., the nature of the flow very close to the free surface, including the role of the free-surface boundary conditions and the structure of turbulence, effects of geometry and turbulence on wave-induced separation, wake bias, and pacesetting issues for cfd advancements).

This paper concerns one of the aforementioned issues for further study, i.e., the nature of the flow very close to the free surface, including the role of the free-surface boundary conditions. Laminar-flow solutions are presented for the Sw/fp flow field, including the exact free-surface boundary conditions. The work presents for the first time solutions to the exact governing Navier-Stokes (NS) equations and boundary conditions for a solid-fluid juncture blw with waves. Some additional turbulent-flow solutions are also presented; however, these are preliminary due to the current uncertainty in prescribing appropriate turbulence free-surface boundary conditions and treatment of the meniscus boundary layer.

The complete results are extensive and provided by Choi [8]. In the following, the most important aspects of the solutions are discussed and example results are presented. First, overviews are given of the physical problem, including order-of-magnitude estimates (ome), and precursory and relevant work, and the computational method. Then the computational conditions, grids, and uncertainty are described and results presented and/or discussed for small, medium, and large wave-steepness Ak (where A and k are the wave amplitude and number, respectively) for laminar and turbulent flow. Lastly, a summary and conclusions are made, including recommendations for future study and implications with regard to practical applications.

PHYSICAL PROBLEM AND PRECURSORY WORK

Consider the development of the blw for a ship moving steadily at velocity U_0 in an incompressible viscous fluid (figure 1). Following [1], the flow in the neighborhood of the body blw/free-surface juncture is divided into five regions (figure 2): (I) potential flow; (II) free-surface boundary layer; (III) body blw; (IV) solid-fluid juncture blw with waves; and (V) meniscus boundary layer.

The flow in region I is well known, i.e., ome and analytical and cfd methods are well established. The situation is similar for region II, at least for laminar flow, e.g., the analytical solution provided in Appendix A of [8]. Table 1 of [8] provides inviscid and viscous Stokes-wave solutions for regions I and II. In region III, the effects of the free surface are primarily transmitted through the external-flow pressure field and, here again, ome and cfd methods are available. The precursory work mentioned earlier and described later has been very successful in documenting the nature of the flow in this region. In region IV, the effects of the free surface are due both to the influences of the external-flow pressure field and the kinematic and dynamic requirements of the free-surface boundary conditions, which alters both the mean and turbulent velocity components. Presently, the only available information for region IV is that provided by [1], i.e., ome and preliminary calculations for the Sw/fp flow field, including approximate free-surface boundary conditions. Some relevant work, which is also useful in understanding the flow in region IV is described later. Region IV is the topic of this paper. The flow in region V is presently poorly understood, involving surface-tension and contact-line effects. Region V is neglected in this paper, but, as discussed later, recommended for future study.

Order-of-Magnitude Estimates

[1] provides a discussion of the ome for regions I through III and a derivation for those for region IV in connection with the determination of appropriate small-amplitude-wave and more approximate free-surface boundary conditions. In regions I through III, the important nondimensional parameters are Ak and Reynolds number (Re) or related blw thickness $\varepsilon = \delta/L$ or δ/λ (where δ is the body or free-surface boundary-layer or wake thickness, δ_b, δ_{fs}, δ_w, respectively, L is the body characteristic length, and $\lambda = 2\pi/k$ is the wave length). For sufficiently

large Re and slender bodies, the ome for regions I through III in terms of these parameters are provided in table 1. In region IV, the ome were derived in consideration of both those for region III, with the assumption of thin-boundary-layer theory, and the requirements of the free-surface boundary conditions. Additionally, Ak/ε is shown to be an important parameter. However, the assumption of thin-boundary-layer theory for region III led to an error for one of the estimates, i.e., W_z[1]; therefore, an updated derivation is provided as follows.

In consideration of the flow in regions I and III, the ome for $V = (U,V,W)$, η, $\partial/\partial x$, and $\partial/\partial y$ are:

$$V = (1,\varepsilon,Ak)$$
$$\eta = (Ak) \tag{1}$$
$$\partial/\partial x = (1)$$
$$\partial/\partial y = (\varepsilon^{-1})$$

Next, the normal and tangential dynamic and continuity-equation free-surface boundary conditions (see later), respectively

$$\frac{\eta_x}{Re}\left(\frac{\partial W}{\partial z} + \frac{\partial U}{\partial x}\right) + \frac{\eta_y}{Re}\left(\frac{\partial W}{\partial y} + \frac{\partial V}{\partial z}\right)$$
$$+ p + \frac{\eta}{Fr^2} - \frac{2}{Re}\frac{\partial W}{\partial z} = 0 \tag{2}$$

$$\eta_x\left(-p - \frac{\eta}{Fr^2} + \frac{2}{Re}\frac{\partial U}{\partial x}\right) + \frac{\eta_y}{Re}\left(\frac{\partial U}{\partial y} + \frac{\partial V}{\partial x}\right)$$
$$- \frac{1}{Re}\left(\frac{\partial U}{\partial z} + \frac{\partial W}{\partial x}\right) = 0 \tag{3}$$

$$\frac{\eta_x}{Re}\left(\frac{\partial V}{\partial x} + \frac{\partial U}{\partial y}\right) + \eta_y\left(-p - \frac{\eta}{Fr^2} + \frac{2}{Re}\frac{\partial V}{\partial y}\right)$$
$$- \frac{1}{Re}\left(\frac{\partial V}{\partial z} + \frac{\partial W}{\partial y}\right) = 0 \tag{4}$$

$$\frac{\partial U}{\partial x} + \frac{\partial V}{\partial y} + \frac{\partial W}{\partial z} = 0 \tag{5}$$

are used, i.e., using (3)-(5), respectively, to eliminate U_z, V_z, and W_z in (2), solving for p, and with (1) results in the ome for p:

$$p = -\frac{\eta}{Fr^2} - \frac{2}{Re(1 - \eta_x^2 - \eta_y^2)}\left[(1 + \eta_x^2)\frac{\partial U}{\partial x}\right.$$
$$+ \eta_x\eta_y\left(\frac{\partial U}{\partial y} + \frac{\partial U}{\partial x}\right) + \left.(1 + \eta_y^2)\frac{\partial V}{\partial y}\right]$$
$$= (Ak/Fr^2) \tag{6}$$

---

[1] Subscripts are used to denote derivatives, as indicated here, or in defining certain variables, as indicated in the Nomenclature.

Finally, using (3)-(5) with (1) and (6) results in the ome for U_z, V_z, and W_z, respectively:

$$\frac{\partial U}{\partial z} = \frac{1}{1 - \eta_x^2}\left[4\eta_x\frac{\partial U}{\partial x} + \eta_y(1 + \eta_x^2)\left(\frac{\partial U}{\partial y} + \frac{\partial V}{\partial x}\right)\right.$$
$$+ 2\eta_x(1 + \eta_y^2)\frac{\partial V}{\partial y} - (1 - \eta_x^2)\frac{\partial W}{\partial x}$$
$$\left. - Re\,\eta_x\,\eta_y^2\left(p + \frac{\eta}{Fr^2}\right)\right]$$
$$= (Ak/\varepsilon^2) \tag{7}$$

$$\frac{\partial V}{\partial z} = \frac{1}{1 - \eta_y^2}\left[4\eta_y\frac{\partial V}{\partial y} + \eta_x(1 + \eta_y^2)\left(\frac{\partial U}{\partial y} + \frac{\partial V}{\partial x}\right)\right.$$
$$+ 2\eta_y(1 + \eta_x^2)\frac{\partial U}{\partial x} - (1 - \eta_y^2)\frac{\partial W}{\partial y}$$
$$\left. - Re\,\eta_y\,\eta_x^2\left(p + \frac{\eta}{Fr^2}\right)\right]$$
$$= (Ak/\varepsilon) \tag{8}$$

$$\frac{\partial W}{\partial z} = -\frac{\partial U}{\partial x} - \frac{\partial V}{\partial y}$$
$$= (1) \tag{9}$$

The ome for region IV are provided in table 1 and, as will be shown later, are confirmed by the present results. Note that the only differences with those provided previously by [1] are for W_z, as mentioned earlier, and that a single estimate is not provided for $\partial/\partial z$.

Thus far, no distinction has been made between the flow in the blw regions, which is not necessary, except for the far-wake (fw) region, i.e., hereafter, the blw refers to the boundary-layer and near- and intermediate-wake in distinction from the fw. The fw requires a different ome derivation. In this case, in consideration of the flow in region I and the asymptotic two-dimensional zero-pressure gradient fw solution [9], the ome for V, ∂U, η, η_x, η_y, $\partial/\partial x$, and $\partial/\partial y$ are:

$$V = (1,\varepsilon/\sqrt{x},Ak)$$
$$\partial U = (Ak)$$
$$(\eta,\eta_x,\eta_y) = (Ak,Ak,Ak) \tag{10}$$
$$\partial/\partial x = (1/x)$$
$$\partial/\partial y = [1/(\varepsilon\sqrt{x})]$$

Next, following the usual derivation for region III both for the blw and a similar derivation as provided earlier for region IV both for the blw, the ome for regions III and IV for the fw are derived. These are also provided in table 1 and, here again, as will be shown later, are confirmed by the present results.

Regions III Calculations and Experiments

[1] identified the model problem of a combination Sw/fp flow field (figure 3), which facilitated the isolation and identification of the most important features of the wave-induced effects. Numerical results were presented for laminar and turbulent flow utilizing first-order boundary-layer equations and both small-amplitude-wave and more approximate zero-gradient free-surface boundary conditions. Subsequently [2], results from a towing-tank experiment were presented utilizing a unique, simple foil-plate model geometry, which simulates the Sw/fp flow field. Mean-velocity profiles in the boundary-layer region and wave profiles on the plate were measured for three wave-steepness conditions. For medium and large steepness, the variations of the external-flow pressure gradients were shown to cause acceleration and deceleration phases of the streamwise velocity component and alternating direction of the crossflow, which resulted in large oscillations of the displacement thickness and wall-shear stress as compared to the zero-steepness condition. The measurements were compared and close agreement was demonstrated with the results from the turbulent-flow calculations with the zero-gradient approximation for the free-surface boundary conditions. Also, wave-induced separation was discussed, which was present in the experiments, and the starting point was predicted by the laminar-flow calculations under certain conditions.

More recently [3], results were presented from extensions of both the previous experimental and theoretical work: the measurement region was extended into the wake where both mean-velocity and wave-elevation measurements were made; and a state-of-the-art cfd method was brought to bear on the present problem, in which the Reynolds-averaged NS (RaNS) equations were solved for the blw region with zero-gradient free-surface boundary conditions. Measurements and calculations were performed for the same three wave-steepness conditions. The trends were even more pronounced for the wake than shown previously for the boundary-layer region. Remarkably, the near and intermediate wake displayed a greater response, i.e., a bias with regard to favorable as compared to adverse pressure gradients [8]. The measurements were compared and close agreement was demonstrated with results from the RaNS calculations. Additional calculations were presented, including laminar-flow results, which aided in explicating the characteristics of

the near and intermediate wake, the periodic nature of the fw, and wave-induced separation.

Very little is known about wave-induced separation, i.e., three-dimensional boundary-layer separation near the free-surface induced by waves and accompanied by a large disturbance to the free surface itself. The additional laminar-flow computational results of [3] enabled, for the first time, a detailed study, including the flow pattern in the separation region. A saddle point of separation and a focal point of attachment were indicated on the plate and mean free surface, respectively. As the wave steepness increased, the saddle point moved downwards and towards the trailing edge, whereas the focal point moved downstream and away from the plate surface. The U and W components displayed, respectively, flow reversal and complex S-shaped profiles. A longitudinal vortex was generated in which the vortical motion was counterclockwise with respect to the flow direction and towards the free surface and clockwise with respect to the flow direction and in the main stream direction above (i.e., in the reverse-flow region) and below the saddle point, respectively. The identification of these features of wave-induced separation was considered very significant and invaluable, but with some caution and to some extent preliminary due to the approximate nature of the free-surface boundary conditions used in the calculations. This paper also addresses this issue.

RELEVANT WORK

Relevant work concerns viscous-free-surface flow, i.e., solutions of the viscous-flow equations, including various treatments of the free-surface boundary conditions, for a variety of applications, i.e: free-wave problems, open-channel flow, free-surface jet flow, vortex/free-surface interaction, and ship blw's for nonzero Froude number (Fr). In [8], the critical issues with regard to the implementation of the free-surface boundary conditions and the various treatments utilized are discussed. Also, for the latter applications, the most important results are summarized both with regard to experimental information and physical understanding and computational studies. The discussions are useful for the evaluation and interpretation of the present solutions with regard to their significance and the role of the free-surface boundary conditions. The conclusions with regard to the relevant work are summarized as follows (see [8] for references).

A variety of cfd formulations of viscous-free-surface flow are possible with the ability to predict a wide class of flows; however, none have fully implemented the free-surface boundary

conditions or resolved the free-surface boundary layer and taken into account complicating factors such as the meniscus boundary layer, etc. Turbulence free-surface interaction has been investigated for certain idealized geometries (i.e., open-channel flow, free-surface jet flow, and a submerged tip vortex) all of which indicate similar free-surface effects: constant turbulent kinetic energy (i.e., zero gradient) with a redistribution of energy between the turbulence velocity components, i.e., the vertical turbulence velocity is damped and the horizontal and streamwise components are increased. Free-surface jet flow also displays effects due to jet-induced waves and free-surface induced lateral spreading. The idealized geometries are different than ship blw's in that the source of turbulence does not pierce the free surface and the role of gravity waves is minimal. Considerable experimental and computational information is available for vortex/free-surface interaction for laminar flow and clean free surfaces, which indicates complex features involving interrelated free-surface deformation, secondary-vorticity generation, and vorticity reconnection; however, a complete understanding of the physics is lacking, i.e., most studies are descriptive and controversey exists as to the physical mechanisms. The role of surfactants and turbulence are insufficiently understood. Although certain progress has been made in the understanding of the practical application of ship blw's for nonzero Fr, the detailed flow structures, including turbulence and the micro-scale flow are poorly understood.

COMPUTATIONAL METHOD

The computational method is based on extensions of [3] for region IV calculations, including the use of a two-layer k-ε turbulence model [10]. [3] is a modified version of the large-domain viscous-flow method of [11] for small-domain calculations and free-surface boundary conditions. Only a brief review of the basic viscous-flow method is provided, but with a detailed description of the present solution domain and boundary conditions. Further details are provided in [8] as well as [10,11] and associated references.

In the viscous-flow method, the RaNS equations are written in the physical domain using Cartesian coordinates (x,y,z). For laminar-flow calculations, the equations reduce to the NS equations by simply deleting the Reynolds-stress terms and interpreting (U,V,W) and p as instantaneous values. The governing equations are transformed into nonorthogonal curvilinear coordinates (ξ,η,ζ) such that the computational

domain forms a simple rectangular parallelepiped with equal grid spacing. The transformation is a partial one since it involves the coordinates only and not the velocity components (U,V,W). The transformed equations are reduced to algebraic form through the use of the finite-analytic method. The velocity-pressure coupling is accomplished using a two-step iterative procedure involving the continuity equation based on the SIMPLER algorithm. Both fixed and free-surface conforming grids were used for the calculations. In both cases, a simple algebraic technique was used whereby the longitudinal and transverse sections of the computational domain are surfaces of constant ξ and η, respectively; and, moreover, the three-dimensional grids were obtained by simply "stacking" the two-dimensional grid for the transverse plane.

The Sw/fp solution domain and coordinate system are shown in figure 3. In terms of the notation of figure 3, the boundary conditions are as follows. On the inlet plane S_i, ϕ is specified from the Stokes-wave solutions (i.e., table 1 of [8]) and typical free-stream values for (k,ε). On the body surface S_b, the no-slip condition is imposed. On the symmetry planes S_{cp} and S_d, $\partial(U,W,p,k,\varepsilon)/\partial y = V = 0$ and $\partial(U,V,p,k,\varepsilon)/\partial z = W = 0$, respectively. On the exit plane S_e, axial diffusion is negligible so that $\partial^2\phi/\partial x^2 = p_x = 0$. On the outer boundary S_o, the edge conditions are specified from the Stokes-wave solutions (i.e., table 1 of [8]) and zero-gradient conditions for (k,ε).

On the free-surface S_η (or simply η), there are two boundary conditions

$$\partial\eta/\partial t + V\cdot\nabla\eta = 0 \tag{11}$$

$$\tau_{ij}\,n_j = \tau^*_{ij}\,n_j \tag{12}$$

where $\eta(x,y,t)$ is the wave elevation (interpreted as Reynolds averaged for turbulent flow), τ_{ij} and τ^*_{ij} are the fluid- and external-stress tensors, respectively, the latter, for convenience, including surface tension, and $n_j = (\eta_x,\eta_y,-1)/\sqrt{\eta_x^2+\eta_y^2+1}$ is the unit normal vector to η. The kinematic boundary condition expresses the requirement that η is a stream surface and the dynamic boundary condition that the stress is continuous across it. Note that η itself is unknown and must be determined as part of the solution. Boundary conditions are also required for the turbulence parameters (k,ε).

(11) can be put in the form:

$$\partial\eta/\partial t = W - U\eta_x - V\eta_y = 0 \qquad (13a)$$

on $z = \eta$. (13a) is solved for η using finite differences and two different strategies for regions of unseparated and separated flow. For unseparated flow, (13a) is solved in steady form

$$0 = W - U\eta_x - V\eta_y \qquad (13b)$$

using a backward difference for the x-derivative, a central difference for the y-derivative, and a tridiagonal-matrix algorithm. For separated flow, (13a) is solved in unsteady form using backward differences for the t- and x-derivatives, a central difference for the y-derivative, a tridiagonal-matrix algorithm, and an iterative procedure whereby the steady-state solution is obtained. In both cases, a special treatment was required for $(y,z) = (0,\eta)$, which is singular due to the incompatibility of simultaneously satisfying both the no-slip and free-surface boundary conditions. Furthermore, this point is embedded in the meniscus boundary layer, region V; thus, a rigorous treatment is beyond the scope of the present paper. For laminar flow, the approximation was made that the wave elevation was assumed constant across the first three grid points $(y/\delta \lesssim .03)$. For turbulent flow, an interpolation procedure was used to obtain the wave elevation across the first ten grid points, i.e., the value at $y = 0$ was assumed .9 of the value at $y^+ \approx 10$ and intermediate values were obtained using a cubic spline. The number of grid points and the wave elevation value at $y = 0$ were determined based on trial and error to minimize the residuals and error in satisfying the dynamic free-surface boundary condition. The assumption used for laminar flow is satisfactory, i.e., it has a minimal influence over a small portion of the overall region of interest. However, the assumption used for turbulent flow requires further justification since it has a large influence over a significant portion of the region of interest such that, as already mentioned, region V is recommended for future study.

(12) and (5) are used to derive free-surface boundary conditions for V and p in conjunction with the solution for η. The external stress and surface tension were neglected in (12), i.e.

$$\tau_{ij}n_j = 0 \qquad (14)$$

on $z = \eta$.

For laminar flow,

$$\tau_{ij} = -p^*\delta_{ij} + \frac{1}{Re}\left(\frac{\partial U_i}{\partial x_j} + \frac{\partial U_j}{\partial x_i}\right) \qquad (15)$$

where p^* is the static pressure, i.e., $p^* = p + \frac{z}{Fr^2}$. Substituting (15) into (14) results in the normal- and two tangential-stress free-surface boundary conditions, i.e., (2)-(4), on $z = \eta$, which can be solved for p, U_z, and V_z to provide the free-surface boundary conditions for p, U, and V, respectively:

$$p = -\frac{\eta}{Fr^2} + \frac{2}{Re}\frac{\partial W}{\partial z} - \frac{\eta_x}{Re}\left(\frac{\partial U}{\partial z} + \frac{\partial W}{\partial x}\right)$$
$$- \frac{\eta_y}{Re}\left(\frac{\partial V}{\partial z} + \frac{\partial W}{\partial y}\right) \qquad (16)$$

$$\frac{\partial U}{\partial z} = -\frac{\partial W}{\partial x} - \eta_x Re(p + \frac{\eta}{Fr^2})$$
$$+ 2\eta_x\frac{\partial U}{\partial x} + \eta_y\left(\frac{\partial U}{\partial y} + \frac{\partial V}{\partial x}\right) \qquad (17)$$

$$\frac{\partial V}{\partial z} = -\frac{\partial W}{\partial y} - \eta_y Re(p + \frac{\eta}{Fr^2})$$
$$+ 2\eta_y\frac{\partial V}{\partial y} + \eta_x\left(\frac{\partial U}{\partial y} + \frac{\partial V}{\partial x}\right) \qquad (18)$$

For the physical domain, the terminology normal and tangential refers to the mean free surface [i.e., (2)-(4) are the components of the stress in each of the Cartesian coordinate directions (z,x,y), respectively, on $z = \eta$]; however, upon transformation into the computational domain, it refers to the actual free surface $z = \eta$. Finally, (5) is solved for W_z to provide the free-surface boundary condition for W

$$\frac{\partial W}{\partial z} = -\frac{\partial U}{\partial x} - \frac{\partial V}{\partial y} \qquad (19)$$

Equations (16)-(19) were implemented in finite-difference form using backward differences for the z-derivatives and central differences for the x- and y-derivatives, for (16) and (19) and a backward and central differences, respectively, for the x- and y-derivatives for (17) and vice versa for (18).

For turbulent flow,

$$\tau_{ij} = -p^*\delta_{ij} + \frac{1}{Re}\left(\frac{\partial U_i}{\partial x_j} + \frac{\partial U_j}{\partial x_i}\right) - \overline{u_i u_j} \qquad (20)$$

However, the same conditions (16)-(19) apply for turbulent flow with V interpreted as the mean velocity. The kinematic free-surface boundary condition in terms of velocity fluctuations is

$$-u\,\eta_x - v\,\eta_y + w = 0 \qquad (21)$$

Multiplying (21) by u, v, and w and Reynolds averaging results in, respectively

$$-\overline{uu}\,\eta_x - \overline{uv}\,\eta_y + \overline{uw} = 0 \qquad (22)$$

$$-\overline{uv}\,\eta_x - \overline{vv}\,\eta_y + \overline{vw} = 0 \qquad (23)$$

$$-\overline{uw}\,\eta_x - \overline{vw}\,\eta_y + \overline{ww} = 0 \qquad (24)$$

Substituting (20) into (14) and using (22)-(24) to eliminate the Reynolds-stress terms results identically in (16)-(18), but with V interpreted as the mean velocity. Note that this derivation neglects the effects of free-surface fluctuations. Equation (19) is also valid for the mean-velocity components. The finite-difference procedures for turbulent flow were the same as those described earlier for laminar flow.

Reasonable approximations for free-surface boundary conditions for k and ε are simply zero-gradient conditions

$$\frac{\partial k}{\partial z} = 0 \qquad (25)$$

$$\frac{\partial \varepsilon}{\partial z} = 0 \qquad (26)$$

on z = η, which are implemented in finite-difference form using backward differences for the z-derivatives.

In summary, for laminar flow, the exact free-surface boundary conditions are given by (13) and (16)-(19). The corresponding turbulent-flow approximation are these same conditions and (25)-(26). Approximate treatments of the free-surface boundary conditions are now considered, which are useful in assessing various approximations used in the precursory and relevant work, i.e., flat free-surface, inviscid, and zero-gradient conditions.

The flat free-surface conditions are obtained from the exact conditions under the approximation that $\eta_x = \eta_y = 0$ in the dynamic free-surface boundary conditions, whereupon (16)-(18) reduce to

$$p = -\frac{\eta}{Fr^2} + \frac{2}{Re}\frac{\partial W}{\partial z} \qquad (27)$$

$$\frac{\partial U}{\partial z} = -\frac{\partial W}{\partial x} \qquad (28)$$

$$\frac{\partial V}{\partial z} = -\frac{\partial W}{\partial y} \qquad (29)$$

The inviscid conditions are obtained from the flat free-surface conditions under the additional assumption that the normal and tangential gradients of the normal velocity are negligible, whereupon (27)-(29) reduce to

$$p = -\frac{\eta}{Fr^2} \qquad (30)$$

$$\frac{\partial U}{\partial z} = 0 \qquad (31)$$

$$\frac{\partial V}{\partial z} = 0 \qquad (32)$$

(27-(29) and (30)-(32) in conjunction with (13) and (19) are solved in a similar manner as described earlier for the exact conditions, including, for turbulent flow, (25)-(26). The zero-gradient conditions are obtained from the inviscid conditions under the additional assumption that (30) and (19) are replaced by zero-gradient conditions

$$\frac{\partial p}{\partial z} = 0 \qquad (33)$$

$$\frac{\partial W}{\partial z} = 0 \qquad (34)$$

which in conjunction with (31)-(32) are solved in a similar manner as described earlier for the exact conditions, including, for turbulent flow, (25)-(26); however, in this case, (13) is not required since η is no longer present in the equations.

The exact and approximate free-surface boundary conditions are to be applied on the exact free-surface z = η, which is obtained as part of the solution. However, with the additional assumption that the wave elevation is small, all of the above conditions can be represented by first-order Taylor series expansions about the mean wave-elevation surface (i.e., z = 0). In the following, this will be referred to as the Taylor-series approximation.

COMPUTATIONAL CONDITIONS, GRIDS, AND UNCERTAINTY

The computational conditions were based on [1-3], i.e., Ak = (0, .01, .11, .21), Re = 10^5 and 1.64 x 10^6 for laminar[2] and turbulent flow, respectively, and L = λ = 1. Typical values for δ_b (at the trailing edge), δ_w (in the near wake), and δ_{fs} (at the edge of the blw) are (.015, .02, .0018) and (.02, .03, .0004) for laminar and turbulent

---

[2] The Re = 2 x 10^4 value used in [1,3] was modified for the present work to the value Re = 10^5 in conformity with other researchers.

flow, respectively. The corresponding Ak/ε values for both laminar and turbulent flow are $O(1)$ and $O(10)$ for small and medium and large steepness, respectively.

The laminar-flow calculations were performed for all four Ak values utilizing the exact, flat free-surface, inviscid, and zero-gradient conditions applied both on $z = \eta$ (exact) and 0 (Taylor-series approximation). For zero steepness, the calculations were begun with a zero-pressure initial condition for the pressure field. For nonzero steepness, the complete zero-steepness solution was used as an initial condition. The solutions were built up in stages starting with small Ak values and achieving partial convergence and then incrementally increasing Ak until reaching the desired value and final convergence. For each $Ak > 0$, initially coarse-grid calculations were performed utilizing the zero-gradient condition applied on $z = 0$. These were then used as the initial guess for the fine-grid calculations utilizing the exact and approximate conditions applied both on $z = 0$ and η. For the cases involving free-surface conforming grids (i.e., conditions applied on $z = \eta$), usually three updates (i.e., grid regenerations) were sufficient for convergence. Partial views of the coarse and typical fine grids used in the calculations are shown in figure 4. For the coarse grid, 170 axial, with 50 over the plate and 120 over the wake, 24 transverse, and 9 depthwise grid points were used, i.e., imax was $170 \times 24 \times 9 = 36720$. For the fine grid, 179 axial, with 5 before the leading edge, 54 over the plate and 120 over the wake, 24 transverse, and 25-27 depthwise, with 16-18 over the free-surface boundary layer, grid points were used, i.e., imax was $179 \times 24 \times 27 = 115992$.

The turbulent-flow calculations were performed for all four Ak values utilizing the zero-gradient conditions applied on $z = 0$ and, for $Ak = .01$, utilizing the exact and zero-gradient conditions on $z = \eta$ and 0. The procedure for obtaining the solutions was similar to that for laminar flow. Transition was fixed at $x = .05$, which corresponds to the turbulence stimulators in the experiments. For the coarse grid, 187 axial, with 49 over the plate and 138 over the wake, 24 transverse, with 15 in the inner layer, and 9 depthwise grid points were used, i.e., imax was $187 \times 24 \times 9 = 40392$. The fine grid was similar, except 28 depthwise, with 12 over the free-surface boundary layer, grid points were used, i.e., imax was $187 \times 24 \times 28 = 125664$.

The detailed grid information, and values of the time, velocity, pressure-correction, and pressure under-relaxation factors and total number of global iterations itl used in obtaining

both the laminar and turbulent solutions are provided in [8]. The average job run CRAY hours and central memory were 1.05 and 1.17 hours and 1.5 megawords for 100 global iterations for the fine-grid laminar and turbulent solutions, respectively.

Due to the complexity of the present calculations, it was not possible to carry out extensive grid dependency and convergence tests; however, these were done previously both for the basic viscous-flow method [11] and for other applications. The convergence criterion was based on the residual

$$R(it) = \sum_i \sum_j \sum_k (|\phi(it-1)| - |\phi(it)|) / \sum_i \sum_j \sum_k |\phi it-1| \quad (35)$$

and error(x,y,z) in satisfying the dynamic free-surface boundary conditions (17), (18), and (16), respectively, i.e., that R(it) and the error (x,y,z) be of order 10^{-4}. Typical convergence histories and error-bar charts are provided in [8] and figure 5, respectively.

LAMINAR-FLOW SOLUTIONS

First, the small wave-steepness $Ak = .01$ results are discussed in detail for both the macro and micro scales: the macro scale corresponds to $\lambda = L = 1$ and includes region III, whereas the micro scale corresponds to the body blw and free-surface boundary-layer thicknesses and is restricted to region IV. Second, the medium and large wave-steepness $Ak = .11$ and .21 results are discussed with particular reference to the influences of increasing Ak, including wave-induced separation. In general, only detailed results are presented in which the exact free-surface boundary conditions were utilized; however, in the discussion of the error-bar charts, reference is made to the various approximate treatments discussed earlier.

The discussion focuses on the differences between the $Ak = 0$ or equivalently deep solutions and the nonzero wave-steepness $Ak = .01, .11,$ and .21 solutions through the presentation of dependent variable differences from their deep values

$$\Delta\phi = \phi - \phi(deep) \quad (36)$$

where ϕ is any of the relevant dependent variables of interest, e.g., V, p, ω, etc.; thereby, accentuating the wave-induced effects. The equivalence between the $Ak = 0$ and deep solutions is indicated by the form of the governing equations and free-surface boundary conditions with $\eta = \eta_x = \eta_y = W = 0$ (except for small leading- and trailing-edge effects for the

former case, which were neglected since only zero-gradient conditions were used). Furthermore, note that both the Ak = 0 and deep solutions correspond to the Blasius solution and corresponding two-dimensional wake, both of which are recovered to within a few percent, except for leading- and trailing-edge and near-wake effects. In general, results are presented and/or discussed for both the blw and fw regions.

In order to confirm the ome for regions III and IV and for evaluation of the relative contributions of various terms in the equations of interest, average values over the blw thickness are evaluated and designated with an overbar

$$\bar{\phi}(x) = \frac{1}{\delta} \int_0^\delta \phi \, dy \tag{37}$$

where, in this case, ϕ is any relevant dependent variable or equation, i.e., (13b), (16)-(19), and the vorticity difference, vorticity-transport equation, and free-surface vorticity flux, respectively

$$\Delta\omega = (\Delta\omega_x, \Delta\omega_y, \Delta\omega_z) \tag{38}$$

$$= (\frac{\partial(\Delta W)}{\partial y} - \frac{\partial(\Delta V)}{\partial z}, \frac{\partial(\Delta U)}{\partial z} - \frac{\partial(\Delta W)}{\partial x}, \frac{\partial(\Delta V)}{\partial x} - \frac{\partial(\Delta U)}{\partial y})$$

$$U\frac{\partial\omega_x}{\partial x} + V\frac{\partial\omega_x}{\partial y} + W\frac{\partial\omega_x}{\partial z} \tag{39a}$$

$$= \omega_x\frac{\partial U}{\partial x} + \omega_y\frac{\partial U}{\partial y} + \omega_z\frac{\partial U}{\partial z} + \frac{1}{Re}\nabla^2\omega_x$$

$$U\frac{\partial\omega_y}{\partial x} + V\frac{\partial\omega_y}{\partial y} + W\frac{\partial\omega_y}{\partial z} \tag{39b}$$

$$= \omega_x\frac{\partial V}{\partial x} + \omega_y\frac{\partial V}{\partial y} + \omega_z\frac{\partial V}{\partial z} + \frac{1}{Re}\nabla^2\omega_y$$

$$U\frac{\partial\omega_z}{\partial x} + V\frac{\partial\omega_z}{\partial y} + W\frac{\partial\omega_z}{\partial z} \tag{39c}$$

$$= \omega_x\frac{\partial W}{\partial x} + \omega_y\frac{\partial W}{\partial y} + \omega_z\frac{\partial W}{\partial z} + \frac{1}{Re}\nabla^2\omega_z$$

$$q_x = (-\eta_x\frac{\partial\omega_x}{\partial x} - \eta_y\frac{\partial\omega_x}{\partial y} + \frac{\partial\omega_x}{\partial z})/\sqrt{\eta_x^2+\eta_y^2+1} \tag{40a}$$

$$q_y = (-\eta_x\frac{\partial\omega_y}{\partial x} - \eta_y\frac{\partial\omega_y}{\partial y} + \frac{\partial\omega_y}{\partial z})/\sqrt{\eta_x^2+\eta_y^2+1} \tag{40b}$$

$$q_z = (-\eta_x\frac{\partial\omega_z}{\partial x} - \eta_y\frac{\partial\omega_z}{\partial y} + \frac{\partial\omega_z}{\partial z})/\sqrt{\eta_x^2+\eta_y^2+1} \tag{40c}$$

Figures for $\bar{\phi}$ are included where appropriate in which the numbered dashed and solid lines designated on the figures correspond to the various terms in the equations with the numbering proceeding term by term from left to right. In most cases, the dashed line corresponds to the term representing the left-hand side of the equation. In the cases of (16)-(18) and the

vorticity-transport equation, the dashed line represents the sum of all the terms, which, of course, should be zero. In discussing such figures, $\bar{\phi}$ is identified in symbol with an overbar or in words with inclusive terms simply referred to in symbol without an overbar or by number. Note that the solutions are for the primitive variables V and p subject to the free-surface boundary conditions (13b) and (16)-(19), whereas equations (38)-(40) are derived, which in conjunction with the integration procedure (37) introduces some error; however, $\bar{\phi}$ are still useful in evaluating the solutions. $\bar{\phi}$ are evaluated at z = .1 and η for the macro- and micro-scale flows, respectively. Appendix B in [8] provides a summary of the ome for the various variables or equations of interest, including a listing of the confirmations and exceptions based on the blw averaged values.

Lastly with regard to the presentation of the results, the analysis was facilitated by color graphics through the use of PLOT3D from which certain of the present figures were reproduced in black and white. Note that in such figures - W is shown in conformity with the PLOT3D coordinate system (figure 3), i.e., negative values correspond to downward flow and positive values to upward flow.

Small Steepness

First, the results for the macro-scale flow are discussed. Figure 6 displays the free-surface velocity profiles $\Delta V/Ak$ vs. y for various axial locations. The streamwise ΔU and depthwise ΔW components display the pressure-gradient induced acceleration and deceleration phases and alternating direction, respectively. The transverse component ΔV indicates outward flow over most of the plate and inward flow near the trailing edge and over most of the wake. Note that the ome conform to table 1, i.e., V = (1,ε,Ak) and (1,ε/x,Ak) for the blw and fw, respectively. Also, noteworthy for laminar flow, is the broad region of large velocity gradients over δ. The results at larger depths are qualitatively similar, but with reduced amplitudes due to the exponential depthwise decay of the streamwise p_{ex} and depthwise p_{ez} external-flow pressure gradients.

Figure 7 displays the wall-shear stress $\Delta\tau_w/\tau_w$(deep), wake-centerplane velocities ΔU_{cp} and ΔV_{cp}, and displacement thickness $\Delta\delta^*$ vs. x for various depthwise locations. The wave-induced oscillations are evident as is the wake bias. The oscillations persist to large depths, i.e.,

223

wave effects are discernible up to about $z = .5$; however, the largest variations are near the free surface and, subsequently, decay rapidly towards the deep solution. The amplitudes of the oscillations are large, especially in the near and intermediate wake. The large values of $\Delta\delta^*$ near the trailing edge are associated with wave-induced separation, which occurs in this region for sufficiently large Ak. The wake bias [8] refers to the fact that the flow in the near and intermediate wake is considerably more responsive to the effects of the favorable as compared to the adverse external-flow pressure gradients, i.e., the magnitude of the overshoots in response to favorable p_{ex} and p_{ez} are much larger than those in response to adverse p_{ex} and p_{ez}. Subsequently, there is transition region where the differences between the maximum and minimum amplitudes decay such that ultimately in the fw ($x \gtrsim 4$) a periodic state is recovered in which ΔU_{cp}, ΔW_{cp}, and $\Delta\delta^*$ all appear to oscillate with equal maximum and minimum amplitudes about the deep (i.e., two-dimensional) solution with, in some cases, a constant offset due to the wave-induced streaming velocities [8]. In the former cases, the ome of the oscillations is (Ak), which conforms to table 1. These trends are evident at all depths, but with reduced amplitudes. The distances over which the bias and transition occurs and magnitude of the streaming velocities depends on Ak and laminar- vs. turbulent-flow conditions, i.e., the bias and streaming velocity magnitude and extent are largest for small Ak and laminar flow.

Figures 8 and 9 display ΔV and $\Delta\omega$ contours, respectively, and vividly display the macro-scale wave-induced effects: acceleration and deceleration of the streamwise velocity component; alternating direction of the depthwise component (e.g., in the boundary-layer region, strong downward flow near $x = .25$, the indication of S-shaped profiles near $x = .5$ and 1, and strong upward flow near $x = .75$); depthwise decay of wave-induced effects; increased response, which propagates to larger depths, for the near- and intermediate-wake regions, including wake bias; and significant streamwise- and depthwise-vorticity components. Note the vertical scale and that the wave-induced effects persist to about $z = .5$. The blw averaged values of the vorticity components indicate that $\omega = (W_y, U_z - W_x, -U_y)$, which conforms to the table 1 ome (Ak/ε,1,1/ε) and $(\frac{Ak}{\varepsilon\sqrt{x}}, \frac{Ak}{x}, \frac{Ak}{\varepsilon\sqrt{x}})$ for the blw and fw,

respectively, with the exception of the $-W_x$ term for the blw, which the ome indicates O(Ak).

Lastly, with regard to the Ak = .01 macro-scale solution, the results for the contours and blw averaged values of the convection (terms 1-3), stretching (terms 4-6, i.e., combined stretching/turning unless stated otherwise), and diffusion (term 7) terms of the streamwise, transverse, and depthwise vorticity-transport equations, respectively, are discussed. The contours for streamwise and stretching terms of the depthwise equation display the wavy nature of the flow, whereas the contours for the transverse equation and for the convective and diffusion terms of the depthwise equation are nearly zero and constant with depth, respectively. In the case of the streamwise equation, this is consistent with the nature of ω_x (= W_y) itself, whereas in the case of the depthwise equation, this is consistent with the dominant stretching (and turning) terms, i.e., $\omega_y W_y + \omega_z W_z$ and the nature of W_y and W_z. The blw averaged values indicate that for the blw, the streamwise, transverse, and depthwise equations primarily represent balances between, respectively: convection, stretching, and diffusion terms 1, 2, 4, 5, 6, and 7; convection, stretching, and diffusion terms 1, 2, 5, 6, and 7; and convection and diffusion terms 1, 2, and 7. Similarly for the fw, the streamwise, transverse, and depthwise equations primarily represent balances between, respectively: convection and diffusion terms 1 and 7; convection, stretching, and diffusion terms 1, 3, 6, and 7; and convection and diffusion terms 1 and 7. For each equation, in most cases, the dominant terms conform to the table 1 ome, i.e., respectively, for the blw $(Ak/\varepsilon,1,\varepsilon^{-1})$ and for the fw $[Ak/(\varepsilon x^{3/2}), Ak/x^2, Ak/(\varepsilon x^{3/2})]$. The exceptions to the ome are for the ω_x term $\omega_x U_x = (Ak/\varepsilon)$ for the blw, which the results indicate higher order; and the ω_x and ω_y terms $\omega_y U_y = (Ak^2/\varepsilon x^{3/2})$ and $W\omega_{yz} = (Ak/x)^2$ and $\omega_z V_z = (Ak/x^{5/2})$, respectively, for the fw, which the results indicate lower order. Note that for the blw deep solution the only component of vorticity is $\omega_z = -U_y = (\varepsilon^{-1})$, such that the streamwise and depthwise vorticity equations are identically zero and the depthwise equation is an exact balance between convection and diffusion terms 1 and 7 with ome (ε^{-1}).

Based on the results for the vorticity-transport equation and associated ome and vorticity production $\omega(y = 0) = (-U_y, 0, W_y)$ and flux $q_w = (-Rep_z, 0, Rep_x)$ on the plate, the nature

of the vorticity transport in region III is as follows. For the blw: ω_z is produced/fluxed on the plate due to $\omega_z(y = 0)$ and q_{wz}, respectively, and transported by a balance of convection and diffusion terms 1, 2, and 7 (= ω_{zyy}); ω_y is created by turning term 6 (= $\omega_z V_z$) and transported by a balance of convection, stretching, and diffusion terms 1, 2, 5, and 7 (= ω_{yyy}); and ω_x is produced/fluxed on the plate due to $\omega_x(y = 0)$ and q_{wx}, respectively, and created by turning terms 5 and 6 (= $\omega_y U_y$ + $\omega_z U_z$) and transported by a balance of convection and diffusion terms 1, 2, and 7 (= ω_{xyy}). For the fw: ω_x and ω_z are transported by a balance of convection and diffusion terms 1 and 7 (= ω_{xyy} and ω_{zyy}, respectively), whereas ω_y is created by turning term 6 (= $\omega_z V_z$) and transported by a balance of convection and diffusion terms 1 and 7 (ω_{yyy}).

Next, the results for the micro-scale flow are discussed. The differences between the exact and various approximate treatments of the free-surface boundary conditions are displayed in the error-bar chart for the dynamic free-surface boundary condition (figure 5). First, consider the results utilizing the Taylor-series approximation. The zero-gradient conditions lead to appreciable errors for all three stress components. The inviscid conditions reduce the errors substantially (i.e., by two orders of magnitude) and somewhat for the normal and transverse components, respectively, and have minimal effect on the streamwise component. The flat free-surface conditions have errors similar to those just described. The exact conditions substantially reduce the error for the streamwise component (i.e., by one order of magnitude) and somewhat for the normal and transverse components. The results utilizing the exact free surface are similar to those just described for the approximate treatments, i.e., have a minimal influence; however, for the exact conditions the errors for all three components are somewhat reduced. In summary, for small Ak = .01, the zero-gradient conditions lead to substantial errors, the inviscid and flat free-surface conditions reduce the error for the normal component, and the exact conditions additionally reduce the error for the streamwise and transverse components. Application of the conditions on the exact free surface has a minimal influence, except for the exact condition, which displays a slight reduction in error for all three components. Note that appreciable errors in satisfaction of the exact conditions correspond to the generation of erroneous vorticity near the free surface.

Figure 10a displays the solution of the kinematic free-surface boundary condition (13b) for the wave-elevation $\Delta\eta$ and slopes $\Delta\eta_x$ and $\Delta\eta_y$ calculated using finite differences. The former are seen to correlate with W and the latter with - W in the blw and W in the fw, which, at least in magnitude, is expected both from physical reasoning and the form of (13). In the fw ($x \gtrsim 4$), $\Delta\eta$ monotonically decreases in amplitude such that $\Delta\eta_x \to \Delta\eta_y \to 0$. Figure 10b shows $\overline{\eta_x}$ and $\overline{\eta_y}$ evaluated both using (13b) and finite differences. The dominant terms for the blw are, respectively, W/U and - η_xU/V, whereas for the fw, in the latter case, the dominant term is W/V. η, η_x, and η_y conform to the expected ome, i.e., for the blw and fw (Ak,Ak,Ak/ε) and(Ak,Ak,Ak), respectively.

Figures 11a-d display ΔV contours and the blw averaged values of the dynamic and continuity-equation free-surface boundary conditions $\overline{U_z}$, $\overline{V_z}$, $\overline{W_z}$, and $\overline{p}$ evaluated using (17)-(19), and (16), respectively. The ΔU and ΔV contours display large variations, including islands of large magnitudes, whereas those for ΔW and Δp indicate relatively smooth variations. Note the vertical scale and that the effects of the free-surface boundary conditions penetrate to a depth of about $z \approx .04$ ($\approx \lambda/25 \approx 3\delta_b$). The table 1 ome are confirmed, i.e.: for the blw, the dominant terms are $\eta_y U_y$ (- W_y + 2$\eta_y V_y$ + $\eta_x U_y$), - (U_x + V_y), and - η/Fr^2 with ome (Ak/ε^2,Ak/ε,1,Ak/Fr^2), respectively, whereas for the fw, the dominant terms are - W_x, - W_y, - (U_x + V_y), and - η/Fr^2 with ome [Ak/x,Ak/($\varepsilon\sqrt{x}$),Ak/x + 1/x$^{3/2}$,Ak/Fr^2], respectively. The exception to the ome is for the V_z term 2$\eta_y V_y$ = (Ak/ε) for the blw, which the results indicate higher order. The trends for $\overline{U_z}$ follow $\eta_y U_y$ such that regions of U_z > and < 0 imply ΔU near the free surface is smaller and larger than at greater depths, respectively, which is also the case for the other velocity components ΔV and ΔW and their derivatives V_z and W_z. In the blw, this is achieved in a remarkable manner, i.e., the maximum/minimum values are below the free surface: in regions of U_z < 0, there is an island of large negative ΔU below the free surface, whereas in regions of U_z > 0, there is an island of large positive ΔU below the free surface. For $x \gtrsim 4$, U_z becomes small, i.e., follows - W_x. The $\overline{V_z}$ trends are complex since all three terms - W_y, $\eta_x U_y$, and 2$\eta_y V_y$ contribute, although the latter term is of relatively smaller magnitude. In the blw, ΔV also displays islands of large positive/negative values below the free surface.

225

In the near and intermediate wake, $V_z > 0$ such that ΔV is smaller near the free surface than at greater depths, but with the minimum value at the free surface itself. For $x \gtrsim 4$, V_z becomes small, i.e., follows - W_y. The trends for $\overline{W}_z$ follow - $(U_x + V_y)$. In the blw, W_z is small such that the variations are also small, except near the trailing edge and in the near and intermediate wake where $W_z < 0$, including islands of minimum values below the free surface. For $x \gtrsim 4$, W_z becomes relatively smaller, i.e., follows - $(U_x + V_y)$. The $\overline{p}$ trends follow - η. The depthwise variations of velocity and pressure are further displayed in figure 12 in which ΔV and p vs. z at $y/\delta = .52$ are shown. Maximum/minimum values below the free surface are evident for all three velocity components, whereas p is nearly uniform.

Figures 13a-d display $\Delta\omega$ contours and the b l w averaged values $\overline{\omega}_x [= W_y - V_z (= -\Delta W_y + 2\eta_y V_y + \eta_x U_y)], \overline{\omega}_y$ $[= U_x (= \eta_y U_y) - W_x]$, and $\Delta\overline{\omega}_z (= \Delta V_x - \Delta U_y)$.

All three components display large variations near the free surface and islands of maximum/minimum values, especially ω_y. The dominant terms for the blw are $2W_y - \eta_x U_y$, $\eta_y U_y$, and U_y, which conform to the table 1 ome $(Ak/\varepsilon, Ak/\varepsilon^2, 1/\varepsilon)$, respectively; however, the ome also indicate that the ω_x term - $2\eta_y V_y = (Ak/\varepsilon)$, but the results indicate higher order. The dominant terms for the fw are $W_y - V_z$, - W_x, and - U_y, which conform to the table 1 ome $[Ak/(\varepsilon\sqrt{x}), Ak/x, Ak/(\varepsilon\sqrt{x})]$, respectively; however, the ome also indicate that the ω_y term $U_z = (Ak/x)$, but the results indicate higher order. Noteworthy are the large values of transverse vorticity ω_y for the blw, which are a direct consequence of the free-surface boundary conditions. For $x \gtrsim 4$, all three vorticity components are negligible. The depthwise variations of vorticity at $y/\delta = .52$ indicate maximum/minimum values below the free surface for all three vorticity components. The fact that the velocity and vorticity components display maximum/minimum values below the free surface is similar and consistent with the oscillatory nature of the viscous Stokes-wave solution for region II (cf. figure 96 of [8]).

The results for the streamwise, transverse, and depthwise vorticity flux both on the free surface (40) and plate are now discussed, including, in the former case, the blw averaged values. Note that q and $q_w > 0$ correspond to vorticity flux out and into the fluid, respectively. On the free surface, the dominant terms for the

blw are - $\eta_y \omega_{xy}$, - $\eta_y \omega_{yy}$, and - $\eta_y \omega_{zy} + \omega_{zz}$, which conform to the table 1 ome $(Ak/\varepsilon^2, Ak/\varepsilon^3, 1/\varepsilon^2)$, respectively; however, the ome also indicate that the (q_x, q_y) terms $(\omega_{xz}, \omega_{yz}) = (Ak/\varepsilon^2, Ak/\varepsilon^3)$, but the results indicate higher order. The dominant terms for the fw are - $\eta_y \omega_{xy}$, - $\eta_y \omega_{yy}$, and - $\eta_y \omega_{zy}$, which conform to the table 1 ome $[Ak^2/(\varepsilon^2 x), Ak^2/(\varepsilon x^{3/2}), Ak^2/(\varepsilon^2 x)]$, respectively; however, the streamwise vorticity-flux terms - $\eta_y \omega_{xy} = (Ak^2/\varepsilon^2 x)$ and $\omega_{xz} = (Ak/\varepsilon x^{3/2})$, but the results indicate higher and lower order, respectively; and the depthwise vorticity-flux terms - $\eta_y \omega_{zy} = (Ak^2/\varepsilon^2 x)$ and $\omega_{zz} = (Ak/\varepsilon x^{3/2})$, but the results indicate higher and lower order, respectively. For $x \gtrsim 2$-3, all three vorticity-flux components are negligible. On the plate, the dominant terms are - $\omega_{xy} = - Re\ p_z$, $\omega_{yy} = 0$, and - $\omega_{zy} = Re\ p_x$ with ome $[Ak/(\varepsilon^2 Fr^2)]$ in the former and latter cases. Note that q can also be expressed by vector identity as [12]

$$q = n \times \nabla \times \omega - (\nabla\omega) \cdot n \qquad (41)$$

The terms on the right-hand side of (41) can be further expanded through the use of the NS equation and vector identity, respectively, to read

$$n \times \nabla \times \omega = n \times [- Re\ (a + \nabla p)] \qquad (42)$$

$$(\nabla\omega) \cdot n = \nabla(\omega \cdot n) - \omega \cdot \nabla n \qquad (43)$$

where a is the acceleration. (42) is a vector tangent to the free surface with magnitude proportional to the sum of the acceleration and piezometric pressure gradient. (43) is the sum of the gradient of the normal component of vorticity and dot product of ω and ∇n, which is related to the surface curvature. Thus, the physical mechanism for q is a combination of these terms. Expansion of (41) and comparison with (40a)-(40c) shows that terms 2, 3, and 4 correspond to [(43), (42), (42)], [(42), (43), (42)], and [(42), (42), (43)], respectively. Lastly, the ome of the momentum equations at the free surface indicate for the blw and fw, respectively

$$WU_z = - Re^{-1}(- \omega_{yz}) = (Ak/\varepsilon)^2$$
$$WV_z = - Re^{-1}(\omega_{xz}) = (Ak^2/\varepsilon) \qquad (44a)$$
$$UW_x + VW_y + WW_z - p_z =$$
$$- Re^{-1}(\omega_{yx} - \omega_{xy}) = (Ak)$$

and

$$UU_x = - Re^{-1}(\omega_{zy}) = (Ak/x)$$

226

$$UV_x = - Re^{-1}(\omega_{xz} - \omega_{zx}) = (\varepsilon/x^2) \qquad (44b)$$
$$UW_x = - Re^{-1}(\omega_{xy}) = (Ak/x)$$

which relate certain q terms [i.e., right-hand sides of (44)] to certain terms of the tangential and normal components of the acceleration and piezometric pressure gradient on the free surface [i.e., left-hand sides of (44)].

Lastly, with regard to the Ak = .01 micro-scale flow, the results for the vorticity-transport equation are discussed. The contours for all three equations and terms display significant variations with depth, especially for the transverse equations. The blw averaged values indicate that for the blw the streamwise, transverse, and depthwise equations primarily represent balances between, respectively: stretching terms 5 and 6; convection and diffusion terms 3 and 7; and convection, stretching, and diffusion terms 1, 2, 6, and 7. In the former case, the balance is actually between convection, stretching, and diffusion terms 1, 2, 4, 5, 6, and 7 (= ω_{xyy}) with ome (Ak/ε) or convection and diffusion terms 3 and 7 (= ω_{xzz}) with ome (Ak/ε)^3; since, $\omega_y U_y + \omega_z U_z$ = - $W_x U_y + V_x U_z$ = (Ak/ε) due to the cancellation of the $U_z U_y$ = (Ak/ε^3) terms. Similarly for the fw, the streamwise, transverse, and depthwise equations primarily represent balances between: convection and diffusion terms 1 and 7. For each equation, in most cases, the dominant terms conform to the table 1 ome, i.e., respectively, for the blw [Ak/ε or (Ak/ε)^3, Ak^3/ε^4, ε^{-1}] and for the fw [Ak/($\varepsilon x^{3/2}$), Ak/x^2, Ak/($\varepsilon x^{3/2}$)]. The exceptions to the ome are for the ω_x terms Vω_{xy} = (Ak/εx^2) and Wω_{xz} = $\omega_x U_x$ = $\omega_y U_y$ = $\omega_z U_z$ = (Ak^2/$\varepsilon x^{3/2}$) for the fw, which the results indicate lower order. Consistent with ω, all three equations indicate negligible values for x $\gtrsim$ 4.

Based on the results for the vorticity-transport equation and associated ome, vorticity production ω(y=0) on the plate and flux both on the plate q$_w$ and free surface q the nature of the vorticity transport in region IV is as follows. For the blw: ω_z is produced/fluxed on the plate due to ω_z(y = 0) and both on the plate and free surface due to q$_{wz}$ and q$_z$, respectively, and transported by a balance of convection, stretching, and diffusion terms 1, 2, 6, and 7 (= ω_{zyy}); ω_y is fluxed on the free surface due to q$_y$ and transported by a balance of convection and diffusion terms 3 and 7 (= ω_{yzz}); and ω_x is produced/fluxed on the plate due to ω_x(y = 0) and both on the plate and free surface due to q$_{wx}$ and

q$_x$, respectively, and created by turning terms 5 and 6 (= $\omega_y U_y + \omega_z U_z$) and transported by a balance of convection, stretching, and diffusion terms 1, 2, 4, 5, 6, and 7 (= ω_{xyy}) or convection and diffusion terms 3 and 7 (= ω_{xzz}). For the fw: ω is fluxed on the free surface due to q and transported by a balance of convection and diffusion terms 1 and 7.

Medium and Large Steepness

The trends for the medium- and large-steepness macro-scale flow are similar to those described earlier for small steepness, with the exception of the influences of wave-induced separation. The wave-induced separation flow patterns for both Ak = .11 and .21 are nearly identical with those obtained previously [3] in which the zero-gradient approximation was utilized for the free-surface boundary conditions, although the effects of the free-surface boundary conditions cause a small increase in the size of the separation region. Also evident is that the wave-induced effects when normalized by Ak are larger for Ak = .01.

The trends for the micro-scale flow are also similar to those described earlier for Ak = .01, except the following: there is an increased influence of satisfying the free-surface boundary conditions on the exact free-surface z = η; the wave elevation and slopes show complex behavior in the separation region, especially for Ak = .21; the depthwise velocity and pressure profiles indicate that the ΔU variations are reduced, whereas those for ΔV, ΔW, and Δp are increased; and the variations are confined to a narrower region close to the free surface. Also, in general, the table 1 ome are confirmed.

TURBULENT-FLOW SOLUTIONS

The small-wave steepness Ak = .01 results are discussed for both the macro and micro scales in which the turbulent-flow approximation to the exact free-surface boundary conditions is utilized, i.e., (13), (16)-(19), and (25)-(26). Note that, as was the case for laminar flow, the Ak = 0 and deep solutions are equivalent due, here again, to the use of the zero-gradient condition and, additionally, an isotropic eddy viscosity. Both the Ak = 0 and deep solutions correspond to benchmark two-dimensional flat-plate boundary layer and wake turbulent-flow solutions within a few percent, except for leading- and trailing-edge and near-wake effects. In [8] results are also presented for Ak = .11 and .21 in which the zero-gradient approximation to the free-surface boundary conditions was utilized and

comparisons were made with the precursory data and calculations, which validated the performance of the two-layer k-ε model.

Figures 14 and 15 display $\Delta V/Ak$ and ΔV_y vs. y and y^+ and $\Delta\tau_w/\tau_w$(deep), ΔU_{cp}, ΔW_{cp}, and $\Delta\delta^*$ vs. x, respectively. Comparison to the corresponding laminar-flow solutions indicates similar tendencies, although the influences of turbulence are clearly evident, i.e.: typical turbulent profiles with a narrow region of large velocity gradients very close to the wall and wake centerplane; reduction in overshoots, three-dimensionality, and wake bias and streaming velocities; and wave-induced separation is not present. The ΔV_y profiles indicate that the region of large velocity gradient is confined to $y^+ < 10$. As will be discussed next, this has direct consequences with regard to the micro-scale flow. In general, the table 1 ome are confirmed.

The results for the error-bar chart for turbulent flow (figure 5) indicate that the differences between the errors for the zero-gradient and turbulent-flow approximation to the exact free-surface boundary conditions are similar to those for laminar flow; however, it is also evident that the error has not been reduced to the same level. Figures 16-18 display, respectively, $\Delta\eta$, $\Delta\eta_x$, $\Delta\eta_y$, and ΔV and $\Delta\omega$ contours. Comparison to the corresponding laminar-flow solutions indicate, as was the case for the macro-scale flow, similar tendencies, although, here again, the influences of turbulence are clearly evident, i.e., in this case, the effects of the free-surface boundary conditions are confined to a very narrow region close to the wall and free surface, which correlates with the region of large velocity gradients ($y^+ < 10$). This should not be surprising in view of the similarities between the exact laminar-flow free-surface boundary conditions and those presently used for turbulent flow. However, this underscores the need for confirmation of appropriate turbulence free-surface boundary conditions and refined treatment of region V for turbulent-flow conditions. In general, the table 1 ome are confirmed.

SUMMARY AND CONCLUSIONS

Definitive results have been presented, which, for the first time, document the nature of the flow for a solid-fluid juncture blw with waves, including the role of the free-surface boundary conditions. Overviews of the physical problem, including ome, precursory and relevant work, and the computational method were given. The computational conditions, grids, and uncertainty were described and results presented for small,

medium, and large wave-steepness for laminar and turbulent flow.

The laminar and turbulent macro-scale flow (i.e., at scales corresponding to the wave length $\lambda = L = 1$) exhibits all of the features of the wave-induced effects described for the blw region in the precursory work. Additionally, the nature of the vorticity production/flux/transport is explicated. Furthermore, at this scale, the effects of the free-surface boundary conditions are not discernible, which is also consistent with the precursory work in which it was found that most of the results could be explicated in terms of the external-flow pressure gradients without consideration of the role of the free-surface boundary conditions.

The laminar micro-scale flow (i.e., at scales corresponding to the body blw and free-surface boundary-layer thicknesses) indicates that the free-surface boundary conditions have a profound influence on the flow in the region close to the free surface, i.e., $z \lesssim .04$ ($\approx \lambda/25 \approx 3\delta_b$). Appreciable errors are introduced through approximations to the exact free-surface boundary conditions, which corresponds to the generation of erroneous vorticity near the free surface. The blw wave elevation and streamwise and transverse slopes correlate with the depthwise velocity component. The streamwise and transverse velocity components and vorticity components display large variations, including islands of large magnitudes (i.e., maximum/minimum values), whereas the depthwise velocity component and pressure indicate relatively smooth variations. All three components of vorticity flux on the free surface indicate significant values. The vorticity-transport equations display complex balances between convection, stretching/turning, and diffusion. For $x \gtrsim 3\text{-}4$, the effects of the free-surface boundary conditions become negligible. The wave-induced effects when normalized by wave steepness are larger for small than for medium and large steepness with the exception of the large influence of wave-induced separation; however, the free-surface boundary conditions have a relatively small influence on this catastrophic event. In general, the ome are confirmed for both the blw and fw, which confirms the importance of the parameter Ak/ε for characterizing the micro-scale flow.

The turbulent micro-scale flow results are similar and consistent with those for laminar flow, but must be considered preliminary due to the present uncertainty in appropriate treatment of

the turbulence free-surface boundary conditions and meniscus boundary layer for this condition. Clearly, both these areas are imperative for future study. For this purpose, current work involves further towing-tank experiments using laser-doppler velocimeter measurements for the foil-plate model, including the region close to the free surface, and development of cfd methods, including moving contact-line boundary conditions and RaNS methods utilizing nonisotropic turbulence models and large-eddy and/or direct numerical simulations.

Lastly, the present work has several implications with regard to the practical application of ship blw's for nonzero Fr. In particular, the free-surface boundary conditions have been shown to have an important influence in regions of large velocity gradients and wave slopes, including significant free-surface vorticity flux and complex momentum and vorticity transport in a layer close to the free surface all of which scale with the parameter Ak/ε. Note that the present Ak/ε values = $O(1) - O(10)$ are similar to those for model and full-scale practical applications. Also, although turbulent-flow conditions prevail for practical applications, the boundary layer is relatively thick (in distinction from the present thin blw turbulent-flow condition), especially over the afterbody and wake, such that the region of influence of the free-surface boundary conditions is expected to be large over a significant portion of the blw (i.e., more similar to the present laminar- than turbulent-flow solutions), which will affect the detailed flow near the free surface, i.e., velocity, pressure, and vorticity values and gradients, bubble entrainment, and triggering of wave breaking and -induced separations, etc.; thereby, impacting the overall ship performance, including signatures and propeller-hull interaction. In conclusion, methods for calculating ship blw's for nonzero Fr (e.g., [6,7]) should be extended to include more exact free-surface boundary conditions and clearly it is all the more imperative that progress be made on both areas designated earlier for future work. It has been remarked that the most important layer of the ocean is the top millimeter, i.e., microlayer [13], which, at least for some multiple of this physical dimension, may also be the case for ship blw's.

ACKNOWLEDGMENTS

REFERENCES

1. Stern, F., " Effects of Waves on the Boundary Layer of a Surface-Piercing Body," J. of Ship Research, Vol. 30, No. 4, Dec. 1986, pp. 256-274.

2. Stern, F., Hwang, W.S., and Jaw, S.Y, "Effects of Waves on the Boundary Layer of a Surface-Piercing Flat Plate: Experiment and Theory," J. of Ship Research, Vol. 33, No, 1, March, 1989, pp. 63-80.

3. Stern, F., Choi, J.E., and Hwang, W.S, "Effects of Waves on the Wake of a Surface-Piercing Flat Plate : Experiment and Theory," J. of Ship Research, Vol. 37, No. 2, June 1993, pp. 102-118.

4. Toda, Y., Stern, F., and Longo, J., "Mean-Flow Measurements in the Boundary Layer and Wake and Wave Field of a Series 60 $C_B = 0.6$ Ship Model-Part 1: Froude Numbers 0.16 and 0.316," J. of Ship Research, Vol. 36, No. 4, Dec. 1992, pp. 360-377.

5. Longo, J., Stern, F., and Toda, Y., "Mean-Flow Measurements in the Boundary Layer and Wake and Wave Field of a Series 60 $C_B = 0.6$ Ship Model-Part 2: Scale Effects on Near-Field Wave Patterns and Comparisons with Inviscid Theory," J. of Ship Research, Vol. 37, No. 1, March, 1993, pp. 16-24.

6. Tahara, Y., Stern, F., and Rosen, B., "An interactive Approach for Calculating Ship Boundary Layers and Wakes for Nonzero Froude Number," J. of Computational Physics, Vol. 98, No.1, Jan, 1992, pp. 33-53.

7. Tahara, Y and Stern, F. , "Validation of an Interactive Approach for Calculating Ship Boundary Layers and Wakes for Nonzero Froude Number," to appear Computers and Fluids, 1994.

8. Choi, J.E., "Role of Free-Surface Boundary Layer Conditions and Nonlinearities in Wave/Boundary-Layer and Wake Interaction," Ph.D. Thesis, The University of Iowa, Dec. 1993.

9. Schlichting, H., "Boundary-Layer Theory," McGraw Hill Book Company, New York, 1979.

10. Chen, H.C. and Patel, V.C. , "The Flow around Wing-Body Junctions," Proc. Symposium on Numerical and Physical Aerodynamic Flows, Vol. 4, 1989.

11. Patel, V.C., Chen, H.C., and Ju, S., "Ship Stern and Wake Flow: Solutions and the Fully-Elliptic Reynolds-averaged Navier-Stokes

Equations and Comparisons with Experiments," J. of Computational Physics, Vol. 88, June 1990, pp. 305-336.

12. Rood, E.P., "Interpreting Vortex Interactions With a Free Surface," to appear J. of Fluids Engineering, 1994.

13. MacIntyre, F., "The Top Millimeter of the Ocean," Scientific American, Vol. 230, No.5, 1974, pp. 62-77.

14. Newman, J.N., "Recent Research on Ship Waves," Proc. 8th Symposium on Naval Hydrodynamics, Pasadena, CA, Aug. 1970, pp. 519-545.

Table 1. Order-of-magnitude estimates.

Region	I	II	III		IV		fw:
			blw	fw	blw	fw	$x \gtreqless$
U	1	1	1	1	1	1	
∂U	Ak	Ak	1	Ak	1	Ak	
V			ε	ε/x	ε	ε/x	
W	Ak	Ak	Ak	Ak	Ak	Ak	
p	Ak	Ak			Ak/Fr^2	Ak/Fr^2	
η	Ak	Ak			Ak	Ak	
η_x	Ak				Ak	Ak	
η_y					Ak/ε	Ak	
$\partial/\partial x$	1	1	1	$1/x$	1	$1/x$	
$\partial/\partial y$			$1/\varepsilon$	$1/(\varepsilon\sqrt{x})$	$1/\varepsilon$	$1/(\varepsilon\sqrt{x})$	
$\partial/\partial z$	1	1	1	$1/x$		$1/x$	
U_z	Ak^2	Ak^2	1	Ak/x	Ak/ε^2	Ak/x	4
V_z			ε	ε/x^2	Ak/ε	$Ak/(\varepsilon\sqrt{x})$	3
W_z	Ak^2	Ak^2	Ak	Ak/x	1	Ak/x	3
ω_x			Ak/ε	$Ak/(\varepsilon\sqrt{x})$	Ak/ε	$Ak/(\varepsilon\sqrt{x})$	3
ω_y		Ak^2	1	Ak/x	Ak/ε^2	Ak/x	3
ω_z			$1/\varepsilon$	$Ak/(\varepsilon\sqrt{x})$	$1/\varepsilon$	$Ak/(\varepsilon\sqrt{x})$	3
q_x					Ak/ε^2	$Ak^2/(\varepsilon^2 x)$	3
q_y					Ak/ε^3	$Ak^2/(\varepsilon x^{3/2})$	3
q_z					$1/\varepsilon^2$	$Ak^2/(\varepsilon^2 x)$	3
vorticity-transport equation							
streamwise			Ak/ε	$Ak/(\varepsilon x^{3/2})$	$(Ak/\varepsilon)^3$	$Ak/(\varepsilon x^{3/2})$	3
transverse			1	Ak/x^2	Ak^3/ε^4	Ak/x^2	3
depthwise			$1/\varepsilon$	$Ak/(\varepsilon x^{3/2})$	$1/\varepsilon$	$Ak/(\varepsilon x^{3/2})$	3
Re		$1/\varepsilon^2$	$1/\varepsilon^2$	$1/\varepsilon^2$	$1/\varepsilon^2$	$1/\varepsilon^2$	
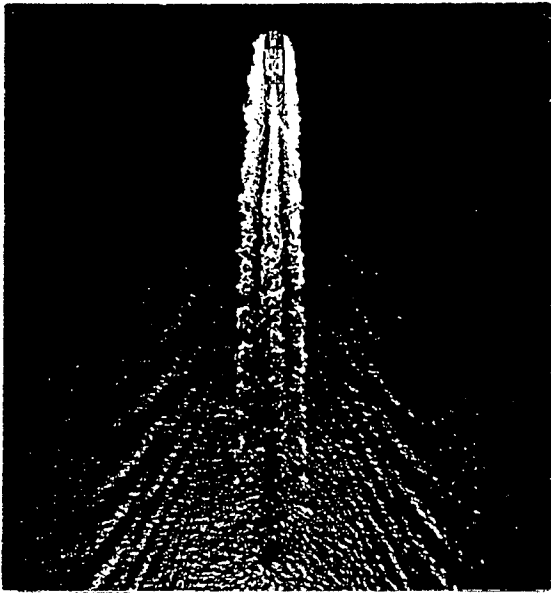
Figure 1. Wave/boundary-layer and wake interaction [14].
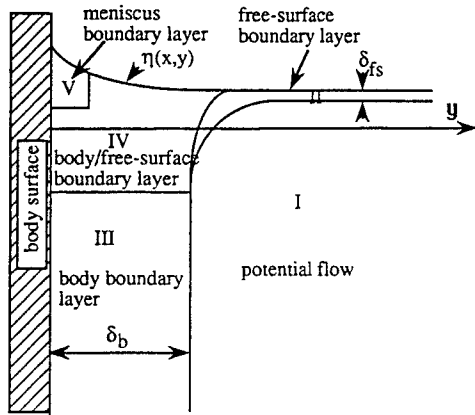
(a) boundary layer
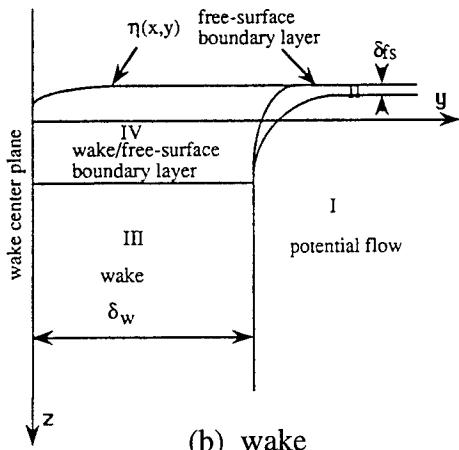
(b) wake

Figure 2. Flow-field regions.
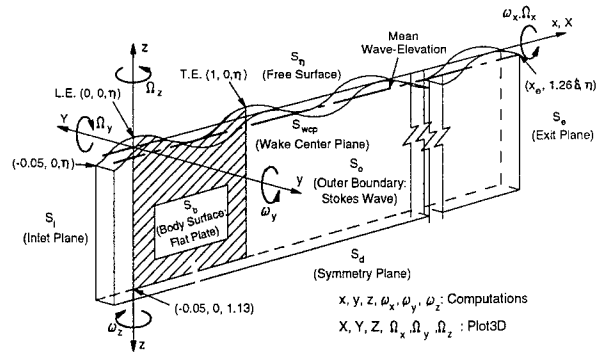
(a) physical domain
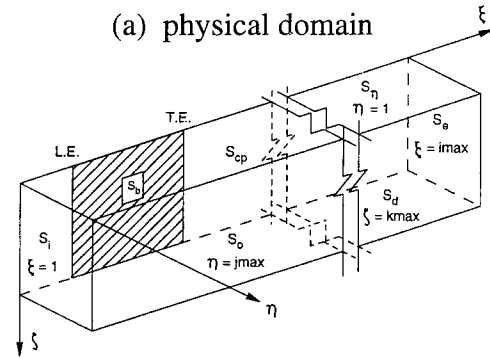
(b) computational domain

Figure 3. Stokes-wave/flat-plate flow field: solution domain and coordinate systems.
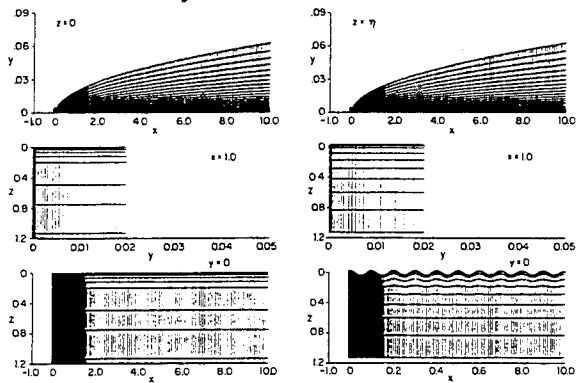
(a) coarse grid (b) typical surface-conforming fine grid

Figure 4. Laminar-flow computational grids.

Dynamic Free-surface Condition
■ error(z)
▨ error(x)
▥ error(y)
1. zero-gradient at z=0
2. inviscid at z=0
3. flat free-surface at z=0
4. exact at z=0
5. inviscid at z=η
6. flat free-surface at z=η
7. exact at z=η

■ error(z)
▨ error(x)
▥ error(y)

laminar   turbulent
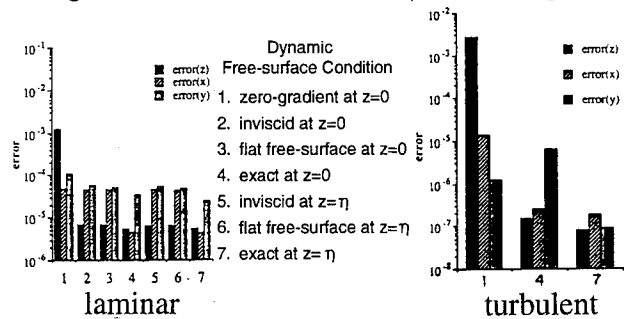
Figure 5. Error-bar chart: Ak=.01.

Figure 7. Wall shear stress, wake-centerplane velocities, and displacement thickness for various depthwise locations: laminar flow and Ak=.01.

Figure 6. Free-surface velocity profiles for various axial locations: laminar flow and Ak=.01.

(a) streamwise

(b) transverse

(c) depthwise

Figure 9.   Macro-scale vorticity: laminar flow and Ak=.01.

(a) streamwise

(b) transverse

(c) depthwise

Figure 8.   Macro-scale velocity: laminar flow and Ak=.01.

(a) streamwise

(b) transverse

(c) depthwise

Figure 11. Micro-scale velocity: laminar flow and Ak=.01.
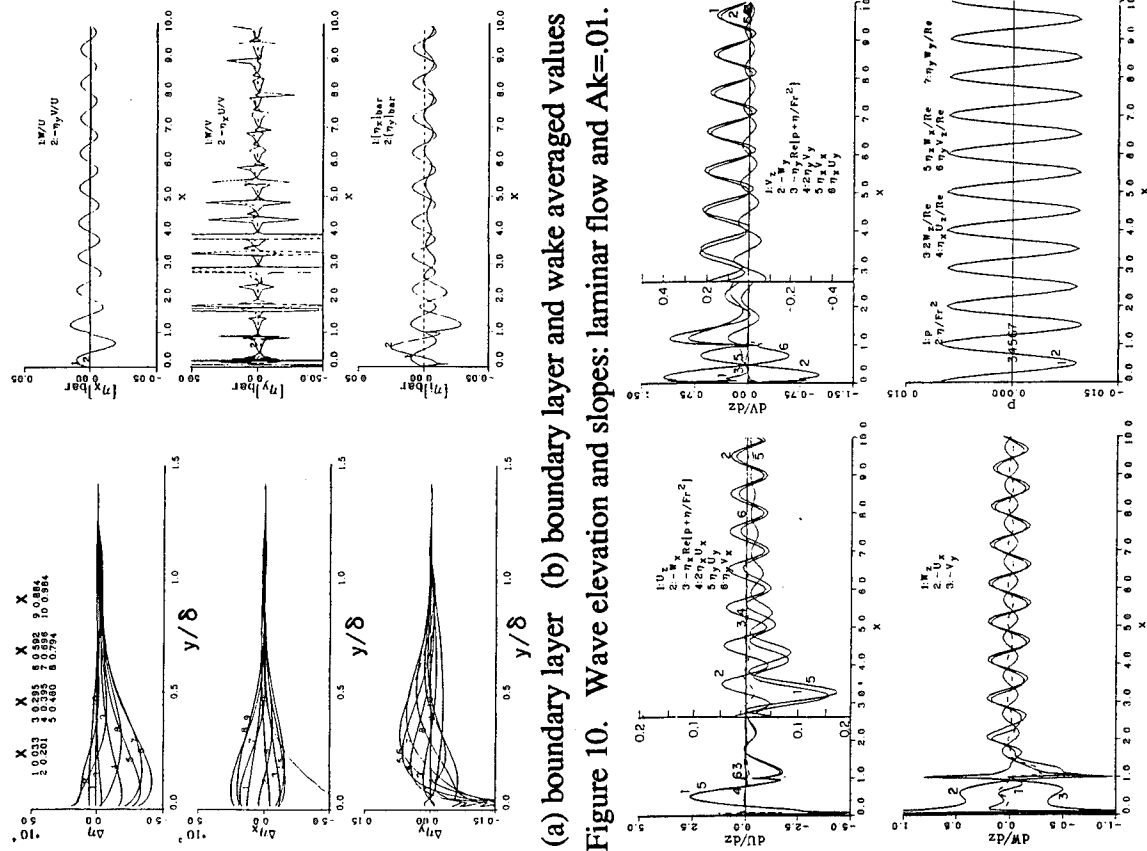
(a) boundary layer (b) boundary layer and wake averaged values

Figure 10. Wave elevation and slopes: laminar flow and Ak=.01.

(d) boundary-layer and wake averaged values

(a) streamwise

(b) transverse

(c) depthwise

(d) boundary-layer and wake averaged values

Figure 13. Micro-scale vorticity: laminar flow and Ak=.01.
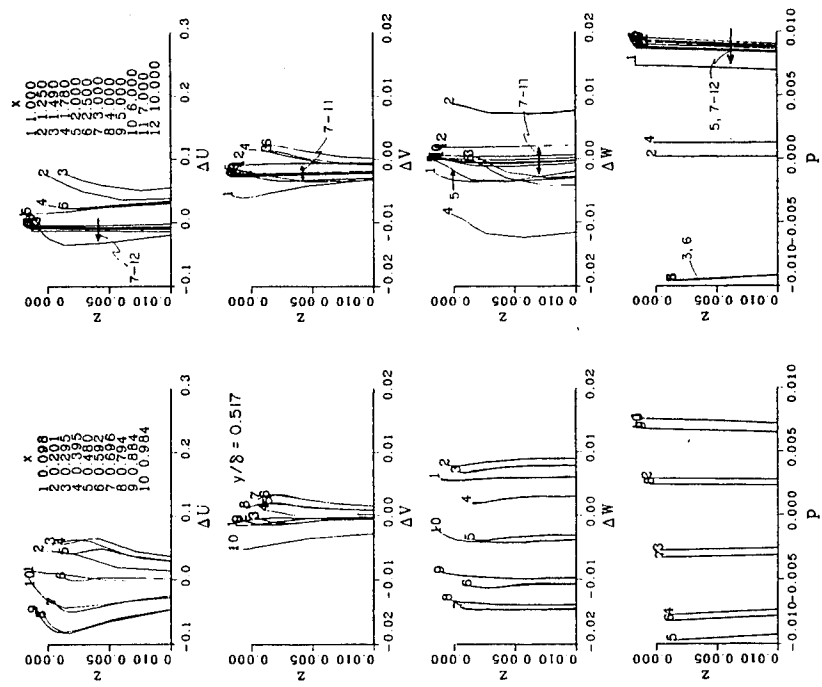
Figure 12. Depthwise variation of velocity and pressure: laminar flow and Ak=.01.

235
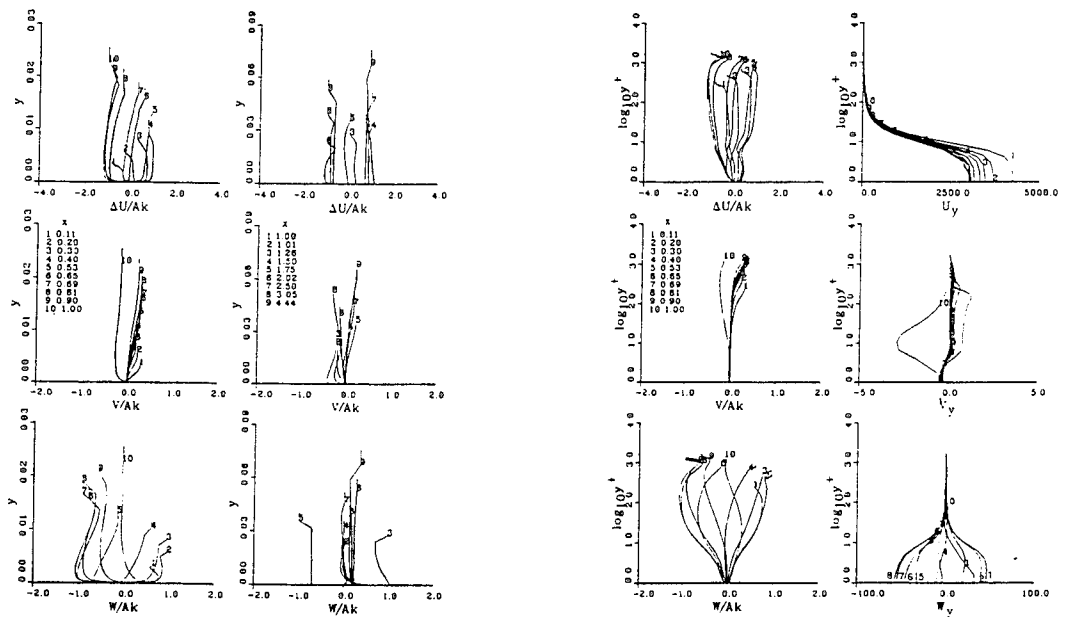
(a) velocity　　　　　　　(b) velocity and velocity gradient in wall coordinates

Figure 14.　Free-surface profiles for various axial locations: turbulent flow and Ak=.01.
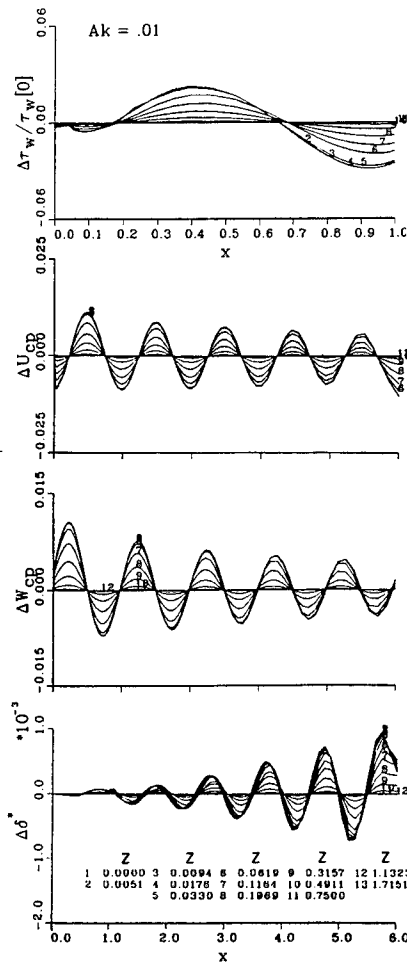
Figure 15.　Wall shear stress, wake-centerplane velocities, and displacement
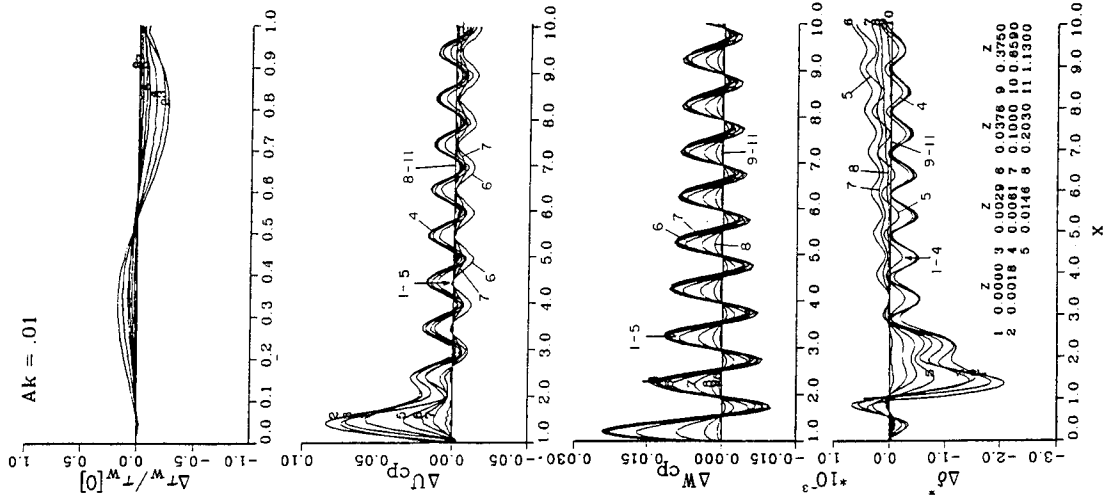thickness for various depthwise locations: turbulent flow and Ak = .01.

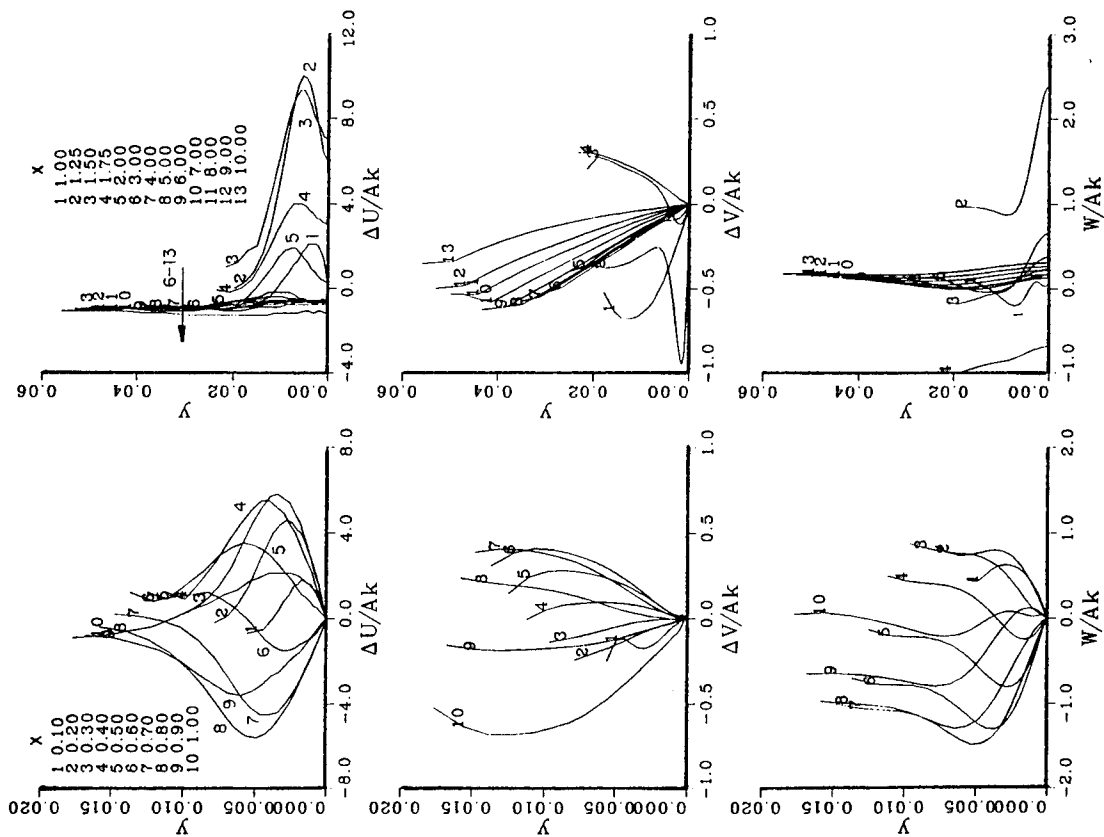

boundary layer
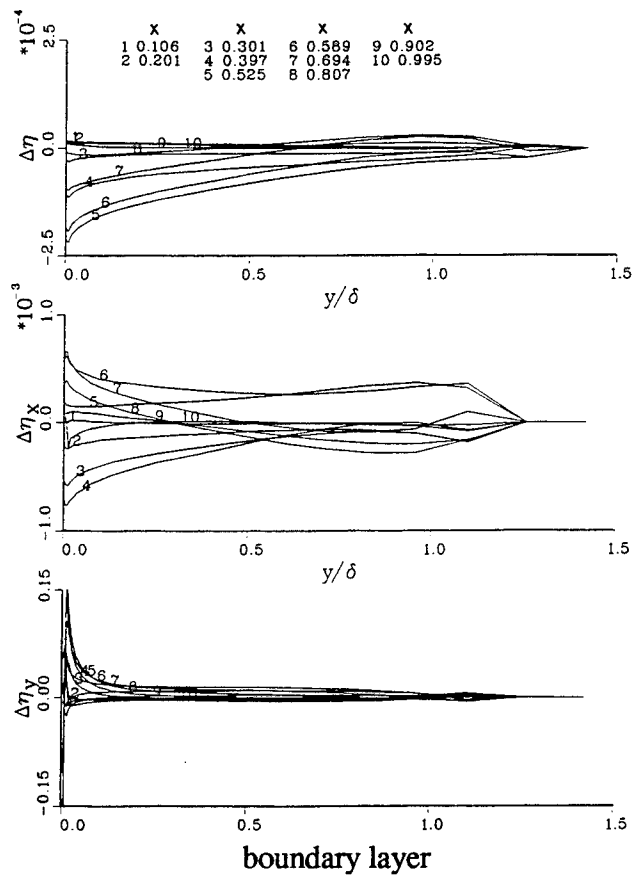
Figure 16.　Wave elevation and slopes: turbulent
flow and Ak=.01.

236

transverse

Figure 18. Micro-scale vorticity: turbulent flow and Ak=.01.

streamwise

Figure 17. Micro-scale velocity: turbulent flow and Ak=.01.

237

DISCUSSION
by Professor M. Tulin, University of California, Santa Barbara

How important are the intersection effects for the wave pattern, or wave resistance, and for the stern wake (propeller plane) pattern?

Author's Reply
We thank both the oral and written discussers of our paper for their pertinent remarks.

The free-surface boundary conditions have been shown to have an important influence in regions of large velocity gradients and wave slopes. For practical applications, the boundary layer is relatively thick, especially over the afterbody and wake, such that the region of influence of the free-surface boundary conditions is expected to be large over a significant portion of the blw, which will effect the detailed flow near the free surface, i.e., velocity, pressure, and vorticity values and gradients, bubble entrainment, and triggering of wave breaking and induced separations, etc.; thereby, impacting the overall ship performance, including signatures and propeller-hull interaction.

DISCUSSION
by Professor K. Mori, Hiroshima University, Japan.

Are the boundary conditions of (25) and (26) obtained from experimental data? According to our experiments [1], although the phenomena are not the same, the conditions seem too strong.

1. Mori, K. and Shin, M., Proc. of 17th Sym. on Naval Hydrodynamics (1989).

Author's Reply
The turbulence free-surface boundary conditions (25)-(26) are not based on experimental data, but rather seem reasonable approximations in view of the available turbulence/free-surface interaction experimental data for idealized geometries. As pointed out in the text, procurement of experimental data for more relevant geometries and determination of appropriate turbulence free-surface boundary conditions are imperative for future study.

238

Direct Numerical and Large-Eddy Simulations of Turbulent Free-Surface Flows

D.G. Dommermuth (Science Applications International Corporation, USA)
E.A. Novikov (University of California, San Diego, USA)

ABSTRACT

Direct numerical simulations and large-eddy simulations of free-surface turbulence are performed to investigate the turbulent structure near the free surface, the roughening of the surface, and the dissipation and scattering of waves by turbulence. Recent laboratory measurements that show tendency of two-dimensional turbulence at the free surface are not supported by the present numerical simulations. In the absence of waves, the surface disturbance (surface roughness) is directly proportional to the component of the pressure that is induced by the vortical portion of the subsurface flow. Simple formulas for predicting surface roughness, which include the effects of hydrostatics and capillarity, are provided. The scattering and dissipation rates of wave energy due to turbulence are the same order as laminar dissipation for a 5cm gravity-capillary wave at an moderate Froude number. Turbulent scattering and dissipation are dominated by the effects of parasitic capillary waves and surfactants. In the far wake of a ship the effects of turbulent scattering and dissipation are minimal.

NOMENCLATURE

R_e:	Reynolds number
R_λ:	Taylor Reynolds number
F_r:	Froude number
W_e:	Weber number
ρ:	Density
σ:	Surface tension
g:	Gravity
ν:	Kinematic viscosity
(x, y, z):	Cartesian coordinates
t:	Time
u_i:	Total velocity field
U_i:	Rotational velocity field
ϕ:	Potential field
η:	Free-surface elevation
n_i:	Unit normal on free surface
(u, v, w):	Total velocity components
(U, V, W):	Rotational velocity components
Π:	Total pressure
P:	Vortical component of pressure
P_a:	Atmospheric pressure
C:	Correlation coefficient
Δ:	Grid spacing
τ_{ij}:	SGS stress tensor
μ:	Scattering or dissipation rate
$\mathcal{F}$:	Filter operator

1 INTRODUCTION

Direct numerical simulations (DNS) of ship wakes are very difficult. Based on Kolmogorov's scaling laws the work and storage requirements of a direct numerical simulation are proportional to Re^3 and $Re^{9/4}$ respectively, where Re is the Reynolds number. Doubling the Reynolds number leads to an order of magnitude increase in the amount of work that is necessary to compute a turbulent flow. So for a ship wake, where the Reynolds number is $O(10^9)$ based on ship length and velocity, direct numerical simulations are impossible now and in the forseeable future.

Large-eddy simulations (LES) attempt to overcome this problem by directly computing the large-scale features of the flow and analytically modeling the small-scale features. The basic assumption of LES is that the small-scale motion is statistically more universal even though the large-scale motion may strongly depend on geometry, external forces, boundary conditions, and initial conditions. Successful implementations of LES methods include studies of homogeneous turbulence, turbulent channel flow, and weather prediction. Here, we use LES to perform preliminary studies of turbulent free-surface flows.

LES formulations decompose the velocity field into its resolvable and subgrid-scale (SGS) components. The effectiveness of a LES formulation depends on how well the SGS stresses are modeled. The SGS stresses are typically formulated in terms of a turbulent eddy viscosity. Smagorinsky's [36] method is the most widely used SGS model in large-eddy simulations, but as Moin [22] discusses there are several problems associated with this model including:

1. The optimal choice of the coefficient in the expression for the eddy viscosity depends on the type of flow;

2. The limiting behavior of the SGS model is not correct near walls *or free surfaces*;

3. The model is too dissipative in laminar flow regions; and

4. The model does not allow transfer of energy from small scales to large scales.

Attempts to alleviate these problems have not been very successful, but there has been some progress. For example, Schumann [34] modifys the behavior of the SGS stresses near walls. As a result, Schumann's simulations of turbulent channel flow agree with experiments slightly better than those of Deardorff [4] whose SGS stress formulation does not account for anisotropy.

Besides modifying the behavior of the SGS stresses near boundaries, another improvement to the Smagorinsky model is to use the resolved flow field to predict the subgrid scales. The basic idea is to extrapolate from the resolved flow the behavior of the SGS stresses. For example, Germano, et al [9], use extrapolation to predict the Smagorinsky coefficient. The effects of their model vanish in the case of laminar flow. Lilly [15] has recently proposed a modification to the extrapolation scheme that uses a least-squares technique to remove a source of singularity.

We use Germano's scheme with Lilly's modification to study free-surface turbulence. A Helmholtz formulation is used to decompose the flow field into potential and vortical fields [6], and an adjustment procedure is used to eliminate the generation of spurious high-frequency waves due to imbalances in the initial conditions [7]. Fully-nonlinear free-surface boundary conditions are satisfied on the exact position of the free surface, and a preconditioned multigrid solution scheme is used to solve the nonlinear elliptic boundary-value problems [8].

We provide the mathematical and numerical formulations of our LES and DNS capabilities in Sections 2-4. The performance of the LES and DNS capabilities is illustrated by several validation studies in Sections 5 & 6. We then use the DNS capability to investigate the turbulent structure near the free

surface, the roughening of the surface by turbulence, and the scattering and dissipation of surface waves by turbulence in Section 7.

2 MATHEMATICAL FORMULATION

2.1 Field Equations

Consider the unsteady incompressible flow of a Newtonian fluid under a free surface, and let $\overline{u}_i(x,t) = (\overline{u}, \overline{v}, \overline{w})$ represent the filtered three-dimensional velocity field as a function of time. Here, the overbar denotes the large-eddy filter. Applying Helmholtz's theorem gives

$$\overline{u}_i = \frac{\partial \overline{\phi}}{\partial x_i} + \overline{U}_i \, , \qquad (1)$$

where $\overline{\phi}(x,y,z,t)$ is a filtered velocity-potential which describes the irrotational flow and $\overline{U}_i = (\overline{U}, \overline{V}, \overline{W})$ is a filtered solenoidal-field which describes the vortical flow such that

$$\frac{\partial^2 \overline{\phi}}{\partial x_i^2} = 0 \qquad (2)$$

$$\frac{\partial \overline{U}_i}{\partial x_i} = 0 \, . \qquad (3)$$

Since $\overline{\phi}$ satisfies Laplace's equation and the divergence of the rotational field $\overline{U}$ is chosen zero, the total velocity field $\overline{u}$ conserves mass. Note that $\overline{U}$ may contain a portion of the irrotational field depending on how the boundary conditions are defined.

Based on this Helmholtz decomposition of the velocity field, define the total-pressure $\overline{\Pi}$ in terms of a vortical pressure $\overline{P}$ and an irrotational pressure as follows:

$$\overline{\Pi} = \overline{P} - \frac{\partial \overline{\phi}}{\partial t} - \frac{1}{2} \nabla \overline{\phi} \cdot \nabla \overline{\phi} - \frac{1}{F_r^2} z \, . \qquad (4)$$

Here, the velocity and pressure terms are respectively normalized by u_c and ρu_c^2, where u_c is the characteristic velocity and ρ is the density. $F_r^2 = u_c^2/g\ell_c$ is the Froude number and ℓ_c is the characteristic length. The vertical coordinate z is positive upward, and the origin is located at the mean free surface. Substituting these decompositions (1 & 4) into the Navier-Stokes equations gives

$$\frac{\partial \overline{U}_i}{\partial t} + \overline{u}_j \frac{\partial \overline{U}_i}{\partial x_j} + \overline{U}_j \frac{\partial^2 \overline{\phi}}{\partial x_i \partial x_j} =$$
$$- \frac{\partial \overline{P}}{\partial x_i} + \frac{\partial \tau_{ij}}{\partial x_j} + \frac{1}{R_e} \frac{\partial^2 \overline{U}_i}{\partial x_j^2} \, , \qquad (5)$$

where $R_e = u_c \ell_c/\nu$ is the Reynolds number and ν is the kinematic viscosity. The SGS stress tensor is defined by

$$\tau_{ij} = \overline{u}_i \overline{u}_j - \overline{u_i u_j} \, . \qquad (6)$$

The divergence of the momentum equations (5) used in combination with the mass-conservation equations (2 & 3) can be used to derive a Poisson equation for the vortical pressure:

$$\frac{\partial^2 \overline{P}}{\partial x_i^2} = - \frac{\partial \overline{U}_j}{\partial x_i} \frac{\partial \overline{U}_i}{\partial x_j}$$
$$-2 \frac{\partial \overline{U}_j}{\partial x_i} \frac{\partial^2 \overline{\phi}}{\partial x_i \partial x_j} + \frac{\partial^2 \tau_{ij}}{\partial x_i \partial x_j} \, . \qquad (7)$$

As shown by Dommermuth (1993a), the vortical pressure is also subject to a solvability condition because we impose Neumann boundary conditions [6].

2.2 Free-Surface Boundary Conditions

The Helmholtz decomposition of the velocity field requires that an additional boundary condition be imposed on the free surface. An expedient boundary condition that can be

241

specified is that the normal component of the rotational velocity is zero on the free surface:

$$\overline{U}_i \cdot \overline{n}_i = \frac{-\overline{U}\overline{\eta}_x - \overline{V}\overline{\eta}_y + \overline{W}}{\sqrt{\overline{\eta}_x^2 + \overline{\eta}_y^2 + 1}} = 0 , \qquad (8)$$

where $z = \overline{\eta}(x, y, t)$ is the filtered free-surface elevation and $\overline{n}_i$ is the filtered unit-normal on the free surface. (The subgrid-scale terms in this equation and in the succeeding free-surface boundary conditions will be neglected.) The preceding constraint which is imposed on the rotational velocity field means that the evolution of the free-surface elevation is entirely prescribed in terms of the free-surface elevation itself and the velocity potential as follows:

$$\frac{\partial \overline{\eta}}{\partial t} + \overline{\eta}_x \overline{\phi}_x + \overline{\eta}_y \overline{\phi}_y - \overline{\phi}_z = 0 , \qquad (9)$$

where everything is evaluated on the exact position of the free surface, $z = \overline{\eta}$.

The normal stress on the free surface must balance with the atmospheric pressure and the surface tension:

$$\frac{d\overline{\phi}}{dt} + \frac{1}{2}(\overline{\phi}_x^2 + \overline{\phi}_y^2 - \overline{\phi}_z^2) + (\overline{\eta}_x \overline{\phi}_x + \overline{\eta}_y \overline{\phi}_y)\overline{\phi}_z$$

$$+\frac{1}{F_r^2}\overline{\eta} = -\frac{1}{W_e}\frac{\partial \overline{n}_i}{\partial x_i} + \overline{P} - \overline{P}_a$$

$$-\frac{\overline{n}_i \overline{n}_j}{R_e}\left(\frac{\partial \overline{u}_i}{\partial x_j} + \frac{\partial \overline{u}_j}{\partial x_i}\right) , \qquad (10)$$

where $\overline{P}_a$ is the atmospheric pressure, $W_e = \rho u_c^2 \ell_c / \sigma$ is the Weber number, and σ is the surface tension. $d/dt = \partial/\partial t + \nabla\overline{\phi} \cdot \nabla$ is a substantial derivative. In addition to the normal-stress condition there are also two tangential-stress conditions that are provided in Dommermuth [6].

The normal stress condition (10) and the corresponding tangential stress conditions are appropriate only if the free-surface boundary-layer is sufficiently resolved. Since

it is difficult to resolve the boundary-layer of a ship wake, a boundary-layer approximation is required in a LES formulation.

Longuet-Higgins [17], Lundgren [18] and Dommermuth [8] provide examples of free-surface boundary-layer formulations. For a clean free surface the boundary-layer approximation of the normal stress condition is

$$\frac{d\overline{\phi}}{dt} + \frac{1}{2}(\overline{\phi}_x^2 + \overline{\phi}_y^2 - \overline{\phi}_z^2) + (\overline{\eta}_x \overline{\phi}_x + \overline{\eta}_y \overline{\phi}_y)\overline{\phi}_z$$

$$+\frac{1}{F_r^2}\overline{\eta} = -\frac{1}{W_e}\frac{\partial \overline{n}_i}{\partial x_i} + \overline{P} - \overline{P}_a$$

$$+ \underbrace{\frac{4}{R_e}(\overline{\phi}_{xx} + \overline{\phi}_{yy})}_{\text{Boundary-Layer Term}} . \qquad (11)$$

This equation correctly predicts the laminar dissipation for small amplitude waves. The two tangential stress conditions are essentially free-slip boundary conditions, and they can be derived by eliminating the potential-flow and shear-stress terms in Equation (16) of Dommermuth [6].

The boundary-layer approximation models the dominate effects of scattering and dissipation of waves by turbulence through the combination of the kinematic condition for the rotational velocity (Equation 8) and the vortical pressure term ($\overline{P}$) in the normal stress condition (Equation 11). The generation of vorticity by spatial and temporal changes in the free-surface elevation is not modeled, but the boundary-layer approximation does model the dissipation of waves due to the direct action of viscosity. The boundary-layer term that models this effect is highlighted in Equation (11).

The Helmholtz formulation separates the potential portion of the flow from the vortical portion of the flow. This requires twice as many elliptic solves as a primitive-variable formulation, but this disadvantage is offset by the following advantages:

- The terms that excite spurious high-

frequency waves can be eliminated using a simple adjustment procedure [7].

- The confluence of boundary conditions that occur at the intersection of the free surface and the ship hull can be rigorously treated without using *ad hoc* extrapolation schemes.

- SGS models for the vortical flow can be developed independently of the potential flow. As a result, the potential flow will not adversely affect the turbulence model.

- The potential portion of the flow can be used in a Lagrangian formulation to model steep waves. This ensures that the grid lines will not cross, unlike a Lagrangian formulation of the primitive-variable equations.

2.3   SGS Models

Based on exact results for the conditionally-averaged vorticity field [23, 24, 26], we expect that the conditionally-averaged SGS stress tensor has a local part $(\tau^{(\ell)})$, which is generally nonanalytical, and a global analytical $(\tau^{(g)})$ part:

$$\langle \tau_{ij} \rangle = \tau_{ij}^{(\ell)} + \tau_{ij}^{(g)} , \qquad (12)$$

where $\langle \rangle$ denotes conditional averaging with fixed $\overline{u}_i$. The local part is a function of the filtered deformation and rotation tensors, taken at the same space-time location where the SGS is evaluated:

$$\overline{D}_{ij} = \frac{1}{2} \left(\frac{\partial \overline{u}_i}{\partial x_j} + \frac{\partial \overline{u}_j}{\partial x_i} \right)$$

$$\overline{R}_{ij} = \frac{1}{2} \left(\frac{\partial \overline{u}_i}{\partial x_j} - \frac{\partial \overline{u}_j}{\partial x_i} \right) . \qquad (13)$$

Except for some degenerate situations, Lund and Novikov (1992) show that $\tau^{(\ell)}$ can be expressed as a function of six terms:

$$\tau^{(\ell)} = \sum_{m=1}^{6} c_m \overline{\tau}^{(m)} , \qquad (14)$$

where c_m are nondimensional coefficients. The nondimensional coefficients can be determined (*a priori*) from a DNS data-set, or dynamically (*a posteriori*) in a LES using, for example, a test-filter procedure such as Germano, et al's (1991).

For simplicity, let $\overline{\tau}^{(m)}$, $\overline{\mathbf{D}}$, $\overline{\mathbf{R}}$, and $\mathbf{I}$ be the matrices associated with the corresponding tensor quantities. Here, $\mathbf{I}$ is the identity matrix associated with δ_{ij}. Then the $\overline{\tau}^{(m)}$ are

$$\overline{\tau}^{(1)} = \overline{\Delta}^2 |\overline{\mathbf{D}}| \overline{\mathbf{D}}$$

$$\overline{\tau}^{(2)} = \overline{\Delta}^2 \overline{\mathbf{D}}\,\overline{\mathbf{D}}$$

$$\overline{\tau}^{(3)} = \overline{\Delta}^2 \overline{\mathbf{R}}\,\overline{\mathbf{R}}$$

$$\overline{\tau}^{(4)} = \overline{\Delta}^2 (\overline{\mathbf{D}}\,\overline{\mathbf{R}} - \overline{\mathbf{R}}\,\overline{\mathbf{D}})$$

$$\overline{\tau}^{(5)} = \overline{\Delta}^2 |\overline{\mathbf{D}}|^{-1} (\overline{\mathbf{D}}\,\overline{\mathbf{D}}\,\overline{\mathbf{R}} - \overline{\mathbf{R}}\,\overline{\mathbf{D}}\,\overline{\mathbf{D}})$$

$$\overline{\tau}^{(6)} = \overline{\Delta}^2 |\overline{\mathbf{D}}|^2 \mathbf{I} , \qquad (15)$$

where $\overline{\Delta}$ is the grid scale and $|\overline{\mathbf{D}}| = \sqrt{tr(\overline{\mathbf{D}}\,\overline{\mathbf{D}})}$. $\overline{\tau}^{(1)}$ corresponds to Smagorinsky's closure [36].

Equation (14) has been tested *a priori* using a DNS data-set of homogeneous turbulence [13]. The conclusions based on this test are: (1) The degenerate situations have zero statistical measure; (2) The Smagorinsky term is dominant, but other terms can make significant contributions; (3) $\overline{\tau}^{(4)}$ is important for turbulent flows with shear; and (4) The coefficients c_m have high spatial variations, which indicates that the local representation $\tau^{(\ell)}$ is insufficient and a global representation $\tau^{(g)}$ is required.

For $\tau^{(g)}$ we assume that it is quadratic and as a first approximation that it involves only one additional filtering. (We denote the first filter by a overbar and the second filter by a overhat.) We also impose the necessary condition of Galilean invariance (the addition of a constant velocity should not affect

243

the SGS stress), which is obvious in Equation (6). From these conditions and symmetry, it follows that $\tau^{(g)}$ has only two terms:

$$\tau^{(g)} = c_7 \, \widehat{\tau}^{(7)} + c_8 \, \widehat{\tau}^{(8)} \qquad (16)$$

$$\widehat{\tau}^{(7)} = \widehat{\overline{u}_i}\widehat{\overline{u}_j} - \widehat{\overline{u}_i\overline{u}_j}$$
$$\widehat{\tau}^{(8)} = \overline{u}_i\overline{u}_j + \widehat{\overline{u}_i\overline{u}_j} - \widehat{\overline{u}_i}\overline{u}_j - \overline{u}_i\widehat{\overline{u}_j} \,. \qquad (17)$$

The term $\widehat{\tau}^{(7)}$ has already appeared in the literature [1, 37], but the term $\widehat{\tau}^{(8)}$ appears to be new. Based on preliminary investigations of homogeneous turbulence by Lund and Novikov, $\widehat{\tau}^{(7)}$ and $\widehat{\tau}^{(8)}$ correlate equally well with *a priori* tests of DNS[1]. Based on these tests $\widehat{\tau}^{(7)}$ may be more desirable than $\widehat{\tau}^{(8)}$ because it is less complex.

The choice of the second filter is very flexible, and may even change during a simulation to achieve optimal performance. However, in the current study, we have not investigated this possibility, and we use the same first and second filters.

Zhang, Street, and Koseff [39] use the combination of $\overline{\tau}^{(1)}$ and $\widehat{\tau}^{(7)}$ to study a lid-driven cavity flow. They propose using this combination to model turbulent free-surface flows. Here, we consider several combinations of the SGS models in a test filter approach to model turbulent free-surface flows.

2.4   Test Filter Approach

Based on Germano, et al's technique, we define two filtering operators: one is the grid filter ($\overline{\mathcal{F}}$), denoted by a overbar, while the other is the test filter ($\widetilde{\mathcal{F}}$), denoted by a tilde [9]. The mesh of the test filter ($\widetilde{\Delta}$) is bigger than the grid scale ($\overline{\Delta}$).

When $\overline{\mathcal{F}}$ is applied to the Navier-Stokes equations, the SGS stresses are given by Equation (6). When $\widetilde{\mathcal{F}}$ and $\overline{\mathcal{F}}$ are applied simultaneously, the SGS stresses are

$$T_{ij} = \widetilde{\overline{u}}_i\widetilde{\overline{u}}_j - \widetilde{\overline{u_i u_j}} \,. \qquad (18)$$

The anisotropic and isotropic portions of the SGS stresses are modeled separately for both the grid and test filters. Here, we illustrate the test filter approach for the anisotropic stresses:

$$\tau_{ij} - \frac{\delta_{ij}}{3}\tau_{kk} = \sum_m c_m \Big(\overline{\tau}_{ij}^{(m)} - \frac{\delta_{ij}}{3}\overline{\tau}_{kk}^{(m)}\Big)$$
$$T_{ij} - \frac{\delta_{ij}}{3}T_{kk} = \sum_m b_m \Big(\widetilde{\overline{\tau}}_{ij}^{(m)} - \frac{\delta_{ij}}{3}\widetilde{\overline{\tau}}_{kk}^{(m)}\Big) \,,$$
$$(19)$$

where the m subscripts and superscripts denote some combination of the local and global portions of the SGS stress model. The c_m and b_m are unknown coefficients.

The *resolved turbulent stresses* ($\mathcal{L}_{ij}$) are related to τ_{ij} and T_{ij} as

$$\mathcal{L}_{ij} = T_{ij} - \widetilde{\tau}_{ij} = \widetilde{\overline{u}}_i\widetilde{\overline{u}}_j - \widetilde{\overline{u}_i\overline{u}_j} \,. \qquad (20)$$

The model of the resolved turbulent stresses can be evaluated by subtracting the test-scale filtering of τ_{ij} from T_{ij} using the relations provided in equation (19):

$$\mathcal{L}_{ij}^{\circ} = \sum_m \Big(b_m\widetilde{\overline{\tau}}_{ij}^{(m)} - \widetilde{\mathcal{F}}(c_m\overline{\tau}_{ij}^{(m)})\Big)^{\circ} \,, \qquad (21)$$

where ()$^{\circ}$ indicates the trace-free part and $\widetilde{\mathcal{F}}$ is a linear function that applys the test filter (see Section 4).

For Formula (21) a generalization of Lilly's least-squares-technique allows us to solve for the unknown coefficients using the five independent equations for the anisotropic portion of the resolved SGS stress [15]. As shown by Lund and Novikov [13], the resulting coefficients may have a high spatial variation. We use volume averaging to circumvent this problem. As a result, the c_m coefficient

can be brought outside of the filter operator. We also assume that the coefficients do not depend on the level of filtering so that $c_m = b_m$.

3 NUMERICAL FORMULATION OF DNS

The Navier-Stokes equations, and the boundary and initial conditions are discretized using 4th-order finite differences. The momentum equations (5), kinematic condition (9), and the normal stress condition (10) are integrated with respect to time using a third-order Runge-Kutta scheme. Each stage of the Runge-Kutta scheme is formulated to inhibit the accumulation of errors in the divergence of the rotational flow field [11]. The rotational pressure is used to project the rotational velocity onto a solenoidal field (3 & 7) with zero normal velocity on the free surface (8). Aliasing errors are controlled using 5th-order upwind-biasing of the convective terms [30]. Laplace's equation for the potential (2) and Poisson's equation for the rotational pressure (7) are solved at each stage of the Runge-Kutta scheme, and a solvability condition is enforced for the rotational pressure. A preconditioned multigrid solution scheme is used to solve the three-dimensional elliptic equations [8]. The z-coordinate is mapped onto a flat plane, and the grid is stretched to resolve the free-surface boundary layer [6]. This mapping is applied to Laplace's equation (2), the Poisson equation for the pressure (7), the momentum equations (5), and all the boundary conditions. Periodic boundary conditions are used on the sides of the domain and free-slip boundary conditions are used on the bottom.

4 NUMERICAL FORMULATION OF LES

The design of grid and test filters is difficult for inhomogeneous problems such as turbulent free-surface flows because Fourier decompositions are not readily available along all of the coordinate axes. The resolution of our fourth- and fifth-order finite-difference schemes also makes it difficult to implement a test filter approach because only the lower half of the energy spectrum is resolved well. This problem is compounded by weak Nyquist-wavelength instabilities that occur in one-sided finite-difference formulas near the free surface. We treat these problems by applying filters in physical space that have resolution and accuracy properties that are consistent with our finite-difference operators.

Let ψ_i represent a discrete variable at gridpoint i, then the grid-filter $(\overline{\mathcal{F}})$ and test-filter $(\widetilde{\mathcal{F}})$ operators are

$$\overline{\mathcal{F}}(\psi_i) = \overline{\psi}_i = (772\psi_i \\ + 210(\psi_{i+1} + \psi_{i-1}) - 120(\psi_{i+2} + \psi_{i-2}) \\ + 45(\psi_{i+3} + \psi_{i-3}) - 10(\psi_{i+4} + \psi_{i-4}) \\ + (\psi_{i+5} + \psi_{i-5}))/1024 + O(\Delta^{10}) \quad (22)$$

$$\widetilde{\mathcal{F}}(\psi_i) = \widetilde{\psi}_i = (28\psi_i + 19(\psi_{i+1} + \psi_{i-1}) \\ + 2(\psi_{i+2} + \psi_{i-2}) \\ - 3(\psi_{i+3} + \psi_{i-3}))/64 + O(\Delta^4), \quad (23)$$

where Δ is the grid spacing. The discrete Fourier transforms of the grid- and test-filters are

$$\widehat{\overline{\mathcal{F}}}(\kappa) = (386 + 210\cos(\kappa) \\ - 120\cos(2\kappa) + 45\cos(3\kappa) \\ - 10\cos(4\kappa) + \cos(\kappa))/512 \quad (24)$$

$$\widehat{\widetilde{\mathcal{F}}}(\kappa) = (14 + 19\cos(\kappa) \\ + 2\cos(2\kappa) - 3\cos(3\kappa))/32, \quad (25)$$

where the hat symbol (^) denotes the Fourier transform and $0 \leq \kappa \leq \pi$ is the nondimensional wavenumber.

Figure 1 shows the Fourier transforms of the filters. Near $\kappa = 0$ both filters are equal

to one. This region corresponds to long-wavelength quantities that are resolved well with a minimal number of grid points. As $\kappa/\pi \to 1$, the Fourier amplitudes of both filters approach zero. This region corresponds to the Nyquist wavenumbers. As designed, the test filter has less bandwidth than the grid filter.

Based on the Fourier transforms, we can define effective length-scales for the filters:

$$\overline{\Delta} = \frac{\pi\Delta}{\int d\kappa\, \widehat{\overline{\mathcal{F}}}(\kappa)} = \frac{256\Delta}{193} \qquad (26)$$

$$\widetilde{\Delta} = \frac{\pi\Delta}{\int d\kappa\, \widehat{\widetilde{\mathcal{F}}}(\kappa)} = \frac{16\Delta}{7}. \qquad (27)$$

These scales indicate that the middle portion of the velocity spectrum is used to determine the model coefficients in the test-filter approach.

The filters in Equations (22 & 23) are applied along all three coordinate axes, in the middle of the domain, at the edges of the periodic boundary, and at the free-slip bottom. Near the free surface, however, we have developed one-sided filters that have similar accuracy and resolution characteristics. Our filters, unlike the more traditional box-car filters, commute with the other finite-difference operators that are used in the LES. This property is required in the derivation of the SGS stress tensor.

We consider several different SGS stress models. These models are summarized in Table 1 below:

Type	Model
I	$c_1\overline{\Delta}^2|\overline{\mathbf{D}}|\overline{\mathbf{D}}$
II	$c_7(\overline{\overline{u}_i\overline{u}_j} - \overline{\overline{u}_i}\,\overline{\overline{u}_j})^\circ$
III	$c_1\overline{\Delta}^2|\overline{\mathbf{D}}|\overline{\mathbf{D}} + c_7(\overline{\overline{u}_i\overline{u}_j} - \overline{\overline{u}_i}\,\overline{\overline{u}_j})^\circ$
IV	$c_6\overline{\Delta}^2|\overline{\mathbf{D}}|^2\mathbf{I}$
V	$c_7^\circ(\overline{\overline{u}_k\overline{u}_k} - \overline{\overline{u}_k}\,\overline{\overline{u}_k})/3\mathbf{I}$
VI	Grid Filter $(\overline{\mathcal{F}})$

Table 1: *SGS Stress Models.*

The first type of closure, which we label Type I, is a conventional technique for modeling

turbulent dissipation. Comparisons to DNS simulations indicate that although Type I closures provide desirable dissipation effects, the details of the flow are not predicted well. The Type II closure is designed to provide better prediction of the SGS stresses. The Type III closure attempts to combine the desirable dissipation effects of the Type I closure with the better prediction of the detailed flow characteristics using the Type II closure. The Types IV and V closures model the isotropic SGS stresses. Most LES absorb the isotropic SGS stresses into the pressure-gradient term in the Navier-Stokes equations, but in free-surface flows these terms are required to predict turbulent roughening of the free surface. A Type IV or V closure is used in combination with the Types I, II, and III closures. A Type VI closure applies the grid filter (see Equation 22) without any SGS stress model.

5 DNS VALIDATION STUDIES

The convergence of the DNS capability is illustrated using exact gravity-waves, viscous Airy-waves, triad interactions, wave-current interactions, and Gerstner's waves as benchmarks. The numerical simulations of exact gravity-waves provide a test of the nonlinear formulation of the inviscid free-surface boundary conditions, and similarly the simulations of viscous Airy-waves test the formulation of the viscous stress conditions. The investigations of Triad interactions demonstrate the capability to simulate the nonlinear interactions of three-dimensional gravity-capillary waves. The investigation of wave-current interactions tests the coupling between the potential and vortical portions of the Helmholtz formulation when the shear is strong and the wave nonlinearity is weak. Gerstner's wave, which is fully-nonlinear and rotational, provides a final validation of our DNS capability.

One measure of a numerical scheme's performance is determined by how well it conserves energy. The vector product of the total velocity with the momentum equations, integrated over the fluid volume, gives a formula for the conservation of energy. The transport theorem in conjunction with the divergence theorem may be used to simplify the resulting equation. Upon substitution of the exact free-surface boundary conditions, the following formula is derived:

$$
\frac{d}{dt}\left(\int_V \frac{U_i U_i}{2} + \frac{1}{2}\int_{S_o}\eta_t\phi + \frac{1}{2F_r^2}\int_{S_o}\eta^2 \right.
$$
$$
\left. + \frac{1}{W_e}\int_{S_o}\left(\sqrt{1+\eta_x^2+\eta_y^2}-1\right)\right) = -\int_{S_o}\eta_t P_a
$$
$$
-\frac{2}{R_e}\int_{S_f} n_i \frac{\partial\phi}{\partial x_j}\frac{\partial^2\phi}{\partial x_i \partial x_j} - \frac{4}{R_e}\int_V \frac{\partial^2\phi}{\partial x_i \partial x_j}\frac{\partial U_i}{\partial x_j}
$$
$$
-\frac{1}{R_e}\int_V \left(\frac{\partial U_i}{\partial x_j}+\frac{\partial U_j}{\partial x_i}\right)\frac{\partial U_i}{\partial x_j}, \qquad (28)
$$

where S_f is the free surface and S_o is the projection of the free surface onto the xy-plane. The first term (dE_{uu}/dt) represents the change in kinetic energy integrated over the material volume of the fluid (V) of the vortical portion of the flow. The second and third terms $(dE_{\phi\phi}/dt$ & $dE_{\eta\eta}/dt)$ represent the changes in the kinetic and potential energies of the waves. The fourth term (dE_s/dt) is the superficial energy due to surface extension. The first term on the right-hand side (dW_{pa}/dt) represents the power input by atmospheric forcing. The last few terms (dW_ν/dt) represent the power expended by viscous stresses. This term can be expressed as a function of the total velocity:

$$
\frac{dW_\nu}{dt} = -\frac{1}{R_e}\int_V \left(\frac{\partial u_i}{\partial x_j}+\frac{\partial u_j}{\partial x_i}\right)\frac{\partial u_i}{\partial x_j},
$$

which shows by virtue of the quadratic terms and the symmetry properties that dW_ν/dt will result in a net decrease in energy. Note that the work due to stresses on all other boundaries besides the free surface is assumed to be zero.

Based on the preceding formula for the conservation of energy, we define the accumulation of absolute error:

$$
\mathcal{E}_a(t) = \int_0^t d\tau \left| \frac{d}{d\tau}\left(E_{uu}+E_{\phi\phi}+E_{\eta\eta}+E_s \right.\right.
$$
$$
\left.\left. -W_{pa}-W_\nu\right)\right| .
$$

This error normalized by the initial kinetic, potential, and superficial energies provides one basis for quantifying numerical convergence:

$$
\mathcal{E}_{ene}(t) = \frac{\mathcal{E}_a(t)}{(E_{uu}+E_{\phi\phi}+E_{\eta\eta}+E_s)_{t=0}} . \quad (29)
$$

Comparisons to exact analytic solutions provide additional tests of the numerical scheme's convergence. For example,

$$
\mathcal{E}_\eta(t) = \frac{1}{a_o A}\int_{S_f}|\eta-\tilde\eta| , \qquad (30)
$$

measures the difference between the exact free-surface elevation (η) and the approximate free-surface elevation $\tilde\eta$ at any instant of time. Here, a_o is the initial wave amplitude and $A = LW$ is a surface area, where L and W are respectively the length and width of the computational domain. The maximum absolute difference in the free-surface elevation is

$$
\mathcal{E}_{\eta max}(t) = \frac{1}{a_o}\text{MAX}|\eta-\tilde\eta| . \qquad (31)
$$

Equations (30 & 31) test the convergence of the irrotational portion of our Helmholtz equation solver. A test of the rotational portion of the numerical scheme is provided by

$$
\mathcal{E}_\omega(t) = \frac{1}{\omega_o^s A}\int_{S_f}|\omega^s-\tilde\omega^s| , \qquad (32)
$$

where ω^s is the surface vorticity and ω_o^s is a characteristic surface-vorticity. For a surface

247

wave, $\omega_o^s = 2ka_o\Omega$, k is the wavenumber, a_o is the initial wave amplitude, $\Omega^2 = (k/F_r^2 + k^3/W_e)\tanh(kh)$ is the wave frequency, and h is the depth. For two-dimensional simulations, $\omega^s = \omega_y|_{z=\eta}$, where $\omega_y|_{z=\eta}$ is the y-component of vorticity evaluated on the free surface.

5.1 Test Case I: Exact Gravity-Wave

Table 2 shows the numerical errors as a function of the spatial and temporal resolution when an exact gravity-wave is used as initial conditions. The solution to the exact gravity-wave is calculated based on the techniques of Schwartz [35], but instead of using perturbation expansions, we use Newton iteration to solve the nonlinear equations. The characteristic length is the wavelength $\ell_c = \lambda$, and the characteristic velocity is $u_c = \sqrt{g\lambda}$. The depth is equal to the wavelength. The solution is inviscid and capillarity is not modeled.

$\lambda/\Delta x$	$T/\Delta t$	$\mathcal{E}_{\eta_{max}}(T)$	$\mathcal{E}_\eta(T)$	$\mathcal{E}_{ene}(T)$
24	80	1.6(−2)	4.5(−3)	3.1(−3)
24	160	1.5(−2)	4.4(−3)	2.4(−3)
48	80	2.6(−3)	7.2(−4)	6.7(−4)
48	160	1.3(−3)	4.0(−4)	6.2(−5)

Table 2: *Gravity wave convergence test.* (The numbers in the parentheses denote exponents of ten.)

The steepness is $\epsilon = 0.35$, where by definition $\epsilon = \frac{1}{2}k(\eta_{max} - \eta_{min})$. This corresponds to 80% of the limiting steepness for a gravity wave. The horizontal grid spacing is Δx, the time step is Δt, and the wave period is T. The horizontal and vertical grid-spacings are equal in this two-dimensional simulation. Four V-cycle multigrid iterations are used during each stage of the Runge-Kutta algorithm, and six Jacobi iterations are used during each V-cycle (see [8]). Table 2 illustrates that the fourth-order spatial-accuracy of the numerical scheme is recovered if the time steps are sufficiently small. The maximum error for the highest resolution case is 0.1%.

5.2 Test Case II: Viscous Airy-Wave

Table 3 shows the numerical errors as a function of the spatial and temporal resolution when a viscous Airy-wave is used as initial conditions. The solution to the Airy wave is calculated based on minor extensions to Lamb's solution to account for finite depth [12]. Here, the finite-depth effects are very weak because the depth is equal to the wavelength. The characteristic velocity is the minimum phase speed for a gravity-capillary wave $u_c = (4g\sigma/\rho)^{1/4}$. The characteristic length is the wavelength of this wave $\ell_c = 2\pi(\sigma/\rho g)^{1/2}$. Based on these scales $F_r^2 = \pi^{-1}$, $W_e = 4\pi$, and $R_e = 2^{3/2}\pi(\sigma/\rho)^{3/4}/g^{1/4}\nu \approx 4000$. For this illustration of the numerical scheme's convergence, a lower Reynolds number is simulated, $R_e = 500$.

$\lambda/\Delta x$	$\delta/\Delta z_o$	$T/\Delta t$	$\mathcal{E}_\eta(T)$	$\mathcal{E}_\omega(T)$	$\mathcal{E}_{ene}(T)$
24	1	500	1.2(−2)	2.7(−1)	6.0(−3)
24	2	500	1.1(−2)	4.8(−2)	2.5(−3)
48	4	1000	1.0(−2)	2.7(−2)	9.1(−4)
96	8	2000	9.9(−3)	2.6(−2)	2.7(−3)

Table 3: *Airy wave convergence test.*

The leading-order solutions $(O(\epsilon^2, R_e^{-1}))$ for the free-surface elevation and the surface vorticity are

$$\eta = a_o \exp(-\frac{2k^2}{R_e}t)\cos(kx - \Omega t)$$

$$\omega^s = -2ka_o\Omega \exp(-\frac{2k^2}{R_e}t)\cos(kx - \Omega t).$$

Similar approximations for ϕ and U_i are used to initialize the fully-nonlinear numerical scheme. The initial wave steepness is very low ($\epsilon = 0.01$) to account for differences between the analytic approximation and the fully-nonlinear solution. The horizontal resolution varies from 24 to 96 grid points per

wavelength. The same number of grid points are used in the vertical plane, but the grid spacing is slightly stretched to resolve the free-surface boundary layer. The laminar boundary-layer thickness is $\delta = R_e^{-1/2}$. The number of grid points in the free-surface boundary-layer is $\delta/\Delta z_o$, where Δz_o is the vertical grid-spacing at the free surface.

Table 3 illustrates that the numerical scheme predicts the correct attenuation of the wave to within the accuracy of Lamb's approximation. The free-surface elevation is correctly predicted to within one percent, even when the resolution of the free-surface boundary-layer is very poor. The calculations of the surface vorticity improve as the resolution of the free-surface boundary-layer increases. The energy is conserved to within 0.1% for a moderate resolution case, but the energy conservation is poorer for the highest resolution case probably because of insufficient multigrid iterations.

5.3 Test Case III: Triad Resonance

Our study of triad resonances is motivated by the need to model short waves for the purposes of remote sensing applications. The derivation of the analytic solution is based on a perturbation expansion in terms of powers of the wave steepness and a Taylor series expansion about the plane $z = 0$. The first-order solution in infinite depth is

$$\eta^{(1)} = \sum_{i=1}^{3} a_i(\tau) \exp\left(i(\mathbf{k_i} \cdot \mathbf{x} - \Omega_i t)\right)$$

$$\phi^{(1)} = \sum_{i=1}^{3} -i\frac{a_i(\tau)\Omega_i}{k_i} \exp\left(k_i z + i(\mathbf{k_i} \cdot \mathbf{x} - \Omega_i t)\right) \, ,$$

where a_i are the slowly-varying complex amplitudes of the resonant triad, and $\mathbf{k_i}$ and Ω_i are their respective wavenumbers and wave frequencies. $\tau = \epsilon t$ is a slow time expansion. We could also allow slow variations in space [19] and weak viscous effects [18, 8],

but for the purposes of our demonstration a slow-time expansion is sufficient.

The triad of waves will resonate if the following conditions are satisfied:

$$\mathbf{k_1} + \mathbf{k_2} = \mathbf{k_3}$$
$$\Omega_1 + \Omega_2 = \Omega_3 \, ,$$

where for deep water, the dispersion relationship is

$$\Omega_i^2 = \frac{1}{W_e}k_i^3 + \frac{1}{F_r^2}k_i \, .$$

At each order of the approximation, evolution equations for a_i are derived by eliminating secular terms. These *free* waves generate *bound* harmonics. The bound waves are the particular solutions to the governing equations after the secular terms have been eliminated. This solution procedure has been automated using Macsyma, a symbolic algebra code.

We consider a special case that illustrates the directional spreading of wave energy due to triad interactions:

$$\mathbf{k_1} = (k_1 \cos(\theta), k_1 \sin(\theta))$$
$$\mathbf{k_2} = (k_1 \cos(\theta), -k_1 \sin(\theta))$$
$$\mathbf{k_3} = (2k_1 \cos(\theta), 0) \, .$$

where θ is the angle of incidence of the two gravity waves ($\mathbf{k_1}$ & $\mathbf{k_2}$) relative to the capillary wave ($\mathbf{k_3}$). The wavenumber that characterizes this case is

$$k_1^2 = \frac{(2\cos(\theta) - 1)W_e}{(4\cos(\theta)^3 - 2)F_r^2} \, .$$

Based on the preceding equation, resonance can occur only for $\cos(\theta) < 2^{-1/3} \approx 37.5 \deg$. These waves are long-crested gravity-capillary waves. The equations that govern the envelop are

$$\frac{da_1}{d\tau} = -iF(\theta)k_1\Omega_1 a_2^* a_3$$

$$\frac{da_2}{d\tau} = -iF(\theta)k_1\Omega_1 a_1^* a_3$$

$$\frac{da_3}{d\tau} = -iF(\theta)\cos(\theta)k_1\Omega_1 a_1 a_2,$$

where $F(\theta) = (\cos(\theta))^2 + 2\cos(\theta) - 2)$.

The characteristic velocity is the minimum phase speed for a gravity-capillary wave $u_c = (4g\sigma/\rho)^{1/4}$. The characteristic length is the inverse wavenumber of this wave $\ell_c = (\sigma/\rho g)^{1/2}$. Based on these scales $F_r^2 = 2$ and $W_e = 2$. The solution is inviscid. The angle of incidence is $\theta = \arctan(\frac{1}{2})$. The numerical solution is initialized with $\epsilon_1 = \epsilon_2 = 0.05$ and $\epsilon_3 = 0$. Two hundred time steps are used per gravity-wave period ($T = 2\pi/\Omega_1$), and the duration of the simulation is 35 gravity-wave periods. The grid resolution along the $x-$, $y-$, & $z-$axes is $24 \times 48 \times 24$. The depth that is used in the numerical simulation is sufficiently deep to neglect finite-depth effects.

Figure 2 compares the modal amplitudes of the analytic and numerical solutions. The agreement is very good initially, but then the solutions begin to diverge after about ten gravity-wave periods. The theory predicts that all of the gravity-wave energy goes into the capillary wave, whereas the numerical solution shows a periodic behavior. This discrepancy is due to a special phase dependence in the analytic theory that can be eliminated by extending the theory to higher order. (We plan to demonstrate this result in a subsequent paper.) The numerical solutions also show a high-frequency behavior due to high-order interactions that are not modeled by the analytic theory. The numerical simulation conserved energy to within four percent after 35 gravity-wave periods ($\mathcal{E}_{ene}(35T) = 0.037$).

5.4 Test Case IV: Wave-Current Interactions

As a test of the coupling between the potential and vortical portions of our Helmholtz formulation, consider the interaction of a wave with a shear current. A linear analysis of this flow leads to Rayleigh's stability equation subject to the kinematic and dynamic free-surface boundary conditions [38]. Our current profile has the following general form:

$$U(z) = U_0 + U_1 \cos(\frac{\pi}{2h}(z + h)),$$

where U_0 and U_1 are the amplitudes of the mean and sinusoidal portions of the current and h is the depth. The characteristic length is the wavelength of the surface disturbance $\ell_c = \lambda$, and the characteristic velocity is $u_c = \sqrt{g\lambda}$. The depth is equal to the wavelength. The solution is inviscid and capillarity is not modeled.

For $U_1 = -U_0$ the current is highest at the mean free-surface ($z = 0$), and the shear is highest at the mean free surface and the bottom. For our test case all of the eigenvalues are real and the flow is stable. As initial conditions, we choose the eigenmode with the highest eigenvalue. The phase speed of this wave is approximately $c \approx \sqrt{g/k} + U(0)$. Twenty-four grid points are used per wavelength and one hundred time steps are used per wave period. Two wave steepnesses and two currents are chosen to show the convergence of the fully-nonlinear numerical solution to the linear analytic solution as the steepness and shear are reduced.

U_0	ϵ	$\mathcal{E}_\eta(T)$	$\mathcal{E}_\omega(T)$	$\mathcal{E}_{ene}(T)$
0.1	0.01	2.3(−2)	1.5(−3)	1.0(−4)
0.1	0.02	2.5(−2)	2.9(−3)	4.5(−4)
0.2	0.01	4.9(−2)	2.1(−3)	7.8(−5)
0.2	0.02	5.0(−2)	4.4(−3)	2.6(−4)

Table 4: *Wave-current convergence test.*

Table 4 illustrates the convergence of the numerical scheme as a function of the wave

steepness and the shear. The error in the surface vorticity ($\mathcal{E}_\omega$) is normalized by $\omega_o^s = |U_1|\pi/2h$. The errors in the free-surface elevation are halved when the magnitude of the shear is halved. Similarly, the errors in the surface vorticity are halved when the wave steepness is halved. The kinetic and potential energy is conserved to within .05% for all cases.

5.5 Test Case V: Gerstner's Wave

Table 5 shows the numerical errors as a function of the spatial and temporal resolution and the nonlinearity when Gerstner's wave is used as initial conditions[12]. A Newton-Raphson technique is used to convert Gerstner's Lagrangian coordinates to our Eulerian coordinates. Then a boundary-value problem is solved to convert from the primitive-variable formulation of Gerstner to our Helmholtz decomposition. The characteristic length is the wavelength $\ell_c = \lambda$, and the characteristic velocity is $u_c = \sqrt{g\lambda}$. The depth is equal to the wavelength. The solution is inviscid and rotational. Capillarity is not modeled.

z_s	$\lambda/\Delta x$	$T/\Delta t$	$\mathcal{E}_\eta(T)$	$\mathcal{E}_\omega(T)$	$\mathcal{E}_{ene}(T)$
-0.1	24	50	1.9(−2)	3.0(−2)	3.1(−2)
-0.1	48	100	7.5(−3)	7.3(−3)	1.3(−2)
-0.2	24	50	3.1(−3)	1.1(−3)	9.6(−3)
-0.2	48	100	1.2(−3)	1.7(−4)	4.3(−3)

Table 5: *Gerstner's wave convergence test.*

The wave steepness, $\epsilon = \pi H/\lambda$, is a function of z_s: $\epsilon = \exp(kz_s)$, where k is the wavenumber and $z_s = 0$ corresponds to a cycloid. The two entries in the table for $z_s = -0.1$ and -0.2 correspond to $\epsilon = .53$ and .28. The error in the surface vorticity is normalized by $\omega_o^s = 2\Omega$, where Ω is the wave frequency.

The errors in the surface vorticity show that the fourth-order accuracy is approached as the grid resolution is increased. However, the convergence of the free-surface solution is not as rapid. A closer inspection of the numerical results shows that the

cusp that occurs at the crest of the Gerstner wave is smoothed out. Another factor that contributes to the slower convergence is the finite-depth effects that are present in the numerical solution, but not the analytic solution. Even with these limitations, the accuracy of these numerical simulations is comparable to the simpler gravity-wave case.

6 LES PERFORMANCE STUDIES

The LES formulation is tested *a priori* using a DNS dataset of three-dimensional homogeneous turbulence and *a posteriori* using numerical simulations of free-surface turbulence. The DNS code that is used to generate the dataset of homogeneous turbulence uses the same finite-difference operators and multigrid solver as the free-surface code. The study of homogeneous turbulence allows us to perform high-resolution simulations of a flow that is less complex than free-surface turbulence. The LES studies of free-surface turbulence include comparisons to moderate-resolution DNS studies of turbulence without waves, turbulence with waves, and waves without turbulence. These numerical simulations allow us to assess the performance of the test-filter approach and the SGS closures under a variety of conditions.

6.1 A Priori Tests

The *a priori tests* of the SGS models are based on a DNS simulation of homogeneous turbulence. Based on a length scale of $\ell_c = 5cm$ and a rms-velocity scale of $u_c = 4cm/s$, the Reynolds number is $R_e = 2000$. These scales are chosen to match our free-surface turbulence studies, which we will discuss later. As initial conditions, we used white noise with zero mean that was projected onto a solenoidal velocity field. A 128^3 numerical simulation was run until the kinetic energy decayed to about 25% of its initial value. Then the velocity field was rescaled so that

the rms velocity was equal to one. This process was repeated until the shape of spectrum did not change. The Taylor Reynolds number at this point was $R_\lambda = 46$.

Figure 3 compares energy spectrums of numerical simulations to the measurements of Comte-Bellot and Corrsin [2]. The energy density and the wavenumbers are normalized using Kolmogorov units. The numerical simulations include the results of 128^3 psuedo-spectral simulations (labeled I and II), and eight-point and six-point upwind-biased finite-difference codes[2]. The first spectral simulation was allowed to naturally decay. The second spectral simulation forced the lowest wavenumbers to make the spectrum stationary. The six-point FDM scheme is used in our free-surface code. The results of the eight-point FDM scheme are included to illustrate convergence.

The finite-difference codes compare as well to the experiments as the spectral codes. Moreover, the finite-difference codes show no evidence of an energy pileup at the highest wavenumbers, unlike the spectral codes. Except for the energy pileup, a nonstationary spectrum may explain the poorer agreement of the first spectral simulation with the experimental data. The poorer agreement of the second spectral simulation at the lower wavenumbers may be attributed to the forcing. As expected, the eight-point finite-difference scheme shows slightly better agreement with the experimental data at the highest wavenumbers. However, considering that this slight discrepancy is occuring at the Nyquist wavenumbers, the excellent agreement of both finite-difference codes with the experimental data is remarkable. We are currently investigating the performance of the finite-difference codes at higher Reynolds numbers on a CM-5 computer.

The DNS dataset from the eight-point finite-difference code is used to generate synthetic LES velocity fields using different filters.

The SGS stress tensor is calculated using the definition in Equation (6). Then volume-averaged SGS coefficients are calculated using Lilly's least-squares procedure. Table 6 provides the SGS coefficients and the correlation coefficients. The effective length-scale of each filter is Δ_e, and Δ is the grid spacing. As the ratio Δ_e/Δ gets larger, more energy is filtered out. Two of the filters correspond to the grid and test filters that are defined in Equations (22 & 23). The third filter is a very coarse second-order accurate filter. The correlation coefficient is defined below:

$$\mathcal{C}^{(m)} = \frac{<\tau_{ij}\tau_{ij}^m>}{\sqrt{<(\tau_{ij})^2><(\tau_{ij}^m)^2>}}, \quad (33)$$

where τ_{ij} is the SGS stress tensor and τ_{ij}^m is the model SGS stress tensor. The brackets denote volume averaging.

Type	Δ_e/Δ	C_1	C_6	C_7	$\mathcal{C}^{(m)}$
I	256/193	8.10(-3)	-	-	0.06
I	16/7	2.55(-2)	-	-	0.17
I	16/5	5.59(-2)	-	-	0.26
II	256/193	-	-	1.20	0.95
II	16/7	-	-	1.40	0.94
II	16/5	-	-	1.81	0.90
III	256/193	1.92(-4)	-	1.20	0.95
III	16/7	-5.28(-4)	-	1.40	0.94
III	16/5	4.72(-3)	-	1.80	0.90
IV	256/193	-	-9.81(-3)	-	0.25
IV	16/7	-	-3.94(-2)	-	0.69
IV	16/5	-	-1.36(-1)	-	0.87
V	256/193	-	-	1.20	0.95
V	16/7	-	-	1.58	0.95
V	16/5	-	-	2.20	0.98

Table 6: *SGS and correlation coefficients.*

In Table 6 the correlation of the global model (Types II and V) is much better than the local models (Types I and IV), and the combination of a local model with the global model (Type III) does not improve the performance of the global model alone (Type II). In general, the correlations of the global models slightly decrease as the coarseness of the filter increases, whereas the correlations

---

[2]Dr. Thomas Lund at Nasa Ames provided us with the spectral results.

of the local models improve. All of the SGS coefficients increase as coarseness increases.

The Type I model with $\Delta_e/\Delta = 16/5$ roughly corresponds to one case that Lund and Novikov investigated using a spectral code with a sharp-cutoff filter and volume averaging [13]. For this case their correlation coefficient ($C = 0.24$) agrees with our results. As a possible explanation of the excellent correlation coefficients for the global model, consider the correlation between the energy density $(u_k u_k)$ and the filtered energy-density $(\overline{u}_k \overline{u}_k)$. For even the coarsest filter, this correlation exceeds 0.97. This implies that most of the kinetic energy is concentrated in the lowest wavenumbers, which helps to explain the excellent correlation of the global model. Moreover, as noted by Meneveau, et al (1992), although the global model captures a significant portion of the SGS energy, its wavenumber content is too high to be resolved by a LES formulation [20]. So it is possible for the global model to have a high correlation in a static test, like we have just performed, and still perform less well in a dynamic test as we will see in next section.

6.2 A Posteriori Tests

Table 8 in Section 9 at the end of this paper provides the details of six DNS studies of free-surface turbulence. These DNS studies, which include simulations of subsurface turbulence without waves, turbulence with waves, and waves without turbulence, are compared to low-resolution LES. The LES studies and the DNS studies that they are compared to are provided in Table 9.

The initial assignment of the subsurface-velocity field is similar to the procedure Dommermuth (1993a) discusses in his Appendix C [6]. The initial shape of the subsurface-velocity spectrum is $\kappa^{-5/3}$. The mean velocity components are zero. To ensure that the LES and DNS studies use identical initial conditions, only low wavenumbers ($\kappa \leq 12\pi$) that will fit into the LES are excited. Free-

slip boundary conditions are initially used on the plane $z = 0$. If a surface wave is also present, then the subsurface-velocity field is periodically extended above the plane $z = 0$. A boundary-value problem is solved to set the normal-component of the surface velocity to zero (see Equation 8). The initial rms velocity of the subsurface-velocity field is set to one, whether or not a surface wave is present. The surface wave is assigned using an exact Gravity wave, and the generation of spurious high-frequency waves due to imbalances in the initial conditions is eliminated using an adjustment procedure (see [6], [7], & [8]). The simulations are run for about 2.5 wave periods, or more than two small-scale eddy-turnover times (t_o) for the lowest Froude-number runs and almost six turnover times for the highest Froude number, where $t_o = \lambda_o/u_o$, λ_o is the final Taylor microscale, and u_o is the final rms velocity.

The spectrum of the total-velocity field is calculated by taking the Fourier transform in the horizontal plane of $(\eta + D)^{1/2}\vec{u}$ where D is the depth and $\eta + D$ accounts for the vertical extent of the fluid. The Fourier coefficients are squared and integrated over the depth. Finally, the energy density is summed over wavenumber shells to calculate the one-dimensional spectrum $E(\kappa)$. Details of a similar procedure are provided in Dommermuth (1993a).

Figures 4 & 5 compare the spectra of the DNS to the LES for cases with and without surface waves. Both figures include the spectrum of the total velocity field $(E(\kappa))$ and the spectrum of the wave energy $(S(\kappa))$. By comparing the initial velocity spectra to the final velocity spectra (see Figures 4a & 5a), we observe that the higher wavenumbers $(\kappa > 12\pi)$ of the DNS runs have filled in according to Kolmogorov's law $(E(\kappa) \propto \kappa^{-5/3})$. The spectra of wave energy in Figure 4b show a buildup of energy for wavenumbers $\kappa > 2\pi$ relative to the initial conditions. This buildup corresponds to the formation of parasitic capillary waves on the front face of the

gravity wave (see [3], [16], & [8]). With no initial wave, the spectra of wave energy correspond to surface roughness (see Section 7.2). Since roughness is proportional to pressure, the spectra of roughness should behave as

$$S(\kappa) \propto \frac{\kappa^{-7/3}}{(\frac{1}{F_r^2} + \frac{\kappa^2}{W_e})^2},$$

where the $\kappa^{-7/3}$ dependence is associated with the pressure [21] and the denominator includes free-surface effects (see Section 7.2). This trend is illustrated in Figure 5b.

Comparing the LES and DNS velocity spectra in Figures 4a & 5a shows that low-resolution LES ($24 \times 24 \times 25$) tend to decay less rapidly than the DNS for the lowest few wavenumbers. This anomaly is reduced when the resolution of the LES is increased (see 'LES 6' run in Figure 5a). We speculate that once a sufficient portion of the turbulent energy cascade is captured by the LES, then this problem will be eliminated. However, we will require DNS with higher resolution or experimental measurements to validate LES with higher resolution.

The higher wavenumbers ($\kappa > 12\pi$) of the LES velocity spectra (see Figures 4a & 5a) decay more rapidly than the DNS because the current formulation of the LES applys a grid filter. (see Equation 22). Without the grid filter, the LES break down due to a buildup of energy at the Nyquist wavenumbers. The differences between the SGS models are relatively small. In fact, just the grid filter (LES runs 1, 5, and 6) without a SGS model performs as well as the more complex LES formulations (LES runs 2-4). Whether this trend will continue at higher resolution is not clear.

The dissipation in a LES is provided by the SGS model, the viscous terms in the Navier-Stokes equations, and the grid filter. The grid filter for the low-resolution LES provides about 75% of the dissipation, 20% is provided by the viscous terms, and the final 5%

is provided by the SGS models. However, the global SGS model (Type II) sometimes provides a small net increase in energy (see LES run 2). The inclusion of the Smagorinsky model (Type III) does not reverse this trend in a test filter approach because the global model dominates (see LES run 3). This dominant behavior is also observed in the *a priori tests*. The Smagorinsky model (Type I) always provided some dissipation. This explains why the low wavenumbers associated with this model agree slightly better with the DNS (see LES run 4 in Figure 4a).

The volume-averaged coefficient of the global model is nearly constant ($c_7 \approx 1.0$) during the simulations (LES runs 2 & 3) for both the anisotropic and isotropic portions of the SGS stresses. The Smagorinsky coefficient rises to a peak value of about $c_1 = 0.36$ during the developing stage of the flow (LES run 4), and then steadily decreases to a value of $c_1 = 0.22$ at the end of the simulation. When the Smagorinsky model is used in combination with the global model (LES run 3), the magnitude of the Smagorinsky coefficient is an order of magnitude less and its sign varies. The coefficient of the isotropic model (Type IV) is almost constant ($c_6 = -0.60$, LES run 4). Overall, the coefficient's magnitudes are higher than what we had expected based on the *a priori* tests. As the resolution of the LES increases, we conjecture that the magnitude of the coefficients will go down.

Figures 6a-d compare LES and DNS free-surface cuts as a packet of parasitic capillary waves forms on the front face of the gravity wave. The wave is propagating from right to left. The initial conditions are a pure gravity wave (see parts a & b), and the parasitic capillary waves form from rest due to a parametric resonance near the crest (see parts c & d). The wave length of the ripples is determined by the condition that the phase velocity of the ripples is equal to the phase velocity of the gravity wave plus the local water-particle velocity of the gravity wave [16]. When the subsurface flow is free of turbulence, the 5cm

254

wave that is modeled in Figures 6a-d will form nine ripples on the front face of the gravity wave, and the wavelength and the amplitude of these ripples will steadily decrease down the face of the gravity wave [8].

Although LES cannot resolve the ripples that are observed in the DNS data that is plotted in Figures 6c & d, Part (d) shows that the 'mean' slope is predicted well by the LES. Since the attenuation of wave energy due to viscosity is proportional to the wavenumber squared, the inability of the LES to resolve the ripples could give the wrong wave dissipation. This effect may explain why the LES predicts a slightly higher wave amplitude than the DNS (see Figure 6c). This mechanism for wave dissipation is a very sensitive function of the gravity wave's steepness, and it warrants additional investigation using LES with higher resolution.

For these low-resolution LES the wavy portion of the flow is not separated from the vortical flow in the SGS stress models. As our modeling capabilities improve, this separation may be required to model the different physical processes that are associated with the different components of the flow. Our Helmholtz formulation provides a natural technique for performing this separation.

7 NUMERICAL RESULTS

Based on a combination of model-scale measurements and numerical predictions of the Taylor length scale and the rms turbulent velocity in a ship wake, we expect Taylor Reynolds numbers $R_\lambda = O(10^5 - 10^6)$ and Taylor Froude numbers $F_\lambda = O(10^{-1} - 10^{-3})$ that depend on the distance aft. We do not expect strong interactions between the subsurface turbulence and the surface waves in the far wake of the ship, where the Froude number is low, but we still need to quantify the types of interactions and their behavior as a function of the Froude number. Here, we use the results of the DNS to investigate the structure of turbulence near the free sur-

face, turbulent roughening of the free surface, and turbulent scattering and dissipation of waves at the low Taylor Froude numbers $(O(10^{-1} - 10^{-2}))$ that would occur several ship lengths astern of the ship. The longest wave lengths that we model correspond to a C-Band radar at an angle of incidence of 30 degrees. The numerical details of the DNS are provided in Table 8 in Section 9 at the end of this paper.

As the characteristic velocity and length scales, we choose the rms velocity of the turbulence and the wavelength of the ambient wave. In physical units, we simulate rms turbulence velocities from 2-4cm/s interacting with a 5cm gravity-capillary wave. This leads to Taylor Reynolds of $R_\lambda = O(50 - 100)$. Based on our earlier simulations of homogeneous turbulence (see §6.1, the resolution of the bulk flow is adequate. The free-surface boundary layer, however, is not resolved. Since our primary goal is to model the work that the turbulence performs on the waves, we choose to use the DNS free-surface boundary conditions (see Equation 10) as if the boundary-layer is fully resolved. (For example, the prediction of turbulent roughening of the free surface does not require resolving the free-surface boundary layer, see Section 7.2.) Upon further validation of our free-surface boundary-layer formulation (see Equation 11), we will incorporate that capability into our DNS code. A preliminary validation study is provided in Dommermuth (1993c).

7.1 The Turbulent Structure Near the Free Surface

Laboratory measurements of a turbulent vortex-tube interacting with a free surface show the formation of whirls [32, 33]. The observed persistence and amalgamation of these whirls is characteristic of two-dimensional turbulence. Whether this behavior is common to turbulent free-surface flows in general is questionable because this particular

vortex-tube experiment had a moving stagnation point on the free surface where the whirls would naturally tend to collect [31, 5, 6]. This issue is addressed using a DNS of a more general turbulent free-surface flow.

For any function $F(x, y, z, t)$ such as vorticity, we can define an one-dimensional energy operator (E_{1d}):

$$E_{1d}(F; \hat{z}, t) = \frac{1}{2} \int \int dx dy \frac{(\eta + D)}{D} F^2 \,,$$

where $\hat{z} = (z + D)/(\eta + D)$ is a mapping, and D is the depth. (The free surface corresponds to $\hat{z} = 1$ and $z = \eta$, and the bottom corresponds to $\hat{z} = 0$ and $z = -D$.) The operator E_{1d} provides a vertical distribution of energy for a function F. An integral of E_{1d} with respect to $\hat{z}$ multiplied by the depth D provides the total energy in the fluid volume.

Figures 7a & b provide the enstrophy distribution for the vertical component of vorticity $(E_{1d}(\omega_z))$ and the energy distribution for the horizontal components of velocity $(E_{1d}(u) + E_{1d}(v))$. The vertical component of vorticity corresponds to the whirls that are observed in laboratory experiments. As time increases, Figure 7a shows that $E_{1d}(\omega_z)$, after a small initial increase, actually decreases by about 25% near the free surface $(\hat{z} = 1)$ and the free-slip bottom $(\hat{z} = 0)$. In the interior of the fluid for $\hat{z} = 0.75$, 0.50, and 0.25 the enstrophy increases and actually more than doubles in one case. There is no evidence that the vertical component of vorticity tends to persist longer at the free surface for this low Reynolds number simulation.

Figure 7b shows that the horizontal velocity components have at least 50% more energy near the free surface and the free-slip bottom than in the interior of the flow. The high velocities near the boundaries of the fluid are due to horizontal vortices interacting with their images. These high horizontal velocities may actually inhibit the connection of normal vorticity with the free surface. Granted, these results are for a single real-

ization of a turbulent flow at a low Reynolds number, but they do not support the notion that the flow near the free surface behaves like two-dimensional turbulence.

7.2 Free-Surface Roughness

We define roughness as the free-surface disturbance that is caused by subsurface turbulence in the absence of ambient waves. At low Froude numbers, the free-surface elevation is hydrostatically balanced with the component of the pressure that is induced by the vortical portion of the flow:

$$\eta = F_r^2 P \,. \qquad (34)$$

If capillarity is important, then

$$\widehat{\eta} = \frac{\widehat{P}}{\frac{1}{F_r^2} + \frac{\kappa^2}{W_e}} \,, \qquad (35)$$

where the hat symbol (^) denotes the Fourier transform and κ is the horizontal wavenumber. As the Froude number increases, dispersive effects may become important, then

$$\hat{\eta}(t) = \frac{\kappa}{\omega} \int_o^t du \widehat{P} \sin(\omega(t - u))$$
$$\exp(\frac{-2\kappa^2}{R_e}(t - u)) \,, \qquad (36)$$

where $\omega^2 = \kappa/F_r^2 + \kappa^3/W_e$ is the wave frequency.

In Table 7 we compare the preceding formulas to two DNS of a fully-nonlinear free-surface flow (see Runs 1 & 4 in Table 8). Two additional DNS with free-slip boundary conditions on the "free surface" are used to calculate the vortical component of the pressure. This pressure is inserted into the three formulas for roughness. Table 7 provides the correlation coefficients between the free-surface and free-slip wall calculations. The symbols C_{34}, C_{35}, and C_{36} respectively correspond to the correlation coefficients for Equations (34, 35, & 36). The results are for the final time step.

256

DNS Run	C_{34}	C_{35}	C_{36}
1	0.939	0.998	0.999
4	0.767	0.907	0.928

Table 7: *Roughness correlation coefficients.*

The correlation coefficients for DNS Run 1 are better than DNS Run 4 because Run 1 has a lower Froude number and less nonlinearity. Comparing the coeffients C_{35} to C_{34} in Table 7 shows that capillary effects are important for the $5cm$ and smaller disturbances that Runs 1 and 4 model. Dispersive effects do not appear to be as important because the C_{36} coefficients are only slightly better than the C_{35} coefficients. Overall, the good agreement of the free-slip-wall simulations with the fully-nonlinear free-surface simulations provides strong support for using simple free-slip-wall formulations to perform roughness calculations.

7.3 Turbulent Scattering of Waves

We define turbulent scattering as the directional spreading of surface waves due to interactions with subsurface turbulence. In our simulations the surface wave is initially propagating along the $x-$axis, and then the interactions of the wave with the turbulence move wave energy off of the $x-$axis. One measure of how much scattering has occurred in our numerical simulations is the amount of potential energy that has nonzero $y-$wavenumbers, which we denote as E_s. The operator E_s also includes the effects of roughness, but its effect on E_s is minimal because the total potential energy due to roughness is less than 0.2% of the wave potential energy.

Figure 8 plots the turbulent scattering of wave energy for the two different Froude numbers in Table 8. The two curves are initially flat due to the effects of the adjustment procedure, but then the slopes of the curves develop a mean component. The slope of the fitted curve in the figure is equal to the mean slope of the numerical data. Based on this fitted curve, we estimate that the rate of turbulent scattering (μ_s) is

$$\mu_s = \frac{1}{4}E_p , \qquad (37)$$

where E_p is the initial potential energy. (Note that the time t is normalized by the ratio of the rms turbulent velocity to the wavelength.) Equation (37) represents a spreading of wave energy that can act like an apparent dissipation. Let E_o equal the total wave energy, which includes the kinetic, potential, and superficial energy, then the laminar rate of energy decay (μ_l) is

$$\mu_l = -\frac{4\kappa^2}{R_e}E_o , \qquad (38)$$

where $\kappa = 2\pi$ is the wavenumber of the surface wave. If we assume that the scattering formula in Equation (37) is equally valid for the kinetic and superficial energy components, then for a Reynolds number $R_e = O(10^3)$, the apparent dissipation due to scattering is the same order as the attenuation due to laminar decay.

Another scattering mechanism that is important for gravity-capillary waves is the triad resonance that is discussed in Section 5.3. The rate of scattering of wave energy due to a triad resonance (μ_r) is proportional to the wave steepness ($\mu_r \propto \kappa a$, where κ is the wavenumber and a is the wave amplitude). For short steep waves, especially wind-driven waves, this mechanism is as effective as turbulence for scattering wave energy. This is illustrated in Figure 2, where we observe that over 75% of the gravity-wave energy has scattered after only fifteen wave periods. However, triad resonances, unlike turbulent scattering, have a nonlinear recurrence that may limit their overall effectiveness.

Figure 9 plots the x-component of the free-surface slope for two different Froude numbers at roughly the same nondimensional time $t/F_r = 8.35$. The scattered potential energies relative to the initial potential wave energies are the same order at this time. This

257

indicates that the long, energy-containing waves, are about equally scattered. We observe, however, that the short parasitic capillary waves are steeper and appear to be more scattered for the higher Froude number case. This is confirmed by analysis of two-dimensional wave spectra. The waves are propagating from right to left along the x−axis.

7.4 Turbulent Dissipation of Waves

We define turbulent dissipation as the attenuation of surface waves due to interactions with subsurface turbulence. The total wave energy E_w is

$$E_w = \frac{1}{2} \int_{S_o} \eta_t \phi + \frac{1}{2F_r^2} \int_{S_o} \eta^2 + \frac{1}{W_e} \int_{S_o} (\sqrt{1 + \eta_x^2 + \eta_y^2} - 1) ,$$

where the first three terms on the right-hand side of the equation are respectively the wave kinetic energy, the wave potential energy, and the wave superficial energy. Let E_{w1}, E_{w2}, and E_{w3} respectively represent the energy with an ambient wave but no turbulence, the energy with an ambient wave and turbulence, and the energy with turbulence but no ambient wave. We define the change of wave energy (E_d) due to the actions of turbulence as

$$E_d = E_{w1} - (E_{w2} - E_{w3}) .$$

In our DNS runs, we neglect E_{w3} because it never exceeds .2% of E_o, where E_o is the initial value of E_{w1}.

Figure 10 plots the turbulent dissipation of the wave energy for the two different Froude numbers in Table 8. The two curves are initially flat due to the effects of the adjustment procedure, but then the slopes of the curves develop an oscillatory and a mean component.

The period of the oscillations is roughly equal to the wave period, which would suggest that the amplitude of the oscillations is proportional to the wave amplitude. This possible dependency will be investigated in a future paper.

The mean offset in the slope represents a net decrease in the wave energy. The slope of the fitted curve in the figure is equal to the mean slope of the numerical data. Based on this fitted curve, we estimate that the turbulent dissipation rate (μ_t) is

$$\mu_t = 4E_o F_r . \tag{39}$$

Comparing the turbulent dissipation rate relative to the turbulent scattering rate shows that turbulent dissipation decreases more rapidly as the Froude number decreases (see Equation 37). For Froude numbers $O(10^{-1} - 10^{-2})$, the turbulent dissipation rate is the same order as the turbulent scattering rate and the laminar dissipation rate (see Equation 38). However, all of these effects are less than the dissipation rates associated with the formation of parasitic capillary waves (μ_c) and the effects of surfactant films (μ_f).

In the case of parasitic capillary waves, Dommermuth's numerical simulations and Longuet Higgins' theoretical predictions show that $\mu_c = O(5\mu_l - 10\mu_l)$ for steep 5cm gravity capillary waves [8, 16]. Pillips shows that in the inextensible limit of a surfactant film that $\mu_f = O(10\mu_l)$ for a 5cm gravity-capillary wave [29].

Our turbulent-dissipation rate is four times lower than the dissipation rate that Olmez & Milgram (1992) measure [28]. We note, however, that the laminar decay rate that they measure is two times higher than theory. Two possible explanations that could explain the differences between our predictions, their measurements, and theory include the effects of the poor resolution of the free-surface boundary layer in the numerical simulations and the effects of a surfactant film that may have been present in the Michi-

gan towing-tank facility even with the use of scrubbers[3].

8 CONCLUSIONS

Comparisons between the LES and DNS indicate that the LES should be performed at higher resolution to resolve a sufficient portion of the turbulent energy cascade. For the present low-resolution LES, the global stress model (Type II closure) provides excellent prediction of the SGS stresses, but the wavenumber content is too high to be resolved in a LES formulation. For the same resolution, a grid filter with no SGS model works as well as the closure models that we have tested to date. These trends require investigation at higher resolution. The next step in SGS modeling will also require a detailed study of the structure of turbulence [25, 27].

DNS studies of free-surface turbulence do not provide evidence that whirls will persist on the free surface due to the effects of two-dimensional turbulence at low Reynolds numbers. DNS studies show that free-surface roughness is proportional to the component of the pressure that is induced by the vortical portion of the flow. Since turbulent dissipation relative to turbulent scattering is a higher order function of the Froude number, its effects will diminish more rapidly in a ship wake. The turbulent scattering and dissipation of 5cm surface waves are dominated by the effects of parasitic capillary waves and surfactants for Froude numbers that would correspond to a region that is several ship lengths aft of the stern.

These DNS results are tempered by our inability to resolve the free-surface boundary layer. We propose to overcome this problem by using the boundary-layer formulation of the free-surface boundary conditions that

we provide in Equation (11). This boundary condition is already incorporated into our LES capability. The boundary-layer formulation enables us to simulate the dominate dissipative effects of parasitic capillary waves while still maintaining an ability to predict free-surface roughness, and turbulent scattering and dissipation.

References

[1] Bardina, J., Ferziger, J.H., and Reynolds, W.C. (1980) Improved subgrid-scale models for large-eddy simulations. AIAA 80-1357.

[2] Comte-Bellot, G. and Corrsin, S. (1971) Simple Eulerian time correlation of full and narrow-band velocity signals in grid-generated 'isotropic' turbulence. *J. Fluid Mech.*, **48**, 273-337.

[3] Cox, C.S. (1958) Measurements of slopes of high-frequency wind waves. *J. Mar. Res*, **16**, 199-225.

[4] Deardorff, J.W. (1970) A numerical study of three-dimensional turbulent channel-flow at large Reynolds numbers. J. Fluid Mech., **41**, 453-480.

[5] Dommermuth, D.G. (1992) The formation of U-shaped vortices on vortex tubes impinging on a wall with applications to free surfaces. *Phys. Fluids*, A bf 4(4), 757-769.

[6] Dommermuth, D.G. (1993a) The laminar interactions of a pair of vortex tubes with a free surface. *J. Fluid Mech.*, **246**, 91-115.

[7] Dommermuth, D.G. (1993b) The initialization of vortical free-surface flows. *J. Fluids Eng.* To appear.

---

[3]In a private conversation, Prof. Milgram noted that he has since measured dissipation rates in another facility that are similar to his previous measurements.

[8] Dommermuth, D.G. (1993c) Efficient Simulation of short- and long-wave interactions with applications to capillary waves. *J. Fluids Eng.* To appear.

[9] Germano, M., Piomelli, U., Moin, P., and Cabot, W.H. (1991) A dynamic subgrid-scale eddy viscosity model. *Phys. Fluids*, A 3(7), 1760-1765.

[10] Gharib, M., Wegand, A., Dabiri, D., and Novikov, E. (1993) Interaction of small-scale turbulence with a free surface. Submitted for publication.

[11] Hirt, C.W., Nichols, B.D., and Romero, N.C. (1975) SOLA-A numerical solution algorithm for transient fluid flows. *Los Alamos Scientific Lab.* Report No. LA-5852.

[12] Lamb, H. (1932) Hydrodynamics. *Dover.*

[13] Lund, T.S. and Novikov, E.A. (1992) Parameterization of subgrid-scale stress by the velocity gradient tensor. In *Annual Research Briefs.* Center for Turbulence Research, NASA-Ames Research Center and Stanford University.

[14] Leighton, R.I., Swean, T.F., Handler, R.A., and Swearingen, J.D. (1991) Interaction of vorticity with a free surface in turbulent open channel flow. In *Proceedings of the 29th Aerospace Sciences Meeting, Reno, NV*, AIAA 91-0236.

[15] Lilly, D.K. (1991) A proposed modification of the Germano subgrid-scale closure method. *Phys. Fluids*, A 4(3), 633-635.

[16] Longuet-Higgins, M.S. (1963) The generation of capillary waves by steep gravity waves. *J. Fluid Mech.*, 16, 138-159.

[17] Longuet-Higgins, M.S. (1991) Theory of weakly damped Stokes waves: a new formulation and its physical interpretation. *J. Fluid Mech.*, preprint.

[18] Lundgren, T.S. (1989) A free-surface vortex method with weak viscous effects. In *Mathematical Aspects of Vortex Dynamics*, ed. by R.E. Caflisch, SIAM, pp. 68-79.

[19] McGoldrick, L.F. (1970) On Wilton's ripples: a special case of resonant interactions. *J. Fluid Mech.* 42, 193-200.

[20] Meneveau, C., Lund, T.S., and Moin, P. (1992) Search for subgrid scale parameterization by projection pursuit regression. In *Studying Turbulence Using Numerical Simulation Databases - IV.* Center for Turbulence Research, NASA-Ames Research Center and Stanford University.

[21] Monin, A.S. and Yaglom, A.M. (1975) Statistical Fluid Mechanics II. *The MIT Press, Cambridge, MA*

[22] Moin, P. (1990) I. The subgrid scale modeling group. In *Studying Turbulence Using Numerical Simulation Databases - III, Proceedings of the 1990 Summer Program.* Center for Turbulence Research, NASA-Ames Research Center and Stanford University.

[23] Novikov, E.A. (1991) Solutions of exact kinetic equations for intermittent turbulence. In *Monte-Verita Symposium on Turbulence, Switzerland*, preprint.

[24] Novikov, E.A. (1992a) Self-amplification of turbulent 3D vorticity field and 2D vorticity gradient. *J. Phys.*, A 25, 657.

[25] Novikov, E.A. (1992b) Probability distributions for three-dimensional vectors of velocity increments in turbulent flow. *Phys. Rev. A, Rapid Comm.*, 46 (10), R6147.

[26] Novikov, E.A. (1993a) A new approach to the problem of turbulence, based on the conditionally-averaged Navier-Stokes equations. *Fluid Dyn. Res.*, 12 (10).

[27] Novikov, E.A. (1993b) Statistical balance of vorticity and a new scale for vortical structures in turbulence. *Phys. Rev. Let.*, Submitted.

[28] Olmez, H.S. and Milgram, J.H. (1992) An experimental study of attenuation of short water waves by turbulence. *J. Fluid Mech.*, 239, 133-156.

[29] Phillips, O.M. (1980) The Dynamics of the Upper Ocean. *Cambridge University Press.*

[30] Rai, M.M and Moin, P. (1991) Direct simulations of turbulent flow using finite-difference schemes. *J. Comp. Phys.*, 96, 15-53.

[31] Sarpkaya, T. and Suthon, P. (1991) Interaction of a vortex couple with a free surface. *Exp. Fluids*, 11 205-217.

[32] Sarpkaya, T. (1992) Interaction of a turbulent vortex with a free surface. In *Proc. 19th Symp. on Naval Hydro., Seoul, Korea.*

[33] Sarpkaya, T. (1992) Three-dimensional interactions of vortices with a free surface. In *Proceedings of the 30th Aerospace Sciences Meeting, Reno, NV*, AIAA 92-0059.

[34] Schumann, U. (1975) Subgrid scale model for finite difference simulations of turbulent flows in plane channels and annuli. *J. Comp. Phys.*, 18, 376-404.

[35] Schwartz, L.W. (1974) Computer extension and analytic continuation of Stokes' expansion for gravity waves. *J. Fluid Mech.*, 62, 553-578.

[36] Smagorinsky, J. (1963) General circulation experiments with the primitive equations. *Mon. Weather Rev.*, 91, 99-164.

[37] Speziale, C.G. (1985) Galilean invariance of subgrid-scale stress models. *J. Fluid Mech.*, 156, 55.

[38] Triantafyllou, G.S. and Dimas, A.A. (1989) Interaction of two-dimensional separated flows with a free surface at low Froude numbers. *Phys. Fluids*, A 1(11), 1813-1821.

[39] Zhang, Y., Street, R.L., and Koseff, J.R. (1993) Thoughts on the development of a dynamic subgrid-scale model for free- surface flow. In *1993 Free-Surface Vorticity Workshop, Pasadena.*

9 TABLES

	DNS 1	DNS 2	DNS 3	DNS 4	DNS 5	DNS 6
Includes Wave?	no	yes	yes	no	yes	yes
Includes Turbulence?	yes	no	yes	yes	no	yes
ℓ_c	5cm	5cm	5cm	5cm	5cm	5cm
u_c	2cm/s	2cm/s	2cm/s	4cm/s	4cm/s	4cm/s
H/λ	-	.07	.07	-	.07	.07
R_e	1000	1000	1000	2000	2000	2000
F_r^{-2}	1230.	1230.	1230.	306.	306.	306.
W_e^{-1}	3.70	3.70	3.70	0.925	0.925	0.925
R_λ	62	-	62	63	-	63
Δt	0.0003	0.0003	0.0003	0.0006	0.0006	0.0006
N_t	601	801	801	601	801	801
δ_t^{-1}	14.0	14.0	14.0	7.0	7.0	7.0

Table 8: *Data for DNS runs.*

The 'Includes Wave?' item indicates whether a fully-nonlinear gravity wave is present in the initial conditions. Similarly, the 'Includes Turbulence?' item indicates whether the initial conditions include a subsurface-velocity field. The length of the wave is ℓ_c and the initial rms velocity of the subsurface velocity field is u_c. $H/\lambda = H/\ell_c$ is the initial wave steepness. R_e, F_r, and W_e are respectively the Reynolds, Froude, and Weber numbers based on the characteristic scales ℓ_c and u_c. R_λ is the Taylor Reynolds number at the final time step. The time step is Δt, and N_t is the number of time steps. The adjustment factor is δ_t (see [6]). The component of the pressure that is induced by the vortical flow, the viscous normal stresses, and the effects of capillarity are all adjusted[4]. The length (x), width (y), and depth (z) of the computation domain are respectively $L = 1$, $W = 1$, and $D = 1$. The number of grid points along the x-, y-, and z-axes are respectively $I_{max} = 96$, $J_{max} = 96$, and $K_{max} = 97$. The maximum allowable wavenumber in the free-surface elevation is $\kappa_{max} = 64\pi$. Wavenumbers that exceed this value are bandpassed filtered. Three multigrid iterations and six V-cycle Jacobi iterations are used to solve the elliptic equations (see [8]).

	LES 1	LES 2	LES 3	LES 4	LES 5	LES 6
DNS Run	6	6	6	6	4	6
Model Types	VI	II & V	III & V	I & IV	VI	VI
Resolution	$24 \times 24 \times 25$	$24 \times 24 \times 25$	$24 \times 24 \times 25$	$24 \times 24 \times 25$	$24 \times 24 \times 25$	$48 \times 48 \times 49$
κ_{max}	24π	24π	24π	24π	24π	32π
Δt	0.0012	0.0012	0.0012	0.0012	0.0012	0.0009

Table 9: *Data for LES runs.*

The 'DNS Run' item is the DNS run in Table 8 that corresponds to the LES run. The 'Model Types' item is the SGS Model from Table 1 that is used in the LES. The resolution is the number of grid points along the x-, y-, and z-axes. The maximum allowable wavenumber in the free-surface elevation is κ_{max}. Wavenumbers that exceed this value are bandpassed filtered. Δt is the time step. All of the LES runs use 601 time steps.

---

[4]The adjustment procedure uses an exponential function $(\exp(-\delta_t^2 t^2))$ to slowly couple the free-surface waves with the subsurface turbulent flow.
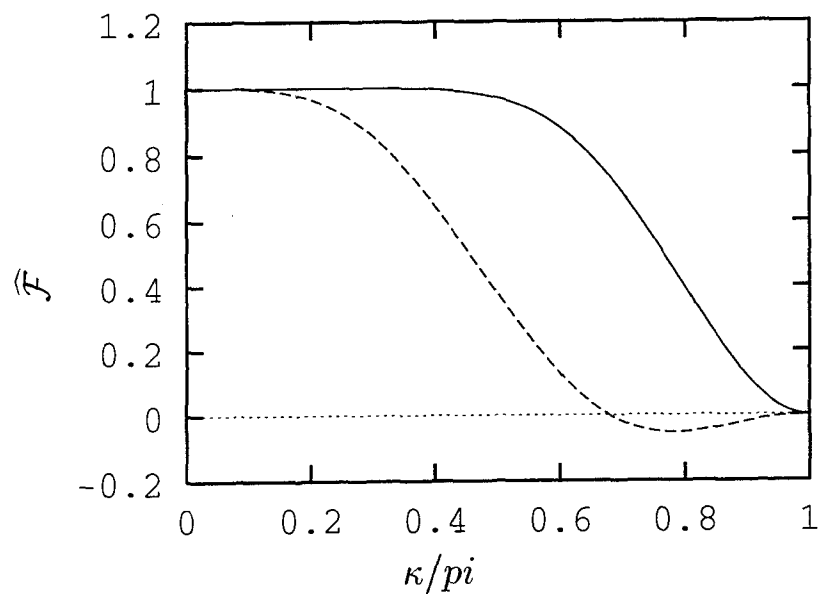
Figure 1: *Fourier-Transformed Filters.*
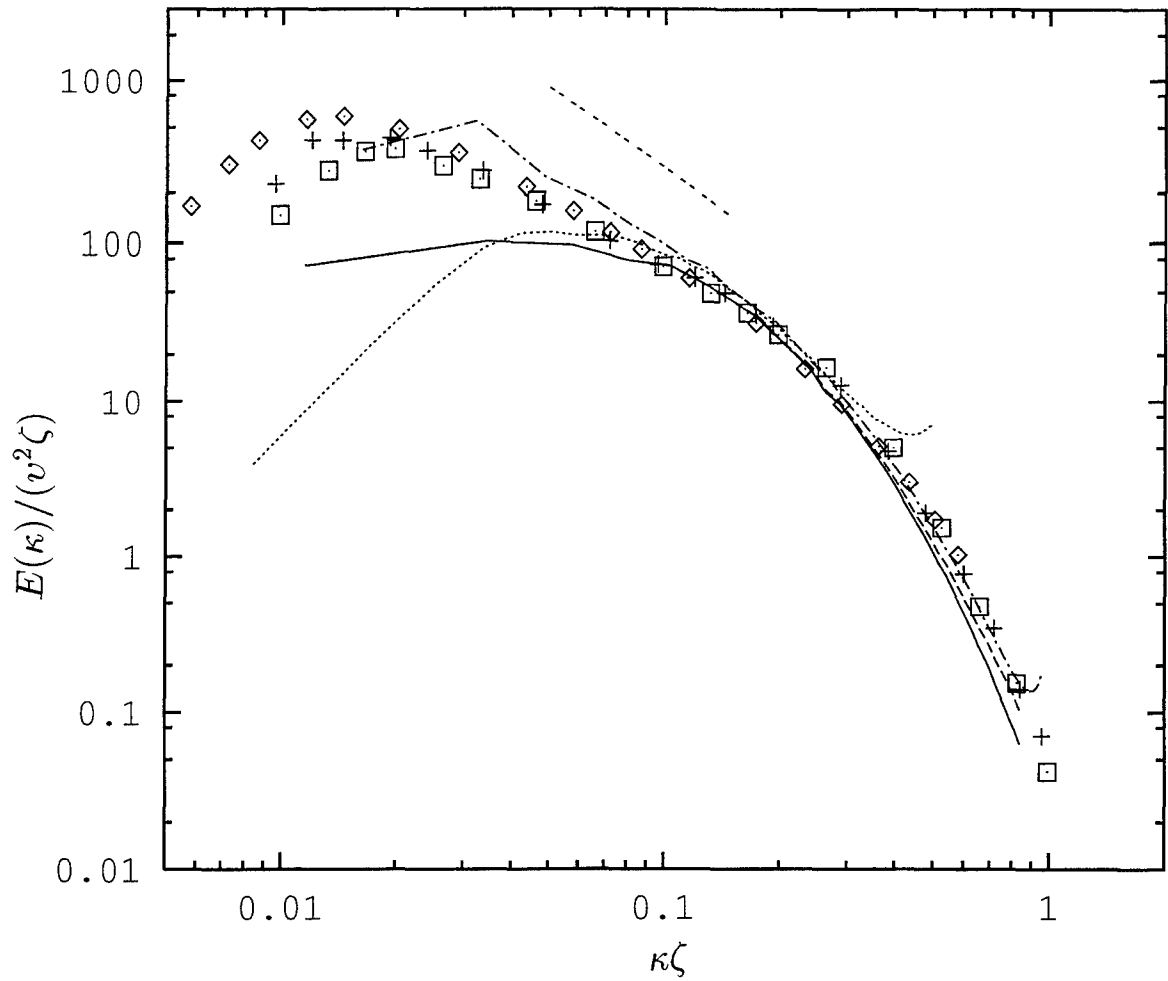
GRID filter ———
TEST filter - - - -
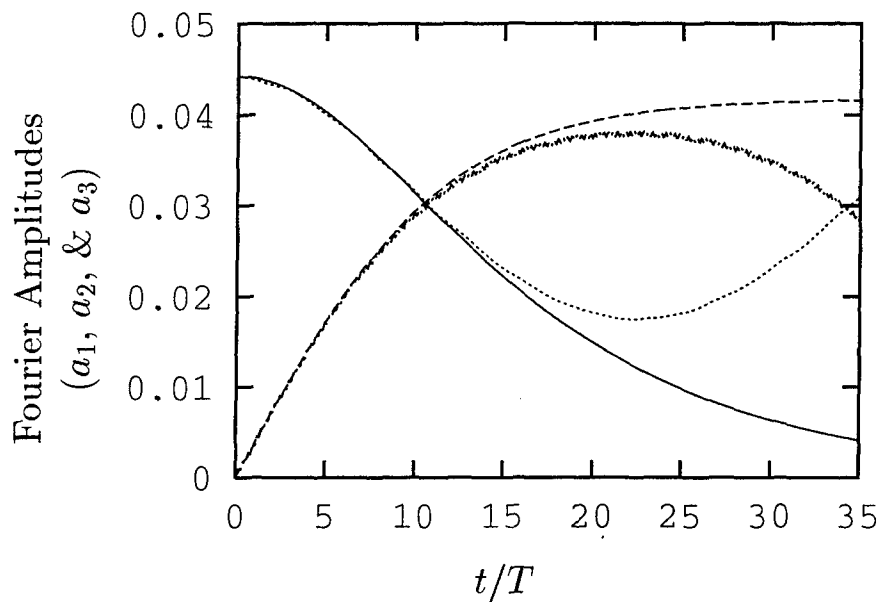
Figure 2: *Triad Resonances.* The Fourier amplitudes of the gravity waves ($a_1 = a_2$) and the capillary waves (a_3) are plotted versus time.

Theory (gravity) ———
Theory (capillary) - - - -
FDM (gravity) ·········
FDM (capillary) - ·· - ··

Figure 3: *Energy Spectrum of Homogeneous Turbulence.* The energy density $(E(\kappa))$ and wavenumber (κ) are normalized by the Kolmogorov length (ζ) and velocity (v) microscales.

Fig. 4a
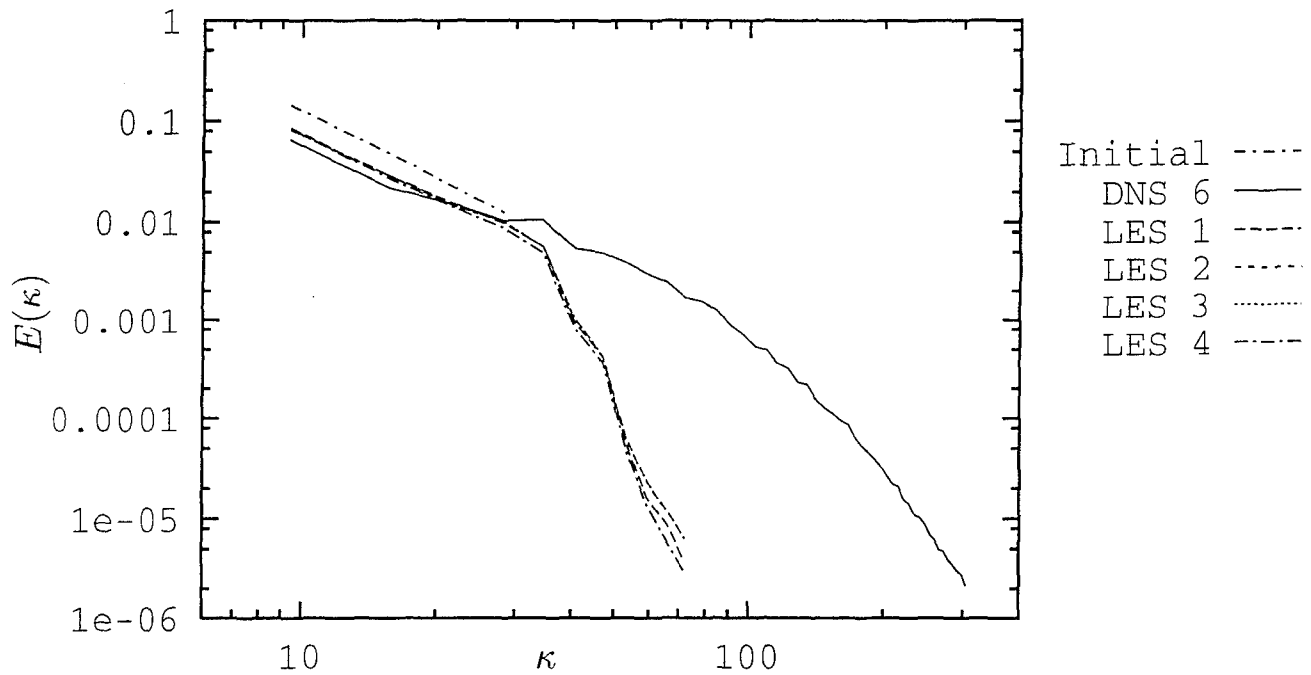
Fig. 4b
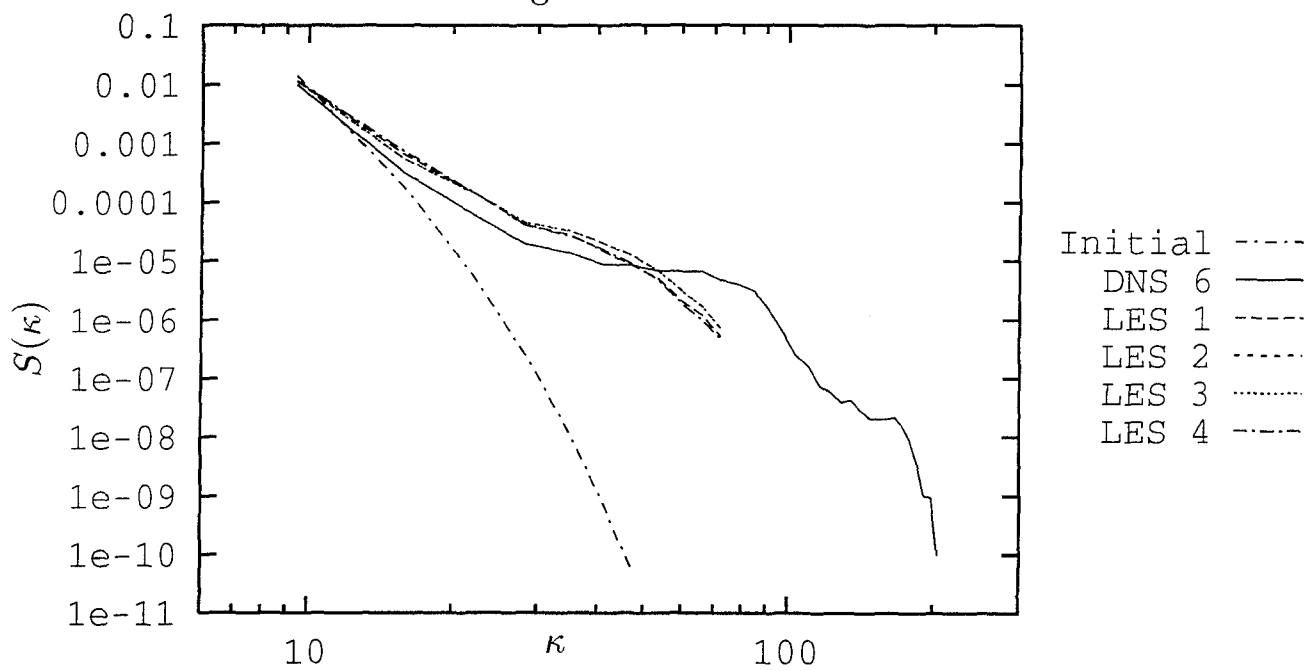
Figure 4: *Comparison of DNS and LES Spectra.* Initial conditions include subsurface turbulence <u>with</u> a surface wave. (a) LES and DNS runs are total-velocity spectra at time $t = 0.36$. (b) LES and DNS runs are wave energy spectra at time $t = 0.36$. The initial conditions are also shown.

Fig. 5a
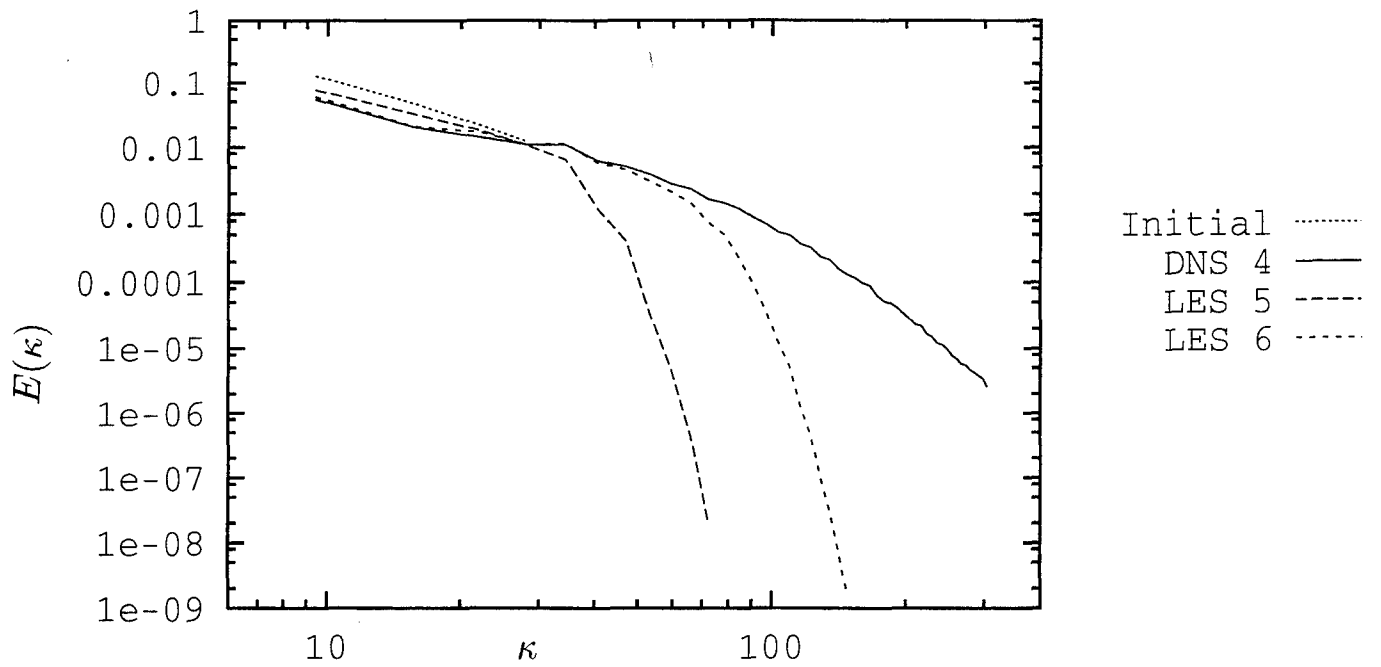
Fig. 5b
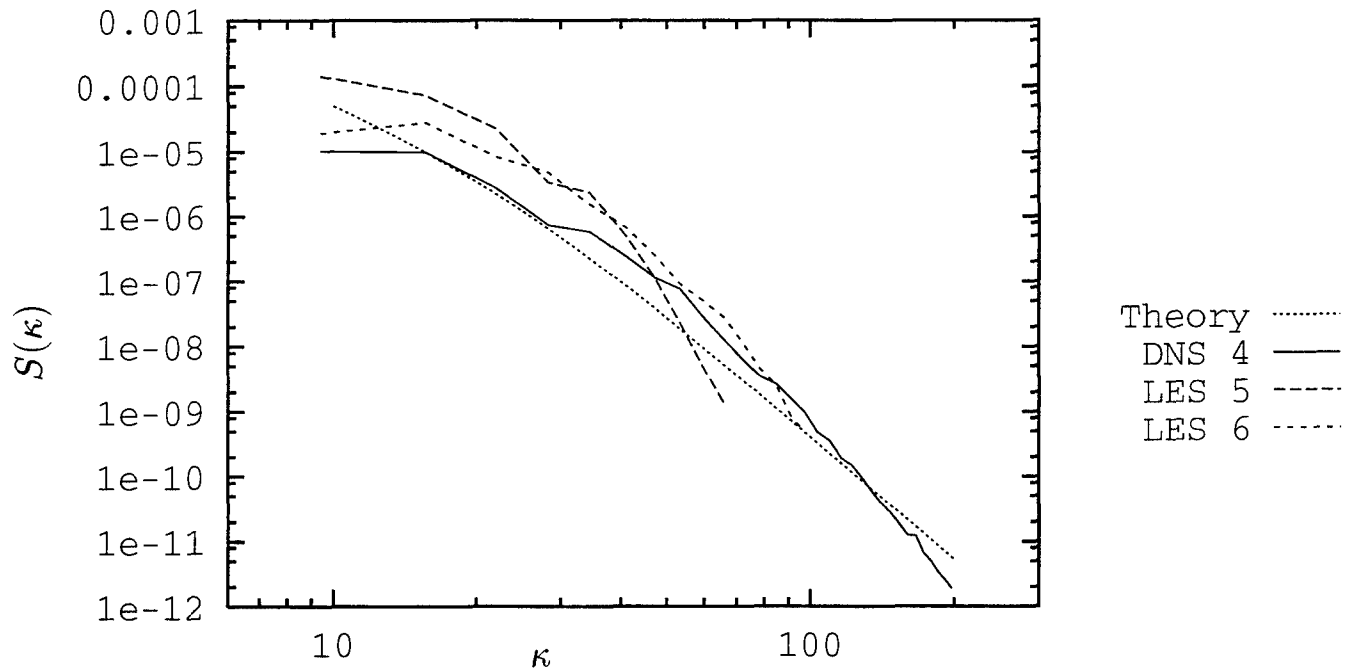
Figure 5: *Comparison of DNS and LES Spectra.* Initial conditions include subsurface turbulence <u>without</u> a surface wave. (a) Total-velocity spectra at time $t = 0.36$. (b) Wave energy spectra at time $t = 0.36$. The initial conditions for the total-velocity spectrum are shown. The initial wave energy is zero, corresponding to no wave.
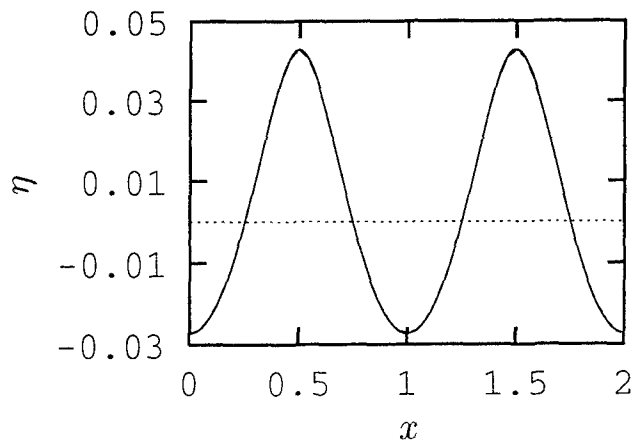
Fig. 6a

DNS 6 (t=0) ———
LES 4 (t=0) -----
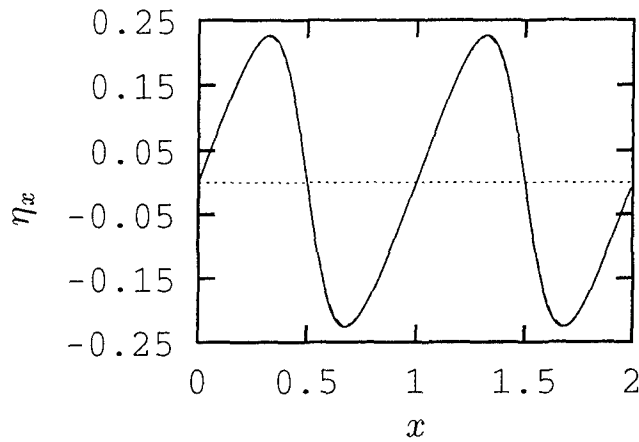
Fig. 6b

DNS 6 (t=0) ———
LES 4 (t=0) -----
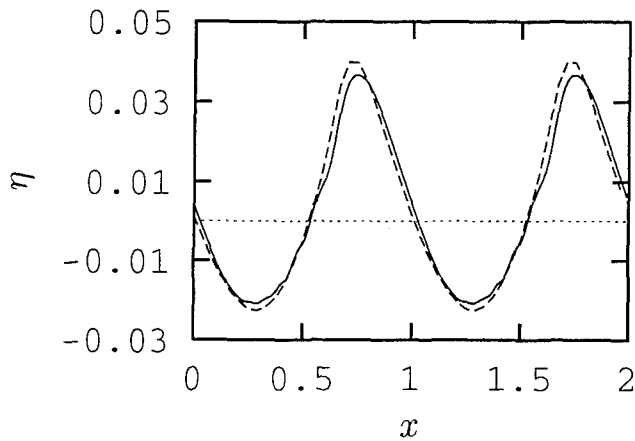
Fig. 6c

DNS 6 (t=0.36) ———
LES 4 (t=0.36) -----
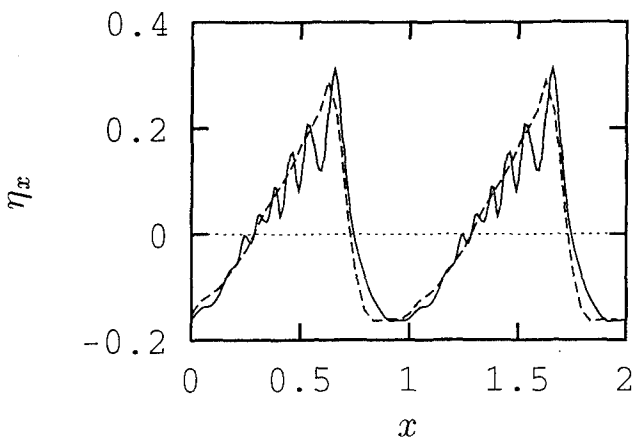
Fig. 6d

DNS 6 (t=0.36) ———
LES 4 (t=0.36) -----

Figure 6: *Comparison of DNS and LES Free-Surface Cuts.* (a) Initial elevation. (b) Initial slope. (c) Final elevation. (d) Final slope. The cut is averaged along planes parallel to the x-axis, and the data is periodically extended to double the length of the domain.

Fig. 7a

$\hat{z}=1.00$ ——
$\hat{z}=0.75$ -----
$\hat{z}=0.50$ ········
$\hat{z}=0.25$ ··········
$\hat{z}=0.00$ —·—·—

Fig. 7b

$\hat{z}=1.00$ ——
$\hat{z}=0.75$ -----
$\hat{z}=0.50$ -----
$\hat{z}=0.25$ ··········
$\hat{z}=0.00$ —··—··—
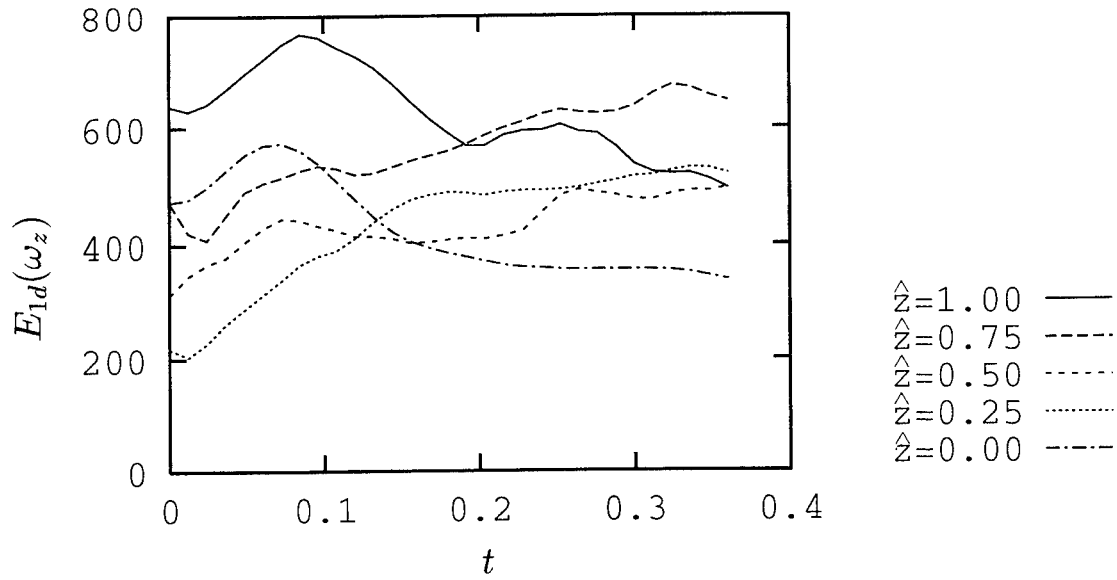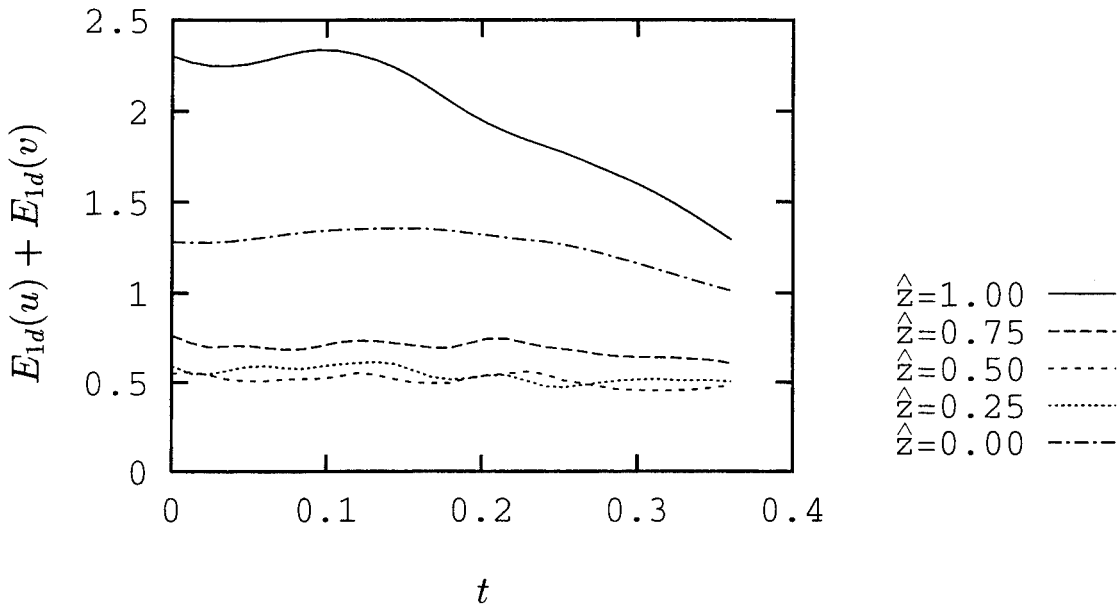
Figure 7: *Vertical Distributions of Enstrophy and Energy.* (a) Vertical component of vorticity. (b) Horizontal components of velocity. The plots are based on DNS Run 4.
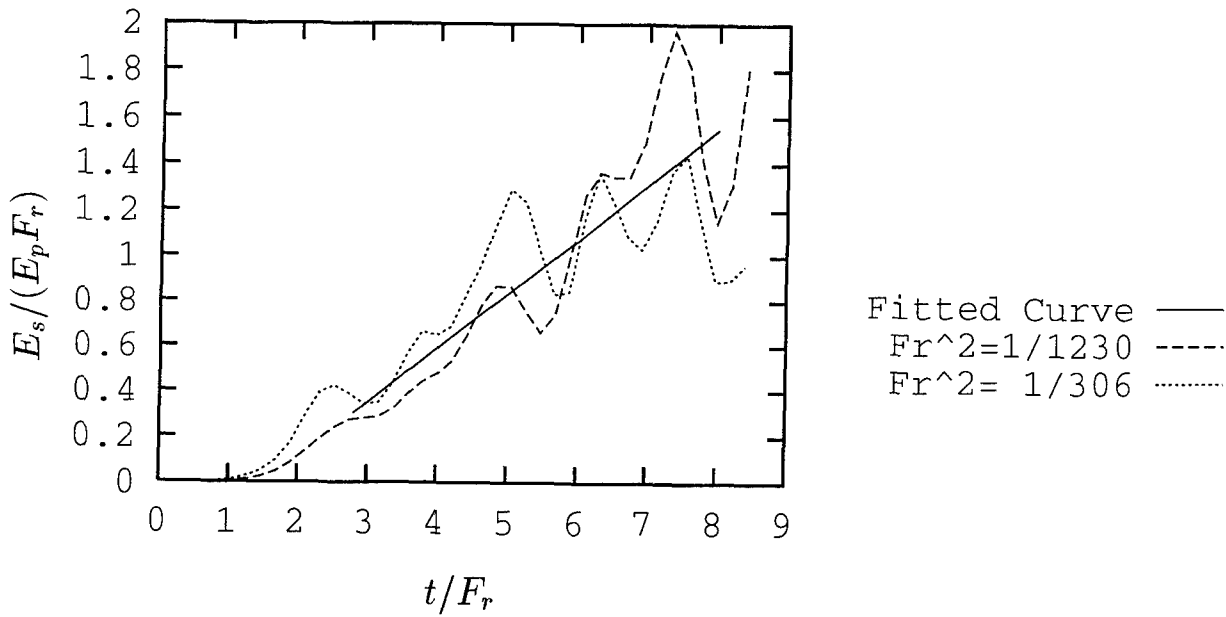
Figure 8: *Turbulent Scattering of 5cm Waves.* E_s is the scattered potential wave energy and E_p is the initial potential wave energy.
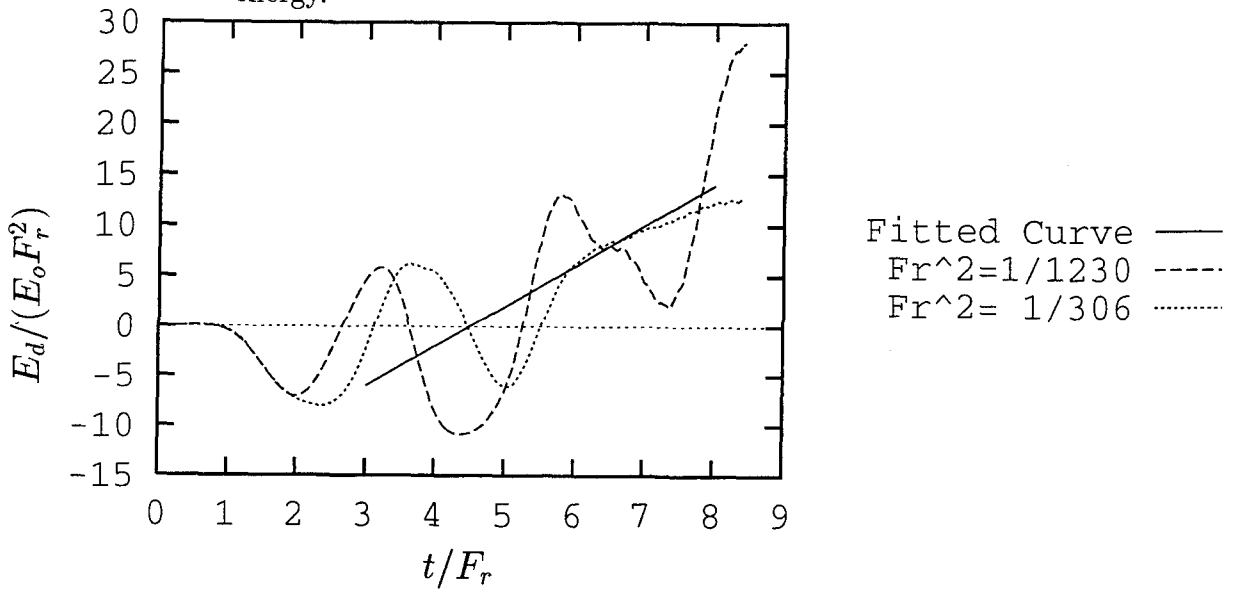
Figure 10: *Turbulent Dissipation of 5cm Waves.* E_d is the wave energy that is dissipated by turbulence and E_o is the initial total wave energy.

Figure 9b.
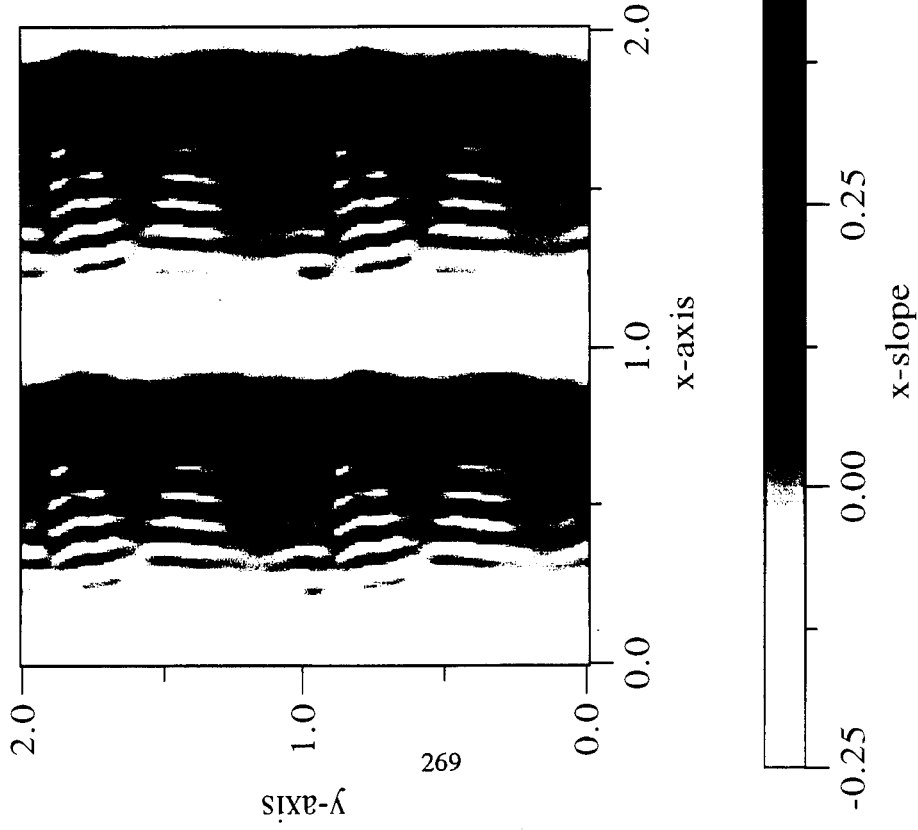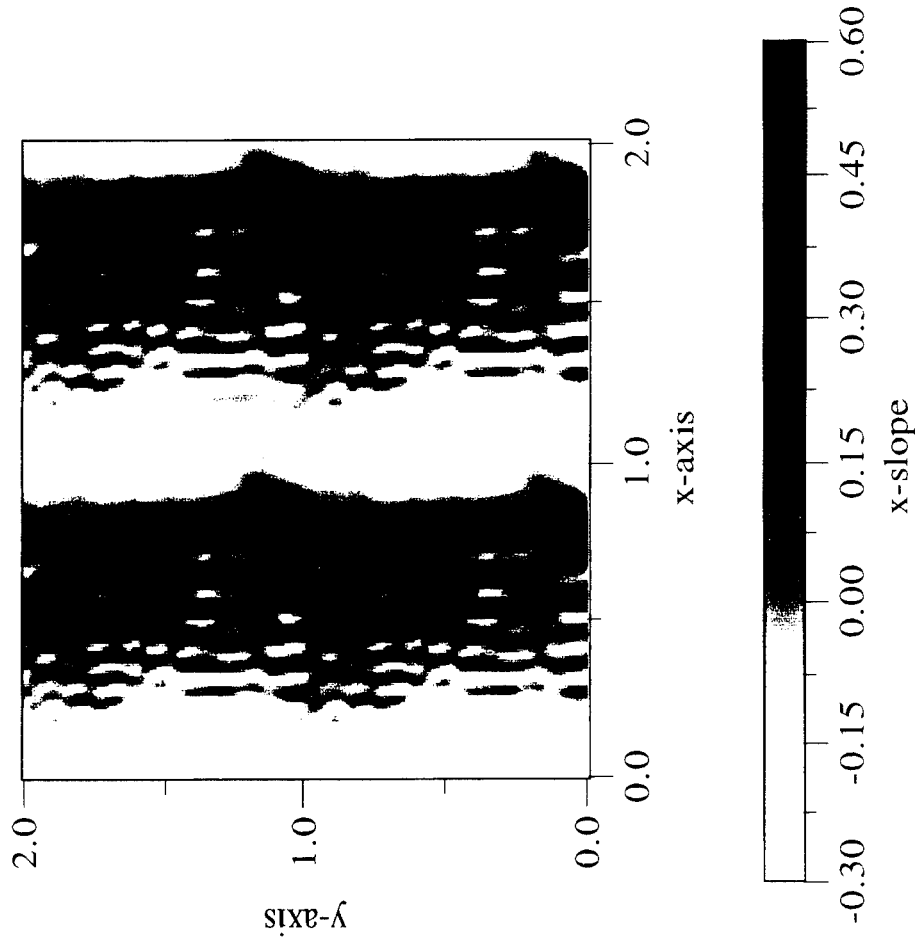
Figure 9a.

Figure 9: *Scattered Parasitic Capillary Waves.* (a) DNS run 3, $F_r^{-2} = 1230$. (b) DNS run 6, $F_r^{-2} = 306$.

DISCUSSION

by Dr. Thomas T. Huang, David Taylor Model basin

Did you define or quantify the characteristics of numerical dissipation in comparison with the physical dissipation you presented in the paper?

Author's Reply

The numerical validation studies that we performed indicate that numerical dissipation is minimal.

DISCUSSION

by Dr. H. Haussling, Naval Surface Warfare Center

The authors have presented impressive results which help us understand the interactions of turbulence with a free surface. When the decomposition of the pressure field was described in the talk, it was mentioned that this decomposition might be useful in Reynolds-averaged Navier-Stokes computations about ships. Could this suggestion be discussed in more detail?

Author's Reply

A Helmholtz decomposition provides a rigorous treatment of the intersection of the ship hull with the free surface. As a result, unlike conventional RANS techniques, extrapolation is not required to project velocities from the free surface onto the ship hull where the no-slip condition is satisfied. This extrapolation is required in RANS simulations because otherwise the free-surface could not rise up the hull.

The Helmholtz formulation decomposes the flow field into its wavy and vortical parts. The wavy portion (f) of the flow allows the free surface to rise up the wall, and the vortical portion ($\overline{u}$) of the flow enforces the no-slip condition on the wall. Since the flow is decomposed into two parts, an additional kinematic boundary condition is required on the free surface. For small free-surface slopes, this additional boundary condition is approximately that the vertical component of the vortical flow is ($w \approx 0$). The no-slip condition on the wall requires that $w \approx \phi_2$.

A Helmholtz formulation also allows the use of boundary-layer approximations in the free-surface boundary conditions. This prevents the excessive dissipation of waves that is observed in RANS simulations of free-surface flows.

270

Computation of Free-Surface Flows Around 3-D Hydrofoil and Wigley Ship by N-S Solver

S.H. Kwag and K.S. Min
(Hyundai Maritime Research Institute, Korea)

ABSTRACT

Computations are carried out to simulate the free-surface flows around the Wigley model. The Navier-Stokes equation is solved by a SIAF (semi-implicit approximate factorization) method where the body-fitted coordinate system and the wall function are invoked. The numerical merit is that each line of block pentadiagonal system is decoupled from others and highly vectorized coding is possible. Calculations are made at the Reynolds number of 10^6 and the Froude numbers are 0.25, 0.289 and 0.316. The free-surface waves are compared with those by the explicit method and experiments. In the latter part, the flow characteristics of 3-D submerged foil is investigated. Flows of five different cases are simulated and compared each other to discuss the free-surface effect on the hydrofoils where the submergence depth and angle of attack are imposed. Through the numerical simulation, it is found that the lift and drag are seriously influenced by the free-surface waves. The righting moment, which comes from the non-symmetrical lift distribution along the span, is also calculated for the heeled case.

NOMENCLATURE

$\varPhi$: non-dimensional pressure
Re : Reynolds number, $U_o \cdot L / \nu$
Fn : Froude number, $U_o / \sqrt{gL}$
$\triangle t$: time increment
U,V,W : contravariant velocities
q : velocity vector in matrix form
ζ : free-surface amplitude
K : pressure gradient term
n : n^{th} time step
L : ship length or chord length

INTRODUCTION

Free-surface flow around ship is one of the most complicated flows because there are various nonlinear phenomena and viscous-inviscid interaction. Recently, with the aid of the rapid development of computer technology, methods called NS solvers, in which the governing equations of the flow are discretized and computed, have become very popular[1-5]. Among them, the finite-difference solution methods for the Navier-Stokes equation with free-surface seem to be the most promising because of their generality. However, there are much more difficulties to be overcome in the development of free-surface flow solvers such as the treatment of free-surface boundary condition, especially the viscous and turbulence conditions on the free-surface. Another shortcoming is a long computation time.

In the present paper, the explicit finite-difference method for the Navier-Stokes solver[6], is extended to the semi-implicit approximation method. The advantage of the present method[7] is that the partial differential equations are changed to the ordinary ones. The equations form a system with block pentadiagonal matrices in three dimensional case and can be efficiently solved. Through the

approximate factorization, each line of block system in any of the three sweeps is completely decoupled from others and therefore highly vectorized coding is possible. Through the numerical study, it is confirmed that the present method is very efficient in reducing the computation time and also keeping the accuracy in the results. The computation time can be reduced to a large extent because the marching time interval is increased to several times in the magnitude. It is because the method is, by nature, unconditionally stable. This numerical merit encourages us to challenge the full-scale computation with free-surface.

In the latter part, the free-surface interaction is investigated for 3-D submerged hydrofoil because there is a recent trend to develop high speed ships such as the hydrofoil craft. Duncan[8] and Coleman[9] made some experiments on the 2-D wings and discussed the flow characteristics as well as the wave breaking. The pressure data are available from Nishiyama[10]. The calculation results can be seen in Suzuki et al[11] through the FDM and BEM analyses even though they are 2-dimensional. Hino[12] and Mori[13] solved 2-dimensional N-S and Euler equations with the nonlinear free-surface conditions and reviewed on the submerged advancing hydrofoil by calculating the lift and drag forces. In the ship hydrodynamics, the wing is strongly affected by the free-surface and vice versa because the wing usually works near the free-surface. In spite of many research works, there are still a lot of unclear problems. In this sense, it is no doubt necessary to investigate the interaction between the lifting body and free-surface. One of the motivations for the present 3-D lifting body research is that, if we directly solve the N-S equation, there is no need to introduce the so-called Kutta condition which is obscure in 3-D cases. Many researchers have tried to solve the problems by the potential flow approach in which an appropriate modelling of the wake leaving from the trailing edge of the wing is necessary or the wake is solved iteratively. A difficulty is to find a universal and exact model for the Kutta condition. The N-S solver does not include such a problem if the no-slip condition is imposed on the body surface. The no-slip condition used for the viscous flow simulation realizes the shock-free condition for the pressure. The 3-D effect is simultaneously investigated besides the study of interaction with free-surface. The tip vortex, which is a part of the results, shows that the rotational magnitude of velocity is much affected by the submergence depth and 3-dimensionality of the wing. As concerns the resistance, the induced drag is intrinsically explained because it may be an inherent component of forming the pressure drag. The nonlinear property of waves and the interaction of a viscous flow with waves render the fluid motion much more difficult to simulate numerically.

NUMERICAL SIMULATION OF SHIP WAVES

Basic Equation

Numerical simulation of 3-D free-surface flow is carried out by solving the N-S equation basically following to the MAC method. The mean velocity components u, v and w exclusive of the fluctuation components at (n+1) time step are determined by using a forward-time difference as follows.

$$
\begin{aligned}
u^{n+1} &= (F^n - \Phi_x)\Delta t \\
v^{n+1} &= (G^n - \Phi_y)\Delta t \\
w^{n+1} &= (H^n - \Phi_z)\Delta t
\end{aligned}
\qquad (1)
$$

where

$$
\begin{aligned}
F^n =\ & \frac{u^n}{\Delta t} + \frac{1}{Re}\nabla^2 u - (u^n\frac{\partial u}{\partial x} + v^n\frac{\partial u}{\partial y} + w^n\frac{\partial u}{\partial z}) \\
& + \frac{\partial}{\partial x}\{\nu_t(2\frac{\partial u}{\partial x})\} + \frac{\partial}{\partial y}\{\nu_t(\frac{\partial u}{\partial y} + \frac{\partial v}{\partial x})\} \\
& + \frac{\partial}{\partial z}\{\nu_t(\frac{\partial v}{\partial z} + \frac{\partial w}{\partial y})\}
\end{aligned}
$$

$$
\begin{aligned}
G^n =\ & \frac{v^n}{\Delta t} + \frac{1}{Re}\nabla^2 v - (u^n\frac{\partial v}{\partial x} + v^n\frac{\partial v}{\partial y} + w^n\frac{\partial v}{\partial z}) \\
& + \frac{\partial}{\partial x}\{\nu_t(\frac{\partial u}{\partial y} + \frac{\partial v}{\partial x})\} + \frac{\partial}{\partial y}\{\nu_t(2\frac{\partial v}{\partial y})\} \\
& + \frac{\partial}{\partial z}\{\nu_t(\frac{\partial v}{\partial z} + \frac{\partial w}{\partial x})\}
\end{aligned}
\qquad (2)
$$

$$
\begin{aligned}
H^n =\ & \frac{w^n}{\Delta t} + \frac{1}{Re}\nabla^2 w - (u^n\frac{\partial w}{\partial x} + v^n\frac{\partial w}{\partial y} + w^n\frac{\partial w}{\partial z}) \\
& + \frac{\partial}{\partial x}\{\nu_t(\frac{\partial u}{\partial z} + \frac{\partial w}{\partial x})\} + \frac{\partial}{\partial y}\{\nu_t(\frac{\partial v}{\partial z} + \frac{\partial w}{\partial y})\} \\
& + \frac{\partial}{\partial z}\{\nu_t(2\frac{\partial w}{\partial z})\}
\end{aligned}
$$

272

and

$$\Phi^n = p + \frac{z}{F_n^2} \tag{3}$$

All the variables are on the cartesian coordinate system(x, y, z) where x is in the uniform flow direction, y in the lateral, and z in the vertical direction respectively ; u, v and w are the velocity components in the x-, y- and z-direction, respectively. They are normalized by the representative length and reference velocity. Subscripts denote the differentiations with respect to the referred variables and superscripts the values at the referred time step. The term Δt stands for the time increment, p the pressure and ν_t the eddy viscosity. Re and Fn are Reynolds and Froude numbers respectively based on L and U_o, and

$$\nabla^2 = \frac{\partial}{\partial x^2} + \frac{\partial}{\partial y^2} + \frac{\partial}{\partial z^2} \tag{4}$$

Differentiating (1) with respect to x, y and z, we can have

$$\nabla^2\Phi = F_x + G_y + H_z - (u_x^{n+1} + v_y^{n+1} + w_z^{n+1})/\Delta t \tag{5}$$

The last term in (5) is expected to satisfy the continuity condition. (5) can be solved by the relaxation method. The new free-surface at the (n+1)th time-step is calculated by moving the marker particles by

$$
\begin{aligned}
x^{n+1} &= x^n + u^n\Delta t \\
y^{n+1} &= y^n + v^n\Delta t \\
z^{n+1} &= z^n + w^n\Delta t
\end{aligned}
\tag{6}
$$

The oncoming flow is accelerated from zero to the given constant velocity. Third-order upstream differencing is used for the convection terms with the fourth-order truncation error which is written as, for example ;

$$
\begin{aligned}
&U(\frac{\partial f}{\partial x})_{i,j,k} \\
&= U_{i,j,k}\frac{f_{i-2,j,k} - 8f_{i-1,j,k} + 8f_{i+1,j,k} - f_{i+2,j,k}}{12} \\
&\quad + |U_{i,j,k}|\frac{f_{i-2,j,k} - 4f_{i-1,j,k} + 6f_{i,j,k} - 4f_{i+1,j,k} + f_{i+2,j,k}}{4}
\end{aligned}
\tag{7}
$$

SIAF Scheme

To solve the N-S equations more efficiently, the SIAF method is used. The 3-D equations are used in the computation, but 2-D basic equations are only described for brief understanding. The turbulence model is not particularly remarked here because of the same applicability as in the explicit method. The N-S equation can be written in the non-conservative vector form as follows.

$$q_t + uq_x + wq_z = \frac{1}{Re}\nabla^2 q - K \tag{8}$$

where

$$q = \begin{bmatrix} u \\ w \end{bmatrix}, \quad K = \begin{bmatrix} \Phi_x \\ \Phi_z \end{bmatrix} \tag{9}$$

The numerically-generated, body-fitted coordinate system gives the transformation.

$$
\begin{aligned}
\xi &= \xi_{(x,z,t)} \\
\zeta &= \zeta_{(x,z,t)} \\
t &= t
\end{aligned}
\tag{10}
$$

It offers the advantages of generality and flexibility and, most importantly, transforms the computational domain into a simple rectangular region with equal grid spacing. Through transformations, (8) can be written for the velocity component q as

$$q_t + Uq_\xi + Wq_\zeta = \frac{1}{Re}\nabla^2 q - K' \tag{11}$$

where U and W are the unscaled contravariant velocity components and K' is transformed from K in terms of (ξ, ζ)

$$
\begin{aligned}
U &= \xi_t + u\xi_x + w\xi_z \\
W &= \zeta_t + u\zeta_x + w\zeta_z \\
K' &= \begin{bmatrix} \Phi_\xi\xi_x + \Phi_\zeta\zeta_x \\ \Phi_\xi\xi_z + \Phi_\zeta\zeta_z \end{bmatrix}
\end{aligned}
\tag{12}
$$

The Laplacian operator gives

$$
\begin{aligned}
\nabla^2 &= a_1\frac{\partial^2}{\partial\xi^2} + a_2\frac{\partial^2}{\partial\zeta^2} + a_3\frac{\partial}{\partial\xi} \\
&\quad + a_4\frac{\partial}{\partial\zeta} + a_5\frac{\partial^2}{\partial\xi\partial\zeta}
\end{aligned}
$$

273

$$a_1 = \xi_x{}^2 + \xi_z{}^2 \qquad a_3 = \xi_{xx} + \xi_{zz}$$
$$a_2 = \zeta_x{}^2 + \zeta_z{}^2 \qquad a_4 = \zeta_{xx} + \zeta_{zz}$$
$$a_5 = 2(\xi_x \zeta_x + \xi_z \zeta_z) \tag{13}$$

The implicit form of (11) is as follows.

$$\frac{q^{n+1} - q^n}{\Delta t} + (Uq_\xi)^{n+1} + (Wq_\zeta)^{n+1}$$
$$= \frac{1}{Re}(\nabla^2 q)^{n+1} - K'^{n+1} \tag{14}$$

The (n) and (n+1) mean the time-step, where the value at (n+1) is treated as unknown. The linearization and truncation give

$$U^{n+1} = U^n + \frac{\partial U^n}{\partial q^n} \frac{\partial q^n}{\partial t} \Delta t + O(\Delta t^2)$$
$$W^{n+1} = W^n + \frac{\partial W^n}{\partial q^n} \frac{\partial q^n}{\partial t} \Delta t + O(\Delta t^2)$$
$$q^{n+1} = q^n + \frac{\partial q^n}{\partial t} \Delta t + O(\Delta t^2) \tag{15}$$
$$\nabla^2 q^{n+1} = \nabla^2 q^n + \nabla^2 \frac{\partial q^n}{\partial t} \Delta t + O(\Delta t^2)$$

The convective terms can be written as

$$(Uq_\xi)^{n+1} = U^n q^n{}_\xi + U^n \frac{\partial q^n{}_\xi}{\partial t} \Delta t$$
$$+ q^n{}_\xi \frac{\partial U^n}{\partial q^n} \frac{\partial q^n}{\partial t} \Delta t + O(\Delta t^2)$$
$$(Wq_\zeta)^{n+1} = W^n q^n{}_\zeta + W^n \frac{\partial q^n{}_\zeta}{\partial t} \Delta t$$
$$+ q^n{}_\zeta \frac{\partial W^n}{\partial q^n} \frac{\partial q^n}{\partial t} \Delta t + O(\Delta t^2) \tag{16}$$

The finite-difference scheme gives

$$\Delta U^n = \frac{\partial U^n}{\partial t} \Delta t = \frac{U^{n+1} - U^n}{\Delta t} \Delta t$$
$$= U^{n+1} - U^n$$
$$\Delta W^n = \frac{\partial W^n}{\partial t} \Delta t = \frac{W^{n+1} - W^n}{\Delta t} \Delta t$$
$$= W^{n+1} - W^n \tag{17}$$
$$\Delta q^n = \frac{\partial q^n}{\partial t} \Delta t = \frac{q^{n+1} - q^n}{\Delta t} \Delta t$$
$$= q^{n+1} - q^n$$

The governing equation is written as

$$\frac{\Delta q^n}{\Delta t} + U^n q^n{}_\xi + U^n \Delta q^n{}_\xi + q^n{}_\xi \frac{\partial U^n}{\partial q^n} \Delta q^n$$
$$+ W^n q^n{}_\zeta + W^n \Delta q^n{}_\zeta + q^n{}_\zeta \frac{\partial W^n}{\partial q^n} \Delta q^n \tag{18}$$

$$= \frac{1}{Re}(\nabla^2 q^n + \nabla^2 \Delta q^n) - K'^n$$

In above equation, $K'^{(n+1)}$ is approximated as $K'^{(n)}$ because it is not easy to get the solution at the (n+1) time step. The fourth and seventh terms of above equation are approximately factored.

$$q^n{}_\xi \frac{\partial U^n}{\partial q^n} \Delta q^n = \frac{\partial q^n}{\partial \xi} \frac{\partial U^n}{\partial q^n} \Delta q^n = \frac{\partial U^n}{\partial \xi} \Delta q^n$$
$$= U^n{}_\xi \Delta q^n \tag{19}$$
$$q^n{}_\zeta \frac{\partial W^n}{\partial q^n} \Delta q^n = \frac{\partial q^n}{\partial \zeta} \frac{\partial W^n}{\partial q^n} \Delta q^n = \frac{\partial W^n}{\partial \zeta} \Delta q^n$$
$$= W^n{}_\zeta \Delta q^n$$

Rearranging (18) with respect to $\triangle q^n$, we get

$$\left[I + \Delta t \left\{ U^n{}_\xi + \left(U^n - \frac{a_3}{Re} \right) \frac{\partial}{\partial \xi} - \frac{a_1}{Re} \frac{\partial^2}{\partial \xi^2} \right\} \right]$$
$$\cdot \left[I + \Delta t \left\{ W^n{}_\zeta + \left(W^n - \frac{a_4}{Re} \right) \frac{\partial}{\partial \zeta} \right. \right.$$
$$\left. \left. - \frac{a_2}{Re} \frac{\partial^2}{\partial \zeta^2} \right\} \right] \Delta q^n = \Delta t Q^n \tag{20}$$

$$Q^n = -(U^n q^n{}_\xi + W^n q^n{}_\zeta) + \frac{1}{Re}(a_1 q^n{}_{\xi\xi}$$
$$+ a_2 q^n{}_{\zeta\zeta} + a_3 q^n{}_\xi + a_4 q^n{}_\zeta + a_5 q^n{}_{\xi\zeta}$$
$$+ a_5 \Delta q^n{}_{\xi\zeta}) - K'^n$$

Here it is not possible to calculate $\triangle q^n$ in the above equation. It is approximated as

$$\Delta q^n{}_{\xi\zeta} = \Delta q^{n-1}{}_{\xi\zeta} + O(\Delta t^2) \tag{21}$$

Therefore, through the approximate factorization, the partial differential equations are changed to the ordinary ones.

$$\left[I + \Delta t \left\{ U^n{}_\xi + \left(U^n - \frac{a_3}{Re} \right) \frac{\partial}{\partial \xi} \right. \right.$$
$$\left. \left. - \frac{a_1}{Re} \frac{\partial^2}{\partial \xi^2} \right\} \right] \Delta q^{*n} = \Delta t Q^n$$
$$\left[I + \Delta t \left\{ W^n{}_\zeta + \left(W^n - \frac{a_4}{Re} \right) \frac{\partial}{\partial \zeta} \right. \right. \tag{22}$$
$$\left. \left. - \frac{a_2}{Re} \frac{\partial^2}{\partial \zeta^2} \right\} \right] \Delta q^n = \Delta q^{*n}$$

The above set of equations form a system with block pentadiagonal matrices in three dimensional case and can be efficiently solved. Through an approximate factorization, each line

of block pentadiagonal system in any of the three sweeps is decoupled completely from others, and therefore highly vectorized coding is possible.

Boundary Conditions

1) On the free-surface, the boundary condition requires zero tangential stress and a normal stress which balances any externally applied forces. The application of these conditions requires a knowledge of not only the location of the free-surface at each grid but also its slope and curvature. In the present calculation, the shape of the free-surface is not known a priori; it is defined by the position of the marker particles. The z-coordinate of the free-surface is rearranged by a linear interpolation in proportion to the newly calculated projected area at each time step. On the free-surface, the exact pressure condition is imposed because the uppermost grid is always identical to the free-surface. By this scheme, it is expected that the free-surface condition, i.e., the constant pressure condition, can be directly applied.

2) On the body surface, the wall function approach is used to reduce the computation time. With the wall condition, the minimum grid spacing in the direction normal to the body surface should be small enough to resolve the viscous sublayer in the boundary layer.

3) At upstream boundary, the uniform flow condition is used; $\triangle q=0$. At downstream boundary, zero extrapolation in ξ-direction is used. On the symmetric plane, $q_\eta=0$ and $\triangle q_\eta$ $=0$ is applied. At outer boundary, the zero-gradient extrapolation is used.

Turbulence Model

The turbulence model used is the Baldwin-Lomax zero-equation algebraic model, whose original form is the Cebeci-Smith model. It is widely used in the aerodynamic computation and also in the incompressible flow computation around a ship. In the present study, flow is enforced to be turbulent from the fore end of a ship. The free-surface effect on turbulence is not included in the model. There has not been any turbulence model that can be

well applied to the boundary layer and wake of a surface-piercing body like a ship. Therefore, in the present calculation, the simple zero equation model is used.

COMPUTED RESULTS

Wigley Case

The SIAF method is applied to Wigley model with free-surface. The aim is to compare the present results with those of explicit method. The Reynolds number is 10^6 and Froude numbers are 0.25, 0.289 and 0.316. For the numerical stability and efficiency, the grid scheme near the hull surface is required to be orthogonal to it and the grid size should change smoothly. The number of grids is 74x29x19 and the computed domain is $-0.7 \leq x/L \leq 1.5$, $0.0 \leq y/L \leq 0.5$ and $-0.1745 \leq z/L \leq 0.0$. The time increment is 0.002. In order to check the convergence of the computation, the wave pattern and drag coefficients are compared along the marching time step as shown in Fig.1 and Fig.2 where Cp, Cf and Ct are the pressure, frictional and total resistance coefficients respectively. Although the wave seems to be still developed further, we can assume that it is converged at t=3.0 where t is the non-dimensional time. It can be supported by the results as shown in Fig.2. The calculated frictional resistance, which is directly derived from the difference of the velocities at the two points, is still larger than the Schoenherr's. The frictional drag calculated by the present method is much closer to the Schoenherr's than that by the explicit method.

Fig.3 shows the comparison of wave contour calculated at Froude number of 0.289. The difference between (a) and (b) is hardly seen, but there remains still a need for the free-surface improvement when compared with the experiments. It seems to be partly due to the narrow computing domain in the lateral direction. Fig.4 shows the time history of wave pattern at Froude number of 0.25. The bow and stern waves are developed reasonably. Fig.5 shows the wave profile along the hull

surface. The Reynolds number of the measurement is 3.59×10^6. Both the SIAF and explicit method simulate the waves well around the bow, but slight discrepancies are still observed in the aft half of the hull. Fig.6 shows the velocity vectors at Froude number of 0.316 on several transverse sections in which the vortical motion is observed around the keel. It seems not so easy to calculate the cross flows accurately at the stern part considering some aspects in the numerical point of views. The assumption of symmetry or the steady flows should be pointed out. The unsteadiness and non-symmetry observed in experiment should be taken into account in the numerical simulation. Of course, the grid used in the computing domain is still coarse and it can be a cause not able to capture completely the details of the fluid motions.

Through the numerical study, it is confirmed that the SIAF method is very efficient in reducing the CPU time and also keeping the accuracy in the computational results. The computing time can be reduced to less than half because the time increment is increased to several times as large. It is because the SIAF method is, in its numerical property, un-conditionally stable. This numerical experiment encourages us to challenge the ship-scale calculation including the free-surface in the near future.

Foil Case

Computations are carried out to investigate the flow characteristics of 3-D submerged hydrofoil with free-surface. The foil of NACA 0012 section is located beneath the undisturbed free-surface with 10 and 20 degrees of angle of attack. The span shape is an ellipse of aspect ratio 3 as shown in Fig.7 where L is the chord length and s the span of the wing. The Froude and Reynolds number are 0.567 and 10^3 respectively.

To discuss the interaction of the pressure between the wing and the free-surface, calculations are tried for five cases by changing the submergence depth and angle of attack whose conditions are tabulated in Table 1. Here d is the submergence depth and a angle of attack. The without-free-surface case, the case 1, is also tried for the purpose of comparison where the wave elevation is imposed to be zero which may correspond to the unbounded case or the infinite submergence depth. In the case 5, the wing is heeled but only one side is calculated. The number of grid is 61x32x44 for case 1, 71x32x44 for case 2, 71x32x36 for cases 3 and 4 and 61x32x36 for case 5 respectively. Fig.8 shows the grid scheme for case 2. The time increment is 0.001 for all the time steps and the minimum spacing is 0.002 near the wing surface. A numerical difficulty in the computation is that the residual is not so small in magnitude at the leading edge due to a rapid change of geometry in the H-H grid topology. The rapid change of geometry renders the computation unstable at the leading edge, so that a large number of iteration is needed in solving the Poisson equation. This may be a defect of the non-staggered grid system which does not use a very fine grid near the leading edge. To reduce the residual value, the cross-differentiation is put to zero at the leading edge.

An appropriate computing domain is demanded for the wave development behind the trailing edge and the grid should be very small. However, as seen in Fig.8, both are not enough in the present simulation. Thus we should limit ourselves only to the discussion of the hydrodynamic trend for flow properties around the 3-D wing. Fig.9 shows the velocity vector for case 1, without free-surface. The separation occurs on the suction side around the midchord. The velocity defect can be seen behind the trailing edge. The z-component velocity is seen both on the upper and lower boundaries. The shock-free flow is well simulated. Fig.10 shows the results for case 2 in which the free-surface wave becomes weaker towards the tip because the wing shape is of elliptic finite-span type. It is observed that the flow is modest and does not differ so much from case 1. This means the free-surface effect is small enough at d/L=0.8. Fig.11

shows the results of cases 3 and 4. The free-surface wave is considerably developed in case 3. In case 4, the free-surface is more considerably developed. Although any numerical breakdown is not observed, the wave does not develop in downstream. This is probably due to the coarse grid used in the present computation which can not follow the steep waves. By the effect of free-surface, the remarkable velocity defect is seen under the wave crest.

Fig.12 shows the pressure contours of case 2 in spanwise direction. The intensity of pressure becomes weaker near the tip because of the 3-dimensionality. Here all the pressures are defined as the dynamic pressures normalized by ρU_o^2. Fig.13 shows the comparison of the pressure contours of cases 3 and 4. Fig.14 shows the pressure contour on the corresponding grid plane of wing surface for case 4. Near the tip, the pressure gradient is somewhat modest, which may be partially due to a large grid skew around there. However, the result seems to be reasonable considering the vortex generation behind the tip. Fig.15 and Fig.16 show the chordwise pressure distribution for case 3 and 4, respectively. The effect of angle of attack is shown comparatively between cases 3 and 4; the suction pressure around the tip significantly differs between the two cases. The steeper angle of attack makes the interaction of free-surface stronger and gives influence on the flow properties.

Fig.17 shows the chordwise velocity vectors for cases 2, 3 and 4. Here i=39 corresponds to the trailing edge and i=33 and 41 to x/L=0.75 and 1.08 respectively. As the effect of the tip suction, strong whirls are observed. That of case 2 is much more intensive than that of case 3; it means that the velocity fields around the tip may be influenced by the free-surface waves. In a shallow depth of case 3, the y-component velocity is reduced in magnitude entirely around the wing surface. The flow direction of case 2 behind the trailing edge is partly opposite to that of case 3. The velocity of case 4 is more accelerated than that of case 3. This is because a larger angle of attack

produces much steeper suction at the tip and it makes the velocity-components stronger. Fig.18 shows the chordwise vorticity distribution at the trailing edge for cases 2, 3 and 4. The strength of vorticity supports the characteristics of the y- and z-velocity components shown in Fig.17. As explained above, the intensity and region of the vorticity are modest for the shallower case.

Fig.19, Fig.20 and Fig.21 show the pressure distribution on the foil; the comparison for with- and without-free-surface is made in Fig.19; the effect of submergence depth is presented in Fig.20 and angle of attack in Fig.21. The pressure is continuous on the trailing edge as expected for the whole span. The no-slip condition satisfies the shock-free condition automatically. This can be an important advantage of N-S solver over calculations based on the potential flow assumption. When the submergence depth is shallow, the resultant pressure for the lift contribution is less due to the free-surface effect. In other words, the free-surface wave is strongly affected by the submergence depth and the angle of attack and it eventually affects the pressure distribution on the foil. The generated waves render the mutual interaction with the submerged wing body by keeping the balance in the momentum flux. The large-amplitude waves, under the suspected breaking, have much influence on the lift and drag force because the pressure and velocity fields are seriously affected by the waves.

The comparison of lift and drag coefficient is made. Here the coefficients are non-dimensionalized by $\rho U_o^2 S$ where S is the projected area of foil. Fig.22 shows the lift coefficients. It is reasonable that the lift for case 1 is larger than that for case 2. This is well supported by referring to the pressure difference between the upper- and lower-side of the wing in Fig.19 where the enclosed area for the case 1 is larger in appearance. Case 3 is much lower in the lift than case 2. This can be also explained by the pressure distribution on the wing surface in Fig.20. The free-surface makes the lift less. This is consistent to our

common experience that the lift is decreased when the hydrofoil craft becomes airborn condition. Case 4 shows extremely large lift than case 3 due to the effect of angle of attack; the lift is twice larger.

Fig.23 shows the comparison of drag ; pressure drag C_{DP} and frictional drag C_{DF} ; no significant difference in the friction component is observed among all cases. This is physically reasonable because the frictional drag depends not so much on the free-surface wave and angle of attack but rather on the Reynolds number. The pressure drag includes the wave-making resistance and the induced drag also. Although the wave-making resistance of case 3 may be larger than that of case 2, the pressure drag of case 3 is less than that of case 2. This may be mainly due to the difference in the induced drag. The pressure drag of case 4 is much larger than that at the attack angle of 10°. The drag/lift ratio is about 0.4, which is surprisingly large.

Here all the computations are restricted only within t=3.0. Therefore we should not jump into a decisive conclusion, but the numerical results can be very useful in understanding the wing problem with free-surface. The free-surface wave effect should be considered together with its wave-breaking phenomena. Needless to say, the pressure drag is in close connection with the lift force. The existence of the free-surface makes the understanding of the drag/lift ratio more complicated due to the wave-making resistance. As a special application, the heeled condition is additionally imposed on the case 4 to investigate 3-D lifting flow characteristics in more details. The heeled condition produces asymmetric lift distribution along the span to yield a righting moment for the hydrofoil. For the present calculation, the computation is tried at the heel angle of 5° and the angle of attack 20° , which is categorized as case 5. Due to the limitation of computer capacity, only one side is taken as a computational domain. For the boundary condition, a simple "symmetric condition" is used on the symmetric plane for the velocity and pressure. So this case corresponds to the flow

about a wing with a negative dihedral angle. We extend, however, the computed results to the study of the heeled wing assuming that the influence of the other side is small enough. Fig.24 shows the pressure distribution along the span compared with the non-heeled case 4. General findings are that there can not be seen any significant differences around the symmetric plane but the flows are affected by the free-surface near the tip. This can be explained as a heeled effect because the submergence depth is gradually deepened along the span. The change of submergence renders influence on the free-surface, which makes the pressure changing around the tip. The starboard side (y>0) of Fig.24 shows the spanwise distribution of the cases 4 and 5. The heeled case, case 5, is larger in the magnitude of lift. The lift and drag are compared with the case 4 in Fig.22 and Fig.23. The lift of case 5 is a little greater than that of case 4, but the frictional and pressure drags are nearly the same. The extrapolation of the lift from starboard to port side (y<0) gives the chain line distribution in Fig.25. The lift difference between the two sides gives the righting moment of 0.89×10^{-2}. It can be pointed out that the righting moment can be expected, when the foil is heeled, which comes from the non-symmetrical lift distribution along the span.

CONCLUSION

Numerical computations are carried out to simulate the free-surface flows around 3-D bodies. Through the numerical studies, the effectiveness and usefulness of the present method are demonstrated. Findings through the study are summarized as follows.

(1) The SIAF method is very efficient in reducing the computation time and also keeping the accuracy in the computational results. The computed free-surface waves are compared with those by the explicit method and experiments. The CPU time is reduced to less than half because each line of block pentadiagonal system in any of the three sweeps is decoupled completely from others and the highly vectorized

coding is possible.

(2) The 3-D hydrofoil calculation shows that the free-surface wave is strongly affected by the submergence depth and the angle of attack. The generated wave renders the mutual interaction with the submerged wing by keeping the balance in the momentum flux. The effect of free-surface is clearly elucidated through some examples. The no-slip condition used for the viscous flow simulation realizes the shock-free condition for the pressure around the trailing edge automatically, which proves to be one of the merits of the present numerical simulation. The large-amplitude waves, under the suspect of breaking, have much influence on the lift and drag force because the pressure and velocity gradients are seriously affected by the waves. The calculated lift and drag coefficients are qualitatively quite valuable in understanding the wing problem with free-surface.

ACKNOWLEDGEMENT

REFERENCES

1. Kodama, Y., "Grid Generation and Flow Computation for the Practical Ship Hull Forms and Propellers Using the Geometrical Method and the IAF Scheme", 5th Int. Conf. on Num. Ship Hydro. 1989, part 1, pp.41-54

2. Hino, T., "Computation of a Free Surface Flow around an Advancing Ship by the Navier-Stokes Equations", 5th Int. Conf. on Num. Ship Hydro., 1989, part 1, pp.69-82

3. Patel, V.C., Chen, H.C. and Ju, S., "Ship Stern and Wake Flows: Solutions of the Fully Elliptic Reynolds-Averaged Navier-Stokes Equations and Comparisons with Experiments", Iowa Institute of Hydraulic Research, The University of Iowa, IIHR Report No.323, 1988

4. Stern, F. and Kim, H.T., "Computation of Viscous Flow around a Propeller-Shaft Configuration with Infinite-Pitch Rectangular Blades", 5th Int. Conf. on Num. Ship Hydro., 1989, part 2, pp.408-423

5. Sato, T., Miyata, H., Baba, N. and Kajitani, H., "Finite-Difference Simulation Method for Waves and Viscous Flows about a Ship", Jour. of Soc. Naval Arch. of Japan, Vol.160, 1986

6. Mori, K., Kwag, S.H. and Doi, Y., "Numerical Simulation of Ship Waves and Some Discussions on Bow Wave Breaking and Viscous Interaction of Stern Waves", Proc. 18th Symp. on Naval Hydro, 1990

7. Beam, R.M. and Warming, R.F., "An Implicit Factored Scheme for the Compressible Navier-Stokes Equations", AIAA Jour., Vol.16, No.4, 1978

8. Duncan, J.H., "The Breaking and Non-Breaking Wave Resistance of a Two-Dimensional Hydrofoil", Jour. Fluid Mech., Vol.26, 1983, pp.507-520

9. Coleman, R.M., "Nonlinear Calculation of Breaking and Non-Breaking Waves behind a Two-Dimensional Hydrofoil", Proc. 16th Symp. on Naval Hydrodynamics, 1986, pp.51-62

10. Nishiyama, T., "Experimental Investigation of the Effect of Submergence Depth upon the Hydrofoil Section Characteristics ", Jour. of Soc. Naval Arch. of Japan, Vol.105, 1959, pp.7-21 (in Japanese)

11. Suzuki, K. and Hino, T., "Comparison of Calculation Method for 2-D Free-Surface Flow about Hydrofoil", Open Forum on Num. Ship Hydro., Tokyo, 1987, pp.107-128

12. Hino, T., "Numerical Computation of a Free Surface Flow around a Submerged Hydrofoil by the Euler/Navier-Stokes Equations", Jour. of Soc. Naval Arch. of Japan, Vol.164, 1988, pp.9-17

13. Mori, K. and Shin, M., "Sub-Breaking Wave: Its Characteristics, Appearing Condition and Numerical Simulation", Proc. 17th Symp. on Naval Hydro., 1989

Table 1 Study cases for systematic analysis

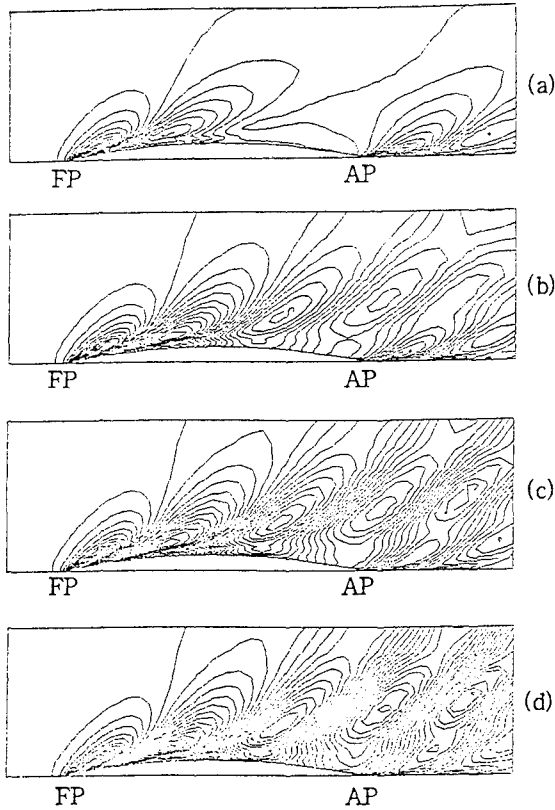|	case 1	case 2	case 3	case 4	case 5
free-surface	no	yes	yes	yes	yes
d/L	0.8	0.8	0.4	0.4	0.4
attack-angle α	10°	10°	10°	20°	20°
heel-angle	0°	0°	0°	0°	5°

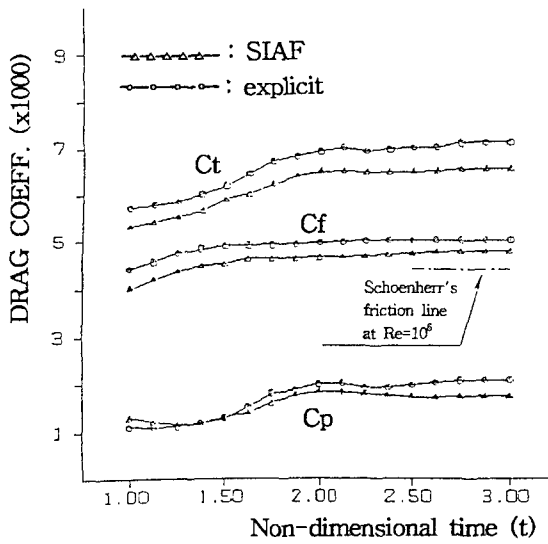Fig.1 Time history of free-surface wave contour at Fn=0.316 (a) t=1.0 (b) t=2.0 (c) t=2.5 (d) t=3.0

Fig.2 Time history of drag coefficients at Fn=0.316

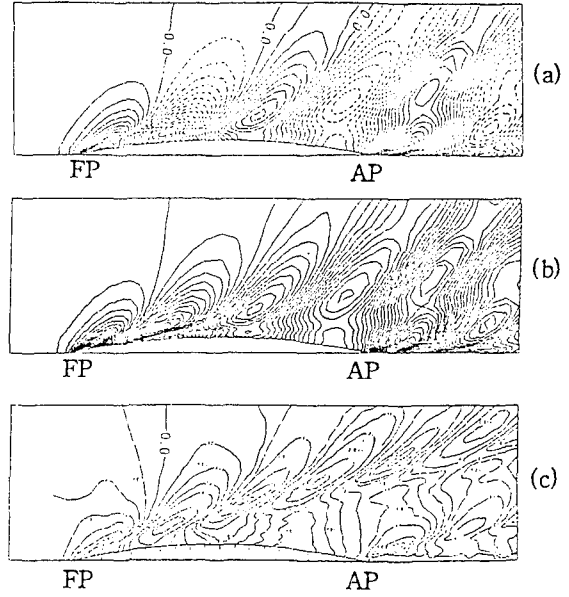Fig.3 Comparison of free-surface wave contour at Fn=0.289 (a) explicit method (Re=10^6) (b) SIAF(10^6) (c) experiment (3.59×10^6)
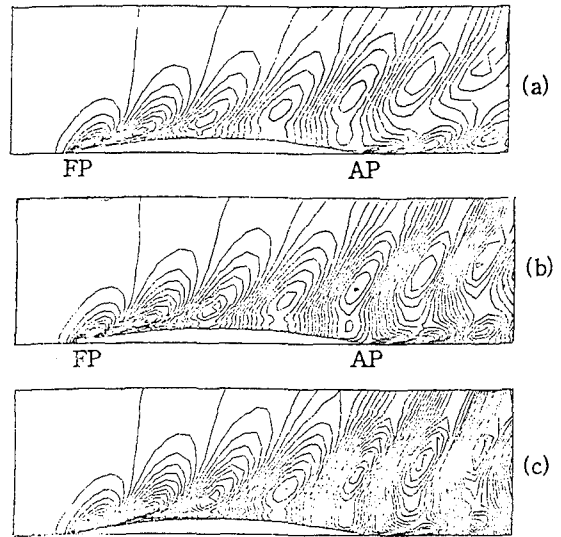

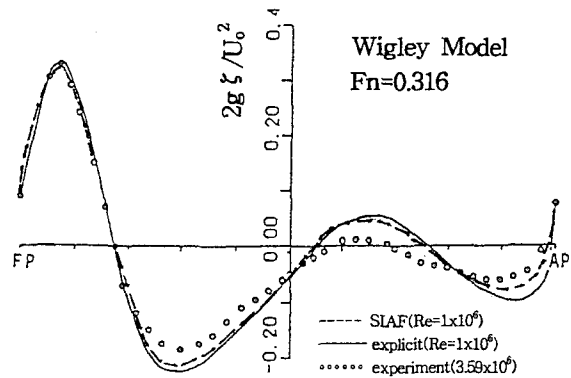Fig.4 Time history of free-surface wave contour at Fn=0.25 (a) t=1.0 (b) t=2.0 (c) t=3.0
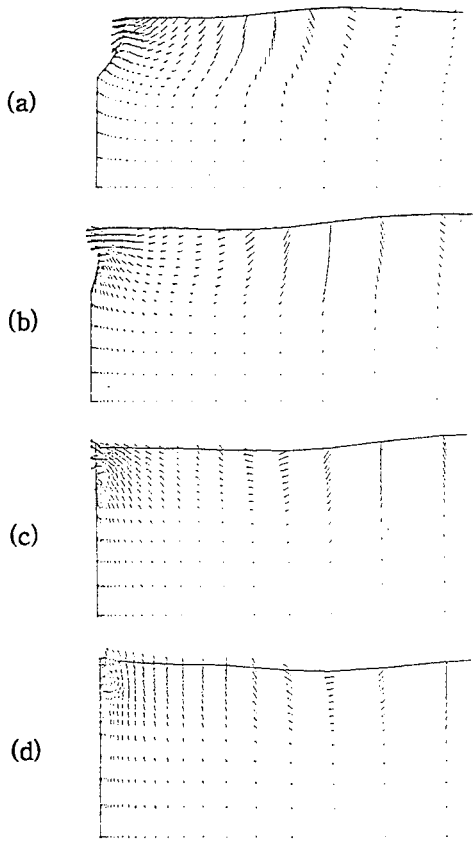

Fig.5 Free-surface wave profile at hull surface

280

Fig.6 Velocity vectors on transverse sections
at Fn=0.316 (a) x/L=0.84 (b) x/L=0.94
(c) x/L=1.00 A.P. (d) x/L=1.06
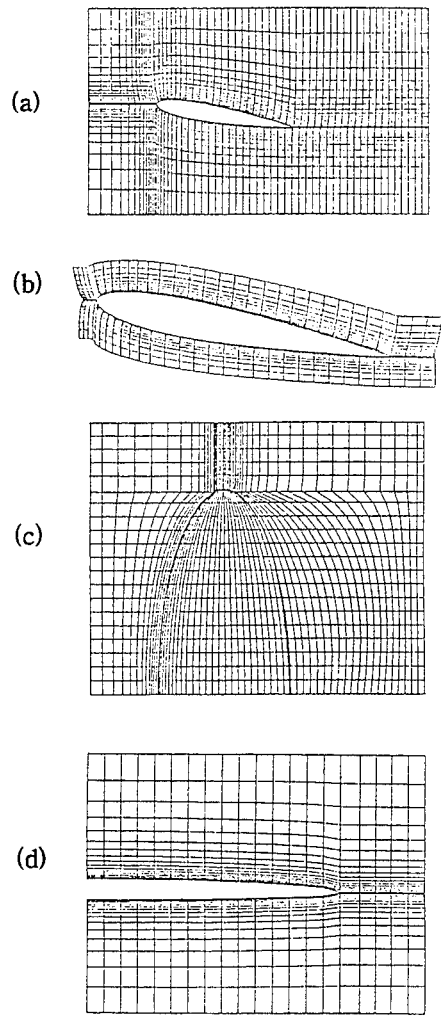
Fig.8 Grid view for case 2 (a) x–z plane
(b) Closed–up view (c) x–y plane
(d) y–z plane
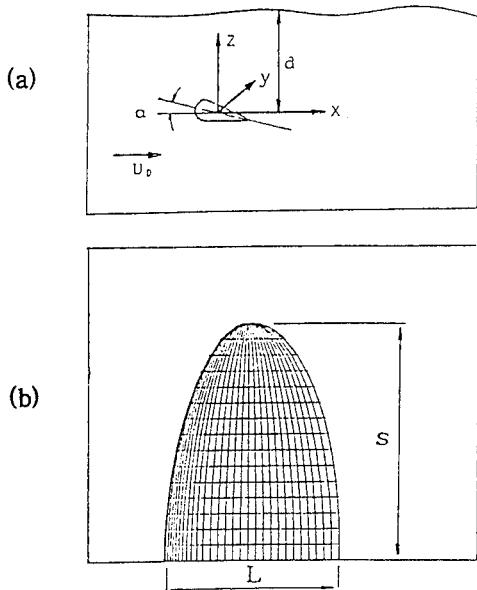
Fig.7 Coordinate system and elliptic span view
of 3–D submerged hydrofoil
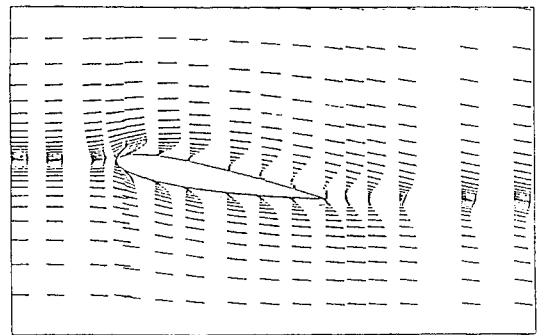
Fig.9 Velocity vector for case 1
(symmetric plane, j=3)
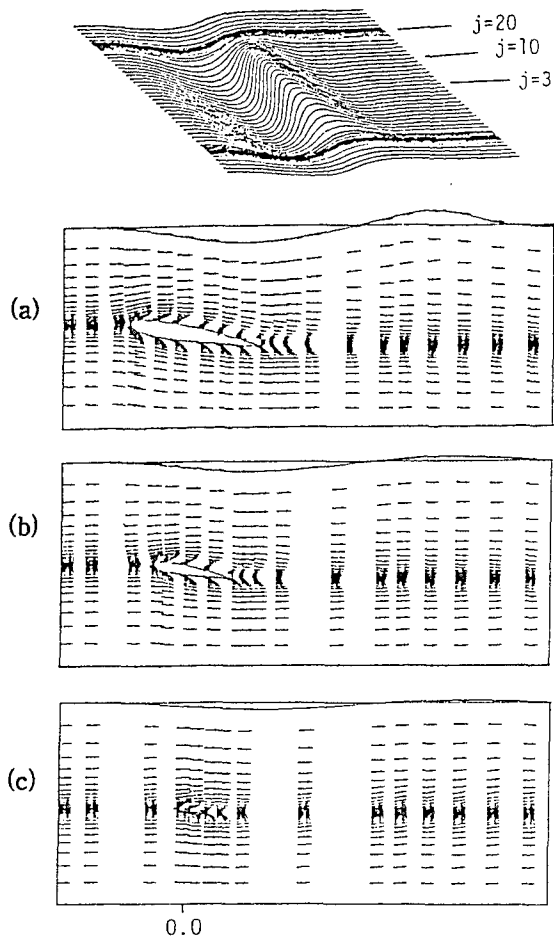
Fig.10 Free-surface profile and velocity vectors
on the three parallel surfaces of case 2
(a) j=3   (b) j=15   (c) j=20 (near tip)
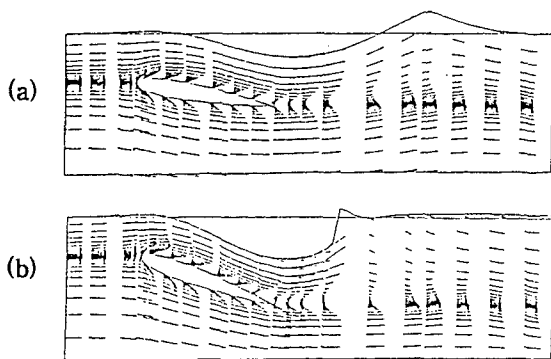
Fig.11 Free-surface profile and velocity vectors
on the symmetric plane, j=3
(a) case 3   (b) case 4
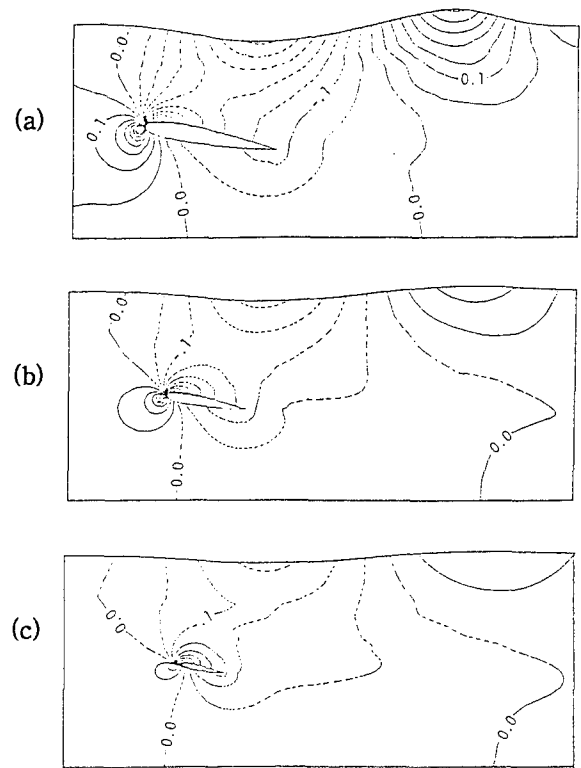
Fig.12 Pressure contours for case 2
(a) j=3   (b) j=15   (c) j=18
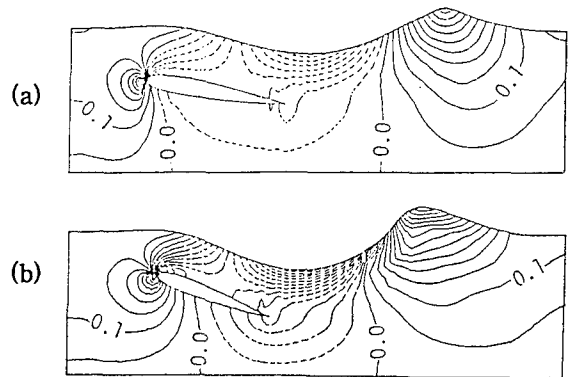
Fig.13 Pressure contours for cases 3 and 4
(a) case 3, j=3   (b) case 4, j=11
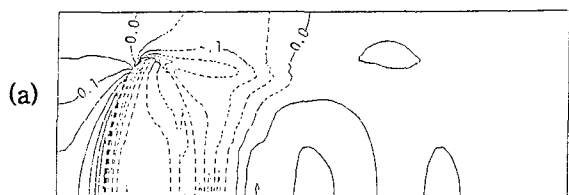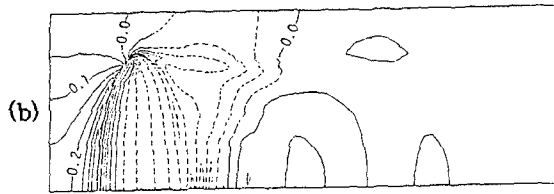
Fig.14 Pressure contour on wing surface
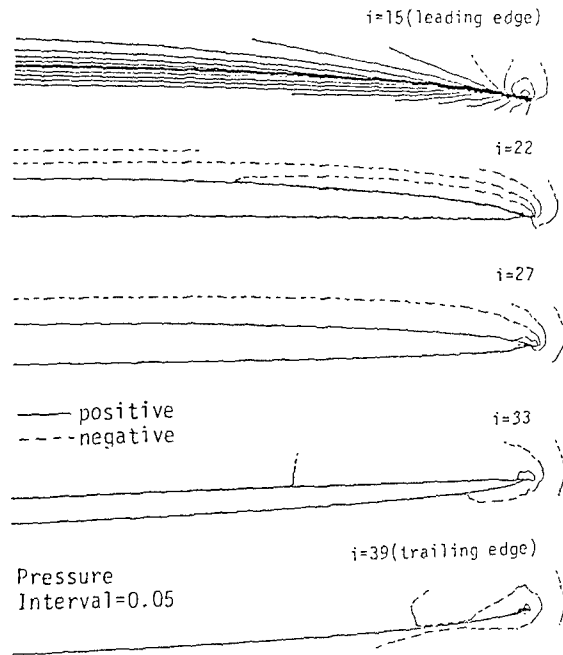for case 4 (a) suction side
(b) pressure side

Pressure
Interval=0.05

i=15(leading edge)

i=22

i=27

—— positive
- - - - negative

i=33

i=39(trailing edge)

Fig.16 Chordwise pressure contours for case 4

i=15(leading edge)

i=22

i=27

—— positive
- - - - negative

i=33

Pressure
Interval=0.05

i=39(trailing edge)

Fig.15. Chordwise pressure contour for case 3
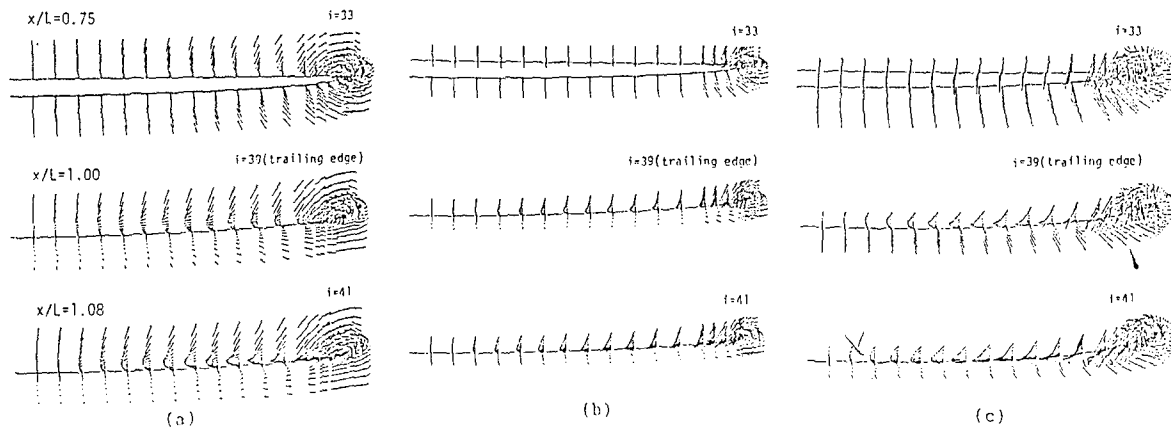
Fig.17 Chordwise velocity vectors at i=33,39
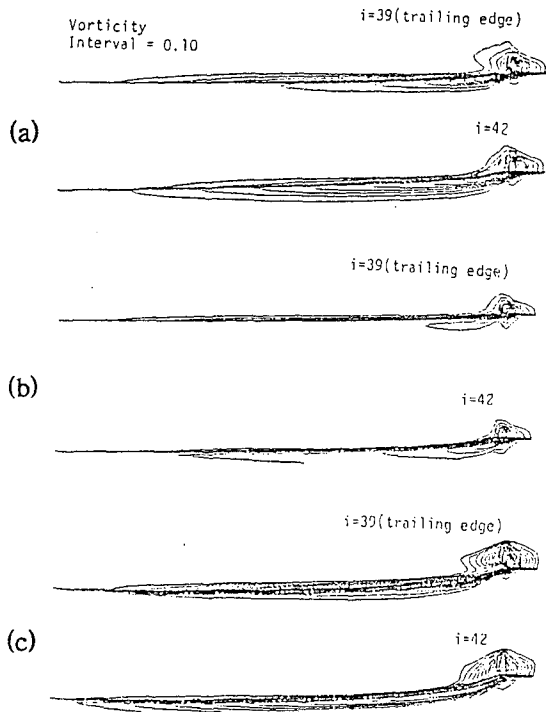and 41 (a) case 2 (b) case 3 (c) case 4

283

Fig.18 Chordwise vorticity contours at i=39 and 42 (a) case 2 (b) case 3 (c) case 4
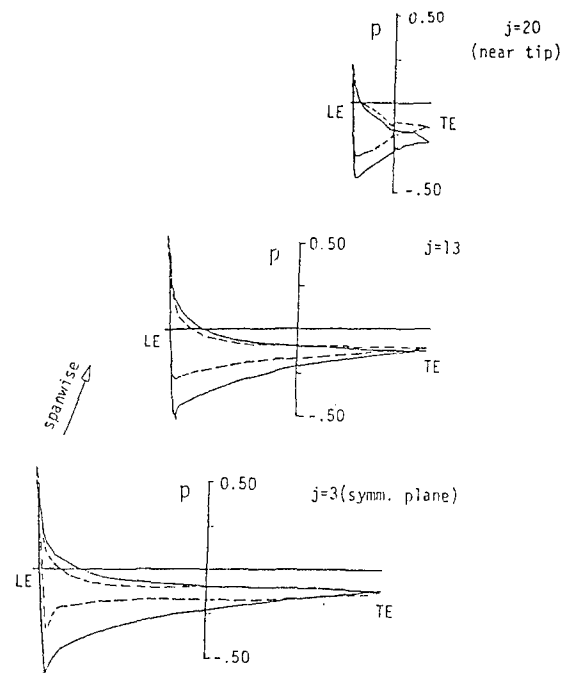

Fig.20 Comparison of spanwise pressure distribution on wing surface. Lower;suction, upper;pressure (——— ;case 2, - - - ;case 3)
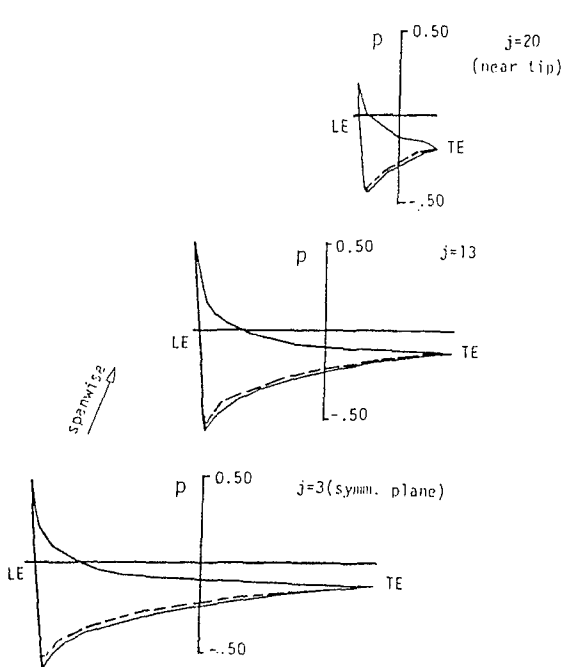

Fig.19 Comparison of spanwise pressure distribution on wing surface Lower;suction, upper;pressure (——— ;case 1, - - - ;case 2)
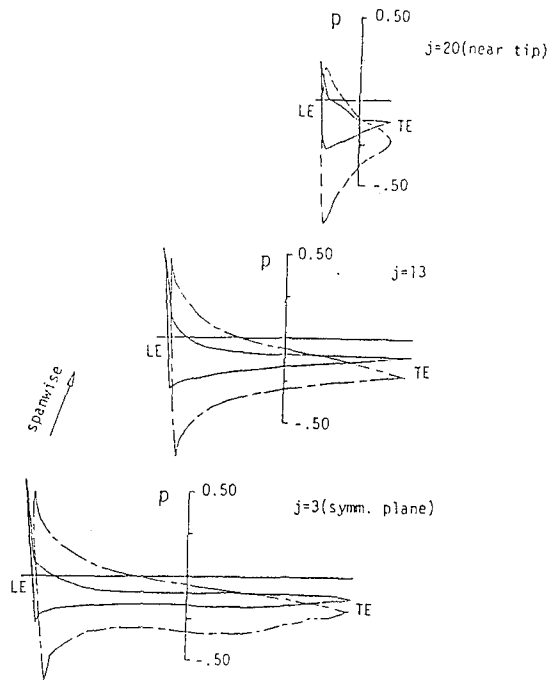

Fig.21 Comparison of spanwise pressure distribution on wing surface Lower;suction, upper;pressure (——— ;case 3, - - - ;case 4)
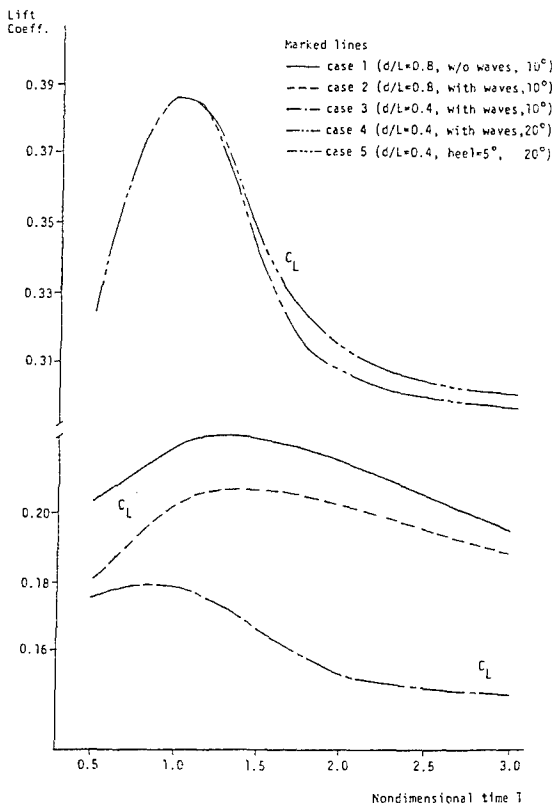
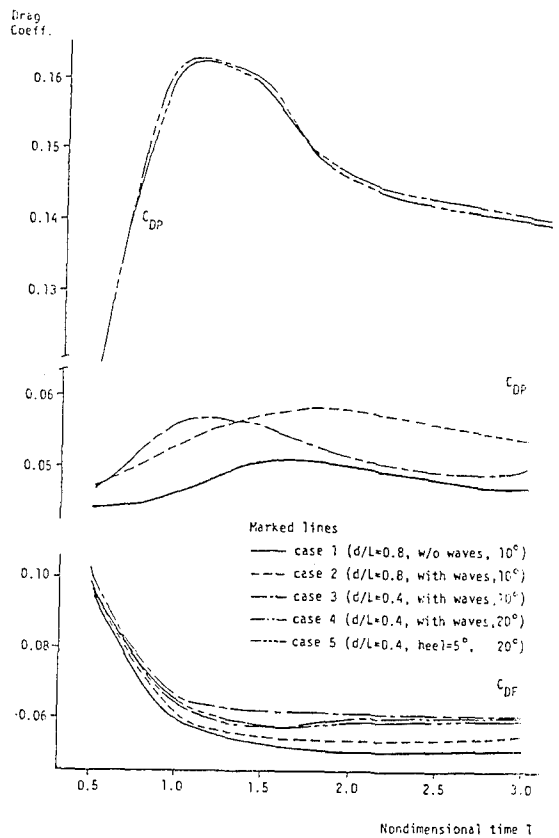Fig.22 Comparison of lift coefficients
for cases 1, 2, 3, 4 and 5

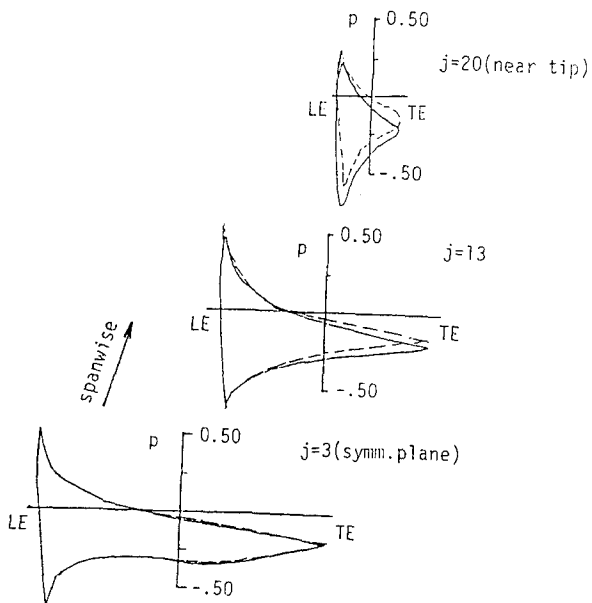Fig.23 Comparison of drag coefficients
for cases 1, 2, 3, 4 and 5

Fig.24 Comparison of spanwise pressure
distribution on wing surface
Lower;suction, upper;pressure
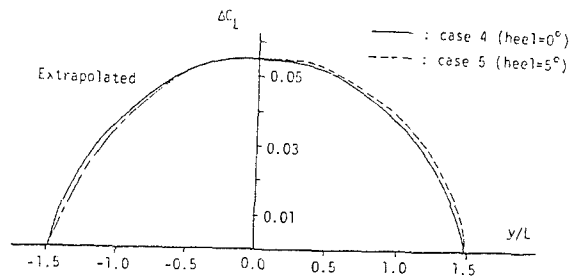(————;case 4, - - -;case5)

Fig.25 Spanwise lift distribution of port and
starboard sides

285

DISCUSSION
by Dr. T. Hino, Ship Research Institute, Japan

The authors use two time-integration methods in solving the Navier-Stokes equations: one is the SIAF method and the other is the explicit method. In Figure 2, time history of drag coefficients shows that the two methods give different converged solutions. If the spatial discretizations of the two methods are identical, the solutions should converge to the same value. What causes the difference?

Author's Reply
In the calculation, the frictional drag is directly obtained by the difference of the velocities at the two points near the hull surface, and the pressure drag by the integration of the pressure on the hull surface. One of the numerical inconsistencies may be the different treatment of boundary conditions near the hull surface.

The explicit method has a very simple boundary condition by nature inside the hull surface. However, the implicit factorization method gives much more complicate boundary condition inside the hull surface in which the contravariant velocities are invoked to handle the boundary conditions. The reason of the difference can't be clearly explained, but it is certain that there is a numerical contradiction between the two applications.

DISCUSSION
by Professor K. Mori, Hiroshima University, Japan.

Owing to the introduction of the IAF scheme, you increased the time interval by four times. This may be okay for the momentum equations, but may not for the computation of free-surface elevation. Higher approximation should be introduced for the wave calculations also if you increase the time step.

Author's Reply
According to our results, the free-surface elevation is almost the same between the two methods even though authors increase the time interval by four times. One of the advantages in the present scheme is the reduction of the computational time with the similar results to the explicit ones. However, in order to get the

improved free-surface, higher approximation and/or new boundary conditions at the downstream or lateral side may be necessary for the free-surface development.

DISCUSSION
by Dr. Y.T. Lee, David Taylor Model Basin

The grid systems used in this paper, particularly the one used for the Wigley case 74X29X19, are too coarse both in Y and Z directions. This implies that the solutions obtained are basically Euler solutions. The inconsistent results shown in Fig. 2 for drag coefficients at large time from two different approaches may be related to error in the viscous term.

Author's Reply
The grid system used in the computation is too coarse as you commented. In this connection, authors have an experience to calculate the full Navier-Stokes equations at two Reynolds numbers. One is 10^4 and the other 10^6. According to the calculated results, the effect of Reynolds number is obviously seen. It means that the coarse grid doesn't always give the results based on the Euler solutions. Authors agree that the coarse grid may be related to some errors in course of the long iterative procedure.

DISCUSSION
by Professor J. Feng, Penn State University

Four very simple questions:
(1) Would the authors explain why a nonconservative formulation was chosen for convective terms instead of a conservative form?

(2) A five-point differencing was used for viscous flux differencing. This leads to a penta-diagonal matrices, which are more expensive to solve than a tri-diagonal system form a three-point plus two half-point formulation.

(3) Three dimensional ADI are not unconditional stable

(4) A seemingly non-changing Ct/Cf/Cp is not a good criteria of convergence. In fact, Fig. 2 seems to suggest that the solutions are far from converging. At convergence, the explicit and the semi-explicit scheme should approach a common

numerical solution since they share the same right-hand terms. But more importantly, the fact that the two group of curves are flat and the different appears to imply numerical results will not converge easily or may even never converge at all.

Author's Reply

(1) Non-conservative form has better stability property. The conservative form is dominantly used with compressible equations.

(2) A five-point central differencings are used to increase the solution accuracy with a given number of grid points, thus resulting in block pentadiagonal systems. At points adjacent to the point of singularity or solid wall boundary, the three-point differencing formula are used for the first and second derivatives.

(3) A three-level sweep scheme allows the spatial terms to be included efficiently in a spatially factored algorithm without upsetting the unconditional stability.

(4) Please refer to the reply on the Hino question.

Numerical Prediction of Ship Generated Internal Waves in a Stratified Ocean at Supercritical Froude Numbers

M.P. Tulin, P. Wang, and Y. Yao
(University of California, Santa Barbara, USA)

ABSTRACT

Here we develop a non-linear theory for the solution of the near and intermediate internal wave field caused by a ship passing through a stratified ocean. The theory is mainly composed of a perturbation cross flow theory and is asymptotic to the case of very high supercritical ship speeds in the regime of greatest interest for modern ships, and to the case of small density differences. FEM is employed for numerical implementation.

Calculations have been carried out to distances from 10 to 80 ship lengths behind the stern for several speeds, F, and pycnocline distributions, $\rho(z)$. The formation of a propagating trough followed by a crest, and successive waves has been found. A comparison of the predictions with experiments carried out in our laboratory, shows good agreement between measured and calculated wave patterns and amplitudes.

NOMENCLATURE

x, y, z : moving Cartesian coordinates

s : path of the water particle

$\rho(z)$: vertical density distribution

ρ_1 : density of the upper homogeneous layer

ρ_2 : density of the lower homogeneous layer

$\Delta\rho$: density difference, $\Delta\rho = \rho_2 - \rho_1$

H : depth of water

h : mid depth of the pycnoclines

δ : thickness of pycnoclines

U_s : ship speed

L : ship length

D : ship depth

ε : scale parameter, $\varepsilon = D / L$

F_L : Froude number scaled with the ship length ,

$$F_L = U_s / \sqrt{gL}$$

F_h : densimetric Froude number scaled with h ,

$$F_h = U_s / \sqrt{gh\Delta\rho/\rho_2}$$

$\vec{u}_0$: homogeneous velocity vector in x-y-z space,

$$\vec{u}_0 = (u_0, v_0, w_0)$$

$\vec{\tilde{u}}$: perturbation velocity vector in y-z plane,

$$\vec{\tilde{u}} = (\tilde{v}, \tilde{w})$$

$\vec{u}$: sum of homogeneous and perturbation velocity vectors in x-y-z space, $\vec{u} = (u, v, w)$

q : water particle speed

ϕ_0 : potential of 3-D homogeneous flow

ψ : stream function of 2-D perturbation flow

$\vec{\omega}$: vorticity vector, $\vec{\omega} = (\omega_x , \omega_y , \omega_z)$

∇p : pressure gradient

$\wedge$: denoting nondimensionalized variables

N_i : high order Hermite shape functions,

i = 1, ..., 12

H_i : standard bilinear shape functions,

i = 1, ..., 4

INTRODUCTION

The discovery that ships create internal waves when traveling in stratified water is due to Ekman (1904). In fjords and similar highly stratified water bodies ($\Delta \rho = O(10^{-3} \sim 10^{-2})$), the surface disturbances due to the subsurface disturbances may be readily observed. Radar remote sensing makes ship internal waves even more readily detected, and has caused renewed interest in the subject. Internal waves are dispersive and the dispersion relation depends on the vertical density distribution and may be calculated from it. The far field kinematical wave pattern due to a localized moving disturbance may also be predicted from the dispersion relations using ray methods, Keller and Munk (1970), or equivalent asymptotics, Yih(1990), Tulin & Miloh (1990). The latter, further, found an expression for the amplitudes in the far field, in terms of an amplitude function, following the technique introduced for ship waves by Havelock (1934).

The celerity of the first fundamental, and fastest, wave, c^*, is approximately 30-50 cm/sec in both the ocean and fjords. The wave patterns depend upon $F_h = U_s / c^*$. The so-called dead-water phenomena resulting in greatly enhanced ship resistance occurs for $F_h = O(1)$; for these speeds, the wave pattern is essentially transverse, see Miloh & Tulin (1988). However, the speed of modern ships is normally sufficiently high so that $F_h >> 1$, and in this case the waves are solely divergent, within a half angle, β, where $\sin\beta = 1 / F_h$.

In the case of a two layer fluid, and for waves of small amplitude, wave fields may be calculated utilizing appropriate source-like singularities to represent bodies. This has been done: see, for example, Miloh, Tulin & Zilman(1992), where same examples of wave fields for different regimes in F_h are shown.

The specific calculation of the near field displacement patterns was first carried out by Tulin & Miloh (1990) using a shallow pycnocline (long wave) approximation. The resulting calculations revealed an upwelling in the near wake behind the ship, accompanied by negative deflections on either side, the triple lobe pattern. They have suggested that the far field has its origin in and results from the relaxation of the triple-lobe pattern, and may therefore be predicted from it.

Conceivably, suitably large forcing of the pycnoclines could result in the generation and propagation of soliton disturbances just outside the half angle, β. It would therefore be desireable to have available a theoretical method for the prediction of ship internal waves including non-linear terms.

In the present work we take advantage of the strongly divergent nature of the wave pattern for $F_h >> 1$ to develop a numerical calculation method for the theoretical prediction of both near and far field internal wave patterns for arbitrary vertical density distributions and for slender ships of arbitrary cross section, including the dominant non-linear terms.

Very recently, Wong & Calisal (1993) have presented a numerical cross flow theory, with results. This interesting theory differs from that presented here in several respects : the forcing is calculated as part of the cross flow, whereas here the forcing is taken from the homogeneous flow; the density distribution corresponds to a two layer fluid. Their theory seems therefore most appropriate in the case of relatively shallow, sharp pycnoclines.

The validation of theory has been handicapped by a lack of systematic data. Therefore, Ma & Tulin (1992) carried out experiments on ship internal waves utilizing a small stratified tank and a small towed model of length, 45 cm. Longitudinal wave cuts at various transverse distances have been made for a spheroidal model, half submerged, over a range of F_h, both close to and much larger than unity, Ma (1993).

Here we describe the new theory and present specific calculations in four cases for which experimental data have been obtained in our laboratory. Satisfactory comparisons are made, so that the present method can be effectively used for the numerical study of ship internal waves, including non-linear effects.

The examples given here are for a simple spheroidal hull shape and simple pycnocline distributions, but the program created may be used for more general hull shapes and density distributions.

CROSS FLOW THEORY

We consider here an incompressible and inviscid fluid with a variation of density ρ in the vertical direction. The density profile is typified by a shallow layer of water with constant density ρ_1 above, and an infinite depth of water with higher constant density ρ_2 beneath, pycnoclines where the density changes continuously from ρ_1 to ρ_2. A ship with small ratio of draft D to length L passes above or through the pycnoclines, its speed U_s is much larger than the limiting speed of internal waves, $c^* \cong \sqrt{gh\Delta\rho/\rho_2}$, as shown in figure 1. In these supercritical cases (densimetric Froude Number $F_h =$

$U_s / c^* >> 1$), the internal wave patterns generated are essentially divergent, the waves propagate in the the direction transverse to the ship's direction, and the wave pattern is contained within a half angle to the ship's direction of $\sin^{-1}(1/F_h)$. In a medium with small density differences, and for $F_h >> 1$, the velocities in the near field of the ship can be composed of the sum of the homogeneous field, with no density gradients, and a perturbation field, representing the internal wave field, where the latter (and only the latter) is assumed two-dimensional in the cross flow plane, and becomes the entire disturbance in the far field.

We consider the generation and propagation of these ship internal waves in a frame of reference stationary relative to the ship. In a coordinate system fixed in the moving ship, with the x-axis ($\vec{i}$) downstream, y-axis ($\vec{j}$) transverse and z-axis ($\vec{k}$) upward, see figure 1, the velocity field is decomposed, as discussed above, into :

$$\vec{u} = \vec{u}_0 + \vec{\tilde{u}} \qquad (1)$$

where ,

$$\vec{u} = u\,\vec{i} + v\,\vec{j} + w\,\vec{k}$$
$$\vec{u}_0 = u_0\,\vec{i} + v_0\,\vec{j} + w_0\,\vec{k} \qquad (2)$$
$$\vec{\tilde{u}} = \tilde{v}\,\vec{j} + \tilde{w}\,\vec{k}$$

and (u_0, v_0, w_0) is the homogeneous flow field with potential ϕ_0 driven by the passing ship, where it is usually but not necessarily appropriate to consider the free surface to be a rigid lid. This double model flow can be calculated by standard methods. In the specific calculations given here, we consider the flow past spheroids, so that the homogeneous ship flow is represented by a linear source distribution m(x) on the free surface, $-L/2 \le x \le L/2$:
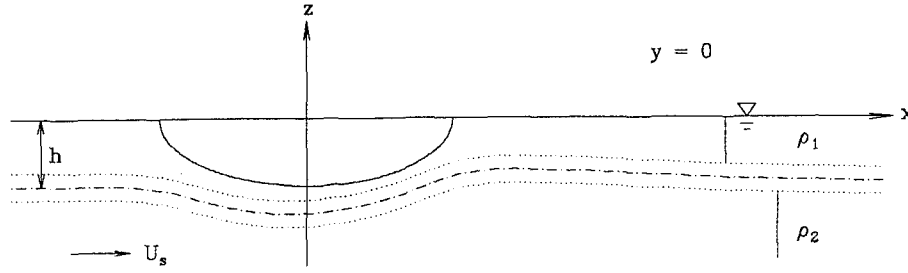
Figure 1 : A Stationary Flow Due to Ship Passing Over Pycnoclines, Actual Calculations. The Vertical Scale Has Been Stretched.
$(\Delta\rho/\rho_2=10^{-3}, F_h=5, D/L=0.1, h/D=1, \delta/h=0.4)$

$$\phi_0 (x,y,z) = U_s x - \frac{1}{4\pi} \int_{-\frac{L}{2}}^{\frac{L}{2}} \frac{m(\xi)\,d\xi}{\sqrt{(x-\xi)^2 + y^2 + z^2}} \qquad (3)$$

$$m(x) = - 8\pi U_s (D/L)^2 x \qquad (4)$$

The flow field, $\vec{u}$, causes the isopycnics to become inclined to the horizontal. Then, the pressure and density gradients interact to create vorticity in the region of stratification. This vorticity first creates a narrow region of displacements within the wake behind the ship, and these displacements relax to form internal waves propagating transversely.

The vorticity arises in accord with Fridman's relation (Kochin et al, 1948), where the forcing is through the pressure term on the right,

$$\frac{D}{Dt}\vec{\omega} - (\vec{\omega}\cdot\nabla)\vec{u} = \frac{1}{\rho^2}(\nabla\rho \times \nabla p) \qquad (5)$$

where

$$\vec{\omega} = \omega_x \vec{i} + \omega_y \vec{j} + \omega_z \vec{k}$$

$$= (\frac{\partial w}{\partial y} - \frac{\partial v}{\partial z})\vec{i} + (\frac{\partial u}{\partial z} - \frac{\partial w}{\partial x})\vec{j} + (\frac{\partial v}{\partial x} - \frac{\partial u}{\partial y})\vec{k} \qquad (6)$$

Since both the ship and the internal wave pattern are slender, $\frac{\partial}{\partial x}/\frac{\partial}{\partial y}$, $\frac{\partial}{\partial x}/\frac{\partial}{\partial z} = O(\varepsilon) \ll 1$ in the near field, where $\varepsilon = (F_h)^{-1} \ll 1$ in the far field; for the same reason, the perturbations in u above are $O(\varepsilon)$ and smaller than v,w. Therefore, from (6), $\omega_y, \omega_z / \omega_x = O(\varepsilon)$:

$$\vec{\omega} \cong \omega_x \vec{i}$$

$$= (\frac{\partial \widetilde{w}}{\partial y} - \frac{\partial \widetilde{v}}{\partial z})\vec{i} \qquad (7)$$

Applying (5) in x direction, the first term of the LHS may be written in the steady case : $q\frac{\partial \omega_x}{\partial s}$, where q is the flow speed on the streamsurface. Within the same approximation, we obtain,

$$q\frac{\partial \omega_x}{\partial s} - \omega_x\frac{\partial u}{\partial x} = \frac{1}{\rho^2}(\frac{\partial \rho}{\partial y}\frac{\partial p}{\partial z} - \frac{\partial \rho}{\partial z}\frac{\partial p}{\partial y}) \qquad (8)$$

The pressure can be expressed in terms of the velocity field through Euler's equation :

292

$$\frac{D\vec{u}}{Dt} - g\vec{k} = -\frac{1}{\rho}\nabla p \qquad (9)$$

then (8) becomes,

$$\omega_x = u\int_{s_0}^{s}\{\frac{1}{\rho u}[\underbrace{\frac{\partial\rho}{\partial z}(u\frac{\partial v}{\partial x}+v\frac{\partial v}{\partial y}+w\frac{\partial v}{\partial z})}_{[1]}$$

$$\underbrace{-\frac{\partial\rho}{\partial y}(u\frac{\partial w}{\partial x}+v\frac{\partial w}{\partial y}+w\frac{\partial w}{\partial z}}_{[2]}\underbrace{-g}_{[3]})]\}\frac{ds}{q}$$

$$(10)$$

where [1] represents the horizontal inertial accelerations, [2] the vertical inertial accelerations, and [3] the gravitational acceleration.

The magnitude of these terms in the near field may be understood by introducing nondimensional variables appropriate to the near field :

$$\hat{x} = x/L \; ; \qquad \hat{y} = y/D \; ; \qquad \hat{z} = z/D \; ;$$

$$\hat{u} = u/U_s \; ; \qquad \hat{v} = v/(U_s\varepsilon) \; ; \qquad \hat{w} = w/(U_s\varepsilon) \; ;$$

$$\hat{s} = s/L \; ; \qquad \hat{q} = q/U_s \; ;$$

$$\hat{\rho} = \rho/\rho_2 \; ; \quad \widehat{\frac{\partial\rho}{\partial y}} = \frac{\partial\rho}{\partial y}\cdot(\frac{\delta}{\Delta\rho}) \; ; \quad \widehat{\frac{\partial\rho}{\partial z}} = \frac{\partial\rho}{\partial z}\cdot(\frac{\delta}{\Delta\rho}) \; ;$$

$$\hat{\omega}_x = \omega_x\frac{\delta}{(\Delta\rho/\rho_2)U_s\varepsilon} \; ;$$

$$F_L = U_s/\sqrt{gL}$$

$$(11)$$

then Eq (10) becomes,

$$\hat{\omega}_x = \frac{\hat{u}}{\hat{\rho}}\int_{\hat{s}_0}^{\hat{s}}\frac{1}{\hat{u}}\{\widehat{\frac{\partial\rho}{\partial z}}(\hat{u}\frac{\partial\hat{v}}{\partial\hat{x}}+\hat{v}\frac{\partial\hat{v}}{\partial\hat{y}}+\hat{w}\frac{\partial\hat{v}}{\partial\hat{z}})$$

$$-\widehat{\frac{\partial\rho}{\partial y}}(\hat{u}\frac{\partial\hat{w}}{\partial\hat{x}}+\hat{v}\frac{\partial\hat{w}}{\partial\hat{y}}+\hat{w}\frac{\partial\hat{w}}{\partial\hat{z}}-\frac{1}{\varepsilon F_L^2})\}\frac{d\hat{s}}{\hat{q}} \qquad (12)$$

The gradient $\frac{1}{\hat{\rho}}\widehat{\frac{\partial\rho}{\partial z}}$ is O(1), but $\frac{1}{\hat{\rho}}\widehat{\frac{\partial\rho}{\partial y}}$ is in ratio to the former by the factor tan(α), where α is the tilt of the pycnoclines from the horizontal. Since F_L is normally in the range 0.1 ~ 0.3, the term εF_L^{-2} dominates within the second bracket.

In the y-z cross flow plane, we introduce a stream function ψ to represent the perturbation flow or the internal wave field $(\tilde{v}, \tilde{w})$, which satisfies,

$$\tilde{v} = \frac{\partial\psi}{\partial z} \; , \qquad \tilde{w} = -\frac{\partial\psi}{\partial y} \qquad (13)$$

then from Eq. (7), we deduce the Poisson Equation in nondimensional form, which governs the generation and oscillation of the internal waves in the cross flow plane, with the vorticity as its forcing term,

$$\frac{\partial^2\hat{\psi}}{\partial\hat{y}^2} + \frac{\partial^2\hat{\psi}}{\partial\hat{z}^2} = -\hat{\omega}_x \qquad (14)$$

where,

$$\hat{\psi} = \psi\frac{\delta}{(\Delta\rho/\rho_2)U_sD^2\varepsilon} \qquad (15)$$

Because the whole flow field is symmetric about the mid-line of the ship, or the x-axis, we take

293

the cross flow as a closed flow in half of the y-z plane with a continuous streamline of value zero on the whole boundary. Considering the fact that surface wave modes and internal wave modes are uncoupled and the amplitude ratio of these two wave systems is of order of $\Delta\rho/\rho_2$ (Phillips, 1967), we approximate the free surface as a rigid-lid. The infinite boundary in the y direction can be moved to a position where the leading internal wave has yet to arrive. The bottom boundary can also be taken where the disturbances have sufficiently decayed in depth.

The generation of vorticity and the deflection of the pycnoclines, or the oscillation of internal waves, are mutual and simultaneous, so Eqs (12) and (14) are coupled in a complex way. In the numerical simulation however, they can be decoupled by an iteration technique or simply by separating their calculation by an infinitesimal time interval. We choose the latter since the internal waves are long waves of steepness around one tenth and the velocity field changes very slowly. The calculation may be made by marching downstream since there is no upstream influence between the vorticity and the internal wave field.

In the x direction, the Lagrangian Method can be used to follow the fluid particles from one cross plane to another, resulting in pycnoclines in each new cross plane, and thus a three dimensional internal wave picture can be drawn. The starting cross plane is at $x = x_0$, some distance before the bow of the ship, where the homogeneous flow field is still uniform and pycnoclines are still horizontal, as no vorticity has yet been generated.

In succeeding sections, the caps on nondimensional variables will be deleted for simplicity.
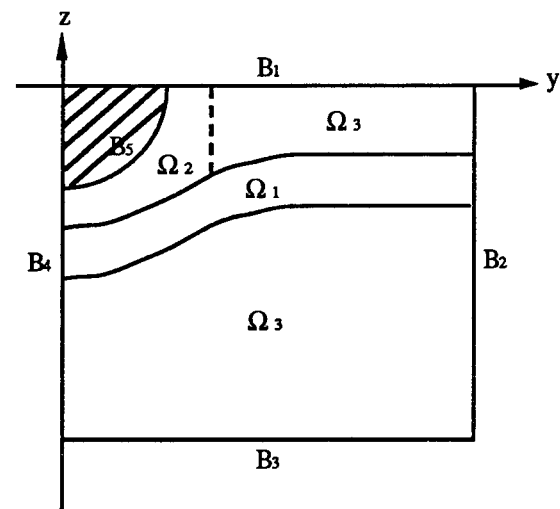
NUMERICAL IMPLEMENTATION

The physical problem discussed above can be described mathematically as an initial value problem in time, or in the x direction, which is solved by marching forward, plus successive boundary value problems in the y-z plane. Two corresponding computational domains are shown in figure 2.
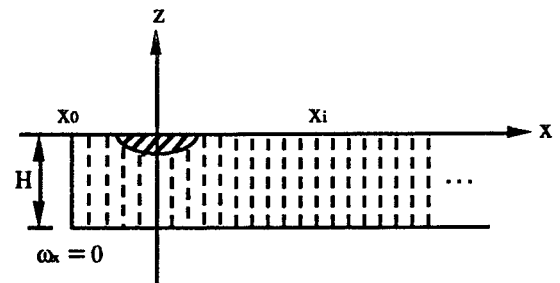
(a) Side View
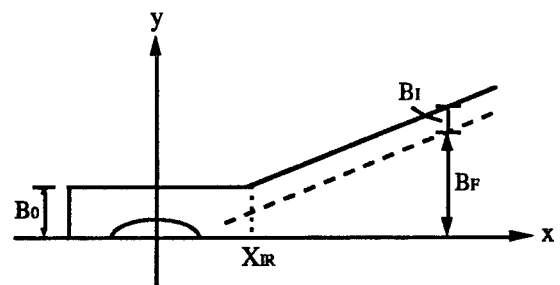
(b) Top View

(c) Back View

Figure 2 : Schematic Computational Domains

294

It can be seen in figure 2(b) that the breadth of the cross flow domain will continually increase after some distance along the x direction at $x = x_{IR}$ in view of the divergent property of internal waves. B_0 is selected to allow a full depression under the ship; B_F is the front of the transverse waves obtained from far field theory (Tulin & Miloh, 1990), and B_I is a constant distance added on B_F.

As discussed in the section above, velocity and vorticity fields can be solved separately at infinitesimal time intervals, or infinitesimal distances in the x direction. At the begining cross plane, $x = x_0$, the vorticity is zero, the velocity field is taken from the homogeneous flow, $\vec{u_0}$; the pycnoclines are horizontal with an imposed density profile, and then the first vorticity increment can be calculated, using Eq.(12), where $\vec{u} = \vec{u_0}$. In the successive ith y-z plane, $x = x_{i-1} + \Delta x$, the position of the pycnoclines is obtained by following fluid particles from the (i-1)th plane to the ith plane, where the distance the particles have travelled is $\Delta s = q (\Delta x / U_s)$; density gradients can also be calculated from the deflection of the pycnoclines, and the velocity field, $\tilde{\vec{u}}$, is obtained by solving the Poisson equation, Eq.(14), with vorticity integrated from the previous section as the forcing, Eq (12), wherein $\vec{u} = \vec{u_0} + \tilde{\vec{u}}$. Marching through a sufficient distance after the ship, first a triple-lobed wake displacement pattern, and subsequently a three dimensional dispersive internal wave pattern appears. For Δx reasonably small, a high accuracy of simulation can be achieved.

The essence of the current theory is the perturbation cross flow in the y-z plane governed by the Poisson Equation, with vorticity penetrating the plane as its forcing. So the crux of the numerical implementation is in solving a two dimensional boundary value problem with an elliptic P.D.E. as its field equation, and Dirichlet conditions around the whole boundary.

Finite Difference and Finite Element Methods are two numerical techniques available for this problem, but the latter is more suited to modelling curved boundaries, like the ship hull boundary, and when non-uniform gridding is used. To allow for a large field simulation which consumes considerable CPU resources, a graded spatial discretization is preferred, and refined meshes in the z-direction are used within the pycnoclines, where the density of the fluid changes rapidly; the size of the meshs which are away from the pycnoclines increase gradually upward or downward. In the y-direction, the size of the mesh increases gradually proceeding outwards since internal waves propagate outwards with the longest wave in the front. To catch the interfacial movement of the pycnoclines, the easiest way is by always following their particles, so the grids have to be on the wavy changing pycnoclines. For all these reasons, the Finite Element Method is employed for the current task.

In the classical Galerkin finite element method, the weight functions are chosen to be equal to the element shape functions. A discrete analog of the continuous physical system, which is governed by the Poisson equation, is given by,

$$\int_{\Omega} N_i \left(\frac{\partial^2 \psi}{\partial y^2} + \frac{\partial^2 \psi}{\partial z^2} + \omega_x \right) d\Omega = 0 \qquad (16)$$

where N_i are the weight functions; Ω represents the whole calculation domain in the y-z plane. Integrating by parts to reduce the second order

295

derivatives to the first order, and expressing Eq.(16) as a finite sum of integrations on piecewise continuous elements, we obtain,

$$\Sigma \{ \int\int_{\Omega_e} (\frac{\partial N_i}{\partial y} \frac{\partial \psi^{(e)}}{\partial y} + \frac{\partial N_i}{\partial z} \frac{\partial \psi^{(e)}}{\partial z}) dydz$$

$$+ \int_{\partial\Omega_e \cap (B_4+B_5-B_2)} N_i \frac{\partial \psi^{(e)}}{\partial y} dz$$

$$+ \int_{\partial\Omega_e \cap (B_1+B_5-B_3)} N_i \frac{\partial \psi^{(e)}}{\partial z} dy$$

$$= \Sigma \{ \int\int_{\Omega_e} N_i (\omega_x)^{(e)} dy\, dz \} \qquad (17)$$

where Ω_e is the integration domain in each element in the y-z plane, B_i, i = 1, 2, ..., 5, is the boundary of the computational domain as indicated in figure 2(c), and $\partial\Omega_e$ is the integration boundary of elements on those boundaries; $\Psi^{(e)}$ and $(\omega_x)^{(e)}$ are the interpolated stream function and vorticity distribution variables in each element represented by linear interpolation of their discrete values on element nodes.

The selection of the type of element is very important for the success of the current numerical approach. We follow particles in the x direction by their velocity to complete a stationary three dimensional wave pattern. And vorticity involves velocity derivatives. So the accurate approximation of first and second order derivatives of the stream function is crucial in the numerical simulation of ship generated internal waves. We choose a high order Hermite element, because it has both the variable and its first order partial derivative all as unknowns, and allows the second order derivatives,

which do not occur in the governing equation, to be differentiated based on the velocity field which is interpolated by a linear combination of its discrete nodal values.

Considering both accuracy and computer time expenses, and comparing two polynomial bases for triangles and quadrilaterals, Eq (18) and (19), four node cubic Hermite elements are employed to partition the computational domain into finite elements. This allows the continuity condition to be satisfied on nodes of elements. Continuity of the stream function and tangential velocities across element boundaries are also preserved.

$$\{P\}_3 = \{1\ \xi\ \eta\ \xi^2\ \xi\eta\ \eta^2\ \xi^3\ \xi^2\eta\ \xi\eta^2\ \eta^3\} \qquad (18)$$

$$\{P\}_4 = \{1\ \xi\ \eta\ \xi^2\ \xi\eta\ \eta^2\ \xi^3\ \xi^2\eta\ \xi\eta^2\ \eta^3\ \xi^3\eta\ \xi\eta^3\} \qquad (19)$$

The stream function in each element is thus interpolated by a linear combination of its nodal values using 4-node cubic Hermite shape functions N_i (i=1, ..., 12),

$$\psi^{(e)} = \sum_{i=1}^{12} N_i (\xi, \eta)\, \psi_i \qquad (20)$$

Element coordinates and all the other variable functions, like velocity, density and vorticity, are interpolated using the standard bilinear shape functions H_i (i = 1, ..., 4) that is,

$$y = \sum_{i=1}^{4} H_i (\xi, \eta)\, y_i\ ; \qquad z = \sum_{i=1}^{4} H_i (\xi, \eta)\, z_i\ ;$$

$$v^{(e)} = \sum_{i=1}^{4} H_i (\xi, \eta)\, v_i\ ; \qquad w^{(e)} = \sum_{i=1}^{4} H_i (\xi, \eta)\, w_i\ ;$$

$$\rho^{(e)} = \sum_{i=1}^{4} H_i (\xi, \eta)\, \rho_i\ ;$$

$$\omega_x^{(e)} = \sum_{i=1}^{4} H_i (\xi, \eta)\, (\omega_x)_i$$

$$(21)$$

296

Variable derivatives are carried out based on interpolated variable functions and transformed from local (ξ, η) to a general (y, z) coordinate system by the Jacobian operator.

It should also be mentioned that all variable derivatives, except velocity, calculated on grids except at corners of the domain are averaged on the surrounding elements with equal weight.

The cubic Hermite shape functions N_i and the bilinear shape functions H_i , and their first order partial derivatives $\partial N_i / \partial \xi$, $\partial N_i / \partial \eta$ and $\partial H_i / \partial \xi$, $\partial H_i / \partial \eta$ are available in the literature. With careful geometrical treatment of the physical domain and application of standard procedures in FEM, the stream function and velocity field can be solved together with sufficient accuracy.

We divide the y-z cross flow domain Ω into three parts, Ω_1, Ω_2, and Ω_3, as shown in figure 2(c). The first part, Ω_1, like a stream tube, includes all pycnoclines and is bounded by upper and lower interfaces with two constant density layers. The second part, Ω_2 , is the region in the upper layer and is near the boundary of the ship, where the mesh construction is a little harder than in the other two

parts. The third part Ω_3 represents the remaining part of the whole domain, including the layer beneath the pycnoclines and the right part of the upper layer. In Ω_2 and Ω_3 , the vorticity is equal to zero, and no fluid particles need to be followed from one section to another.

In Ω_1, one big stream tube is divided into multiple smaller ones, along which elements are distributed with neighboring segments being near-orthogonal to the streamlines, or the pycnoclines, as shown in figure 3. The element breadth increases gradually in the outflow direction.

Near the ship boundary, high curvatures are involved including two singular points. Generalized coordinates are normally more suitable for this kind of boundary. But here a band of the computational domain is predetermined by the physical flow, characterized by the oscillation of pycnoclines, the grid generation cannot be done automatically in the whole computational domain by algebraic mapping or by solving partial differential equations. To avoid complex manipulations or manual intervention during grid generation, a simpler technique is used in Ω_2 at the cost of local element distortion near the
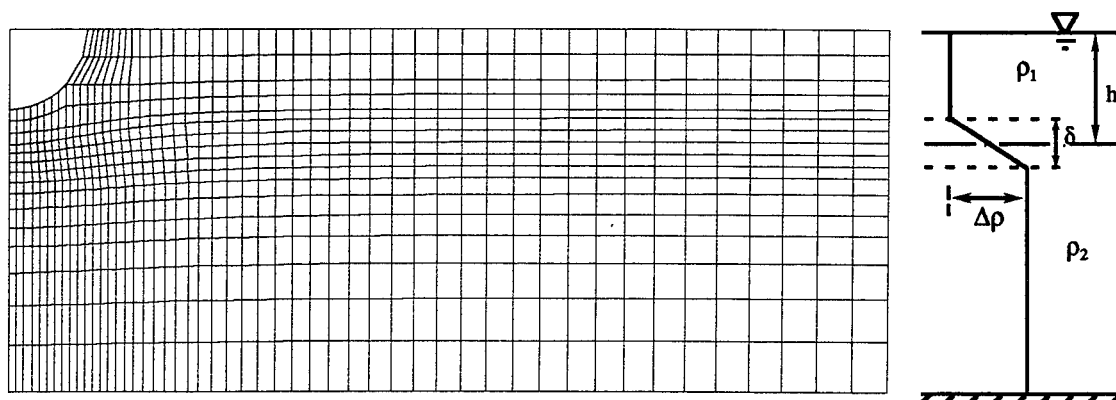

Figure 3 : On the Left, an Example of Grid Distribution in y-z Cross Plane, the Blank Part on Left-Upper Corner Represents a Quarter of a Section of a Double Hull Ship. On the Right, an Example of a Vertical Density Distribution.

ship boundary. This has little effect on the internal wave calculation.

In Ω_3, meshes are formed comparatively free of any restrictions, and stretching out in the y direction and in the upward or downward direction within the upper and lower layers.

An example of grid generation is shown in figure 3. It can be seen that more grids are concentrated in the left part in the pycnoclines, whereas in the right and lower part of the domain, the mesh distribution is quite loose. It is reasonable to expect that the efficiency of the computation can be even more enhanced, by using a split-time technique, or a split-marching technique for the stationary flow; however this technique has not been implemented in the current stage.

RESULTS & DISCUSSION

The numerical code developed based on the above theory and computational techniques has been tested with regard both to the finite element solution of the Poisson equation, and the convergence of wave amplitudes for different marching steps in the x direction.

As a test flow, we consider a simple closed flow with a stream function,

$$\psi = \sin(k_y y) \sin(k_z z) \qquad (22)$$

where,

$$k_y = \frac{y}{B} \pi n, \qquad k_z = \frac{z}{H} \pi m, \qquad n, m = 1, 2, \qquad (23)$$

B and H are the breadth and height of the physical domain, so $\psi = 0$ on the entire boundary.

The velocity field for this stream function is,

$$v = \frac{\partial \psi}{\partial z} = k_z \sin(k_y y) \cos(k_z z)$$

$$(24)$$

$$w = -\frac{\partial \psi}{\partial y} = -k_y \cos(k_y y) \sin(k_z z)$$

An x component of vorticity exists within the whole flow field, and its value can be calculated directly from the known stream function, Eq (22),

$$\omega_x = -\left(\frac{\partial^2 \psi}{\partial y^2} + \frac{\partial^2 \psi}{\partial z^2} \right)$$

$$= [(k_y)^2 + (k_z)^2] \sin k_y y \sin k_z z \qquad (25)$$

We do the inverse problem numerically using our code, and compare the velocity field, solved from the Poisson equation, with the exact solution given in Eq (24). High resolution is achieved with 8 to 12 grids distributed uniformly in a half wave length, see figure 4.

In the x direction, as far as proper marching steps are concerned, the convergence test is carried out in the region from upstream ($\hat{x} = \hat{x}_0 = -0.8$) to midship ($\hat{x} = 0$), where a big depression always occurs, with a larger displacement than elsewhere. A range of $\Delta\hat{x}$ from 0.005 to 0.05 was tested, and the wave amplitude and vorticity converge very well when $\Delta\hat{x}$ is less than 0.025, see figure 5; the errors relative to $\Delta\hat{x} = 0.005$ are shown in table 1.

Table 1 : Convergence Test -- Relative Errors

$\Delta\hat{x}$	$\Delta\eta/\eta_{0.005}$	$\Delta\omega_x/(\omega_x)_{0.005}$
0.01	0.14%	0.75%
0.025	0.38%	4%
0.05	0.77%	10%

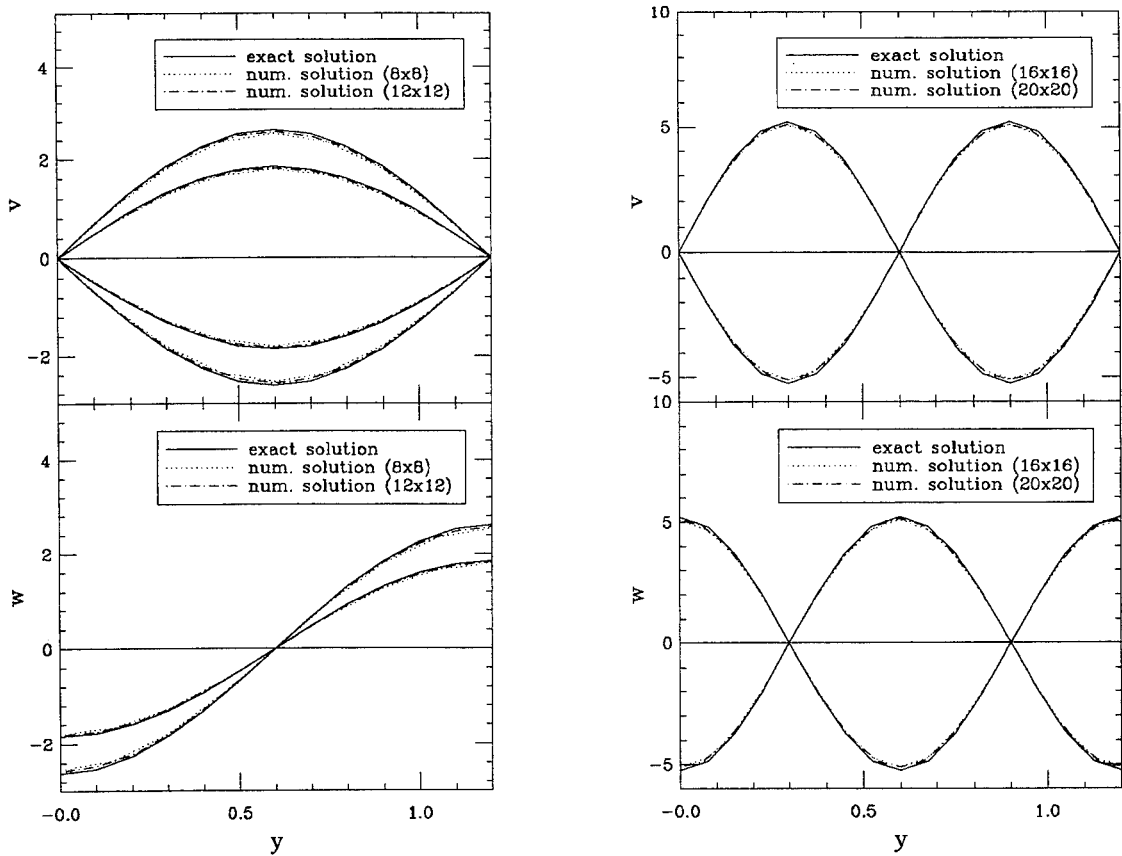With the confidence obtained so far, we did a series of calculations with the physical conditions

Figure 4 : Numerical Test of the Finite Element Solution of the Poisson Eq.
B=H=1.2, Velocities at Five Equally Spaced Positions of z (for v) &
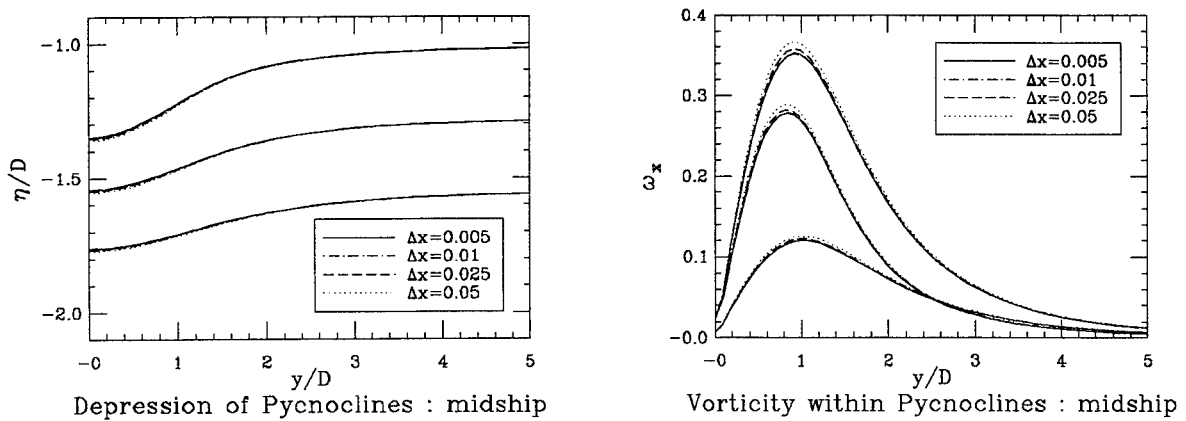y (for w) Are Compared. Left, n=m=1; Right, n=m=2

Figure 5 : Convergence Test for Marching Steps in the x Direction, $\Delta\hat{x}$. Three Bunches
of Lines in Each Plot Correspond to Upper, Mid and Lower Interfaces.
(F=4.76, D/L=0.097, h/D=1.28, δ/h=0.42, $\Delta\rho/\rho$=0.0036)

299

listed in table 2, selected from tank experiments carried out in our laboratory; the case numbers are the same as used in the experiments.

An internal wave field as long as 80 ship lengths is simulated for case 41(c), figure 6(a) & (b),

Table 2 : Physical Conditions of the Numerical Simulations (D/L = 0.097)

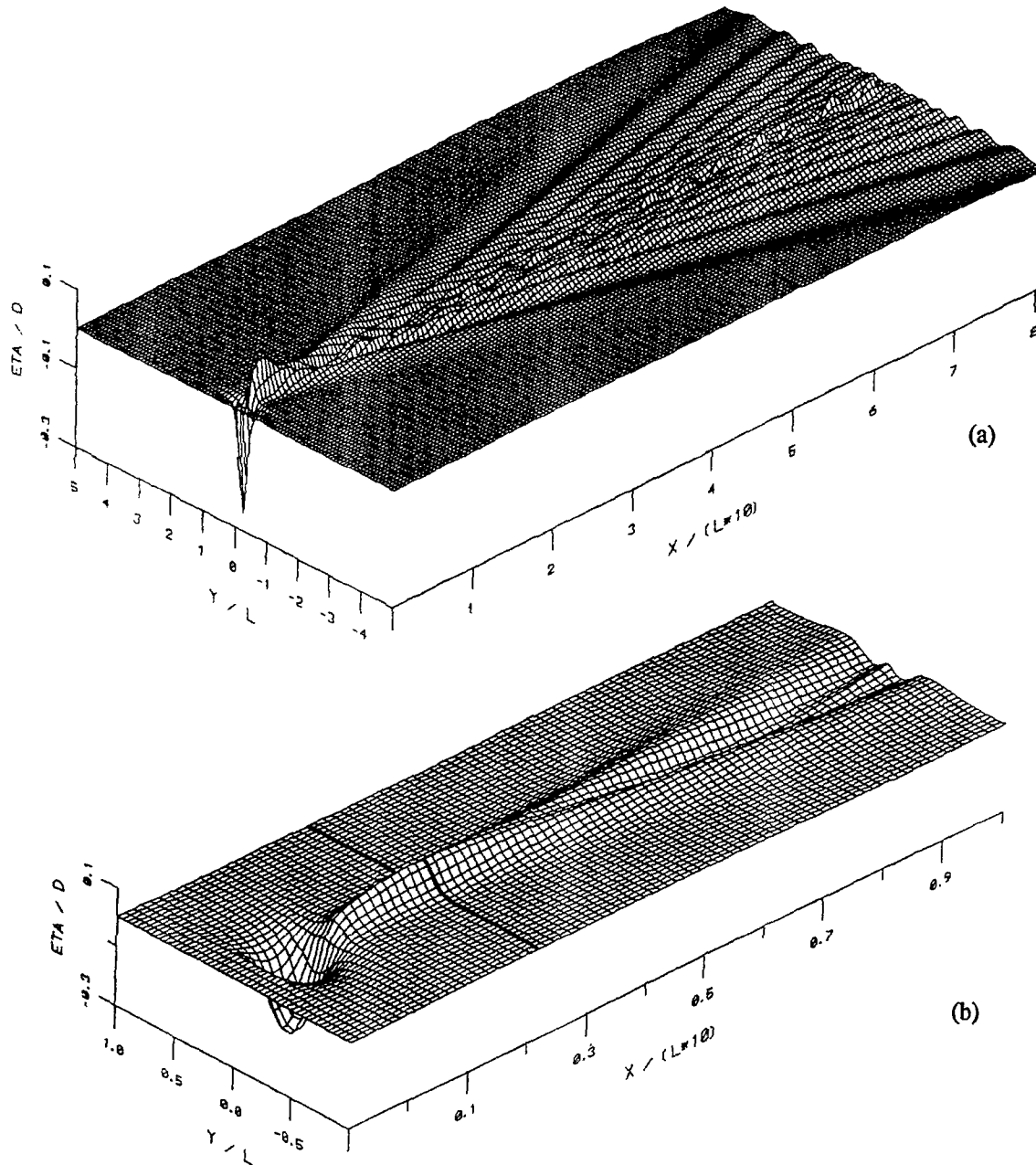| Case No.	h/D	δ/D	Δρ/ρ₂	F_h
41 (c)	1.28	0.54	0.0034	10.
41 (b)	1.28	0.54	0.0034	4.8
28 (b)	0.96	0.29	0.0036	5.9
25 (c)	0.78	0.39	0.0041	6.5

Figure 6 : Ship Internal Waves, Case 41(c), the Darkened Line Is the Cut for Triple Lobe.
(a) Near and Intermediate Field;   (b) Near Field, Blown up from (a) .

300

which covers the near and intermediate internal wave field. It can be clearly seen that : a big displacement appears just under the ship; and starting immediately after the ship, a central peak accumulates gradually which separates and pulls up the down lobe until a typical triple-lobe pattern in the transverse direction forms; then, this deformation relaxes and produces dispersive waves which propagate outwards, with the longest waves in the front.

The kinematic wave pattern, represented by the phase lines corresponding to crests and troughs, has been compared with far field theory (Tulin & Miloh, 1990), and very good agreement is obtained, as shown in figure 7.

Occuring one and a half ship lengths after the stern of the ship, case 41c, where the centerline amplitude reaches its peak, a triple-lobe pattern with a sharp peak and two shallow troughs appears as shown in figure 8(a); its vertical velocities are shown in figure 8(b), which, with a little shift, is similar to the triple-lobe distribution, and has an almost zero velocity at the central point as intended. It was suggested by Tulin & Miloh (1990) that the far field internal wave pattern may be calculated upon the assumption that the far field wave pattern originates from the initial conditions represented in the triple lobed pattern. In that case, they showed that the entire far field may be represented by a complex amplitude function, which is readily calculated from a Fourier transform of the triple lobed pattern, amplitudes and velocities.

This calculation has been carried out here, see figure 9. The real part of the transform of the triple-lobe amplitudes, centers at kh around one and decreases slowly in each direction, case 41c; the imaginary part, originating from the vertical

velocities in the triple-lobe pattern, has an infinite value at kh equal to zero and decreases fast when kh increases. The modulus of these two parts composes the amplitude function which can be used together with the far field kinematic pattern to represent the far field internal wave field.

In figure 10, downstream wave cuts at increasing transverse distance, y/D, are shown from two different calculations together with experimental data: the current direct numerical calculation, and the far field calculation using the calculated amplitude function. We get very good agreement between the two kinds of calculations, and generally good agreement with the experimental data.

More simulations are carried out for a densimetric Froude number around five and for different depths of pycnoclines. Results are shown from figure 7 to figure 10. It is seen that, very good agreement is also obtained for case 41(b) between current direct calculation and the calculation using the far field theory for both the kinematic wave pattern and wave amplitudes. With the success of the calculation of the amplitude function and the confirmation of the far field theory, in the case 28(b) and 25(c) we halted the direct calculation at the triple-lobe pattern, and then calculated the amplitude function, used it to predict the far field internal wave pattern using the far field theory.

A detailed comparison of the results is shown in Figure 10(a) to (d). In 10(a) and (b) very good agreement is seen between the present numerical far field calculations (−·−) and predictions made from the analytical theory of Tulin and Miloh based on amplitude functions computed from triple-lobed patterns calculated numerically using the present theory (······). This agreement suggests that
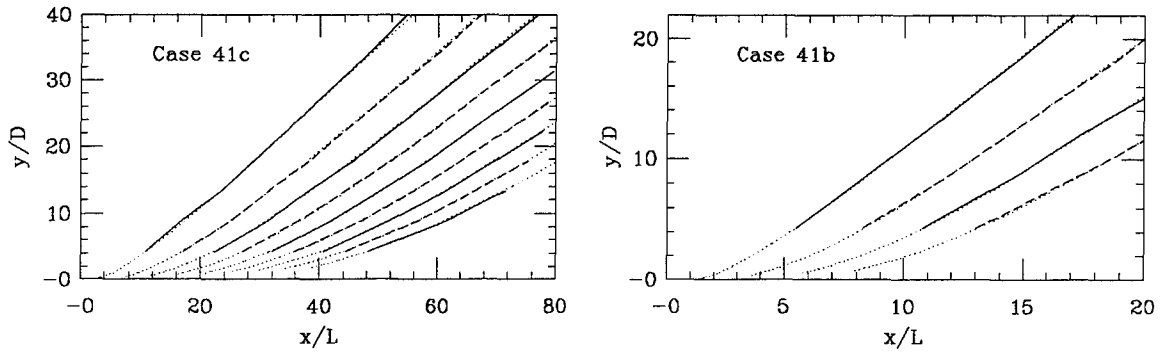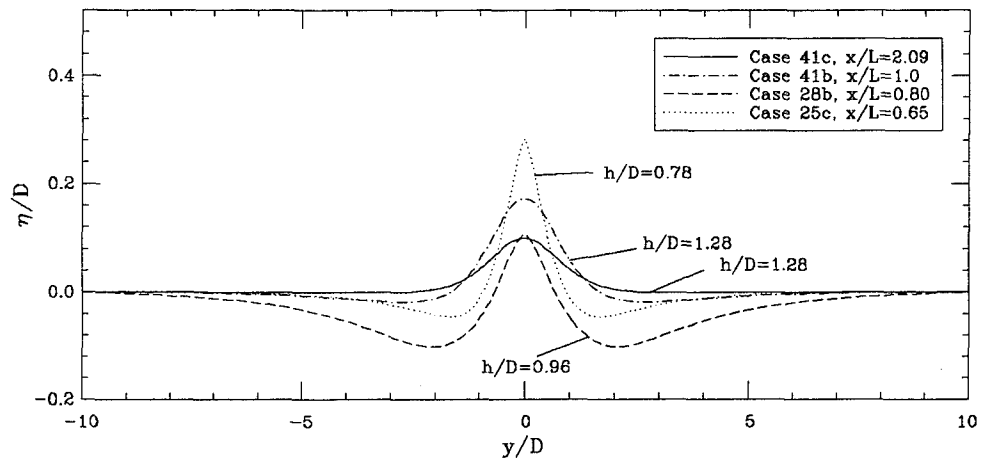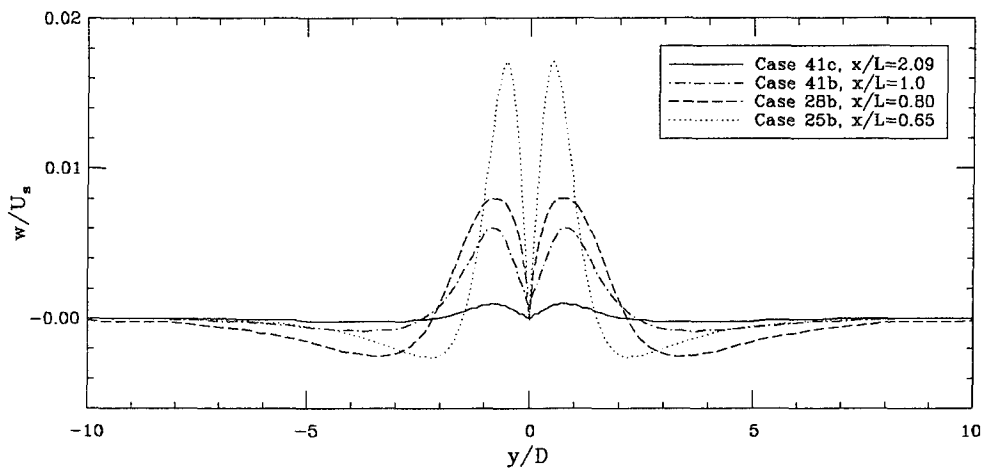
Figure 7 : Far Field Phase Lines. ——, Crests, – · – , Troughs, Both from Direct Numerical Calculations ; ······ , Crests and Troughs, from Far Field Theory.

(a) Amplitudes

(b) Vertical Velocities

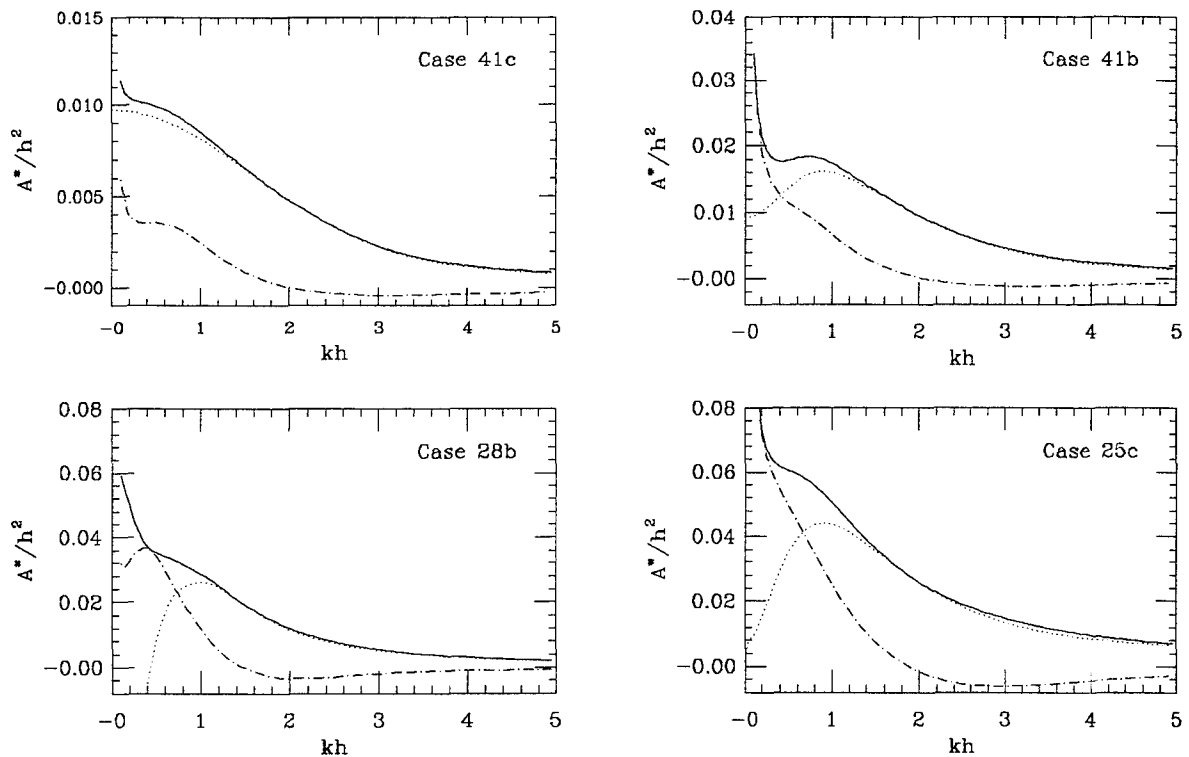Figure 8 : Triple-Lobe Patterns in the Near Field Wake.

Figure 9 : Far Field Amplitude Functions.

these detailed numerical calculations need only be carried out in the near field aft to the triple-lobe, providing that the waves are sufficiently small.

The experimental results (——) shown for comparison have been obtained in a small stratified tank using a towed model 45cm long (Ma & Tulin, 1992). The effects of the turbulent wake of the model are evident in the roughness of the wave patterns close to the model track and sufficiently aft. The amplitudes found in the experiments and predicted theoretically are, in general, comparable —— there certainly exists no major discrepancies in magnitudes, although a tendancy for theory to underpredict seems present; it must be kept in mind that the turbulent wake is not modeled here. In general, the agreement improves for cuts at the center of the larger transverse distances. A comparison of both theory and experimental measurements at much larger scales would be highly desireable.

A kh-map is shown in figure 11, in the case of 41b, which gives a clear view of the distribution of wave lengths in the patterns, and is helpful when far field wave amplitudes are analyzed using the amplitude function.

The CPU time needed for calculation in the near field to the triple-lobe pattern is only around 265 seconds, and for far field calculation to 80 ship lengths in case 41c, 371 minutes. All these calculations have been carried out on an IBM 9000.

303

Figure 10(a) : Longitudinal Wave Cuts at Transverse Distances from the Ship, Case 41c,
from y/D = 4.35 to y/D = 40.35 in intervals of Δy/D = 4.5 , Where
——— , Experimental Data, – · – , Direct Calculation Using Current Theory,
······ , Results From Far Field Theory Using Triple-Lobe Pattern From
Direct Calculation

Figure 10(b) : Longitudinal Wave Cuts at Transverse Distances from the Ship, Case 41b,
from y/D = 4.35   to   y/D = 40.35   in intervals of Δy/D = 4.5 , Where
—— , Experimental Data, – · – , Direct Calculation Using Current Theory,
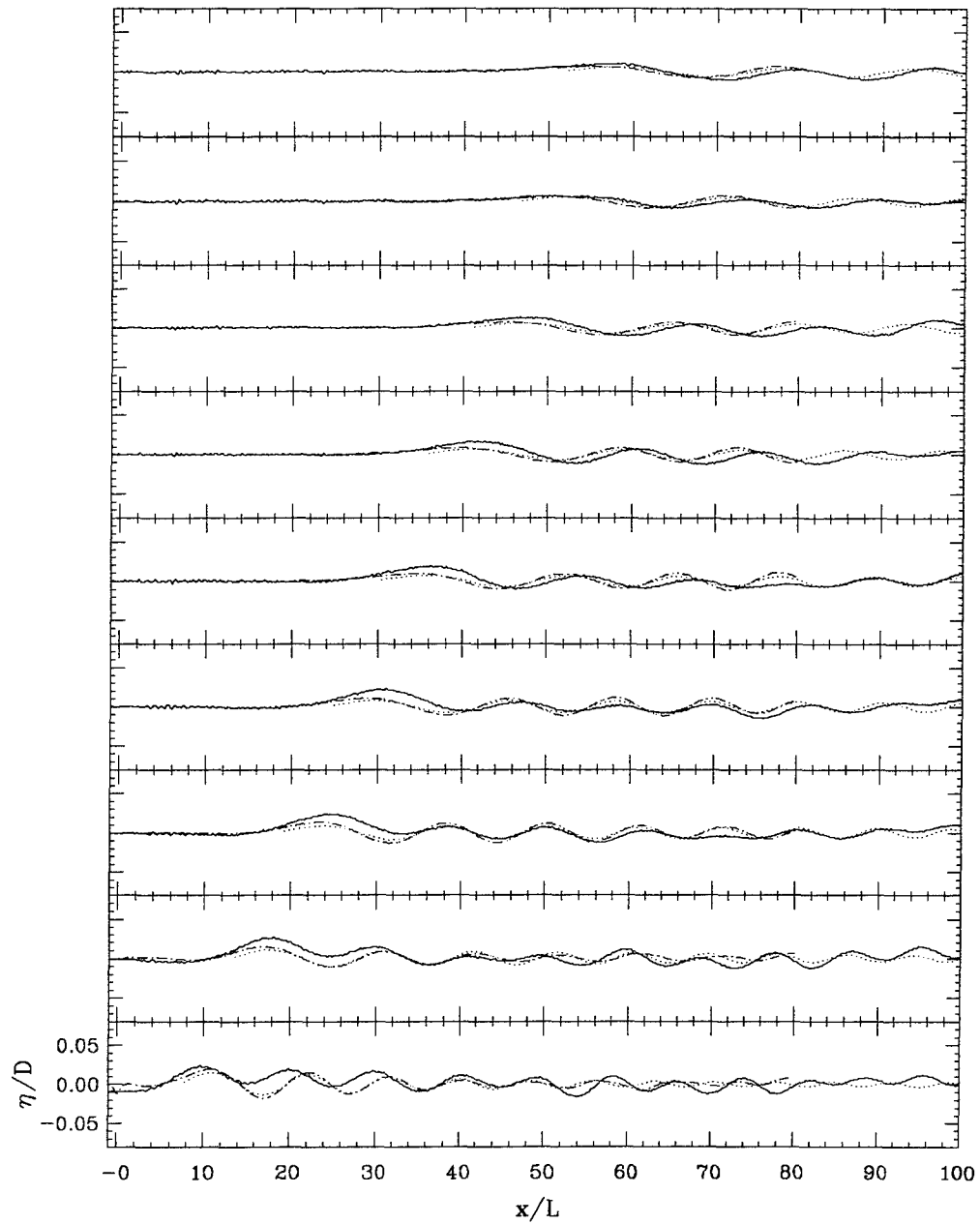······ , Results From Far Field Theory Using Triple-Lobe Pattern From
Direct Calculation
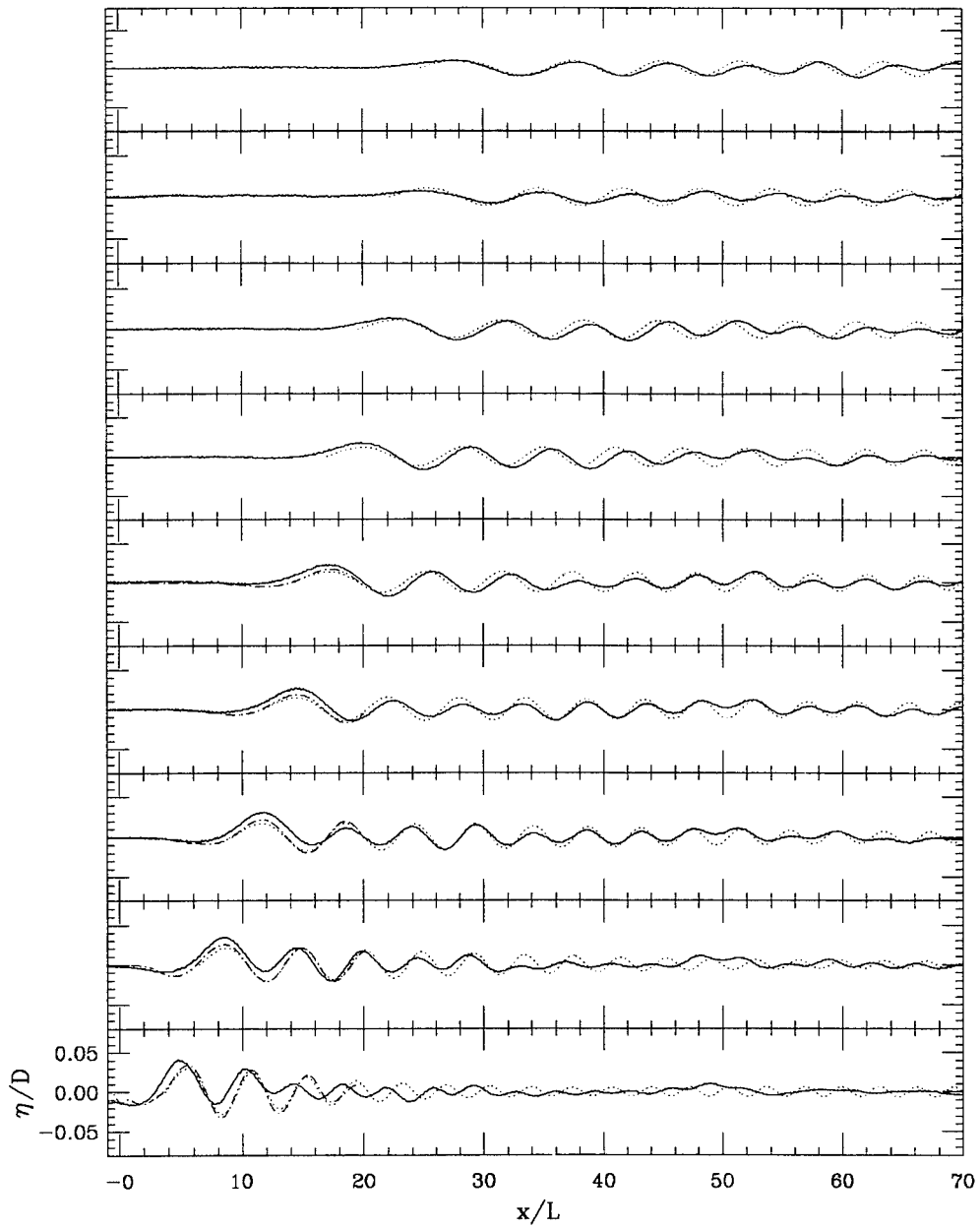
Figure 10(c) : Longitudinal Wave Cuts at Transverse Distances from the Ship, Case 28b,
from y/D = 5 to y/D = 32 in intervals of $\Delta y/D = 4.5$, Where
—— , Experimental Data, ······ , Results From Far Field Theory Using
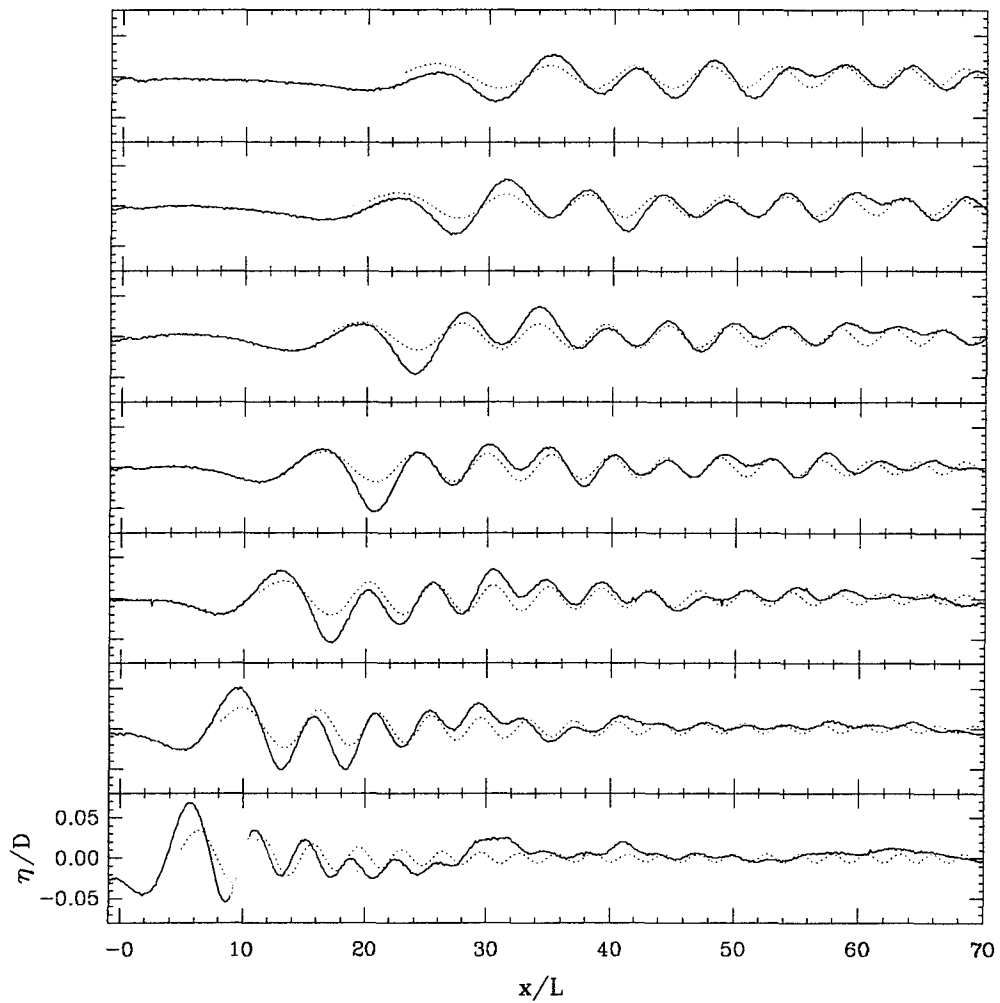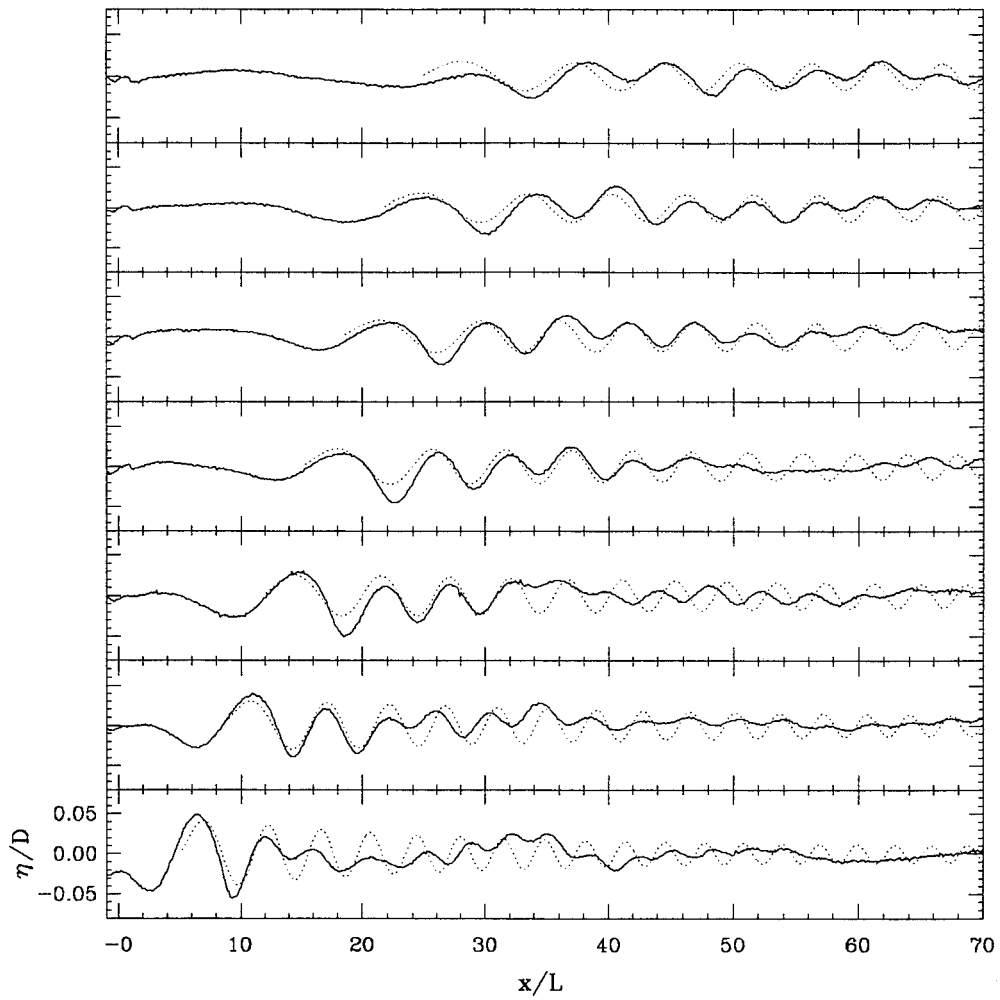Triple-Lobe Pattern From Direct Calculation

Figure 10(d) : Longitudinal Wave Cuts at Transverse Distances from the Ship, Case 25c
from y/D = 5 to y/D = 32 in intervals of Δy/D = 4.5 , Where
—— , Experimental Data, ······ , Results From Far Field Theory Using
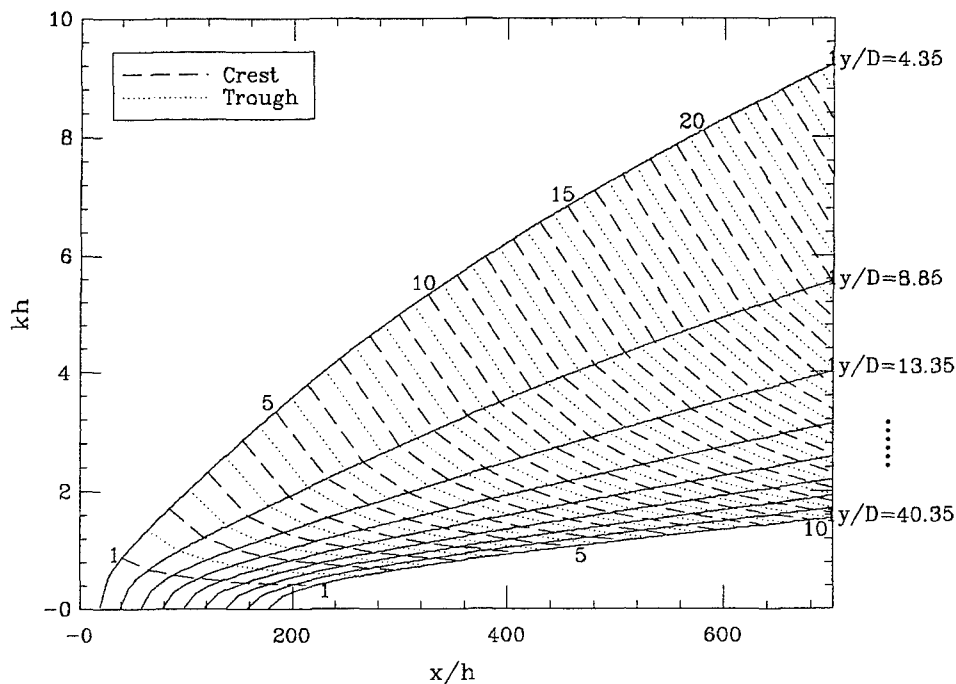Triple-Lobe Pattern From Direct Calculation

307

Figure 11 : a Typical kh-map of the Far Field of Ship Internal Waves Showing
the Distribution of Wave Lengths in Wave Pattern and in Space

SUMMARY & CONCLUSIONS

A numerical method has been developed which is appropriate for slender bodies of arbitrary cross section traveling in a stratified ocean at sufficiently large densimetric Froude numbers, $F_h \gg 1$.

This method assumes an inviscid flow field composed of a double model flow about the ship in homogeneous water plus a perturbation flow slowly varying in the x direction and therefore 2D in the cross flow plane. The 2D cross flow is described by the Poisson equation for the cross flow stream function, where the forcing is provided by the down stream vorticity, induced by deflections of the pycnoclines. The resulting solution satisfies the boundary conditions everywhere on the ship hull. The vorticity is calculated by a marching procedure, using an algorithm based on Fridman's Equation.

The method is applicable to arbitrary density profiles in depth and to arbitrary ship cross sections, and is non-linear in the cross flow plane and allows the propagation of solitons, none of which are generated in the examples given here.

The numerical method utilizes higher order Hermite finite elements and has been convergence tested.

Total calculations have been made for four cases for which small model experimental data on

308

the far field wave pattern exist. These were taken in our own laboratory.

The present computational method predicts a far field kinematical pattern in very good agreement with the predictions of analytical far field theory.

The computations show the development in the near field of a narrow pattern of deflections behind the ship, arising from the initial reaction of the pycnoclines to the depression by the ship hull. These deflections in the wake on the ship track, are upwards and reach a peak behind the ship, at which station the cross section of the depression pattern is upwards in the center and downwards on either side. The triple lobe pattern was originally discovered by Tulin & Miloh, 1990.

Far field amplitudes deduced from the analytic theory of Tulin & Miloh, using an amplitude function calculated from the triple lobe pattern computed here, are in very good agreement with the far field fully numerical calculations.

The results found here thus tend to confirm the triple lobe pattern as the source of initiation of the far field wave pattern. This places an emphasis on the calculation of the near field, and reduces the computing time by orders of magnitude.

The magnitude of computed wave amplitudes are in good general agreement with our experimental results, with same tendency for theory to underpredict, and for detailed comparisons to improve with increasing transverse distance from the ship.

Considering the influence which the turbulent wake might be expected to have on the flow in the direct wake of the ship, the agreement between small scale theory and these numerical predictions must be regarded as very good.

Additional comparisons with large scale experiments would be highly desireable.

ACKNOWLEDGEMENT

REFERENCES

Ekman, V. W., 1904. On Dead Water. *The Norwegian North Polar Expedition 1893-1896*, vol. V, Ch. XV, Christiania

Havelock, T. H. "The Collected Papers of Sir Thomas Havelock on HYDRODYNAMICS," *ONR/ACR-103*, pp. 377-389

Keller, J.B. & Munk, W. H., 1970, "Internal Wave Wakes of a Body in a Stratified Fluid", *Physics of Fluid*, Vol. 13, pp.1425-1431

Kochin, N. E., Kibel, I. A. & Roze, N. V., "Theoretical Hydromechanics," 1948

Ma, H & Tulin, M. P., 1993. "Experimental Study of Ship Internal Waves : The Supersonic Case", *Journal of OMAE* , Vol. 115, No.1, pp. 16-22.

Ma, H. , 1993. Dissertation, OEL, UCSB

Miloh, T. & Tulin, M. P., 1988. "a Theory of Dead Water Phenomena," *Proc. of the 17th Symposium on Naval Hydrodynamics*, National Academy Press, 1988

Miloh, T., Tulin, M. P. & Zilman, G., 1992. "Dead-Water Effects of a Ship Moving in Stratified Seas", *Proc. of the 11th Intl Conf. on OMAE, 1992*, Vol I, Part A, pp. 59-67

Phillips, O. M., Dynamics of the Upper Ocean, Cambridge, 1969.

Tulin, M. P. & Miloh, T., 1990. "Ship Internal Waves in a Shallow Thermocline: the Supersonic Case", *Proc. of the 18th Symposium on Naval Hydrodynamics*, National Academy Press, 1990

Wong, H. L. & Calisal S. M., 1992. "Waves Generated by a Ship Travelling in Stratified Water," Proc. of the 3rd Intl. Offshore & Polar Engr. Conference, 1993

Yih, C. S., "Patterns of Ship Waves," Engineering Science, Fluid Dynamics, World Scientific Publishers, 1990.

SESSION 6

WAVY/FREE-SURFACE FLOW:
VISCOUS-INVISCID INTERACTION

Displacement Thickness of a Thick 3-D Boundary Layer

L. Landweber, A. Shahshahan, and R.A. Black

(University of Iowa and Loras College, USA)

ABSTRACT

Thin-boundary-layer solutions for displacement thickness were published in the fifty's. More recently, semi-empirical methods of computing displacement thickness were developed in connection with interactive methods of computing viscous flows about bodies. In the present work, the determination of the displacement thickness is recognized as a member of the class of "ill-posed problems" (IPP), in which small or random errors in the data defining a problem result in much larger errors in its solution. Otherwise, the displacement thickness of a given viscous flow can be well-defined mathematically by generalizing the thin-boundary-layer solution. Rational solutions can then be obtained by applying the suggestions for controlling growth of errors given in the IPP literature.

The theory assumes that, exterior to a boundary layer, the flow is irrotational, that this irrotational flow can be continued into the boundary-layer region, and that this flow is singularity-free in that region. That is accomplished by means of a Fredholm integral equation of the first kind which, appropriately is a classical example of an IPP. The procedure is illustrated by applying it to a Wigley form.

INTRODUCTION

We suppose that a given double body of a ship form is at rest in a uniform stream U_∞ of an incompressible fluid parallel to its centerplane, and that the vector velocity field $\underline{v}$ of the mean flow within the boundary layer and wake (BLW) of the ship form is known. Outside the BLW, we assume that the mean flow $\underline{v}$ is irrotational and coincides there, with a small error, with an irrotational vector $\underline{V}$ which may be continued as an irrotational velocity field $\underline{V}$ into the BLW. Let S_3 be a member of the family of viscous-flow stream surfaces, lying exte-

rior to the BLW, of which the body itself, S_0 is the defining member. Then S_3 also defines a different family of irrotational flow stream surfaces of $\underline{V}$ extending into BLW. The displacement-thickness surface S_1 is defined as that member of the latter family which satisfies the flux condition that the flux of $\underline{v}$ between S_0 and S_3 is equal to the flux of $\underline{V}$ between S_1 and S_3. See Fig. 1.

If S_2 is another surface, not necessarily a stream surface, but closer to the edge of BLW, S_2 may replace S_3 in the above definition of S, since we assume $\underline{v} = \underline{V}$ between S_2 and S_3. The above definition implicitly assumes that $\underline{V}$ is singularity-free in the space between S_1 and S_2, except for a surface distribution on the centerplane of the wake. If that condition is not satisfied, then an exact solution for S_1 does not exist, although useful, approximate solutions may be found.

If the body has a well-defined stagnation point, the dividing streamline would be, by symmetry, a straight line, generating the given body in the viscous flow and S_1 in the irrotational flow. This is seen to satisfy the flux condition, since, far upstream, the velocity fields of $\underline{v}$ between S_0 and S_3 and of $\underline{V}$ between S_1 and S_3, coincide. See Fig. 1.

Moore [1] and Lighthill [2] have treated the present subject for thin boundary layers. Both defined the displacement-thickness surface S_1 as a stream surface, but neither introduced a flux condition. Moore terminated his analysis with a first-order partial differential equation (PDE) for the displacement thickness, derived from the stream-surface condition, the equations of continuity, and the thin boundary-layer approximations. Lighthill rederived Moore's equations, but also obtained explicit solutions for the displacement thickness and the equivalent source distribution on the body surface. Lighthill assumed that the stream surface of $\underline{V}$ which passes through the stagnation point(s) is the displacement-thickness surface. This assumption which is also made in the present work, can be

justified for symmetric flows about double models without a free surface, because then a free-surface boundary layer and wavebreaking are not present ahead of the bow and the stagnation points are well-defined.

In Stern, Yoo and Patel [3] an interactive method of computing the viscous flow about a 3-D body, involving displacement thickness, was developed. Beginning with an assumed first approximation, a succession of displacement bodies and the corresponding irrotational- and viscous-flow fields were computed iteratively. In that work, each transverse section of the S_1-surface was assumed to be an ellipse of dimensions satisfying approximately a mean, local flux condition. Nevertheless, their viscous-flow results were in good agreement with experimental data and those computed by a large-domain method.

At the request of Fred Stern (FS), the present work was undertaken by Landweber (LL). It will be seen that an important phase of the project is the calculation of the continued irrotational flow into the boundary layer and wake (BLW). For that purpose, a method using a Fredholm integral equation of the first kind for determining the source distribution on the surface of the body equivalent to the displacement effect of the boundary layer, was proposed by LL and FS assigned an M.S. candidate, RA Black, to work with LL on the validation of the procedure. After verifying that the equivalent source distributions could be obtained with sufficient accuracy, the next step was to calculate the irrotational velocity field of the sources. For that purpose, a complicated Hess-Smith computer program [4] for the velocity field of a source distribution of constant strength on a flat quadrilateral panel was available; but, by transforming the integrals to ones over the centerplane of the body the projected panels became rectangular, and the integrals could be expressed more simply in closed form in terms of elementary functions. Since these results may be new and useful, they will be presented here.

Equivalent source distributions are of interest not only for calculating the effects of waves on the boundary layer of a ship, but also for the effects of the boundary layer on the wavemaking of a ship form. This was shown for the Weinblum very thin form by Kang [5] and by Shahshahan and Landweber [6] for the Wigley form, both using equivalent centerplane distributions. It will be of interest to calculate the wave-making resistance of the Wigley form using the present results for the equivalent source distribution on the body surface, although this is not done in the present work.

Here we shall derive a generalized version of Moore's partial differential equation, without applying the thin-boundary-layer approximations. Since the only application planned was to the

Wigley form, it seemed most convenient to work in rectangular Cartesian coordinates, although the generalized PDE had also been derived in nonorthogonal coordinates. The PDE was then solved by a method of finite differences, using a method suggested by Lax [7].

The plan of the present work is as follows:

1. Obtain a source distribution on the body surface y_0 and the centerplane of the wake as the numerical solution of an integral equation of the first kind, using given data for the viscous-flow velocity field exterior but close to the edge of the boundary layer.

2. Apply that source distribution to compute the irrotational velocity field within the boundary layer and wake.

3. Apply the irrotational and viscous-flow velocity fields to compute the auxiliary displacement thicknesses α and β defined in Eq. (4). Also compute the derivatives of the velocity components at y_0 occurring in Eq. (11).

4. Use method of finite differences to solve the partial differential equation (10) and (11) for δ_1, defined in (4).

NATURE OF THE PROBLEM

Let us suppose that the edge of the BLW is defined by a contour surface at $H = 0.990\ H_\infty$, where H denotes the total head at the contour and H_∞ the asymptotic value of the total head at great distances upstream or lateral to the body. Had H been defined by $H = 0.995\ H_\infty$, the edge of the BLW would be much farther from the centerplane and the error in assuming irrotational flow there would be reduced, but the accuracy of analytical continuation of that flow into the BLW region would be greatly diminished. Indeed, the procedure adopted here to continue the potential flow strongly suggests that the present work is on an "ill-posed problem," in which small or random errors in the data defining a problem results in much larger errors in its solution, as defined by Tikhonov and Arsenin in [8].

The simplest case of an ill-posed problem is a set of linear, algebraic equations, $A\underline{x} = \underline{b}$, where A is a matrix and x and b are vectors. This has an exact solution when the A is nonsingular (i.e. its determinant is not zero); but if A is nearly singular and the right member is subject to errors, the resulting errors in the solution would be amplified. Another classic case is the Fredholm integral equation of the first kind, which, in general does not

have an exact solution. If discretized by means of a quadrature formula, this case reduces to the previous one, yielding approximate solutions with possibly large errors.

The literature on ill-posed problems presented in [8] indicates that it is possible to get useful results by use of supplementary information, such as requiring smoothness of the solution, or by a process called "regularization" developed by Tikhonov in a series of six papers from 1963-65. The method of constructing approximate solutions is called the "regularization method." This method requires finding or constructing a regularization operator which transforms the equation of the ill-posed problem so that approximate, stable solutions (i.e. solutions without error amplification) could be found. Construction of this operator appears to be a difficult task. Twelve years prior to Tikhonov's work on this concept, Landweber [9] had shown that the integral operator of an integral equation of the first kind transforms the equation into one with a symmetric kernel with which stronger convergence properties of an iteration formula could be proved. In that sense, the original operator of the ill-posed problem could serve as a regularization operator. Reference [9] is not included among the 221 papers listed in the Bibliography of [8].

FORMULATION OF STREAM-SURFACE EQUATIONS

The equation of continuity and the stream-surface equation will now be applied to generalize the thin boundary-layer treatments of Moore [1] and Lighthill [2] for a double ship form. Let (x,y,z) denote a rectangular Cartesian coordinate system with origin at the forward stagnation point, the x-axis parallel to the uniform stream and positive in the downstream direction, with the x- and z-axes lying in the vertical centerplane, and the z-axis positive upwards. Let (u,v,w) and (U,V,W) denote the components of $\underline{v}$ and $\underline{V}$. Also let $y = y_0(x,z)$, $y = y_1(x,z)$, $y = y_2(x,z)$ denote the equations of a given hull surface S_0, its displacement thickness surface S_1 and a surface S_2, near but exterior to BLW, respectively. At S_0, the velocity components will be designated by

$$\underline{V}_0 = \underline{V}(x,y_0,z) = \hat{i}U_0 + \hat{j}V_0 + \hat{k}W_0$$

where $\hat{i}, \hat{j}, \hat{k}$ denote unit vectors in the x,y,z-directions; and there, by the nonslip condition,

$$\underline{v}_0 = \underline{v}(x,y_0,z) = \hat{i}u_0 + \hat{j}v_0 + \hat{k}w_0 = 0 \tag{1}$$

Since $\underline{V}$ is irrotational, we have

$$\nabla \times \underline{V} = 0, \qquad \nabla^2 \underline{V} = 0 \tag{2}$$

and on S_2, we assume

$$u_2 = U_2, v_2 = V_2, w_2 = W_2 \tag{3}$$

We also define the three auxiliary displacement thicknesses

$$\delta_1 = y_1 - y_0, \qquad \alpha = \frac{1}{U_\infty} \int_{y_0}^{y_2} (U - u) dy,$$

$$\beta = \frac{1}{U_\infty} \int_{y_0}^{y_2} (W - w) dy \tag{4}$$

These definitions of α and β assume that V and W are singularity-free for $y_0 \leq y \leq y_2$. We also assume that α and β are of the order $O(\delta_1)$ for a body of unit length.

The equations of continuity for $\underline{v}$ and $\underline{V}$ are

$$\frac{\partial u}{\partial x} + \frac{\partial v}{\partial y} + \frac{\partial w}{\partial z} = 0 \quad \frac{\partial U}{\partial x} + \frac{\partial V}{\partial y} + \frac{\partial W}{\partial z} = 0 \tag{5}$$

Then, integrating equations (5) with respect to y from y_0 to y_2, taking their difference and applying (1) and (3), we obtain

$$V_0 = \int_{y_0}^{y_2} \left[\frac{\partial}{\partial x}(U - u) + \frac{\partial}{\partial z}(W - w) \right] dy \tag{6}$$

or, applying (4) and the Leibnitz rule for the derivative of an integral, we get

$$V_0 = U_\infty(\alpha_x + \beta_z) + U_0 y_{0x} + W_0 y_{0z} \tag{7}$$

where subscripts x and z denote partial differentiation with respect to the indicated variable.

The condition that the y_1 surface be a stream surface is

$$V_1 = U_1 \frac{\partial y_1}{\partial x} + W_1 \frac{\partial y_1}{\partial z} =$$

$$U_1 \frac{\partial}{\partial x}(y_0 + \delta_1) + W_1 \frac{\partial}{\partial z}(y_0 + \delta_1) \tag{8}$$

where

$$\underline{V}_1 = \underline{V}(x, y_1, z)$$

315

Since the y_1 surface is unknown, we transfer (8) to the known surface y_0 by means of the Taylor expansions

$$U_1 \doteq \left[U + \delta_1 U_y + \frac{1}{2} \delta_1^2 U_{yy} \right]_0$$

$$V_1 \doteq \left[V + \delta_1 V_y + \frac{1}{2} \delta_1^2 V_{yy} \right]_0$$

$$W_1 \doteq \left[W + \delta_1 W_y + \frac{1}{2} \delta_1^2 W_{yy} \right]_0$$

which, substituted into (8), gives

$$\left[V + \delta_1 V_y + \frac{1}{2} \delta_1^2 V_{yy} \right]_0$$

$$\doteq \left[U + \delta_1 \frac{\partial U}{\partial y} + \frac{1}{2} \delta_1^2 \frac{\partial^2 U}{\partial y^2} \right]_0 \frac{\partial}{\partial x}(y_0 + \delta_1) \qquad (9)$$

$$+ \left[W + \delta_1 \frac{\partial W}{\partial y} + \frac{1}{2} \delta_1^2 \frac{\partial^2 W}{\partial y^2} \right]_0 \frac{\partial}{\partial z}(y_0 + \delta_1)$$

By substituting for V_0 from (7), replacing V_y by $-U_x - W_z$, V_{yy} by $-V_{xx} - V_{zz}$ and neglecting the δ_1^3 terms, we obtain

$$(P_x + Q_z)_0 \doteq R(x, z, \delta_1) \qquad (10)$$

where

$$R = -\left[\delta_1 \left(y_{0x} U_y + y_{0z} W_y \right) + \frac{1}{2} \delta_1^2 \left(y_{0x} U_{yy} \right. \right.$$

$$\qquad (11)$$

$$\left. \left. + y_{0z} W_{yy} \right) \frac{1}{2} \frac{\partial}{\partial x} \left(\delta_1^2 U_y \right) + \frac{1}{2} \frac{\partial}{\partial z} \left(\delta_1^2 W_y \right) \right]_0$$

and

$$P(x,z) = U \delta_1 - U_\infty \alpha, \quad Q(x,z) = W \delta_1 - U_\infty \beta$$

Here the left member is clearly of order $O(\delta_1)$. The first term of the right member also seems to be of order $O(\delta_1)$; but, as will be seen, computationally, its effect is that of a second-order term, and the remaining terms are of even higher order, at least for the Wigley form. We also observe that the homogeneous form of (11) when $R = 0$, is essentially Moore's partial differential equation expressed in rectangular, Cartesian coordinates.

CONTINUATION OF OUTER IRROTATIONAL FLOW INTO BOUNDARY LAYER

Source Distribution on Body

Let Φ denote the velocity potential of the irrotational flow about the displacement body in a uniform stream and ϕ that of the disturbance potential. Then

$$\Phi = \phi + U_\infty x \qquad (12)$$

and V, the y-component of $\underline{V}$, is given by $v = \dfrac{\partial \phi}{\partial y}$ in the exterior of BLW according to (3). Since $\underline{v}$ is given, grad Φ is known on y_2, but we shall require only V.

We assume that potential flow ϕ is generated by a source distribution $\sigma(x_Q, z_Q)$ on the hull surface y_0 and the centerplane of the wake may be written as

$$\phi(P) = -\int_{S_Q} \frac{\sigma(Q)}{r_{PQ}} dS_Q \qquad (13)$$

where P denotes a point exterior to BLW and r_{PQ} the distance between points P and Q,

$$r_{PQ} = \left[\left(x_P - x_Q \right)^2 + \left(y_P - y_Q \right)^2 + \left(z_P - z_Q \right)^2 \right]^{1/2}$$

Then, differentiating with respect to y_P, we obtain

$$V_P = -\int_{S_Q} \sigma(Q) \frac{\partial}{\partial y_P} \left(\frac{1}{r_{PQ}} \right) dS_Q =$$

$$\qquad (14)$$

$$\int_{S_Q} \sigma(Q) \frac{y_P - y_Q}{r_{PQ}^3} dS_Q$$

a Fredholm integral equation of the first kind.

By applying a quadrature formula of order N, (14) can be reduced to a set of N linear equations for σ_Q, i=1,2...N which can be solved by a computer using available software. It is well known, however, that small changes in V_P in (14) may cause large changes in σ_Q when the set of linear equations is nearly singular; i.e. when the determinant of the coefficients is nearly zero. This was verified in several test cases in which the velocity was computed at points exterior to a body due to an assumed source distribution on the surface of the

body. Then the relation between the source distribution and the velocity was treated as an integral equation of the first kind to try to recover the source distribution. This preliminary work yielded the conclusions that double precision should be used and that an iteration formula for integral equations of the first kind due to Landweber [9] yielded useful results even when a linear-equation solver had failed.

In order to derive the convergence properties of the iteration formula of [9], the original kernel of the integral equation was transformed into a symmetric one. Since that requires a large number of additional integrations for a 3-D problem, it is customary to assume that the iteration formula with the original kernel would have similar convergence properties. In general, integral equations of the first kind do not have exact solutions, but a sequence of approximate solutions can be found which converges in the mean, i.e. the integral of squares of the errors becomes very small. In practice, the successive approximations are monitored so that the sequence can be stopped when the errors are as small as desired, or, in case of initial convergence and then divergence, when the errors begin to grow. An important difference between the preliminary tests of the integral equation method on a Wigley form and a calculation of the unknown function is that, in the former case, the exact solution was known, and, in the latter case, the existence of a solution was uncertain.

The equation of the Wigley form for which results were computed is

$$y_0 = \pm \frac{bx}{\ell^2}(2\ell - x)\left(1 - \frac{z^2}{h^2}\right) \qquad (15)$$

Here the body length is $L=2\ell$, b is half the beam and h is the draft. We take $L = 1$, $b = 0.10\ell$ and $h = 0.125\ell$. The limits of integration of the integral in (14) are taken to extend over the double body and over the centerplane of the wake for an additional ship length L and for z varying from -h to +h. The integral in (14) may then be written as

$$\int_0^{2L} \int_{-h}^{h} \mu(Q) \frac{y_P - y_{0Q}}{r_{PQ}^3} dx_Q dz \qquad (16)$$

$$\mu(Q) = \sigma(Q)\left[1 + y_{0x}^2 + y_{0z}^2\right]^{1/2}$$

Since $\mu(Q)$ is the same in the four quadrants of a transverse section, the four terms with $y_Q \neq 0 (0 < x < L)$ and the two terms with $y_Q = 0$ $(L \leq x \leq 2L)$ can be collected into a single expression

for integration over the first quadrant of Q's for any point P in the first quadrant,

$$V_P = \int_0^{2L} \int_0^{h} \mu(Q)K(P,Q)dx_Q dz_Q \qquad (17)$$

where

$$K(P,Q) = \lambda\left[\frac{y_P - y_{0Q}}{r_{1PQ}^3} + \frac{y_P + y_{0Q}}{r_{2PQ}^3} + \frac{y_P + y_{0Q}}{r_{3PQ}^3} + \frac{y_P - y_{0Q}}{r_{4PQ}^3}\right]$$

with $\lambda=1$ when $y_Q \neq 0$ and $\lambda = 1/2$ when $y_Q = 0$, and

$$r_{1PQ}^2 = \left(x_P - x_Q\right)^2 + \left(y_P - y_{0Q}\right)^2 + \left(z_P - z_Q\right)^2$$

$$r_{2PQ}^2 = \left(x_P - x_Q\right)^2 + \left(y_P + y_{0Q}\right)^2 + \left(z_P - z_Q\right)^2$$

$$r_{3PQ}^2 = \left(x_P - x_Q\right)^2 + \left(y_P + y_{0Q}\right)^2 + \left(z_P + z_Q\right)^2$$

$$r_{4PQ}^2 = \left(x_P - x_Q\right)^2 + \left(y_P - y_{0Q}\right)^2 + \left(z_P + z_Q\right)^2$$

The integral in (17) may be interpreted as extending over the centerplane; although $y_0(x,z)$ is not replaced by zero, i.e. the unknown source distribution is still on the body. Adopting the iteration formula of [9], but with the original kernel, we obtain

$$\mu_P^{(n+1)} = \mu_P^{(n)} + C\left[V_P - \int_0^{2L} \int_0^{h} \mu_Q^{(n)}K(P,Q)dx_Q dz_Q\right] \qquad (18)$$

Here P and Q have the coordinates (x_P, y_P, z_P) and $(x_Q, y_0(x_Q, z_Q), z_Q)$, and V_P and the integral are functions of the coordinates of P. Hence, in the present coordinate system we must take (x_P, z_P) and (x_Q, z_Q) as the same array of numbers and interpret the iteration as giving a corrected source distribution at the same points Q. "C" is a constant, selected so as to accelerate the convergence. To initiate the iteration, the selected value of $\mu_Q^{(1)}$, suggested by slender-body theory is

$$\mu_Q^{(1)} = \frac{U_\infty}{4\pi}\left(1 - \frac{x}{\ell}\right)\left(1 - \frac{z^2}{h^2}\right), \quad 0 < x < L$$

$$\mu_Q^{(1)} = 0, L \le x \le 2L \tag{19}$$

Equation (18), discretized by the panel method of the next section, becomes

$$\mu_P^{(n+1)} = \mu_P^{(n)} + C\left[V_P - \Sigma_{x_i}\Sigma_{z_j}\mu_{ij}^{(n)}K_{ij}\Delta x_i \Delta z_i\right] \tag{20}$$

results, obtained with 70 values of x and 13 values of z, with C=1, are shown in Figures 2, 3a and 3b.

Velocity Field of a Source Distribution

The basic PDE given in (10) and (11) requires that U, V, W, and their first two derivatives with respect to y at y_0, be calculated. Also, $\alpha(x, y_0, z)$, and $\beta(x, y_0, z)$ defined in (4), and α_x and β_z at y_0 must be computed. To obtain the latter quantities, the irrotational flow field within the region bounded by y_0 and y_2 is needed.

Hess, J.L. and Smith, A.M.O. [9] have furnished a formulation for calculating the velocity field for a flat quadrilateral panel on which a source distribution of constant strength is distributed. For forms such as Wigley's for which the potential can be expressed in terms of rectangular panels on the centerplane, it was possible to derive a much simpler set of formulas for U, V and W, by making one additional approximation. As in [4], we assume that the panels are flat; so that the direction cosines of the normals are constant on each panel, and that σ_Q's on each panel are also constant. The additional approximation is that y_{0Q} is replaced by y_0 - value corresponding to the center of the rectangle, y_{0c}; i.e. a constant for each panel.

The velocity potential for a rectangular panel of dimensions 2a and 2b may now be written as

$$\Phi = x - \mu_c \int_{x_c-a}^{x_c+a}\int_{z_c-b}^{z_c+b} \frac{1}{r_{PQ}}dx_Q dz_Q \tag{21}$$

$$r_{PQ} = \left[(x_Q - x_P)^2 + (y_{0c} - y_P)^2 + (z_Q - z_P)^2\right]^{1/2}$$

The results for U, V, W can be readily obtained by operating on the double indefinite integral, with $\xi = x_Q - x_P$, $\mu = y_{0Q} - y_P$, $\zeta = z_Q - z_P$,

$$I(\xi,\eta,\xi) = \iint\frac{d\xi d\varsigma}{r_{PQ}}, r_{PQ} = \left[\xi^2 + \eta^2 + \varsigma^2\right]^{1/2} \tag{22}$$

Then

$$-\frac{\partial I}{\partial x_P} = \frac{\partial I}{\partial \xi} = \int\frac{d\varsigma}{r_{PQ}} = \ell n(r_{PQ} + \varsigma) \tag{23}$$

the constant of integration vanishing when the integration limits of (21) are introduced. Similarly

$$-\frac{\partial I}{\partial z_P} = \frac{\partial I}{\partial \varsigma} = \ell n(r_{PQ} + \xi) \tag{24}$$

We also have

$$-\frac{\partial I}{\partial y_P} = \frac{\partial I}{\partial \eta} = -\iint\frac{\eta}{r_{PQ}^3}d\xi d\varsigma$$

$$= \eta\varsigma\int\frac{d\xi}{r_{PQ}(\xi^2 + \eta^2)} = -\arctan\frac{\xi\varsigma}{\eta r_{PQ}} \tag{25}$$

Then, introducing the integration limits in (23), we get

$$U_{Pc} = 1 + \mu_c \ell n(r_{PQ} + \varsigma)\Big|_{x_c-a}^{x_c+a}\Big|_{z_c-b}^{z_c+b}$$

$$1 + \mu_c \ell n\frac{(r_{Pc1} + z_c - b - z_P)(r_{Pc2} + z_c + b - z_P)}{(r_{Pc3} + z_c - b - z_P)(r_{Pc4} + z_c + b - z_P)} \tag{26}$$

where

$$r_{Pc1}^2 = (x_c - a - x_P)^2 + (y_c - y_P)^2 + (z_c - b - z_P)^2$$

$$r_{Pc2}^2 = (x_c - a - x_P)^2 + (y_c - y_P)^2 + (z_c - b - z_P)^2$$

$$r_{Pc3}^2 = (x_c - a - x_P)^2 + (y_c - y_P)^2 + (z_c - b - z_P)^2$$

$$r_{Pc4}^2 = (x_c - a - x_P)^2 + (y_c - y_P)^2 + (z_c - b - z_P)^2$$

Similarly, from (25),

$$V_{PC} =$$

$$-\mu_c\left[\arctan\frac{(x_c - a - x_P)(z_c - b - z_P)}{r_{Pc1}(y_c - y_P)}\right.$$

$$+\arctan\frac{(x_c + a - x_P)(z_c + b - x_P)}{r_{PQ2}(y_c - y_P)}$$

$$-\arctan\frac{(x_c + a - x_P)(z_c - b - z_P)}{r_{PQ3}(y_c - y_P)} \tag{27}$$

$$-\arctan\frac{(x_c - a - x_P)(z_c + b - z_P)}{r_{PQ4}(y_c - y_P)}$$

and from (24),

$$W_{Pc} = \mu_c \ell n \frac{\left(r_{Pc1} + x_c - a - x_P\right)\left(r_{Pc2} + x_c + a - x_P\right)}{\left(r_{Pc3} + x_c + a - x_P\right)\left(r_{Pc4} + x_c - a - x_P\right)}$$

(28)

These expressions must be summed over all the panels for a fixed point P. Here we can again take advantage of symmetry in the y-z plane for $0<x_c<L$ to collect four terms and to collect two terms for $L<x_c<2L$ with the same μ_c.

The approximation of replacing y_Q in the integrations introduces appreciable errors in panels for points P close to a panel on y_0. Since these constitute a small percentage of the total number of panels usually used, that error may be acceptable.

Velocity distributions computed from (26, 27, 28) are shown in Fig. 4.

SOLUTION OF STREAM-SURFACE EQUATION

We can now consider a procedure for solving (10) and (11) for δ_1. Initially, the case R = 0, equivalent to Moore's PDE for thin boundary layers, was treated, i.e., with $U_\infty = 1$,

$$P_x + Q_z = R$$

$$P = U_0\delta_1 - \alpha \qquad Q = W_0\delta_1 - \beta$$

(29)

with the boundary conditions

$\delta_1(0,z) = 0$ at the bow
$\delta_{1z}(x,0) = 0$ at the waterline by symmetry
$\delta_{1z}(x,h) = 0$ at the keel by symmetry

Equation (29) was discretized by the method suggested by Lax [7]. The finite-difference formulation of (29) is

$$P_{i+1,j} = \overline{P}_{i,j} + \frac{\Delta x}{2\Delta z}\left(Q_{i,j-1} - Q_{i,j+1}\right) + \frac{\Delta x}{2}\left(R_{i,j+1} + R_{i,j-1}\right)$$

(30)

where

$$\overline{P}_{i,j} = \frac{1}{2}\left(P_{i,j+1} + P_{i,j-1}\right)$$

Here i and j denote indices for increasing values of x and z respectively. This gives a marching procedure in the x-direction. Using this formulation and

the aforementioned boundary conditions, the case R=0 was solved. Typical results are shown in Figure 5. Since R was found to be very small, its effect on the calculated values of ϕ_1 was too small to show graphically. Thus, the thin-boundary-layer approximation is very good for the Wigley form.

ACKNOWLEDGMENT

REFERENCES

1. Moore, F.K., "Displacement Effect of a Three-Dimensional Boundary Layer," NACA Report 1124, 1953.

2. Lighthill, M.J., "On Displacement Thickness," Journal of Fluid Mechanics, Vol. 4, Part 4, 1958, pp. 383-392.

3. Stern, F., Yoon, S.Y. and Patel, V.C., "Viscous-Inviscid Interaction with Higher-Order Viscous-Flow Equations," IIHR Report No. 304.

4. Hess, J.L. and Smith, A.M.O., "Calculation of Nonlifting Potential Flow About Arbitrary Three-Dimensional Bodies," Douglas Aircraft Report E.S. 40622, 1962.

5. Kang, S.-H., "Viscous Effects on the Wave Resistance of a Thin Ship," Ph.D. Thesis, The University of Iowa, July 1978.

6. Shahshahan, A. and Landweber, L., "Boundary-Layer Effects on the Wave Resistance of a Ship Model," Journal of Ship Research Vol. 34, No. 1, March 1990, pp. 29-37.

7. Lax, P.P., "Weak Solutions of Nonlinear Hyperbolic Equations and Their Numerical Computations," Communications on Pure and Applied Mathematics, Vol. 7, 1954.

8. Tikhonov, A.M. and Arsenin, V.Y., "Solutions of Ill-Posed Problems," Published by V.H. Winston & Sons, Distributed by John Wiley & Sons, New York, 1977.

9. Landweber, L., "An Iteration Formula for Fredholm Integral Equations of the First Kind," American Journal of Mathematics, Vol. 73, No. 3, July 1951.
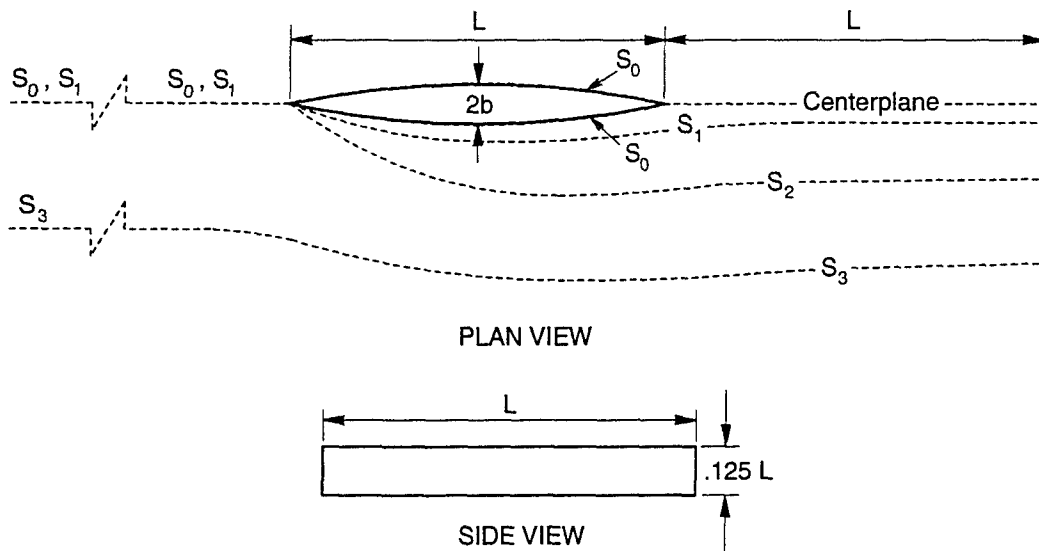
Figure 1. Sketch of Wigley hull showing stream surfaces S_0, S_1 and S_3, and a surface S_2 exterior to the BLW.
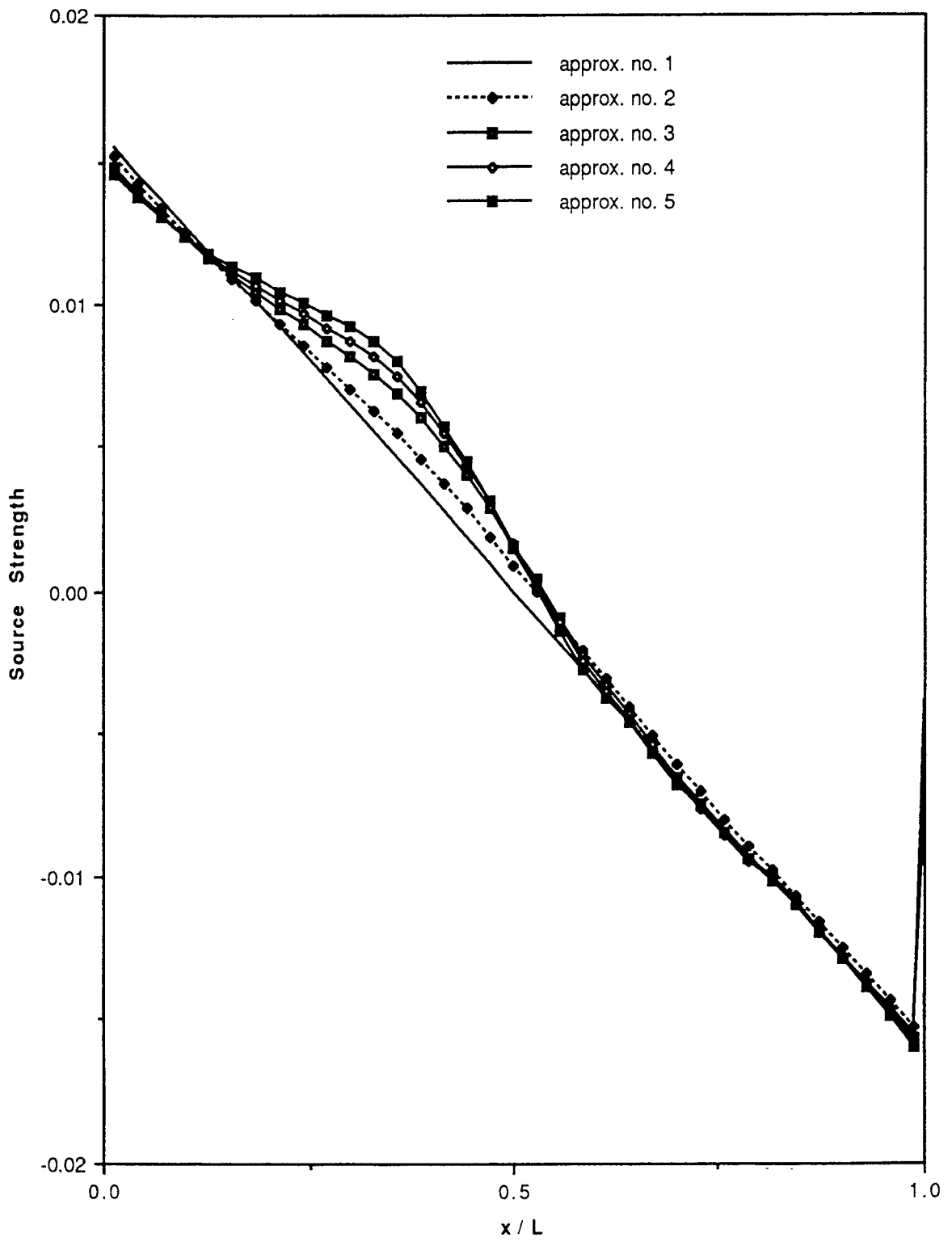
Fig. 2   Source distributions on Wigley form at various iterations at z/h =1/26
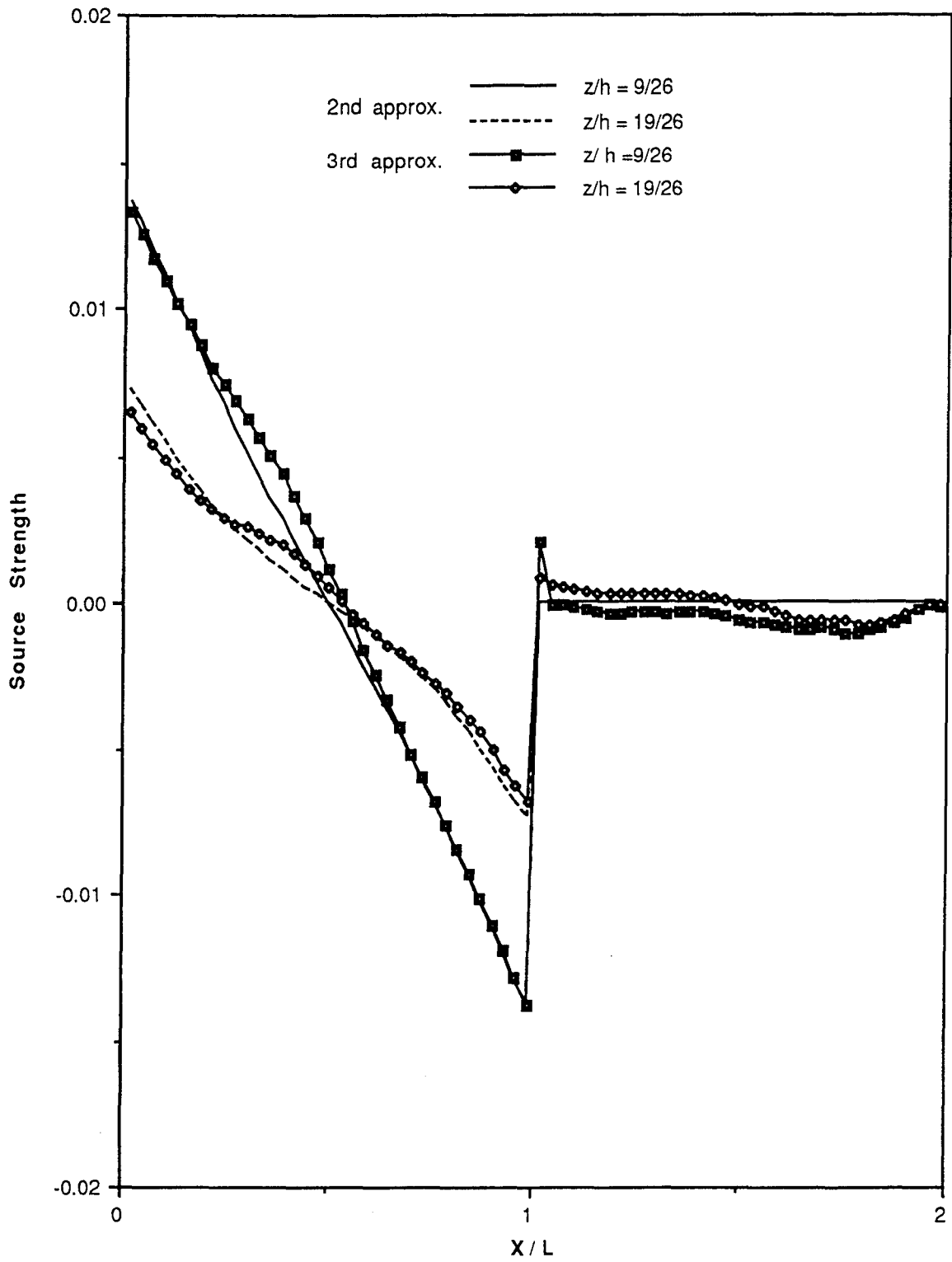
321

Fig. 3a Source distribution on Wigley form and wake centerplane
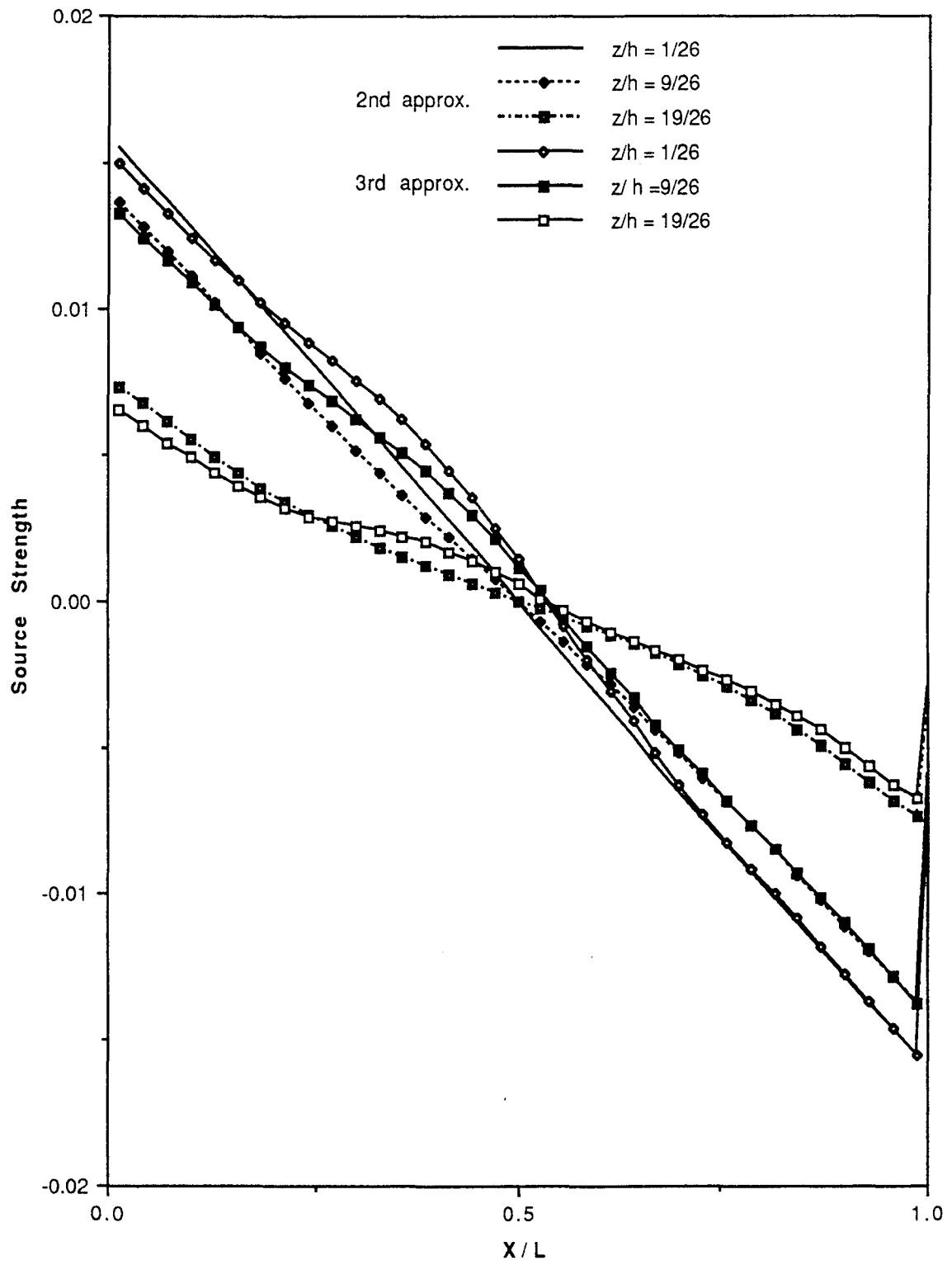at second and third approximations for two values of z/h

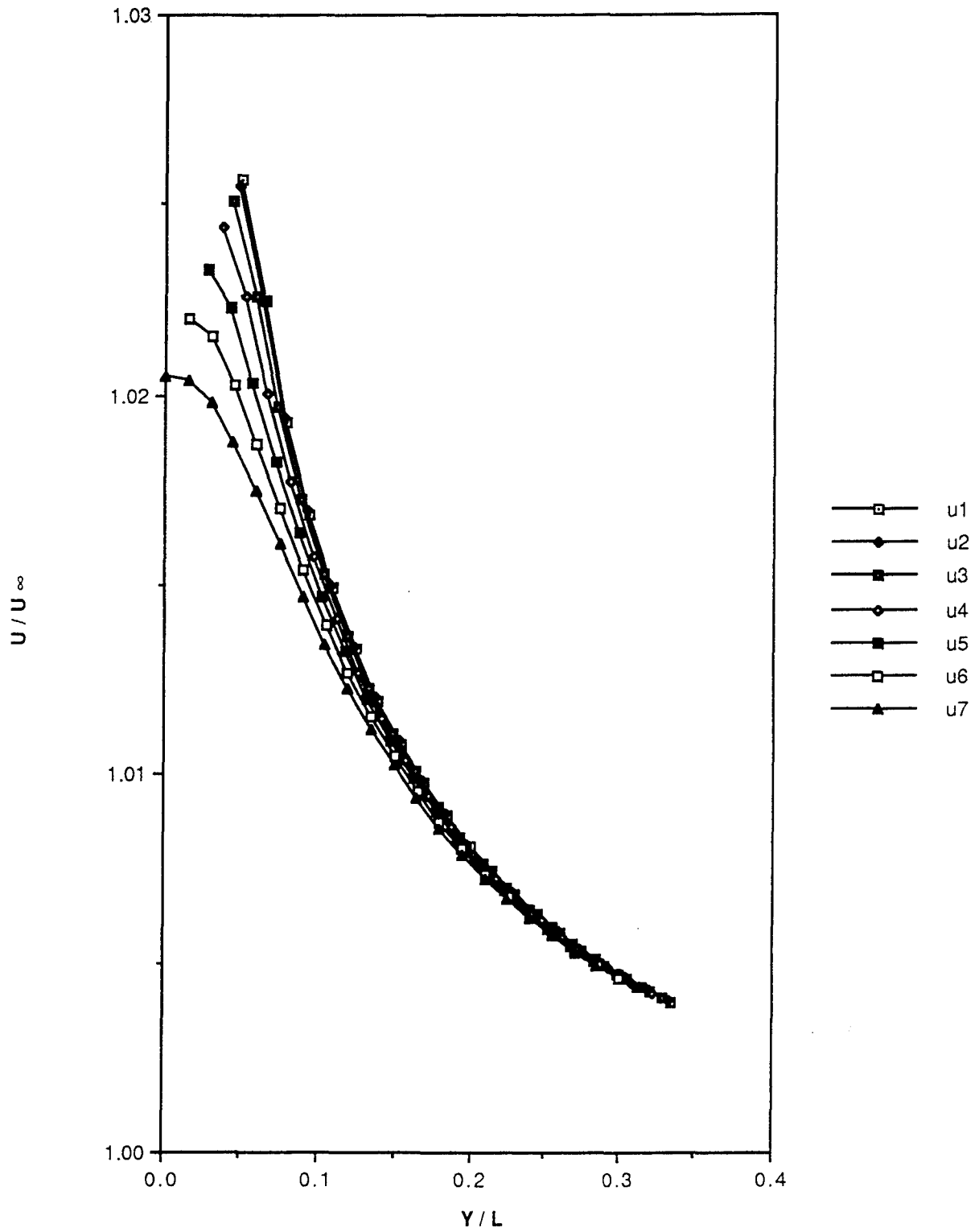Fig. 3b Expansion of part of figure 3a.

U/U∞ at X/L=0.5

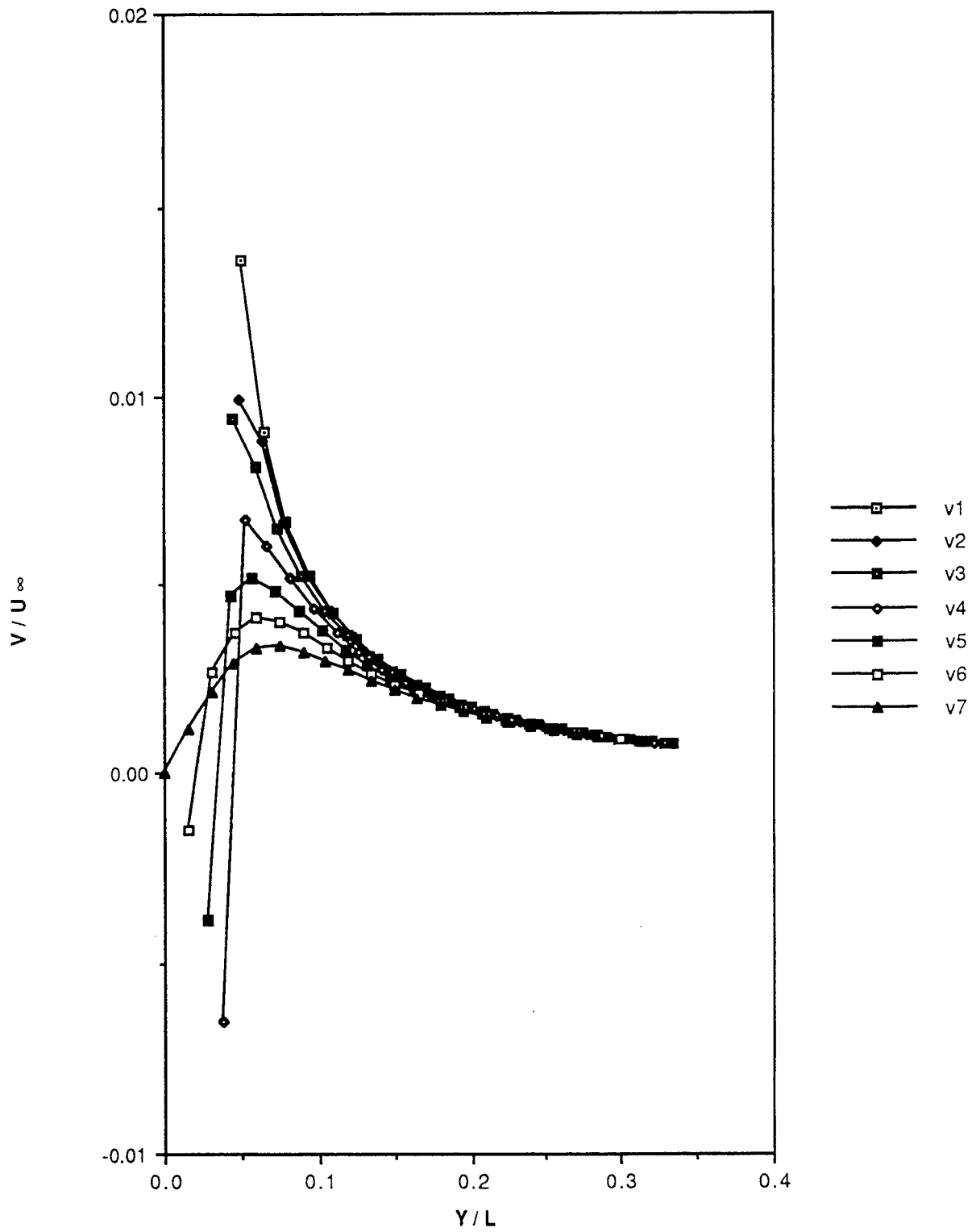Figure 4a. Irrotational velocity field in BLW.

V/U∞   at   X/L=0.5
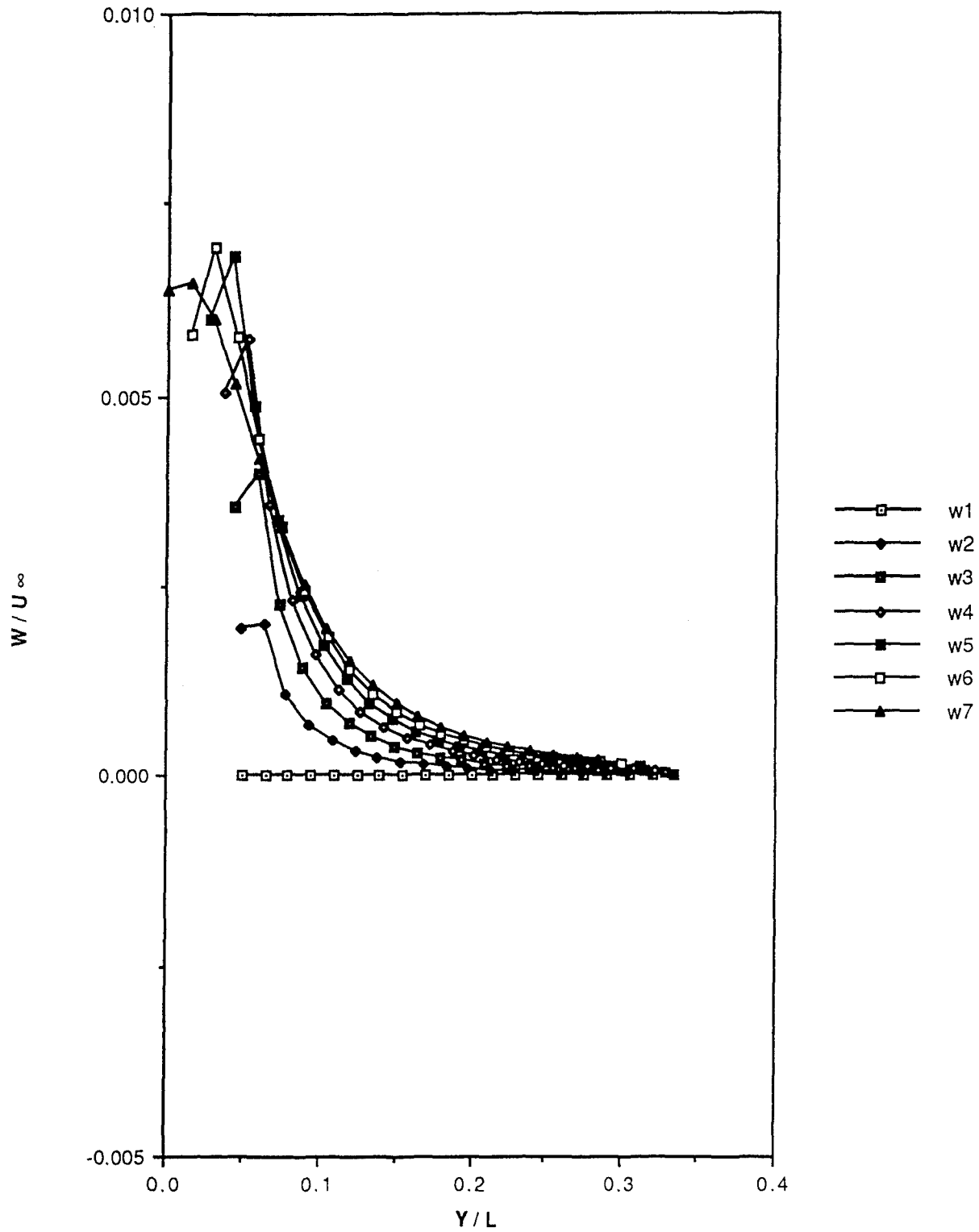
Figure 4b. Irrotational velocity field in BLW.

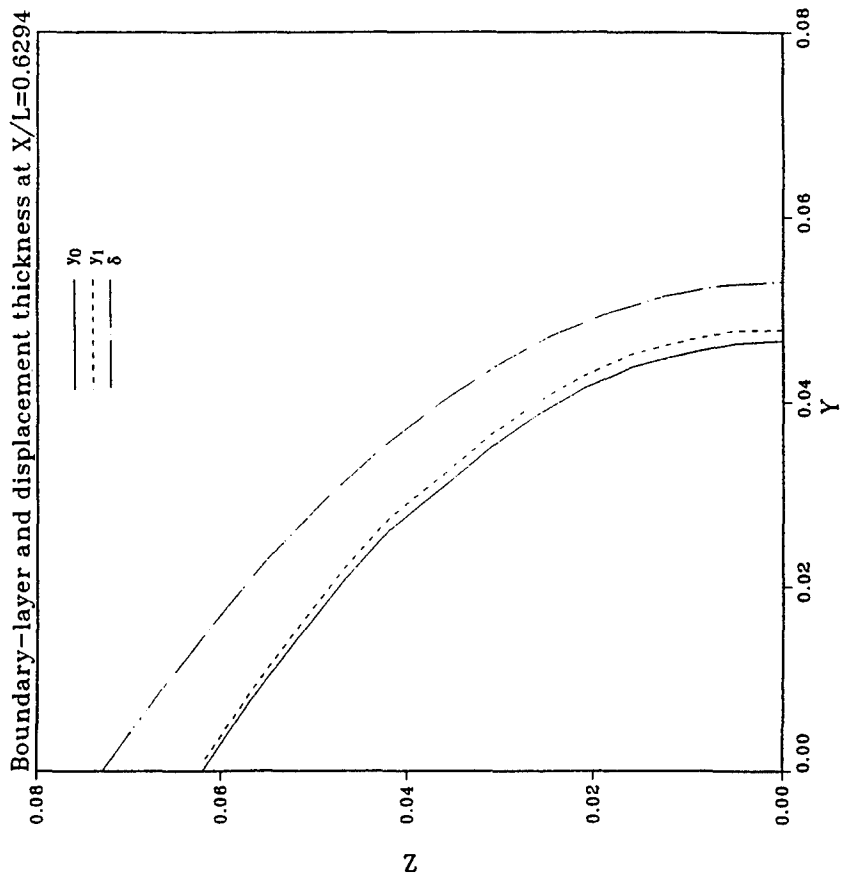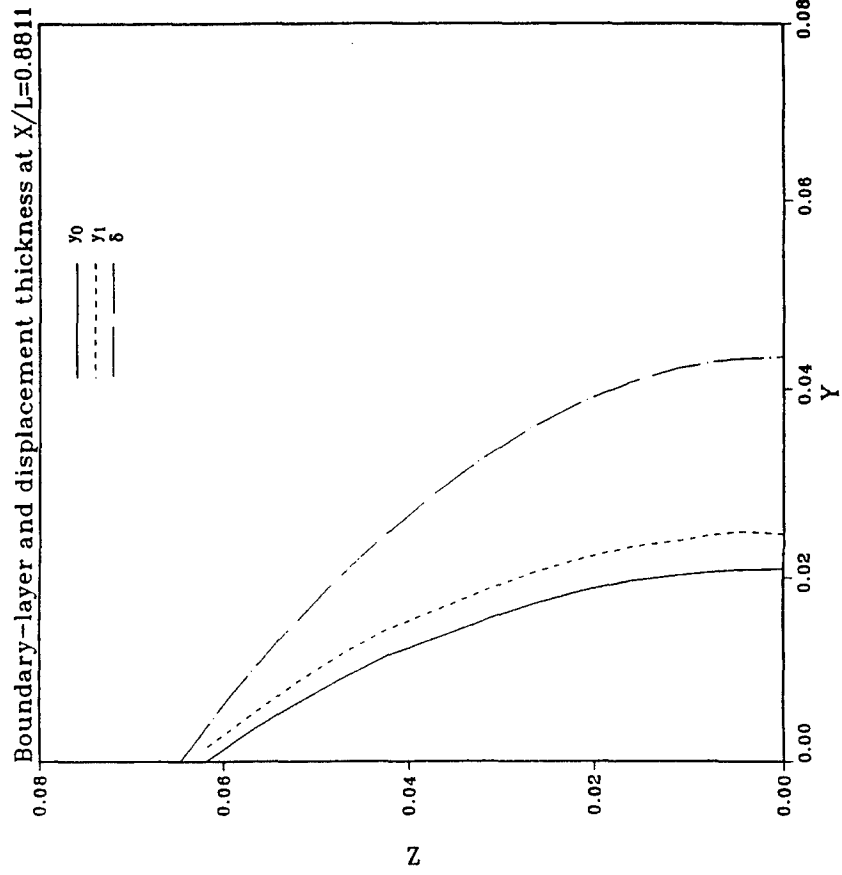Figure 4c. Irrotational velocity field in BLW.

Figure 5. Computed displacement-thickness surface y_1 relative to y_0 and δ for two transverse sections.

DISCUSSION
by Professor F. Stern, University of Iowa, USA.

How well would your method of computing displacement bodies work with hull geometries that create more complex stern flows (i.e. Series 60 and HSVA tanker) than the Wigley hull?

Author's Reply

For application of our method to more ship-like forms, some of the special geometric properties of the Wigley form, of which we took advantage, would not be available. For example, the-turn-of-the-bilge is usually sharp for a merchant ship. When that is the case, the procedure of projecting the integral equation for the source distribution on the hull onto the vertical centerplane would have to be modified. That would complicate the discretization of the integral equation by means of flat panels. We would then prefer to use quadrature formulas instead of panels to compute the source distribution and its irrotational-flow field.

The more complex stern flows about ship-like forms would affect the determination of the viscous flow. Since we assumed that that flow was given, our method of determining the displacement thickness is unaffected. The same remark applies to bow flows (free-surface boundary layer, wave breaking, bilge vortices, necklace vortices).

Domain Decomposition in Free Surface Viscous Flows

E. Campana, A. Di Mascio, P.G. Esposito, and F. Lalli
(INSEAN, Italian Ship Model Basin, Italy)

ABSTRACT

In the present paper the computation of the steady free surface flow past a ship hull is performed by a domain decomposition approach. Viscous effects are taken into account in the neighbourhood of solid walls and in the wake by solving the Reynolds Averaged Navier–Stokes equations, whereas the assumption of irrotationality in the external flow allows a description by a potential model. Free surface boundary conditions have been implemented in a linearized form at the undisturbed waterplane. Suitable matching conditions are enforced at the interface between the viscous and the potential region. The numerical results obtained for the HSVA tanker and the S60 hull (C_b=0.6) are compared with experimental data available in the literature.

NOMENCLATURE

$\mathcal{B}, \mathcal{B}'$	the wetted ship hull and its image
$\mathcal{D}$	fluid domain
$\mathcal{D}_p$	potential flow domain
$\mathcal{D}_v$	viscous flow domain
$Fr = \dfrac{U}{\sqrt{gL}}$	Froude number
g	acceleration of gravity
$\mathcal{H}(x, y)$	free surface elevation
J	jacobian
L	ship hull length
$\mathbf{l}$	unit vector tangent to the double model streamlines on $z = 0$
l	parameter defined along the double model streamlines on $z = 0$
$\mathbf{n}$	unit vector normal to Γ, oriented toward $\mathcal{D}_p$)
N_{NS}	number of iterations in the Navier–Stokes solver
$N = NS + NC$	number of boundary elements L_k used
NS	boundary elements arranged on $\mathcal{S}$
NC	boundary elements arranged on Γ
$P(x, y, z)$	field point
p	pressure
p_0	double model pressure
$Q \equiv (x_Q, y_Q, z_Q)$	source point
$\mathbf{q} \equiv (p, u, v, w)$	
$Re = \dfrac{UL}{\nu}$	Reynolds number
$\mathcal{S}$	free surface
$\mathcal{S}_p$	free surface $\in \mathcal{D}_p$
$\mathcal{S}_v$	free surface $\in \mathcal{D}_v$
$\mathbf{u} = (u, v, w)$	fluid velocity expressed in Cartesian components
$\mathbf{u}_0$	double model fluid velocity
U	free stream velocity
$\mathbf{V}_k, \mathbf{V}'_k$	influence matrices
$\mathcal{V}_n$	boundary condition for φ on Γ
$\tilde{\mathcal{V}}_n$	boundary condition for $\tilde{\varphi}$ on Γ

x, y, z	Cartesian coordinates in the body-fixed frame of reference
β	pseudo-compressibility coefficient
Γ	interface between $\mathcal{D}_p$ and $\mathcal{D}_v$
Γ^*	secondary interface (overlapping)
ε_e	fourth order artificial dissipation coefficient
ε_i	second order artificial dissipation coefficient
ν	kinematic viscosity of water
ν_T	eddy viscosity coefficient
$\Phi = \varphi + \tilde{\varphi}$	velocity potential (defined in $\mathcal{D}_p$)
φ	potential of double model
$\tilde{\varphi}$	perturbation potential
σ	simple layer density for φ
$\tilde{\sigma}$	simple layer density for $\tilde{\varphi}$
$\underline{\underline{\tau}}$	stress tensor

INTRODUCTION

The prediction of the total drag of a hull in forward motion is a major task in ship design. To this aim, numerical fluid dynamics is a useful engineering tool for computing both pressure and viscous stresses on a body piercing the surface of the sea. Furthermore, it is possible to get detailed information on the wake past the hull; the knowledge of the velocity field in the aft region can help designers to improve the performance of the propeller and avoid cavitation.

However, the numerical simulation of this flow field is a difficult problem to deal with, because of the extremely large Reynolds numbers encountered in practical problems ($\sim 10^8 \div 10^9$), and the moving boundary at the air-water interface. The solution of the Navier-Stokes equations generally requires such a large amount of CPU time that this kind of codes becomes unfeasible for a customary usage in ship design. On the other hand, the codes based on potential flow models, although much faster than the former, are unable to mimic the formation and growth of the boundary layer and the wake.

In view of the problems mentioned above, the zonal approach concepts can be fruitfully exploited to save CPU time. In the proposed numerical algorithm the full viscous model is solved only in the neighbourhood of rigid boundaries and in the wake, while the external flow, where viscous effects are supposed to be negligible, is simulated by means of a potential model.

The present approach is quite different from the classical boundary layer-potential flow interactive methods based on the concept of displacement thickness. Applications of these schemes can be found in [1], where an integral boundary layer approach is used, or in [2], where the displacement thickness is computed by the solution of the Navier-Stokes equation close to the ship hull. In both cases, the boundary of the potential flow domain is determined by the displacement body. This kind of approach may cause some difficulties when dealing with full-form hulls and transom sterns, where the definition of the displacement thickness is not an easy task, especially when boundary layer separation occurs. In view of such applications, the present method is not based on the concept of displacement thickness, but we define a fixed decomposition of the fluid domain, with a matching surface located *a priori*. In each domain, a suitable physical model able to grasp the relevant features of the flow is chosen and a proper numerical method is used: a Boundary Element Method is implemented for the solution of the external potential flow, whereas the Reynolds Averaged Navier-Stokes equations in the inner domain are discretized by a Finite Volume technique.

The Dawson model [3], in which the double model flow is the basis flow for the linearization, has been chosen for the free-surface external flow. The choice of a linear potential model is dictated by the need of CPU time saving; at the same time, the Dawson model was preferred with respect to other linear solvers because it allows a satisfactory representation of the free surface pattern also when dealing with full form hulls [4].

With a zonal approach, however, problems related to the matching conditions for the external and the internal solutions arise. Although the coupling procedure in unbounded flows is quite well established [5], the use of the zonal approach for solving free surface flows still needs to be investigated.

In the following sections, the viscous and inviscid solvers are described and the coupling procedure is analyzed. Finally some numerical examples are discussed and compared with experimental data.

MATHEMATICAL MODEL

In the following, we consider the steady flow around a rigid body $\mathcal{B}$ submerged or floating in an incompressible fluid of infinite depth, bounded upwards by a free surface $\mathcal{S}$ and unbounded in the other directions.

The fluid is assumed inviscid and the flow irrotational in the outer region $\mathcal{D}_p$ of the fluid domain $\mathcal{D}$, whereas viscosity effects are taken into account in the inner region $\mathcal{D}_v$ (Fig. 1).
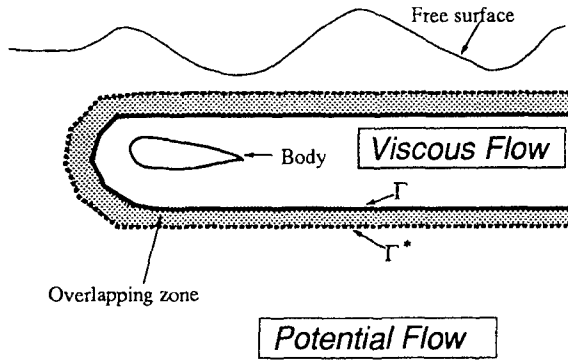

Figure 1: Computational sub-domains and overlapping zone

We assume a body-fixed reference frame with the x-axis oriented along the uniform stream U and the z-axis positive upwards.

The variables have been nondimensionalized with respect to the body length L and the uniform stream velocity U.

The Outer Region

The fluid velocity $\mathbf{u} = (u, v, w)$ can be written as the gradient of a scalar function Φ:

$$\mathbf{u}(x, y, z) = \nabla \Phi(x, y, z) \tag{1}$$

The potential Φ, harmonic in $\mathcal{D}_p$, is split into the double model term φ and the wave term $\tilde{\varphi}$:

$$\Phi(x, y, z) = \varphi(x, y, z) + \tilde{\varphi}(x, y, z) \tag{2}$$

The double model potential φ describes the flow past the body $\mathcal{B}$ and its image $\mathcal{B}'$, symmetric with respect to the (x, y)-plane; namely, $\varphi_z(x, y, 0) \equiv 0$. The double model potential satisfies the Neumann BC's

$$\frac{\partial \varphi}{\partial n} = \mathcal{V}_n \qquad on\ \Gamma \tag{3}$$

where $\mathcal{V}_n$ is the boundary condition to be specified later on, while Γ is the matching surface.

At the free surface $\mathcal{S} : z = \mathcal{H}(x, y)$ the pressure is constant, so that by Bernoulli's theorem we find the dynamic condition:

$$\mathcal{H}(x, y) = \frac{Fr^2}{2} \{ 1 - |\nabla \Phi[x, y, \mathcal{H}(x, y)]|^2 \} \tag{4}$$

where surface tension has been neglected.

To get the linear form introduced by Dawson [3], we neglect the squares of $\tilde{\varphi}$; if l is the curvilinear abscissa defined along the double model streamlines lying on $z = 0$, the dynamic condition gives:

$$\mathcal{H}(x, y) = \frac{Fr^2}{2} [1 - (\varphi_l^2 + 2\varphi_l \tilde{\varphi}_l)] \tag{5}$$

The linearized form of the kinematic condition, combined with (5), yields:

$$\varphi_l^2 \tilde{\varphi}_{ll} + 2\varphi_l \varphi_{ll} \tilde{\varphi}_l + \frac{1}{Fr^2} \tilde{\varphi}_z = -\varphi_l^2 \varphi_{ll} \tag{6}$$

Therefore the wave potential can be computed by (6) on $z = 0$ and by the following Neumann boundary condition:

$$\frac{\partial \tilde{\varphi}}{\partial n} = \tilde{\mathcal{V}}_n \qquad on\ \Gamma \tag{7}$$

where $\tilde{\mathcal{V}}_n$ is the boundary condition for the perturbation potential. Finally, the asymptotic behavior of the wave potential $\tilde{\varphi}(x, y, z)$ at infinity must be specified, i.e. waves should never propagate upstream. This gives the radiation condition:

$$\lim_{x \to -\infty} |\nabla \tilde{\varphi}(x, y, z)| = 0 \tag{8}$$

for every fixed (y, z) in $\mathcal{D}_p$.

The solution of the mathematical model described above can be represented by means of a simple layer potential distributed over Γ and the part $\mathcal{S}_p$ of the free surface included inside $\mathcal{D}_p$ [6]:

$$\varphi(P) = \int_\Gamma \sigma(Q) \left[\frac{1}{|P - Q|} + \frac{1}{|P - Q'|} \right] dS_Q \tag{9}$$

$$\tilde{\varphi}(P) = \int_{\Gamma \cup \mathcal{S}} \tilde{\sigma}(Q) \frac{1}{|P - Q|} dS_Q \tag{10}$$

where $P = (x, y, z) \in \mathcal{D}_p$, $Q = (x_Q, y_Q, z_Q) \in \Gamma \cup \mathcal{S}_p$, $Q' = (x_Q, y_Q, -z_Q)$.

Such definitions can be introduced in formulas (3) and (6-7), obtaining the integral equations whose discretization and numerical solution will be discussed in the next section. The double model potential can be computed independently by solving a standard Fredholm integral equation of the second kind for $\sigma(Q)$.

The Inner Region

In the inner region $\mathcal{D}_v$ a turbulent viscous model has to be used to simulate the boundary layer growth and wake formation.

A pseudo-transient formulation due to Chorin [7] is used to solve the steady state incompressible Reynolds Averaged Navier-Stokes equations. In this scheme the continuity equation is replaced by a transient counterpart

$$\frac{\partial p}{\partial t} + \beta \nabla \cdot \mathbf{u} = 0 \tag{11}$$

where $\mathbf{u} = (u, v, w)$ is the velocity vector expressed in Cartesian components, p is the pressure and β is the pseudo-compressibility factor. The resulting system of conservation laws is

$$\frac{\partial \mathbf{q}}{\partial t} + \frac{\partial \mathbf{F}^1}{\partial x} + \frac{\partial \mathbf{F}^2}{\partial y} + \frac{\partial \mathbf{F}^3}{\partial z} =$$
$$\frac{\partial \mathbf{q}}{\partial t} + \frac{\partial \mathbf{F}^i}{\partial x_i} = 0 \tag{12}$$

where

$$\mathbf{q} = \begin{pmatrix} p \\ u \\ v \\ w \end{pmatrix}$$

$$\mathbf{F}^1 = \begin{pmatrix} \beta u \\ u^2 + p - \tau_{xx} \\ uv - \tau_{yx} \\ uw - \tau_{zx} \end{pmatrix}$$

$$\mathbf{F}^2 = \begin{pmatrix} \beta v \\ vu - \tau_{xy} \\ v^2 + p - \tau_{yy} \\ vw - \tau_{zy} \end{pmatrix} \tag{13}$$

$$\mathbf{F}^3 = \begin{pmatrix} \beta w \\ wu - \tau_{xz} \\ wv - \tau_{yz} \\ w^2 + p - \tau_{zz} \end{pmatrix}$$

In the previous equation $\underset{=}{\tau}$ is the stress tensor, including the turbulent part generated by the Reynolds averaging procedure. If an eddy viscosity turbulence model is introduced to evaluate the Reynolds stresses, $\underset{=}{\tau}$ can be written as

$$\underset{=}{\tau} = (\frac{1}{Re} + \nu_T) \left[(\nabla \mathbf{u}) + (\nabla \mathbf{u})^T \right] \tag{14}$$

being Re the Reynolds number and ν_T the kinematic eddy viscosity. In the present paper the Baldwin-Lomax turbulence model [8] has been used.

If $(\xi, \eta, \zeta) = (\xi_1, \xi_2, \xi_3)$ is a curvilinear coordinate system, equation (12) can be recast in the form

$$\frac{\partial \mathbf{q}}{\partial t} + \frac{1}{J} \frac{\partial}{\partial \xi_k} \left[J \xi_{k,i} \mathbf{F}^i \right] = 0 \tag{15}$$

where J is the Jacobian and $(\cdot)_{,i} \equiv \frac{\partial(\cdot)}{\partial x_i}$.

Apart the surface Γ^* at which the potential and the viscous solutions are matched, the boundary conditions imposed are the standard ones for Navier-Stokes computations. At solid walls no slip conditions are enforced, whereas at the midplane symmetry conditions are imposed:

$$\begin{aligned} \frac{\partial u}{\partial \zeta}\bigg|_{y=0} &= 0 \\ \frac{\partial w}{\partial \zeta}\bigg|_{y=0} &= 0 \\ v\big|_{y=0} &= 0 \\ \frac{\partial p}{\partial \zeta}\bigg|_{y=0} &= 0 \end{aligned} \tag{16}$$

At the outflow the velocity and the pressure fields are assumed to be fully developed, thus zero streamwise gradients are assumed. On the free surface, the boundary conditions to be satisfied are the following:

$$\left.\begin{aligned} \frac{\partial \mathcal{H}}{\partial t} + u\frac{\partial \mathcal{H}}{\partial x} + v\frac{\partial \mathcal{H}}{\partial y} &= w \\ p &= \frac{\mathcal{H}}{Fr^2} \\ \tau_{xz} &= 0 \\ \tau_{yz} &= 0 \end{aligned}\right\} \quad on \; z = 0 \tag{17}$$

NUMERICAL MODEL

Potential Solver

For the numerical solution of the problem described in the previous section, we discretize $\Gamma \cup \mathcal{S}_p$ into $N = NS + NC$ plane quadrilateral elements $L_k, k = 1, \ldots, N$. NC denotes the number of panels located on Γ and NS the number of those located on the average free surface $\mathcal{S}_p$. Let $P \equiv (x, y, z)$, $Q \equiv (x_Q, y_Q, z_Q)$ and $Q' \equiv (x_Q, y_Q, -z_Q)$. The discrete form of the integral equation for $\sigma(P)$ is the following:

$$\sum_{\substack{k=NS+1 \\ k \neq i}}^{N} \sigma_k \left\{ \frac{\partial}{\partial n_P} \int_{L_k} \left[|P - Q|^{-1} + \right. \right.$$

$$\left| P - Q' \mid^{-1} \right] dS_Q \Bigg\}_{P=P_i} - 2\pi\sigma_i =$$

$$\mathcal{V}_n(P_i) \qquad (18)$$

for $i = NS + 1, \ldots, N$. Equation (18) can be rewritten in the following form:

$$\sum_{\substack{k=NS+1 \\ k \neq i}}^{N} \sigma_k[\mathbf{n}(P_i) \cdot (\mathbf{V}_k(P_i) + \mathbf{V}'_k(P_i))]$$

$$-2\pi\sigma_i = \mathcal{V}_n(P_i) \quad (19)$$

where

$$\mathbf{V}_k(P) = \int_{L_k} \frac{P-Q}{\mid P-Q \mid^3} dS_Q \qquad (20)$$

$$\mathbf{V}'_k(P) = \int_{L_k} \frac{P-Q^*}{\mid P-Q' \mid^3} dS_Q \qquad (21)$$

The discrete forms of equations (6-7) are obtained:

$$\sum_{\substack{k=1 \\ k \neq i}}^{N} \tilde{\sigma}_k[\mathbf{n}(P_i) \cdot \mathbf{V}_k(P_i)] - 2\pi\tilde{\sigma}_i = \tilde{\mathcal{V}}_i(P_i)$$

$$(i = NS + 1, \ldots, N) \qquad (22)$$

$$[\varphi_l(P_i)]^2 \sum_{\substack{k=1 \\ k \neq i}}^{N} \tilde{\sigma}_k \mathbf{l}(P_i) \cdot \nabla[\mathbf{l}(P_i) \cdot \mathbf{V}_k(P_i)]$$

$$+ 2\varphi_l(P_i)\varphi_{ll}(P_i)] \sum_{\substack{k=1 \\ k \neq i}}^{N} \tilde{\sigma}_k \mathbf{l}(P_i) \cdot \mathbf{V}_k(P_i)$$

$$+ \frac{1}{Fr^2}[\sum_{\substack{k=1 \\ k \neq i}}^{N} \tilde{\sigma}_k V_{zk}(P_i) + 2\pi\tilde{\sigma}_i] =$$

$$-[\varphi_l(P_i)]^2\varphi_{ll}(P_i) \quad (i = 1, \ldots, NS) \qquad (23)$$

where $\mathbf{l}(P_i)$ is the unit vector tangent to the direction l, and

$$\varphi_l(P_i) = \sqrt{\varphi_x^2(P_i) + \varphi_y^2(P_i)}$$

In order to avoid numerical dispersion, we compute the derivatives of $\mathbf{V}_k(P)$ analitically; in fact the numerical dispersion can significantly affect the wave pattern, as shown in [6]. The radiation condition (8) is enforced in the following discrete form:

$$\sum_{k=1}^{N} \tilde{\sigma}_k \frac{\partial}{\partial x} V_{xk}(P_j) = 0, \quad \sum_{\substack{k=1 \\ k \neq j}}^{N} \tilde{\sigma}_k V_{zk}(P_j) = -2\pi\tilde{\sigma}_j$$

where $j = 1, \ldots, N_j$ is the index set corresponding to all panels on the first upstream row. These equations replace the $2N_j$ equations (23) corresponding to the first upstream and the last downstream row.

Navier–Stokes Solver

A well established implicit scheme developed by [9] has been used in order to ensure reliable results and robustness needed for the interactive method.

A finite volume technique is used to discretize equation (12). The inner region $\mathcal{D}_v$ is divided in hexahedra V_{ijk}. The application of the Gauss' theorem in the control volume V_{ijk} yields

$$\frac{\partial \mathbf{q}_{ijk}}{\partial t} + \mathbf{R}(\mathbf{q})_{ijk} = 0 \qquad (24)$$

with

$$\mathbf{R}(\mathbf{q})_{ijk} = \frac{1}{V_{ijk}} \oiint_{S_{ijk}} \mathcal{F} \cdot \mathbf{n} \, dS = 0 \qquad (25)$$

where S_{ijk} is the boundary of V_{ijk}, $\mathbf{n} = (n_x, n_y, n_z)$ is the outer normal to S_{ijk} and $\mathcal{F} = (\mathbf{F}^1, \mathbf{F}^2, \mathbf{F}^3)$. In the numerical approximation of equation (24) the values of $\mathcal{F}$ on the faces of cell V_{ijk} are needed for the discretization of Equation (24): a simple averaging of neighbouring points is used to obtain velocity and pressure, while the stress tensor is evaluated by centered differencing.

The time marching procedure is that suggested by Beam and Warming [10]

$$\frac{\mathbf{q}^{n+1} - \mathbf{q}^n}{\Delta t} =$$

$$(1 - \theta) \left. \frac{\partial \mathbf{q}}{\partial t} \right|^n + \theta \left. \frac{\partial \mathbf{q}}{\partial t} \right|^{n+1} =$$

$$-(1 - \theta)\mathbf{R}(\mathbf{q}^n) - \theta\mathbf{R}(\mathbf{q}^{n+1}) \qquad (26)$$

where $0 \leq \theta \leq 1$. Using a Taylor expansion, equation (26) becomes

$$\left[\delta\mathbf{q} + \frac{\theta\Delta t}{J} \frac{\partial}{\partial \xi_l} \left(J\xi_{l,m}\mathbf{A}^m \delta\mathbf{q} + \right. \right.$$

$$\left. \left. J\xi_{l,m}\mathbf{B}^{m,r} \frac{\partial \delta\mathbf{q}}{\partial \xi_r} \right) \right]^n = -\Delta t\mathbf{R}(\mathbf{q}^n) \quad (27)$$

where $\delta\mathbf{q}^n = \mathbf{q}^{n+1} - \mathbf{q}^n$, $\mathbf{A}^m$ and $\mathbf{B}^{m,r}$ are the jacobians of $\mathbf{F}^m$:

$$\mathbf{A}^m = \frac{\partial \mathbf{F}^m}{\partial \mathbf{q}}$$

$$\mathbf{B}^{m,r} = \frac{\partial \mathbf{F}^m}{\partial \mathbf{q}_{\xi_r}} \qquad (28)$$

A direct solution of the system of algebraic equations (27) would be too expensive, thus an approximate factorization technique is used to reduce it to the solution of three simpler problems, with block tridiagonal coefficient matrix:

$$\left[\mathbf{I} + \theta\Delta t \left(\mathcal{A}^1 + \mathcal{A}^2 + \mathcal{A}^3 \right) \right] \delta\mathbf{q}^n \simeq \qquad (29)$$

$$\left(\mathbf{I} + \theta\Delta t\mathcal{A}^1 \right) \left(\mathbf{I} + \theta\Delta t\mathcal{A}^2 \right) \left(\mathbf{I} + \theta\Delta t\mathcal{A}^3 \right) \delta\mathbf{q}^n$$

within an accuracy of the order $O(\Delta t)$. The operator $\mathcal{A}$ introduced in the factorization is defined as

$$\mathcal{A}^l = \frac{1}{J}\frac{\partial}{\partial \xi_l}\left(J\xi_{l,m}\mathbf{A}^m + J\xi_{l,m}\mathbf{B}^{m,l}\frac{\partial}{\partial \xi_l}\right) \quad (30)$$

with no summation on l. It can be noticed that all the second order mixed derivative in $\delta\mathbf{q}$ were discarded in the implicit part of the system to maintain the tridiagonal structure. This approximation, however, does not affect the steady state solution.

To improve the numerical stability of the scheme, a fourth order artificial dissipation term is added to the right hand side of (29). Thus the flux at the interface $\xi_1|_{i+\frac{1}{2},j,k}$ is modified according to

$$\tilde{\mathcal{F}}\cdot\mathbf{n}|_{i+\frac{1}{2},j,k} = \mathcal{F}\cdot\mathbf{n}|_{i+\frac{1}{2},j,k} \quad (31)$$
$$+ \varepsilon_e\overline{V}(\mathbf{q}_{i+2,j,k} - 3\mathbf{q}_{i+1,j,k} + 3\mathbf{q}_{i,j,k} - \mathbf{q}_{i-1,j,k})$$

being $\overline{V}$ is the average volume of the two neighbouring cells. A second order term is added to each tridiagonal operator in the left-hand side

$$\tilde{\mathcal{A}}^l = \frac{1}{J}\frac{\partial}{\partial \xi_l}\left(J\xi_{l,m}\mathbf{A}^m \right. \quad (32)$$

$$\left. + J\xi_{l,m}\mathbf{B}^{m,l}\frac{\partial}{\partial \xi_l} - \varepsilon_i\overline{V}\frac{\partial}{\partial \xi_l}\right) \quad (33)$$

The final form of the system of equations is, then

$$\left(\mathbf{I} + \theta\Delta t\tilde{\mathcal{A}}^1\right)\left(\mathbf{I} + \theta\Delta t\tilde{\mathcal{A}}^2\right)\left(\mathbf{I} + \theta\Delta t\tilde{\mathcal{A}}^3\right)\delta\mathbf{q}^n =$$
$$- \Delta t\tilde{\mathbf{R}}(\mathbf{q}^n) \quad (34)$$

where $\tilde{\mathbf{R}}(\mathbf{q}^n)$ is the residual that includes the artificial dissipation terms.

It can be shown that the steady state solution is second order accurate and that the above scheme is unconditionally stable if $\theta \geq 0.5$ in the linear case. The reader is referred to [9] and [10] for a detailed discussion.

In the implementation of the numerical code, all the metric terms in the above relations were computed in a finite volume fashion, i.e. the Jacobian J_{ijk} was set equal to the volume cell V_{ijk} and the terms like $J\xi_i$ at the cell interfaces $\xi = const.$, for instance, are computed as

$$\begin{aligned}
J\xi_x|_{i+\frac{1}{2},j,k} &= n_x\Delta S_{i+\frac{1}{2},j,k} \\
J\xi_y|_{i+\frac{1}{2},j,k} &= n_y\Delta S_{i+\frac{1}{2},j,k} \quad (35) \\
J\xi_z|_{i+\frac{1}{2},j,k} &= n_z\Delta S_{i+\frac{1}{2},j,k}
\end{aligned}$$

where (n_x, n_y, n_z) is the outer normal to the interface and $\Delta S_{i+\frac{1}{2},j,k}$ is the area of the interface between (i,j,k) and $(i+1,j,k)$.

A speedup in the computation can be achieved if a local time step is used

$$\Delta t_{ijk} = CJ_{ijk}^{\frac{1}{3}} \quad (36)$$

with C a stability parameter.

Applications of this scheme to ship flow calculation can be found, for instance, in [11] or in [12].

MATCHING ALGORITHM

The numerical algorithm used to couple the inner and the outer solution is the most important step of the whole procedure. The choice of the exchanged variables and the location of the matching surface may deeply affect the convergence rate or even cause the failure of the algorithm. In fact, in the previous version of the method [13], a non-overlapping domain decomposition scheme was used. The values of the tangential component of the velocity and the pressure of the potential field at the matching surface were used as boundary conditions for the Navier–Stokes solver, while the normal component of the viscous solution was used as Neumann condition in the potential flow. With this kind of approach, the convergence was reached within round-off errors but the convergence rate was not very satisfactory and some relaxation factors had to be used when matching the solutions. Furthermore, non-smooth transition from the inner to the outer domain was observed.

In the present work, the algorithm has been changed: the flow domain is divided in two subdomains that overlap over a small region, as illustrated in Fig. 1 for a two-dimensional case. These subdomains are bounded by Γ and Γ^*, which are the boundaries in the flow field for the potential and viscous zones, respectively. The thickness of
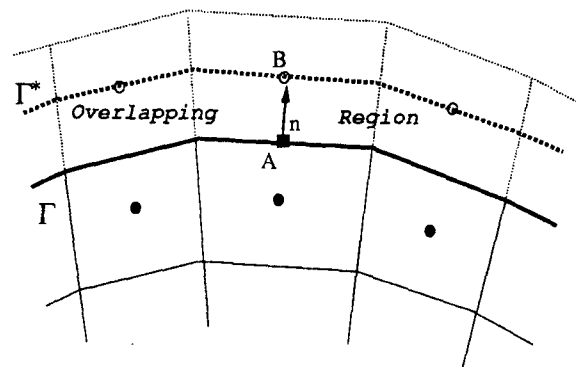
Figure 2: Location of the exchanged variables at the matching interfaces

334

the overlapping region is equal to half the heigth of the outermost cells in the inner grid (Fig. 2). In the iterative coupling procedure, the solution computed in the first domain is used to feed the solution in the other domain with the boundary conditions, that is:

- from the potential solver we get the velocity vector and the pressure at the grid point B on Γ^* (see Fig. 2); these values are forced as boundary conditions on the viscous flow

$$\mathbf{u}|_{\Gamma^*} = \nabla\Phi|_{\Gamma^*}$$
$$p|_{\Gamma^*} = \tfrac{1}{2}\left(1 - \nabla\Phi \cdot \nabla\Phi\right)\big|_{\Gamma^*} \tag{37}$$

- the normal component of the velocity at the control point A on Γ (see Fig. 2) is computed from the viscous flow solution. This value is then used as a Neumann condition for the potential problem

$$\frac{\partial\Phi}{\partial n}\Big|_{\Gamma} = \mathbf{u} \cdot \mathbf{n}|_{\Gamma} \tag{38}$$

This new scheme improves the convergence rate, makes the relaxation factors unnecessary and ensures a smooth transition across the matching surface.

However, the coupling procedure deserves a more detailed discussion. In fact, as mentioned before, the potential flow field is expressed as the sum of a double model potential φ and a wave potential $\tilde{\varphi}$. This linearized form [3], has been chosen because it gives a satisfactory description of the wave pattern also in case of non-slender hull, when compared with the Neumann–Kelvin linear problem. In order to keep the same representation of the potential flow, the multidomain solution has to be consistent with this decomposition, and therefore the solution is computed in two steps:

1. *Double Model Solution:* The solution is computed with the condition

$$w_0 = 0; \quad \frac{\partial u_0}{\partial z} = 0; \quad \frac{\partial v_0}{\partial z} = 0; \quad \frac{\partial\varphi}{\partial z} = 0 \tag{39}$$

on the waterplane $z = 0$, while the matching conditions on Γ and Γ^* are

$$\mathbf{u}_0|_{\Gamma^*} = \nabla\varphi|_{\Gamma^*}$$

$$p_0|_{\Gamma^*} = \tfrac{1}{2}\left(1 - \nabla\varphi \cdot \nabla\varphi\right)_{\Gamma^*} \tag{40}$$

$$\frac{\partial\varphi}{\partial n}\Big|_{\Gamma} = \mathbf{u}_0 \cdot \mathbf{n}|_{\Gamma}$$

where $\mathbf{u}_0$ and p_0 are the velocity vector and the pressure in the inner double model solution.

2. *Free Surface Solution:* Once the double model flow is solved with the desired accuracy, the free surface flow is computed. A linearised free surface condition is used in both domains on the water plane. However, the matching condition to be forced are slightly more complex than in the previous step. In fact, the potential $\tilde{\varphi}$ is a perturbation with respect to the double model flow and therefore it must be related to the difference between the velocity field in the free surface viscous domain and the double model velocity field in the same domain. At the same time, the viscous solution, which is not split, must be related the total potential:

$$\mathbf{u}|_{\Gamma^*} = \nabla(\varphi + \tilde{\varphi})|_{\Gamma^*}$$

$$p|_{\Gamma^*} = \tfrac{1}{2}\left(1 - \nabla(\varphi + \tilde{\varphi}) \cdot \nabla(\varphi + \tilde{\varphi})\right)_{\Gamma^*}$$

$$\frac{\partial\tilde{\varphi}}{\partial n}\Big|_{\Gamma} = \mathbf{u} \cdot \mathbf{n}|_{\Gamma} - \mathbf{u}_0 \cdot \mathbf{n}|_{\Gamma} \tag{41}$$

It is easy to verify that if (40) and (41) are summed, the global matching condition (37)–(38) are satisfied for the total potential Φ and the viscous solution $(\mathbf{u}, p)$.

The application of the multidomain decomposition technique in the form described above would be too much expensive. In fact, it implies the iterative solution of the Navier–Stokes equations for $(\mathbf{u}, p)$ assigned on Γ^* at each global step. This "inner" convergence seems not to be required when computing a steady state solution. In all the test cases we have performed, the Navier–Stokes solver was iterated for a fixed number N of steps (typically $1 \leq N_{NS} \leq 100$) and the algorithm never failed to converge. However, the number of sub–iterations affects the global convergence rate. We are not able to give a definite answer to this regard because only few test computations have been performed.

Finally, it is worth noticing that the CPU time spent in the computation of the potential solution is small compared to the total CPU time. In fact, the LU factorization of the matrix of the linear system for φ and $\tilde{\varphi}$ is performed once, since the viscous solver only affects the RHS. Next inviscid steps are simply obtained by backsubstitution.

335

NUMERICAL RESULTS

All the test cases presented in this section were computed with a workstation RISC/6000 Mod. 540 equipped with 128 Megabyte of RAM with peak performances equal to 60 MFLOPS.

Before the discussion of the numerical results, a few comments on the convergence behaviour of the algorithm may be worth doing. The procedure described above, as shown in Fig. 3, is consistent, in the sense that the discrete problem can be solved with any desired accuracy, up to round-off errors. The jump, clearly recognizable in the plot, is experienced when the free surface flow computation begin, starting from the converged double body flow. In this case (Wigley hull), 975 panels have been arranged on Γ, 1050 panels on the undisturbed free surface, while the grid for the viscous problem is $65 \times 15 \times 15$. However, in the applications such a fine resolution is not required: a tolerance equal to 10^{-3} generally suffices for practical purposes.

Figure 4: Computational grid showing part of the matching surface Γ

the ship lenght. The potential solution is updated every $N_{NS} = 10$ viscous steps. The pressure contourlines on the hull have been depicted in Fig. 5:

Figure 3: Convergence history of L_2 norm of the mass residual

Figure 5: Pressure contour map: comparison between present method (solid line) and full viscous solution (dashed line) for the HSVA-tanker. Levels: -0.5,-0.45, ...,0.5

A Double Model Flow: the HSVA-tanker

The proposed algorithm has been applied in two different problems. At first, the coupling algorithm has been tested for a double model flow at $Re = 5 \times 10^6$ past a typical bluff hull, such as the HSVA-tanker (Fig. 4); the grid in the viscous region is $65 \times 14 \times 14$, while 910 panels are on the matching surface. In this test case Γ is located at a distance from the hull equal to $L/10$, where L is
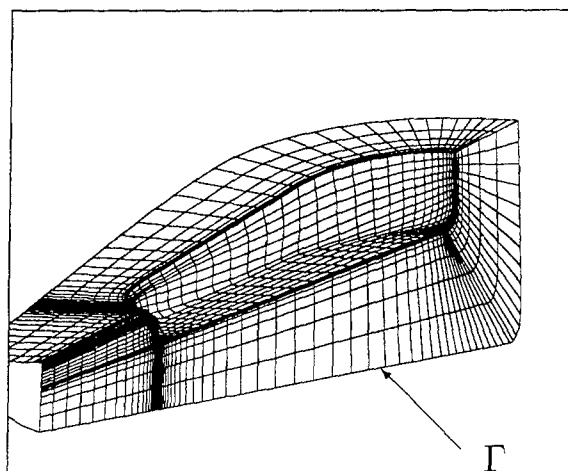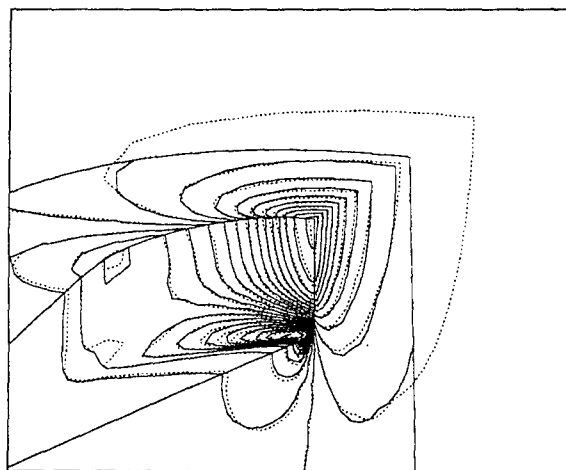
the present method reproduces with a rather good agreement the results of the full viscous computation on a grid $80 \times 30 \times 24$. The comparison of the performances of the two algorithm is very encouraging: the required CPU times are 4h with the zonal approach and 24h in the full viscous computation. In Fig. 6 the computed pressure is compared with experimental data ([14]). It can be seen that the agreement is quite good.
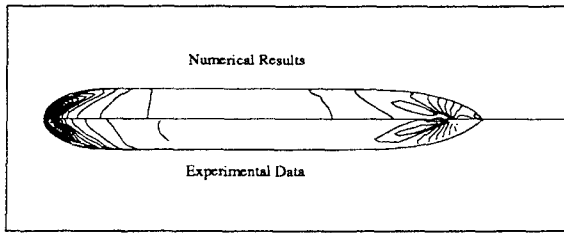
336

Figure 6: Pressure contour map: comparison between numerical results (top half) and and experimental data [14] (bottom half) for the HSVA-tanker. Levels: -0.5,-0.475, . . . ,0.5

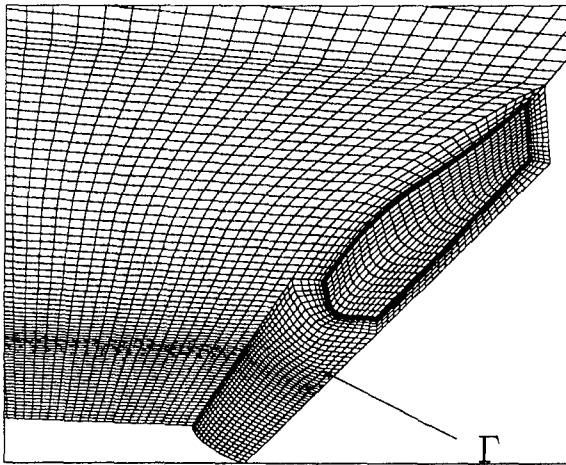## A Free Surface Flow: the S60 Hull (C_b=0.6)

Figure 7: Computational grid showing part of the matching surface Γ

For the S60 C_b=0.6 model non-zero Froude number computations have been performed. Details of the grid can be observed in Fig. 7: the 77 × 25 free surface panels are arranged in a H-shaped grid that face the C-grid 70 × 15 × 15 in the viscous inner region. Numerical constraints related to both Reynolds and Froude number have to be satisfied in the grid spacing. In the computation reported in this sub-section, we have $Re = 4.5 \times 10^6$ and $Fr = 0.300$, 0.316. The grid lines were clustered at the hull surface to have a sufficient resolution in the boundary layer: the size of the first grid cell near the body is 10^{-5} in the normal direction. The nodes in streamwise direction were arranged to have at least 23 grid points per wave lenght (according to the linear 2D wave lenght formula). Regarding to the location of the matching surface, the viscous domain should be chosen as narrow as possible to improve
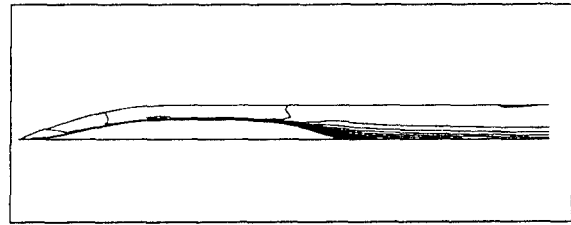

Figure 8: Top view of the boundary layer and the wake for the double model case
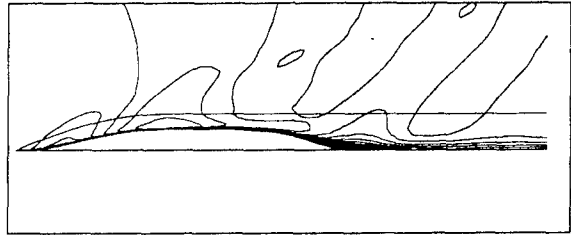

Figure 9: Top view of the boundary layer and the wake for the free surface flow

the efficiency of the numerical scheme in practical applications. In any case, all the relevant viscous effect must be confined inside the inner region. In the numerical tests, starting from a distance of $L/2$, Γ has been moved closer to the body up to $L/20$. No significant changes in the solution have been observed. However, $L/20$ cannot be considered the closest distance at which Γ can be located, since we have not performed further test cases. The analysis of this problem will be carried on more deeply in the future. In the computations reported in Figs. 8 and 9 (contour lines of the u components of the velocity for the double body flow and for $Fr = 0.316$, respectively) it is shown that the boundary layer and the wake are clearly confined inside $\mathcal{D}_v$.
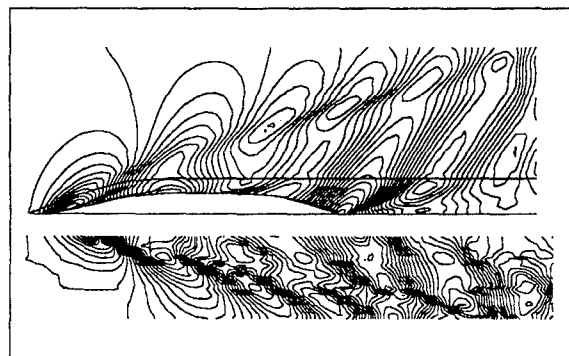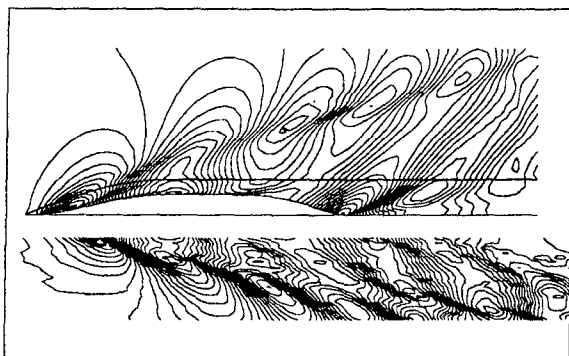

Figure 10: Free surface elevation: comparison between numerical results (top half) and experimental data [16] (bottom half) for the S60 — $Fr = 0.300$. Levels of $\mathcal{H}/Fr^2$: -0.1,-0.09,. . . ,0.1

337

Figure 11: Free surface elevation: comparison between numerical results (top half) and experimental data [16] (bottom half) for the S60 — $Fr = 0.316$. Levels of $\mathcal{H}/Fr^2$: -0.1,-0.09,...,0.1
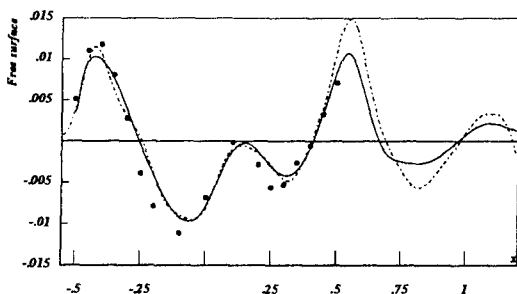

Figure 13: Free surface elevation along the hull at $Fr = 0.316$. — present method; - - - inviscid computation; •: experiment [16]

Figure 12: Free surface elevation along the hull at $Fr = 0.300$. — present method; - - - inviscid computation; •: experiment [16]

Figure 14: Pressure at the stern of the S60 hull at $Fr = 0.16$: comparison between numerical results (solid line) and experimental data [16] (dashed line). Levels: -0.06,-.05 ,...,0.1

The wave patterns are shown in Figs. 10 and 11 for two values of Froude number: 0.300 and 0.316 ($Re = 4.5 \times 10^6$). The computed solutions are compared with experimental measurements [15]. The inner and the outer solution seem to be very well matched, whereas the comparison with the experimental measured wave profiles is rather encouraging. Concerning the wave profiles along the hull, the potential solution (dotted line) seems to fit better the experimental data [15, 16] in the bow zone, with respect to the present solution (solid line). The rather unsatisfactory prediction at the bow may be due to the poor grid resolution, since only 15 points were used in girthwise direction. Upwind discretization of the free surface boundary condition in the inner region may be another cause of the bow wave underestimation.

Finally, the pressure on the hull surface at the stern is compared with measured values at $Fr = 0.16$ in Fig. 14. Also in this case, the numerical prediction is satisfactory.
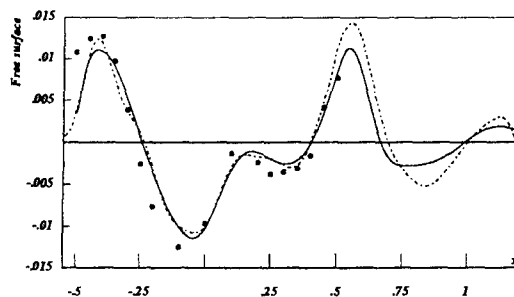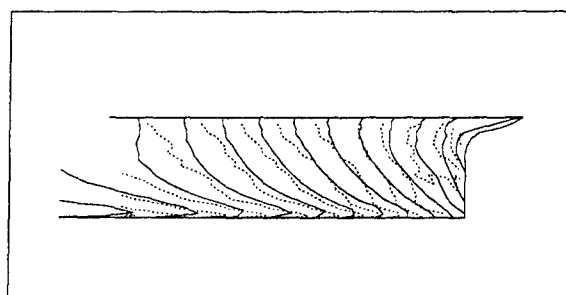
CONCLUDING REMARKS

The numerical solution of a domain decomposition model for free surface steady viscous flows has been obtained; the preliminary results seem to be rather encouraging. The coupling algorithm between the viscous and the potential solvers is implemented by a robust iterative scheme. The CPU saving with respect to a full Navier–Stokes code is apparent and promising. Further numerical experiments are needed to analyze the dependence of the solution on the grid refinement and on the thickness of the viscous region. Moreover, in the viscous region, the wave amplitude is rather underestimated: this problem might be solved by a grid refinement, or by a more accurate implementation of the free surface boundary conditions for Navier–Stokes equations.

ACKNOWLEDGEMENTS

338

REFERENCES

[1] M. Ikehata, Y. Tahara,"Influence of Boundary Layer and Wake on Free Surface Flow around a Ship Model", Nav. Arch. and Ocean Eng., Vol.26, p.71 (1988).

[2] Tahara, Y., Stern, F., "An Interactive Approach for Calculating Ship Boundary Layer and Wakes for Nonzero Froude Number", Proc. XVIII O.N.R., Ann Arbor, Michigan, 1990.

[3] Dawson, C.W.,"A Practical Computer Method for Solving Ship-Wave Problems", 2nd Int. Conf. on Numerical Ship Hydro., Berkeley, 1977.

[4] Lalli, F., Campana, E., Bulgarelli, U., "Ship Waves Computations", 7th Inter. Workshop on Water Waves and Floating Bodies, Val de Reuil, France, May 1992.

[5] Lock, R.C., Williams, B.R. (1987), "Viscous–Inviscid Interactions in External Aerodynamics", Prog. Aerospace Sci., 24, pp.51-171.

[6] Bassanini, P., Bulgarelli, U., Campana, E., Lalli, F., "The Wave Resistance Problem in a Boundary Integral Formulation", to be published on Surv. Math. Ind..

[7] A.J. Chorin, J. Comput. Phys., Vol.2, pp.12-26 (1967)

[8] Baldwin, B.S., Lomax, H. "Thin Layer Approximation and Algebraic Model for Separated Turbulent Flows", AIAA Paper 78-257, (1978)

[9] Kwak,D., Chang, J.L.C., Shanks, S.P., Chakravarthy, S.R., "A Three-Dimensional Incompressible Navier–Stokes Flow Solver Using Primitive Variables", AIAA J., Vol.24, pp.390-396 (1986)

[10] R.M. Beam, R.F. Warming, "An Approximate Factorization Scheme for the Compressible Navier–Stokes Equations", AIAA J., Vol.16, pp.393-402 (1978)

[11] Di Mascio, A., Esposito, P.G., "Numerical Simulation of Viscous Flows past Hull Forms", The Second Osaka Inter. Coll. on Viscous Fluid Dyn. in Ship and Ocean Tech., Sept. 27-30, 1991

[12] Kodama, Y., "Grid Generation and Flow Computation for Practical Ship Hull Forms and Propelleres Using the Geometrical Method and the IAF Scheme", Fifth International Conference on Numerical Ship Hydrodinamics, pp. 71-85, Hiroshima 1989

[13] Campana, E., Di Mascio, A., Esposito, P.G., Lalli, F., "Viscous–Inviscid Coupling in Ship Hydrodynamics", XI Australasian Fluid Mech. Conf., Hobart (Australia), 1992.

[14] Knaack, T., Kux, J., Wieghart, K., "On the Structure of the Flow Field on Ship Hulls", Osaka International Colloquium on Ship Viscous Flow, 1985

[15] Toda, Y., Stern, F., Tanaka, I., Patel, V.C. IIHR Report No. 326, Iowa Institute of Hydraulic Research, The University of Iowa, Nov. 1988

[16] Toda, Y., Stern, F.,Longo, J., IIHR report No.352, Iowa Institute of Hydraulic Research, The University of Iowa 1991.

DISCUSSION

by Dr. Yoshiaki Kodama, Ship Research Institute, Tokyo, Japan.

I would like to congratulate the authors on this successful computation of free-surface flows using the domain decomposition method and ask the following questions:

(1)   On the free surface boundary of the inner region, five boundary conditions are needed, in agreement with the number of unknowns, i.e., u, v, w, p, and H (wave height). However, in Eq. (17) only four boundary conditions are given. What is the fifth boundary condition used?

(2)   Linearized free surface boundary conditions are used in the computations. How much does this approximation effect the computed results?

<u>Author's Reply</u>

We thank Dr. Kodama for his comments and discussions.

In response to the first question, on the free surface boundary of the inner region one of the unknown velocity components can be simply obtained by the continuity equation. The combination of this with the boundary conditions (17) give the complete set of conditions for the five unknowns.

Concerning the second question, it may be said that the limits of the linearized formulation re widely known, that is, its influence on the wave amplitude, wave shape and wave length. Aware of this, we decided to use the linearized formulation because of its simplicity. In fact, at the present stage of our research, we are mostly interested in the consequences of the use of the domain decomposition approach. We devoted our efforts in solving a few problems arising out of its use: the investigation on the effective CPU time reduction, on the smoothness of the solution at the matching boundary and on the robustness of the matching algorithm.

DISCUSSION

by Dr. P. M. Gresho, Lawrence Livermore National Laboratory, USA

In spite of your good-looking and converged solutions, I am disturbed by your matching boundary conditions for the viscous incompressible Navier-Stokes equations. You seem to specify all components of velocity and the pressure. The NS equations, however, are well-posed with just the velocity specified on the boundary of the solution domain (the pressure on the boundary is part of the solution!) and are over specified, and thus ill-posed, if you also specify the pressure. How do you account for this, or explain/justify you boundary conditions?

<u>Author's Reply</u>

Dr. Gresho is quite right, of course, regarding the number of boundary conditions to be imposed for the Navier-Stokes equations. At the matching boundary, continuity of pressure and normal velocity should be imposed, while a discontinuity on tangential velocity at the matching boundary should be allowed. However, in the overlapping region, we also expect the viscous term to be small and, moreover, the grid to be so coarse that viscous effects cannot be resolved. Therefore, for practical computation, we suppose that the model is the same on both domains in the overlapping zone, i.e., the algorithm works as if a homogeneous domain decomposition technique with overlapping were implemented.

The above discussion is not rigorous, being justified only on computational ground. From the theoretical point of view, doubts remain when the grid size goes to zero, in which case a discontinuity must be accepted on tangential velocity at the viscous-inviscid interface.

Interactive Zonal Approach for Ship Flows Including Viscous and Nonlinear Wave Effects

H.-C. Chen (Texas A&M University, USA)
W.-M. Lin and K.M. Weems
(Science Applications International Corporation, USA)

ABSTRACT

A hybrid numerical method for the prediction of ship flows including both viscous and nonlinear wave effects is presented. In this method, a zonal approach which combines a free-surface potential flow calculation and the Reynolds-Averaged Navier-Stokes (RANS) method is used. The linear potential flow calculation provides the ship-generated waves away from the ship. The RANS method in the near field resolves the turbulent boundary layer, the wake flows, and the nonlinear waves around the ship hull. The kinematic and dynamic free-surface boundary conditions are satisfied on the exact free surface in the RANS solution domain. The viscous-inviscid interaction is captured through a direct matching of the velocity and pressure fields in an overlapped RANS and potential flow computation region.

Extensive results are presented for the Series 60 $C_B = 0.6$ parent hull form at Froude numbers (Fr) = 0.0 (double body), 0.160 and 0.316. The coupled RANS and potential flow method successfully resolves the hull boundary layer, the near wake, and the nonlinear free surface waves. The results clearly demonstrate the feasibility of the coupling approach and therefore enables us the use of a rather small RANS solution domain for efficient and accurate resolution of near-field ship flows.

INTRODUCTION

In the study of the body-wave interaction problems, potential flow methods are normally used. Viscous effects are included only empirically or in an integral sense to approximate overall viscous damping forces. This simplification in many cases is justifiable and also practically essential to keep the complexity of the problem in reasonable bounds. However, viscous effects are important to many ship free-surface flow related problems, such as roll motion, bow flow, stern flow and wake, detailed inflow to the propeller, and propeller/hull/wave interactions. In order to improve our understanding of the interaction between the viscous flow and wave field and to enhance our capability in the design and evaluation of new advanced ships, it is necessary to develop a prediction method which considers both the viscous and nonlinear wave effects.

In principle, both the viscous and wave effects can be calculated directly using the complete Reynolds-Averaged Navier-Stokes (RANS) equations for the entire flow field with an appropriate free surface boundary condition. This approach has been employed by Miyata et al. [1],[2] and Hino [3], among others, for ships in straight courses. These calculations, however, often require the use of a very large solution domain and an excessively large number of grid nodes to achieve adequate resolution of the entire flow field. Since the viscous effects are usually confined to a small region surrounding the ship hull and in the ship wake, it is desirable to use the simpler potential flow theories, instead of the complete RANS equations, for the wave field outside the viscous flow region. A zonal, interactive numerical approach which combines the RANS and potential flow calculations can therefore be an effective method for accurate resolution of ship free-surface flow problems.

The interaction among free-surface waves, the boundary layer, and wake flows has been the sub-

ject of many previous studies. Most of these studies, however, have focused on either viscous effects on wavemaking or wave effects on the boundary layer and wakes. A review of these works was given by, among others, Shahshahan & Landweber [4] and Stern [5]. More recently, Tahara et al. [6] and Toda et al. [7], [8] employed the displacement body concept of Lighthill [9] and developed an interactive approach to calculate ship boundary layers, wakes and wave field for a Wigley hull form. In their studies, the RANS method was coupled with the SPLASH free surface code of Rosen [10]. A simplified displacement body was used to account for the viscous effect in an approximate manner. The evaluation of displacement thickness, however, was found to be rather sensitive to small velocity changes in the outer part of viscous boundary layers. Furthermore, the validity of the displacement body concept also becomes questionable for problems involving thick boundary layers, wakes and/or regions of massive flow separation.

In view of the difficulties encountered in the displacement body approach, Chen and Lin [11] have explored several alternative coupling schemes including velocity/pressure matching, stream surface iteration, and field vorticity methods. Unlike the displacement body and the body vorticity methods proposed by Lighthill [9], these new coupling schemes do not rely on the thin boundary layer assumptions and are directly applicable to thick boundary layer as well as separated flow regions. Numerical results in Chen and Lin [11] for several axisymmetric bodies and three-dimensional double body ship forms clearly demonstrate that the velocity/pressure coupling scheme is the most accurate and efficient approach in capturing the viscous-inviscid interactions.

In this paper, the velocity/pressure coupling scheme is employed for the calculation of steady ship free-surface flow problems. The multiblock RANS method of Chen and Korpus [12] is extended for nonlinear free-surface flow calculations. Free surface potential flow methods are used to provide the wave field away from the ship hull. For the viscous-inviscid coupling, several major modifications are necessary for both the potential flow and the RANS methods. For completeness, the potential flow methods, the multiblock RANS methods, and the viscous-inviscid coupling scheme are briefly described. Calculations were performed using the Series 60 C_B

= 0.6 parent hull form to examine the general performance of the interactive RANS and potential flow coupling method. Numerical solutions were obtained for the double-body flow (Fr = 0.0) and the steady ship free surface flow at Fr = 0.16 and 0.316. Detailed comparisons have been made with available experimental data to evaluate the general performance of the present interactive RANS/potential flow coupling approach.

POTENTIAL FLOW METHODS

For the solution of ship waves in the outer field, two potential-flow codes have been used. The SLAW (Ship Lift and Wave) code is a Dawson type steady ship wave panel code [13]. The LAMP (Large-Amplitude Motion Program) code utilizes a time-domain Green function approach [14]. Both methods and their respective advantages and disadvantages will be discussed here.

SLAW Calculations

The SLAW code was developed for computing the inviscid, irrotational, steady free surface flow around a ship operating on or near the free surface [13]. SLAW's basic formulation follows Dawson's method [15] for computing the hydrodynamic flow around a ship operating on the free surface. In this method, low order singularity panels are distributed over the body surface, S_B, and a local region of the mean free surface, S_F, as shown in Figure 1. Source panels are used for the free surface panels while body panels can either be source panels [16] for non-lifting problems or source and dipole panels [18] for lifting problems like sailing yachts running upwind. The lifting (source/dipole) singularity model includes dipole wake sheets for modeling vortex wakes and enforcing the Kutta condition on wake shedding edges.

SLAW satisfies an exact Neumann condition on S_B and a linearized free surface boundary condition on S_F, which is derived from the general form of the kinematic and dynamic free surface boundary conditions shown below:

$$\vec{\nabla}\Phi \cdot \hat{n} = 0 \qquad z = \zeta(x,y) \quad (1)$$

$$|\vec{\nabla}\Phi|^2 = U_\infty^2 + V_\infty^2 - 2g\,\zeta \qquad z = \zeta(x,y) \quad (2)$$

where Φ is the velocity potential, $\hat{n}$ the unit normal vector to the free surface, $\zeta(x,y)$ the free

surface elevation, g the gravitational acceleration, and U_∞ and V_∞ are the x and y components of the inflow velocity at infinity. To linearize these conditions, Φ is divided into the double body potential, Φ^{DB}, and a free surface perturbation potential, ϕ:

$$\Phi = \Phi^{DB} + \phi \qquad (3)$$

After substituting this definition into Equations (1) - (2), higher order terms of the perturbation potential can be dropped to get the following linearized free surface boundary condition on the mean free surface:

$$2(\Phi_x^{DB}\Phi_{xx}^{DB} + \Phi_y^{DB}\Phi_{xy}^{DB})\,\phi_x$$
$$+2(\Phi_x^{DB}\Phi_{xy}^{DB} + \Phi_y^{DB}\Phi_{yy}^{DB})\,\phi_y$$
$$+\Phi_x^{DB^2}\,\phi_{xx} + 2\Phi_x^{DB}\Phi_y^{DB}\,\phi_{xy} + \Phi_y^{DB^2}\,\phi_{yy} + g\phi_z$$
$$= -\Phi_x^{DB^2}\Phi_{xx}^{DB} - 2\Phi_x^{DB}\Phi_y^{DB}\Phi_{xy}^{DB} - \Phi_y^{DB^2}\Phi_{yy}^{DB}$$
$$on \ z = 0 \qquad (4)$$

In addition, a radiation condition must be imposed to avoid upstream waves. SLAW uses Jensen's upstream collocation point shift [17] technique to enforce the radiation condition, rather than upstream differencing used by Dawson and others. Since this technique eliminates the dispersion error and wave damping associated with the upstream differencing, SLAW's free surface solution is more suitable for the present zonal calculation than many other free surface potential flow methods.

Since the free surface boundary condition is linearized about the double body (Fr=0.0) flow, the double body potential is first calculated by imposing a normal velocity condition at the control point of each body panel:

$$\vec{\nabla}\Phi^{DB} \cdot \hat{n} = V_N^{DB} \qquad (5)$$

where V_N^{DB} is the specified double body normal velocity and $\hat{n}$ is the surface unit normal vector. The resulting system of linear equations can then be solved to get double body singularity strength for each body panel. Note that, because the double-body solution is solved separately and completely, SLAW is set up so that it can be used to compute Fr=0.0 problems (i.e. no free surface) simply by stopping the calculation after the double-body solution.

After the double body problem is solved, the perturbation potential is calculated by satisfying the linearized free surface boundary condition shown in Equation (4) at the control point of each free surface panel and the following perturbation velocity condition on each body panel:

$$\vec{\nabla}\phi \cdot \hat{n} = V_N - \vec{\nabla}\Phi^{DB} \cdot \hat{n} = V_N - V_N^{DB} \qquad (6)$$

where V_N is the total specified normal velocity and V_N^{DB} is the double body specified normal velocity. The resulting system of linear equations can then be solved for the perturbation singularity strength on each body and free surface panel.

Once the double body and perturbation singularities have been computed, flow quantities like potential, velocity, and pressure can be computed at field points anywhere in the fluid domain by calculating the influence of each panel on the specified field point. Note, however, that the edge singularity of the constant source and dipole panels make this type of influence calculation inaccurate for field points which are close (less then one half of a panel length) to a panel edge. For these cases, the field point quantities are interpolated from quantities computed at the panel control points and at field points "far" from panel edges.

SLAW Self-Consistency Test

For a conventional ship wave calculation, S_B is simply the hull surface and the specified normal velocities, V_N^{DB} and V_N, are zero for all panels. For the RANS/Potential Flow interaction problem where SLAW is being used to compute the outer flow region, S_B is an arbitrary matching surface and the specified normal velocities, V_N^{DB} and V_N, are computed from the RANS solution for the inner flow region. Once either type of calculation has been done, the potential flow velocities and pressures on the RANS matching surface can be computed using SLAW's field point velocity routine. Special subroutines were added to the SLAW code to make the RANS/SLAW interaction virtually automatic.

Because the double body and total specified normal surface velocities, V_N^{DB} and V_N, are specified separately, two procedures for matching the SLAW and RANS velocities are possible:

1. Compute an iterative RANS/SLAW double-body solution (Fr=0.0) first, using the double body RANS velocities on the matching surface as V_N^{DB}, then turn on the free surface effects, using the complete RANS velocity as V_N.

2. Iterate between the complete (with free surface) RANS and SLAW solutions from the beginning, using the complete RANS velocity on the matching surface as V_N^{DB} and V_N.

The first procedure has been used by Campana et al. [19]. The advantage of the this procedure is that it is completely consistent with the SLAW formulation. The disadvantage is that it requires iterating the RANS and SLAW calculations to convergence twice, first with the free surface effects neglected, and then with the free surface effects accounted for. The advantage of the second procedure is that its single iteration loop is simpler to implement and requires less computation. A possible disadvantage is that the specified normal velocities for SLAW's "double-body" solution, which are interpolated from the inner RANS solution, are no longer double-body (Fr = 0.0) velocities. Numerically, this is no problem, since the free surface potential can be calculated as a perturbation about any basis potential solution. Likewise, the linearized free surface boundary condition used by SLAW will be valid for any basis potential as long as it has $\frac{\partial \Phi}{\partial z} = 0.0$ on $z = 0.0$, which is implicitly satisfied by the singularity model used to compute the "double-body" flow. However, the RANS solution contains free surface effects and will not typically have $\vec{V} \cdot \hat{n} = 0.0$ at the mean free surface. In addition, the free surface effects in the RANS solution will appear in the nonlinear terms of the free surface boundary condition rather than the linear terms. Since it was not possible to predict *a priori* the effects of these "inconsistencies" on the SLAW calculation, a series of test calculations were done.

In order to verify the validity of using the SLAW code to compute a zonal flow field and to investigate what velocity matching procedure was required, a series of test calculation were performed for a Wigley parabolic hull at Fr=0.340 in which the the SLAW code was used to calculate both the complete and the outer flow field. First, SLAW was used to compute the complete flow field, with the ship hull itself used as S_B and the matching velocities, V_N^{DB} and V_N, set to zero. The computed free surface elevation contours for this calculation are shown in the top plot of Figure 2. As part of this calculation, both double body ($\vec{V}^{\text{DB}}$) and total ($\vec{V}^{\text{FS}}$) field point velocities were computed on a cylindrical "matching" surface which extended the entire length of the computational domain.

Two SLAW calculations were then made for the outer computation domain, with the "matching" surface used as S_B. In the first outer domain calculation, the specified double body velocity on S_B was set to be the normal component of the double body field point velocity computed in the complete domain calculation, and the specified total velocity S_B was set to be the normal component of the total field point velocity:

$$V_N^{\text{DB}} = \vec{V}^{\text{DB}} \cdot \hat{n} \tag{7}$$

$$V_N = \vec{V}^{\text{FS}} \cdot \hat{n} \tag{8}$$

This test calculation is the equivalent of the RANS/SLAW velocity matching procedure 1 above. Computed free surface elevation contours for this calculation are shown in the middle plot of Figure 2. These contours match the outer part of the complete domain contours almost exactly, confirming both the validity of the SLAW zonal calculation and the implementation of the field point velocity calculation and zonal interaction routines.

In the second outer domain calculation, both the specified double body and the specified total normal velocity on S_B were set to the the normal component of the total field point velocity computed in the complete domain calculation:

$$V_N^{\text{DB}} = V_N = \vec{V}^{\text{FS}} \cdot \hat{n} \tag{9}$$

This test calculation is the equivalent of the RANS/SLAW velocity matching procedure 2 above. The computed free surface elevations for this calculation are shown in the bottom plot of Figure 2. Again, these contours match the outer part of the complete domain contours almost exactly, verifying that SLAW zonal calculation can be made by matching the total velocity only and that first iterating to find the RANS/SLAW double body solution is not necessary. A similar zonal test calculation for the Series 60 hull confirmed that only the total velocity had to be matched.

LAMP Calculations

In our earlier study (Chen and Lin [20]), a three-dimensional time-domain program LAMP [14] was used. The LAMP code is generally used to compute the flow around a ship moving with forward speed in a seaway. In the LAMP approach, the exact body boundary condition is satisfied on the instantaneous wetted surface of the moving body while the free-surface boundary conditions

are linearized. The problem is solved using a panel method with distribution of the transient free-surface Green function for a step-function source below the free surface [21].

For the steady ship wave solution, the unsteady LAMP code is run for a ship started from rest and accelerated until it reaches a constant forward speed corresponding to the specified Froude number. The calculation is continued until a steady state is reached. It was found in [14] that the starting condition will affect only the initial transient behavior of the solution and has no effect on the steady-state solutions. For the RANS/LAMP interaction problem where LAMP is being used to compute the outer flow region, an arbitrary matching surface is used with the specified normal velocities computed from the RANS solution for the inner flow region.

The RANS/LAMP velocity-pressure coupling for the viscous free-surface flow problems was established by Chen & Lin in [20]. However, several issues remain to be addressed to ensure a general and robust RANS/LAMP coupling. First, the LAMP method, unlike the SLAW method described above, requires a closed matching surface which will have to cut through the viscous wake region. A discrete vortex model is needed in the LAMP computation domain to account for the viscous effect in the wake. Without the discrete vortex model, the LAMP solution can only be used for the initial "bare-body" calculation of velocities and pressures at the outer matching surface. Iteration between RANS and LAMP cannot be done. Secondly, the time-domain approach is computationally more expensive than SLAW for steady-state problems. However, the time-domain approach may be necessary for unsteady problems.

The numerical results obtained by RANS/LAMP coupling approach has been reported in details in Chen and Lin [20]. In the present study, we shall present only the potential flow results obtained by using the SLAW code.

MULTIBLOCK RANS METHOD

In the present study, the multiblock RANS method of Chen and Korpus [12] has been employed for the solution of viscous boundary layers, wakes and nonlinear free surface waves in the near field. We shall briefly describe the general-

ized RANS method in the following:

Governing Equations

Consider the nondimensional Reynolds-Averaged Navier-Stokes equations for incompressible flow in a orthogonal curvilinear coordinate system (x^1, x^2, x^3, t):

$$U^i_{,i} = 0 \qquad (10)$$

$$\frac{\partial U^i}{\partial t} + U^j U^i_{,j} + \overline{(u^i u^j)}_{,j}$$
$$+ g^{ij} p_{,j} - \frac{1}{Re} g^{jk} U^i_{,jk} = 0 \qquad (11)$$

where

$$g^{ij} = \delta_{ij}/h_i^2 \ ,$$
$$g_{ij} = \delta_{ij} h_i^2$$

and U^i, $\overline{u^i u^j}$, and p represent contravariant velocities, Reynolds stresses, and pressure, respectively. The quantities g_{ij} and g^{ij} represent metric and conjugate metric tensors in orthogonal curvilinear coordinates, and the h_i's represent associated metric scale factors. The Reynolds number $Re = U_o L/\nu$ is based on a characteristic length L, a reference velocity U_o and the kinematic viscosity ν.

The Reynolds stresses are related to the corresponding mean rate of strain e^{ij} through an isotropic eddy viscosity ν_t,

$$-\overline{u^i u^j} = 2\nu_t e^{ij} - \frac{2}{3} g^{ij} k, \qquad (12)$$

$$e^{ij} = \frac{e(ij)}{h_i h_j} = \frac{1}{2}(g^{ik} U^j_{,k} + g^{jk} U^i_{,k}) \qquad (13)$$

where $k = g_{ij}\overline{u^i u^j}/2$ is the turbulent kinetic energy. The quantities e^{ij} and $e(ij)$ represent contravariant and physical components of the rate-of-strain tensor respectively. Substitution into (11) yields momentum equations:

$$\frac{\partial U^i}{\partial t} + U^j U^i_{,j} + g^{ij}(p + \frac{2}{3}k)_{,j} - 2\nu_{t,j} e^{ij}$$
$$- \frac{1}{R_u} g^{jk} U^i_{,jk} = 0 \qquad (14)$$

The quantity $1/R_u = 1/Re + \nu_t/\sigma_u$ represents the effective turbulent viscosity.

Equations (14) are closed using the two-layer turbulence model of Chen and Patel [22]. In the two-layer approach, the transport equations for

turbulent kinetic energy and its dissipation rate can be written as:

$$\frac{\partial k}{\partial t} + U^j k_{,j} - (\frac{1}{R_k} g^{ij} k_{,j})_{,i} - G + \varepsilon = 0 \quad (15)$$

$$\frac{\partial \varepsilon}{\partial t} + U^j \varepsilon_{,j} - (\frac{1}{R_\varepsilon} g^{ij} \varepsilon_{,j})_{,i}$$

$$- \frac{\varepsilon}{k} C_{\varepsilon 1} G + C_{\varepsilon 2} \frac{\varepsilon^2}{k} = 0 \quad (16)$$

where

$$G = \nu_t (U^i_{,m} U^m_{,i} + g_{ij} g^{mn} U^i_{,m} U^j_{,n}) \quad (17)$$

The effective viscosities in (15) and (16) are taken as $1/R_k = 1/Re + \nu_t/\sigma_k$, and $1/R_\varepsilon = 1/Re + \nu_t/\sigma_\varepsilon$, respectively, and the coefficients $(C_\mu, C_{\varepsilon 1}, C_{\varepsilon 2}, \sigma_u, \sigma_k, \sigma_\varepsilon)$ are fixed constants equal to (0.09, 1.44, 1.92, 1.0, 1.0, 1.3).

In the near-wall region, the rate of turbulent dissipation is specified in terms of k rather than being computed from (16). From Chen and Patel [22]:

$$\varepsilon = \frac{k^{3/2}}{\ell_\varepsilon} \quad (18)$$

where ℓ_ε is a dissipation length scale equal to $C_\ell y[1 - exp(-R_y/A_\varepsilon)]$. With k and ε known, the eddy viscosity is found from:

$$\nu_t = C_\mu \sqrt{k} \ell_\mu \quad (19)$$

where

$$\ell_\mu = C_\ell y[1 - exp(-R_y/A_\mu)]$$

The constants C_ℓ, A_μ and A_ε are chosen to yield a smooth distribution of eddy viscosity between the two regions, and take the values ($C_\ell = \kappa C_\mu^{-3/4}$, $\kappa = 0.418$, $A_\mu = 70$, $A_\varepsilon = 2C_\ell$).

For calculations around practical geometries, Equations (14) through (16) have been transformed into body-fitted coordinates $t = \tau$, $x^i = x^i(\xi^1, \xi^2, \xi^3, \tau)$:

$$\frac{1}{J} \sum_{i=1}^{3} \sum_{j=1}^{3} \frac{\partial}{\partial \xi^i} [b^i_j U(j)] = 0 \quad (20)$$

$$\frac{\partial U(i)}{\partial \tau} + \sum_{j=1}^{3} C^j_{U(i)} \frac{\partial U(i)}{\partial \xi^j} - \frac{1}{R_U} \nabla^2 U(i)$$

$$+ s_{U(i)} = 0 \quad (21)$$

$$\frac{\partial k}{\partial \tau} + \sum_{j=1}^{3} C^j_k \frac{\partial k}{\partial \xi^j} - \frac{1}{R_k} \nabla^2 k + s_k = 0 \quad (22)$$

$$\frac{\partial \varepsilon}{\partial \tau} + \sum_{j=1}^{3} C^j_\varepsilon \frac{\partial \varepsilon}{\partial \xi^j} - \frac{1}{R_\varepsilon} \nabla^2 \varepsilon + s_\varepsilon = 0 \quad (23)$$

where $U(i) = h_i U^i$ are physical components of the contravariant velocity vector. The curvature parameters K_{ij}, geometric coefficients α_{ij}, convection coefficients C^j_ϕ, source functions s_ϕ and Laplacian operator ∇^2, are given in Chen et al. [23].

Multiblock Capability

In the present multiblock approach, the solution domain is first decomposed into a number of smaller sub-regions which are solved on a block by block basis. Within each computational block, the finite-analytic numerical method of Chen et al. [23] was employed to solve the unsteady RANS equations in a general curvilinear, body-fitted coordinate system. Complete continuity across block intersections is maintained by adding a one-cell overlap at each face. Thus, each point that is interior to the domain is also interior to at least one block. Block interface boundary conditions are updated by copying from the interior of adjacent blocks.

The current implementation requires continuity of grid lines across block faces, but not the one-to-one matching of the faces themselves. Any face can be divided into sub-sections that match different blocks, or that can be assigned different boundary conditions. Each block is allowed arbitrary dimension and orientation as long as the assembly of all blocks covers the entire solution domain. This multiblock structure has been further generalized in the present study to provide a flexible interface with the SLAW and LAMP codes in the potential flow computational block.

For three-dimensional flow calculations involving large number of grid nodes, a data management system was incorporated to circumvent the computer memory restrictions. The multiblock solution procedure requires only one block at a time, and reads the variables for that block as they are needed. Boundary data is stored in separate files since it may be needed a number of times during solution of any given block. The boundary files are relatively small, and can be read many times per iteration without slowing the computation. For the present interactive RANS/SLAW method, the SLAW solutions on any matching boundary can be readily treated as boundary data files in RANS calculations.

346

VISCOUS-INVISCID COUPLING

In the interactive RANS/SLAW calculations, the solutions in the RANS and SLAW solution domains are obtained separately. In order to capture the interaction between the viscous boundary layers and inviscid wave field, the velocity/pressure matching scheme developed by Chen and Lin [11] was employed to provide the viscous-inviscid coupling between the RANS and SLAW solutions.

If the RANS solution domain is large enough to capture the entire viscous-inviscid interactions, it will not be necessary to update the SLAW solutions in the outer region. In practical applications, however, it is desirable to reduce the RANS domain to take full advantage of the efficiency and accuracy of the potential-flow solver, particularly for computing the inviscid wave field in free surface problems. When the RANS outer boundary is placed in the region where the interaction between the RANS and SLAW solutions remains significant, it is necessary to perform iteration between the RANS and the SLAW solutions so that the viscous effects on the free surface can be properly accounted for in subsequent SLAW calculations.

As noted earlier, the present velocity/pressure coupling scheme matches both the velocity and pressure fields directly at the matching boundaries. SLAW is run first to calculate the inviscid wave field for the bare hull. This provides the velocity and pressure boundary conditions for the RANS solver on the outer matching boundary embedded in the SLAW solution domain. The RANS method is then employed for the solution near the ship hull. The iteration between the RANS and the SLAW solutions is done by constructing an imaginary SLAW solution boundary (inner matching boundary) which lies outside the viscous boundary layers and wakes, but still embedded in the RANS solution domain. The SLAW solution is recomputed by using the matching surface as S_B and the normal component of the RANS velocities as the specified SLAW normal velocities. Since the RANS normal velocities are used to specify the V_N distribution for the SLAW calculations, the new far-field potential flow solutions will contain the influences of near-field viscous and nonlinear wave effects modeled in the RANS calculation.

In order to account for the viscous-inviscid in-teractions between the RANS and SLAW solutions, both the pressure and tangential velocity on the RANS outer boundary are matched directly to the SLAW solution. However, since the RANS and SLAW methods have different level of discretization errors, a direct matching of all three velocity components often leads to spurious pressure gradients along the RANS matching boundary. In order to ensure smooth pressure and velocity distributions between the viscous and inviscid flow domains, the normal velocity must be adjusted to eliminate any mass sources which may arise from incompatible pressure/velocity matching boundary conditions. In the present study, the SIMPLER/PISO coupling scheme has been modified to ensure the conservation of mass and momentum across block boundaries. In particular, the contravariant velocity components leaving (or entering) the matching face have been adjusted so that the continuity equation will be satisfied at all times. The modified SIMPLER/PISO scheme was then employed to compute the pressure field and update the velocity field in the RANS domain. The same procedure has also been used by Hubbard and Chen [24] in a Chimera RANS method to maintain smooth pressure and velocity distributions across arbitrary overlapping and embedding chimera grid blocks. A more detailed description of the modified SIMPLER/PISO pressure solver were given in Hubbard and Chen [24].

For double-body ship flows without the presence of free surface waves, the potential flow solutions can be obtained effectively even with large number of panels on the hull surface. This has been demonstrated in Chen and Lin [11] for SSPA 720 Cargo Liner using 1250 (50 x 25) hull panels and 1850 (74 x 25) off-body points on a cylindrical matching boundary locates at a distance of 0.1 ship length (L) from the centerline. In this case, the potential flow panelization corresponded exactly to the RANS surface grid. With the presence of the free surface effects, however, panels must also be distributed on the local pottion of the free surface, so it is necessary to reduce the number of hull and free surface panels in potential flow calculations in order to keep the computational efforts within reasonable bounds. In most calculations performed here, the SLAW panel distributions on the inner matching boundary were constructed by taking only the odd $(2\xi^1 - 1, 2\xi^3 - 1)$ nodes of the RANS numerical grid in the longitudinal and girthwise directions. The free surface panels were then automatically

generated by the SLAW code in order to resolve the ship wave. By generating the body panels in this manner, the specified normal velocities for the SLAW panels could be taken directly from the even $(2\xi^1, 2\xi^3)$ grid nodes of the RANS solution without resorting to interpolation.

Because of the needs for extensive refinement of hull and free surface panels at low speeds, the computational effort required for SLAW calculations increase rapidly at low Froude numbers. In addition, SLAW calculations have not been well validated at extremely low speeds. Detailed measurements by Toda et al. [7], [8], however, indicated that the free surface wave effects are negligible at low speeds except near the bow and stern. Since the viscous-inviscid interactions are quite weak at low Froude numbers, it is probably more effective to use a larger RANS solution domain and move the overlap region completely outside the interactive zone. This enables us to match the RANS solutions directly with bare-body SLAW solutions and avoid time-consuming RANS/SLAW interactive calculations. This non-interactive approach provides a powerful alternative to the SLAW or other potential flow codes for low speed simulations when the viscous effects are equally or more important than the wave effects.

Free Surface Boundary Conditions

As noted earlier, both SLAW and LAMP satisfy linearized free surface boundary conditions. In the initial phase of this study, the free surface boundary conditions in RANS domain were also linearized to simplify the coupling between the RANS and potential flow methods. Within the context of the linear wave theory, the dynamic and kinematic free surface boundary conditions were specified at the mean free surface of the RANS solution domain. Both the surface tension and viscous shear stresses on the free surface were neglected. The wave profile was calculated from the kinematic boundary conditions using a time-marching scheme. The pressure distribution on the mean free surface was then updated using the dynamic free surface conditions. Preliminary results exhibit some unrealistically large waves within the hull boundary layer. This is believed to be caused by the incompatibility of viscous boundary layer flow and inviscid wave field near the hull and free surface intersection. A detailed study of both the hull and free surface boundary layer including free surface turbulence

is obviously needed in order to address the mixed-boundary shear flow in this region. Since such a study is well beyond the scope of the present research, we have adopt a rather crude approximation to treat this complex body/wave intersection problem. In the present study, this problem was circumvented by allowing the free surface within a small viscous layer (about 0.001 L) near the body to move like an inviscid flow with Neumann (zero gradient) boundary conditions.

In addition to the free surface and hull interaction problem, it was noted that the linearization of free surface boundary conditions also contributed to the underprediction of wave profiles at high Froude numbers. Measurements at Fr=0.316 by Toda et al. [7], [8] indicated that the maximum elevation change between the primary wave crest and wave trough amounts to nearly 50% of the ship draft. It is, therefore, desirable to apply the dynamic boundary condition on the exact free surface rather than the mean free surface for accurate resolution of viscous boundary layer and wake flows beneath the actual free surface. In the present study, the kinematic and dynamic free surface boundary conditions are applied on the exact free surface location. This is achieved by a simple stretching of the z coordinates in the vertical direction after a new free surface wave profile has been obtained from the integration of the exact kinematic free surface condition. It is recognized that this simple stretching procedure may lead to significant distortion of the hull forms. In order to minimize this distortion, the coordinate stretching was applied only to upper portion of the numerical grid near free surface while the remaining grids still conformed exactly with the original hull form. If more accurate representation of hull form is desired, it will be necessary to map the entire ship hull, including the exact hull geometry above the calm water level, into a parametric space. A parametric resplining of hull surface panels can then be performed to conform with the exact hull geometries. No such parametric resplining has been performed in the present study.

RESULTS AND DISCUSSIONS

In the present study, the RANS/SLAW method described above was employed for calculations of the viscous and wave fields around the Series 60 $C_B = 0.6$ parent hull. Calculations were performed for two different Froude numbers, Fr =

0.16 and 0.316, to facilitate a detailed comparison of numerical results with the velocity, pressure and wave elevation measurements documented in Toda et al. [7], [8]. For completeness, a double-body (Fr = 0.0) calculation for the same hull has also been performed to quantify the effects of free surface waves at different Froude numbers. In this section, important numerical results are summarized and compared with available data for detailed assessment of the general performance of the present RANS/SLAW interactive approach.

Numerical Grid

In the present calculations for the Series 60 C_B = 0.6 parent hull form, a 85 × 36 × 29 body-fitted numerical grid shown in Figure 3 was employed to cover the entire viscous flow region. The grids was generated using an interactive gridding code GRIDGEN developed by Steinbrenner et al. [25]. The first station in axial direction was located at X/L = -0.5 upstream of the bow, and the last station was placed at X/L = 2.0 in the wake where viscous diffusion is negligible. There are 49 streamwise and 29 girthwise stations on the hull itself. In addition, 12 stations were used upstream of the bow while 24 stations were employed for the resolution of ship wake flows. In the radial direction, 36 grid nodes were used between the hull surface and the RANS outer boundary located at R/L = 0.3. The SLAW matching boundary was chosen to be constant-ξ^2 coordinate surface with several grid-cells overlap between the RANS and SLAW solution domains. In double body calculations, the grid is uniformly distributed in the girthwise direction to provide appropriate resolution of the three-dimensional boundary layer on the ship hull. For non-zero Froude number cases, however, the numerical grids has been re-splined to improve the resolution near free surface. In the present RANS calculations, the numerical grid was divided into four blocks to facilitate the implementation of the two-layer turbulence model and various boundary conditions. Furthermore, an extra station (ξ^3 = 30) representing the mirror-image of ξ^3 = 28 station was added on the other side of the keel plane (ξ^3 = 29) so that the flow on the keel plane can be calculated directly.

For nonzero Froude number calculations, it was necessary to adjust the solution domain to conform with the exact free surface profiles. As noted earlier, this was achieved by stretching only the upper portion of the coordinate surfaces beneath the free surface once the new wave profile is obtained from the integration of kinematic free surface boundary conditions. For high Froude number case considered here, the elevation change between the primary wave crest and trough can amount to about 50 % of the ship draft. Consequently, considerable grid adjustments are required in order to conform with the exact free surface profiles and resolve the nonlinear wave effects.

In the bare body SLAW calculations for double-body and Fr = 0.316 cases, a 24 × 14 hull surface panel distribution was employed by selecting only the odd nodes from the RANS hull surface grid. The free surface panels were generated by adding 9 panels upstream and 17 downstream of the hull, and 21 panels in the transverse direction. This results in a total of 336 body panels and 882 free surface panels. For subsequent interactive calculations, the matching surface panels were again constructed by selecting the odd nodes from a constant-ξ^2 coordinate surface in the RANS grid. The new free surface grid needed for SLAW calculations was generated by adding 2 stations upstream and 3 stations downstream of the matching surface panels. In the transverse direction, 19 panels were used with outer boundary located at Y/L = 1.192. Overall, 588 (42 × 14) body panels and 855 free surface panels are used for the interactive SLAW calculations. Since the CPU time increases quadratically with the number of panels, the use of coarse panels enables us to reduce the run time to about 1/16 of the fine-grid calculations.

For the low Froude number (Fr = 0.160) calculations, it was necessary to increase the number of body and free surface panels for proper resolution of the short wavelength, small amplitude free surface waves at low speeds. In the present bare-body SLAW calculations, the downstream boundary was placed at X/L = 1.52 instead of 2.0 to reduce the computational efforts. On the hull surface, 840 (60 × 14) body panels were used to resolve the free surface waves. In addition, 2880 (96 × 30) free surface panels have been constructed by adding 8 panels upstream and 32 panels downstream of the hull. Since more panels and considerably longer run time will be needed for subsequent interactive calculations, it was decided to omit the interactive coupling between the RANS and SLAW solutions. As noted earlier, it is probably more effective to use a larger RANS solution

domain rather than performing RANS/SLAW interactive coupling for low speed calculations.

Interactive RANS/SLAW Coupling

Before describing detailed numerical results for the selected test cases, we shall carefully examine the general performance of the proposed velocity/pressure coupling approach with or without the presence of free surface waves. Interactive RANS/SLAW calculations were performed first for a double-body model of the Series 60 $C_B = 0.6$ parent hull at a Reynolds number Re $= 5 \times 10^6$. Figure 4 shows the convergence history of the pressure along the waterline and wake centerline. It is seen that the solutions converged in just two interactive RANS/SLAW coupling cycles. Similar level of convergence has also been observed in our earlier RANS/LAMP calculations (Chen and Lin [11]) for other hull forms with much smaller RANS domain and stronger viscous-inviscid interactions.

The surface pressure distributions obtained by interactive RANS/SLAW method are in close agreement with the SLAW bare-hull solutions up to about 80% of the body length. The sharp reduction of hull pressure in the stern region is obviously due to the rapid thickening of hull boundary layers in that area. For completeness, the pressure and vertical velocity contours for both the non-interactive (zeroth iteration) and interactive (second iteration) solutions are shown in Figure 5 to further illustrate the effectiveness of the present interactive coupling scheme. The dashed ($\xi^2 = 30$) and dotted ($\xi^3 = 36$) lines in these plots represent, respectively, the inner SLAW and outer RANS matching boundaries. Only the outer part of the SLAW solutions were plotted in the overlap region since accurate evaluation of the off-body velocities in the vicinity of the body can only be achieved with local refinement of surface panels. In the non-interactive solutions, there are very significant differences between the RANS and SLAW solutions in the overlap region. The discrepancies are particularly noticeable in the stern region where the viscous effects has led to rapid thickening of the hull boundary layers. It is noted in Figure 5(c) that the RANS vertical velocities differ considerably from the corresponding potential flow solutions, indicating the presence of strong viscous effects. In order to properly account for the viscous effects, the RANS velocities normal to the matching boundary have been used

to specify V_N in subsequent SLAW calculations. This has led to dramatic improvement of the predicted vertical velocity contours near the SLAW inner matching boundary. Similarly, the modified SIMPLER/PISO scheme was also found to be very effective in maintaining smooth pressure distributions in the overlap region. The slight discrepancies in the overlap region are most likely due to the use of coarser matching surface panels in SLAW calculations.

It should be remarked here that, in double-body calculations, both the RANS and SLAW matching surfaces remain fixed. This enables us to match pressure and velocities directly on the same grid nodes without any interpolation. For nonzero Froude number calculations, however, the free surface grids in RANS solution domain have to be adjusted to provide accurate resolution of nonlinear free surface waves. On the other hand, the SLAW code still uses calm-water hull and free surface panels in the context of linear wave theory. This has caused some inconsistencies on both the SLAW and RANS matching boundaries since only the underwater portion of the hull geometry will be retained in SLAW calculations. In present implementation of velocity/pressure coupling approach, the two solutions have been matched in the transformed plane ξ^i without considering the actual grid deformations caused by nonlinear wave effects. This incompatibility can be readily removed if a fully nonliner potential flow method is used for the calculations of free surface waves in the far field.

Despite the inconsistencies mentioned above, the velocity/pressure coupling approach appears to be quite effective even for the high Froude number cases. This is clearly evident from the convergence history shown in Figure 6 for Fr = 0.316 case. It is noted that the wave elevations along the waterline and wake centerline converged in just two to three RANS/SLAW iterations. The interactions between the viscous boundary layer and free surface flows completely altered the potential flow wave profiles in the stern and wake regions. In particular, the free surface waves decay very quickly along the wake centerline due to the convergence of low momentum fluid towards the ship stern and the centerplane of the wake. It is also seen from Figure 7 that the wave elevations along waterline and wake centerline ($y = 0$) are rather insensitive to different choices of SLAW inner matching boundaries.

Figure 8 shows a detailed comparison of the axial velocity contours between the non-interactive and interactive solutions. The dashed and dotted lines again represent the SLAW and RANS matching boundaries. It should be remarked here again that the SLAW solutions were evaluated on the calm water surface $z = 0$, while the RANS results were obtained on the exact free surface $z = \zeta$. Since the amplitude of the primary wave amounts to about 25 % of the ship draft, the nonlinear wave effects and the associated grid deformations may lead to significant distortion of the plotted axial velocity contours. These must be borne in mind when comparing the linear SLAW and nonlinear RANS solutions in the overlap region.

The most notable feature of the non-interactive solutions shown in Figure 8 is the absence of the viscous wake in the bare-hull potential flow solutions. In addition, there is a rather abrupt change in the slope of non-interactive velocity contours near the RANS outer boundary. This is obviously caused by the stern boundary layer and viscous wake which occupied about 1/3 of the RANS solution domain. In particular, the viscous wake pushed the SLAW velocity contours away from the wake centerline and forced the formation of new axial velocity contours outside the viscous wake. Consequently, the interactive RANS/SLAW solutions shown in Figure 8(b) exhibit a weaker wave pattern with longer wavelengths in comparison with potential flow solutions. The interactive RANS and SLAW solutions are in fairly good agreement in the overlap region.

For completeness, detailed pressure and axial velocity contours are shown in Figure 9. For clarity, only the RANS solutions were plotted in the overlap region. Interactive RANS/SLAW calculations have been performed for two different inner matching surfaces at $\xi^2 = 30$ (RANS/SLAW 1) and $\xi^2 = 32$ (RANS/SLAW 2). It appears that the RANS/SLAW 1 matching surface may be too close to the viscous wake. The matching between RANS and SLAW solutions, however, improves significantly in RANS/SLAW 2 with the overlap region located outside the viscous wake. A systematic domain dependence study may be needed to guide the selection of both the inner and outer matching boundaries.

Finally, we shall examine some preliminary low Froude number (Fr = 0.16) results to facilitate the discussion of Froude number effects. In potential flow calculations of low Froude number free surface flows, very fine panels and prolong simulation time are often required in order to resolve the short wavelength, small amplitude free surface waves observed at low speeds. Since the interaction between the far field free surface waves and the viscous boundary layers and wakes becomes quite weak at low Froude numbers, it is possible to neglect the free surface wave effects on the RANS outer boundary without significant effects on the viscous free surface flows in the near field. In our earlier RANS/LAMP calculations (Chen and Lin [20]), the near-field RANS solutions were matched directly with the double-body potential flow solutions to avoid lengthy time-domain LAMP computations. Although it appears that double-body matching conditions gave reasonable results for low Froude number simulations in the near field, it is still desirable to match the RANS solution directly with the potential flow free surface waves in order to ascertain the effects of matching conditions on the near-field viscous flow. A non-interactive RANS/SLAW calculation has been performed here to examine general features of the low Froude number free surface ship flows.

Figure 10 shows the numerical grid and calculated wave patterns for Fr = 0.160 case. The SLAW free surface panels in the inner region was removed to facilitate the comparison of RANS and SLAW grid distributions. The potential flow wave patterns shown in Figure 10(b) reveals a quite complex system of short wavelength, small amplitude waves. It is evident that the RANS numerical grid must be refined in both longitudinal and transverse directions to provide adequate resolution of all detailed flow features at this Froude number. The refinement of RANS grid is currently in progress.

Despite the coarseness of the numerical grids, preliminary RANS calculations have been performed to examine the general features of near-field low Froude number flows. Figures 10(c) and 10(d) show the calculated axial velocity and pressure contours. The influence of pressure and velocity matching conditions on the RANS outer boundary appear to be confined to a narrow region and have very little effects on the near-field free surface flows. In view of this, we shall focus our attention on the near-field RANS solutions for the present study. It is also seen that the low Froude number results closely resemble the double-body

solutions except in the bow and stern regions. More detailed comparisons will be made in later sections for further assessment of the near field solutions.

Double-Body Results

In order to facilitate a direct comparison of free surface wave effects between low and high Froude numbers cases, we shall present both the Fr = 0.160 and 0.316 results in the same plots. Furthermore, comparisons will also be made with double body solutions for more detailed examinations of complex interactions between the turbulent boundary layers, ship wakes and nonlinear free surface waves. For simplicity, we shall examine first the double-body turbulent boundary layer and wake flows without the complications due to surface waves. This enables us to establish a baseline solution for the assessment of free surface wave effects. In this section, we shall discuss only the basic flow features associated with double-body models. All the double-body solutions are shown as part (a) in Figures 11 through 14 to facilitate the comparisons and discussion of free surface effects at different Froude numbers.

Figure 11(a) shows the calculated double body pressure and axial velocity contours on the hull surface as well as the waterline and keel planes of symmetry. The pressure and axial velocity contours at selected transverse sections are shown in Figures 12(a) and 13(a). Together, they provide a detailed description of the three-dimensional pressure and axial velocity fields. For the double-body models considered here, strong pressure variations were observed in both the bow and stern regions due to the rapid changes of hull geometry in these areas. In the absence of free surface waves, it is seen that the boundary layer remains thin up to about 80% of the ship hull. Beyond that, a thick boundary layer develops quickly due to rapid changes in stern geometry and the accompanied three-dimensional pressure gradients around the hull surface.

Figure 14(a) shows the transverse velocity vector plots at several axial stations. The complex secondary flow patterns were generated by the geometrically-induced pressure gradients in the girthwise direction. The present solutions successfully captured the development of the bow bilge vortex (x = 0.4), the convergence of crossflow in the stern region (x = 0.8 & 0.9), and the

evolution of the stern bilge vortex in the near wake (x = 1.1). The convergence of the crossflow in the stern region is responsible for the thickening of stern boundary layer and near wake flows shown in Figure 13(a).

Nonzero Froude Number Results

Measurements performed recently by Toda et al. [7], [8] for the Series 60, $C_B = 0.6$ parent hull indicated very significant differences between the high and low Froude number data due to the wave-induced effects. In general, both the amplitude and length of the ship generated waves increase as Froude number becomes higher. At Fr = 0.16, the free surface effects are negligible except near the bow and stern regions. The measured pressure and velocity profiles also resemble those for the double body ship models. At higher Froude number of 0.316, the interactions between the viscous boundary layer, wake and free surface waves become much more profound near the bow, the afterbody, and in the wake. In these areas, both the viscous and free surface flows are significantly altered due to boundary layer, wake and wave interactions.

As described earlier, calculations have been performed for both Fr = 0.160 and 0.316 cases to examine the free surface effects. For the Fr = 0.160 case, we shall focus only on the comparison of near field flows. Figure 11 shows a comparison of pressure and axial velocity contours at different Froude numbers. At the low Froude numbers, it is seen that the pressure on the free surface differs considerably from that for the double-body case. But the wave effects was clearly confined to a small layer just beneath the free surface. This is also evident from Figure 12(b) which shows the pressure contours on several transverse sections. Note that the pressure contours on each transverse section are nearly identical to the corresponding double-body results shown in Figure 12(a) except in a small region just below the free surface. The wave-induced pressure gradients, however, are very large within this small surface layer.

Figure 13(b) and 14(b) show the axial velocity and crossflow vectors at several transverse stations. As expected, the influence of the free surface waves was also seen to be confined to a thin surface layer. It is interesting to note that the vertical velocity component changes rather dras-

tically near the free surface even though the cross-flow patterns returned quickly to the double-body pattern underneath the free surface. The magnitude of the surface vertical velocity is, in fact, comparable to that obtained for Fr = 0.316 case and is directly associated with the large wave-induced pressure gradients near the free surface. Both the crossflow patterns and the wave-induced pressure gradients can be explicated by the wave elevations shown in Figure 15.

With the increase of Froude number or ship speed, both the free surface wave elevations and wavelengths increase. As can be seen clearly in Figures 12 through 14, the wave elevation has large difference at x = 0.1 and at x = 0.4. Note that the amplitude of the bow wave is about 25 % of the ship draft. It is also seen from perspective views shown in Figures 15 and 16 that the nonlinear free surface waves induced very strong pressure gradients, both in the longitudinal and transverse directions. The presence of these wave-induced pressure gradients have led to significant modifications of the viscous boundary layer and wake flows shown in Figures 13 and 14. Compared to the Fr = 0.160 results, the wave-induced effects were also observed to penetrate much deeper into the fluid domain. Both the pressure and velocity contours plots reveal a strong interaction between the viscous boundary layer and wake, and the nonlinear free surface wave field. Most of the interaction can again be explicated as a result of the wave elevations and the wave-induced pressure gradients. For completeness, the free surface profiles are shown in Figures 15 and 16 to facilitate the discussion of wave-induced effects.

For high Froude number case, the wave-elevation contours reveal complex wave patterns consisting of both transverse and diverging wave systems. Close to the hull surface, it is seen that both the bow- and stern-wave systems were initiated with crests and the shoulder wave systems with troughs. Away from the ship hull, there is a complex interaction between the bow-, shoulder- and stern-wave systems, which creates the overall wave patterns shown in Figures 15 and 16. Compare to the Fr = 0.160 results, there is a much more distinct diverging wave system, especially in the bow and stern areas. Furthermore, it is also evident from the pressure contours shown in Figures 11 and 12 that the wave-induced pressure gradients remained very significant for a large portion of the underwater hull surface. These

pressure gradients are responsible for the development and evolution of crossflow patterns shown in Figure 14. It is quite clear that the wave-induced effects have altered both the magnitude and direction of the crossflow vectors up to about 50% of the ship draft.

Figure 15 shows the nonlinear waves in the RANS solution domain. A perspective view of the complete wave patterns in both the RANS and SLAW domains are also shown in Figure 16. The wave elevations were normalized by $1/Fr^2$ to reveal the complex wave patterns for both cases. The actual wave elevation for Fr = 0.160 case is about 1/4 of that for the high Froude number Fr = 0.316 case. At Fr = 0.160, the hull surface pressure is nearly identical to those calculated for the double-body model. The wave effects on the viscous boundary layer and wake flows are rather small, except in the bow and stern areas. The wave pattern itself, however, is quite complex in the near field. For double body calculations, the wave field will be completely suppressed by requiring the vertical velocity to be zero on the free surface. This can only be achieved with a nonzero pressure field (i.e., the double-body pressure) on the mean free surface. For nonzero Froude number calculations, on the other hand, the dynamic free surface boundary condition requires the total pressure to be zero (i.e., equal to ambient pressure) on the free surface. In practice, no matter how small the Froude numbers are, gravity waves must be generated in order to balance the fictitious double-body pressure gradients on the free surface. Note that the dynamic pressure on the free surface is always proportional to the wave elevation, normalized by Fr^2, when both the surface tension and viscous stresses are neglected. At low Froude numbers, the dynamic pressure returns rapidly from the free surface values to the double body distributions within a small surface layer. Therefore, a large wave-induced pressure gradient is produced across the surface layer. This leads to the development of large vertical velocities observed in Figure 14 near the free surface.

Finally, the calculated and measured wave profiles along the ship hull are shown in Figure 17 for both Froude numbers. For Fr = 0.160 case, the wave elevations predicted by the non-interactive RANS method are in excellent agreement with the measured data in the bow and forebody regions. The wave elevations for the afterbody, however, was somewhat underpredicted. The underprediction in the stern region is most likely

caused by the inadequate grid resolutions noted earlier. For completeness, the bare-hull potential flow wave elevations are also shown in Figure 17(a) to quantify the viscous effects. It is seen that the viscosity plays a dominant role in eliminating the short wavelength, small amplitude waves at low speeds.

For high Froude number (Fr = 0.316) case, it is seen from Figure 17(b) that the wave elevations obtained by interactive RANS/SLAW method are in very good agreement with the measured values over the entire ship. The bare-body potential flow solutions overpredicted the wave elevation in the stern region, but underpredicted the amplitude of the primary wave in the bow region. The over-prediction of stern waves is obviously due to the negligence of viscous effects due to thick boundary layer and wake flows. The underprediction of the bow wave, however, must be attributed to the use of linearized free surface conditions in SLAW bare-body calculations. It is noted that the wave elevation changes by as much as 0.03 of ship length or 50% of the ship draft. Although this wave amplitude may still be considered small compared to wavelength, it is quite clear that the viscous boundary layer and wake flows will be greatly influenced by the nonlinearity in the free surface wave field. Consequently, it is necessary to adjust the RANS solution domain in order to properly account for the nonlinear wave effects due to local changes in underwater geometry at each transverse section.

It should be emphasized that both the viscous and wave effects have been included directly in the present RANS calculations, even though the surface tension and viscous stresses on the free surface had been neglected due to a lack of understanding on the physical processes and mathematical modeling of the free surface turbulence. The inclusion of both the viscous and wave effects enables us to capture the complete interaction between the wavemaking and viscous boundary layer and wake in the near field. In particular, the wave-induced effects were formally included by requiring the dynamic free surface boundary conditions to be satisfied on the exact free surface. On the other hand, the influence of viscous boundary layer and wake flows on the free surface waves was captured automatically when the kinematic boundary conditions were used to update the free surface wave profiles.

CONCLUSIONS

An interactive numerical method which combines the Reynolds-Averaged Navier-Stokes (RANS) method and the free-surface potential flow calculations has been developed for the prediction of ship flows including both the viscous and nonlinear free-surface wave effects. In this zonal approach, the RANS method is employed to resolve the viscous boundary layer, wake and the nonlinear free-surface waves around the ship hull while the potential flow method is used to provide the wave information outside the viscous region. For high Froude number cases where the wave effects are significant, the near-field RANS solution is matched with the SLAW solution. Iterations between the two solutions are performed to capture the interaction between the viscous and the wave effects. Only one to two iterations is needed to achieve a converged solution. At low Froude numbers, the wave effects outside the RANS domain are insignificant and the RANS solutions are matched with the SLAW solution without iteration.

In the present RANS calculations, the dynamic free surface boundary conditions are satisfied on the exact free surface and, therefore, it is possible to capture the strong interaction between the nonlinear waves, the boundary layer, and wake flows underneath the exact free surface. With further modifications in the adaptive grid generation procedure, the present method can be readily generalized for the prediction of nonlinear wave effects arose from arbitrary ship motions.

Calculations have been performed for the Series 60, $C_B = 0.6$ parent hull for both low and high Froude number cases. The numerical solutions clearly demonstrated the feasibility of coupling the RANS and SLAW methods in an interactive approach for detailed resolution of both the viscous and the free-surface wave effects. This enables us to use a rather small RANS solution domain for efficient and accurate resolution of the interaction between wavemaking and viscous boundary layer and wake.

All of the RANS calculations presented here were performed on CRAY YMP supercomputers. The CPU time required is about 440 CPU seconds for every 100 time steps. Normally, 200 to 300 times steps are needed to achieve complete convergence for a non-interactive solution. In the subsequent interactive calculations, 50 to 100 more time steps

354

were used for each interactive RANS/SLAW coupling solution. A complete RANS calculation for the near-field viscous flow with three interactive coupling cycles takes about 30 to 45 CPU minutes. The SLAW calculations for double-body and $Fr = 0.316$ cases were performed on an IRIS R4000-50 GTX workstation, while the $Fr = 0.160$ results were obtained on a IBM RS6000/550 workstation. Depending on the Froude Number, the SLAW calculations of the potential flow waves take about 5 to 80 ($Fr = 0.160$ case) CPU minutes for one solution on the workstations. In general, a complete RANS and potential flow coupling solution may be obtained in less than 1 CPU hour on a CRAY YMP. This demonstrates the efficiency of the method presented in this paper and shows the feasibility of using this type of advanced numerical method for evaluation of practical problems.

The method developed in the present study is very general. With the present velocity/pressure coupling approach, it is possible to use the most suitable and efficient solver for each different flow region to provide maximum flexibility, accuracy and efficiency. With some modifications, the method can be readily generalized for the study of nonlinear unsteady interaction of ship and waves, effect of propulsor on stern flows, and other near-field ship flow problems.

ACKNOWLEDGEMENT

References

[1] Miyata, H. and Nishimura, S., "Finite-Difference Simulation of Nonlinear Waves Generated by Ships of Arbitrary Three-Dimensional Configuration," *Journal of Computational Physics*, Vol. 60, No. 3, pp. 391-436, 1985.

[2] Miyata, H., Zhu, M. and Watanabe, O., "Numerical Study on a Viscous Flow with Free-Surface Waves About a Ship in Steady Straight Course by a Finite-Volume Method," *Journal of Ship Research*, Vol. 36, No. 4, pp. 332-345, 1992.

[3] Hino, T., "Computation of a Free Surface Flow around an Advancing Ship by the Navier-Stokes Equations," *Proc. 5th International Conference on Numerical Ship Hydrodynamics*, 1989, Hiroshima, Japan.

[4] Shahshahan, A. and Landweber, L., "Interactions Between Wavemaking and the Boundary Layer and Wake of a Ship Model," IIHR Report No. 302, 1986, Iowa Institute of Hydraulic Research, The University of Iowa, Iowa City, IA.

[5] Stern, F., "Effects of Waves on the Boundary Layer of a Surface-Piercing Body," *Journal of Ship Research*, Vol. 30, No. 4, pp. 256-274, 1986.

[6] Tahara, Y., Stern, F. and Rosen, B., "An Interactive Approach for Calculating Ship Boundary Layers and Wakes for Nonzero Froude Number," Proc. 18th ONR Symposium on Naval Ship Hydrodynamics, 20-24 August, 1990, Ann Arbor, MI.

[7] Toda, Y., Stern, F. and Longo, J., "Mean-Flow Measurements in the Boundary Layer and Wake and Wave Field of a Series 60 C_B = .6 Ship Model for Froude Numbers .16 and .316," IIHR Report 352, 1991, Iowa Institute of Hydraulic Research, The University of Iowa, Iowa City, Iowa.

[8] Toda, Y., Stern, F. and Longo, J., "Mean-Flow Measurements in the Boundary Layer and Wake and Wave Field of a Series 60 C_B = .6 Ship Model - Part 1 : Froude Numbers .16 and .316," *Journal of Ship Research*, Vol. 36, No. 4, pp. 360-377, 1993.

[9] Lighthill, M.J., "On Displacement Thickness," *J. of Fluid Mechanics*, Vol. 4, Part 4, 383-392, 1958.

[10] Rosen, B., "SPLASH Free Surface Code : Theoretical/Numerical Formulation," South Bay Simulation Inc., Babylon, NY, 1989.

[11] Chen, H.C. and Lin, W.M., "Interactive RANS/LAMP Coupling Schemes and Their Applications to Ship Flows," SAIC-91/1021, February 1991, Science Applications International Corporation, Annapolis, MD.

[12] Chen, H.C. and Korpus, R., "A Multi-block Finite-Analytic Reynolds Averaged Navier-Stokes Method for 3D Incompressible Flows," *Proc. ASME Fluid Engineering Conference*, Washington, D.C., June 20-24, 1993.

[13] Letcher, J., Weems, K., Oliver, C., Shook, D., and Salvesen, N., "SLAW: Ship Lift and Wave, Theory, Implementation, and Numerical Results, SAIC Technical Report 89/1196, 1989.

[14] Lin, W.M. and Yue, D.K.P., "Numerical Solutions for Large-Amplitude Ship Motions in the Time-Domain", *Proc. 18th Symp. Naval Hydro.*, The University of Michigan, Ann Arbor, MI, USA, 1990.

[15] Dawson, C., "A Practical Computer Method for Solving Ship-Wave Problems" *Proc, 2nd International Conference on Numerical Ship Hydrodynamics*, University Extension Publishers, Berkeley, CA, 1977, pp 30-38.

[16] Hess, J., and Smith, A., "Calculation of Nonlifting Potential Flow about Arbitrary Three-Dimensional Bodies", *Journal of Ship Research*, Vol 8, 1964, pp 20-24.

[17] Jensen, P., "On the Numerical Radiation Condition in the Steady-State Ship Wave Problem", *Journal of Ship Research*, Vol 31, pp 14-22, 1987.

[18] Morino, L., Chen, L.-T., and Suciu, E., " Steady and Unsteady Oscillatory Subsonic and Supersonic Aerodynamics around Complex Configurations", *AIAA Journal*, Vol 13, pp 368-374, 1975.

[19] Campana, E., Di Mascio, A., Esposito, P.G., and Lalli, F., "A Multidomain Approach to Free Surface Viscous Flows", Abstract submitted to the Eighth International Workshop on Water Waves and Floating Bodies, St. John's, Newfoundland, Canada, May 1993.

[20] Chen, H.C. and Lin, W.M., "Interactive RANS/LAMP of Ship Flows Including Viscous ans Wake Effects," SAIC Technical Report 92/1049, 1992.

[21] Stoker, J.J.,"Water Waves," *Pure and App. Math.*, Volume IV., 1957.

[22] Chen, H.C. and Patel, V.C., "Near-Wall Turbulence Models for Complex Flows Including Separation," *AIAA Journal*, Vol. 26, No. 6, pp. 641-648, June 1988.

[23] Chen, H.C., Patel, V.C. and Ju, S., "Solutions of Reynolds-Averaged Navier-Stokes Equations for Three-Dimensional Incompressible Flows," *Journal of Computational Physics*, Vol. 88, No. 2, pp. 305-336, 1990.

[24] Hubbard, B, and Chen, H.C., "A Chimera Reynolds-Averaged Navier-Stokers Methods for 3D Incompressible Flows," Texas A & M Research Foundation, COE Report No. 328, 1993.

[25] Steinbrenner, J.P., Chawner, J.R. and Fouts, C.L., "The GRIDGEN 3D Multiple Block Grid Generation System," Vols. I & II, WRDC-TR -90-3022, 1990, Wright Patterson AFB, OH.
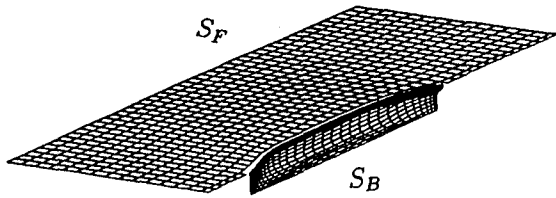
Fig. 1: SLAW Potential Flow Panel Model.
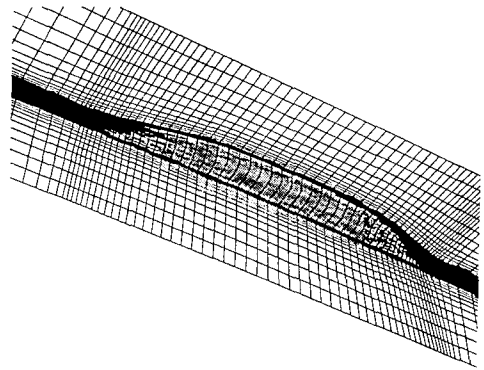
Fig. 3: Partial View of RANS Grid.

Complete Domain Calculation
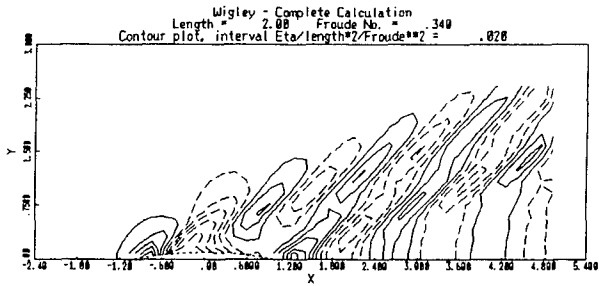
Fig. 4: Convergence History; Double-Body.
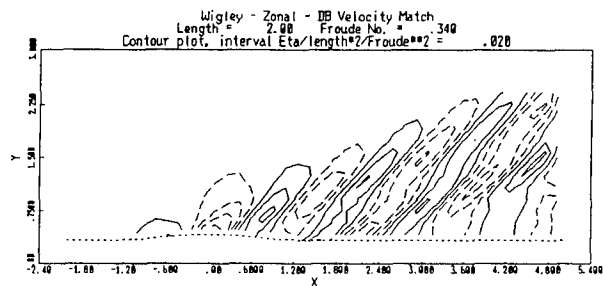
Outer Domain Calculation - $V_N^{DB} = \vec{V}^{DB} \cdot \hat{n}$, $V_N = \vec{V}^{FS} \cdot \hat{n}$
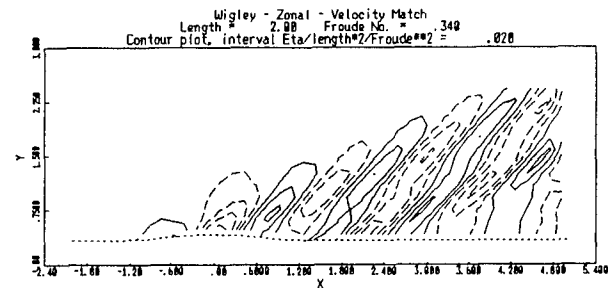
Outer Domain Calculation - $V_N^{DB} = V_N = \vec{V}^{FS} \cdot \hat{n}$
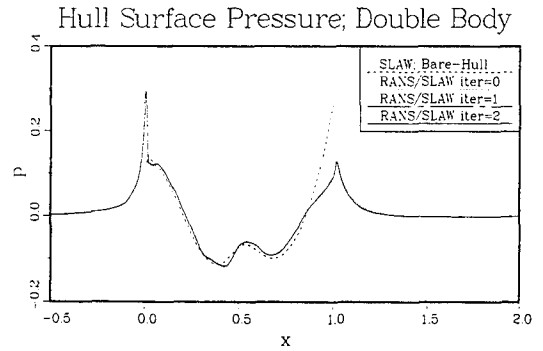
Fig. 2: SLAW Zonal Test Calculation.

357
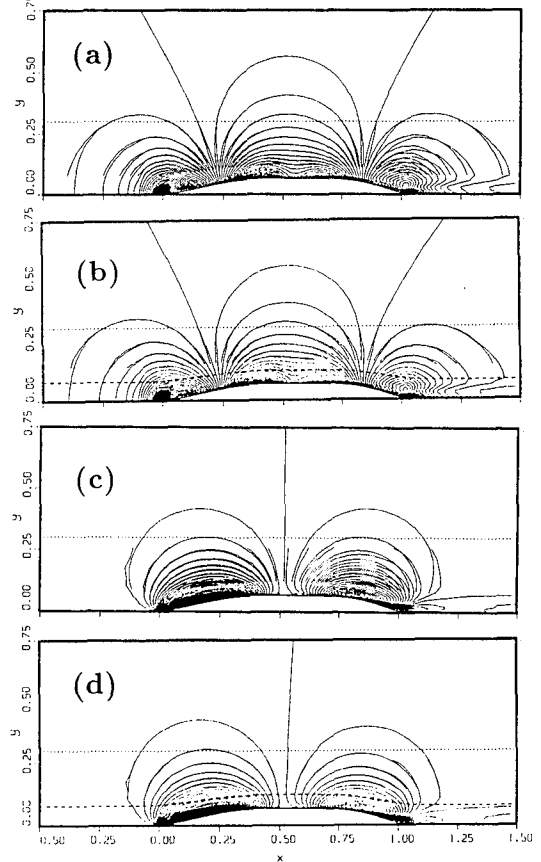
Fig. 5: (a) Non-interactive and (b) Interactive Pressure Contours, (c) Non-interactive and (d) Interactive Vertical Velocity Contours; Fr = 0.

Wave Profile ; Fr = 0.316
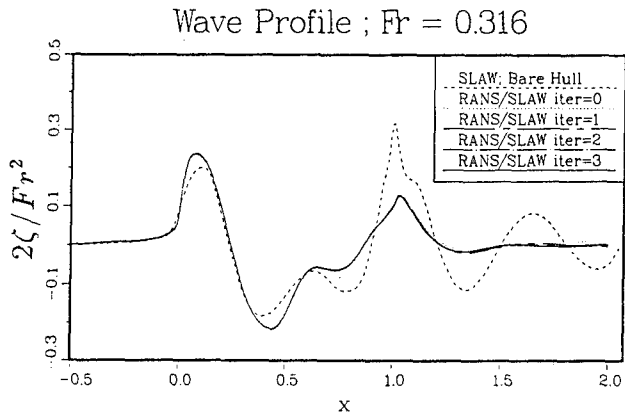
Fig. 6: Convergence History; Fr=0.316.

Wave Profile ; Fr = 0.316
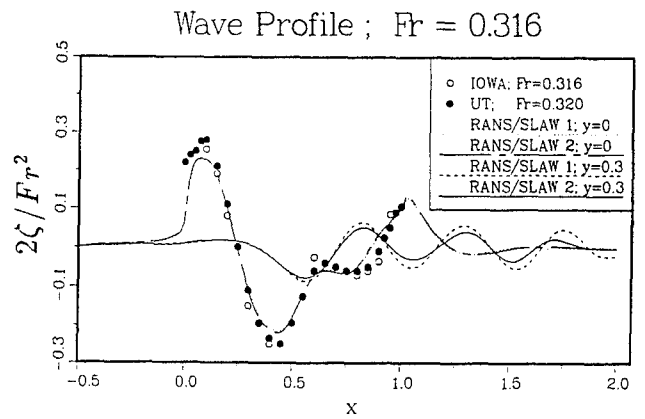
Fig. 7: Influence of SLAW Matching Boundary.
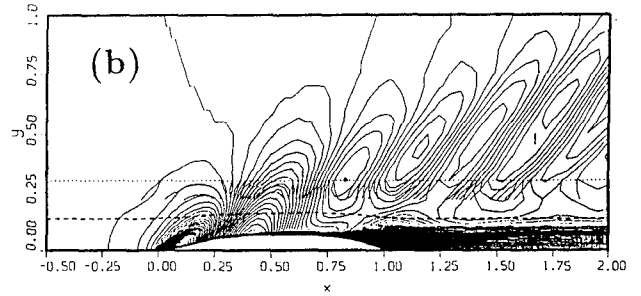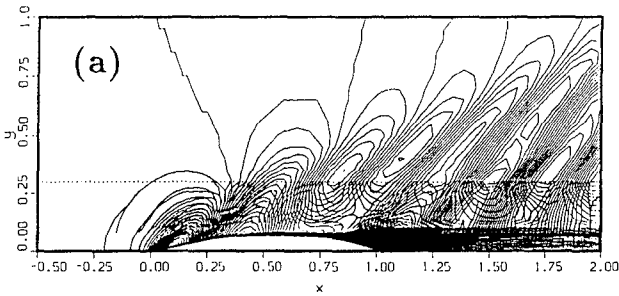
Fig. 8: Fr = 0.316 Wave Patterns: (a) Non-interactive, (b) Interactive.
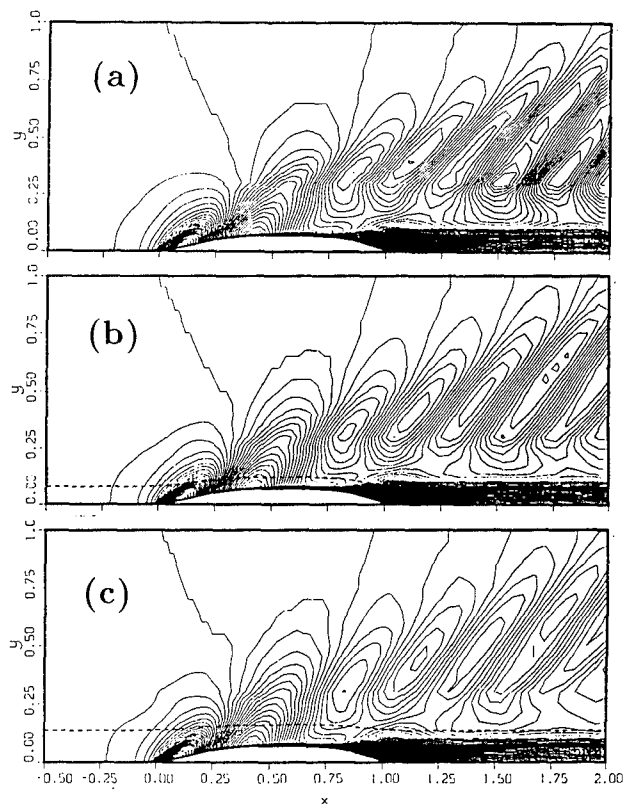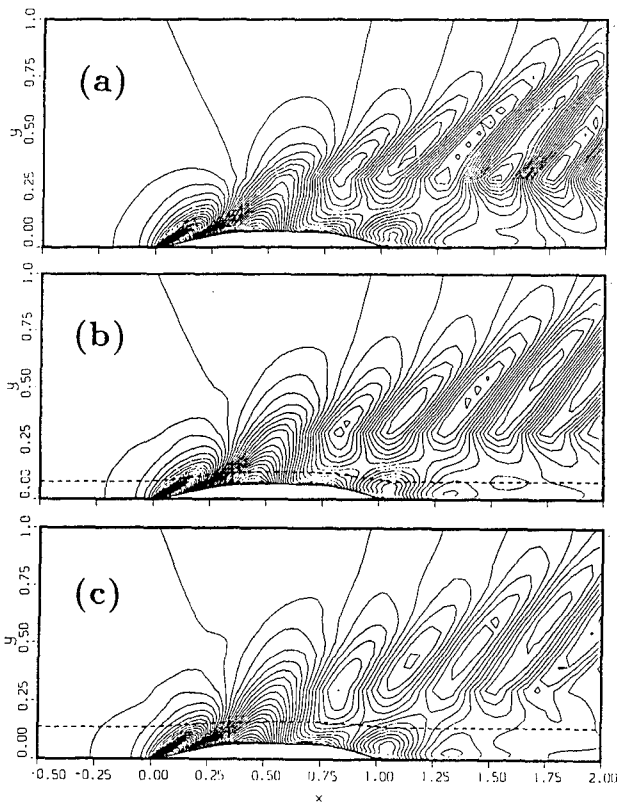
Fig. 9: Fr = 0.316 Pressure (left) and Axial Velocity (right) Contours: (a) Non-interactive; $\xi^2 = 1$, (b) RANS/SLAW 1; $\xi^2 = 30$, (c) RANS/SLAW 2; $\xi^2 = 32$.
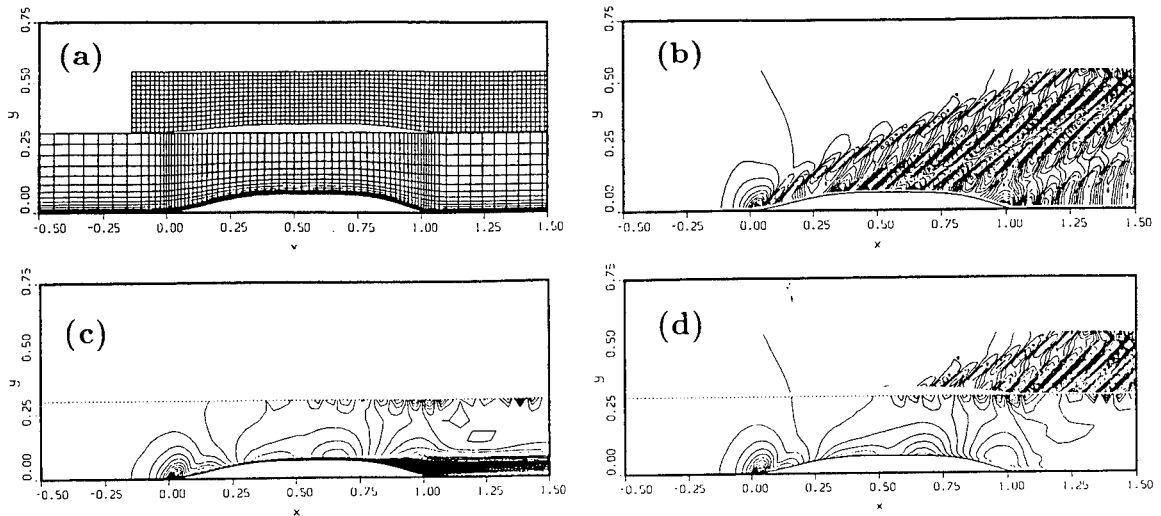
Fig. 10: Fr = 0.160 Solutions: (a) Numerical Grid, (b) Bare-Hull SLAW Wave Patterns, (c) RANS Axial Velocity Contours, (d) RANS/SLAW Pressure Contours.
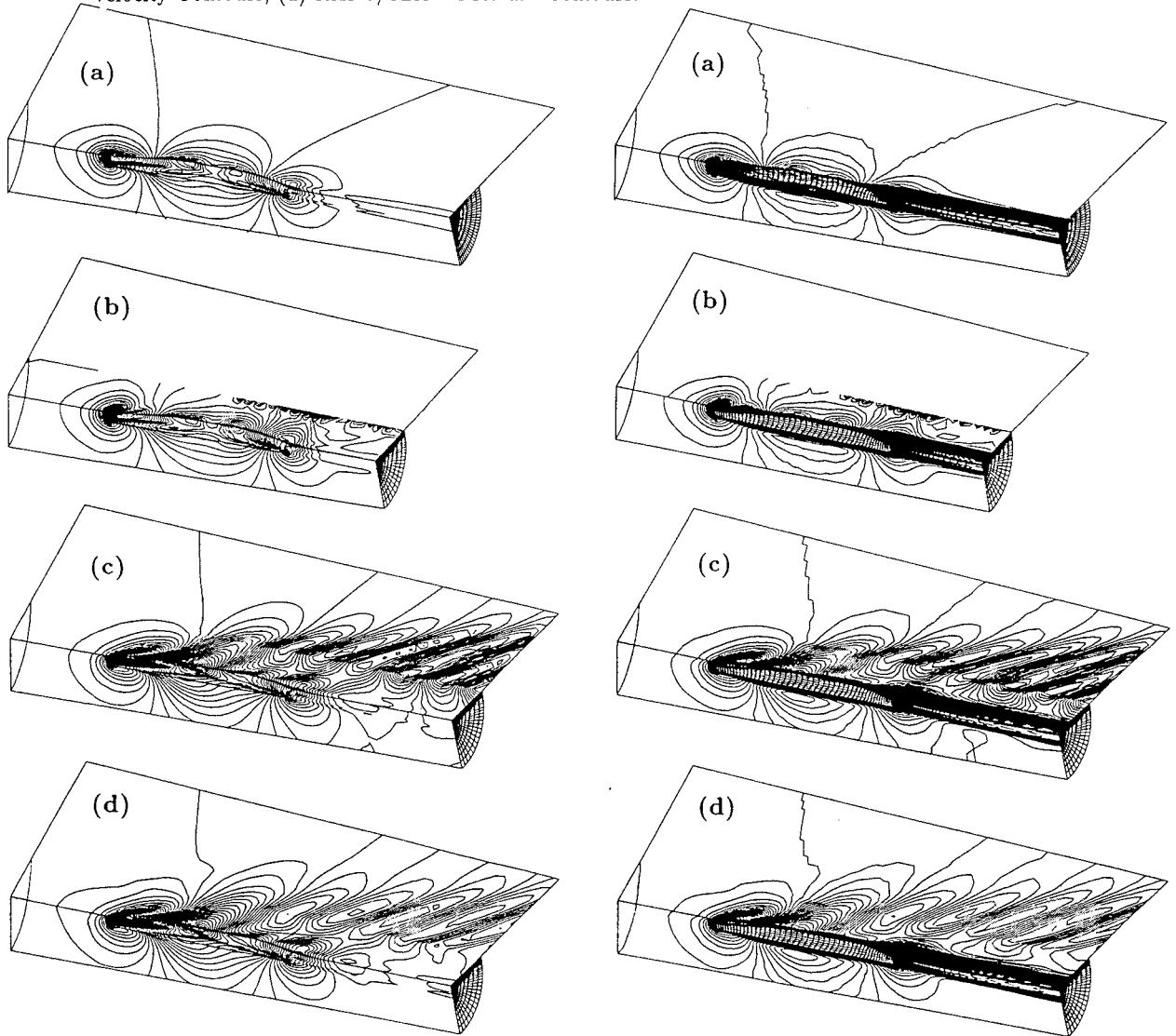
Fig. 11: Pressure (left) and Velocity (right) Contours: (a) Interactive Double-Body, (b) Non-interactive Fr = 0.160, (c) Non-interactive Fr = 0.316, (d) Interactive Fr = 0.316.

359
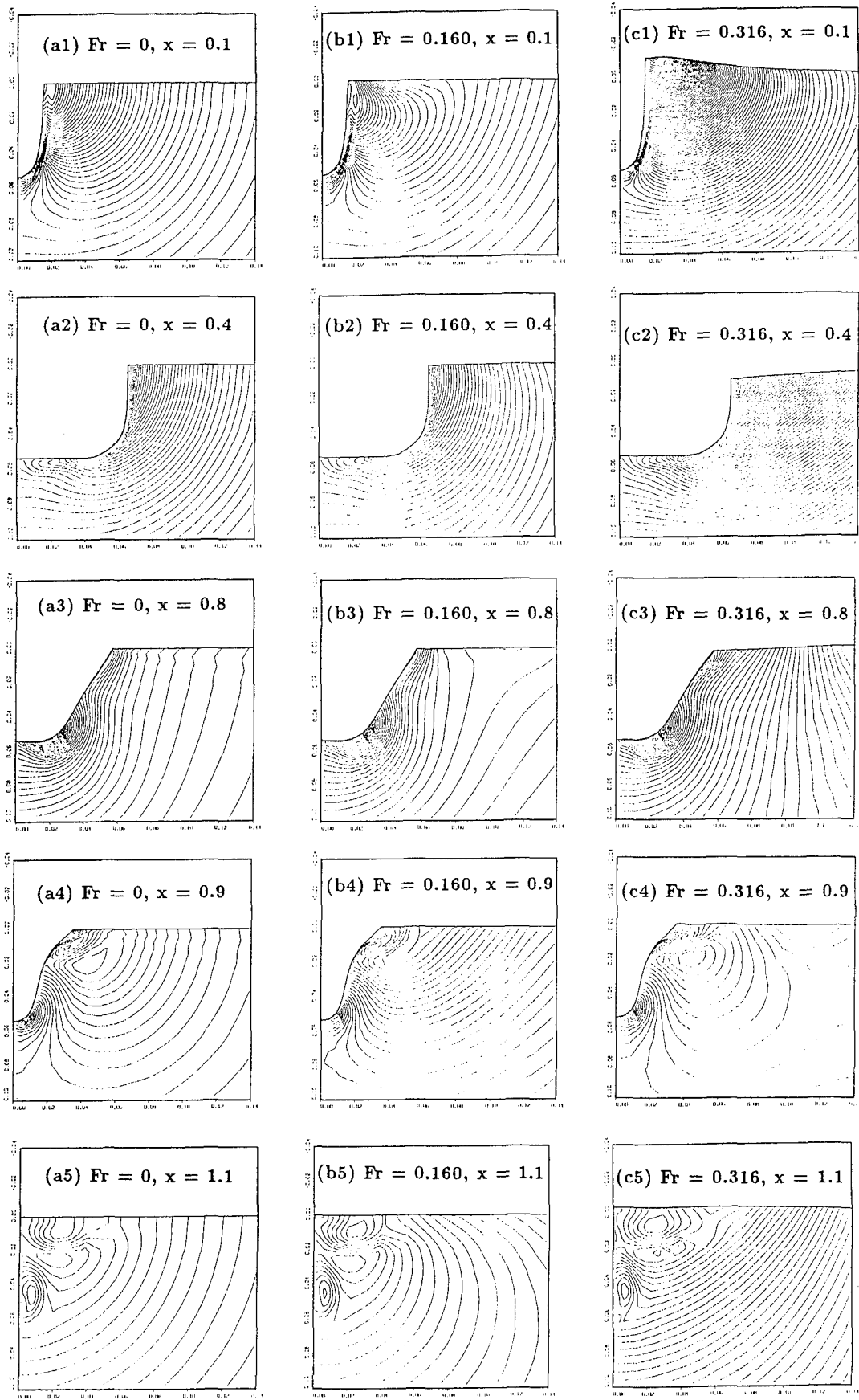
Fig. 12: Pressure Contours: (a) Double-Body, (b) Fr = 0.160, (c) Fr = 0.316.
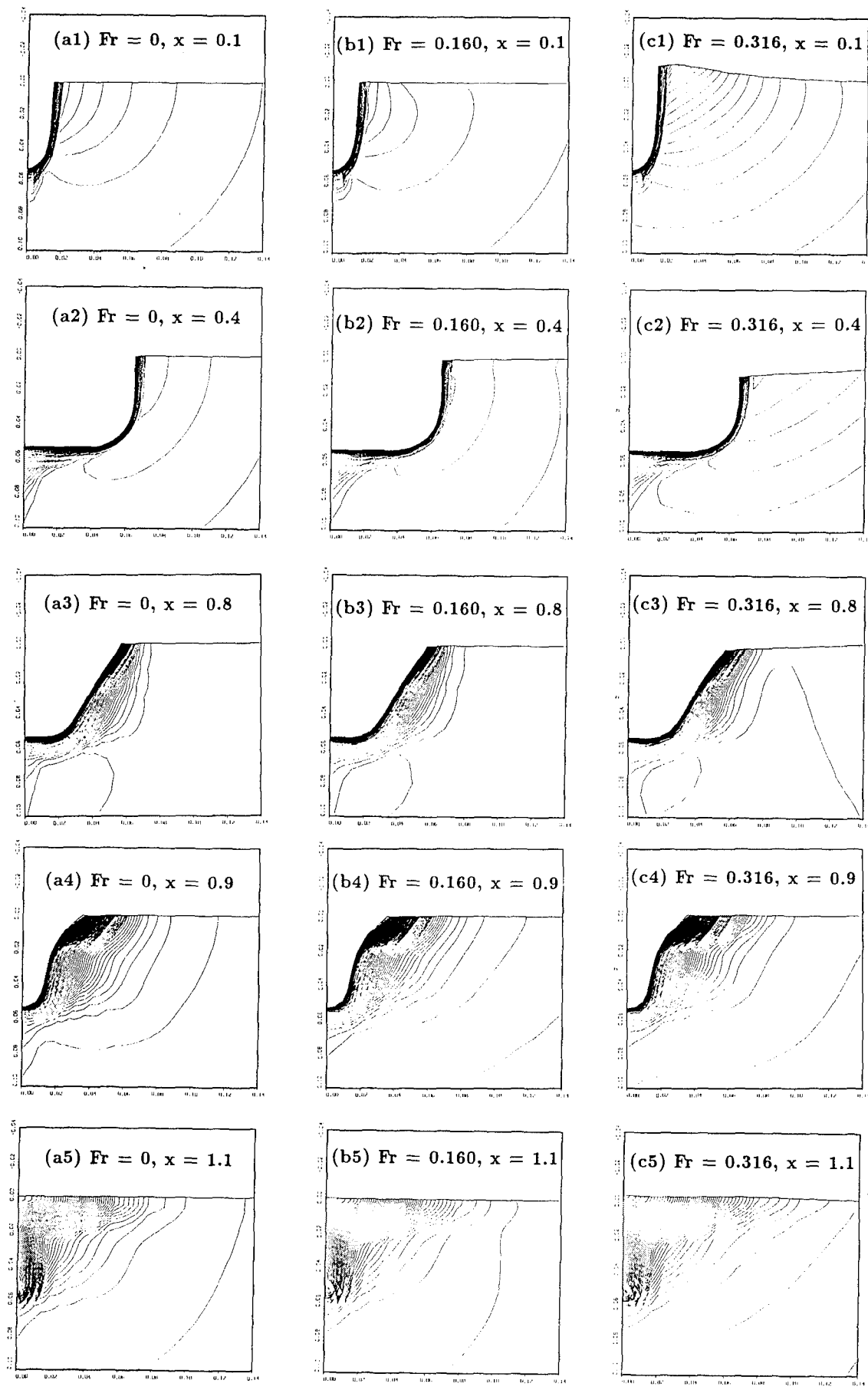
Fig. 13: Axial Velocity Contours: (a) Double-Body, (b) Fr = 0.160, (c) Fr = 0.316.

361
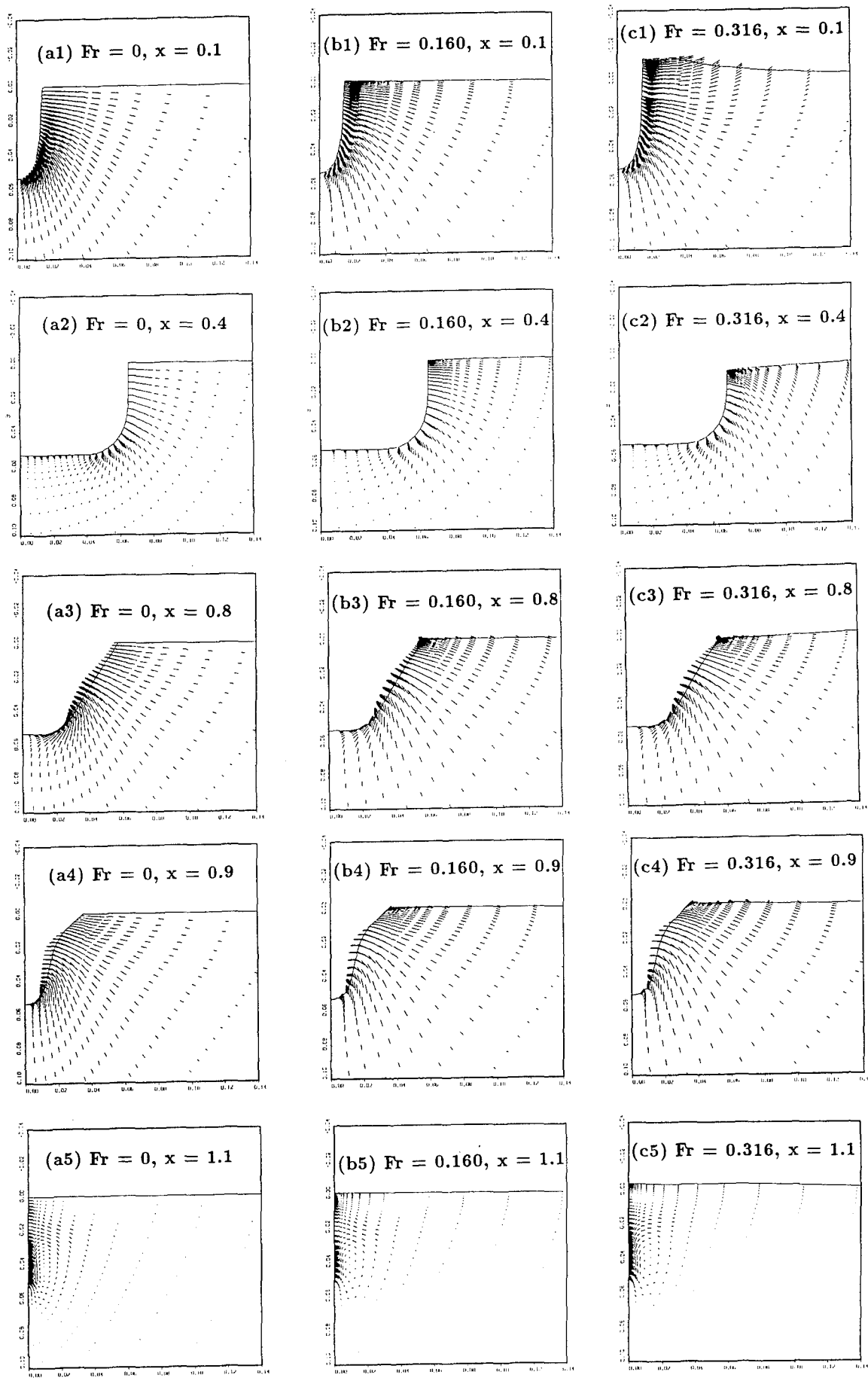
Fig. 14: Crossplane Velocity Vectors: (a) Double-Body, (b) Fr = 0.160, (c) Fr = 0.316.

Fr = 0.160
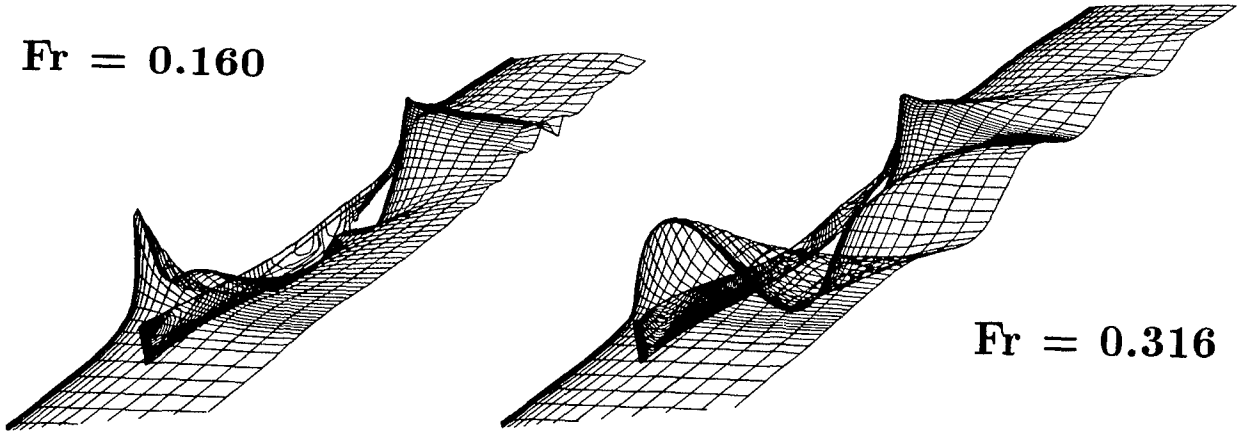
Fr = 0.316

Fig. 15: Nonlinear Waves (ζ/Fr^2) in RANS Solution Domain.
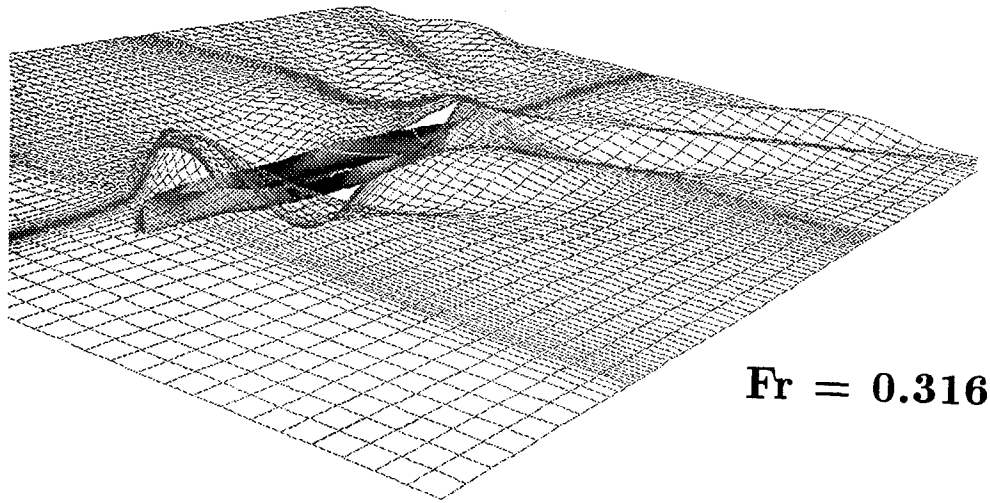
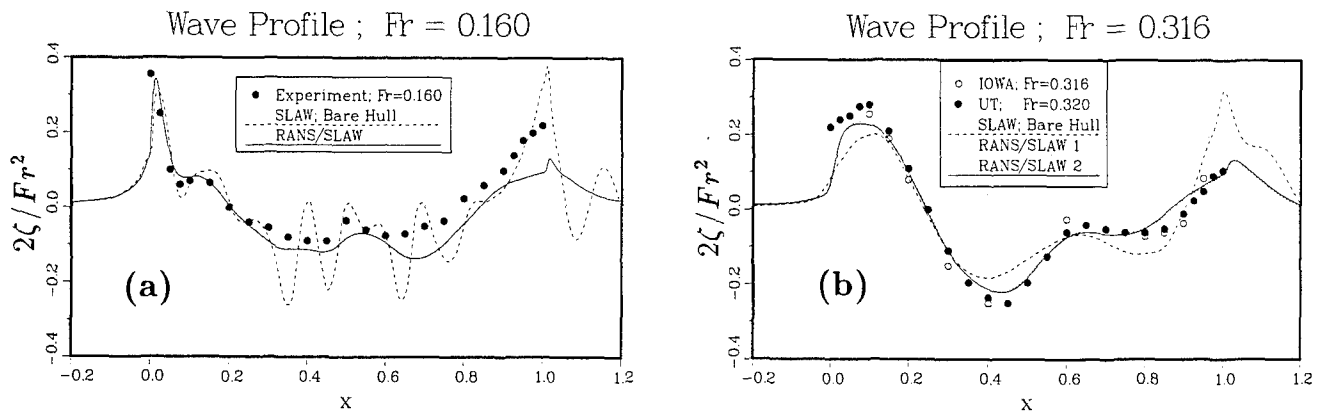Fr = 0.316

Fig. 16: Perspective View of Free Surface Waves.

Fig. 17: Comparison of Wave Profiles on Hull Surface and Along Wake Centerline.

SESSION 7

VISCOUS FLOW: NUMERICAL METHODS

Navier-Stokes Computations of Ship Stern Flows: A Detailed Comparative Study of Turbulence Models and Discretization Schemes

G.B. Deng, P. Queutey, and M. Visonneau
(Ecole Centrale de Nantes, France)

ABSTRACT

A fully elliptic numerical method for the solution of the Reynolds Averaged Navier Stokes Equations is applied to the flow around the HSVA Tanker. The weaknesses of the simulation are analysed by comparing several discretisation schemes and grids as well as several turbulence models. Grid refinement in the near wake or application of new accurate discretisation schemes have a little effect on the quality of the solution in the wake. Systematic comparisons of various turbulence models and numerical experiments suggest that the solution is essentially affected by a too high level of turbulence viscosity in the core of the longitudinal vortex.

NOMENCLATURE

Variables

(x,y,z)	cartesian coordinates
U	average velocity vector
p	pressure
t	time
Re	Reynolds number
$\mathbf{uu}$	Reynolds stress tensor
k	turbulent kinetic energy
ε	rate of turbulence dissipation
I	Identity tensor
ν_T	eddy viscosity
$C_\mu, C_{\varepsilon 1}, C_{\varepsilon 2}, \sigma_k, \sigma_\varepsilon$	k-ε coefficients
$R_{eff}, R_k, R_\varepsilon$	effective Reynolds numbers
G	production
ξ, η, ζ	curvilinear coordinates
u, v, w	contravariant components of the velocity
U,V,W	cartesian components of the velocity
J	jacobian
b^i_j	j component of the contravariant vector b^i
g^{ij}	contravariant metric tensor
S_{U^l}	source term for the momentum equations
S_k	source term for the k transport equation
S_ε	source term for the ε transport equation
C_{NB}	influence coefficients at point C
A, B	normalized convective velocities
$\hat{U}_C$	pseudo-velocity at point C

Operators

Div	divergence
∇	gradient
∇^2	laplacian
∇^T	transposed gradient

1. INTRODUCTION

Advances in numerical solution methodology along with increased computer storage and speed have made it possible to seek numerical solutions of the three-dimensional Reynolds Averaged Navier Stokes Equations (RANSE) for moderately complex ship hulls. With the development of computers, wind tunnel or towing tank experiments are no more the only way to get information on ship performances and CFD tools appear to be able to generate an overwhelming amount of information on the flow with a level of details and flexibility which seems out of reach of a reasonable experimental approach. These computations are nevertheless mostly confined to double models, in which wave effects are absent, to

367

bare hulls without appendages or propulsors and conducted at laboratory Reynolds numbers. However, even for these simple configurations, it is crucial to locate as accurately as possible the limitations of numerical simulations in order to know (i) which level of details can be reasonably captured by a CFD tool, (ii) what are the leading weaknesses of the simulation and (iii) how to improve the accuracy of the numerical prediction.

From that point of view, the so-called HSVA tanker is known as the best documented test case among all the available experimental ship flow data bases. It is why it was chosen as one of the two testcases of the 1990 SSPA-CTH-IIHR Workshop on Ship Viscous Flow which was held at Goteborg [1]. Some nineteen organizations coming from twelve countries participated in the Workshop and all of them calculated the first test case i.e. the flow around the HSVA tanker at the laboratory Reynolds number Re=5.0 10^6 on which this paper will be entirely focussed.

Despite its seemingly geometric simplicity, the flow around this hull is rather complex. As the flow progresses along the hull, the geometry of the body gradually forces the boundary layer to pack in an area whose girthwise dimension decreases, implying a progressive convergence of the streamlines in some regions of the hull. Continuity requires a large normal velocity, a strong thickening of the boundary layer occurs often associated to the birth of a longitudinal vortex motion which is slowly relaxed in the wake at large distances downstream from the ship.

A more detailed understanding of the flow is provided by the visualisation of the limiting streamlines (Figure 1 from [1]), actually the print of the flow on the hull; it clearly indicates the existence of a well defined line of convergence located just beyond the keel plane of symmetry. It is also quite clear that the behaviour of the limiting streamlines is complex since two convergence lines are visible. The first one (S1 line) is S-shaped and demarcates a vertical wall flow region and a small zone of flow reversal. The second convergence line (S2 line) is located just beyond the keel plane of symmetry and joins the S1 line at the end of the hull. Consequently, since this region seems to be characterized by a rapid normal variation of the velocity orientation from the wall to the so-called logarithmic region, it is plausible to think that such a complex three-dimensional behaviour can be hardly simulated by a wall function approach which cannot account for the high twist angle (>90°) between the wall flow and the external streamlines directions.

Even more interesting are the measurements of the pressure and velocity components made at several cross-sections. Figs 2-a-b-c from [1] show the axial velocity contours at several locations, namely, x/L=0.908, 0.976 and 1.005. The longitudinal velocity contours indicate a very characteristic "hook" shape in the central part of the wake correlated with the core of the longitudinal vortex. This small region is characterised by a nearly uniform U component, a linear variation of the vertical component W preceding a maximum and again an "hook" shape of the pressure contours. These features confirm the existence of an intense longitudinal bilge vortex emanating from the hull and leads us to classify the HSVA tanker as an U-shaped hull rather than a V-shaped hull for which the longitudinal vortex is far more intense and does not create this very characteristic hook shape of the longitudinal velocity contours.

The Goteborg workshop's results indicated that great progress has been made through the development of methods based on the Reynolds-Averaged Navier Stokes Equations. These methods generally simulate the gross features of the wake and predict the shape and location of the velocity contours with reasonable accuracy even on the rather coarse meshes recommended for the simulations. Nevertheless, neither the central part of the wake with this hook shaped velocity contour nor the entire wall flow behaviour can be captured by the methods presented at this time.

The description of this phenomena could be of crucial importance for the design since the designer's task is to devise the best hull geometry leading to improvments to propulsive efficiency through better hull form/propeller matching. This is often a compromise between V-shaped stern sections which are associated to lower viscous resistance and less intense longitudinal bilge vortex and U-shaped stern sections for which the more intense longitudinal bilge vortex create an higher propulsive efficiency which partly compensates for the higher resistance. It is therefore fundamental to determine if the solution of the RANSE enables us to distinguish between the flows associated to U-shaped or V-shaped geometries without ambiguity.

During the workshop, several hypotheses were put forward to explain the incapability of the RANSE-based methods to describe accurately the central part of the bilge vortex. Two types of explanations may be evocated, the first one favouring the discretization inaccuracies and the second one emphasizing the weaknesses of the turbulence modelisation.

It is sensible to stress the numerical inaccuracy since the threedimensional grids are often too coarse to capture the details of the flow especially if we consider that most of the discretisation schemes are only first order accurate when the flow is dominated by the convection and not aligned with the coordinate lines. The numerical solution produced by such discretisation schemes is always too diffusive and local inhomogeneities such

368

as this hook shape are filtered by a too high artificial viscosity.

On the other hand, it is reasonable to stress the weaknesses of the classical turbulence modelisation for this class of stern flows. As it was pointed out by V.C. Patel in [2], the turbulence in stern flows seems to behave in a very specific way. Let us compare with him the behaviour of the measured kinetic energy k plotted in outer variables, with U_0 and δ as scales of velocity and length for two different flows, a thick boundary layer stern flow around the SSPA hull and a traditional flat plate flow (Fig. 3 from [2],[15]). The measurements for the strong thick boundary layer indicate a two layer structure, leading V.C. Patel to wonder if a single set of scaling parameters is adequate to modelize this flow. The outer zone is actually characterized by a lower level of the turbulence intensity, meaning that the conventional turbulence model might generate again a too diffusive flow.

Then, the conjecture could be stated in these terms. What is the respective importance of the artificial viscosity compared with the likely inadequacy of the turbulence modelling? Actually, these aspects are strongly tied up if we think that the turbulence numerically produced by the discretised k-ε transport equations is somewhat modified by various numerical inaccuracies among which might be quoted the discretisation errors, an unsufficient level of coupling between the source terms of the turbulence transport equations or an unsatisfactory level of convergence for the non-linearities. This is why some authors consider it safer to use a simpler 0 equation turbulence model like a Baldwin-Lomax model.

The aim of this paper can be summarised as follows: (i) to determine what is the respective weight of the numerics compared to the turbulence modelisation for this class of stern flows, (ii) to show what has to be improved in the future to use the RANSE based methods as a reliable design tool in the naval architecture context.

This paper is outlined as follows. In section 2, the alternative curvilinear formulations are described as well as the turbulence models used in the present study. Section 3 is devoted to a brief survey of the two numerical methods being the subject of comparisons. In section 4, the conditions of the computations are described and the relative influence of turbulence models and numerical approaches upon the simulation is investigated. Some concluding remarks are mentionned in Section 5.

2. EQUATIONS

2.1 The Basic Equations

We consider the equations of motion in cartesian (x,y,z) coordinates for incompressible flows. The exact RANSE of continuity and momentum of the mean flow in dimensionless form are given by equations (2.1), (2.2) and (2.3):

$$\text{div}\mathbf{U} = 0 \tag{2.1}$$

$$\frac{\partial \mathbf{U}}{\partial t} + \nabla \mathbf{U}\mathbf{U} + \nabla p + \nabla.\mathbf{uu} = \frac{1}{Re}\nabla^2 \mathbf{U} \tag{2.2}$$

$$\frac{\partial \mathbf{U}}{\partial t} + \mathbf{U}.\nabla \mathbf{U} + \nabla p + \nabla.\mathbf{uu} = \frac{1}{Re}\nabla^2 \mathbf{U} \tag{2.3}$$

$\mathbf{U}$, p and $\mathbf{uu}$ are respectively the velocity vector, the pressure and the Reynolds stress tensor. The resulting turbulent closure problem is solved by means of the classical k-ε turbulence model in which the Reynolds stress is linearly related to the mean rate of strain tensor through an isotropic eddy viscosity as follows:

$$\mathbf{uu} = \frac{2}{3}k\mathbf{I} - \nu_T(\nabla \mathbf{U} + \nabla^T \mathbf{U}) \tag{2.4}$$

If the k-ε turbulence model is used, the eddy viscosity ν_T is classically given by:

$$\nu_T = C_\mu \frac{k^2}{\varepsilon} \tag{2.5}$$

where the adimensional turbulent kinetic energy k and its dimensionless rate of dissipation ε are governed by the following transport equations:

$$\frac{\partial k}{\partial t} + \mathbf{U}.\nabla k = \text{div}(\frac{1}{R_k}\nabla k) + G - \varepsilon \tag{2.6}$$

$$\frac{\partial \varepsilon}{\partial t} + \mathbf{U}.\nabla \varepsilon = \text{div}(\frac{1}{R_\varepsilon}\nabla \varepsilon)$$

$$+ C_{\varepsilon 1}\frac{\varepsilon}{k}G - C_{\varepsilon 2}\frac{\varepsilon^2}{k} \tag{2.7}$$

where G is the turbulence generation term:

$$G = \nu_T \nabla \mathbf{U}:(\nabla \mathbf{U} + \nabla^T \mathbf{U}) \tag{2.8}$$

The effective Reynolds numbers R_k, R_ε, Reff have been defined by:

$$R_{eff}^{-1} = \nu_T + R_e^{-1}; R_k^{-1} = \frac{\nu_T}{\sigma_k} + R_e^{-1};$$

$$R_\varepsilon^{-1} = \frac{\nu_T}{\sigma_\varepsilon} + R_e^{-1} \tag{2.9}$$

369

Unless specified, the constants in the previous equations are taken to their standard values (2.10):

$$C_\mu = .09 \; ; \; C_{\varepsilon 1} = 1.44 \; ; \; C_{\varepsilon 2} = 1.92 \; ;$$
$$\sigma_k = 1.00 \; ; \; \sigma_\varepsilon = 1.30.$$

In order to avoid the wall function approach, several near wall k-ε models are compared in this study. For the sake of brevity, the details concerning their implementation, which can be found in [4], [13] and [14], are omitted here. For a significant increase of numerical troubles and computing time (because the integration is carried out to $y^+ \approx 1$), the delicate problem of the three-dimensional specification of the log-law , dealt with only in [5], is avoided.

The algebraic Baldwin-Lomax model [6] is also evaluated because it is less expensive in terms of CPU effort and rate of convergence.

2.2 The Equations In The Transformed Coordinate System

For hydrodynamic applications, a numerical coordinate transformation is highly desirable in that it greatly facilitates the application of the boundary conditions and transform the physical domain in which the flow is studied into a parallelepipedic computational domain $\left\{ \xi^i \right\} = \left\{ \xi, \eta, \zeta \right\}$.

The partially transformed RANSE are given by the following relations *in a fully conservative developped form*. The contravariant components of the velocity are defined by $\left\{ u^i \right\} = \left\{ u, v, w \right\}$ and the physical cartesian components by $\left\{ U_i \right\} = \left\{ U, V, W \right\}$:

$$\frac{1}{J} (J u^i)_{\xi^i} = 0 \quad \text{with} \quad J u^i = b^i_j U_j \qquad (2.11)$$

$$\phi_t + \frac{1}{J} \left[(J u \phi)_\xi + (J v \phi)_\eta + (J w \phi)_\zeta \right]$$
$$= \frac{1}{J} [(\frac{J g^{12}}{R_\phi} \phi_\xi)_\xi + (\frac{J g^{22}}{R_\phi} \phi_\eta)_\eta$$
$$+ (\frac{J g^{33}}{R_\phi} \phi_\zeta)_\zeta] + S_\phi \qquad (2.12)$$

with $\phi = U, V, W, k, \varepsilon$ where:

$$S_\phi = \frac{1}{J} [(\frac{J g^{12}}{R_\phi} \phi_\eta)_\xi + (\frac{J g^{13}}{R_\phi} \phi_\zeta)_\xi$$
$$+ (\frac{J g^{21}}{R_\phi} \phi_\xi)_\eta + (\frac{J g^{23}}{R_\phi} \phi_\zeta)_\eta \qquad (2.13)$$

$$+ (\frac{J g^{31}}{R_\phi} \phi_\xi)_\zeta + (\frac{J g^{32}}{R_\phi} \phi_\eta)_\zeta] - s_\phi$$

while $R_\phi = R_{eff}$ if $\phi = U, V, W$;
$R_\phi = R_k$ if $\phi = k$;
$R_\phi = R_\varepsilon$ if $\phi = \varepsilon$

Also,

$$S_{U_l} = \left[b^i_l (p + \frac{2}{3} k) \right]_{\xi_i} - \left[\nu_T \frac{b^i_m b^j_l}{J} U_{m \xi_j} \right]_{\xi_i}$$

$$S_k = G - \varepsilon \quad \text{and} \quad S_\varepsilon = C_{\varepsilon 1} \frac{\varepsilon}{k} G - C_{\varepsilon 2} \frac{\varepsilon^2}{k}$$

The alternative *convective form* needs to be introduced (2.14):

$$\phi_t + (\frac{1}{J} b^1_j \alpha^j_\phi - \frac{f^1}{R_\phi}) \phi_\xi$$
$$+ (\frac{1}{J} b^2_j \alpha^j_\phi - \frac{f^2}{R_\phi}) \phi_\eta$$
$$+ (\frac{1}{J} b^3_j \alpha^j_\phi - \frac{f^3}{R_\phi}) \phi_\zeta = \qquad (2.14)$$
$$\frac{1}{R_\phi} \left\{ (g^{11} \phi_{\xi\xi} + g^{22} \phi_{\eta\eta} + g^{33} \phi_{\zeta\zeta}) + S_\phi \right\}$$

where:

$$\alpha^j_\phi = \sigma_\phi U^j - \frac{1}{J} (b^1_j \nu_{T\xi} + b^2_j \nu_{T\eta} + b^3_j \nu_{T\zeta})$$
$$S_\phi = 2(g^{12} \phi_{\xi\eta} + g^{13} \phi_{\xi\zeta} + g^{23} \phi_{\eta\zeta}) - s_\phi$$

The additional source terms contain classically the pressure gradients and the turbulence contributions:

$$S_{U^l} = \frac{1}{J} \left[b^i_l (p + \frac{2}{3} k) \right]_{\xi_i}$$
$$- \left[\nu_T \frac{b^i_m b^j_l}{J} U_{m \xi_j} \right]_{\xi_i} \qquad (2.15)$$

$$S_k = G - \varepsilon ;$$

$$S_\varepsilon = C_{\varepsilon 1} \frac{\varepsilon}{k} G - C_{\varepsilon 2} \frac{\varepsilon^2}{k} \qquad (2.16)$$

Endly, the metric coefficients involved in the transformation are given. They are the contravariant base, $\{b^i\}$, normalized by the Jacobian, J, of the transformation and the metric tensor g:

$$b^k_i = (b^k)_i; \, b^k = \frac{\partial r}{\partial \xi^i} \times \frac{\partial r}{\partial \xi^j};$$

$$g^{ij} = J^{-2} b^i b^j; \quad (2.17)$$

$$J = \frac{1}{3}[(xb^1_1 + yb^1_2 + zb^1_3)_\xi$$
$$+ (xb^2_1 + yb^2_2 + zb^2_3)_\eta \quad (2.18)$$
$$+ (xb^3_1 + yb^3_2 + zb^3_3)_\zeta]$$

The convective form needs the functions f^j which can be seen as purely geometrical convective coefficients or defined as stretching functions:

$$f^j = \frac{1}{J} \frac{\partial (Jg^{ij})}{\partial \xi^i} \quad (2.19)$$

3. THE NUMERICS

In order to clarify the role played by the accuracy of the discretisation schemes, two approximation methods are evaluated. Before detailing the differences, let us first recall their common characteristics. For each of them, a cell-centered layout is used in which pressure, turbulence and velocity unknowns share the same location. This strategy simplifies coding and leads to significant savings in computational time and storage. Even if a steady solution is looked for, a local time step ensuring a fixed amount of diagonal dominance with respect to the momentum equations, is devised to accelerate the convergence towards the steady state. Endly, the momentum and continuity equations are coupled through the well known (one step) PISO procedure already detailed in [7].

3.1 Method 1

The Convection Diffusion Schemes

The momentum equations are written down under their convective form (2.14). When the Multi-exponential scheme is used, the normalized transport equation is splitted as follows :

$$2 A \phi_\xi - \phi_{\xi\xi} = D2 - (R \phi_t + S_\phi) \quad (3.1)$$
$$2 B \phi_\eta - \phi_{\eta\eta} = D1 - (R \phi_t + S_\phi) \quad (3.2)$$

where $D1$ and $D2$ are defined as:

$$-D1 = 2A\phi_\xi - \phi_{\xi\xi}, \quad (3.3)$$
$$-D2 = 2B\phi_\eta - \phi_{\eta\eta}, \quad (3.4)$$

Using an exponential scheme for every equation and summing gives the so-called multi-exponential scheme:

$$(C_U + C_D + C_N + C_S)\phi_C = C_U \phi_U + C_D \phi_D$$
$$+ C_N \phi_N + C_S \phi_S - (R\phi_t + S_\phi) \quad (3.5)$$

where:

$$C_{U(D)} = \frac{Ae^{+(-)Ah}}{h \sinh Ah}; C_{N(S)} = \frac{Be^{+(-)Bk}}{k \sinh Bk} \quad (3.6)$$

The multi-exponential scheme is very similar to the hybrid scheme. Its coefficients are always positive. It is second order accurate when the cell Reynolds numbers A, B are small, and it behaves as an upwind scheme when A, B dominate. Although the accuracy is similar to that of the hybrid scheme, this scheme is preferred since the coefficients resulting from this discretization vary smoothly, this factor is favorable for convergence.

The Uni-exponential scheme is a skew upwind exponential scheme designed to decrease the numerical diffusion occuring in the previous scheme when the flow is not aligned with the grid lines. The idea is briefly outlined below for a 2D equation. After normalisation, the 2D transport equation can be written as:

$$(\phi_{ss} - 2\sqrt{A^2 + B^2}\phi_s)$$
$$+ (\phi_{\xi\xi} + \phi_{\eta\eta} - \phi_{ss}) = S_\phi \quad (3.7)$$

where s is the local advection direction. The first term can be expressed by an exponential discretization, while other second derivatives are discretised by centered differences. A parabolic interpolation fonction is used to express the intermediate values ϕ_U and ϕ_D in terms of dependent variables, for instance:

$$\phi_U = \phi_{NW}\eta_U(\eta_U + 1)/2$$
$$- \phi_W(\eta_U + 1)(\eta_U - 1) \quad (3.8)$$
$$+ \phi_{SW}\eta_U(\eta_U - 1)/2$$

which results in a 9 points formula.

$$\phi_C = \sum_{NB} C_{NB}(C)\phi_{NB} - C(C)S_\phi(C) \quad (3.9)$$

Extension to the 3D case is straightforward and a 27 points formula is obtained. The 3D Uni-exponential scheme is not a positive scheme, but this fact does

not induce any troubles, neither in the convergence, nor in the monotony of the solution. Nevertheless, this scheme is only first order accurate when the flow is dominated by a balance between convection and pressure gradient.

The Continuity Equation

The fully conservative formulation is retained. The discretised form is a balance between unknown mass fluxes:

$$\left[Ju^1\right]_d - \left[Ju^1\right]_u + \left[Ju^2\right]_n - \left[Ju^2\right]_s$$
$$+ \left[Ju^3\right]_e - \left[Ju^3\right]_w = 0 \qquad (3.10)$$

with $Ju^i = b_l^i U_l$

On the both sides of the control volume interface, the discretised momentum equations are available and can be written as:

$$U_l(C) = \hat{U}_l(C) - C(C)b_l^j(C)\frac{\partial p}{\partial \xi^j}(C) \qquad (3.11)$$

where the contributions of neighbouring points and source term (except the pressure gradient) are accumulated into the pseudo-velocity $\hat{U}_l(C)$.

We must now reconstruct the contravariant velocity components u^i needed at the control volume interfaces to enforce continuity and to avoid the chequerboard pressure oscillations.

$$Ju^i = b_l^i U_l$$
$$(3.12)$$

Instead of interpolating U_l from available neighbouring values of the same species, U_l is linked to other dependent variables through a local *'pseudo-physical'* approximation of momentum equation at the control volume interface [8].

$$U_l(d) = \overline{\hat{U}}_l(d) - \overline{C}(d)b_l^j(d)\frac{\partial p}{\partial \xi^j}(d) \qquad (3.13)$$

A linear interpolation (in the computational domain) is used to build $\overline{\hat{U}}_d$ and $\overline{C}(d)$ but the pressure gradient is rediscretised at the respective interface. This is why this reconstruction is called "pseudo-physical". Using the relation (3.12), the contravariant components are now given by:

$$u^i = \frac{1}{J}b_l^i\overline{\hat{U}}_l - \overline{C}\frac{1}{J}b_l^i b_l^j \frac{\partial p}{\partial \xi^j}$$
$$= \frac{1}{J}b_l^i\overline{\hat{U}}_l - \overline{C}Jg^{ij}\frac{\partial p}{\partial \xi^j} \qquad (3.14)$$

Using relation (3.13), the mass fluxes are gathered in (3.10) to provide a pressure-pseudo-velocity equation which does not admit chequerboard oscillating solutions.

3.2 Method 2

The Convection Diffusion Scheme

The major drawback of the previous discretisation schemes comes from the fact that the local variations of the convection or diffusion coefficients as well as the source term are not accounted for in the influence coefficients. The CPI (Consistent Physical Interpolation) scheme, based on a fully conservative formulation of the momentum equations, was proposed recently by the authors to remedy this weakness [9]. Its name stems from the fact that the fluxes are reconstructed from auxiliary (momentum) equations which are rediscretised at the interfaces of the control volume. This discretisation provides a "dynamical interpolation formula" linking the interfacial unknowns to the neighbouring cell-centered unknowns. For instance, the 2D reconstruction formula for the unknown u at the interface e is given by:

$$U_e = \hat{U}_e + \sum_{NB} B_{eNB}^U p_{NB} \;;$$
$$V_e = \hat{V}_e + \sum_{NB} B_{eNB}^U p_{NB} \qquad (3.15a,b)$$

with:

$$\hat{U}_e = \sum_{NB} C_{eNB}^U U_{NB} \;;$$
$$\hat{V}_e = \sum_{NB} C_{eNB}^U V_{NB} \qquad (3.16a,b)$$

The pseudo-velocities $\hat{U}_e$ are no more interpolated from the available neighbouring $\hat{U}_{NB}$ like in the previous approach. They are linked to the surrounding velocities U_{NB} through a discretisation of an auxiliary momentum equation. This is why the CPI approach is a generalisation of the previous recontruction: (i) this is a physical reconstruction, (ii) this technique is applied not only to the continuity equation but also to the momentum equations. For the sake of compacity, the details concerning the stencil and the

372

discretisation scheme which can be found in [9], are omitted here.

After elimination of the interfacial unknowns and combination of the various fluxes, the CPI method yields a stable second-order accurate twenty-seven point stencil in the three-dimensional case.

The Continuity Equation

The available reconstructed mass fluxes are gathered into the continuity equation which provides a new pressure-pseudo velocities equation.

4. THE RESULTS

The Grid Topology

The flow domain covers $0.5 < x/L < 3$, L being the length of the ship; $r_s < r/L < 1$. Starting from an a priori specified surface grid distribution, a volumic mesh is generated using a transfinite interpolation procedure. A new O-O topology is preferred to the previous H-O grid topology [7]. This new topology enables us to optimize the number of points describing the hull and makes it possible a better description of the near wake flows. The fact that no a priori grid line is aligned with the dominant flow direction could appear as a disadvantage. Actually, since the fully elliptic RANSE are retained here, and since no particular anisotropic splitting is involved in the discretisation schemes, we think that the results are not too penalised by this choice. At the very most may we fear a slight increase of false diffusion in some parts of the flow domain. This likely drawback is largely compensated for by the fact that this fully body fitted grid allows a correct handling of the propeller boss, which was not possible with $x = x(\xi)$ grids used in [7].

The Boundary Conditions

Inlet velocity profiles ($\xi = 1$) are generated in accordance with the method of Coles and Thompson [10] which needs the specification of δ, U_τ and Q_e. These values are estimated from the specified data [11], [12] where:

$$\theta_{11} = \int_0^\infty \frac{U_e - U}{Q_e} \frac{U}{Q_e} dy \; ; \quad \delta_1 = \int_0^\infty \frac{U_e - U}{Q_e} dy \; ;$$

$$H_{12} = \frac{\theta_{11}}{\delta_1} \text{ and } C_f = \frac{\tau_w}{\frac{1}{2}\rho U_\infty^2}$$

in order to match the solution to the measured data at X/L=0.646. However, it is felt that the influence of inlet conditions is forgotten at the stations on the afterbody and in the wake.

Neumann conditions are used for the planes of symmetry ($\xi = \xi_{max}$, $\zeta = 1$ and $\zeta = \zeta_{max}$). No slip conditions is enforced on the hull ($\eta = 1$) and free stream conditions (U=1, V=W=0) are applied at the outer surface ($\eta = \eta_{max}$). Velocity profiles are slightly modified to enforce the global mass continuity constraint; hence, linear extrapolation is used for the extraneous pressure boundary conditions on all the surfaces limitating the flow domain instead of the usual Dirichlet condition p=0.

The First Results

Computations with Method 1 associated to a two-layer k-ε model [4] are performed on a 80x40x51 fully body fitted grid based on an O-O topology described before (Grid I). Figure 4 shows a perspective view of this grid. The clustering of the grid close to the hull is such that the boundary layer is always described by more than 25 points, the first point being located in the viscous sublayer ($y^+ = 1$). The longitudinal pressure distributions are presented in figs. 5a-b. A very good agreement with the experimental results is observed on the waterline while the pressure distribution on the keel line presents the same trends as in [7], i-e an overestimation of about 40% near x/L=0.875. However, the spike that was present at X/L=0.90 in our previous computations [7] has disappeared here.

Girthwise pressure distributions at several x-stations (figs 6a-b-c) exhibit the same trends as in [7].

The computational and experimental skin friction lines on the hull surface are presented in figs 7a-b. They both indicate that the flow close to the stern separates along an S convergence line (S1 line). The excellent agreement of the results with visualisation data is due to the eviction of the wall function approach associated to the use of a fully body fitted grid on which the propeller boss can be correctly accounted for. Nevertheless, the convergence line present in the visualisation data near the keel line (S2 line) is completely missed by the computations. The calculated skin friction lines go up from the keel line and cross this region without any distortion.

The axial velocity contours at the propeller plane (x/L=0.976) are presented in figs 8a-b-c. Two convection-diffusion schemes have been employed to generate the computational results; the first one is the multi-exponential scheme based on a 7 points stencil and the second one is the uni-exponential one which leads to a 27 points stencil. They are both first order accurate when the flow is dominated by a balance between convection and pressure forces but the last one is preferred because the extraneous

corner points enable a more accurate representation of the convective direction and leads to a reduction of the directional numerical viscosity. Nevertheless, even if the results are improved when the Uni-exponential scheme is used - the axial velocity contours have a bulge on a level near the propeller centerline - the characteristic hook shape present in the measured velocity contours is not found by the computations.

Endly, the velocity components U, V, W as well as pressure data are compared more extensively in figs 9-10-11. For each series of plots, the evolution is considered with respect to y for several depths z=cste. Here again, the calculations exhibit a correct agreement with the data except in the region close to the core of the longitudinal vortex. The experimental U profiles are characterised by a non-monotonicity which is forgotten by the computations. The maximum of W profiles is underestimated in the computations, indicating that the calculated longitudinal vortex is less intense than its experimental counterpart.

The results of these simulations are in good agreement with the experimental measurements. The gross features of the wake such as the thin shear layer near the keel, the accumulation of low speed flow in the middle part of the hull and the related occurence of a longitudinal vortex are correctly captured by the computations. However, the simulated flow seems more regular than the experimental one and some very specific details, such as the low speed region in the vicinity of the propeller disk associated to the hook-shaped velocity contours, appear filtered by the simulation. Actually, the computed flow looks like the flow around a slender hull, which makes questionable the use of the results of simulations to improve the geometry via an interactive design process.

Influence of Discretisation Errors

Therefore, it is necessary to identify the parameters which have a dominant influence on the quality of the simulation for such hulls. As pointed before, the influence of the discretisation scheme does not seem negligible. In order to clarify the degree of importance of discretisation errors, two categories of tests are conducted.

Test 1

For the first test, the usual methodology based on the Uni-exponentiel scheme and a Baldwin-Lomax model is retained (Method 1). The computations are performed on a refined mesh (121x61x60) (Grid II) based on the same O-O topology. The clustering of discretisation points is such that about twice more points per direction are present into the propeller disk region. Figure 12 shows the girthwise Cp distribution for three

locations, namely, x/L=0.64, 0.87 and 0.94. For the first two stations, no spectacular improvment can be noticed. However, the strong gradient near the keel plane of symmetry is better captured on the finer grid. Figure 13 presents a visualisation of skin-friction lines on the hull which is not noticeably different from the one obtained on Grid I. Figure 14 shows the longitudinal velocity contours in the propeller disk. Again, no evident improvment can be noticed so that it seems that the results are more or less grid independant.

Test 2

In order to assess the influence of the discretisation errors, a new convection diffusion scheme (CPI) leading to a totally new methodology, has been applied to this problem (Method 2). A Baldwin-Lomax turbulence model is again used here and the computations are performed on Grid I. Figures 15-16 show the girthwise Cp distributions and the wall flow which are not significantly different from the results obtained with Method 1 on Grid I. Figure 17 shows the axial velocity contours at x/L=0.976. The bulge is now slightly more developped but the innermost contours do not reveal any hook-configuration.

Several numerical tests have been performed to evaluate the weight of numerical inaccuracies. Neither the computation on a refined grid, nor the use of a new discretisation method, have improved the computed simulation in the near wake. As a matter of fact, even if the global characteristics are slightly improved, the characteristic hook-shaped contours are not predicted in the propeller disk region. These numerical tests indicate that (i) the solution is more or less grid independent on Grid I, (ii) the simulated flow is too diffusive, (iii) the turbulence modelisation plays a major role in the mechanisms giving birth to these uneven vortex features.

Influence Of The Turbulence Modelisation Errors

To evaluate the influence of the classical newtonian turbulence models, the Baldwin-Lomax model has been compared to several k-ε models (Chen & Patel [4], Nagano &Tagawa [13], Deng & Piquet [14]) for which the wall function approach is always discarded. For the sake of brevity, the results are just mentionned and not analysed in detail. The k-ε models should be more accurate since the eddy viscosity depends on the two quantities k and ε which are obtained by solving transport equations. However, the supremacy of the k-ε models over the algebraic Baldwin-Lomax model is not demonstrated for this class of flows. As it was pointed out in [1], the aforementionned tested models produce

essentially the same too diffusive flow, especially in the near wake region.

In order to get an idea of what has to be modified to improve the simulation, a last "heretic" computation has been performed by reducing the level of the eddy viscosity by a factor 2.5 in the core of the longitudinal vortex. Figure 18 shows the axial velocity contours at x/L=0.976. The hook-shaped configuration is now captured and figs 19a-b confirm the very good agreement between this computation and the experiments. The U component profiles are non-monotonic in the core of the longitudinal vortex and the W component profiles indicate that the predicted vortex is now far more intense. At last, fig. 20 shows a visualisation of the wall flow. It is very interesting to notice that the S2 convergence line is now present, which underlines the correlation between the extent and intensity of the longitudinal vortex and its trace on the hull. This numerical experiment indicates clearly that the turbulent eddy viscosity is the key parameter which controls the near wake of the flow. The classical turbulence models seem to produce a too high level of eddy viscosity in the central part of the wake which hides the characteristics of discretisation schemes.

5. CONCLUSION

A detailed analysis of several numerical approaches and turbulence models has been performed in this work. The various discretisation schemes which have been evaluated, produce a similar flow in the near wake, characterized by a too moderate longitudinal vortex and no hook-shaped isowake contours. The computations on a refined grid revealing the same weaknesses, it is sensible to think that errors coming from the turbulence modelling are mainly responsible for the inaccuracies of the RANSE computations. This hypothesis is confirmed by the spectacular effect of a local reduction of the eddy viscosity. Therefore, the development of new turbulence models including more physics (Reynolds stress models, improvment of k-ε models, curvature effects,?..) seems to be the only way to improve the quality of RANSE based simulations for this class of flows.

REFERENCES

1. L. Larsson, V.C. Patel & G. Dyne (Eds) Proceedings of 1990 SSPA-CTH-IIHR Workshop on Ship Viscous Flow. Flowtech Int. Report N°2, 1991.
2. V.C. Patel "Ship Stern and Wake Flows: Status of Experiment and Theory", Proc. 17th Symp. on Naval Hydrodyn., The Hague, The Netherlands, 1988, pp. 217-240.
3. M. Wolfhstein "The Velocity and Temperature Distribution in One- Dimensional Flow with Turbulent Augmentation and Pressure Gradient", Int J. Heat Mass Transfer, Vol.12, 1969, pp. 301-318.
4. H.C. Chen & V.C. Patel "Practical Near-Wall Turbulence Models for Complex Flows Including Separation", AIAA-87-1300, 1987.
5. V.C. Patel, H.C. Chen & S. Ju "Ship Stern and Wake Flows: Solutions of the Fully Elliptic Reynolds Averaged Navier Stokes Equations and Comparisons with Experiments", IIHR Rept. 323, Iowa City, Iowa, 1988.
6. B.S. Baldwin and H. Lomax "Thin Layer Approximation and Algebraic Model for Separated Turbulent Flows", AIAA Paper 78-257, 1978.
7. J. Piquet & M. Visonneau "Computation of the Flow past a Shiplike Hull", Proc. 5th. Int. Conf. Num. Ship Hydrodynamics, Hiroshima, Mori, K.H. Ed., 1989.
8. C.M. Rhie & W.L. Chow "A Numerical Study of the Turbulent Flow past an Isolated Airfoil with Trailing Edge Separation", AIAA-82-0998, 1982.
9. G.B. Deng, J. Piquet, P. Queutey & M. Visonneau "A Fully Implicit and Fully Coupled Approach for the Simulation of Three-Dimensional Unsteady Incompressible Flows" Paris GAMM Workshop, Notes on Num. Fluid Mech., Vol 36, M. Deville, T.H. Lê & Y. Morschoine Eds., 1991.
10. T. Cebeci, K.C. Chang and K. Kaups "A Three Dimensional General Method for Three-dimensional Laminar and Turbulent Boundary Layers on Ship Hulls", Proc. 12th ONR Symp. Naval Hydro., Washington, 1978.
11. L. Larsson (Ed.) (1980) Proceedings of SSPA-ITTC on Ship Boundary Layers. SSPA Report N°90.
12. K. Wieghardt and J. Kux "Nomineller Nachström auf Grund von Windkanal versuchen", Jahrb. der Schiffbautechnischen Gesellschaft (STG), 1980, pp. 303-318.
13. Nagano, Y. & Tagawa, M. "An Improved k-ε Model for Boundary-Layer Flows", J. Fluids Eng., 100, 1990, pp. 33-39.
14. Deng G.B. & Piquet J. "K-ε Turbulence Model for Low Reynolds Number Wall-Bounded Shear Flow ", Proc. " 8th Turbulent Shear Flow ", 26-2, Münich , 1991.
15. Lofdahl, L. "Measurements of the Reynols Stress Tensor in the Thick Three-Dimensional Boundary Layer near the Stern of a Ship Model", SSPA, Goteborg, Sweden, Report N°61, 1982.
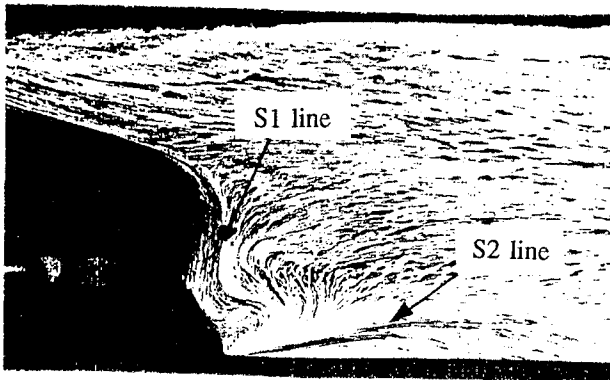
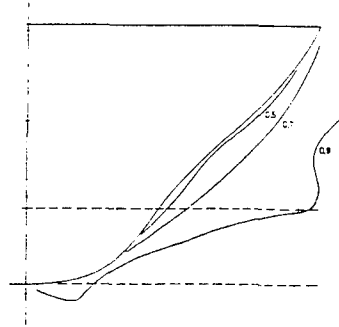Figure 1- HSVA Tanker-Limiting streamlines (from [1]).

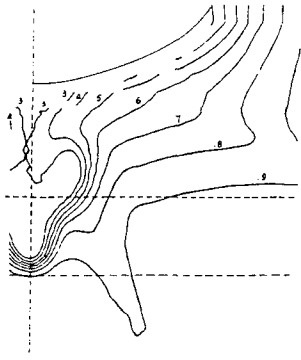Figure 2a- HSVA Tanker- Axial velocity contours-x/L=0.908 (from [1]).

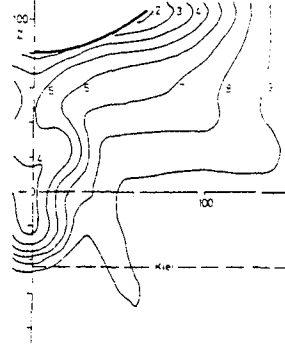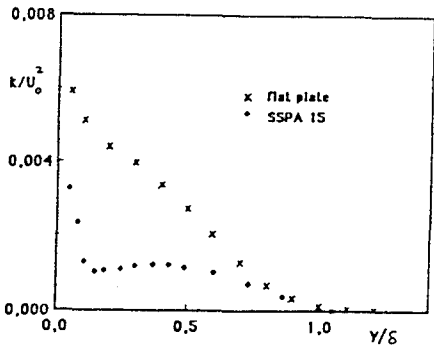Figure 2b- HSVA Tanker- Axial velocity contours-x/L=0.976 (from [1]).

Figure 2c- HSVA Tanker- Axial velocity contours-x/L=1.005 (from [1]).

(d) Turbulent kinetic energy in outer variables

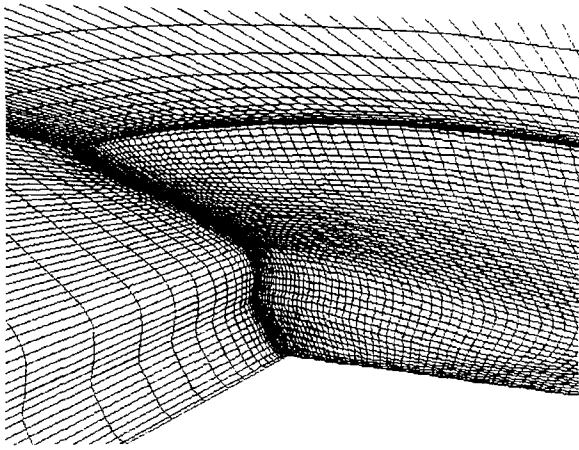Figure 3- Turbulence measurements in stern flow (from [2], [15]).
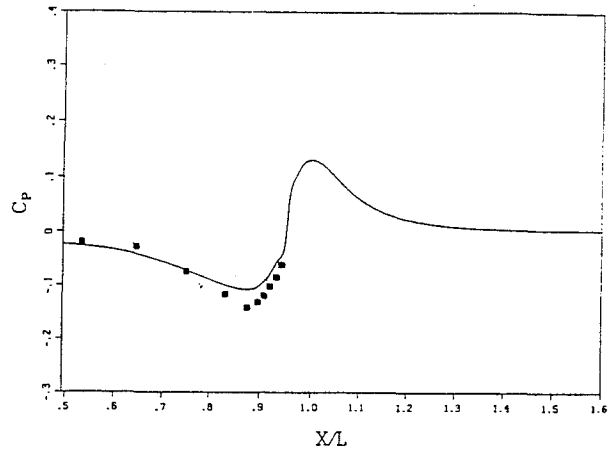
Figure 4- Perspective view of Grid I.
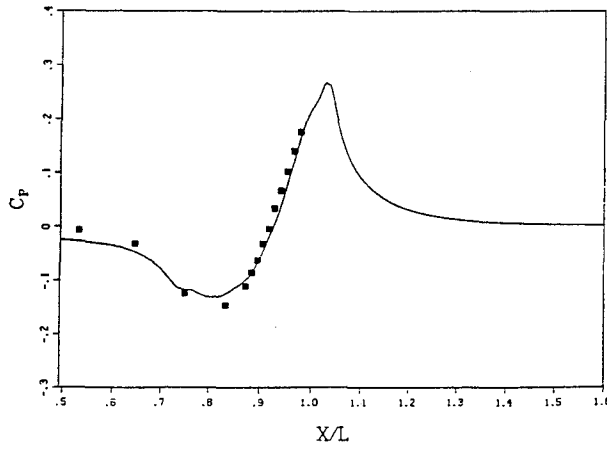

Figure 5a- Cp distribution along the keel line.

Figure 5b- Cp distribution along the waterline.
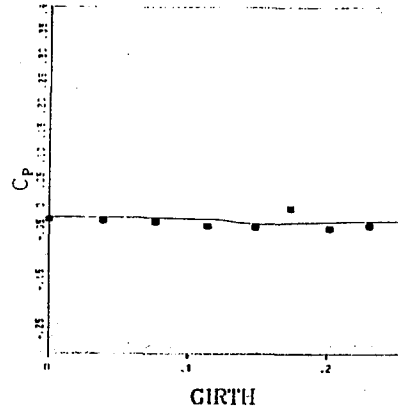
Figure 6a- Girthwise Cp distribution- x/L=0.64.
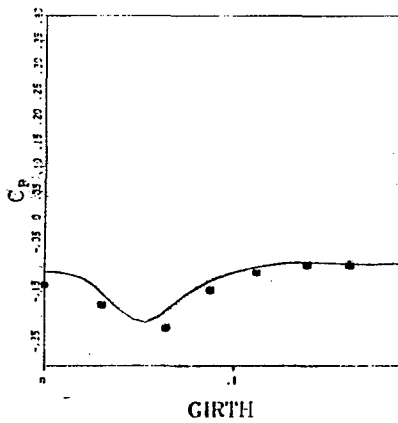
Figure 6b- Girthwise Cp distribution- x/L=0.87.
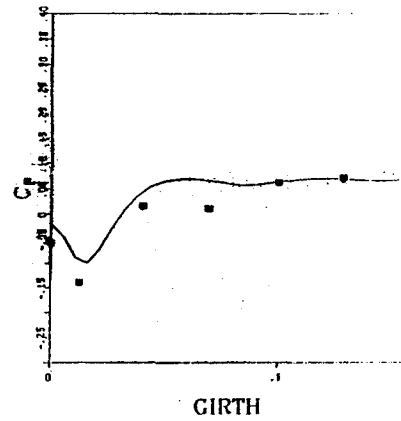
Figure 6c- Girthwise Cp distribution- x/L=0.94.
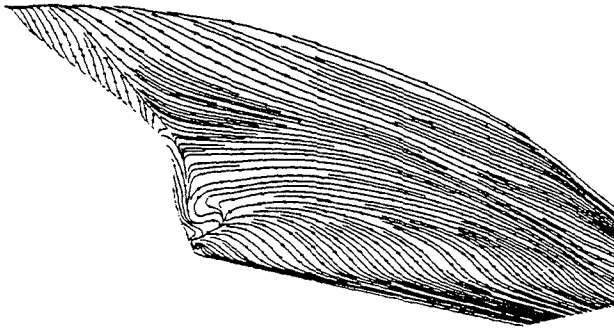
Figure 7a- Computed wall flow.
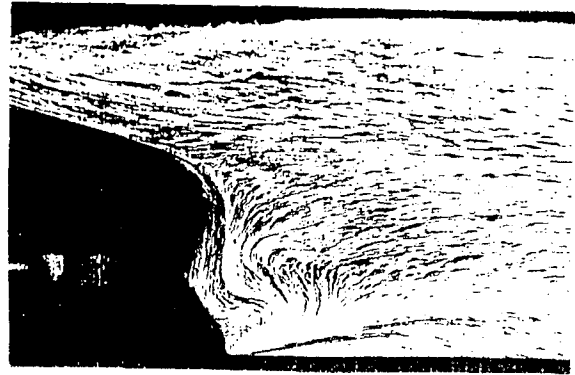
Figure 7b- Experimental wall flow.

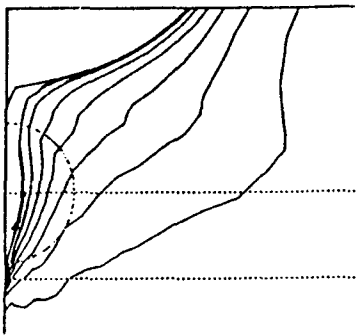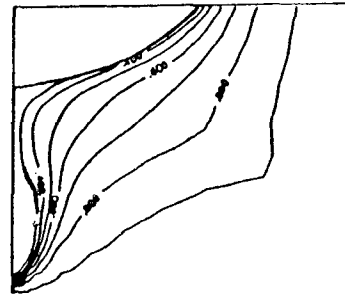Figure 8a- Axial velocity contours- 7 points Multi-exponential scheme- x/L=0.976.

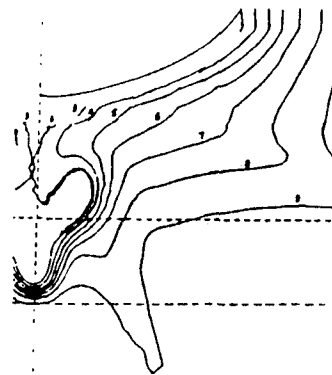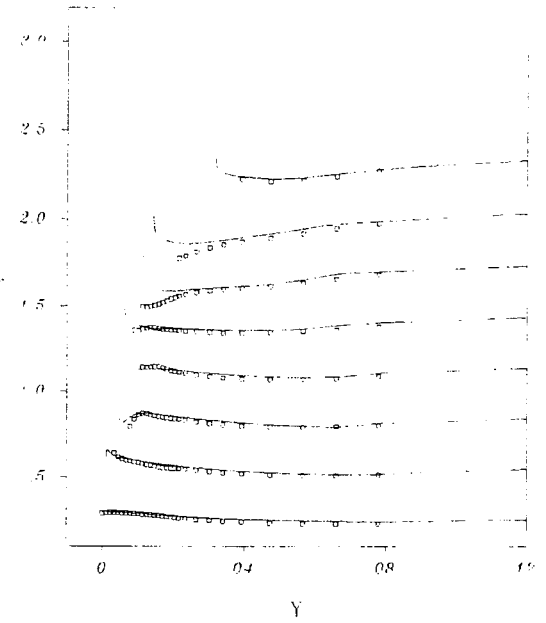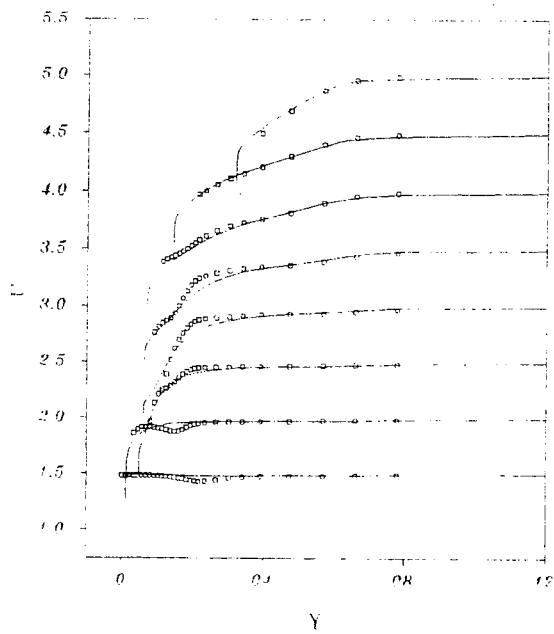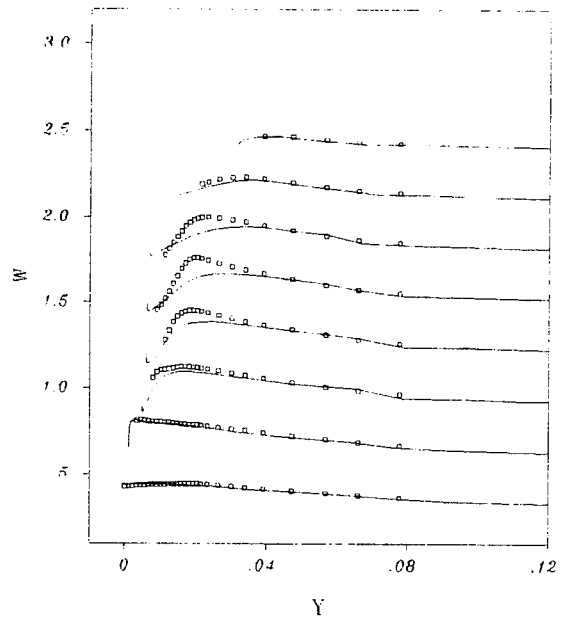Figure 8b- Axial velocity contours- 27 points Uni-exponential scheme- x/L=0.976.

Figure 8c- Axial velocity contours- Experiments-x/L=0.976.

HSVA TANKER (80*40*51) X/L= 0.9548

HSVA TANKER (80*40*51) X/L= 0.9548

Figure 9- U (upper left), V (upper right), W (lower left) and P (lower right) profiles as functions of y, for several depths z=cste, measurements; ---, computations- x/L=0.954

379
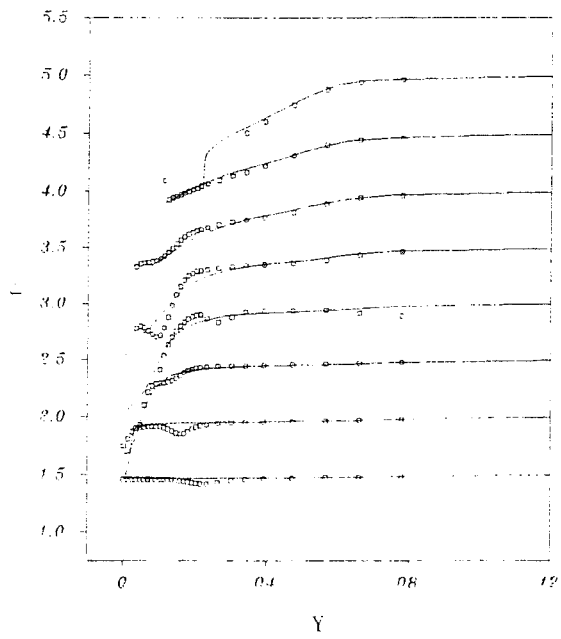
Figure 10- U (upper left), V (upper right), W (lower left) and P (lower right) profiles as functions of y, for several depths z=cste, measurements; ---, computations- x/L=0.969
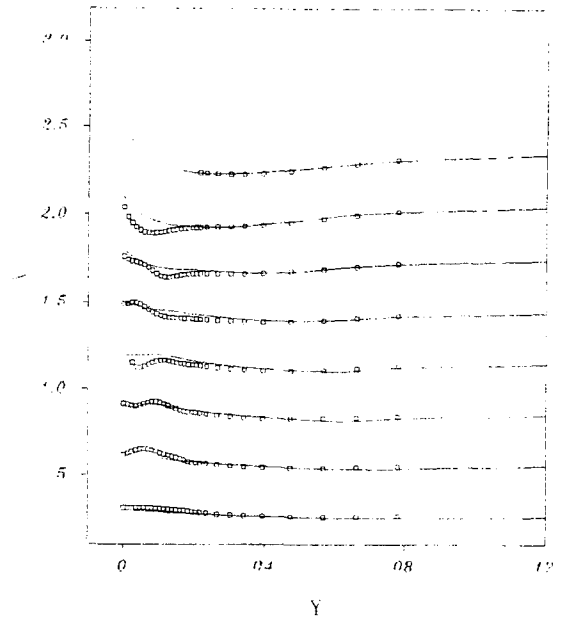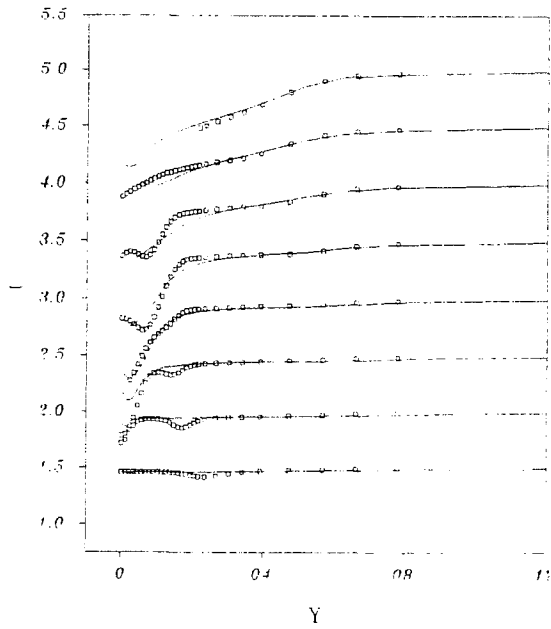
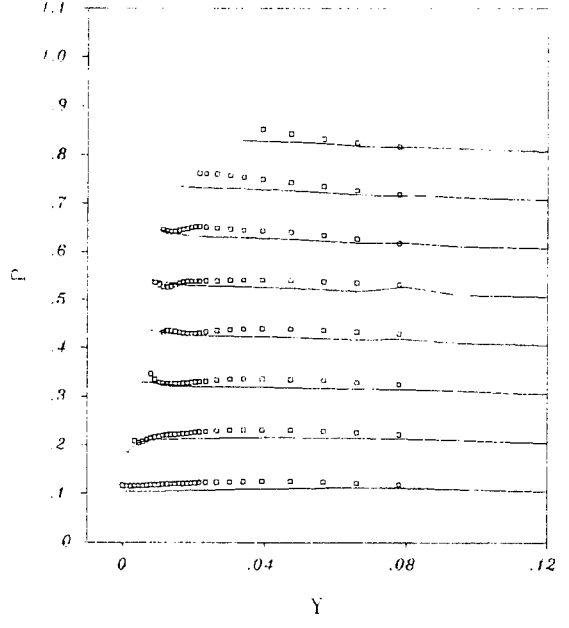HSVA TANKER (80*40*51) X/L= 0.9881
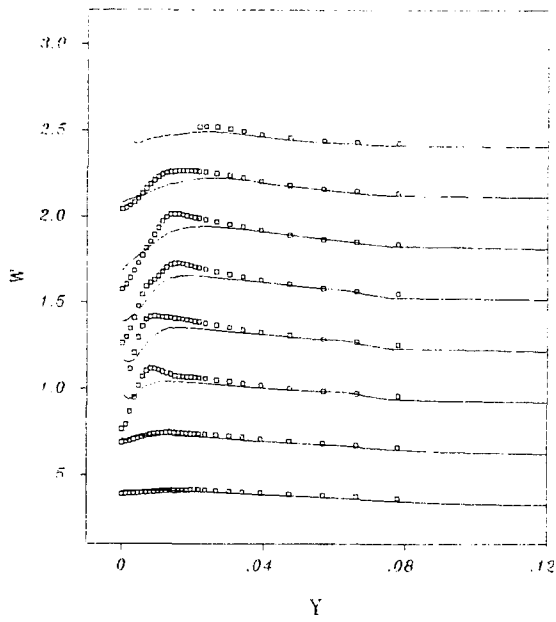
HSVA TANKER (80*40*51) X/L= 0.9881
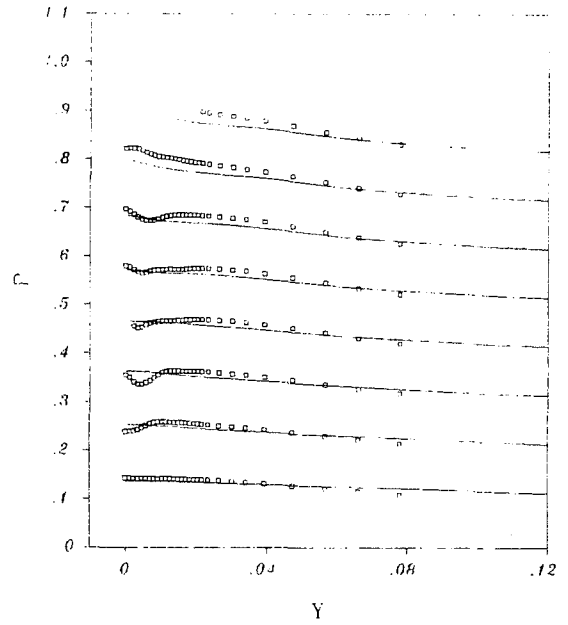
Figure 11- U (upper left), V (upper right), W (lower left) and P (lower right) profiles as functions of y, for several depths z=cste, measurements; ---, computations- x/L=0.988
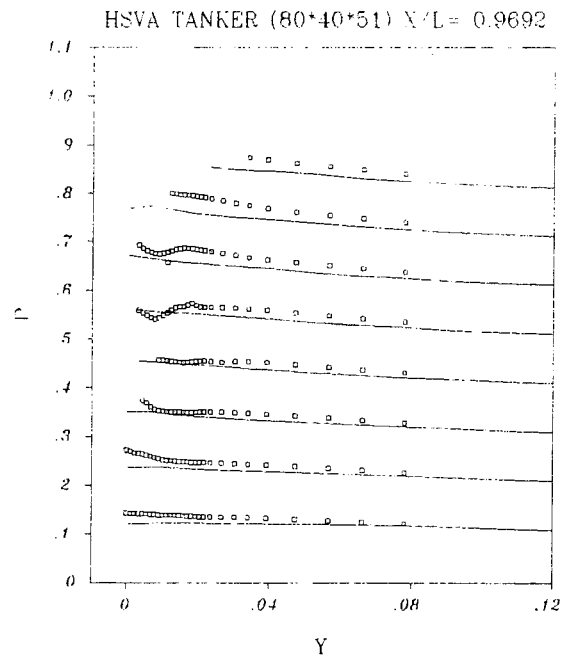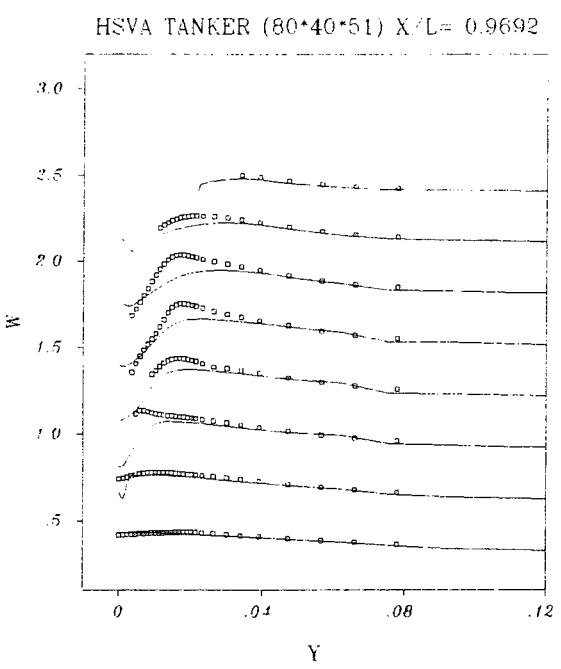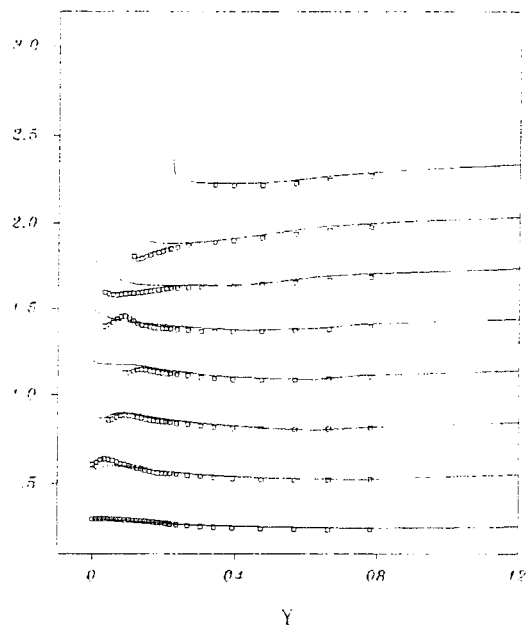
381
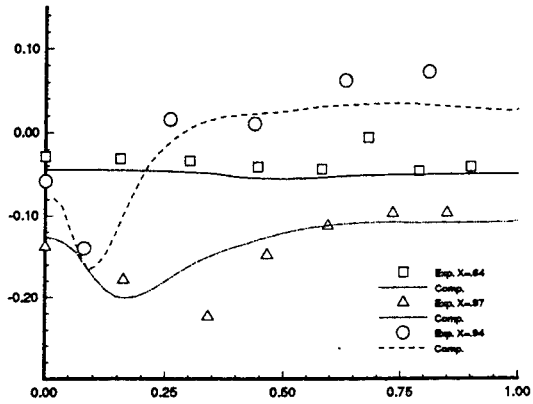
Figure 12- Girthwise Cp distributions- Uni-exponential scheme- Grid II.
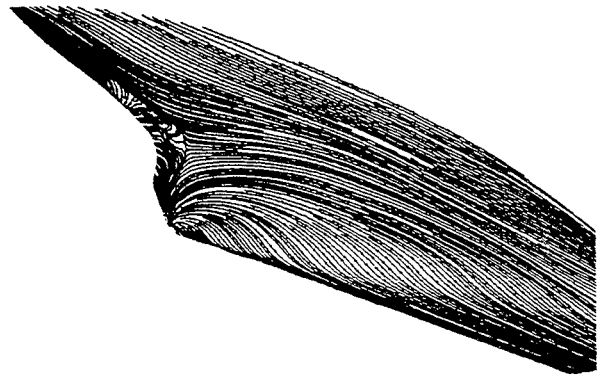
Figure 13- Wall flow- Uni-exponential scheme- Grid II.
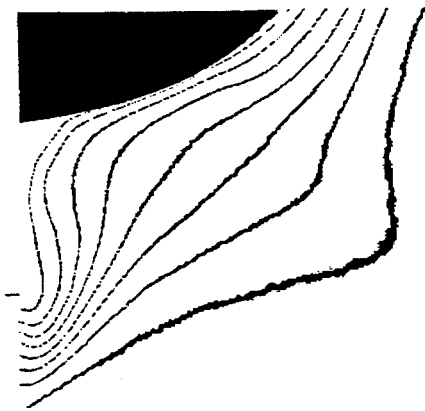
Figure 14- Axial velocity contours- Uni-exponentiel scheme- x/L=0.976-Grid II.
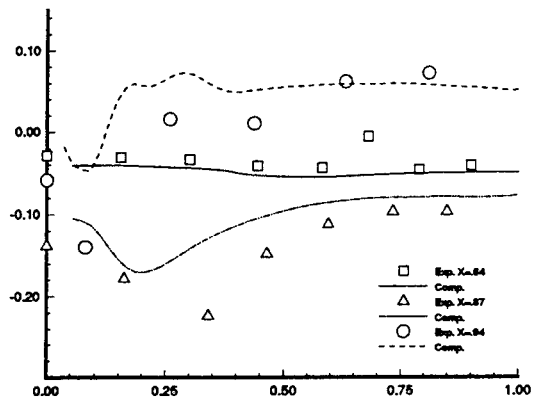
Figure 15- Girthwise Cp distributions- CPI scheme- Grid I.
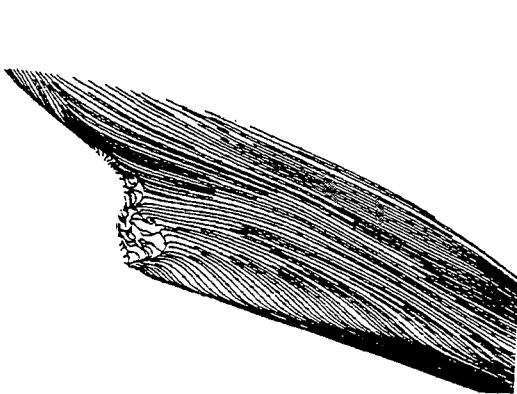
Figure 16- Wall flow- CPI scheme- Grid I.
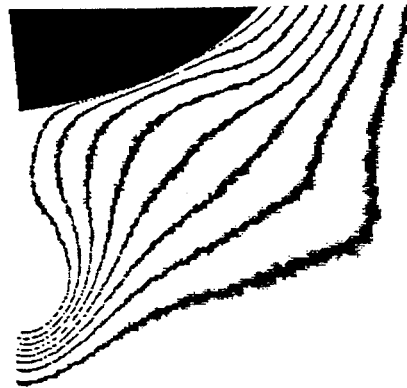
Figure 17- Axial velocity contours- CPI scheme- x/L=0.976-Grid I.

382
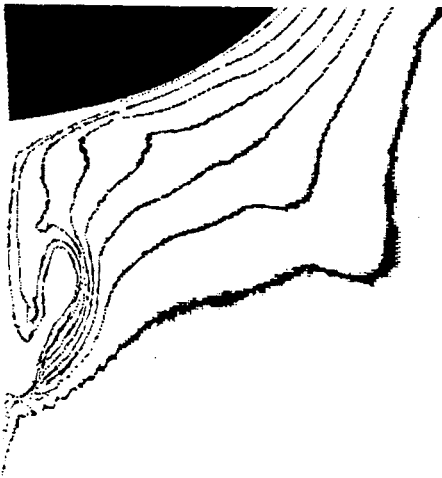
Figure 18- Axial velocity contours- Reduction of the turbulence viscosity- x/L=0.976-Grid I.
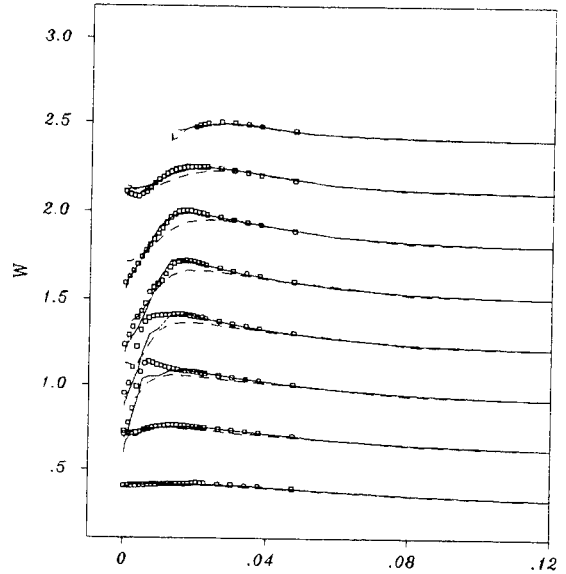
Figure 19b- W profiles as functions of y, for several depths z=cste, measurements; ---, Standard Uni-exp. computations; — ν_T modified computations. x/L=0.978-Grid I.
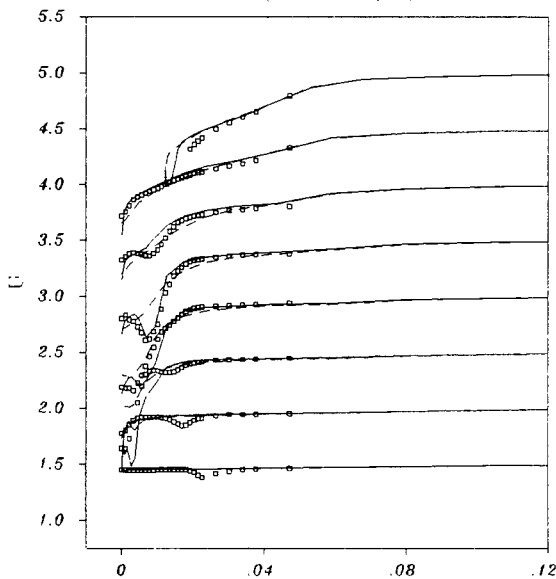
Figure 19a- U profiles as functions of y, for several depths z=cste, measurements; ---, Standard Uni-exp. computations; — ν_T modified computations. x/L=0.978-Grid I.
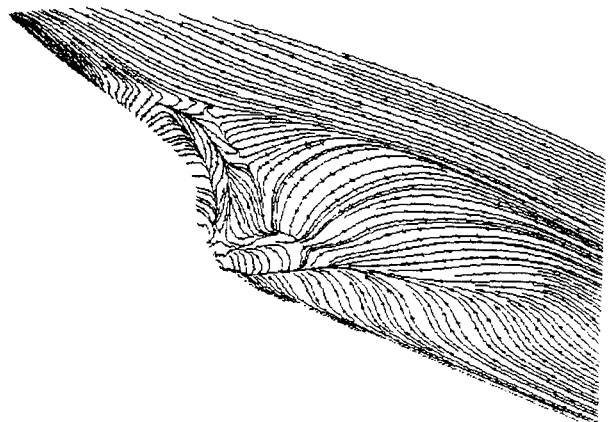
Figure 20- Wall flow- Computations with a reduction of eddy viscosity-Grid I.

by Dr. Yoshiaki Kodama, Ship Research Institute, Tokyo, Japan.

The authors conducted a rather definitive work which answers most of the questions raised in the 1990 SSPA Workshop, with respect to the disagreement between the measured and computed wake distributions of the HSVA tanker. I agree with the authors that the turbulence model is mainly responsible for the disagreement. I would, thus, like to ask the authors how can we improve the available turbulence models in order to accurately predict the wake distributions?

Author's Reply
We believe that it is time to implement new turbulence models which are not based on the eddy viscosity concept if the simulation of complex three-dimensional flows is aimed. Encouraging results are already obtained with several full Reynolds stress closures employed to computed three dimensional flows (see [1] & [2] for instance). However, it is now difficult to evaluate the likely numerical difficulties associated with the eviction of turbulent viscosity. We guess that the correct treatment of the turbulent coupling will require severe improvements of the present methodology.

References
Sotiropoulos, F. and Patel, V.C., "Numerical Calculation of Turbulent Flow through a Circular-to Rectangular Transition Duct Using Advanced Turbulence Closure," AIAA Paper 93-3030, AIAA 24th Fluid Dynamics Conference (1991).
Chen, H.C., "Calculations of Submarine Flows by a Multiblock Reynolds-Averaged Navier-Stokes Method," Proc. of the 2nd Int. Symp. on Engineering Turbulence Modelling and Measurements (1993).

DISCUSSION
by Professor Lars Larsson, FlowTech International and Chalmers University

This is a very interesting and careful study of the flow around one of the test cases of the 1990 SSPA-CTH-IIHR Workshop on Ship Viscous Flow. A new and effective grid is used and grid independence is reasonably well-demonstrated. Different discretization schemes and two standard turbulence models are used. The results seem to verify what was suspected at the Workshop, namely that the results are rather insensitive to variations of this kind. Good results are obtained in all cases for the outer part of the wake, but the central part is wrong.

The drastic improvement in the results caused by the ad hoc change to the eddy viscosity in the vortex is extremely interesting, and the excellent results obtained in this way seem to indicate that it is the turbulence model that has caused the problems everyone has had so far. The reduction in turbulence levels in the thick part of the boundary layer is well-known from experiments and our group tried a more drastic variation already at the Workshop, namely to set $\nu_T = 0$ aft of X/L = 0.8. This gave a slight improvement, but not at all as large as in the present paper. However, turbulence data are available for the HSVA tanker (see the paper by Dr. Kux et al. at the Osaka Colloquium in 1985) and it would be very interesting to see whether the present ad hoc modification of the turbulence model is substantiated by that data.

Author's Reply
At this time, we did not make any comparisons with turbulence data since they were not available to us. However, it is planned to make such comparisons for the CFD Workshop devoted to the "Improvement of Hull Forms Design" which will be held in Tokyo in 1994. It will be interesting to check if these ad-hoc modifications of the turbulence model improve also the description of turbulence data.

DISCUSSION
by Steve Watson, Hampshire, DRA

To which method did you apply your viscosity ?

Author's Reply

In this paper, the reduction of turbulent viscosity was done for calculations conducted with method I. Since then, the same modification was applied to calculations associated with method II with a similar effect on the near wake.

DISCUSSION
by Prof. A. Y. Odabasi, Technical University of Istanbul, Turkey

I would like to congratulate the authors for an excellent paper and even better presentation. I would like to provide some additional information which may assist in their future work:

(1) The measure offered by Prof. M. Tulin, already exists in turbulent shear flow calculations, known as the effects of extra strain rates, largely advocated by Prof. P. Bradshaw of Stanford University (ex-Imperial College, London) and his proposals were published by AGARD.

(2) During the PHIVE project, jointly conducted by BSRA and NMS, three models were tested in the large wind tunnel and these measurement included turbulent quantities up to (including) triple velocity correlation terms. Energy balance near vortex cores in the stern region showed that these the dissipation was balanced by diffusion (not by production as is the case near the wall). This feature was brought out in Ref. [16]. Unless transport equations reach to a maturity to model turbulence as measured these anomalies will continue

References:

[16] Odabasi, A.Y., and Davies, M.E., " Structure of complex turbulent shear flow," Proc. 3rd Symp. on Numerical and Physical Aspects of Aerodynamic Flows, Long Beach, CA, 1985

Author's Reply

We are aware of many works concerned with curvature effects related to specific configurations. However, we do not know any general approach which could be used in a general purpose computational code to modify the turbulent viscosity in complex three-dimensional flows. Moreover, it is difficult to determine if the reduction of turbulent stresses is mainly due to curvature effects.

DISCUSSION
by Professor M. Tulin, University of California at Santa Barbara

You reported significant improvements in comparisons, when you reduced the Reynolds stress in the longitudinal vortex by a factor of 2.5. In flows with significant streamline curvature the pressure gradients normal to the streamlines can strongly effect the turbulent fluctuations in the normal direction. This is an effect analogous to that due to vertical density gradients in the ocean and the atmosphere; in these cases vertical turbulence can be, and often is strongly suppressed and becomes strongly isotropic. I mention this because there is a large literature on the subject (see Monin's book, for example). I am quite sure that this analogy has already been carried over to homogeneous flows with curved streamlines and applied to flows with vortices, etc. This effect is not part of the Baldwin-Lomax model, but it should be added; this would result in anisotropic Reynolds stresses.

Author's Reply

Thank you for your comments and helpful remarks but we feel that it is not easy to sensitize the turbulent viscosity to the complex streamline curvature that occurs in such a situation.

DISCUSSION
by Dr. A. J. Musker, Defense Research Agency, Haslar, England

A previous Haslar study [1], published in the wake of the 1990 Gothenburg Workshop, indicated that future CFD validation studies should avoid attempts at improving the accuracy of discretization schemes and recommended instead "(that) a comprehensive assessment of different wall treatments and turbulence models (should be undertaken)." The present study confirms that the solution is insensitive to the numerical scheme but is extremely sensitive to local changes in turbulence diffusivity.

In the most recent Haslar study (presented at this Conference), we cite the presence of the upstream support wire as the possible cause of the "hook" observed in the contours for axial velocity in the propeller plane. Our only evidence for this is the observation that when the

support wire used in the experiment was included (albeit crudely) in the RANS calculation it had the effect of introducing a hook downstream. The only other occasion where a hook was observed, in any of our predictions without the support wire, occurred when the (current) solution was far removed from convergence. If such a solution was then driven more and more towards convergence the hood would eventually vanish. I would be interested to learn whether the present authors have observed similar behavior and whether they are confident that the solution displayed in Figure 18 had truly converged.

Notwithstanding the above cautionary note, the findings in the present paper offer an entirely different, less troublesome, and more exciting explanation for the presence of the hook - namely, that it is associated with a reduced eddy diffusivity within the core of the longitudinal bilge vortex. I say less "troublesome" because our own investigation casts unwanted doubt on the validity of the experiment data which were carefully measured and compiled by the Hamburg team; I say "exciting" because this new finding supplies us with a tantalizing lead which will allow the CFD community to focus attention on the turbulence models with a view to introducing some consistent mechanism for attenuating the eddy diffusivity within such a vortical flow.

The community will want to know which team is right - is the hook caused by the presence of the support wire? Or is it caused by the inherent properties of the turbulent fluid? Time will tell, but I'm bound to say that the case for the former, resting as it does on an imperfect grid, is much weaker in the light of the authors' findings. This paper is an excellent example of what can be achieved by systematic validation studies and I offer the authors my sincere congratulations.

Author's Reply

We agree with Dr. Musker and confirm that it is very important to get a converged solution, although it is almost impossible to reduce the non-linear residuals to machine-zero for this kind of flows. Actually, the evolution of near-wall quantities appears to provide a trustable sensor of practical convergence for this class of applications, once the non-linear L2-residuals are reduced by 3 to 4 orders of magnitude. The flow

resulting from a local reduction of turbulent viscosity obeys these criteria.

Concerning this particular flow, we noticed that an intense unsteady longitudinal vortex appeared if the computations are started in laminar regime. Once the turbulence model is activated, this vortex and the associated hook-shaped structure slowly disappear to give the well-known unsatisfactory results. Then, if we start from this turbulent solution and reduce the turbulent viscosity by an ad-hoc factor in the ad-hoc region, the intensity of the longitudinal vortex grows again, then stabilizes during several hundreds of non-linear iterations, giving birth to the distorted wake pattern and the secondary line of convergence illustrated in this paper.

DISCUSSION
by Dr. Ming Zhu, University of Tokyo

Have you ever seen the flow separation in your computed results? With our numerical study (see our paper in the present conference), we found that the distortional wake pattern in the propeller plane is produced by the flow separation in which phenomenon the Reynolds stress intensity is observed, in many experiment, lower than those in thin turbulent boundary layer. That means that if the flow separation can not be revealed in the numerical simulation, it may be quite difficult to simulate the distortional wake pattern well.

Author's Reply

As indicated in your very interesting paper presented at this conference, the reduction of turbulent shear stresses is due to the conjunction of two phenomena: (i) the thickening of the boundary layer, (ii) the occurrence of a longitudinal flow reversal region near the hub of the hull. However, we guess that the distorted wake pattern observed in the propeller plane is not only due to the presence of this small separated region. Indeed, a small separated region was simulated in our first calculations presented at the Goteborg's Workshop in 1990 but nevertheless, we were not able to capture neither the hook-shaped structure of isowakes nor the longitudinal skin friction convergence line.

Effects of Turbulence Models on Axisymmetric Stern Flows Computed by an Incompressible Viscous Flow Solver

C.H. Sung, J.F. Tsai, T.T. Huang, and W.E. Smith
(David Taylor Model Basin, USA)

ABSTRACT

An incompressible Reynolds-averaged Navier-Stokes (RANS) computational procedure which employs multigrid, multiblock,and local refinement techniques is presented. The effects of grid spacing and grid stretching on the convergence rate of pressure residuals are investigated. In the computation of turbulent flow over an axisymmetric body the grid distributions in the streamwise, azimuthal, and normal-to-the-wall directions and the grid stretching factor normal to the wall are varied. Quantification of computation errors by a solution-to-solution comparison is used to achieve a grid-independent numerical solution. Numerous computations using a three-dimensional computer code with a multigrid capability are then made on four axisymmetric bodies at a Reynolds number (R_L) about 10^7 to investigate the variation of grid distribution requirements at higher R_L. The grid distributions are refined to adapt to the local flow conditions on the body. More grid points are needed in regions of rapid pressure variation and finer grid density is required for flow at a higher Reynold number. The total grid cell number is proportional to the square of (R_L/y_1^+) and inversely proportional to the aspect ratio of the first grid cell normal to the wall. A grid independent numerical solution has been obtained from the present RANS computer code when the average value of y_1^+ is less than 7, and the rate of solution convergence is controlled by avoiding the use of grid cells with an excessively large aspect ratio and extreme grid stretching. Comparisons with experiment are presented for axial velocity and turbulent shear stress profiles in the stern regions of four axisymmetric bodies are used to evaluate and validate various turbulence models. The root-mean-square (RMS) differences of the measured and computed flow variables are given.

Two modifications to the Baldwin-Lomax turbulence model are shown to improve the predictions of axisymmetric stern flows.

A brief description is also given of a new numerical approach based on multiblock, multigrid and local refinement techniques that has been implemented in IFLOW. Prediction of three-dimensional complex flows at high Reynolds numbers can be accomplished along with a fine spatial resolution and reduced requirements for computer memory and cpu time.

NOMENCLATURE

a_x = axial-to-normal aspect ratio of the 1st grid cell from the wall

a_θ = circumferential-to-normal aspect ratio of the 1st grid cell from the wall

A^+ = 26, Eq.(5)

C = chord length of hydrofoil

C_τ, C_f = local, mean skin friction coefficient

C_F(ITTC)= the 1957 ITTC friction correlation line

C_{cp} = 1.2, Eq.(6)

C_h = 1.55, $\delta = C_h y_{max}$

C_{kleb} = 0.65, Eq.(6)

C_β = 0.01, Eq.(8)

E = preconditioned matrix, Eq.(2)

F,G,H = flux vectors in x,y,z directions, Eq.(2)

$F(y)$ = $y|\omega|[1 - e^{-y^+/A^+}]$

F_{wake} = $y_{max} F_{max}$

$F_{kleb}(y) = \{ 1 + 5.5[C_{kleb}(y/y_{max})]^6 \}^{-1}$
in boundary layer

$F_{kleb} = \{1 + 5.5[C_{kleb} \dfrac{|y - y_{max}|}{(\dfrac{U_{dif}}{|\omega|_{max}})}]^6\}^{-1}$ in wake

387

$$\hat{G} = \sqrt{\frac{(C_h y_{max} + r_o)^2 - r_0^2}{11(C_h y_{max})^2}}$$

$$\text{and } \hat{G} = 1.0, \text{ for } C_h y_{max} / r_o < 0.2,$$

k   = 0.4, von Karman constant, Eq.(5)

K   = 0.0168, Clauser constant

L   = length of axisymmetric body

l   = mixing length

N   = total number of data points or grid cells

MW   = computer memory in million words

n_x, n_θ, n_y = grid cell numbers in axial, circumferential, and normal to the wall directions

$$\hat{P} = (\frac{1}{3} + \frac{2}{3} e^{-C_\beta \hat{\beta}}),$$

$$\hat{\beta} = \frac{y_{max}}{\tau_w} \frac{1}{2} (\frac{\partial p}{\partial x} + |\frac{\partial p}{\partial x}|),$$

BL   = Baldwin-Lomax turbulence model

q   = primitive flow variable vector, Eq(2)

$R_n = R_L = U_\infty L / \nu_\infty$, $R_n = R_C = U_\infty C / \nu_\infty$

R_{max} = maximum radius of the hull

r   = radius, r_0 = hull radius

u,v,w = velocity components in x,y,z directions

x,y,z = coordinate system

U_∞ = reference velocity

u_τ = frictional velocity, $\rho u_\tau^2 = \tau$

v^c = computed flow variable

v^m = measured flow variable

y_1 = distance from the wall to 1st grid cell center

y_{max} = value of y at the maximum of F(y)

y_1^+ = $u_\tau y_1 / \nu$

y^+ = $u_\tau y / \nu$, y = distance from the wall

$$u_{dif} = (\sqrt{u^2 + v^2 + w^2})_{max} - (\sqrt{u^2 + v^2 + w^2})_{|\omega|_{max}}$$

$-u'v'$ = turbulent shear stress

t   = a parameter in Table 1, 95% confidence limit = t x RMS

α, β = preconditioned parameters, $\alpha = -1$, $\beta = 1$

δ = boundary layer thickness

ρ = mass density of fluid

ν = kinematic viscosity of fluid

ν_t = eddy viscosity

$\nu_{t_{inner}}$ = inner eddy viscosity, Eq.(4, 5)

$\nu_{t_{outer}}$ = outer eddy viscosity, Eq.(4,6)

$[\nu_{t_{outer}}]_{BL} = \nu_{t_{outer}}$ of the original BL model

$[\nu_{t_{outer}}]_G = [\nu_{t_{outer}}]_{BL} \hat{G}^2$

$[\nu_{t_{outer}}]_{GP} = [\nu_{t_{outer}}]_{BL} \hat{G}\hat{P}$

$\nu_{t_{wake}}$ = eddy viscosity in wake, Eq.(9)

Δu = computed velocity difference at two R_L's

ω = vorticity, Eq.(6)

$|\omega|_{max}$ = maximum value of $|\omega|$

τ = wall shear stress

τ_{ij} = Reynolds stress tensor, Eq.(3)

INTRODUCTION

Recent advances in Computational Fluid Dynamics (CFD) based on numerical solutions of the Reynolds-Averaged Navier-Stokes (RANS) equations have demonstrated a capability to predict the physics of complex flows as measured in model experiments. Computer codes have been developed for hydrodynamic applications where the flows are treated as incompressible and the Reynolds numbers are high (order of 10^6 to 10^9). However, such codes must be thoroughly validated in order to assess their utility and limitations as design tools. There are many types of errors which the validation process seeks to identify and, hopefully, eliminate. These include numerical errors, physical model errors, and even coding errors. In this paper, a RANS code, IFLOW (Sung and Griffin[1], Sung et. al.[2], and Tsai et. al.[3]) is used as a vehicle to quantify such error sources. The numerical errors associated with grid resolution, grid stretching and convergence rate of the pressure residuals are investigated. Quantification of these errors by solution-to-solution comparison is essential in order to achieve a grid-independent numerical solution. The most critical physical errors are induced by the turbulence model. The errors associated with the turbulence model can only be evaluated after a grid-independent solution is obtained. Performance of the turbulence model can then be assessed by comparisons of measured and computed results. In this paper the measured pressures, skin friction, turbulence shear stress and axial velocity profiles of turbulent axisymmetric stern flows are used to evaluate computed results using various grid resolutions. The RMS differences between the measured and computed flow variables are used to quantitatively assess the validity of the numerical technique.

In the computation of turbulent flow over an axisymmetric body, the grid distributions in the streamwise, circumferential, and normal-to-the-wall directions and the grid stretching in the normal-to-the-wall direction are varied to obtain a grid-independent numerical solution. The distributions and spacings of the flow-adapted grids are successively refined. More grid points are needed in the region of rapid pressure variation and

finer grid density is required for flow at higher Reynolds numbers. The center of the first grid cell normal to the wall (y_1) must be set inside the viscous sublayer to obtain a grid-independent solution. This requirement is satisfied by keeping the average value of $y_1{}^+ = u_\tau\, y_1/\upsilon$ less than 7, where u_τ is the frictional velocity and υ is the kinematic viscosity of the fluid. The rate of solution convergence is monitored during the computation to identify the presence of grid cells with excessively large aspect ratios.

Computation of body drag at high values of Reynolds number is a major challenge for any CFD code. The effects of grid resolution and turbulence models on the computed total fcitional drag coefficients of the axisymmetric bodies are presented. This demonstrates the status of CFD drag prediction by an incompressible RANS code. An example is also given of RANS computations at two Reynolds numbers to address one aspect of scale effects.

DESCRIPTION OF NUMERICAL METHOD

The three-dimensional, incompressible, Reynolds-averaged Navier-Stokes equations is solved using the artificial compressibility approach first proposed by Chorin [4] and subsequently generalized and improved by Turkel [5,6]. This approach has been successfully used by Chang and Kwak [7], Kwak et al. [8], and many others. The formulation of IFLOW [1,2,3] developed at the David Taylor Model Basin is outlined in the following

$$Eq_t + F_x + G_y + H_z = 0,$$

or

$$q_t + E^{-1}F_x + E^{-1}G_y + E^{-1}H_z = 0 \qquad (1)$$

where the subscripts indicate partial derivatives with respect to time t, and the three coordinates x, y, and z. The preconditioned matrix E and the column vectors of the dependent variables q and of the three components of fluxes F, G and H are defined as

$$E = \begin{bmatrix} \beta^{-2} & 0 & 0 & 0 \\ (1+\alpha)\beta^{-2}u & 1 & 0 & 0 \\ (1+\alpha)\beta^{-2}v & 0 & 1 & 0 \\ (1+\alpha)\beta^{-2}w & 0 & 0 & 1 \end{bmatrix},$$

$$q = \begin{bmatrix} p^* = \dfrac{p}{\rho} \\ u \\ v \\ w \end{bmatrix}$$

$$F = \begin{bmatrix} u \\ u^2 + p^* - \mathcal{T}_{xx} \\ uv - \mathcal{T}_{xy} \\ uw - \mathcal{T}_{xz} \end{bmatrix},$$

$$G = \begin{bmatrix} v \\ uv - \mathcal{T}_{yx} \\ v^2 + p^* - \mathcal{T}_{yy} \\ vw - \mathcal{T}_{yz} \end{bmatrix},$$

$$H = \begin{bmatrix} w \\ uw - \mathcal{T}_{zx} \\ vw - \mathcal{T}_{zy} \\ w^2 + p^* - \mathcal{T}_{zz} \end{bmatrix} \qquad (2)$$

where p is the pressure, ρ is the constant density, u, v and w are the three Cartesian components of the mean velocity and the Reynolds stresses are defined as

$$\mathcal{T}_{ij} = R_n^{-1} V \left\{ \frac{\partial u_i}{\partial x_j} + \frac{\partial u_j}{\partial x_i} \right\}$$

$$i, j = 1, 2, 3 \qquad (3)$$

where $\mathbf{u} = (u_1, u_2, u_3) = (u, v, w)$, $(x_1, x_2, x_3) = (x, y, z)$, V is the sum of the kinematic and eddy viscosities, and R_n is the Reynolds number. The variables are nondimensionalized by the free stream condition at infinity in the following manner: u, v and w by U_∞; p and τ by $\rho_\infty U_\infty^2/2$; x, y and z by L; $R_L = R_n = U_\infty L/\nu_\infty$, L is the body length; and α and β^{-2} are the preconditioned parameters. Numerical experiments indicate that the choice of $\alpha = -1$ and $\beta = 1$ is adequate.

The spatial discretization is based on the cell-centered central difference finite-volume formulation. An explicit one-step, five-stage Runge-Kutta time-stepping scheme is used. In this scheme only three evaluations of the artificial dissipation term are made at the first, the third and

the fifth stages with an appropriate weighting at each stage to increase the stability limit. Specifically, the parabolic stability limit along the real axis has been raised to 9 which is advantageous in terms of stability when solving the Navier-Stokes equations. The three techniques used to accelerate the rate of convergence are local time-stepping, implicit residual smoothing and multigridding. The local time step size when defined to include both the convective and the viscous terms has been found to be more stable than that which is estimated by including only the convective term. Three smoothing parameters are used in the residual smoothing technique. These parameters are fixed as constants but are self-adjusting to flow characteristics, and are properly scaled to reduce the undesirable effect arising from high aspect ratios of the grid cells. It is essential to add an appropriate amount of artificial dissipation to suppress spurious oscillations which occur in all central difference schemes. The conventional unidirectional dissipation where the dissipation is proportional only to the maximum eigenvalue of the flux Jacobian in that coordinate direction has been modified to appropriately blend the maximum eigenvalues in all three coordinate directions. Numerical experiments with the revised artificial dissipation terms with carefully devised boundary conditions for the dissipation terms have demonstrated that the revised dissipation models are robust and accurate in the calculation of the flow problems which include high aspect ratio grid cells.

The multigrid method developed by Jameson [9] to accelerate solution convergence has been adopted. By the cyclic use of a sequence of fine to coarse grids, the multigrid technique is very effective in damping the solution modes with long wave lengths which are primarily responsible for slow convergence. Both V- and W-cycle multigrid techniques are used. Boundary conditions are updated at each Runge-Kutta stage of every grid level in the fine-to-coarse path, but they are not updated in the coarse-to-fine path. This practice is mainly used to avoid introducing boundary condition interpolation errors. For ease of coding the grid cell numbers in all the coordinate directions used in a coarse grid is selected to be half of that in the fine grid.

The boundary conditions used on the solid wall are that the three velocities and the normal pressure gradients are all zero. The far field boundary conditions which include both the inflow and the outflow through the boundaries are based on a zero-gradient for the three velocities and a non-reflecting condition for the pressure ; Hedstrom [10], and Rudy and Strikewerda [11]. The non-reflecting boundary condition is particularly important for computation in a relatively small domain and has been carefully implemented.

TURBULENCE MODEL

A simple modification of Baldwin-Lomax turbulence model [12] is used in this paper. The Baldwin-Lomax formulation of eddy viscosity is similar to the algebraic eddy-viscosity model of Cebeci and Smith [13] but is easier to implement in the RANS code. The inner and outer eddy viscosity of the turbulent wall model are defined as

$$\nu_t = \begin{cases} \nu_{t_{inner}} & (0 < y \leq y_c) \\ \nu_{t_{oute}} & (y_c \leq y) \end{cases} \qquad (4)$$

where y is the normal distance from the wall, and y_c is the value of y at which the values of eddy viscosity from the inner and outer formulas are equal.

$$\nu_{t_{inner}} = \ell^2 |\omega| \qquad (5)$$

Where $\ell = ky[1 - e^{-y^+/A^+}]$, and

$$|\omega| = \left| \sqrt{\left(\frac{\partial v}{\partial x} - \frac{\partial u}{\partial y}\right)^2 + \left(\frac{\partial u}{\partial z} - \frac{\partial w}{\partial x}\right)^2 + \left(\frac{\partial w}{\partial y} - \frac{\partial v}{\partial z}\right)^2} \right|$$

;

and

$$\nu_{t_{outer}} = KC_{cp}F_{wake}F_{kleb}(y). \qquad (6)$$

For a wall boundary layer, $F_{wake} = y_{max}F_{max}$, and

$$F_{kleb}(y) = \{ 1 + 5.5[C_{kleb}(y/y_{max})]^6 \}^{-1},$$

where F_{max} is the maximum value of $F(y) = y|\omega|[1 - e^{-y^+/A^+}]$ that occurs in a profile and y_{max} is the corresponding value of y at which it occurs. The $K_{kleb}(y)$ is the Klebanoff intermittency factor. The constants used are: $k=0.4$, $A^+= 26$, $y^+= yu_\tau/\nu$ ($\rho u_\tau^2 = \tau_w$ = wall shear stress), $C_{kleb}= 0.65$, $C_{cp}=1.2$, and $K = 0.0168$ = the Clauser constant.

In the stern regions of axisymmetric bodies the standard Baldwin-Lomax model overpredicts the values of turbulent shear stresses and streamwise velocities. Two simple modifications to the standard Baldwin-Lomax model are made for these

flows. The modifications are made based on the experimental data of Huang et al. [14,15,16] and are applied only to the values of $v_{t_{outer}}$ as

$$[v_{t_{outer}}]_G = [v_{t_{outer}}]_{BL} \hat{G}^2 \qquad (7)$$

and

$$[v_{t_{outer}}]_{GP} = [v_{t_{outer}}]_{BL} \hat{G}\hat{P}$$

$$V_t = [v_{t_{outer}}]_{GP} \tanh\{\frac{v_{t_{inner}}}{[v_{t_{outer}}]_{GP}}\} \qquad (8)$$

where

$$\hat{P} = (\frac{1}{3} + \frac{2}{3}e^{-C_\beta \hat{\beta}}),$$

$$\hat{\beta} = \frac{y_{max}}{\tau_w}\frac{1}{2}(\frac{\partial p}{\partial x} + |\frac{\partial p}{\partial x}|),$$

$$\hat{G} = \sqrt{\frac{(C_h y_{max} + r_o)^2 - r_0^2}{11(C_h y_{max})^2}} \quad for \ \frac{C_h y_{max}}{r_0} \geq 0.2,$$

and $\hat{G}=1.0$ for $C_h y_{max}/r_0 < 0.2$.

The constants $C_\beta = 0.01$ and $C_h = 1.55$ ($C_h y_{max} = \delta$ = the boundary-layer thickness), were obtained by conducting numerical experiments using the measured velocity profiles of Huang et al., and r_0 is the local radius of the hull. The modified turbulence model used in equations (7) and (8) will be referred to as BL-G, and BL-GP, respectively, and both are simple modifications of the Baldwin-Lomax (BL) model. The letters G indicate the modification is based on the flow geometry of an axisymmetric boundary layer, Eq(7), and GP indicates that the modification is based on the flow geometry and pressure gradient, Eq(8). The modifications apply in the stern region where the axial pressure gradient is positive (adverse).

In the symmetric wake of a single axisymmetric body or a two-dimensinal foil the modified eddy viscosity of Renze, Buning, and Rajagopalan [17] is used,

$$v_{t_{wake}} = KC_{cp}F_{wake}F_{kleb}(y) \qquad (9)$$

where

$$u_{dif} = (\sqrt{u^2 + v^2 + w^2})_{max} - (\sqrt{u^2 + v^2 + w^2})_{|\omega|_{max}}$$

$$F_{kleb} = \{1 + 5.5[C_{kleb}\frac{|y - y_{max}|}{(\frac{u_{dif}}{|\omega|_{max}})}]^6\}^{-1}$$

The value of y_{max} is set at $|\omega|_{max}$ and the Klebanoff function is applied outside of y_{max}. Inside of y_{max} the eddy viscosity is constant and is set equal to the computed value of $v_{t_{wake}}$ at y_{max}. The wake becomes asymmetric when the axisymmetric body or foil is at angle of attack. The center line of the asymmetric wake is set at the location of the minimum velocity in the wake. The values of y_{max} are set at two locations of $|\omega|_{max}$ from upper and lower wake. The value of $v_{t_{wake}}$ takes the maximum value from either side of the wake center line. Inside the two locations of y_{max} the eddy viscosity is constant and the Klebanoff function is applied outside of y_{max}.

The problem of multiple peaks in the Baldwin-Lomax F_{max} function has previously been reported by Degani and Schiff [18]. The modification of the Baldwin-Lomax model made by Degani and Schiff is implemented in the IFLOW code for an axisymmetric body at angle of attack. The differentiation between the vorticity within the attached boundary layers from the vorticity on the surfaces of separated vortices is made to select a length scale based on the thickness of the attached boundary layers rather than one based on the radial distance between the body surface and the surfaces of separated vortices. This modification eliminates the possibility of locating the value of y_{max} at the surface of the separated vortex and causing an excessively large eddy viscosity.

RESULTS AND DISCUSSION

The comparison of the typical rates of convergence of single grid, 3-level V-cycle multigrid and 3-level W-cycle multigrid based on the calculations on a 96x32x48 grid of a complex appendage-flat plate juncture flow at $R_c=6.2\times10^5$ is shown in Fig. 1, where R_c in the Reynolds number based on the chord length of the appendage. The residual is defined as the RMS difference between the nondimensional pressures at the (n+1)th and nth cycle, p^{n+1} and p^n,

391

$$\text{Residual}=[\ \Sigma_i^N(\ p_i^{n+1}-p_i^n)^2/N]^{1/2},$$
$$i=1,2,3...,N \qquad (10)$$

where N is the total number of points. As expected, the W-cycle multigrid converges fastest and the single the slowest. The results presented in this paper are for converged residuals of $3x10^{-3}$ to 10^{-4} which indicate satisfactorily convergence of the numerical solutions. Around 100 V-cycle multigrid iterations were generally sufficient to achieve the converged numerical solutions with the residuals less than $3x10^{-3}$.

Computation of the flow field and drag of an axisymmetric body at a high Reynolds number is a major challenge to CFD capability. The effects of grid resolution and turbulence models on the computed flow field and drag coefficients of the axisymmetric Suboff model [16] and the DTNSRC Axisymmetric Body 1, 2 and 5 [14,15] are presented to illustrate the status of the incompressible IFLOW RANS code. The grid-independent solution is defined ideally as the solution of the finite difference equations that approaches the exact solution of the corresponding partial differential (RANS) equations as the grid spacing approaches zero. Since no exact solution of the RANS equations is available for an axisymmetric body at high Reynolds numbers to validate the numerical results, it is necessary to generate numerous numerical solutions for various grid spacings and distributions to compare with experimental measurements. Validation of a RANS computer code can only be made by this tedious numerical-experimental comparison. Quantification of measurement uncertainties are generally available for high-quality experiments. The root-mean-square (RMS) value of the difference between the computed and measured values of the flow variables, respectively defined as v^c and v^m, is

$$\text{RMS Difference}=[\ \Sigma_i^N(v_i^c-v_i^m)^2/N]^{1/2},$$
$$i=1,2,3...,N \qquad (11)$$

where N is the total number of data values used in the comparison. In the presentation of the following results the measurement uncertainties, the RMS differences, and the average values of $y_1^+=u_\tau\ y/\upsilon$ for the first grid center normal to the wall are reported for all the computations. The grids are distributed in the axial, circumferential, and radial directions of the axisymmetric body. The distribution of axial grids is selected according to the magnitude of the axial pressure gradient on the body; finer grids are used in the regions of higher pressure gradient. The distribution of circumferential grids is chosen to keep the aspect ratios of grids within the limit that provides good solution convergence (residuals of less than $3x10^{-3}$ in about 100 iteration cycles). The distribution of radial grids, made to resolve the boundary layer characteristics on the hull, requires that y_1^+ of the first grid center from the wall be limited to less than the thickness of the laminar sublayer. The effects of grid distribution on the computed pressure and skin friction coefficients on the body, the axial velocity and turbulent shear stress profiles at two axial locations of x/L=0.904 and 0.978 on the Suboff Axisymmetric Body have been shown in Reference 3. The computed RMS differences of the flow variables as a function of the average values of y_1^+ for the Suboff model are shown in Fig. 2. The Reynolds number based on the body length is $1.2x10^7$. As shown in Fig. 2 and the results of Reference 3 when the average value of y_1^+ of the first grid center from the wall is smaller than 7 every computed viscous flow variable approaches a grid-independent solution. It was found that the computed pressure coefficients approach the grid-independent solution faster than the computed skin friction coefficients.

The effect of turbulence model parameters on the computed results can be evaluated after a grid-independent solution has been achieved. An example of the effect of choice of turbulence model parameters on the computed viscous flow variables with a 112x32x64 grid ($5.5< y_1^+< 7.9$) is shown in Table 1 and Figs. 3 and 4. It is evident that the original Baldwin-Lomax turbulence model must be modified for thick stern boundary layers. The standard Bladwin-Lomax turbulence model was found to overpredict the measured eddy viscosity by as much as a factor of 4, mixing length by a factor of 2, and Reynolds stress by a factor of 2. These discrepancies will generally cause an overprediction of axial velocities in the propeller plane by up to10% of the free stream velocity. The prediction of full-scale ship speed and propulsor rotation speed imposes stringent accuracy requirements for experimental and computational data. Therefore, continued improvement of experimental and computational accuracy is essential to meet CFD validation requirements. The turbulence model we proposed here is an interim rather than a final solution. Critical examination of the measured and computed Reynolds stresses and velocity profiles, as illustrated in this paper is helpful for assessing the validity of turbulence models. Without such a careful examination and detailed comparison, the utility of CFD can be seriously

compromised. Table 1 indicates that the two modified Baldwin-Lomax turbulence models (BL-G, and BL-GP) with the value of the average y_1^+ smaller than 7, the RMS differences between the computed and measured pressures, skin frictions, axial velocities, and turbulent shear stresses are within the measurement uncertainties. Furthermore, Table 1 shows that the computed total frictional drag coefficients, C_f, are almost equal to or smaller than the value of the standard ship-model correlation line of the 1957 International Towing Tank Conference , $C_F(ITTC)$, depending on whether the value of y_1^+ for the grid used is smaller than or greater than 7. During the course of computation it was noted that grid cells of excessive aspect ratios reduced the rate of convergence. As a result, the circumferential grid number was increased to reduce the aspect ratios and in turn provided an improved rate of convergence. The total pressure drag of the body was also computed and a slight oscillation with increasing grid density was noted. Further improvement of the pressure drag computation has been made by using a local refinement technique to a generate fine grid around the body.

The modified Baldwin-Lomax turbulence model (BL-GP) was used to predict the flow over the Suboff Axisymmetric Body. The results are shown in Figs. 5 and 6 using a grid of 128X32X88. It is seen that satisfactorily computed results for axial velocity and turbulent shear stress profiles were obtained for an average value of $y_1^+=4.4$. The computed axial velocity profiles at $R_L=6.6\times10^6$ and 2.5×10^7, and the computed profiles of the difference in axial velocity at the two R_L's for the DTNSRDC Axisymmetric Body 1 are shown Fig. 7. These computed results are useful for propulsor design.

The present comparisons of the computed and measured results provide a guide to estimate the minimum number of grid cells in the streamwise (axial), circumferential, and normal-to-the-wall directions, n_x, n_θ, and n_y. In many applications the RANS solutions, which consistently predict flow variables within the measurement uncertainties of the experimental data, will be accepted as grid-independent solutions for engineering applications. The minimum axial and circumferential grid numbers, n_x and n_θ, needed to achieve grid-independent RANS solutions of flows over axisymmetric bodies at high Reynolds numbers may be estimated as

$$n_x = \frac{L}{2a_x y_1} = \frac{1}{2a_x}(\frac{u_\tau}{U_\infty})(\frac{R_L}{y_1^+}) = \frac{1}{2\sqrt{2}a_x}\sqrt{C_f}(\frac{R_L}{y_1^+})$$

$$and \quad n_\theta = \frac{\pi D}{2a_\theta y_1} = \frac{\pi\frac{D}{L}}{2\sqrt{2}a_x}\sqrt{C_f}(\frac{R_L}{y_1^+}) \qquad (12)$$

where y_1 is the first grid center from the wall, a_x and a_θ are the average values of the axial and circumferential aspect ratios of the first grid cell from the wall with respect to $2y_1$, C_f is the mean skin friction coefficient, $R_L=LU_\infty/\nu$ is the Reynolds number based on body length L and free-stream velocity U_∞, $y_1^+=y_1 u_\tau/\nu$, D is the maximum diameter of the body, and ν is the kinematic viscosity. The grid spacings normal to the wall direction are stretched according to a hyperbolic tangent function of two control parameters. The value of n_y has been varied from 36 to 88 and the stretching parameters have also been varied to obtain a grid with the smallest allowable value of y_1^+ that possesses a good rate of solution convergence. The ratios of two adjacent grid spacings, Δ_{n+1}/Δ_n, in each direction are normally limited to $1.2> \Delta_{n+1}/\Delta_n> 0.8$. The total number of grid cells becomes

$$N = 1.5 n_x n_\theta n_y = \frac{4.71\frac{D}{L}}{8a_x a_\theta}(\frac{R_L}{y_1^+})^2 C_f n_y \qquad (13)$$

Here a factor is used to allow for 50% more axial grid cells in the wake. The required computer memory M in units of words may be estimated by assuming that about 50 to 60 (used in the present estimates) 64 bit (8 byte) words of memory are needed for each grid cell. Table 4 of Reference 3, which is generated using the estimates of Equations (12) and (13), provides a guide to select the minimum grid numbers and computer memory required to obtain grid-independent RANS solutions for a range of Reynolds numbers at three typical aspect ratios and at two desired values of y_1^+. The present computer limitation of about 200 megawords (2 gigawords is possible in the near future) of supercomputer memory for CFD production computations with simple grid distributions precludes the use of $y_1^+=1.0$ for $R_L>10^7$. It is evident that a RANS computer code must possess rapid convergence characteristics for large numbers of grid cells with the largest possible aspect ratios in order to perform computations for R_L at about 10^7 to 10^8 and must be able to provide consistent

393

engineering grid-independent solutions for a value of y_1^+ of about 4.0-6.0. It is very difficult to perform an accurate RANS computation at $R_L = 10^9$ with the memory and speed of the present supercomputers with a simple grid distribution technique and it will be a grand challenge for future CFD efforts for many years to come.

RECENT ADVANCES

The value of y_1^+ must be smaller than 7 to achieve a grid-independent solution. It is noted from Eqs.12 and 13 that the grid cell number is proportional to the square of Reynolds number for the same values of y_1^+, n_x and n_θ. The required large grid cell numbers at full-scale Reynolds numbers are the major diffculty and hence the grand challenge for CFD. One seemingly easy approach is to increase the aspect ratios of the grid cells near the wall and to stretch the grid as much as possible away from the wall. However, excessively large aspect ratio of grid cell near the wall and extreme grid stretching anywhere has been found to degrade numerical stability and to slow solution convergence.

A new numerical approach based on a multiblock, multigrid, local refinement method proposed by Sung[19] has been implemented in IFLOW. The multiblock structure makes grid generation for a complex geometry easier. Multigrid techniques significantly accelerate the rate of convergence. The local refinement method provides high spatial resolution of three-dimensional boundary layer and separated vortical flows at reduced computer memory and cpu time. Two sample three-dimensional flow computations for an appendage/flat plate juncture have been made for $R_C = 6.2 \times 10^5$ [1, 20] and are presented in Figs.8, and 9. Traditional grids of 96x48x48 and 192x96x96 were first used. Then three and four levels of local refinement were applied; the performance of IFLOW on a Cray C90 for these two calculations are shown in Table 2. Memory savings of 70% and 92% and reductions of cpu time by factors of 4.3 and 19 respectively have been achieved with the same spatial resolution in the inner viscous layer. The original values of y_1^+ of 8.4 and 3.7, respectively were maintained for this evaluation. It is very interesting to note from Table 2 that both computer memory savings and cpu reductions improve with an increasing numbers of grid cells in the computational domain. The required solution resolution in the dominantly viscous flow region (boundary layer, vortex core, or three-dimensional separated zone) dictates the acceptable spacings of grid cells in that region. It is very desirable to be able to reduce grid spacing locally in the critial region without changing the overall grid. The local refinement technique doubles grid numbers in all three directions for every level of refinement. Multiple levels of local grid refinement with moderate grid stretching can be used to provide fine grid spacings near the wall. Thus, the method provides the required fine spatial resolution in the dominantly viscous region which is relatively small. This also avoids the use of excessively large aspect ratios of the grid cells near the wall or large grid numbers. Furthermore, the results of numerical experimentation indicate that the present multigrid local refinement technique can provide effective numerical communications across the interfaces of all levels of grid refinement without numerical instability. This multiblock, multigrid and local refinement method can be used to predict three-dimensional complex flows at high Reynolds numbers with fine spatial resolution in a numbers of critical regions. The details of the numerical method and code validation will be presented in future publications.

CONCLUSION

An incompressible Reynolds-averaged Navier-Stokes computational procedure is presented. Numerous computations are made on four axisymmetric bodies at high values of Reynolds number (between 6.6×10^6 and 1.2×10^7) to investigate the effects of grid distribution and turbulence model on computed stern flows. The numerical-experimental comparisons are presented for pressure and skin friction coefficients on the body, and axial and turbulent shear stress profiles at several axial locations in the stern region. The root-mean-square (RMS) differences between the measured and computed flow variables are summarized.

It was found that when the average values of y_1^+ for the first grid center from the wall was smaller than 7, the RMS differences between all the measured and computed flow variables were within the measurement uncertainties, and the computed total skin friction coefficients were approaching the values of the standard ship-model correlation line of the 1957 International Towing Tank Conference. It was also noted that the grid cells with excessively large aspect ratios near the wall and extreme grid stretching reduced the rate of solution convergence. Therefore, it is important to monitor the rate of solution convergence during computations and avoid the use of grid cells having extreme grid stretching and excessively large aspect ratios.

Two simple interim modifications of the original Baldwin-Lomax turbulence model were made for the stern regions of axisymmetric bodies.

The two modified turbulence models provide better predictions of the stern flows for two axisymmetric bodies.

Preliminary sample computations indicate that a multiblock (for complex geometry), multigrid(for fast solution), local refinement (for efficient use of grid cells) method can be used to compute complex flows at high Reynolds numbers with considerably reduced computer momery and cpu time.

ACKNOWLEDGEMENT

REFERENCES

1. Sung, C.-H., and Griffin, M. J., " Improvement in Incompressible Turbulent Horseshoe Vortex Juncture Flow Calculations," AIAA Paper 91-0022, AIAA 29th Aerospace Sciences Meeting, Reno, Nevada, January 7-10, 1991.

2. Sung, C.-H., Griffin, M. J., and Coleman, R. M., " Numerical Evalution of Vortex Flow Control Devices," AIAA paper 91-1825, AIAA 22nd Fluid Dynamics, Plasma Dynamics & Laser Conference, Honolulu, Hawaii, June 24-26, 1991.

3. Tsai, J. F., Sung, C. H., Griffin, M. J., and Huang, T. T., " Effects of Grid Resolution on Axisymmetric Stern Flows Computed by an Incompressible Viscous Flow Solver," paper presented at the ASME Summer Fluids Engineering Conference, FED-Vol. 158, pp99-108, June 20-24, 1993.

4. Chorin, A. J.," A Numerical Method for Solving Incompressible Viscous Flow Problems," J. Comp. Phys., vol. 2, pp. 12-26, 1967.

5. Turkel, E.," Preconditioned Methods for Solving Incompressible and Low Speed Compressible Equations," NASA ICASE Report 86-14, 1989.

6. Tuekel, E.," Review of Preconditioning Methods for Fluid Dynamics," NASA ICASE Report 92-47, 1992.

7. Chang, J. L. C., and Kwak, D.," On the Method of Pseudo Compressibility for Numerically Solving Incompressible Flows," AIAA Paper-0252, 1984.

8. Kwak, D., Chang, J. L. C., Shanks, S. P., and Chakravarthy, S.," A Three-Dimensional Incompressible Navier-Stockes Flow Solver Using Primitive Variables," AIAA J., vol. 24, no. 3, pp390-396, 1986.

9. Jameson, A.," Multigrid Algorithms for Compressible Flow Calculation," in Multigrid Methods II, Lecture Notes in Mathematics series, no.1228, Hackbusch, W., and Trottenberg, U. Eds., Spring-Verlag, New York, 1986.

10. Hedstrom, G. W.," Nonreflecting Boundary Conditions for Nonlinear Hyperbolic System," J. Computational Physics, vol. 30, pp222-237, 1979.

11. Rudy, D. H., and Strikewerda, J. C.," Boundary Conditions for Subsonic Compressible Navier-Stokes Equations," Computers and Fluids, vol.9, pp327-338, 1981.

12. Baldwin, B. S., and Lomax, H.," Thin Layer Approximation and Algebraic Model for Separated Turbulent Flows," AIAA paper 78-257, AIAA 16th Aerospace Sciences Meeting, Huntsville, Alabama, January 16-18, 1978.

13. Cebeci, T. and Smith, A. M. O., Analysis of Turbulent Boundary Layers, Academic, New York, 1974.

14. Huang, T. T., Santelli, N., Belt, G.," Stern Boundary-Layer Flow on Axisymmetric Bodies," Paper presented at the 12th Symposium on Naval Hydrodynamics, Wash. D. C., June 5-9, 1978, National Academy of Sciences Wash. D. C., pp 127-157, 1978.

15. Huang, T. T., Groves, N. C., and Belt, G. S., "Boundary Layer Flow on an Axisymmetric Body with an Inflected Stern," DTNSRDC Report 80/064, 1980.

16. Huang, T. T., Liu, H.-L., Groves, N. C., Forlini, T. J., Blanton, J. N., and Gowing, S.," Measurements of Flows Over an Axisymmetric Body with Various Appendages (DARPA SUBOFF Experiments)" Paper presented at the 19th Symposium on Naval Hydrodynamics, Seoul, Korea,August 24-28, 1992.

17. Renze, K. J., Buning, P. G., and Rajagopalan, R. G.," A Comparative Study of Turbulence Models for Overset Grids, AIAA paper

92-0437, AIAA 30th Aerospace Sciences Meeting, Reno, Nevada, Jan. 6-9,1992.

18.   Degani, D., and Schiff, L. B.," Computation of Turbulent Supersonic Flows around Pointed Bodies Having Crossflow Separation," J. Comp. Phys., Vol. 66, pp173-196, 1986.

19.   Sung, C.H.," A Multiblock Multigrid Local Refinement Method for Incompressible Reynolds-averaged Navier-Stokes Equations", 6th Copper Mountain Conference on Multigrid Methods, Copper Mountain, Colorado, April 4-9, 1993.

20.   Devenport, W. J., Dewitz, M. B., Agarwal, N. K., Simpson, R. L., and Poddar, K.," Effects on the Flow Past a Wing Body Junction," AIAA 2nd Tuebulent Shear Flow Control Conference, Tucson, Arizona, March, 1989.
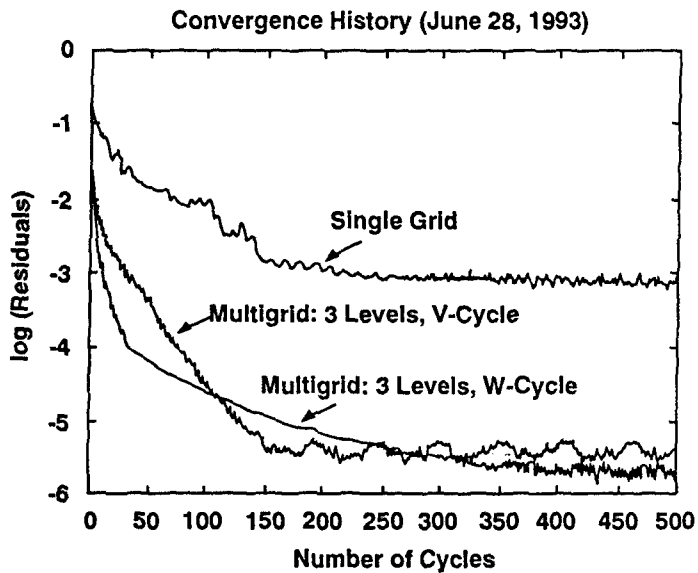
FIGURE 1. TYPICAL RATE OF CONVERGENCE
WITH AND WITHOUT MULTIGRID
FOR 96x32x48 GRID
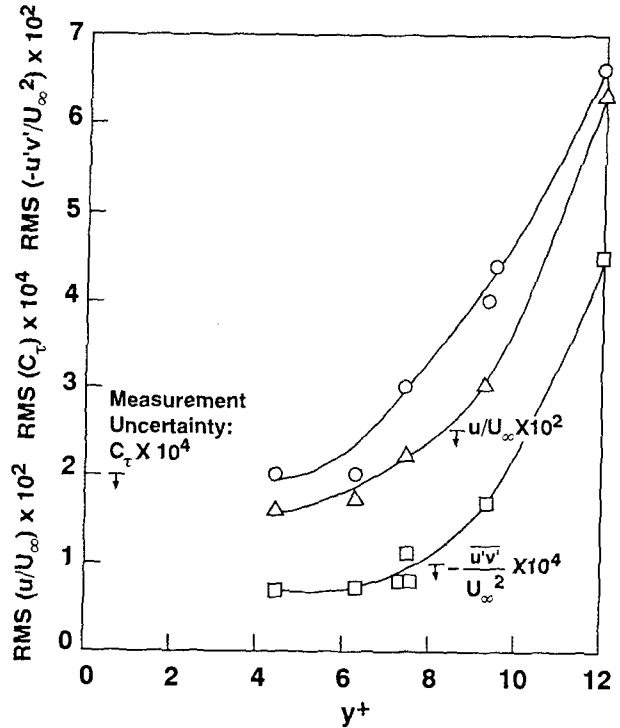
FIGURE 2. RMS DIFFERENCES
BETWEEN MEASURED AND
COMPUTED FLOW VARIABLES
AT VARIOUS VALUES OF y_1^+

a). Suboff Axisymmetric Body
X/L = 0.978, R_L = 1.2 x 10^7
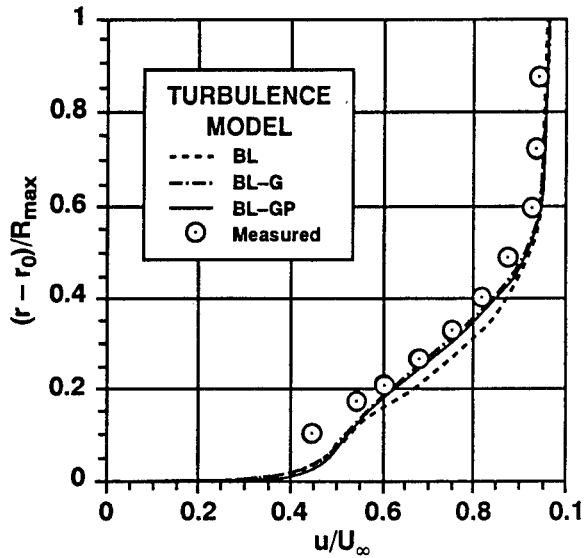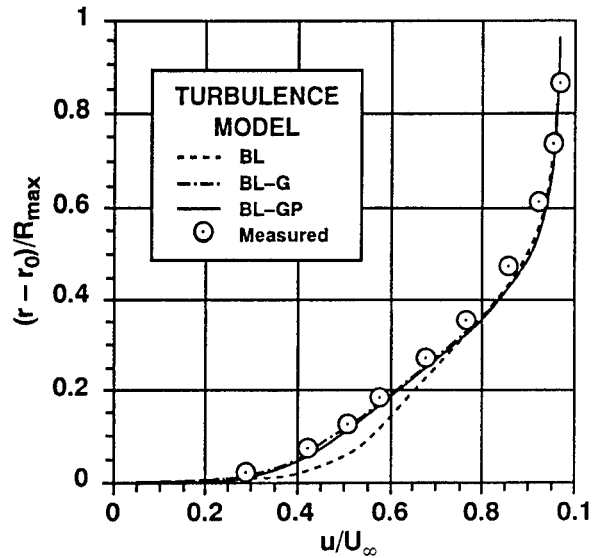
b). DTNSRDC Axisymmetric Body 1
X/L = 0.964, R_L = 6.6 x 10^6

c). DTNSRDC Axisymmetric Body 2
X/L = 0.977, R_L = 6.8 x 10^6
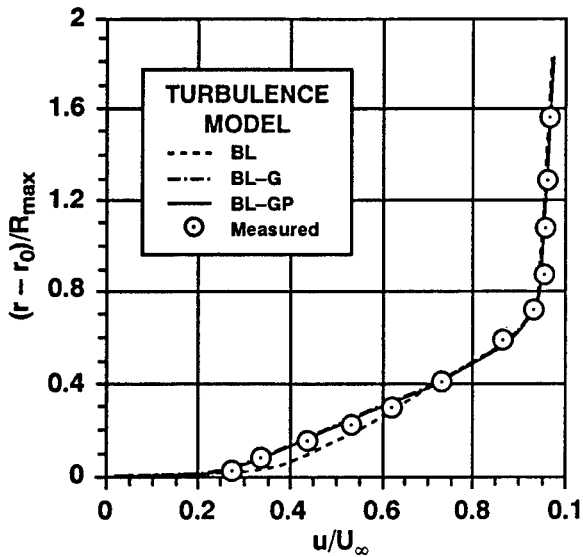
d). DTNSRDC Axisymmetric Body 5
X/L = 0.987, R_L = 9.3 x 10^6
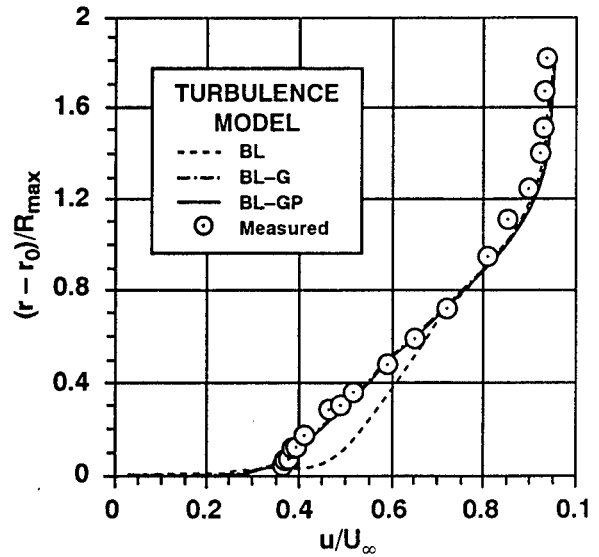
FIGURE 3. THE EFFECT OF TURBULENCE MODEL ON THE COMPUTED
AXIAL VELOCITY PROFILES
Grid 112x32x64, Measurement Uncertainty of $\dfrac{u}{U_\infty}$: ±0.025

397

a). Suboff Axisymmetric Body
X/L = 0.978, R_L = 1.2 x 10^7
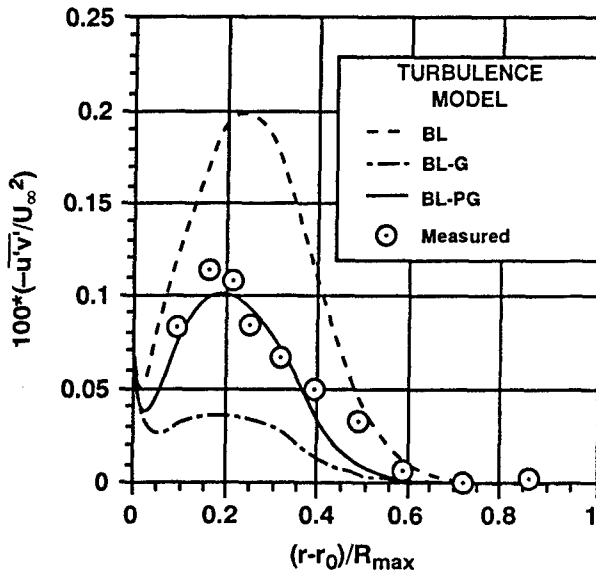
b). DTNSRDC Axisymmetric Body 1
X/L = 0.964, R_L = 6.6 x 10^6
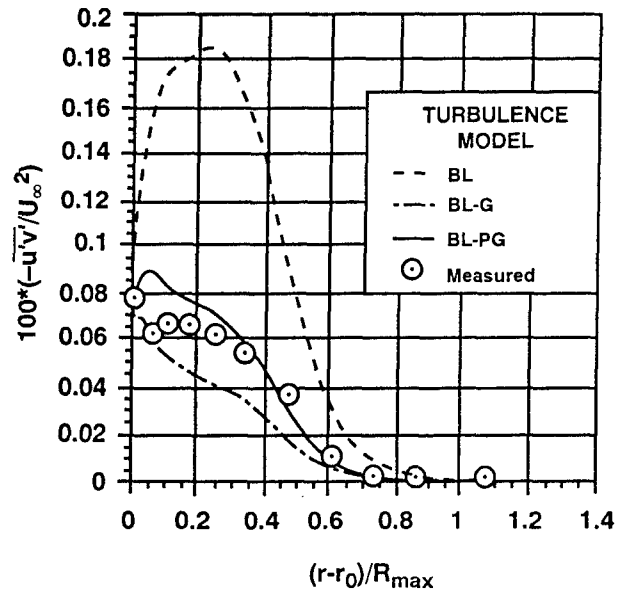
c). DTNSRDC Axisymmetric Body 2
X/L = 0.977, R_L = 6.8 x 10^6
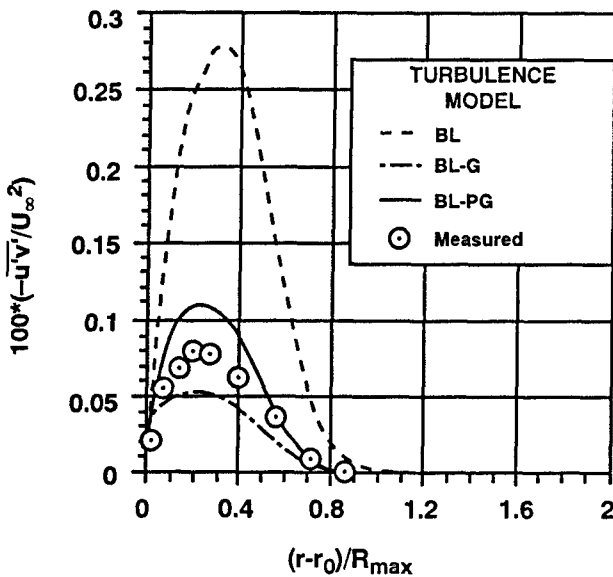
d). DTNSRDC Axisymmetric Body 5
X/L = 0.987, R_L = 9.3 x 10^6
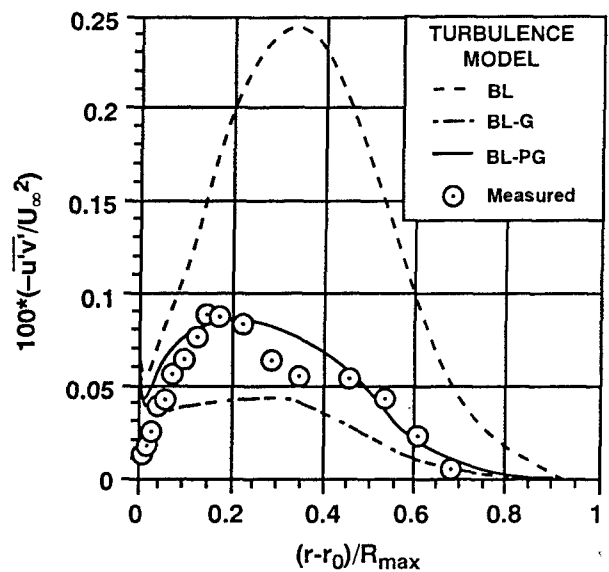
FIGURE 4. THE EFFECT OF TURBULENCE MODEL ON THE COMPUTED
SHEAR STRESS PROFILES

Grid 112x32x64, Measurement Uncertainty of 100 $\left(- \dfrac{\overline{u'v'}}{U_\infty^2}\right)$: ±0.01
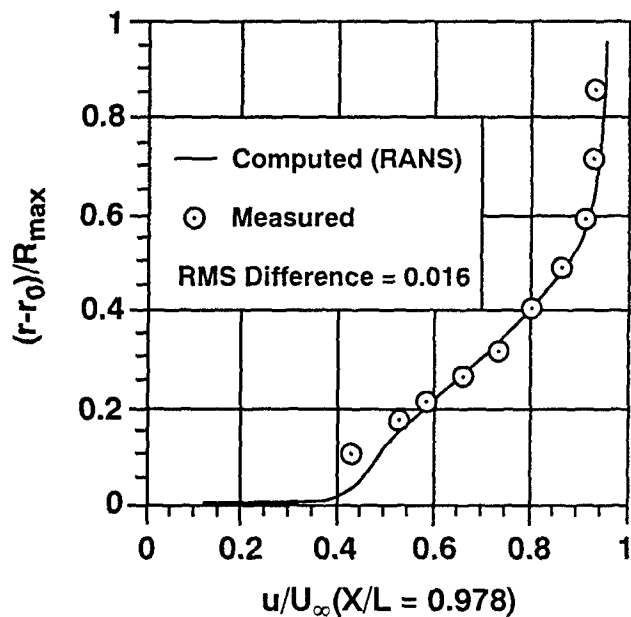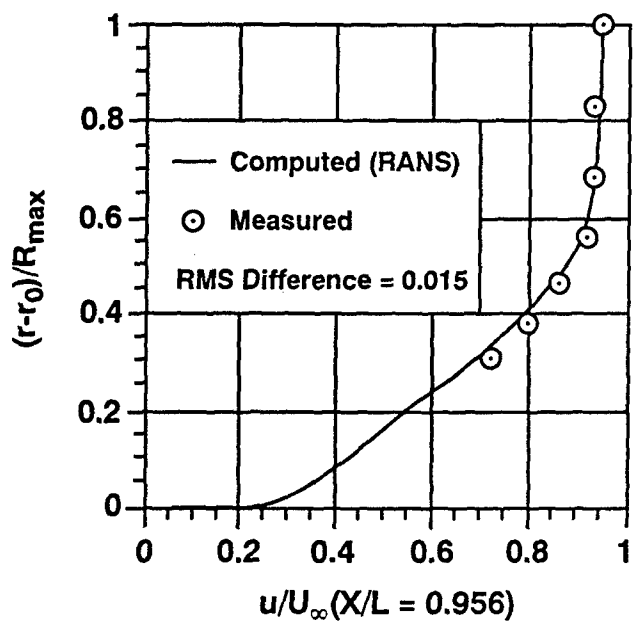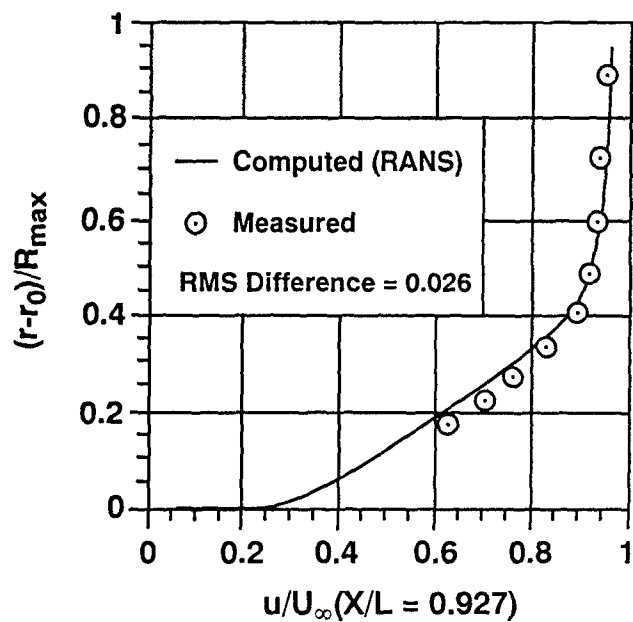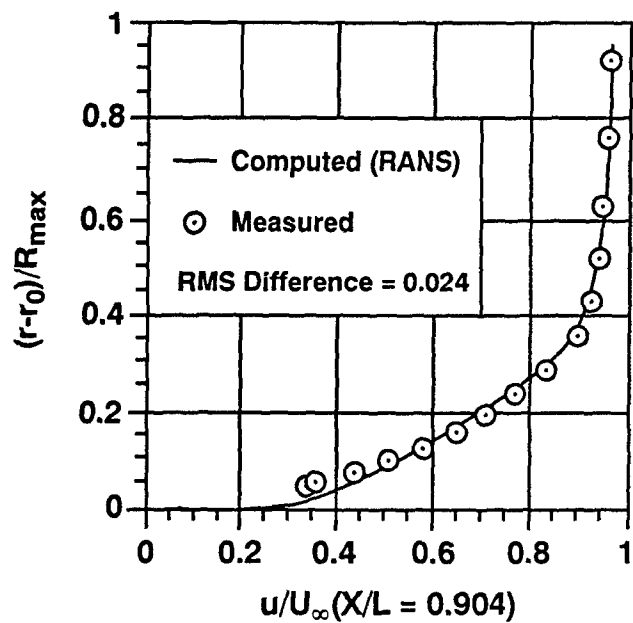
FIGURE 5. COMPARISON OF COMPUTED AND MEASURED
AXIAL VELOCITY PROFILES

Suboff Axisymmetric Body, R_L = 1.2 x 10^7, Grid 128x32x88

Turbulence Model: BL-GP, Measurement Uncertainty of u/U_∞ : ± 0.025
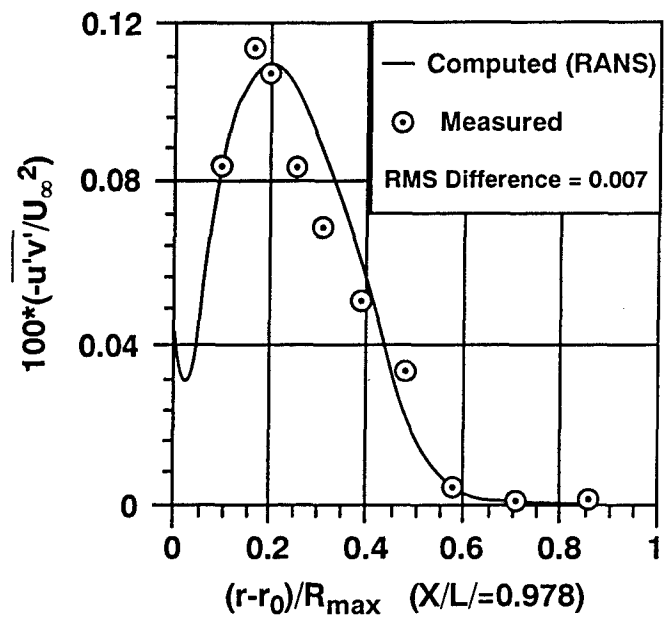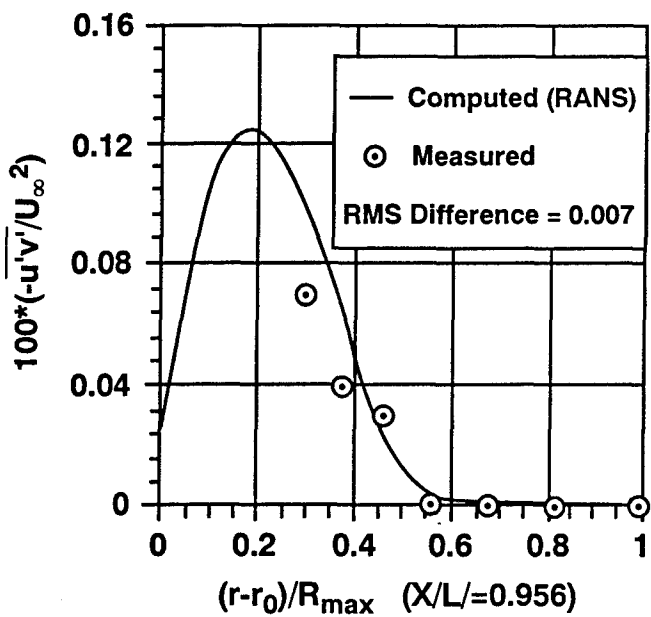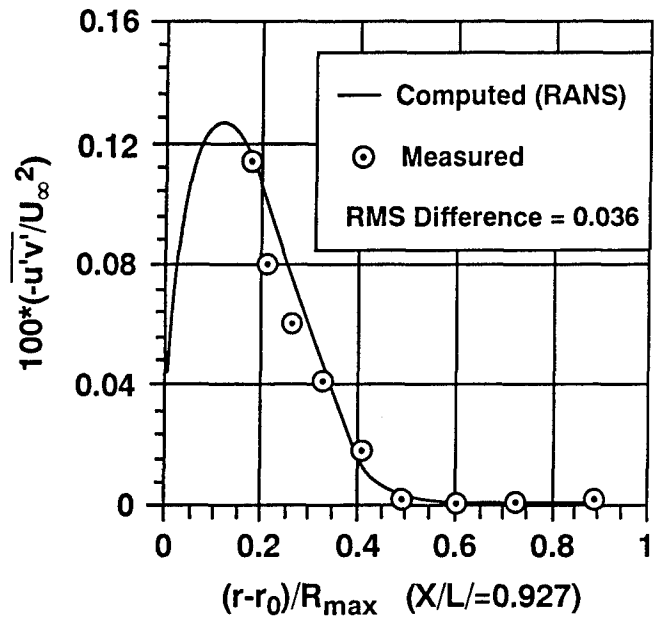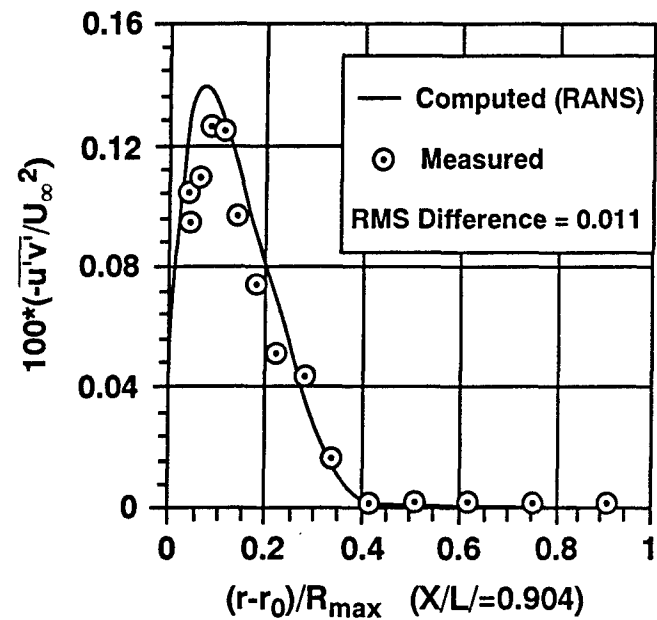
FIGURE 6. COMPARISON OF COMPUTED AND MEASURED
TURBULENT SHEAR STRESS PROFILES

Suboff Axisymmetric Body, R_L = 1.2 x 10^7, Grid 128x32x88

Turbulence Model: BL-GP, Measurement Uncertainty of $100(-\overline{u'v'})/U_\infty^2$: ± 0.01
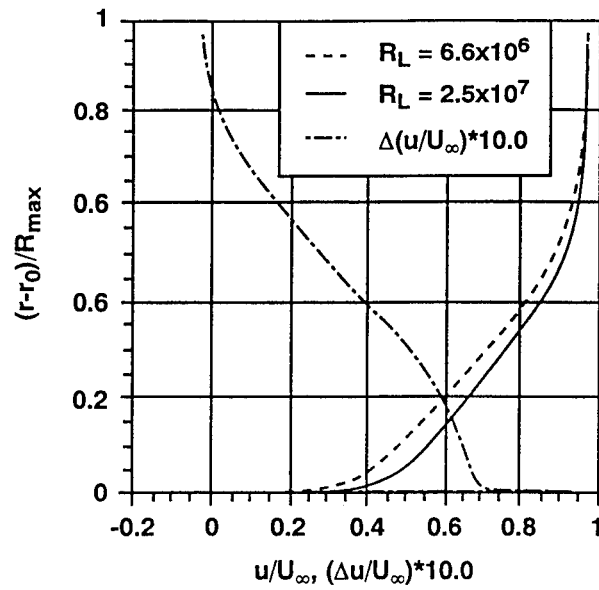
FIGURE 7. COMPUTED AXIAL VELOCITY PROFILE

AT X/L = 0.978, DTNSRDC AXISYMMETRIC BODY 1

R_L= 6.6x10⁶ and 2.5x10⁷

Measurement Uncertainty of u/U∞ = ± 0.025
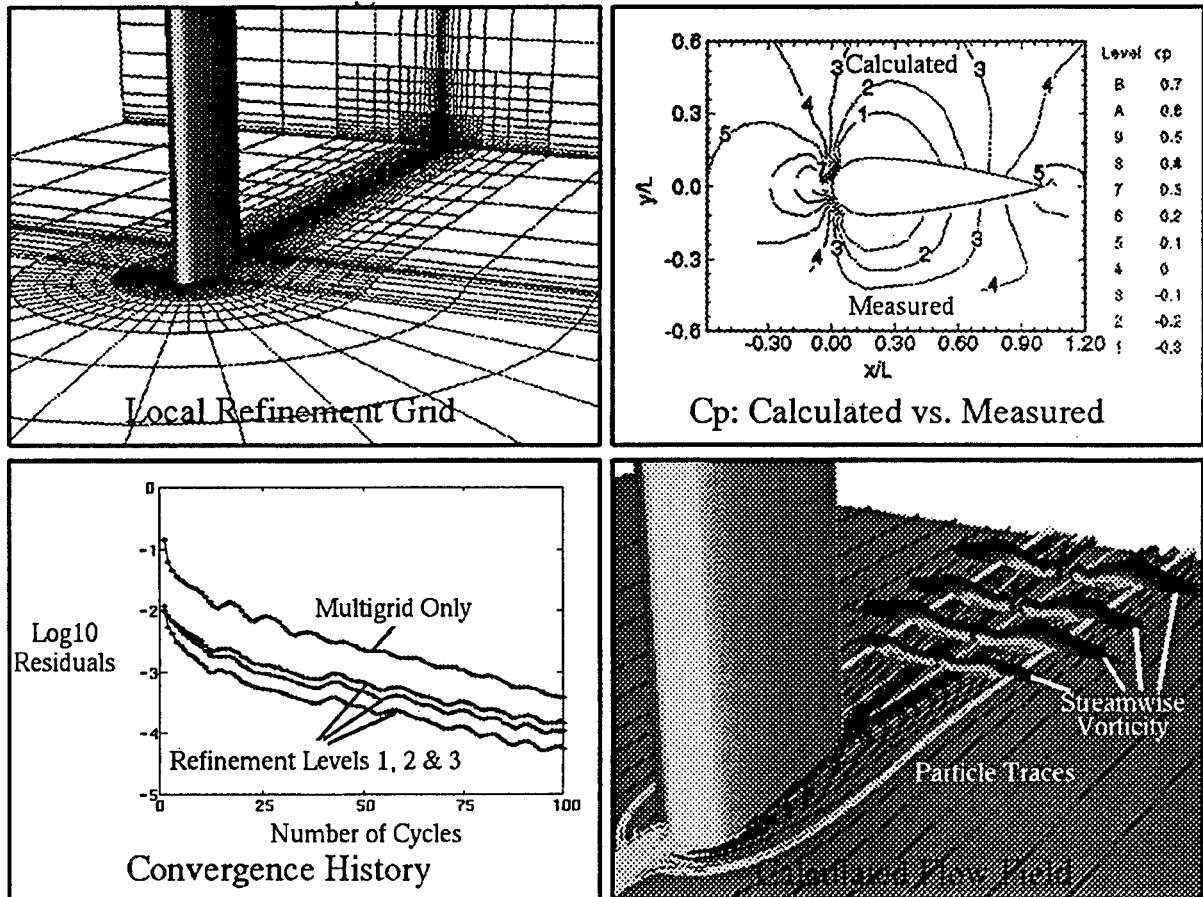
FIGURE 8. MULTIBLOCK MULTIGRID LOCAL REFINEMENT RANS SOLUTION OF A APPENDAGE/FLAT PLATE JUNCTURE FLOW AT R_c=6.2x10⁵, GRID: 96x48x48

401
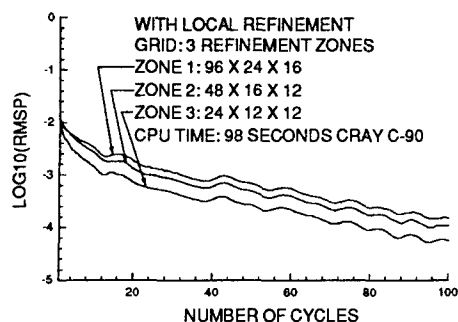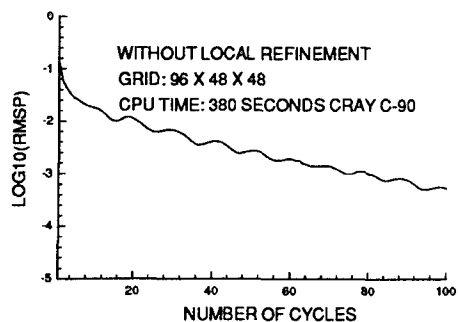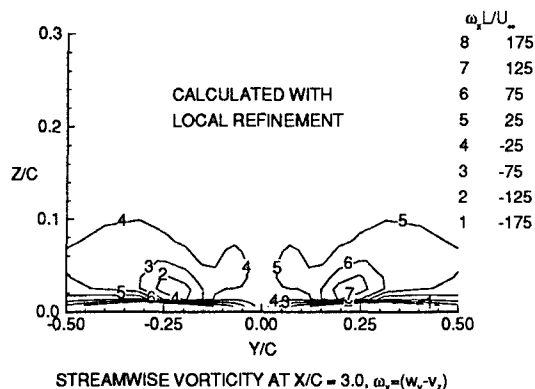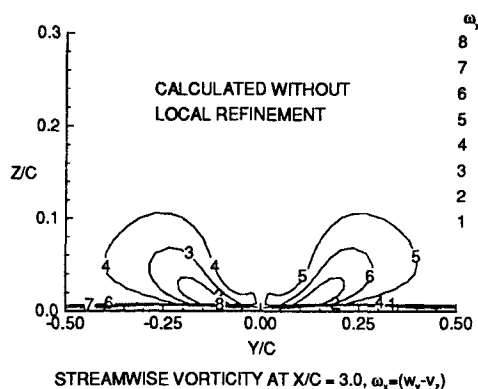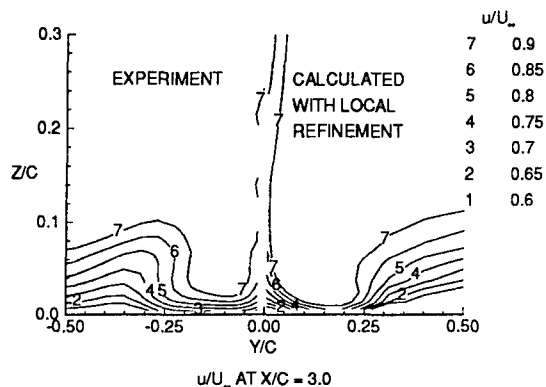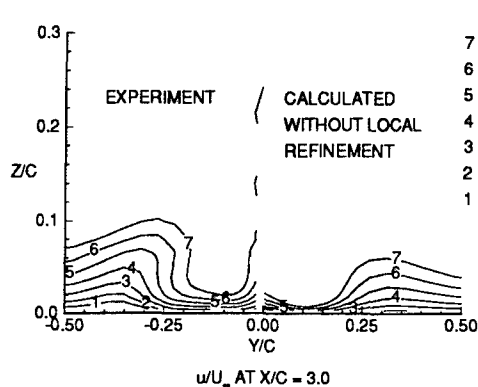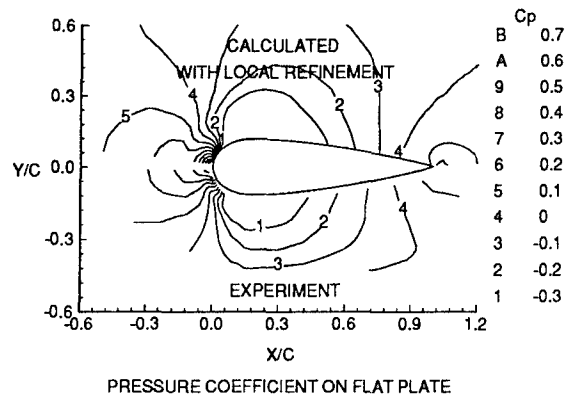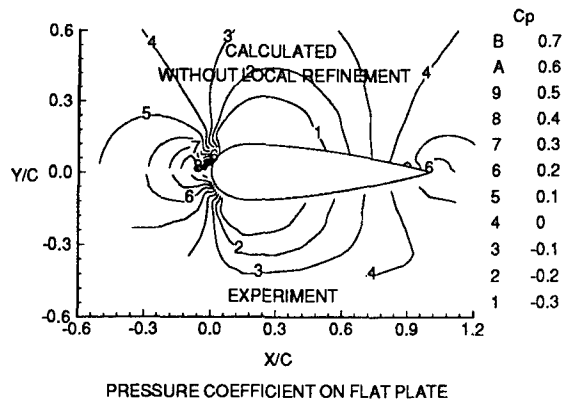
FIGURE 9. COMPARISON OF EXPERIMENT AND MULTIGRID RANS
SOLUTIONS WITH AND WITHOUT LOCAL REFINEMENT FOR APPENDAGE/
FLAT PLATE JUNCTURE FLOWS, R_c=6.2X10^5, U_∞=32m/s, L=0.3045m.

402

a) Suboff Axisymmetric Body, $R_L = 1.2 \times 10^7$

	u/U_∞				$-100\ \overline{u'v'}/U_\infty^2$				C_p	$C_\tau \times 10^4$	$C_f \times 10^3$	y^+ave
Measurement Uncertainty	± 0.025				± 0.01				± 0.015	± 2.0		
X/L	0.904	0.927	0.956	0.978	0.904	0.927	0.956	0.978				
No. of Points	19	14	12	16	19	14	12	16	21	17		
t	2.093	2.145	2.179	2.120	2.093	2.145	2.179	2.120	2.080	2.110		
BL	0.050	0.013	0.007	0.049	0.089	0.111	0.131	0.116	0.023	3.0	2.778	7.658
BL-G	0.032	0.015	0.006	0.024	0.054	0.057	0.035	0.076	0.020	2.6	2.772	7.570
BL-PG	0.032	0.010	0.005	0.030	0.011	0.006	0.007	0.008	0.019	2.5	2.766	7.265

C_F (ITTC) : 2.907×10^{-3}

b) DTNSRDC Axisymmetric Body 1, $R_L = 6.6 \times 10^6$

	u/U_∞				$-100\ \overline{u'v'}/U_\infty^2$				C_p	$C_\tau \times 10^4$	$C_f \times 10^3$	y^+ave
Measurement Uncertainty	± 0.025				± 0.01				± 0.015	± 2.0		
X/L	0.755	0.934	0.964	0.978	0.755	0.934	0.964					
No. of Points	15	14	16	35	12	9	11		11	9		
t	2.131	2.145	2.120	2.000	2.179	2.262	2.201		2.201	2.262		
BL	0.021	0.017	0.043	0.039	0.018	0.062	0.077		0.009	0.9	2.936	7.93
BL-G	0.021	0.011	0.028	0.014	0.019	0.021	0.019		0.010	1.2	2.919	7.78
BL-PG	0.021	0.006	0.020	0.010	0.023	0.009	0.010		0.012	1.0	2.879	7.78

C_F (ITTC) : 3.229×10^{-3}

c) DTNSRDC Axisymmetric Body 2, $R_L = 6.8 \times 10^6$

	u/U_∞				$-100\ \overline{u'v'}/U_\infty^2$				C_p	$C_\tau \times 10^4$	$C_f \times 10^3$	y^+ave
Measurement Uncertainty	± 0.025				± 0.01				± 0.015	± 2.0		
X/L	0.840	0.934	0.970	0.977	0.840	0.934	0.970	0.977				
No. of Points	11	17	14	13	6	14	10	9	12	11		
t	2.201	2.110	2.145	2.160	2.306	2.145	2.228	2.262	2.179	2.110		
BL	0.025	0.028	0.064	0.033	0.022	0.064	0.113	0.115	0.017	2.1	3.217	5.50
BL-G	0.014	0.042	0.026	0.018	0.016	0.008	0.019	0.017	0.020	2.0	3.211	5.51
BL-GP	0.025	0.027	0.037	0.019	0.026	0.014	0.016	0.019	0.015	1.5	3.157	5.35

C_F (ITTC) : 3.212×10^{-3}

d) DTNSRDC Axisymmetric Body 5, $R_L = 9.3 \times 10^6$

	u/U_∞				$-100\ \overline{u'v'}/U_\infty^2$				C_p	$C_\tau \times 10^4$	$C_f \times 10^3$	y^+ave
Measurement Uncertainty	± 0.025				± 0.01				± 0.015	± 2.0		
X/L	0.704	0.831	0.951	0.987	0.704	0.831	0.951	0.987				
No. of Points	21	18	26	27	21	9	13	17	15	14		
t	2.080	2.101	2.056	2.052	2.080	2.262	2.160	2.110	2.131	2.145		
BL	0.019	0.016	0.061	0.058	0.008	0.009	0.160	0.094	0.025	3.76	2.993	5.98
BL-G	0.018	0.016	0.025	0.013	0.008	0.010	0.024	0.026	0.023	2.75	2.978	5.89
BL-GP	0.019	0.015	0.023	0.015	0.008	0.007	0.027	0.018	0.019	2.23	2.926	5.87

C_F (ITTC) : 3.038×10^{-3}

TABLE 1. EFFECT OF TURBULENCE MODELS ON THE RMS DIFFERENCES BETWEEN MEASURED AND COMPUTED FLOW VARIABLES
Grid 112x32x64

Sample Computation 1. 3-Level Local Refinement to Obtain Resolution of 96x48x48 Grid, $y_1^+=8.4$

MULTIGRID	GRID CELLS	MEMORY (MW)	CPU(SEC)/ 100 CYCLES	% SAVING MW	RED. IN CPU TIME
Without Local Refinement	221,184	11.5	430	—	—
With Local Refinement	49,536	3.4	99	70%	4.3

Sample Computation 2. 4-Level Local Refinement to Obtain Resolution of 192x96x96 Grid, $y_1^+=3.7$

MULTIGRID	GRID CELLS	MEMORY (MW)	CPU(SEC)/ 100 CYCLES	% SAVING MW	RED. IN CPU TIME
Without Local Refinement	1,769,472	80.0	3600	—	—
With Local Refinement	71,808	6.16	191	92%	19

TABLE 2. MULTIBLOCK MULTIGRID LOCAL REFINEMENT COMPUTATION OF TURBULENT APPENDAGE/FLAT PLATE JUNCTURE FLOW ON CRAY C90 COMPUTER, $R_C=6.2 \times 10^5$

by Professor V. C. Patel, University of Iowa

I have some questions that could be addressed also to authors of some previous papers in which the Baldwin-Lomax model is used with the first grid point at y^+ around 7 to 10. The questions are:

"Are these the maximum or minimum, or just average values? How do you determine C_f, the friction coefficient? Do you simply use the slope at the wall? Do you make a correction for the pressure gradients, both longitudinal and transverse? If not, how accurate are C_f and related quantities?"

Author's Reply

In our paper the value of y_1^+ at the first grid point around 7 to 10 is meant to say that the maximum value of y_1^+ is 10 and the arithmetic mean value is 7. When one value of y_1^+ is given that is the arithmetic mean value of y_1^+ for all the grid cells on the body.

The local skin-friction coefficient C_f is calculated by

$$C_f = \frac{2\tau}{\rho U_\infty^2} = \frac{2\upsilon}{U_\infty^2}(\frac{\partial u}{\partial y})y = 0$$

where the value of $(\frac{\partial u}{\partial y})y = 0$ is computed at the cell center of the first grid from the wall when the value of y_1+ is less than 7. It is noted that the exact value $(\frac{\partial u}{\partial y})y = 0$ at the wall must be used when the value of y_1^+ is larger than 7, and can be obtained by extrapolating from the velocities parallel to the wall $u(y_1)$ and $u(y_2)$ of the first second grid centers at distances y_1 and y_2 normal to the wall,

$$(\frac{\partial u}{\partial y})y0 = \frac{y_2[u(y_1)-u(y_0)]}{y_1(y_2 - y_1)} - \frac{y_1[u(y_2)-u(y_0)]}{y_2(y_2 - y_1)}$$

where $u(y_0)$ is set equal to 0 at the smooth wall y_0 without drag reduction.

No correction for the pressure gradients was made in computing C_f, but the effect due to the streamwise pressure gradient is added to the

Baldwin-Lomax model. The total skin-friction was integrated from the local skin-friction. The accuracy of the computed local and total skin-friction coefficients is shown in Table 1.

SESSION 8

VISCOUS FLOW: APPLICATIONS 1

A Viscous Flow Simulation of Flow About the 1/40-Scale Model of the U.S. Airship Akron at Incidence Angle

C.-I. Yang (David Taylor Model Basin, USA)

ABSTRACT

A three-dimensional incompressible Navier-Stokes code based on an artifical compressibility, implicit-upwind-relaxation, flux-splitting algorithm is employed to simulate the flow about a 1/40-scale model of the U.S. airship "Akron" at several incidence angles. The distributions of transverse forces along the hull and the integrated moments about the center of buoyancy are computed and comparisons with the measurements are made.

INTRODUCTION

Purely for mathematical interest, the inviscid flow about a body of revolution has long since been formulated and studied in detail. Practically, because of the predominant viscous effect near the boundary, the related flow pattern is much more complicated. especially if the body is at an incidence with respect to the flow direction. The wake of the body becomes turbulent, and various types of cross flow separation take place. The basic hull form of a modern submersible is typically a body of revolution. While maneuvering at high speed, the hull may be subject to severe hydrodynamic forces. Under certain conditions, the moment of the forces about the center of buoyancy of the body may cause instability. In order to achieve a higher envelope of maneuverability and controllability, the designers of the modern submersible have practical interest in predicting the hydrodynamic response for any given planned movement. Such interest can best be served by parallel efforts in enlarging the data base from controlled laboratory environments and developing accurate computational schemes.

Extensive experiments were carried out by various research parties, some of the representive results were reported in references (1-3). More recently, computational efforts based on newly developed numerical schemes derived from the Reynolds Averaged Navier-Stokes (RANS) formulation offer encouraging predictions (4-8).

This report present a study of the accuracy and feasibility of predicting forces and moment on a body of revolution hull form at incidence with a RANS technique. The data obtained from wind tunnel tests of a 1/40-scale model of the U.S. airship "Akron" are used for the purpose of comparison.

DESCRIPTON OF EXPERIMENT

A series of tests was made on a 1/40-scale model of the U.S. Airship "Akron" at the propeller research wind tunnel, Langley Memorial Aeronautical Laboratory (currently, NASA Langley Research Center) in 1932 (9-11). The purpose of the test was to determine the drag, lift, and pitching moments of the bare hull and the hull equipped with fins.

This particular experiment is attractive to us in some aspects: (1) the hull form is very similar to the modern high performance submersible, (2) the Reynolds number is relatively high due to·the large size of the model, and (3) the data are relevent to our study; included are the distributions of the transverse forces along the hull and the moments of the forces about the center of buoyancy.

The model is of hollow wooden construction having 36 sides over the fore part of the hull, fairing into 24 sides near the stern. The length of the hull is 5.98 m.(19.62 ft.), the maximun diameter 1.01 m. (3.32 ft), the fineness ratio 5.9, the

volume $3.27 m^3$ ($115.61 ft^3$). Four hundred pressure orifices, distributed among 26 stations, were placed along one side of the hull. The orifices were connected inside the hull to two photographic-recording multiple manometers. Each manometer consisted of 200 glass tubes placed about the periphery of a drum, a long incandescent light bulb for making the exposures was placed at the center of the drum.

Tests were conducted at several different wind speeds. The maximun speed was 44.70 m/s (100 miles per hour). The corresponding Reynolds number is about 17 million based on the length of the hull. This value is about 1/34 of the full scale ship at a speed of 37.54 m/s (84 miles per hour). The transition from laminar to turbulent flow occured at a local Reynolds number of 814000 based on the axial distance between the nose and the transition point (10). At a wind speed of 44.70 m/s (100 miles per hour), the transition point is about 0.25 m.(10 inches) from nose.

The maximum departure of the observed wind tunnel velocity from a mean value was about ± 0.6 percent. The deflection of the support wire, that is the downstream movement of the model, observed at the maximum velocity of the tunnel with the hull at $0°$ pitch was approximately 1.5×10^{-3} m. (0.06 inch). The sources of error and the precision of measurements are discussed in detail in references 9-11.

NUMERICAL APPROXIMATION

The three-dimensional incompressible RANS equations based on primitive variables are formulated in a boundary-fitted curvilinear coordinate system and solved with an artifical compressibility concept (12). The basic operations of converting the set of differential equations to a system of difference equations may be divided into: spatial differencing and time differencing. The procedure can be described as follows.

Spatial Differencing

The three-dimensional differential operator is first split into three independent one-dimensional operators. The spatial differencing of the inviscid flux in each of these one-dimensional operators is then constructed by an upwind flux-differencing scheme based on Roe's approximate Riemann solver approach (13). In each computational cell the differential operator is linearized around an average state such that the flux difference between two adjacent cells satisfies certain conservative properties. As a result, the flux

at an interface can be expressed in terms of the direction of the travelling waves. Harten's high-resolution total variation dimishing (TVD) technique (14,15) is then applied to enhance the accuracy of the solution to a higher order in the region where its variation is relatively smooth. The undesirable spurious numerical ocillations associated with high order approximations are suppressed by appling a TVD limiter. The viscous flux is centrally differenced with second-order accuracy. The overall discretization is obtained by summing up all the independent discretizations of the flux derivatives in each dimension.

Time Differencing

Since only the steady-state solutions are of interest, a first-order accurate Euler-implicit time differencing scheme is used. The application of the scheme avoids a overly restrictive time-step size when highly refined grids are used to resolve viscous effects. In addition, a spatially variable time step is used to accelerate convergence.

The governing differential equations are then reduced to a system of difference equations in "delta form". In each time step, the corrections to the variables, instead of the variables themselves, are solved. The right hand side of the system is defined as residual. It is the explicit part of the system and has four components, one for each variable. As the solutions advance to their steady-state values through time stepping, the corrections and residuals approach zero.

The system is solved iteratively with a hybrid technique which uses approximate factorization in cross planes in combination with a planar Gauss-seidel relaxation in the third direction. The process is highly vectorizable. Presently, the L_2 norm of the residual is used as a measurement of convergence of the iteration process.

As a result of upwind-differencing, the coefficient matrix of the system becomes diagonal dominant. In addition, the necessity of adding and tuning of a numerical dissipation term for stability reasons, as in some schemes with central differencing, is alleviated.

BOUNDARY CONDITION

The computational domain defined by a C-O grid extends from two body lengths upstream of the nose to two body lengths downstream of the tail in the longitudinal direction, and two body lengths from the body axis in the radial direction. On the body surface, the no-slip condition

is imposed and the normal gradient of the pressure is assumed to vanish. Free stream conditions are specified along the outer boundaries except for the outflow boundary, where the values are computed by using extrapolation. Since the flow field is symmetric with respect to the longitudinal plane of symmetry, only the flow field over half of the body is computed. Reflective conditions are then applied on the plane of symmetry. The values of the characteristic variables along the wake line are obtained by first extrapolating from interior points along each radial grid line and then taking the circumferential average. The normal distance between the body surface and the nearest grid line is 1.0×10^{-5} of the body length; the corresponding y^+ is about 4. Computations are first performed on a grid with a $79 \times 81 \times 83$ distribution in radial, circumferential and streamwise directions respectively. To determine the effect of gridding on the prediction of lift and cross flow separation, a grid with $79 \times 111 \times 83$ distribution is used for a repeat computation. In both cases the circumferential spacing of radial lines is uniformly distributed, The angles between adjacent radial lines are $2.22°$ and $1.62°$ respectively.

TURBULENCE MODEL

The algebraic Balwin-Lomax turbulence model was used by Degani and Schiff (16) in computing the turbulent flows around axisymmetric bodies with crossflow separation. In order to predict multiple secondary crossflow separations at high incidence angle, modification was made such that the turbulence length scale of the outer region is determined by the viscous vorticity imbedded in the boundary layer and not the inviscid vorticity shed from the separation line. The modified model has been successfully used in several occasions to compute the turbulent flows over bodies of revolution at an incidence angle (7,16,17). The details of the modification, implementation and the physical justication can be found in Reference 16.

The behavior of the turbulent boundary layer near the stern region of an axisymmetric body has been studied extensively by Huang et al. (19). It was found that as the boundary layer thickens rapidly over the stern region, the turbulence intensity is reduced and becomes more uniformly distributed. The measured mixing length of the thick axisymmetric stern boundary layer was found to be proportional to the square root of the area of the turbulent annulus between the body surface and the edge of the boundary layer.

This simple similarity hypothesis for the mixing length improved the prediction of the mean velocity distribution in the entire stern boundary layer.

Based on the above observation and results indicated in Reference 7, it is decided that algebraic Baldwin-Lomax turbulance model with Degani-Schiff's correction and Huang's modification is appropriate for present simulation.

RESULTS

The experimental data reported in References 9,11 are massive and extensive. Our present interests are limited to the distributions of transverse forces along the bare hull and the pitching moments about the center of buoyancy of the hull at several given incidence angles. The data were presented in terms of the dynamic pressure (denoted by q) of the air stream and were corrected for the difference between the local static pressure in the stream and the reference pressure. The correction consisted simply of substracting from the pressure at any section of the model the static pressure of the air stream, measured in the absence of the model, at the corresponding point along the axis of the model. The correction reduced the pressure at the stagnation point at the nose of the hull, with the model at $0°$ pitch, to a value equal to the dynamic pressure q. Here, the dynamic pressure q is defined as: $\frac{1}{2}\rho V_\infty{}^2$, where ρ is the density of the air and V_∞ is the air stream velocity. Tests were conducted with the air stream at several different dynamic pressures. The highest value was $1,225.73$ Pa $(25.6 lb/ft^2)$, the equivalent Reynolds number is about 17 millions based on body length. Based on this condition, the numerical simulations were carried out.

Predictions with the potential-based Munk and Upson equations of the transverse force at $15°$ of pitch were shown in Reference 11. Both predictions deviated substantially from the measurements near the stern region. The disagreements are not a surprise, since the distribution of force along the hull is strongly influenced by the surface flow separations. An engineering rational flow model based on a discrete vortex cloud method greatly enhanced the prediction (20). The improvement was attributed to a separation line model that defines the body vortex feeding sheets along the body surface. Flow visualizaton indicated that the separation patterns along a smooth surface can be quite complicated. Any further improvement in prediction at current stage may require a turbulent viscous flow approach. The

411

present numerical simulation assesses the feasibility and accuracy of RANS's predictions.

The profile and wire-framed perspective view of the hull are shown in Figure 1. Pressure distributions along the hull at 0° of pitch are shown in Figure 2, where the pressure is normalized with the dynamic pressure q and the distance from the nose is normalized with the hull length L. The experimental values were obtained from averaging the circumferential measurements at each of the axial locations where the pressure orifices were placed. The viscous flow solution was obtained from a computation on a $79 \times 81 \times 83$ grid. At the mid-section of the hull, there are 28 grid points located inside the boundary layer. The CFL number used in the computation is 10. The L_2 norm of the residual and the lift coefficient during the course of the iteration are shown in Figure 3. The lift force is nomalized with $q(vol)^{2/3}$, where vol is the volume of the hull. The potential flow solution was obtained from a surface panel method VSAERO (21). At zero incidence, experimental data indicate that there exist a small amount of sectional transverse force along the hull at the bow and after portions of the hull. It was assumed that the air flow was not strictly axial or that the model was not exactly symmetrical.

The transverse forces along the hull at several incidence angles are shown in Figure 4. Notice that the integration of the areas underneath the curves gives the total normal forces acting on the hull. The experiment data are obtained from Table V in Reference 11. The computational results are obtained from solutions based on two grids with different densities in circumferential direction. At a given incidence, the difference between the two computational results is insignificant. Noticeable differences between experimental and computational results can be found in the stern region. The predicted and measured total transverse forces on the hull, normalized with $q(vol)^{2/3}$, are shown in Figure 5 and the values are given in Table 1. The discrepancy is more perceptible at higher incidence. It was reported (11), that at high-speed, high-pitch-angle condition, the model was observed to be quite unsteady.

The axial location of the center of bouyancy of the hull is 2.77 m. (9.10 ft.) from the nose. The pitching moment about the center has two parts: (1) moment (M_1) of the transverse force and (2) moment (M_2) of the longitudinal force. The experiment value M_1 was obtained by tak-

ing the moment of the area of the transverse force curves in figure 4 about the center of buoyancy by means of a mechanical integrator. To obtain M_2, curves with transverse force at each axial location plotted against the corresponding cross-sectional area, were constructed. M_2 values were then obtained by integrating the areas under the curves. The contribution of the longitudinal forces to the total moment is about 4%, and it is opposite in direction to that due to the transverse force. Lift and moment coefficients are shown in Figure 6. The Lift is normalized with $q(vol)^{2/3}$, and the moment is normalized with $q(vol)$. The values are tabulated in Tables 2 and 3 respectively. The computed values of M_1 and M_2 are listed in parenthesis.

In general, the measurements and the predictions are in good agreement, Noticeable differences occur only at higher incidence.

Computations have been carried out both on CRAY-YMP and CONVEX-3080 machines. Estimated CPU times are about 40μ sec per grid per iteration on CRAY-YMP and 200μ sec per grid per iteration on CONVEX-3080 in the vector mode.

CONCLUSIONS

Numerical simulations of flow about a 1/40-scale model of U.S. Airship "Akron" were carried out with RANS formulation. The effort is an attempt to predict the hydrodynamic force acting upon a body of revolution type hull form at incidence. Good and encouraging results are obtained. Further enhencement in accuracy and computational efficiency requires a improved turbulence model and a multigrid type approach. Data bases obtained with modern techniques under controlled environments are needed for validation of numerical schemes.

ACKNOWLEDGEMENT

REFERENCES

1. Ramaprian, B.R., Patel, V.C., and Choi, D.H.,"Mean-flow Measurements in the Three-dimensional Boundary Layer over a

Body of Revolution at Incidence," Journal of FluidMechanics, Vol.103, 1981, pp.479-504.

2. Intermann, G.A., "Experimental Investigation of the location and Mechanism of Local Flow Separation on a 3-Caliber Tangent Ogive Cylinder at Moderate Angles of Attack," M.S. Thesis, Universith of Florida, Gainesville, FL. 1986

3. Kim, S.E., and Patel, V.C., "Separation on a Spheroid at Incidence: Turbulent Flow," The Second Osaka International Colloquium on Viscous Fluid Dynamics in Ship and Ocean Technology, September 27-30, 1991,Osaka.

4. Vatsa, V.N., Thomas, J.L., and Wedan, B.W., " Navier-Stokes Computations of Prolate at Angle of Attack," AIAA Journal, Vol. 26,NO.11. 1989, pp.986-993.

5. Degani. D., Schiff, L.B., and Levy, Y., "Numerical Prediction of Subsonic Turbulent Flow over Slender Bodies at High Incidence," AIAA Journal, Vol.29, No.12, 1991, pp.2054-2061.

6. Hartwich, P.M., and Hall, R.M.,"Navier-Stokes Solution for Vortical Flow over a Tangent-Ogive Cylinder,"AIAA Journal, Vol.28,No.7, 1990, pp.1171-1179.

7. Sung, C-H., Griffin, M.J., Tsai, J.F., and Huang, T.T., "Incompressible Flow Computation of Force and Moments on Bodies of Revolution at Incidence," AIAA-93-0787, 31st Aerospace Science Meeting and Exhibit, Jan. 11-14, 1993, Reno, NV.

8. Meir, H.V., and Cebeci, T., "Flow Characteristic of a body of Revolution at Incidence," 3rd Symposium on Numerical and Physical Aspects of Aerodynamic Flows, Long Beach, California, 1985

9. Freeman, H.B., "Force Measurement on a 1/40-Scale Model of the U.S. Airship "Akron"," T.R. No.432, NACA, 1932.

10. Freeman, H.B., "Measurements of Flow in the Biundary Layer of a 1/40-Scale Model of the U.S. Airship "Akron"," T.R. No.430, NACA, 1932.

11. Freeman, H.B.,"Pressure-Distribution Measurements on the Hull and Fins of a 1/40-Scale Model of the U.S. Airship "Akron"," T.R. no.443, NACA, 1933

12. Chorin, A.,"A Numerical Method for Solving Incompressible Viscous Flow Problems," Journal of Computational Physics, Vol.2, No.1, August, 1967, pp.12-26.

13. Roe, P.L.,"Approximate Riemann Solvers, Parameter Vectors, and Difference Schemes," Journal of Computational Physics, Vol.43, No.2, 1981, pp.357-372.

14. Harten, A., "High Resolution Scheme for Hyperbolic Conservation Laws," Journal of Computational Physics, Vol.49, No.3, 1983, pp.357-393.

15. Yee, H.C., Warming, R.F., and Harten, A.,"Implicit Total Variation Diminishing (TVD) Schemes for Steady-State Calculations," Journal of Computational Physics, No.57, 1985, pp.327-360.

16. Degani, D., and Schiff, L.B., "Computation of Turbulent Supersonic Flows around Pointed Bodies Having Crossflow Separation," Journal of Computational Physics, Vol.66, No.1, 1986, pp.173-196

17. Vatsa, V.N.,"viscous Flow Solutions for Slender Bodies of Revolution at Incidence," Computers Fluids, Vol.20, No.30, 1991, pp.313,320

18. Gee, K., Cummings, R.M., and Schiff, L.B.,"Turbulence Model Effects on Separated Flow about a Prolate Spheroid," AIAA Journal, Vol.30, No.3, 1992, pp.655-664

19. Huang, T.T., Santelli, N., and Bolt, G.,"Stern Boundary Layer Flow on Axisymmetric Bodies," 12th Symposium on Naval Hydrodynamics, Washington D.C., June 1978.

20. Mendenhall, M.R., and Perkins, S.,"Prediction of the Unsteady Hydrodynamic Characteristics of Submersible Vehicles," The Proceedings, 4th International onference on Numerical Ship Hydrodynamics, Washington D.C.,Sept. 24-27 1985.

21. Maskew, B., "Prediction of Subsonic Aerodynamic Characteristics - A Case for low-order Panel Methods," AIAA-81-0252, AIAA 19th Aerospace Sciences Meeting, January, 1981.
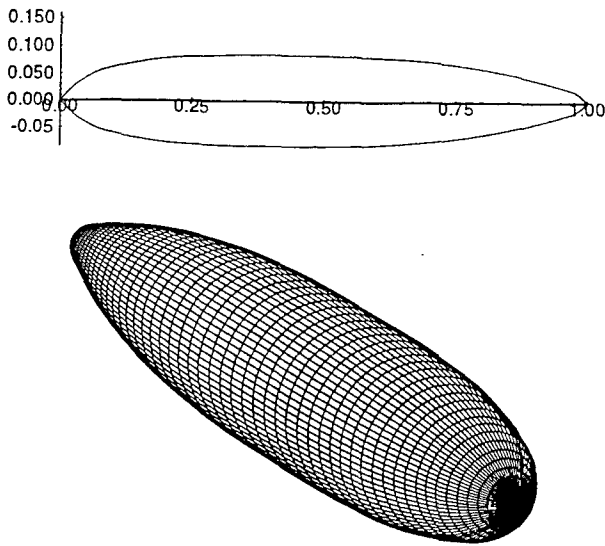
Figure 1. Profile and perspective
view of bare hull

(a) Navier-Stokes Solution

(b) Potential Flow Solution
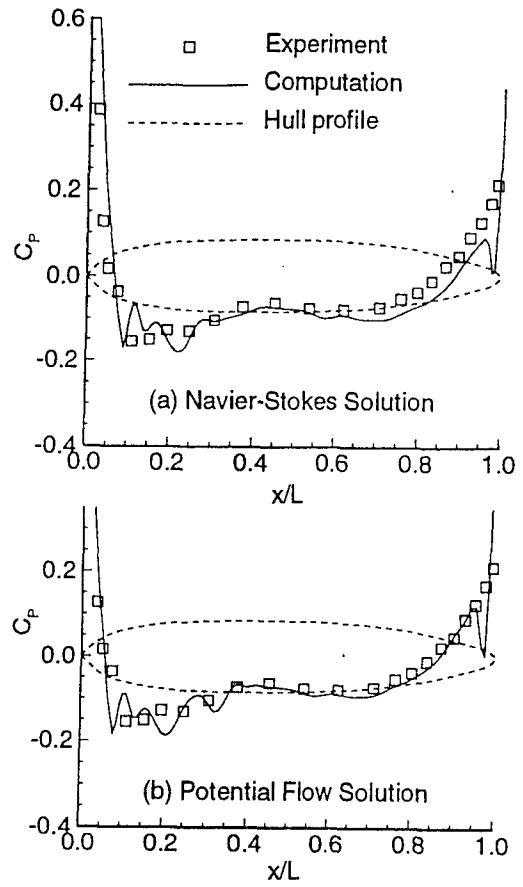
Figure 2. Pressure distribution
along hull at 0° pitch
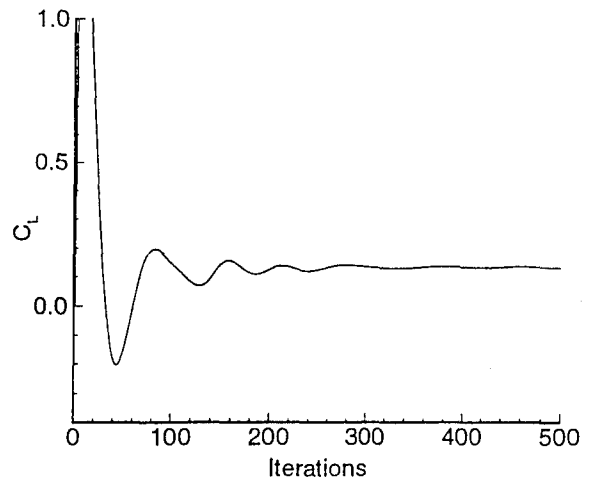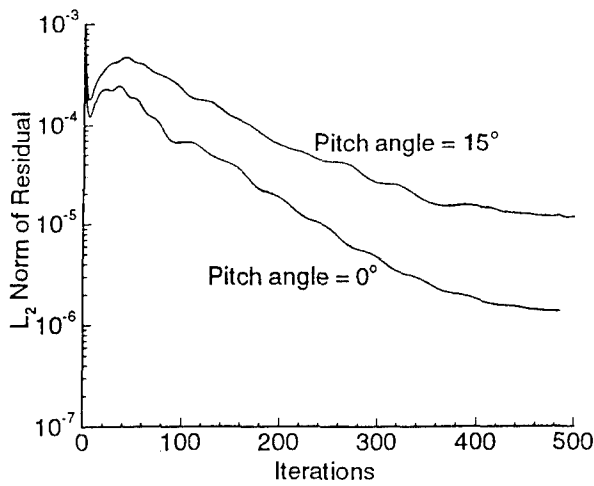
Figure 3. L_2 norm of residual and C_L at 15° pitch

414
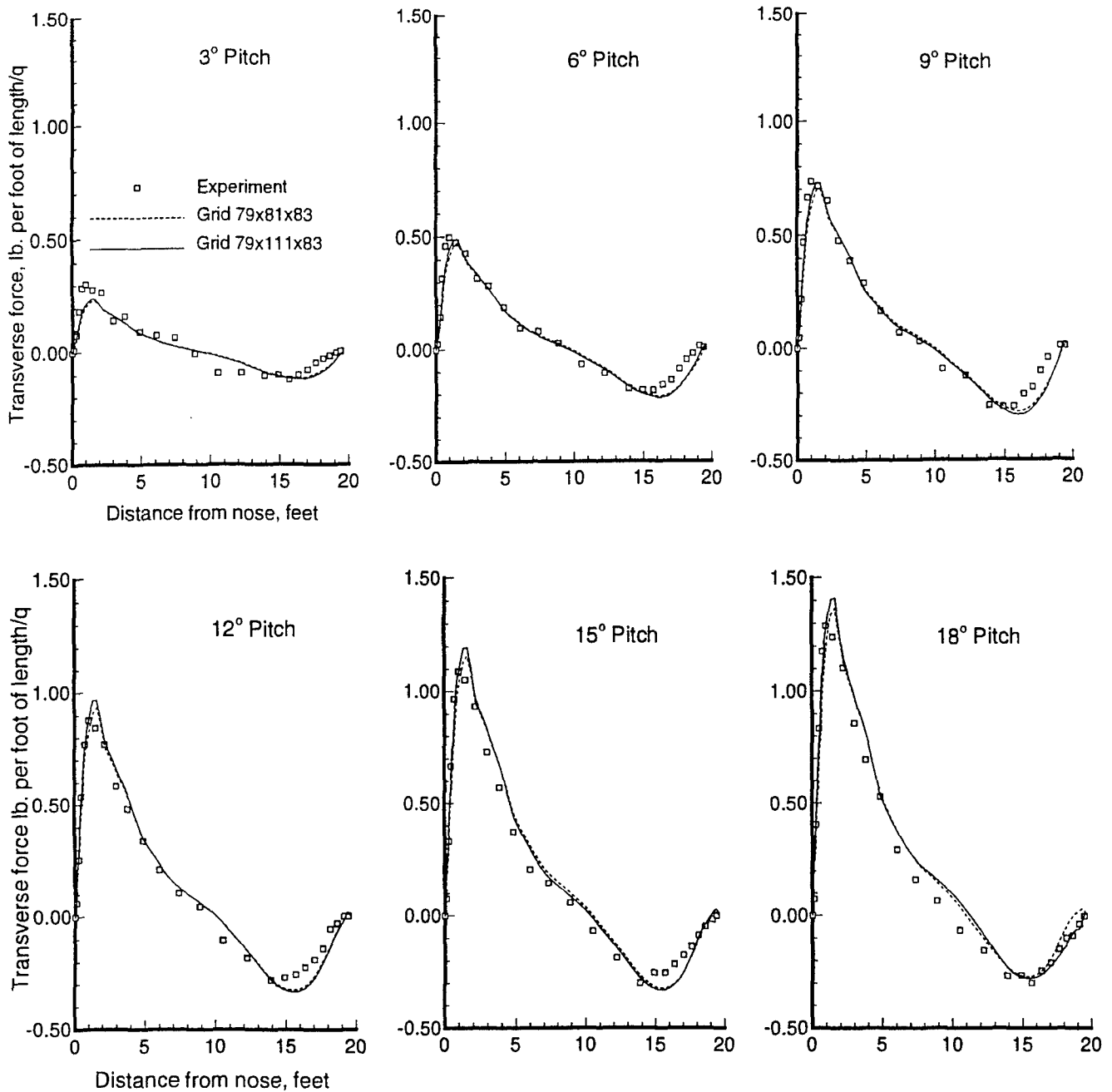
Figure 4. Transverse force along hull at incidences

415
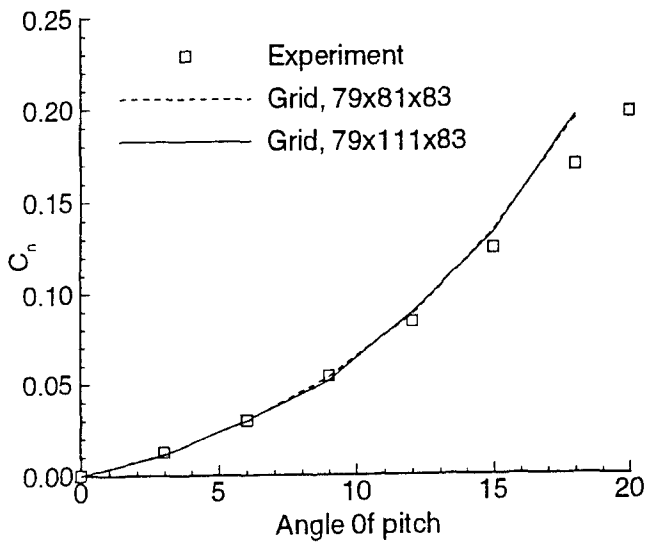
Figure 5. Transverse force coefficients

Table 1. Transverse Force Coefficients.

Incidence Angle (degrees)	Experiment	Computation	
		Grid # 1	Grid # 2
3	0.0127	0.0114	0.0110
6	0.0300	0.0294	0.0297
9	0.0541	0.0536	0.0515
12	0.0845	0.0883	0.0895
15	0.1246	0.1343	0.1330
18	0.1690	0.1939	0.1956

Grid # 1 : 79x81x83
Grid # 2 : 79x111x83

Table 2. Lift Coefficients.

Incidence Angle (degrees)	Experiment	Computation	
		Grid # 1	Grid # 2
3	0.011	0.011	0.011
6	0.029	0.028	0.027
9	0.054	0.051	0.047
12	0.080	0.083	0.081
15	0.115	0.125	0.121
18	0.155	0.178	0.173

Grid # 1 : 79x81x83
Grid # 2 : 79x111x83

Table 3. Pitching Moment Coefficients.

Incidence Angle (degrees)	Experiment	Computation	
		Grid # 1	Grid # 2
3	0.078	0.081 (0.084, -0.003)	0.081 (0.084, -0.003)
6	0.150	0.156 (0.162, -0.006)	0.153 (0.159, -0.006)
9	0.212	0.222 (0.230, -0.008)	0.222 (0.230, -0.008)
12	0.260	0.276 (0.286, -0.010)	0.271 (0.282, -0.010)
15	0.307	0.316 (0.327, -0.011)	0.310 (0.322, -0.012)
18	0.348	0.339 (0.352, -0.013)	0.347 (0.360, -0.015)

Grid # 1 : 79x81x83
Grid # 2 : 79x111x83
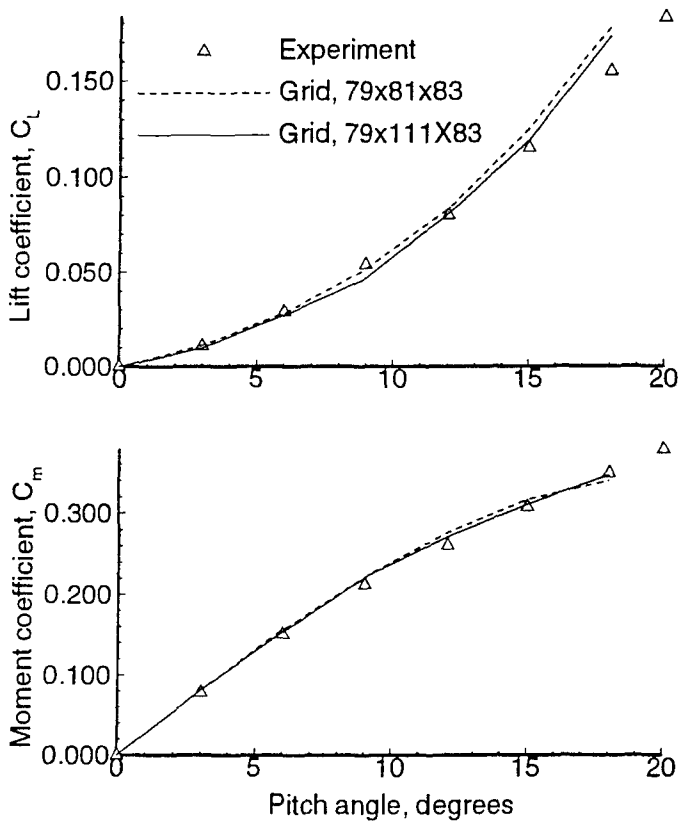
Figure 6. Lift and moment coefficients

416

The Prediction of Nominal Wake Using CFD

A.J. Musker, S.J. Watson, P.W. Bull, and C. Richardsen
(Defence Research Agency, England)

ABSTRACT

A study of the effect of systematically applying different CFD methods and associated parameters is described for the case of the HSVA tanker. Attention is focussed on the propeller plane and the nominal wake in particular. The viscous solutions are compared with an inviscid solution and with experiment data in an attempt to discover how well current codes perform in terms of practical predictions of propeller inflow. It has been found that the flow in the outer region of the propeller disc can be defined with reasonable accuracy. However, the methods fail to describe the flow at the half-radius position.

NOMENCLATURE

C_μ constant of proportionality for the eddy viscosity

k turbulence kinetic energy

L_{pp} length between forward perpendiculars

r radial length from propeller axis

R_D radius of grid domain

R propeller radius

U_t tangential fluid velocity

U_x axial fluid velocity at propeller plane

U_∞ free-stream fluid velocity

w Taylor wake fraction

w_1 average circumferential wake fraction

w_2 volumetric mean wake fraction

x longitudinal distance from forward perpendicular

ϵ turbulence diffusion rate

θ angle between propeller radius and horizontal radius

INTRODUCTION

In recent years a great deal of effort has been spent on developing numerical techniques to solve the Navier-Stokes equations of fluid motion. For practical reasons, these fundamental equations need to be 'Reynolds-averaged' and, in so doing, some error is incurred in the modelling. Additional errors are incurred in the choice of the closing turbulence model and also in the various numerical processes invoked to solve the equations. These processes include the discretisation scheme, the grid resolution, cell disposition and quality, choice of solution algorithm and choice of convergence criteria.

This paper describes some recent experiences in predicting the nominal wake of a surface ship using advanced computational fluid dynamics procedures. The paper is the third in a series on CFD validation originating from the CFD Section at the Defence Research Agency, Haslar [1, 2]; these studies concentrate on the issue of numerical verification. A validated CFD capability should enable the designer to make use of the computed velocity field in the propeller plane to aid in the design of a suitable propeller. Not only would this enable more candidate hulls to be assessed and placed in rank order of performance, but it might also permit significant reductions in design costs to be gained.

Whilst the ship hydrodynamics community must continue to support and encourage the development of new methods to aid in ship design, it should, every once in a while, stop to examine the capability that *currently* exists and then match that capability to the *requirements* of the naval designer. In this way, any serious shortfall in

417

capability will be identified and this should determine the level of effort required to improve the methods. In the authors' opinion, such a 'definition of capability' for stern flows is still lacking in the ship hydrodynamics literature; the most recent qualitative attempt was made by Larsson, Patel and Dyne [3].

In their study, an international workshop was organised to establish how accurately the velocity field could be predicted in the stern region of a model tanker which had been tested in a wind-tunnel at the University of Hamburg. The workshop attracted 19 teams from many nations and provided an excellent forum for establishing the world-wide capability. It also highlighted the extreme difficulty facing the CFD teams with respect to the sensitivity of their predictions to the choice of the various numerical methods and parameters associated with the conduct of their calculations.

An additional but related difficulty facing the organisers concerned the lack of any control relating to these parameters - particularly the grid size. Nearly all the participants 'broke the rules' imposed by the organisers and this made the task of comparing the predictions associated with the various methods very difficult. Half of the teams managed to produce results which resembled the experiment measurements, and one or two performed rather better than this but were still regarded by the workshop participants as insufficiently accurate.

This paper concentrates on the first of the two test-cases under investigation in the above workshop, namely, the problem of predicting the nominal wake (by which is meant the propeller is absent) for the HSVA hull at a Reynolds number of 5×10^6. The investigation was initiated in response to a growing awareness within the International Towing Tank Conference (ITTC) community that in recent years too little attention has been paid to issues relating to the validation of CFD.

The authors use computational fluid dynamics (CFD) methods to calculate the fluid velocity in the propeller disc to deduce the Taylor wake fraction and the associated radial and circumferential distributions of wake. This is compared with experiment data in a systematic manner and under reasonably well controlled numerical conditions. The k-ϵ turbulence model is used throughout,

although subtle differences exist between the codes concerning the wall treatment.

Control over the investigation is imposed by ensuring that the datum conditions for the computer runs, for example the number of computational cells for the two types of grid, structured and unstructured, remain approximately the same.

Clearly, there is considerable scope for improving this approach to numerical verification through additional effort and expense (perhaps using finer grids, or more sophisticated turbulence models). However, statements concerning accuracy can still be made, albeit pragmatic ones, based on a typical set of default conditions derived on the basis of wide experience in using these methods. It is hoped that the investigation will help the community to judge the present capability of available CFD codes, as applied to the practical prediction of nominal wake.

SOLUTION METHODS

Overview

The solution methods which are appropriate for solving the RANS (Reynolds-Averaged Navier-Stokes) equations fall into three broad categories: finite difference, finite volume and finite element methods. Each method has certain apparent advantages depending on the complexity and nature of the application, although it has to be said that practically no research has been undertaken aimed at ranking the performance of the methods for typical naval problems. Indeed, this is one of the aims of the Haslar team. In this study, five methods were tried, although two of them were similar in terms of the detailed solution technique employed. For the purpose of the present paper, we shall refer to the different methods by a simple numbering system.

Finite difference methods rely on replacing individual partial derivatives by algebraic equivalents which are local to a particular location, or cell, within the fluid domain. The finite analytic method also falls into this category except that the difference equations are related to locally analytic forms of the master equations (Method 1).

Finite volume methods use integral formulations of the RANS equations applied to a large number of control volumes constructed using

the computational grid. Such methods offer the advantage of examining fluxes through a well-defined volume and as such allow local continuity to be satisfied more easily (Method 2).

Finite element methods rely on expressing the local variation of each primitive variable within a cell (or element) by a shape function. The equations are re-cast in terms of the various shape functions chosen and a set of residuals is formed. These are weighted on the basis of the coefficients used in the shape function and the equations are solved for zero weighted residuals; this is the basis of the so-called Galerkin method. In principle this method ought to be the most accurate, but it can be memory intensive and therefore expensive to run (Method 3).

All the methods require the generation of a computational grid of cells. This can be performed either algebraically, using trans-finite interpolation, or numerically, using a set of Poisson equations relating the physical space to a convenient logical computational space (in which grid lines are straight and parallel and orthogonal in the coordinate directions). In the latter procedure, the governing master equations are transformed into a curvilinear, body-fitted coordinate system which maps across to the computational grid.

A severe restriction imposed by many CFD methods is that they are designed to work on only 'structured' grids in which cells are arranged in contiguous order in a logical space. For appended bodies, the structured approach can only be used by assembling blocks of structured grids together such that the total grid containing all the blocks fills the physical domain. The flow code then has to be organised so that information at block boundary faces can be easily communicated to adjacent block faces with the minimum of distortion. This is the basis of the multi-block approach (Method 4).

For the finite volume and finite element codes, however, the grid can be totally unstructured and the equations need not be transformed to a curvilinear coordinate system. In principle, this should lead to greater flexibility in the disposition and clustering of cells for regions within the domain where high gradients of velocity occur, and may allow greater flexibility with regard to building grids around complex geometries. Of course, this extra flexibility is gained at the considerable expense of more computer time and memory, since the move away from a contiguous ordering of cells imposes a need to store the cell connectivity in the form of additional look-up tables.

The different methods used in the present study will now be outlined.

Method 1

This method was developed by Patel, Chen and Ju at the Iowa Institute of Hydraulic Research and has been partially validated by them in a separate report [4]. The method, now embodied in the RANSSTERN computer code, employs the three-dimensional RANS equations for steady, incompressible flow. The Reynolds stresses are related to the corresponding mean rate of strain using the eddy viscosity concept. The eddy viscosity is calculated from the standard two-equation k-ϵ model with convective transport equations for the turbulence kinetic energy and dissipation rate. All of the equations are written in dimensionless form, using a partial transformation, where only the independent coordinate variables are transformed from the physical domain to a logical computational domain. The coordinate transformation is defined using a set of Poisson equations with the computational coordinates as the dependent variables and the Cartesian coordinates as the independent variables. A cylindrical polar coordinate system is used as the basic physical coordinate system, with velocity components in the axial, radial and circumferential directions.

The momentum and turbulence equations are recast using transformations into the computational domain and rearranged into general convective transport equations with suitable source terms. These equations are discretised using the finite-analytic (FA) method which reduces them to a set of fully implicit equations, in space and time, which can be solved by a tridiagonal matrix algorithm. The continuity equation, however, is solved using a modified version of the SIMPLER algorithm [5], which produces equations for pressure correction terms and pressure using a staggered grid. These equations are also discretised using the finite analytic method and solved using a tridiagonal matrix algorithm.

The complete solution is obtained firstly by solving the momentum, pressure correction and turbulence equations in planes marching downstream and then by solving the pressure equations in planes

marching upstream. This ensures that the elliptic nature of the equations is maintained and improves the convergence rate of the solution. An iterative procedure is used to link the pressure field to the velocity and turbulence fields. Although the calculation is steady-state, the method uses a time-marching technique in which a time step corresponds to one outer iteration, the steady-state solution being obtained after sufficient time steps. The convergence rate is controlled using suitable values of the time step and successive under-relaxation parameters.

The wall function on the ship surface uses a two point formulation and the effects of pressure gradients on the flow in the wall region are taken into account using a generalised law of the wall due to Chen and Patel [6].

Method 2

This method was developed by Lonsdale and Webster [7] of the United Kingdom Atomic Energy Authority and is now embodied in the ASTEC computer code. The method represents a major extension of ideas and techniques for two-dimensional flows reported by Baliga and Patankar [8]. Features held in common with method 1 include the application of the three dimensional RANS equations subject to the assumptions of steady, incompressible flow, and the eddy viscosity concept calculated from the convective transport equations for k and ϵ. The constants used for the k-ϵ model in both methods were identical. Method 2 uses a standard logarithmic wall function (without the pressure gradient correction incorporated in method 1).

The underlying approach, however, is very different from, and conceptually simpler than, method 1. The most obvious difference relates to the solution of the equations in the physical space rather than a transformed computational space. As a consequence, method 2 uses very different discretisation procedures.

Integral forms of the RANS equations are solved numerically by applying them to control volumes which surround each node within the domain. The velocity components are defined at each node and the pressure is defined at each cell centre. A cell is here restricted to an eight-noded hexahedron. The control volumes are constructed around the cell nodes by firstly joining the centroids

of each cell face to the centroid of the cell. In this manner each hexahedral cell is divided into eight smaller hexahedra - each one of which includes a cell node. The smaller hexahedra associated with neighbouring cells surrounding a given node are then joined to define a control volume.

A purely geometrical approach is used to quantify the various terms appearing in the integral equations. For example, the divergence theorem of Gauss is invoked to convert the pressure gradient term to a surface integral of pressure. The latter is easily evaluated by summing the contributions from individual faces of a given control surface, subject to the assumption that the pressure for a face is given by the pressure for the element containing the face. Indeed it is a feature of the method that any flux associated with a control surface face is calculated using only nodal information belonging to the element containing the face.

The diffusion term is treated in a similar manner to the pressure gradient term. In this case, the fluid velocity gradients are defined for each control surface by linear interpolation of the current velocity components applied to sets of tetrahedra constructed within each element. The advection term is calculated using a skew-upwind hybrid differencing scheme. This scheme allows various blends of central and upwind differencing to provide the usual compromise between accuracy and stability. In addition, however, the scheme also allows upwind discretisation in the local stream-wise direction in an attempt to reduce the amount of false numerical diffusion associated with highly skewed flows. This facility is provided by a set of weighting factors applied to the nodes of the upwind element face. These factors are set according to the point of intersection of an element streamline (emanating from a given downstream node) and the upwind face of the corresponding element.

The resulting discretised equations are solved using a segregated approach. The momentum equations are solved using a Gauss-Seidel solver; for the continuity equation, the SIMPLE algorithm is applied and the equation is solved using a pre-conditioned conjugate gradient method. A modification of the Rhie and Chow [9] procedure is used to improve the stability of the pressure correction scheme applied at each element. Although a pseudo-unsteady approach is also used in this method, the time step can be chosen to be very large.

Method 3

The suite of computer programs, FIDAP (written by Fluid Dynamics International [10]) can be used to simulate a variety of flow conditions. FIDAP is a Petrov-Galerkin based finite element method for computational meshes which can be either structured or unstructured.

Tri-linear basis functions were used for velocity, except in those cells abutting hull surfaces; piece-wise constants were used for pressure. The discretized equations of motion are solved in a segregated manner with the equations for each variable being solved in turn using the preconditioned conjugate gradient technique. Note that streamline up-winding was used to enhance the stability of the discretized transport equations.

Pressure correction is employed to ensure mass conservation. In the modelling of the effect of the hull shear layer, FIDAP uses a wall function approach with the turbulent kinetic energy providing the velocity scale for the wall functions. For mesh cells abutting the hull, FIDAP uses a single velocity profile, the so-called Reichardt law, to modify the velocity basis function in the direction normal to the wall. Similarly, the eddy viscosity is modified using a van Driest damping factor normal to the wall.

Method 4

The DRA code, RANSBLOCK, is a suite of computer programs which is based on the multi-block technique for solving the RANS equations for complex geometries. The multi-block technique decomposes the flow domain into a number of blocks and uses a communication strategy to transfer global conservation of mass and momentum. RANSBLOCK uses a transformation from body-fitted coordinates to logical computational coordinates for each block in the domain. The coefficients for the discretisation scheme are evaluated using the finite analytic approach, in an identical manner to RANSSTERN. RANSBLOCK uses a structured block scheme and is fully three-dimensional, which gives considerable flexibility for generating body fitted meshes, unlike RANSSTERN which is limited to parallel x-planes.

As in RANSSTERN, the Chen and Patel [6] wall function is used; this includes a correction term for the prevailing pressure gradient.

The overall solution strategy involves the calculation of velocity, mass source and turbulence fields for each block using the momentum, pressure correction and turbulence equations. These results are communicated to adjoining blocks using interpolation schemes for each block. The pressure field is then calculated for each block. The complete process is repeated a number of times until the continuity equation is satisfied to within a given tolerance.

Method 5

This method provides a non-lifting potential flow solution to the problem. The method, embodied in the DRA code known as BRAC, is a panel method and was devised by the first author for predicting non-linear wave resistance [11]. However, in this instance, the code was run at negligible Froude number in order to provide a basis for assessing the improvement to be gained by adopting a fully viscous method using a RANS code.

CONDUCT OF INVESTIGATION

Run Attributes

The aim of the investigation was to record changes in the numerical solution arising from changes in the details associated with implementing a particular method or problem specification. Such details will be referred to as 'attributes'. The particular attributes chosen for the investigation were:

a.   Turbulence Model

The k-ϵ model was used with three different values of C_μ (the constant of proportionality relating the eddy viscosity to the computed ratio k^2/ϵ). The values used were C_μ, $\frac{1}{2}C_\mu$ and $2C_\mu$. Alternatively, the modified k-ϵ model due to Chen and Kim [12] could be chosen instead.

b.   Grid

Six different grids were generated. Three of these were plane-by-plane structured grids, as required by Method 1; the resolutions were 21,168 cells (datum standard), 64,584 cells (medium resolution) and 390,818 cells (high resolution). Two unstructured grids were included, although

they were unstructured only in transverse planes; both represented attempts to concentrate cells around regions of high curvature and near the propulsor disc. The 'unstructured 1' grid comprised 21,756 hexahedral cells, whilst the 'unstructured 2' grid comprised 21,854 cells which were mostly hexahedral but included some wedge cells near the stern. Finally, a 3D surface-by-surface (as opposed to plane-by-plane) structured grid, was also included.

The grids filled a cylindrical domain whose nominal dimensions were $x/L_{pp} = 0.3$ to $x/L_{pp} = 2.5$, and $R_D/L_{pp} = 0.75$, where L_{pp} is the length of the ship, x is the distance measured from the bow, and R_D is the radial distance from the longitudinal axis.

c.   Alignment of model in computational domain

The longitudinal axis of the model could be chosen to be either parallel to the onset flow or to make a small angle (in pitch and/or yaw) to the onset flow (in such cases, the removal of symmetry planes doubled, or quadrupled, the number of computational cells). This attribute was included in the investigation to determine how sensitive the flow-field in the experiment might have been to small errors in model alignment.

d.   Inclusion of supporting wire

In the wind-tunnel experiment [13], the stern region of the model was supported by a thin wire on each side. The wire was connected to the keel of the hull at $x/L_{pp} = 0.81$ (the authors are indebted to Dr J Kux for providing this information) and formed an angle of 45^0 to the horizontal. In the calculations, this wire could be either ignored or modelled (albeit crudely by invoking a no-slip boundary condition at nodes nearest to the wire).

Strategy

The verification process can be conveniently described in terms of an imaginary machine. Associated with this machine is a set of five switches, each of which can change the setting of an attribute in accordance with the options available, as described above.

The datum set of attributes was:

a.   turbulence: standard k-ε
b.   plane-by-plane structured grid (23,750) (as used in ref [2])
c.   model axis parallel to onset flow
d.   wire ignored

This datum set of attributes corresponds to all the switches being set at 'zero', as shown in Table 1.

In order to exercise proper control over the investigation, no more than two switch settings were allowed to have non-zero values for a given run. For example, if the model was inclined (see the 'alignment attribute in Table 1), with the alignment switch set to 1, 2 or 3, then all other switches would have been set to zero (the datum setting).

It was not possible to test all the methods with all the switch positions; however, all the methods were applied to the datum case (all switch settings set to zero). The actual runs performed are indicated in Tables 2 to 5. Each 'yes' entry is a single run, with all other attribute switches set to zero.

DATA REDUCTION

Attention was focussed exclusively on the velocity field within a prescribed area in the propeller plane (defined to be a plane through the propeller position and perpendicular to the longitudinal axis). This area extended to two propeller diameters below the hull and to 1.5 propeller diameters outwards from the centre-plane. Within this region, each data set was linearly interpolated onto a uniform reticle for ease of comparison.

The following parameters were calculated for each computer run:

a.   the Taylor wake fraction, w, at the radius of the propeller disc, and at half the radius:

$$w(r,\theta) = U_x(r,\theta)/ U_\infty$$

b. average circumferential Taylor wake fraction, w_1:

$$w_i(r) = (1/2\pi U_\infty) \int_0^{2\pi} U_x(r,\theta) \, d\theta$$

c. the circumferential variation in the tangential velocity component, U_t, at the radius of the propeller disc, and at half the radius.

d. contours of constant axial velocity.

e. volumetric mean wake fraction, w_2:

$$w_2 = (1/\pi U_\infty R^2) \int_0^R \int_0^{2\pi} r U_x(r,\theta) \, dr d\theta$$

All integrations were performed using Simpson's rule after demonstrating that the arithmetic was sensibly independent of the chosen step-length.

DISCUSSION OF RESULTS

A project of this nature generates a huge amount of data; specifically, 120 graphs were produced for analysis, together with the 20 values of mean volumetric wake fraction. Accordingly, this section will concentrate on the salient features and trends observed in the results. For convenience, all the runs are listed in Table 6 so that the reader can associate a particular run with the method and switch setting(s) identified in the Tables 1-5; note that only runs 10 and 12 had more than one non-zero switch setting.

In all the subsequent plots, the experiment data are indicated by open circular symbols, and the CFD data by spline curves derived from the raw calculations. Plots involving circumferential variations are displayed according to the convention that θ increases from $-\pi/2$ at the bottom of the (imaginary) propeller disc to $+\pi/2$ at the top (nearest the double body symmetry plane). Plots involving radial variations (w_1) increase from zero (centre of disc) to the outer radius of the disc. The predicted values for the volumetric mean wake fraction, w_2, are shown in the right-hand column of Table 6. For all the predictions shown in the following figures, the run number is indicated so that the reader can recover the particular switch settings from Tables 1-6.

We shall start with the effect of changing the flow solution method for the datum cases, where all the switches were set to zero. The results are shown in Figures 1 to 6.

With the possible exception of Method 1 (run 1), which strays significantly from the experiment data, the Taylor wake fraction at the edge of the propeller disc (Figure 1) is predicted reasonably accurately. The viscous effects are clearly captured, as can be seen by comparing all the predictions with Method 5 (run 20) - the inviscid model. At half the radius, however, all the methods fail to describe the shape of the experiment curve. The circumferential variation of the wake fraction is shown in Figure 3. Again, the shape of the experiment curve is not depicted in any of the predictions, although in quantitative terms all the viscous codes have succeeded in reducing w_1 to its correct value at the edge of the disc. At half the radius, errors are typically 30%.

Figure 4 shows the tangential velocity at the radius of the disc. Interestingly, the inviscid code (run 20) performs better than all the viscous codes - a fortunate consequence of the location of the circumference of the disc with respect to the measured cross-flow; the inviscid code does not generate vortical features and this result should be regarded as coincidental.

The situation is very different at half the disc radius (Figure 5), where the longitudinal vorticity is high. Clearly the flow is dominated by viscous effects, and these are reflected in the predictions only in the sense of a general trend towards correctly increasing U_t compared with inviscid theory. The axial velocity contours are compared with experiment, using all the methods, in Figure 6. Note that the so-called 'hook' [3] in the experiment curve is missing from all the predictions.

Method 3 was used to investigate the sensitivity of the predictions to changes in the attitude of the model with respect to the inflow. These 'perturbations' were introduced in an attempt to discover whether a small alignment error in the wind-tunnel might help to explain the differences observed within the core of the vortical flow. The only positive conclusion that can be drawn from this

exercise is that the discrepancy diminishes slightly when the double-body hull is pitched by an angle of plus two degrees (Figure 7). However, the oscillating character of the experiment data is still not reproduced.

The effect of changing the turbulence representation in Method 2 is shown in Figure 8 for the case of U_t at the disc radius. Significant improvements are found when C_μ is halved (run 6) and when the Chen and Kim model is used (run 8). This suggests that either k is over-predicted, or that ϵ is under-predicted, in the standard k-ϵ model. However, the predictions of U_t at the edge of the disc are no better than those of Method 5 (the inviscid method), so it is possible that all the viscous solutions suffer from too much numerical diffusivity compared with the eddy diffusivity computed from the standard 2-equation model.

Method 1 was used to assess the effect of the cell density on the solution; some results for the wake fraction at the edge of the disc are shown in Figure 9. Although the calculated values of w at the bottom of the disc $(-\pi/2)$ are too high, there is clearly an improvement to be gained by adopting a denser grid (runs 3 and 4).

The multi-block code (Method 4) was used to study the effect of switching from a standard (vertical) plane-by-plane (PBP) grid (run 18) to a more versatile (non-vertical) surface-by-surface (SBS) grid (run 19); the results are shown in Figure 10. Here, the peak at approximately -1 radian is more clearly described by the SBS grid compared with the PBP grid. However, the SBS grid tends to under-predict slightly at the top of the disc.

Figure 11 shows the effect of changing from a structured grid (run 5) to an unstructured grid (run 11). A clear improvement is noticed, similar to the observation made above regarding the effect of halving C_μ, suggesting that the unstructured grid is less diffusive than the structured grid.

We now come to the effect of incorporating the support wire. This was investigated by simply applying a no-slip boundary condition at nodes nearest to the wire but without any attempt to cluster cells around it. Consequently, some features of the flow in the propeller plane are adversely affected by this crude modelling. This is exemplified in Figure 12, where the momentum

deficit is greatly increased (run 9) compared with the datum case without the wire (run 5). However, at the half-radius position (Figure 13), there is a considerable improvement in the top-most region of the disc compared with the datum runs shown in Figure 2. Similarly, although the absolute values of the circumferentially-averaged wake fraction, w_1 (Figure 14), are too low compared with the datum run (run 5), the prediction with the wire (run 9) does exhibit the point of inflection in the region of r/L = 0.005. The comparisons for U_t at the edge of the disc, and at the half-radius position, are shown in Figures 15 and 16. Note that there was little improvement, in terms of general trends, associated with the use of the Chen and Kim turbulence model or the unstructured grid (runs 10 and 12 - not shown).

Attention must now be drawn to a somewhat surprising outcome of this investigation. Figure 17 shows a comparison between run 5 (the datum run for Method 2) and run 9 (with the wire included) for the case of the constant axial velocity contours. It can be seen that there is a very pronounce 'hook' which appears in the experiment and is reproduced in run 9; this Figure should be compared with Figure 6, which displays the datum runs for all the methods. It must be emphasised that the only change to the datum run was the application of a set of no-slip conditions to those nodes closest to the wire; the grid and all other features remained the same.

Finally, the volumetric mean wake fraction, w_2, is listed in Table 6 for all the runs performed. The mean of all the runs (excluding the inviscid method) is 0.39, compared with the experiment value of 0.37 as calculated using the same procedures as those employed in the analysis of the CFD data.

CONCLUSIONS

A numerical verification study into the effects of the choice of solution algorithm, turbulence model, grid, model alignment and model support arrangements has been conducted for the case of the HSVA tanker at a Reynolds number of $5x10^6$. The propeller was absent throughout the investigation. The following conclusions are drawn:

a. RANS methods provide a good overall description of the flow near the edge of the propeller disc. In this region, the predictions are

424

reasonably independent of the choice of solution method adopted.

b. The predictions break down in the region within the disc; specifically, the predictions were generally poor at the half-radius position. In this region, changing the choice of solution method brought about changes in the solution which were comparable in magnitude with the changes associated with the choice of computational grid.

c. Changes to the standard k-ϵ turbulence model, including drastic changes to the constant of proportionality for the eddy viscosity, produced relatively little change in the predicted wake. The observed changes were considerably smaller than those associated with the choice of other attributes.

d. Changes arising from the use of different grids resulted in significant changes to the solution. Switching from a plane-by-plane grid to a 3D surface-by-surface grid, from a coarse to a fine grid, and from a structured grid to an unstructured grid, led to improvements in the predictions at the edge of the disc.

e. Simulations of the effect of poor model alignment in the wind-tunnel have demonstrated that a 2^0 error in yaw or pitch creates a greater change to the nominal wake than any change brought about by the choice of any of the numerical attributes associated with the generation of a solution for a naked hull.

f. By appending the hull to a support wire attached to the keel at $x/L_{pp} = 0.81$, as was done in the experiment, and applying a no-slip boundary condition to nodes closest to the wire, the solution was observed to change radically. No attempt was made to wrap a stretched grid around the wire, as this would have disrupted the control of the experiment (since the cell count would have increased dramatically). Although the crude approach adopted led to worse quantitative predictions of the nominal wake, it dramatically improved the qualitative prediction of the axial velocity contours. Specifically, the so-called 'hook' was captured in the solution.

Further work is planned to confirm what is now a mere suspicion; namely, that the failure to describe the measured axial velocity contours, using RANS methods, may be due to the actual experiment conditions having been neglected.

REFERENCES

1. Musker, A. J., "Stability and Accuracy of a Non-Linear Model for the Wave Resistance Problem," Proceedings of the 5th International Conference on Numerical Ship Hydrodynamics, Hiroshima, September 1989.

2. Musker, A. J., Atkins, D. J., Watson, S. J. and Bull, P. W., "A Comparison of Two Navier-Stokes Methods Applied to the Stern Region of the HSVA Tanker," Proceedings of the 2nd International Colloquium on Viscous Fluid Dynamics in Ship and Ocean Technology, Japan, September, 1991.

3. Larsson, L. and Patel, V. C., "Proceedings of the 1990 SSPA-CTH-IIHR Workshop on Ship Viscous Flow," Goteborg, September 1990.

4. Patel, V. C., Chen, H. C. and Ju, S., "Ship Stern and Wake Flows: Solutions of the Fully-Elliptic Reynolds-Averaged Navier-Stokes Equations and Comparisons with Experiments," IIHR Report No 323, April 1988.

5. Patankar, S. V., "Numerical Heat Transfer and Fluid Flow," McGraw-Hill, New York, 1980.

6. Chen, H. C. and Patel, V. C., "Calculation of Trailing Edge, Stern and Wake Flows by a Time-Marching Solution of the Partially Parabolic Equations", IIHR Report No 285, 1985.

7. Lonsdale, R. D. and Webster, R., "The Application of Finite Volume Methods for Modelling Three-Dimensional Incompressible Flow on an Unstructured Mesh," Proceedings of the 6th International Conference on Numerical Methods in Laminar and Turbulent Flow, Swansea, England, July 1989.

8. Baliga, B. R. and Patankar, S. V., "A Control Volume - Finite Element Method for Two Dimensional Fluid Flow and Heat Transfer," Numerical Heat Transfer, 6, pp 245 - 261, 1983.

9. Rhie, C. M. and Chow, W. L., "Numerical Study of the Turbulent Flow Past an Airfoil with Trailing Edge Separation," AIAA Journal 21, No 11, 1983.

10. FIDAP User Manual Volume 1 - Theory. Fluid Dynamics International Inc., Evanston, IL, USA. April 1991.

425

11. Musker, A. J., "Panel Method for Predicting Ship Wave Resistance," Proceedings of the 17th Symposium on Naval Hydrodynamics, The Hague, 1989.

12. Chen, Y.-S and Kim, S.-W, "Computation of Turbulent Flows Using an Extended k-ε Turbulence Closure Model," NASA Report CR-179204, October 1987.

13. Wieghardt, K and Kux, J. Nomineller Nachstrom auf Grund von Windkanalkversuchen, Jahrbuch der Schiffbautechnischen Gesellschaft (STG), Springer Verlag, pp 303 - 318, 1980.

Table 1 - Switch/Attribute Matrix

switch #	turbulence	grid	alignment	wire
0 (datum)	k-ε	standard structured	perfect	ignored
1	½C$_\mu$	unstructured 1	± 2^0 yaw	included
2	2C$_\mu$	unstructured 2	+ 2^0 pitch	-
3	Chen and Kim	medium structured	- 2^0 pitch	-
4	-	high structured	-	-
5	-	3D	-	-

Table 2 - Verification Runs for Method 1

switch #	turbulence	grid	alignment	wire
1	no	no	no	no
2	no	no	no	-
3	yes	yes	no	-
4	-	yes	-	-
5	-	no	-	-

Table 3 - Verification Runs for Method 2

switch #	turbulence	grid	alignment	wire
1	yes	yes	no	yes
2	yes	no	no	-
3	yes	no	no	-
4	-	no	-	-
5	-	no	-	-

Table 4 - Verification Runs for Method 3

switch #	turbulence	grid	alignment	wire
1	no	no	yes	no
2	no	yes	yes	-
3	no	no	yes	-
4	-	no	-	-
5	-	no	-	-

Table 5 - Verification Runs for Method 4

switch #	turbulence	grid	alignment	wire
1	no	no	no	no
2	no	no	no	-
3	no	no	no	-
4	-	no	-	-
5	-	yes	-	-

Table 6 - Description of Run Numbers

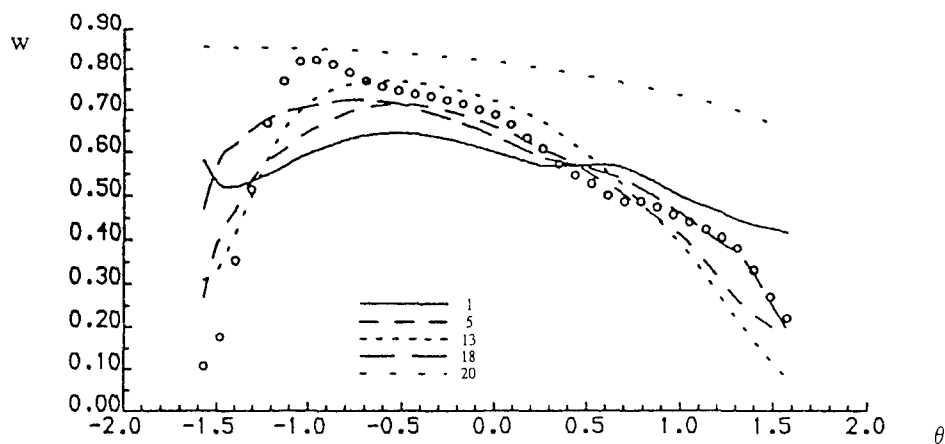| Run #	Method	Switch Setting(s)	w_2
1	1	datum #0	0.46
2	1	turbulence #3	0.48
3	1	grid #3	0.46
4	1	grid #4	0.50
5	2	datum #0	0.38
6	2	turbulence #1	0.40
7	2	turbulence #2	0.43
8	2	turbulence #3	0.41
9	2	wire #1	0.21
10	2	wire #1, turbulence #3	0.23
11	2	grid #1	0.41
12	2	wire #1, grid #1	0.33
13	3	datum #0	0.44
14	3	alignment #1	0.33/0.51
15	3	alignment #2	0.31
16	3	alignment #3	0.21
17	3	grid #2	0.40
18	4	datum #0	0.45
19	4	grid #5	0.46
20	5	see text	0.78

Figure 1 Taylor wake fraction at r=R (comparison of methods)

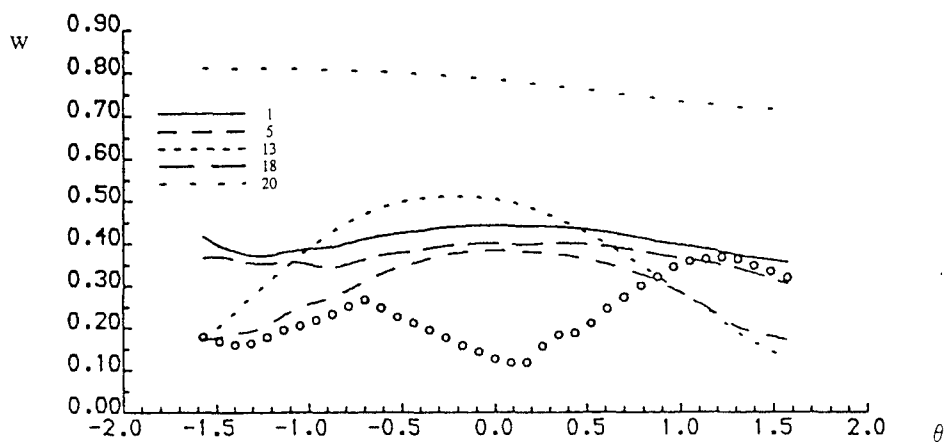Figure 2 Taylor wake fraction at r=R/2 (comparison of methods)
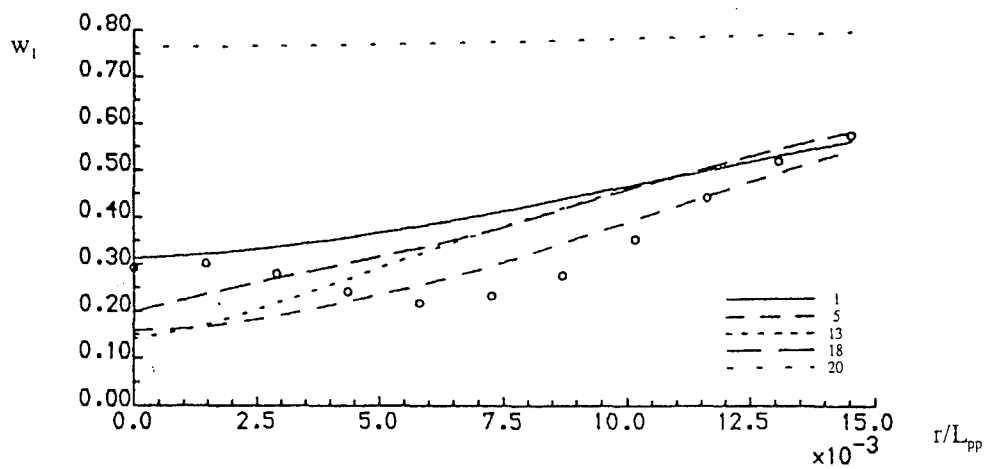
Figure 3 Average circumferential wake fraction (comparison of methods)
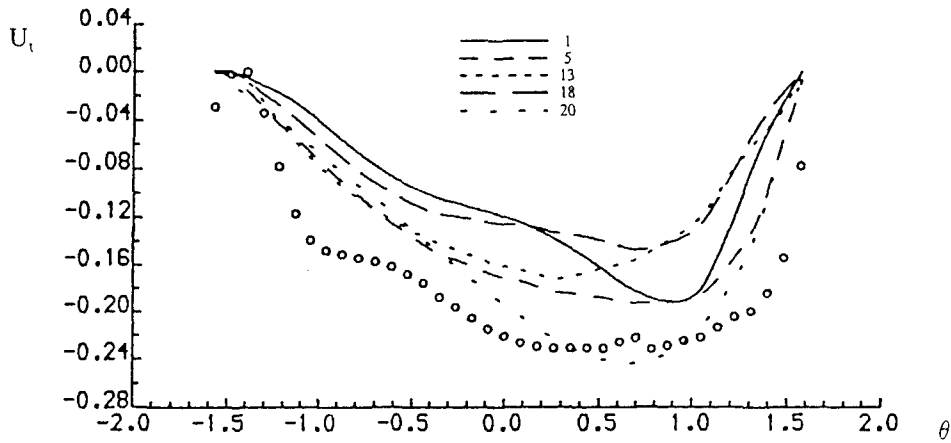
Figure 4   Tangential velocity at r=R (comparison of methods)
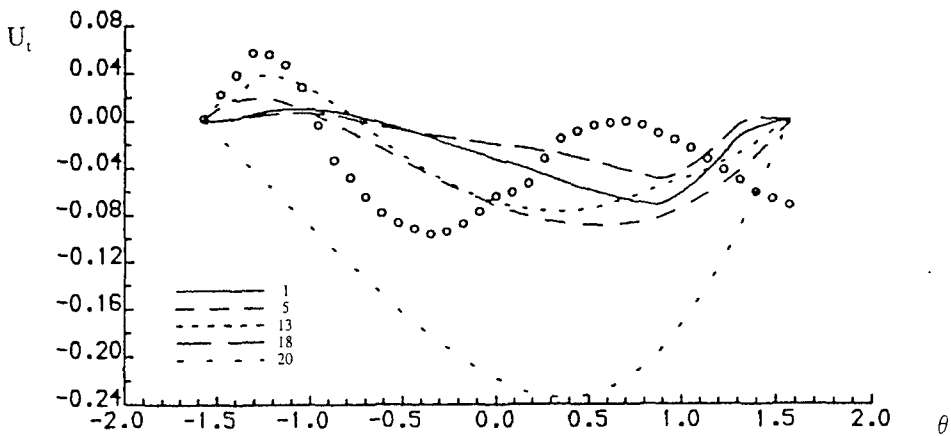
Figure 5   Tangential velocity at r=R/2 (comparison of methods)
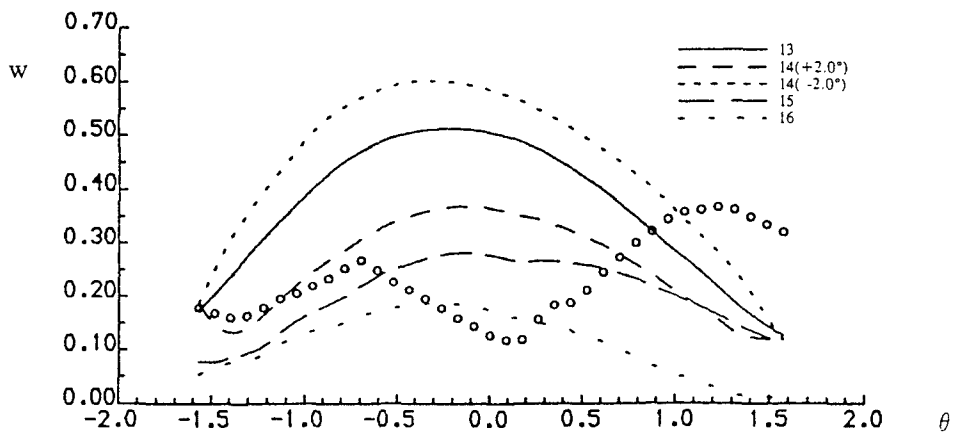
Figure 7 Taylor wake fraction at r=R/2 (effect of misalignment)
(NB Figure 6 follows Figure 7)
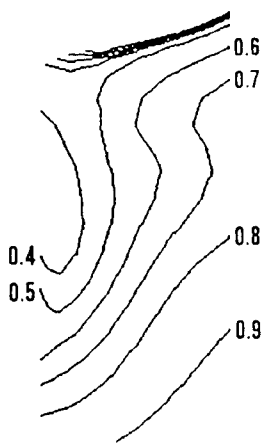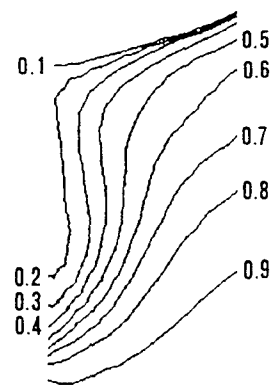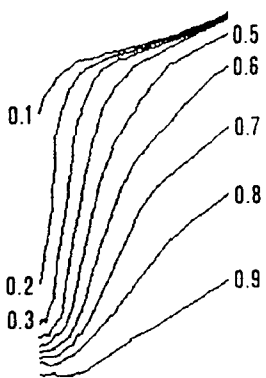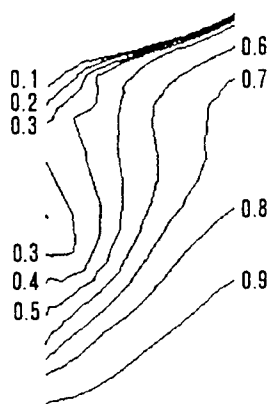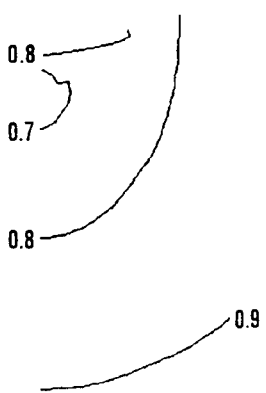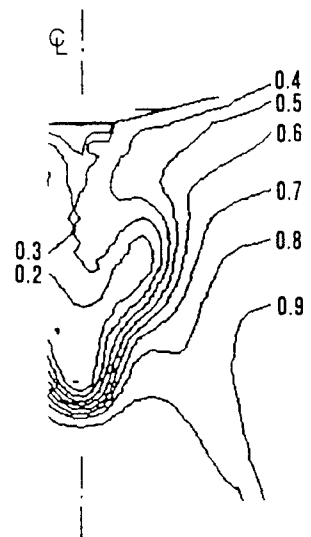
Figure 6 Axial velocity contours (comparison of methods)

431
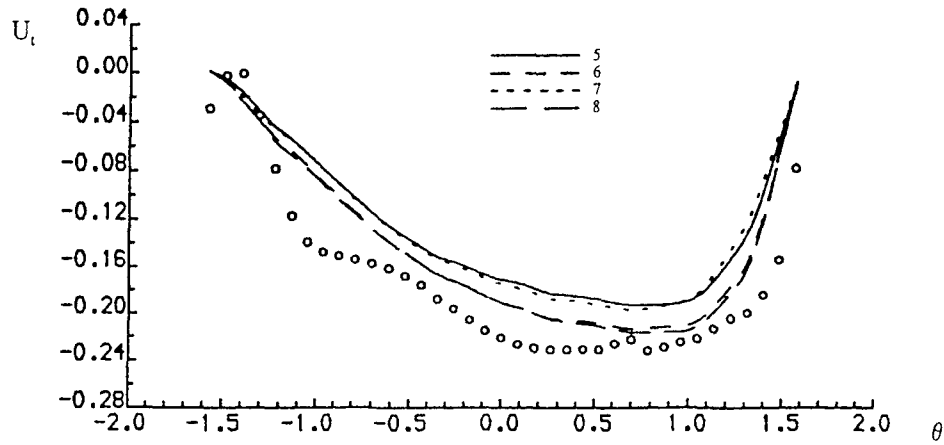
Figure 8　Tangential velocity at r＝R (effect of turbulence model)
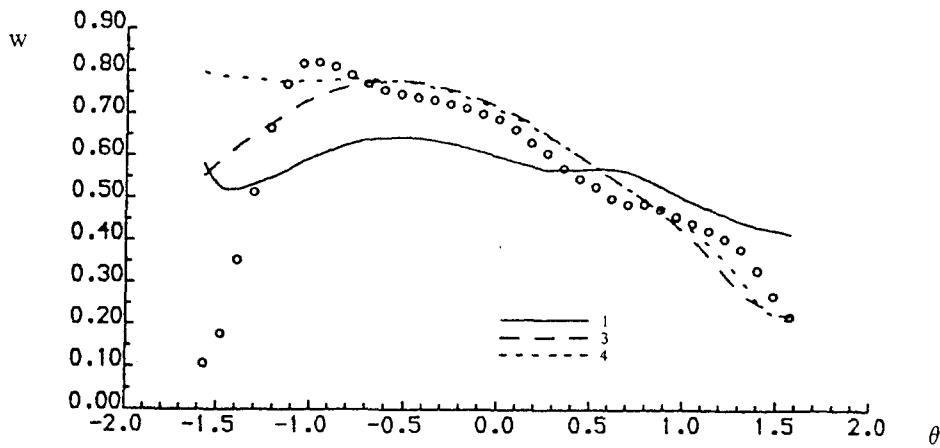
Figure 9　Taylor wake fraction at r＝R (effect of cell density)
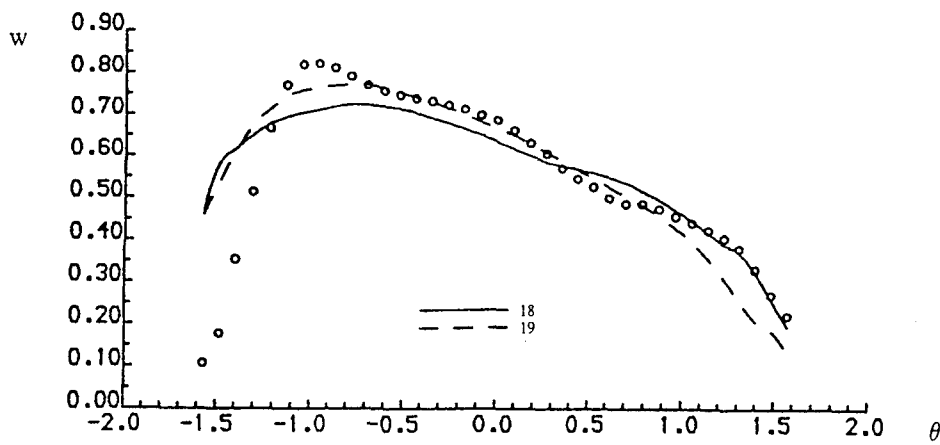
Figure 10　Taylor wake fraction at r＝R (effect of SBS grid - run 19)

432
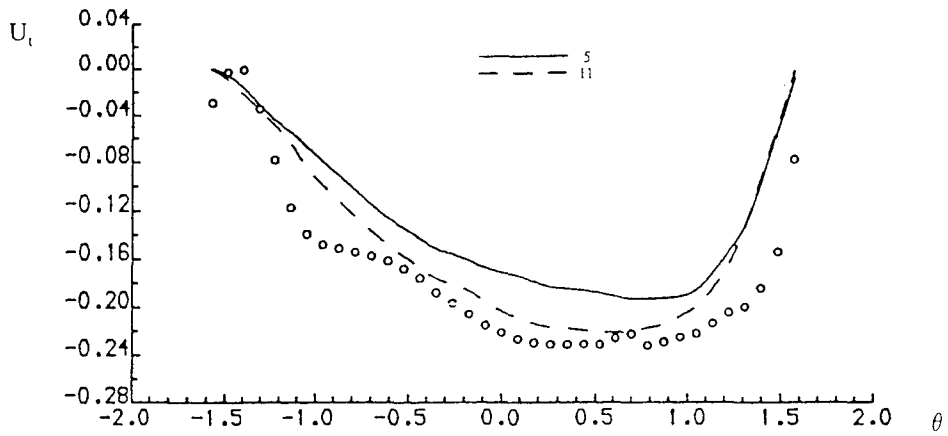
Figure 11 Tangential velocity at r = R (effect of unstructured grid - run 11)
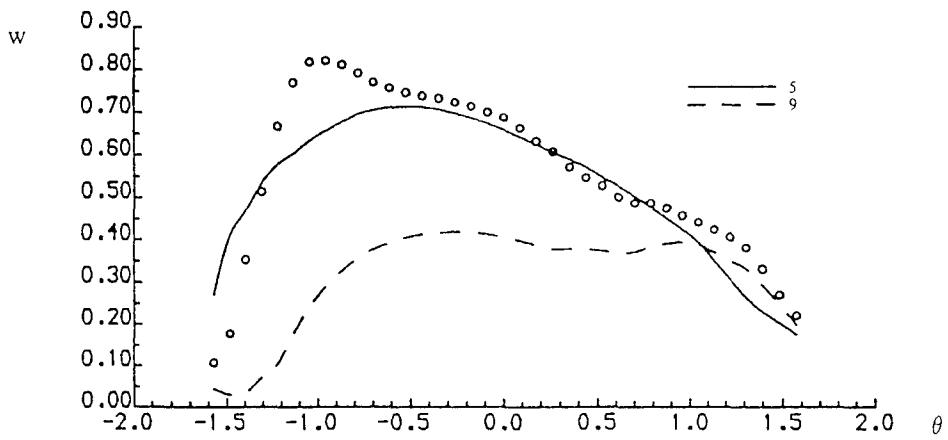
Figure 12 Taylor wake fraction at r = R (effect of wire - run 9)
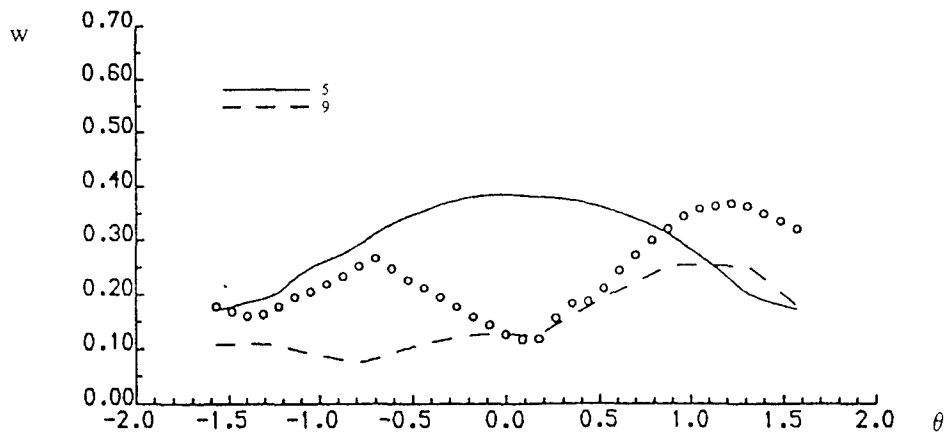
Figure 13 Taylor wake fraction at r = R/2 (effect of wire - run 9)

433
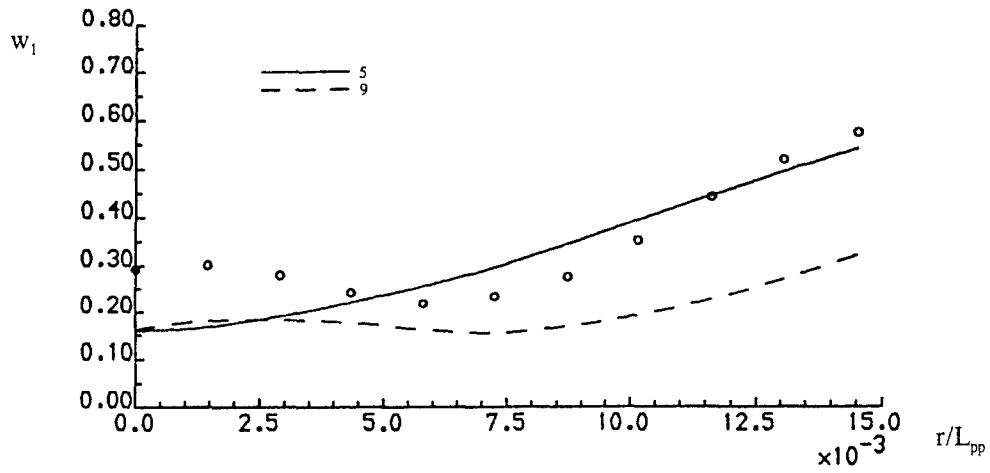
Figure 14 Average circumferential wake fraction (effect of wire - run 9)
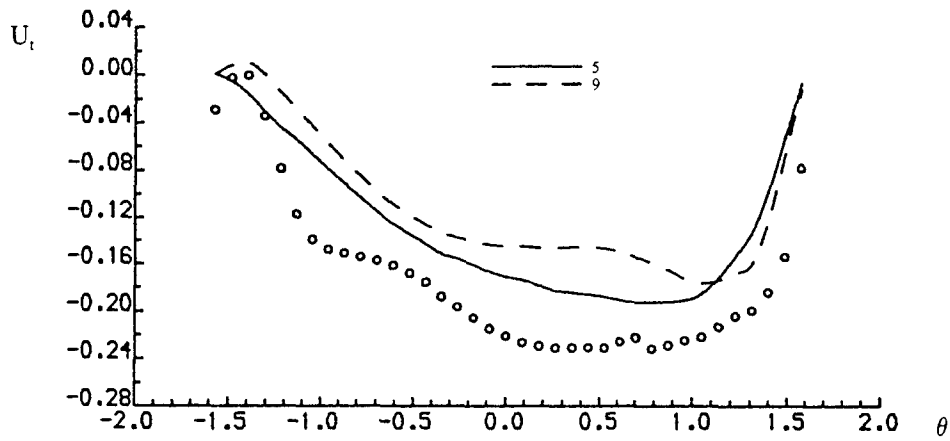
Figure 15 Tangential velocity at r=R (effect of wire - run 9)
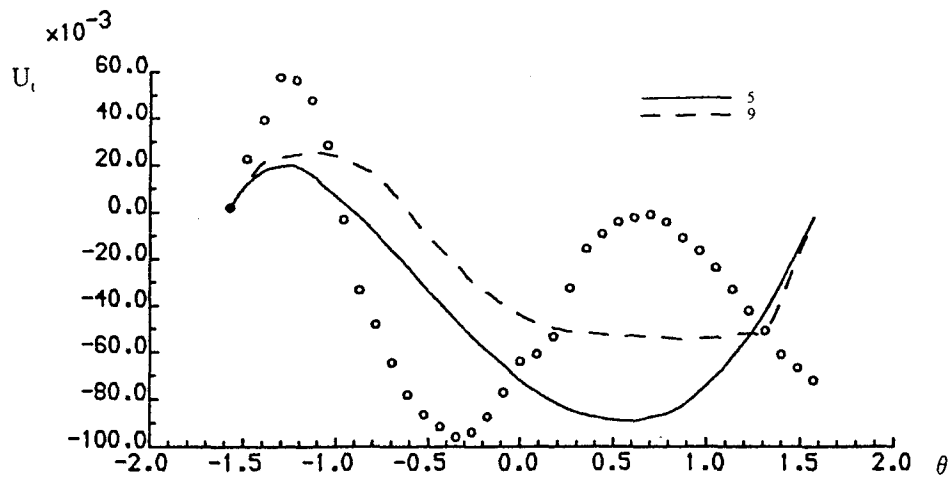
Figure 16 Tangential velocity at r=R/2 (effect of wire - run 9)

434
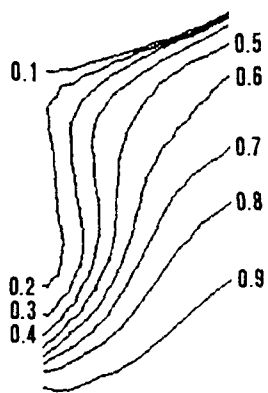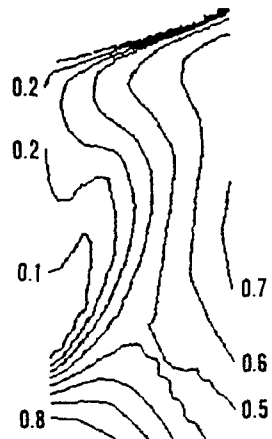
datum run (run 5)   with wire (run 9)   experiment

Figure 17 Axial velocity contours showing effect of support wire

DISCUSSION
by Professor D. L. Whitfield, Mississippi State University.

To simulate the influence of the support wire on the experimental measurements you stated you adjusted the computed velocity. Another way the authors might consider simulating the support wire numerically would be to use the drag force of the wire (which can be estimated rather accurately) as a body force in the equations used for the numerical simulation. This approach is simple to use and doesn't require extensive grid modifications other than, perhaps, some aligning of the grid in the region of the support wire.

Author's Reply
To clarify any confusion, note that we simulated the presence of the support wire by specifying values of velocity as boundary conditions at grid points lying near to the actual physical position of the wire throughout its length and not by modifying computed velocities.

As to representing the wire as a body force in the equations of motion, we agree that this approach would be worthy of further investigation. However, although Professor Whitfield's comments about the modifications to the mesh are valid, we believe that the mesh would have been optimal had it been designed to accommodate the presence of the wire at the outset, so as to avoid numerical complications and ambiguities.

DISCUSSION
by Dr. J. Kux, Institut für Schiffbau, Universitat Hamburg

The authors are to be complimented for this thorough study of wake prediction by applying different CFD methods to the case of the HSVA tanker.

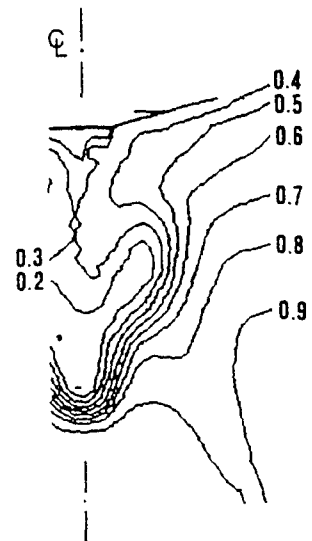As originator of the experimental data about the flow field of the so called HSVA1 test case, I feel that some remarks concerning the wake of this hull form should be appended here. The authors claim, though at present as "a mere suspicion," that their failure in reproducing the experimental findings "may be due to the actual

experiment conditions having been neglected" and here the main point alluded to, is the suspension wire with its wake interfering with the double model wake in the region scanned. Since this is - if really the wake is basically altered due to the wire - a severe objection against this data set to be used as test case, the matter should be thoroughly ventilated. At the moment a new run with the HSVA1 double model in the wind tunnel with changed support wire location is not feasible. Therefore it is appropriate to review evidence against the cited suspicion. This has to include a critical discussion of the arguments presented, as well as a search for cases with similar wake details (hoods) from model investigations where no supporting wires were present, a summary of our scrutiny of the details of the wire wake and of computational evidence, that the hood may well be obtained with no need to simulate wires, but merely by slightly increasing the sophistication of the turbulence model use.

The basic problem when comparing two flows, here one measured with one computed, is the choice and weighting of the criteria on which to base figures of merit. There are several quantities such as scalar (i.e., pressure), vector (i.e., mean velocity, wall shear-stress) and even tensorial (i.e., Reynolds-stress) fields which should enter the comparison. Here a singular feature, the famous "hook," a detail of the isoline pattern of the longitudinal component of the mean velocity field, has been overemphasized and shown to be reproducible by a computational intervention, without the vortical pattern of the transverse components of the mean velocity, which has to go with it, being depicted for this computational attempt. The feature "hook" has been achieved by a questionable technique of an artificial non-slip boundary condition on some nodes close to the wire, at locations which are not disclosed in the paper. Further details of the fields are not shown: Does the wall shear-stress distribution, or the distribution of k, the kinetic energy of turbulence, obtained with this wire simulation, compare qualitatively better or worse to the experimental findings than without wire simulation? It should not be overlooked, that, as stated by the authors, quantitatively this crude intervention led to a deterioration of predictions.

Now if we look for evidence of "hooks" in wake velocity patterns from towed models, (no

suspension wires, no struts) we readily hit upon such: merely a few will be cited. Tanaka (1988, Figure 23, Page 345) shows such a wake pattern for three geosims of a tanker, Ogiwara in its contribution relating to one of the new test cases to be proposed by the Resistance and Flow Committee of the ITTC, the "Ryuko Maru," presents such an isoline pattern (Figure 10, Section C), and for the other test case, the so called Hamburg Test Case, towed in the HSVA [Betram et al., 1992], the vestige of a "hook" appears in the nominal wake (Abb. 5-30) (as in the experimental findings from the double model of this hull in the wind tunnel at the IfS), which develops into a enormous "hook" under the action of the propeller at certain propeller-loadings (Abb. 5-38). Finally, also in this conference we have seen a similar pattern [Suzuki et al. 1993] (Figure 6), for the nominal wake developing behind the so called propeller open boat in an experiment designed to investigate the interaction of the propeller slipstream with the rudder.

The velocity field for the HSVA1 test case was thoroughly investigated by us several years ago, when we were first faced with the details disclosed by the experiment. One step was the computation of the vorticity field, the curl of the vector field of the mean velocity. In the wake of the wire, vorticity values were derived, but this vorticity was aligned - as to be expected - with the wire direction and no longitudinal component of the vorticity appeared. In the area of interest, there is, of course, a superposition of this vorticity to the one from the flow field. Nevertheless, specifically in the core domain of the longitudinal vortex, and therefore at the "hook," this original vorticity is strongly aligned with the velocity vector, i.e., we have high helicity there (while over most of the region, vorticity and velocity tend to be almost at right angles), an alignment process initiated by the three-dimensional thick boundary layer, where the vorticity vector, due to the cross flow, leaves its circumferential direction (originally in a transverse plane as in a nearly two dimensional boundary layer) initiating the formation of the characteristic longitudinal vortex. The wire-induced vorticity, being aligned neither with the vortex core vorticity nor with the original boundary layer vorticity, it does not seem likely that the wire wake induces a basically different flow pattern from that which would develop in the absence of the wire.

Different authors managed to reproduce the "hook," in the near past, in their computational studies. At the Gothenburg workshop [Larsson et al., 1991], Zhu & Miyata (Figure 8), at the Osaka Colloquium 1991, Sung et al [Sung et al, 1991] (Figure 20), and at this conference Zhu et al., [Zhu et al 1993] (Figure 12c), using hybrid turbulence model and Deng et al., [Deng et al., 1993] (Figure 18), with an unconventional localized change of the eddy viscosity otherwise obtained by the standard k-ε-model. In the last mentioned contribution, a quite reasonable resulting wall shear-stress directional pattern is presented too. Remarkably in this paper, these results were obtained by reducing the value of the (scalar) eddy viscosity in the core of the longitudinal vortex thus enhancing the inhomogeneity of the simulated turbulence considerably in contrast to the model prediction. The simple change of the eddy viscosity by a factor, as in the paper here discussed, could not be expected to render any dramatic influence, since the scalar viscosity is differentiated (multiplied to the symmetrised stress tensor) in the momentum equations. This shows that the nowadays popular use of a scalar eddy viscosity, common to all the components of the Reynolds tensor, is an oversimplification. Any anisotropy deviation from that of the stress tensor is suppressed. Even when we accept a scalar eddy viscosity, in the k-ε-model, k is a scalar by definition, while ε is the trace of what originally entered the scene as a tensor, the dissipation in the transport equations of the Reynolds stress tensor components, a tensor with an anisotropy that is sacrificed both, to keep the model simple and since no sound empirical indications are available to model it.

References
1. Bertram, V., Chao, K.Y., Lammers, G., and Laudan, J., "Entwicklung und Verifikation Numerischer Verfahren zur Antriebsleistungsprognose, Phase 2," Report No. 1579, The Hamburg Ship Model Basin, HSVA, 1992
2. Deng, G.B., Queutey, P., and Visonneau, M., "Navier-Stokes Computation of Ship Stern Flows: A Detailed Comparative Study of Turbulence Models and Discretization Schemes," Proceedings of the Sixth

International Conference on Numerical Ship Hydrodynamics, Iowa City, Iowa, 1993

3. Larsson, L., Patel, V.C., and Dyne, G., Editors: "Ship Viscous Flow," Proceedings of the 1990 SSPA-CTH-IIHR Workshop, Gothenburg, Research Report No. 2, Flowtech International AB, 1991

4. Sung, C.H., Griffin, M.J., Smith, W.E., and Huang, T.T., "Computation of Viscous Ship Stern and Wake Flow," The Second Osaka International Colloquium on Viscous Fluid Dynamics in Ship and Ocean Technology, Osaka, 1991, Proceedings

5. Suzuki, H., Toda, Y., and Suzuki, T., "Computation of Viscous Flow Around a Rudder Behind a Propeller - Laminar Flow Around a Flat Plate Rudder in Propeller Slipstream," Sixth International Conference on Numerical Ship Hydrodynamics, Iowa City, Iowa, 1993, Proceedings

6. Tanaka, I., "Three-Dimensional Ship Boundary Layer and Wake," Advances in Applied Mechanics, Vol. 26, 1988, Pages 311-359

7. Zhu, M., Yoshida, O., Miyata, H., and Aoki, K., "Verification of the Viscous Flow-Field Simulation for Practical Hull Forms by a Finite-Volume Method," Proceedings of the Sixth International Conference on Numerical Ship Hydrody-namics, Iowa City, Iowa, 1993

Author's Reply

Dr. Kux is right to point out that the "hook" for the HSVA1 experiment data is by no means unique, but it should not be forgotten that the other examples cited were not, in my opinion, subjected to the same degree of rigorous scrutiny as was exercised by the Hamburg term. Experiments involving supporting struts for models show that junction vortices formed where a strut joins a model can be extremely persistent and can interfere with measurements well downstream. Of course, as Dr. Kux rightly points out, in the HSVA1 case the axis of vorticity is parallel to the wire downstream and away from the model. But at the junction with the hull, the vorticity associated with the developing shear layer will be deflected as the fluid streams past the wire. Consequently, I believe it is possible that the wire represents a source of interference to the measured nominal wake and that one should not ignore its presence on the grounds, for example, that its diameter is

small or that other precedents may have been set for models towed in a tank (without support wires).

On the other hand, the work presented by Deng et al at this Conference has opened up the possibility that the hook is indeed a feature of the flow-field and not, as we have suggested, an aberration caused by the wire. It is always possible, of course, that the wire itself was responsible, in a fortuitous way, for numerically attenuating the eddy diffusivity within the bilge vortex further downstream! This needs to be confirmed and is now being investigated at Haslar.

I am unaware of any hook having been predicted unequivocally by other teams. It was my understanding that the 1990 Gothenburg Workshop prediction by Zhu and Miyata was later withdrawn after an error had been detected in the computer code (reported at the 1991 Osaka Colloquium). The numerical results for the SR196 hull series presented by Zhu. Yoshida and Miyata at this Conference do not, in my opinion, show clear signs of any hook - although it is prominent in the experiment. The results of Sung et al at the 1991 Osaka Colloquium show a very weak hook (compared with the experiment) but only for their medium grid data; the two other grids, one with eight times as many cells and the other with eight times fewer cells, show no trace whatsoever of a hook.

On a more general note, one very useful outcome of the recent ITTC effort to place CFD validation very firmly on the ship hydrodynamics agenda, has been the realization that systematic studies can indeed point to possible explanations of observed phenomena. In the case of the notorious "hook", we now have two pointers as to its possible cause and I hope very much that other teams will now join the effort to resolve this elusive riddle. While our computers may converge towards a sound numerical solution, we must step back and converge towards a sound physical solution. Whether this will involve a closer look at the precise details of the experiment, or - now more likely - a closer look at how our turbulence models can be made to deal more adequately with vortical regions, remains to be seen.

Numerical Prediction of Viscous Flows Around Two Bodies by a Vortex Method

Y.M. Scolan and O. Faltinsen
(University of Trondheim, Norway)

ABSTRACT

Viscous incompressible flows around two identical circular cylinders are simulated by using a Mixed Euler-Lagrange Method. The Vortex-In-Cell Method is combined with the Operator Splitting Technique and a Random Method. The vorticity field is represented by a set of discrete vortices which are transported in the fluid by solving the Navier Stokes equations in the subcritical flow regime. The interaction of two bodies is studied through the combination of the Conformal Mapping Technique and the Green's Theorem. The obtained results show that the physical phenomena can in general be satisfactory predicted for two cylinders in either side-by-side or tandem arrangements. Comparisons are made with experimental data for oscillating and steady ambient flows. The presented method may handle two arbitrary cross-sectional shapes. The model may also be extented to super-critical flow regimes.

NOMENCLATURE

C_i contour of cylinder $N^o i$
d distance between the centers of the two circular cylinders
a radius of one circular cylinder
ρ mass density of the fluid
U amplitude of the ambient harmonic oscillatory flow velocity or the ambient steady flow velocity
L characteristic length of one body $(L = 2a)$
T period of the oscillatory ambient flow velocity
ν kinematic viscosity coefficient
f_o frequency of vortex shedding
Δt time step

Re Reynolds number $(Re = \frac{UL}{\nu})$
KC Keulegan-Carpenter number $(KC = \frac{UT}{L})$
β Stokes parameter $(\beta = \frac{Re}{KC})$
St Strouhal number $(St = \frac{f_o L}{U})$
C_D drag coefficient
C_L lift coefficient
C_M mass coefficient

THEORETICAL MODEL

The numerical scheme is a combination of the Vortex-In-Cell Method (VIC) as it has originally been introduced by (1) and the Operator Splitting Technique used by (2) to simulate the transport of vorticity. For the two past decades the VIC Method has been continuously improved. Therefore the theory will not be detailed in the present paper but the main features of the basic method are recalled. For more details one can refer to (3) and also to the significant contributions by (4,5,6,7).

The Vortex-In-Cell Method and the Random Method

Since planar flows are considered here, the equations are formulated in terms of the vorticity ω and the stream function ψ. In the Poisson equation

$$\Delta \psi = -\omega \qquad (1)$$

the right hand side (ω) is represented by a set of Lagrangian particles (or vortices) with positions (x_l, y_l) carrying each a certain amount of circulation (Γ_l) constant in time:

$$\omega(x, y) = \sum_{l=1}^{N_v} \Gamma_l \delta(x - x_l)\delta(y - y_l) \qquad (2)$$

439

Here δ is the Dirac delta function. The vorticity field is distributed on the cell-nodes of an Eulerian mesh which covers a limited computational domain. This is done by the Area Weighting Scheme as it has been originally proposed by (1). In the present method the Poisson equation will always be solved in an annular domain. The Elliptic Solver is decomposed in a Finite Difference Method for the resolution in the radial direction and a Fast Fourier Transform for the azimuthal direction.

The generation of vortices takes place on the body contours in order to respect the no-slip condition. The local tangential component of the velocity provides the circulation of the new set of discrete vortices. The vorticity is transported in the fluid by solving the Navier Stokes equation in the laminar flow regime. The Operator Splitting Technique (OST) is used. The **convection** step consists of moving the vortices with their local velocity without change of their circulation. The convection motion is performed by a second order Runge-Kutta integration scheme. The **diffusion** step consists of superimposing a random walk to the the position of the vortices. The random numbers are distributed according to a normal law with a zero mean value and a standard deviation $\sqrt{2\nu\Delta t}$, where Δt is the time step and ν is the kinematic viscosity coefficient.

The whole process described above is repeated in time. That leads to a continuous production of vorticity. The Kelvin Theorem (zero total circulation around a curve surrounding the generated vorticity from the bodies) must be respected since no vorticity exists at the initial instant.

Due to the way that the effect of diffusion is simulated, it should be noted that all the local variables (vorticity, stream function, velocity...) and therefore the forces themselves may be affected by a small random component: this grows with $\sqrt{\Delta t/Re}$.

As the number of vortices increases in time, it is necessary to reduce the number of vortices if one wants to perform long simulations in time. This can be achieved in two ways. One concerns the treatment of vortices which enter the body due to the random walk. The technique which is used here is similar to the one presented in (6). The vortices which enter the body contour, are coalesced at the nearest nodes of the contour mesh. Then new vortices are re-injected into the fluid at a certain radial distance. This distance is chosen in the same sequence of random numbers as for the diffusion process. This technique allows one to keep constant

the rate of circulation per time step, and leads to a considerable decrease of the number of vortices present in the fluid. This optimization is particularly important for ambient oscillatory flows when many vortices remain close to the body contour due to the reversal of the flow. However this advantage still holds, but to a lesser extent, for steady incident current. In this case the coalescence of vortices far away from the bodies is the best way of reducing the number of vortices. In practice the coalescence occurs in a special region which overlaps a part of the wake far away from the bodies. As soon as this zone contains vortices enough, the coalescence happens. More details will be given later in the text in connection with the numerical modelling of the physical problem.

Extension to Multi-body Configurations

The modelling of viscous flows around multiple cylinders has been investigated for the past decade. The validation has been essentially done by comparisons with experimental data for two identical circular cylinders of radius a spaced with a distance d between the centers.

The already existing techniques consist of using several levels of overlapping meshes in the physical plane (see (6)). The successive solutions from the coarsest mesh to the finest ones provide the boundary conditions of all intermediate Boundary Value Problems (BVP). Results for the pressure have been compared with experiments in the turbulent flow regime. Those experiments have been performed in a wind tunnel (see (9) and (10)). Numerical results for two staggered cylinders are available in (11) where comparisons are made with experimental data as well. However, if one cylinder is directly situated in the wake of the second, the Vortex-In-Cell Method applied to supercritical flow regimes has difficulties. The reason is lack of accuracy in modelling the flow in the gap. The shortest gap of two tandem cylinders computed by (11), is two diameters between the cylinder centers. More recently, one can find in (12), results by using the Vortex-In-Cell Method in combination with a Random Method. They used three levels of overlapping meshes to solve the Poisson equation. The generation of vortices is otherwise achieved through an integral equation which provides directly the circulation of the newly created discrete vortices. Besides they reported that in experiments, "some aspects of large-scale wake behaviour associated with vortex shedding

440

are similar at low Reynolds numbers (100—200) and at high Reynolds numbers (greater than 10^4). Thus, for the tandem arrangement, they computed the drag force at a low Reynolds number $Re = 200$ for a spacing varying from $d/a = 2.4$ up to $d/a = 14$.

In this paper, only moderate subcritical flows are considered. The smallest computed gap is $d/a = 2.5$. Numerical difficulties may occur at a smaller gap. This has not been systematically investigated. However, it should be noted that the limitation on the value of the gaps, in the present numerical model, is connected to the discretization of the fluid domain in the close vicinity of each solid contour. In order to avoid several levels of overlapping meshes, the combination of a Conformal Mapping and the Green's Theorem is used. The convection of all the vortices present in the fluid at one time step requires three solutions of the Poisson equation. The first one will be obtained in a transformed plane. The Conformal Mapping transforms the physical fluid domain (limited by the boundaries of the two circles) into a simpler computational domain. Different types of transformation may be used. The main criteria for choosing adequate transformations are:

- the conservation (through the transformation) of both the geometrical boundary and the conditions which are prescribed on them,

- the suitability of the simplest mesh in the computational domain of the transformed plane to the physical phenomenon of interest.

This actually leads to a transformation which preserves the boundary contour as streamlines whatever the plane, and also refines the physical mesh in the gap between the two cylinders. The chosen transformation has been widely used for solving compressible flows around multi-foils. The analytical developments may be found in (13) and applications are available in (14) or (15).

The VIC Method provides a solution in the transformed plane. However this solution may not be accurate enough all over the boundary layers close to each solid boundary. Therefore additional problems should be solved for each body. The VIC Method is solved for each cylinder, in a domain (as regular as possible) surrounding the body. The outer boundary of that domain is also a circle. On this boundary a condition is established by using the Green's Theorem. Thus,

two sub-problems are successively solved in the physical plane.

Mapping of two cylinders into an annulus

The exterior domain of two arbitrary cylinders C_1 and C_2 may be mapped into an annular domain bounded by two concentric circular cylinders. The notations (see (16)) are described in figure $(1)_{(a,b)}$. The physical and transformed geometries are defined in the z-plane and the ζ-plane, respectively. The radius of cylinder $N°i$ is r_i in the physical plane. Later in the text, the radii will be chosen equal and denoted by a. The position of the center of cylinder $N°i$ is z_i. The distance between the two cylinders is denoted $d = |z_2 - z_1|$. The angle Θ is the orientation of the line joining the two centers relative to the x-axis. In the transformed plane, the radius of cylinder $N°i$ is R_i and the position of the center of the concentric cylinders is denoted ζ_o. The equation of the transformation may be written:

$$\frac{\zeta - \zeta_o}{R_1} = \frac{te^{i\Theta}}{r_1} \frac{d(z - z_1) - s(z_2 - z_1)}{d(z - z_1) - t(z_2 - z_1)} \quad (3)$$

with

$$\begin{cases} s\,t = r_1^2 \\ (d - s)\,(d - t) = r_2^2 \end{cases} \quad (4)$$

and

$$\frac{R_2}{R_1} = \frac{r_2}{r_1} \left| \frac{t}{d - t} \right| \quad (5)$$

In the general case two constants are arbitrary and for simplicity one can fix: $\zeta_o = 0$ and $\min_i(R_i) = 1$, so that the governing equation is:

$$\zeta = C\,R_1\,\frac{z\,d + A}{z\,d + B} \quad (6)$$

with

$$\begin{cases} A & = & -dz_1 - s(z_2 - z_1) \\ B & = & -dz_1 - t(z_2 - z_1) \\ C & = & \frac{te^{i\Theta}}{r_1} \end{cases} \quad (7)$$

The image of physical infinity in the transformed plane is located at $\zeta_\infty = CR_1$.

Since a constant mesh is used in the azimuthal direction of the transformed plane, the size of the cells varies considerably from one solid contour to the other one.

441

The complex inverse Jacobian[1] of the transformation is:

$$\frac{d\zeta}{dz} = \frac{C\,R_1\,(B-A)\,d}{(z\,d+B)^2} \qquad (8)$$

$$= \frac{d(CR_1-\zeta)^2}{C\,R_1\,(B-A)} \qquad (9)$$

The mapping derivative $\frac{d\zeta}{dz}$ has no singular point since $z = -B/d$ is always located inside one of the two bodies. When $|z| \to \infty$ or alternatively $\zeta \to \zeta_\infty$, the mapping derivative behaves as $\frac{1}{|z|^2}$. The Jacobian itself (i.e. $\frac{dz}{d\zeta}$) is singular at infinity.

The relation between the two complex velocities in the z- and ζ-planes are:

$$W_z = W_\zeta \frac{d\zeta}{dz} \qquad (10)$$

From this last relation, one can show that an uniform current in the physical plane is represented in the transformed plane by a doublet located precisely at $\zeta = \zeta_\infty$. The complex velocity at ζ_∞ behaves as:

$$W_\zeta^\infty \propto \frac{1}{(CR_1-\zeta)^2} \qquad (11)$$

Figures $(2)_{(a,b)}$ illustrate the Conformal Transformation. The arrow-plot shows the velocity pattern around two staggered cylinders in unseparated flow. The uniform current is directed horizontally from the left to the right. The starting point of each arrow is the image of the regular polar mesh nodes shown in the transformed plane. The image of the infinity and origin of the physical plane are also marked in the transformed plane. The mesh in the transformed plane has been expanded exponentially in the radial direction. This causes an approximately constant distance between mesh points along the line joining the centers of the two bodies in the physical plane.

SOLUTION OF THE BOUNDARY VALUE PROBLEM

Due to the linearity of the Poisson equation, the stream function can be decomposed into the following three components:

---

[1]The Jacobian of the transformation between the physical and transformed planes (respectively z and ζ) is defined as $J = dz/d\zeta$. The proper definition of the Jacobian is the ratio of the infinitely small areas of the two planes: $|dz/d\zeta|^2$.

- the unperturbed flow component (ψ_∞) corresponding to the ambient flow without any solid contours and no vortices in the fluid,

- the perfect fluid component (ψ_p) representing the perturbation of the ambient flow due to the bodies, but without any free vorticity in the fluid,

- the vortex component (ψ_v) taking into account the presence of the vortices around the solid boundaries.

The perfect fluid solution (ψ_p) is obtained by the Boundary Integral Equation Method (BIEM). The vortex solution (ψ_v) is calculated from the solutions of the VIC Method in both the transformed and the physical planes.

The Perfect Fluid Solution

This solution depends only on the geometry, the direction of the unperturbed flow $\vec{u}_\infty$ and varies linearly with $|\vec{u}_\infty|$. This solution is obtained by solving the following BVP for the stream function ψ_p:

$$\begin{aligned}\Delta\psi_p &= 0 \\ \vec{\nabla}\psi_p \cdot \vec{t} &= -\vec{u}_\infty \cdot \vec{n} \quad \text{on } (C_i)_{i=1,2} \\ |\vec{\nabla}\psi_p| &\to 0 \qquad \text{when } |z| \to \infty \end{aligned} \qquad (12)$$

A right-handed coordinate system $(\vec{n}, \vec{t}, \vec{k})$ is defined on the body contour. The unit normal vector $\vec{n}$ points into the fluid domain and the direction of $\vec{t}$ is anti-clockwise. The solution of equation (12) is represented by a distribution of sources and dipoles over the body contours. The resulting integral equation is solved by a Collocation Method. The singularity strengths vary linearly over each segment of discretization. Since the two cylinders are fixed in the plane, the matrix of the linear equation system does not depend on time but only on the geometry. This means that the perfect fluid solution can be calculated once and for all. The linear equation system is solved by a classical direct elimination scheme of the Gauss type. The velocity is also represented with an integral form by differentiating the basic integral equation for ψ_p. The total perfect fluid velocity is finally given by:

$$\vec{u} = \text{curl}(\psi_p\vec{k}) + \vec{u}_\infty \qquad (13)$$

In practice the contours of the two unit circles are each discretized into 90 segments.

442

The convergence tests showed this discretization is fine enough to have accurate results whatever the relative position of the two cylinders is. The perfect fluid velocity is calculated in the physical plane for points that are images of the polar mesh nodes defined in the transformed plane (see figures $(2)_{(a,b)}$). Thus the perfect fluid velocity at any point of the physical plane is interpolated from the values given on that mesh.

The Vortex Solution

The vortex solution gives the velocity induced by the free vortices in the fluid. The computation is divided in two main steps. A first solution is obtained in the transformed plane. This gives the convection velocity of vortices which are located beyond a certain distance from the solid boundaries. Then the Poisson equation is solved successively on two polar meshes surrounding each circular body. The latter solution gives the convection velocity of vortices close to the body contours. Figure $(1)_{(a,b)}$ give the notations of the different domains where a standard BVP is solved.

The BVP in the transformed plane

This BVP is posed in the annular domain defined by the polar coordinates $\zeta = \rho e^{i\lambda}$ and it is bounded by $R_2 < |\zeta| < R_1$. One must find the solution of:

$$\begin{aligned} \Delta\psi_v &= -\omega \quad |\zeta| \in [R_2, R_1] \\ \psi_v &= c_v^{(i)}(t) \quad \text{on } C_1 \cup C_2 \end{aligned} \quad (14)$$

where $c_v^{(i)}(t)$ are only functions of time (t). If one denotes $\delta\psi_v$ the jump of the stream function between the two bodies, then it can be calculated as the flux of velocity between the two bodies by using:

$$\begin{aligned} \delta\psi_v &= c_v^{(2)} - c_v^{(1)} = \int_{P_1}^{P_2} \vec{\nabla}\psi_v \cdot d\vec{\ell} \quad (15) \\ &= \int_{P_1}^{P_2} \vec{u}_v \cdot d\vec{n} \quad \text{with} \quad d\vec{n} = d\vec{\ell} \wedge \vec{k} \end{aligned}$$

The integration is performed between the points P_1 and P_2 which are located on the two solid contours, respectively C_1 and C_2. The vector $d\vec{\ell}$ is directed from C_1 to C_2. The set of vectors $(d\vec{n}, d\vec{\ell}, \vec{k})$ is right-handed. The quantity $\vec{u}_v$ is the physical velocity induced by the vortices only in the presence of the solid contours. This velocity is obtained at a

certain time instant from the solution calculated at the previous time step on the polar meshes surrounding each body.

A particular solution of the BVP defined in equation (14) may be obtained by taking $\omega = 0$. The solution can be written:

$$\psi_v^l(\rho, \lambda) = A(t) \log\rho + B(t) \quad (16)$$

where $A(t), B(t)$ are two functions of time. The velocity in the transformed plane is:

$$\vec{u}_v^l(\zeta) = -\frac{\delta\psi_v}{\log(R_2/R_1)} \frac{\vec{\lambda}}{\rho} \quad (17)$$

which can be expressed with its complex form in the physical plane by using equation (10):

$$W_v^l(z) = \frac{\delta\psi_v}{\log(R_2/R_1)} \frac{d\zeta}{dz} \frac{ie^{-i\lambda}}{\rho} \quad (18)$$

This solution represents a flow whose intensity increases in the gap but vanishes rapidly elsewhere.

The general vortex solution is calculated with the VIC Method. The problem given by equation (14) is solved with homogeneous Dirichlet conditions on the two solid boundaries. The computational domain is annular and the mesh is polar. The azimuthal step is constant and the number of segments is $N_\lambda = 2^7 = 128$. This is a power of 2 in order to solve the Poisson equation by using a Fast Fourier Transformation. There are N_{rad}^{C2} nodes in the radial direction. The mesh is refined exponentially close to the inner contour in order to have approximately a constant radial step in the gap of the physical plane.

The sum of the particular and general vortex solution provides the velocity $\vec{u}_v$ induced by the vortices (and only them) in the presence of the two solid contours. Finally, by adding the perfect fluid solution given by equation (13), the resulting velocity is used to convect the vortices which are located outside the outer boundary of two polar meshes surrounding each body.

The BVPs in the physical plane

In order to represent accurately the boundary layer which is formed around each solid contour, the Poisson equation is solved in an annular domain around each body. The

inner and outer boundaries are respectively the solid contours $(C_j)_{j=1,2}$ and the circles $(\Sigma_j)_{j=1,2}$ of radius r_{Σ_j} centered at the position z_i. The radii $(r_{\Sigma_j})_{j=1,2}$ are chosen so that the two outer boundaries $(\Sigma_j)_{j=1,2}$ do not intersect, but they may touch in one point.

The two BVPs are solved successively and separately in the physical plane. The calculation of the boundary conditions for each BVP is described in a coordinate system centered at the position z_i. The cartesian and polar coordinates are denoted respectively (x, y) and (r, θ) whatever the BVP since those are solved separately and in an exactly similar way.

The interaction between the two bodies appears in the outer boundary conditions. On the boundary (Σ_j) one has to match the two components of the velocity. This is achieved by using the Green's second identity, which relates the following two functions:

- the **total** stream function ψ,

- a test function φ which is harmonic.

The resulting integral equation is:

$$\int_{\Omega_e} \varphi \, \omega \, ds = \qquad (19)$$

$$\int_{\partial \Omega_e} \left[\psi \, \varphi_{,n} - \varphi \, \psi_{,n} \right] d\ell$$

where n denotes the outward normal on the contour $(\partial \Omega_e)$ The domain Ω_e is limited by the outer boundary (Σ_j), the boundary of the other cylinder $(C_i)_{i \neq j}$ and a circular control surface (Σ_∞) extending to infinity. The integral over the solid contour $(C_i)_{i \neq j}$ vanishes. This follows from the Gauss Divergence Theorem, the fact that this surface is a streamline and that the normal gradient of the stream function $(\psi_{,n})$ is exactly the tangential velocity. The latter must vanish on the contour due to the no-slip condition. It remains finally the contribution of the surfaces (Σ_j) and (Σ_∞) in the integral equation (19). On the surface (Σ_∞) the vorticity vanishes. Hence, the total stream function ψ is matched on (Σ_∞) with the stream function of the unperturbed flow plus the stream function of a dipole in order to take into account the presence of the bodies. The behavior of ψ and its radial gradient on the surface (Σ_∞) is:

$$\psi \quad \propto \quad -(\vec{u}_\infty \cdot \vec{\theta}) \left(r + O(\frac{1}{r}) \right) \quad (20)$$

$$\psi_{,r} \quad \propto \quad -(\vec{u}_\infty \cdot \vec{\theta}) \left(1 + O(\frac{1}{r^2}) \right) \quad (21)$$

The test function is otherwise calculated by using the Method of Separation of Variables. The only possible set of solutions is:

$$\varphi_m(r, \theta) = \left(\frac{r_{\Sigma_j}}{r} \right)^m e^{im\theta} \qquad (22)$$

where m is a positive integer number. The function φ_m is singular at the origin z_i, which is outside the domain Ω_e.

The stream function is decomposed in a truncated Fourier Series of the polar angle (θ), i.e.

$$\psi(r, \theta) = \frac{1}{2} \widehat{\psi}^0 \qquad (23)$$

$$+ \sum_{n=1}^{\frac{N_\theta}{2} - 1} (\widehat{\psi}^{nc} \cos n\theta + \widehat{\psi}^{ns} \sin n\theta)$$

The number of modes of the Fourier development is $\frac{N_\theta}{2}$ and N_θ denotes also the number of nodes in the azimuthal direction of the polar mesh. The expressions of ψ and φ are included in the Green's identity (19):

$$\pi \left\{ \begin{array}{l} r_{\Sigma_j} \widehat{\psi}_{,r}^{mc} + m \widehat{\psi}^{mc} \\ r_{\Sigma_j} \widehat{\psi}_{,r}^{ms} + m \widehat{\psi}^{ms} \end{array} \right\}_{r = r_{\Sigma_j}}$$

$$= \int_{\Omega_e} \omega \left\{ \begin{array}{l} \Re(\varphi_m) \\ \Im(\varphi_m) \end{array} \right\} ds \qquad (24)$$

$$+ 2 \pi \, r_{\Sigma_j} \, \delta_{m1} \left\{ \begin{array}{l} - \quad \vec{u}_\infty(t) \cdot \vec{y} \\ \vec{u}_\infty(t) \cdot \vec{x} \end{array} \right\}$$

Here δ is the Kroenecker symbol and m is an integer number of the interval $[0, \frac{N_\theta}{2} - 1]$. The equation for the mode 0 reduces to:

$$\pi \, r_{\Sigma_j} \left(\widehat{\psi}_{,r}^0 \right)_{r = r_{\Sigma_j}} = \int_{\Omega_e} \omega \, ds \qquad (25)$$

The right hand side of the last equation represents exactly the amount of circulation which lies outside the surface (Σ_j) and therefore balances the circulation which is inside the polar mesh due to the Kelvin Theorem. In the computations one may increase the stability of the simulations by taking the average of the total circulations lying inside and outside the surface (Σ_j):

$$\int_{\Omega_e} \omega \, ds = \frac{1}{2} \left(\sum_{r_l > r_{\Sigma_j}} \Gamma_l - \sum_{r_l < r_{\Sigma_j}} \Gamma_l \right) \quad (26)$$

444

The development for the non-zero modes may be pursued by using equation (2). The integral term in the right hand side of equation (24) may be developed as:

$$\int_C \omega \, \varphi_m^{(e)} ds = \sum_{r_l > r_{\Sigma_j}} \Gamma_l \left(\frac{r_{\Sigma_j}}{r_l}\right)^m e^{im\theta_l} \quad (27)$$

The outer boundary condition is a mixed (or Fourier) condition. This condition is written for a given mode m and depends only on the radius r_{Σ_j}. For body $N°j$, the BVP posed in the polar mesh may now be written as:

$$\begin{array}{ll} \psi = c_j & \text{on } C_j \\ \Delta\psi = -\omega & r < r_{\Sigma_j} \\ f(\widehat{\psi}^m) = F^m(t) & r = r_{\Sigma_j} \end{array} \quad (28)$$

where the last condition is defined by equation (24). In order to be consistent, the two first equations are Fourier tranformed. Then, the resulting BVP is classicaly solved for each mode by a Finite Difference Method. The solution ψ gives, after differentiation, the total velocity which is used to convect the vortices lying inside the two polar meshes. The non-homogeneous Dirichlet condition in the BVP defined by equation (28) does not affect the results for the velocity.

NUMERICAL PARAMETERS

Two parameters govern the physics of the problem. These are the Keulegan - Carpenter number $KC = \frac{UT}{L}$ and the Reynolds number $Re = \frac{UL}{\nu}$, where U and T are respectively the amplitude and the period of the oscillating current velocity, L is a characteristic length of the body shape. In the following applications, L denotes the diameter of one cylinder, that is to say $L = 2a$. A third coefficient is usually introduced for the oscillating flows: the Stokes Parameter $\beta = \frac{Re}{KC}$. In addition, for steady flows the Strouhal number $St = \frac{f_o L}{U}$ where f_o is the frequency of the vortex shedding, will be used.

The force acting on each body is calculated at each time instant of a simulation. The instantaneous force $F(t)$ follows from integration of the Cauchy Stress Tensor whose radial and tangential components correspond respectively to the effect of the pressure and the skin friction.

For steady incident flows, the drag coefficient (C_D) is calculated in the direction on the ambient flow, and the lift coefficient (C_L) is calculated in the transverse direction.

The force coefficients for oscillating ambient flows are partially defined by the Morison's equation which states that the force $F(t)$ in the direction of the ambient planar flow $u(t)$ can be written:

$$\begin{aligned} F(t) &= \frac{1}{2} \rho \, C_D \, L \, u(t)|u(t)| \\ &+ \frac{\pi}{4} \rho \, L^2 \, C_M \, \frac{du(t)}{dt} \end{aligned} \quad (29)$$

Here $|.|$ denotes the absolute value. The velocity oscillates at the circular frequency of oscillation $\underline{\omega}$ and behaves as $u(t) = U \sin(\underline{\omega} t)$. The drag coefficient C_D characterizes the force in phase with the ambient fluid velocity. The mass coefficient C_M is connected with the force in phase with the ambient fluid acceleration. These two main coefficients are calculated from the history of the force by Fourier averaging over one cycle. This is performed according to the following two formulas:

$$C_D = \frac{1}{\frac{1}{2}\rho U^2 L} \frac{3\underline{\omega}}{8} \int_0^T F(t) \sin(\underline{\omega} t) dt \quad (30)$$

$$C_M = \frac{1}{\frac{1}{2}\rho U^2 L} \frac{KC\underline{\omega}}{\pi^3} \int_0^T F(t) \cos(\underline{\omega} t) dt \quad (31)$$

RESULTS AND DISCUSSIONS

Computations have been performed for two arrangements of cylinders:

- two tandem cylinders in either oscillating or steady ambient flows,

- two side-by-side cylinders in a steady ambient flow.

Comparisons have been made with available experimental data. The numerical parameters are given for each arrangement and type of flow.

Two Cylinders in a Tandem Arrangement and in an Oscillating Ambient Flow

The two gaps $d/a = 4$ and $d/a = 8$ are investigated at a Stokes parameter $\beta = 534$. Comparisons are made with two sets of experimental data: by ([17]) at $\beta = 534$ and by ([18]) at $Re = 2.5 \cdot 10^4$ and $d/a = 3$ and 5.

The time simulations are always performed over a number of cycles of oscillations (N_c) as large as possible. N_c decreases mainly with an increasing Keulegan-Carpenter number and to a lesser extent with

445

an increasing Reynolds number. The final force coefficient is the mean value over the total number of simulated cycles. Besides, the standard deviations, for each coefficient, are calculated over the total number of cycles of oscillations, in order to quantify how the force coefficients vary from one cycle to another cycle.

The time step has been chosen in order to have 100 time step per period up to $KC = 2.5$ that is to say $\frac{U\Delta t}{L} = \frac{KC}{100}$. However, for higher KC, the time step is limited to $\frac{U\Delta t}{L} = 0.025$.

The simulations for two tandem cylinders have been performed by imposing numerical symmetry about the axis going through the centers of the two cylinders. This is necessary in order to avoid numerical difficulties with a possible orbital current generated during the reversal of the flow. As a matter of fact, a slight asymmetry of the boundary condition on the outer radius $(r = r_{\Sigma_j})_{j=1,2}$, may induce an orbital current along the body contour. This amplifies very rapidly since the tangential velocity, calculated on the solid contour, provides the strengths of the newly created discrete vortices. Therefore the production of vortices carrying each a very large circulation, affects seriously the stability of the time simulation. The imposed symmetry can be justified up to $KC \approx 4$. However beyond that limit the use of the numerical symmetry is more questionnable. As a matter of fact, it has been observed by (19) that the wake behind one circle starts to be asymmetric in the interval $KC \in [4, 8]$.

The figures $(3)_{(a,b)}$ and $(4)_{(a,b)}$ show the results at respectively $d/a = 4$ and $d/a = 8$. The drag coefficients are identical for the two cylinders at small KC numbers. The minimum value of C_D appears at $KC = 2.4$ and $KC = 2$ for $d/a = 4$ and $d/a = 8$, respectively. Then the drag coefficient increases with increasing KC-numbers to almost constant values of $C_D \approx 1.2$ for $d/a = 4$ and $C_D \approx 1.3$ for $d/a = 8$. The results show a small oscillatory behavior of C_D as a function of KC for $KC > 6$. This is most pronounced at $d/a = 4$. The comparison with experimental data can be made in the interval $KC \in [5, 8]$. In that range the present numerical results and the experimental data by (17) do not show the same trend. Beyond $KC = 6$, whatever the spacing, the computed drag coefficient does not increase but remains close to a constant value. However the numerical values match well with the experimental data by (18). These experimental

data have been obtained at a high subcritical Reynolds number $Re = 2.5 \cdot 10^4$ while the highest Reynolds number in the present computations is $Re = 4272$.

Concerning the mass coefficient, an asymptotic limit can be calculated at $KC = 0$. For the two gaps $d/a = 4$ and $d/a = 8$ the mass coefficient tends respectively to $C_M \approx 1.97$ and $C_M \approx 2.06$. These values can also be compared to theoretical results for a single circular cylinder. For example (20) obtained an asymptotic expansion for small KC-numbers of the mass coefficient as a function of the Stokes parameter (β). According to (20), $C_M = 2.09$ for $\beta = 534$.

For $KC \in [5, 10]$ the computed mass coefficients do not follow the decreasing trend shown by the experimental data in (17). But the present numerical data and the experimental data by (18) match well at $KC \approx 8$.

Tables (1) to (4) summarize also the performed computations. The results show that the number of simulated cycles decreases as the KC-number increases. The reason is that the maximum number of discrete vortices has been reached (this is fixed to 200.000 in the computer program). In connection with the decreasing number of simulated cycles, one should note the increasing standard deviation with increasing KC-number.

Two Tandem Cylinders in a Steady Incident Flow

For the tandem arrangement in steady incident flow, (21) reported that there exists a critical spacing in the subcritical and laminar flow regimes. This critical spacing may vary in the interval $d/a \approx [6.8, 7.6]$. Below these values, vortex shedding does not occur from the upstream cylinder but only from the downstream cylinder. Beyond this critical value, vortex shedding occurs separately from each cylinder. Results are obtained here for a spacing $d/a = 6$ (that is to say below the critical spacing) at low Reynolds numbers $Re \in [100, 500]$. The numerical parameters of the time simulation are the following:

- the time step is $\frac{U\Delta t}{a} = 0.05$ and the simulations are performed over 1000 time steps,

- the radial discretization in the transformed plane is $N_{rad}^{C2} = 200$,

446

- in the physical plane the radius of the outer boundary is $r_{\Sigma_j}/a = 2$ and the number of radial nodes N_r varies with the Reynolds number from $N_r = 21$ to 60.

The coalescence of vortices takes place in a annulus domain defined by $\frac{|z|}{a} \in [10., 11.5]$ and centered at the middle of the line joining the centers of the two cylinders. A grid of 5 radial nodes and $N_\theta = 128$ azimuthal nodes covers this annulus. Only that part of the annulus which overlaps the wake is used. The coalescence consists of replacing the vortices enclosed in that region by new vortices at the nodes of the grid. A necessary requirement is that the total circulation is constant before and after the coalescence. In the computations performed in this paper the coalescence occurred at time intervals $\frac{0.5L}{U}$.

In the range of computed Reynolds numbers and below $\frac{Ut}{a} = 20$, the instantaneous force signal, whatever the cylinder, reaches very rapidly a local maximum. Then the drag force of the upstream cylinder stabilizes around a positive constant value while the drag force of the other cylinder decreases rapidly to a negative value. Figure (5) gives an example of the force signal at $Re = 100$. From the time history of the in-line force, the drag coefficient is calculated from the average of the instantaneous force over the interval $\frac{Ut}{a} \in [20, 50]$.

The present numerical results for C_D are compared in figure (6) with:

- experimental data by (22) for $Re = 3400$,

- experimental data by (23) for $Re \in [6.10^4, 2.10^5]$,

- numerical results by (12).

The experimental data (see (24) p17) for a single cylinder are also plotted in order to show the effect of interference. The difference in the drag force between the two cylinders is noticeable. In particular the negative drag force acting on the dowstream cylinder should be noted. This follows from the presence of two large rolled-up vortices between the two cylinders. For higher Reynolds number than $Re = 1000$, instabilities of the large scale vortical structures may occur in the gap. In that case longer time simulations are necessary for good estimations of the average drag coefficients.

Two Side-by-side Cylinders in a Steady Incident Flow

The influence of the gap width on the coefficients of the flow is studied at $Re = 200$. Higher Reynolds number could be handled with the present numerical model, however long simulations are necessary in order to obtain the coefficients of the flow accurately enough. The studied spacings vary in the interval $d/a \in [2.5, 8]$. The parameters of the time simulations are the following:

- the time step is $\frac{U \Delta t}{a} = 0.1$ and the simulations are performed over 1000 time steps,

- the radial discretization in the transformed plane varies with the spacing and the number of radial nodes is fixed by the condition $N_{rad}^{C2} = 100\frac{d}{a} - 200$,

- in the physical plane the radius of the outer boundary r_{Σ_j} is chosen as large as possible and the number of radial nodes is never less than 10,

- the parameters for the coalescence are identical to those used for the tandem cylinders in a steady incident flow.

The force coefficients are calculated in the interval $\frac{Ut}{a} \in [20, 100]$ where all transient effects have disappeared. The Strouhal number is obtained by using a spectral analysis of the lift force signal over the same time interval.

The results are shown in figures (7) to (10). Comparisons are made with the experimental data reported by (21) and (25), and the numerical results by (12). The interval of studied spacings covers two typical regimes of vortex shedding for two circular cylinders in a side-by-side arrangement. A classification has been done by (21). In the first regime[2] ($d/a \in [2.4, 4]$) the vortex shedding is characterized by "narrow and wide wakes which are formed behind two identical pipes, respectively, and the gap flow forms a jet biased towards the narrow wake. The flow is bistable, i.e. the biased jet can switch in the opposite direction at irregular time intervals, and the narrow and wide wakes interchange behind the tubes". In the next regime ($d/a \in [4, 8]$), "both nearwakes are equal in size but the two vortex streets are coupled and mirror along the gap axis. The vortex shedding is synchronized, both in phase

---

[2] the exact limits of the interval of spacing (d/a) for each regime may vary with the Reynolds number

447

and frequency". In the present computations the critical spacing, i.e. the limit between the two regimes, is about $d/a = 4$. This is in agreement with the observations by (21) and the numerical results by (12). This is illustrated in figure (7) where the Strouhal number is plotted. Three frequencies may be identified according to (12) and (25) in connection with the bistable regime of the biased flow. It was the measurements of harmonic modes of vortex shedding that gave these three frequencies in (12) and (25). In the present results, only two frequencies appear clearly through the spectral analysis of the lift force signals. The analysis is difficult at $d/a = 4$. For higher values of d/a, the Strouhal number is close to the experimental value ($St \approx 0.19$) for a single circle at $Re = 200$ (see (24) p32).

The computed drag coefficients are shown in figure (8). Below $d/a = 4$, the numerical results do not reach a minimum as shown by the experimental data by (21) and (25) and also by the numerical data by (12). However there is a large difference in Reynolds numbers between the present numerical results and the experimental data reported by (21) and (25). Above $d/a = 6$ the calculated drag coefficient approaches the experimental value of $C_d \approx 1.5$ for a single cylinder at $Re = 200$ (see (24) p17).

The lift force is decomposed into a mean value and an oscillating component. The mean value (C_{L_m}) is plotted in figure (9). The sign of the lift forces on the two cylinders are opposite and act in a repulsive manner. The amplitude of the oscillating component (C_{L_o}) is plotted in figure (10) for $d/a > 4$, where the spectral analysis of the lift force signal provides only one sharp peak.

CONCLUSIONS

A theoretical model for viscous flows around two cylinders is presented. This model is based on the Vortex-In-Cell Method combined with a Random Method. The interaction is taken into account by using a conformal mapping technique and the Green's Theorem. The numerical results are validated by studying two identical cylinders in tandem and side-by-side arrangements. The force coefficients are calculated for both steady and oscillating ambient flows and compared with experimental data. The agreement is generally good. The present model can handle two cylinders of arbitrary shape by using additional conformal transformations.

BIBLIOGRAPHIC REFERENCES

1. Christiansen J.P., "Numerical simulation of hydrodynamics by the method of point vortices.", Journal of Computational Physics 13, , 1973, pp 363–379.
2. Chorin A.J., "Numerical study of slightly viscous flow.", Journal of Fluid Mechanics, Vol. 57, part 4, 1973, pp 785–796.
3. Scolan Y.M. and Faltinsen O.M., "Numerical prediction of vortex shedding around bodies with sharp corners at arbitrary KC-numbers" Osaka Colloquium '91, Japan, 1991.
4. Smith P.A., "Computation of viscous flows by the Vortex Method", Ph.D. Thesis, University of Manchester, 1986.
5. Smith P.A. and Stansby P.K., "Impulsively started flow around a circular cylinder by the vortex method", Journal of Fluid Mechanics Vol. 194, 1988, pp 45–77.
6. Smith P.A. and Stansby P.K., "An efficient surface algorithm for random - particle simulation of vorticity and heat transport", Journal of Computational Physics, Vol. 81, n° 2, 1989.
7. Smith P.A. and Stansby P.K., "Viscous oscillatory flows around cylindrical bodies at low Keulegan - Carpenter numbers using the Vortex Method", Journal of Fluid and Structures, Vol. 5, 1991, pp 339–361.
8. Stansby P.K.and Dixon A.G., "Simulation of flows around cylinders by a lagrangian vortex scheme", Applied Ocean Research, Vol. 5, N° 3, 1983.
9. Turner J.T., "Measurement of the mean and fluctuating pressure levels around a circular cylinder in the wake of another.", Report on an experimental study carried out for A/S Veritas Research, Simon Engineering Laboratories, University of Manchester, 1985.
10. Penoyre R. and Stansby P.K., "Pressure distribution on a circular cylinder in the wake of an upstream cylinder in a duct", Internal report 1986, Simon Engineering laboratories, University of Manchester.
11. Vada T. and Skomedal N.G., "Simulation of supercritical viscous flow around two cylinders in various configurations" Technical Report n° 86-2020, A.S. Veritas Research, 1986.
12. Slaouti A. and Stansby P.K., "Flow around two circular cylinders by the Random-vortex method", Journal of Fluid and Structures, Vol. 6, 1992, pp 641–670.
13. Lagally M., "The frictionless flow in a region around two circles", Translated in NACA TM-626, 1929.

14. Ives D.C., "A modern look on conformal mapping including multiply connected regions", AIAA Journal, Vol. 14, n^o8, 1976, pp 1006–1011.

15. Suddhoo A., "Inviscid compressible flow past multi–element airfoils", PhD thesis, University of Manchester, 1985.

16. Kober H., "Dictionnary of conformal representations", Dover publications, inc. 1957.

17. Sortland B., "Force measurements and flow visualization on circular cylinders", Internal report n° 86-0218, Marintek, 1987.

18. Ikeda Y., Horie H. & Tanaka N., "Viscous interference effect between two circular cylinders in harmonically oscillating flow", Journal of the Kansai Society of Naval Architects, 1985.

19. Bearman P.W., "Vortex trajectories in oscillatory flow", Proceedings of the International Symposium on Separated Flow Around Marine Structures, NTH, Trondheim, 1985.

20. Wang C.Y., "On high-frequency oscillating viscous flows", Journal of Fluid Mechanics, Vol.32, 1968, pp 55–68.

21. Zdravkovich M.M., "The effects of interference between circular cylinders in cross flow", Journal of Fluid and Structures, Vol. 1, 1987, pp 239–261.

22. Tanida Y.,Okajima A. and Watanabe Y., "Stability of a circular cylinder oscillating in uniform flow or in a wake", Journal of Fluid Mechanics, Vol.61, part 4, 1973, pp 769–784.

23. Okajima A., "Flows around two tandem circular cylinders at very high Reynolds numbers", Bulletin of the JSME, Vol. 22, n^o166, 1979.

24. Schlichting H., "Boundary-Layer Theory",McGraw-Hill Edt, 1979.

25. Williamson C.H.K., "Evolution of a single wake behind a pair of bluff bodies", Journal of Fluid Mechanics, Vol. 159, 1985, pp 1–18.

KC	N_c	C_{Df}	$\sigma_{C_{Df}}$	C_{Dp}	$\sigma_{C_{Dp}}$	C_M	σ_{C_M}
0.5	10	0.94	0.03	2.21	0.07	1.97	0.01
1.0	10	0.47	0.02	1.12	0.03	1.96	0.01
1.5	10	0.31	0.01	0.82	0.04	1.96	0.02
2.0	10	0.24	0.01	0.71	0.04	1.95	0.02
2.5	10	0.19	0.01	0.71	0.05	1.92	0.02
3.0	10	0.15	0.01	0.84	0.13	1.86	0.02
3.5	10	0.13	0.01	0.92	0.14	1.82	0.06
4.0	10	0.11	0.01	1.04	0.14	1.77	0.10
4.5	10	0.10	0.01	1.08	0.17	1.74	0.06
5.0	10	0.09	0.01	1.06	0.18	1.76	0.06
5.5	8	0.08	0.01	1.06	0.13	1.79	0.08
6.0	8	0.07	0.00	0.95	0.23	1.77	0.12
6.5	7	0.07	0.01	1.10	0.19	1.72	0.11
7.0	6	0.06	0.00	1.09	0.18	1.74	0.09
7.5	6	0.06	0.00	0.92	0.11	1.83	0.15
8.0	6	0.05	0.00	0.98	0.10	1.86	0.12

Table (1): Tandem cylinders in oscillating ambient flow with the gap width $d/a = 4$; variation of the numerically calculated force coefficients of the cylinder N^o1 with the Keulegan Carpenter number KC at $\beta = 534$; C_{Df}: drag coefficient due to skin friction; C_{Dp}: drag coefficient due to pressure; C_M: mass coefficient; σ: standard deviation of each coefficient through a total of N_c cycles of oscillation.

KC	N_c	C_{Df}	$\sigma_{C_{Df}}$	C_{Dp}	$\sigma_{C_{Dp}}$	C_M	σ_{C_M}
0.5	10	0.93	0.02	2.32	0.10	1.97	0.01
1.0	10	0.47	0.01	1.22	0.07	1.97	0.02
1.5	10	0.31	0.01	0.87	0.04	1.96	0.01
2.0	10	0.23	0.01	0.72	0.04	1.95	0.02
2.5	10	0.18	0.01	0.74	0.07	1.92	0.02
3.0	10	0.15	0.01	0.82	0.13	1.87	0.03
3.5	10	0.13	0.01	0.94	0.12	1.83	0.04
4.0	10	0.12	0.01	1.03	0.15	1.84	0.03
4.5	10	0.10	0.01	1.02	0.12	1.80	0.04
5.0	10	0.09	0.00	1.05	0.16	1.78	0.05
5.5	8	0.08	0.01	1.08	0.37	1.74	0.15
6.0	8	0.07	0.01	0.91	0.42	1.90	0.14
6.5	7	0.07	0.00	1.03	0.13	1.81	0.09
7.0	6	0.06	0.00	0.97	0.14	1.85	0.11
7.5	6	0.06	0.00	1.16	0.20	1.75	0.09
8.0	6	0.06	0.00	1.06	0.10	1.76	0.14

Table (2): Tandem cylinders in oscillating ambient flow with the gap width $d/a = 4$; variation of the numerically calculated force coefficients of the cylinder N^o2 with the Keulegan Carpenter number KC at $\beta = 534$; C_{Df}: drag coefficient due to skin friction; C_{Dp}: drag coefficient due to pressure; C_M: mass coefficient; σ: standard deviation of each coefficient through a total of N_c cycles of oscillation.

KC	N_c	C_{Df}	$\sigma_{C_{Df}}$	C_{Dp}	$\sigma_{C_{Dp}}$	C_M	σ_{C_M}
0.5	10	0.98	0.02	2.61	0.12	2.06	0.01
1.0	10	0.49	0.02	1.38	0.09	2.06	0.02
1.5	10	0.33	0.01	0.98	0.06	2.05	0.02
2.0	10	0.25	0.01	0.83	0.04	2.04	0.02
2.5	10	0.20	0.01	0.91	0.08	1.99	0.01
3.0	10	0.16	0.00	1.08	0.17	1.92	0.02
3.5	10	0.14	0.01	1.11	0.20	1.94	0.04
4.0	10	0.12	0.01	1.22	0.17	1.94	0.06
4.5	10	0.11	0.01	1.14	0.17	1.94	0.10
5.0	9	0.10	0.00	1.17	0.17	1.91	0.08
5.5	8	0.09	0.00	1.19	0.14	1.88	0.05
6.0	7	0.08	0.00	1.20	0.12	1.89	0.08
6.5	7	0.07	0.00	1.22	0.21	1.92	0.12
7.0	6	0.07	0.00	1.20	0.14	1.93	0.19
7.5	6	0.06	0.00	1.16	0.08	1.81	0.03
8.0	5	0.06	0.00	1.17	0.04	1.84	0.09

Table (3): Tandem cylinders in oscillating ambient flow with the gap width $d/a = 8$; variation of the numerically calculated force coefficients of the cylinder N^o1 with the Keulegan Carpenter number KC at $\beta = 534$; C_{Df}: drag coefficient due to skin friction; C_{Dp}: drag coefficient due to pressure; C_M: mass coefficient; σ: standard deviation of each coefficient through a total of N_c cycles of oscillation.

KC	N_c	C_{Df}	$\sigma_{C_{Df}}$	C_{Dp}	$\sigma_{C_{Dp}}$	C_M	σ_{C_M}
0.5	10	0.97	0.04	2.63	0.11	2.07	0.02
1.0	10	0.49	0.02	1.34	0.07	2.06	0.01
1.5	10	0.33	0.01	0.98	0.05	2.05	0.02
2.0	10	0.25	0.01	0.83	0.03	2.04	0.02
2.5	10	0.20	0.01	0.89	0.05	1.99	0.01
3.0	10	0.16	0.00	0.98	0.11	1.94	0.02
3.5	10	0.14	0.01	1.11	0.16	1.92	0.03
4.0	10	0.12	0.01	1.14	0.21	1.94	0.06
4.5	10	0.11	0.00	1.13	0.11	1.94	0.04
5.0	9	0.09	0.00	1.17	0.10	1.94	0.09
5.5	8	0.09	0.01	1.18	0.11	1.84	0.08
6.0	7	0.08	0.00	1.18	0.11	1.87	0.08
6.5	7	0.07	0.00	1.12	0.13	1.86	0.08
7.0	6	0.07	0.00	1.14	0.20	1.87	0.14
7.5	6	0.06	0.00	1.10	0.19	1.95	0.23
8.0	5	0.06	0.00	1.08	0.26	1.92	0.18

Table (4): Tandem cylinders in oscillating ambient flow with the gap width $d/a = 8$; variation of the numerically calculated force coefficients of the cylinder N^o2 with the Keulegan Carpenter number KC at $\beta = 534$; C_{Df}: drag coefficient due to skin friction; C_{Dp}: drag coefficient due to pressure; C_M: mass coefficient; σ: standard deviation of each coefficient through a total of N_c cycles of oscillation.
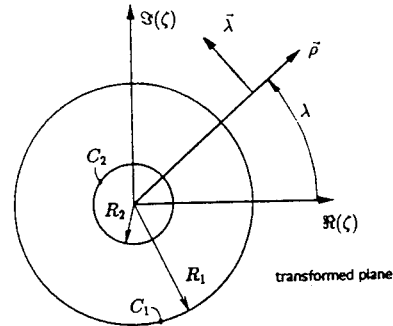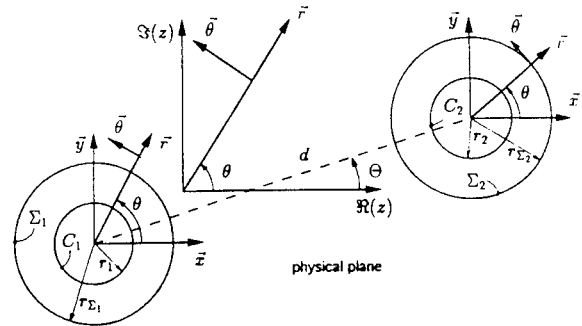

Figure 1: Conformal Mapping for two cylinders – Notations in the physical and the transformed planes
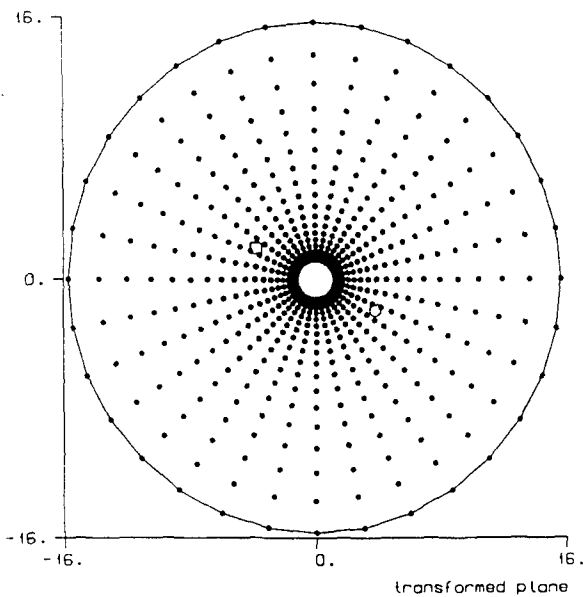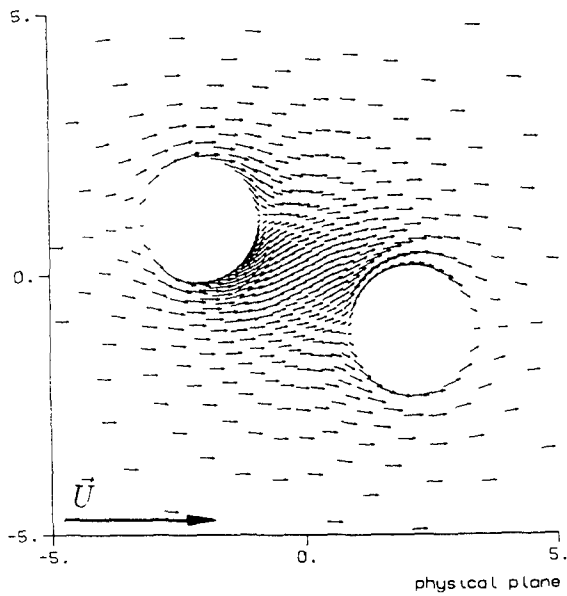
Figure 2: Unseparated flow around two staggered cylinders. The direction of the ambient flow is indicated by the big arrow. The arrow plot shows the velocity field calculated by equation (13). The start point of each arrow in the physical plane is the image of one mark (•) in the transformed plane. The image of the physical origin and infinity are marked with (o) and (□), respectively.
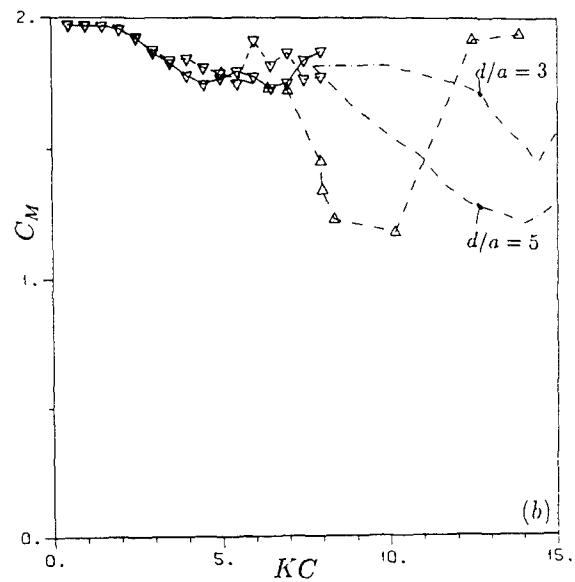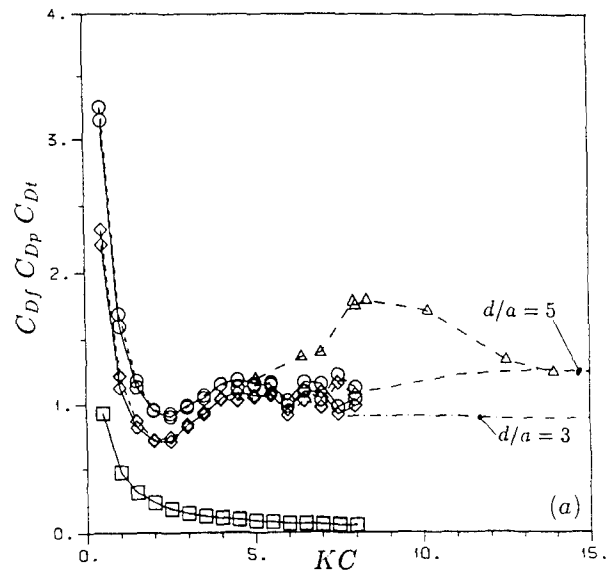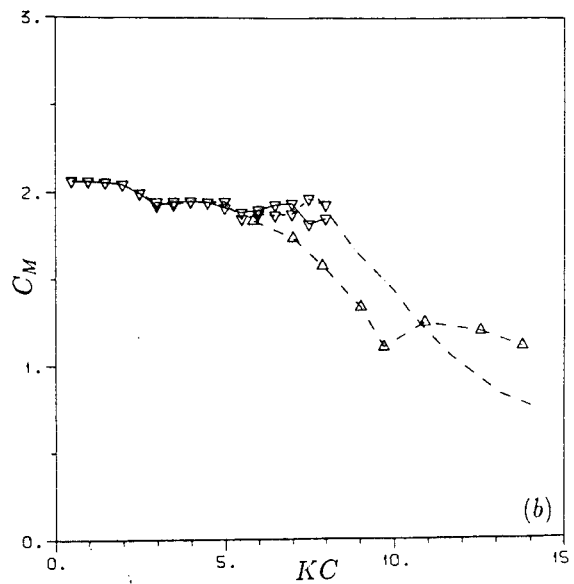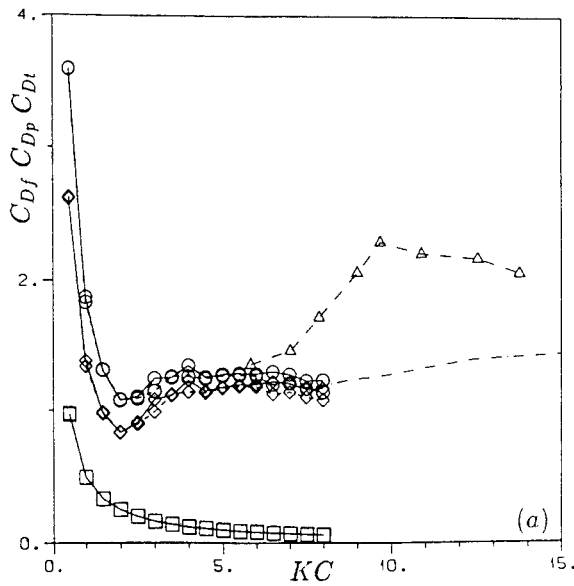
Figure 3: Force coefficients of two tandem circles at $\beta = 534$ with the gap width $d/a = 4$; drag and mass coefficients respectively in figure (a) and (b); (———): cylinder N^o1; (– – –): cylinder N^o2; ($\triangle$): experimental data from (17); (□): drag due to friction (present method); ($\diamond$): drag due to pressure (present method); (o): total drag (present method); (∇): mass coefficient (present method); (–·–·–): experimental data from (18) at $Re = 2.5 \cdot 10^4$ and $d/a = 3$ and 5.

451

(a)

(b)

Figure 4: Force coefficients of two tandem circles at $\beta = 534$ with the gap width $d/a = 8$; drag and mass coefficients respectively in figure (a) and (b); (——): cylinder $N°1$; (– – –): cylinder $N°2$; (Δ): experimental data from (17); ($\Box$): drag due to friction (present method); ($\diamond$): drag due to pressure (present method); ($\circ$): total drag (present method); (∇): mass coefficient (present method); (—·—·—): experimental data from (18) at $Re = 2.5 \cdot 10^4$ and $d/a = 8$.
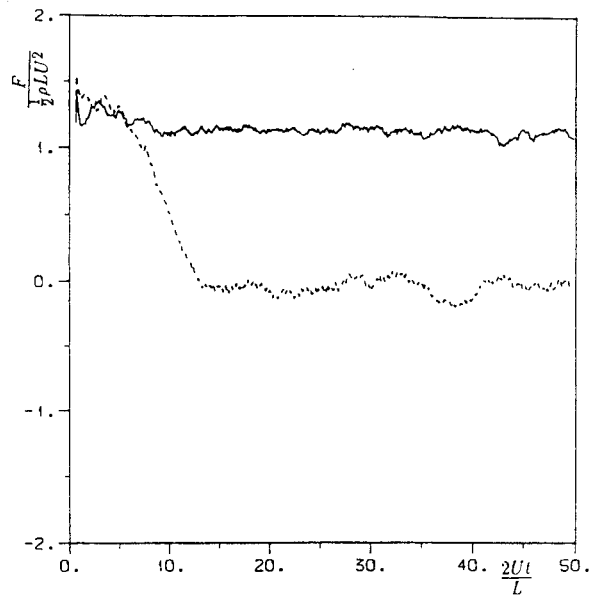

Figure 5: Drag force signal (F_x) of two tandem circles with spacing $d/a = 6$ in a steady ambient flow at $Re = 100$; (——): upstream cylinder; (- - - - - -): dowstream cylinder.
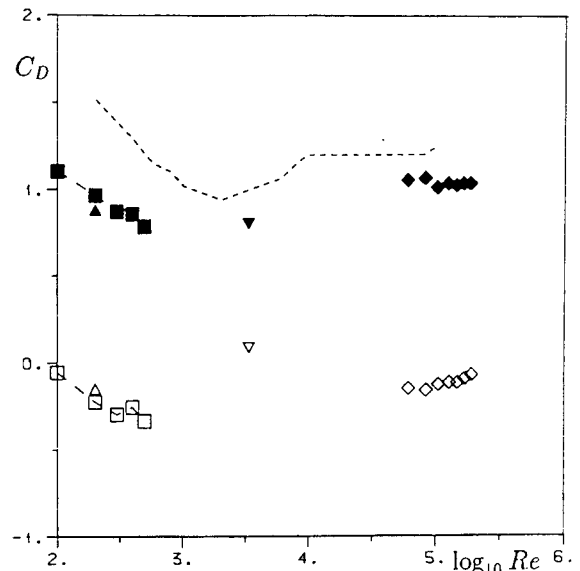

Figure 6: Drag coefficients C_D for two tandem cylinders with the spacing $d/a = 6$; the empty marks are connected to the downstream cylinder; (– – –): experimental data from (24) for a single cylinder; (∇): experimental data from (22); ($\diamond$): experimental data from (18); (Δ): numerical results from (12); ($\Box$): present numerical results
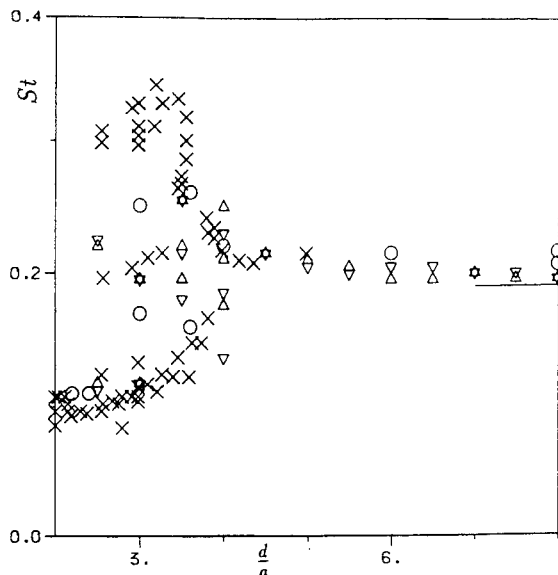
452

Figure 7: Strouhal number of two side-by-side cylinders in a steady incident flow at $Re = 200$; ($\times$): experimental data reported by (21) and (25); (Δ): upper cylinder (present numerical results); (∇): lower cylinder (present numerical results); ($\circ$): numerical results from (12) for $Re = 200$; (———): experimental data for a single cylinder reported by (24) for $Re = 200$.

Figure 8: Drag coefficients of two side-by-side cylinders in a steady incident flow at $Re = 200$; (Δ): upper cylinder (present numerical results); (∇): lower cylinder (present numerical results); ($\circ$): numerical results from (12) for $Re = 200$; ($+, \times, *$): experimental data reported by (21) and (25) at $Re = 8 \cdot 10^3$, $2.5 \cdot 10^4$ and $6 \cdot 10^4$, respectively; (———): experimental data for a single cylinder reported by (24) for $Re = 200$.
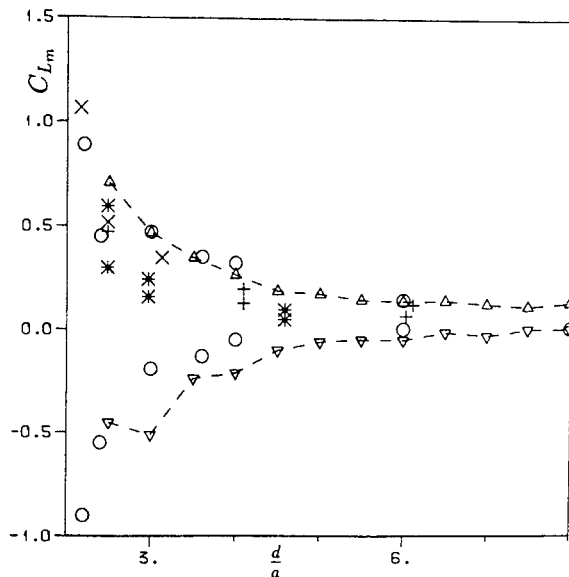

Figure 9: Mean value of the lift coefficients of two side-by-side cylinders in a steady incident flow at $Re = 200$; (Δ): upper cylinder (present numerical results); (∇): lower cylinder (present numerical results); ($\circ$): numerical results from (12); ($+, \times, *$): experimental data reported by (21) and (25) at $Re = 8 \cdot 10^3$, $2.5 \cdot 10^4$ and $6 \cdot 10^4$, respectively.
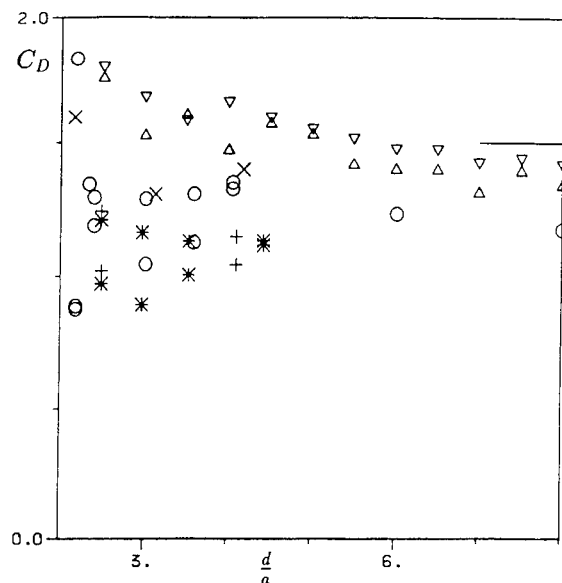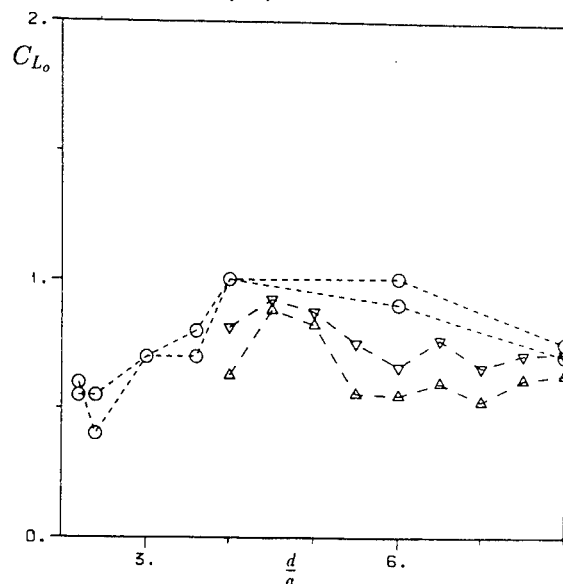

Figure 10: Amplitude of the oscillatory component of the lift coefficients of two side-by-side cylinders in a steady incident flow at $Re = 200$; (Δ): upper cylinder (present numerical results); (∇): lower cylinder (present numerical results); ($\circ$): numerical results from (12).

453

SESSION 9

VISCOUS FLOW: APPLICATIONS 2

Numerical Simulation of the Effect of Fillet Forms on Appendage-Body Junction Flow

D. Li and L.-D. Zhou

(China Ship Scientific Research Center, PRC)

ABSTRACT

The possibility of using a fillet form to control the horseshoe vortex flow caused by the turbulent shear flow around wing-body junction has been investigated numerically. A numerical method for the solution of three dimensional incompressible, Reynolds-averaged Navier-Stokes equations with the two-equation (k,ε) turbulence model has been developed to evaluate the effect of fillet forms on appendage-body junction vortex flow. The wing investigated is NACA0020. The Reynolds number based on a chordlength is 1.0×10^5. Three configurations including a baseline, a triangle fillet form, and a constant radius convex arc fillet form along the entire wing/flat-plate junction are presented. It is shown that a suitable convex filet form can significantly improve the stability of junction horseshoe vortex and reduce the strength of vortex and the non-uniformity in the wake velocity profile. It is also demonstrated the capability of the numerical approach in the design of vortex flow control devices.

1. INTRODUCTION

When an laminar or turbulent boundary layer on a surface encounters a wing or other protuberances projecting from that surface, a complex and highly three-dimensional flow results. The most significant feature of this flow is the generation of a horseshoe vortex or a set of horseshoe vortices. This horseshoe vortex forms around the nose of the wing and its legs trail downstream into the wake and forms streamwise vortices in the wake. This phenomena occurs at many places including wing/fuselage intersections in aerodynamics, appendage/hull junctions in hydrodynamics, and blade/hub junctions in propellers and turbomachinery, etc.. As a consequence of the generation of the horseshoe vortices, the drag is in general increased and the

wake velocity profile becomes significantly non-uniform. This can be a great nuisance in marine applications where a propeller operating in a non-uniform wake results in significant unsteady forces.

As well known, when a boundary layer encounters a protruded bluff body, the streamwise vortex in the form of the horseshoe vortex cannot be prevented from being generated. However, it is possible to minimize the strength of the horseshoe vortex by some flow control devices such that the resulting wake will be less non-uniform and the unsteady forces will be reduced. Experimental and numerical investigations on the use of fillet forms to reduce the interference effects have been reported before [1-5]. In these papers, the type of fillet forms are all concave. According to observation and analysis of our experimental research on the effect of fillet form[6], the strength and the unsteadiness of the horseshoe vortex and non-uniform of wake may be effectively reduced by designing a suitable convex fillet form. Here, a numerical investigation was carried to evaluate the effectiveness of the convex forms and to demonstrate the capability of the numerical approach in the design of vortex flow control devices.

A general purpose computer code for the solution of the complete three-dimensional Reynolds-averaged Navier-Stokes equation has been developed [7]. In this numerical procedure, the 3D Navier-Stokes equation is solved by finite-volume scheme in a nearly-orthogonal body-fitted coordinate system. The pressure-velocity coupling is treated with SIMPLEC algorithm [8] using a non-staggered grid. The Rhie-Chow algorithm [9] is chosen to avoid the well known problems due to chequerboard oscillations in the pressure and velocity fields which are traditionally associated with the naive use of non-staggered grids. The system of algebraic equations formed by the assembly of the convection-diffusion and pressure equations are solved by the strongly implicit procedure (SIP) algorithm and the preconditioned conjugate gradients (PCG) algorithm [7]. The two-

equation k-ε model with wall functions is used for the turbulent flow involving separation and vortices.

This numerical procedure is used in the present investigation. Three configurations including a baseline configuration consisting of a wing mounted on a flat-plate junction, a triangle fillet form, and a constant radius convex arc fillet form along the entire wing/flat-plate junction are presented here. The numerical solutions were used to evaluate the relative effectiveness of the three configurations. Particular emphasis is placed on the discussion of effectiveness of convex fillet forms on the stability of the horseshoe vortex.

2. NUMERICAL METHOD

2.1 Governing Equations

We consider the governing equations in Cartesian coordinates $(x^i, t) = (x, y, z, t)$ for unsteady, three-dimensional, incompressible flow. The complete three-dimensional Reynolds-averaged equations of continuity and momentum of the mean flow are

$$\frac{\partial \rho U^i}{\partial x^i} = 0 \tag{1}$$

$$\frac{\partial U^i}{\partial t} + \frac{\partial}{\partial x^j}(\rho U^j U^i + \rho \overline{u^j u^i}) = -\frac{\partial p}{\partial x^i} + \frac{\partial}{\partial x^j}(\mu(\frac{\partial U^j}{\partial x^i} + \frac{\partial U^i}{\partial x^j})) \tag{2}$$

where $U^i = (U, V, W)$ and $u^i = (u, v, w)$ are, respectively, the Cartesian components of the mean and fluctuating velocities, t is time, p is pressure, ρ is mass density, and μ is dynamic viscosity.

If the Reynolds stresses $\overline{u^i u^j}$ are related to the corresponding mean rate of strain through an isotropic eddy viscosity v_t,

$$-\overline{u^i u^j} = v_t(\frac{\partial U^i}{\partial x^j} + \frac{\partial U^j}{\partial x^i}) - \frac{2}{3}\delta_{ij}k \tag{3}$$

where $k = (\overline{uu} + \overline{vv} + \overline{ww})/2$ is the turbulent kinetic energy. Here, v_t is related to the turbulent kinetic energy k, and its rate of dissipation ε, by the two-equation k-ε model

$$v_t = C_\mu \frac{k^2}{\varepsilon}, \qquad \mu_t = \rho v_t \tag{4}$$

and k and ε are obtained from the transport equations

$$\frac{\partial k}{\partial t} + \frac{\partial \rho U^i k}{\partial x^i} = \frac{\partial}{\partial x^i}\left(\frac{\mu_t}{\sigma_k}\frac{\partial k}{\partial x^i}\right) + \rho(G - \varepsilon) \tag{5}$$

$$\frac{\partial \varepsilon}{\partial t} + \frac{\partial \rho U^i \varepsilon}{\partial x^i} = \frac{\partial}{\partial x^i}\left(\frac{\mu_t}{\sigma_k}\frac{\partial \varepsilon}{\partial x^i}\right) + \rho\frac{\varepsilon}{k}(C_1 G - C_2\varepsilon) \tag{6}$$

where G the rate of production of k is defined by

$$G = v_t \sum_{i=1}^{3}\sum_{j=1}^{3}(\frac{\partial U^i}{\partial x^j} + \frac{\partial U^j}{\partial x^i})^2 \tag{7}$$

and $(C_\mu, C_1, C_2, \sigma_k, \sigma_\varepsilon)$ are constants whose values are (0.09, 1.44, 1.90, 1.0, 1.3).

It is convenient to rewrite the equation of continuity and the transport equations(1),(2),(5),(6) for momentum(U,V,W) and turbulence quantities(k, ε) in the following general form:

$$\frac{\partial \phi}{\partial t} + \frac{\partial}{\partial x^i}(\rho U^i \phi) = \frac{\partial}{\partial x^i}\left(\Gamma^\phi \frac{\partial \phi}{\partial x^i}\right) + S^\phi \tag{8}$$

where ϕ again represents any one of the convective transport quantities (U,V,W,k,ε). The scalar diffusivity Γ^ϕ and source functions S^ϕ for U^i, k and ε are, respectively,

$$\left.\begin{aligned}\Gamma^\phi &= \mu + \mu_t \\ S^\phi &= -\frac{\partial}{\partial x^i}(p + \frac{2}{3}\rho k) + \frac{\partial}{\partial x^j}\left((\mu + \mu_t)\frac{\partial U^j}{\partial x^i}\right)\end{aligned}\right\} \quad \phi = U^i \tag{9a}$$

$$\Gamma^k = \mu_t/\sigma_k, \qquad S^k = \rho(G - \varepsilon) \tag{9b}$$

$$\Gamma^\varepsilon = \mu_t/\sigma_\varepsilon, \qquad S^\varepsilon = \rho\frac{\varepsilon}{k}(C_1 G - C_2\varepsilon) \tag{9c}$$

2.2 Body-Fitted Coordinate Systems

In order to extend the capabilities of the difference methods to deal with complex geometries, a curvilinear coordinate transformation is used to map the complex flow domain in physical space to a simple (i.e. rectangular) flow domain in computational space. In other words, the Cartesian coordinate system $(x^i) = (x, y, z)$ in the physical domain is replaced by a curvilinear coordinate system $(\xi^i) = (\xi, \eta, \zeta)$ such that boundaries of the flow domain correspond to surfaces ξ^i = constant.

For the present application to wing-body junction flow with fillet forms, the body-fitted numerical grids were generated by a system of elliptic partial differential (Possion) equations of the form of

$$\nabla^2 \xi^i = f^i \quad (i = 1, 2, 3) \tag{10}$$

458

Here, ∇^2 is the Laplacian operator in Cartesian coordinates x^i. The nonhomogeneous source functions f^i may be assigned appropriate values to yield desirable grid distributions. In practical applications, the inverse transformation of equation(10) is used to obtain the coordinate transformation relations $x^i = x^i(\xi^i)$, i.e.,

$$\nabla^2 x^i = 0 \quad (i=1,2,3) \tag{11}$$

where ∇^2 is the Laplacian operator in the transformed plane.(ξ^i). Using the transformation relations, the equation(11) can be rewritten as,

$$g^{jk}\frac{\partial^2 x^i}{\partial \xi^j \partial \xi^k} + f^j\frac{\partial x^i}{\partial \xi^j} = 0 \tag{12}$$

where g^{jk} is the inverse metric tensor[7]. The grid-control functions f^i were determined by the specified boundary-node distribution in this paper.

The body-fitted numerical grids generated by above method is a general non-orthogonal coordinate system. In order to simple the calculation and ensure the accuracy of solution, it is important to ensure that the grid is nearly orthogonal at boundaries. In present study, a corrective method[7] is used to generate nearly orthogonal grids.

2.3 Transformation of the Equations

The price that has to be paid for the simplicity of implementing boundary conditions using body-fitted coordinate systems is the increase in complexity of the governing equations when the Cardesian coordinates is transformed to the non-orthogonal coordinate system(ξ^i). The vector operation in the transformed plane is

$$\nabla \bullet V = \frac{1}{\sqrt{g}}\frac{\partial}{\partial \xi^i}(\sqrt{g}V^i) = \frac{1}{\sqrt{g}}\frac{\partial \hat{V}^i}{\partial \xi^i} \tag{13}$$

where $\hat{V}^i$ are the normal flux components of V, as defined in [7]. It is convenient to write equation(8), in the steady state, in the equivalent form:

$$\frac{\partial I^i}{\partial x^i} = S \tag{14}$$

where I^i is called the total(i.e. convective + diffusive) flux, and is given by:

$$I^i = \rho U^i\phi - \Gamma\frac{\partial \phi}{\partial x^i} \tag{15}$$

Using the expression (13) for the covariant divergence, we obtain immediately:

$$\frac{1}{\sqrt{g}}\frac{\partial}{\partial \xi^i}(\sqrt{g}I^{i}) = S \quad \Leftrightarrow \quad \frac{\partial \hat{I}^i}{\partial \xi^i} = \sqrt{g}\,S \tag{16}$$

i.e. exactly the same form as equation(14), with the effective total flux given in contravariant and normal components by:

$$\hat{I}^i = \sqrt{g}I^{i} = \rho\hat{U}^i\phi - \sqrt{g}g^{ij}\Gamma\frac{\partial \phi}{\partial \xi^j} \tag{17}$$

Summarizing, the governing equations in computational space are:

$$\frac{\partial \hat{I}^i}{\partial \xi^i} = \sqrt{g}\,S \tag{18}$$

$$\hat{I}^i = \rho\hat{U}^i\phi - \Gamma^{ij}\frac{\partial \phi}{\partial \xi^j} \tag{19}$$

where $\hat{U}^i$ the normal flux components are the scalar products of velocity vector U with the area vectors

$$\hat{U}^i = \sqrt{g}U^i = U\bullet A^{(i)} \tag{20}$$

and

$$\Gamma^{ij} = \sqrt{g}g^{ij}\Gamma \tag{21}$$

Note that the effective diffusion tensor Γ^{ij} is a symmetric tensor, by virtue of the fact that g^{ij} is symmetric. Also, it is diagonal if and only if g^{ij} is diagonal, so the effective diffusion tensor is orthotropic if and only if the coordinate transformation is orthogonal, and it is fully anisotropic if and only if the coordinate transformation is strictly non-orthogonal. Due to its importance in the subsequent discretization process, we give the tensor multiplier in (21) a special symbol:

$$G^{ij} = \sqrt{g}\,g^{ij} \tag{22}$$

and we call G^{ij} the geometric diffusion coefficients.

2.4 Discretization of Equations

The discretisation of the advection-diffusion equation is now straightforward. Integrating (18) over a control volume in computational space, we obtain, since computational space control volumes are unit cubes:

459

$$[\hat{f}^1]_u^d + [\hat{f}^2]_n^s + [\hat{f}^{3'}]_e^w = <\sqrt{g}\,S>_p \qquad (23)$$

where nn(nearest neighboring face) = u, d, n, s, e, or w as shown in Figure 1. Using (19), we have:

$$\hat{f}_{nn}^i = \left(\rho\hat{U}^i\phi - \Gamma^{ij}\frac{\partial\phi}{\partial\xi^j}\right)_{nn} \qquad (24)$$

or

$$\hat{f}_{nn}^i = C_{nn}^i\phi_{nn} - D_{nn}^{ij}\left(\frac{\partial\phi}{\partial\xi^j}\right)_{nn}, \quad i = \begin{cases}1, & nn=u,d\\2, & nn=n,s\\3, & nn=e,w\end{cases} \qquad (25)$$

where C_{nn}^i, D_{nn}^{ij} are the convection and anisotropic diffusion coefficients defined by:

$$C_{nn}^i = (\rho\hat{U}^i)_{nn} = (\rho U\cdot A^{(i)})_{nn} \qquad (26)$$

$$D_{nn}^{ij} = \Gamma_{nn}^{ij} = \Gamma_{nn}G_{nn}^{ij} \qquad (27)$$

The standard convection and diffusion coefficients are given by:

$$C_{u,d} = C_{u,d}^1 \qquad C_{n,s} = C_{n,s}^2 \qquad C_{e,w} = C_{e,w}^3$$
$$D_{u,d} = D_{u,d}^{11} \qquad D_{n,s} = D_{n,s}^{22} \qquad D_{e,w} = D_{e,w}^{33}$$

The Rhie-Chow algorithm[9] is used for the interpolation of velocity components to control volume faces required for the computation of convection coefficients. We employ hybrid differences, i.e. central differences when mesh Peclet number is less than 2 and upwind differences when mesh Peclet number is greater than 2, for the values of ϕ on control volume faces appearing in the convection term of equation (25). We employ central differences for the normal and 'cross-derivatives' of ϕ appearing in the diffusion term of (25) (See Figure 2). For example, we have:

$$\left(\frac{\partial\phi}{\partial\eta}\right)_u = \frac{1}{4}(\phi_N - \phi_S + \phi_{UN} - \phi_{US})$$

$$\left(\frac{\partial\phi}{\partial\zeta}\right)_u = \frac{1}{4}(\phi_E - \phi_W + \phi_{UE} - \phi_{UW}), \qquad \text{etc.}$$

Explicitly, we obtain, substituting (25) into the discretisation equation (23):

$$\left(\sum_{nn}a_{nn} + s_m\right)\phi_p - \sum_{nn}a_{nn}\phi_{NN} - S' = <|J|S>_p \qquad (28)$$

where ϕ_{NN} are the values of ϕ at nearest neighboring points, a_{nn} are the standard matrix coefficients obtained using hybrid differencing normal to control volume faces, and s_m is a mass source term, i.e.

$$a_U = \max(\tfrac{1}{2}|C_u|, D_u) - \tfrac{1}{2}C_u$$
$$a_D = \max(\tfrac{1}{2}|C_d|, D_d) + \tfrac{1}{2}C_d \qquad \text{etc.} \qquad (29)$$
$$s_m = C_u - C_d + C_n - C_s + C_e - C_w$$

S' is the extra term arising from the cross-derivatives due to the non-orthogonality of the grid:

$$S' = \left[D^{12}\frac{\partial\phi}{\partial\eta} + D^{13}\frac{\partial\phi}{\partial\zeta}\right]_d^u + \left[D^{21}\frac{\partial\phi}{\partial\xi} + D^{23}\frac{\partial\phi}{\partial\zeta}\right]_s^n + \left[D^{31}\frac{\partial\phi}{\partial\xi} + D^{32}\frac{\partial\phi}{\partial\eta}\right]_w^e \qquad (30)$$

In full, we have:

$$
\begin{aligned}
4S' =\ & (\phi_U - \phi_D)(D_n^{21} - D_s^{21} + D_e^{31} - D_w^{31})\\
& + (\phi_N - \phi_S)(D_u^{12} - D_d^{12} + D_e^{32} - D_w^{32})\\
& + (\phi_E - \phi_W)(D_u^{13} - D_d^{13} + D_n^{23} - D_s^{23})\\
& + \phi_{UN}(D_u^{12} + D_n^{12}) - \phi_{US}(D_u^{12} + D_s^{12})\\
& + \phi_{UE}(D_u^{13} + D_e^{13}) - \phi_{UW}(D_u^{13} + D_w^{13})\\
& - \phi_{DN}(D_d^{12} + D_n^{12}) + \phi_{DS}(D_d^{12} + D_s^{12})\\
& - \phi_{DE}(D_d^{13} + D_e^{13}) + \phi_{DW}(D_d^{13} + D_w^{13})\\
& + \phi_{NE}(D_n^{23} + D_e^{23}) - \phi_{NW}(D_n^{23} + D_w^{23})\\
& - \phi_{SE}(D_s^{23} + D_e^{23}) + \phi_{SW}(D_s^{23} + D_w^{23}) \qquad (31)
\end{aligned}
$$

and inserting (31) into (28) gives the requires linear equations for ϕ over a 19-point difference molecule. However, we employ a deferred correction approach, whereby the extra terms S' are absorbed into the source term on the right hand side of equation (28). Thus, linearising the source term in the usual fashion:

$$<|J|S> = V_c<S> = s_\phi + s_0\phi_p$$

we obtain the linear equations:

460

$$a_p \phi_p - \sum_{nn} a_{nn} \phi_{NN} = s_\phi + S' \qquad (32)$$

where

$$a_p = \sum_{nn} a_{nn} - s_p, \qquad s_p = s_0 - s_m$$

Therefore, the 19-point molecule is reduced to a 7-point molecule, and the use of hybrid differencing to compute the matrix coefficients of this 7-point molecule guarantees diagonal dominance of the resulting matrix if the linearisation of the source term is chosen so that $s_p \le 0$.

2.5 Velocity-Pressure Coupling Algorithm

If the pressure is known, equation (32) can be employed to solve equation (18) for U, V, W, k, ε. In practice, however, the pressure is not known a priori and must be determined by requiring the velocity field to satisfy the equation of continuity (1). Here, we derive the pressure-correction equation obtained by applying the SIMPLEC algorithm [8] to the momentum equations (32) for Cartesian velocity components on the non-staggered grid.

Let U^{i*}, P^* denote the most recently updated velocity and pressure fields after the linearised momentum equations have been solved. From the equations (32), we may write the momentum equations in the form:

$$U^i_p{}^* = \sum_{nn} \frac{a_{nn} U^i_{NN}{}^*}{a_p} + S'_{U^i} - B^k_i \frac{\partial P^*}{\partial \xi^k} \qquad (33)$$

where S'_{U^i} are the remaining source terms after the pressure gradient source terms have been removed (i.e. the non-pressure gradient and the non-orthogonality source terms) divided by the matrix diagonal $a_{p,}$, and B^k_i is the matrix multiplier of the computational space pressure gradients:

$$B^k_i = \frac{A^k_i}{a_p} \qquad (34)$$

Now a solution U^{i*} of (33) does not in general satisfy the continuity equation; it has a residual mass source:

$$m_p = [\rho \hat{U}^{1*}]^u_d + [\rho \hat{U}^{2*}]^n_s + [\rho \hat{U}^{3*}]^e_w$$
$$= C_u{}^* - C_d{}^* + C_n{}^* - C_s{}^* + C_e{}^* - C_w{}^* \qquad (35)$$

The term in (35) involve the values of the normal velocity components on mass control volume faces, and these must be approximated somehow from the velocity components U^{i*}_p at mass control volume centers. The prescription for doing this is the whole crux of the Rhie-Chow algorithm.

The main idea of the SIMPLEC algorithm is to find update velocity and pressure fields U^{i**}, P^{**} obeying the discrete momentum equations and the discrete continuity equation:

$$U^i_p{}^{**} = \sum_{nn} \frac{a_{nn} U^i_{NN}{}^{**}}{a_p} + S'_{U^i} - B^k_i \frac{\partial P^{**}}{\partial \xi^k} \qquad (36)$$

$$[\rho \hat{U}^{1**}]^u_d + [\rho \hat{U}^{2**}]^n_s + [\rho \hat{U}^{3**}]^e_w = 0 \qquad (37)$$

We use the term $\frac{a_{nn}}{n\hat{n}^a_p} U^i_p$ to minus the bath hand of (36) and (37):

$$(1 - \sum_{nn} \frac{a_{nn}}{a_p}) U^i_p{}^* = \sum_{nn} \frac{a_{nn}(U^i_{NN}{}^* - U^i_p{}^*)}{a_p} + S'_{U^i} - B^k_i \frac{\partial p^*}{\partial \xi^k} \qquad (38)$$

$$(1 - \sum_{nn} \frac{a_{nn}}{a_p}) U^i_p{}^{**} = \sum_{nn} \frac{a_{nn}(U^i_{NN}{}^{**} - U^i_p{}^{**})}{a_p} + S'_{U^i} - B^k_i \frac{\partial p^{**}}{\partial \xi^k} \qquad (39)$$

Assuming:

$$p' = p^{**} - p^*, \qquad U^{i'} = U^{i**} - U^{i*}$$

and

$$\sum \frac{a_{nn}(U^{i'}_{NN} - U^{i'}_p)}{a_p} = 0$$

we obtain the following formulae for the velocity- and pressure-corrections by (39) – (38):

$$U^{i**} = U^{i*} - B^k_i \frac{\partial p'}{\partial \xi^k} \qquad (40)$$

where

$$B'^k_i = \frac{B^k_i}{(1 - \frac{a_{nn}}{n_i\partial p})} \qquad (41)$$

Thus we obtain update velocity and pressure fields satisfying exact mass continuity and approximately satisfying the discrete momentum equations.

It follows that the corrected values of the normal velocity flux components $\hat{U}^i = A^i_j U^j$ are given by:

$$\hat{U}^{i**} = \hat{U}^{i*} - C^{ij}\frac{\partial p'}{\partial \xi^j} \qquad (42)$$

where

$$C^{ij} = A^i_k B^j_k = \frac{A^i_k A^j_k}{a_p} = \frac{\sqrt{g}}{a_p}G^{ij} \qquad (43)$$

The pressure-correction equation is obtained by substituting (42) into the continuity equation (37). We obtain:

$$b_p P'_p = \sum_{nn} b_{nn} P'_{NN} + S' - m_p, \qquad b_p = \sum_{nn} b_{nn} \qquad (44)$$

where

$$b_{U,D} = (\rho C^{11})_{u,d}$$

$$b_{N,S} = (\rho C^{22})_{n,s}$$

$$b_{E,W} = (\rho C^{33})_{e,w} \qquad (45)$$

and S' are the additional terms due to non-orthogonality. It can be obtained by (30) for $\phi = P$ and

$$D^{ij}_{nn} = (\rho C^{ij})_{nn} = \left(\rho\frac{\sqrt{g}}{a_p}G^{ij}\right)_{nn} \qquad (46)$$

2.6 Solution Procedure

The system of algebraic equations is formed by the assembly of the convection-diffusion and velocity-pressure correction equations (28) and (44). This approach ignores the non-linearity of the underlying differential equations. Therefore iteration is used at two levels; an inner iteration to solve for the spatial coupling for each variable and an outer iteration to solve for the coupling between variables. Thus each variables is taken in sequence, regarding all other variables as fixed. By always

reforming coefficients using the most recently calculated values of the variables.

In present paper, the U, V, W equations are solved by the SIP algorithm with 5 internal iterations; the P pressure equation is solved by the PCG algorithm with 30 internal iterations; the k, ε equations are solved by the ADI (Alternating-Direction-Implicit) algorithm with 4 internal iterations. different iteration methods. The mass source residual, the error in continuity, is chosen as stopping criteria for the outer iteration.

3. CFD VISUALIZATION

One of the great problems with three-dimensional flow calculations is that of interpreting the sheer amount of outputs of the numerical method. Thus an integrated CFD visualization system VISPLOT [10] is developed to process and analysis the numerical results of this paper. The VISPLOT has a friend user-interface which converts the results into a database and allows the user to dialogue with computer and database. Three forms of data processing are carried out: on one-dimensional grid lines, two-dimensional grid planes, or full three-dimensional graphics. The facilities of VISPLOT include:

a) Color contours of scalar quantities in grid slices and planes.
b) Profiles of the variables on arbitrary lines through the computational domain.
c) Velocity vector plots.
d) Particle tracks.
e) Full exploitation of color to bring out the features of the flow, for example, to overlay velocity vector plots with contours of the pressure.
f) 3D plot of grid distribution, geometry of problems, or velocity fields etc..

4. RESULTS AND DISCUSSION

We have selected the same configuration used in our experiments[6]. The wing is 25.9 cm chord length, consisting of a 3:2 semielliptic leading edge and a NACA 0020 aft section. The baseline configuration consists of the wing mounted on the flat-plate(See Fig. 3(a)). The triangle fillet form is a triangle form of side length 0.1C along entire wing/flat-plate junction(See Fig. 3(b)). The Convex arc fillet form is a circular arc form of radius 0.1C along entire wing/flat-plate junction(See Fig. 3(c)). Here, C is chord length of the wing. All computations of turbulent junction flows with and without fillet forms were made on the 50×30×30 nearly-orthogonal grids(See Fig. 3). The solution

domain consisted of a semicircular cylinder of radius R/C = 1.5 attached to a rectangular region 0 < X/C < 2.5, 0 < Y/C < 1.5, 0 < Z/C < 1.5. The first spacing normal to the flat-plate and wing is on the order of 0.001C. The mass source residual less than 10^{-4} was chosen to judge whether convergence has been achieved. In generally the solution became convergence at about 180 cycle outer iterations using about 8 CPU hours on a PC-486/50.

As mentioned earlier, the main objective of using a fillet form is to weaken the horseshoe vortex generated. A simple method can be used to judge these fillet forms with minimum ambiguity on whether the vortex generated in one form is stronger or weaker than the vortex generated by another form. It is by comparing the sharpness of the kinks in the C_p profiles near the leading edge. Sharper kinks in the C_p profiles imply that a stronger vortex has been generated. Applying this criterion to the Cp profiles of the baseline, the triangle fillet form and the convex arc fillet form shown in Figures 4(a), 4(b), and 4(c), it can be seen that the strong kinks exist in the C_p profile of the baseline. But the kinks also exist in the C_p profiles of the fillet forms. This implies that the strength of vortex generated will not be effectively reduced by unsuited fillet forms.

The velocity vector fields in the symmetry plane in front of the leading edge of the baseline, the triangle fillet form and the convex arc fillet form are shown in Figures 5(a), 5(b), and 5(c). It can be seen that the vortex generated by the baseline is an elliptic form but the vortices generated by the fillet forms are circular forms. It means that the vortex generated by the baseline is unstable and will become low-frequently oscillating vortex but the vortex generated by the fillet forms, specially by the convex fillet form, may be stable and adhere the junctions. It is very similar with the observation of our experiments [6]. It implies that the convex fillet form can control the unstable vortex generated by the junction configuration.

Figures 6(a), 6(b), and 6(c) of velocity vectors in transverse section x/C = 2.14 clearly show the streamwise vortices in the wake formed by ahead horseshoe vortices. These vortices cause the wake velocity profiles becoming significantly nonuniform (See Figure 7(a), 7(b), and 7(c)). The velocity fields around the leading edge of wing at z/C = 0.01 horizontal plane are shown in Figures 8(a), 8(b), and 8(c). They show the flow reversal in fornt of the wing associated with the ahead vortex.

5. CONCLUSIONS

An improved numerical method for the solution of the complete three-dimensional incompressible, Reynolds-averaged Navier-Stokes equation based on finite-volume scheme in a non-staggered grid has been applied to evaluate the effect of fillet forms on wing-body junction flow. Three configurations including a baseline, a triangle fillet form, and a convex arc fillet form were considered. The computed pressures on the entire flat-plate are first used to discuss the effectiveness of the fillet forms in terms of the ability of each to reduce the strength of the horseshoe vortex. The velocity vector fileds in the symmetry plane ahead leading edge of the wing are used to analysis the ability of each to improve the stability of the horseshoe vortex. It has been demonstrated that the numerical approach is a valuable tool for evaluation of the effectiveness of the fillet forms and the design of vortex flow control devices. It is the main purpose of this paper.

REFERENCES

1. Sung, C.H., Michael, J.G., and Roderick, M.C., "Numerical Evaluation of Vortex Flow Control Devices," AIAA paper 91-1825, AIAA 22nd Fluid Dynamics, Plasma Dynamics & Lasers Conference, June 24-26, 1991, Hawaii.

2. Kubendran, L.R., Bar-sever, A. and Harvey, W.D., "Juncture Flow Control Using Leading-Edge Fillets," AIAA Paper 85-4097, 1985.

3. Kubendran, L.R., Bar-sever, A. and Harvey, W.D., "Flow Control in a Wing/Fuselage-type Juncture," AIAA Paper 88-0614, 1988.

4. Pierce, F.J., Frangistas, G.A. and Nelson, D.J., "Geometry Modification Effects on Junction Vortex Flow," Symposium on Hydrodynamic Performance Enhancement for Marine Application, Newport, RI, November, 1988.

5. Sung, C.H., and Yang, C.I., "Control of Horseshoe Vortex Juncture Flow Using A Fillet," Symposium on Hydrodynamic Performance Enhancement for Marine Application, Newport, RI, November, 1988.

6. Li, D.,and Zhou, L.D., "The Effect of Juncture Form on Appendage-Body juncture Flow," Osaka Colloquium '91, Japan.

7. Li, D., "Viscous Flow Around Body-Wing Junctures," Ph.D. Thesis, China Ship Scientific Research Center, 1992.

8. Von Doormal, J.P. and Raithby, G.D., " Enhancements of the SIMPLE Method for Predicting Incompressible Fluid Flows," Numerical Heat Transfer, Vol 7, pp147-163, 1984.

9. Rhie, C.M. and Chow, W.L., "Numerical Study of Turbulent Flow Past an Airfoil with
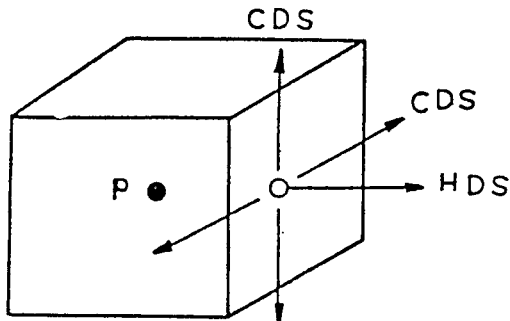
Trailing Edge Separation," AIAA Journal, Vol 21,
No. 11, pp 1525-1532, 1983.

10. Li, D. and Zhou, L.D., "Computational
Fluid Dynamics Visualization System," To be
Published in Journal of Hydrodynamics, 1993

(a) Unfilleted Case
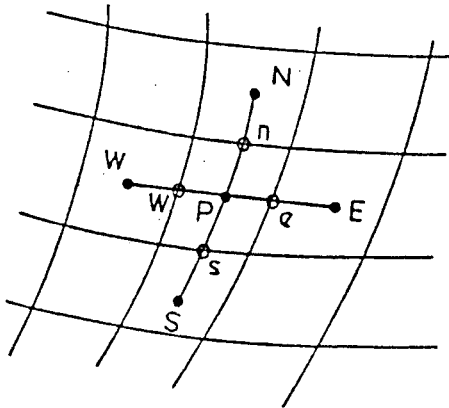
• = Mass control volume centers
o = Mass control volume face centers
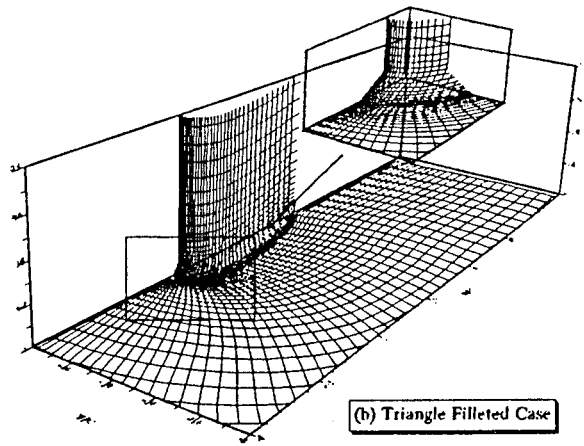
Figure 1. Grid Structure and Numerical
Molecule

(b) Triangle Filleted Case

CDS

CDS

P ●   ○ ──→ HDS

CDS = Central Difference Scheme.
HDS = Hybrid Difference Scheme.

(c) Convex Arc Filleted Case

Figure 2. Difference Schemes for Normal and
Cross-Derivatives.
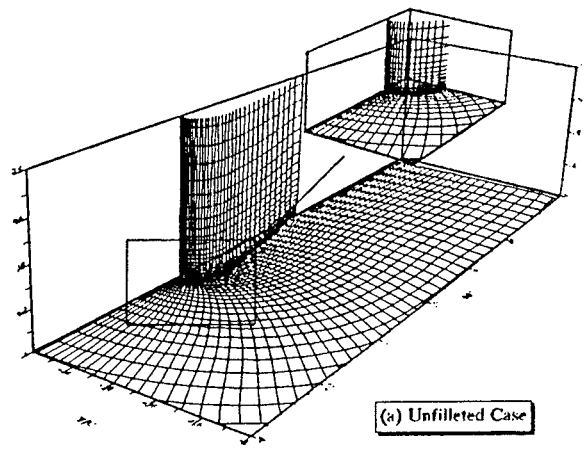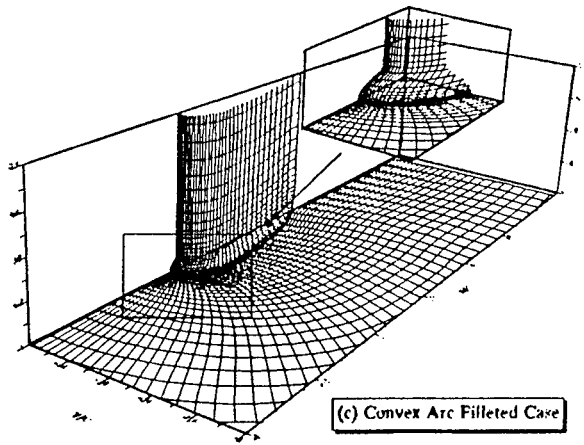
Figure 3.Geometric Configuration of Junction and
Computational Grids

464
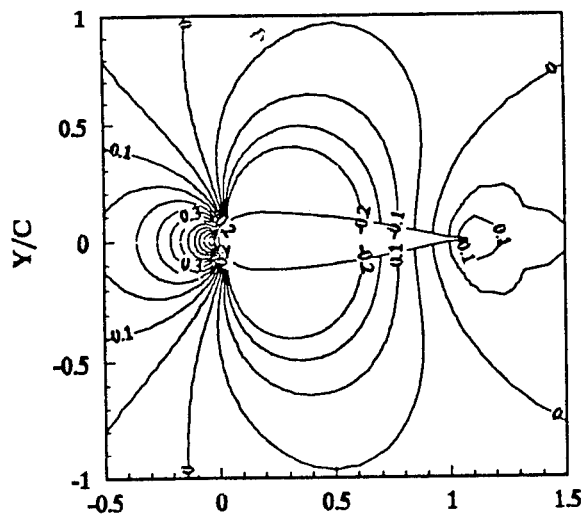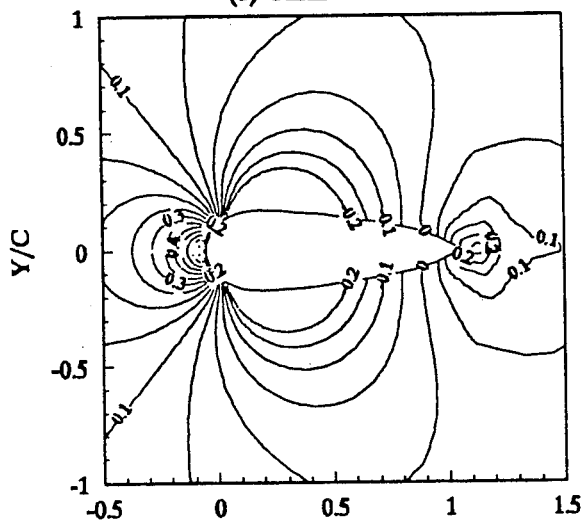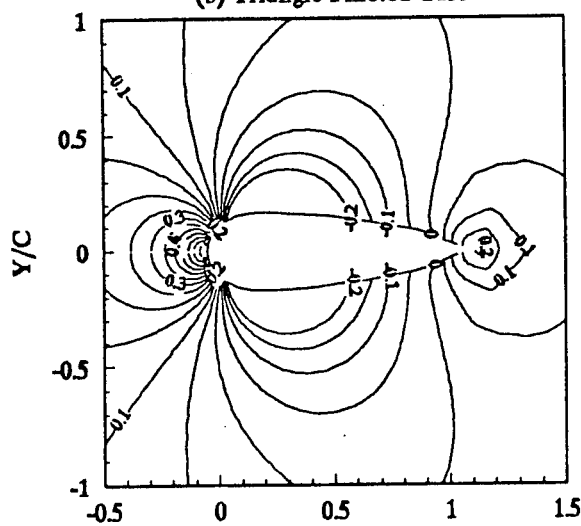
Figure 4. Pressure Coefficient C_p Profiles on The Flat-Plate
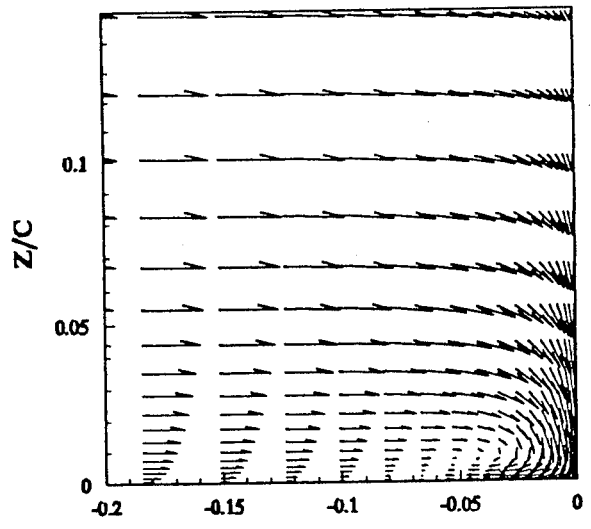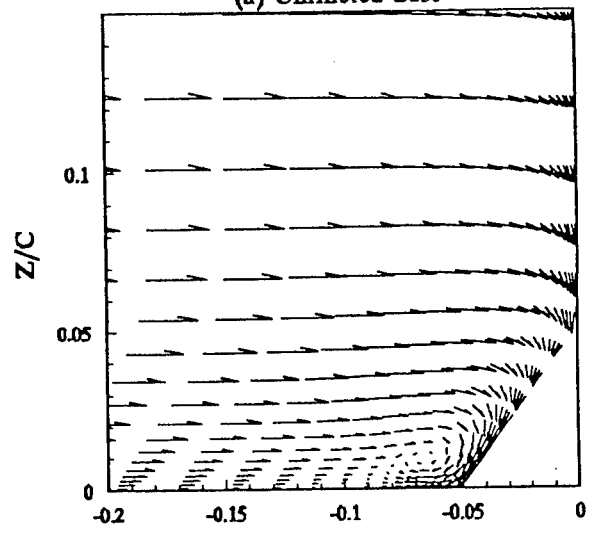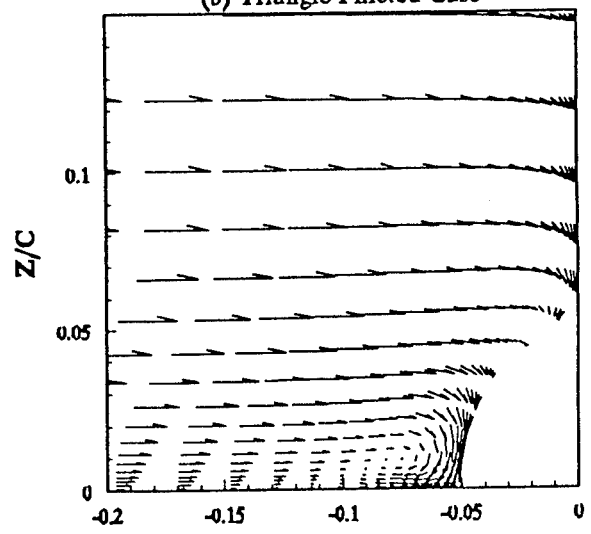
Figure 5. Velocity Vectors in The Symmetry Plane in Front of Wings

465
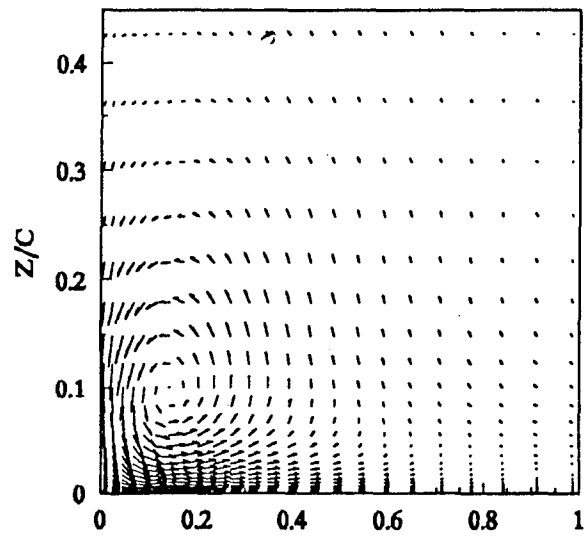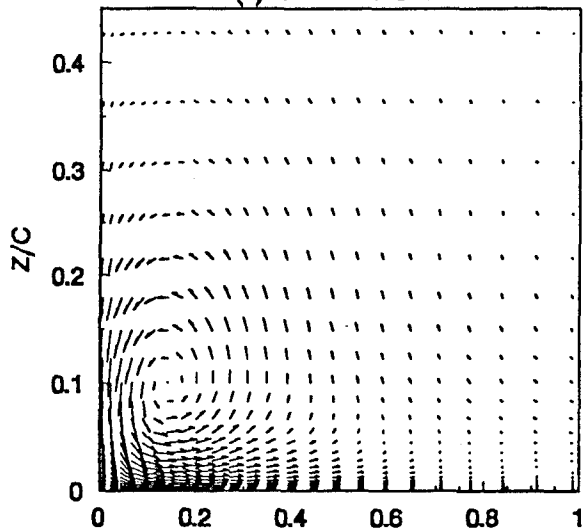
(a) Unfilleted Case

(b) Triangle Filleted Case
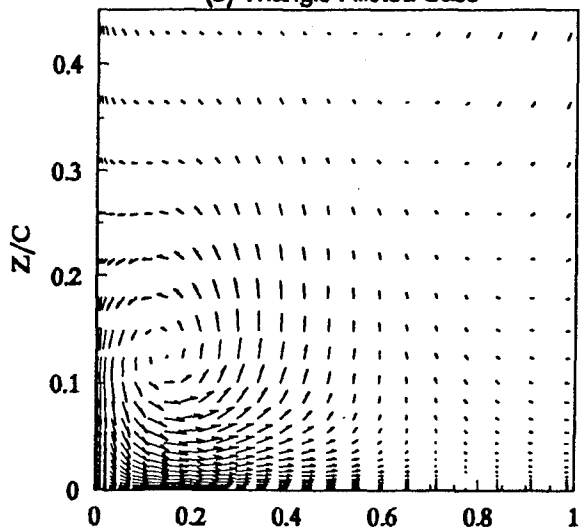
(c) Convex Arc Filleted Case

Figure 6. Velocity Vectors in Transverse Section
X/C = 2.14

(a) Unfilleted Case

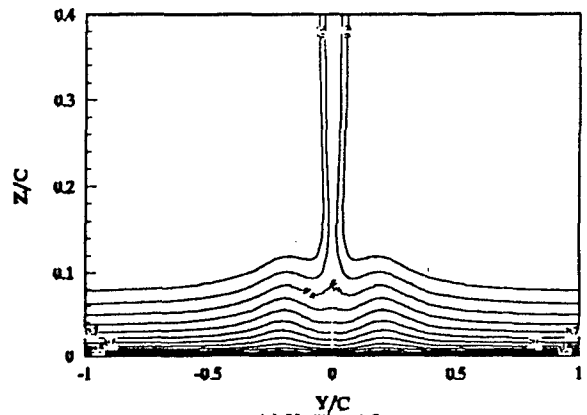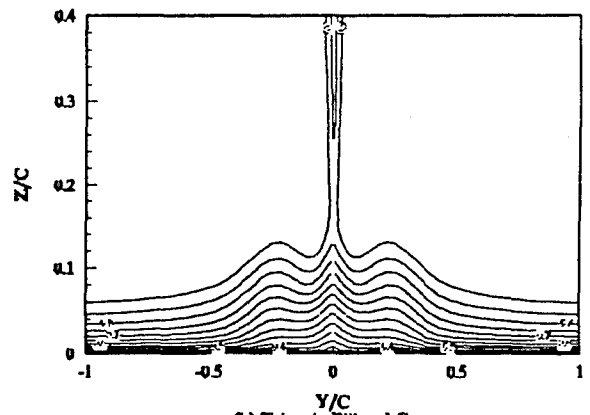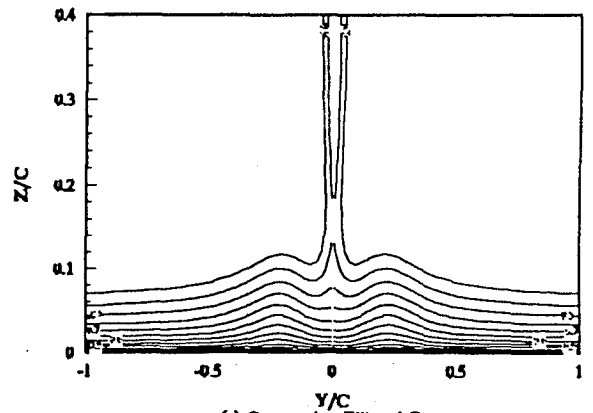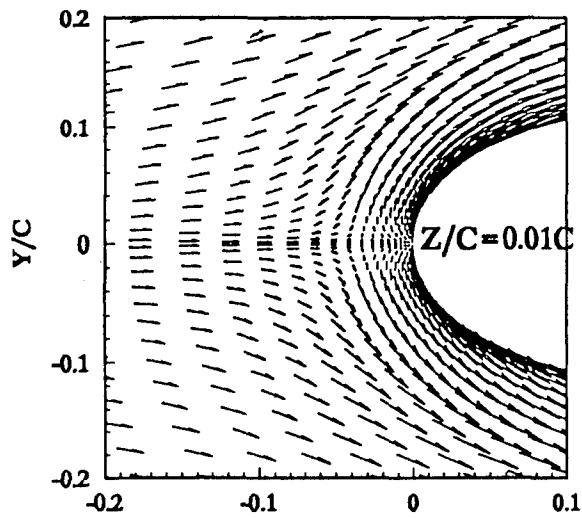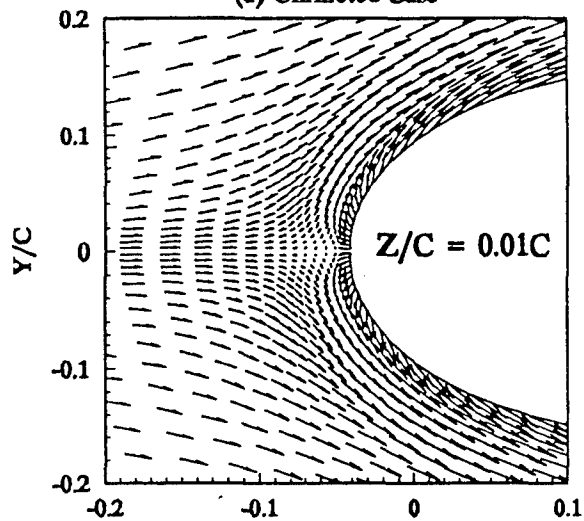
(b) Triangle Filleted Case

(c) Convex Arc Filleted Case
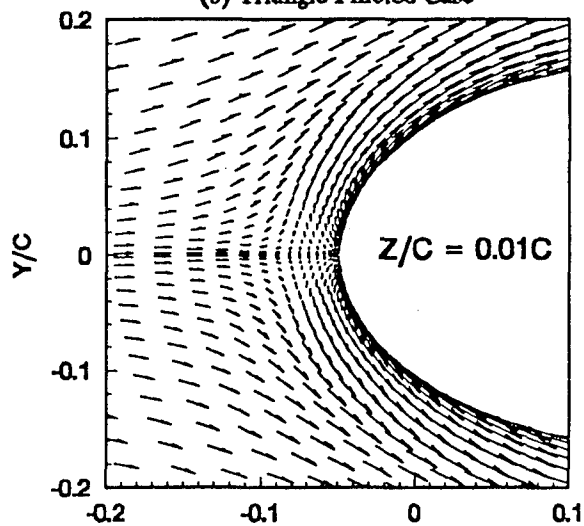
Figure 7. Streamwise Velocity in Transverse
Section X/C=2.14

466

Figure 8. Velocity Vectors Around Leading Edge of
Wing at Z/C = 0.01

Verification of the Viscous Flow-Field Simulation for Practical Hull Forms by a Finite-Volume Method

M. Zhu, O. Yoshida, and H. Miyata (University of Tokyo, Japan)
K. Aoki (Isuzu Motors Ltd., Japan)

ABSTRACT

A hybrid turbulence model based on the sub-grid scale (SGS) turbulence model combined with the Baldwin-Lomax turbulence model is introduced into the Navier-Stokes simulation of the viscous flow about the ship model with practical hull configuration. The aim is to develop a numerical method able to cope with the low-Reynolds-stress flow structure near the ship stern. The agreement between the computed results and the measurement indicate the feasibility of this approach to clarify some of the important features of ship stern flow. The stern flow structures of three-dimensional flow separation, the generation of the longitudinal vortex, and the resulting distorted wake pattern are studied and discussed.

INTRODUCTION

The accurate prediction of viscous ship stern flow is important in the evaluation of the ship powering performance. One of the most difficult requirements is to predict the distorted wake pattern in the propeller disk for full ship form. This wake pattern is the result of evolution of the longitudinal vortex which is generated by the flow separation, in the thick turbulent boundary layer about the ship stern. Due to its complex nature, it is not surprising that this wake pattern can not be predicted well in the numerical calculations based on the Reynolds-Averaged Navier-Stokes equations (RANS). The three-dimensional flow separation and the evolution of the longitudinal vortex are presently not modeled very well as shown in the proceedings of the Second SSPA-CTH-IIHR Workshop [1]. In the most successful RANS simulation, the turbulence model is the k-ε two equation model with the wall function or Baldwin-Lomax zero equation model. However, since both models are substantially tuned for the ordinary turbulent boundary layer, the eddy viscosity is too large to properly model the Reynolds stress distributions about the ship stern, which is inconsistent to the observed flow structure there. The measured turbulent shear stresses are found to become smaller in magnitude gradually towards the stern and to fluctuate inside the boundary layer in contrast with the classical boundary layer theory [2] [3] [4] [5]. Some of the flows exhibit quite complicated features, indicating the failure of explanation by the ordinary turbulence structure theory [6]. This is a problem in the flow structure model which may not able to be overcome by the refinement of the numerical solver [7] [8].

It is encouraging to note that turbulence modeling can be improved by CFD (Computational Fluid Dynamics) research combined with the experimental research for the investigation of turbulence structure about the ship stern. However, this approach has not been fully utilized. There is a limited number of research based on CFD databases in the area of ship hydrodynamics. This is the uncertainty of the measurement due to the complexity of the ship stern flow, and then it is quite difficult to make a reasonable model for the numerical simulation. Therefore it is quite difficult to validate the numerical results.

The purpose of this paper is to clarify the flow structure which makes the ship stern flow so complicated to experimentally measure and so difficult to predict in numerical calculations. It is supposed that it is due to the three-dimensional flow separation and the evolution of the induced longitudinal vortex. It is contrary to the viscous flow about a fine ship almost exhibiting minimum or no flow separation which can be predicted quite accurately, such as the hull form of Series 60 model ($C_B = 0.6$) [7]. However, very few RANS

simulations have successfully predicted flow separation for full ship form.

The flow separation phenomenon has been investigated in the experiment for simple flow geometry. Simpson [9] described the flow structure in a turbulent separating boundary layer. He showed the large scale vortical motions induced by the flow separation do not significantly contribute to the turbulent shear stresses but distort the mean flow and produce the low-frequency pressure fluctuation. He concluded that this flow behavior makes this type of flow difficult to calculate accurately. Since the influence of thick turbulent boundary layer over the ship hull near the stern is strong, the frequency of the field fluctuations (mainly the pressure fluctuations on the body surface) may not be as low as described by Simpson. It is really possible that the flow structure is changed by the flow separation over the hull as the bifurcation of flow geometry by shifting the frequency of the flow motions of most significant energy to the smaller frequency region in the Fourier space.

This frequency shift is very important to clarify the phenomenon because it opens the possibility how we can capture the stern flow separation phenomenon in the numerical simulation with the present computer capacity. If the boundary layer flow was not so dominant, the field fluctuations from flow separation would not be in the high-frequency region as shown numerically by Zhu et al. [10] for a car-like body. This point should be clarified for the ship stern flow.

For the full ship stern, the low-intensity Reynolds shear stress and the distorted wake pattern are both present. Moreover, the low-intensity Reynolds shear stress can be found not only in the flow separation phenomenon but also in the thick boundary layer almost without flow separation in the case of a modified spheroid of revolution as shown by Patel et al. [11]. Therefore, the low-intensity turbulent shear stress may be related to the flow structure which is mostly responsible for the flow separation phenomenon. This correlation gives us the guidance to tune turbulence model in the present study.

Therefore, the validation of CFD requests the calculation to be capable of capturing the following important features of the ship stern flow.

1. The three-dimensional flow separation from the hull surface;

2. The evolution of the induced longitudinal vortex and its interaction with the turbulent boundary layer;

3. The vortex structure near the propeller plane and the resultant distorted wake pattern inside the propeller disk; and

4. The difference of flow structure due to the change of stern hull configuration.

The above four points may serve as the checking point to verify the degree of resolution and the appropriateness of the numerical method. The flow separation phenomenon is firstly and mostly necessary to be accurately simulated. However, unfortunately, very few measurements of the turbulence on a ship model stern are available for this validation. In this study, we will consider the macroscopic feature of the flow phenomenon about the ship stern and show some detailed turbulent structure by use of the eddy viscosity distribution of the tuned turbulence model in connection with the change of flow structures.

In the present study, the adopted numerical method is an advanced version of a finite-volume solution method developed for the ship viscous flow called WISDAM-V by Zhu, Miyata and Kajitani [12] and Miyata, Zhu and Watanabe [13]. The calculated results [12] [13] demonstrated the suitability of using the sub-grid scale turbulence model to cope with some important features of ship stern flow in their LES-like numerical simulations. In this paper, a combined turbulence model based on the Baldwin-Lomax turbulence model and the sub-grid scale turbulence model is tuned in order to carry out simulations for the purpose of ship design.

This paper presents four topics. The advanced version of WISDAM-V method for viscous flow about the ship hull is first introduced. Secondly, the influence of the boundary condition for the sub-grid scale turbulence model is verified for the case of the viscous flow past a modified spheroid [11]. Thirdly, we tune a hybrid turbulence model based on the Baldwin-Lomax turbulence model and the sub-grid scale turbulence model in the application to the viscous flow about actual ship models. Fourthly, with the aid of computer graphics (CG) technique, we study and discuss the structure of the three-dimensional flow separation from the hull surface due to the ship stern configuration and the generation of the longitudinal vortex, and the resultant distortional wake pattern in the case of an actual ship hull with different stern hull configurations (SR 196 series tanker model).

WISDAM-V FINITE-VOLUME METHOD

Numerical formulation

The WISDAM-V finite-volume solution method is similar to the previous study [12] [13] in some aspects. However some modifications are made. As shown in Fig. 1, the pressure is defined at the center of the cell and the velocity components are defined at the center of respective cell surface. Therefore the staggered arrangement is shifted half diagonally in comparison with the previous studies [12]. The Cartesian coordinates are chosen as the basic coordinate system in the physical region, and the governing equations are formulated in an approach so-called "partial transformation". The respective area vector is defined as follows as shown in Fig. 1, for example,

$$S^1 = S_{abcd} = r_{ac} \times r_{bd} \qquad (1)$$

and the volume of the cell is calculated from the surface area and the diagonal length of the cell.

$$J = \frac{1}{3} (S_{abcd} + S_{aa'bb'} + S_{bb'cc'}) \cdot r_{bd} \qquad (2)$$

The Jacobian J and the area vector S^m defined in this way satisfy the geometry conservation law, i.e., the sum of the cell volumes equals the total volume of the flow region [14].

For the incompressible viscous flow, the Navier-Stokes equation can be written into the following conservative form,

$$\frac{\partial u}{\partial t} + div\ T = F \qquad (3)$$

here, F is the external force, u is the velocity, and the stress tensor T is defined as

$$T = p\bar{I} + uu - \frac{1}{R} def\ u \quad ; \quad R = \frac{V\ L}{v}, \qquad (4)$$

where all of the variable is nondimensionalized by the streamwise velocity V and the ship length L. I is the unit tensor, v is the kinematic molecular viscosity of the fluid, p is the pressure divided by the fluid density, R is the Reynolds number and the fluid deformation is defined as,

$$def\ u\ = grad\ u + (grad\ u)^T. \qquad (5)$$

Therefore the stress tensor T in Eq.(4) is composed of the normal stress of pressure, nonlinear stress, viscous stress.

Separating the pressure term from the others, Eq.(3) becomes,

$$\frac{\partial u}{\partial t} = - grad\ p + f, \qquad (6)$$

and

$$f = div\ \bar{\tau}, \qquad (7)$$

Then the stresses in Eq.(7) are

$$\bar{\tau} = - uu + \frac{1}{R} def\ u. \qquad (8)$$

By use of the area vector of Eq.(1) and the Jacobian of Eq.(2), Eqs. (6) and (7) have their vector forms as follows.

$$\frac{\partial u^i}{\partial t} = - \frac{1}{J} \frac{\partial}{\partial \xi^j} (S_k^j p\ \delta^{ik}) + f^i, \qquad (9)$$

and

$$f^i = \frac{1}{J} \frac{\partial}{\partial \xi^j} (S_k^j\ \tau^{ik}), \qquad (10)$$

where the stress tensor of Eq.(8) becomes,

$$\tau^{ij} = - u^i u^j + \frac{1}{R} (2\ e^{ij}), \qquad (11)$$

and the strain tensor is

$$e^{ij} = \frac{1}{2} \left(\frac{\partial u^i}{\partial x^m} \delta^{mj} + \frac{\partial u^j}{\partial x^n} \delta^{in} \right). \qquad (12)$$

Therefore, Eqs.(9) to (11) can be rewritten as follows,

$$\frac{\partial u^i}{\partial t} = - \frac{1}{J} \frac{\partial}{\partial \xi^j} (S_k^j p\ \delta^{ik}) + \frac{1}{J} \frac{\partial}{\partial \xi^j} (S_k^j\ \tau^{ik}). \qquad (13)$$

In order to perform a time dependent calculation, explicit time-marching is employed for the convection term and partial implicit time-marching for the diffusion term. The partial implicit finite-difference scheme for the diffusion term is used same as the previous studies [12] [13] and is abbreviated here. The finite-difference scheme is quite different from the previous studies [12] [13] and is described here in detail. A third-order accurate upwind finite-difference scheme is introduced within

471

the non-uniform flux-difference splitting framework [15] [7]. The inviscid flux can be considered in following form.

$$F^j = \left(S_k^j \cdot u^k \right) q = U^j q,$$ (14)

where q is the arbitrary velocity component, U^j is the volume flux (mass flux) in j sweep, and F^j is the inviscid flux for q in j sweep. Since q is defined on the each cell surface, as shown in Fig. 2, the first order flux for the upwind scheme is written in the following form.

$$F_i^j = \frac{1}{2}\left(U_i^j - |U_i^j| \right) q_{i+\frac{1}{2}} + \frac{1}{2}\left(U_i^j + |U_i^j| \right) q_{i-\frac{1}{2}}$$ (15)

Following the non-uniform flux-difference splitting method for the third order scheme by Sawada et al.[15], Eq.(15) becomes

$$F_i^j = \frac{1}{2}\left(U_i^j - |U_i^j| \right) q_i^+ + \frac{1}{2}\left(U_i^j + |U_i^j| \right) q_i^-$$ (16)

where q_i^+ and q_i^- are defined as follows.

$$q_i^- = q_{i-\frac{1}{2}} + \Phi_1^- \delta q_{i-1} + \Phi_2^- \delta q_i,$$ (17a)

$$q_i^+ = q_{i+\frac{1}{2}} + \left(1 - \Phi_2^+ \right) \delta q_i - \Phi_1^+ \delta q_{i+1}$$ (17b)

where

$$\delta q_i = q_{i+\frac{1}{2}} - q_{i-\frac{1}{2}},$$ (18)

and

$$\Phi_1^- = \frac{h_i\, h_{i+1}}{\left(h_{i-1} + h_i + h_{i+1} \right)\left(h_{i-1} + h_i \right)},$$ (19a)

$$\Phi_2^- = \frac{h_i\left(h_{i-1} + h_i \right)}{\left(h_{i-1} + h_i + h_{i+1} \right)\left(h_i + h_{i+1} \right)},$$ (19b)

$$\Phi_1^+ = \frac{h_i\, h_{i+1}}{\left(h_i + h_{i+1} + h_{i+2} \right)\left(h_{i+1} + h_{i+2} \right)},$$ (19c)

$$\Phi_2^+ = \frac{h_{i+1}\left(h_{i+1} + h_{i+2} \right)}{\left(h_i + h_{i+1} + h_{i+2} \right)\left(h_i + h_{i+1} \right)}.$$ (19d)

Here h_i is the conjugate length of the coordinate system and is defined as follows.

$$h_i = \left(\frac{J}{|S|} \right)_i.$$ (20)

The continuity equation for the incompressible flow is as follows.

$$div\,(u) = 0,$$ (21)

and its vector form is written as

$$\frac{1}{J}\frac{\partial}{\partial \xi^j}\left(S_k^j\, u^k \right) = \frac{1}{J}\frac{\partial U^j}{\partial \xi^j} = 0.$$ (22)

Solution Procedure

It is well known that the MAC-type algorithm is one of the best solution procedure for the time-dependent, incompressible viscous flow at a high Reynolds number. Suppose the flow field is determined in the (n)-th time step, the velocity of (n+1)-th time step can be written in the fractional step manner.

$$a - u^{(n)} = \Delta t\, f,$$ (23a)

$$u^{(n+1)} - a = -\Delta t\, \nabla^{(n+1)} p^{(n+1)},$$ (23b)

where ∇ is the Laplacian operator. If the pressure increase is defined as δp,

$$p^{(n+1)} = p^{(n)} + \delta p.$$ (24)

The artificial compressibility method is introduced for the coupling of the pressure increase and the continuity condition as follows.

$$\frac{\delta p}{\delta \omega} + \nabla^{(n+1)} \cdot u^{(n+1)} = 0$$ (25)

By introducing Eq.(23), Eq.(22b) becomes,

$$\begin{aligned} u^{(n+1)} &= -\Delta t\, \nabla^{(n+1)}\left(p^{(n)} + \delta p \right) + a \\ &= -\Delta t\, \nabla^{(n+1)}\delta p - \Delta t\, \nabla^{(n+1)} p^{(n)} + a \\ &= -\Delta t\, \nabla^{(n+1)}\delta p + \widehat{u}, \end{aligned}$$ (26)

where $\widehat{u}$ is the velocity predictor using the pressure of (n)-th time step as follows,

$$\widehat{u} = -\Delta t\, \nabla^{(n+1)} p^{(n)} + a.$$ (27)

Introducing Eq.(25) into Eq.(26), the following matrix equation for δp can be obtained.

$$\left(1 - \delta \omega \Delta t\, \nabla^{(n+1)} \cdot \nabla^{(n+1)} \right)\delta p = -\delta \omega\, \nabla^{(n+1)} \cdot \widehat{u},$$ (28)

where $\delta \omega = \Delta t$ in the present study. Eq.(28) is solved by means of the approximation factorization method. Therefore, the pressure and the velocity are solved by the simultaneous iterative method by employing

472

Eqs.(27), (28) and (24). The pressure is assumed to be converged at every time step when the pressure residual satisfies the following criterion at the (m)-th iteration step.

$$|p^{(m+1)} - p^{(m)}| < 10^{-4}. \qquad (29)$$

Boundary and initial condition

No-slip condition is imposed on the hull body surface and no wall function is used [12] [13]. Since in the present paper, only the viscous problem is dealt with, the symmetric condition is imposed on the still water plane boundary. The velocity is given uniformly on the inflow boundary, and the zero-normal-gradient condition on the downstream boundary. The side boundary is set sufficiently far from the hull so that the velocity is set by the zero-normal-gradient and the pressure is set at zero. As for the initial condition of the computation, the water is still and then gradually accelerated to the steady streamwise speed in 0.5 dimensionless time.

TURBULENCE MODEL

Ship Flow and SGS Turbulence Model

The sub-grid scale turbulence model was applied to the ship viscous problem by Miyata, Sato and Baba [16] for the case of Wigley model at the Reynolds number 10^4. Zhu, Miyata and Kajitani [12] and Miyata, Zhu and Watanabe [13] introduced a finite-volume method (WISDAM-V) as well as the sub-grid scale turbulence model to achieve the numerical prediction of turbulent ship flow at a model-test Reynolds number. They employed the sub-grid scale model in a RANS-like manner rather than the well known large-eddy simulation (LES).

By use of the sub-grid scale model, the flow simulated in the region of thin turbulent boundary layer results a unrealistic velocity profile. On the other hand, for full ship form such as the HSVA tanker, the use of the sub-grid scale turbulence model [17] [13] leads to a better prediction of the flow separation and the distorted wake pattern in the propeller disk than the other RANS simulations with the conventional models [1].

Therefore, the sub-grid scale model in the expression of the Smagorinsky formula [18] fails in the simulation of thin boundary layer but has some relevance to the flow structure about the ship stern of full form. One of the practical possibility is that the length scale employed in the sub-grid scale model is small than the thin boundary layer so as to be relevant to the low-Reynolds-stress structure as observed in the experiments [2] [3] [4] [5]. On the

other hand, for the pure large-eddy simulation, as discussed by Moin [19], there are several problems associated with the sub-grid scale model as,

1. The optimal choice of the coefficient in the expression for the eddy viscosity depends on the type of flow;
2. The limiting behavior of the SGS model is not correct near walls or free surface;
3. The model is too dissipative in laminar regions; and
4. The model does not allow transfer of energy from small scales to large scale.

It is not so difficult to find that, for the viscous ship flow, there are common problems as discussed by Moin. Some of inappropriateness of sub-grid scale model for the application to the ship case, such as the coefficients of the model, have been adjusted in the WISDAM-V method[17]. With respect to the grid resolution, their correlations with the artificial dissipation term in the numerical scheme have also been discussed.

Following Smagorinsky et al. [18] and the other extensive expression, the eddy viscosity of the sub-grid scale model is defined as follows.

$$v_s = L_s^2 \left(2\overline{e^{ij}} \, \overline{e_{ij}} \right)^{\frac{1}{2}} = L_s^2 |\omega| \qquad [30]$$

where e^{ij} is the fluid strain defined in Eq.(12) and ω is the vorticity vector. L_s is the length scale which should be adjusted in the case of interest. Since in the present study the turbulence model is incorporated in a RANS manner, the following expression is used instead of $1/R$ in the calculation.

$$\frac{1}{R_T} = \frac{1}{R} + v_s \qquad [31]$$

SGS model for a modified spheroid

In order to validate the body boundary condition of turbulence model, the numerical tests for the viscous flow past a modified spheroid is carried out. The prolate spheroid of six to one proportion is used. A conical tail piece is used to preserve the flow over the tail without flow separation. The mean flow measurements as well as turbulence measurements have been carried out by Patel et al.[11] and are available for the validation of the turbulence model [20].

Following the measurement, the Reynolds number based on the spheroid length and streamwise velocity is set at 2.75×10^6 in the calculation. Fig.3 showed the O-H grid system around the modified

473

spheroid. The total grid points is 135,642 (141x26x37). The minimum mesh spacing of the innermost velocity point from the body surface is 5×10^{-5}, and time increment is set at 1×10^{-4}. The simulation is carried out until the dimensionless time T reaches 2.5.

We tested two cases for the length scale of turbulence model. In the case A, the length scale is set as follows.

$$L_s = min \left(0.1 J \tfrac{1}{3}, \; 0.5 \Delta x^1, \; 0.5 \Delta x^2, \; 0.5 \Delta x^3 \right)$$
[32]

In the case B, the Van Driest wall damping function is introduced into the length scale.

$$L_s = D_f min \left(0.1 J \tfrac{1}{3}, \; 0.5 \Delta x^1, \; 0.5 \Delta x^2, \; 0.5 \Delta x^3 \right)$$
[33]

where

$$D_f = 1 - exp \left(- y^+ / A^+ \right)$$
[34]

and y^+ is the normal viscous unit from the body surface and A^+ is set at 26.

The comparison of the radial distribution of the axial velocity between the two cases of calculation and the experiment is shown in Fig.4. The comparison of the afterbody pressure distribution along the longitudinal axis is shown in Fig.5. It is noted that the numerical results are improved by introducing the Van Driest wall damping function. Especially for the pressure distribution, the numerical results of case B showed an excellent agreement with the experiment. However, the velocity distribution needs to be improved near the body surface.

Hybrid turbulence model for ship flow

For the flow about a full ship hull with long parallel middle body a hybrid turbulence model is designed [21]. Assume that the eddy viscosity of SGS model is v_s, and that of Bladwin-Lomax model [22] is v_b, the hybrid turbulence model is defined in the following way.

$$v_h = \begin{cases} v_b & , \text{when } x_{FP} \leq x \leq x_{Midship} \\ \beta v_b + \left(1 - \beta \right) v_s & , \text{when } x_{Midship} \leq x \leq x_{AP} \\ v_s & , \text{when } x_{AP} \leq x \end{cases}$$
[35]

where β is defined as a function of prismatic coefficients of the hull in the present study as follows.

$$\beta = \left(C_p \right)^{\alpha}$$
[36]

Fig.6 shows the distributions of prismatic curve of SR196A (see next section) along the streamwise axis and its rooted curve as an example. Yoshida tested this model in detail and recommended $\alpha = 0.5$ [21].

CONDITION OF SIMULATION

A series of full tanker hull named SR196 after the same name of project [23], are employed for the verification of the present method. The displacement of the full-scale ship is 230,000 ton, the length is 320 m and the service speed is 14 kt (7.202 m/s). The principal particulars of the original full-scale ship and 4 m testing model are listed in Table 1. The stern configuration is designed as mariner type for its employment of low-frequency, large-diameter propeller.

There were 9 types of model hull derived from the original hull proposed for testing [23]. In the present study, three types of hull are adopted. They have common fore part and common prismatic curve but different framelines of after part as shown in Fig.7. The original hull is called SR196A, the modification with V-shaped stern is SR196B and the U-shaped is SR196C.

The computational conditions are listed in Table 2. About 65,000 grid points are allotted in the computational domain. Fig.8 is the grid about the bulbous bow and stern of SR196A hull.

The Reynolds number in the calculation is 106. The time increment is set at 5×10^{-4}. The minimum grid spacing is set at 10^{-4}. This grid spacing ensures the first grid point is set inside the sublayer in the ordinary turbulent boundary layer.

The computation spends almost two days for one case on a engineering workstation (130MIPS).

ANALYSIS OF NUMERICAL RESULTS

The time sequence of simulated viscous resistance coefficients of SR196A is shown in Fig.9. The resistance coefficients are defined as follows.

$$C_v = C_{vp} + C_f,$$
(37a)

$$C_{vp} = \frac{\int_{hull} \left(-p\, \delta^{ij}\, n_{ij}\, dS \right)}{\frac{1}{2} \rho\, V^2\, A} \qquad (37b)$$

$$C_f = \frac{\int_{hull} \left(\frac{1}{R_e} e^{ij}\, n_{ij}\, dS \right)}{\frac{1}{2} \rho\, V^2\, A} \qquad (37c)$$

where A is the wetted surface area of the hull, C_v is the total viscous resistance coefficient, C_{vp} is the viscous pressure resistance coefficient and C_f is the frictional resistance coefficient. One can find the increase of resistance during the acceleration and the convergence of solution within a few dimensionless time unit. The friction resistance coefficients are predicted fairly well for all of the cases. However, the viscous pressure resistance coefficients are overpredicted and fluctuate in time.

The simulated eddy viscosities of several transverse sections along the waterline No.3 are shown compared with the boundary layer theory [24] in Fig. 10. The eddy viscosity is nondimensionalized by the wall frictional velocity u_w and the momentum thickness δ_2 of the boundary layer. The distance y from the hull surface is also nondimensionalized by δ_2. The lateral velocity profiles at the same position are shown in Fig. 11 fitted to the empirical wall law. It is because that, along waterline no.3, both the change of the hull form and the difference between three hulls are also most significant as shown in Fig.7.

Figs.10 and 11, for both the eddy viscosity and the velocity profile, indicate that the flow structures along this waterline are still those of a developing turbulent boundary layer at S.S.2. The agreements between the calculation and the theory for both eddy viscosity and velocity profile are fairly good. However, at S.S.1, the eddy viscosity becomes smaller and the velocity profile exhibits its departure from the wall law, indicating that the flow changes its structure during the part of hull between S.S.2 to S.S.1.

The velocity profile at S.S.1 shows a skewness during the viscous unit $y^+ = 100 \sim 400$. SR196C (U-shape) shows the largest change while SR196B (V-shape) shows the smallest, indicating the correlation of the velocity profile with the hull form.

The comparisons of longitudinal velocity distribution between the calculation and the experiment [23] in the transverse sections S.S.1, S.S.1/2 and propeller plane are shown in Figs.12a, 12b and 12c. Although the Reynolds number of the experiment (4×10^6) is different from the present calculation (10^6), the evolution of the thick boundary layer as well as the distorted wake pattern are revealed in the calculation. However, the changes of the wake pattern inside the propeller disk due to the difference of hull form are not predicted so distinctly by comparison with the experiment.

The 3D contour map of iso-longitudinal vortex around the after part of SR196C hull is shown in Fig.13. It is interesting to note that the flow structure may not be described so clearly by the the drawing of the value of longitudinal vortex component. This is because the flow near the stern always diverge from the keel toward the free surface. It creates a circulation which has a main component in the same direction with the longitudinal axis as those of bilge vortex or separated vortex.

In order to elucidate the vortex structure related to the flow separation, in the present paper, the vorticity is decomposed into the following two parts as shown in Fig.14.

the helicity or Lamb scalar:
$$L_s = \omega \cdot u \qquad (38a)$$

the inertial vortex force or Lamb vector:
$$L_v = \omega \times u \qquad (38b)$$

where ω is the vorticity vector and u is the velocity vector. Yamada and Miyata [25] showed that the separated vortices are clarified by use of these values. In a flow separation associated wind noise problem, Zhu et al.[10] showed that the helical vortex can be employed to distinctly clarify the flow separation phenomenon.

The 3D contour maps of iso-helicity around the after part of SR196B, SR196A and SR196C hulls (from upper side) are showed in Fig.15. It is not surprising that the three-dimensional flow separation phenomenon is described definitely by using the helical vortex. It is worth to be mentioned that there is a strong correlation between the separated vortex structure and the low-pressure part on the hull surface.

It may be safe to say that the present numerical method is capable of elucidating some flow features caused by the difference of hull form. The vortex structures seem to be more three-

dimensional when the hull form changes from V-shape to U-shape. The separated vortex forms a "hook" shape during its interaction with the hull. This is why the velocity profile at S.S.1 was more skewed for SR196C. This "hook" shaped vortex structure may be directly responsible for the distorted wake pattern inside the propeller disk. However, as shown in Fig.15, the vortex seems to be dissipated when it passes the propeller position so that the simulated wake pattern is not so distorted as shown in Fig.12. Considering the grid spacing employed in the present work, both the resolution and the turbulence modeling should be further improved by the collaboration with the experimental investigation in the near future.

CONCLUSIONS

A numerical solution method (WISDAM-V method) has been developed for the viscous flow about a full ship model with practical hull configuration. A hybrid turbulence model is tuned and incorporated into the numerical method in order to cope with the low-Reynolds stress flow structure near the ship stern. Numerical tests have been carried out for a series of SR196 tanker model. It seems that this method is capable of predicting the distorted wake pattern and clarifying the difference of ship stern configuration.

In the present study, the possible correlation between the separated vortex structure and the wake pattern in the propeller plane has been discussed. For the accurate prediction of wake pattern, it is quite important for the numerical simulation to reveal the flow separation as well as the evolution of separated vortex. This work showed the possibility and importance of turbulence modeling for thick boundary layer.

REFERENCES

[1] Larsson, L., Patel, V. C. and Dyne, G. (editors), Proc. of the 1990 SSPA-CTH-IIHR Workshop on Ship Viscous Flow, Gothenburg, 1991.

[2] Knaack, T., Kux, J. and Wieghardt, K., " On the Structure of the Flow Field on Ship Hulls", Proc. Osaka Int. Colloq. Ship Visc. Flow, Osaka, 1985, pp.192-208.

[3] Fukuda, K. and Fujii, A., "Turbulence Measurement in Three Dimensional Boundary Layer and Wake around a Ship Model", J. Soc. Naval Architects of Japan, Vol. 150, Dec. 1981, pp.85-98; "Turbulence Measurement in Three Dimensional Boundary Layer and Wake around a Ship Model (Second Report), J. Soc. Naval Architects of Japan, Vol. 153, June, 1983, pp.29-41. (in Japanese)

[4] Löfdahl, L. and Larrson, L., "Turbulence Measurements Near the Stern of a Ship Model", J. Ship Research, Vol.28, No.3, 1984, pp.186-201.

[5] Knaack, T., "Laser-Doppler Velocity Measurement on a Double Model of a Ship in a Wind Tunnel", Inst. Schiffbau, Univ. Hamburg, Report 439, 1984; "LDV Measurement of the Reynolds Stresses in the Wake of a Ship in a Wind Tunnel", Inst. Schiffbau, Univ. Hamburg, Report 499, 1990. (in German)

[6] Townsend, A. A., The Structure of Turbulent Shear Flow, Cambridge University Press, 2nd Ed., 1976.

[7] Kodama, Y., "Computation of Ship's Resistance Using an NS Solver with Global Conservation - Flat Plate and Series 60 (CB=0.6) Hull -", J. Soc. of Naval Archit. of Japan, Vol. 172, Dec. 1992, pp.147-156.

[8] Deng, G. B., Piquet J. and Visonneau M., "Viscous Flow Computation Using a Fully Coupled Technique", Proc. of the Second Osaka Int. Colloq. on Visc. Fluid Dyns in Ship and Ocean Tech., Osaka, 1991, pp.186-202

[9] Simpson, R. L., "Turbulent Boundary-Layer Separation", Ann. Rev. Fluid Mech. 21, 1989, pp.205-234.

[10] Zhu, M., Hanaoka, Y. and Miyata, H., "Numerical Study on the Mechanism of Wind Noise Generation About the Front Pillar of a Car-Like Body", submitted to ASME J. Fluid Engrg., 1993.

[11] Patel, V. C., Nakayama, A. and Damian, R., "Measurements in the Thick Axisymmetric

Turbulent Boundary Layer near the Tail of a Body of Revolution", J. Fluid Mech., Vol.63, Part 2, 1974, pp.345-367.

[12] Zhu, M., Miyata, H. and Kajitani, H., "A Finite-Volume Method for the Unsteady Flow About a Ship in Generalized Coordinate System", J. Soc. Naval Archit. of Japan, vol.167, 9, 1990, pp.9-15.

[13] Miyata, H., Zhu, M. and Watanabe, O., "Numerical Study on a Viscous Flow with Free-Surface Waves About a Ship in Steady Straight Course by a Finite-Volume Method", J. Ship Research, Vol.36, No.4, Dec. 1992, pp.332-345.

[14] Vinokur, M., "Review Article: An Analysis of Finite-Difference and Finite-Volume Formulations of Conservation Laws", J. Comput. Phys., Vol.81, 1989, pp.1-52.

[15] Sawada, K. and Takanashi, S., "A Numerical Investigation and Wing/Nacelle Interferences of USB configuration", AIAA Paper 87-0455, 1987.

[16] Miyata. H., Sato, T. and Baba, N., "Difference Solution of a Viscous Flow with Free-Surface Wave About an Advancing Ship", J. Comput. Phys., Vol. 72, No.2, 1987, pp.393-421.

[17] Zhu, M., "A Finite-Volume Solution Method for Unsteady, Three-Dimensional Turbulent Flows About A Full Ship Model", PhD. Thesis, Dept. Naval Architecture and Ocean Engineering, The University of Tokyo, 1991.

[18] Smagorinsky, J., Manabe, S., and Holloway, J., L., "Numerical Results from a Nine-Level General Circulation Model of the Atomsphere", Monthly Weather Review, 93, Dec. 1965, pp.727-768.

[19] Moin, P., I. The subgrid scale modeling group. In Studying Turbulence Using Numerical Simulation Databases - III, Proceedings of the 1990 Summer Program. Center for Turbulence Research, NASA-Ames Research Center and Stanford University, 1990.

[20] Aoki, K., Zhu, M. and Miyata, H., "Finite-Volume Simulation of 3-D Vortical Flow-Fields about Road Vehicles with Various After-Body Configuration", 7th Int. Pacific Conf. on Auto. Engrg., Pheonix, Nov., 1993.

[21] Yoshida, O., "Verification of Turbulence Model in the Numerical Simulation of Viscous Ship Stern Flow", Master Thesis, Dept. Naval Architecture and Ocean Engineering, The University of Tokyo, 1993. (in Japanese)

[22] Baldwin, B. S. and Lomax, H., "Thin Layer Approximation and Algebraic Model for Separated Turbulent Flows", AIAA paper 75-257, 1978.

[23] Research on the Design of Ship Stern Hull Configuration --- Viscous Flow: Project SR 196, the Shipbuilding Research Association of Japan, 1985.

[24] Cebeci, T. and Bradshaw, P., Momentum Transfer in Boundary Layer, Hemisphere Publishing, 1977.

[25] Yamada Y. and Miyata H., "Computational Study of Large Eddy Structure of Flows past Bluff Body and Oceanic Topography", J. Soc. Naval Archit. Japan, Vol.173, 1993.
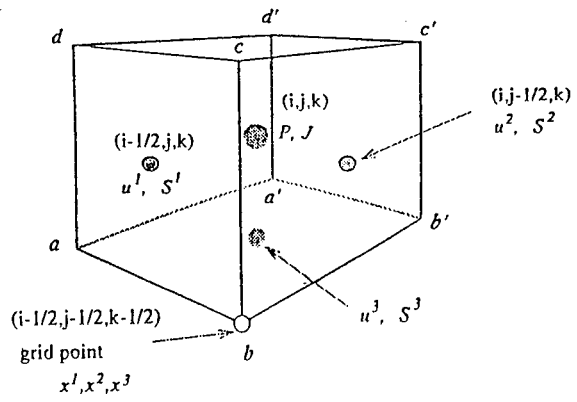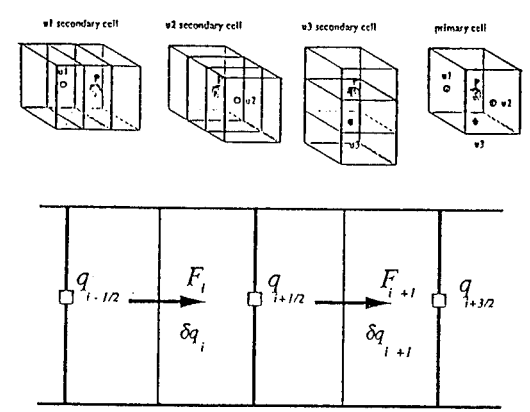
Fig. 1   Variable arrangement

Fig. 2   Definition of the invisid flux

Particulars	Model	Ship
L_{pp} (m)	4.0000	320.00
B (m)	0.6663	53.30
d (m)	0.2413	19.30
C_B	0.8017~0.8027	0.802
F_n	0.17 (Experiment)	0.129 (Service Speed)
R_e	4.007×10^6	2.305×10^9

Table   1   Principal particulars of SR 196 hull models

Condition	SR196 A, B, C
grid points (total amount)	91 x 23 x 31 (64,883)
computational domain length	2.5
computational domain width	1.0
computational domain depth	1.0
minimum grid spacing	1.0×10^{-4}
time increment	5.0×10^{-4}
time steps for acceleration	1000
time of simulation	2.5 ~ 3.0
Reynolds number	10^6
turbulence model	hybrid model

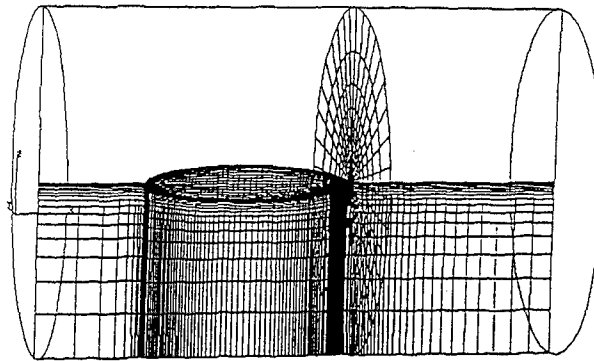Table   2   Condition of simulation

Fig. 3   Grid system about the modified spheroid

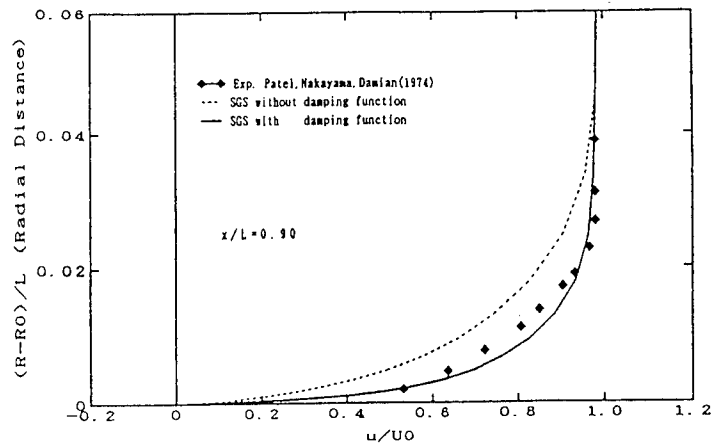Fig. 4   Radial distribution of the axial velocity: x/L=0.90
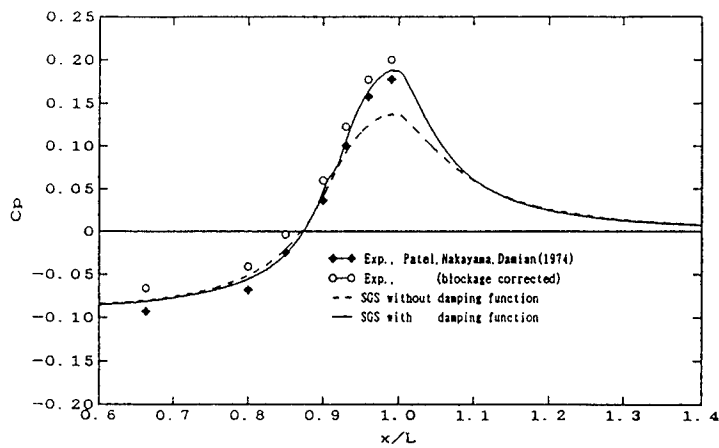
Fig. 5   Afterbody pressure distribution along the longitudinal axis
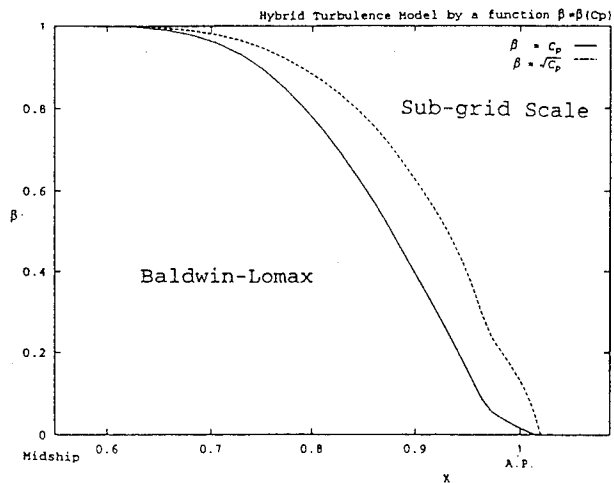
Fig. 6   Definition of hybrid turbulence model for viscous ship flow
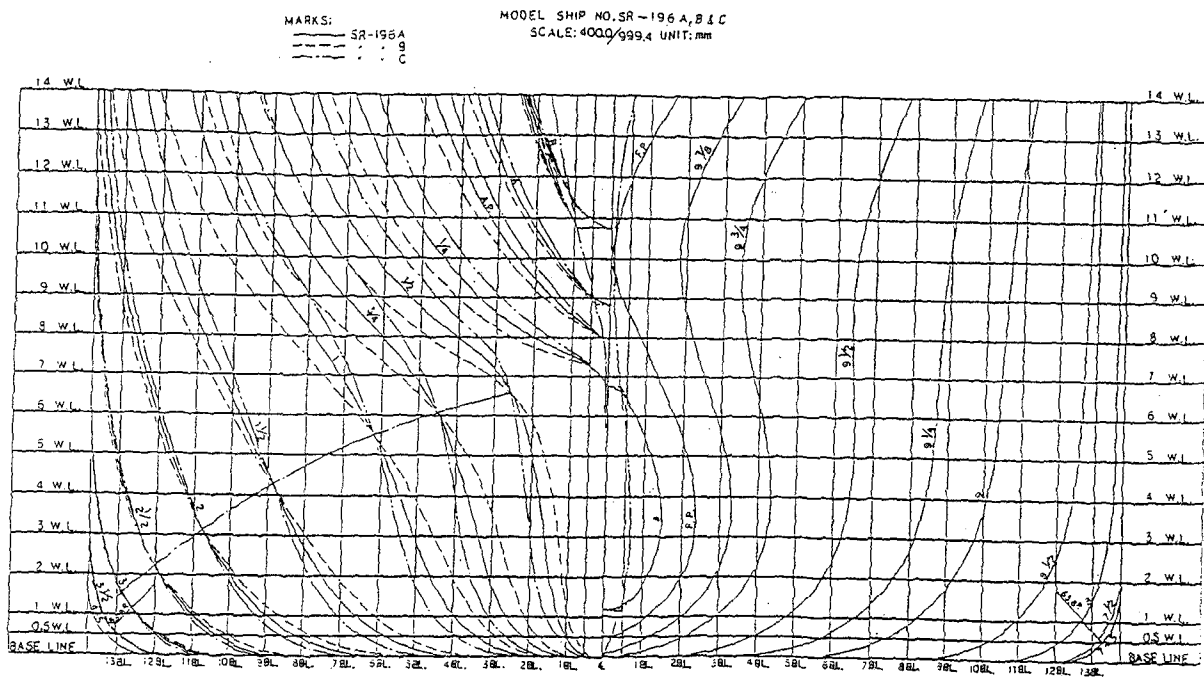
Fig. 7　　　　Body plan of SR 196 tanker series
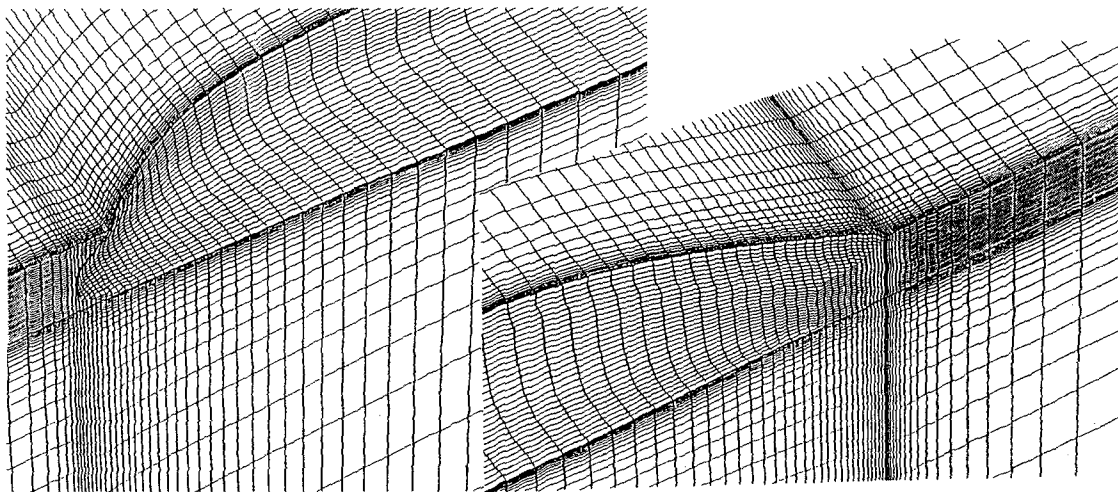
Fig. 8　　　　Grid system about SR 196A ship model (about bow and stern)
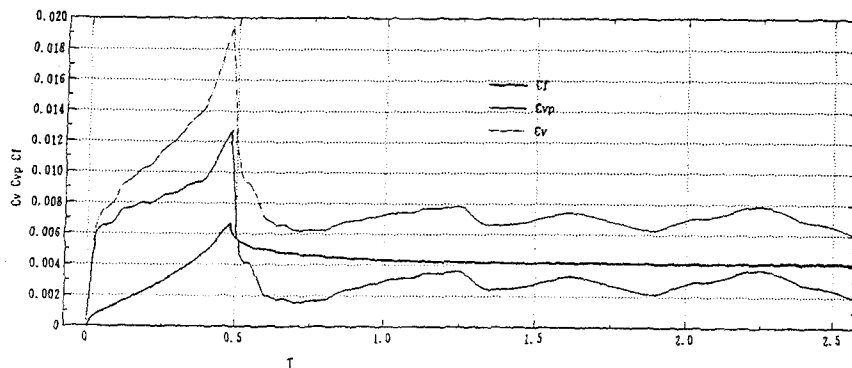
Fig. 9　　　　Time sequence of the computed force coefficients of SR196A hull
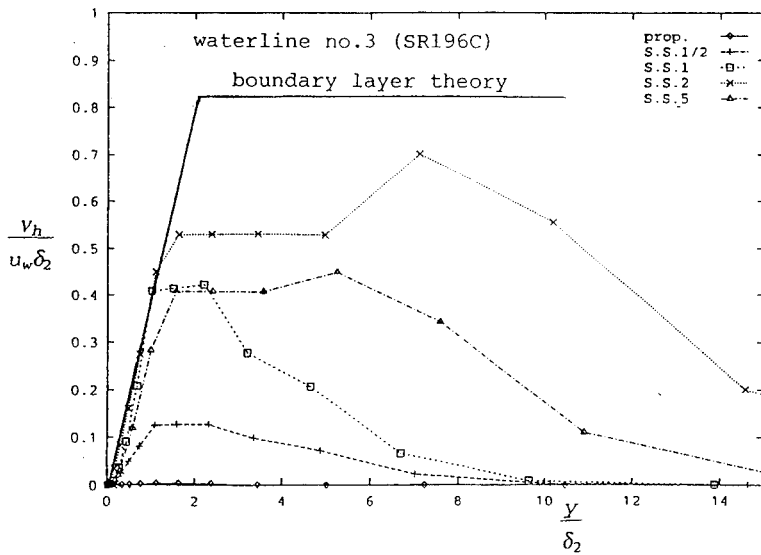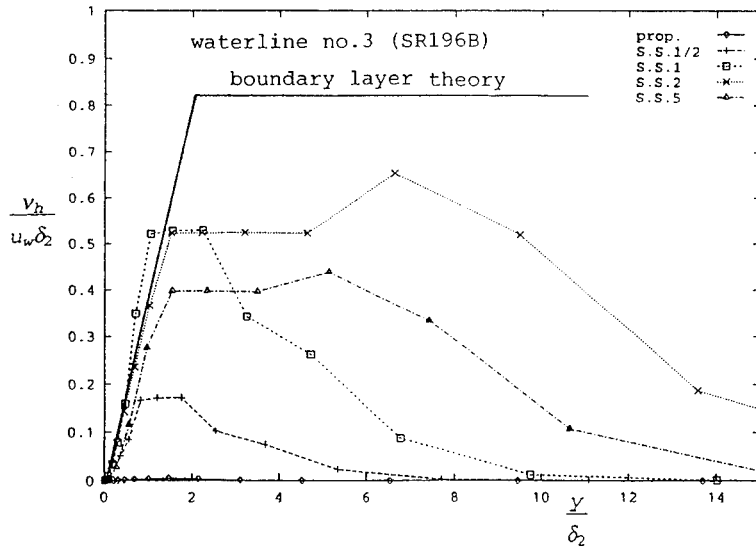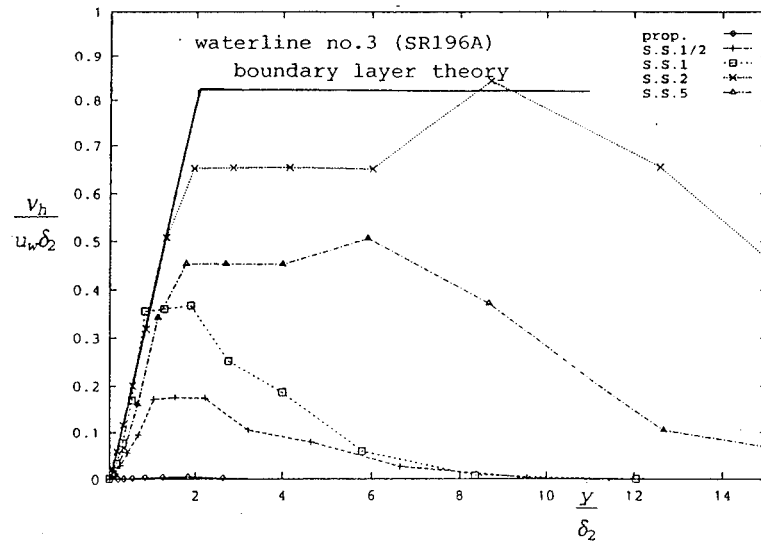
Fig. 10   Eddy viscosity distribution of the tuned turbulence model along waterline no.3

481
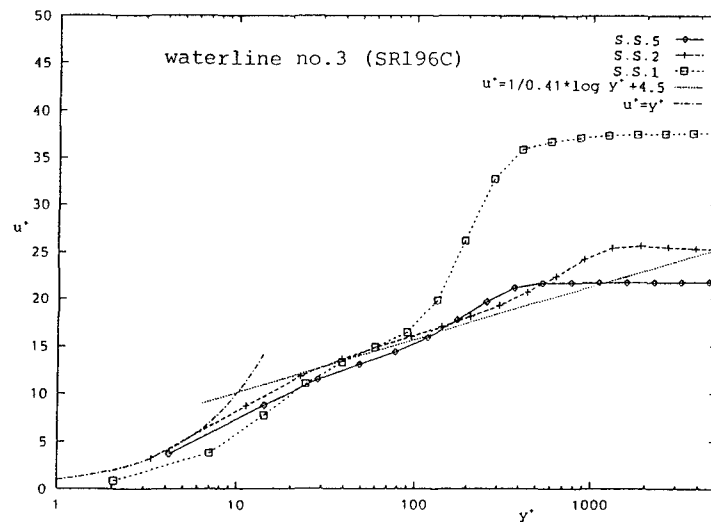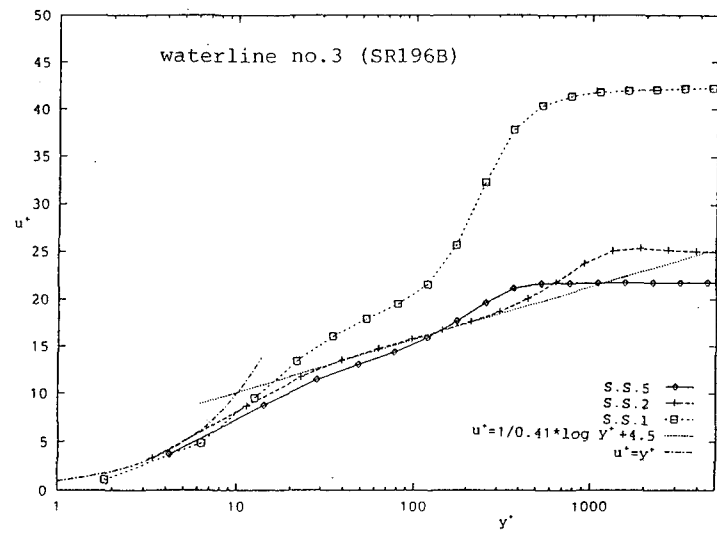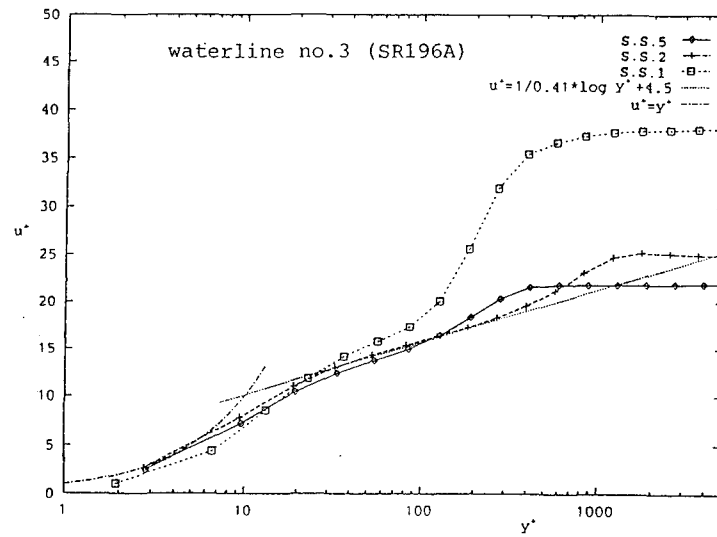
Fig. 11   Velocity profile along waterline no.3

0.5
v/U,w/U

S R 1 9 6 A

Eexperiment   Calculation

S R 1 9 6 B

Eexperiment   Calculation

S R 1 9 6 C

Eexperiment   Calculation
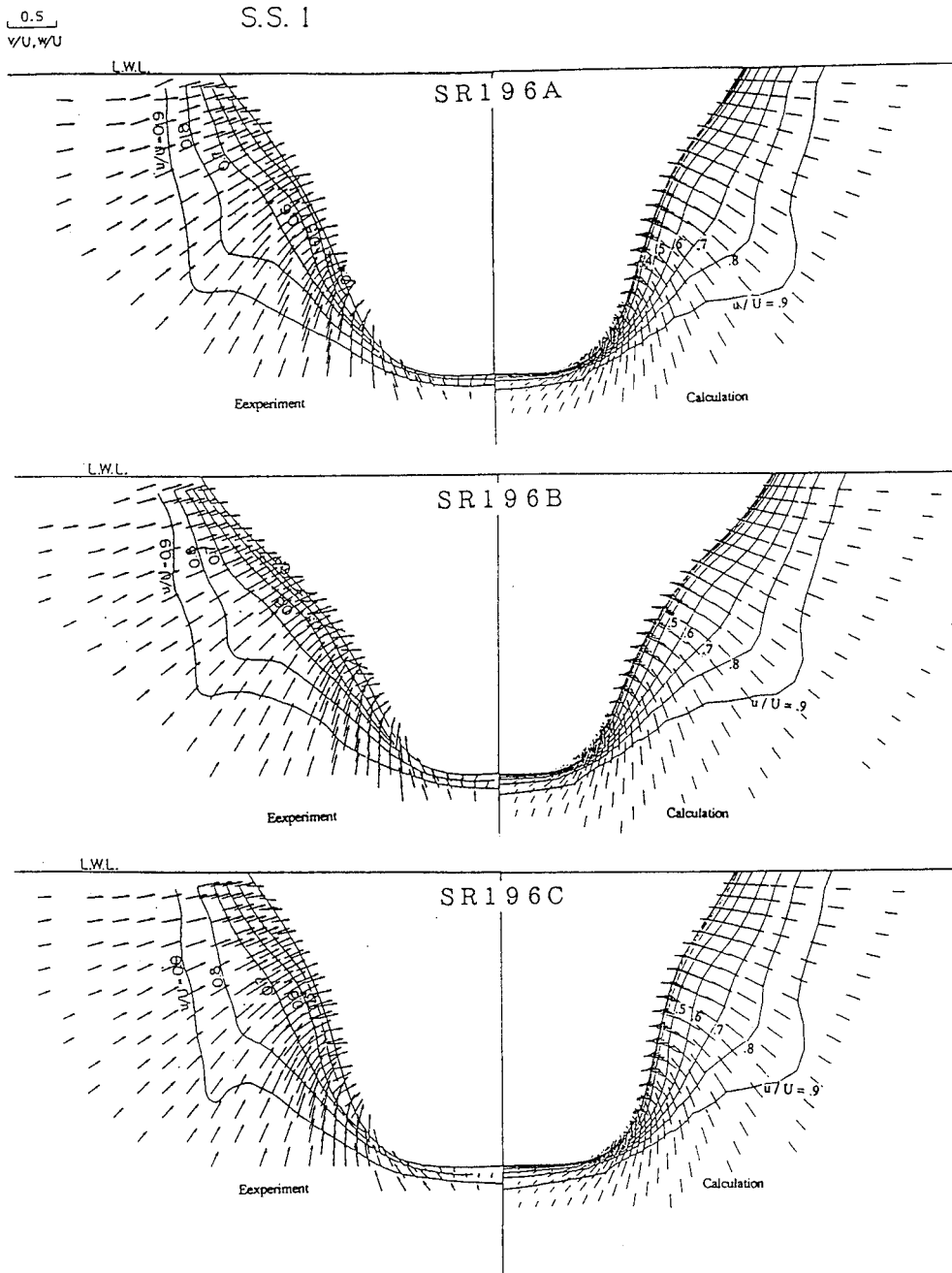
Fig. 12a   Comparison of longitudinal velocity between the calculation and the experiment: S.S.1
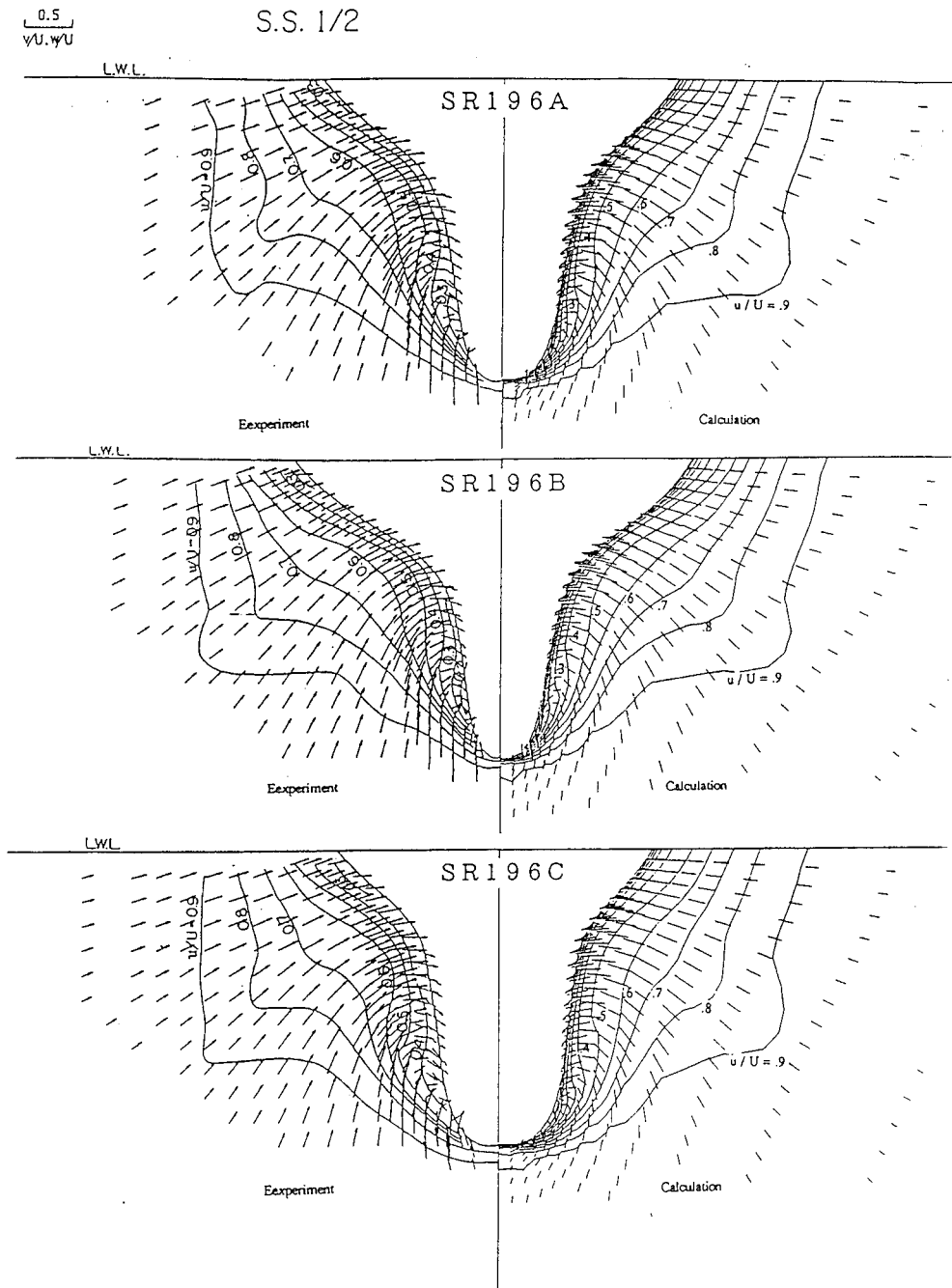
Fig. 12b   Comparison of longitudinal velocity between the calculation and the experiment: S.S.1/2
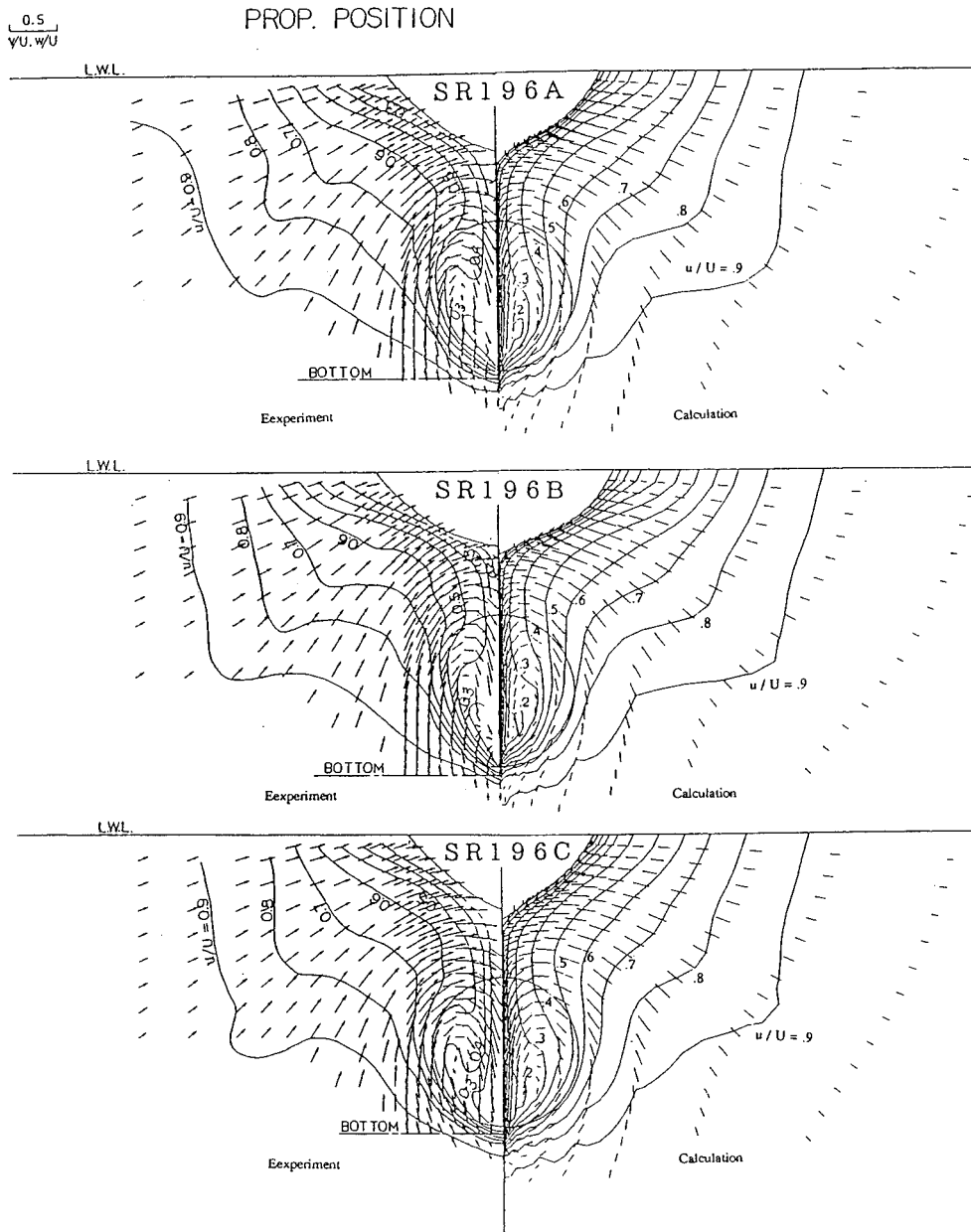
Fig. 12c   Comparison of longitudinal velocity between the calculation and the experiment: propeller plane

485
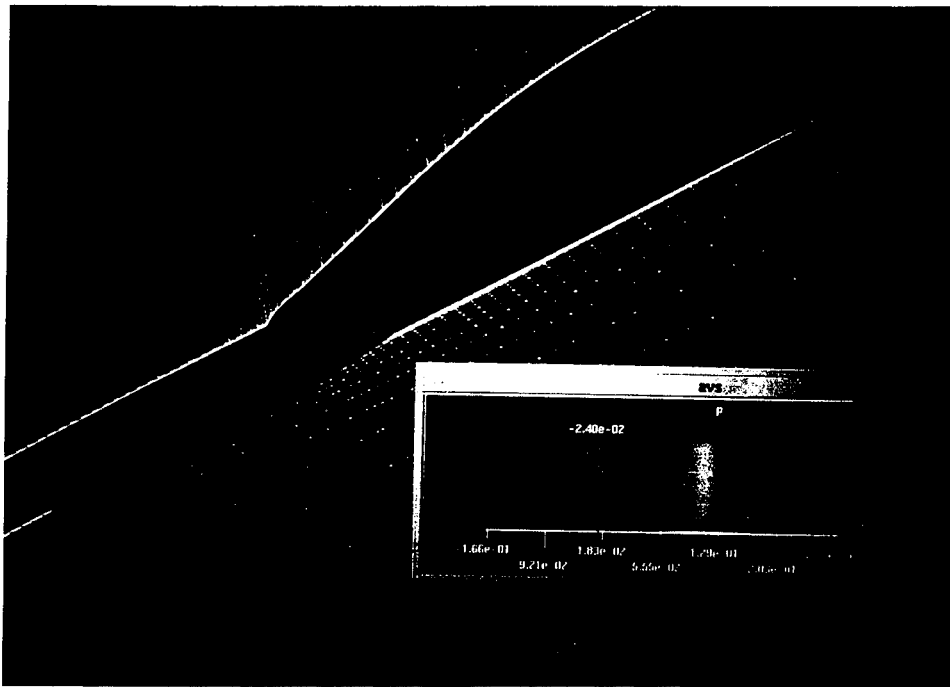
Fig. 13   Three-dimensional iso-longitudinal vortex contour about the afterbody hull of SR196C

Inertial Vortex Force :

$$L_v = \omega \times u$$

Helicity :

$$L_s = \omega \cdot u$$

ω : Vorticity Vector
u : Velocity Vector
ψ : Swirl Angle

Fig. 14   Decomposition of vorticity component

486

Fig. 15   Three-dimensional iso-helicity contour about the afterbody hull
From the upper :   SR196 B (V type hull)
                    SR196 A (Original hull)
                    SR196 C (U type hull)

Hydrodynamical Design of Super-Slender-Twin-Hull Ferries by CFD Techniques

H. Miyata, T. Ohmori (University of Tokyo, Japan)
E.M. Kamal (Ishikawajima-Harima Heavy Industries Co. Ltd., Japan)

Abstract

Two CFD techniques are applied in the course of developing a new-type fast ferries named Super-Slender-Twin-Hull. Since this ship is of displacement type and the design Froude number is from 0.4 to 0.8, minimization of wave resistance is of major importance. After pursuing the optimal particulars, the TUMMAC-IV method for ship waves is employed to have the hull-form of minimum wave resistance. By imposing appropriate boundary conditions on the centerline and the bottom the wave systems of a catamaran in both deep and shallow waters are simulated. For the design of the after body the WISDAM-V method, which employs boundary-fitted coordinate system and finite-volume discretization, is used. The difference of the buttock flow due to shortening the length of the after body, the effect of waves on the viscous flow, the effect of the asymmetric hull geometry on the wake are studied. The oblique tow simulation is performed with this method by giving proper inflow boundary conditions. It is demonstrated that the present method can predict lateral force and yaw moment quite correctly.

1. Introduction

Computational Fluid Dynamics (CFD) is now on the new stage of putting the stress on the application to scientific and engineering purposes in a variety of fields. We still have important problems of CFD technique to which continuous efforts should be exerted for improvement . The turbulence models now available are not suitable for separating flow and the resolution of the turbulent flow at high Reynolds number is insufficient. Treatments of moving interface is not yet at the satisfactory level. The grid system must be more conveniently generated with the smallest degree of topological singularity. However, the research works made in the last decade show that the accuracy is on quite a satisfactory level, for the free-surface waves without involving wave breaking, and that the turbulent motions of relatively larger scale including the secondary or longi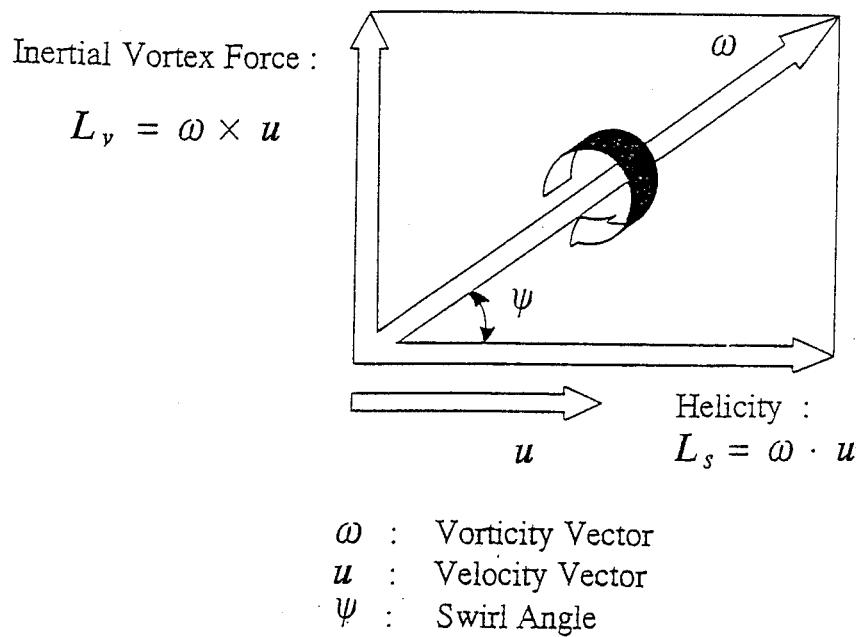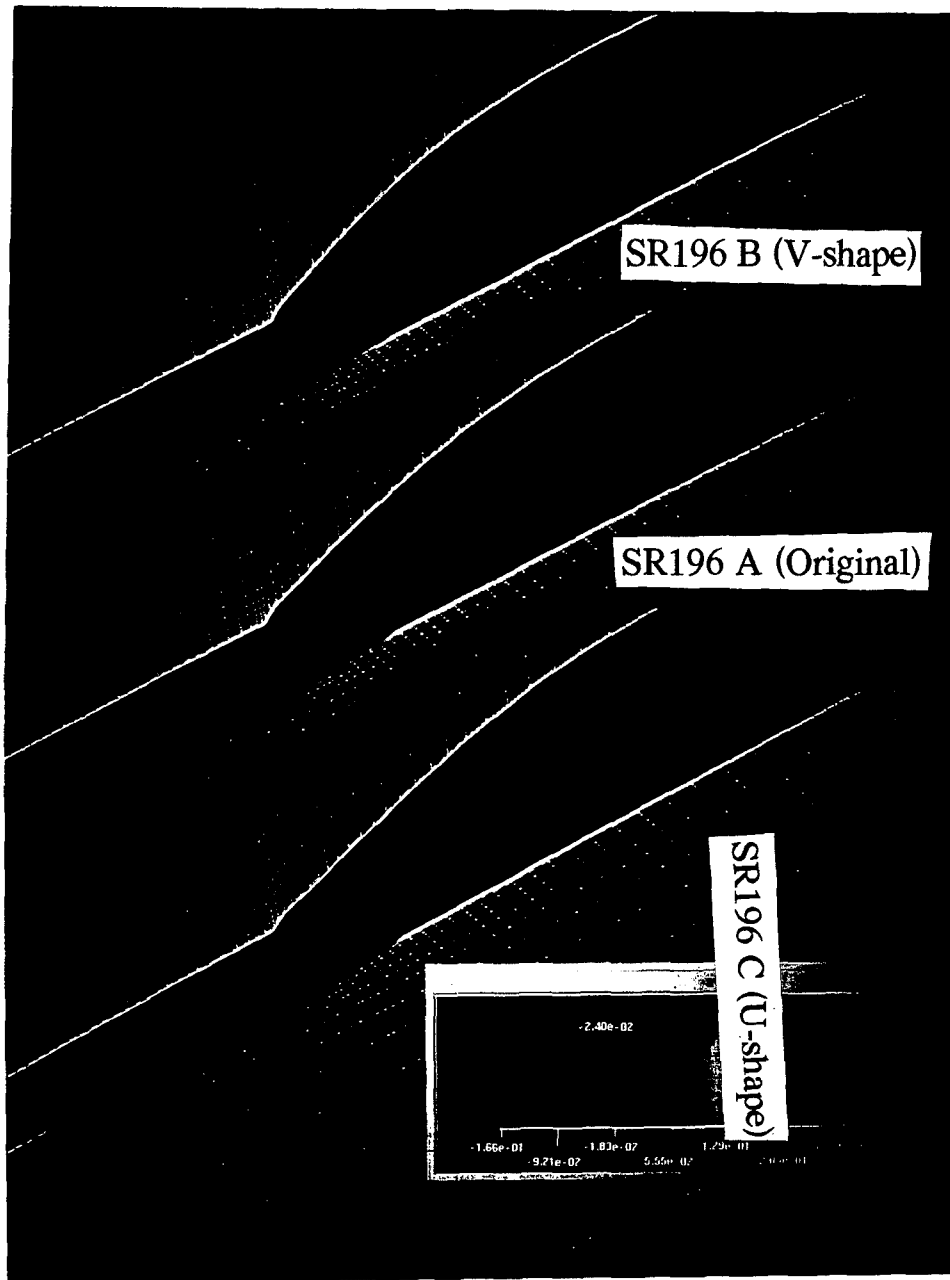tudinal vortices are resolved by the finite-volume simulation techniques in the curvilinear, boundary-fitted coordinate system. Although we are not sufficiently sure to what extent the degree of resolution ability should be raised for respective problems, some examples of applicational approach seem to provide us promising results. The turbulent flow simulations are also going to be on the applicational stage.

The TUMMAC-IV code and WISDAM-V code with modification are used in the course of the development of a new-type fast ferry " Super-Slender-Twin-Hull " (SSTH) . The SSTH is composed of two extremely slender demihulls, which provide sufficiently small degree of wave resistance and relatively lower magnitude of motion transfer functions due to the long ship length, double-stair-bow (DSB) and properly designed hull-form. The development was commenced in 1987 by IHI with the collaboration of the authors' laboratory, and a trials ship was constructed in 1991 and served for the experiments at sea. The principal particulars and the overall configuration are shown in Figs. 1, 3 and in Table 1. The development and the full-scale experiments are reported in Ref. [1] [2].

Because the SSTH is a displacement-type ship, the optimization of the hull configuration, from all of the fluid-dynamical aspects, is of essential importance. A tremendous amount of water basin experiments were performed at the experimental tanks of both IHI and the University of Tokyo. Linear potential theories were used for the determination of the preliminary prismatic curve and for the estimation of motions in waves. The CFD techniques were used for the improvement of the details of the hull-forms.

489

Since the hull-form was of the extremely slender type, the classical linear theories were also very useful. The hybrid use of physical experiments, computational simulations and linear analyses seemed to be most effective for the development of a new ship system with completely new configuration.

In this paper, the TUMMAC-IV code for ship waves is used for the design of the fore-body configuration of minimum wave resistance. Demihulls with both symmetric and asymmetric waterlines are served for numerical simulation and not only the optimal prismatic curve but also the optimal degree of asymmetry are derived by modifying the original code so that it may cope with catamarans. The waves in shallow water are also studied. The WISDAM-V code, which is a finite-volume simulation method for the viscous flow about a ship, is used for the detailed understanding of the viscous flow fields, such as the viscous interaction with waves. It is also used for the estimation of the side-force and yaw-moment on the oblique tow condition.

PART-I FORE-BODY DESIGN
BY WAVE MAKING SIMULATION

2. FSSW and TUMMAC-IV Method

The nonlinear characteristics of bow waves were experimentally clarified and the newly recognized waves were called free-surface shock waves (FSSW) due to the analogical features with the supersonic shock waves. [3] [4] . They indicated that linear theories cannot cope with this nonlinear wave making. Linear theories including the double-model linear theory called modified Rankine source method are based on the assumption that the order of magnitude of perturbation velocities is sufficiently lower than that of the advance speed. However, perturbation velocity is usually of the same order of magnitude in the vicinity of a bow where the most significant waves are generated. This situation is exaggerated in the case of a ship with a blunt bow for which the region of high perturbation velocities occupies a large area. The effect of a bow bulb is most obvious on the FSSW formation as seen in Fig. 3. Furthermore, the steep wave slope and discontinuous velocity field of FSSW do not permit us to employ any kind of linear theory.

The TUMMAC-IV method [5] [6] was initially developed in 1979 when the important part of the characteristics of FSSW were elucidated. It is a finite-difference solution method for the Navier-Stokes or Euler equation. It is solved in the time marching procedure in the rectangular coordinate system. The free-surface condition is fulfilled on the exact location of the free-surface and ingenious techniques are devised so that the free-slip body boundary condition is implemented with sufficient degree of accuracy in the body boundary cells of which shape varies depending on the curvature of the hull-form. The degree of agreement in bow waves is excellent as shown in Fig. 4.

In order to assure whether this method can be used in the practical design procedure, the accuracy in the relative magnitude of wave energy and integrated pressure distribution on hull surfaces is most important. Better full-form of smaller wave resistance can be obtained by such degree of accuracy. We can recall a large number of theoretical works which conjecture the accurate estimation of the absolute value of wave resistance for a simple hull-form. This does not always guarantee the ability of practical application as the history of wave making resistance suggests. It is well known that the wave resistance is sensitively changed due to a delicate difference of lines rather than many other forces. The usefulness of wave making simulation is verified only when this sensitive change of wave formation is realized in the simulation. The practical use of the TUMMAC-IV method which started in 1985 is based on thorough examination from this standpoint. One of the typical examples is described in Ref. [7]. Although the satisfactory accuracy is not achieved, the systematical variation of the FSSW formation is also exemplified in Ref. [8].

3. Monohull Design

3. 1 Optimization procedure

The optimum hull-form of catamaran is based on the optimum hull-form of monohull. Therefore, the development of hull-form was started with the optimization of monohull. The length-beam ratio of conventional ships, including warships, had been less than 12, with which the value of wave resistance coefficient on the last hump is extremely large and the required horsepower exceeds economical limit. This is avoided very easily by increasing the length-beam ratio.

The design point of minimum resistance is determined by compromising the decreasing wave resistance and the increasing frictional resistance due to the elongation of the monohull at the constant volume for buoyancy.

When the first approximation of the optimal particulars of monohull is derived. The slender body theory is employed for the improvement of the prismatic curve of the monohull. For this slender hull, at high Froude numbers, the nonlinearity of the waves is not very dominant. Therefore, this second stage is very economically performed.

In the third stage, the lines (especially near the bow) is improved by the numerical simulation of the waves on the fore-part of the hull. The hull-form is systematically modified and the modified offsets are put into the computation. Since the rectangular coordinate system is employed in the TUMMAC-IV method, the grid generation (cell division) is automatically made and the grid spacing is absolutely common to all modifications.

490

3. 2 Towing test results

The optimal monohull configuration is not derived only from the viewpoint of resistance. The motion properties must be carefully studied since the slamming phenomenon can take place at relatively low angle of pitching for the long, shallow-drafted ship. Therefore, in the above-mentioned procedure of monohull optimization, motion tests are successively made at the towing tank.

After preliminary optimization of the prismatic curve, the frame-lines and the profile of the monohull in the above-mentioned procedure , the optimal length-beam ratio is experimentally determined. The results of towing test with three ship models with various length-beam ratio are shown in Fig. 5. By the dimensions of M-L3, the total resistance reached almost minimal level for a monohull.

4. Catamaran Design

4. 1 Optimization procedure

Design is made of a SSTH catamaran of which displacement is greater than 500ton and the service speed is 40kt .

When the distance between the two demihulls are sufficiently large, the combination of two optimal demihulls makes the optimal catamaran, because the interaction of two demihulls can be ignored. However, since the length-beam ratio of SSTH configuration is around 5, the flow between two demihulls is remarkably influenced by the interaction of the waves from two demihulls. Therefore, the optimization of each demihull must be made by considering the wave interactions on the second stage. The optimal configuration may not be a symmetric one, since the wave resistance is usually increased by the amplification of waves due to the interaction of the two wave systems from two demihulls.

The optimal monohull configuration obtained in the procedure described in the previous section is used as a component of a catamaran and its configuration is improved by the simulation of the TUMMAC-IV method which is modified so that it may cope with the catamaran case.

4. 2 Modification of TUMMAC-IV

The computational domain for wave simulation is schematically shown in Fig. 6. Only the fore part is considered and the region of computation is devided into inner and outer parts. The flows of both parts are separately computed, which means that the flow is assumed not to go across the centerline of each demihull.

For the flow simulation in the inner region, the centerline condition is imposed on the side boundary as shown in Fig. 7. This is very easily implemented simply by giving zero normal velocity on this surface instead of the zero-normal-gradient condition.

4. 3 Computation and results

About 40,000 grid points were allocated in each part of the computational domain and the grid spacing is variable in the vertical direction, which is especially important for SSTH, because the wave height is very small in comparison with the ship length. The flow is accelerated from the still condition to the steadily advancing condition by 400 time steps and the steady state of the waves was researched at the 700-th time step.

The results of a series simulation are summarized in the wave contour maps in Figs. 8 and 9 for the outer and inner part, respectively. The wave hight is normalized with respect to the head of the uniform stream. Keeping the symmetric configuration the demihull 's prismatic curve is modified from M-P1 to M-P2, which unexpectedly resulted in higher waves outside and lower wave depression near the midship although the maximum wave height on the centerline of the catamaran is slightly reduced.

The demihull configuration is further modified and a bow-bulb like configuration is given to M-P3 and M-P4. With the same prismatic curve, these two models have different degree of asymmetry about the centerline of a demihull. When the beam-length of the inner hull is set at 66.67 percent of the outer hull, the displacement volume of the inner hull is 40 percent of the total displacement volume. In this way 40 percent of the displacement is alloted on the inner part of M-P3 and 45 percent on that of M-P4. As shown in Fig. 9, the maximum wave height on the centerline of the catamaran is about 30 percent reduced by the 40 to 60 percent distribution of M-P3. However, the waves outside are significantly accentuated and the integrated wave energy of M-P3 is much larger than M-P4. In this process, the optimal catamaran configuration is derived and its quantitative properties of resistance coefficient are obtained through towing tests.

5. Wave Making in Shallow Water

5. 1 Bottom condition

For the TUMMAC-IV method the flow simulation in a restricted water region can be very conveniently performed as is anticipated in the treatment of centerline condition of a catamaran. By simply imposing zero vertical velocity on the point where the vertical velocity is defined in the staggered grid system as shown in Fig. 11 the free-slip bottom boundary condition is implemented. The pressure on the lowest pressure point below the bottom by half of the vertical spacing is extrapolated from the pressure above, through the relation of the Navier-Stokes equation in the vertical direction.

5. 2 Simulation results

The condition of the computation is shown in Fig. 10 and only the fore-part of a catamaran M-P4 is served for the computation. The other conditions of

491

computation are the same with the cases described in the previous section.

The obtained wave contour maps are shown in Fig. 12. It can be seen that the bow waves are reduced on both sides of a demihull and that the free-surface is remarkably suppressed in between the two demihulls. The wave field is quite different from the case in deep water.

PART-II AFTBODY DESIGN BY VISCOUS FLOW SIMULATION

6. WISDAM-V Method

For the viscous flow, simulation for a ship with smooth surface of gentle curvature a boundary-fitted curvilinear coordinate system must be employed. Since the viscous flow is intrinsically unsteady, the time-marching solution procedure, preferably explicit time-accurate one, is most suitable. Due to the limited number of grid points, the longitudinal or girthwise spacing may be 1000 times larger than the grid spacing normal to the hull surface. In such a grid system, the conservation laws of mass and momentum are difficult to fulfill in the finite-difference scheme. Therefore, the finite-volume scheme is often employed in the simulation techniques for flows about bodies of complex geometry.

Since the two-equation turbulence model is not suitable for the separated flow, and many experiences indicate insufficient evolution of the flow with intense vorticity, the subgrid-scale (SGS) turbulence model is employed in the WISDAM-V method. Because an outer flow about a body of complex geometry is treated here and then the periodic condition cannot be imposed at the inflow and outflow boundaries, the SGS turbulence model is used in a very averaged manner. However, the long experience with this turbulence model both in the TUMMAC and WISDAM methods suggests that the complicated 3D structure of vortices in the thick boundary layer and separated flow is more realistically resolved with this model than others. In order to meet the use of the SGS turbulence model, no wall-function is imposed on the body surface. Therefore, the damping function and the length-scale of the turbulence model must be carefully tuned depending on the Reynolds number and the grid spacing. All the computations by the WISDAM-V method in this paper are performed at the Reynolds number 1×10^6, which is of the same order with the experiments with a small ship model.

The WISDAM-V method is developed with the above-mentioned considerations. The detailed description of the method and numerical tests are already reported in Ref. [7] [8] [9] and they are not repeated in this paper.

7. Effect of Asymmetric Hull on Viscous Flow

7. 1 Condition of computation

Since a hull-form of asymmetric configuration turned out to be useful from the resistance point of view, the viscous flow field about the asymmetric after-body must be studied for the proper design of the hull and propeller (SSTH is propelled either propeller or water-jet installed on both of the demihulls.)

The so-called O-H type grid system is employed for a demihull and both starboard and port side flow-fields are considered so that it may cope with the asymmetrical hull as well as the oblique tow condition. The catamaran configuration is not taken into account because the interaction of viscous flow between two demihulls is supposed to be negligibly small. The transverse view of the grid system is shown in Fig. 13. The length of a ship is devided into 80 grid poinds and the smallest spacing on the hull surface in the direction normal to the hull is less than $y^+ = 5$, where y^+ is the viscous unit. The total number of grid points is around 10^5 in all cases in this paper. Since a stern configuration of transom type is employed for SSTH, a dummy hull is attached in order to avoid topological singularity at the after end.

The computation is started from the still condition and the flow is accelerated to the condition of 40kt by 2000 time steps with the time increment of 2×10^{-4}, where time is made dimensionless with respect to the ship length and the steady advance speed of a ship. Almost steady viscous flow field is attained when the dimensionless time T exceeds 2.0. The drawings of the flow-field in this paper are all for the steady state.

The WISDAM-V method has an advanced version which can simulate the free-surface flow with the free-surface-fitted moving grid system. The grid generation is performed in each time step and the free-surface conditions are implemented on the exact location of the free-surface. The viscous free-surface condition is introduced in a very approximate manner, i. e. , the normal stress is ignored assuming the small curvature of the free-surface and the tangential stress is set to be vanished on the free-surface by giving zero-normal-gradient of horizontal velocity in the thin free-surface layer of which thickness is around 5×10^{-4}. Therefore, the grid system is also attracted to the free-surface.

7. 2 Computation and results

The results of viscous flow simulation for the demihull M-P4 with asymmetric configuration are shown in Figs. 14 to 16. It is noted that the difference of the pressure distribution between two sides of the hull is rather small and the asymmetrical distribution of wake and vorticity does not seem to be influential to the propeller design. It is obviously shown that one pair of longitudinal vortex is present at the stern. This

is much simpler and weaker than the case of a tanker, for which the magnitude of vorticity is 10 times larger and more than two pairs of longitudinal vortices are generated [8].

7. 3 Simulation with free-surface

The simulation by another WISDAM-V version with free-surface is performed on the model M-P4 slightly modified by cutting off the stern end.

The results are shown in Figs. 17 and 18. The waves are very gentle due to the extreme slenderness of the hull. However, the comparison between Fig. 18 and Fig. 16 very clearly indicates that the vorticity field is remarkably influenced by the presence of free-surface. The vortical motions around the bow look intensified and another pair of longitudinal vortices appear near the keel owing to the action of the free-surface waves.

8. Comparison of Buttock Flow

8. 1 Condition of computation

In case a propeller is installed at the stern, its diameter is of the same magnitude with the draft due to the high horsepower for the high service speed. Therefore, the stern configuration is inevitably of the buttock flow type but for such a long ship the suitable configuration is not well known.

The M-P1 hull form is used and the buttock flow configuration is modified as shown in Fig. 19. The length of the after-body of the shortened one is one half of the longer one.

The WISDAM-V method without free-surface is employed and the computation is continued for 10,000 time steps with the time increment of 1×10^{-4}.

8. 2 Simulation results

The results of simulation are shown in Figs. 20 to 22. Relatively high pressure region is caused by the relatively steeper upward slope. These results in the pressure drag coefficient of the shorter version 2.14×10^{-4}, while that of the longer version -0.6×10^{-7}. Although the absolute value is not reliable, the difference between two hulls seems to be well explained. As shown in Fig. 22, the intensity of longitudinal vortex is doubly magnified for the shorter stern. This pair of longitudinal vortex seems to be inevitably generated by the upward variation of the stern configuration.

9. Oblique Tow Simulation

9. 1 Condition of computation

For high-speed ships, the directional stability is more important than low-speed ships, while the catamaran configuration and the use of water-jet units often deteriorate this property. In this section, an oblique tow test is achieved in the numerical simulation as a first step to the directional stability simulation. Only a demihull is used for the computation current.

The oblique flow condition is implemented by giving Ucos β and Usin β for the streamwise and lateral velocity components at the inflow boundary, where β is the oblique tow angle. In the stage of flow acceleration to the steady advance speed, the lateral velocity component in the x^2 direction is also accelerated in a way similar to that in the x^1 direction. The computational domain is stretched laterally so that a complete oblique tow condition is implemented.

The angle of oblique tow is set at 5 degrees and the double-model flow version of the WISDAM-V method is used. The time increment is set at 2.0×10^{-4} and the computation is continued to the dimensionless time T = 2.7.

9. 2 Simulation results

The time-history variations of resistance, lateral force and yawing moment are shown in Fig. 23, in which almost steady state is attained after T = 2.0. These forces and moment are normalized with respect to the velocity head $1/2 \rho U^2$ and 2/3 power of volume or volume itself for forces and moment, respectively.

The flow-field and pressure distribution at the steady state are shown in Figs. 24 to 26. Wakes are seriously distorted and the structure of vortices are deformed and the strength of vortices is amplified. It is noted that the contour interval in Fig. 24 (right) is five-times magnified than those in Figs 16 and 18.

In Fig. 26, the pressure difference between face and back sides of the hull is most obvious at the bow and it is gradually reduced on the after-part of the hull. This pressure distribution on the waterlines is supposed to be caused partly by the usual nature of pressure distribution of a wing section and partly by the buttock flow configuration of the after-part. The detailed pressure distribution on the oblique tow condition seems to be very useful for the understanding of the generation of asymmetric force and moment.

The computed lateral force and yawing moment are compared with the measured results in Figs. 27 and 28. The experiments were conducted at the University Tokyo Tank with a 2.8m long model. The model was steadily fixed to the carriage and obliquely towed at the Froude number 0.2. The forces and moment were measured by a load- cell unit. The towing speed was varied up to Fn = 0.30 and the effect of the free-surface motions were studied, and the variation was from 0.032 to 0.041 for the lateral force and from 0.17 to 0.19 for the yawing moment. The agreement seems to be very satisfactory.

A number of research works are known for the theoretical explanation of the forces in the oblique tow condition, quite recently by Tahara [10]. The pressure distribution in Fig. 26 indicates that a simpler

method with some postulations may give satisfactory agreement. However in the hull-form with more complicated stern configuration, the resolution of the 3D vortical flow-field may be of substantial importance.

10. Conclusions

Two numerical simulation techniques are applied in the process of developing a new-type, high-speed ship. Since hydrodynamical properties determine the most important part of a high-speed ship, the assistance of such numerical tools are very useful.

In this paper, two quite different numerical methods are used. Since the grid spacing is too coarse in the region little away from the hull where wave making is still important, the WISDAM-V method is not yet applied to the process of searching a hull-form of minimum wave resistance with sufficient reliability. However, when sufficient number of grid points can be allotted on the free-surface, all the computations will be performed by the WISDAM-V method and all features and values related with resistance will be simultaneously simulated. If the movement of a ship can be treated by use of a moving grid technique, a considerable part of " numerical tank " will be completed.

The hull-form development of SSTH was conducted by the collaboration with the Technology Development Division and the Research Institute of IHI. This paper describes a part of this work mostly parformed at the University of Tokyo. The authors are grateful to Mr. R. Ono, Mr. H. Nogami, Mr. S. Mizoguchi, Mr. Y. Shirose and all other members of the SSTH project at IHI.

References

1. H. Miyata et al. , Fast ferry by super-slender twin hull, Proc. IMAS'91 (The Institute of Marine Engineers International Conference) Sydney, 1991.

2. A. Abe et al. , Full-scale experiment and advanced design of SSTH ferries, Proc. Intersociety High Performance Marine Vehicle Conference and Exhibit (American Society of Naval Engineers), Arlington, USA, 1992.

3. T. Inui et al. , Experimental investigations on the wave making in the near-field of ships, J. Kansai Soc. Naval Archit. Vol. 173 (1979).

4. H. Miyata. et al. , Nonlinear ship waves, Adv. Appl. Mech. Vol. 24, (1984).

5. H. Miyata et al. , Finite-difference simulation of nonlinear waves generated by ships of arbitrary three-dimensional configuration, J. Comput. Phys. Vol. 60-3, 1985.

6. H. Miyata et al. , Finite-difference simulation of nonlinear ship waves, J. Fluid Mech. vol. 157, (1985) .

7. Y. Maekawa et al. , A method of optimizing hull-forms by use of the finite-difference technique TUMMAC-IV, Intern. Symposium on Ship Resistance and Powering Performance, Shanghai, China (1989).

8. K. Aoki et al. , A numerical analysis of nonlinear waves generated by ships of arbitrary waterline (First report) (Second report) , J. Soc. Naval Archit. Japan Vol. 154, 155, (1983) (1984).

9. O. Watanabe et al. , Numerical simulation of a . O. Watanabe et al. , Numerical simulation of a viscous flow with free-surface wave about a ship by a finite-volume method, J. Soc. Naval Archit. Japan Vol. 171 (1992) (in Japanese).

10. H. Miyata et al. , Numerical study on a viscous flow with free-surface waves about a ship in steady straight course by a finite-volume method, J. Ship Research (to appear).

11. O. Yoshida et al. , Verification of the viscous flow-field simulation for practical hull-forms by the finite-volume method WISDAM-V, J. Soc. Naval Archit. Japan (to appear) (in Japanese).

12. Y. Tahara, A boundary-element method for calculating free-surface around a yawed ship, J. Kansai Soc. Naval Archit. (to appear).
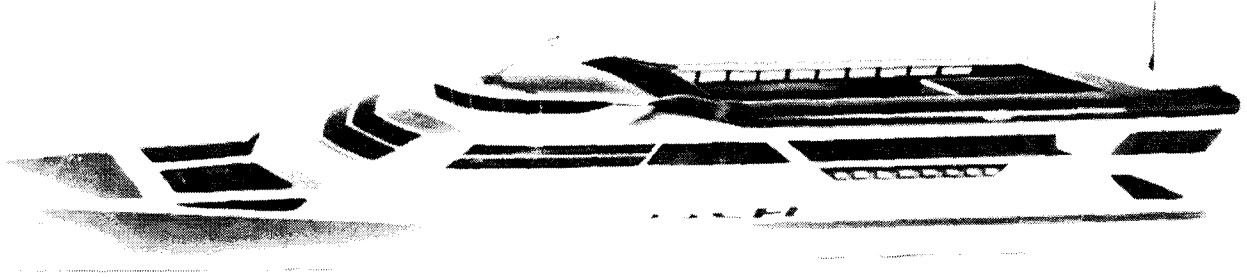
Fig. 1   Artist impression of SSTH ferry (75m craft)

Table 1   Principal particulars of SSTH ferry design

IHI Super Slender Twin Hull (SSTH) ferry design
Approximate dimensions and performance when fitted with propellers

	90m craft	Trials craft
Length bp	75.0m	24.0m
Breadth moulded	19.4m	5.6m
Depth moulded	4.9m	1.9m
Draught	2.3m	0.7m
Gross tonnage	3600tonnes	52tonnes
Capacity		
-passengers	400	68
-cars	80	-
Maximum speed	40knots	28.5knots
Main engines	4 × high speed diesels	2 × high speed diesels
	4 × 7000ps	2 × 605ps
Propulsion system	waterjet	propeller
Range	200n miles	100n miles

Fig. 2   SSTH30 trials craft off Yokohama

495
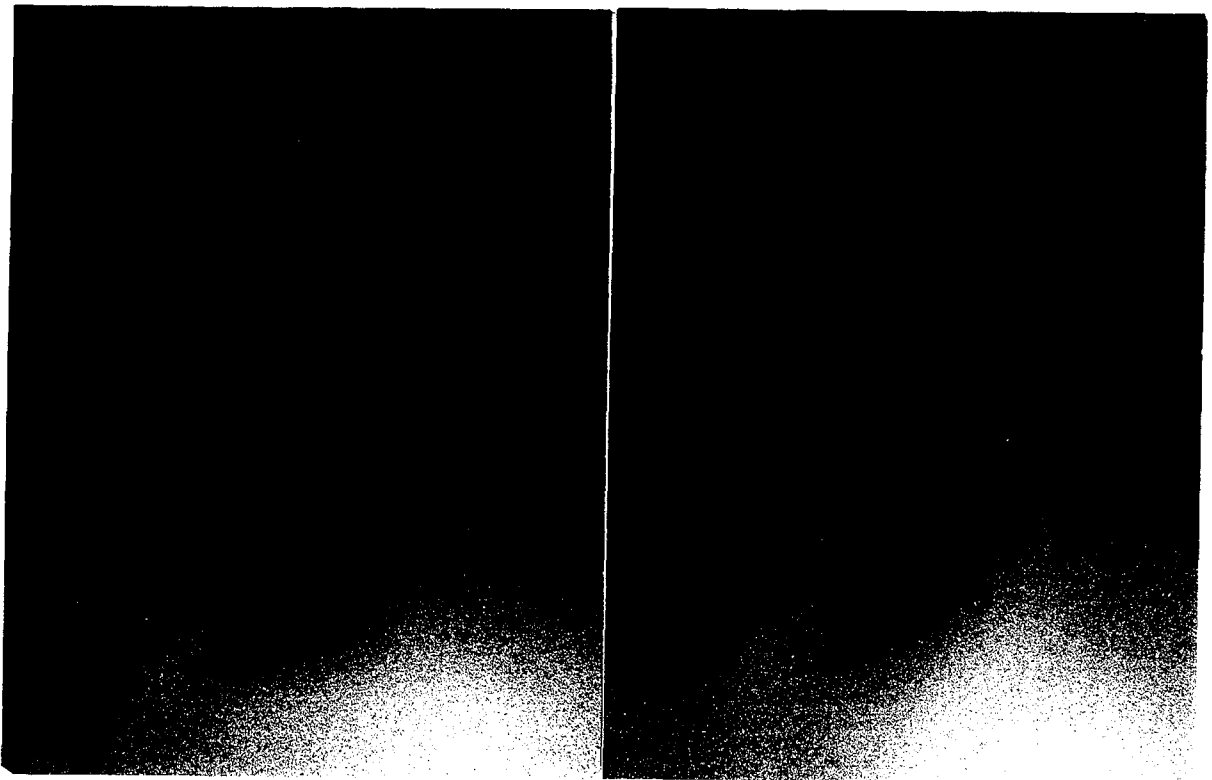
Fig. 3   Bow wave pictures of a simple ship
model without bulb (left) and with a bulb
(right).
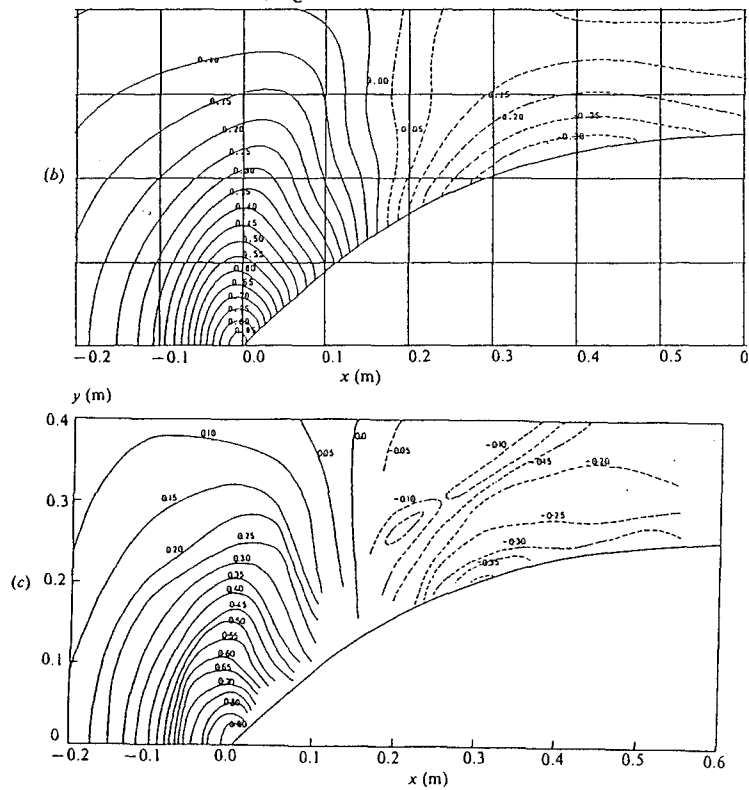
Fig. 4   Comparison of wave contour maps of
bow waves of a tanker
model, simulation (upper) and
experiment (lower).

Ct

V (kt)

Cw

V (kt)
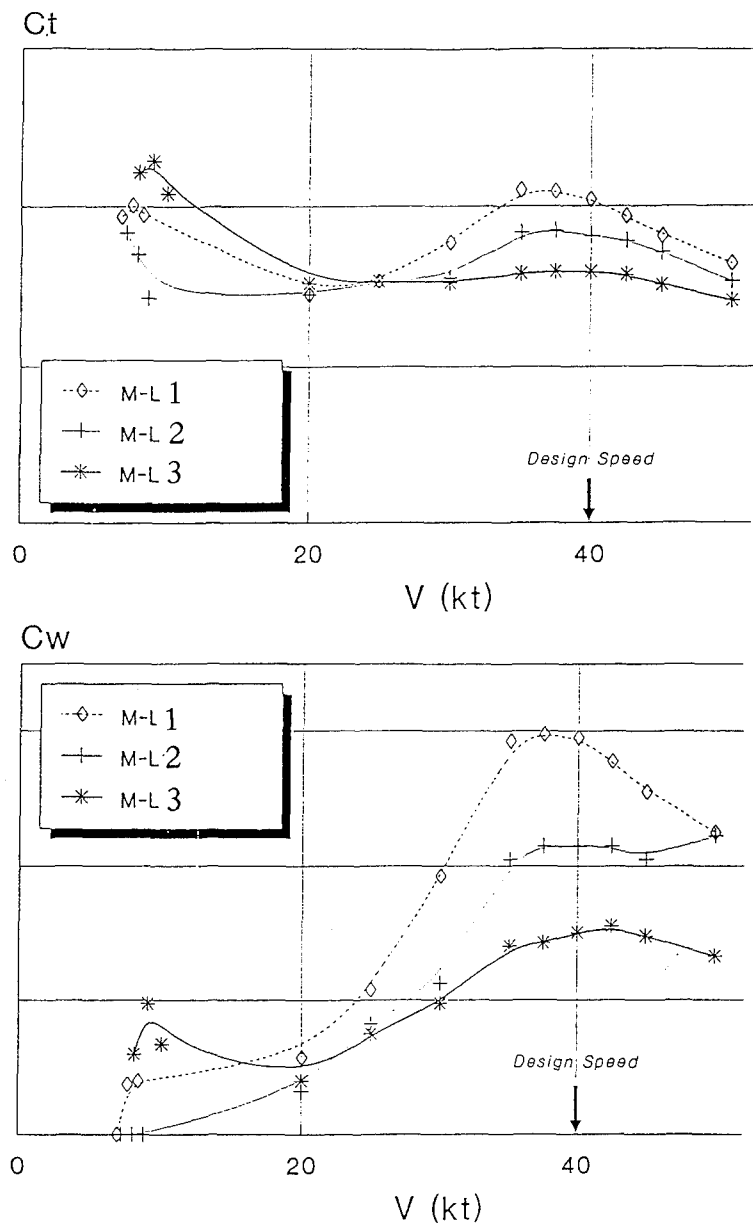
Fig. 5   Comparison of total and wave resistance
curves due to the difference of
slenderness.

497
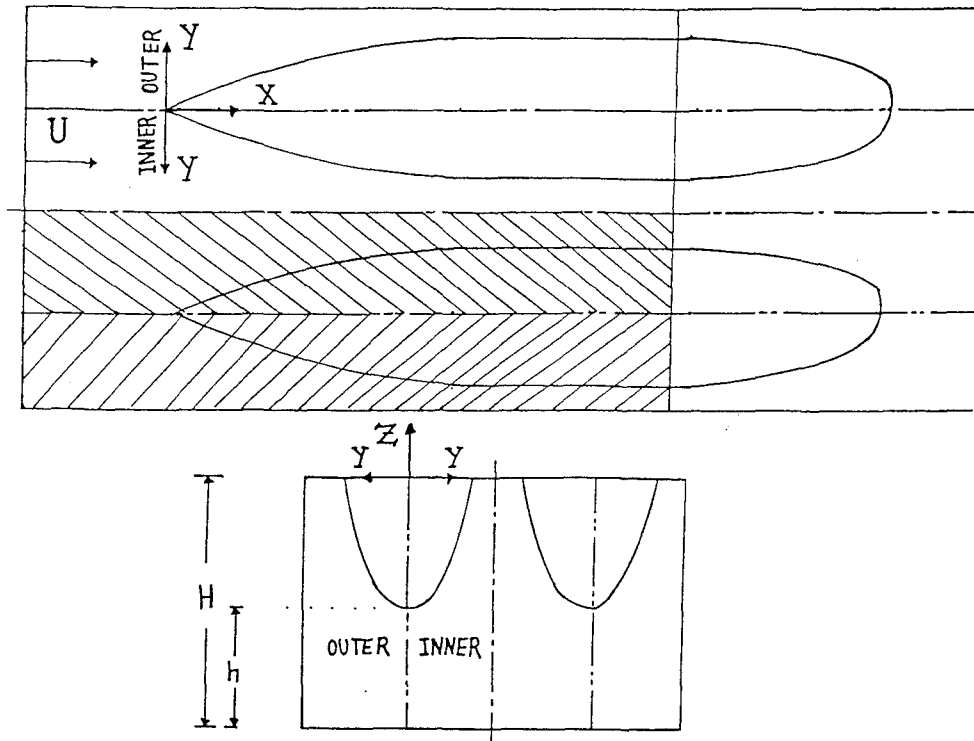
Fig. 6   Computational domain for the
          approximate treatment of a catamaran
          hull for TUMMAC-IV simulations.
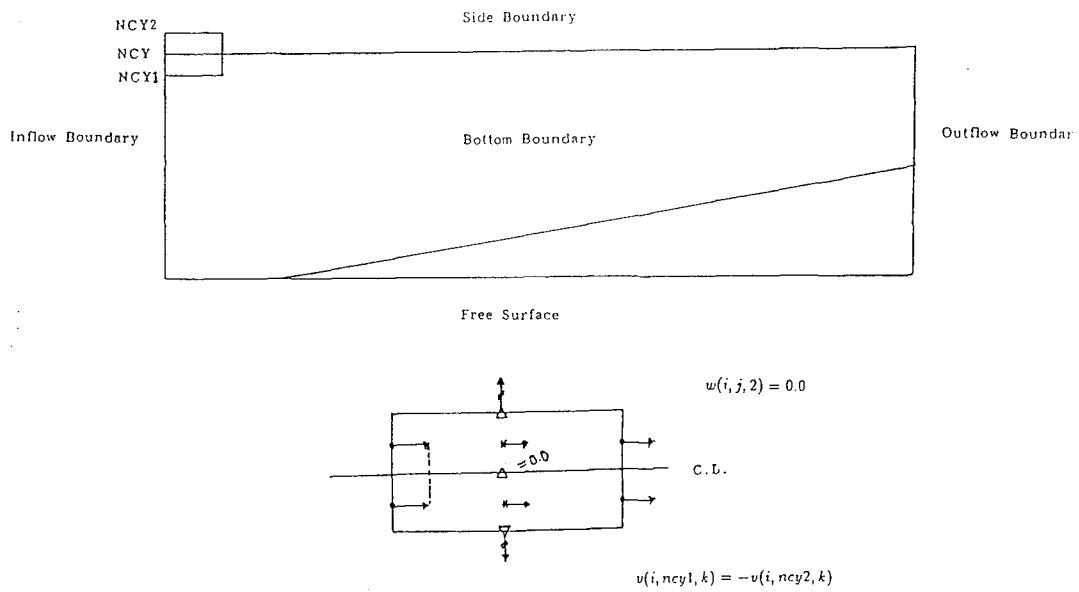
Fig. 7   Boundary conditions for the inner side of
          a catamaran
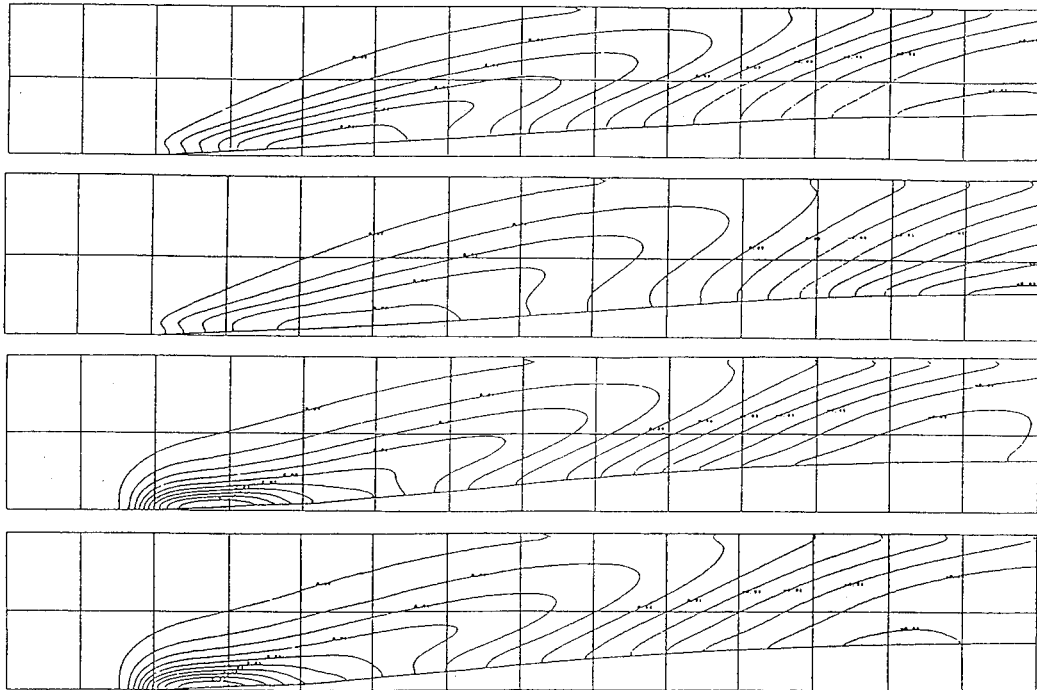
Fig. 8 Comparison of simulated wave contours
in the outer region of a catamaran at
40kt, contour interval is 0.01
nondimensional wave height, M-P1,
M-P2, M-P3 and M-P4 from above, the
contour interval is 0.05.
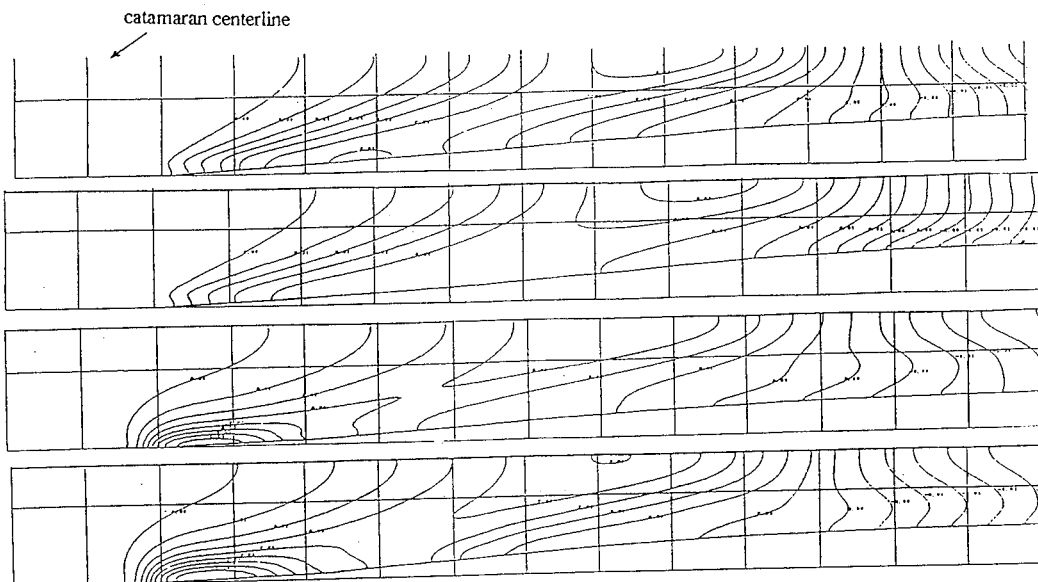
Fig. 9 Same as Fig. 8, in the inner region of a
catamaran, top-side of each
figure coincides with the catamaran
centerline.
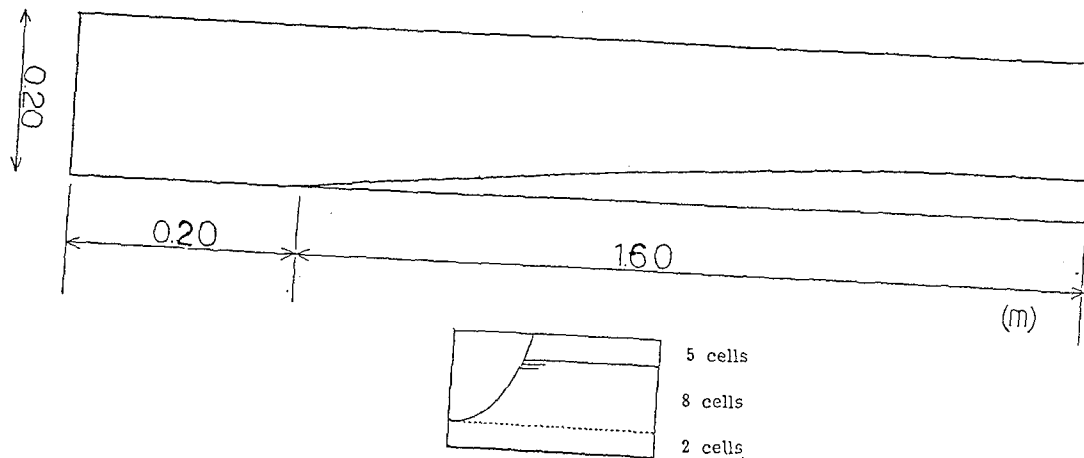
Fig. 10   Computational domain for the shallow
water case.

$$P_{k=1} = P_{k=2} + dZ(1)/dt * (w(i,j,2) - wc(i,j,2))$$
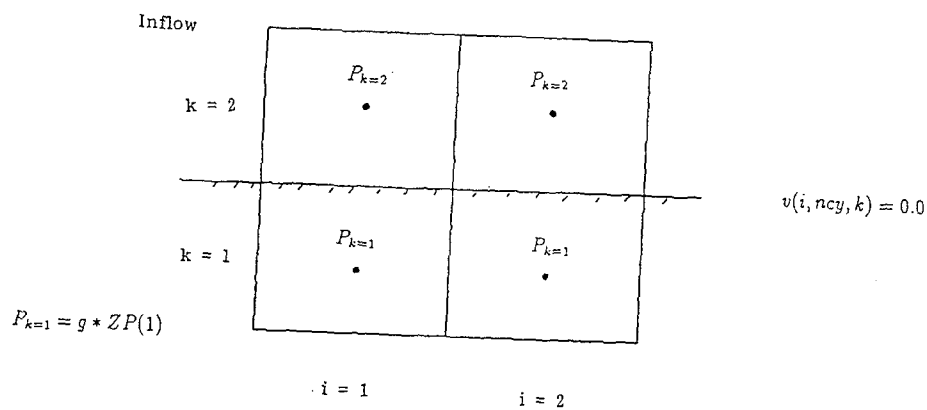
Fig. 11   Bottom boundary condition.
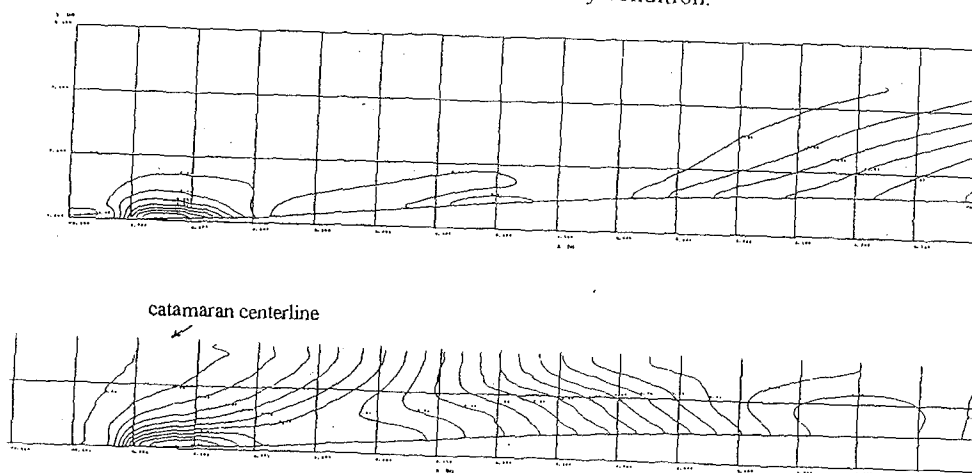
Fig. 12   Simulated wave contours of the outer (
above) and inner (below) regions,
the contour interval is 0.05.
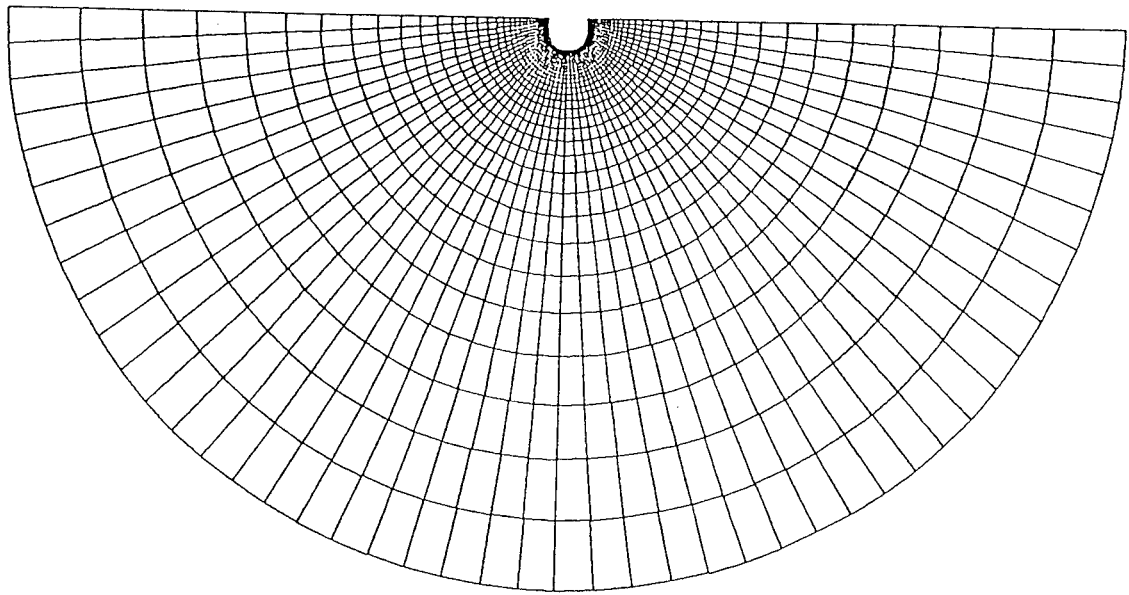
Transverse Section of Grid System

Fig. 13   Transverse section of grid system
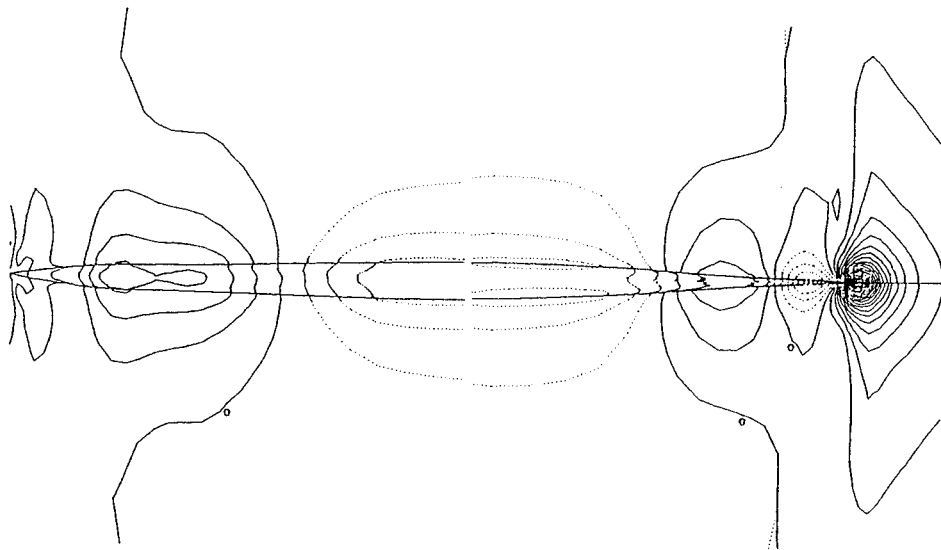
Pressure Fields   Waterplane, con-
l= 2 × 10⁻³

Fig. 14   Pressure contours of M-P4 on hull
surface and water plane, the contour
interval is 2×10^{-3}, bow field (right
)and stern field (left).

Pressure Coefficient of M60C (2)
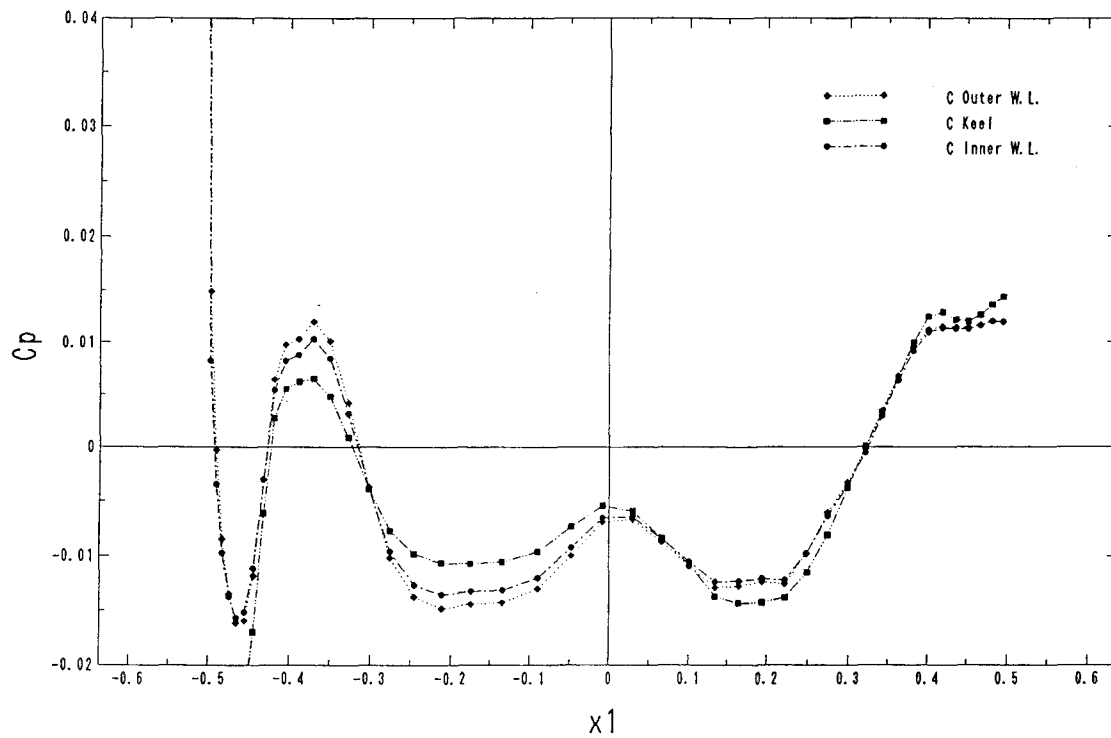
Fig. 15   Longitudinal distribution of pressure on
three lines of a hull.

X = - 0.46
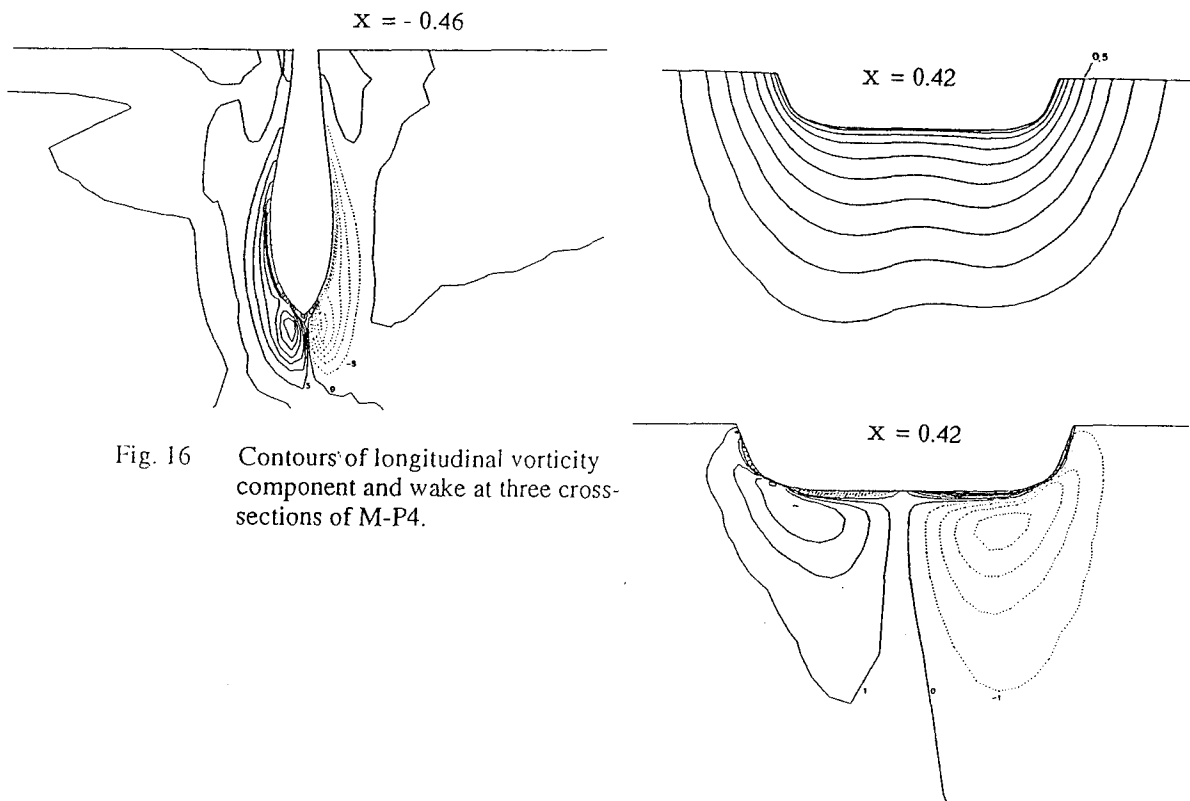
Fig. 16   Contours of longitudinal vorticity
component and wake at three cross-
sections of M-P4.

502
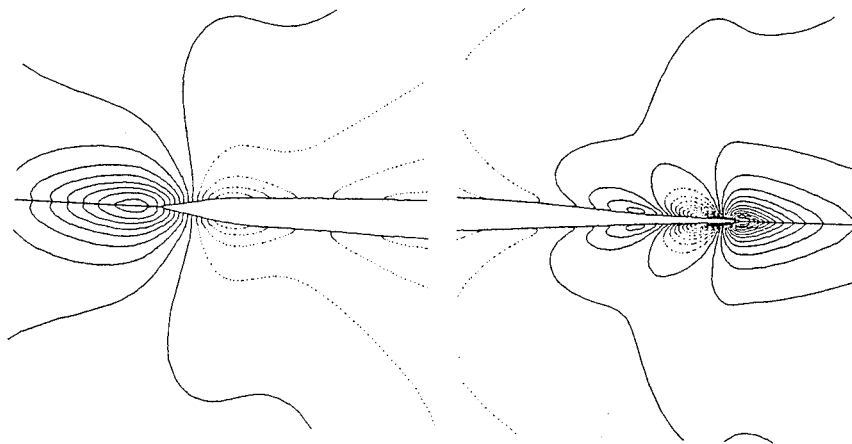
Fig. 17   Simulated bow (right) and stern (left)
           wave systems for M-P4 with
           short stern.

x = - 0.46
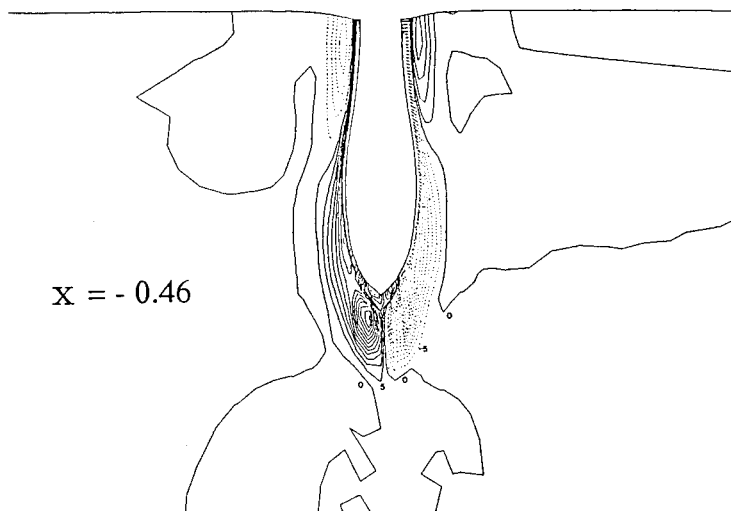
Fig. 18   Contours of longitudinal vorticity
           component of M-P4 with short stern,
           simulation with free-surface.
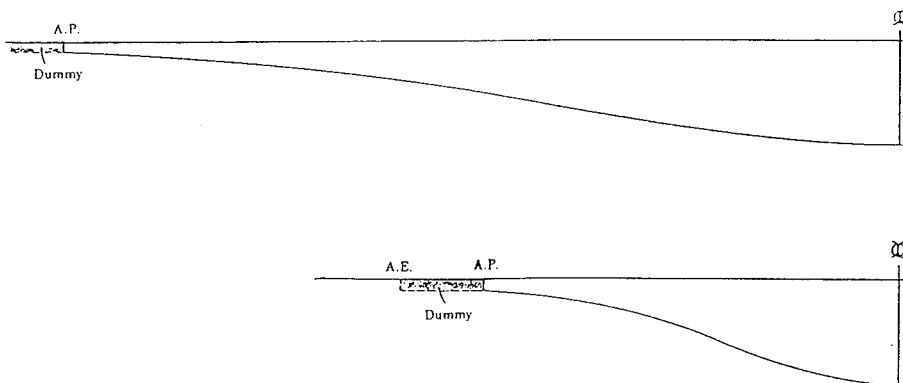
Fig. 19   Comparison of hull profile of M-P1
           (upper) shortened model   (lower).

503
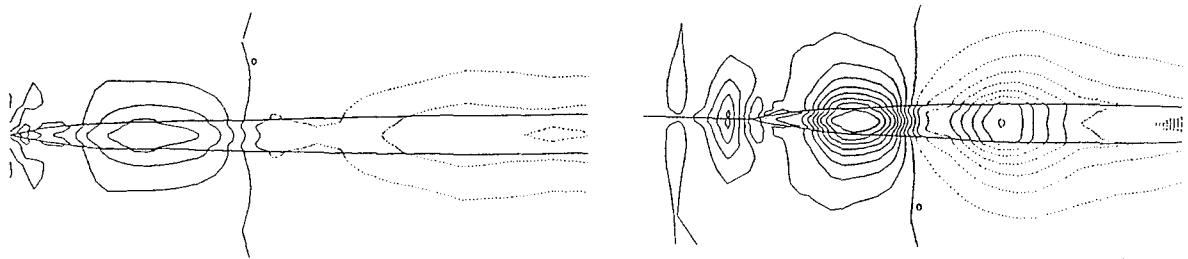
Fig. 20   Comparison of pressure contours on hull
surface and waterplene, M-P1
(left) and shortened model (right), the
contour interval is 2×10^{-3}
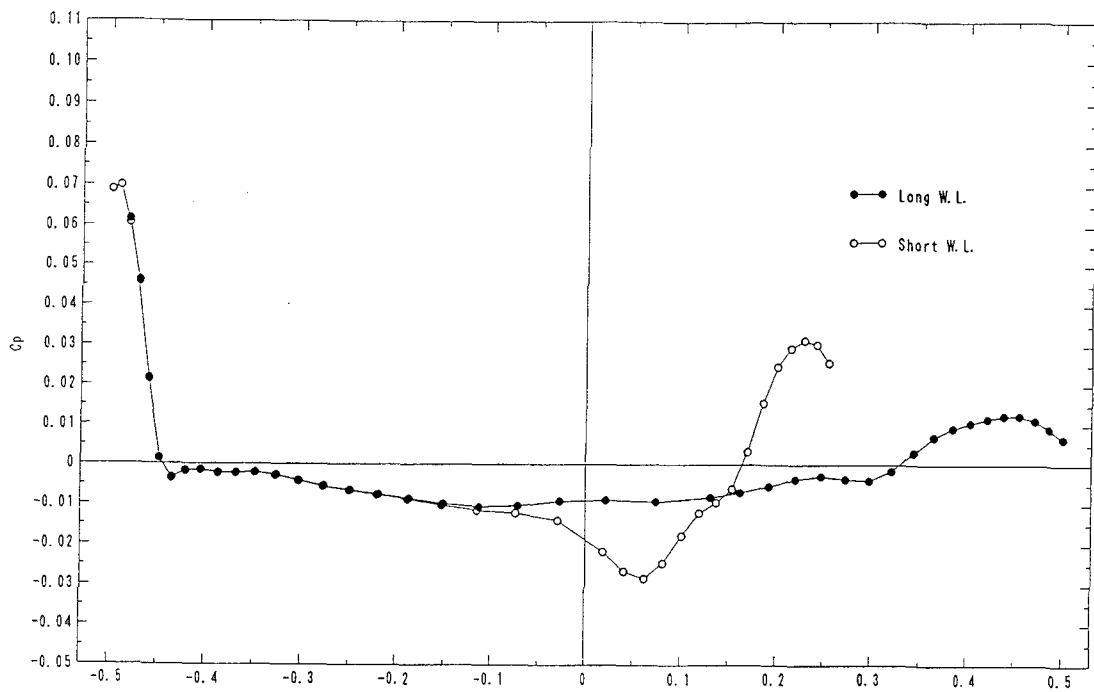
Fig. 21   Comparison of pressure coefficient along
waterlines of M-P1 and shortened
model.
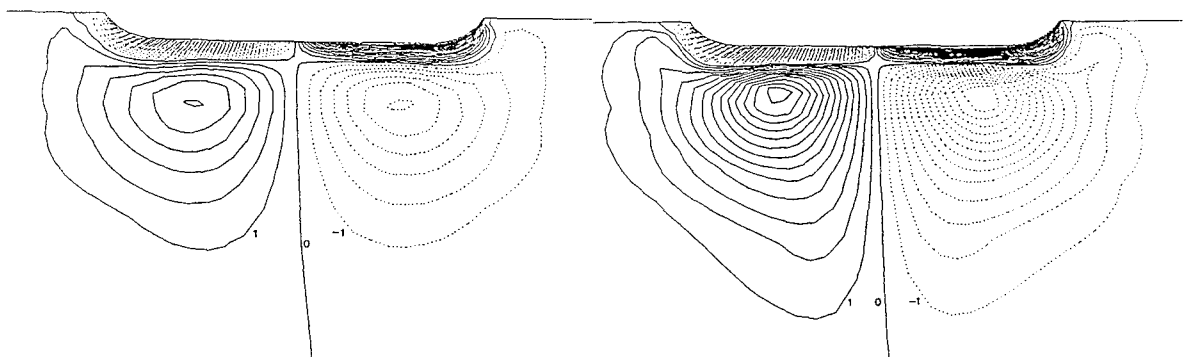
Fig. 22   Comparison of longitudinal vorticity
contours at the stern end of M-P1
and the shortened model.

504
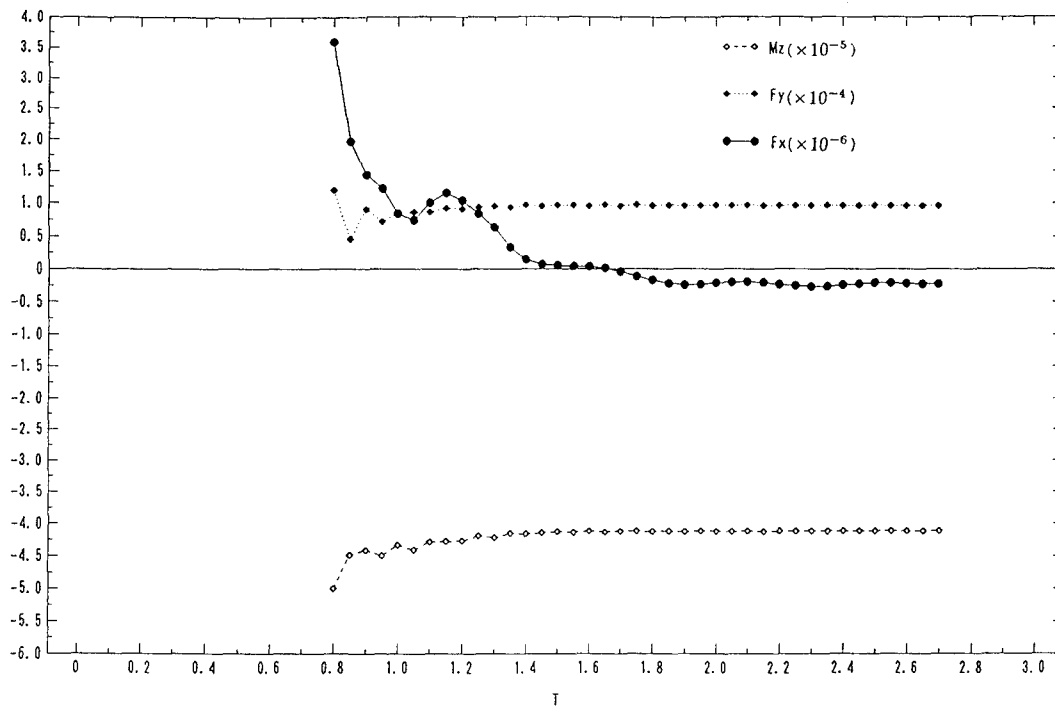
Fig. 23   Time-historical variation of forces and
moment in the simulation of the
oblique tow case.
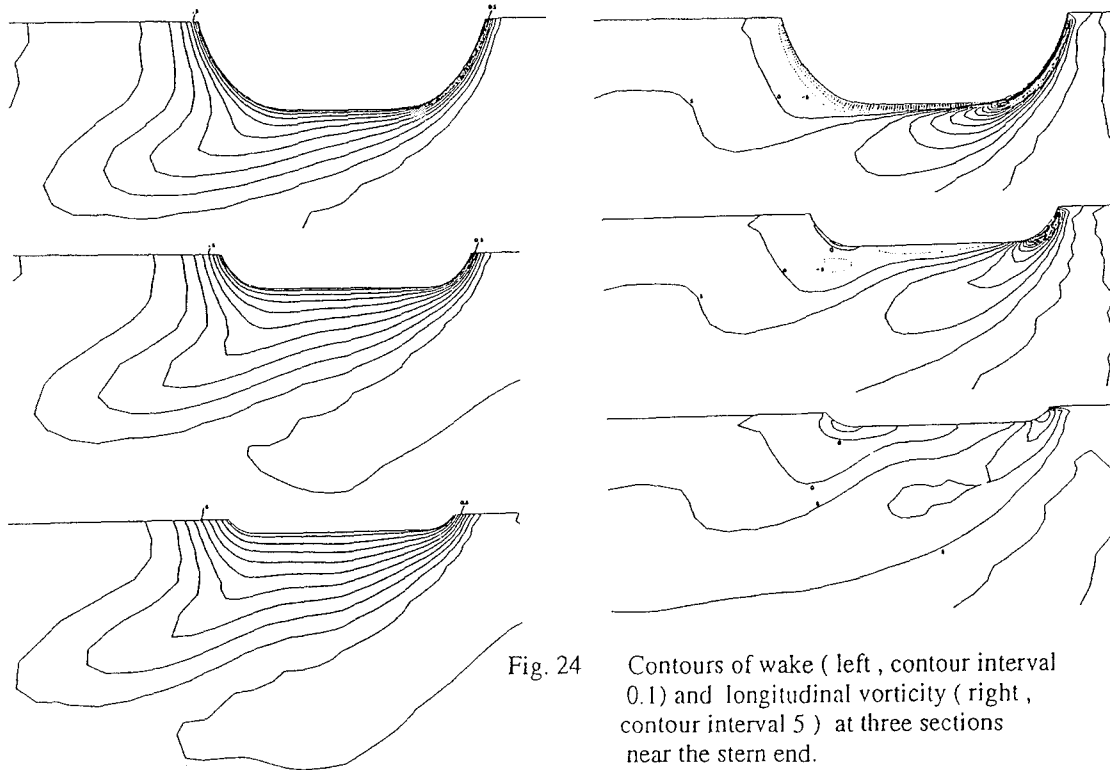
Fig. 24   Contours of wake (left , contour interval
0.1) and longitudinal vorticity (right ,
contour interval 5) at three sections
near the stern end.
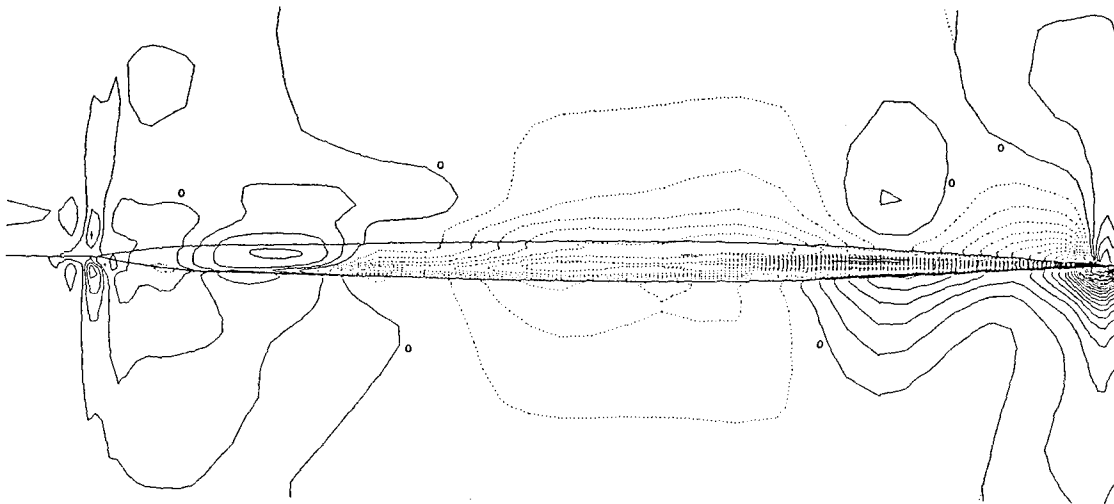
Fig. 25   Pressure distribution on the hull surface
            and waterplane of the 5° oblique
            tow case, the contour interval is 2×10^{-3}.
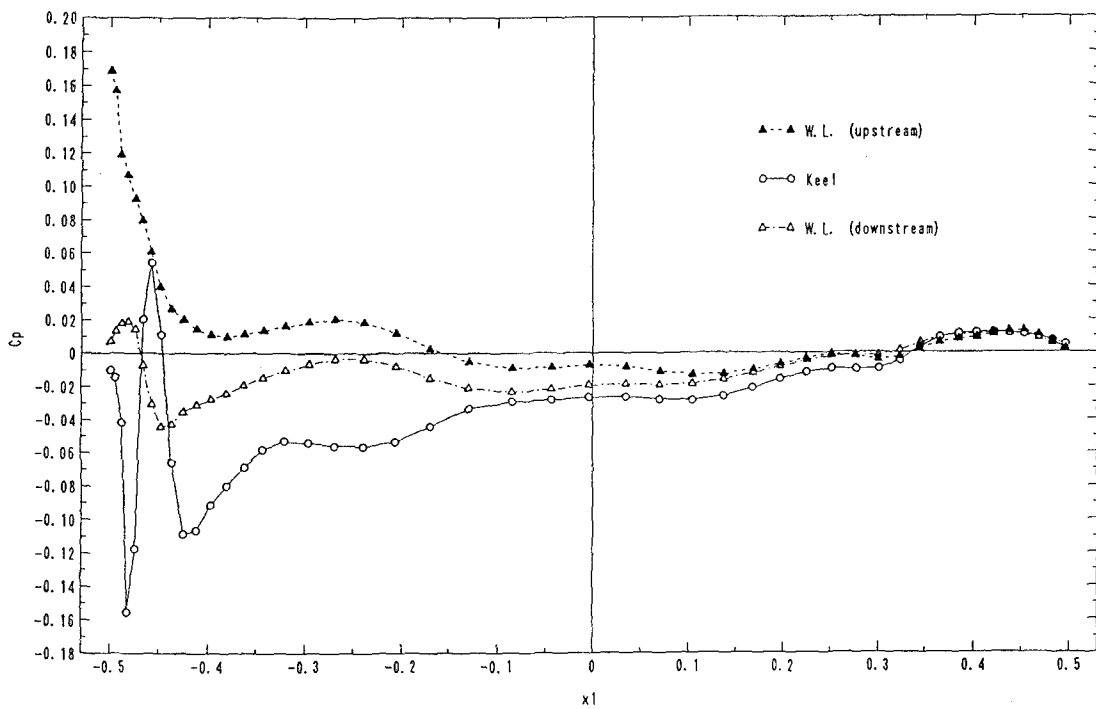
Fig. 26   Longitudinal distribution of pressure on
            the hull surface.
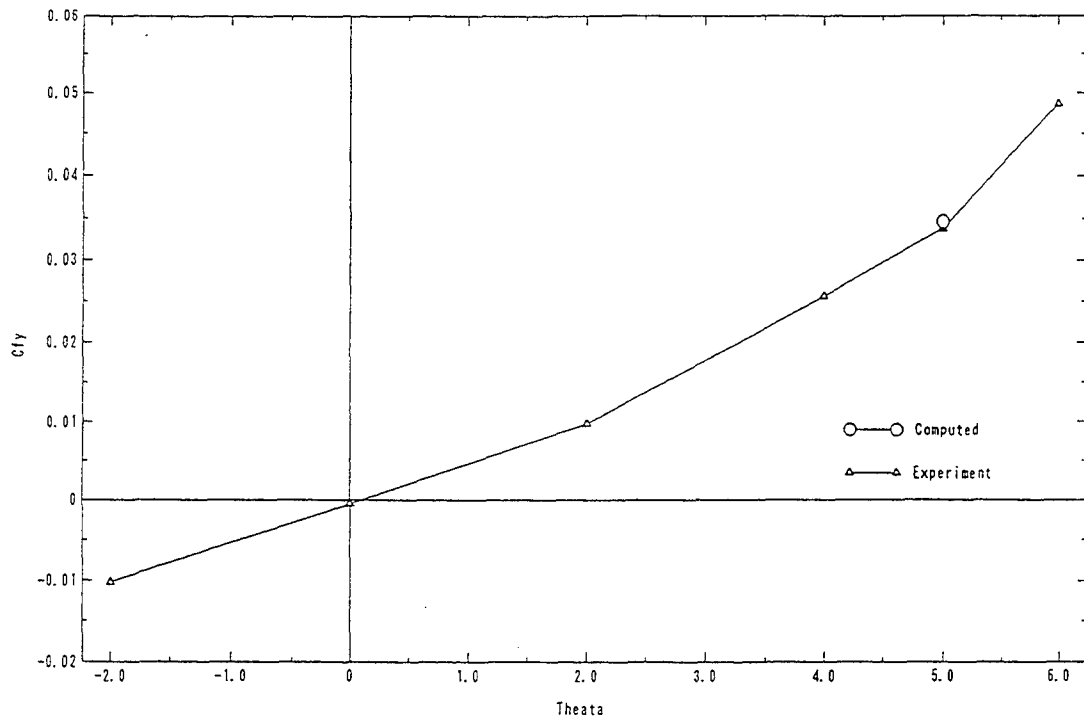
Fig. 27　Lateral force vs. oblique tow angle.
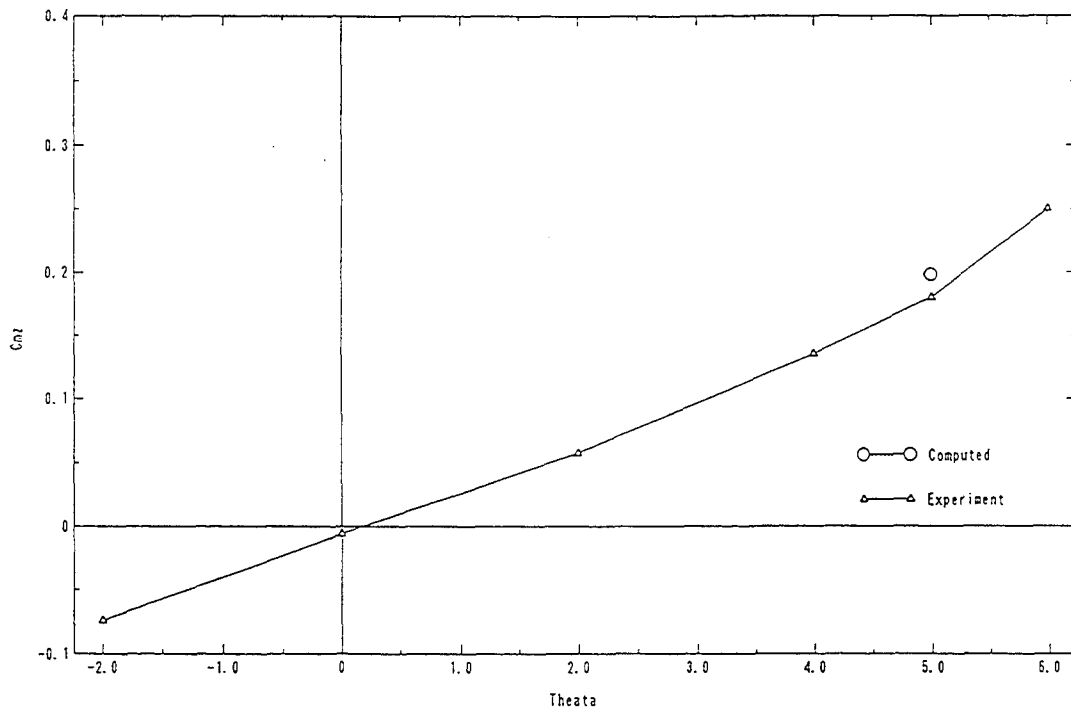
Fig. 28　Yaw moment coefficient vs. oblique tow
angle.

DISCUSSION
by Dr. J. Ando and Dr. K. Nakatake
Kyushu Univ., Japan.

We would like to congratulate the authors for developing SSTH by concerted applications of several numerical techniques. We are interested in the flow field in the stern region where the propeller is operating. According to our experience, the free surface effect on the stern flow becomes large at high speeds. A comparison between Fig. 18 with Fig. 16 in your paper indicates the strong effect of the free surface on the vorticity field. You showed the calculated flow field near the stern region without free surface. If the free surface is considered, however, we believe that the flow field will be fairly different. Would you comment on this point?

Author's Reply

As the discussors suggest, the interaction of the free-surface with the viscous motion is most important at the stern. This is especially true for high-speed vessels and has been one of the major objectives of the researches at the author's laboratory. However, we have not yet reached the satisfactory results due partly to the nonlinearity of the free-surface motion and partly to the inadequacy of the turbulence modelling.

DISCUSSION
by Dr. Raven
MARIN

According to your presentation, you used two (2) criteria to select the best hull form from the wave-resistance point of view:

- the peak wave heights in between the demi-hulls;
- the integrated wave energy in the entire domain.

The former is not necessarily related to the wave resistance. Could you clarify the second criterion?
Is this a wave pattern analysis approach, or anything else representative of radiated wave energy?

Author's Reply

One of the shortcomings of such CFD simulation of waves in a restricted region is that the dispersive spread of wave system is not well realized. Therefore, the estimation of the relative magnitude of wave resistance must be made by either integration of wave energy in the computational domain or integration of the surface pressure distribution. For local modification of the hull form the use of the former is useful and the letter for other cases if pressure integration is carefully performed.

DISCUSSION
by Dr. Marshall P. Tulin
Ocean Engineering Laboratory, UCSB

The authors do not provide section plans for the hulls, which are the subject of the paper. It is therefore difficult to analyze their results. Could they provide a sketch showing section plans?

Author's Reply

The purpose of our paper is to demonstrate the extent the CFD techniques can be applied to very practical problems. Unfortunately we cannot show details of the lines, because it is really practical.

SESSION 10

LIFTING-SURFACE FLOW: INVISCID METHODS

The Nonlinear Numerical Prediction of Unsteady Sheet Cavitation for Propellers of Extreme Geometry

N.E. Fine (Engineering Technology Center, USA)
S.A. Kinnas (Massachusetts Institute of Technology, USA)

Abstract

The unsteady flow around cavitating marine propellers is treated in nonlinear theory by employing a low-order potential based boundary element method. The solution is found in the time domain. The kinematic and dynamic boundary conditions, which are fully three dimensional, nonlinear and time-dependent, are satisfied on an approximate surface consisting of the propeller surface beneath the cavity and the portion of the blade wake surface overlapped by the cavity. An efficient and robust algorithm is developed to predict arbitrary cavity shapes, including so-called "mixed" cavity planforms in which the blade is partially cavitating at inner radii and supercavitating near the tip. In previous works, it has been shown that the present solution represents the first iteration of a completely nonlinear solution in which the exact boundary conditions are satisfied on the exact flow boundary. The main emphasis of the present work is to investigate the performance of the method for extreme propeller geometries, such as those with large amounts of skew, rake or pitch. The effect of the hub on the solution is investigated and shown to have more effect on heavily pitched propellers than on moderately pitched ones. The importance of including the crossflow terms in the dynamic boundary condition is also ivestigated for extreme propeller geometries.

1 Introduction

With recent increases in the demand for heavily loaded efficient marine propellers, the occurrence of cavitation has become less and less avoidable. As a result, it has become the task of the hydrodynamicist to predict the cavitation characteristics of a propeller at the design stage, with the expectation that analytical methods can be used to avoid excessive cavitation within an appropriate range of ship speed. Computational tools for the *reliable* prediction of propeller cavitation are therefore in high demand. Moreover, these tools must be applicable to propellers of extreme geometry (high skew, rake or twist) which have become very common in recent years.

The approach taken in this work is to treat propeller cavitation strictly as sheet cavitation. The travelling bubbles and bubble clouds which often are entrained in the wake of the sheet cavity, or precede the occurrence of sheet cavitation in the incipient stage, are not included in the present analysis. Viscosity will also be neglected in this work, and the inflow will be assumed to be free of vorticity. The advantage of this approach lies in its relative mathematical simplicity. The governing equation is Laplace's equation for the perturbation potential. The use of surface singularities and the now classic application of Green's 3rd identity are well suited for such a problem.

Despite the relative simplicity, however, the problem is far from trivial. The main difficulty arises from the need to determine the cavity free-surface on which the pressure is prescribed. The fact that a portion of the flow boundary is unknown makes the problem nonlinear. In addition, the inherent complexity of solving three dimensional flows around extreme geometries adds to the difficulty of the analysis. Furthermore, the cavity extent and volume variation in time resulting from nonaxisymmetries in the inflow is strongly nonlinear, making it impossible to solve in the frequency domain.

The main disadvantages of treating only sheet cavitation in potential flow result from the combined neglect of viscosity, tip and hub vortex cavitation, bubble cavitation, and cloud cavitation.

However, there are two additional rationales for taking the potential flow avenue. First, it is believed that the first-order contributor to dynamically varying blade loads and radiated pressures is the transient sheet cavity [28]. Second, many or all of the neglected phenomena may be included as refinements to the potential flow solution. For example, a viscous-inviscid boundary layer interaction could be used to model the effects of viscosity. As another example, a local tip solution, including a cavitating tip vortex, could be matched to the outer sheet cavity solution. The potential of such a model to capture most of the physics at reasonable computational expense is the motivation for obtaining an *accurate* and *efficient* potential flow solution which is able to treat a wide class of geometries including highly skewed, raked or pitched propellers. At this stage of development, it is also important to investigate the effects of the parameters which *are* included in the model. For example, the effect of the hub may be investigated to determine its importance to the solution for various geometries and operating conditions. Also, the importance of the crossflow terms in the dynamic boundary condition may be investigated. Finally, the method should be interrogated to determine if it predicts multiple solutions. These are the goals of the present work.

2 Formulation

The mathematical formulation first appeared in [15]. The formulation will be repeated here, but with more detail on the dynamic boundary condition in the wake (section 2.2.2). Details of the numerical implementation are provided in the next section.

Consider a cavitating propeller subject to a nonuniform inflow $U_W(x_S, r_S, \theta_S)$, with the subscript S denoting the ship-fixed coordinate system in which the wake is defined. U_W is assumed to be the *effective* wake. Some details of the geometry are shown in Figure 1. The solution is found in the (x, y, z) coordinate system, which rotates with the propeller. The propeller is assumed (without loss of generality) to be right-handed and to rotate at a constant angular velocity ω. The inflow relative to the propeller is

$$U_{\mathrm{in}}(x, y, z, t) = U_W(x, r, \theta - \omega t) + \omega \times x \quad (1)$$

where $r = \sqrt{y^2 + z^2}$, $\theta = \tan^{-1}\left(\frac{z}{y}\right)$, $x = (x, y, z)$.
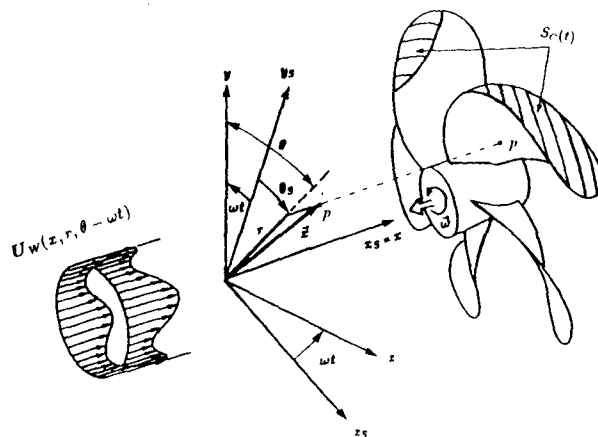
Figure 1: The propeller and cavity geometry, coordinate systems, and nonuniform inflow. x_S, y_S, z_S represent the ship-fixed coordinate system; x, y, z represent the propeller-fixed coordinate system. The point p is a point on the propeller surface, defined by the vector $\vec{x}$ from the origin of the propeller-fixed system.

For the moment, assume that the propeller has a developed sheet cavity whose time-dependent surface is denoted by $S_C(t)$, as shown in Figure 1. The fluid is assumed to be inviscid and the resulting flow to be incompressible and irrotational. In this case, the time-dependent total flow velocity $q(x, y, z, t)$, can be written in terms of the perturbation potential, $\phi(x, y, z, t)$, as follows:

$$q(x, y, z, t) = U_{\mathrm{in}}(x, y, z, t) + \nabla\phi(x, y, z, t). \quad (2)$$

The goal is to determine the potential field $\phi(x, y, z, t)$, as well as the cavity surface $S_C(t)$[1]. Once ϕ is known, the pressure distribution may be computed by numerically differentiating the potentials and applying Bernoulli's equation. The unsteady blade load distribution may then be determined by integrating the pressure. Knowing $S_C(t)$, the cavity volume history may be computed. In the following sections, the equations and boundary conditions necessary for the solution will be derived.

2.1 Green's Formula

The perturbation potential $\phi_p(x, y, z, t)$ at any point p which lies either on the wetted blade (or

---

[1]The leading edge of the cavity will be assumed to be *known*, the rest of the surface $S_C(t)$ is to be determined. See section 6 for related discussion.
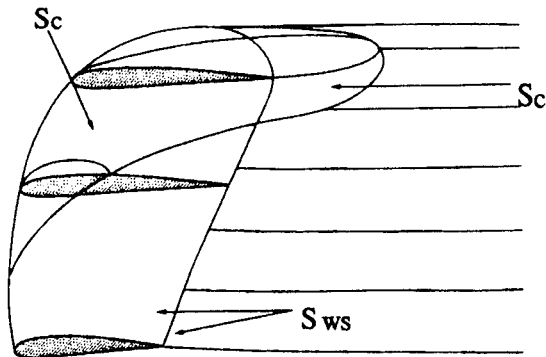
Figure 2: Definition of the flow boundaries on which the boundary conditions should be satisfied.

Figure 3: The approximate cavity surface on which the boundary conditions are applied.

hub) surface[2], $S_{WS}(t)$, or on the cavity surface, $S_C(t)$, (both surfaces are shown in Figure 2) must satisfy Green's third identity:

$$2\pi\phi_p(t) =$$

$$\int_{S_{WS}(t)\cup S_C(t)} \left[\phi_q(t)\frac{\partial G(p;q)}{\partial n_q(t)} - G(p;q)\frac{\partial\phi_q}{\partial n_q}(t)\right] dS +$$

$$\int_{S_W(t)} \Delta\phi_w(r_q,\theta_q,t)\frac{\partial G(p;q)}{\partial n_q(t)} dS; p \in (S_{WS}\cup S_C)$$

(3)

The subscript q corresponds to the variable point in the integrations. $\hat{n}_q(t)$ is the unit vector normal to the surface of the propeller, the cavity, or the wake. The unit normal points *into* the fluid (on the wake surface, $\hat{n}_q(t)$ is oriented such that it points towards the same horizon as the normal on the *suction* side of the blade). $\Delta\phi_w(r,\theta,t)$ is the potential jump across the wake sheet, $S_W(t)$, and $G(p;q) = 1/R(p;q)$ is Green's function, where $R(p;q)$ is the distance from the field point p to the variable point q.

Equation (3) expresses the perturbation potential on the surface formed by the union of the cavity and blade surfaces, $S_{WS}(t)\cup S_C(t)$, as a superposition of the potentials induced by a continuous source distribution, G, and a continuous dipole distribution, $\frac{\partial G}{\partial n}$, on $S_{WS}(t)\cup S_C(t)$, and a continuous

dipole distribution on the trailing wake surface, $S_W(t)$. The application of Green's 3rd identity to problems in potential flow is classic [18, 22, 26], while applications to propeller and rotor flows are more recent [21, 23, 7, 8, 10, 16].

Ultimately, the exact nonlinear potential flow solution will be found when the kinematic and dynamic boundary conditions (which may be applied simultaneously with Green's formula (3)) are satisfied on the *exact* flow boundary. However, we face the usual problem that the position of the cavity surface is unknown. As a first iteration towards the fully nonlinear solution, we apply the boundary conditions on an *approximate* flow boundary. If the blade is experiencing only partial cavitation, then the approximate boundary coincides with the blade surface (including the part of the blade beneath the cavity). This surface will be referred to as S_{CB}. On the other hand, if the blade is supercavitating, the upper and lower sides of the supercavity downstream of the blade trailing edge are collapsed to a single surface and the two sides of the collapsed cavity surface are taken to coincide with the two sides of the zero-thickness trailing wake sheet (see discussion below). This surface will be referred to as $S_{CW}(t)$. Thus the approximate flow boundary consists of the blade surface, S_{CB}, and the portion of the trailing wake sheet which is overlapped by the cavity, $S_{CW}(t)$.

A sketch of the approximate boundary is shown in Figure 3. The geometry of the wake, $S_W(t)$ will from here on be assumed to be invariant in time and identical to the steady-flow relaxed wake

[2]The wetted blade surface is that part of the blade which is not cavitating.

513

corresponding to the circumferentially averaged inflow [6]. The approximate flow boundary therefore coincides with that of the fully wetted solution, as described by Hsin [8].

A justification for making this approximation as well as a measure of its effect on the cavity solution is given in [3] and [15].

As a result of the linearization of the part of the supercavity downstream of the blade trailing edge, the surface $S_{CW}(t)$ may be considered to be a force-free surface. The pressure across the collapsed cavity surface must therefore be continuous and equal to the cavity pressure p_c. The pressure across the blade wake surface must also be continuous. Therefore, it is possible to consider these two surfaces to coincide, with the condition of pressure continuity being

$$
\begin{aligned}
p^+ &= p^- = p_c \quad \text{on } S_{CW}(t) \\
p^+ &= p^- = p \quad \text{on } S_W.
\end{aligned}
\tag{4}
$$

Satisfying the boundary conditions on the approximate boundary described above may be viewed as the first iteration towards a fully nonlinear solution. In the fully nonlinear solution, subsequent iterations are found by satisfying the dynamic boundary condition on an updated cavity surface, where the kinematic boundary condition is used to update the surface, as described in section 2.3. The solution is then considered to be converged when the cavity surface does not change (to within a tolerance) between two consecutive iterations. However, it was discovered that, using the present potential based panel method, the first iteration solution (where Green's formula is satisfied on the approximate boundary) *is extremely close to the converged nonlinear solution* for a wide range of operating conditions [13, 14, 3]. As a result, it is deemed unnecessary to go beyond the first iteration towards the fully nonlinear solution. In view of the high computational cost involved in regridding and re-computing influence coefficients, the importance of this conclusion cannot be overstated.

Considering the approximate boundary, the first integral on the right-hand-side of equation (3) may be decomposed into integrals over the blade surface and the portion of the wake which is overlapped by the cavity (denoted S_{CB} and S_{CW}, respectively, in Figure 3). The exact form of Green's formula depends on the location of the field point, which will either be on S_{CB} or on S_{CW}. Each case will be considered separately in the following.

2.1.1 Field Point on S_{CB}

If the field point is on the blade surface S_{CB}, the local contribution is extracted from the first integral in equation (3) and Green's formula becomes

$$
2\pi\phi(t) =
$$

$$
= \int_{S_{CB}} \left[\phi_q(t)\frac{\partial G(p;q)}{\partial n_q} - G(p;q)\frac{\partial \phi_q}{\partial n_q}(t) \right] dS -
$$

$$
- \int_{S_{CW}(t)} G(p;q) \left(\frac{\partial \phi_q}{\partial n_q}^+(t) - \frac{\partial \phi_q}{\partial n_q}^-(t) \right) dS +
$$

$$
+ \int_{S_{CW}(t) \cup S_W} (\Delta\phi_w(r,\theta,t))\frac{\partial G(p;q)}{\partial n_q} dS
\tag{5}
$$

where the superscripts $+$ and $-$ correspond to the upper and lower sides of the wake surface, respectively. Note that the wake surface has been divided into S_{CW} and S_W, as shown in Figure 3.

The velocity normal to S_{CW} is discontinuous across the surface. The jump in $\frac{\partial \phi}{\partial n}$ defines a source distribution, of density $q_w(t)$, which represents the cavity thickness:

$$
q_w(t) \overset{\text{def}}{=} \frac{\partial \phi_q}{\partial n_q}^+(t) - \frac{\partial \phi_q}{\partial n_q}^-(t).
\tag{6}
$$

The potential is also discontinuous across S_W, where the jump $\Delta\phi_w(r,\theta,t)$ is related to the local circulation history.

Inserting (6) into (5) yields:

$$
2\pi\phi(t) =
$$

$$
= \int_{S_{CB}} \left[\phi_q(t)\frac{\partial G(p;q)}{\partial n_q} - G(p;q)\frac{\partial \phi_q}{\partial n_q}(t) \right] dS -
$$

$$
- \int_{S_{CW}(t)} q_w(t)G(p;q)\, dS +
$$

$$
+ \int_{S_{CW}(t) \cup S_W} \Delta\phi_w(r,\theta,t)\frac{\partial G(p;q)}{\partial n_q} dS \quad \text{on } S_{CB}.
$$

$$
\tag{7}
$$

2.1.2 Field Point on S_{CW}

Now consider the case where the field point is on the upper side of the collapsed cavity surface in the wake, $S_{CW}(t)$. Extracting the local contribution from the integral over S_W on the right hand side of (3) and using the expression $\phi^+(t) + \phi^-(t) =$

$2\phi^+(t) - \Delta\phi_w(r,\theta,t)$ yields an expression for the potential on the upper wake surface ϕ^+:

$$4\pi\phi^+(t) = 2\pi\Delta\phi_w(r,\theta,t)$$

$$+ \int\limits_{S_{CB}} \left[\phi_q(t)\frac{\partial G(p;q)}{\partial n_q} - G(p;q)\frac{\partial\phi_q}{\partial n_q}(t) \right] dS -$$

$$- \int\limits_{S_{CW}(t)} q_w(t)G(p;q)\, dS +$$

$$+ \int\limits_{S_{CW}(t)\cup S_W} \Delta\phi_w(r,\theta,t)\frac{\partial G(p;q)}{\partial n_q} dS \quad \text{on } S_{CW}.$$

$$(8)$$

A detailed derivation of (8) may be found in [3]. Equations (7) and (8) define the potential $\phi(t)$ on the blade surface beneath the cavity, S_{CB}, and the potential $\phi^+(t)$ on the wake sheet, $S_{CW}(t)$, in terms of the following distributions of singularities:

- continuous source and normal dipole distributions on S_{CB} of strength $\frac{\partial\phi_q}{\partial n_q}(t)$ and $\phi(t)$, respectively

- a source distribution on $S_{CW}(t)$ of strength $q_w(t)$

- a normal dipole distribution on the entire wake sheet $S_{CW}(t) \cup S_W$ of strength $\Delta\phi_w(r,\theta,t)$.

On the wake sheet $S_{CW}(t)\cup S_W$ the dipole strength $\Delta\phi_w(r,\theta,t)$ is convected along the assumed wake surface with angular speed ω, in order to ensure that the pressure jump in the wake is equal to zero:

$$\Delta\phi_w(r,\theta,t) = \Delta\phi_T\left(r, t - \frac{\theta - \theta_T(r)}{\omega}\right);$$

$$t \geq \frac{\theta - \theta_T(r)}{\omega}$$

$$\Delta\phi_w(r,\theta,t) = \Delta\phi_w^{fw}\left(r, t - \frac{\theta - \theta_T(r)}{\omega}\right);$$

$$t < \frac{\theta - \theta_T(r)}{\omega} \quad (9)$$

where r,θ are the cylindrical coordinates of the wake surface and $\theta_T(r)$ is the θ coordinate of the blade trailing edge at radius r. $\Delta\phi_w^{fw}(r)$ is the unsteady fully wetted flow potential jump in the wake. $\Delta\phi_w^{fw}(r)$ is known since the unsteady fully wetted flow solution is found before the unsteady cavity solution.

Note that the wake convection given by (9) is identical to the fully wetted convection [17]. This is allowed by the linearization of the supercavity in the wake, where the two force-free surfaces are considered as one.

Everywhere on S_{CB} and $S_{CW}(t)$, either the source distribution is known (a *Neumann* boundary condition) or the dipole distribution is known (a *Dirichlet* boundary condition). Green's formulae (7) and (8) may then be discretized and rewritten as a linear system of equations by employing the boundary conditions and shifting all of the known quantities to the right-hand-side.

2.2 Dynamic Boundary Condition

The dynamic boundary condition (DBC) requires that the pressure everywhere inside and on the cavity be constant and equal to the known cavity pressure, p_c. Bernoulli's equation with respect to the propeller fixed system is

$$\frac{p_o}{\rho} + \frac{1}{2}|U_W|^2 = \frac{\partial\phi}{\partial t} + \frac{p_c}{\rho} + \frac{1}{2}|q_t|^2 - \frac{1}{2}\omega^2 r^2 + gy_S.$$

$$(10)$$

where ρ is the fluid density and r is the distance from the axis of rotation. Here q_t is the total velocity on the cavity surface. p_o is the pressure far upstream on the shaft axis; g is the gravitational constant and y_S is the vertical distance from the horizontal plane through the axis of rotation, as shown in Figure 1. y_S is defined as negative in the direction of gravity.

After some manipulation, and using the definition of the cavitation number:

$$\sigma_n \stackrel{\text{def}}{=} \frac{p_o - p_c}{\frac{\rho}{2}n^2 D^2}, \quad (11)$$

where $n = \frac{\omega}{2\pi}$ and D are the propeller revolutions per unit time and diameter, respectively, we find that the magnitude of the total cavity velocity satisfies

$$|q_t|^2 = n^2 D^2 \sigma_n [1 - f(s)] + |U_W|^2 +$$

$$+ \omega^2 r^2 - 2gy_S - 2\frac{\partial\phi}{\partial t}. \quad (12)$$

The function $f(s)$ corresponds to a pressure recovery law at the trailing edge of the cavity along the arc s on the surface of each spanwise blade section. The pressure recovery is given by an algebraic expression over a specified portion of the cavity near its trailing edge. This termination model is described in detail in [3].

Since the cavity boundary consists of two parts — one coinciding with the cavitating portion of the blade surface and the other with the cavitating portion of the wake surface — further derivation of the dynamic boundary condition will be considered on each surface separately.

2.2.1 DBC on the Blade Cavity

In addition to the expression (12), the cavity velocity q_t may also be expressed in terms of the directional derivatives of the perturbation potential and the components of the inflow along the same curvilinear coordinates [10]. The coordinate system[3] on the cavity surface consists of s (chordwise) and v (spanwise), as shown in Figure 3:

$$q_t = \frac{1}{\|\hat{s} \times \hat{v}\|^2} \left[\left(\frac{\partial \phi}{\partial s} + U_s\right) [\hat{s} - (\hat{s} \cdot \hat{v})\hat{v}] + \left(\frac{\partial \phi}{\partial v} + U_v\right) [\hat{v} - (\hat{s} \cdot \hat{v})\hat{s}] \right] + \left(\frac{\partial \phi}{\partial n} + U_n\right) \hat{n} \tag{13}$$

with $\hat{s}$ and $\hat{v}$ being the unit vectors corresponding to the coordinates s and v, respectively, and with $\hat{n}$ being the unit normal vector to the assumed cavity. U_s, U_v, and U_n are the s, v and n components of the relative inflow, U_{in}.

If s, v and n were located on the correct cavity surface, then the normal velocity, $\frac{\partial \phi}{\partial n} + U_n$, would vanish. However, this is not the case since the cavity curvilinear coordinates are approximated with those on the propeller surface. Nevertheless, in applying the dynamic boundary condition, the normal velocity is assumed to be vanishingly small. In the fully nonlinear scheme, the normal velocity vanishes as the solution converges. As shown in [3] it was found that leaving the normal velocity term out of the dynamic boundary condition has only a small effect on the solution.

Equations (12) and (13) may then be combined to form an equation which is quadratic in the unknown chordwise perturbation velocity, $\frac{\partial \phi}{\partial s}$. The two solutions to the quadratic equation represent potential gradients which are positive and negative in the direction of *increasing* s. The positive root is chosen to ensure that the cavity velocity points in the direction of increasing s. We can now express $\frac{\partial \phi}{\partial s}$ in terms of the cavitation number, the inflow velocity, and the *unknown* derivatives $\frac{\partial \phi}{\partial v}$ and $\frac{\partial \phi}{\partial t}$:

$$\frac{\partial \phi}{\partial s}(s, v, t) = -U_s + \left(\frac{\partial \phi}{\partial v} + U_v\right)\cos\theta + \\ + \sin\theta \sqrt{|q_t|^2 - \left(\frac{\partial \phi}{\partial v} + U_v\right)^2} \tag{14}$$

with θ being the angle between s and v, as shown in Figure 3. Here $|q_t|^2$ is defined as in equation (12). Equation (14) is integrated once to form a Dirichlet boundary condition on ϕ:

$$\phi(s, v, t) = \phi(0, v, t) + \\ \int_0^s \left[-U_s + \left(\frac{\partial \phi}{\partial v} + U_v\right)\cos\theta + \\ + \sin\theta\sqrt{|q_t|^2 - \left(\frac{\partial \phi}{\partial v} + U_v\right)^2} \right] ds \tag{15}$$

The integral on the right-hand-side of (15) is determined by trapezoidal quadrature. Since (15) defines the strength of the dipole distribution on the cavity, it may be directly substituted into Green's formula 7.

According to the dynamic boundary condition (15), ϕ depends on both its spanwise and time derivatives. These terms will be treated as knowns and will be updated in a time-stepping scheme which will be discussed later. The influence of the crossflow term $\frac{\partial \phi}{\partial v}$ was studied first for the case of partially cavitating 3-D hydrofoils and it was found that the global dependence of the solution on the crossflow term was small. This result will be shown in section 4.2, where it will also be demonstrated for the propeller solution. For a discussion of the convergence of the time-derivative with iterations and its effect on the solution, see [3] or [15].

2.2.2 DBC on the Wake Cavity

The dynamic boundary condition on the cavitating portion of the wake, S_{CW}, may also be written as a Dirichlet condition on ϕ^+. In this case, consider the orthogonal system (s, u, n), shown in Figure 4. Assuming that s is the direction of the mean velocity, the total velocity on the upper side of the wake sheet may be written

$$V^+ = V_s^+ \hat{s} + V_u^+ \hat{u} + V_n^+ \hat{n}.$$

---

[3]In general non-orthogonal.

516
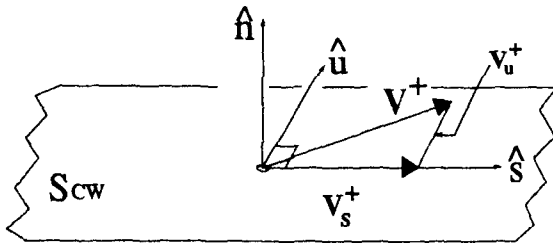
Figure 4: Velocity diagram on the wake surface.

Figure 5: Definition of the cavity surface defined with respect to the blade surface.

The normal velocity V_n^+ will be omitted from the dynamic boundary condition, as it was from (13), with the same justification.

Applying Bernoulli's equation, which is used to define the total velocity on the cavity q_t, we have

$$V_s^+ = \sqrt{|q_t|^2 - (V_u^+)^2}. \qquad (16)$$

The dynamic boundary condition on S_{CW} may thus be written

$$\frac{\partial \phi^+}{\partial s} = -U_s + \sqrt{|q_t|^2 - (V_u^+)^2}. \qquad (17)$$

Equation (17) may be integrated once to form a Dirichlet boundary condition on the potential on the upper wake surface, ϕ^+:

$$\phi^+(s, u, t) = \phi(0, v, t) + \int_{s_{TB}}^{s} \left[-U_s + \right.$$

$$\left. + \sqrt{|q_t|^2 - (V_u^+)^2} \right] ds. \qquad (18)$$

The integral in (18) is computed by trapezoidal quadrature. Equation (18) defines the potential ϕ^+ on the upper side of the wake and may be directly substituted into Green's formula (8).

2.3 Kinematic Boundary Condition

Since the dynamic boundary condition is applied on the portion of the boundary which is encompassed by the cavity, the other boundary condition, namely the kinematic condition, may be used to determine the position of the actual cavity surface once the singularity strengths have been determined. In this section, the most useful form of the kinematic boundary condition (KBC) will

be derived. As in the previous section, the cavity boundary will be divided into two zones which will be considered separately.

2.3.1 KBC on the Blade Cavity

The kinematic boundary condition on the cavity is the requirement that the substantial derivative of the cavity surface vanishes:

$$\frac{D}{Dt}\left[n - h(s, v, t) \right] =$$

$$= (\frac{\partial}{\partial t} + q_t \cdot \nabla)\left[n - h(s, v, t) \right] = 0 \qquad (19)$$

where n is the coordinate normal to the blade surface (with unit vector $\hat{n}$) and $h(s, v, t)$ is the thickness of the cavity normal to the blade at the point (s, v) at time t. Expressing the gradient in terms of the local directional derivatives

$$\nabla = \frac{[\hat{s} - (\hat{s} \cdot \hat{v})\hat{v}] \frac{\partial}{\partial s} + [\hat{v} - (\hat{s} \cdot \hat{v})\hat{s}] \frac{\partial}{\partial v}}{\|\hat{s} \times \hat{v}\|^2}$$

$$+ \hat{n}\frac{\partial}{\partial n}, \qquad (20)$$

performing the dot product with q_t (as defined in (13)) and substituting the result in (19) yields the following partial differential equation for the cavity thickness:

$$\frac{\partial h}{\partial s}\left[V_s - \cos\theta V_v \right] + \frac{\partial h}{\partial v}\left[V_v - \cos\theta V_s \right]$$

$$= \sin^2\theta(V_n - \frac{\partial h}{\partial t}) \qquad (21)$$

where

$$V_s \stackrel{\text{def}}{=} \frac{\partial \phi}{\partial s} + U_s, \quad V_v \stackrel{\text{def}}{=} \frac{\partial \phi}{\partial v} + U_v, \quad V_n \stackrel{\text{def}}{=} \frac{\partial \phi}{\partial n} + U_n.$$

517
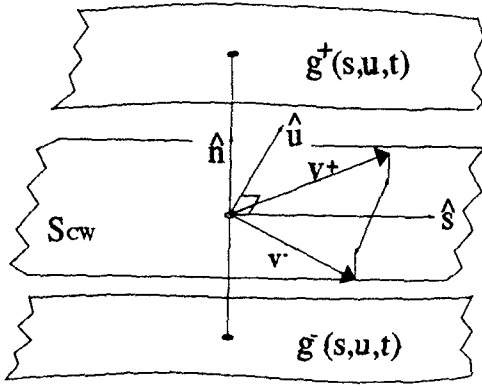
Figure 6: Definition of the cavity surface defined with respect to the wake surface.

2.3.2 KBC on the Wake Cavity

The kinematic boundary condition on the cavity surface in the wake may be derived in a similar fashion, except that now both surfaces of the supercavity must be considered

$$\frac{D}{Dt}\left(n - g^+(s, u, t)\right) =$$

$$= \left[\frac{\partial}{\partial t} + V^+ \cdot \nabla\right]\left(n - g^+(s, u, t)\right) = 0$$

$$\frac{D}{Dt}\left(n - g^-(s, u, t)\right) =$$

$$= \left[\frac{\partial}{\partial t} + V^- \cdot \nabla\right]\left(n - g^-(s, u, t)\right) = 0$$

$$(22)$$

where $g^\pm(s, u, t)$ defines the upper and lower cavity surfaces, as shown in Figure 6. Note that (s, u, n) is an orthogonal system. V^+ and V^- are the total velocities on the upper and lower sides of the wake (also shown in Figure 6), respectively, and may be written

$$V^\pm = V_s^\pm \hat{s} + V_u^\pm \hat{u} + V_n^\pm \hat{n} \qquad (23)$$

The upper and lower cavity surfaces, $g(s, u, t)^\pm$, may be written

$$g(s, u, t)^\pm = C(s, u, t) \pm \frac{1}{2}h_w(s, u, t),$$

where C is the cavity camber in the wake and h_w is the cavity thickness. The quantities g, C and h_w are all taken along the normal to the wake surface. These quantities are also shown in Figure 7.

Expanding equations (22) we find that

$$V_n^+ - \left[\frac{\partial C}{\partial t} + \frac{1}{2}\frac{\partial h_w}{\partial t}\right] =$$
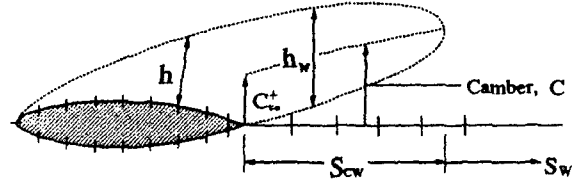
Figure 7: Definition of the cavity camber and height for a supercavitating section of the propeller blade.

$$= V_s^+\left[\frac{\partial C}{\partial s} + \frac{1}{2}\frac{\partial h_w}{\partial s}\right] + V_u^+\left[\frac{\partial C}{\partial u} + \frac{1}{2}\frac{\partial h_w}{\partial u}\right]$$

$$V_n^- - \left[\frac{\partial C}{\partial t} - \frac{1}{2}\frac{\partial h_w}{\partial t}\right] =$$

$$= V_s^-\left[\frac{\partial C}{\partial s} - \frac{1}{2}\frac{\partial h_w}{\partial s}\right] + V_u^-\left[\frac{\partial C}{\partial u} - \frac{1}{2}\frac{\partial h_w}{\partial u}\right]$$

$$(24)$$

Taking the difference between the two equations in (24) and assuming that $\hat{s}$ coincides with the direction of the mean velocity so that

$$V_s^+ = V_s^- \qquad (25)$$

yields

$$q_w(t) - \frac{\partial h_w}{\partial t} = V_s^+\frac{\partial h_w}{\partial s} + 2V_u^+\frac{\partial C}{\partial u} \qquad (26)$$

Here we have used the definition of the wake source strength (6) and the following equalities:

$$V_u^+ = -V_u^- \quad \text{and} \quad V_n^+ = -V_n^- \qquad (27)$$

which readily follow from the assumption (25) and the fact that the free vorticity must follow the mean velocity vector.

To be consistent with the dynamic boundary condition, we assume that the spanwise crossflow velocity is small. Thus, applying equation (16), and the assumption of small spanwise slope of the camber $C(s, u, t)$, the kinematic boundary condition (26) reduces to

$$\frac{\partial h_w}{\partial s}|q_t| = q_w(t) - \frac{\partial h_w}{\partial t}. \qquad (28)$$

Note that the cavity height on the blade and in the wake, both shown in Figure 7, are defined differently and so are given separate symbols.

The position of the cavity surface over the blade surface is determined by adding the cavity thickness h normal to the blade surface at the midspan

518

of the panel boundaries. In the wake, the cavity camber $C(s, u, t)$ must first be determined. An expression for $C(s, u, t)$ may be found by adding the two equations (24) and dividing through by two:

$$V_s^+ \frac{\partial C}{\partial s} = -\frac{\partial C}{\partial t} + U_n + \frac{1}{2}\left(\frac{\partial \phi^+}{\partial n} + \frac{\partial \phi^-}{\partial n}\right)$$
$$-V_u^+ \frac{\partial h_w}{\partial u} \qquad (29)$$

where U_n is the inflow velocity normal to the wake sheet. Equation (29) is numerically integrated to determine the camber surface in the wake. At the trailing edge of the blade, the continuity of camber and thickness is imposed:

$$C_{te}^+ = \frac{1}{2} h_{w_{te}}^- \qquad (30)$$
$$h_{w_{te}}^+ = h_{w_{te}}^-.$$

Here, the superscripts $+$ and $-$ denote just upstream and just downstream of the trailing edge, respectively. C_{te}^+ is the value of the camber just upstream of the trailing edge. It is determined by adding $\frac{h}{2}$ to the trailing edge along the blade normal (see Figure 7). The quantity $h_{w_{te}}^-$ is determined by interpolating the upper cavity surface over the blade at the trailing edge and computing its normal offset from the wake sheet. The upper and lower surfaces of the cavity in the wake are then determined by adding and subtracting half of the cavity thickness h_w from the camber surface. This defines the cavity surface at the midspans of all the spanwise strips. The surface of the cavity at the strip boundaries are determined by interpolation and extrapolation.

2.3.3 KBC on the Wetted Blade

The kinematic boundary condition on the wetted portion of the blade, $\tilde{S}_{WS}$, defines the source strength there in terms of the known inflow velocity:

$$\frac{\partial \phi_q}{\partial n_q}(t) = -U_{in}(x_q, y_q, z_q, t) \cdot \hat{n}_q; \qquad q \in S_{WS}(t) \qquad (31)$$

where x_q, y_q, z_q are the coordinates of the point q with respect to the propeller fixed system. As in the case of fully-wetted flow, this boundary condition may be directly substituted in Green's formula.

2.4 The Kutta Condition

The Kutta condition requires that the fluid velocity be finite at the blade trailing edge. It was found

necessary, in the fully wetted steady flow propeller solution, to satisfy a nonlinear Kutta condition which ensures pressure equality between the suction and pressure sides at the trailing edge [20]. The so-called pressure Kutta condition was later refined by Kinnas and Hsin [16], who developed an efficient iterative solution. In the present work, an extension of Morino's steady Kutta condition is applied. Development of a pressure Kutta condition for the cavitating propeller is left for the future.

The value of the dipole strength, $\Delta\phi_T(r, t)$, at the blade trailing edge at time t is

$$\Delta\phi_T(r, t) = \phi_T^+(r, t) - \phi_T^-(r, t) = \Gamma(r, t) \qquad (32)$$

where ϕ_T^+ and ϕ_T^- are the values of the potential at the blade trailing edge at radius r on the suction side and the pressure side, respectively. The potential jump there is also equal to the circulation Γ at time t around the blade section at radius r. This condition is equivalent to requiring the shed vorticity from the blade trailing edge to be proportional to the time rate of change of the circulation around the blade (Kelvin's law). An extension of Morino's Kutta condition for steady flow [24], in which the potential jump at the trailing edge of the blade is simply replaced by the potential jump at the nearest control points, is applied.

3 Implementation

The objective of the numerical analysis is to invert equations (7) and (8) subject to the kinematic boundary condition (31), the dynamic boundary conditions (15) and (17), and the Kutta condition. These equations, however, assume that the cavity extent is *known*. Since it is not, an iterative solution will be employed. This will be described in detail later in this section. First, we will describe how Green's formulae and the boundary conditions are satisfied *for a given guess of the cavity extent*. To accomplish this, we first tag one blade with the label "key blade". The solution at a given time step will be obtained only for the key blade, with the influence of the other blades corresponding to an earlier solution of the key blade. The key blade surface is discretized into N chordwise and M spanwise quadrilateral panels with the corners lying on the blade surface S_{CB} and with the control points located at the panel centroids. An example of a discretized blade is shown in Figure 8. The source and normal dipole distributions on each panel are approximated with constant strength distributions.
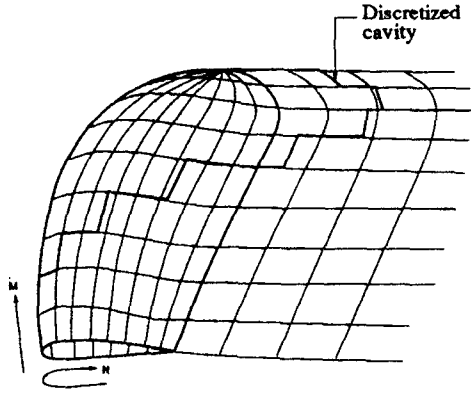
Figure 8: Discretization of the propeller blade, the cavity, and their trailing wakes; N=16, M=9.

The trailing wake is discretized into panels at constant angular intervals $\Delta\theta_W = \omega\Delta t$ with Δt being the time step. The blade and trailing wake discretization is identical to that in the case of fully wetted unsteady flow [8, 17, 16]. If we call

$N_{WS} = $ Number of wetted blade panels

$N_{CB} = $ Number of cavitating blade panels

$N_{CW} = $ Number of cavitating wake panels,

then, among the discrete sources and dipoles, we have N_{WS} known source strengths, via (31), N_{CB} known dipole strengths, via (15) and N_{CW} known dipole strengths, via (18). The following are then unknown and must be solved for: N_{WS} dipole strengths on the wetted blade, N_{CB} source strengths on the cavitating blade and N_{CW} source strengths in the supercavitating wake.

3.1 Discrete Green's Formulae

Prior to substituting the expressions for the known singularity strengths, the discrete Green's formulae (7) and (8) appear as follows:

$$\sum_{k=1}^{N_B}\sum_{m=1}^{M}\left\{\sum_{n=1}^{N}\left[A_{inm}^{k}\phi_{nm}^{k}(\tilde{n}) - B_{inm}^{k}\frac{\partial\phi^{k}}{\partial n}_{nm}(\tilde{n})\right]-\right.$$

$$-\sum_{l=1}^{NC_m}C_{ilm}^{k}Q_{nm}^{k}(\tilde{n})+$$

$$\left.+\sum_{l=1}^{N_W}W_{ilm}^{k}\Delta\phi_{w_{lm}}^{k}(\tilde{n})\right\}=0 \quad i=1,...,N\times M$$

(33)

and

$$4\pi\phi_i^k(\tilde{n}) =$$

$$=\sum_{k=1}^{N_B}\sum_{m=1}^{M}\left\{\sum_{n=1}^{N}\left[D_{inm}^{k}\phi_{nm}^{k}(\tilde{n}) - E_{inm}^{k}\frac{\partial\phi^{k}}{\partial n}_{nm}(\tilde{n})\right]-\right.$$

$$-\sum_{l=1}^{NC_m}F_{ilm}^{k}Q_{lm}^{k}(\tilde{n})+$$

$$\left.+\sum_{l=1}^{N_W}W_{ilm}^{*k}\Delta\phi_{w_{lm}}^{k}(\tilde{n})\right\} \quad i=1,...,N_{CW}$$

(34)

where $\tilde{n}$ is the discrete time step, N_B is the number of blades, N_W is the number of panels on each strip of the wake, and N_{C_m} is the number of cavitating panels on each strip of the wake.

In equations (33) and (34), the indices i and j map quantities to panels. For example, $\phi_i(\tilde{n})$ is the potential at the control point on the ith panel at the $\tilde{n}^{th}$ time step. However, each panel may also be identified as the nth panel on the mth strip, so ϕ_i may also be written ϕ_{nm}. In what follows, these indexing alternatives will be used interchangeably to maximize compactness.

A_{inm}^{k} and B_{inm}^{k} are defined as the potentials induced at the ith control point on the key blade by a unit strength dipole and a unit strength source at the nth panel on the mth strip of the kth blade ($k=1$ refers to the key blade). When the ith control point lies on the nth panel of the mth strip of the key blade, then

$$A_{inm}^{1} = 2\pi \quad \text{for} \quad i\longleftrightarrow(n,m).$$

C_{inm}^{k} is the potential induced at the ith panel on the key blade due to a unit strength source at the nth panel on the mth strip of the wake of the kth blade. W_{iml}^{k} is the potential induced at the ith control point on the key blade by a unit strength dipole at the lth panel of the mth strip of the wake of the kth blade. D_{inm}^{k}, E_{inm}^{k}, F_{inm}^{k} and W_{iml}^{*k} are defined similarly, noting that

$$W_{inm}^{*1} = 2\pi \quad \text{for} \quad i\longleftrightarrow(n,m).$$

The shape of the surface bounded by the edges of each quadrilateral panel is approximated by a hyperboloidal surface, and the corresponding influence coefficients are determined analytically. The need for hyperboloidal panels was found to be necessary for the convergence and consistency of the steady flow propeller solution, especially when applied to extreme geometries [16, 25, 7]. Discussion of the computation of these influence coefficients may be found in [27] and [8].

520

Equations (33) and (34) may be regrouped to reflect the fact that at any given time step only the potentials on the key blade are unknown, while the rest are assumed to be known. Equation (33) becomes

$$\sum_{m=1}^{M}\left\{\sum_{n=1}^{N}\left[A_{inm}\phi_{nm} - B_{inm}\frac{\partial\phi}{\partial n}_{nm}\right] - \right.$$

$$\left. - \sum_{n=1}^{N_{C_m}}C_{inm}Q_{nm} + W_{i1m}\Delta\phi_{w_{1m}}\right\} = \left\{\text{RHS}\right\}_{S_{CB_i}}$$

$$i = 1, ..., N \times M \quad (35)$$

and (34) becomes

$$\sum_{m=1}^{M}\left\{\sum_{n=1}^{N}\left[D_{inm}\phi_{nm} - E_{inm}\frac{\partial\phi}{\partial n}_{nm}\right] - \right.$$

$$\left. - \sum_{n=1}^{N_{C_m}}F_{inm}Q_{nm} + W_{i1m}^{\bullet}\Delta\phi_{w_{1m}}\right\} =$$

$$= 4\pi\phi_i + \left\{\text{RHS}\right\}_{S_{CW_i}} \quad i = 1, ..., N_{CW} \ (36)$$

where

$$\left\{\text{RHS}\right\}_{S_{CB_i}} =$$

$$= -\sum_{k=2}^{N_B}\left\{\sum_{m=1}^{M}\sum_{n=1}^{N}\left[A_{inm}^{k}\phi_{nm}^{k} - B_{inm}^{k}\frac{\partial\phi}{\partial n}^{k}_{nm}\right] - \right.$$

$$\left. \sum_{n=1}^{N_{C_m}}C_{inm}^{k}Q_{nm}^{k} + \sum_{l=2}^{N_W}W_{iml}^{k}\Delta\phi_{w_{1m}}^{k}\right\}$$

$$(37)$$

and

$$\left\{\text{RHS}\right\}_{S_{CW_i}} =$$

$$- \sum_{k=2}^{N_B}\left\{\sum_{m=1}^{M}\sum_{n=1}^{N}\left[D_{inm}^{k}\phi_{nm}^{k} - E_{inm}^{k}\frac{\partial\phi}{\partial n}^{k}_{nm}\right] - \right.$$

$$\left. \sum_{n=1}^{N_{C_m}}F_{inm}^{k}Q_{nm}^{k} + \sum_{l=2}^{N_W}W_{iml}^{\bullet k}\Delta\phi_{w_{1m}}^{k}\right\}.$$

$$(38)$$

In (35) and (36) the superscript $k = 1$ is implied. In (37) and (38) the potential ϕ_{nm}^{k} is equal to
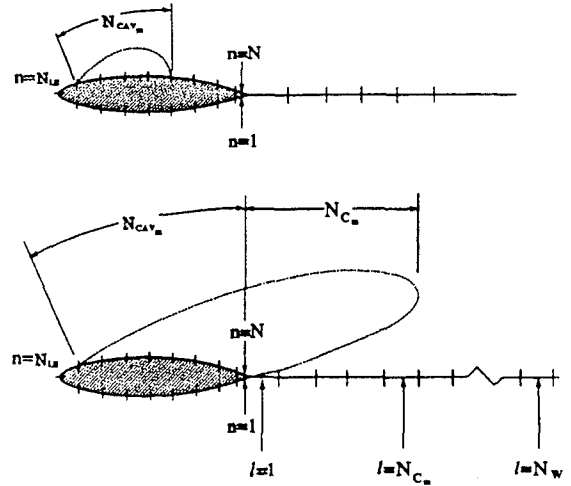
Figure 9: Index system for discrete equations.

ϕ_{nm}^{1} taken from the key blade solution at a previous time step, corresponding to the current location of blade k. The same equivalence is true for the source strengths $\frac{\partial\phi}{\partial n}^{k}_{nm}$ and Q_{nm}^{k} and the wake dipole strengths $\Delta\phi_{w_{1m}}^{k}$.

3.2 Discrete Boundary Conditions

The boundary conditions may now be discretized and incorporated in Green's formulae (35) and (36).

The discrete version of the kinematic boundary condition on the blade (31) is

$$\frac{\partial\phi}{\partial n}_{jm} = -U_{in_{nm}} \cdot \hat{n}_{nm}.$$

$$n = 1, ..., N_{LE}; N_{LE} + N_{CAV_m}, ..., N$$
$$m = 1, ..., M \quad (39)$$

where $U_{in_{nm}}$ is the inflow velocity at the current time step, defined at the nth control point on the mth spanwise strip of the blade. The system of indexing is shown in Figure 9.

A single discrete equation may be written to replace the dynamic boundary conditions on the blade (15) and in the wake (18)

$$\phi_{(N_{LB}+n)m} = \phi_{0_m} + \Psi_{nm}$$

$$n = 1, ..., N_{CAV_m} + N_{C_m}$$
$$m = 1, ..., M \quad (40)$$

s=0

S_i
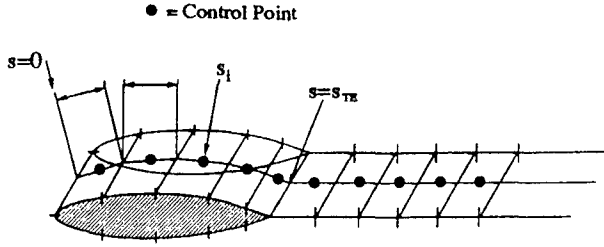
s=s_{TE}

Figure 10: Definition of the arclength on a spanwise strip, used in the trapezoidal integration of $\frac{\partial \phi}{\partial s}$.

Cavity Surface

h_{im} $h_{(i+1)m}$

$h_{i(m-1)}$ M

$h_{i(m-2)}$ M-1

M-2

i-1

i   i+1

$h_{(i+1)(m-1)}$

$h_{(i+1)(m-2)}$

• = Control Point

Figure 11: Schematic of $h(s, v, t)$ computation.

where

$$
\Psi_{nm} \stackrel{def}{=} \begin{cases} \int_0^{s_{nm}} \left[\frac{\partial \phi}{\partial s} \text{ from } (14) \right] ds \\ \qquad n = 1, ..., N_{CAV_m} \\ \\ \int_0^{s_{TE_m}} \left[\frac{\partial \phi}{\partial s} \text{ from } (14) \right] ds \\ \quad + \int_{s_{TE_m}}^{s_{nm}} \left[\frac{\partial \phi}{\partial s} \text{ from } (17) \right] ds \\ \qquad n = N_{CAV_m} + 1, ..., N_{CAV_m} + N_{C_m} \\ \\ m = 1, ..., M \end{cases}
$$

(41)

and s_{TE_m} is the value of s at the trailing edge of the blade on the mth spanwise strip, as shown in Figure 10. The integrals in equation (41) are computed by trapezoidal quadrature. The values of the integrands are computed at the control points and at the leading edge of cavity, where $s = 0$. The arclength between two consecutive control points is approximated by the sum of the linear distances between the control points and the panel edges (see Figure 10)

$$
s_{nm} = \frac{1}{2} \Delta s_{1m} + \sum_{j=1}^{n-1} \frac{1}{2} (\Delta s_{jm} + \Delta s_{(j+1)m})
$$

The quantity ϕ_0 in (40) is the perturbation potential at the detachment point of the cavity. It is also an unknown. This term is expressed as a cubic extrapolation in terms of the unknown potentials on the wetted panels on the same strip adjacent to the cavity detachment. The implementation of this term is discussed in detail in [3].

3.3 Cavity Height Computation

Once the problem has been solved for a guessed cavity planform, and $\frac{\partial \phi}{\partial n}$ on the cavity panels is

known, the cavity height ($h(s, v, t)$ on the blade and $h_w(s, v, t)$ in the wake) can be determined by integrating the partial differential equations (21) and (28). This is accomplished by replacing the partial derivatives of h and h_w with two-point backwards difference formulae and solving for h and h_w recursively. Note that the derivatives are defined at the control points. The finite difference models of the derivatives are as follows (h_w may be substituted for h):

$$
\frac{\partial h}{\partial s} \approx \frac{h_{(i+1)m}^{\hat{n}} - h_{im}^{\hat{n}}}{\Delta s_i}
$$

$$
\frac{\partial h}{\partial v} \approx \frac{3h_{im}^{\hat{n}} - 4h_{i(m-1)}^{\hat{n}} + h_{i(m-2)}^{\hat{n}}}{3\Delta v_1 - \Delta v_2}
$$

$$
\frac{\partial h}{\partial t} \approx \frac{h_{im}^{\hat{n}} - h_{im}^{\hat{n}-1}}{\Delta t}
$$

where

$$
h_{im} = \frac{1}{2}(h_{(i+1)m}^{\hat{n}} + h_{im}^{\hat{n}})
$$

Refer to Figure 11 for clarification. Substitution of the finite differences in (21) and (28) yields recursive formulae for $h_{i+1}^{\hat{n}}$ and $h_{w_{i+1}}^{\hat{n}}$ in terms of previously computed quantities. The height of the cavity at its trailing edge, $\delta(r, t)$, will in general be non-zero, unless we have guessed the correct cavity planform. The means by which we arrive at the correct planform will be discussed next.

3.4 The Cavity Planform

As mentioned earlier, the extent (planform) of the unsteady cavity is unknown and must be determined as a part of the solution. The local cavity length (defined as the arclength of the projection of the cavity on the nose-tail helix) is given at each radius r by the function $l(r, t)$. For a given cavitation number, σ_n, the cavity planform $l(r, t)$ will be determined from the requirement:

$$\delta(l(r, t), r; \sigma_n) \stackrel{\text{def}}{=}$$
$$\stackrel{\text{def}}{=} h(l(r, t), r, t) \; [\text{or } h_w(l(r, t), r, t)] = 0. \tag{42}$$

Equation (42) requires that the cavity close at its trailing edge; this requirement will be used as the basis of an iterative solution to find the cavity planform. In discrete form, equation (42) becomes:

$$\delta_m(l_1(t), l_2(t), ..., l_M(t); \sigma_n) = 0; \quad m = 1, ..., M \tag{43}$$

where δ_m is the openness of the cavity trailing edge at the mth spanwise strip and l_m is the value of $l(r, t)$ at the midspan of the same strip. At each time t the vector $L = [l_1, l_2, ..., l_M]^T$ must be determined by solving the M equations (43). The algorithm to do that is described in detail in [3]. In summary, the planform is determined by solving the system of equations (35) and (36) using an initial guess of L^4. For that initial guess, the openness of the cavity at its trailing edge, δ_m, is determined for all m by integrating equations (21) and (28). If $\delta_m \neq 0$, the cavity planform L is updated by applying a Newton-Raphson (secant) scheme on equations (43) and the process is repeated until the δ_m vanishes for all m, to within a prescribed tolerance.

The algorithm is depicted in Figure 12 for the case of a highly pitched propeller (geometry provided in [3]) . In this figure, the computed trailing edge cavity heights, δ_m, are shown for a series of guesses of the cavity planform. The cavity closes at all spanwise strips for only one solution, and this is the correct cavity planform for the given cavitation number and operating conditions.

For arbitrary cavity planforms, one must address the possibility that the cavity trailing edge does not coincide with a panel boundary. Since the singularity distributions span integral panel lengths, a provision must be made for "splitting"

---

[4] A good guess is the final planform L from the previous time step.
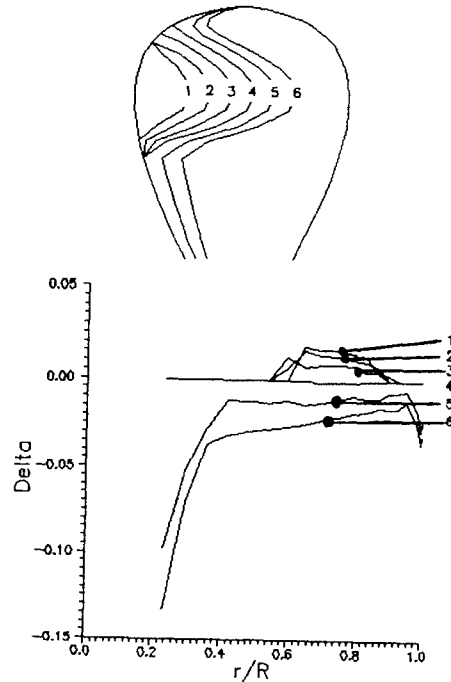
Figure 12: Cavity openness (bottom) corresponding to several cavity planforms (top). Notice that $\delta_m = 0$ for all m for only one of the planforms. The propeller is a heavily pitched (tip unloaded) test propeller whose geometry is given in [3].

a panel into a cavitating part and wetted part[5]. The so-called "split-panel" method (introduced in [13]) allows cavity planforms to be smooth and independent of the discretization. The price paid for that luxury is the introduction of a small amount of error in the solution. The details of the split-panel method, as well as a discussion of the error it introduces, is provided in [3].

3.5 Time-Marching Scheme

The time marching scheme is identical to that used in the fully wetted solution, and is described in detail in [8]. The main features of the scheme will be outlined here for the sake of completeness.

Time is discretized into equal increments, Δt. During one time step, each propeller blade rotates through an incremental angle $\Delta \theta = \omega \Delta t$. At each time step, the solution is found for the key blade only, while the singularities on the other blades are assumed to be known. Before proceeding to the next time step, vorticity is shed downstream

---

[5] The other option of *repanelling* the surface to ensure that the cavity ends at a panel boundary is considered too computationally expensive.

along the assumed wake surface through an angular distance equal to the incremental rotation $\Delta\theta$. This enforces the equality of the strength of the shed vorticity and the time rate of change of the circulation on the blade. The strength of the circulation is given in terms of the potential jump at the trailing edge of the blade

$$\Gamma(r,t) = \Delta\phi_T(r,t) = \phi_T^+(r,t) - \phi_T^-(r,t)$$
$$= \phi_{Nm} - \phi_{1m}.$$

and the potential jump at the first wake panel is given by

$$\Delta\phi(r,t) = \frac{\Gamma(t) + \Gamma(t - \Delta t)}{2}. \qquad (44)$$

Thus, the vorticity convection is used to define the wake dipole strengths. Although this an extension of Morino's Kutta condition in steady flow, it is not equivalent to the Kutta condition he applied in unsteady flow [24].

The solution is initiated by the fully wetted *steady* solution. Next, the fully wetted *unsteady* solution is obtained, which then serves as the "initial guess" for the unsteady cavity solution. The unsteady cavity solution is turned on when the key blade is at the 6 O'Clock position, so that it is likely to start out fully wetted. This was found to be an important time-saving measure in the linear solution by Lee [19]. The singularity strengths on the other blades and their wakes are taken from earlier key blade solutions. During the first revolution of the key blade, the singularities on another blade are taken either from the fully wetted solution or from the cavity solution when the key blade was in the same angular position. For subsequent revolutions, the other blade singularities are taken from previous cavity solutions when the key blade was in the same angular position.

4 Some Results

4.1 Uniqueness of the Solution

For some values of cavitation number, equations (43) may accept more than one solution. For example, it is a well known fact that, in two dimensions, for some cavitation numbers there exist *three* solutions (corresponding to two partial cavities and one supercavity). Our method has also predicted multiple solutions for three dimensional hydrofoils. For a complete discussion of that result, see [3] or [4]. On the other hand, no multiple solutions have been found for propellers. Figure 13
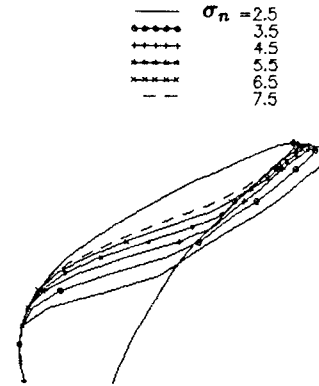
Figure 13: Investigation of multiple solutions for propellers. No multiple solutions were found for any of the cavitation numbers tried here for this geometry and operating condition. The propeller is an AO-177 operating in steady flow at $J = 0.6$.

shows a series of cavity planforms corresponding to different cavitation numbers. Note that there is a smooth one-to-one correlation between cavitation number and cavity planform for this geometry. Moreover, each predicted planform shown in Figure 13 has been determined using two different initial guesses, one a spanwise uniform short cavity $l(r) = 0.5$ and the other a spanwise uniform long cavity $l(r) = 1.5$. Each resulting planform was the same for the two initial guesses. While this does not necessarily preclude the existence of multiple solutions, it does show that, if they exist, they are difficult to find using this method.

4.2 The Crossflow Terms

It was mentioned in section 2.2 that the crossflow terms $\frac{\partial\phi}{\partial v}$ and V_u^+ in the dynamic boundary conditions (15) and (18), respectively, were found to have only a small effect on the solution. This will be shown for three geometries in this section. First, Figure 14 shows the cavity planforms on an elliptic hydrofoil from two consecutive iterations where, in between iterations for the cavity planform, the velocities $\frac{\partial\phi}{\partial v}$ and V_u^+ are updated. The first term is computed by numerically differentiating the potentials using second-order accurate central differences (except for $m = 1$ and $m = M$, where forward and backward differences are used, respectively). The second term is computed with central differences far downstream in the wake. Since the wake is assumed to be force-free, the crossflow velocity is constant in the streamwise direction for steady flow. Note that the cavity planforms do not change significantly between the two

$\frac{r}{R}$	$\frac{P}{D}$	$\frac{tk}{D}$	sk(°)	$\frac{C}{D}$	$\frac{l_{max}}{C}$	$\frac{l_{max}}{C}$
0.20	1.12	0.000	0.0	0.207	0.049	0.041
0.30	1.22	0.006	2.2	0.246	0.044	0.040
0.40	1.29	0.021	7.1	0.272	0.037	0.036
0.50	1.32	0.041	13.1	0.282	0.031	0.030
0.60	1.31	0.065	20.0	0.268	0.030	0.024
0.70	1.25	0.091	27.7	0.232	0.030	0.017
0.80	1.14	0.109	34.5	0.182	0.028	0.011
0.90	0.97	0.117	40.3	0.118	0.026	0.006
0.95	0.86	0.117	42.8	0.081	0.025	0.004
1.00	0.72	0.115	45.0	0.001	0.000	0.002

Table 1: The AO-177 propeller geometry.

iterations. No change was found when an additional iteration was tried. This example shows that the crossflow terms have little effect for supercavitating hydrofoils.

To gauge the importance of the crossflow terms for partially cavitating hydrofoils, a rectangular foil at $\alpha = 3°$ is tested for $\sigma = 0.5$ with and without inclusion of the crossflow terms. The results, shown in Figure 15, indicate that $\frac{\partial \phi}{\partial v}$ has a negligible effect on the solution, since the two cavity planforms are nearly indistinguishable.

The third geometry is an AO-177 propeller whose geometry is given in Table 1. Shown in Figure 16 are cavity planforms on the test propeller geometry for consecutive crossflow iterations. From this it is clear that, for the propeller solution, the crossflow term also has a negligible effect on the cavity planform.

4.3 The Hub Effect

The hub geometry may be included in the solution. Hyperboloidal panels are placed on the surface of the hub and Green's formula is satisfied, subject to the kinematic boundary condition. The modelling of the hub has been described by J.T. Lee [20] for the case of fully wetted flows. Figure 17 shows a typical blade and hub discretization. For the cavity solution, the hub is assumed to be fully wetted and the following kinematic boundary condition is applied:

$$\frac{\partial \phi_q}{\partial n_q}(t) = -U_{\text{in}}(x_q, y_q, z_q, t) \cdot \hat{n}_q; \qquad q \in S_H \quad (45)$$

where S_H is the surface of the hub. The discretized Green's formulae (35) and (36) are essentially unchanged, because the hub may be viewed as an extension of the wetted blade surface. The additional equations applied on the hub surface are also
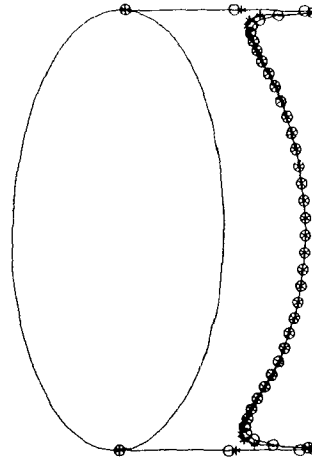
Figure 14: Convergence of the cavity planform with updating of the crossflow terms. Elliptic hydrofoil with maximum thickness-to-chord ratio of 6% at the midspan, tapering elliptically to zero thickness at the tip. $\alpha = 3°$, $\sigma = 0.2$.
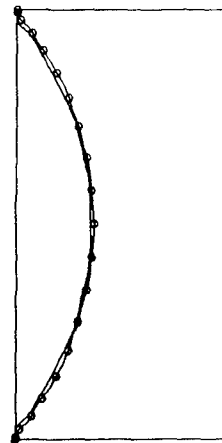
Figure 15: Convergence of the cavity planform with updating of the crossflow terms. Rectangular hydrofoil at $\alpha = 3°$, $\sigma = 0.5$, $\frac{l_0(y)}{c(y)} = .014$.

525
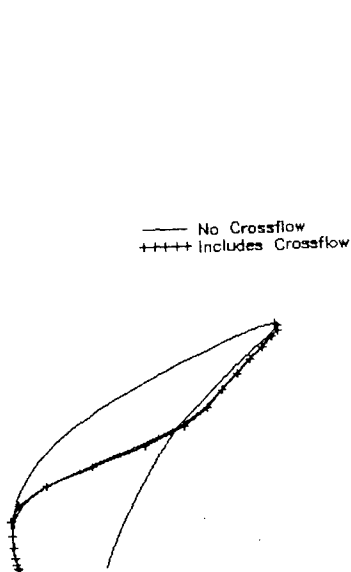
Figure 16: Convergence of the cavity planform with updating of the crossflow terms for the AO-177 propeller.
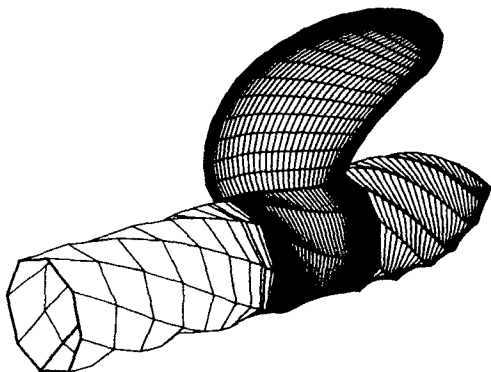
Figure 17: Typical blade and hub discretization.
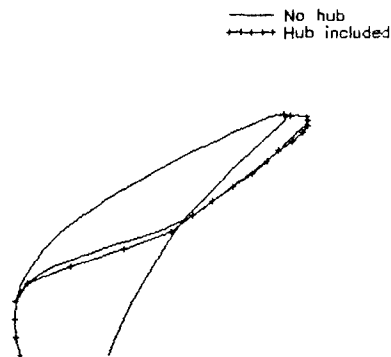
Figure 18: Cavity planform with and without inclusion of the hub for the AO-177 propeller at $J_S = 0.6$ and $\sigma = 3.5$ in steady flow.

similar to (35) and (36) and need not be included here.

The effect of the hub on the cavity solution is shown in Figure 18 for the AO-177 propeller at $J_S = 0.6$ and $\sigma_n = 3.5$ in steady flow. Note that the presence of the hub makes the cavity slightly larger at the inner radii because the local increase in circulation.

In the case of a highly twisted propeller, which is lightly loaded at the tip, the hub effects are noticeably larger. Figure 19 shows the cavity solution for a modified N4381 propeller (see [3] for a description of the geometry) in steady flow with and without the hub. Notice that the presence of the hub causes a marked increase in the cavity length at inner radii.

4.4 Comparison to Linear Theory

Figure 20 shows a comparison between the cavity planform computed by the present method (labeled PROPCAV, which is the name of the program) and those computed by linear theory and linear theory with leading edge corrections (labeled PUF-3A [11, 12]). The computations are done for steady flow conditions on the one-bladed AO-177 propeller. Linear theory is seen to overpredict the cavity extent, as it does in 2-D. We see here that the cavity extent is overpredicted by linear theory in both spanwise and chordwise directions. The linear theory with leading edge corrections also overpredicts the extent. A comparison is then made for the same propeller in nonuniform axial wake inflow. In this case, the hydrostatic terms are

526
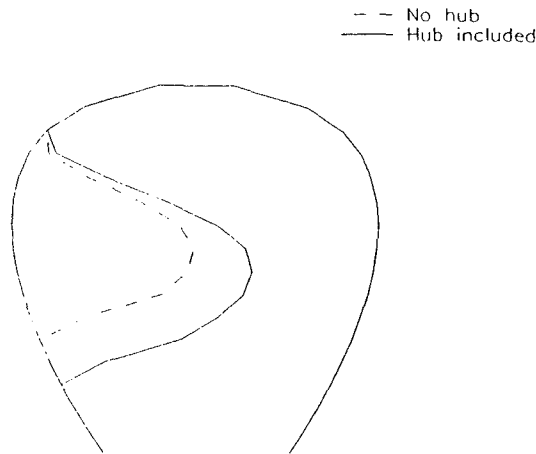
Figure 19: Cavity planform with and without inclusion of the hub for a highly pitched propeller (taken from [3]).

—— PROPCAV
+++++ PUF—3A Nonlinear
- - PUF—3A Linear
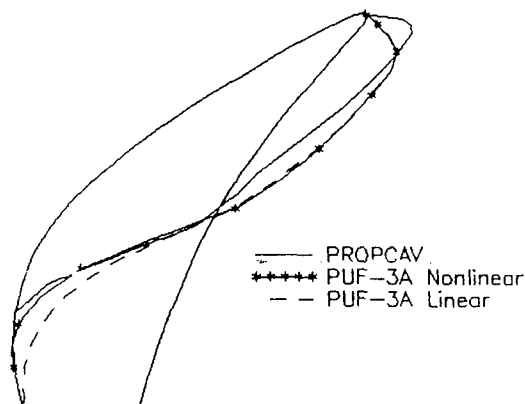
Figure 20: Cavity planforms predicted by PUF-3A (with and without the leading edge correction) and the present method (implemented in the code PROPCAV) on the AO-177 propeller at $J_s = 0.6$ and $\sigma = 2.7$ in uniform flow.
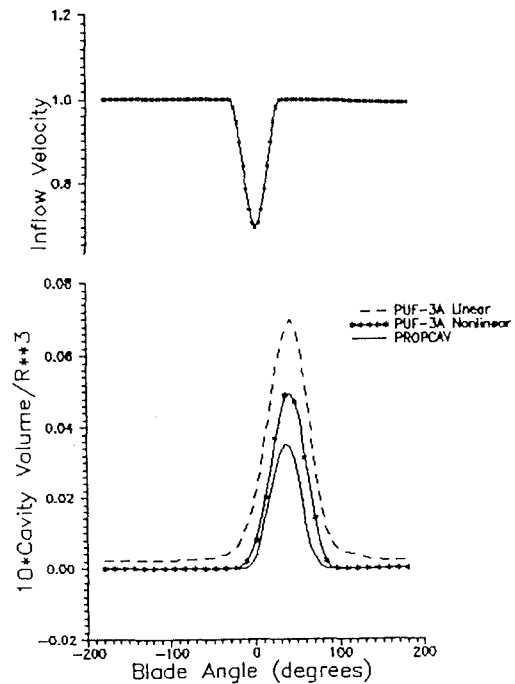
Figure 21: Cavity volume histories predicted by PUF-3A (with and without the leading edge correction) and the present method on the AO-177 propeller at $J_s = 0.95$, $Fr = 4.981$ and $\sigma = 2.6$ in nonuniform flow (bottom plot). The inflow wake field (top plot) is an axial flow with a 30% wake dent symmetric in θ about $\theta = 0$.

turned on ($Fr = n^2 D/g = 4.981$). The advance coefficient and the cavitation number are kept the same as in the steady flow case. The cavity volume histories predicted by the three methods are shown in Figure 21.

5 Conclusions

A potential based boundary element method has been developed for the analysis of unsteady sheet cavitation for propellers of extreme geometry. The method is able to predict, in an efficient and robust manner, arbitrary unsteady cavity planforms on a blade discretization which is fixed in time. An extensive investigation of the solution for varying cavitation number revealed no multiple solutions, such as were found for three dimensional hydrofoils in an earlier work [14]. The method was used to validate the predictions of linear theory (with and without leading edge corrections). It was found that linear theory, with *and* without the leading edge correction, overpredicts the cavity extent and volume for propellers of extreme geometry. Contrary to this, it was reported in an earlier work that the linear theory with leading edge correc-

527

tions came reasonably close to the nonlinear result for a more conventional propeller geometry [15].

6   Future Research

As mentioned in section 1, the fundamental assumptions made in order to admit a potential flow solution render the model incomplete. The effects of viscosity, tip and hub vortex cavitation, bubble and cloud cavition, and the cavity trailing edge flow are all unaccounted for in the present model. However, the present model is amenable to inclusion of many of these effects. For instance, the effects of viscosity may be included via an interactive viscous/inviscid boundary layer solution, similar to the one developed by Hufford for fully wetted flows [9]. The boundary layer solution could be used to determine the thickness of the cavity wake so that the openness of the cavity correctly correlates to the sectional drag coefficient. A model for determining the correct detachment point, by correlating the point of laminar separation or turbulent transition to the point of cavity detachment (as suggested by several previous researchers [1, 5]), may also be implemented. A preliminary two-dimensional numerical study of the effects of viscosity on hydrofoil cavitation is underway and shows promising results [29].

A model of the cavitating tip vortex may be added to improve the solution at the tip. This could be accomplished by treating the tip vortex as an inner problem, the solution of which should be matched to the outer solution from the present method. The inner problem could be treated by a boundary element method with a grid which is chosen to fit a vortex with an assumed core radius (possibly determined semi-empirically). In determining the flow at the tip, as well as the trajectory of the tip vortex, methods for the modelling of fully wetted tip flows may be applied. As shown experimentally by Arndt et al [2] the trajectory of the tip vortex does not seem to be sensitive to the value of the cavitation number.

A firm foundation, in the form of an accurate inviscid solution, is required to build our more physical models. The vortex/source lattice method, as implemented in the code PUF-3A, is not a very strong foundation due to the neglect of blade thickness and the crude treatment of the propeller tip geometry. The present method, however, is an accurate inviscid solution and will serve as a good base for implementing the additional models.

7   Acknowledgements

References

[1] H. Arakeri. Viscous effects on the position of cavitation separation from smooth bodies. *Journal of Fluid Mechanics*, vol 68(No. 4):pp 779–799, 1975.

[2] R.E.A. Arndt, V.H. Arakeri, and H. Higuchi. Some observations of tip vortex cavitation. *Journal of Fluid Mechanics*, 229:pp 269–289, 1991.

[3] N. E. Fine. *Non-linear Analysis of Cavitating Propellers in Nonuniform Flow*. PhD thesis, Department of Ocean Engineering, MIT, 1992.

[4] N.E. Fine and S.A. Kinnas. A Boundary Element Method for the Analysis of the Flow Around 3-D Cavitating Hydrofoils, March 1992. Recommended for publication in Journal of Ship Research.

[5] J.P. Franc and J.M. Michel. Attached cavitation and the boundary layer: Experimental investigation and numerical treatment. *Journal of Fluid Mechanics*, vol. 154:pp 63–90, 1985.

[6] D.S. Greeley and J.E. Kerwin. Numerical methods for propeller design and analysis in steady flow. *Trans. SNAME*, vol 90, 1982.

[7] T. Hoshino. Hydrodynamic analysis of propellers in steady flow using a surface panel method. In *Proceedings of the Spring Meeting*, number 1-6. The Society of Naval Architects of Japan, May 1989.

[8] Ching-Yeh Hsin. *Development and Analysis of Panel Method for Propellers in Unsteady Flow*. PhD thesis, Department of Ocean Engineering, MIT, September 1990.

[9] G. Hufford. Viscous flow around marine propellers using boundary layer strip theory. Master's thesis, Massachusetts Institute of Technology, May 1992.

[10] J.E. Kerwin, S.A. Kinnas, J-T Lee, and W-Z Shih. A surface panel method for the hydrodynamic analysis of ducted propellers. *Trans. SNAME*, 95, 1987.

[11] J.E. Kerwin, S.A. Kinnas, M.B. Wilson, and McHugh J. Experimental and analytical techniques for the study of unsteady propeller sheet cavitation. In *Proceedings of the Sixteenth Symposium on Naval Hydrodynamics*, Berkeley, California, July 1986.

[12] S.A. Kinnas. Leading edge correction to the linear theory of cavitating hydrofoils and propellers. In *Int. Symp. on Propeller and Cavitation*, Hangzhou, China, September 1992.

[13] S.A. Kinnas and N.E. Fine. A Numerical Nonlinear Analysis of the Flow Around 2-D and 3-D Partially Cavitating Hydrofoils. *Journal of Fluid Mechanics*. To appear.

[14] S.A. Kinnas and N.E. Fine. Analysis of the flow around supercavitating hydrofoils with midchord and face cavity detachment. *Journal of Ship Research*, 35(3):pp. 198–209, September 1991.

[15] S.A. Kinnas and N.E. Fine. A nonlinear boundary element method for the analysis of unsteady propeller sheet cavitation. In *Proceedings of the Nineteenth Symposium on Naval Hydrodynamics*, Seoul, Korea, August 1992.

[16] S.A. Kinnas and C-Y. Hsin. A boundary element method for the analysis of the unsteady flow around extreme propeller geometries. *AIAA Journal*, March 1992.

[17] S.A. Kinnas, C-Y. Hsin, and D.P. Keenan. A potential based panel method for the unsteady flow around open and ducted propellers. In *Proceedings of the Eighteenth Symposium on Naval Hydrodynamics*, pages 667–685, Ann Arbor, Michigan, August 1990.

[18] Sir Horace Lamb. *Hydrodynamics*. Cambridge University Press, sixth edition, 1932.

[19] Chung-Sup Lee. *Prediction of Steady and Unsteady Performance of Marine Propellers with or without Cavitation by Numerical Lifting Surface Theory*. PhD thesis, M.I.T., Department of Ocean Engineering, May 1979.

[20] Jin-Tae Lee. *A Potential Based Panel Method for the Analysis of Marine Propellers in Steady Flow*. PhD thesis, MIT, Department of Ocean Engineering, 1987.

[21] B. Maskew. Prediction of subsonic aerodynamic characteristics: A case for low-order panel methods. *Journal of Aircraft*, vol 19(no 2):pp 157–163, February 1982.

[22] Jack Moran. *An Introduction to Theoretical and Computational Aerodynamics*. John Wiley and Sons, 1984.

[23] L. Morino and B.K. Bharadvaj. A unified approach for potential and viscous free-wake analysis of helicopter rotors. *Vertica*, vol 12(no 1/2), 1988.

[24] L. Morino, Jr. Kaprielian, Z., and S.R. Sipcic. Free wake aerodynamic analysis of helicopter rotors. Technical Report CCAD-TR-83-01, Boston University, MAY 1983.

[25] Luigi Morino and Ching-Chiang Kuo. Subsonic potential aerodynamic for complex configurations : A general theory. *AIAA Journal*, vol 12(no 2):pp 191–197, February 1974.

[26] J.N. Newman. *Marine Hydrodynamics.* The MIT Press, Cambridge, Massachusetts, 1977.

[27] J.N. Newman. Distributions of sources and normal dipoles over a quadrilateral panel. *Journal of Engineering Mathematics*, vol 20:pp 113–126, 1986.

[28] M.P. Tulin. An analysis of unsteady sheet cavitation. In *Proceedings of the 19th ATTC Conference*, pages 1049–1079, 1980.

[29] R. Villeneuve. The effects of viscosity on hydrofoil cavitation, June 1993.

Numerical Modelling of Propeller Tip Flows

S.A. Kinnas, S. Pyo, C.Y. Hsin, and J.E. Kerwin
(Massachusetts Institute of Technology, USA)

Abstract

An improved panel arrangement is introduced for the analysis of flows at the tips of three-dimensional hydrofoils. Only round tip planforms are considered. The proposed grid is normal to the leading edge outline and adapted to the force-free wake geometry at the trailing edge. The location of the tip vortex detachment point is also determined in the process. It is shown that, when an existing boundary element method is applied on the proposed grid, the accuracy of the results improves substantially, not only at the tip but elsewhere on the hydrofoil. In addition, previous differences between results from the boundary element method and a vortex-lattice method (modified to include the thickness/loading coupling) are reconciled when the proposed grid is utilized.

1 INTRODUCTION

Accurate prediction of the flow at the tips of 3-D hydrofoils or propeller blades is essential in determining the characteristics of the tip vortex and its susceptibility to cavitation, as well as in assessing the overall hydrodynamic performance of these devices at off-design and/or cavitating flow conditions.

A Boundary Element Method (BEM) for the analysis of propeller flows (including the presence of the hub and duct) has been developed [8],[14]. The method is a low-order BEM based on Green's formula with respect to the perturbation potential. The method was recently extended to include unsteady flow effects [11],[5]. To ensure zero pressure jump across the blade trailing edge an iterative Kutta condition was applied. Recent improvements include: (a) the de-

velopment of a computationally efficient Newton-Raphson scheme for the application of the iterative pressure Kutta condition, which improved the overall convergence of the method [5], [10], (b) the treatment of highly twisted panels with hyperboloidal rather than planar geometry panels, which improved the convergence of the method for highly skewed propeller blades [5], [6] and, (c) the development of a Blade Orthogonal Grid (BOG), which improved the accuracy of the predicted pressure distributions at the blade tips [6].

A systematic effort to assess the accuracy of this BEM in predicting the flow around lifting surfaces has been carried out. In several applications (such as 3-D rectangular hydrofoils or high aspect ratio propeller blades) the BEM has been found to predict spanwise circulation distributions which are *consistent* with those predicted from lifting surface theory [5]. This means that the circulation distributions predicted by BEM for lifting surfaces with thickness *smoothly* (often linearly with thickness) extrapolate to the circulation distribution for the same lifting surface with zero thickness. The zero thickness circulation distribution is predicted by a lifting surface Vortex Lattice Method (VLM), since the BEM formulation becomes degenerate in this case.

For other cases however, especially for lifting surfaces with wide circular tips (similar to those of propeller blades), the circulation distributions predicted by the BEM have been found not to be consistent to those predicted by the VLM [5]. In order to solve this problem our efforts have been concentrated into investigating the results from applying the BEM and the VLM on a circular planform hydrofoil. In this case, it has been found that the BEM predicts a circulation distribution, which is quite different (not only at the tip but elsewhere) before and after the application of the iterative pressure Kutta condition.

In the present work, the primary cause of the problems associated with the application of the BEM on round planform hydrofoils is identified, and a new grid arrangement is proposed which is shown to improve the performance of the BEM appreciably.

2 BOUNDARY ELEMENT METHOD (BEM)

The fundamentals of the BEM are described in [8], [14] and [6]. In brief, the method is based on the classical Green's third identity (applied on the body surface S_B):

$$
\begin{aligned}
2\pi\phi \;=\; & \int_{S_B} \left[\phi \frac{\partial G}{\partial n} - G \frac{\partial \phi}{\partial n} \right] dS \\
& + \int_{S_W} \Delta\phi \frac{\partial \phi}{\partial n} dS
\end{aligned}
\tag{1}
$$

where the Green's function G is the unit strength source in three dimensions; ϕ is the perturbation potential; S_W is the trailing wake surface.

The BEM implementation involves:

- Constant strength dipole and source panels.

- Hyperboloidal panel geometry (critical for highly twisted body geometries).

- An Iterative Pressure Kutta (IPK) condition which determines the appropriate strength $\Delta\phi$ in the wake, in order for the pressure jump across the trailing edge to be equal to zero at all spanwise locations.

Two grid arrangements have been used. They are described in the next two sections:

2.1 The conventional grid

The conventional grid has been used traditionally for vortex-lattice applications on 3-D hydrofoils or propeller blades [13], [3]. It has also been called the "constant radii" grid. The panel edges are located along the intersections of the blade with cylinders concentric with the axis of propeller rotation. In the case of three dimensional hydrofoils the panels are arranged along the intersections of the hydrofoil with planes normal to the planform. The conventional grids for a propeller blade and a circular planform hydrofoil are shown in Figures 1 and 2, respectively.
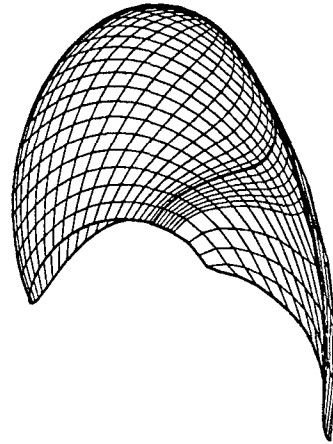
Figure 1: The conventional grid on a propeller blade and its trailing wake.
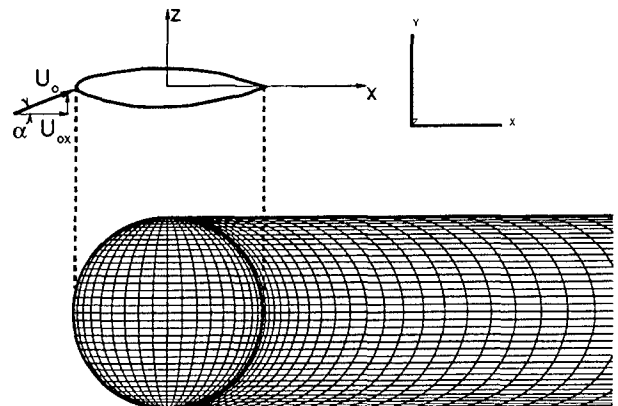
Figure 2: The conventional grid on a circular planform hydrofoil and its trailing wake.

532

As stated earlier, the BEM has been validated extensively for several hydrofoil and propeller blade geometries. From these studies it has been found that that the results from applying the BEM for "wide" round tip geometries either do not converge when applying the IPK condition, or do not seem to be consistent with the lifting surface zero thickness results. In order to investigate this peculiar behavior of the BEM we decided to test the simplest round tip propeller at the simplest possible inflow. That is the Circular Planform Hydrofoil (CPH) with zero camber, subject to a uniform inflow, U_o, at an angle of attack α. The maximum thickness to local chord ratio is kept constant along the span. A modified NACA66 thickness form [2] is used at each spanwise location. In order to avoid any ambiguity concerning the shape of the wake it was decided to force the wake to lie on the xy plane[1] as shown in Figure 2. At first, it was also decided not to contract the wake. In other words, we assumed that the vorticity vector in the wake was parallel to the x axis [2].

The spanwise circulation distribution (symmetric with respect to midspan and thus shown only over half of the span) predicted by the BEM applied for the CPH and for two thickness to chord ratios are shown in Figures 3 and 4. The circulation distribution "before" the IPK condition corresponds to the Morino Kutta condition in which the dipole strength in the wake is taken equal to the difference of the potentials at the panels at the two sides of the trailing edge [15]. This condition has been found to produce pressure distributions which do not match at the trailing edge, especially in the vicinity of the tip, as for example is shown in Figure 5. The circulation distribution "after" the IPK condition, corresponds to the modified wake dipole strength (thus circulation) which ensures pressure equality at the trailing edge. Notice the large difference over the span between the circulation distributions before and after the IPK condition, especially for the 20% thickness to chord ratio CPH, shown in Figure 4. This large difference in circulation has been caused by the relatively small adjustment of the trailing edge pressures in the vicinity of the tip, as shown in Figure 5. Also notice the "peculiar" behavior (sharp change in the slope) of the circulation distribution after the IPK condition, at the tip.

---

[1] Which, in the case of uncambered hydrofoils, is the same as the bisector plane of the trailing edge angle.

[2] The validity of this assumption will be examined later in this paper.

Figure 3: Circulation distribution on a circular planform hydrofoil; $[\tau/c]_{max} = 0.1$, $\alpha = 5.73°$. Predicted by applying the BEM on the conventional grid; before and after applying the Iterative Pressure Kutta (IPK) condition.

Figure 4: Circulation distribution on a circular planform hydrofoil; $[\tau/c]_{max} = 0.2$, $\alpha = 5.73°$. Predicted by applying the BEM on the conventional grid; before and after applying the Iterative Pressure Kutta (IPK) condition.
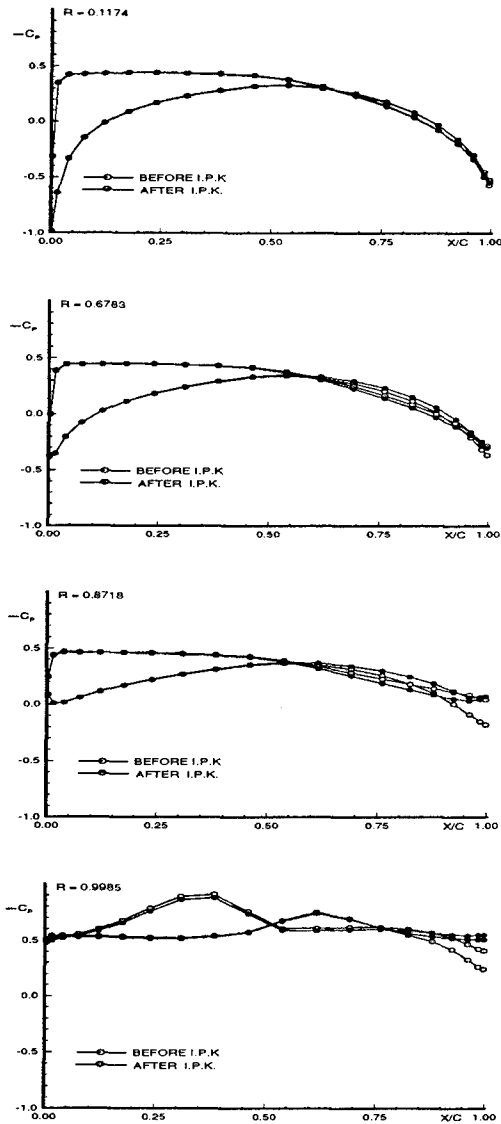
Figure 6: The blade orthogonal grid on a circular planform hydrofoil and its trailing wake.

2.2 The blade orthogonal grid

The blade orthogonal grid was introduced in [6]. The grid lines are normal to the blade outline [6], as shown for the CPH in Figure 6. When the BEM was applied on this grid, it was found that the surface pressures at the tips of non-lifting bodies were computed more accurately than when the BEM was applied on the conventional grid [6]. This is the consequence of concentrating more panels at the tip as well as of producing much less distorted panels (of which the sides are of comparable size and almost orthogonal to each other) than the conventional grid. The blade orthogonal grid was also found to improve the convergence of the IPK condition in the case of lifting hydrofoils or propeller blades. This is a direct consequence of the fact that the trailing edge pressures (which drive the IPK condition) at the tips were computed more accurately now than in the case of the conventional grid. The circulation distributions for the CPH are shown in Figure 7. Notice that the difference between the circulation distributions before and after the IPK condition is now larger than that for the conventional grid. An explanation for this will be given in Section 2.3. Also notice that the circulation distribution after the IPK condition is very similar (also "peculiar") to that in the case of the conventional grid. The results shown in this and the previous section indicate that there must be something fundamentally wrong either with the implementation of the IPK condition and/ or with the utilized grids.

Figure 5: Pressure coefficients predicted from BEM applied on the conventional grid (before and after the IPK condition); circular planform hydrofoil, $[\tau/c]_{max} = 0.2$, $\alpha = 5.73^\circ$. $C_p = (p - p_\infty)/\rho/U_o^2/2$.

2.3 Flow at the trailing edge

In order to understand the behavior of the flow at the trailing edge, the total velocity vectors on both sides of the CPH are shown in Figure 8. The
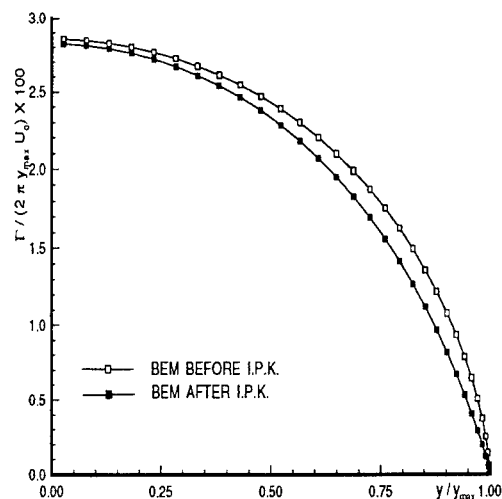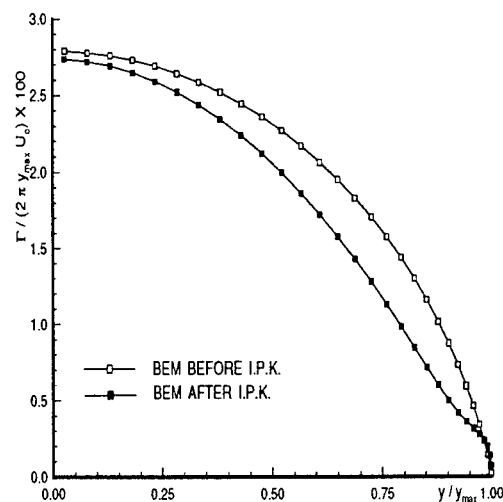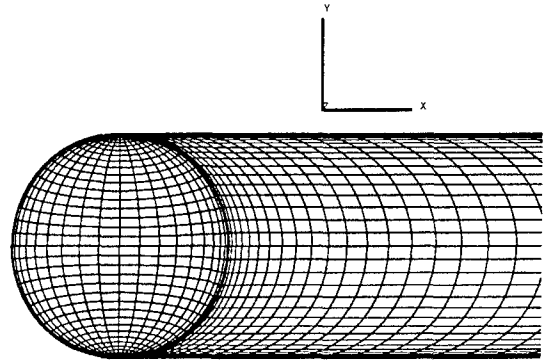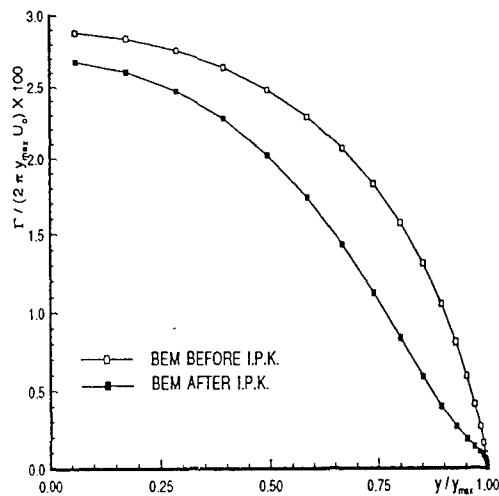
Figure 7: Circulation distribution on a circular planform hydrofoil; $[\tau/c]_{max} = 0.2$, $\alpha = 5.73°$. Predicted by applying the BEM on the blade orthogonal grid; before and after applying the IPK condition.

direction of the vorticity vector in the wake is also shown. Notice that the velocity vectors, V^+ and V^- at the suction and pressure sides of the trailing edge, respectively, have equal magnitudes as a result of the IPK condition[3]:

$$|V^+| = |V^-| \qquad (2)$$

On the other hand, the direction of the mean velocity vector, $V_m = [V^+ + V^-]/2$, is very different from that of the wake vorticity vector γ. This will result in a pressure jump in the wake given by:

$$\Delta p_W = \rho\, |V_m \times \gamma| \qquad (3)$$

where ρ is the flow density.

In other words, even though the IPK condition has ensured the equality of pressures at the trailing edge on the blade, it has no way to force the zero pressure jump condition in the wake. Instead, we must align the vorticity vector, i.e. wake geometry, with the mean velocity vector at the trailing edge. Therefore, our earlier assumption of no contraction in the wake must be withdrawn. It would also seem natural for the grid on the blade to be aligned with the mean velocity vector at the trailing edge. A justification for this is given next.

The total potentials Φ^+ and Φ^- at the suction and pressure sides at the trailing edge, respectively, may be expressed as follows:

---

[3] The IPK condition was found to affect the magnitude of the trailing edge velocities more than their directions

$$\Phi^+ = \Phi_1 + V_s^+ \Delta s$$
$$\Phi^- = \Phi_N + V_s^- \Delta s \qquad (4)$$

where Φ_1 and Φ_N are the total potentials at the control points of the trailing edge panels at the suction and pressure sides, respectively; Δs is the distance of the control points from the trailing edge measured along the "chordwise" grid direction on the planform [4], s, as shown in Figure 9; V_s^+ and V_s^- are the projections of the total trailing edge velocities V^+ and V^-, respectively, along s.

The Morino Kutta condition [15] at the trailing edge is:

$$\Delta\Phi = \Phi^+ - \Phi^- \qquad (5)$$

On the other hand, the numerical implementation of equation (5) requires:

$$\Delta\Phi_M = \Phi_1 - \Phi_N \qquad (6)$$

Thus, the discretization error, E, in implementing the Morino condition (i.e. before the IPK condition), may be expressed, by making use of equations (4), (5) and (6), as follows:

$$E = \Delta\Phi - \Delta\Phi_M = \Delta s\, [V_s^+ - V_s^-] \qquad (7)$$

According to equation (7), in order to minimize the difference between the circulations before and after applying the IPK condition, we should have:

$$V_s^+ = V_s^- \qquad (8)$$

In light of equation (2), equation (8) is equivalent to requiring that the mean velocity vector V_m is aligned with the grid direction s on the planform. This explains the larger difference between the circulation distributions before and after the IPK condition, in the case of the blade orthogonal grid than in the case of the conventional grid, stated earlier. In the case of the blade orthogonal grid the angle between V_m and the s direction is larger than in the case of the conventional grid.

2.4 The flow adapted grid

Based on the preceeding investigation the grid should have the following characteristics:

- Be adapted to the resulting flow in the wake.

---

[4] In gegenal different from the grid direction in the wake.

Figure 10: The effect of thickness sources (or sinks) on the flow field in the wake of a circular planform hydrofoil. The effect of sinks on the wake is stronger than that of sources.

- Be continuous at the trailing edge (thus also adapted with the wake flow).

- Be orthogonal at the leading edge (this will result in more accurate pressure predictions at the leading edge).

The proposed grid is called the *flow adapted* grid. It is defined as follows.

IN THE WAKE:

The total velocity, V_t, in the wake may be decomposed as:

$$V_t = V_\tau + V_\gamma^B + V_\gamma^W + U_o \qquad (9)$$

where $V_\tau, V_\gamma^B, V_\gamma^W$ are the induced velocities due to the sources on the hydrofoil surface, the vorticity (or dipoles) on the hydrofoil and, the vorticity in the wake , respectively; U_o is the inflow velocity.

Given that the wake geometry is assumed to lie on the x, y plane, the induced velocity due to the thickness sources will be the predominant contribution in the total wake velocity[5]. Thus, the total velocity vector in the wake may be approximated as:

$$V_t = V_\tau + U_{ox} \qquad (10)$$

Figure 8: Velocity vectors on the suction and pressure sides at the trailing edge of the circular planform; $[\tau/c]_{max} = 0.2$, $\alpha = 5.73°$. Predicted by applying the BEM on the blade orthogonal grid; after the IPK condition. The trailing vorticity vector, γ, is also shown.

Figure 9: Schematic of the paneling on a 3-D hydrofoil and its wake in the vicinity of the trailing edge.

where U_{ox} is the x component of the inflow velocity. V_τ may be expressed as:

---

[5]The vorticity distribution on the hydrofoil and its trailing wake will primarely induce velocities normal to the xy plane.

536
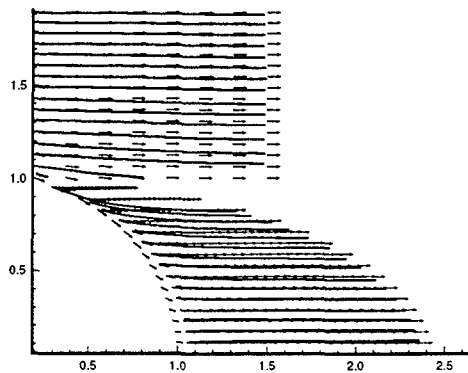
Figure 11: Velocity flow field and streamlines around a circular planform hydrofoil; $[\tau/c]_{max} = 0.2$. Only the effect of thickness sources is included. The upper right quadrant of the CPH is only shown.

$$V_\tau = \int_S q_\tau(x,y)\frac{\boldsymbol{R}}{4\pi R^3}dxdy \qquad (11)$$

$q_\tau(x,y)$ is the thickness source distribution, which for planar 3-D hydrofoils is given as follows:

$$q_\tau(x,y) = U_{ox}\frac{\partial \tau}{\partial x} \qquad (12)$$

where $\tau(x,y)$ is the thickness distribution and $\boldsymbol{R}$ is the vector connecting the point in the wake and the source point on the hydrofoil surface.

The integral in equation (11) is determined by discretizing the source distribution into line sources, arranged with a constant spacing in the spanwise direction and a full cosine spacing in the chordwise direction, as described in [3]. In particular, since the thickness sinks at the aft part of the hydrofoil are closer to the wake than the thickness sources at the forward part, it is expected that the combined effect will contract the wake, as shown schematically in Figure 10. The resulting total velocity flow field and the corresponding streamlines[6] for the circular planform hydrofoil with 20% thickness to chord ratio, are shown in Figure 11, where the expected contraction in the wake shape can be clearly seen. The shape of each of the streamlines may be determined by integrating the velocity flow field shown in Figure 11. Instead, we determine the following parameters for each streamline, shown in Figure 12:

• Its starting point y_{te}, x_{te} at the trailing edge.
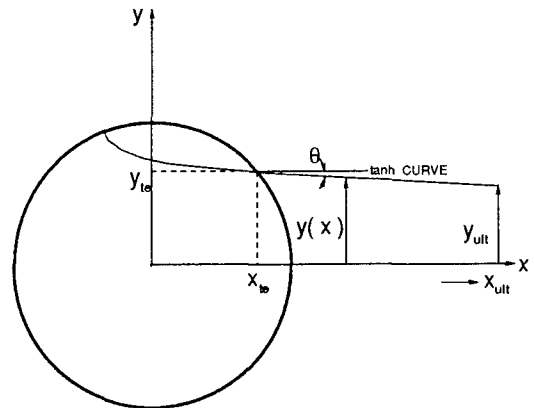
Figure 12: The geometry of wake streamlines.

• Its contraction angle, θ, at the trailing edge.

• Its distance, y_{ult}, from the x axis far downstream.

and then approximate its shape $y(x)$ by the expression:

$$y(x) = y_{te} - (y_{te} - y_{ult})\tanh X \qquad (13)$$

with X defined as

$$X = \frac{\theta\,(x - x_{te})}{y_{te} - y_{ult}} \qquad (14)$$

AT THE TIP:

The outer wake streamline in the case of the conventional and the blade orthogonal grid is parallel to the x axis, starting from the tip of the hydrofoil (defined as the point of maximum y). In the present case the starting point (we also call it the "computational" tip) and the shape of the outer wake streamline are deterined by searching among the streamlines for the one which starts at the largest y location and does not intersect the planform. Due to the contraction of the wake, the computational tip (it may also be seen as the tip vortex detachment point) will be downstream from the actual tip.

ON THE PLANFORM:

Having determined the location of the tip vortex detachment point, A_{tip}, the grid on the planform is determined, by modifying the algorithm on which the blade orthogonal grid was based [6], as follows:
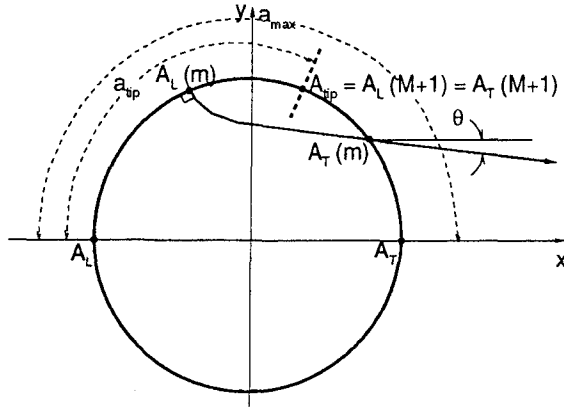
Figure 13: The geometry of grid lines. The location of the "computational" tip, A_{tip}, is taken downstream of the actual tip due to the contraction of the wake.

Figure 14: Flow adapted grid on circular planform hydrofoil; $[\tau/c]_{max} = 0.2$, $\alpha = 5.73°$. The trailing wake is aligned with the inflow, adjusted for the influence of the sources (and sinks) representing the hydrofoil thickness.

First, the arcs $A_L A_{tip}$ and $A_T A_{tip}$, shown in Figure 13, are divided into M half-cosine intervals, with M being the number of "spanwise" panels. The correspoding arclenghts are given as

$$a_{le}(m) = a_{tip} \cos \beta_m$$
$$a_{te}(m) = a_{max} - (a_{max} - a_{tip}) \cos \beta_m$$

$$\text{for} \quad m = 1, 2, \cdots, M$$

where $a_{le}(m)$, $a_{te}(m)$ are the lengths of the arcs $A_L A_L(m)$ and $A_T A_T(m)$, respectively, with β_m defined as

$$\beta_m = \frac{\pi}{2}\left(1 - \frac{m-1}{M}\right) \qquad (15)$$

In the case of the blade orthogonal grid, each $A_L(m)$ is connected with $A_T(m)$ via B-spline curves which are normal to the blade outline. In the present case, the grid lines are still normal to the blade outline at the leading edge, but now they form an angle with the x axis at the trailing edge, which is equal to the corresponding wake contraction angle θ, defined earlier. The arcs of these grid lines are then divided into $N/2$ full-cosine spaced intervals, with N being the number of "chordwise" panels. The grid on both sides of the 3-D hydrofoil is then determined by moving the grid of the planform normal to the planform and by an amount equal to $\pm\tau/2$.

The proposed flow adapted grid for the circular planform hydrofoil with 20% thickness to

chord ratio, is shown in Figure 14. The grids for various thickness to chord ratios are shown in Figure 15. Notice that as the thickness reduces, the wake contraction and the distance between the computational and the actual tip also reduce.

The circulation distribution predicted from applying the BEM on the flow adapted grid for the CPH are shown in Figure 16. Notice that the circulation distributions before and after applying the IPK condition are closer to each other than they were in the case of the conventional and the blade orthogonal grid. Also notice that the circulation distribution now extends only up to the location of the computational tip and that its values after the IPK condition does not show the previously observed "peculiar" behavior at the tip. The predicted flow at the trailing edge is also shown in Figure 17, where it can be seen that the mean velocity vector is now practically aligned to the trailing wake vorticity vector. Small differences in the directions of the V_m and γ vectors at the trailing edge may be attributed to our restricting the wake on the xy plane. It is anticipated that relaxing the wake and aligning the grid on the planform at the same time, it would further reduce the difference between the circulation distributions before and after the IPK condition. Performing the complete wake relaxation and the corresponding planform grid alignment was outside the scope of the present work.

538

Figure 17: Velocity vectors on the suction and pressure sides at the trailing edge of the circular planform; $[\tau/c]_{max} = 0.2$, $\alpha = 5.73°$. Predicted by applying the BEM on the flow adapted grid; after the IPK condition. The trailing vorticity vector is also shown.
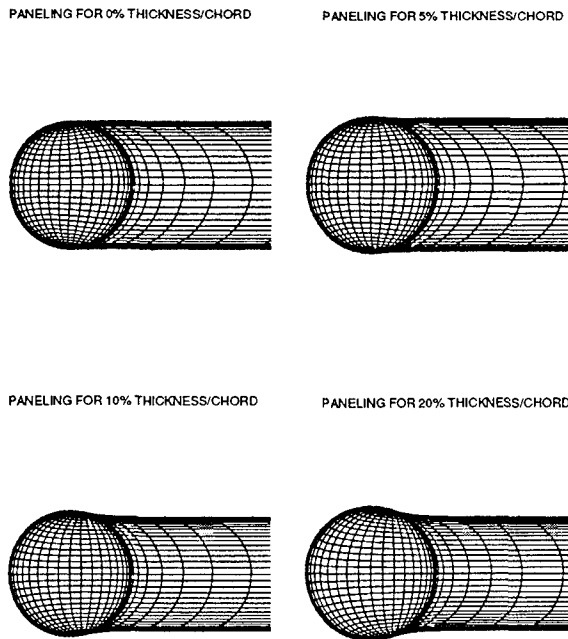
Figure 15: Flow adapted grids for circular planform hydrofoils with different thickness/chord ratios.
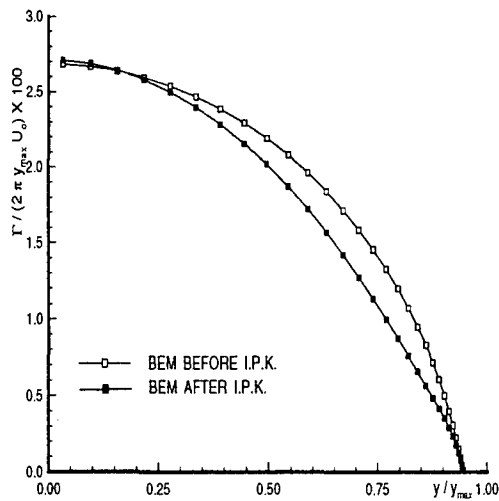
Figure 16: Circulation distribution on a circular planform hydrofoil; $[\tau/c]_{max} = 0.2$, $\alpha = 5.73°$. Predicted by applying the BEM on the flow adapted grid; before and after applying the IPK condition.
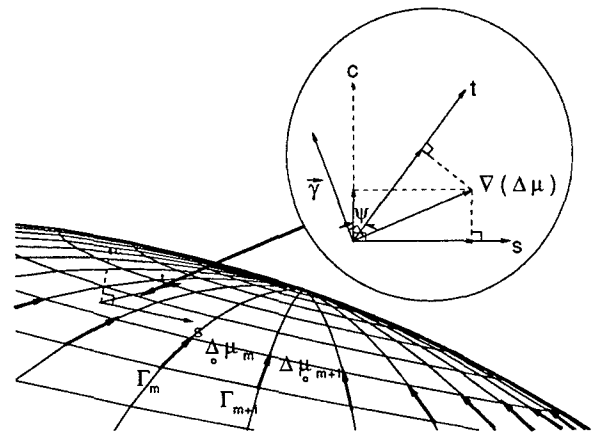
Figure 18: Grid lines in the vortex-lattice method.

539

3 VORTEX-LATTICE METHOD (VLM)

The fundamentals of the Vortex Lattice Method are described in [13] and [3]. The method models the lifting surface (3-D hydrofoil or propeller blade) with a lattice of line vortices and sources, distributed on the mean camber surface and the trailing wake. This method has recently been modified to account for the coupling between thickness and loading [9]. The modified VLM has been applied on 3-D hydrofoils and propeller blades (by using conventional grids) and has produced results which for most applications are strikingly close to those from applying the BEM method [9], even in the case of highly skewed propeller blades [6]. In the present work we have extended the implementation of the thickness/loading coupling in the case of general grids, as shown in Figure 18. The method is summarized in the following steps:

- Solve the zero thickness VLM problem and determine the strengths, $\Gamma's$, of the line vortices, by satisfying the kinematic boundary condition at appropriately selected control points on the planform:

$$V_\Gamma \cdot n = -U_{on} \qquad (16)$$

where V_Γ is the velocity vector induced by all discrete vortex horseshoes on the planform and its wake; U_{on} is the component of the inflow normal to the planform, i.e. $U_{on} \equiv U_o \cdot n$, with n being the unit normal vector to the planform, pointing towards the positive z axis shown in Figure 2.

- Evaluate the potential jumps, $\Delta\mu$'s, across the planform, by using the following algorithm:

$$\Delta\mu_m = \Delta\mu_{m-1} + \Gamma_m ; \quad m = 1,...,M \quad (17)$$

with $\Delta\mu_0 \equiv 0$. Equation (17) is applied along each s grid line. The resulting $\Delta\mu$'s are asigned at the control points of the VLM.

- Determine the vorticity vector γ on the planform by using the formulas:

$$\gamma = \gamma_s s + \gamma_c c$$

$$\gamma_s = -\frac{\partial(\Delta\mu)}{\partial c} =$$

$$= \left[\frac{\partial(\Delta\mu)}{\partial s}\sin\psi - \frac{\partial(\Delta\mu)}{\partial t}\right]\frac{1}{\cos\psi}$$

$$\gamma_c = \frac{\partial(\Delta\mu)}{\partial s} \qquad (18)$$

where s, t are the arclenghts along the two grid directions (in general non-orthogonal); c is the arclength on the planform in directions normal to s; s and c are the unit vectors along s and c respectively; ψ is the angle between the c and t directions; γ_s and γ_c are the components of γ along the s and c directions, respectively. Equations (18) are the result of the following equations or definitions:

$$\gamma = n \times \Delta V \qquad (19)$$
$$\Delta V \equiv V^+ - V^- \qquad (20)$$
$$V^+ - V^- = \Delta(\nabla_S \mu) \qquad (21)$$
$$\nabla_S \equiv s\frac{\partial}{\partial s} + c\frac{\partial}{\partial c} \qquad (22)$$
$$\Delta(\nabla_S \mu) = \nabla_S(\Delta\mu) \qquad (23)$$
$$\gamma = n \times \nabla_S(\Delta\mu) \qquad (24)$$

- Evaluate the additional normal velocity V^c due to the thickness/loading coupling by using the expression:

$$V^c = \nabla_S \cdot \left[\frac{(\gamma \times n)\tau}{4}\right] =$$
$$= \frac{1}{4\lambda l^*}\left[\frac{\partial(\lambda\gamma_c^*)}{\partial s} - \frac{\partial(l^*\gamma_s^*)}{\partial t} - \frac{\partial(\mu l^* \gamma_c^*)}{\partial s}\right] \quad (25)$$

where

$$\gamma_s^* = \gamma_s\tau$$
$$\gamma_c^* = \gamma_c\tau$$
$$\mu = \frac{-\frac{\partial x_p}{\partial s}\cdot\frac{\partial x_p}{\partial t}}{\left|\frac{\partial x_p}{\partial s}\right|^2}$$
$$\lambda = \left|\frac{\partial x_p}{\partial t}\right|$$
$$l^* = \left|\frac{\partial x_p}{\partial s}\right|$$

$$(26)$$

with x_p being the vector expressing the mean camber surface (the xy plane in the case of a planar 3-D hydrofoil) and τ being the hydrofoil thickness distribution. The second part

of equation (25) gives ∇_S in terms of functions of the non-orthogonal coordinates s and t, shown in Figure 18. This expression has been derived by applying a similar procedure to that described in Appendix 1 of [9].

- Modify the kinematic boundary condition of the zero thickness problem by replacing U_{on} with U_{on}^{mod} at the RHS of equation (16):

$$U_{on}^{mod} = U_{on} - V^c + v_q^n \qquad (27)$$

where v_q^n is the induced normal velocity due to the thickness source distribution. For planar 3-D hydrofoils, $v_q^n = 0$

- Solve the VLM problem with the modified kinematic boundary condition to find the new γ_{mod} distribution.

The derivatives involved in equations (18) and (25) are evaluated by splining the corresponding functions and then by taking the derivatives of the spline interpolations.

The VLM method has been applied on the circular hydrofoil planform and the results are described in the next section.

4   BEM VS. VLM

Due to the lack of analytic solutions for lifting 3-D hydrofoils with thickness, there is no direct way to validate the accuracy of different numerical methods (VLM's or BEM's) for such applications. To our knowledge, the only analytic solution for 3-D hydrofoils is the one by Jordan [7] for a circular planform hydrofoil with zero thickness. The predicted circulation distribution from applying the VLM on this hydrofoil has been found to agree very well to the analytic solution, even with a 5 by 5 grid [4]. The BEM formulation, however, becomes degenerate for zero thickness, and thus it cannot be applied to this problem. The consistency test, already mentioned in the introduction, is not a direct test, since it requires extrapolations of the results from applying the BEM at a progression of gradually thinning sections.

Instead, in this work, we compare the results from applying the BEM to those from applying the VLM, including the thickness/ loading coupling. Such comparisons are shown in Figure 19. Notice the large difference between the circulation distributions in the case of the conventional and the blade orthogonal grid. This is a consequence of the fact that the effect of velocities due

to thickness on the Kutta condition, is ignored in the VLM. If this effect is superimposed to the trailing velocity vectors predicted by the VLM, the magnitudes of the velocity vectors and thus pressures at the two sides of the trailing edge will not be equal. Thus, in this case the pressure jump at the trailing edge is non-zero, in addition to being non-zero in the wake (as explained in Section 2.3). However, when applying the VLM on the flow adapted grid, the velocity due to thickness changes the magnitudes of the velocities at the two sides of the trailing edge by the same amount, thus preserving the zero pressure jump across the trailing edge. The good agreement of the circulation distributions predicted from applying the BEM and the VLM on the flow adapted grid, shown at the bottom of Figure 19, is attributed to the fact that *both* methods satisfy the zero pressure jump condition at the trailing edge on the planform, as well as in the wake.

5   RESULTS

The BEM is applied on three hydrofoils with the following characteristics:

- Elliptic chord distribution in the spanwise direction.

- Aspect Ratio AR=3.

- Modified NACA66 thickness distribution with 20% maximum thickness to chord ratio (constant in the spanwise direction)

- Sweep angle varying from -45° (forward sweep) to 0° and 45°.

The circulation distributions predicted from applying the BEM on the conventional and the flow adapted grid are shown in Figure 20. Notice that as the sweep angle decreases the difference between the two circulation distributions increases. This is due to the drastic contraction of the wake geometry, also shown in Figure 20, as the planform is swept forward. The wake contraction is increasing as the planform is swept forward, because the source sinks at the aft part of the planform, shown in Figure 10, have a stronger effect on the wake streamlines at the tip.

Finally, the elliptic planform hydrofoil used in the experiment by Arndt et al. [1] is analyzed by the present method. In particular, the trajectory of the tip vortex is determined, by considering only the effect due to hydrofoil thickness, as descibed in Section 2.4. The spanwise
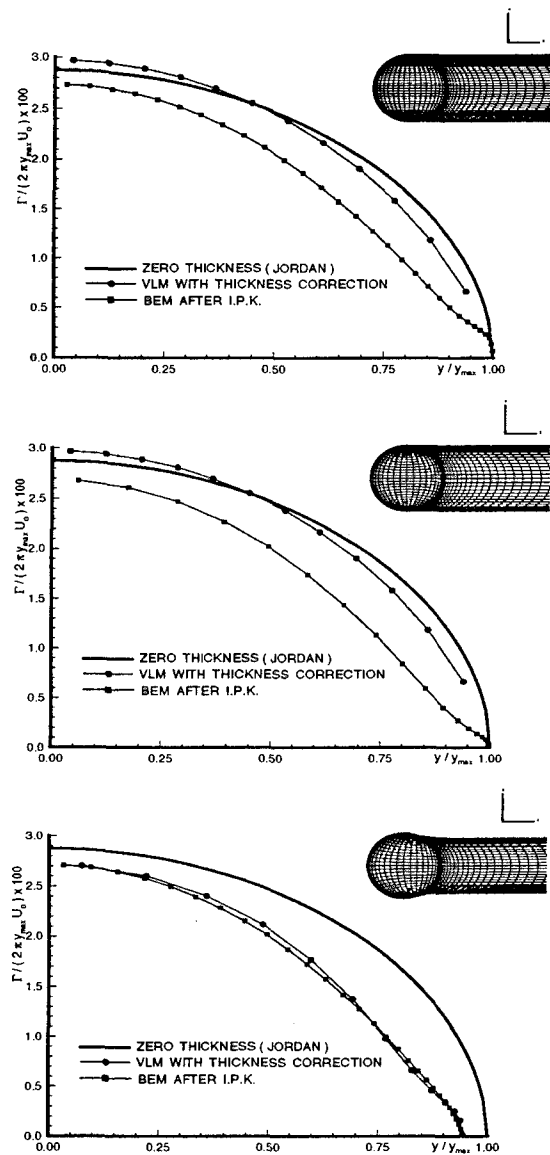
Figure 19: Circulation distributions predicted from BEM (after the IPK condition) and VLM (including the thickness/ loading coupling) for different grid arrangements. The analytical solution for zero thickness (Jordan, 73) is also shown. Circular planform hydrofoil, $[\tau/c]_{max} = 0.2$, $\alpha = 5.73°$. Original grid (top). Orthogonal grid (middle). Proposed grid (bottom).
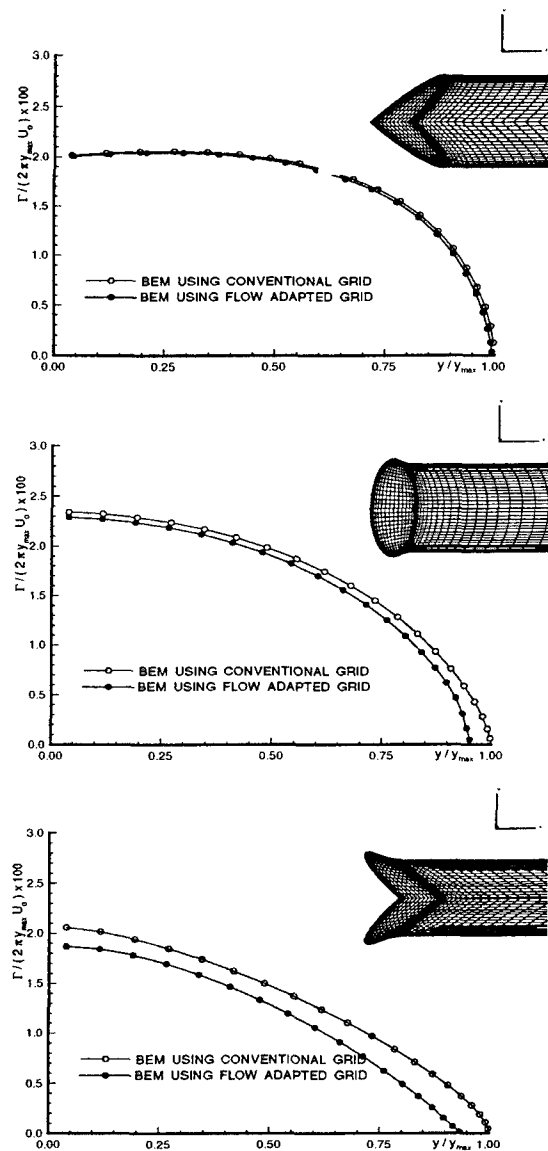
Figure 20: Effect of wake geometry on circulation predicted by BEM for three hydrofoils with elliptic chord distribution along the span; $[\tau/c]_{max} = 0.2$, $\alpha = 5.73°$, aspect ratio AR=3. 45° backward sweep (top) no sweep (middle) 45° forward sweep (bottom). The corresponding flow adapted grids are also shown.
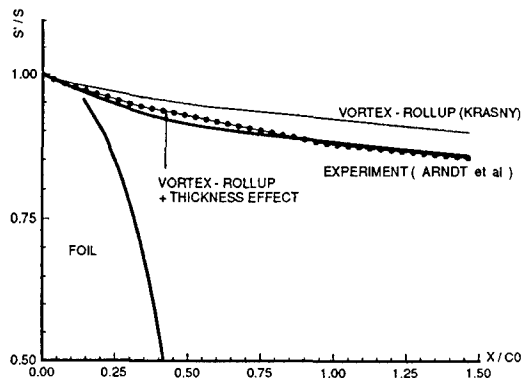
Figure 21: Tip vortex trajectories predicted from analysis and measured in experiment. Elliptic planform hydrofoil; $\alpha = 15.5^{\circ}$, $[\tau/c]_{max} = 0.15$, aspect ratio $AR = 3$.

coordinates of this trajectory are then superimposed to those of the tip vortex trajectory predicted by Krasny [12], who only included the effects of the wake sheet rollup. The results are shown, together with the experimental results, in Figure 21. Notice that, under the examined condition, the effects of the wake sheet rollup and that of the hydrofoil thickness on the predicted tip vortex trajectory are equally important, and that when both are included, the trajectory of the tip vortex matches the observed very well. However, in order to validate the prediction methods completely, more comparisons with experiments at several conditions are required. In addition, further computations, which also include the effects of viscosity on the hydrofoil loading, thus on the strength of the wake vortex sheet, must be carried out.

6 CONCLUSIONS

The performance of a boundary element method, when applied for the prediction of flows around lifting surfaces with round tips, has been addressed. Previous grid arrangements have been found to be incompatible with the application of a pressure Kutta condition at the trailing edge. It has been concluded that an improved grid arrangement should have the following characteristics:

- Be adapted to the mean velocity vector at the trailing edge.

- Converge to a point at the tip which coincides with the tip vortex detachment point.

When a flow adapted grid was applied on a circular planform hydrofoil, the performance of the boundary element method was found to improve substantially. In addition, the results from applying a vortex-lattice method on the same grid, were found to be in very good agreement to those from the boundary element method. Thus, previous differences between the results from the boundary element and the vortex-lattice method, have been reconciled.

ACKNOWLEDGEMENTS

References

[1] R.E.A. Arndt, V.H. Arakeri, and H. Higuchi. Some observations of tip-vortex cavitation. *Journal of Fluid Mechanics*, 229:pp. 269–289, 1991.

[2] T. Brockett. *Minimum Pressure Envelopes for Modified NACA-66 Sections with NACA a=0.8 Camber and Buships Type I and Type II Sections*. Report 1780, DTNSRDC, Teddington, England, Feb 1966.

[3] D.S. Greeley and J.E. Kerwin. Numerical methods for propeller design and analysis in steady flow. *Trans. SNAME*, vol 90, 1982.

[4] J.L. Guermond. About collocation methods for marine propeller design. In *Proceedings of the Propellers '88 Symposium*, pages 1–9 (paper No. 8), Soc. Naval Arch. & Marine Engnrs., Virginia Beach, VA, September 1988.

[5] Ching-Yeh Hsin. *Development and Analysis of Panel Method for Propellers in Unsteady Flow*. PhD thesis, Department of Ocean Engineering, MIT, September 1990.

[6] C-Y. Hsin, J.E. Kerwin, and S.A. Kinnas. A panel method for the analysis of the flow around highly skewed propellers. In *Proceedings of the Propellers/Shafting '91 Symposium*, pages 1–13 (paper No. 11), Soc. Naval Arch. & Marine Engnrs., Virginia Beach, VA, September 1991.

[7] Peter F. Jordan. Exact solutions for lifting surfaces. *AIAA Journal*, 11(8), August 1973.

[8] J.E. Kerwin, S.A. Kinnas, J-T Lee, and W-Z Shih. A surface panel method for the hydrodynamic analysis of ducted propellers. *Trans. SNAME*, 95, 1987.

[9] S.A. Kinnas. A general theory for the coupling between thickness and loading for wings and propellers. *Journal of Ship Research*, 36(1):pp. 59–68, March 1992.

[10] S.A. Kinnas and C-Y. Hsin. A boundary element method for the analysis of the unsteady flow around extreme propeller geometries. *AIAA Journal*, 30(3):688–696, March 1992.

[11] S.A. Kinnas, C-Y. Hsin, and D.P. Keenan. A potential based panel method for the unsteady flow around open and ducted propellers. In *Proceedings of the Eighteenth Symposium on Naval Hydrodynamics*, pages 667–685, Ann Arbor, Michigan, August 1990.

[12] R. Krasny. Computation of vortex sheet roll-up in the Trefftz plane. *Journal of Fluid Mechanics*, 184:pp. 123–155, 1987.

[13] C.E. Lan. A quasi vortex-lattice method in thin wing theory. *Journal of Aircraft*, vol. 11(no. 9), 1974.

[14] Jin-Tae Lee. *A Potential Based Panel Method for The Analysis of Marine Propellers in Steady Flow*. PhD thesis, M.I.T., Department of Ocean Engineering, August 1987.

[15] Luigi Morino and Ching-Chiang Kuo. Subsonic potential aerodynamic for complex configurations : a general theory. *AIAA Journal*, vol 12(no 2):pp 191–197, February 1974.

Time-Dependent Inviscid Flow Analysis of Rotor-Stator Systems

Y.T. Lee (David Taylor Model Basin, USA)
J. Feng and C.L. Merkle (The Pennsylvania State University, USA)

ABSTRACT

A time-accurate hybrid panel/Euler computational method for unsteady 2-D/3-D inviscid incompressible flows through a rotor-stator system is presented. The method represents the boundary surfaces by distributing constant-doublet (for 3-D) or piecewise linear-vortex (for 2-D) and constant-source singularities on discrete panels. A local coordinate is assigned to each independently moving object. Blade shed vorticity is convected using the Euler equation. A nonlinear unsteady pressure-type Kutta condition is applied that enforces zero blade trailing-edge loading at each time step. Example problems of the near-encounter between a vortex and an airfoil, as well as unsteady loading on a foil by upstream flapper foils demonstrate the validity of the techniques. Results of rotor-stator calculations indicate that unsteady interactions play an important role in the rotor-stator system. Time-accurate unsteady results are much closer to experimental measurements than are quasi-unsteady approximations that are commonly used.

NOMENCLATURE

C_p pressure coefficient
c   chord of the foil
CD   velocity potential due to doublet
CDL   velocity potential due to linearly distributed vortex
CDU   velocity potential due to uniformly distributed vortex
CD1   coefficient defined in Eq. (7)
CD2   coefficient defined in Eq. (7)
CS   velocity potential due to uniformly distributed source
D   scalar matrix defined in Eq. (20)

ds   differential surface element
$\underline{dv}$ differential volume element
$\underline{E}$ vector matrix defined in Eq. (20)
f   reduced frequency based on half chord length
G   Green's function
H   cascade spacing or pitch
ITS   total time steps
N   total number of panels
NS   total number of surface patches
n   surface normal
$\underline{p}$ local static pressure
r   distance vector
S   panel length
s   surface tangent
t   time
T   period
$\underline{U}$ reference velocity
$\underline{u}$ total velocity
$\underline{u}_B$ surface moving velocity
$\underline{u}_m$ mean velocity, defined in Eq. (16)
$\underline{u}_o$ flow onset velocity
v_t velocity defined in Eq. (13)
x,y,z   global ground-fixed coordinate
α angle of attack
Γ circulation around a foil or an isolated vortex
γ vortex or doublet strengths
$\delta\Omega$ boundary surfaces
$\underline{\kappa}$ ratio of panel lengths
ξ vorticity vector
ρ fluid density
$\underline{\sigma}$ source strength
ϕ unit vector potential
ϕ disturbance velocity potential
ϕ_∞ inflow velocity potential
Ω flow domain

Sub- or Superscripts
b   body or airfoil
e   exact solution

k	iteration number
s	tangent to the surface
u	upper surface
v	vortex
W	wake
ℓ	lower surface

INTRODUCTION

Many unconventional marine propulsors, such as counterrotating propellers or propellers with preswirl stators, consist of multiple-blade-row configurations. The flow structure in such geometries is very complex. The wakes shed by upstream blades are nonuniform and time dependent due to the relative motion between the upstream and downstream blade rows. Further, these wakes interact with the downstream blades, generating wake wrapping and wake cutting. Previous studies (1,2) have suggested that such a complex flow is still primarily inviscid and that time-dependent interactions can be properly addressed in an inviscid flow fashion, provided that the vortex shedding and its evolution are handled correctly.

Unsteady potential-flow calculation methods (3,4,5,6) have been developed for propellers and turbomachinery for many years. These methods have demonstrated their capability in many practical design problems. Most of these methods include effects of vortex shedding but do not trace the vorticity field. Instead the shed vorticity is placed on a prescribed path. These approaches are effective in cases where wake vortex effects are small. For large amplitude unsteady motions like marine propeller flows, however, the effect of the blade shed wake becomes important both for the force prediction and also for the other flow induced phenomena. For example, the authors' recent results (7) in predicting blade/vortex interaction noise indicate that correct modelling and tracing of blade shed vorticity is necessary for the accurate prediction of noise generated by acceleration or deceleration of vorticity during blade/vortex and wake/vortex interactions.

In the present paper, a time-accurate hybrid panel/Euler method is developed for inviscid flow through rotor-stator configurations. The unsteady Kutta condition is enforced at the blade trailing edge to account for the neglected viscosity effect. In order to effectively simulate the blade shed vorticity, the vortical wake is modelled using Kelvin's conservation law of vorticity and the appropriate Euler's equation. For developing an efficient calculation scheme and also generating smooth wake vorticity, a vortex splitting and merging procedure is used to reduce vorticity tracing instability due to vortex interactions.

To demonstrate the features of the method, Chow's analytic solution (8) is first presented and compared for a "strong" incoming vortex interacting with a foil. Secondly, MIT's flappers and foil flow simulations (9) are shown by using the multiple-blade-row cascade calculation method. Lastly, a turbine stator-rotor interaction result (10) based on unsteady calculations and quasi-unsteady calculations are presented and compared with measurements.

GOVERNING EQUATIONS

For inviscid incompressible flows past a rotor-stator system, the velocity u at a field point p and time t is given by the integral relation (11),

$$
\vec{u}(p,t) = \nabla \int_{\delta\Omega} u_n G ds \\
- \nabla \times [\int_{\delta\Omega} \vec{\xi}_b G ds + \int_\Omega \vec{\xi} G dv] \tag{1}
$$

The surface integrals are performed on the boundary surface $\delta\Omega$ for surface normal velocity u_n and surface vorticity ξ_b. The volume integral is an integration in the flow domain Ω for the shed vorticity ξ, whose motion is governed by the Euler equation,

$$
\frac{\partial \vec{\xi}}{\partial t} + \vec{u} \cdot \nabla \vec{\xi} = 0 \tag{2}
$$

The quantity G is the Green function, which is given by $-1/4\pi r$ for three-dimensional flows and by $1/2\pi \ln (1/r)$ for two-dimensional flows.

The system given in Eqs. (1) and (2) must satisfy the following boundary condition and auxiliary conditions. On the blade surface, the flow tangency condition becomes

$$
u_n = \vec{u}_b \cdot \vec{n} \tag{3}
$$

where $\overline{u}_b$ is the velocity of the blade surface. This boundary condition is augmented by the Kutta condition, which requires zero pressure loading and permits a tangential slip velocity at the trailing edge.

$$
p^u = p^\ell \quad \text{at the trailing edge .} \tag{4a}
$$

where u and ℓ represent upper and lower surfaces of the blade. For 3-D problems, the two components of the surface vortex ξ are not independent, but their spanwise and tangential derivatives are related by

$$\frac{\partial \xi_1}{\partial x_2} = \frac{\partial \xi_2}{\partial x_1} \quad . \tag{4b}$$

More conveniently, the surface vortex sheet can be replaced by an equivalent doublet sheet which satisfies Eq. (4b) automatically.

For 2-D flows, Eq. (4b) is reduced to a simple restraint of total circulation conservation on the blade surface $\delta\Omega$ and in the wake Ω,

$$\int_{\delta\Omega} \xi_b ds + \int_{\Omega} \xi dv = constant \quad . \tag{4c}$$

The solution of Eqs. (1) and (2) along with the conditions of Eqs. (3) and (4) is accomplished by means of a hybrid panel/Euler solution procedure. This procedure discretizes the blade surfaces into panels. The governing equations then are transformed into a velocity potential form and are enforced at panel control points located at the center of each panel. The boundary condition is implemented by directly substituting u_n from Eq. (3) into Eq. (1). The calculation of the unsteady force and moment on each moving foil is reduced to an integration using the unsteady Bernoulli equation in a body-fixed coordinate system,

$$C_p = \frac{p - p_\infty}{\rho U^2 / 2} = -2\frac{\partial \phi}{\partial t} - \vec{u}\cdot(2\vec{u}_b + \vec{u}) + u_o^2 \quad . \tag{5}$$

Here ϕ is the disturbance velocity potential and u_o is the onset flow velocity. The panel method then solves for the surface doublet or vortex strengths. The vorticity shed from the trailing edge of the foil is determined by satisfying the Kutta condition to account for the viscosity effect. The induced velocity at each wake vortex location is computed and used to enforce Eq. (2) for vortex convection.

NUMERICAL IMPLEMENTATIONS

Surface Singularities

The surface $\delta\Omega$ is discretized into small discrete flat elements (surface panels for 3-D and line segments for 2-D) with the control point located at the centroid. The normal to the surface is approximated by the perpendicular to the flat element. The constant source strength on each element is given by Eq. (3). The strengths of the constant 3-D doublet or the linear 2-D vortex are obtained from solving Eq. (1).

The 2-D velocity potential at an ith element due to a jth element which contains linearly distributed

vortices of strength $\gamma(\xi) = (\gamma_j + \gamma_{j+1})/2 + (\gamma_{j+1} - \gamma_j)\xi/2S_j$, and a constant source σ_j is given by

$$\phi_{ij} = CD1_{ij}\gamma_j + CD2_{ij}\gamma_{j+1} + CS_{ij}\sigma_j \quad , \tag{6}$$

where

$$CD1_{ij} = \frac{1}{2}(CDU_{ij} - CDL_{ij})$$
$$CD2_{ij} = \frac{1}{2}(CDU_{ij} + CDL_{ij}) \quad , \tag{7}$$

and CDU_{ij} and CDL_{ij}, given in Ref. (2), represent the velocity potentials due to the uniformly and the linearly distributed vortices. The quantity CS_{ij}, which is due to the uniformly distributed source, is given in Ref. (2). The corresponding 3-D velocity potential at an ith element due to a jth constant doublet γ_j is

$$\phi_{ij} = CD_{ij}\gamma_j + CS_{ij}\sigma_j \quad , \tag{8}$$

where CD_{ij} is the influence coefficient of the doublet.

Equation for Vortex/Doublet Strengths

For a unique solution outside of the surface $\delta\Omega$ described by Eq. (1), the flow inside the surface $\delta\Omega$ can be assumed at rest. If each body/foil surface $\delta\Omega$ is divided into N segments, the quiescent interior flow condition requires

$$\phi_i = constant \quad or$$
$$\Delta\phi = \phi_{i+1} - \phi_i = 0 \qquad i = 1, 2 \ldots, N-1 \quad . \tag{9}$$

The no-penetration boundary condition, Eq. (3), is imposed at the control point of each element.

For the two-dimensional case, a set of linear algebraic equations for the bound vortex γ_i is formed by expanding Eq. (9) as

$$(CD1_{i,1} - CD1_{i-1,1})\gamma_1 + (CD2_{i,N} - CD2_{i-1,N})\gamma_{N+1}$$
$$+ \sum_{j=1}^{N-1}(CD1_{i,j+1} - CD1_{i-1,j+1} + CD2_{i,j} - CD2_{i-1,j})\gamma_{j+1}$$
$$= \sum_{j=1}^{N}(CS_{ij} - CS_{i,j-1})\frac{\partial\phi}{\partial n_j} - \sum_{j=1}^{ITS}\gamma_{wj}\phi_{wj} \tag{10}$$
$$i = 1, 2 \ldots, N-1 \quad ,$$

where ITS represents the total number of time steps. This gives N-1 equations for the N+1 unknown values of γ. Hence two extra equations are required for obtaining a unique solution for 2-D problems. These

547

conditions are given later.

For 3-D flows the disturbance potential at infinity approaches zero. Consequently Eq. (9) is simplified to $\phi_i = 0$.

In this case, the 3-D doublet strengths are obtained from the equations

$$\sum_{j=1}^{N} CD_{i,j}\gamma_j = \sum_{j=1}^{N} CS_{ij}\frac{\partial\phi}{\partial n_j} - \sum_{j=1}^{ns} \gamma_{wj}\phi_{wij} \qquad (11)$$

$$i=1,2....,N .$$

Because we use uniform doublets in the 3-D case, Eq. (11) represents a unique system of N equations and N unknowns.

In both the 2-D (Eq. (10)) and the 3-D (Eq. (11)) cases, the vorticity shed at the trailing edge is given by the Kutta condition. This discussion follows.

Kutta Condition

The Kutta-Joukowski condition implicitly accounts for viscous effects otherwise neglected in potential-flow theory. In the present numerical method this is enforced by means of a pressure condition at the trailing edge. Accordingly, the pressures on the upper and the lower surfaces are required to be equal. For 3-D panels, upper and lower surfaces are referred to each specific strip of panels in the chordwise direction. This condition does not restrain the trailing edge from having a variation of pressure in the time domain or spanwise along the trailing edge.

Using the unsteady form of the Bernoulli equation (Eq. (5)), one obtains

$$2\frac{\partial}{\partial t}(\phi_u - \phi_\ell) + [(\vec{u}+\vec{u}_B)_u \cdot (\vec{u}+\vec{u}_B)_u$$
$$-(\vec{u}+\vec{u}_B)_\ell \cdot (\vec{u}+\vec{u}_B)_\ell] = 0 . \qquad (12)$$

Since the impermeability boundary condition is applied on $\delta\Omega$, the flow on the upper and lower surfaces is tangent (superscript s) to both surfaces.

For two-dimensional problems, the scalar relations,

$$\phi_u - \phi_\ell \equiv \Gamma = \sum_{j=1}^{N} \frac{1}{2}(\gamma_j + \gamma_{j+1})S_j$$
$$\bar{v}_t \equiv \frac{1}{2}(V_o^{su} - V_o^{s\ell} + u^{su} - u^{s\ell} + u_B^{su} - u_B^{s\ell}) , \qquad (13)$$

allow Eq. (12) to be recast into the form,

$$(1+\frac{S_1}{2VT})\gamma_1 + \sum_{j=1}^{N-1}\frac{S_j+S_{j+1}}{2VT}\gamma_{j+1} + (1+\frac{S_N}{2VT})\gamma_{N+1}$$
$$= \frac{-\Gamma(t-\Delta t)}{VT} - V_o^{su} - V_o^{s\ell} . \qquad (14)$$

where $VT = 2(\Delta t)\bar{v}_t$ and Γ is the circulation of the airfoil defined as positive in a clockwise direction. The total blade circulation Γ is linearly dependent on the shedding vortex strength γ_W as explained in the next section. Equation (14) is nonlinear in γ because VT is not a constant. In the present study, Eq. (14) is solved iteratively to account for this nonlinearity. Both Yao et al. (12) and Kim and Mook (13) ignored this nonlinearity and applied a more restricted Kutta condition at the trailing edge by requiring $\gamma_1 = \gamma_{N+1} = 0$ and placing a wake vortex of unknown strength there. As shown later, the nonlinear approach gives improved solutions.

For the present 2-D system, Eq. (14) provides one of the two additional equations needed for solving Eq. (10). A second additional equation is needed to obtain a unique γ-distribution for a lifting body. This condition is provided by requiring the tangential velocity gradients along the trailing edge on both the upper and lower surfaces to be identical,

$$(\frac{\partial\gamma}{\partial s})_u = (\frac{\partial\gamma}{\partial s})_\ell . \qquad (15)$$

Requiring the equality of velocity gradients on both surfaces further ensures the smooth merger of the two flows. When second-order backward differencing is used, Eq. (15) is transformed to

$$\kappa[\kappa_\ell(2+\kappa_\ell)\gamma_1 - (1+\kappa_\ell)^2\gamma_2 + \gamma_3]$$
$$-\gamma_{N-1} + (1+\kappa_u)^2\gamma_N - \kappa_u(2+\kappa_u)\gamma_{N+1} = 0 \qquad (16)$$

where $\kappa_u = S_{N-1}/S_N$, $\kappa_\ell = S_2/S_1$ and $\kappa = S_{N-1}(1+\kappa_u)/S_2(1+\kappa_\ell)$. Hence Eqs. (10), (14) and (16) form a determinate system of nonlinear equations for determining γ for a 2-D lifting configuration. They are solved using an iterative scheme.

For 3-D flows Eq. (12) has to be enforced at every panel along the blade trailing edge in the spanwise direction. Consequently, the analog of Eq. (14) for 2-D flow becomes a set of nonlinear matrix equations in 3-D flows. This system again requires iterative numerical procedures. For the 3-D case, Eq. (12) becomes

$$\frac{p_u - p_\ell}{1/2 \rho u_o^2} = 2\frac{\partial}{\partial t}(\phi_u - \phi_\ell) \tag{17}$$
$$+ [(\vec{u} + \vec{u}_B)_u + (\vec{u} + \vec{u}_B)_\ell] \ [(\vec{u} + \vec{u}_B)_u - (\vec{u} + \vec{u}_B)_\ell] \ .$$

The perturbed form of Eq. (17) can be cast as

$$2\frac{\partial}{\partial t}\Delta(\phi_u - \phi_\ell) + 2\vec{u}_m \cdot \Delta(\vec{u}_u - \vec{u}_\ell) = \frac{\Delta p}{1/2 \rho u_o^2} ,$$
$$where \tag{18}$$
$$\vec{u}_m = \frac{1}{2}[(\vec{u} + \vec{u}_B)_u + (\vec{u} + \vec{u}_B)_\ell]$$

is the mean velocity at the blade trailing edge, and $\Delta p = p_u - p_\ell$, is the pressure difference between the upper and lower surfaces. In order to drive Δp to zero we adjust the shed vortex strength. This provides a mechanism for vortex shedding in 3-D calculations.

Calculation of Shed Vorticity

Kelvin's theorem states that the total circulation of the fluid at any instant is conserved. This condition provides a mechanism for shedding vorticity into the wake. For 2-D calculations a uniformly distributed vortex segment with strength γ_w is generated at each time step in the wake adjacent to the foil trailing edge. The length S_w of the vortex segment is set equal to the distance the trailing edge moves between $t-\Delta t$ and t. At a subsequent time step this uniform line vortex is replaced by a discrete concentrated vortex of equivalent strength located at the center of the segment. The generated trailing-edge vortex segment is related to the total foil circulation, Γ, as

$$\frac{\Gamma(t) - \Gamma(t - \Delta t)}{\Delta t} + \frac{S_w(t)\gamma_w(t)}{\Delta t} = 0 \ . \tag{19}$$

The model depicted in Eq. (19) yields numerically stable solutions that are insensitive to the time-step used. When the nonlinear pressure condition is selected for solving Eq. (14), representative calculations based upon the concentrated vortex model used by Kim and Mook (13) for modeling the trailing-edge vorticity generation were found to be dependent on the time step used

Following the shedding process at the trailing edge, the wake vortices are convected downstream and develop a vorticity field. In the 2-D form of the present numerical scheme, these vortices are tracked through the flow field using Lagrangian techniques. The convection of these discrete vortices is modeled

by a predictor-corrector scheme, given in Ref. (2).

The shed vorticity distribution in 3-D flows is obtained by solving Eq. (18) iteratively by relating the nonzero Δp to $\Delta\gamma_w$ by

$$[\Delta(\phi_u - \phi_\ell)] = D[\Delta\gamma_w]$$
$$[\Delta(\vec{u}_u - \vec{u}_\ell)] = \vec{E}[\Delta\gamma_w] \tag{20}$$

where D and $\overline{E}$ are both matrices representing the disturbed velocity potential and induced velocity due to $\Delta\gamma_w$ of unit strength. These matrices are only dependent on the blade geometries and are required to be calculated only once. Thus Eq. (18) becomes

$$[\Delta\gamma_w] = (D + \Delta t \ \vec{u}_m \cdot \vec{E})^{-1} \Delta t \ [\frac{\Delta p}{1/2 \rho u_o^2}] \ . \tag{21}$$

The sub-iteration formula at each time step to update shed vorticity strength is then given by

$$\gamma_w^{(k+1)} = \gamma_w^{(k)} + \Delta\gamma_w^{(k)} \ . \tag{22}$$

Vortex Core Splitting and Merging

As Eq. (19) indicates, a vortex is generated at each time step. This mechanism of generating wake shed vorticity will produce tracing instability when the wake vortices start interacting with one another (14). A remedy for redistributing and splitting the vortex cores was proposed by Mook et. al. (14). In addition to the predictor-corrector tracing method mentioned above, the present vortex convection scheme also adopts Mook's splitting and merging techniques. When any pair of vortices is within $1/4 \ u_o \ \Delta t$, a merging process takes place to reduce the number of vortices. On the other hand, when the distance between two vortices becomes larger than $1.5 \ u_o \ \Delta t$, a linear splitting process is used. The total circulation around the entire wake and airfoil is, however, maintained exactly. This vortex core splitting procedure maintains reasonably uniform spacing between vortices.

Cascade Formulation

For a 2-D cascade of blades with pitch H, each blade generates circulation. If the cascade runs along the y-axis, there exists an upwash far upstream of the cascade and a downwash far downstream. In conjunction with a specified inflow onset condition, an extra term is needed to ensure a unique upstream inflow condition, i.e.

549

$$\phi_\infty = y \sum_{mj=1}^{MJ} \frac{\Gamma_{mj}}{2H_{mj}} \qquad (23)$$

for a multi-blade-row cascade flow, where MJ is the total number of blade rows, H_{mj} is the mj-th cascade spacing or pitch, and Γ_{mj} is the blade circulation from the mj-th cascade.

A complete integration of the velocity potentials for the source and the vortex distributions on each segment was performed numerically for the cascade modification. The detailed formulation as well as the modification in Green function for a cascade can be found in Ref. (2).

Gauss-Seidel Solution Procedure

For a 2-D problem, the governing matrix equations are usually small in size, even for multi-row cascade and therefore a direct solver can be used to solve Eq. (10) efficiently. For a 3-D problem, however, the size of the matrix equations is at least an order of magnitude larger than that of the 2-D ones and often reaches a few thousands or more. Consequently, direct matrix solvers are too expensive to execute for matrix equations of this scope.

In the present paper a two-level multi-block Gauss Seidel procedure is developed for obtaining solutions of 3-D problems. First, the left-hand side of Eq. (11) is partitioned on the basis of the larger surface patches such as those on the blade and hub. Thus Eq. (11) becomes

$$\sum_{i,j=NPS(\ell)}^{NPE(\ell)} CD_{i,j}\gamma_j^{(k+1)} = RHS + \sum_{l=1,l\neq\ell}^{NS} \sum_{i,j=NPS(\ell l)}^{NPE(\ell l)} CD_{ij}\gamma_j^* \qquad (24)$$

$$\ell f=1,2.....,NS ,$$

where NPS(ℓ) and NPE(ℓ) are the starting and ending panel numbers on surface patch ℓ, RHS is the right-hand-side terms of Eq. (11), NS is the total number of surface patches, and γ_j^* is the latest value of γ_j. On the ℓf-th surface patch, $\gamma_j^{(k+1)}$ is updated by

$$[CD_{i,j}\Delta\gamma_i^{(k+1)}] = [RHS^* - \sum_j CD_{ij}\gamma_j^{(k)}]$$

for nonlifting section

or

$$\begin{bmatrix} CD_{i_1 i_1} & CD_{i_1 i_2} \\ CD_{i_2 i_1} & CD_{i_2 i_2} \end{bmatrix} \begin{bmatrix} \Delta\gamma_{i_1} \\ \Delta\gamma_{i_2} \end{bmatrix} = \begin{bmatrix} RHS_{i_1}^* - \sum_j CD_{ij}\gamma_j^{(k)} \\ RHS_{i_2}^* - \sum_j CD_{ij}\gamma_j^{(k)} \end{bmatrix} \qquad (25)$$

for lifting scetion

where RHS* denotes the right-hand-side terms of Eq. (24), and i_1 and i_2 are indices of the two trailing-edge panels on the same strip of the blade. The advantage of Eq. (25) is that it retains the dominant terms in the left-hand-side matrix of Eqs. (24).

RESULTS AND DISCUSSIONS

The unsteady rotor-stator interaction includes both potential-flow and wake effects. The validation of the current calculation method for a complex rotor-stator system therefore involves two validations of fundamental flow phenomena. The first of these is to demonstrate that the shed vortices from a foil (or cascade) are accurately computed. The second is to demonstrate that the interaction between a vortex and a foil is properly computed. Both of these fundamental phenomena have been demonstrated in Ref. (7).

The capability for accurately modelling shed vorticity was demonstrated by comparing the predicted wake behind an oscillating airfoil with experimental measurements (15). Although the present inviscid approach can not predict the viscous (velocity defect) wake at low blade oscillation frequency, it predicts well the jet-like wake for high frequency oscillation. The vortex and blade interaction process was also demonstrated in Ref. (7) by the computation of the interaction between a free traveling vortex encountering a stationary airfoil (11). The results indicate that the current method is able to accurately predict the interaction forces acting on the foil due to a passing vortex.

A third phenomenon that occurs in rotor-stator interactions is wake vortex cutting. An Example of this was given by Chow and Huang (8) who presented an analytical solution based on conformal mapping for a close encounter between a Joukowski airfoil and a moving vortex. The flow phenomenon described by Chow assumes that a "neutral release" position exists for the incoming vortex which divides the vortex trajectories into those either above or below the airfoil.

550
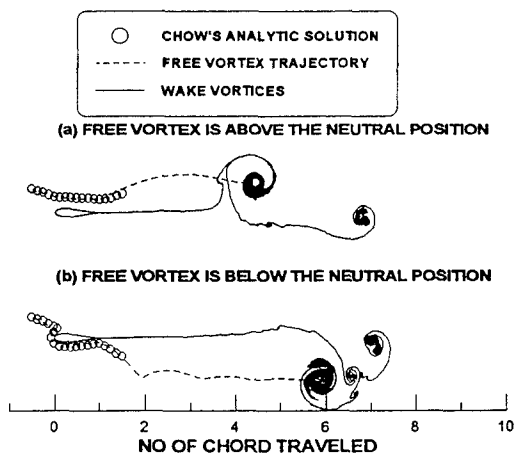
Figure 1. Predicted instability of a vortex
interacting with a Joukowski foil

Representative calculations for vortices on either side of the neutral release point are presented in Figs. 1 and 2 along with corresponding solutions from Chow and Huang. Figure 1 compares the trajectories of the free vortex at representative time steps for both methods. Because Chow's analytical solution extends only a chord length downstream of the airfoil, the comparison is limited to this region. For perspective we also present a snapshot of the wake vortices at the last time step of our calculation. The curved trajectories wrapping around the airfoil and the large amplitude wake roll-up indicate a very strong interaction between the vortex and the airfoil and thus provide a more critical validation for the present calculation scheme than that in Ref. (7). The corresponding force comparisons for these calculations are given in Fig. 2. When the free vortex travels above the foil, it is first absorbed by the foil as the foil's lift increases. After the vortex passes the trailing edge, the foil repels the vortex and its lift is also dropped. The lift on the foil is eventually leveled off as the vortex travels far downstream. Similarly, when the vortex starts from a location above the foil and travels to the lower side of the foil's surface, it is again absorbed by the foil. As the vortex gets too close to the foil surface, the surface vorticity of the foil starts repelling the free vortex. At this moment, the lift of the foil drops suddenly and the vortex is repelled backward and starts moving towards lower side of the foil. On the foil's lower side, the trajectory of the vortex is much closer to the foil surface than that on the upper-side motion. During this period, the lift of the foil increases as the vortex moves towards the trailing edge. When the vortex is in the vicinity of the trailing edge, it starts interacting with the shed wake vorticity originating from the foil

trailing edge. The spike in the predicted lift distribution near the trailing edge is related to the this strong interaction and depends also upon the Kutta condition used. Nevertheless, the present predicted lift distributions compare favorably with Chow's solutions.
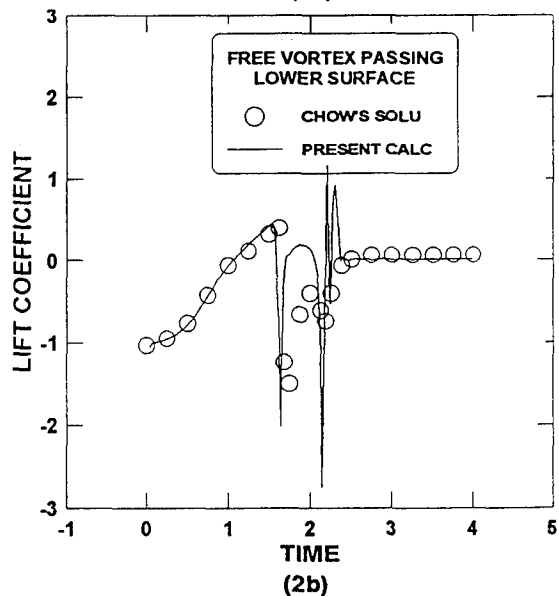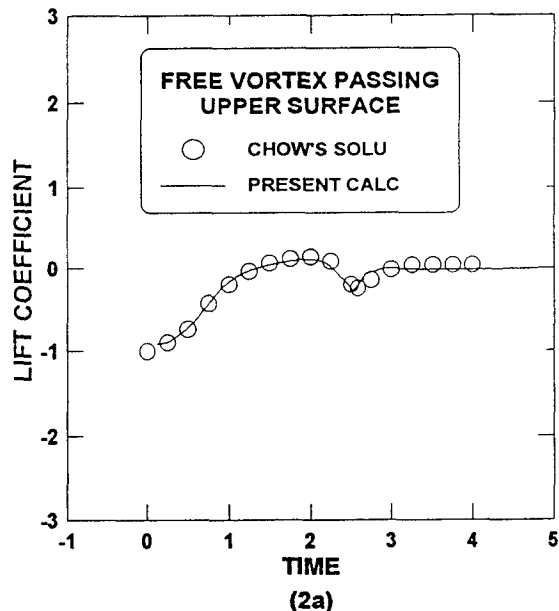
Figure 2. Comparisons of present predicted force on the Joukowski foil with Chow's solutions

An additional demonstration of the effectiveness of the present method, and one that is much more similar to a rotor-stator interaction, is the flapper and foil experiment recently carried out at MIT (9,18). In this experiment detailed measurements of the unsteady flowfield around a foil were measured using the setup shown in Fig. 3. In this experiment two small NACA 0025 flapping foils of 3-inch chord were configured

551

upstream of a larger stationary foil, referred to as the "foil" in the later text, of 18-inch chord. The flappers performed synchronized sinusoidal motions of 6-degree amplitude at a reduced frequency of 3.62. The flappers generate periodic wake fluctuations which impose an unsteady condition on the foil. Velocity and pressure measurements at a Reynolds number of 3.78×10^6 were taken on the foil and around the foil in a rectangular box downstream of the flappers and enclosing the foil, as shown by the dash line in the Fig. 3. The box measurements were intended to provide upstream and downstream boundary conditions for Navier-Stokes computations. Unsteady flow separation was observed on the suction side near the trailing edge of the foil.
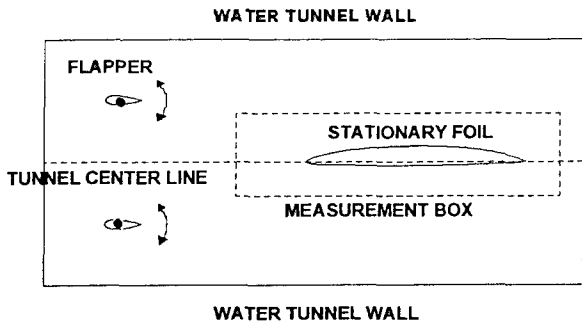
Figure 3. Schematic of MIT Flapping Foil experiment
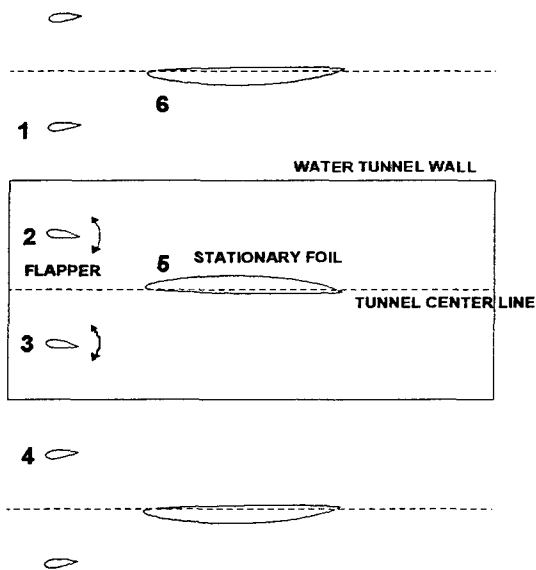
Figure 4. Six-row computational cascade for simulating MIT's flapper and foil experiment

To simulate this flow configuration, a series of image blades were added to the geometry shown in Fig. 3 to incorporate the effects of the tunnel walls. Because of the asymmetry of the foil, the complete

system of flappers, foil and image blades is a six-blade-row cascade system as shown in Fig. 4. Since a thick boundary layer exists in the aft region of the foil, a displacement thickness obtained from boundary-layer calculations based on steady solutions to the six row cascade system was added to the foil surface. Computed steady foil surface pressures with and without the displaced thickness correction are shown in Fig. 5. Comparisons of steady pressure distributions for calculations with and without the flappers and its image cascades are nearly the same.
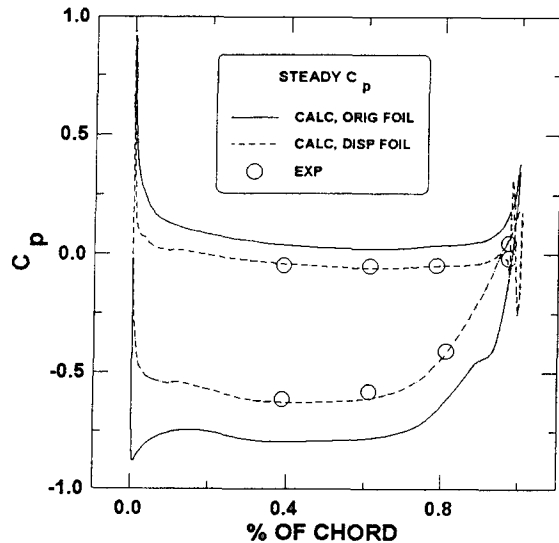
Figure 5. Predicted steady-state pressure distributions on MIT's foil
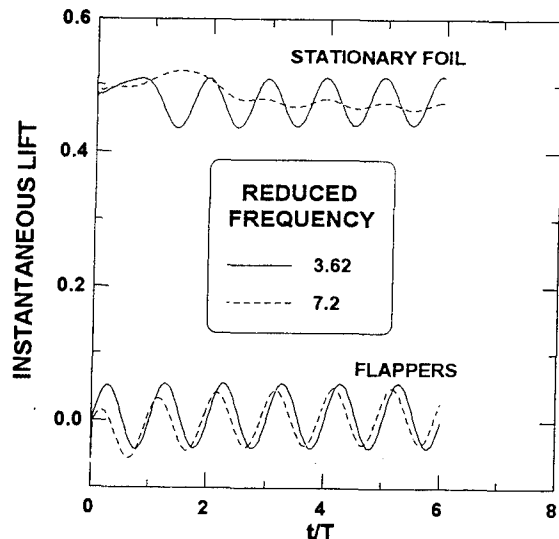
Figure 6. Predicted unsteady lifts on MIT's foil and flappers

552

The unsteady calculations were started at t = 0 from the steady solution. Figure 6 shows the instantaneous lift distributions of the flappers and the foil plotted against nondimensional time at reduced frequencies of 3.62 and 7.2. The foil transient lasts about one period and the calculation extends for six periods with 50 time steps in each period. The corresponding time-averaged mean pressure distributions from the unsteady calculation (reduced frequency of 3.62) are shown in Fig. 7 along with the envelopes of the unsteady solution. These are compared with the measured means and measured local maxima and minima, indicated by I-bars. The calculated mean unsteady pressure agrees well with the measurements. Since the present calculation uses an open trailing-edge for the displaced foil, fluctuations in the predicted pressure distributions exist near the trailing edge, as seen in Fig. 7. Figures 8 and 9 present comparisons of the time history, amplitude and phase angle of C_p at several locations on the stationary foil. Overall, these comparisons in Fig. 8 show the unsteady effects are quantitatively reasonable, but the amplitude are significantly larger than the experimental results. Near the trailing edge the overprediction becomes worse. This is likely due to the aforementioned pressure fluctuation introduced by the open trailing edge (see comparison at x/c=0.972 on Fig. 8).
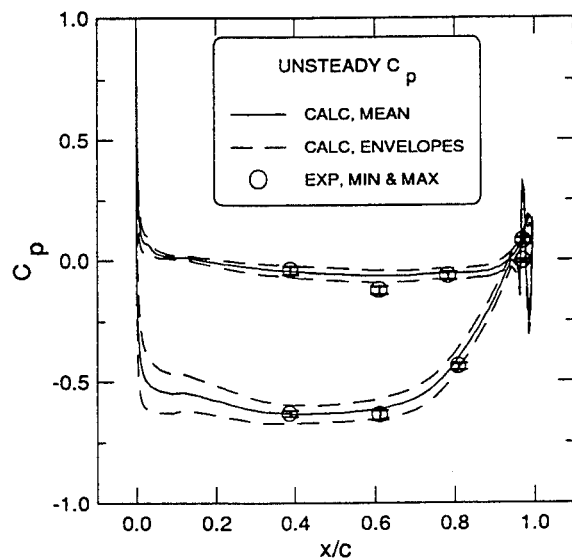
This overprediction is further demonstrated in Fig. 9 by the amplitude of the first harmonic of the pressure distribution around the airfoil. Again the computed amplitude on the suction side (SS) are much larger than the experimental measurements. Close inspection of the measured time history on Fig. 8, however, shows that the experimental variation of the pressure is predominantly a double frequency variation that is twice the reported flapper frequency. For this reason, the calculation was repeated at the double frequency (7.2 reduced frequency) for the flappers. The history of this lift was previously shown in Fig. 6. As this figure shows the amplitude of the fluctuating lift on both flappers is about the same for both high and low frequencies, but that for the stationary foil the amplitude is reduced considerably at the higher frequency. This phenomenon is also evident in the time history and the fundamental harmonic (7.2 reduced frequency) of the pressure distribution (Figs. 8 and 9). Both figures show predictions of unsteady pressures and its amplitudes. These results show that predictions at high frequency agree surprisingly well with measured values. This suggests a possible discrepancy in the measured frequency of the flapper motion. Corresponding comparisons of the phase distribution of the pressure fluctuation around the foil are also given in Fig. 9 for both reduced frequencies. The predictions show little effect of frequency on the suction side, whereas on the pressure side the predictions show a strong phase lead near the leading edge at the lower frequency. As usual in such comparisons, the phase angle predictions do not compare as well with experiments. This phase comparison thus provides no illumination of the above dilemma.

Figures 10 through 11 show predictions of the rotor-stator interaction for the UTRC single stage, low speed turbine (10). The turbine consists of a 22-blade stator with pitch H=0.854c and a 28-blade rotor with pitch H=0.813c. Both the stator and the rotor have round trailing edges. The gap between the two blade rows is 15% of the stator chord. The rotor operates at a reduced passing frequency of 2.8, based on the turbine diameter.

To reduce the computation effort the 22 stator blades versus 28 rotor blades were simulated at the blade number ratio of 21 stator blades versus 28 rotor blades. This enables us to use three representative stator blades and four rotor blades. Trajectories of the shed vorticity patterns at four different time steps during the start-up period of the stator-rotor interaction, are shown in Fig. 10. As the wakes develop from the rest condition they initially follow a straight line behind the trailing edges of both the stator

Figure 7. Predicted time-averaged unsteady pressure distributions and unsteady pressure envelopes on MIT's foil

Figure 8. Time histroy of C_p at various locations of the foil

554

Figure 9. Comparisons of amplitude and phase angle of the first harmonic of C_p
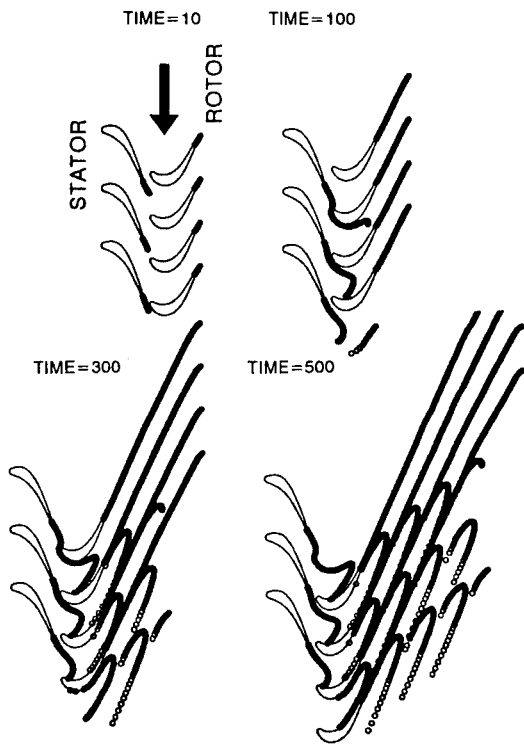
Figure 10. Snapshots of predicted vortex patterns at each time step for UTRC's stator-rotor turbine
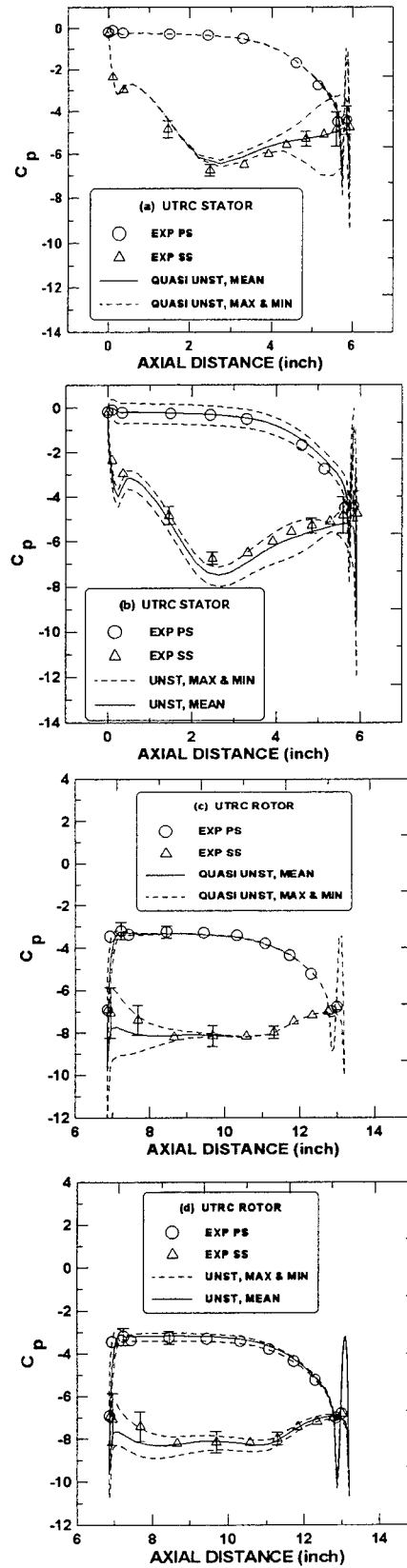
Figure 11. Pressure predictions on UTRC's stator-rotor turbine

555

and the rotor (t=10). At later times the stator wake begins to roll up as it enters the moving rotor (t=100). This roll-up of the stator wakes continues, and as they are cut by the rotor they begin to approach a periodic state (t=300 and t=500). Throughout, the wakes from the rotor remain essentially straight.

The time-averaged pressure distribution from one period of the later stages of the calculation in Fig. 10 are given in Fig. 11 along with the mean experimental measurements for both the stator (Fig. 11b) and the rotor (Fig. 11d). For reference we also show passage-averaged pressure distributions from quasi-unsteady stator-rotor calculations (Figs. 11a and 11c). These quasi-unsteady calculations were performed as a series of steady state calculations with various relative positions for the rotor-stator blades. Wake vortex shedding was neglected.

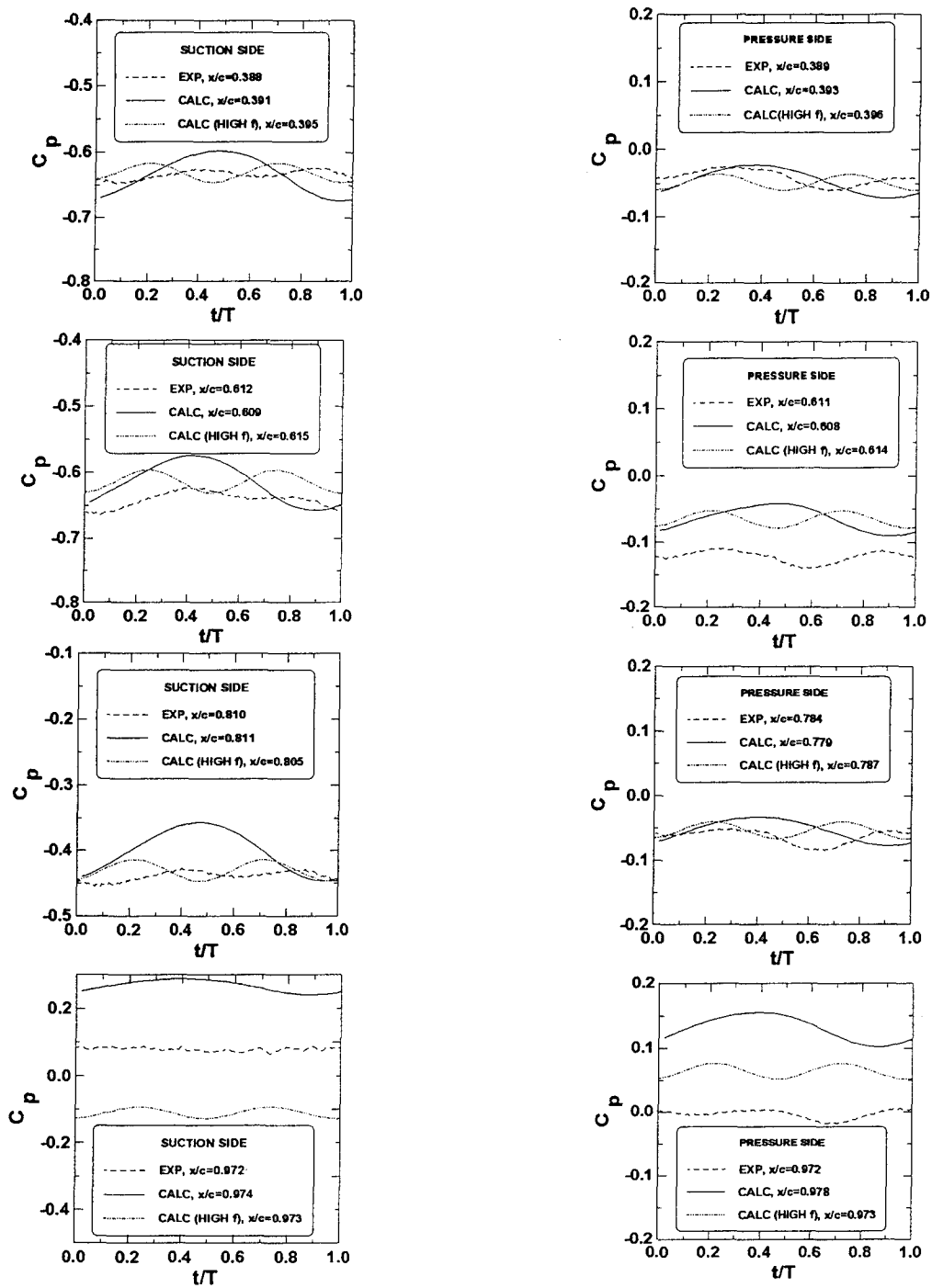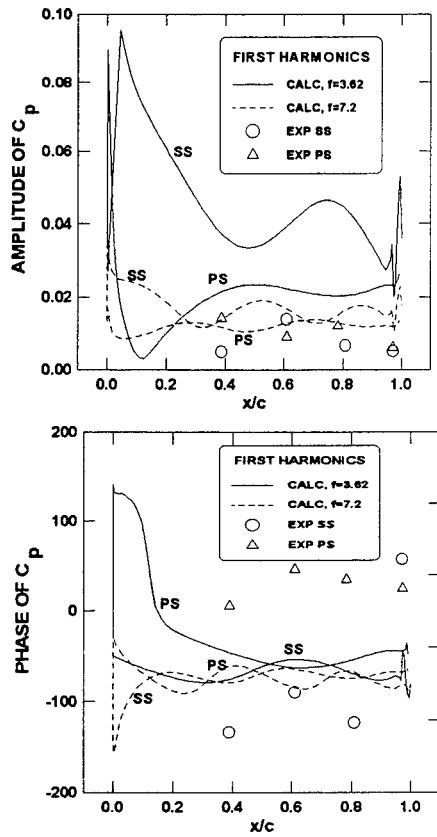The averaged pressure distributions from both the quasi-unsteady calculation and the fully unsteady calculations are in good agreement with experimental measurements. It suggests that for preliminary estimates, especially at an initial stage of design when a large number of comparison studies are needed in a short time period, quasi-unsteady computations should be appropriate for providing reasonable performance predictions. The envelopes of the maxima and minima for both the unsteady and the quasi-unsteady calculations are shown in Fig. 11 along with the corresponding experimental measurements. This comparison clearly shows that the fully unsteady computation which includes vortex shedding and a convection effect has a distinctive advantage over the quasi-unsteady result. First the time-dependent loading is spread evenly over most of the blade. This even spreading of the unsteady loading over the entire blade surfaces is confirmed by the experimental measurements. The quasi-unsteady calculations predict the maxima and minima, variations are restricted to locations near the trailing edge of the stator and the leading edge of the rotor, and the magnitudes of the fluctuations in these regions are very large, far exceeding the experimental measurements. The primary reason for this even spreading of the pressure fluctuations in the true unsteady calculation is the presence of the wake vortex field. The wake vortices are continuously cut by blades as they are convected downstream through the rotor passages. These rolled up vortices have a significant impact on the unsteady pressure distribution on both the rotor and the stator. Clearly, the computational structure of the wake rollup (see Fig. 10) would be impossible to describe in advance.

CONCLUSIONS

A time-accurate hybrid panel/Euler prediction method is presented for unsteady incompressible flows through a rotor-stator system. By tracing wake vorticity, this method is capable of predicting complex flow features such as wake cutting and wake wrapping in rotor-stator systems.

The time-averaged blade pressure distribution predicted by the present approach is in good agreement with experimental measurements. Current results also suggest that for rotor-stator systems quasi-unsteady approaches are appropriate for time-mean performance predictions.

For time-dependent solutions of multiple-blade-row cascade flows, results obtained from the present fully unsteady approach compare well with experimental measurements. Details of the flowfield, such as wake vortex shedding, wake-wrapping and wake-cutting, are simulated for rotor-stator systems from the flow transient to the fully developed periodic stage. For rotor-stator systems quasi-unsteady approaches overpredict the unsteady loading in the strong interacting area of the blade and considerably underpredict in the weak interacting area. By including the complex vortex convection in the flowfield, the present method predicts a much more evenly distributed unsteady pressure as the measurement indicates.

Calculations on the MIT's flapping foil simulation have suggested that the multiple blade row cascade calculation method has correctly modelled the unsteady water-tunnel flow. The unsteady lift on the flappers is independent of its vibrating frequency, but the amplitude (the mean is the same) of the lift on the stationary foil reduces as the flappers move faster. The predictions based on the higher frequency flapper motion, however, agrees better with the measurements in local pressure distributions.

Our results also suggest that the multi-row blade interactions in many rotor-stator systems are inviscid in nature and can be analyzed with more efficient and inexpensive approaches, such as the present method.

The present time-accurate approach can be applied to other unsteady flow problems such as blade passage noise predictions and unsteady cavity flow predictions in rotor-stator systems.

ACKNOWLEDGEMENTS

Basin. Partial computational results were obtained using the facilities sponsored by the NASA Ames Numerical Aerodynamic Simulation Program.

REFERENCES

1. Giles, M.B., "Calculation of Unsteady Wake/Rotor Interaction," AIAA J. of Propulsion and Power, Vol. 4, No. 4, 1988, pp. 356-362.

2. Lee, Y.T., Bein, T.W., Feng, J., and Merkle, C.L., "Unsteady Rotor Dynamics in Cascade," ASME J. of Turbomachinery, Vol. 115, 1993, pp. 85-93.

3. Kerwin, J.E., and Lee, C.S., "Prediction of Steady and Unsteady Marine Propeller Performance by Numerical Lifting-Surface Theory," SNAME Transactions, Vol. 86, 1978, pp. 218-253.

4. Preuss, R.D., Suciu, E.M., and Morino, L., "Unsteady Potential Aerodynamics of Rotors with Applications to Horizontal-Axis Windmills," AIAA Journal, Vol. 18, No. 4, 1980, pp. 385-393.

5. Idris, B.M., Maruo, H., and Ikehata, M., "Theoretical Analysis of Unsteady Characteristics of Marine Propeller in Ship's Wake," J. of the Society of Naval Architects of Japan, Vol. 156, 1984, pp. 60-68.

6. Shoji, H., and Ohashi, H., "Lateral Fluid Forces on Whirling Centrifugal Impeller (1st Report: Theory," Transactions of the ASME, Vol. 109, 1987, pp. 94-109.

7. Lee, Y.T., Feng, J., and Merkle, C.L., "Prediction of Vortex and Linear Cascade Interaction Noise," ASME Paper 93-GT-314, 1993.

8. Chow, C.Y., and Huang, M.K., "Unsteady Flows About a Joukowski Airfoil in the Presence of Moving Vortices," AIAA Paper No. 83-0129, 1983.

9. Kerwin, J., Keenan, D., Mazel, C., Horwich, E., and Knapp, M., "MIT/ONR Flapping Foil Experiment: Unsteady Phase," MIT/ONR FFX Workshop, David Taylor Model Basin, March 1993.

10. Dring, R.P., Joslyn, H.D., Hardin, L.W., and Wagner, J.H., "Turbine Rotor-Stator Interaction," ASME J. of Engineering for Power, Vol. 104, 1982, pp. 729-742.

11. Lee, D.J., and Smith, C.A., "Distortion of the Vortex Core During Blade/Vortex Interaction," AIAA Paper 87-1243, 1987.

12. Yao, Z.X., Garcia-Fogeda, P., Liu, D.D., and Shen, G., "Vortex/Wake Flow Studies For Airfoils in Unsteady Motions," AIAA Paper 89-2225, 1989.

13. Kim, M.J., and Mook, D.T., "Application of Continuous Vorticity Panels to General Unsteady Incompressible Two-Dimensional Lifting Flows," J. of Aircraft, Vol.23, No.6, 1986, pp. 464-471.

14. Mook, D.T., Roy, S., Choksi, G., and Dong, B., "Numerical Simulation of the Unsteady Wake Behind an Airfoil," J. of Aircraft, Vol. 26, No. 6, 1989, pp. 509-514.

15. Koochesfahani, M.M., "Vortical Patterns in the Wake of an Oscillating Airfoil," AIAA J., Vol. 27, No. 9, 1989, pp. 1200-1205.

16. Fuhs, D., "Comparisons of Calculations and Measurements," MIT/ONR Flapping Foil Workshop, Washington D.C., March 29-30, 1993.

DISCUSSION
by Dr. S. Kinnas, MIT

The authors presented an interesting application of inviscid flow methods for practical design. It would be very interesting also if they show convergence tests of the involved methods, in particular, with number of panels and time step size for different values of reduced frequency of the incoming gust.

Author's Reply

The numerical convergence for steady flow calculations has been reported in reference (2) of the main text. Numerical errors, defined as the root-mean-square values of the differences between the calculated C_p and the exact C_p distributions, were presented based on different panel numbers for both circular cylinder and NACA 0010 airfoil. It was concluded that the present approach generates results with an accuracy better than the second order methods and the panel number in the order of 100 for airfoil geometries is adequate to drive the error down to 10^{-5}.

For unsteady flows, the panel size is also governed by two other factors. First, the size of the panels near the foil trailing edge should not be larger than the distance between two successive vortices shed from the trailing edge. That is

$$\Delta s = \Delta t \bullet U_o \qquad (A1)$$

where $\Delta t = 2\pi / \omega n_t$ and n_t is the number of time steps in one period. And Eq. (A1), in terms of reduced frequency $f = \omega c / 2u_o$, becomes

$$\Delta s = \frac{\pi}{f} \bullet \frac{c}{n_t} \qquad (A2)$$

Second, when downstream foils cutting through a vortical wake shed from upstream foils, the size of the panels adjacent to the wake vortices is limited to the distance traveled by the vortices in one time step during the close encounter between the vortex and the foil. This condition requires a similar constrain as shown in Eq. (A2) for panels in the front one-third of the foil.

For a typical calculation with a reduced frequency of 10, a normalized unity chord length and freestream velocity, and 25 time steps in one

calculation period, $c / \Delta s$ is about 80. On the average, we use 25 to 50 time steps and 160 to 300 panels to represent periodic foil motion in unsteady flows.

SESSION 11

WAVY/FREE-SURFACE FLOW: SHIP MOTIONS

The Simulation of Ship Motions

H.B. Bingham, F.T. Korsmeyer, J.N. Newman, and G.E. Osborne
(Massachusetts Institute of Technology, USA)

Abstract

A three-dimensional panel method is used to solve the linearized ship motions problem for a ship traveling with steady forward speed through quasi-random incident waves. The exact initial-boundary-value problem is linearized about a uniform flow, and recast as an integral equation using the transient free-surface Green function. This integral equation is discretized in space by using planar panels, on which the potential is assumed to be constant, and in time by using the trapezoid rule. Collocation is performed at the centroids of each panel.

A technique for approximating the asymptotics of the solution is presented and used to reduce the required length of the computations. Results are shown for a Wigley hull, with and without a steady forward speed. The calculated hydrodynamic coefficients are compared to experiments, as well as to the calculations of two frequency-domain solutions, and a simulation is performed of the ship traveling through a Pierson-Moskowitz sea.

1 Introduction

Since the time when Haskind [6] and Cummins [3] put the superposition principle for transient ship motions on a solid foundation, much work has been focused on calculating the requisite impulse-response functions, or the analogous frequency-response functions. The linearized theory (elegantly reviewed by Ogilvie [22]), has been implemented for practical ship motions calculations, originally using strip theory methods, and more recently by way of three-dimensional panel methods. For solving problems involving a steady for-

ward speed, the most promising panel methods fall into two categories: solutions using the transient free-surface Green function, where only the ship surface is discretized; and Rankine methods, where singularities are distributed on both the hull and a portion of the free-surface. The present work falls into the first category. Frequency-domain results using Rankine methods have been presented in the last few years, (e.g.: [2]; [20]) and Nakos et al. [19] have recently extended their Rankine, frequency-domain method to the time domain. Solutions using the transient free-surface Green function have been reported by several investigators (e.g.: [9]; [10]; and [14]). More recently the *body-exact* formulation (where the body boundary condition is applied on the exact instantaneous position of the hull, while the free-surface condition remains linearized) has been used to extend the technique to large amplitude body motions (e.g.: [1]; [16]; [17]).

We have developed a computer code for the transient hydrodynamic analysis of ships and other bodies. The material in this paper is based on our experience in developing and using this code which is called TiMIT (*Ti*me domain *MIT*). We discuss theoretical and practical issues which are germane to the robust and efficient calculation of impulse-response functions, and their subsequent use in performing a simulation of a ship traveling in a seaway. In Sections 2 and 3, we review the linearized formulation of the transient ship motions problem. Section 4 describes the numerical solution, and presents some techniques which can be used to improve the computational efficiency. In particular, we show how a knowledge of the asymptotic behavior of the solution, combined with an appropriate choice of an impulse, may be used to reduce the required length of the computational record. Section 5 presents the results of a simulation of a Wigley hull travel-

ing through a Pierson-Moskowitz spectrum of incident waves. Finally, some concluding remarks appear in Section 6.

2 Equations of Motion

During normal operating conditions the ship's weight, along with the steady, hydrodynamic sinkage force and trim moment acting on it, are all balanced by the hydrostatic pressure acting on the hull, while its steady resistance is overcome by the propulsion. These forces are in balance, and we will focus upon the unsteady perturbations about this equilibrium condition. Through Newton's law, the dynamics of a ship's unsteady oscillations are governed by a balance between the inertia of the ship and the external forces acting upon it. This balance is complicated by the existence of radiated waves, as a consequence both of the ship's own motions and its scattering of the incident waves. This means that waves generated by the ship at any given time will persist indefinitely and, in principle, affect the ship at all subsequent times, a situation which is described mathematically by a convolution integral. Having assumed that the system is linear, the equations of motion may be written in a form which is essentially identical to the model proposed by Cummins [3]:

$$\sum_{k=1}^{6} [(M_{jk} + a_{jk})\ddot{x}_k(t) + b_{jk}\dot{x}_k(t)$$

$$+(C_{jk} + c_{jk})x_k(t) + \int_{-\infty}^{t} d\tau \, K_{jk}^{(0)}(t-\tau)x_k(\tau) \,]$$

$$= X_j(t),$$

$$j = 1, 2, ..., 6, \qquad (1)$$

where the exciting forces on the right-hand side may be determined from:

$$X_j(t) = \int_{-\infty}^{\infty} d\tau \, K_{jD}(t-\tau)\zeta(\tau) \qquad (2)$$

as proposed by King [8].

In equation (1), the ship's displacement from its mean position in each of its six rigid-body modes of motion is given by x_k, and the overdots indicate differentiation with respect to time. The excitation of the ship is provided by $\zeta(t)$, a time history of the incident wave elevation at some prescribed reference point on the free-surface. The ship's inertia matrix is M_{jk}, and the linearized hydrostatic restoring force coefficients are given
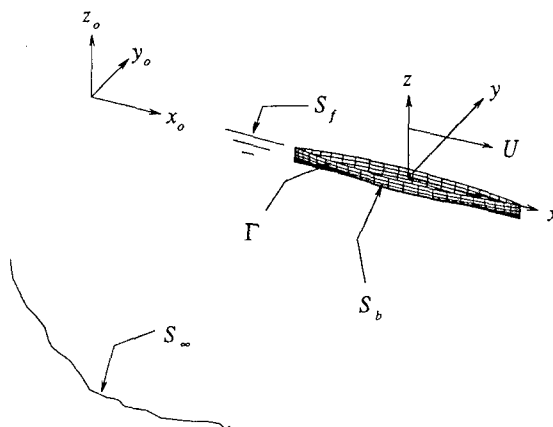
Figure 1: The reference frames and surfaces of the problem.

by C_{jk}. The hydrodynamic coefficients and the kernel of the convolution on the left-hand side of (1), and the kernel of the convolution on the right-hand side of (2), make up a set of radiation and diffraction impulse-response functions: the combination of a_{jk}, b_{jk}, c_{jk}, and $K_{jk}^{(0)}(t)$ is the force on the ship in the jth direction due to an impulsive motion in mode k, while the function $K_{jD}(t,\beta)$ is the force on the ship in the jth direction due to a uni-directional impulsive wave elevation incident from a heading angle of β. Equation (1) differs from the usual form only because the free-surface memory is represented as a convolution with the ship's displacement rather than with its velocity. This choice is convenient in practice because it produces a kernel which vanishes for large time (see Section 4).

With the hydrodynamic and hydrostatic coefficients in hand, a simulation of the ship translating in an ambient wave field may be carried out by integrating in time the above system of six coupled differential equations.

3 Hydrodynamics

3.1 The Exact Problem

Consider a three-dimensional body in a semi-infinite fluid with a free-surface, as shown in Figure 1. The ship moves through an incident wave field with velocity $\vec{U}(t)$, and is allowed to perform small unsteady oscillations about its mean position in any of its six degrees of freedom. The fluid is assumed to be ideal and the flow irrotational, free of separation or lifting effects. Two

562

coordinate systems will be employed in the ensuing derivations: the $\vec{x}_0$ system is fixed in space, and the $\vec{x}$ system is fixed to the mean position of the ship. At $t = 0$, these two coordinate systems coincide.

Subject to the above assumptions, the fluid velocity may be described by the gradient of a scalar velocity potential, $\vec{V}(\vec{x}_0, t) = \vec{\nabla}\Phi(\vec{x}_0, t)$. Conservation of mass requires that this potential satisfy the Laplace equation everywhere in the fluid:

$$\nabla^2 \Phi = 0. \tag{3}$$

The pressure in the fluid, $p(\vec{x}_0, t)$, is given by Bernoulli's equation,

$$p = -\rho(\Phi_t + \frac{1}{2}V^2 + gz_0) + p_a, \tag{4}$$

where g is the acceleration due to gravity, ρ is the fluid density, and p_a is the atmospheric pressure, which is assumed to be constant. (Partial differentiation is indicated when the independent variables x, y, z, t appear as subscripts.) If surface tension is neglected and the pressure on the free-surface is set equal to zero, a combined free-surface boundary condition may be written:

$$
\begin{aligned}
\Phi_{tt} + \quad & 2\nabla\Phi \cdot \nabla\Phi_t \\
+ \quad & \tfrac{1}{2}\nabla\Phi \cdot \nabla(\nabla\Phi \cdot \nabla\Phi) \\
+ \quad & g\Phi_{z_0} = 0 \qquad \text{on } z_0 = \zeta,
\end{aligned}
\tag{5}
$$

where $\zeta(x_0, y_0, t)$ is the unknown free-surface elevation. Since the free-surface condition is second order in time, two initial conditions are required, and it will suffice to let

$$\left.\begin{array}{c}\Phi = 0 \\ \Phi_t = 0 \end{array}\right\} \quad \text{on } z_0 = 0, \text{ for } t < T_0 \tag{6}$$

On the submerged portion of the hull the normal components of the fluid velocity and the ship velocity must be equal:

$$\vec{n} \cdot \vec{\nabla}\Phi = \vec{V}_s \cdot \vec{n} \qquad \text{on } S_b(t), \tag{7}$$

where $S_b(t)$ is the exact position of the ship surface, $\vec{V}_s(\vec{x}_0, t)$, is the velocity of a point on the ship, and $\vec{n}$ is the unit vector normal to the ship surface. Because of the initial conditions, fluid motions caused by the ship will go to zero at spatial infinity for all finite time,

$$\nabla\Phi \to 0, \qquad |\vec{x}| \to \infty, \, t < \infty.$$

3.2 Linearization

In order to make further progress both the free-surface and the body boundary conditions, as well as the Bernoulli equation, will be linearized. Let us now use the coordinate system fixed to the mean position of the ship, which is traveling along the x_0-axis with a constant speed U. We will assume that the ship was accelerated to this speed at some time in the past and that all transients due to this acceleration have decayed to zero. The total velocity potential, in the ship fixed reference frame, will be decomposed as follows:

$$\Phi = \bar{\Phi} + \bar{\phi} + \sum_{k=1}^{6} \phi_k + \phi_I + \phi_S. \tag{8}$$

The combination of $\bar{\Phi}(\vec{x})$ and $\bar{\phi}(\vec{x})$ is the potential due to the steady-state limit of the ship's uniform translation at forward speed U. This will be referred to as the *steady* problem. The *radiation* problem ensues when this translating ship is forced with some prescribed motion in a single rigid body mode k. The potential due to this motion is $\phi_k(\vec{x}, t)$. If the steadily translating (but otherwise motionless) ship encounters an incident wave system with potential $\phi_I(\vec{x}, t)$, the scattering of those waves by the ship will be described by the potential $\phi_S(\vec{x}, t)$. This is the *diffraction* problem. Note that in the moving coordinate system, the fluid velocities in the far field will tend to those of the free stream and the undisturbed incident wave:

$$\vec{\nabla}\Phi \to -U\hat{i} + \vec{\nabla}\phi_I, \quad \text{as } |\vec{x}| \to \infty, \, t < \infty$$

where $\hat{i}$ is the unit vector in the x-direction. Velocities described by the function $\bar{\Phi}$ in the above decomposition are assumed to be $\mathcal{O}(1)$, while the remaining potentials describe velocities which are small perturbations to this basis flow. Far from the ship the basis flow must tend to the free stream, however the choice of $\bar{\Phi}$ is not unique.

If the decomposition of equation (8) is used in equations (7) and (5), the free-surface and body boundary conditions may be linearized about the mean positions of the ship and free-surface boundaries. The simplest choice of a basis flow, and the one that will be used here, is the free-stream alone:

$$\bar{\Phi} = -Ux.$$

This choice leads to the familiar Neumann-Kelvin linearization of the pressure, the free-surface condition and the body boundary conditions:

$$p = -\rho(\phi_t - U\phi_x) \tag{9}$$

563

$$\left(\frac{\partial}{\partial t} - U\frac{\partial}{\partial x}\right)^2 \phi + g\frac{\partial\phi}{\partial z} = 0, \quad \text{on } z = 0 \quad (10)$$

$$\vec{n}\cdot\nabla\bar{\phi} = \qquad U n_1 \qquad (11)$$
$$\vec{n}\cdot\nabla(\phi_I + \phi_S) = \qquad 0$$
$$\vec{n}\cdot\nabla\phi_k = \quad n_k\dot{x}_k + m_k x_k.$$

In equations (9) and (10), ϕ is used to represent any of the above mentioned perturbation potentials and the linearized body boundary conditions in equation (11) are to be applied on $\bar{S}_b$, the mean position of the ship surface. The generalized unit normal n_k is defined by

$$(n_1, n_2, n_3) = \quad \vec{n} \qquad (12)$$
$$(n_4, n_5, n_6) = \quad \vec{r}\times\vec{n}$$

The steady and the unsteady potentials are coupled through the presence of the so-called *m-terms* in the body boundary condition. For this linearization the m-terms simply reduce to

$$m_k = (0, 0, 0, 0, U n_3, -U n_2)$$

Other linearizations can be derived by making a different choice of basis flow, $\bar{\Phi}$.

3.3 The Integral Equation

The foregoing initial-boundary-value problem can be recast as an integral equation by making use of the transient free-surface Green function. The three perturbation problems described above all satisfy the same boundary-value problem, with the exception of the body boundary condition. Consequently, the same integral equation may be used to solve for any of these potentials. The integral equation is derived by applying Green's theorem to the transient free-surface Green function and the time derivative of the potential. This Green function is derived in Wehausen [24]:

$$G(\vec{x}; \vec{\xi}, t) = G^{(0)}(\vec{x}; \vec{\xi}) + G^{(f)}(\vec{x}; \vec{\xi}, t) \qquad (13)$$

where
$$G^{(0)} = \left(\frac{1}{r} - \frac{1}{r'}\right) \qquad (14)$$

$$G^{(f)} = 2\int_0^\infty dk\, [1 - \cos(\sqrt{gk}\, t)]\, e^{kZ} J_0(kR) \quad (15)$$

$$\left.\begin{array}{c} r \\ r' \end{array}\right\} = \sqrt{(x-\xi)^2 + (y-\eta)^2 + (z\mp\zeta)^2}$$

$$Z = (z + \zeta)$$
$$R = \sqrt{(x-\xi)^2 + (y-\eta)^2},$$

and J_0 is the Bessel function of order zero. It is straightforward to verify that this Green function satisfies the complete linearized initial-boundary-value problem, with the exception of the body boundary condition, equation (11). The result of these manipulations is the following integral equation:

$$2\pi\phi + \int\int_{\bar{S}_b} dS \left(\phi G_n^{(0)} - G^{(0)}\phi_n\right) \qquad (16)$$
$$- \int_{-\infty}^t d\tau \int\int_{\bar{S}_b} dS \left(\phi G_{\tau n} - G_\tau \phi_n\right)$$
$$- \frac{U}{g}\int_{-\infty}^t d\tau \int_{\bar{\Gamma}} dl\, n_1 \left[\, \phi\left(G_{\tau\tau} - U G_{\tau\xi}\right) \right.$$
$$\left. - G_\tau\left(\phi_\tau - U\phi_\xi\right) \,\right] = 0$$

where the ship waterline $\bar{\Gamma}$ is the intersection of $\bar{S}_b$ and the $z = 0$ plane, and the arguments of the Green function in the convolution integrals are retarded (*e.g.* $G_\tau = G_\tau(\vec{x}; \vec{\xi}, t-\tau)$). This equation is identical to that used by King *et al.* [9], or Lin & Yue [16], for example.

The following sections will discuss in more detail the solution of the perturbation potentials.

3.4 Forced Motion Problems

The steady perturbation potential, when solved as the limit of a transient problem, and the radiation potentials are all solutions to similar (and in some cases identical) forced motion problems. The only difference being that in the steady problem it is the steady-state limit which is of interest, while in the radiation problem we seek a transient response.

3.4.1 The Radiation Problem

For each radiation problem, the steadily translating ship is moved impulsively in mode k, and the force on the ship in mode j (*i.e.* the corresponding radiation impulse-response function) is calculated. In principle, there are any number of possible forcings for this problem. An impulsive motion of the ship in any derivative (or integral) of its motion will do; or the motion need not even be impulsive, as long as a convenient Fourier transform exists with which to reconstruct the impulse-response from the non-impulse-response [9]. It is clear from the boundary condition that the solution to one impulsive radiation problem is related to that of any other through some number of time derivatives. For example, the body

564

boundary condition corresponding to an impulsive acceleration of the ship is

$$\vec{n} \cdot \nabla \phi_k = n_k\, H(t) + m_k\, r(t), \qquad (17)$$

where $H(t)$ is the Heaviside step function and $r(t)$ is the ramp function $r(t) = t\, H(t)$. The body boundary condition produced by an impulse in the ship's velocity is the time derivative of equation (17)

$$\vec{n} \cdot \nabla \phi_k = n_k\, \delta(t) + m_k\, H(t). \qquad (18)$$

where $\delta(t)$ is the Dirac delta function. Because this is a linear system, the two solutions are related in the same way, and it can be shown that any canonical radiation potential satisfies

$$\frac{\partial \phi_k^{(n)}}{\partial t} = \phi_k^{(n-1)}$$

where $\phi_k^{(n)}$ is the radiation potential due to an impulse in the nth derivative of the ship's motion. This relationship is not surprising given that the same information can be constructed from any canonical radiation potential. Specifically, the potential due to an arbitrary motion of the ship in mode k, Φ_k, can be written as a convolution of $\phi_k^{(n)}$ with a time history of the nth derivative of the ship's motion in that mode, $d^n x_k / dt^n$.

$$\Phi_k = \int_{-\infty}^{\infty} d\tau\, \phi_k^{(n)}(t - \tau) \frac{d^n x_k(\tau)}{d\tau^n} \qquad (19)$$

The force on the ship in mode j due to this arbitrary motion in mode k is found by integrating the consequent linearized pressure over the body surface

$$F_{jk} = -\rho \int\int_{\bar{S}_b} dS \left(\frac{\partial \Phi_k}{\partial t} - U \frac{\partial \Phi_k}{\partial x} \right) n_j. \qquad (20)$$

This form is computationally inconvenient, since it involves a spatial derivative of the potential, and the calculation may be simplified by using a variant of Stokes' theorem attributed to Tuck [23]:

$$\int\int_{\bar{S}_b} dS\ \left[m_j \Phi_k - n_j (\nabla \bar{\Phi} \cdot \nabla \Phi_k) \right] = \qquad (21)$$

$$- \int_{\Gamma_0} dl\ n_j\ \Phi_k (\vec{l} \times \vec{n}) \cdot \nabla \bar{\Phi},$$

where $\vec{l}$ is the unit vector tangent to the mean waterline. For a wall sided ship, the line integral is identically zero and we may write

$$F_{jk} = -\rho \int\int_{\bar{S}_b} dS\ \left(\frac{\partial \Phi_k}{\partial t} n_j - \Phi_k\, m_j \right). \qquad (22)$$

Given the form of the body boundary condition for this problem, it is natural to consider each radiation potential to be the sum of three terms:

$$\phi_k^{(n)} = \mathcal{N}_k\, \dot{x}(t) + \mathcal{M}_k\, x(t) + \psi_k^{(n)}\, H(t) \qquad (23)$$

where $x(t)$ and $\dot{x}(t)$ must be thought of as the generalized functions appropriate to an impulse in the nth derivative of the ship's motion. The two time constants, $\mathcal{N}_k$ and $\mathcal{M}_k$, are solutions to *pressure release* type problems. They satisfy the following pair of boundary value problems:

$$\nabla^2 \mathcal{N}_k = \quad 0 \quad \nabla^2 \mathcal{M}_k = \quad 0 \qquad (24)$$
$$\mathcal{N}_k = \quad 0 \quad \mathcal{M}_k = \quad 0, \quad z = 0$$
$$\vec{n} \cdot \nabla \mathcal{N}_k = \quad n_k \quad \vec{n} \cdot \nabla \mathcal{M}_k = \quad m_k, \quad \text{on } \bar{S}_b,$$

and may be calculated from the following pair of integral equations

$$2\pi \mathcal{N}_k + \int\int_{\bar{S}_b} dS\ \left(\mathcal{N}_k\, G_n^{(0)} - n_k\, G^{(0)} \right) = 0$$

$$2\pi \mathcal{M}_k + \int\int_{\bar{S}_b} dS\ \left(\mathcal{M}_k\, G_n^{(0)} - m_k\, G^{(0)} \right) = 0.$$

The transient or *memory* potential, $\psi_k^{(n)}$, will depend upon the type of impulse the ship is forced to undergo.

Generally, this problem is solved by giving the ship an impulse in its velocity, which means setting $\dot{x}(t) = \delta(t)$ and letting $n = 1$ in equation (19). Because the position of the ship is changed by this choice of an impulse, we must expect it to produce a steady-state limit to the memory potential, $\psi_k^{(1)}$. Physically, when the ship is displaced from its original position by the impulse, a change occurs in the steady wave pattern which must be reflected in the large time limit of the radiation potential. This is undesirable from a computational standpoint because it tends to increases the required length of the computations (see Section 4). A simple way to avoid a non-zero steady-state limit is to prescribe a forced motion which will bring the ship back to its original position. An impulse in displacement, *i.e.* letting $x(t) = \delta(t)$, is the obvious choice to satisfy this requirement. The body boundary condition in this case becomes

$$\vec{n} \cdot \nabla \phi_k^{(0)} = n_k\, \dot{\delta}(t) + m_k\, \delta(t),$$

and the solution will be

$$\phi_k^{(0)} = \mathcal{N}_k\, \dot{\delta}(t) + \mathcal{M}_k\, \delta(t) + \psi_k^{(0)}\, H(t) \qquad (25)$$

In contrast to using an impulsive velocity, this will produce a radiation problem with a memory term that tends to zero at large time.

565

An integral equation for the impulsive displacement memory potential, $\psi(\vec{x}, t)$, (where the super- and sub-scripts have been omitted for clarity) may be derived by inserting the decomposition of the potential into equation (16). The result is similar to the equation derived by Liapis [15] for the impulsive velocity memory potential:

$$2\pi\psi \ + \int\int_{\bar{S}_b} dS \ \left(\psi G_n^{(0)} - G^{(0)}\psi_n\right) \qquad (26)$$

$$- \int_0^t d\tau \int\int_{\bar{S}_b} dS \ \psi G_{\tau n}$$

$$-\frac{U}{g}\int_0^t d\tau \int_\Gamma dl \, n_1 \ [\ \psi \left(G_{\tau\tau} - U \, G_{\tau\xi}\right)$$

$$-G_\tau \left(\psi_\tau - U \, \psi_\xi\right) \ ]$$

$$= \int\int_{\bar{S}_b} dS \ \left(n_k \, G_{\tau\tau}(t) - G_{\tau\tau n}(t) \, \mathcal{N}_k\right)$$

$$- \int\int_{\bar{S}_b} dS \ \left(m_k \, G_\tau(t) - G_{\tau n}(t) \, \mathcal{M}_k\right)$$

$$+\frac{U}{g}\int_\Gamma dl \, n_1 \ G_\tau(t)\psi(0),$$

where $\psi(0) = \psi^{(0)}(\vec{x}, 0)$ is always non-zero.

Using the decomposition of equation (25) through equation (19) and into equation (22), the complete radiation impulse-response function, which consists of the constant coefficients a_{jk}, b_{jk} and c_{jk} combined with the memory function $K_{jk}^{(n)}$, may be expressed in terms of the the general canonical radiation potentials as follows:

$$a_{jk}(\vec{x}) = \rho \int\int_{\bar{S}_b} dS \, \mathcal{N}_k n_j \qquad (27)$$

$$b_{jk}(\vec{x}) = \rho \int\int_{\bar{S}_b} dS \ (\mathcal{M}_k n_j - \mathcal{N}_k m_j)$$

$$c_{jk}^{(0)}(\vec{x}) = \rho \int\int_{\bar{S}_b} dS \ \psi_k^{(0)}(0)n_j$$

$$c_{jk}(\vec{x}) = -\rho \int\int_{\bar{S}_b} dS \ \mathcal{M}_k m_j$$

$$K_{jk}^{(n)}(t) = \rho \int\int_{\bar{S}_b} dS \ \left(\dot{\psi}_k^{(n)}(t) \, n_j - \psi_k^{(n)}(t) \, m_j\right)$$

where the coefficient, $c_{jk}^{(0)}$, has appeared because $\psi_k^{(0)}(0) \neq 0$, and it must be included with c_{jk} when $n = 0$.

It has been pointed out in the past that the coefficient a_{jk} is a genuine added-mass coefficient which is independent of both time (or frequency) and forward speed. The coefficients b_{jk} and c_{jk} are, on the other hand, functions of the forward
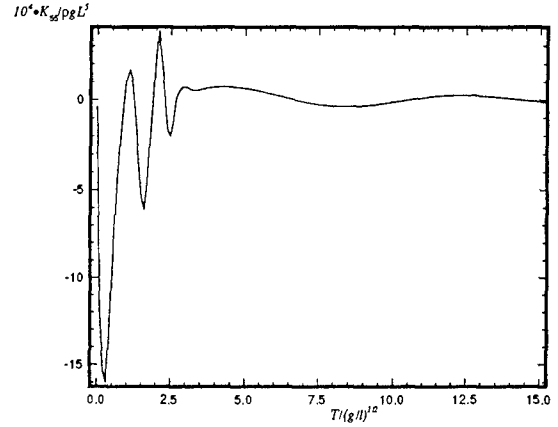
Figure 2: Wigley hull at $Fn = 0.3$, impulsive pitch displacement memory function.
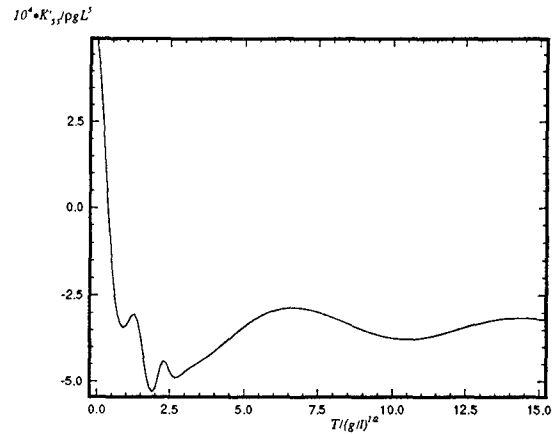
Figure 3: Wigley hull at $Fn = 0.3$, impulsive pitch velocity memory function.
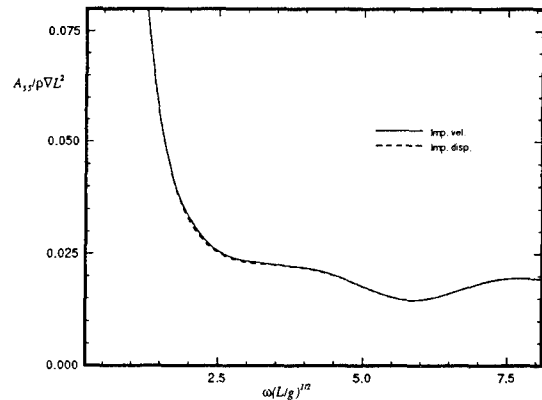
Figure 4: Comparison of the pitch-pitch added-mass coefficient calculated by impulsive displacement and by impulsive velocity of the ship.

566
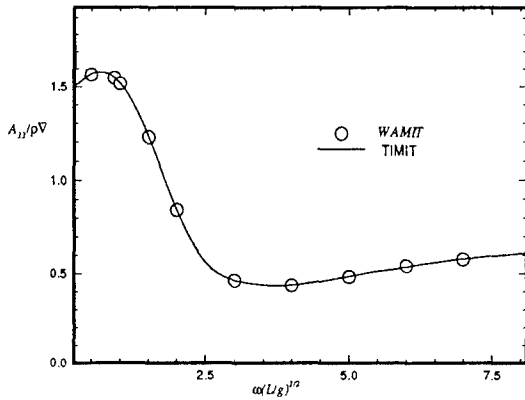
Figure 5: Wigley hull at $Fn = 0.0$, heave-heave added-mass coefficient.

Figure 6: Wigley hull at $Fn = 0.0$, heave-heave damping coefficient.

speed. It can be shown by applying Green's theorem to $\mathcal{N}_k$ and $\mathcal{M}_k$, and using the boundary conditions which they satisfy, that the constants b_{jk} satisfy the following relations,

$$b_{jk} = 0 \qquad \text{for } j = k \qquad (28)$$
$$b_{jk} + b_{kj} = 0 \qquad \text{for } j \neq k$$

Some sample calculations of the pitch memory functions due to both an impulsive displacement and an impulsive velocity appear in Figures 2 and 3. Both calculations have been made for a Wigley hull at a Froude number 0.3.

It can be shown that the impulsive velocity and the impulsive displacement memory functions are related in the same way as the corresponding radiation potentials. That is,

$$\frac{\partial K_{jk}^{(1)}}{\partial t} = K_{jk}^{(0)}.$$

This means that it is possible to calculate $K_{jk}^{(0)}$ from $K_{jk}^{(1)}$, instead of solving the impulsive displacement radiation problem directly, and this may in practice be more convenient.

If the motion of the ship is considered to be time harmonic at frequency ω, then the force on the ship may be written in complex form as

$$F_{jk} = \left(\omega^2 A_{jk}(\omega) - i\omega B_{jk}(\omega) - c_{jk}\right) x_j,$$

and the impulse-response functions calculated using the canonical radiation potentials at any n, are related to the more familiar frequency-response functions (i.e. the added-mass and

Figure 7: Wigley hull at $Fn = 0.0$, pitch-pitch added-mass coefficient.
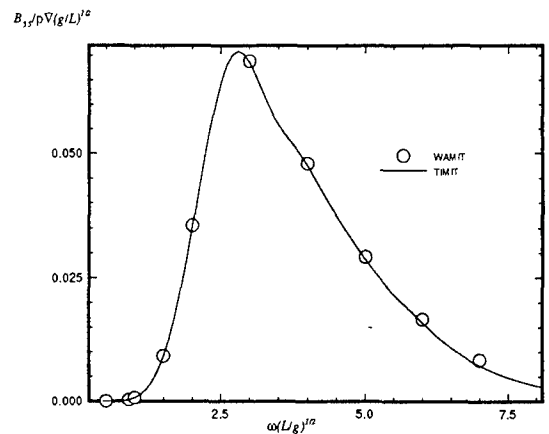
Figure 8: Wigley hull at $Fn = 0.0$, pitch-pitch damping coefficient.

567
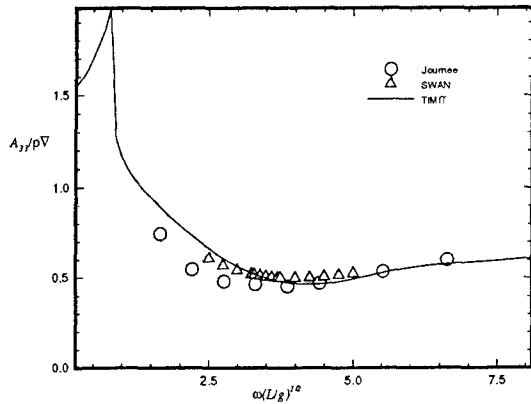
Figure 9: Wigley hull at $Fn = 0.3$, heave-heave added-mass coefficient.

Figure 10: Wigley hull at $Fn = 0.3$, heave-heave damping coefficient.

damping coefficients) through a Fourier transform:

$$-\omega^2 A_{jk}(\omega) \quad +i\omega B_{jk}(\omega) = \qquad (29)$$
$$-\omega^2 a_{jk} + i\omega\, b_{jk}$$
$$+(i\omega)^n \int_0^\infty K_{jk}^{(n)}(t)e^{-i\omega t}\, dt$$

Figure 4 shows a comparison between the added-mass coefficients calculated using the two memory functions shown in Figures 2 and 3. As expected, the results are practically identical.

Calculations made using this method are compared to frequency domain calculations using WAMIT at zero forward speed in Figures 5 through 8. The two solutions for a Wigley hull are in excellent agreement. Comparisons between these two computer codes for more complicated bodies, as well as a description of WAMIT, may be found in Korsmeyer, et al. [10]. Figures 9 through 16 show the results of calculations made for the Wigley hull at a Froude number of 0.3. These results are compared both to the experiments of Journée [7], and to calculations made using the Rankine panel method SWAN [20]. The difference between these two sets of calculated results may be attributed to the fact that SWAN uses a linearization about the double-body flow rather than the Neumann-Kelvin linearization which is used in TiMIT.

3.4.2 The Steady Problem

The steady perturbation potential, $\bar{\phi}(\vec{x})$, can be calculated as the steady-state limit of a particular radiation problem: that of an impulsive accelera-

Figure 11: Wigley hull at $Fn = 0.3$, heave-pitch added-mass coefficient.
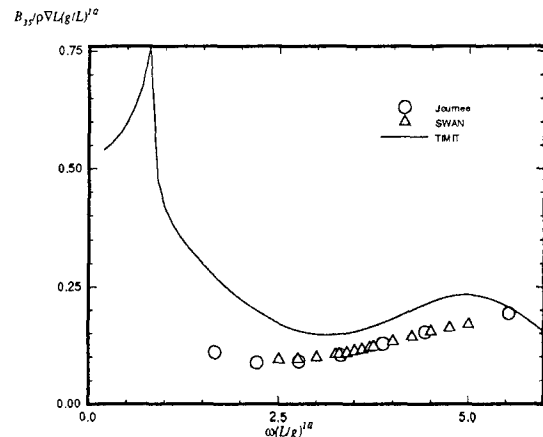
Figure 12: Wigley hull at $Fn = 0.3$, heave-pitch damping coefficient.

568
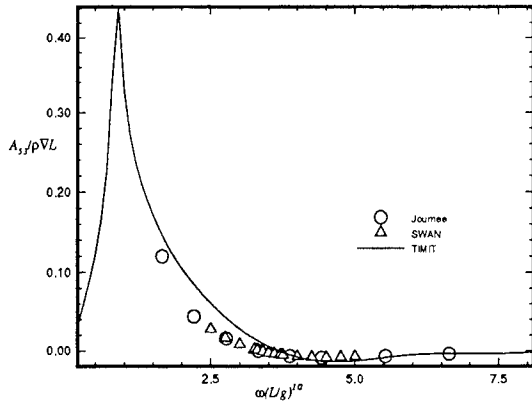
Figure 13: Wigley hull at $Fn = 0.3$, pitch-heave added-mass coefficient.
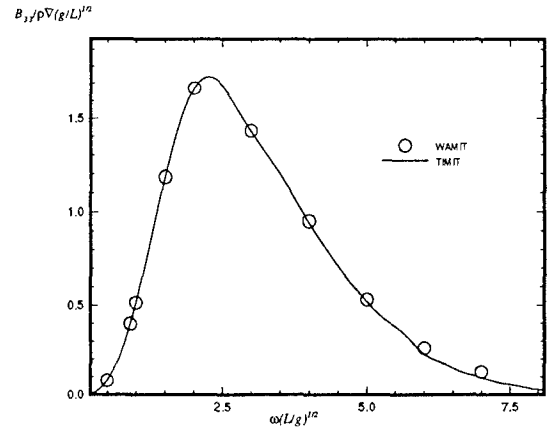

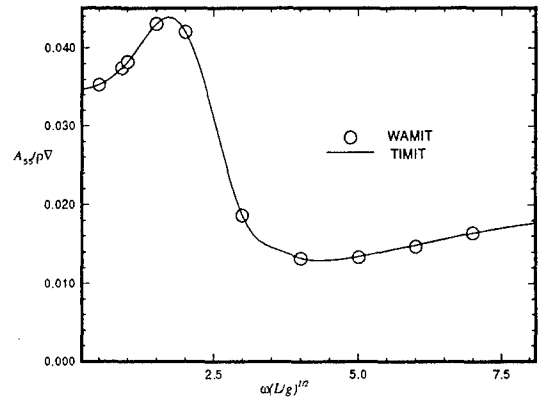Figure 14: Wigley hull at $Fn = 0.3$, pitch-heave damping coefficient.
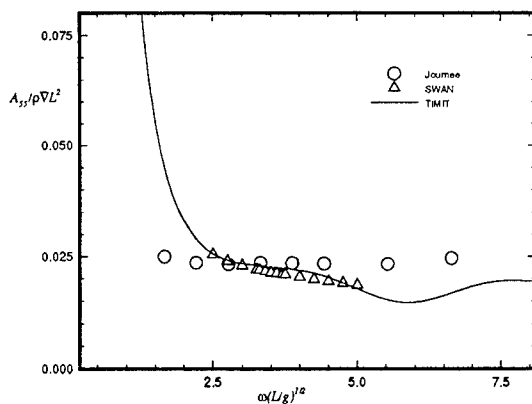
Figure 15: Wigley hull at $Fn = 0.3$, pitch-pitch added-mass coefficient.

Figure 16: Wigley hull at $Fn = 0.3$, pitch-pitch damping coefficient.

tion of the ship to a forward speed U. The boundary conditions for this problem are equations (10) and (17), which in the limit of large time will become the steady-state Neumann-Kelvin conditions

$$U^2 \bar{\phi}_{xx} + g\bar{\phi}_z = 0 \quad \text{on } z = 0$$
$$\bar{\phi}_n = U\,n_1 \quad \text{on } \bar{S}_b.$$

This approach is somewhat indirect, since the Green function for this problem is known (i.e. the Kelvin wave-source potential). The most direct way of calculating the steady potential would be to apply Green's theorem, with the Kelvin wave source potential, and to solve the resulting integral equation for $\bar{\phi}$. However, efforts to calculate the Kelvin wave source potential in a robust and efficient way have not yet been entirely successful. The transient approach, although computationally expensive, is an alternative.

3.5 The Diffraction Problem

The diffraction problem, that of finding the velocity potential for the case of the ship fixed to its mean position in the presence of an incident wave, may be solved to find the transient exciting forces. When the diffraction problem is forced by an impulsive wave elevation, the computed transient forces may be related to impulse-response functions. These impulse-response functions are the kernels of convolutions which can be used to compute the exciting forces and moments which appear on the right-hand side of the equations of motion (1) given an arbitrary, known, incident wave elevation.

569

Equation (16) may be solved for the scattered potential by using the body boundary condition:

$$\frac{\partial \phi_S}{\partial n} = -\frac{\partial \phi_I}{\partial n}, \qquad (30)$$

and the force in mode j, $K_{jD}(t)$, is computed as indicated in (22) with $\Phi_k = \phi_I + \phi_S$, namely the complete diffraction potential.

Two kinds of impulse-response function are of interest and each may be computed by solving canonical problems for scattered potentials. One of these impulse-response functions relates the exciting force to the wave elevation in the earth-fixed reference frame, and the other relates the exciting force to the wave elevation in the ship-fixed reference frame.

In the following convolution, the exciting forces on the ship due to the wave elevation measured at a fixed point in the earth-fixed reference frame, $\zeta_0(t)$, may be computed by

$$X_j(t) = \int_{-\infty}^{\infty} d\tau \, K_{0jD}(t-\tau, \tau)\zeta_0(\tau). \qquad (31)$$

Here the kernel $K_{0jD}(t, t')$ corresponds to the impulse response function of a time-varying linear system. This is due ot the fact that the ship moves in time relative to the reference point where the waves are measured; the ship's response depends on both its position and on the relative time $t - \tau$ since the disturbance. From a different viewpoint, the frequency-domain description of $\zeta_0(t)$ is in terms of the absolute frequency, whereas the description of the ship's exciting force $X_j(t)$ is in terms of the frequency of encounter. Both a phase shift and frequency shift are required to relate these parameters.

$K_{0jD}(t, t')$ is the force on the ship which is found from solving the canonical diffraction problem forced by the incident potential which is the real part of:

$$\phi_I(\vec{x}_0, t, t') = \frac{g}{\pi} \int_{-\infty}^{\infty} d\omega \, \frac{i}{\omega} \exp \left[kz - \right.$$
$$\left. ik\left[(x + Ut)\cos\beta + y\sin\beta\right] + i\omega(t - t')\right], \qquad (32)$$

where the wavenumber k is related to the absolute frequency ω by $k = \frac{\omega^2}{g}$ and β is the angle of wave propagation measured from the positive sense of the x-axis. This incident velocity potential, is a uni-directional wave system which contains all frequencies with equal weight and describes a wave elevation which is the Dirac function in time, $\delta(t-t')$, when viewed from the origin of the earth-fixed reference frame.

An alternative approach is the following convolution, developed by King [8], in which the exciting forces due to the wave elevation measured at a fixed point in the ship-fixed reference frame, $\zeta(t)$, may be computed by

$$X_j(t) = \int_{-\infty}^{\infty} d\tau \, K_{jD}(t - \tau)\zeta(\tau). \qquad (33)$$

Unlike equation (31), the kernel in equation (33) is of the form which corresponds to a time-invariant linear system since the reference point of the waves is fixed with respect to the moving ship.

$K_{jD}(t)$ is the force on the ship which is found from solving the canonical diffraction problem forced by the incident potential which is the real part of:

$$\phi_I(\vec{x}, t) = \frac{g}{\pi} \int_{-\infty}^{\infty} d\omega_e \, \frac{i}{\omega} \exp \left[kz - \right.$$
$$\left. ik\left[x\cos\beta + y\sin\beta\right] + i\omega_e t\right], \qquad (34)$$

where $\omega_e = \omega - Uk\cos\beta$ is the encounter frequency. This incident velocity potential, is also a uni-directional wave system which contains all frequencies, but it describes a wave elevation which is the Dirac function in time, $\delta(t)$, when viewed from the origin of the ship-fixed reference frame.

In the case of $U = 0$ and $t' = 0$, the descriptions (32) and (34) are identical. Note that although these potentials resemble the solution to the two dimensional Cauchy-Poisson problem, that potential describes the evolution of a wave elevation which is initially a Dirac function in space. Here, the spatial concentration of wave elevation is weaker than $\delta(x)$, for instance for $\phi_I(\vec{x}_0, t, t')$:

$$\zeta_0(x_0, y_0, 0, 0) = \frac{1}{2\sqrt{2\pi|x_0|}} \quad U = 0, \ \beta = \pi. \ (35)$$

Continuing with the discussion of the case $U = 0$, $\beta = \pi$, $t' = 0$; at times other than $t = 0$, the waves are dispersed over just one half of the free-surface. For any time $t < 0$, the waves are only in the $x_0 > 0$ half-space, while for $t > 0$, the waves are only in the $x_0 < 0$ half-space. In the former, the waves are coalescing to the impulse, and in the latter they are dispersing from the impulse, hence the Fourier components are always ordered such that the wave length increases with $|x_0|$. The free-surface profiles are illustrated in Figure 17, and discussed further in Section 4.4.

There is no particular significance in choosing to have this temporal impulse occur along a line
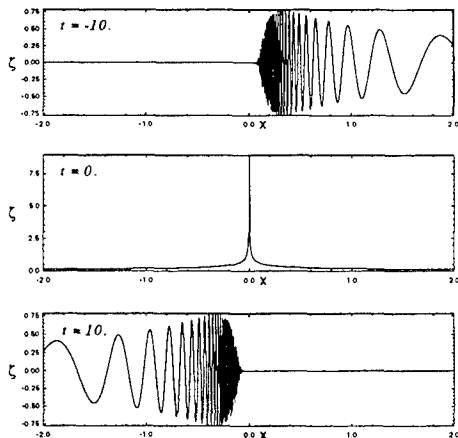
Figure 17: Example free-surface profiles along the x-axis for the case of $U = 0$ and $\beta = \pi$.
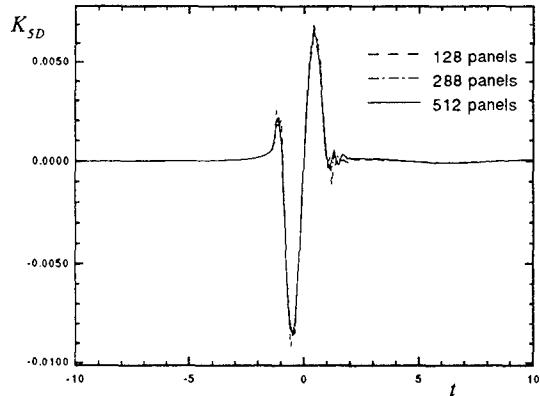
Figure 19: Wigley hull at $Fn = 0.3$, $\beta = \pi$, the pitch exciting moment impulse-response function.
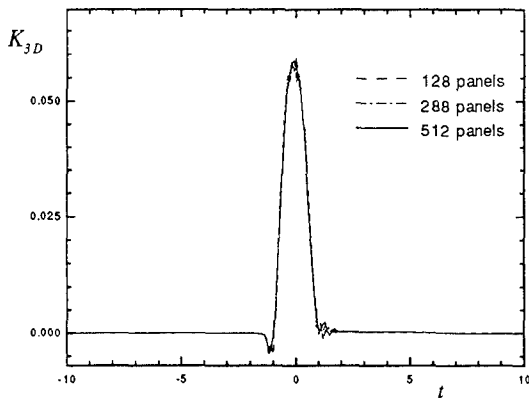
Figure 18: Wigley hull at $Fn = 0.3$, $\beta = \pi$, the heave exciting force impulse-response function.
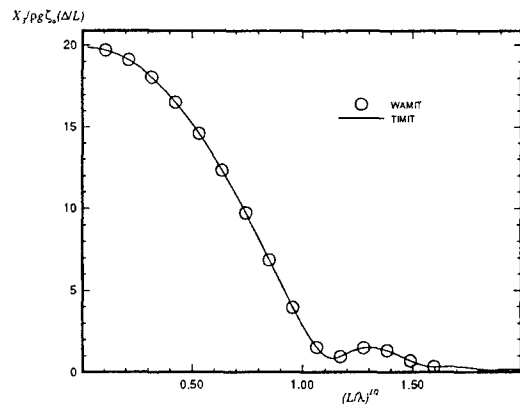
Figure 20: Wigley hull at $Fn = 0.0$, $\beta = \pi$, the heave exciting force amplitude.

through the origin. Any convenient location is acceptable as long as it is accounted for in the interpretation of the impulse-response function or its Fourier transform. In Korsmeyer [11] it is shown that such a shift in the location is equivalent to a phase shift in the frequency domain.

The frequency domain exciting force coefficients are related to $K_{0jD}(t, t')$ and $K_{jD}(t)$ by

$$\frac{X_j(\omega_e)}{\sqrt{1 - 4U\omega_e \cos\beta}} = \frac{1}{\pi} \int_{-\infty}^{\infty} dt\, K_{0jD}(t, 0)e^{-i\omega_e t}, \tag{36}$$

and

$$X_j(\omega_e) = \frac{1}{\pi} \int_{-\infty}^{\infty} dt\, K_{jD}(t)e^{-i\omega_e t}, \tag{37}$$

respectively.

The advantage of $K_{0jD}(t, t')$ over $K_{jD}(t)$ is that the convolution with $\zeta_0(t)$ (the commonly
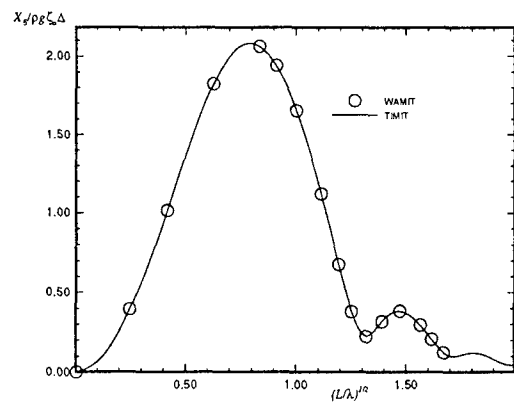
Figure 21: Wigley hull at $Fn = 0.0$, $\beta = \pi$, the pitch exciting moment amplitude.

571
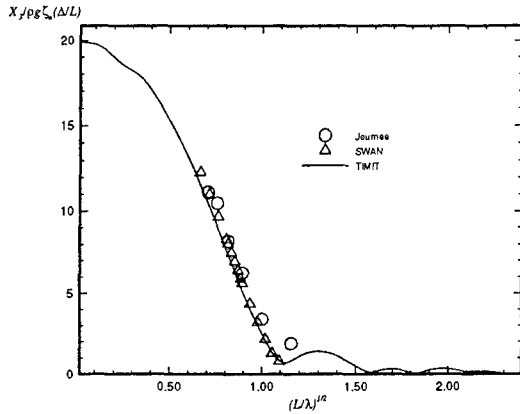
Figure 22: Wigley hull at $Fn = 0.3$, $\beta = \pi$, the heave exciting force amplitude.

Figure 23: Wigley hull at $Fn = 0.3$, $\beta = \pi$, the heave exciting force phase angle.
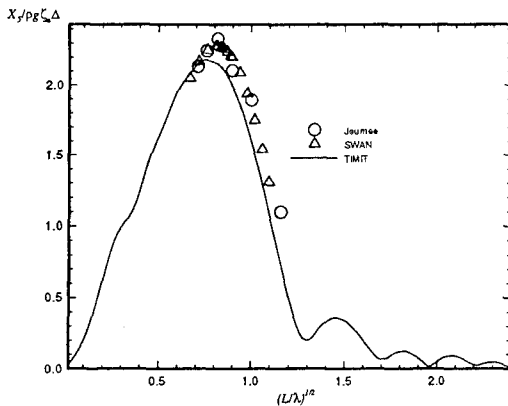
Figure 24: Wigley hull at $Fn = 0.3$, $\beta = \pi$, the pitch exciting moment amplitude.

Figure 25: Wigley hull at $Fn = 0.3$, $\beta = \pi$, the pitch exciting moment phase angle.

available input) avoids the difficulty of the non-unique relationship between encounter and absolute frequencies in following seas. If $K_{jD}(t)$ is used in following seas, three hydrodynamic problems must be solved for three impulse-response functions (one for each of three ranges of absolute frequency) in order to uniquely characterize the response in terms of encounter frequency. On the other hand, $K_{jD}(t)$ is computationally more efficient, particularly in head seas, and the wave elevation $\zeta(t)$ may be readily computed from $\zeta_0(t)$ in Fourier space.

Examples of exciting force impulse-response functions $K_{3D}(t)$ and $K_{5D}(t)$ for a Wigley hull, at a Froude number of 0.3 in head seas, are shown in Figures 18 and 19. These functions are computed for three discretizations. The Wigley hull presents no computational difficulties and so a discretization of only 288 panels is adequate for practically useful results. Note that unlike the radiation force impulse-response functions, the diffraction force impulse-response functions are non-zero at times $t < 0$. This is a result of the dispersion of free-surface waves and the fact that the ship is of finite extent. That is, in head seas for instance, at times $t < 0$ the incident impulsive wave has not yet coalesced, but is already being scattered by the forward sections of the ship. This phenomenon must be accounted for in the convolution on the right-hand side of the equations of motion by the choice of an infinite upper limit of integration in equations (31) and (33).

Comparison of the diffraction impulse-response functions with frequency-domain results may be made through the Fourier transform (36) or (37).

572

Figures 20 and 21 show a comparison of the magnitude of the frequency-domain exciting force coefficients for the heave force and pitch moment on a Wigley hull at a Froude number of 0. The comparison is the Fourier transform of results from TiMIT with calculations conducted in the frequency domain by WAMIT. The results are identical to graphical accuracy, which is expected as these codes are the time-domain and frequency-domain manifestations of the same theory as long as $U = 0$.

Figures 22 through 25 show a comparison of the magnitude and phase angle of the frequency-domain exciting force coefficients for heave force and pitch moment for the Wigley hull at a Froude number of 0.3. The comparison is the Fourier transform of the results from TiMIT shown in Figures 18 and 19 with calculations conducted in the frequency domain by SWAN and experimental results from Journée [7]. As mentioned in Section 3.4.1, the m-terms are treated differently in TiMIT and SWAN and this difference enters into the pitch moment calculation through equation (22). This may account for the fact that the agreement between TiMIT and SWAN is better for the heave exciting force than for the pitch exciting moment. Apparently, using the double-body linearization improves the accuracy of the pitch exciting moment calculation by a small amount.

4   Numerical Issues

There are three major numerical tasks involved in solving the hydrodynamic problems outlined above: calculation of the Green function for pairs of singularity and field points on the representation of the ship hull; calculation of the impulsive incident wave at field points on the ship hull; and solution of the discrete integral equations (16) and (26). The calculation of the Green function is described in detail by Newman [21] and is done to an absolute accuracy of approximately 6 significant digits throughout the computational domain. The computation of the incident potential, along with its temporal and spatial derivatives, is carried out via an extension of algorithms commonly used for the calculation of the complex error function. These algorithms are based on the work of Gautschi [5] and may be found in King [8] and Korsmeyer [13].

4.1   The Discrete Hydrodynamic Problem

The integral equations for the hydrodynamic problems are discretized by subdivision of the hull surface into planar quadrilateral (or triangular) panels upon which the potential is assumed to be constant. A linear system of equations is generated by a collocation scheme where the panel centroids are the collocation points. The convolution terms appear only on the right-hand side, and the convolution is computed by the trapezoid rule (see [12]). If appropriate, the size of the linear system is reduced by exploiting the port and starboard symmetry of the ship. The linear system of equations has a left-hand side matrix which is independent of time, so this matrix may be factored once, with back-substitution used at all subsequent time steps.

The bulk of the computational burden of the solution is in calculating, or fetching from storage, the transient Green function coefficients which appear in the convolution terms. For a zero-speed problem, without exploiting symmetry, the number of coefficients needed at each time step is proportional to $N_t N_P^2$ (where N_t is the number of the current time step and N_P is the number of panels); however, all but N_P^2 have been calculated at previous time steps. If there is sufficient physical memory available, the most efficient strategy is to store the coefficients in memory. If there is not, then they must either all be recalculated at each step, or fetched from storage on disk. On all of the machines that we use (DEC 5000, IRIS Indigo, Cray YMP) storing the coefficients on disk is from three to six times faster than recalculating. The algorithm used to calculate this function requires an average of 1.5 micro seconds on a Cray YMP for one pair of evaluation points at a single time. In the diffraction problem, the incident potential must be calculated at each time step as well, but only N_P evaluations are required and this is not a significant contribution to the overall computational effort.

If the transient coefficients are stored, the space required, whether in RAM or on disk is:

$$\text{Storage} \propto N_P^2 N_T, \qquad (38)$$

where N_T is the total number of time steps. The total cost of the computation, regardless of whether the coefficients are recalculated or stored is:

$$\text{Cost} \propto N_P^2 N_T^2. \qquad (39)$$

There is an N_P^3 term in the cost equation, reflecting the factorization of the left-hand side, but

573

that term is dominated by the N_P^2 term for any typical computation. For the forward-speed problem, additional coefficients are required for the waterline integral.

Clearly it is important to use the coarsest spatial and temporal discretizations which will achieve the desired accuracy. Symmetries should always be exploited when possible as this both reduces the size of the linear system and reduces the number of coefficients which must be computed. Reducing the total time range of the calculation is also possible as is discussed in the next section.

4.2 Asymptotic Continuation

The minimum length of an impulse-response function is determined by the decay of transients in the solution. In principle, the force on the ship continues for all time, but in practice we will feel justified in truncating the record when the force has decayed to some small fraction of its peak value (say .5%). The decay of transients in the solution, with steady forward speed, is fundamentally different from the solution of the zero-speed problem because of the resonance at the critical frequency of $\tau \equiv \frac{\omega U}{g} = 1/4$. At zero speed, the energy associated with the wave system generated by the impulse propagates away from the ship at the group velocity of the various components. At forward speed however, the impulse excites components whose group velocities are approximately equal to the ship's speed, U, and this energy remains in the vicinity of the ship.

This concept can be made more quantitative by considering the asymptotics of the Green function. Newman [21] shows that at zero speed the linearized pressure due to the Green function (equation (13)) is to leading order:

$$G_t \sim \frac{1}{t^3} \quad t \to \infty.$$

When the ship has a steady forward speed, however, the leading order contribution becomes

$$G_t \sim \frac{\sqrt{2}}{U^2 t} \exp\left(\frac{Z}{4U^2}\right) \sin(\omega_c\, t), \qquad (40)$$

where $\omega_c = \frac{g}{4U}$ is the critical frequency of oscillation. This result can be related through a Fourier transform to the results of Dagan & Miloh [4] for the analogous frequency-domain Green function. Asymptotically then, the Green function at forward speed behaves like an oscillation at the critical frequency, which decays at a rate of $\frac{1}{t}$.
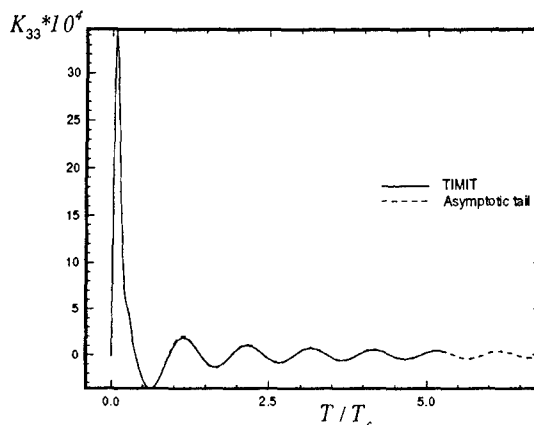
Figure 26: Comparison of the impulse-response function and the proposed asymptotic tail.
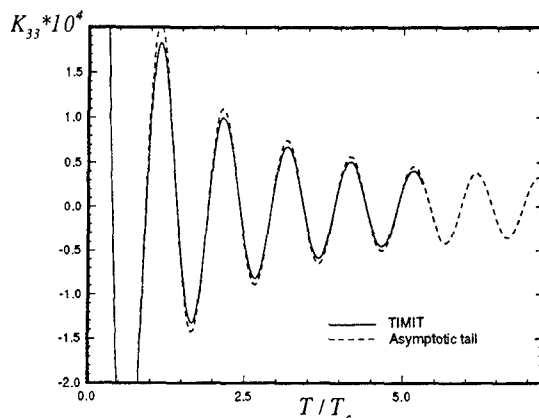
Figure 27: Expanded view of the matching between the asymptotics and the solution.

This behavior in the Green function suggests a similar behavior in the solution to the integral equation, as well as in the impulse-response function. This notion is borne out by numerical experiments, and suggests that a relatively short solution can be extended to any length by matching it to an asymptotic continuation or *tail* which has a form similar to equation (40). Figures 26 and 27 show a comparison between a very long calculation of an impulse-response function and the proposed asymptotic tail. In these figures the non-dimensional impulse-response function and the asymptotic tail are plotted versus the non-dimensional ratio of time to the critical period, $T_c = \frac{2\pi}{\omega_c}$. The two functions have been matched at a peak near $\frac{T}{T_c} = 0.6$.

Despite the good agreement shown in these

574
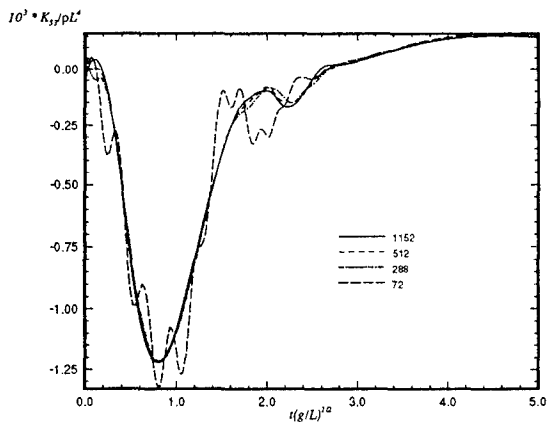
Figure 28: Wigley hull at $Fn = 0.3$, convergence of the pitch-heave response.

Figure 29: Wigley hull at $Fn = 0.3$, convergence of the pitch-pitch response.

figures, this leading-order behavior is based on the potential for a translating source, and is not strictly correct for a collection of singularities such as source and dipole distributions over the panels of a discrete ship geometry. It can be seen in Figure 27, which is an expanded view of the matching shown in Figure 26, that the numerical solution decays slightly faster than $\frac{1}{t}$. This is consistent with the recent work of Liu & Yue [18].

4.3 Convergence

Convergence of transient problems depends on both spatial and temporal discretization. Figures 28 and 29 show the convergence of two radiation impulse response functions with increasing numbers of panels. All the curves are for a Wigley hull at Froude number of 0.3, and each curve which appears in the figures is itself the converged result of a series of calculations using progressively smaller time steps for the same spatial discretization. Figures 30 and 31 are the Fourier transform of the convergence plots shown in Figure 29 to provide a frequency domain perspective on the convergence of the calculations. As can be seen from these figures, and Figures 18 and 19 from Section 3.5, the radiation and diffraction problems appear to have converged to within graphical accuracy using a discretization of 512 panels over the body (256 unknowns).

4.4 Filtering of Short Wavelengths

As in other hydrodynamic problems where a continuous spectrum of wavelengths is present, very small wavelengths exist which are not considered

Figure 30: Wigley hull at $Fn = 0.3$, convergence of the pitch-pitch added-mass coefficient.
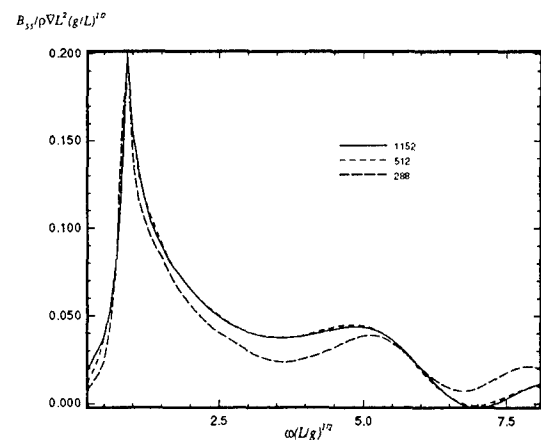
Figure 31: Wigley hull at $Fn = 0.3$, convergence of the pitch-pitch damping coefficient.

to be of physical relevance. These may cause numerical anomalies or errors, since the approximation of the ship's surface by panels upon which the potential is assumed to be constant limits the correct solution to wavelengths substantially longer than the panel dimensions. Since short waves are attenuated exponentially in the vertical direction, this problem is restricted to a relatively thin region adjacent to the free surface.

In the present planar panel method, with the collocation points at the panel centroids, values of the potentials required for the waterline integral in equation (16) are replaced by the corresponding values at the adjacent centroids. This effectively provides an exponential filter to the short wavelengths, scaled in proportion to the panels themselves. This is an *ad hoc* approach, which is justified by convergence tests and visual examination of the resulting computations, as opposed to a more formal numerical analysis. Difficulties can be anticipated if the centroids approach the free surface faster than the scale of the panels is reduced, as might occur if the aspect ratio of the panels is large (horizontal dimension much greater than vertical) or if there is substantial flare at the waterline (panels approaching the horizontal plane).

For example, the presence of very short wavelengths in the incident-wave profile corresponding to either incident potential (32) or (34) (for $U = 0$ and $\beta = \pi$) is illustrated in Figure 17. The profiles shown in this figure are in fact filtered because we are evaluating

$$\zeta(\vec{x}, t) \simeq -\frac{1}{g}\phi_{It}(x, y, -0.001, t). \qquad (41)$$

This is equivalent to the evaluation of the incident potential at the centroids of panels adjacent to the linearized free-surface for a fine discretization of a ship hull.

An alternative filtering scheme for the solution could be based on truncating the integral representation for the Green function, $G^{(f)}$ (15), at some point $k = k_{max}$. This is also an *ad hoc* approach and the truncation point k_{max} would have to be increased systematically with the refinement of the discretization. Such an approach would be expedient if the integral defining $G^{(f)}$ were evaluated numerically. However for efficient transient hydrodynamic analysis, the rapid evaluation of $G^{(f)}$ is critical and is best achieved by evaluating the Green function by analytical expansions and approximations available only for the complete (semi-infinite) range of the integral.

5 Simulation

The simulation of a ship traveling in a seaway is carried out by the temporal integration of the equations of motion (1). For the simulation presented here, the exciting forces are calculated by the convolution appearing in equation (33). This simulation is of a Wigley hull at Froude number 0.3, encountering head seas with a Pierson-Moskowitz spectrum corresponding to 5 meters per second wind speed.

The top of Figure 32 shows a segment of the time history of the incident wave elevation as measured at the origin of the ship-fixed reference frame. The next two time histories in this figure are the heave and pitch responses of the ship respectively.

Validation of these time histories may be made by deducing the frequency-domain response-amplitude operators from the input and output signals:

$$RAO_j = \frac{|X_j(\omega)|}{|\zeta(\omega)|}, \qquad (42)$$

where $X_j(\omega)$ and $\zeta(\omega)$ are obtained by taking the Fourier transforms of the output and input signals respectively. Figures 33 and 34 are plots of the frequency-domain response-amplitude operators compared to experimental results.

We find that the computation of the frequency-domain response-amplitude operators converges more slowly in the vicinity of resonance than at frequencies away from that region, as can be seen in Figures 33 and 34. This is expected since resonance occurs precisely because the determinant of the frequency-domain system of equations of motion becomes small, leading to poor conditioning of this linear system. The convergence of these results is also subject to the reduction of the size of the time-step and the increase of the order of the integration scheme used to solve the time-domain equations-of-motion. A fourth-order Runge-Kutta algorithm is a reasonable choice because it is robust and efficiency is not paramount in this calculation.

To quantify the relatively slow convergence around resonance, we have solved the equations of motion in the frequency domain using the frequency-domain coefficients presented in various figures shown in Section 3, which are the Fourier transforms of time-domain computations. We find that for the Wigley hull in head seas at a Froude number of 0.3, the condition number at the frequency of peak heave and pitch response is approximately twice the value for frequencies

576
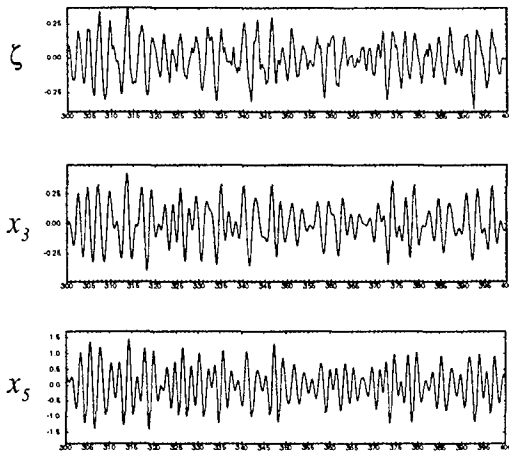
Figure 32: Time histories from a simulation of a Wigley hull at $Fn = 0.3$, $\beta = \pi$. From the top: incident wave elevation in the ship-fixed frame, heave response, pitch response.

away from this peak. It is reasonable to expect that accurate results in the time-domain can only be produced for temporal and spatial discretizations which are sufficiently fine to achieve convergence around resonance.

6 Discussion

A computer code has been developed for the transient hydrodynamic analysis of a ship traveling in a seaway. Results have been presented to demonstrate the convergence of the method for the radiation and diffraction problems, and the calculations are shown to be in satisfactory agreement with both experiments and frequency domain calculations made using other methods. It is also pointed out that the steady problem can be considered to be the large time limit of a particular radiation problem, and the use of an impulse in displacement is suggested as a way of avoiding all steady-state limits in the radiation problem. A technique for extending the impulse response function by asymptotic continuation is also presented and used to reduce the necessary length of the computations.

Topics for the future include improving the calculation of fluid velocities through the use of higher order panels. This is especially important in the steady problem because the forces are determined entirely from gradients of the potential. The calculation of field quantities, such as the free-surface elevation and fluid velocities away from the ship, is also in progress. Real ship forms,
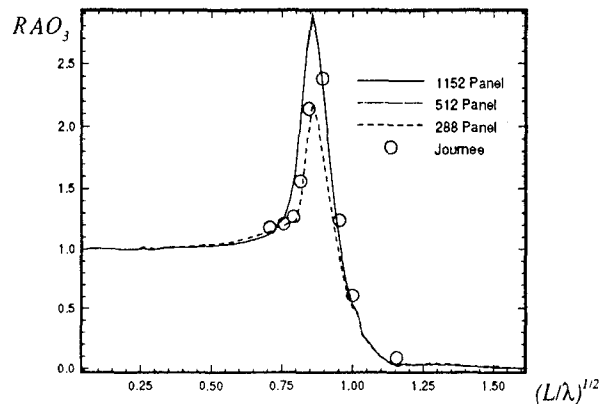
Figure 33: Wigley hull at $Fn = 0.3$, $\beta = \pi$, the heave response-amplitude operator.
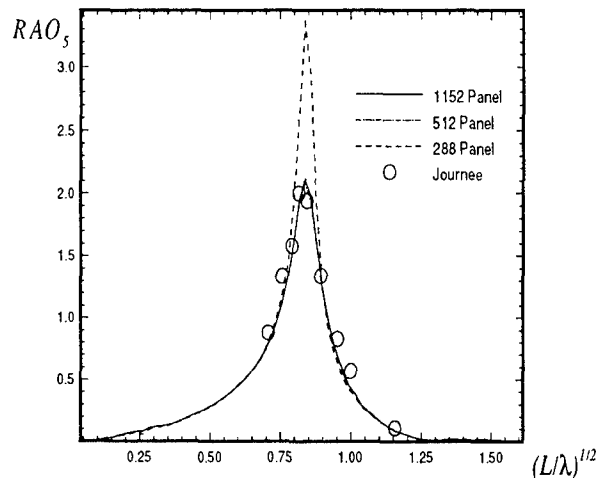
Figure 34: Wigley hull at $Fn = 0.3$, $\beta = \pi$, the pitch response-amplitude operator.

which often have significant flare especially near the stern, present special numerical difficulties for this method of solution and therefore require special care. A ship traveling in following seas is another important topic of further research, and it is not yet clear to us which of the two diffraction formulations discussed in the foregoing will be most useful in this situation.

Acknowledgment

References

[1] R. F. Beck and A. R. Magee. Time domain analysis for predicting ship motions. In *Proc. IUTAM Symp. Dynamics of Marine Vehicles & Structures in Waves*, London, U.K., 1990.

[2] V. Bertram. A Rankine source approach to forward speed difraction problems. In *Proc. 5th Intl. Workshop on Water Waves and Floating Bodies*, Manchester, U.K., 1990.

[3] W. E. Cummins. The impulse response function and ship motions. *Schiffstecknik*, 9:101–109, 1962.

[4] T. Dagan and G. Miloh. Flow past oscillating bodies at resonant frequency. *Proc. 13th Symp. Naval Hydro.*, pages 355–373, 1980.

[5] W. Gautschi. The complex error function. *Collected Algorithms from CACM*, 1969.

[6] M. D. Haskind. Two papers on the hydrodynamic theory of heaving and pitching of a ship. Technical Report 1-12, The Society of Naval Architects and Marine Engineers, 601 Pavonia Ave., Jersey City, New Jersey, 1953.

[7] J. M. J. Journée. Experiments and calculations on four Wigley hullforms. Technical Report 909, Delft University of Technology, Ship Hydromechanics Laboratory, Delft, The Netherlands, 1992.

[8] B. W. King. Time-domain analysis of wave exciting forces on ships and bodies. Technical Report 306, The Department of Naval Architecture and Marine Engineering, The University of Michigan, Ann Arbor, Michigan, 1987.

[9] B. W. King, R. F. Beck, and A. R. Magee. Seakeeping calculations with forward speed using time domain analysis. In *Proc. 17th Symp. Naval Hydro.*, The Hague, Netherlands, 1988.

[10] F. T. Korsmeyer. *The first- and second-order transient free-surface wave radiation problems*. PhD thesis, Massachusetts Institute of Technology, Cambridge, Massachusetts, 1988.

[11] F. T. Korsmeyer. The time domain diffraction problem. In *The Sixth International Workshop on Water Waves and Floating Bodies*, Woods Hole, Massachusetts, 1991.

[12] F. T. Korsmeyer, C. H. Lee, J. N. Newman, and P. D. Sclavounos. The analysis of wave effects on tension leg platforms. In *OMAE Conference*, Houston, Texas, 1988.

[13] F. T. Korsmeyer, J. N. Newman, and G. E. Osborne. The linear, transient, free-surface wave diffraction problem. In preparation, 1993.

[14] S. J. Liapis. *Time domain analysis of ship motions*. PhD thesis, The Department of Naval Architecture and Marine Engineering, The University of Michigan, Ann Arbor, Michigan, 1986.

[15] S. J. Liapis. Time domain analysis of ship motions. Technical Report 302, The Department of Naval Architecture and Marine Engineering, The University of Michigan, Ann Arbor, Michigan, 1986.

[16] W. M. Lin and D. K. P. Yue. Numerical solutions for large-amplitude ship motions in the time domain. In *Eighteenth Symp. on Nav. Hydro.*, Ann Arbor, Michigan, 1990.

[17] W. M. Lin and D. K. P. Yue. Time-domain analysis for floating bodies in mild-slope waves of large amplitude. In *8th Intl. Workshop Water Waves & Floating Bodies*, St. John's, Newfoundland, 1993.

[18] Y. Liu and D. K. P. Yue. On the solution near the critical frequency for an oscillating and translating body in or near a free surface. *J. Fluid Mechanics*, 254:251–266, 1993.

[19] D. E. Nakos, D. E. Kring, and P. D. Sclavounos. Rankine panel methods for time-domain free surface flows. In *6th Intl.*

Conf. Num. Ship Hydro., U. Iowa, Iowa City, 1993.

[20] D. E. Nakos and P. D. Sclavounos. Ship motions by a three dimensional Rankine panel method. In *Eighteenth Symp. on Nav. Hydro.*, Ann Arbor, Michigan, 1990.

[21] J. N. Newman. The approximation of free-surface Green functions. In P. A. Martin and G. R. Wickham, editors, *Wave Asymptotics*, pages 107–135. Cambridge University Press, 1992.

[22] T. F. Ogilvie. Recent progress toward the understanding and prediction of ship motions. In *The Fifth Symposium on Naval Hydrodynamics*, pages 3–128, Bergen, 1964.

[23] T. F. Ogilvie and E. O. Tuck. A rational strip theory for ship motions, part 1. Technical Report 013, The Department of Naval Architecture and Marine Engineering, The University of Michigan, Ann Arbor, Michigan, 1969.

[24] J. V. Wehausen and E. V. Laitone. Surface waves. In *Handbuch der Physik*, pages 446–778. Springer, 1960.

A New Method for the Determination of Resonant States for Fluid-Structure Interaction

O. DeBayser, C. Hazard, and M. Lenoir
(CNRS/ENSTA Centre de l'Yvette, France)
D. Martin (Universite de Rennes, France)

Abstract.

In order to compute the resonant states of a ship on the sea, we investigate a variational formulation for the scattering frequencies of this problem, i.e. the poles of the analytic continuation of the solution operator. A practical method, based on the integral representation of the solution is described, the scattering frequencies are shown to be the solutions of a non-linear eigenvalue problem.

The scattering frequencies and the corresponding eigensolutions provide detailed information about the way energy of incident waves can be stored as waves in the vicinity of the ship or motion along one ore more of its degrees of freedom. They can be used for prediction of the frequency and direction of the incoming waves resulting in the maximum response of the ship along one of its degrees of freedom.

Some preliminary results in that direction are shown here, where the body is a model catamaran, fixed in the waves.

1 Introduction.

We study the linearized sea-keeping problem for an elastic body , i.e., the periodic small motions of an elastic structure which floats (without forward speed) at the free surface of the ocean (in the infinite depth case). We are concerned in particular with the dynamic stability of the structure ; more precisely, the main question is to find the frequency domains which correspond to the highest risks of instability. Indeed, for some values of the frequency, it may happen that the amplitude of the motions of the structure becomes great compared with the amplitude of the incident swell.

This means intuitively that the structure has a tendency to accumulate the energy transmitted by the incident wave. These "resonant frequencies" are not eigenfrequencies of the problem, for the system consisting of the structure coupled with the ocean is not conservative (the energy associated with the scattered wave propagates to infinity). A simple way to determine them is to compute the response curve of the structure, i.e., the total energy of the structure with respect to the frequency of the incident wave (for given amplitude and direction of propagation): the resonant frequencies correspond to the peaks of this curve. However, it is an especially expensive method, since it requires to compute the response of the system for numerous values of the frequency.

The aim of the present paper is to show that the resonant frequencies are nothing but the traces of isolated singularities in the plane of complex frequencies. Indeed, we will see that the sea-keeping problem can be extended analytically to complex values of the frequency, and that this extension has poles in the lower complex half plane: these poles are referred to as "scattering frequencies". They are intrinsic quantities of the system, since they do not depend on the incident swell (as the eigenvalues of a conservative system do not depend on the external forces exerted on it). The knowlegde of these singularities (more precisely, the ones which are near the real frequencies axis) allows not only to locate the peaks of the response curve, but also to obtain an a priori estimate of the response of the system in the vicinity of such frequencies (see [4], [11]).

We present here a way to construct explicitly the analytic continuation of the sea-keeping problem in the plane of complex frequencies, and to

exhibit the singularities of this extension. The principle of the method is quite simple. We begin by reducing the initial problem to an equivalent one set in a bounded domain, thanks to the so-called coupling method between finite elements and integral representation (introduced by Jami and Lenoir [8]). The reduced problem is then extended to complex frequencies using the analytic continuation of the Green function of the sea-keeping problem (Vullierme-Ledard [16]). The scattering frequencies finally appear as the solutions of a nonlinear eigenvalue problem which can be dicretized by finite elements and then solved by a numerical iterative method. In the present paper, the method is described for the general case of the 3-dimensional fluid - structure interation problem. However, the numerical results which are presented here are related to the scattering problem by a fixed rigid body. The case of an elastic floating body is in progress.

In order to focus rather on the numerical aspects of the computation of scattering frequencies, we restrict ourselves to describe the main steps on the method, without going into the mathematical details. For a rigorous mathematical approach, we refer to [11] where the method is applied to the scattering of an acoustic wave by a rigid obstacle. See [16], [4] and soon [6] for the sea-keeping problem. Note that in the finite depth case, an other characterization of the scattering frequencies may be obtained by means of the so-called localized finite element method (see [4] in 2-D, and [5] in 3-D). It is based on a series expansion of the solution instead of an integral representation. In the 2-dimensional case, numerical results are given in [5]. Let us finally mention the paper of Wu, Wang and Price [18] who present an intuitive approach of the notion of scattering frequencies : by an asymptotic analysis of a simplified model, they show in particular how the peaks of the response curve are related to the presence of poles in the complex frequency plane.

2 Resonant states and scattering frequencies.

2.1 Linearized equations.

Consider an elastic body which floats at the free surface of the sea, assumed infinite in both horizontal and downward vertical directions. When the system is at rest, the fluid fills an unbounded
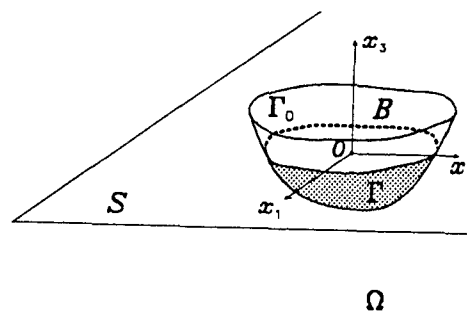
Figure 1: The floating body.

domain Ω whose boundary $\partial\Omega$ consists of the free surface S and the immersed surface Γ of the body. The body fills a bounded domain B : its boundary ∂B consists of Γ and the emerged part Γ_0 which is assumed free. We denote by n either the outer unitary normal to $\partial\Omega$ or the inner normal to ∂B (which coincide on Γ). The coordinate system $(O, \vec{x}_1, \vec{x}_2, \vec{x}_3)$ is defined as shown in Fig. 1: $(O, \vec{x}_1, \vec{x}_2)$ is an horizontal plane parallel to the free surface S, and $(O, \vec{x}_3)$ is the upward vertical direction.

We study the periodic small motions of the coupled system under the action of a given incident monochromatic swell of pulsation ω. Let φ be the velocity potential of the scattered wave and $u = (u_1, u_2, u_3)$, the displacement field of the body. Let $e_{ij}(u)$ and $\sigma_{ij}(u)$ (for $i, j = 1, 3$) be, respectively, the components of the strain and stress tensors given by

$$
\begin{aligned}
e_{ij}(u) &= \frac{1}{2}\left(\partial_{x_j} u_i + \partial_{x_i} u_j\right) \quad \text{and} \\
\sigma_{ij}(u) &= \sum_{k,h} a_{ijkh} \, e_{kh}(u),
\end{aligned}
$$

where a_{ijkh} are the elastic coefficients which are related, in the case of an isotropic material, to the so-called Lamé coefficients λ and μ by the relations

$$
a_{ijkh} = \lambda \delta_{ij}\delta_{kh} + \mu(\delta_{ih}\delta_{jk} + \delta_{ik}\delta_{jh}).
$$

The linearized time-harmonic equations of the problem (expressed in a non-dimensional form) consist in the following system, which will be referred to as problem $\mathcal{P}_\nu$ in the sequel :

$$
\Delta\varphi = 0 \quad \text{in } \Omega, \tag{1}
$$

$$
\partial_n\varphi - \nu\,\varphi = 0 \quad \text{on } S, \tag{2}
$$

$$
\nu\rho\,u_i + \partial_{x_j}\sigma_{ij}(u) = 0 \quad \text{in } B, \tag{3}
$$

$$\sigma_{ij}(u)\, n_j = 0 \quad \text{on } \Gamma_0, \tag{4}$$

$$\sqrt{\nu}\, u.n - \partial_n \varphi = f \quad \text{on } \Gamma, \tag{5}$$

$$\sigma_{ij}(u)\, n_j - \sqrt{\nu}\, \varphi\, n_i = g_i \quad \text{on } \Gamma, \tag{6}$$

$$\lim_{R \to \infty} \int_{\Sigma_R} |\partial_n \varphi - i\nu\, \varphi|^2 \, d\sigma = 0, \tag{7}$$

where ν denotes the pulsation squared ($\nu = \omega^2$), ρ is the (dimensionless) mass density of the body, f and g_i ($i = 1,3$) are given functions on Γ (which depend on the incident swell), and Σ_R is the vertical cylinder $\Sigma_R = \left\{ x \in \Omega; \; x_1^2 + x_2^2 = R^2 \right\}$. We refer for example to [9] and [14] for more details concerning the equations of the fluid and the structure. Laplace's equation (1) is nothing but the conservation of mass. The free surface condition (2) results on one hand from the continuity of the pressure across S, on the other hand from the fact that the velocity of the particles located on S is tangent to S. Eqs. (3) are the dynamics equations in a continuous medium, and (4) expresses that the emerged part Γ_0 of the boundary of B is free. On Γ, the two equations (5) and (6) stand, respectively, for the continuity of the normal velocity and the normal stress. Finally, the radiation condition (7) shows that the energy of the scattered wave radiates towards infinity.

Note that in the case of a rigid body, the strain tensor vanishes at every point of B. It follows that the linearized displacement field has the form $a + b \times x$ (see e.g. [14]) : the system (1) to (7) then simplifies to the problem studied by John [9].

Our aim is to show that this problem extends analytically in the complex ν-plane and above all, to describe how to construct explicitly this extension. Let us point out that we cannot exhibit such an extension simply by replacing ν by a complex number in the equations (1) to (7) of $\mathcal{P}_\nu$. This follows from the so-called "limiting absorption principle" ([10],[4]) which may be explained as follows. Let $\mathcal{P}_\nu$ still denote the problem which is obtained by substituting for ν a complex number. It may be easily seen that this problem is well-posed for every ν such that $\operatorname{Im} \nu \neq 0$, and that its solution decreases exponentially at infinity (when $x_1^2 + x_2^2 \to \infty$). Moreover, if

$$\nu \in \mathcal{C}^+ = \{ z \in \mathcal{C}; \; \operatorname{Im} z > 0 \}$$

tends to a given $\nu_0 \in \mathcal{R}^+$, then the solution of $\mathcal{P}_\nu$ tends locally to the solution of $\mathcal{P}_{\nu_0}$. On the other hand, if

$$\nu \in \mathcal{C}^- = \{ z \in \mathcal{C}; \; \operatorname{Im} z < 0 \}$$

tends to the same point $\nu_0 \in \mathcal{R}^+$, this result does not hold : actually, the limit of the solution of $\mathcal{P}_\nu$

does not satisfy condition (7) any longer. In fact, it verifies

$$\lim_{R \to \infty} \int_{\Sigma_R} |\partial_n \varphi + i\nu\, \varphi|^2 \, d\sigma = 0,$$

which is known as the incoming radiation condition. As a summary, we are able to construct by that way a continuous extension of the initial problem to the upper complex half plane $\mathcal{C}^+$. This extension is regular (since $\mathcal{P}_\nu$ is well-posed for every $\nu \in \mathcal{C}^+$) and no singularity appears in $\mathcal{C}^+$.

The extension of the problem to the lower complex half plane $\mathcal{C}^-$ raises a difficulty which may be understood as follows : noticing that the solution of $\mathcal{P}_\nu$ is exponentially decreasing at infinity for $\nu \in \mathcal{C}^+$, and oscillating for $\nu \in \mathcal{R}^+$, it will clearly become exponentially increasing when $\nu \in \mathcal{C}^-$. In order to remove this difficulty, the method we present in the sequel consists in reducing the initial problem to an equivalent problem set in a bounded domain : the asymptotic behaviour of φ at infinity is explicitly controled by means of an integral representation formula. The reduced problem will then be extended in the complex ν-plane.

2.2 Reduction to a bounded domain.

In this section, ν denotes a real positive number. We recall here the coupling method between finite elements and integral representation (Jami and Lenoir [8]. We will denote by $G_\nu(x, y)$ the Green function (or elementary solution) associated with the sea-keeping problem, i.e., the only solution of

$$\begin{aligned}
\Delta G_\nu(\cdot, y) &= \delta_y \quad \text{in } x_3 < 0, \\
\partial_n G_\nu(\cdot, y) - \nu\, G_\nu(\cdot, y) &= 0 \quad \text{on } x_3 = 0, \\
\lim_{R \to \infty} \int_{\Sigma_R} |\partial_n G_\nu - i\nu\, G_\nu|^2 \, d\sigma &= 0,
\end{aligned} \tag{8}$$

where δ_y is the Dirac measure at point y. Several expression of this function have been obtained (see e.g. Wehausen and Laitone [17], Martin [13], Clément [2]).

$$\begin{aligned}
&G_\nu(x, y) = \\
&\frac{-1}{4\pi} \left(\frac{1}{\|x - y\|} + \frac{1}{\|x - y'\|} + \nu H_\nu(R, Z) \right),
\end{aligned} \tag{9}$$

where y' is symmetric to y with respect to the plane $x_3 = 0$, R and Z are two functions of x and y given by

$$\begin{aligned}
R &= \sqrt{(x_1 - y_1)^2 + (x_2 - y_2)^2}, \\
Z &= x_3 + y_3
\end{aligned}$$

and H_ν is defined by

$$H_\nu(R,Z) =$$
$$2\,\mathrm{Pv}\int_0^{+\infty} \frac{e^{tZ}J_0(tR)}{t-\nu}\,dt + 2i\pi\,e^{\nu Z}J_0(\nu R), \quad (10)$$

where the symbol "Pv" denotes the principal value of the integral, and J_0 is the Bessel function of the first kind and of order 0 (see [X]).

It is well-known that any solution φ of problem $\mathcal{P}_\nu$ satisfies the integral representation formula

$$\varphi = \mathcal{S}_\nu^{\partial_n\varphi} + \mathcal{D}_\nu^\varphi \quad \text{in } \Omega, \quad (11)$$

where we denote by $\mathcal{S}_\nu^a$ and $\mathcal{D}_\nu^b$, respectively, the single and double layer surface potentials with density a and b :

$$\mathcal{S}_\nu^a(x) = -\int_\Gamma a(y)\,G_\nu(x,y)\,d\Gamma_y, \quad (12)$$

$$\mathcal{D}_\nu^b(x) = \int_\Gamma b(y)\,\partial_{n_y}G_\nu(x,y)\,d\Gamma_y. \quad (13)$$

As a consequence, if $\Sigma \subset \Omega$ is surface surrounding Γ as shown in Fig. 2, we have

$$Q^\alpha\varphi = Q^\alpha\mathcal{S}_\nu^{\partial_n\varphi} + Q^\alpha\mathcal{D}_\nu^\varphi, \quad \text{on } \Sigma, \quad (14)$$

where Q^α denotes the boundary operator on Σ

$$Q^\alpha\varphi = (\partial_n\varphi + \alpha\,\varphi)_{|\Sigma}, \quad (15)$$

and α is a complex parameter. Note that the two terms in the right-hand side of (14) simply write

$$Q^\alpha\mathcal{S}_\nu^{\partial_n\varphi}(x) = \int_\Gamma \partial_n\varphi(y)\,Q^\alpha G_\nu(x,y)\,d\Gamma_y,$$

$$Q^\alpha\mathcal{D}_\nu^\varphi(x) = \int_\Gamma \varphi(y)\,\partial_{n_y}(Q^\alpha G_\nu(x,y))\,d\Gamma_y,$$

since Γ and Σ have no point in common : $G_\nu(x,y)$ is thus a regular function, which justifies the permutation of the integral sign with Q^α.

Consider then the bounded domain $\hat{\Omega} \subset \Omega$ located between Γ and Σ, and let $\hat{S}$ denote the part of S contained in the boundary of $\hat{\Omega}$ (see Fig. 2). Property (14) together with Eqs. (1) to (6) of $\mathcal{P}_\nu$ clearly show that the pair $(\varphi_{|\hat{\Omega}}, u)$ (where $\varphi_{|\hat{\Omega}}$ denote the restriction of φ to $\hat{\Omega}$) is a solution of the following problem, denoted by $\hat{\mathcal{P}}_\nu$ in the sequel :

$$\Delta\hat{\varphi} = 0 \quad \text{in } \hat{\Omega},$$
$$\partial_n\hat{\varphi} - \nu\,\hat{\varphi} = 0 \quad \text{on } \hat{S},$$
$$\nu\rho\,\hat{u}_i + \partial_{x_j}\sigma_{ij}(\hat{u}) = 0 \quad \text{in } B,$$
$$\sigma_{ij}(\hat{u})\,n_j = 0 \quad \text{on } \Gamma_0, \quad (16)$$
$$\sqrt{\nu}\,\hat{u}.n - \partial_n\hat{\varphi} = f \quad \text{on } \Gamma,$$
$$\sigma_{ij}(\hat{u})\,n_j - \sqrt{\nu}\,\hat{\varphi}\,n_i = g_i \quad \text{on } \Gamma,$$
$$Q^\alpha\hat{\varphi} = Q^\alpha\mathcal{S}_\nu^{\partial_n\hat{\varphi}} + Q^\alpha\mathcal{D}_\nu^{\hat{\varphi}}, \quad \text{on } \Sigma.$$

Figure 2: The bounded domain.
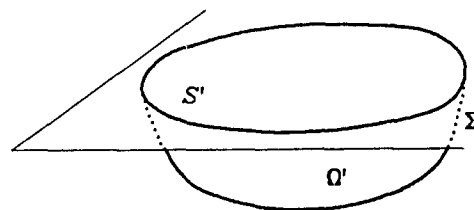
Figure 3: The auxiliary problem.

The point is to prove that for a suitable choice of the parameter α, every solution of this latter problem leads to a solution of $\mathcal{P}_\nu$ by extending $\hat{\varphi}$ outside $\hat{\Omega}$. Using the method described by Jami and Lenoir [8], it may be easily seen that if $(\hat{\varphi}, \hat{u})$ is a solution of $\hat{\mathcal{P}}_\nu$ and if the parameter α has a nonzero imaginary part, then the pair

$$\left(\mathcal{S}_\nu^{\partial_n\hat{\varphi}} + \mathcal{D}_\nu^{\hat{\varphi}}, \hat{u}\right)$$

is a solution of the initial problem $\mathcal{P}_\nu$. More precisely, this result holds provided that α and ν are chosen such that the following auxiliary problem has no solution but zero :

$$\Delta\psi = 0 \quad \text{in } \Omega',$$
$$\partial_n\psi - \nu\,\psi = 0 \quad \text{on } S', \quad (17)$$
$$Q^\alpha\psi = 0, \quad \text{on } \Sigma,$$

where Ω' denotes the domain located inside Σ when the body is removed, and S' is the part of the free surface contained in its boundary (see Fig. 3). In particular, when α is real, this is a classical eigenvalue problem whose solutions form a sequence of real numbers $(\nu_n;\ n \in \mathcal{N})$ which tends to $+\infty$: these values of ν are referred to as "irregular frequencies". If α has a non-zero imaginary part, these frequencies become complex : they are located in the same half plane ($\mathcal{C}^+$ or

$\mathcal{C}^-$) as α. Indeed, by multiplying Lapace's equation by $\bar{\psi}$, integrating in Ω' and using Green's formula, we obtain

$$\int_{\Omega'} |\nabla \psi|^2 d\Omega' - \nu \int_{S'} |\psi|^2 dS'$$
$$+ \alpha \int_{\Sigma} |\psi|^2 d\Sigma = 0,$$

by virtue of the boundary condition in (17). The imaginary part of this expression must be zero. As a consequence, if $\mathrm{Im}\,\alpha$ and $\mathrm{Im}\,\nu$ have opposite signs, the only solution is $\psi = 0$ (since $\psi = 0$ on S' and Σ implies $\partial_n \psi = 0$ by (17), from which we deduce that ψ vanishes everywhere in Ω'). It follows that there is no irregular frequency in the half plane opposite to α.

In the sequel, we will assume that

$$\mathrm{Im}\,\alpha > 0, \qquad (18)$$

which shows in particular that for every real positive ν, the initial problem $\mathcal{P}_\nu$ and the reduced one $\hat{\mathcal{P}}_\nu$ are equivalent.

2.3 Analytic continuation.

By virtue of the equivalence between $\mathcal{P}_\nu$ and $\hat{\mathcal{P}}_\nu$, the extension of $\mathcal{P}_\nu$ to complex frequencies clearly amounts to extending $\hat{\mathcal{P}}_\nu$: this is of course far easier, for the question of the asymptotic behaviour of φ at infinity has now disappeared (since $\hat{\mathcal{P}}_\nu$ is set in a bounded domain). From Eqs. (16) of $\hat{\mathcal{P}}_\nu$, the only difficulty to construct this extension lies in the Green function G_ν. Vullierme-Ledard [16] has shown that G_ν actually has an analytic continuation in the complex plane where $\nu = 0$ is a logarithmic branch point. This means that G_ν may be extended to an infinite-sheeted Riemann ν-plane. However, from a practical point of view, it is enough to consider an extension of G_ν in a simply connected domain of $\mathcal{C} \setminus \{0\}$, as for instance $\mathcal{C} \setminus \mathcal{R}^-$.

A very simple way to prove this analyticity result (first obtained by Vullierme-Ledard) consists in rewriting the expression (10) of H_ν (involved in the definition (9) of G_ν) in the form of a Cauchy integral. First note that from the Cauchy's integral formula, we know that for a positively oriented circle γ of radius ε, whose interior contains ν but not 0, we have

$$2i\pi \, e^{\nu Z} J_0(\nu R) = \int_\gamma \frac{e^{tZ} J_0(tR)}{t - \nu} dt,$$
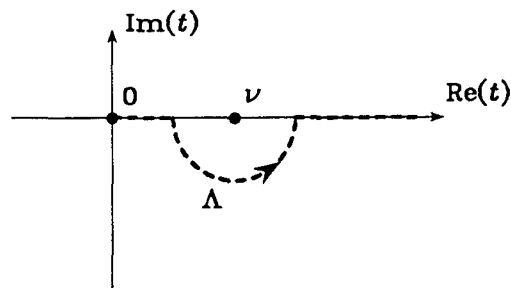
Figure 4: The path Λ for real ν.
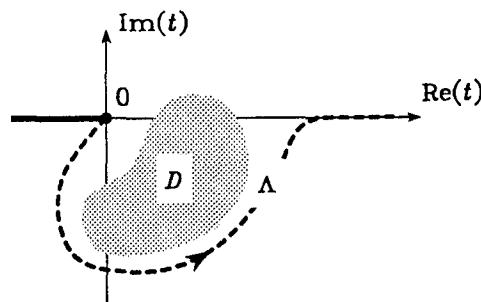
Figure 5: The case of complex ν.

since function $e^{tZ} J_0(tR)$ is analytic (in $\mathcal{C} \setminus \mathcal{R}^-$). From the property

$$e^{\bar{t}Z} J_0(\bar{t}R) = \overline{e^{tZ} J_0(tR)},$$

we deduce

$$\pi \, e^{\nu Z} J_0(\nu R) = \mathfrak{Im} \left\{ \int_{\gamma^-} \frac{e^{tZ} J_0(tR)}{t - \nu} dt \right\},$$

and

$$\mathfrak{Re} \left\{ \int_{\gamma^-} \frac{e^{tZ} J_0(tR)}{t - \nu} dt \right\} \longrightarrow 0, \quad \text{when } \varepsilon \to 0,$$

where γ^- is the part of γ located in $\mathcal{C}^-$. As a consequence, function H_ν may be expressed as follows :

$$H_\nu(R, Z) = 2 \int_\Lambda \frac{e^{tZ} J_0(tR)}{t - \nu} dt, \qquad (19)$$

where Λ denotes a curve in the complex plane such as the one shown in Fig. 4. In fact, we can choose for Λ any curve going from 0 to $+\infty$ which lies below the singular point $t = \nu$.

The analytic continuation of this function does not raise any difficulty. If D is a bounded domain

585

of $\mathcal{C} \setminus \mathcal{R}^-$, we can always find a path Λ which lies below all the points of D (see Fig. 5). For such a path and for fixed R and Z, the integral in (19) defines an analytic function of ν in D (see e.g. Henrici [7]). This is the unique analytic continuation of H_ν in D. The analyticity of the Green function in $\mathcal{C} \setminus \mathcal{R}^-$ follows.

This property allows us to define now problem $\hat{\mathcal{P}}_\nu$ for every $\nu \in \mathcal{C} \setminus \mathcal{R}^-$. The main result concerning this extension of $\hat{\mathcal{P}}_\nu$ lies in the fact that the solution of $\hat{\mathcal{P}}_\nu$ is a meromorphic function of ν. More precisely, if $\hat{S}_\nu$ denotes the solution operator associated with $\hat{\mathcal{P}}_\nu$, i.e., the linear operator which maps the datum (f, g_i) onto the solution $(\hat{\varphi}, \hat{u})$ of $\hat{\mathcal{P}}_\nu$, we have proved that $\hat{S}_\nu$ depends analytically on ν in $\mathcal{C} \setminus \mathcal{R}^-$ except in the vicinity of isolated points which are poles of $\hat{S}_\nu$. This property follows from a theoretical result of Steinberg [15] which concerns the inverse of Fredholm operators (see e.g. [4] for more details). The poles of $\hat{S}_\nu$ are nothing but the values of $\nu \in \mathcal{C} \setminus \mathcal{R}^-$ for which problem $\hat{\mathcal{P}}_\nu$ is ill-posed. In others words, ν is a pole of $\hat{S}_\nu$ if there exists a nonzero pair $(\hat{\varphi}, \hat{u})$ solution of the homogeneous problem associated with $\hat{\mathcal{P}}_\nu$:

$$
\begin{aligned}
\Delta \hat{\varphi} &= 0 \ \text{ in } \hat{\Omega}, \\
\partial_n \hat{\varphi} - \nu \hat{\varphi} &= 0 \ \text{ on } \hat{S}, \\
\nu \rho \hat{u}_i + \partial_{x_j} \sigma_{ij}(\hat{u}) &= 0 \ \text{ in } B, \\
\sigma_{ij}(\hat{u}) \, n_j &= 0 \ \text{ on } \Gamma_0, \\
\sqrt{\nu} \, \hat{u}.n - \partial_n \hat{\varphi} &= 0 \ \text{ on } \Gamma, \\
\sigma_{ij}(\hat{u}) \, n_j - \sqrt{\nu} \, \hat{\varphi} \, n_i &= 0 \ \text{ on } \Gamma, \\
Q^\alpha \hat{\varphi} &= Q^\alpha \mathcal{S}_\nu^{\partial_n \hat{\varphi}} + Q^\alpha \mathcal{D}_\nu^{\hat{\varphi}}, \ \text{ on } \Sigma.
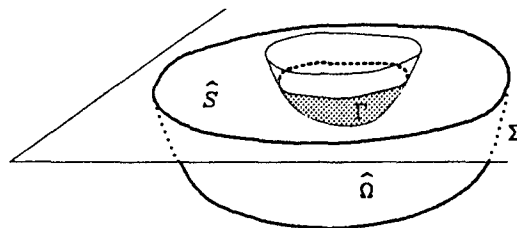\end{aligned}
\tag{20}
$$

Before describing how to compute these poles, let us notice that they can be divided into two families : the irregular frequencies and the scattering frequencies.

- The former family is related to the method which allows us to exhibit the analytic continuation of the initial problem : these are the values of ν for which the reduced problem $\hat{\mathcal{P}}_\nu$ is singular although the initial problem is well-posed. Indeed, it may be easily seen that the solutions of the auxiliary problem (17) are poles of $\hat{S}_\nu$. By virtue of the assumption (18) on the sign of $\mathrm{Im}\,\alpha$, these irregular frequencies are located in the upper complex half plane $\mathcal{C}^+$. They obviously depend on the choice of the boundary Σ, as well as the parameter α, since these are the solutions of (17).

- On the other hand, the scattering frequencies are intrinsic quantities of the system, for they do not depend on the method which allows us to characterize them. They are located either on the real positive axis $\mathcal{R}^+$ or in the lower complex half plane $\mathcal{C}^-$ (since the extension of $\mathcal{P}_\nu$ is well-posed for every $\nu \in \mathcal{C}^+$, see § 2.1).

Of course, among these two families, the scattering frequencies are the poles we are interested to compute.

2.4 Determination of scattering frequencies.

We show in this section that the determination of scattering frequencies amounts to solving a nonlinear eigenvalue problem. Let us first rewrite the homogeneous problem (20) in variational form.

On one hand, multiplying Laplace's equation by a test function $\hat{\psi}$ defined in $\hat{\Omega}$ and integrating by parts leads to

$$
\begin{aligned}
\int_{\hat{\Omega}} \nabla \hat{\varphi} \cdot \overline{\nabla \hat{\psi}} \, d\hat{\Omega} &- \nu \int_{\hat{S}} \hat{\varphi} \, \overline{\hat{\psi}} \, d\hat{S} \\
&- \sqrt{\nu} \int_\Gamma \hat{u} \cdot n \, \overline{\hat{\psi}} \, d\Gamma + \alpha \int_\Sigma \hat{\varphi} \, \overline{\hat{\psi}} \, d\Sigma \quad (21) \\
&- \int_\Sigma \left(Q^\alpha \mathcal{S}_\nu^{\partial_n \hat{\varphi}} + Q^\alpha \mathcal{D}_\nu^{\hat{\varphi}} \right) \overline{\hat{\psi}} \, d\Sigma = 0,
\end{aligned}
$$

by virtue of the boundary conditions on $\hat{S}$, Γ and Σ. On the other hand, multiplying the dynamic equations of the body by a test function $\hat{v} = (\hat{v}_1, \hat{v}_2, \hat{v}_3)$ defined in B yields

$$
\int_B \sum_{ijkh} a_{ijkh} \varepsilon_{kh}(\hat{u}) \, \overline{\varepsilon_{ij}(\hat{v})} \, dB - \nu \int_B \hat{u} \cdot \overline{\hat{v}} \, dB
$$
$$
- \sqrt{\nu} \int_\Gamma \hat{\varphi} \, \overline{\hat{v} \cdot n} \, d\Gamma = 0. \tag{22}
$$

Let $\hat{X}$ (respectively $\hat{Y}$) denote the pair $(\hat{u}, \hat{\varphi})$ (respectively the pair of test functions $(\hat{v}, \hat{\psi})$). Consider then the following sesquilinear forms

$$
m(\hat{X}, \hat{Y}) = \int_{\hat{S}} \hat{\varphi} \, \overline{\hat{\psi}} \, d\hat{S} + \int_B \hat{u} \cdot \overline{\hat{v}} \, dB,
$$

$$
k(\hat{X}, \hat{Y}) = \int_{\hat{\Omega}} \nabla \hat{\varphi} \cdot \overline{\nabla \hat{\psi}} \, d\hat{\Omega}
$$
$$
+ \int_B \sum_{ijkh} a_{ijkh} \varepsilon_{kh}(\hat{u}) \, \overline{\varepsilon_{ij}(\hat{v})} \, dB,
$$

$$c(\hat{X}, \hat{Y}) =$$

$$\int_\Gamma \hat{u} \cdot n \, \overline{\hat{\psi}} \, d\Gamma + \int_\Gamma \hat{\varphi} \, \overline{\hat{v} \cdot n} \, d\Gamma,$$

$$r_\nu(\hat{X}, \hat{Y}) = \alpha \int_\Sigma \hat{\varphi} \, \overline{\hat{\psi}} \, d\Sigma$$

$$- \int_\Sigma \left(Q^\alpha \mathcal{S}_\nu^{\partial_n \hat{\varphi}} + Q^\alpha \mathcal{D}_\nu^{\hat{\varphi}} \right) \overline{\hat{\psi}} \, d\Sigma.$$

The form m represents a mass term, k is a stiffness term, c is a coupling term between the fluid and the structure, and r_ν results from the integral representation formula.

By adding the two variational equations (21) and (22), we finally obtain the variational formulation of the homogeneous problem (20) : a scattering frequencies is a complex value $\nu \in \mathcal{R}^+ \cup \mathcal{C}^-$ such that there exists a non-zero pair $\hat{X} = (\hat{\varphi}, \hat{u})$ which satisfies

$$k(\hat{X}, \hat{Y}) - \sqrt{\nu} \, c(\hat{X}, \hat{Y}) + r_\nu(\hat{X}, \hat{Y})$$
$$= \nu \, m(\hat{X}, \hat{Y}), \qquad (23)$$

for every pair of test functions $\hat{Y} = (\hat{\psi}, \hat{v})$.

This problem may be seen as a nonlinear eigenvalue problem. Indeed, if we denote by $\lambda_k(\nu)$ any eigenvalue of the following (linear) eigenvalue problem

$$k(\hat{X}, \hat{Y}) - \sqrt{\nu} \, c(\hat{X}, \hat{Y}) + r_\nu(\hat{X}, \hat{Y})$$
$$= \lambda_k(\nu) \, m(\hat{X}, \hat{Y}),$$

where ν is considered as a fixed parameter, problem (23) clearly amounts to solving

$$\lambda_k(\nu) = \nu. \qquad (24)$$

This equation is a (nonlinear) fixed point equation (since $\lambda_k(\nu)$ does not depend linearly on ν).

3 Results

3.1 Mélina the finite element code

The numerical results displayed in this paper have been provided by the finite element code Mélina, which has been developped jointly at E.N.S.T.A. and I.R.M.A.R. This fortran code is a library of procedures the most important of which are essentially written to be put together to build straightforwardly a main program to solve P.D.E.'s in either 2 or 3 dimensions. As a matter of fact this set of procedures can be seen as a

rather general toolbox for finite element processing and numerical matrix algebra.

This code has been written as to build easily and quickly a great amount of numerical applications for the solution of P.D.E.'s using a finite element scheme without going through tedious programming. For instance and starting from scratch, the main program and two main procedures which involve the nonlinear computation of 'resonant frequencies' by the secant rule (regula falsi), including the assembly of the matrices of a three-dimensional problem and the computation of eigenvalues using an inverse iteration scheme at each nonlinear iteration, was build in a couple of days by a new user of the code (numerical evaluation of the Green function extended to complex-valued frequency is not included!).

The essential part of the development of such an application of Mélina lies in a direct transcription of a (discretized) variational formulation and the choice of a solving algorithm which in most cases reduces to simple CALL's to the so-called *high level procedures* of the toolbox.

The description of the components of a variational formulation is easily done through the use of a vocabulary of precise keywords. The *sentences* built upon those keywords can be entered either as a data file or as procedure arguments.
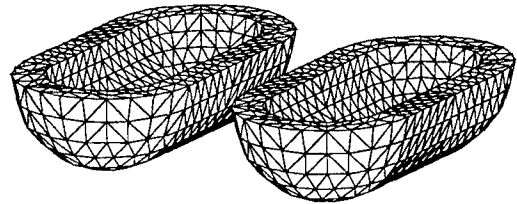
Figure 6: Discretization

Those components or more generally *objects* handled in the code, which are only referred to with their *name*, are closely related (or even symbolically identical) to the entities of the mathematical formulation of the problem. Those objects are for instance (meshed) domains defined in the mesh data file by a name, e.g. 'OMEGA', 'S', 'SIGMA' and associated with a list of elements or element boundaries, integrals terms such as the finite element stiffness matrix corresponding to $\int_{\hat{\Omega}} \nabla \varphi \nabla \psi \, d\omega$ ('RIGID') or the f.e. mass matrix $\int_{\hat{S}} \varphi \psi \, ds$ ('MASS') from equ. 2 of (16), data constants or functions.

With this symbolic representation of data the typical typing of some steps of a solving process reads (though in French!) closely to

- compute f.e. term 'RIGID' on domain 'OMEGA' (with a list of simple attributes, mainly the type of the integrand and quadrature scheme)

- compute f.e. term 'MASS' on domain 'S'

- proceed with the assembly of preconditionning matrix P (with the list of the components of the linear combination)

- proceed with the assembly of the matrix A and if necessary right-hand side b of the linear system

- solve system $Ax = b$ by conjugate gradient preconditionned by matrix P, or compute generalized eigenvalues for $A(\nu)x = \lambda(\nu)Bx$

As the toolbox is mainly used at E.N.S.T.A. for solving wave propagation problems in unbounded domains, two specific tools for their solution have been developped: the computation of the coupling integral terms of the method of coupling of finite element and integral representation [5] and the boundary terms of the localized finite element method (see e.g. [4] in the 2-D case). Moreover as the formulations of those methods generally lead to non-symmetric linear systems with complex coefficients, efficient iterative gradient methods such as the (preconditionned) biconjugate gradient or conjugate gradient squared are available from the toolbox as *high level procedures* (the arguments of which are essentially the names of the matrice(s), right-hand side and solution vectors).

The field of applications which have been developped with Mélina encompasses many wave propagation phenomena such as those involving gravity waves (sea-keeping or wave resistance problems in ship hydrodynamics), acoustic waves (Helmholtz' equation and the like), optical wave guides (or integrated optics problems) and more generally electromagnetic wave problems (Maxwell's equation). A complete description of this finite element code and worked out examples of applications can be found in great details in [3].

3.2 Computional aspects of Green function evaluation

Under the form given in (19) H_ν is not well suited for computational efficiency, we thus give below

the two main expressions we have used for practical implementation of the Green function in the complex domain of frequency ν; similar expressions can be obtained easily for the derivatives of H_ν which are required in the computation of the 'coupling' terms of (21) or discretized sesquilinear form r_ν in (23) (see other expressions in the real positive domain of ν's in [13]).

Using the following integral definition of Bessel first kind function: $J_0(z) = \frac{1}{\pi}\int_0^\pi e^{iz\cos\theta}\, d\theta$, function H_ν (19) can be written as the double integral

$$H_\nu(R,Z) = \frac{2}{\pi}\int_\Lambda\int_0^\pi \frac{e^{\nu Z + i\nu R\cos\theta}}{t - \nu}\, d\theta\, dt\ .$$

After a change of variables of integration and with help of formula $\int_0^\pi (a + ib\cos\theta)^{-1}d\theta = \pi(a^2 + b^2)^{-1/2}$, which holds for any complex a and b with $a^2 + b^2 > 0$, and with the following relation between Bessel second kind function Y_0 and Struve function H_0 ([1] chap. 12):

$$\frac{2}{\pi}\int_0^\infty e^{-zt}(1 + t^2)^{-\frac{1}{2}}dt = H_0(z) - Y_0(z)$$

we get the first expression for H_ν:

$$H_\nu(R,Z) = -2\int_0^{-Z} e^{-\nu t}\big((t+Z)^2 + R^2\big)^{-\frac{1}{2}}dt$$
$$+ \frac{\pi}{2}e^{\nu Z}\big(H_0(\nu R) - Y_0(\nu R) - 2iJ_0(\nu R)\big)\quad (25)$$

which is well suited on the computational point of view for non vanishing R (or practically for a not too large $-Z$ to R ratio).

Another formula for H_ν is obtained by performing the change of integrals in the double integral formula:

$$H_\nu(R,Z) = \frac{2}{\pi}\int_0^\pi e^{\nu q(\theta)}E_1(\nu q(\theta))\, d\theta \quad (26)$$

with $q(\theta) = Z + iR\cos\theta$ and where $E_1(z) = \int_{\Gamma_z} t^{-1}e^{-t}$ is the complex integral exponential function ([1] chap. 5) with a cut in the complex plane along the real positive axis and with a path of integration Γ_z which is any curve starting from z, with Re $z \le 0$, going to $+\infty$ and lying below the origin. This latter formula is used for non vanishing Z (or a rather large $-Z$ to R ratio).

The integrals of expressions (25) and (26) are evaluated using Simpson's quadrature rule. Bessel functions $J_{0(1)}$ and $Y_{0(1)}$ with complex arguments where computed by ascending series [1], rational approximations or Hankel's asymptotic expansions [1] according to the magnitude of their complex argument. Struve functions $H_{0(1)}$ was computed by ascending series [1] or rational approximations found in [12]. A few numerical tests

show that the criterium for switching from expression (25) to expression (26) of H_ν, either for computional accuracy or for time-consuming considerations, is the crossing of the line $-Z = 10 \times R$ of the real (R, Z)–plane.
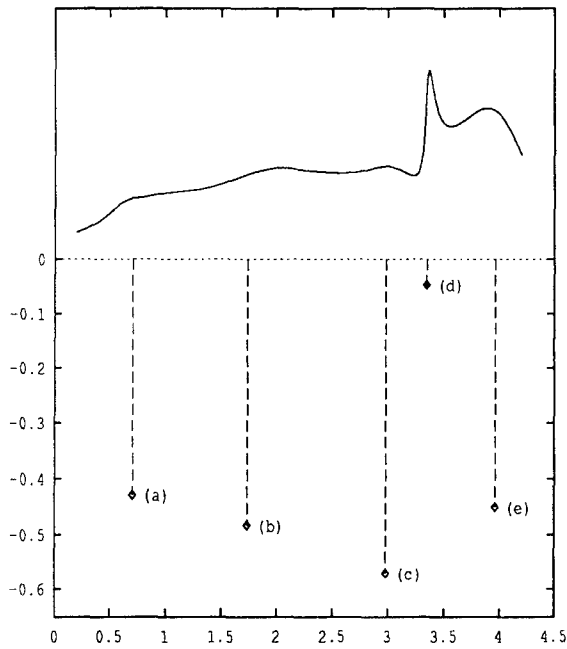
Figure 7: Symmetrical excitation
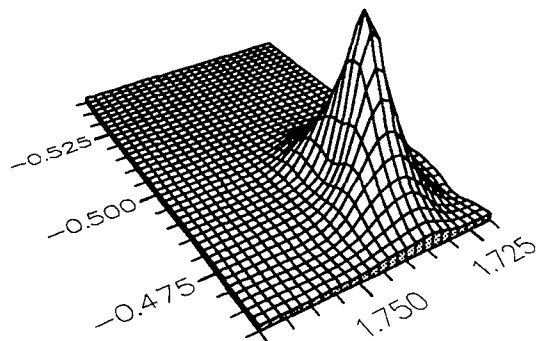
Figure 8: Vicinity of a scattering frequency : symmetrical case

3.3 Numerical experiments

The numerical results given below correspond to the excitation of a two-hull body ('catamaran') floating on an infinitely deep ocean by an incident time-harmonic swell. The non-dimensionnal data of the body as shown on Figure 6 are respectively

2.5 for length and 1. for width and depth of each hull; the hull are 1. apart in the transverse direction. Figures 7 and 9 show response curves of the body, i.e. the total energy transmitted to the body with respects to the real frequency squared (ν). The upper part of figure 7 shows the en-
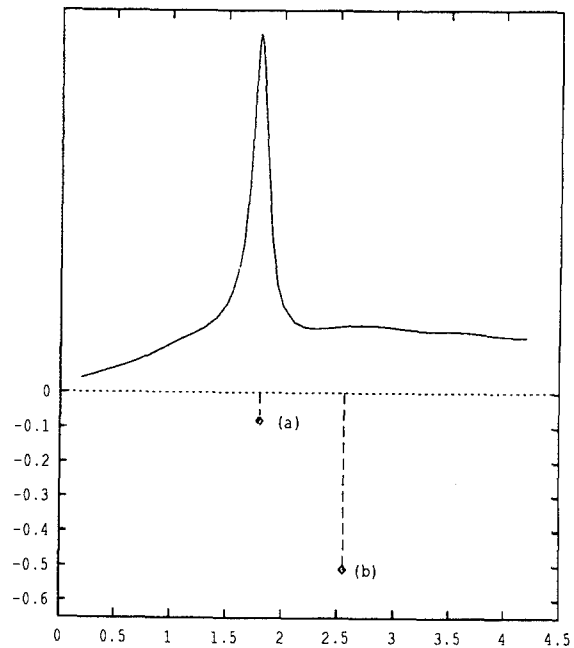
Figure 9: Antisymmetric excitation
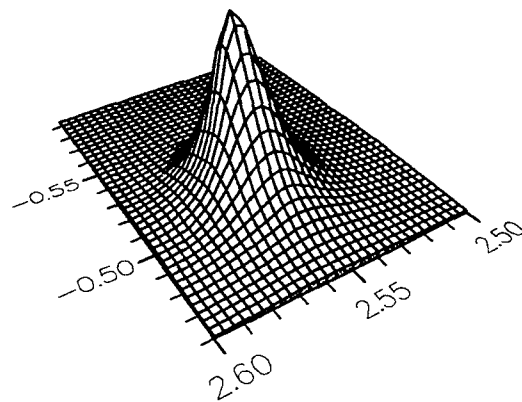
Figure 10: Vicinity of a scattering frequency : antisymmetric case

ergy response curve to an incident swell of the form $\varphi_w(x, y, z) = e^{\nu(z+ix)}$ symmetrized with respect to the vertical planes of coordinates. On the lower part of this figure the scattering frequencies (ν^*) are displayed. As one can see their locations in the direction of $\mathrm{Re}(\nu)$'s are in good agreement with the peaks and bumps of the re-

589

sponse curve, with a shift along the direction of $\text{Re}(\nu)$'s which is predicted by theory as being of order of $(\text{Im}(\nu^*))^2$ [6]. Moreover as is as well shown by theoretical calculations, when considering the expansion of the solution in the vicinity of a given ν^*, the smaller the imaginary part of $\text{Im}(\nu^*)$, the higher and sharper the peak or bump of the response curve. An analogous phenomenon is illustrated on Figure 9, where the energy curve corresponds to an incident swell which is antisymmetric with respect to the transverse direction of the body. Finally on figure 8 (resp. 10), we give the response surface over a complex domain of ν's in the vicinity of the scattering frequency (b) of figure 7 (resp.8). One can easily observe the location of the pole located at (b) of the analytic continuation in C^- as a meromorphic function of ν of the approximated resolvent operator.

References

[1] M. ABRAMOWITZ AND I.A. STEGUN. *Handbook of mathematical functions*. Dover, New York, 1976.

[2] A. CLÉMENT. *Optimisation du calcul de la fonction de Green de la tenue à la mer en profondeur infinie*. Rapport de Recherche N° 165, ENSTA, Palaiseau, France, 1982.

[3] O. DEBAYSER AND D.MARTIN. *Mélina, un code d'éléments finis pour les problèmes extérieurs: application à l'hydrodynamique navale*. In *91ème session de l'ATMA*, Paris, Mars 1991.

[4] C. HAZARD. *Etude des résonances pour le problème linéarisé des mouvements d'un navire sur la houle*. PhD thesis, Université Pierre et Marie Curie, Paris, 1991.

[5] C. HAZARD AND M. LENOIR. *Determination of scattering frequencies for an elastic floating body*. SIAM J. Math. Anal., 24, pp. 1458–1514, 1993.

[6] C. HAZARD, M. LENOIR, AND D. MARTIN. *Integral representation of resonant states*. in preparation.

[7] P. HENRICI. *Applied and computational complex analysis (3 vol.)*. Wiley, New York, 1974.

[8] A. JAMI AND M. LENOIR. *A variational formulation for exterior problems in linear hydrodynamics*. Comp. Meth. Appl. Mech. Eng., 16, pp. 341–359, 1978.

[9] F. JOHN. *On the motion of floating bodies - I*. Comm. Pure Appl. Math., 2, pp. 13–57, 1949.

[10] M. LENOIR AND D. MARTIN. *An application of the limiting absorption principle to the motion of floating bodies*. J. Math. Anal. Appl., 79, pp. 370–383, 1981.

[11] M. LENOIR, M. VULLIERME-LEDARD, AND C. HAZARD. *Variational formulations for the determination of resonant states in scattering problems*. SIAM J. Math. Anal., 23, pp. 579–608, 1992.

[12] Y.L. LUKE. *Mathematical functions and their approximations*. Academic Press, New-York, 1975.

[13] D. MARTIN. *Etude théorique et numérique du problème linéarisé du mouvement sur la houle tridimensionnel*. PhD thesis, Université de Rennes, France, 1980.

[14] J. NECAS AND I. HLAVÁČEK. *Mathematical theory of elastic and elasto-plastic bodies*. Elsevier, Amsterdam, 1981.

[15] S. STEINBERG. *Meromorphic families of compact operators*. Arch. Rational Mech. Anal, 31, 1968.

[16] M. VULLIERME-LEDARD. *Problèmes asymptotiques de l'hydrodynamique navale linéarisée et du couplage fluide-structure*. PhD thesis, Université Pierre et Marie Curie, Paris, 1987.

[17] J.V. WEHAUSEN AND E.V. LAITONE. *Surface waves, in Encyclopedia of Physics*. Volume 9, Springer Verlag, 1960.

[18] X.J. WU, Y. WANG, AND W.G. PRICE. *Multiple resonances, responses, and parametric instabilities in offshore structures*. Journal of Ship Research, 32, No. 4, pp. 91–93, 1988.

Prediction of Nonlinear Hydrodynamic Characteristics of Complex Vessels Using a Numerical Time-Domain Approach

B. Maskew, D.M. Tidd, and J.S. Fraser
(Analytical Methods, Inc., USA)

ABSTRACT

A general purpose numerical flow simulation method is being developed for treating complex hydrodynamic problems associated with arbitrary vessels advancing in large amplitude waves. The objective is to treat conditions experienced by modern high performance vessels that are beyond the scope of traditional linearized approaches.

The method uses a non-linear boundary element approach which treats the free surface deformation and finite amplitude vessel motions in a time-stepping procedure. Boundary layer effects and lifting effects are included in the calculations. The code computes *total* force and moment at each time-step by surface integration of pressure and skin friction loads. Body movement from step to step is computed by direct integration of the equations of motion.

Computed results for pitch and heave transfer functions compare very favorably with measured data for the ITTC S175 standard hull form and for a frigate advancing in head waves. The frigate case includes conditions of green water on the deck.

NOMENCLATURE

Cp	Pressure coefficient $(p - p_{REF})/(1/2\ \rho V_{REF}^2)$
dS	Element of surface
Fr	Froude number, $V_{REF}/\sqrt{gL}$
g	Acceleration due to gravity
L	Hull length
NH	Number of active (wetted) panels on the surfaces

NPAN	Total number of active panels on the free surface and hull(s)
$\vec{n}$	Unit normal to the surface pointing into fluid domain
p	Static pressure
p_{REF}	Ambient atmospheric pressure
$\vec{r}$	Position vector in normalized space
L_{REF}	Reference length, L/2
t	Time
$\vec{v}$	Normalized perturbation velocity, $\vec{v}/V_{REF} = -\nabla\phi$
$\vec{V}$	Perturbation velocity, $-\nabla\Phi$
V_{REF}	Reference speed
x,y,z	Normalized Cartesian coordinates, $x = X/L_{REF}$, etc.
X,Y,Z	Cartesian coordinates, dimensional
s	Surface distance (normalized)
μ	Doublet density, $\phi/4\pi$
σ	Source density, $- (\partial\phi/\partial n)/4\pi$
τ	Normalized time, $t \cdot V_{REF}/L_{REF}$
ρ	Water density
ϕ	Normalized velocity potential, $\Phi/L_{REF}/V_{REF}$
Φ	Velocity potential (units of length^2/time)
$\vec{\Omega}$	Angular velocity (normalized by V_{REF}/L_{REF})
λ	Wave length (dimensional)

INTRODUCTION

Although methods for analyzing ship hydrodynamic characteristics have progressed significantly in recent years, the theoretical prediction of motions of general, complex vessels proceeding in large amplitude waves is still a challenging problem (1). Strip theory, applied initially by Korvin-Kroukovsky (2) and developed further by Ogilvie and Tuck (3), Salveson et al (4), Kim et al (5), among others, is

probably the most accepted, practical tool for predicting motions and sea loads at this time. Even though they are based on linearized assumptions, strip theory methods have been used to analyze non-linear effects (e.g., Chiu and Fujino (6) and Fang et al (7)); however, such applications are questionable, especially when dealing with large amplitude waves and large amplitude motions of general hull forms with possible conditions for slamming and green water on the deck. Also, the inherent difficulties of accounting for the interaction of steady and unsteady flow components in a consistent manner cannot be readily overcome for conditions at high Froude numbers or on hulls with non-vertical sides at the waterline.

Recent developments based on the three-dimensional Rankine panel method offer a potential improvement relative to the traditional strip theory approach. These developments include both frequency domain methods, e.g., Nakos & Sclavounos (8) and also time-domain approaches, for example, King, Beck and Magee (9), Lin and Yue (10), Nakos, Kring and Sclavounos (11). These methods employ body "exact" boundary conditions on the hull, but retain the linearized free surface boundary condition and therefore might miss important effects at the hull/water intersection line due to body flare, body motion, and the dynamic rise and fall of the water surface. Powlowski and Bass (12) presented a practical method for treating large amplitude ship motions in heavy seas. This uses a method of modal potentials and is based on a weak scatter hypothesis. The time-domain calculations use a set of model amplitudes which must be predetermined for each vessel and load condition.

The present work is part of an ongoing development towards a more general capability for complex vessels in large amplitude motions for which linearizing assumptions are inadequate. The basic method is the USAERO time-dependent code (13) which is a low-order boundary element method employing quadrilateral panels of uniform perturbation doublets and sources. The method includes a powerful geometry module with a number of convenient surface modeling features to help with complex paneling problems. Multiple moving frames of reference (user-defined) allow complicated relative motion problems to be treated, including control deflections, etc. The method includes dynamic vortex wake convection for lifting effects and certain extensive separated flow modeling. Routines developed by Dvorak (14) treat unsteady boundary layer characteristics, e.g., displacement effect and skin friction; these are fully coupled within the time-step loop and are driven by the instantaneous surface flow properties. The computed characteristics for boundary layer displacement effect modify the surface boundary condition in the following panel code solution, while the skin friction distribution contributes to the computed force and moment in the next step.

The method was extended for surface piercing vessels with a non-linear treatment of a piece of the free surface in the FSP module (15) (for Free-Surface Program). This applies the kinematic and dynamic boundary conditions on the wavy free surface, using a mixed Eulerian/Lagrangian formulation based on the work of Longuet-Higgens & Cokelet (16). The FSP module addresses the problem of free surface/hull interaction using an automatic repanelling procedure whose purpose is to maintain a "clean" panelling arrangement along the intersection line as the free surface moves relative to the vessel. Although the code can be used to evaluate added mass and damping terms for arbitrary vessels in general forced harmonic motion, the objective behind its development is the step-by-step integration of the equations of motion driven by instantaneous force and moment values.

A wave generator based on a harmonically oscillating velocity potential was added to the upstream "edge" of the free surface (17). This produces a train of incident waves for a moving vessel in a towing tank simulation. Preliminary results for large amplitude motions were presented earlier (18) at the start of a non-linear seakeeping investigation in which the 6 D.O.F., FPI module (19) (for Flight Path Integrator), is coupled with USAERO/FSP. This combined code is also being examined for maneuvering vessels in or near the free surface. Recently, a further extension added the capability for aero-elastic treatment of yacht sails and simultaneous Wind Over Water (WOW) aero/hydrodynamic analysis of complete sailing yachts (20).

The present paper gives further results from the non-linear seakeeping investigation of the coupled USAERO/FSP/FPI code. Calculations are compared with measured data for a frigate model in steep waves (21) and for the S175 ITTC standard container ship model (22). The method is covered in broad outline here as it is described more fully in earlier papers (17, 18). Recent developments include coupling with an "order (N)" iterative solver (23) which has significantly reduced computational

time and storage requirements, thereby removing earlier objections of excessive computational requirements for non-linear time-dependent analyses.

NUMERICAL MODEL

The main features of the numerical model are given below for completeness. A more detailed description of the formulation is included in Ref. 18.

The basis of the model is a time-stepping, boundary element formulation with coupled, unsteady, surface boundary layer analysis. The model includes a nonlinear dynamic treatment of the wake convection and free surface deformation. Body movements are treated step-by-step using a 6 degree-of-freedom (DOF) integration of the equations of motion driven by instantaneous computed forces and moments.

The basic problem to be treated consists of an arbitrary vessel undergoing large amplitude motions in or near the free surface. For generality, the vessel may have fixed or moveable lifting hydrofoils, control surfaces and propulsors. The flow region may extend to infinity or it may be bounded locally in towing tank or canal simulations or in shallow water. The vessel is assigned to a moving-body reference frame whose time-dependent location/orientation is described in a ground-fixed inertial Cartesian coordinate system. This has the X and Y axes in the undisturbed free surface and Z positive upwards, Fig. 1. The fluid motion is assumed to be described by a velocity potential, $\Phi(\vec{R}, t)$ which satisfies Laplace's equation,

$$\nabla^2 \Phi = 0 \qquad (1)$$

Traditionally, Φ is broken down into a number of component parts to aid in the linearizing of boundary conditions. Here, however, no linearizing assumptions are made, so Φ is left as a whole quantity and therefore encompasses such terms as incident wave potential, diffraction potential, radiation potential, etc. The convention adopted here is that the fluid velocity, $\vec{V}$, is the *negative* gradient of the potential, i.e.,

$$\vec{V} = - \nabla \Phi \qquad (2)$$

It is convenient to non-dimensionalize the problem with respect to certain reference quantities. A ref-

erence length, L_{REF} is used to non-dimensionalize the geometry and a reference speed, V_{REF}, is used to non-dimensionalize velocities. (L_{REF} is usually chosen as half the hull length, L, and V_{REF} is the mean speed of the vessel relative to the water.) In non-dimensional space, therefore, we have the quantities,

$$\vec{v} = \vec{V}/V_{REF};$$

$$\phi = \Phi/L_{REF}/V_{REF};$$

$$\tau = t \cdot V_{REF}/L_{REF};$$

$$x = X/L_{REF}, \text{ etc.}$$

The potential flow is solved using Green's Theorem, which is discretized into a surface panel method based on quadrilaterals of uniform source and doublet singularities. This forms a set of simultaneous equations:

$$\sum_{K=1}^{NH} \mu_K C_{JK}$$

$$+ \sum_{K=NH+1}^{NPAN} \sigma_K B_{JK} + E_{JK} = 0 ; \quad J=1,NPAN \qquad (3)$$

where

$$C_{JJ} = -2\pi ,$$

$$E_{JK} = \sum_{K=1}^{NH} \sigma_K B_{JK} + \sum_{K=NH+1}^{NPAN} \mu_K C_{JK}$$

$$+ \sum_{K=1}^{NWS} \mu_{W_K} D_{JK}$$

μ_K, σ_K are the doublet and source densities, respectively, on panel K.

C_{JK}, B_{JK} are the influence coefficients, respectively, for the uniform doublet and source on panel K acting at the control point of panel J (C_{JK} and B_{JK} are given in Maskew (24).

NH is the number of active (i.e., wet) panels on the hull surfaces.

NPAN is the *total* number of active panels on all local wetted surfaces, including the free surface. *NWS* is the total number of free, cross-flow wake segments; this number grows with time. μ_{WK} is the

doublet density at the Kth wake segment, and D_{JK} is the influence coefficient for the linearly varying strength distribution over the pair of wake panels just upstream and just downstream of the segment. The influences of the wake segments that are about to be created at the shedding lines are combined with the local upper and lower shedding panel influences in the first term of Eq. (3) since these segment strengths are unknown at the start of each step. Some influence coefficients have to be re- evaluated at each time step—these include all wake panels, moving free-surface panels, and any hull panels which have relative motion with other hull panels or which have been modified by the repanelling procedure.

On the boundaries representing the "solid" surfaces, the source distribution is determined by the external Neumann Boundary Condition specifying the resultant normal velocity of the fluid.

$$\sigma = \frac{\left(v_{NORM} + v_{BL} + \vec{n} \cdot \vec{v}_b + \vec{\Omega} \cdot \vec{r} \times \vec{n} - \vec{n} \cdot \vec{v}_\infty\right)}{4\pi} \quad (4)$$

where v_{NORM} is the required resultant normal velocity, which is zero for a solid boundary and positive or negative, respectively, for outflow/inflow in propulsor modeling. v_{BL} is the boundary layer displacement effect using the transpiration technique,

$$v_{BL} = \frac{\partial}{\partial s}\left(v_e \delta^*\right) \quad (5)$$

where v_e is the relative flow speed at the edge of the boundary layer and δ^* is the displacement thickness. The derivative is taken with respect to distance in the direction of the local external flow. v_{BL} is zero for stationary boundaries and would be known from the previous step in a time-stepping calculation. $\vec{v}_b(\tau)$ is the body frame velocity and $\vec{\Omega}(\tau)$ is the velocity of rotation about an axis in the body frame. Here, $\vec{r}$ is the position vector of the point in question relative to any point on the rotation axis. $\vec{n}$ is the unit normal to the surface, and $\vec{V}_\infty$ is a possible uniform onset flow. The basic unknown on solid boundaries, therefore, is the doublet term which can be obtained from the solution of Eq. (3) at each step.

The wake doublet distribution, μ_W, is essentially known at each step because it is the accumulation of all previous solutions. Basically, at each step a new set of wake elements is created along wake-shedding lines. Each element takes the instanta-

neous local jump in potential across the shedding line and moves along the local mean velocity vector. This satisfies the unsteady Kutta condition, which is obtained after specifying equal pressure across the separation line,

$$\left(\frac{\partial \mu_W}{\partial \tau}\right) + v_M \left(\frac{\partial \mu_W}{\partial s}\right) = 0 \quad (6)$$

v_M is the mean convection speed and s is measured in the direction of the local mean flow. μ_W is the instantaneous jump in doublet strength across the trailing edge, i.e., μ_W is the newly emerging wake strength.

On the free surface, the initial boundary conditions are that the ϕ and $\partial\phi/\partial n$ (i.e., μ and σ) are zero, and that the pressure is uniform ($Cp = 0$). The ambient pressure is assumed to be transferred directly to the fluid across the free surface, i.e., the effect of surface tension is neglected at this time. The kinematic condition on the free surface is satisfied by moving the particles with the local flow,

$$\frac{d\vec{r}}{d\tau} = \vec{v} \quad (7)$$

Following a particle, the total derivative of ϕ is (from Bernoulli's equation)

$$\frac{d\phi}{d\tau} = \left(\frac{z}{Fr^2} - v^2\right)/2 \quad (8)$$

Assuming for the moment that the free surface displacement z and perturbation velocity $\vec{v}$ are known from the previous step, Eq. (8) can be integrated over a small time step to evaluate the current doublet distribution on the free surface. Given this, Eq. (3) can then be solved for the source distribution, (i.e., $\partial\phi/\partial n$), on the free surface. This, together with the doublet gradient, provides the instantaneous perturbation velocity in Eq. (7). Integrating Eq. (7) then provides the free surface displacement for the next step, and so on.

In summary, the simultaneous solution of Eq. (3) on the instantaneous locations of the free surface and hull configuration at each time step provides the complete doublet and source distributions. Basically, on the hull the source is known and the doublet is unknown, while on the free surface the doublet is known and the source is unknown. On

594

the wake surfaces, the doublet is essentially known and the source is zero.

After solution of the singularity values, the perturbation velocities can be evaluated directly on each panel:

$$\vec{v} = v_N \vec{n} + \vec{v}_T \qquad (9)$$

The normal component, v_N, is obtained directly from the panel source value,

$$v_N = 4\pi\sigma \qquad (10)$$

The tangential component, $\vec{v}_T$, is obtained from the surface gradient of the doublet,

$$\vec{v}_T = -4\pi\nabla\mu \qquad (11)$$

The doublet gradient is evaluated in two directions over each panel using a second-order differencing scheme over three panels in each direction. On the "solid" boundaries, the perturbation velocity is combined with the local velocity, $\vec{v}_s$, due to body motion to give the resultant velocity,

$$\vec{v}_R = \vec{v} - \vec{v}_s$$

Bernoulli's equation then provides the pressure distribution. This may be written in the form of a pressure coefficient using the non-dimensional quantities.

$$Cp = \frac{P - P_{REF}}{1/2\,p\,V_{REF}^2} = -v^2 - \frac{z}{Fr^2} + 2\frac{\partial\phi}{\partial\tau} \quad (12)$$

Where p is the local static pressure, p_{REF} is the reference pressure, which is taken here as the ambient atmospheric value. ρ is the water density (constant). z is the height *above* the undisturbed free surface and F_r represents the Froude number, $V_{REF}/\sqrt{gL}$ where g is the acceleration due to gravity. The z/Fr^2 term represents the hydrostatic pressure coefficient.

Eq.(12) gives the pressure coefficient at a stationary point in the ground fixed frame; the pressure observed at a point moving with velocity, $\vec{v}_s$, relative to the ground-fixed frame is,

$$Cp = v_s^2 - v_R^2 - \frac{z}{Fr^2} + 2\frac{d\phi}{d\tau} \qquad (13)$$

where v_R is the fluid velocity relative to the moving point and $d\phi/d\tau$ is the *total* derivative of ϕ experienced by the moving point.

The pressure coefficient, *Eq.(13)*, can be evaluated at each panel center. The $d\phi/d\tau$ term is evaluated using second-order forward differencing based on the current and two previous solutions.

The pressure distributions can be integrated over the surface of each part of the configurations to provide the force coefficient,

$$\vec{C}_F = -\iint_S \left(Cp\vec{n} - C_f\vec{V}_R|\vec{V}_R|\right)dS \qquad (14)$$

and moment coefficient,

$$\vec{C}_M = \iint_S \left(Cp\vec{n} - C_f\vec{V}_R|\vec{V}_R|\right) \times \vec{r}\, dS \qquad (15)$$

where $\vec{r}$ is the position vector of a surface element relative to a selected moment reference point, and C_f is the skin friction coefficient from a boundary layer analysis based on the current surface velocity distribution.

The above coefficients are based on an area of L_{REF}^2 and a moment arm divided by L_{REF}. They include the effect of hydrostatic pressure (the z/Fr^2 term in *Eq.(13)*), and therefore include the buoyancy force and moment. The 6 DOF response of the vessel to free-surface deformation can therefore be computed by integrating the equations of motion over each time step.

The wetted surfaces of surface-piercing objects, hulls, channel walls, etc. are modified by the deforming free surface and by the movement of the vessel. These effects are accounted for in the numerical treatment of the model.

NUMERICAL PROCEDURE

A brief outline of the numerical procedure is given below; a more detailed account of the basic method is given in Ref. 18. Referring to the numbered steps in the flow chart in Fig. 2.

1. Discretization of the configuration surface into a panel model with uniform source and doublet distributions on quadrilateral panels is fairly standard, except that automatic proce dures distribute the panels over user-defined

patches which may be assigned to various moving frames of reference. Motion/orientation schedules versus time may be defined for each frame by the user.

2. At the outset of a time step the current panel geometry is assembled in the ground-fixed frame based on the instantaneous location/orientation of the various reference frames used in the current configuration.

3. An automatic routine then identifies the instantaneous lines of intersection where the free surface meets the hull(s), and repanels both the hull and free surfaces to the intersection line to ensure a smooth matching of panels at the critical junction. During the process, panels are marked as either "wet" or "dry". Dry panels are temporarily discarded from the current solution process. Another intersection routine monitors vortex wake impingements at solid surfaces and ensures that active wake elements do not arrive *inside* the body regions; this would violate the basic Dirichlet boundary condition of zero flow perturbation inside the bodies.

4. Influence coefficients are assembled for panels acting on collocation points. Solution of the singularities proceeds as follows: the wet panels are assembled and a solution of *Eq. (3)* is processed. On the hull panels the doublet values are the unknown, while the source values are evaluated using the expression in *Eq. (4)*. On the free surface panels, the doublet values are known from the previous time step and the source values are unknown. When the solution has been obtained, the free-surface source distribution provides the normal velocity of the free surface, which is used later (in step 8) when satisfying the kinematic boundary condition on the free surface. Whereas in the earlier calculation (17, 18) several hours of computer time were required to run a wave tank simulation, recent advances in fast iterative solvers have given more than an order of magnitude speed up. Most of the cases reported herein were run using the MIT Fastlap (23) solver, which has now been coupled to USAERO.

5. With the complete set of panel singularities known, the analysis proceeds as follows. First, a two-way derivative of the surface doublet distribution provides the perturbation velocities and, hence, pressures on all surfaces—hull, keel, rudder and free surface. The unsteady pressure term in *Eq. (13)* is evaluated by a second-order finite difference of the doublet values with respect to time. The instantaneous pressure distribution is integrated over each "solid" surface to provide the current force and moment vectors and their spatial distributions. The computed data is stored step-by-step in a plot file for subsequent post processing and graphical display.

6. Instantaneous surface streamlines are traced over the hull, keel, rudder, etc.; unsteady integral boundary layer calculations then provide boundary layer characteristics, such as displacement source term and skin friction coefficient, for the next step. The former modifies the boundary conditions (*Eq. (3)*), while the latter is included in the force and moment integration, *Eqs. (14, 15)*.

7. Wake elements are convected with the local computed flow for the small time step. The local perturbation velocities are evaluated by summing all panel (surface plus wake) singularity contributions. These are added to the appropriate onset flow. A new set of wake panels is constructed along the wake shedding lines at each step according to the local Kutta condition, *Eq. (6)*.

8. The free surface is treated as follows. First the kinematic boundary condition is satisfied by integrating *Eq. (7)* over the small time step. This provides the free surface geometry for the next time step. The new doublet distribution is evaluated by integrating *Eq. (8)* over the small time step. An oscillating potential is applied on the upstream strip of panels which acts as a wave generator.

9. The integrated force and moment values assembled for the body reference frame are transferred to the 6-DOF FPI module. The 6 DOF module solves the equations of motion for a rigid body, assuming that the mass of the body and the mass distribution are constant over time. The 6 DOF module is activated once the force/moment characteristics on the vessel have stabilized, which typically only takes a few time steps to achieve. The starting point is to calculate the hydrodynamic forces and moments acting on the vessel from the coefficients calculated by USAERO/FSP. The external forces such as thrust or gravity are then added to these. Given the force/moments, the nonlinear equations of motion

can be solved for the accelerations, based on computed velocities at the previous timestep. Next, the velocities in the body axes system are updated, based upon known accelerations at the present timestep. This is done using a simple Euler scheme for the calculations described in this paper. Higher order Adams-Bashforth multi-step methods using additional accelerations from previous timesteps have not currently been found to be advantageous. From the velocities, a new orientation of the body in terms of Euler angles can be calculated using a transformation and a further call to the integration scheme. Similarly, the new position of the body relative to the ground-fixed coordinate system can be obtained with a transformation and a final call to the integrator. The new position and orientation of the body is then passed back to USAERO for a revised calculation of the hydrodynamic force/moment data to continue the time-stepping loop of the procedure.

RESULTS

Motions of a Floating Body

As a basic validation exercise of the free motion capability of the method, the decaying motions of a freely floating sphere were computed following an initial displacement of 0.5r where r is the sphere radius. The resulting trace of heave versus time initially follows closely to the measurement of Liapis (25), but with slightly heavier damping (see Fig. 3). The calculated trace is more complicated at a later time when the radiated wave is reflected from the far boundary. The present calculations do not include treatment of the waves arriving at the outer boundaries. Usually, in forward speed cases at least, there has been no need to treat the reflected wave problem. The stationary case, however, needs a wave absorber at the boundary such as the approach described by Nakos et al (11), or Beck and Cao (26).

S175 ITTC Hull Form

A panel model of the S175 hull was constructed using approximately 800 panels. This was placed in a truncated free surface approximately 5L, long by 2.2L wide where L, the length of the hull model, is 3.5 metres in this case. The model was placed 2.5L downstream from the wave-maker.

The hull lines are shown in Fig. 4. A general view of the model and free surface paneling is shown in Fig. 5.

Experimental data reported in Ref. 22 were measured in the U.S. Naval Academy Hydrodynamics Laboratory 116 meter long towing tank. This facility has a dual-flap hydraulically driven wave-maker. Principle characteristics of the S175 hull form—used for comparative studies by the ITTC, are given in the following table.

Length (Lpp)	3.5m
Beam	0.51m
Draft	0.19m
C_B	0.572
Ryy/Lpp	0.24
Displacement	193.2 kg

Table 1. S175 Model Characteristics.

The towing speed case considered here is 1.61m/sec. giving a length Froude number of 0.275.

The calculations start with wave calibration runs in which the period and amplitude of the oscillating velocity potential wave-maker are varied. These cases are run with just the truncated free surface, i.e., the hull model is removed. Precise amplitude and frequency of the generated wave are difficult to obtain at this time, owing to non-linear dependencies. Alternative wave-maker models will be considered in the future. The model will then be extended to include random waves and oblique wave conditions and a Fourier analysis will be applied to the incident wave and the body motion/orientation parameters. In the model used here, the free surface paneling moves with the vessel, thereby eliminating the panel matchup problems encountered in earlier calculations (18) in which the vessel moved through a stationary free surface paneling. In the present model, therefore, the wave-maker strip, being at the upstream "edge" of the free surface, moves with the body frame. It's oscillation is therefore related to the *encounter* frequency rather than the absolute frequency used earlier. Use of this "moving" free surface allows many more wave encounters to be achieved in a realistic computer time. Also, the earlier restriction which required that the hull step movement be closely related to the x-wise panel size on the free surface has now gone.

The present calculations used a time step increment of .03 seconds. This corresponds to

597

approximately 70 time steps for a forward movement of 1 hull length. Fig. 6 shows the transfer functions for pitch, heave, and also acceleration. The latter was measured at a point 0.15 Lpp from the bow perpendicular. The values are plotted as a function of wave slope, ka, for two non-dimensional encounter frequency values, σe of 3.352 and 3.728. k is the wave number, $2\pi/\lambda$, a is the wave amplitude and σe is defined as $\omega_e\sqrt{\dfrac{Lpp}{g}}$. ω_e is the wave encounter frequency.

The heave function is heave amplitude divided by wave amplitude, i.e, z/a; the pitch function is pitch angle divided by wave slope, ka; the acceleration function is $\ddot{z}$ Lpp/(ga). For the experimental data points the amplitudes are the first harmonic term from a Fourier analysis over approximately 10 full cycles. Most of the calculated points are from runs which had less than five wave encounters and so a Fourier analysis was not attempted here: the amplitudes for the calculated points are the average amplitude over the last two wave encounters in each case. This is a temporary measure to get an idea of the general quality of the results, and should be satisfactory at the lower wave slopes where the time traces are fairly regular, but is not very good at the higher wave slopes, especially when the bow takes green water. The latest calculations are covering more cycles thanks to the new matrix solver—and so a Fourier analysis is being added to the routine to process the data.

The calculations compare favorably with the experimental measurements and display the nonlinear characteristics with respect to wave slope. Note that the σ_e values in the calculation are not precisely the same as the experimental values. More calculations are being pursued at the higher wave slopes. There have been some difficulties owing to the bow taking green water. The panel model was constructed without a deck and so when the bow becomes submerged, the calculation does not get the *download* due to water above the deck—consequently, the resulting heave force and pitching moment have an excessive positive value during the part of the cycle when the bow is immersed. Future calculations will include a deck representation in the panel model. However, when pursuing the green-water-on-deck conditions, the question on how detailed a model is required for representing the energy losses in the water jet and spray during slamming encounter has yet to be addressed. The present repanelling procedure in the panel model has to be made more robust before such issues can be addressed with the present approach.

Some general views of the calculated dynamic pressure distribution on the hull at different stages of a wave encounter are shown in Fig. 7. This detailed information can be integrated to provide unsteady shear force and bending moment distribution along the hull.

Frigate Hull

Experimental data are available from a series of tests on a frigate model in steep head waves (21). The results cover fairly extreme conditions, including water on the deck, and cover a range of bow shapes, Fig. 8. The main particulars of the model are given in Table 2 below.

Model Length; Lpp	4.5m
Beam	0.496m
Draft	0.163m
C_B	0.454
Ryy/Lpp	0.277
Displacement	165Kg

Table 2. Frigate Model Characteristics.

The model was free to pitch and heave, but restrained in surge. The conditions used for comparison here are at a Froude number of 0.3.

Fig. 9 shows views of the panel model for the parent hull and free surface, and Fig. 10 shows the time history of the encountered wave height computed about Lpp/4 ahead of the bow. This shows the regular behavior of the computational wave maker. Fig. 11 shows the heave and pitch response function plotted against λ/L. In general, the calculations compare favorably with the measured data. Cases involving steeper waves—i.e., H/λ greater than .02 (where H is the wave double amplitude), also involve water over the bow and need further investigation as discussed for the S175 hull. In the present case, although the deck was panelled, the automatic repanelling procedure did not behave consistently when the bow became submerged. The complete procedure is being reviewed and a more robust scheme will be installed shortly.

Fig. 12 displays the heave and pitch transfer functions plotted against H/λ for a nominal λ/L = 1.2. The calculated heave transfer tends to be higher than the measured value, but the H/λ value for these points is at 1.14 and so is closer to resonance. The computed pitch transfer functions tend to be on the low side but again, because of a slightly lower λ/L, the conditions are moving down the

steep drop off in the pitch versus λ/L data seen in Fig. 11.

Fig. 13 shows a plot of deck wetness as a function of H/λ. The calculated values for the parent hull are simply the average free surface height over the foredeck during an encounter. This is not very precise at this time, and there are uncertainties over the deck solution as discussed above. However, the trends are certainly encouraging. A similar case has been run with the bow2 variation, but did not show any major change in the wetness measurement, whereas the experimental data does show a tendency for reduced wetness level for this hull. It may be that a greater panel resolution should be used when trying to calculate these more extreme cases, however, bad behavior in the repanelling procedure is certainly affecting these results and is partly responsible for spikes seen in the time response curves of the heave force and pitching moment when the bow becomes submerged (see Fig. 14). Although of short duration, the spikes must have some effect on the integrated pitch and heave responses—certainly the troughs in these traces are much sharper than the peaks. Even so, it is encouraging to see the response amplitudes settle down in the last two encounters. The flared hull (bow2) displays a slight phase lag and higher peak values in the heave force and pitching moment compared with the parent hull. This would be consistent with the expected increased flare slam load (computed earlier under forced motion conditions (18)), however, the current difficulties on repanelling as the water goes over the bow may be influencing the trace here and needs further investigation.

Finally, in Fig. 15, four frames show the frigate at various stages in a wave encounter. The colors depict free surface elevation. The conditions are λ/L = 1.2 and H/λ = .021 at Fr = 0.3.

Most of the calculations presented here were run on a Silicon Graphics Indigo workstation. Each case involved approximately 2500 panels and 250 time steps, and took approximately four hours to complete, thanks to the new matrix solver (23).

CONCLUSIONS

The present results show a very encouraging progress in the development of a general non-linear numerical method for treating arbitrary ship motions in waves. Computed response functions for a frigate and for the S175 container ship compare favorably with measured data. With the new iterative matrix solver installed, the turnaround time on a workstation is typically four hours.

Future effort will concentrate on improved repanelling procedures before proceeding to the case of oblique waves.

REFERENCES

1. Faltinsen, O.M., "On Seakeeping of Conventional and High-Speed Vessels", *Journal of Ship Research*, Vol. 37, No. 2, June 1993, pp. 87-101.

2. Korvin-Kroukovsky, B.V., "Investigation of Ship Motions in Regular Waves", *Trans.* SHAME, 63, 1955.

3. Ogilvie, T.F. and Tuck, E.O., "A Rational Strip-Theory of Ship Motion", Part 1, Department of Naval Architecture, The University of Michigan, Ann Arbor, MI, Report No. 013, 1969.

4. Salvesen, N., Tuck, E.O., and Faltinsen, O., "Ship Motions and Sea Loads", *Trans.* SHAME, 250-287, 1970.

5. Kim, C.H., Chou, F.S., and Tein, D., "Motions and Hydrodynamic Loads of a Ship Advancing in Oblique Waves", *Trans.* SNAME, 225-256, 1988.

6. Chiu, F.C. and Fujino, M., "Nonlinear Prediction of Vertical Motions of a Fishing Vessel in Head Sea", Journal of Ship Research, 35, 1, March, 32-39, 1991.

7. Fang, Ming-Chung, Lee, Ming-Ling, Lee, Chwang-Kuo, "Time Simulation of Water Shipping for a Ship Advancing in Large Longitudinal Waves", *Journal of Ship Research*, Vol. 37, No. 2, June 1993, pp. 126-137.

8. Nakos, D.E., and Sclavounos, P.D., "On Steady and Unsteady Ship Wave Patterns,", *Journal of Fluid Mechanics*, 1990, Vol. 215, pp. 263-288.

9. King, B.W., Beck, R.F., and Magee, A.R., "Seakeeping Calculations with Forward Speed Using Time-Domain Analysis," 17th Symposium on Naval Hydrodynamics, 1988.

10. Lin, W.-M., and Yue, D., "Numerical Solutions of Large-Amplitude Ship Motions in the Time Domain," 18th Symposium on Naval Hydrodynamics, 1990.

11. Nakos, D.E., Kring, D.C., Sclavounos, P.D., "Rankine Panel Methods for Time-Domain Free Surface Flows," to be presented in the Sixth International Conference on Numerical Ship Hydrodynamics, Iowa City, Iowa, August 1993.

12. Pawlowski, J.S., and Bass, D.W., "A Theoretical and Numerical Model of Ship Motions in Heavy Seas", Presented at SNAME Annual Meeting, 1991.

13. Maskew, B., *USAERO, A Time-Stepping Analysis Method for the Flow about Multiple Bodies in General Motions, Users' Manual*, Analytical Methods, Inc., Redmond, WA, 1990.

14. Maskew, B. and Dvorak, F.A., "Prediction of Dynamic Stall Characteristics Using Advanced Nonlinear Panel Methods," *Proc. Workshop Unsteady Separated Flows*, USAF Academy, August 1983.

15. Maskew, B., "USAERO/FSP: A Time-Domain Approach to Complex Free-Surface Problems," Symp. High-Speed Marine Vehicles, Naples, Italy, 1991.

16. Longuet-Higgins, M.S. and Cokelet, E.D., "The Deformation of Steep Surface Waves on Water: I. A Numerical Method of Computation," *Proc. R. Soc. London*, A350, 1976, pp. 1-26.

17. Maskew, B., "A Nonlinear Numerical Method for Transient Wave/Hull Problems on Arbitrary Vessels", Presented at 1991 Annual SNAME Meeting, New York, N.Y., November 1991.

18. Maskew, B. "Prediction of Nonlinear Wave/Hull Interaction on Complex Vessels", 19th Symposium on Naval Hydrodynamics, Seoul, Korea, August 1992.

19. Tidd, D.M., "FPI—Flight-Path-Integrator: A Program Module for USAERO for Flight Path Analysis of Arbitrarily Shaped Bodies; Users' Manual", Analytical Methods, Inc., January 1991.

20. Maskew, B., "Numerical Analysis of a Complete Yacht Using a Time-Domain Boundary Element Method," presented at the Third International Seminar on Yacht and Small Craft Design, Castelluccio di Pienza, Italy, 19-23 May 1993.

21. O'Dea, J.F., and Walden, D.A., "The Effect of Bow Shape and Nonlinearities on the Prediction of Large Amplitude Motions and Deck Wetness", *Proc. 15th Symp. on Naval Hydro.*, Hamburg, Germany, 1984.

22. O'Dea, J. (David Taylor Model Basin, USA), Powers, E. (University of Texas at Austin, USA), Zselecsky, J., (U.S. Naval Academy, USA), "Experimental Determination of Nonlinearities in Vertical Plane Ship Motions," *Proc. 19th Symp. on Naval Hydro.*, Seoul, Korea, August 1992.

23. Nabors, K., Korsmeyer, T., White, J., "Multipole Accelerated Preconditioned Iterative Methods for Solving Three-Dimensional Mixed First and Second Kind Integral Equations", *Proc. Copper Mountain Conf. on Iterative Methods*, Copper Mountain, AK, April 1992.

24. Maskew, B., "Program VSAERO Theory Document," *NASA CR-4023*, 1987.

25. Liapis, S.J., "Time-domain Analysis of Ship Motions," Report No. 302, Dept. Naval Arch. Marine Eng., U. Michigan, Ann Arbor, Michigan, 1986.

26. Beck, R.F., Cao, Y., "Nonlinear Computations of Ship Waves and Wave Resistance," to be presented at the Sixth International Conf. on Numerical Ship Hydrodynamics, Iowa, August 1993.
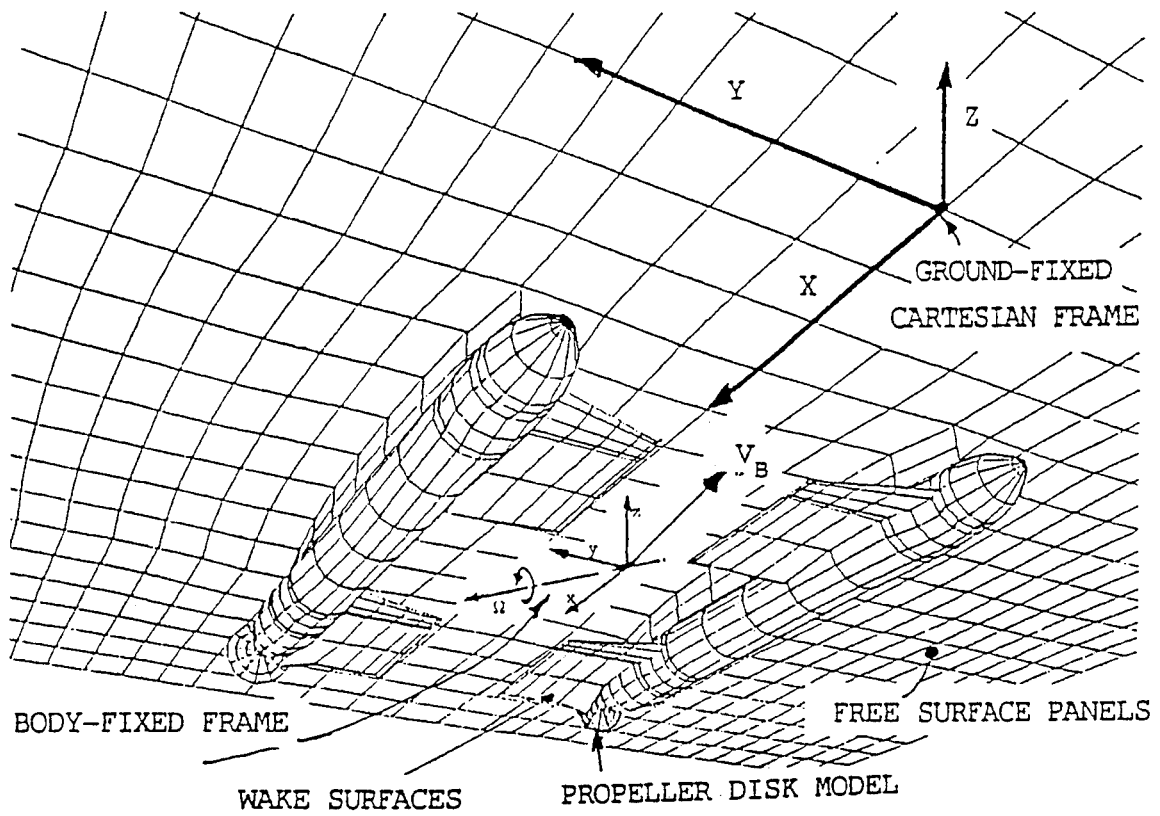
Fig. 1. General Reference System.
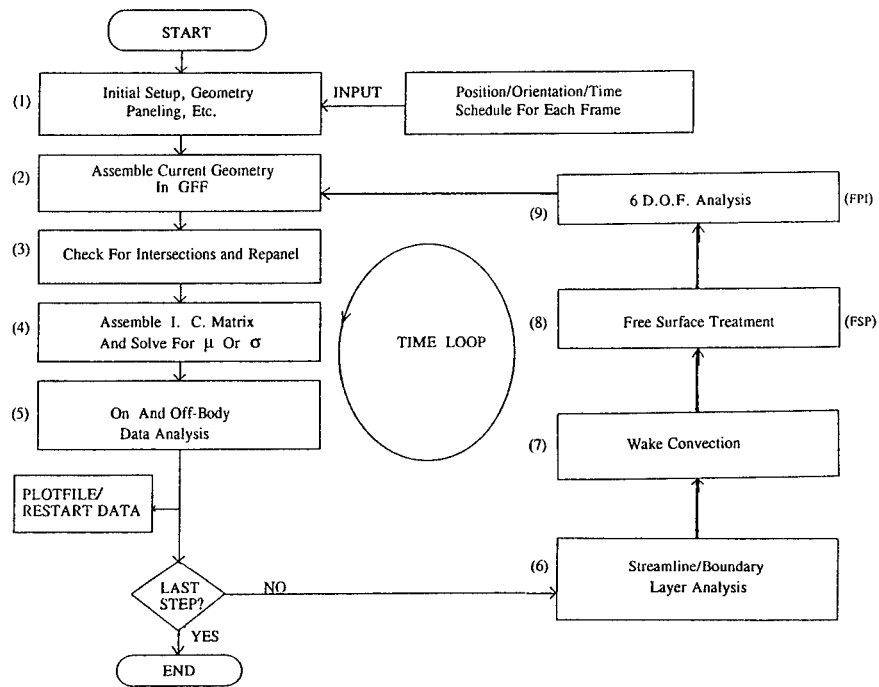
Fig. 2. USAERO/FSP Method Outline.

Fig. 3. Floating Sphere Heave Decay After Displacement
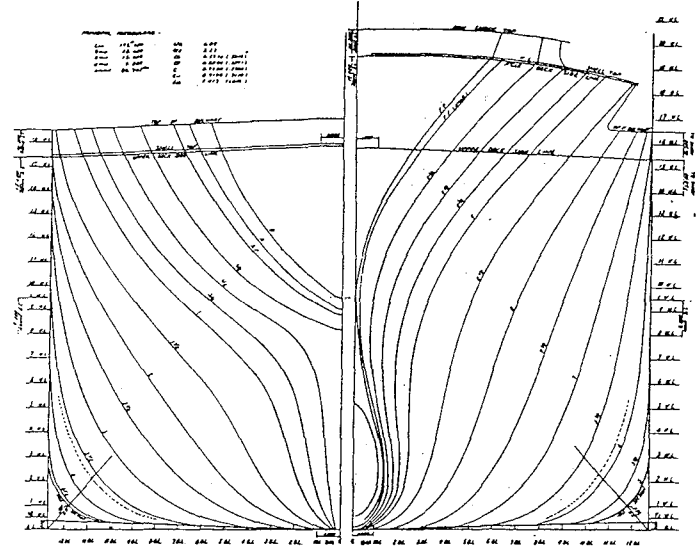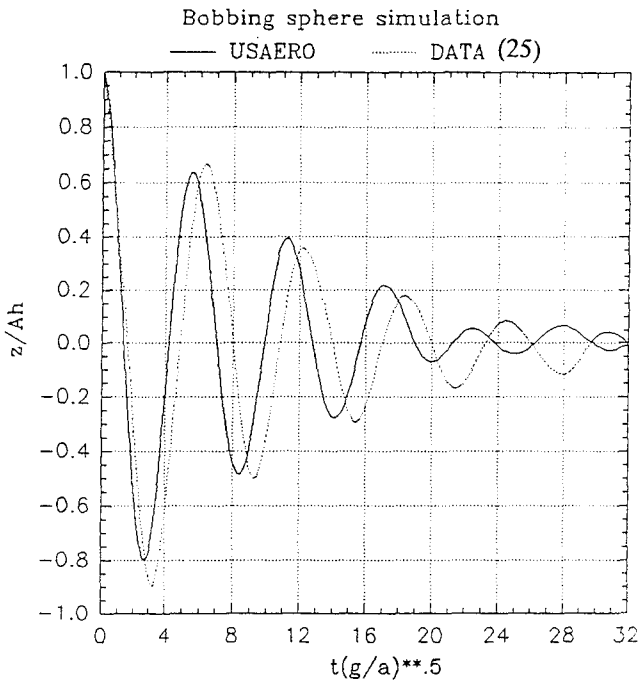
Fig. 4. Lines for the S175 Tanker Hull.
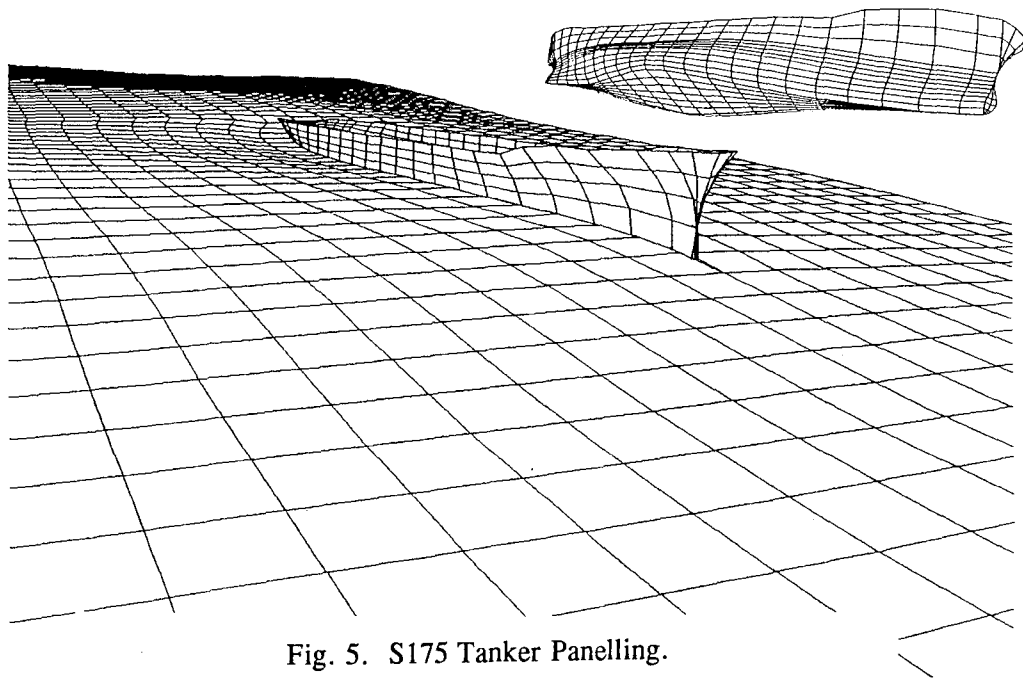
Fig. 5. S175 Tanker Panelling.

602

S175 TANKER
Magnitude of pitch response function Fn=0.275

● USAERO (σ_e = 3.272 – 3.445)   O EXPERIMENT (22)

σ_e = 3.352

● USAERO (σ_e = 3.862 – 3.869)   O EXPERIMENT (22)

σ_e = 3.728

S175 TANKER
Magnitude of heave response function Fn=0.275

● USAERO (σ_e = 3.272 – 3.445)   O EXPERIMENT (22)

σ_e = 3.352

● USAERO (σ_e = 3.862 – 3.869)   O EXPERIMENT (22)

σ_e = 3.728

S175 TANKER
Magnitude of acceleration response function Fn=0.275

● USAERO (σ_e = 3.272 – 3.269)   O EXPERIMENT (22)

σ_e = 3.352

● USAERO (σ_e = 3.862)   O EXPERIMENT (22)

σ_e = 3.728

Fig. 6. Effect of Wave Steepness on Pitch, Heave, and Acceleration Response
Functions for S175 Model Hull at Froude = 0.275.

603
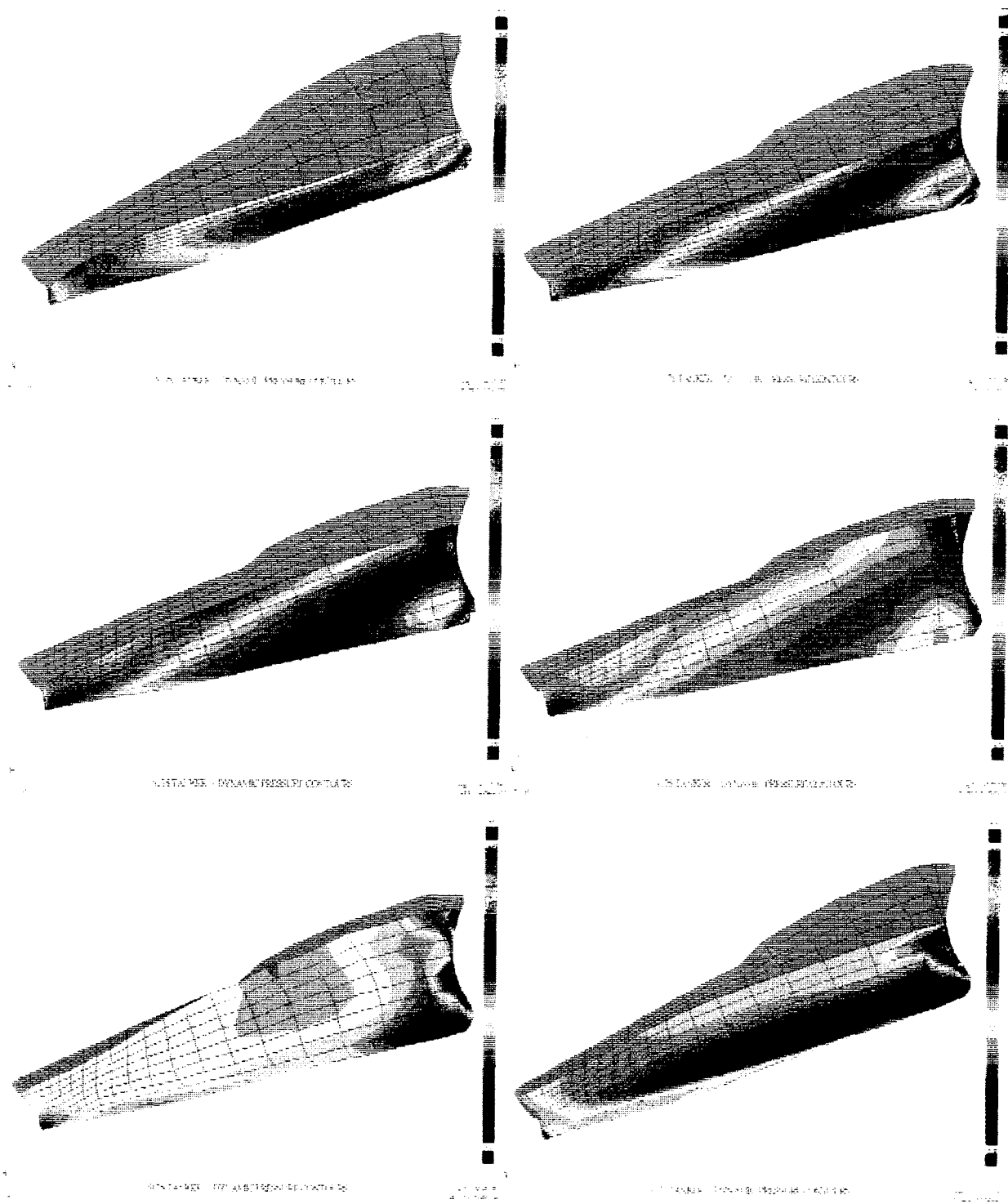
Fig. 7. Computed Dynamic Pressure Contours on S175 Hull During Wave Encounter.

Model Length — 4.5m
Beam — 0.496 m
Draft — 0.163 m
C_B — 0.454
C_x — 0.755

Bow 1
(Decreased Flare)

Bow 2
(Increased Flare)

Bow 3
(Shallow Knuckle)

Bow 4
(Deep Knuckle)
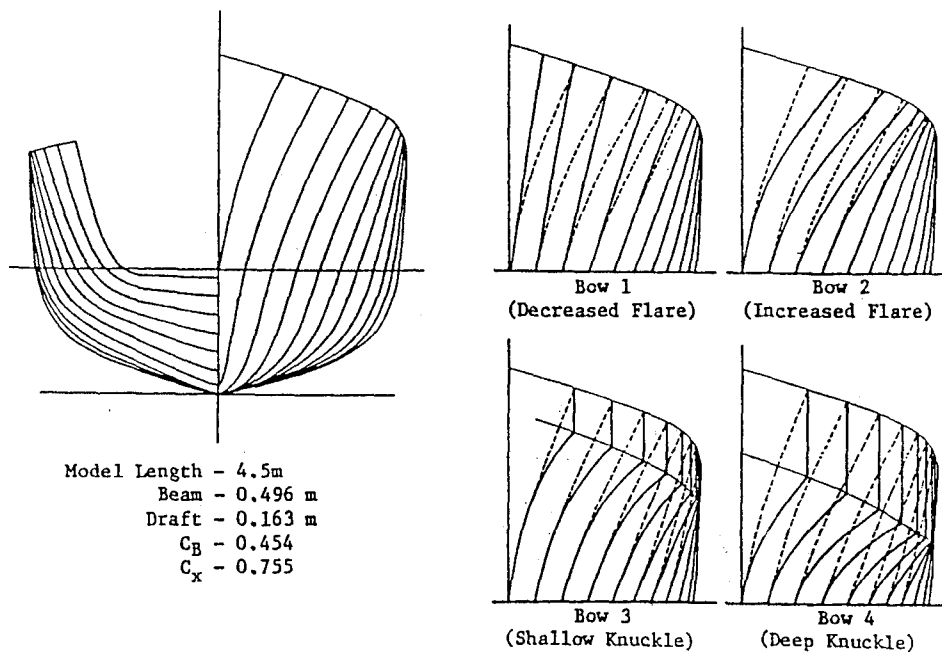
Fig. 8. Frigate Model Lines Showing Bow Variations.
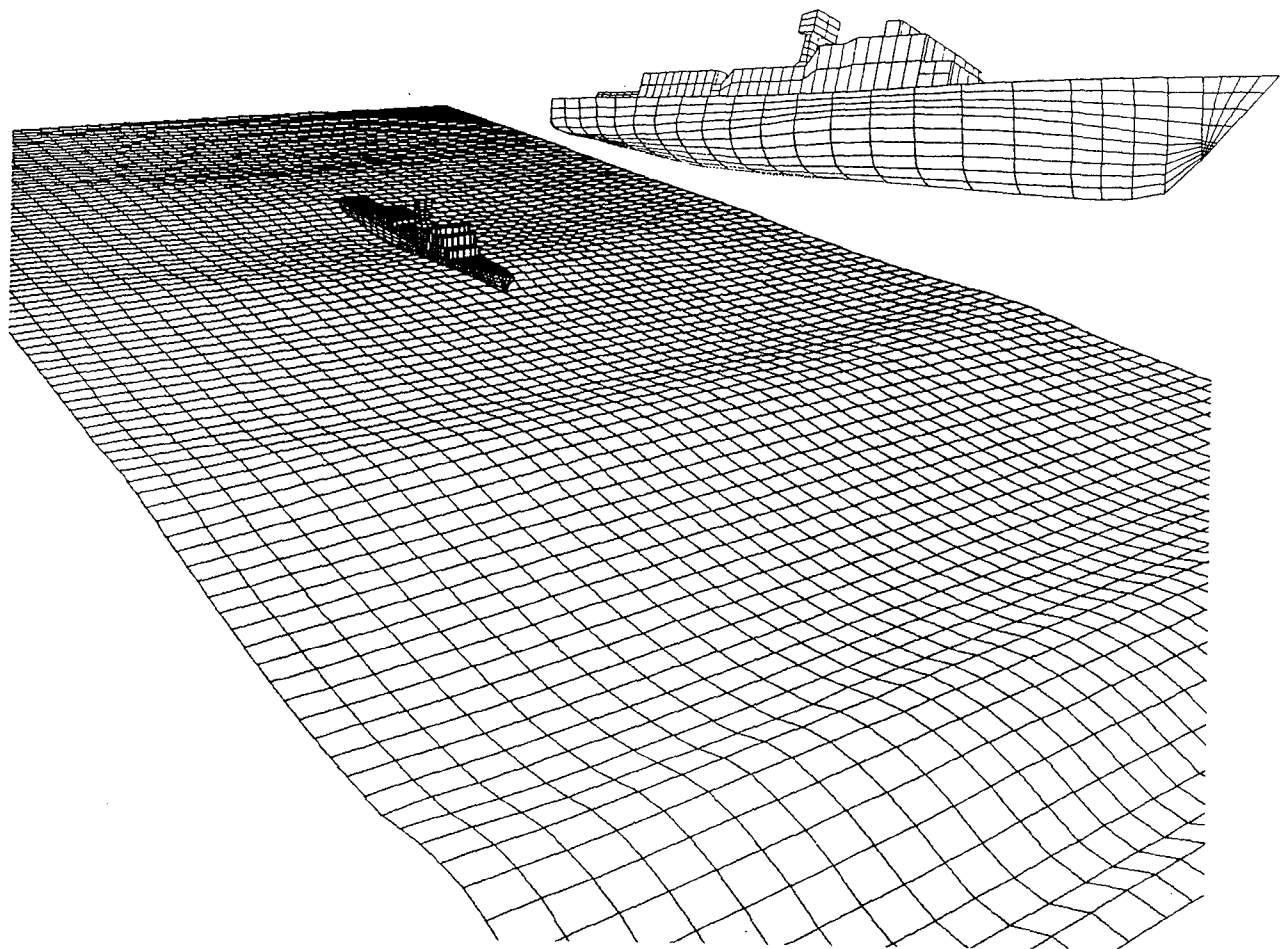
Fig. 9. Free Surface Panelling for Frigate.

605

PANEL 3139 ZWAVE

ZWAVE   Selected Panels 3139
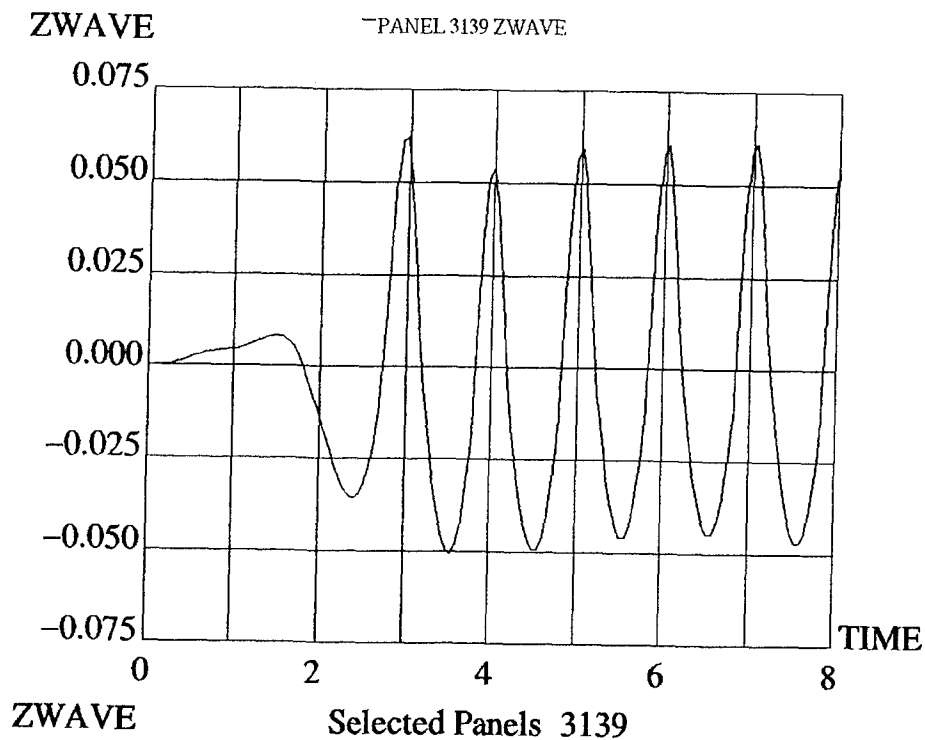
Fig. 10. Wave Height 1m Ahead of Bow for H/λ = 0.02.

PITCH TRANSFER FUNCTION (Fn=0.30)

O EXPERIMENT, H/λ = 0.01 (21)
△ EXPERIMENT, H/λ = 0.03 . .
● USAERO H/λ= 0.009 —→ 0.034

H/λ = 0.034

HEAVE TRANSFER FUNCTION (Fn=0.30)

O EXPERIMENT, H/λ = 0.01 (21)
△ EXPERIMENT, H/λ = 0.03
● USAERO H/λ =0.009 —→ 0.034

H/λ =0.034
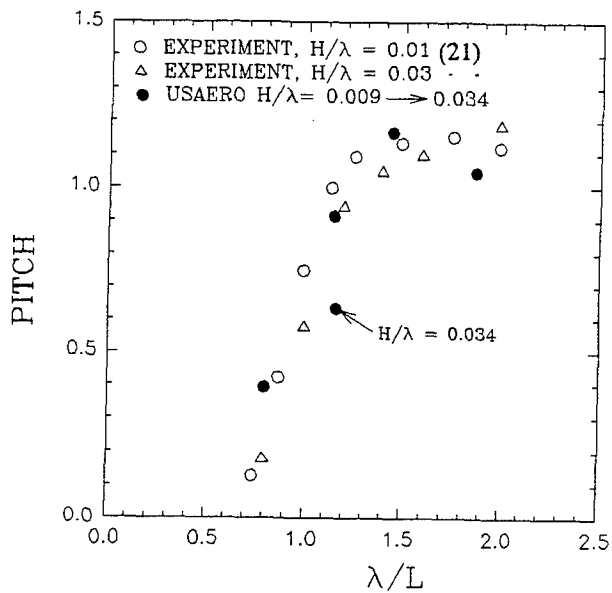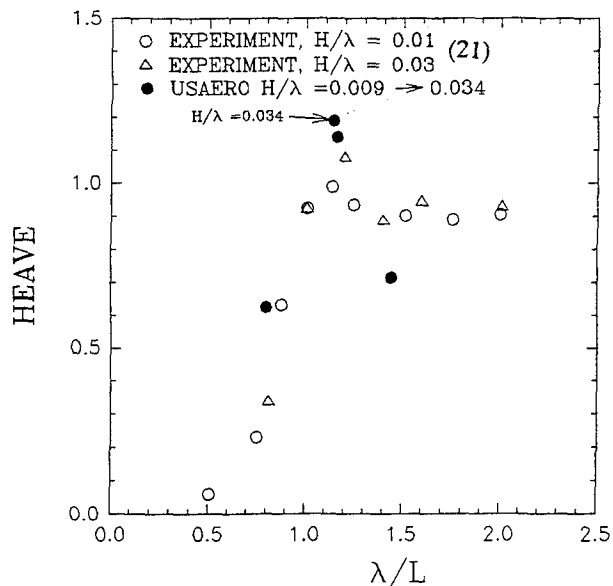
Fig. 11. Effect of Wave Length on Pitch and Heave Transfer Functions.

VARIATION OF MAGNITUDE OF TRANSFER
FUNCTION WITH WAVE STEEPNESS
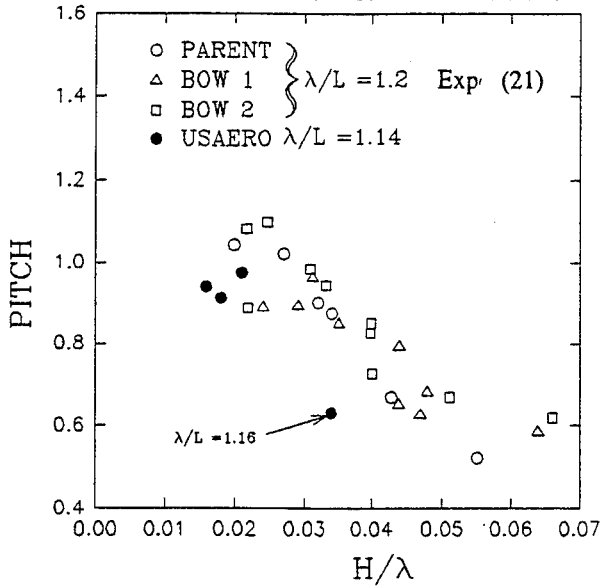
VARIATION OF MAGNITUDE OF TRANSFER
FUNCTION WITH WAVE STEEPNESS
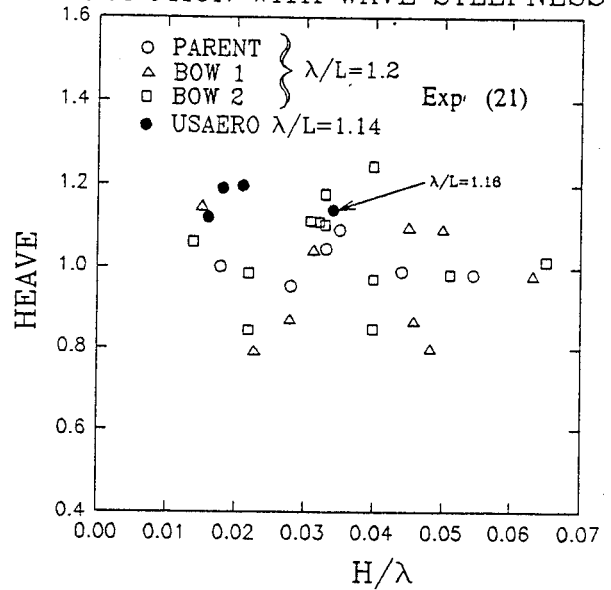
Fig. 12. Effect of Wave Steepness on Pitch and Heave
Transfer Functions.
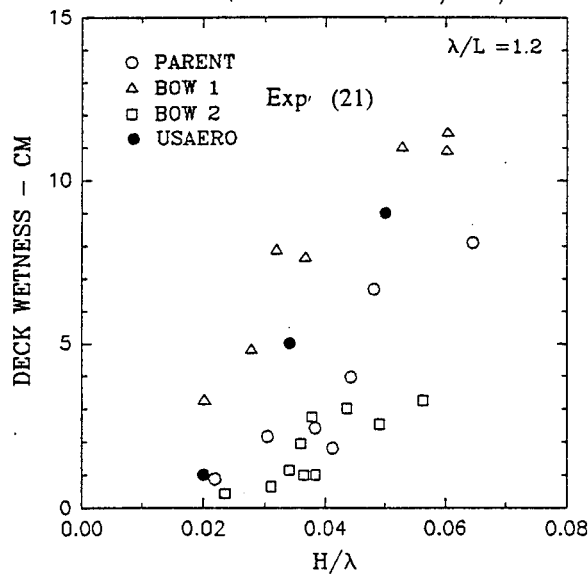
Fig. 13. Effect of Wave Steepness on Deck Wetness.

607
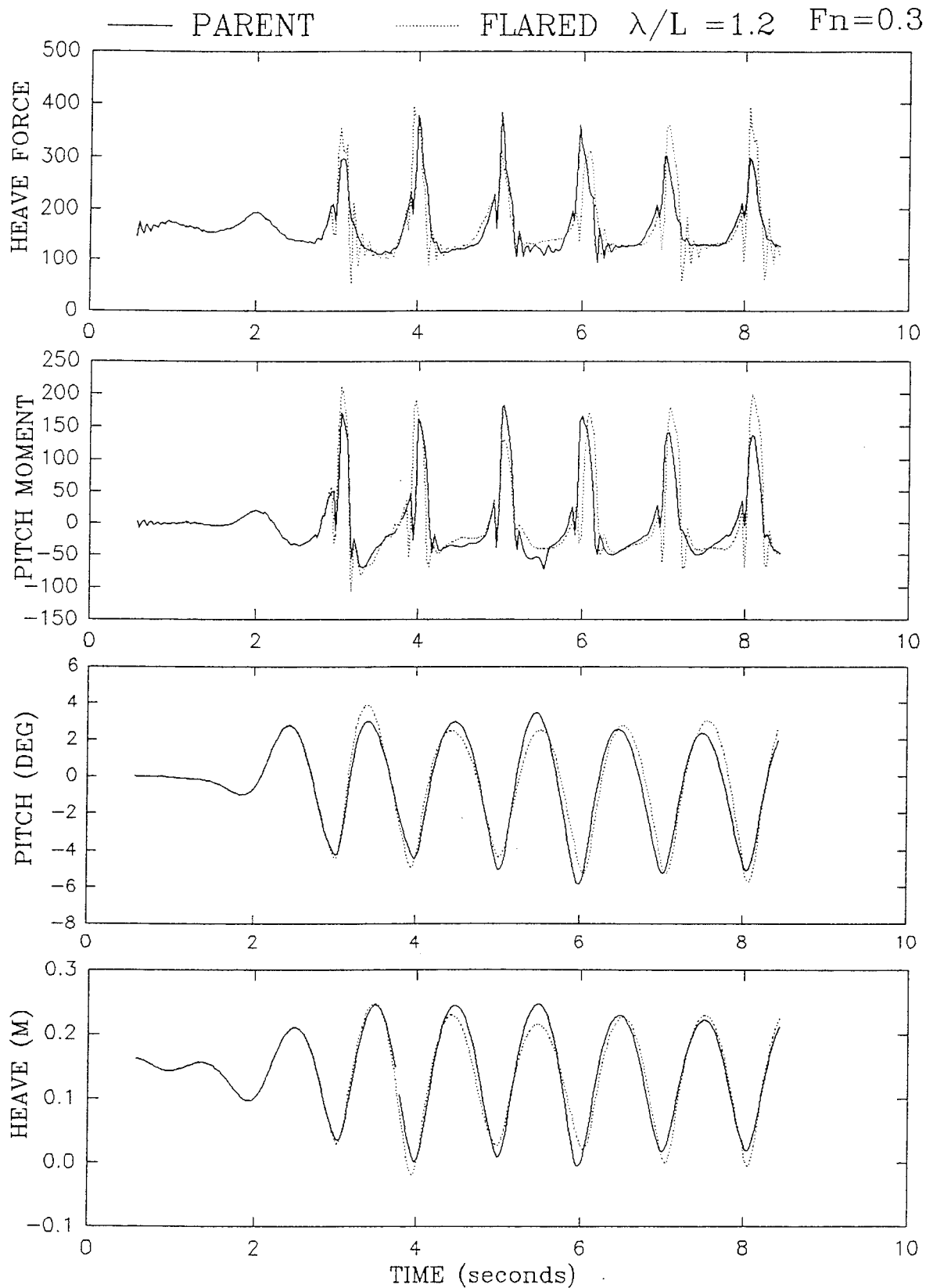
Fig. 14. Calculated Force, Moment and Response Trace for Parent and Bow2;
λ/L = 1.2; H/λ = 0.034.
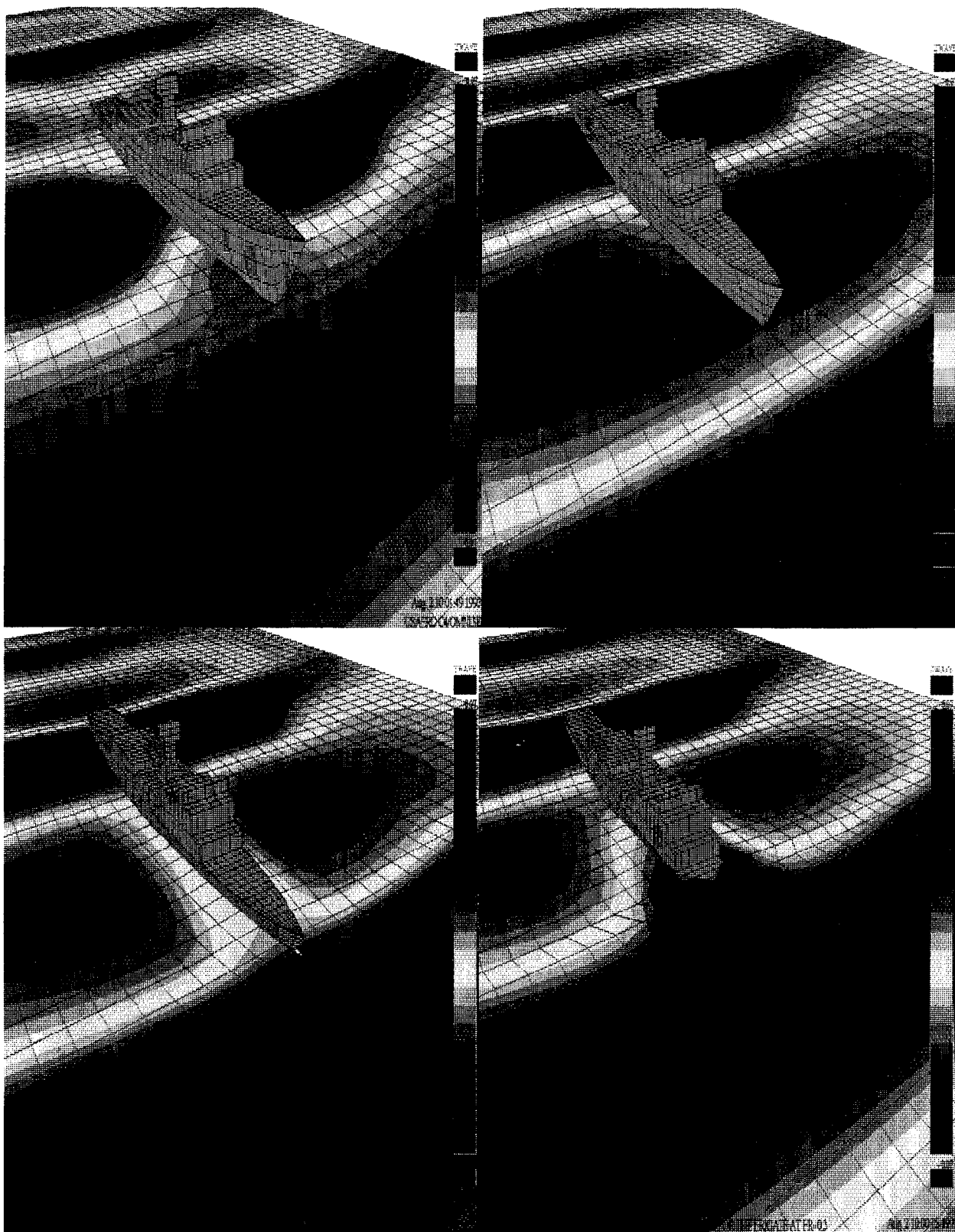
Fig. 15.   General Views of Frigate During Wave Encounter Showing Computed Free Surface
              Elevation Contours, Fr = 0.3, λ/L = 1.2, H/λ = .021.

by Professor E. O. Tuck, University of Adelaide, Australia.

Several times during this talk it has been noted that the agreement between the present computations of heave or pitch motions and experiments is " in the ball park." In view of the fact that, for about 25 years, linear theory (even with the further approximation of strip theory) has inhabited the same ballpark, it would seem that, although the degree of agreement is reasonable, a smaller ballpark is needed in order to justify the expense of the present approach, relative to strip theory. In particular, some form of differencing would seem to be appropriate. In other words, to what (ballpark?) extent does the present program predict nonlinear effects, as measured by the differences between results from large-amplitude and small-amplitude incident waves?

Author's Reply
The non-linear effects are demonstrated in the pitch and heave response functions plotted against wave steepness in Figure 6 for the S175 tanker and in Figure 12 for the frigate. The agreement with measured data is referred to as "ball park" at this stage because these initial results are not at the *precise* wave-length values of the experiments. The numerical wave maker is driven by an oscillating velocity potential, and so the precise wave length and wave amplitude are not controlled directly. A number of cases have yet to be run to provide sufficient information for cross-plots to be generated to complete the figures shown in the paper. Bearing in mind all the complex interactions between the various parts of the method, just getting all this running together and getting "ball park" results was regarded as important progress at this stage.

DISCUSSION
by T. T. Huang, DTMB

Could the authors provide computational uncertainty for the panel number, panel distribution, computation domain and Foude number used for each of computations. A generalized computational uncertainty statement of the USAERO is welcome.

Author's Reply
Detailed sensitivity studies of surface and time discretizations and of free surface truncation as a function of Froude Number have yet to be studied for the *seakeeping* applications of USAERO. Such studies are planned for the third year of this project and will be reported in a future paper. The discretizations used in the resent paper represent "reasonable" (but not necessarily ideal) conditions, based on earlier experience with this code and with its sister code, VSAERO, which has undergone a number of descretization sensitivity studies. The present objectives have been to examine the general behavior of the various parts of the method in the seakeeping applications - i.e., the free surface deformation, the wave maker, the large amplitude free motion of the vessel, the "on-the-fly" repaneling to the free surfce/hull intersection line, and the calculation of the instantaneous body force and moment. These parts must all work smoothly together before starting a detailed sensitivity study.

DISCUSSION
by Dr. Arthur M. Reed, David Taylor Model Basin

This was an informative presentation on a computational tool which has the ability to analyze a number of useful and relevant Navy problems. Thank-you.
I have two questions:
1. You state that your code can include an actuator disk model for a propulsor. What purpose is this intended to serve in the computation?
2. In your non-linear ship motion calculations have you performed any analysis of your results which would indicate which aspects of the non-linear calculations are most important to your results -NL hydrostatics, NL hydrodynamics, etc.?

Author's Reply
1. The actuator disc model in USAERO stems from earlier modeling of aircraft propeller effects on wings, etc. The basic purpose of including it for ship motion calculations is to represent propulsor effects on hull loads; however, current developments, using a blade-element approach, will provide a more complete propulsor modeling capability, including time-

dependent thrust effects and non-uniform inflow effects on thrust and side-force.

2. In general, the code works with the complete unsteady pressure distribution which is integrated at each step to provide the instantaneous force and moment acting on the vessel; the separate contribution of the hydrody-namic, and hydrostatic pressures, have not been examined in detail. However, the current analysis now has the option to display the surface distribution of the "$1-v^2$", the "pzg" and the "$\frac{\partial \phi}{\partial t}$" pressure terms separately. It would be straightforward to integrate these terms separately to provide their respective contributions to the straightforward to integrate these terms separately to provide their respective contributions to the force and moment acting on the hull, thereby allowing the relative magnitudes to be examined.

Rankine Panel Methods for Transient Free-Surface Flows

D.E. Nakos (InTec Software, USA)
D. Kring and P.D. Sclavounos
(Massachusetts Institute of Technology, USA)

ABSTRACT

A Rankine Panel Method is developed for the solution of transient wave-body interactions. In the presence of mean forward speed, the free surface and body boundary conditions are linearized about the double-body flow. The choices of space and time discretization are based on a systematic error and stability analysis. An artificial wave-absorbing beach is designed and employed over the outer portion of the free surface computational domain in order to avoid wave sloshing within the computational basin.

The proposed numerical scheme is applied for the solution of flows around realistic ships with or without mean forward speed. The transient wave resistance problem is considered and the rate of convergence of the resultant forces and moments to their steady values is studied. Forced and free motion simulations are also carried out until steady-state is reached and the resulting forces and motions are compared with computations by the well established frequency domain version of the same Rankine Panel Method.

1. INTRODUCTION

Numerical solutions of the transient wave-ship interactions have recently emerged as a popular alternative to their frequency domain counterparts. Studies with and without mean forward speed have been reported by Wehausen (1967), Liapis (1986), Beck and Liapis (1987) Korsmeyer (1988), King, et al, (1988), Lin and Yue (1990), Beck and Magee (1990), and Maskew(1992).

Over the past 15 years Rankine Panel Methods have been successfully employed by several research teams for the solution of various free sur-face problems ranging from the linearized wave resistance and ship motion problems to nonlinear breaking wave simulations. The use of the simple Rankine source as the elementary singularity is mainly motivated by the resulting flexibility in the choice of the free surface conditions to be satisfied. This property does not only render the Rankine Panel Methods as the sole alternative for nonlinear flows, but it also allows the employment of linearized conditions with variable coefficients. The penalty to be paid by such schemes consists of the necessity to discretize a portion of the free surface surrounding the body, which does not only increase the number of unknowns to be determined, but also may potentially distort the resulting wave pattern due to the introduction of numerical dispersion, dissipation and – most importantly – instabilities.

This study presents the design, implementation and application of a Rankine Panel Method for the solution of transient wave-body interactions in three dimensions. At the presence of mean forward speed, the free surface and body boundary conditions are linearized about the double-body flow, as it is outlined in section 2. Previous studies, in the frequency domain, have illustrated the excellent numerical properties of properly designed Rankine Panel Methods in the frequency domain and the performance of such linearization over a wide range of Froude numbers and frequencies for realistic ship flows(see Sclavounos and Nakos(1988) and Nakos and Sclavounos(1990)).

The numerical scheme adopted by the present study is outlined in section 3 and may be shown to posses very desirable global error and stability properties (see Nakos (1993)). The computational domain, consisting of the hull and a portion of the surrounding free surface, is discretized

by a collection of plane quadrilateral panels over which the unknown functions are represented as biquadratic splines. The time dependence of the solution is modeled by allowing the associated spline coefficients to be time dependent and two alternative time-marching schemes are proposed for the integration of the free surface conditions. Discretization errors are found to be large over length scales of the solution which are comparable to the grid size. A low-pass filtering is designed in order to eliminate such wave components which would, otherwise, propagate at erroneous directions and speeds, therefore jeopardizing the overall accuracy of the numerical solution.

Section 4 undertakes the design and implementation of an artificial wave-absorbing beach for the damping of the reflections due to the truncated free surface domain. The wave absorption mechanism is based on Newtonian cooling (see eg. Israeli and Orszag (1981)) which is distributed over the outer portion of the free surface computational domain. Nakos (1993) has demonstrated the effectiveness of the proposed artificial beach by numerical tests, which is found to be satisfactory as long as the width of the beach is comparable to the length of the waves to be absorbed.

The first numerical simulations are carried out for forced harmonic motions of a vessel at zero forward speed. Section 5 compares the force predictions of the present transient solution to results due to the frequency domain computer code *WAMIT*. The excellent correlation of the two sets of numerical results demonstrates not only the accuracy of the present scheme, but it also serves as a more pragmatic proof of the effectiveness of the adopted artificial beach.

Section 6 presents several simulations of realistic ships advancing steadily at a constant speed. A Series-60 hull and the modified Wigley model are both considered at Froude numbers 0.2 and 0.3. The convergence of the numerical solution with the number of panels is illustrated both with respect to the generated wave patterns and the resultant forces and moments acting on the hull. At low speed the time histories of the forces are shown to contain a slowly-decaying transient oscillation owing to the critical frequency $\omega U/g = 0.25$ which gets excited due to the impulsive start of the vessel.

Forced motion simulations in the presence of constant forward speed are considered in section 7.

The resulting steady-state added mass and damping coefficients compare excellently with related predictions by the frequency domain computer code *SWAN*.

Section 8 presents free motion simulations in the presence of constant forward speed, where the rigid-body equations of motion are solved at each time step. Results are presented for free decay tests and rigid-body response to multichromatic head seas.

2. LINEARIZATION OF BOUNDARY CONDITIONS

The problem requires a formulation for the transient wave flow around at rigid vessel advancing through ambient sea waves. A Cartesian coordinate system $Oxyz$ is utilized with its origin on the calm free surface, its x-axis pointing upstream and its z-axis upwards. The coordinate system will also be fixed to the body. Under the assumptions of inviscid and irrotational flow, the velocity potential Ψ governing the resulting wave flow satisfies Laplace equation in the fluid domain and is subject to the dynamic and kinematic free surface conditions,

$$\left\{ \begin{array}{l} \dfrac{\partial \Psi}{\partial t} = -g\zeta - \dfrac{1}{2}\nabla\Psi \cdot \nabla\Psi \\[2mm] \left(\dfrac{\partial}{\partial t} + \nabla\Psi \cdot \nabla \right)[z - \zeta(x,y,t)] = 0 \end{array} \right\} \quad (2.1)$$

to be imposed at the instantaneous position of the free surface.

Over the wetted portion of the ship hull the normal component of the fluid velocity is equal to the corresponding component of the ship velocity $\vec{V}_B$, or

$$\frac{\partial \Psi}{\partial n} = (\vec{V}_B \cdot \vec{n})(\vec{x},t) = \left(\vec{U} + \frac{\partial \vec{\delta}}{\partial t} \right) \cdot \vec{n} \quad (2.2)$$

applied over the instantaneous position of the vessel. In general, the velocity $\vec{V}_B$ contains the mean forward speed of the vessel $\vec{U}$ and an oscillatory component due to the response $\vec{\delta}$ of the ship to ambient waves. The latter may be decomposed in the six rigid-body degrees of freedom,

$$\vec{\delta} = \vec{\xi}(t) + \vec{\theta}(t) \times \vec{x} \quad (2.3)$$

614

where $\vec{\xi} = (\xi_1, \xi_2, \xi_3)$ and $\vec{\theta} = (\xi_4, \xi_5, \xi_6)$ denote the motions along the translational and rotational rigid-body modes, respectively.

Under the assumption that the total flow Ψ consists of a base-flow Φ, of $O(1)$, and a small amplitude disturbance φ conditions (2.1) and (2.2) may be linearized. This study employs the double-body flow as the basis flow, which satisfies the rigid wall condition over the calm free surface, and offsets the mean forward speed over the mean position of the hull below $z = 0$. The double-body linearization has been employed successfully in the frequency domain by numerous previous studies and its validity has been demonstrated over a wide range of hull shapes, Froude numbers and frequencies (see eg. Nakos and Sclavounos (1990)).

Linearization of (2.1) about the double-body flow leads to

$$\left\{ \begin{array}{l} \dfrac{d\varphi}{dt} + \nabla\Phi \cdot \nabla\varphi = -g\zeta - \left[\dfrac{d\Phi}{dt} + \dfrac{1}{2}\nabla\Phi \cdot \nabla\Phi \right] \\[3mm] \dfrac{d\zeta}{dt} + \nabla\Phi \cdot \nabla\zeta = \dfrac{\partial^2\Phi}{\partial z^2}\zeta + \dfrac{\partial\varphi}{\partial z} \end{array} \right\}$$

$$\text{on } z = 0 \qquad (2.4)$$

where $\zeta = \zeta(x, y, t)$ is the free surface elevation and is assumed to be of the same order as the wave potential φ. The identities $\nabla\Phi \cdot \nabla\Phi_z = 0$ and $d\Phi_z/dt = 0$ over $z = 0$ assist the derivation of (2.4). The Cartesian system $Oxyz$ is selected to translate along with vessel, therefore all time derivatives (d/dt) appearing in (2.4) are augmented by the corresponding convective terms. Conditions (2.4) may be combined to eliminate the wave elevation rendering the free surface condition proposed by Nakos and Sclavounos (1990).

The first term in the second member of the linearized kinematic free surface condition (2.4) follows from the transfer of that condition onto the $z = 0$-plane, by means of an appropriate Taylor expansion. The numerical tests presented in this study do not include the effects of the above term, because of the difficulty to properly handle the singular behavior of $\partial^2\Phi/\partial z^2$ at the bow and stern of surface-piercing vessels. That does not imply, necessarily, that the effects of such term are negligible and the related study is proposed for future research.

Under the assumption of small unsteady displacement, the body boundary condition (2.2) may be transferred onto the mean position of the vessel (see Newman (1978)),

$$\frac{\partial\varphi}{\partial n} = \sum_{i=1}^{6} \left\{ \frac{\partial\xi_i}{\partial t} + \xi_i m_i \right\} \qquad (2.5)$$

where m_i are the so-called m-terms, defined in terms of the velocity field $\vec{W} = \vec{U} - \nabla\Phi$ as follows,

$$\begin{array}{l} (m_1, m_2, m_3) = \dfrac{\partial\vec{W}}{\partial n} \\[4mm] \text{and} \quad (m_4, m_5, m_6) = \dfrac{\partial(\vec{x} \times \vec{W})}{\partial n} \ . \end{array} \qquad (2.6)$$

3. THE DISCRETIZATION ALGORITHM

Consider the enforcement of the Laplace equation in the fluid domain by a distribution of Rankine singularities over the free surface and the wetted portion of the hull. Application of Green's second identity to the velocity potential of the wave flow φ and the Rankine source potential $G(\vec{x}; \vec{\xi}) = 1/2\pi|\vec{x} - \vec{\xi}|$ leads to

$$\varphi(\vec{x}, t) + \iint_{F \cup B} \varphi(\vec{x'}, t)\, G_n(\vec{x}; \vec{x'})\, d\vec{x'}$$

$$- \iint_{F \cup B} \varphi_n(\vec{x'}, t)\, G(\vec{x}; \vec{x'})\, d\vec{x'} = 0 \qquad (3.1)$$

for any finite $\vec{x}$ on the $z = 0$-plane, F, and the mean position of the hull below $z = 0$, B. The contribution of the closing surface at infinity vanishes owing to the decay of both $\varphi(\vec{x'})$ and $G(\vec{x}; \vec{x'})$ as $|\vec{x'}| \to \infty$.

The integral equation (3.1) combined with the linearized conditions (2.4) and (2.5) constitute a system of equations for the solution with respect to the velocity potential φ, the wave elevation ζ and the vertical velocity φ_z over the free surface. The present study elects not to combine (3.1), (2.4) and (2.5) into a single integro-differential equation for φ, for reasons related to the flexibility and modularity of the numerical solution scheme as well as its upgradability with respect to the inclusion of nonlinear effects.

The boundary domain is discretized by a collection of plane quadrilateral panels, over which all three unknowns are approximated, independently, by a linear superposition of biquadratic spline basis functions,
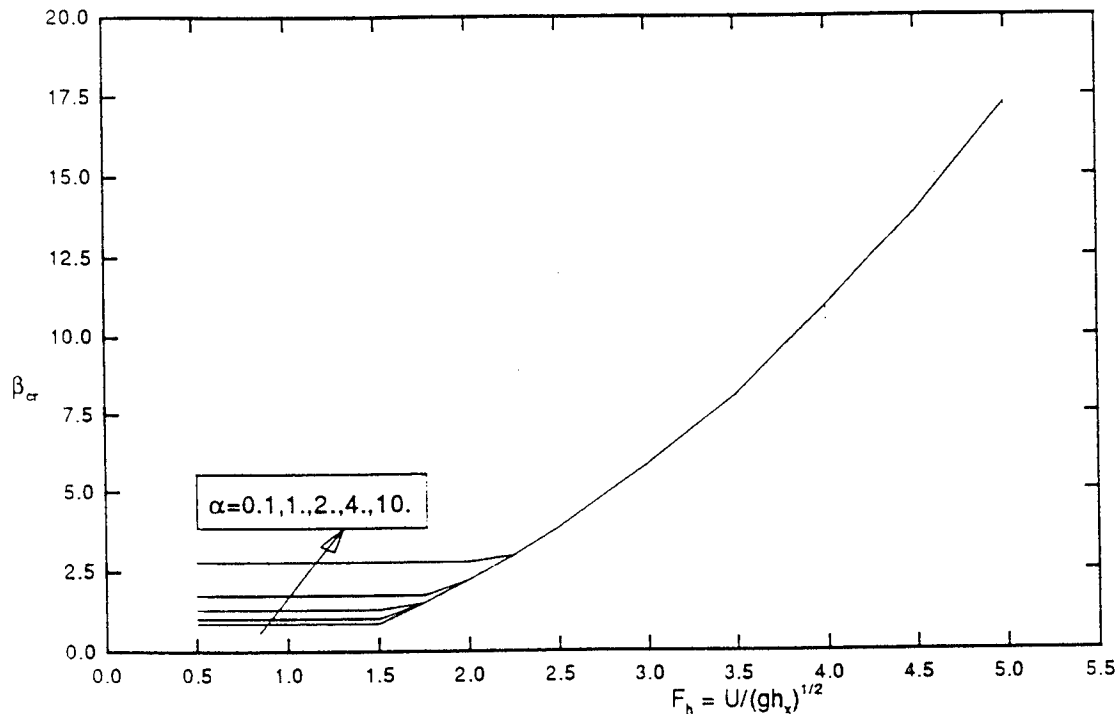
Figure 1. The stability condition for the Emplicit Euler discretization scheme.

$$\varphi(\vec{x}, t) \simeq \sum_j (\varphi)_j(t) \; B_j(\vec{x})$$

$$\zeta(\vec{x}, t) \simeq \sum_j (\zeta)_j(t) \; B_j(\vec{x}) \qquad (3.2)$$

$$\varphi_z(\vec{x}, t) \simeq \sum_j (\varphi_z)_j(t) \; B_j(\vec{x})$$

where B_j is the basis function centered at the j'th panel. The above choice of basis functions provides inter-panel continuity of the unknowns and their gradients. The time dependence of the solution is modeled by allowing the spline coefficients to be time dependent. It is worth noting that these spline coefficients are not equal to the value of the respective unknown at the panel centers, although they are linearly related to them.

The discrete formulation follows from collocation at all panel centers, $\vec{x}_i$, and the employment of a discrete time-marching scheme for the integration of the free surface boundary conditions. Recently, Nakos (1993) presented a systematic algorithm for the evaluation of the numerical attributes of alternative discretization schemes, which hinges upon the introduction of the "discrete dispersion relation" governing the wave propagation over discrete free surface and time, extending in the time domain a related study by Nakos and Scalvounos (1990) for the frequency domain

problem. Comparison of the continuous and discrete dispersion relations allows the rational definition of the consistency, order and stability properties of the numerical solution scheme. After evaluating numerous solution algorithms, two schemes were selected based on their superior performance.

The lower-order scheme employs the explicit and implicit Euler marching for the kinematic and dynamic free surface conditions, respectively, and it may be summarized as follows,

$$\left\{ \begin{array}{l} (\varphi)_j^n B_{ij} + (\varphi)_j^n D_{ij} - (\varphi_z)_j^n S_{ij} = 0 \\[2ex] \dfrac{(\varphi)_j^{n+1} - (\varphi)_j^n}{\Delta t} B_{ij} + (\varphi)_j^{n+1} \left[\nabla \Phi \right]_i^{n+1} \cdot \nabla B_{ij} \\[2ex] \quad = -g(\zeta)_j^{n+1} B_{ij} - \left[\dfrac{d\Phi}{dt} + \dfrac{1}{2} \nabla \Phi \cdot \nabla \Phi \right]_i^{n+1} \\[2ex] \dfrac{(\zeta)_j^{n+1} - (\zeta)_j^n}{\Delta t} B_{ij} + (\zeta)_j^n \left[\nabla \Phi \right]_i^n \cdot \nabla B_{ij} \\[2ex] \quad = (\zeta)_j^n \left[\dfrac{\partial^2 \Phi}{\partial z^2} \right]_i^n B_{ij} + (\varphi_z)_j^n B_{ij} \end{array} \right\}$$
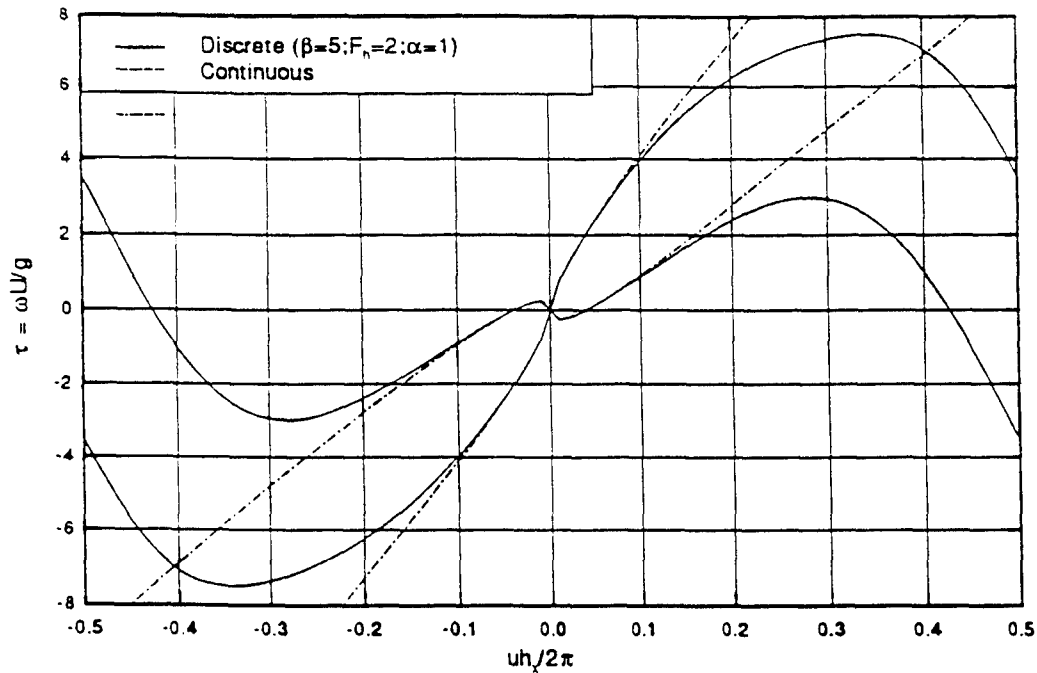
$$(3.3)$$

where summation over the multiply occurring j

616

Figure 2. Continuous vs. discrete dispersion relations.

index is assumed and

$$[\nabla\Phi]_i^n = \nabla\Phi(\vec{x}_i, t^n)$$

$$B_{ij} = B_j(\vec{x}_i)$$

$$S_{ij} = \iint B_j(\vec{x}') \, G(\vec{x}_i; \vec{x}') \, d\vec{x}' \qquad (3.4)$$

$$D_{ij} = \iint B_j(\vec{x}') \, G_n(\vec{x}_i; \vec{x}') \, d\vec{x}' \ .$$

It is shown in Nakos (1993) that the above scheme, referred to as "*Emplicit Euler (EE)*", is neutrally stable under the stability condition illustrated in figure 1. At low mean forward speeds the critical value of the time step scales with the square root of the typical panel size h, while at higher speeds the stability condition imposes a much more restrictive upper bound of Δt scaling with $h^{3/2}$.

A remedy to the severe stability criterion of figure 1 may be found in employing a three-step semi-implicit scheme composed of a Leap-frog marching for the kinematic free surface condition and a Trapezoidal approximation of the dynamic condition (see Vada and Nakos (1993)). This scheme, referred to as "*TLF*", is also neutrally stable under a stability condition which penalizes high forward speed flows less severly.

Unconditionally neutrally stable time-marching schemes may also be designed, but they have the unfortunate property of being fully implicit. Both the *EE* and *TLF* schemes avoid full coupling of the free surface conditions with the integral equation, therefore permitting their successive employment for the evolution of each unknown independently. This is a most welcome attribute, in light of our objective to include non-linear effects.

The matrix form of (3.3), as well as the corresponding TLF formulation, consists of one full and two banded matrices, associated with the integral equation and the free surface conditions respectively. It is worth noting the the full matrix dependents only on the geometrical configuration of the computational domain and therefore, once it is set and LU-decomposed, may be repeatedly employed for all desired simulations.

Under the assumption of infinitely large free surface computational domain, the discrete formulation may be transferred to the frequency domain where the associated *discrete dispersion relation* may be identified. This dispersion relation governs the free wave propagation over the discrete medium established by the numerical algorithm. Under neutral stability, the discrete dispersion relation is directly comparable to its continuous counterpart. A sample comparison between the polars of the discrete and continuous dispersion

617

relations, for the *EE* scheme, is illustrated in figure 2. The discretization density is quantified in terms of the *grid Froude number* $F_h = U/\sqrt{gh_x}$, the *panel aspect ratio* $\alpha = h_x/h_y$ and the *free surface grid number* $\beta = \sqrt{h_x/g}/\Delta t$.

At small wavenumbers and frequencies the continuous and discrete polars coincide, owing to the consistency of the numerical scheme. However, the corresponding polars divert from each other in the neighborhood of length scales that are barely resolved by the grid. Wave components in that region are miss handled by the discretization scheme and they are seen to propagate at erroneous directions, therefore jeopardizing the overall accuracy of the numerical solution. As a remedy, a low-pass filtering technique is employed for the elimination of the short length scales similar to the "smoothing device" proposed by Longuet-Higgins and Cokelet (1976). The adopted filter shape is based on a 7-point polynomial interpolation designed to have no effect on length scales longer than approximately 4-5 panel sizes. Numerical experience with the adopted filtering has shown that it has an uninvited smoothing effect on the local non-radiating disturbance. Minimization of such side influence may be obtained by a relatively infrequent application of filtering which allows "recovery" of the local disturbance.

The discrete dispersion relation may be also interpreted as the *characteristic polynomial* of the underlying time-stepping scheme. The degree of the polynomial depends on the order of the time-stepping scheme, which causes the three-step *TLF* scheme to have three real and distinct roots, under neutral stability. The two principal roots correspond to the roots of the continuous dispersion relation as in the case of the *EE* time-marching algorithm. The third root gives rise to an undamped spurious wave system composed of all wavelengths, that can be resolved by the mesh, and high frequencies comparable to the Nyquist frequency of the discretization, $\pi/\Delta t$, (see Vada and Nakos (1993)). Such phenomenon is frequently encountered in connection with the use of the Leap-Frog scheme and for its remedy Asselin (1972) has proposed an effective asymmetric time-filtering device, which is employed by the present study. Further details of the stability analysis of the present time-domain Rankine panel method may be found in Nakos (1993).

4. WAVE ABSORBING LAYER

Given a sufficiently long simulation interval, the waves generated by the vessel will propagate outwards and interact with the truncation of the free surface computational domain. The effect of the free surface truncation may be interpreted as reflection by a horizontal rigid lid laid over the free surface, outside the computational domain.

Two clearly distinct strategies are suggested in the literature for dealing with such wave reflections. The first is based on enclosing the computational domain inside a control surface over which appropriate radiation conditions are imposed. The present study elects to deal with the truncation error by adopting the second strategy of *wave absorbing layers* as they are reviewed by Israeli and Orszag (1981).

Consider the "Fourier pair" of the linear free surface conditions and the corresponding dispersion relation,

$$\left\{ \begin{aligned} \phi_t &= -g\eta \\ \eta_t &= \phi_z \end{aligned} \right\} \leftrightarrow \omega = \pm \left[g\sqrt{u^2 + v^2} \right]^{1/2} \quad (4.1)$$

A shift of the frequency in the complex plane away from the real axis results in wave damping and may be obtained by introducing Newtonian cooling terms in the kinematic free surface condition, as follows,

$$\left\{ \begin{aligned} \phi_t &= -g\eta \\ \eta_t &= \phi_z - 2\nu\eta + \frac{\nu^2}{g}\phi \end{aligned} \right\} \leftrightarrow \omega = i\nu \pm \left[g\sqrt{u^2 + v^2} \right]^{1/2}$$

$$(4.2)$$

where $\nu > 0$ is the strength of the Newtonian cooling assumed here to be uniformly distributed. In view of the righthand side of (4.2), ν may also be interpreted as the Rayleigh viscosity used for the enforcement of the proper radiation condition in the frequency domain formulation of the problem. Damped free surface conditions at the presence of forward speed follow from (4.2) by adding the proper convective terms to the $\partial/\partial t$ operator.

The design of a wave absorbing layer is based on the employment of the modified free surface conditions (4.2) over the outer portion of the computational domain. This study adopts the recommendations of Israeli and Orszag (1981) for quadratic variation of the cooling strength ν over the damping zone, with zero value and slope along
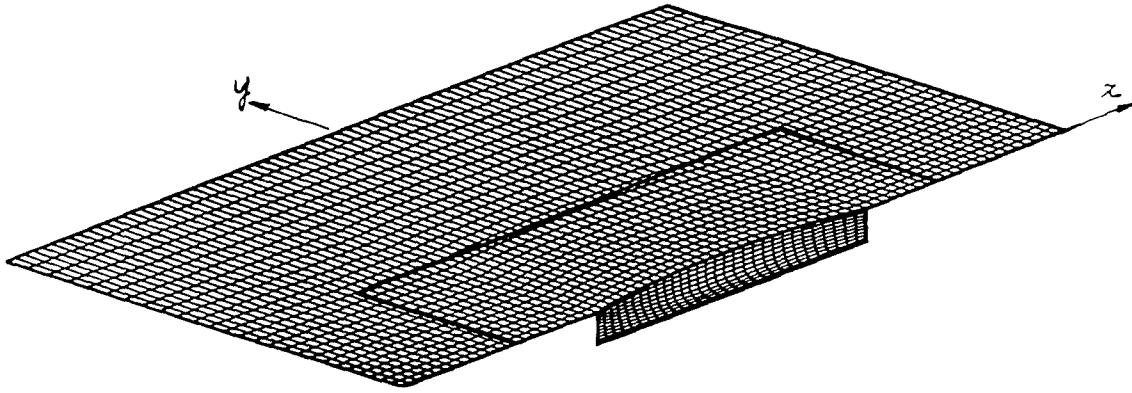
Figure 3. The modified Wigley hull computational domain used for the solution of zero-speed flow. The computational domain outside the square domain drawn on the free surface serves as a numerical beach.

the inside-end of the zone,

$$\nu(\rho) = 3\frac{C_s}{C_w^3}(\rho - \rho_0)^2, \ \ 0 \leq \rho - \rho_0 \leq C_w \quad (4.3)$$

where ρ signifies the radial distance from the wavemaking source, with the damping zone starting at $\rho = \rho_0$ and extending over a width C_w. The overall cooling strength of the zone is dictated by the parameter C_s. Similar wave absorbing devices have been successfully implemented in two dimensions by Baker, Meiron and Orszag (1981) and Cointe (1989).

The effectiveness of the proposed *artificial beach* is extensively tested by Nakos (1993). Its performance depends mainly on the width, C_w, and its successful employment requires minimal tuning. The numerical results of following sections may be considered as a more pragmatic demonstration of the effectiveness of the wave absorption mechanism.

As a general rule, the presence of significant forward speed de-emphasizes the importance of wave absorption. That is because significant waves approach the downstream only portion of the truncation line causing reflections with dispersion characteristics identical to the ones of the main wave field, therefore, propagating downstream and away from the vessel.

5. FORCED HARMONIC MOTIONS AT ZERO FORWARD SPEED

This section discusses the application of the nu-

merical solution algorithm, outlined in the previous sections, for the simulation of wave flows due to forced heave and pitch oscillations of a ship without forward speed. The main purpose of this numerical test is to demonstrate the effectiveness of the adopted artificial beach in realistic situations. The flow around the modified Wigley model is considered. The hull shape and the computational domain are illustrated in figure 3. The free surface grid of figure 3 extends 125% of the waterline length L in the transverse direction and 75% of L upstream and downstream. Due to the transverse symmetry about the centerplane, only the $y > 0$-part of the configuration is discretized. The size and location of the adopted artificial beach is also shown in figure 3. Its width is 75% of L in the transverse direction and 50% of L upstream and downstream. For the following simulations the size of the time step is selected to be $\Delta t = 0.04\sqrt{L/g}$, corresponding to free surface grid number $\beta \simeq 4$. The free surface is assumed to be calm for all time $t \leq 0$, and the hull motion starts impulsively at $t = 0$, oscillating thereafter at a number of selected frequencies ω_k,

$$\xi_i(t) = \sum_k \Xi_i^k \cos\omega_k t, \ t > 0, \ i = 1, ...6, \quad (5.1)$$

where Ξ_i^k is the amplitude of the i'th mode motion at frequency ω_k.

The linearized pressure over the hull is given by Bernoulli equation in terms of the wave potential φ,

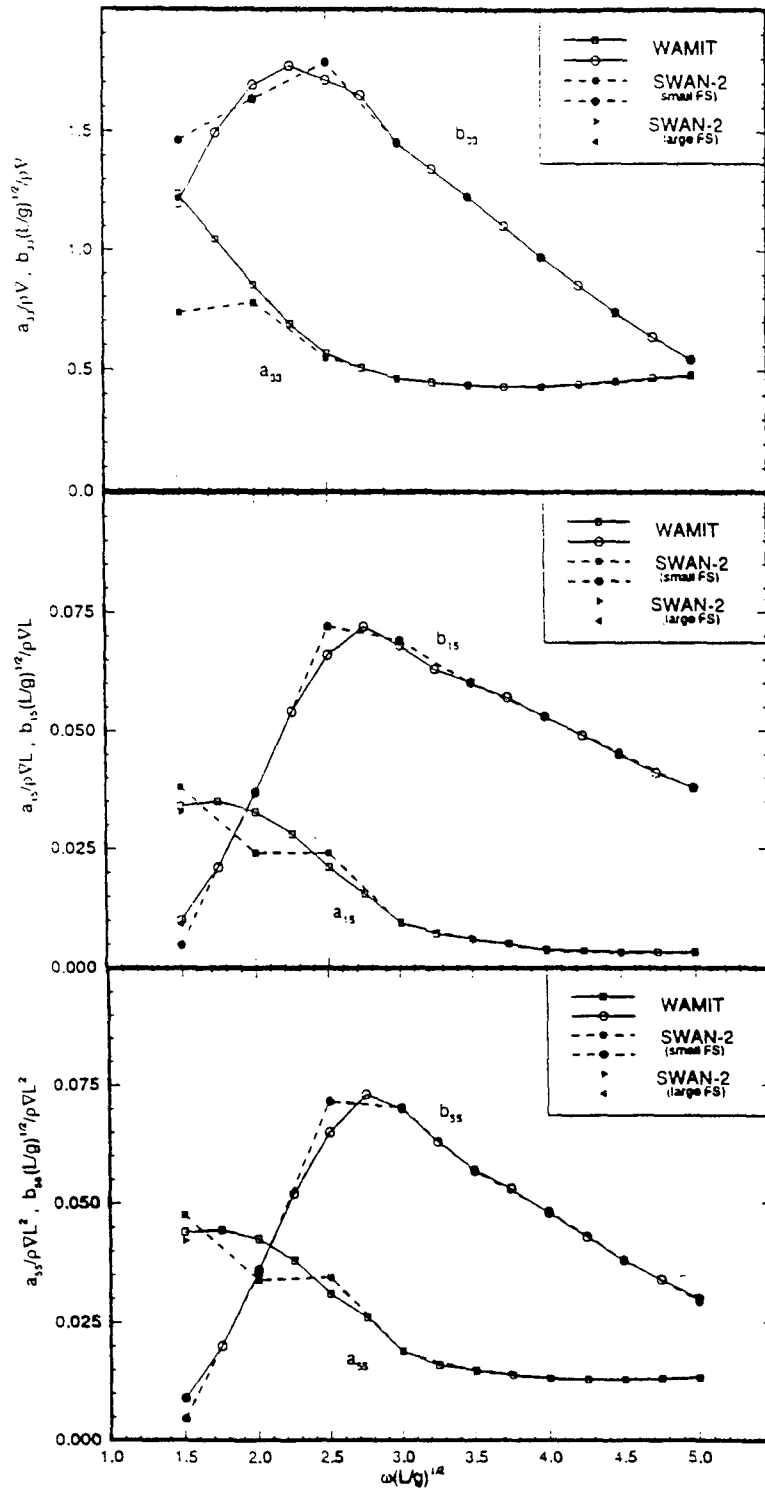$$\frac{p(\vec{x}, t)}{\rho} = -\frac{\partial\varphi}{\partial t} , \quad (5.2)$$

619

Figure 4. Added mass and damping coefficients for the modified Wigley hull at zero forward speed.

and it is evaluated at "half-steps", $(n + \frac{1}{2})\Delta t$, by a two-point centered difference scheme. Numerical experience has shown that employment of the two-point one-sided difference formula for the approximation of (5.2) results in significant discretization errors. An alternative, equally effective, solution is the three-point backward difference scheme for the evaluation of the pressure, which is employed in the freely floating body simulations of section 8.

Two instances of the wave field due to forced sinusoidal heaving and pitching motion of the hull at frequency $\omega\sqrt{L/g} = 3$, were calculated. At zero forward speed, the free wave system contained a single wavelength, which was inversely proportional to the square of the frequency. At all frequencies, the flow was seen to reach rapidly a steady-state. The resulting forces were fitted by a sinusoidal function in order to identify the added mass and damping coefficients shown in figure 4. The results of the present solution algorithm, labeled *SWAN-2*, obtained by the grid of figure 3 (small FS), are compared with results from the frequency domain computer code *WAMIT* (see eg. Korsmeyer et al (1988)), whose accuracy has been verified by systematic convergence tests to a level higher than 1%.

Despite the perfect comparison of the *SWAN-2* and *WAMIT* results at moderate and high frequencies ω, large discrepancies occur in the range $\omega\sqrt{L/g} \leq 2.5$. At these low frequencies, the generated wavelengths are too long to be effectively absorbed by the artificial beach of figure 3. Namely, at $\omega\sqrt{L/g} = 1.5$ the far-field wavelength is almost four times as long as the width of the wave-absorbing layer. Significant errors due to the free surface truncation are, therefore, expected. In order to verify the latter statement, the flow at $\omega\sqrt{L/g} = 1.5$ is also solved using a free surface domain of quadruple the size in each direction and 1/3 of the panel density, referred to as (large-FS). Predictions for the time history of the vertical force due to heave, using the two different computational domain, were calculated. Both simulations appear to reach a steady-state, although this becomes significantly more delayed in the results obtained by the (small-FS) domain. The "corrected" added mass and damping coefficients at $\omega\sqrt{L/g} = 1.5$, resulting from the (large-FS) simulations are superimposed on figure 4 and are seen to compare very well with the corresponding *WAMIT* predictions, despite the relatively low discretization density of the (large-FS)

grid.

The increased accuracy of the results obtained with the (large-FS) domain solidifies the argument that effective wave absorption can be obtained as long as the size of the numerical beach is comparable or larger than the generated wavelengths.

6. STEADY MOTION AT CONSTANT FORWARD SPEED

This section presents applications of the proposed solution algorithm for the prediction of wave flows due to the steady forward motion of ships. The free surface is assumed to be calm for all time less than $t = 0$, when the vessel starts impulsively moving forward at full speed.

The hydrodynamic pressure over the hull surface is given by Bernoulli equation linearized in a manner consistent with the linearization of the free surface conditions,

$$\frac{p(\vec{x}, t)}{\rho} = -\frac{d\varphi}{dt} - \nabla\Phi\cdot\nabla\varphi - \frac{d\Phi}{dt} - \frac{1}{2}\nabla\Phi\cdot\nabla\Phi \quad (6.1)$$

where the time derivatives (d/dt) contain the corresponding convective terms. The pressure distribution is evaluated at half-steps, as explained in the preceding section and integrated over the hull surface to render the time history of the wave resistance, sinkage force and trim moment.

The first simulations involve the Series-60, $c_B = 0.7$, hull advancing at Froude number $F = 0.3$. The hull geometry and the surrounding free surface computational domain are shown in figure 5 along with the selected size of the artificial beach. As discussed in section 4, due to the strongly convective nature of the wave flow no absorbing layer is needed downstream. Two different grid densities are used, the one illustrated in figure 5 with 50 panels along the ship length and a coarser one composed by 30 panels along the ship length. Both grids use the same extend of the free surface computational domain and have panels of unit aspect ratio close to the waterline. The transverse panel size increases in the y-direction geometrically at a ratio of 1.05.

Simulations are carried out until time $t\sqrt{g/L} = 50$ is reached using time steps $\Delta t = 0.03$ and 0.04 for the finer and coarser discretizations, respectively. The predicted wave patterns at the final time step of the simulation are compared in figure 6. Good
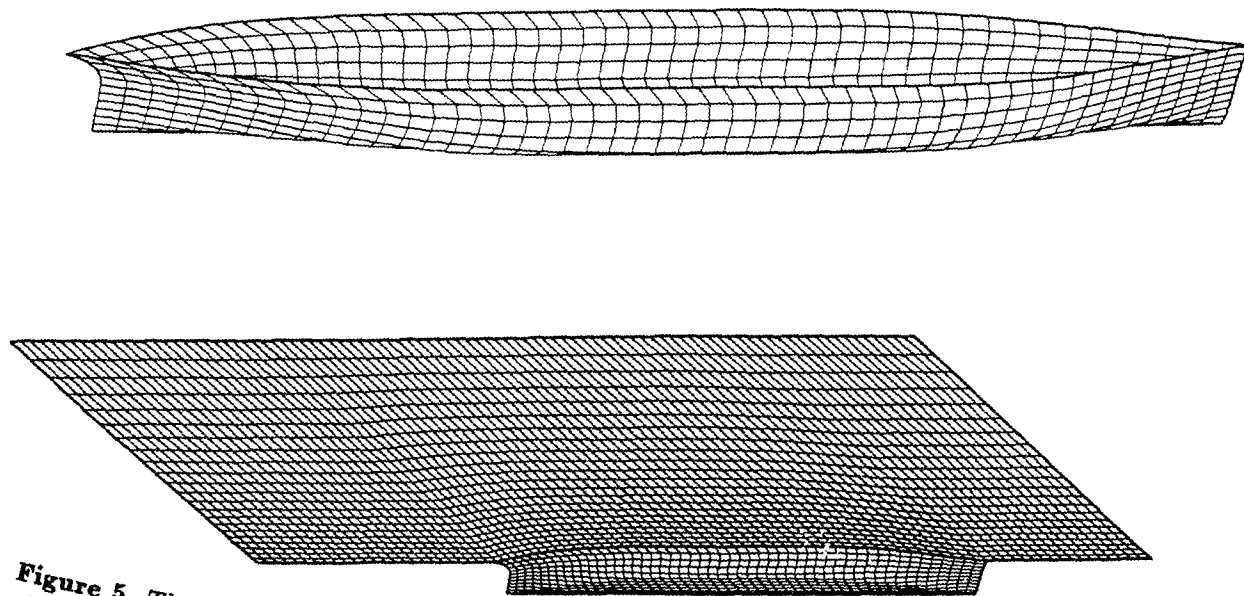
Figure 5. The Series-60, Cb=0.7, hull and computational domain used for solution of the forward speed steady flow.

convergence with the grid density may be observed, especially with respect to the longer length scales of the solution. Shorter diverging wave components are de-emphasized by the coarse discretization mainly due to the application of space-filtering. Figure 6 also shows the pressure distribution over the hull surface which may be seen to be satisfactorily converged.

The time histories of the wave induced forces and moments on the vessel are illustrated in figure 7, as predicted by both the fine and coarse discretizations. All curves show sharp initial transients which settle rapidly to a decaying oscillation at period $T \simeq T_c^l = 8\pi F$, corresponding to the $\tau = 0.25$-singularity which is excited due to the impulsive start of the forward motion. The amplitude of these transient oscillations is, however, smaller than related predictions of Lin and Yue (1990).

The aforementioned "critical" oscillations are much more pronounced in the next simulation which considers the same series-60 hull at Froude number $F = 0.2$. Figure 8 shows the time history of the resultant forces and moments, as predicted by four different computational domains. All grids are of the same density with 50 panels

along the waterline length. Two different values of the free surface extent in the transverse direction (YOUT) and of the transverse width of the
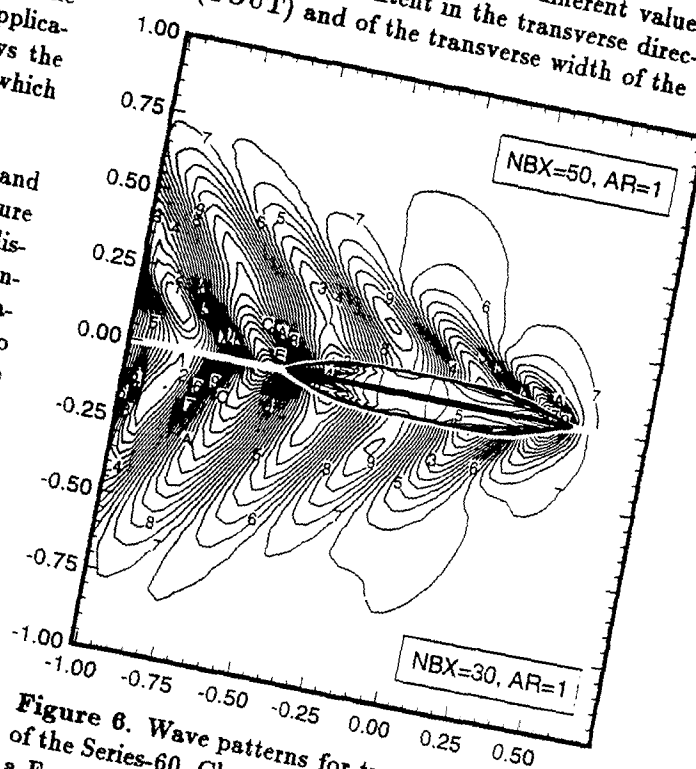
Figure 6. Wave patterns for two discretizations of the Series-60, Cb=0.7, hull in steady motion at a Froude number of 0.3.
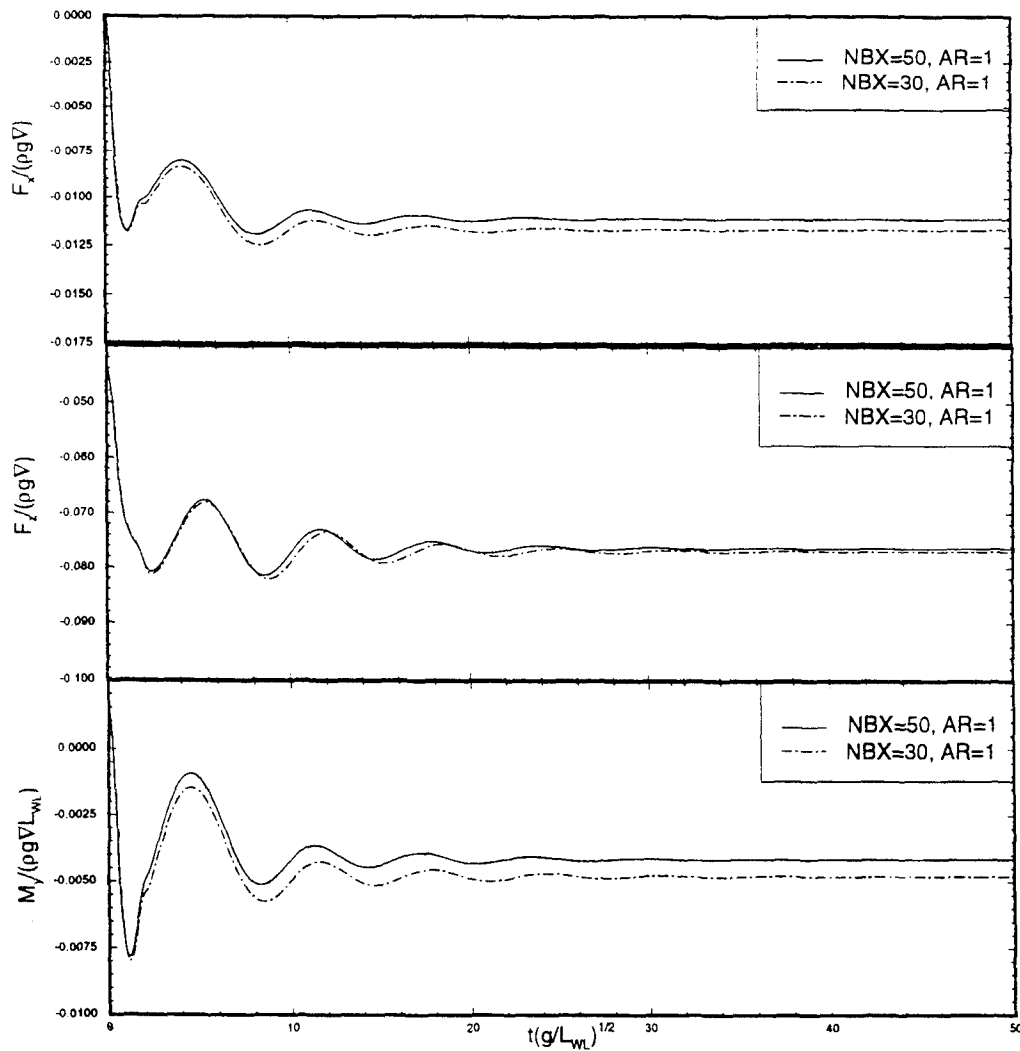
Figure 7. Time history for the Series-60, Cb=0.7, hull in steady motion at a Froude number of 0.3.

artificial beach (C_W) are considered. All records oscillate at approximately the same critical period, T_c, and about the same mean value, but with desperately different amplitudes and phases. Further numerical experimentation has shown that the precise form of the critical transient oscillation depends, almost exclusively, on YOUT and C_w with the general tendency to decrease as the size of the free surface domain and artificial beach increase.

The $\tau = 0.25$—singularity of the forward speed problem which is the underlying cause of the persistent transient oscillations has been been extensively studied over the years. For elementary flows due to translating wave singularities it may be proven that, within linear theory, there exist a wave component with vanishing group velocity whose energy is trapped in the near-field. How-

ever, such studies concentrate on the Neumann linearization of the free surface conditions which is not the framework of the present study. Moreover, the presence of the truncated free surface and wave absorbing layer is expected to have a significant effect on the "trapped" wave component whose wavelength is typically much larger than the overall size of the computational domain.

From the practical standpoint, the transient effect of the critical oscillations causes a significant delay to the onset of the corresponding steady-state and, therefore, increases the computational effort needed for the accurate prediction of the steady-state forces. The idea of filtering any such persisting transients appears very attractive and it is proposed for further study.

623
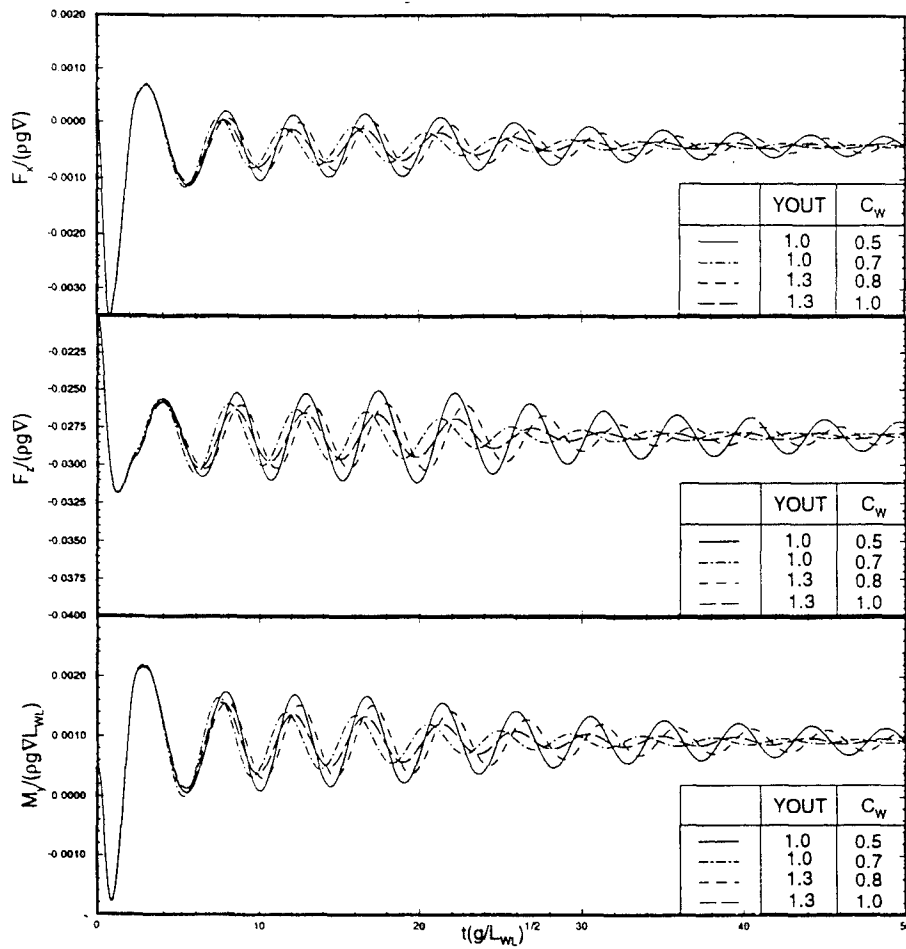
Figure 8. Time history for the Series-60, Cb=0.7, hull in steady motion at a Froude number of 0.2.
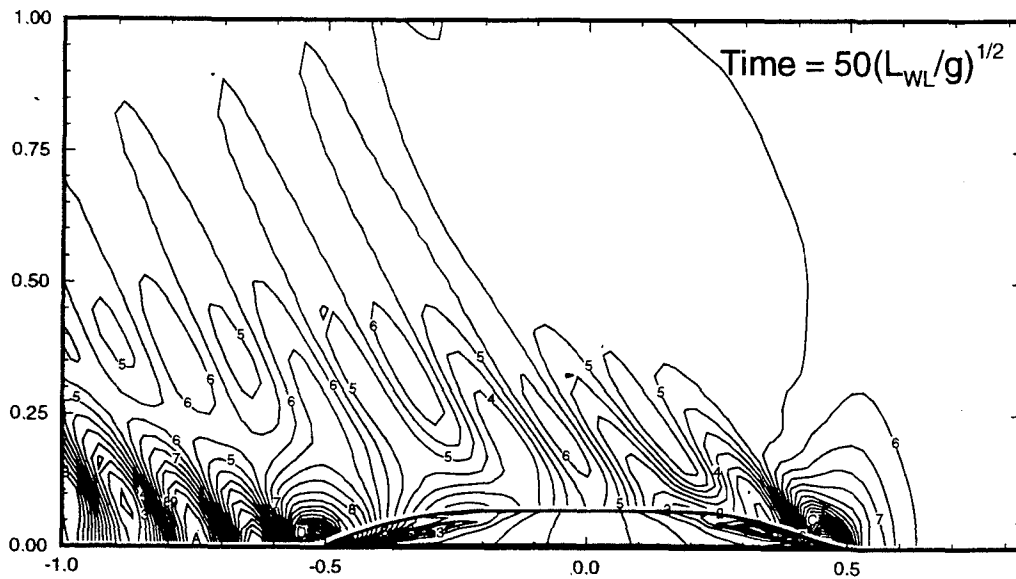
Figure 9. Wave pattern for the Series-60, Cb=0.7, hull in steady motion at a Froude number of 0.2.

624
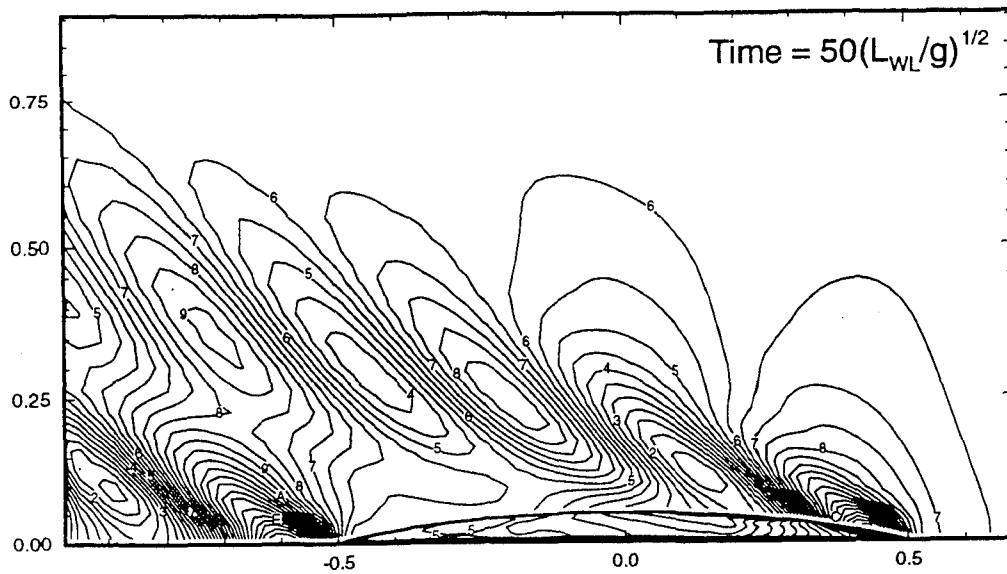
Figure 10. Wave pattern for the modified Wigley hull at a Froude number of 0.3.
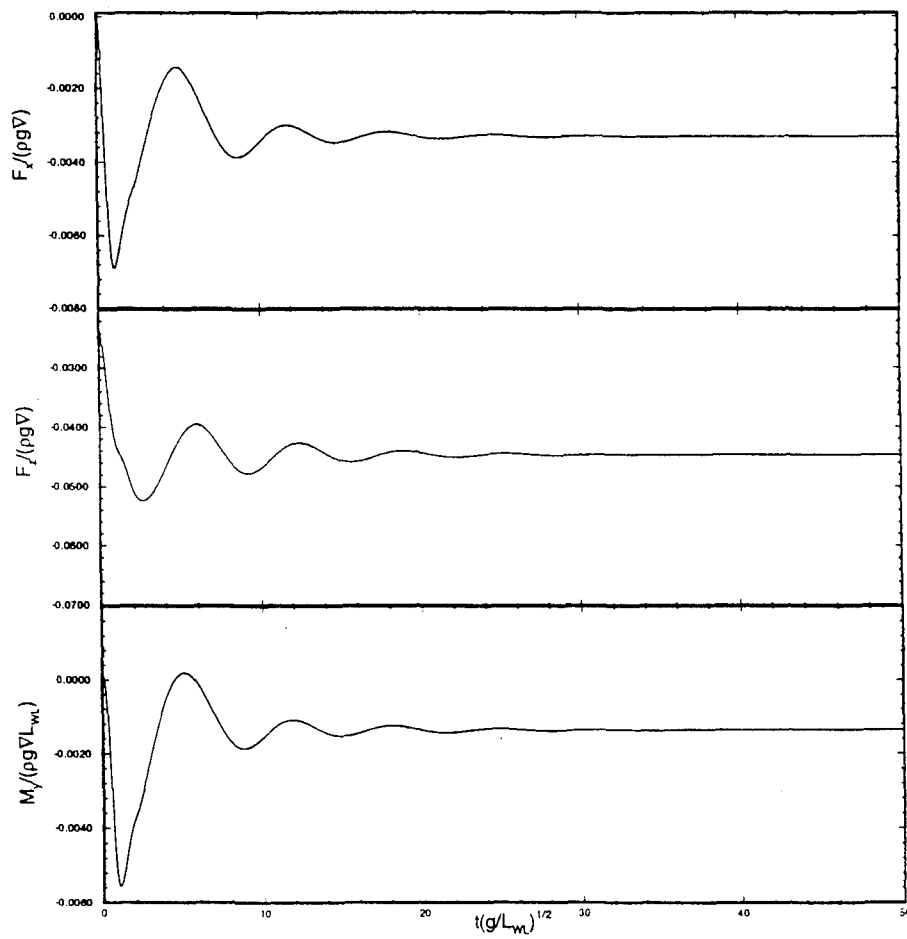
Figure 11. Time history for the modified Wigley hull in steady motion at a Froude number of 0.3.

625
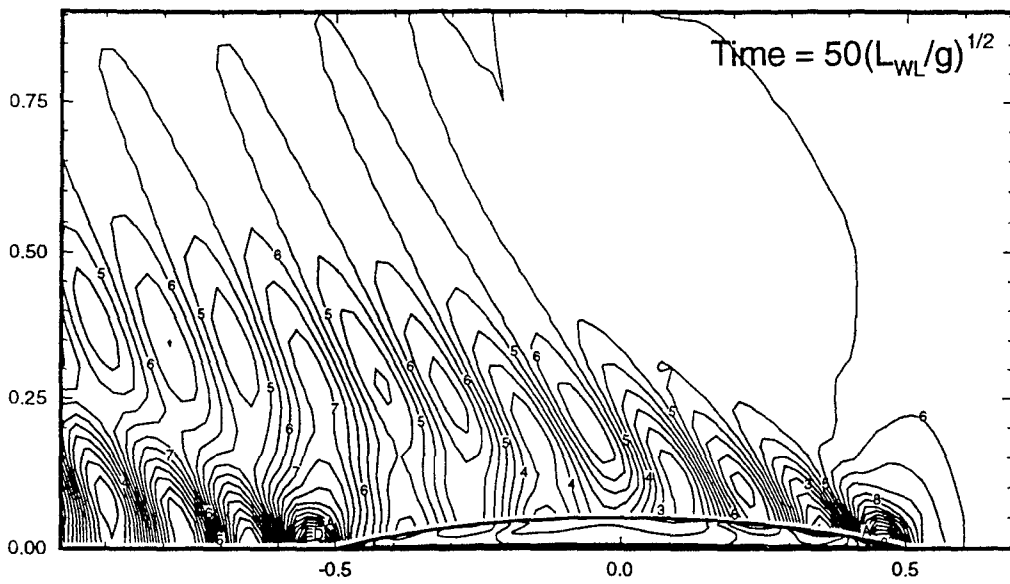
Figure 12. Wave pattern for the modified Wigley hull at a Froude number of 0.2.
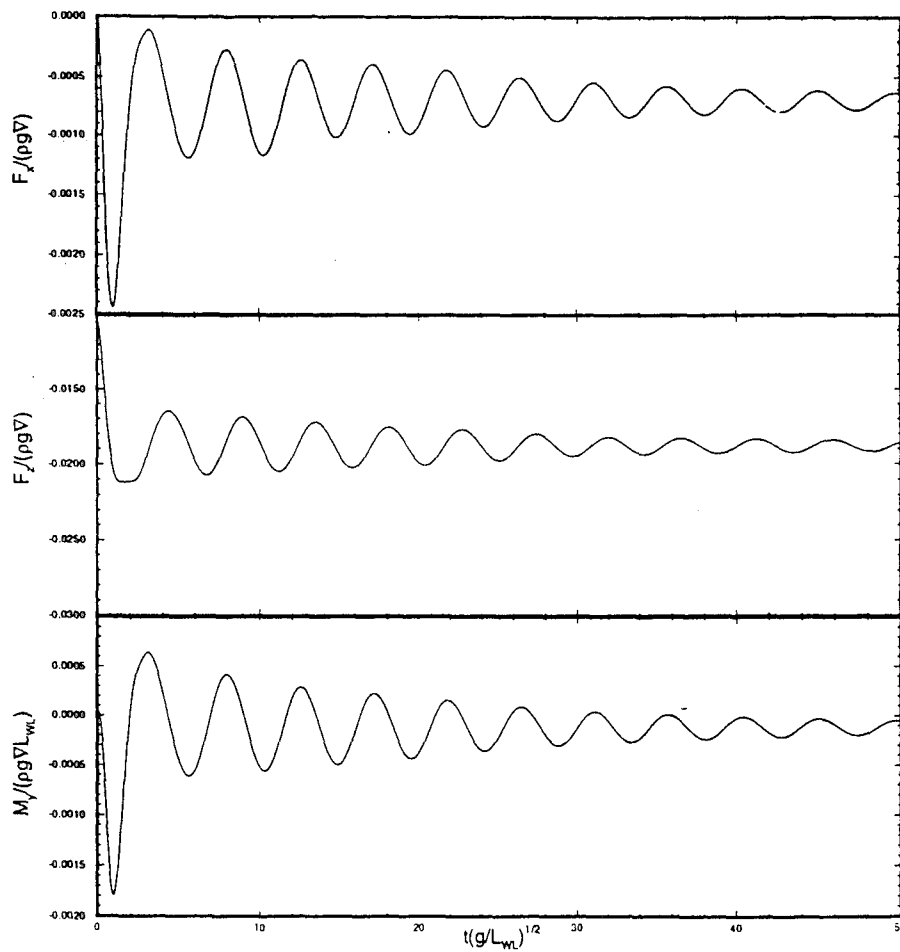
Figure 13. Time history for the modified Wigley hull in steady motion at a Froude number of 0.2.

The insensitivity of all the above conclusions to the hull shape is illustrated by simulations of the modified Wigley model in steady forward motion at Froude numbers 0.3 and 0.2. Like for the Series-60 hull, the simulations are carried out to time $t\sqrt{g/L} = 50$ using a grid density corresponding to 50 panels within the waterline length and a time step of $\Delta t = 0.03$. Figures 9-13 show the predictions for the wave pattern at the final time step and the time history of the forces and moments acting on the hull. Once again, the critical transient oscillations in the force record are much more pronounced at the low speed.

7. FORCED HARMONIC MOTION AT CONSTANT FORWARD SPEED

The simulation of forced harmonic oscillations of
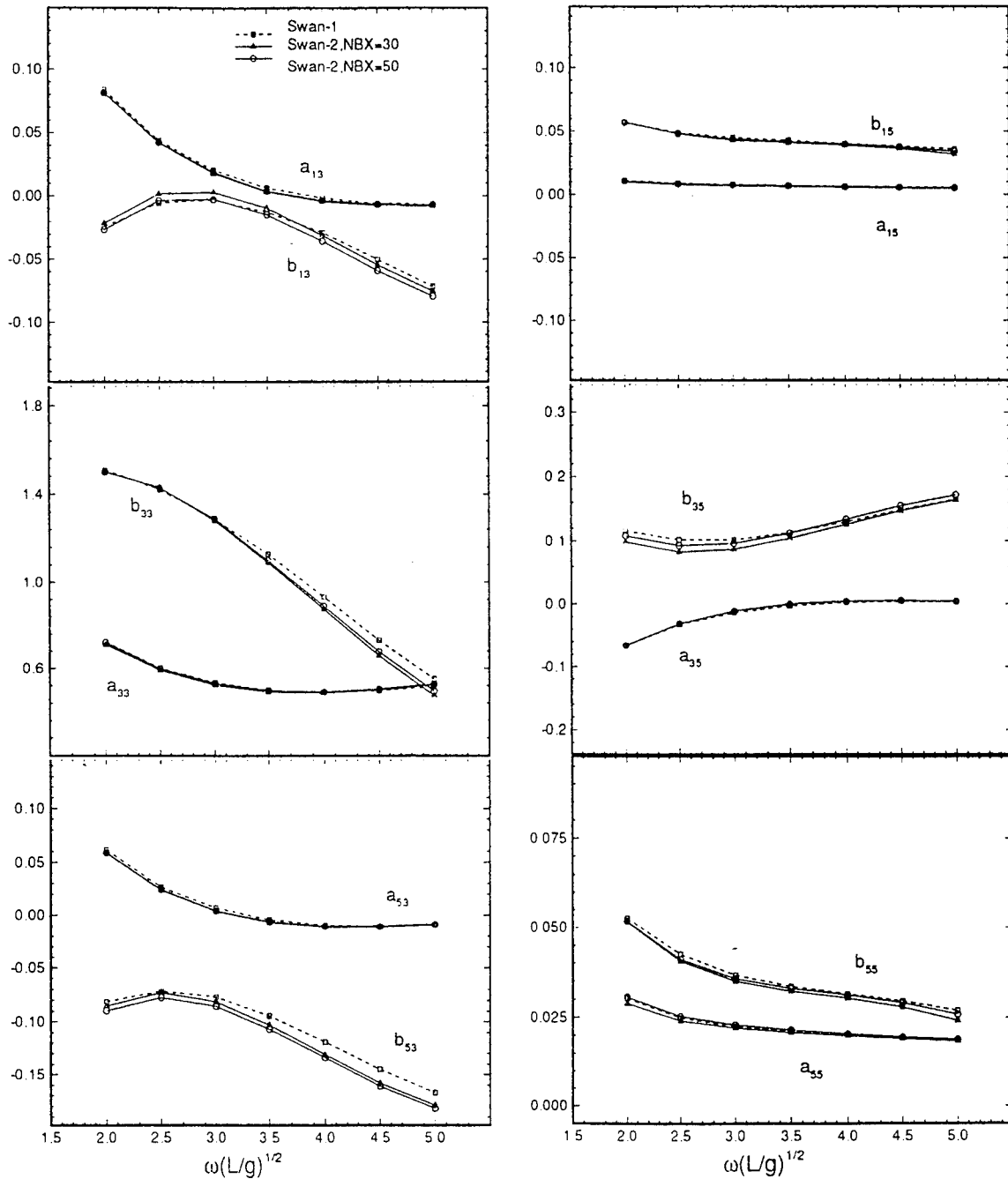
Figure 14. Added mass and damping for the modified Wigley hull at a Froude number of 0.3.

ships advancing at a constant forward speed is the subject of this section. The vessel is considered to be at rest for all time $t \leq 0$, when it suddenly starts moving forward at full speed while oscillating with amplitude given by (5.1).

The wave flow due to the forced harmonic heave and pitch motion of the modified Wigley model and the Series-60, $c_B = 0.7$, is solved by using both the coarse and fine discretizations of section 6. The time history of the resultant forces and moments is evaluated by integrating the pressure,

$$\frac{p(\vec{x}, t)}{\rho} = -\frac{d\varphi}{dt} - \nabla\Phi \cdot \nabla\varphi \qquad (7.1)$$

over the hull surface. Notice that the last two terms of (6.1) are not included in (7.1) since they do not contribute to the steady-state oscillatory forces.
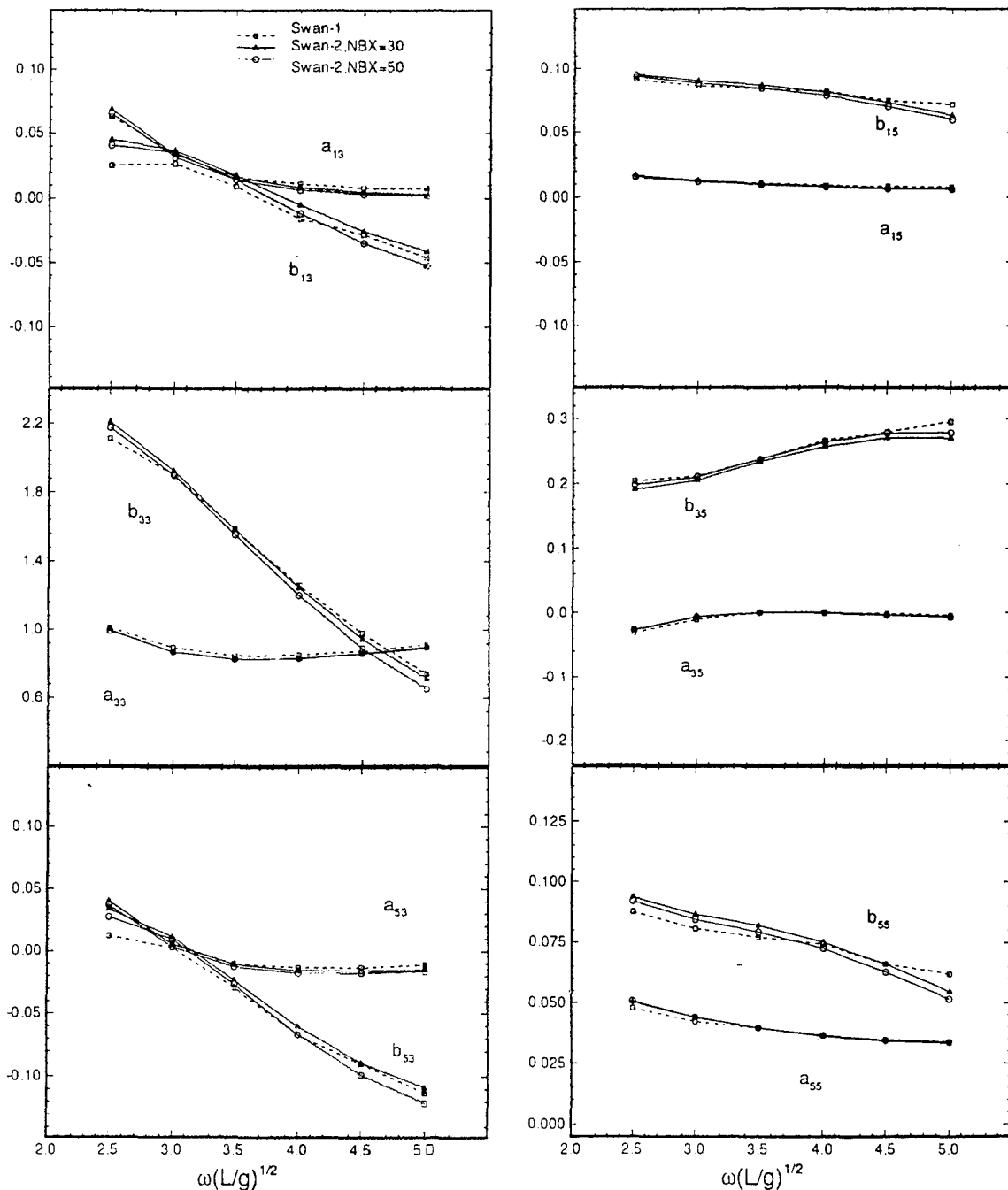
Figure 15. Added mass and damping for the Series-60, Cb=0.7, hull at a Froude number of 0.2.

628

Simulations are carried out until steady-state is reached and the force records are fitted by appropriate sinusoidal functions in order to identify the "frequency domain" added mass and damping coefficients. Figures 14 and 15 compare the predictions of the present time domain solution algorithm *SWAN-2* to computations by the frequency domain solver *SWAN-1* (see Nakos and Sclavounos (1990)), using identical linearization of the free surface and body boundary conditions. Very satisfactory agreement is found both for the modified Wigley model at Froude number 0.3 and the Series-60 hull at Froude number 0.2.

8. FREE MOTION AT CONSTANT FORWARD SPEED

This section presents free motion simulations for ships advancing at a constant forward speed. The vessels start impulsively at $t = 0$ and retain freedom of motion in heave and pitch. Incident head seas can be imposed for the simulation of the resulting ship motions. If the ambient sea state is calm, the simulation becomes a free-decay test where the ship transits from the rest, or static equilibrium, position towards her dynamic equilibrium position, defined by the appropriate steady-state sinkage and trim.

The equation of motion of the hull as a rigid body read as follows,

$$\mathbf{M}\frac{d^2}{dt^2}\vec{\xi}(t) + \mathbf{C}\vec{\xi}(t) = \vec{F}(t) \ , \qquad (8.1)$$

where $\mathbf{M}$ is the inertia matrix, $\mathbf{C}$ are the hydrostatic restoring coefficients, $\vec{\xi}(t)$ are the rigid-body displacements, and $\vec{F}(t)$ is the resultant hydrodynamic force or moment. The initial conditions for the ship can vary. It may be started from a calm rest position or given a specified initial heave and/or pitch displacement and/or velocity. Currently, the time-stepping algrorithm for the integration of the equations of motion (8.1) is based on a semi-implicit backwards differentiation scheme which is only first-order accurate. As discussed at the end of this section, a higher-order scheme with more favorable stability properties is necessary and it is currently being designed.

Within this study three cases of free motion simulation are examined. The first case, illustrated in Figure 16, shows the heave and pitch response of a modified Wigley hull which starts impulsively at $t = 0$ from its calm-water position with a forward speed corresponding to Froude number $F = 0.3$. For all practical purposes, at time $t\sqrt{g/L_{WL}} = 30$ the initial transients have decayed and the solution has approached the corresponding steady-state sinkage and trim.

Figure 16. Modified Wigley hull started impulsively from rest and tending towards a forward speed equilibrium position at a Froude number of 0.3.

Figure 17. Modified Wigley hull started impulsively and dropped from an initial height, $\xi_3/L_{WL} = 0.01$ at three speeds.

Figure 18. Heave and pitch RAO's for the modified wigley hull at a Froude number of 0.3 as predicted by two methods.

630

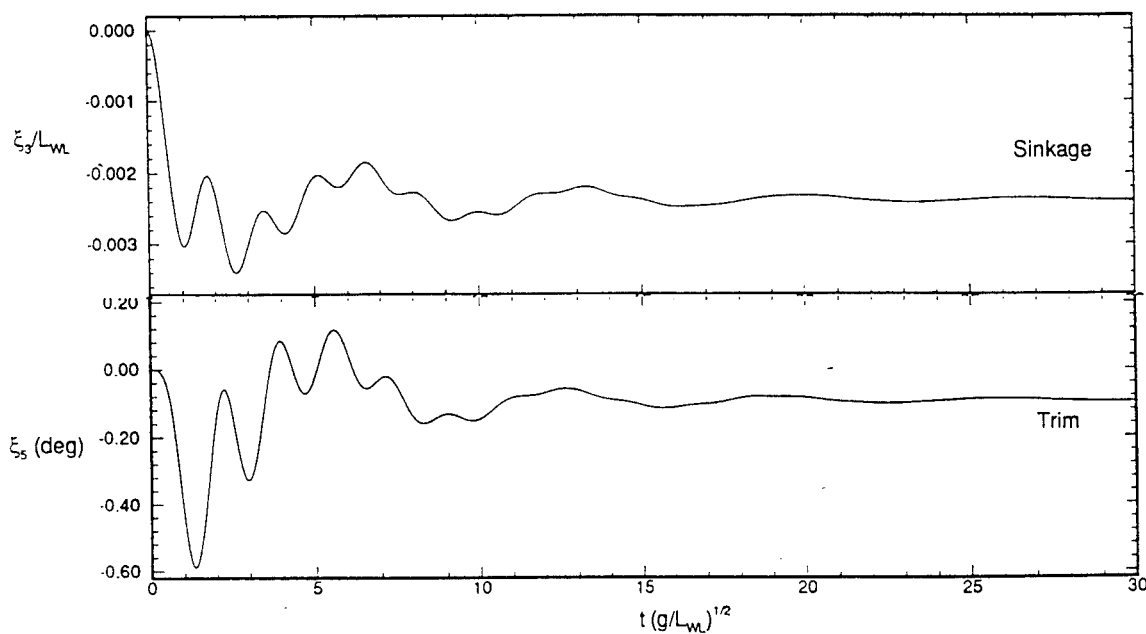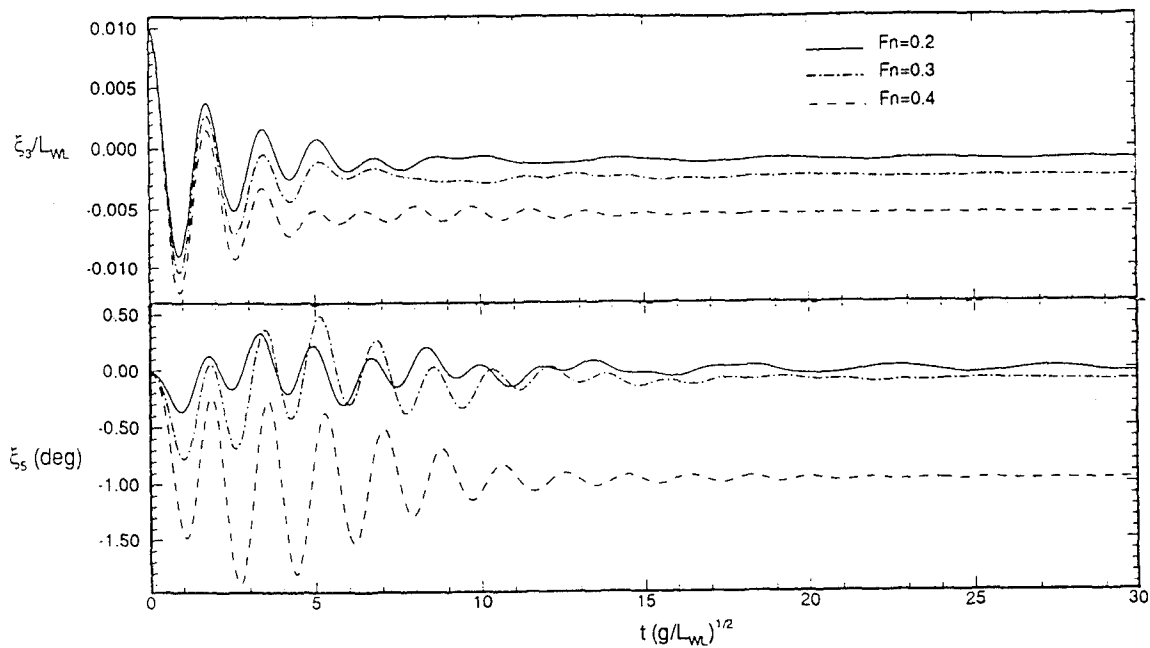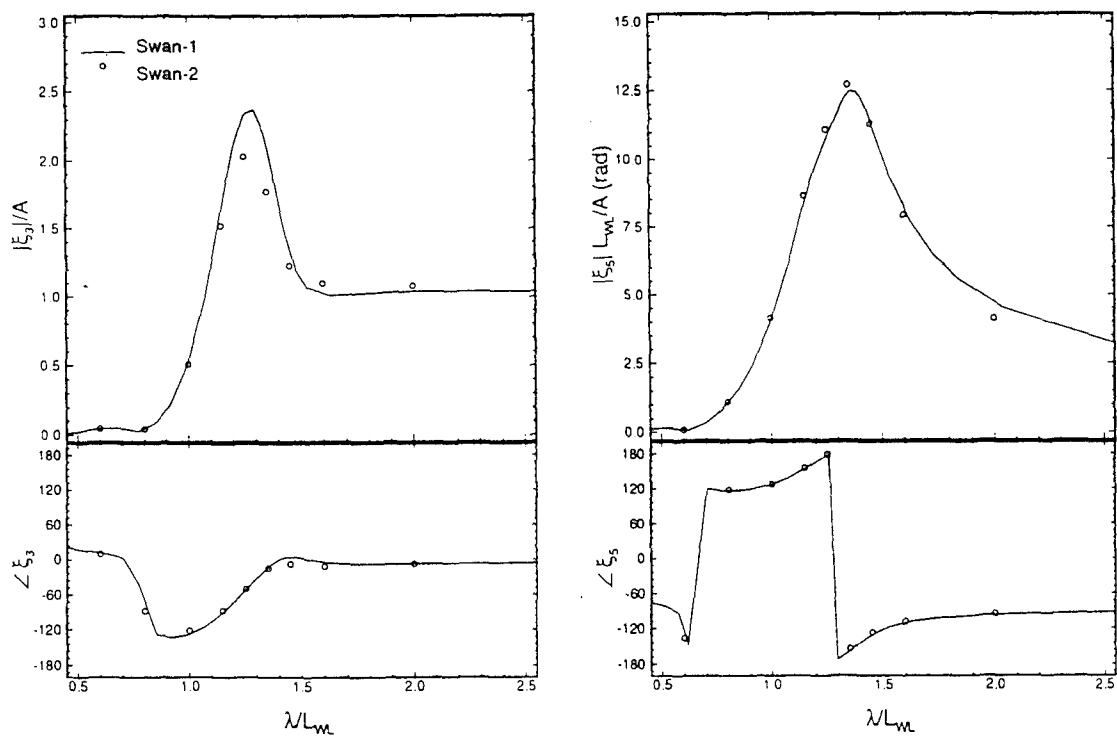The behavior of the transients is worthy of note. Two distinct frequencies are evident is the transient response of figure 16. The shorter period is the natural period of oscillation for the ship at this Froude number and corresponds to the peak in the Response Amplitude Operator curve predicted by the frequency domain solver *SWAN-1*. The longer period corresponds to the critical transient oscillation due to the $\tau = 0.25$—singularity, discussed in preceding sections and it is excited by the impulsive start of the ship.

Subsequently simulations of the same modified Wigley model were carried out at Froude numbers 0.2, 0.3, and 0.4, but this time the vessel was given an initial heave displacement equal to 1% of its waterline length. The predicted motion records are illustrated in figure 17. These tests are instructive in examining the decay of the natural modes of oscillation, and indicate how quickly a hull may reach the steady-state limit, given an initial heave and pitch displacement. The natural period of oscillation of the vessel is evident in the transients excited during the latter simulations. However, the scale of the oscillations at the natural frequency is such that nearly overshadows the critical transient oscillations at period $T_0 = 8\pi F$. The critical oscillations are most noticeable at the lowest Froude number but also affect the modulation of the motions at the higher speeds. Although there was no initial pitch for these free-decay tests, pitch motion did result due to hydrodynamic cross-coupling, which is amplified at higher speeds. After a sufficiently long interval of time the heave and pitch tend towards the sinkage and trim, respectively, appropriate for these speeds.

The predictions of the steady-state sinkage and trim by the present transient solver are considered superior to related computations made by steady-state solvers like *SWAN-1*. That is because the present transient approach incorporates, to leading-order, the effect of the sinkage and trim on the resultant force and moment due to the inclusion of the m-terms in the body boundary condition (2.5). Steady-state solvers may also account for the same effect, but only if they are employed iteratively with respect to the dynamic equilibrium position of the hull.

The last simulation test shows the heave and pitch response of the modified Wigley model advancing at Froude number 0.3 through multichromatic head seas. The time records of the resulting

heave and pitch motions are illustrated in figure 18. The simulation is carried out for a sufficiently long interval of time so that transients have decayed and the motion records may be safely transformed into the frequency domain. The resultant Response Amplitude Operator is compared to related predictions of the frequency domain solver *SWAN-1*.

The predictions of both methods compare very favorably except for the peak magnitude of the heave response amplitude. Numerical convergence difficulties are experienced with respect to the time-step size at the peak of heave response, which may be attributed to numerical dissipation errors in the time-stepping algorithm for the integration of the equations of motion. Efforts are currently focused on analyzing this phenomenon and prescribing a higher-order algorithm for the solution of the equations of motion.

9. SUMMARY AND CONCLUSIONS

The design and implementation are presented of a Rankine Panel Method for the solution of transient wave-body interactions in three-dimensions. In the presence of forward speed the free surface and hull boundary condition are linearized about the double-body flow. The space discretization is based on the approximation of all unknowns in terms of the biquadratic B-spline functions and the time evolution is performed by a neutrally stable time-stepping algorithm. An artificial wave-absorbing beach is designed and employed for the damping of reflections due to the finite free surface computational domain.

Wave flows due to forced and free motions of realistic ship hulls are computed with and without mean forward speed. The simulations are continued until steady-state is reached and the resulting steady-state forces are compared to predictions by well-established frequency-domain solvers. The comparison is excellent for all cases, owing to the optimal design of the time-steeping algorithm and the effectiveness of the employed wave absorption device.

In the presence of forward speed, the onset of steady-state conditions is significantly delayed due to the $\tau = 0.25$—singularity of the corresponding frequency domain problem. The time-records of forces and motions are found to be "contaminated" by a slowly-decaying oscillation

at the critical frequency $\omega U/g = 0.25$, which is excited by the impulsive start-up of the vessel's motion. The wavelengths associated with this critical transient oscillation are often too long to be handled by the adopted extend of free surface computational domain and absorbing artificial beach.

Future extensions of the present formulation and solution scheme include relaxation of the body boundary condition linearization, in order to model large-amplitude ship motions, and solution of the wave flow past ships advancing along arbitrary curvilinear paths which addresses the problem of ship maneuvering in the presence of ambient waves.

ACKNOWLEDGEMENTS

REFERENCES

Asselin, R., 1972, "Frequency filter for time integrations", *Monthly Weather Review*, vol. 100, no. 6.

Baker, G. R., Meiron, D. I., and Orszag, S. A., 1981, "Applications of a generalized vortex method to non-linear free surface flows", *Third International Conference on Numerical Ship Hydrodynamics*.

Beck, R. F. and Liapis, S. J., 1987, "Transient Motions of Floating Bodies at Zero Forward Speed," *Journal of Ship Research*, Vol.31, No.3, pp. 164-176. Beck, R. F. and Magee, A. R., 1990, "Time-Domain Analysis for Predicting Ship Motions,", *Proceedings* Symposium on the Dynamics of Marine Vehicles and Structures in Waves, Brunel University, Amsterdam, pp. 49-65.

Cointe, R., 1989, "Nonlinear simulations of transient free surface flows", *Fifth International Conference on Numerical Ship Hydrodynamics*.

Israeli M., and Orszag S. A., 1981, "Approximation of radiation boundary conditions", *Journal of Computational Physics*, Vol. 41, pp. 115-135.

King, B. W., Beck, R. F., and Magee, A. R., 1988, "Seakeeping calculations with forward speed using time-domain analysis", *Seventeenth Symposium on Naval Hydrodynamics*.

Korsmeyer, F. T., 1988, "The first and second order transient free surface wave radiation problems", Ph.D. Thesis, Dept of Ocean Eng., MIT.

Korsmeyer, F. T., Lee, C.-H., Newman, J. N., and Sclavounos, P. D., 1988, "The Analysis of Wave Effects on Tension-Leg Platforms", *Offshore Mechanics and Arctic Engineering Conference*.

Liapis, S. J., 1986, "Time-domain analysis of ship motions", Report No. 302, Department of Naval Arch. and Marine Eng., University of Michigan.

Lin, W.-M., and Yue, D., 1990, "Numerical solutions of large-amplitude ship motions in the time domain", *Eighteenth Symposium on Naval Hydrodynamics*.

Longuet-Higgins, M. S., and Cokelet, E. D., 1976, "The deformation of steep surface waves on water. I. A numerical method of computation", *Proc. Roy. Soc. Lond.*, Vol. 350, pp. 1-26.

Maskew, B., 1992, "Prediction of Nonlinear Wave/Hull Interactions on Complex Vessels", *Nineteenth Symposium on Naval Hydrodynamics*.

Nakos, D. E., 1993, "Stability of transient gravity waves on a discrete free surface", Submitted for publication.

Nakos, D. E., and Sclavounos, P. D., 1990, "On steady and unsteady ship wave patterns", *Journal of Fluid Mechanics*, Vol. 215, pp. 263-288.

Newman, J. N., 1978, "The theory of ship motions", *Advances in Applied Mechanics*, Vol 18, pp. 221-283.

Newman, J. N., 1985, "The evaluation of free-surface Green functions", *Forth International Conference on Numerical Ship Hydrodynamics*.

Sclavounos, P. D. and Nakos, D.E., 1988, "Stability Analysis of Panel Methods for Free Surface Flows with Forward Speed", *Seventeenth Symposium on Naval Hydrodynamics*.

Vada, T., and Nakos, D. E., 1993, "Time-marching schemes for ship motion simulations", *Eighth International Workshop on Water Waves and Floating Bodies*.

Wehausen, J. V., 1967, "Initial Value Problem for the Motion in an UNdulating Sea of a Body with Fixed Equilibrium Position," *Journal of Engineering Mathematics*, Vol. 1, pp.1-19.

SESSION 12

LIFTING-SURFACE FLOW: STEADY VISCOUS METHODS

Numerical Simulation of Turbulent Flows Around Hydrofoil

C.C.S. Song and C. Chen

(University of Minnesota, USA)

Abstract

The numerical solution to the unsteady compressible flows at small Mach number has always run into trouble due to the disparity between the sound speed and convective speed. The equation of unsteady incompressible flows are even more difficult to solve numerically than that of compressible flows. More importantly, the incompressible flow equations contain no physical information related to pressure waves which is an essential mechanism of rapidly accelerating flow such as hydraulic transients and acoustics. The compressible hydrodynamic equations have been developed to remedy the mathematical and physical shortcomings of the incompressible flow approach. The large eddy simulation approach based on the compressible hydrodynamic equations has been applied to flow around a two dimensional hydrofoil and tip vortex flow around a three dimensional hydrofoil. The simulated mean flow, as well as the turbulent correlations in the two dimensional case have been compared with experimental data. The tip vortex trajectory and the structure of tip vortex core have been studied.

Nomenclature

A^+ constant
A_s projected surface area
a_0 sound speed
C_l lift coefficient
C_0 base chord length
C_s Smagorinsky constant
D damping coefficient
L lift
M Mach number
n normal coordinate of wall
p pressure
p_0 reference pressure
Rc radius of curvature

Re Reynolds number
Re_x Reynolds number based on x
R_θ Reynolds number based on momentum thickness
r radius in polar coordinate
r_c core radius
S_{ij} strain rate tensor
S_t Strouhal number
t time
U reference velocity
u resolved velocity components
u_e velocity at outer flow
u_i' unresolved velocity components
u_t tangential velocity
u_τ shear velocity
V_t mean tangential velocity
x, y, z coordinates
y_w distance from the wall
Δ, Δ_i length scales
Γ circulation
ν molecular viscosity
ν_t turbulent viscosity
ω mean vorticity
ω_m local maximum mean vorticity
ρ density
ρ_0 reference density
θ momentum thickness

1. INTRODUCTION

The compressible hydrodynamics concept has been commonly used to treat hydrodynamic transient. However, in most cases, only one-dimensional situations have been considered. For three dimensional flow phenomena, the commonly used equations are either compressible Navier-Stokes equation for relatively high Mach number flows, or incompressible Navier-Stokes equations for hydrodynamic flows. The incompressible hydrodynamic equations have been

widely used in treating fluid mechanics problems with water as the flow medium. But the incompressible assumption changes the nature of the governing equations from that of hyperbolic type to that of elliptic type. Hence, the traditional numerical method for solving hyperbolic equations cannot be applied. Many difficulties have been encountered in solving the incompressible equations.

In order to obtain the hyperbolic property of the incompressible equation, Chorin [1] has proposed an artificial compressibility method. With this method, one can obtain the steady state solution of incompressible flow in the same way as one solves the compressible Navier-Stokes equations. However, for unsteady hydrodynamic problems, this method does not capture the essential effect of compressibility on fluctuating pressure or flow noise. In most unsteady flows, the weak compressibility of the fluid can contribute a great deal to the pressure field, hence the whole flow phenomena.

The three dimensional compressible hydrodynamic equations, which previously were called the weakly compressible model, has been established by Song and Yuan [2]. This set of equations not only retains the hyperbolic property, but also preserves the hydrodynamic compressibility effect in the equations. By using the property of the small change in density in the case of low Mach number flows, the dynamic part of the flow field is decoupled from the energy equation. But the compressibility effect on the pressure field still remains. Compressible hydrodynamic equations have been successfully used in solving various unsteady, low Mach number flow problems [3, 4].

Flow around foils is a class of common and important phenomena in fluid mechanics. Its significance in engineering practice is evident. Tip vortex as one of the flow pattern in three dimensional cases has not been understood fully; however, its effects on the foil performance is essential. It is theoretically interesting and practically important to understand the principle, origin, and development process of tip vortex.

It is extremely difficult to fully resolve large Reynolds number flows because they contain a very large range of different size eddies. The large eddies simulation (LES) approach, by which large eddies are resolved and small eddies are modeled, has been rapidly developed. The current paper presents numerical simulations of turbulent flows around a two dimensional and a three dimensional hydrofoil by solving the compressible hy-

drodynamic equations with the large eddy simulation method. The tip vortex flow phenomena will be analyzed as well.

2. GOVERNING EQUATIONS FOR LES

2.1 Compressible Hydrodynamic Equations

To implement the large eddy simulation, one needs to apply the cell volume integration over the governing equations, namely, the conservation of mass and momentum equations. A simple volume average method, by which the resolved quantity is treated as a constant over each finite volume, has been used. This is similar to the method introduced by Deardorff [5] and later extended by Schumann [6]. The volume averaged conservation equations have the similar form as the Reynolds average equations. One extra term $\overline{u_i' u_j'}$ is generated from the nonlinear term of the momentum equation. It has been referred as the sub-grid scale Reynolds stress which is analogous to the time averaged Reynolds stress.

Customarily, the sub-grid scale Reynolds stresses are decomposed into the sum of a trace-free tensor and a diagonal tensor. The diagonal tensor part is brought out in a similar way as the dynamic pressure p from the viscosity stress tensor. It is usually combined with pressure as a modified pressure, because they have similar properties, except one is from the molecular viscosity stress tensor, the other is from the unresolved turbulent stress tensor. The modified pressure properly represents the resolved pressure field. The trace-free part of the sub-grid scale Reynolds stress tensor need to be modeled in order to close the set of equations. The model will be discussed in more detail later.

The essential point for deriving compressible hydrodynamic equations is to use the equation of state appropriate to liquids or small Mach number, for which density change in the flow is small. Consider a barotropic flow with low Mach number, one can approximate the equation of state as:

$$p - p_0 = a_0^2 (\rho - \rho_0) \qquad (1)$$

Where p_0 and ρ_0 are reference pressure and density. a_0 is the sound speed, which can be considered as constant. This expression has been widely used in hydraulic transient analysis.

From the above equation, one can solve for

ρ and substitute it into the averaged conservation equation of mass and hence get:

$$\frac{\partial p}{\partial t} + \vec{u} \cdot \nabla p + \rho_0 a_0^2 \nabla \cdot \vec{u} = 0 \qquad (2)$$

By dimensional analysis, one can show that the second term is of order M^2 while the first term is of order $M^2 S_t$. In the case of small Mach number flows, the second term can be ignored. But since the first term is related to the Strouhal number, this term cannot be neglected, especially, when flow is highly time dependent and the Strouhal number is large. It is essential to retain the first term in the continuity equation for flows involving rapid acceleration such as hydraulic transient and hydroacoustics. It also keeps the whole equation set to be of the hyperbolic type. It should also be pointed out that the third term in Eq. (2) is the noise production term.

Similarly, one can substitute the equation of state into the conservation equation of momentum. By considering the density change to be small, one can get the final equation set as following:

$$\frac{\partial \vec{u}}{\partial t} + \nabla \cdot (\vec{u}\vec{u}) = -\frac{1}{\rho_0} \nabla p + \frac{1}{\rho_0} \nabla \cdot \bar{\bar{\tau}} \qquad (3)$$

where $\bar{\bar{\tau}}$ is stress tensor,

$$\tau_{ij} = \underbrace{\rho_0 \nu (\frac{\partial u_i}{\partial x_j} + \frac{\partial u_j}{\partial x_i}) - \frac{2}{3}\rho_0 \nu \frac{\partial u_k}{\partial x_k}\delta_{ij}}_{resolved\ viscosity\ stresses}$$

$$\underbrace{-\rho_0 \overline{u_i' u_j'} + \frac{1}{3}\delta_{ij}\rho_0 \overline{u_k' u_k'}}_{sub-grid\ scale\ Reynolds\ stresses}$$

Eq. (2) and (3) are called compressible hydrodynamic equations. There are four unknowns and four equations. Obviously, this set of equation is closed except that the sub-grid scale turbulent stress need to be modeled. The energy equation has been decoupled. And the equation set has the hyperbolic property and it retains the compressibility effect to the flow field through the continuity equation, Eq. (2).

2.2 SGS Model

The Smagorinsky model is a simple and widely used model for modeling the unresolved sub-grid scale Reynolds stresses. In analogy to the definition for viscosity stresses, the sub-grid scale Reynolds stresses are assumed to be proportional to strain rate of the resolved flow field [7], i.e.

$$-\rho_0 \overline{u_i' u_j'} + \frac{1}{3}\delta_{ij}\rho_0 \overline{u_k' u_k'} = \rho_0 \nu_t (\frac{\partial u_i}{\partial x_j} + \frac{\partial u_j}{\partial x_i}) \quad (4)$$

where ν_t is the unresolved turbulent viscosity, or the sub-grid scale diffusivity. ν_t depends on the length scale of the cell and the strain of the resolved flow field in the following way:

$$\nu_t = (C_s \Delta)^2 (2S_{ij} S_{ij})^{\frac{1}{2}} \qquad (5)$$

$$S_{ij} = \frac{1}{2}(\frac{\partial u_i}{\partial x_j} + \frac{\partial u_j}{\partial x_i})$$

Where Δ represents the filter width, which is taken to be the length scale of the finite volume. There are several ways to decide Δ. According to Bardina et al. [8], a better choice might be:

$$\Delta = (\Delta_1^2 + \Delta_2^2 + \Delta_3^2)^{\frac{1}{2}}$$

where Δ_i is the three dimensions of the finite volume.

C_s is the Smagorinsky constant. Many different values for different flow situations have been used. For homogeneous isotropic turbulence, Lilly [9] determined that $C_s \approx 0.23$. Deardorff [5] used $C_s = 0.1$ for his simulation of turbulent channel flow. And several simulations [10, 11] have used values between 0.1 and 0.23. It is supposed this constant is a universal constant and independent of grid size. But this seems not the case. The simulations that have been carried out by the authors suggested that this constant needs to be adjusted somehow for different mesh systems and flow situations. For the two dimensional simulation to be presented herein, better results have been obtained by using $C_s = 0.14$. And for the primary tip vortex simulation, the tip vortex trajectory is insensitive to this constant.

For turbulence near a solid wall, Eq. (5) has been modified in a similar way as proposed by Moin and Kim [12].

$$\nu_t = (CD\Delta)^2 (S_{ij} S_{ij})^{\frac{1}{2}} \qquad (6)$$

Where D is a non-dimensional damping factor. Van Driet exponential damping function has been used,

$$D = 1 - exp(-y^+/A^+)$$

$$A^+ = 26, \qquad y^+ = y_w u_\tau / \nu$$

It is easy to see, this damping factor will only modify the turbulent viscosity near the solid wall.

3. COMPUTATIONAL CONSIDERATIONS

The size of the largest eddies and the size of the smallest eddies are extremely far apart in turbulent flows. And their difference increases with increasing Reynolds number of the flow. It is very difficult to solve the equations governing the turbulent flows, especially in the case of large Reynolds number flows. In order to gain maximum accuracy with available computer resources, nonuniform mesh system and multi-mesh system has been used.

As the boundary layer on the foil surface and the wake behind the foil are the primary objects in the simulation of flow around two dimensional foil, the computational domain is deliberately divided into two regions. The fine mesh region encloses the foil and covers the wake behind the foil where the gradients are relatively large. The coarse mesh region covers the rest of the computational domain from the lower channel wall to upper channel wall. For the simulation of flow around three dimensional foil, tip vortex is the major objective at this stage of the research. Hence fine mesh has been arranged to resolve the tip part of the foil and the tip vortex behind it. This multi-mesh system has been very beneficial in a sense of using the computer time and memory efficiently.

The artificial interface condition between the fine mesh region and the coarse mesh region is given special attention. For boundary points of the coarse mesh, the primary variables are directly taken from the the corresponding fine mesh region. For boundary points of the fine mesh region, the velocity values and the pressure gradients have been matched to the coarse mesh region. Matching pressure gradient instead of matching pressure itself has enabled the unsteady pressure waves generated by the foil to propagate outward properly. Otherwise, a pressure wave will reflect back and accumulate large errors in the inner zone and hence cause the computation to be broken down.

Wall boundary conditions are very important for the computation. Special attention

should be paid to high Reynolds number flows, since the mesh size usually is not fine enough to resolve the details of the boundary layer. Appropriate partial slip boundary conditions have to be used. Many [3, 6, 13] have used the wall function as a medium to obtain the approximation for the phantom point velocity values. However, the associated assumption of fully developed turbulent boundary layer has limited its usage. Especially it cannot be applied for flow that has laminar boundary layer, transition, as well as turbulent boundary layer. A new way to impose the partial slip condition has been developed for the present simulation in the case of two dimensional flow. By assuming the boundary layer is quasi-steady during a certain time period, say, the time interval of the outer flow calculation increment, one can use the steady boundary layer equations by ignoring the local acceleration term, $\partial \bar{u}/\partial t = 0$.

In the current simulation, Crank-Nicolson's fully implicit second order scheme is used to solve the boundary layer equations. The outer flow conditions are obtained by inputting the pressure field near the wall from the outer flow computation. In the leading part of the foil, the laminar boundary layer is assumed. The transition starting point is determined by laminar boundary layer separation or according to the following criteria [14],

$$R_{\theta tr} = 1.174(1 + \frac{22,400}{Re_{x tr}}) Re_{x tr}^{0.46}$$

where

$$R_\theta = \frac{u_e \theta}{\nu}$$

θ is the momentum thickness of the boundary layer.

Starting from whichever comes first, the turbulent boundary layer equation will be applied. For turbulent boundary layer calculation, Prandtl's mixing length model is used.

After the boundary layer separation, non-slip velocity boundary condition has been used, since after separation, the boundary layer is fairly thick, and the velocity gradient normal to the wall has become much smaller compared with the boundary layer before the separation. Hence, the non-slip boundary condition will be appropriate.

The quasi-steady boundary layer calculation provided the information for imposing the partial slip boundary conditions in the outer flow. It is a novel combination of boundary layer computation and outer flow simulation. For unsteady

638

large eddy simulation, it certainly can improve the accuracy in reflecting the boundary layer effect to the outer flow and flow in the wake.

The pressure condition on the solid walls has been specified in the following way,

$$\frac{\partial P}{\partial n} = -\frac{\rho u_t{}^2}{R_c} \quad (7)$$

Where R_c is the radius of curvature of the wall. This is obvious, since the curved wall will generate a centrifugal force, which will result in a pressure gradient normal to the wall.

Boundary layers along the channel walls are not so interesting for present study; in addition, these boundary layers will not affect the foil wall boundary layer and the wake region. The channel wall has been simply treated with full slip velocity and zero gradient pressure conditions.

The well-known MacCormack predictor-corrector numerical scheme has been used in solving the compressible hydrodynamic equations for large eddy simulation. The scheme is of second order accuracy in time and space.

4. NUMERICAL RESULTS AND DISCUSSIONS

4.1 Flow Around 2-D Foil

A two dimensional foil that has been tested in a water channel by Huang [15] at National Taiwan University has been simulated. The Reynolds number of the flow is 1.6×10^6. And the angle of attack is -5.9.

Fig. 1 shows two instantaneous vorticity fields near the trailing edge of the foil and in the wake. One may note that at pressure side of the foil, a very thin boundary layer is formed, and the vorticity in this layer has a positive sign. On the other hand a relatively thick boundary layer exists at the suction side of the foil. The vorticity is negative in this layer. Apparently, there is no visible separation for the simulated flow. However, the vorticity with opposite sign from two sides of the foil meet at the trailing edge and form a vortex sheet, which is very unstable. Vortices roll-up and negative and positive vortices alternatively shed downstream. A more vivid picture of the
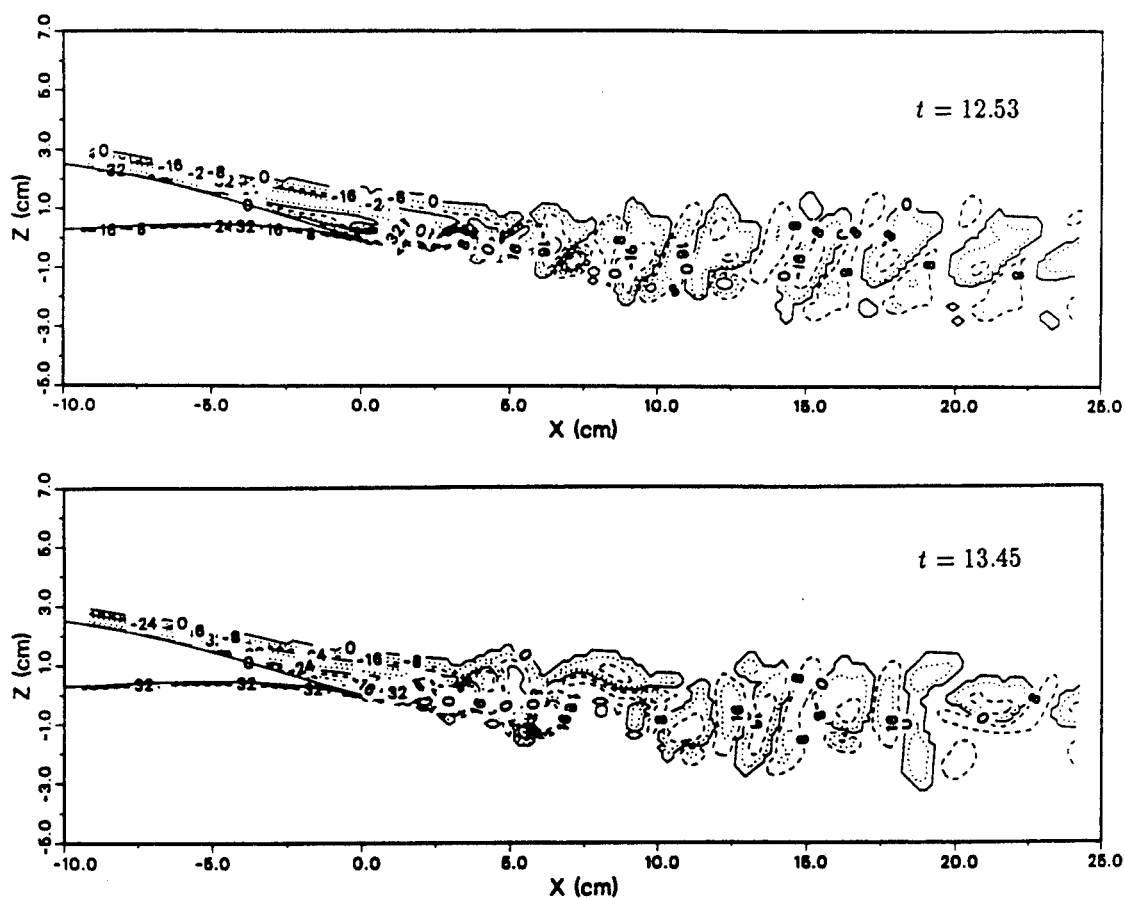

Fig. 1 Instantaneous Vorticity Contours

639

vortex shedding can be seen through animations of color coded pressure and vorticity fields.

The mean flow field around the foil body is shown in Fig. 2. The calculated values are compared with the experimental data. It can be seen they agree very well. The mean flow profiles in the boundary layer are plotted against the experimental measurement in Fig. 3. Again, fairly good agreement has been reached. Mean flow velocity
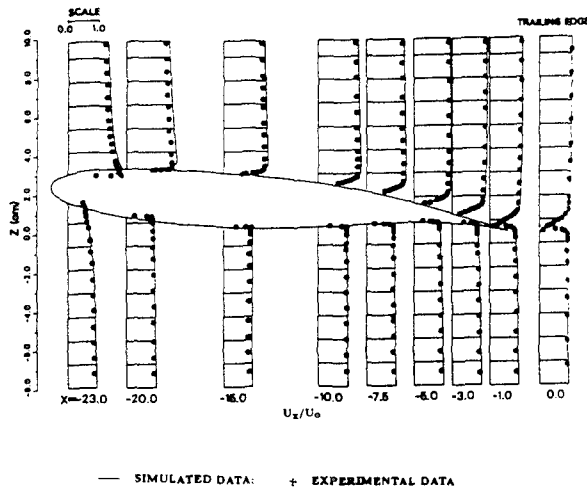
Fig. 2 Simulated and Measured Mean Flow U_x around the Foil
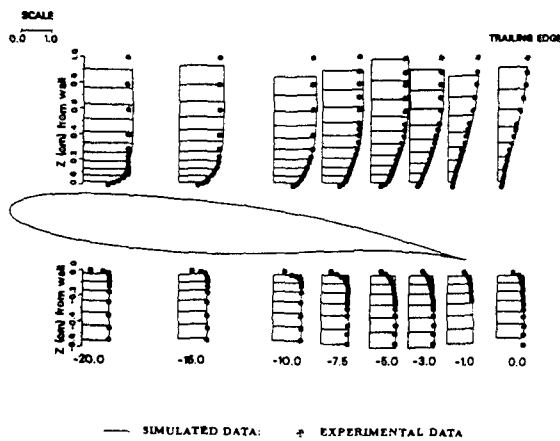
Fig. 3 Simulated and Measured Mean Boundary Layer Profiles

vectors are shown in Figs. 4 and 5 for simulated values and experiment values respectively. The agreement between simulated values and experimental data is quite good. It can be concluded that the mean velocity field can be reproduced by the numerical simulations very well.

As discussed above, the turbulence has been divided into the resolved large scale part and the

unresolved sub-grid scale part. The former is simulated while the latter is modeled through the resolved flow field. Figs. 6(a) and (b) provide the
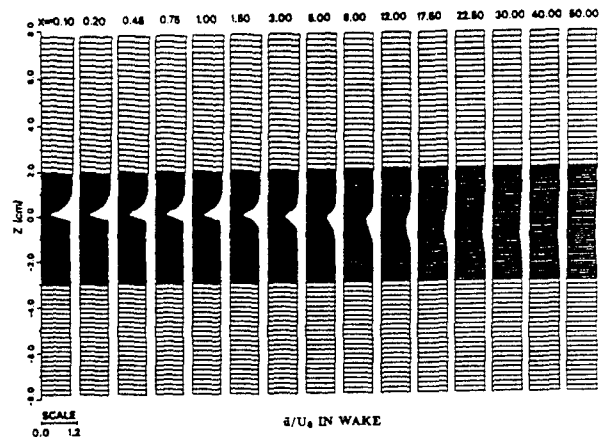
Fig. 4 Simulated Velocity Vectors in the Wake
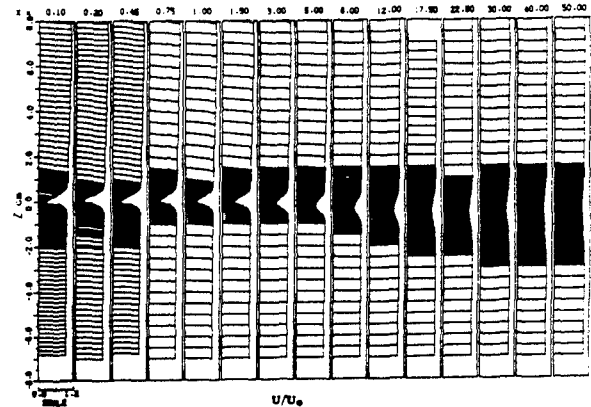
Fig. 5 Measured Velocity Vectors in the Wake

turbulent intensity $\overline{u'v'}/U^2$ for these two parts in several stations in the wake. And the sum of the two parts is plotted in Fig. 6(c). It is interesting to note that in the wake region near the trailing edge, the main contribution is from the modeled part, while in the wake region far from the trailing edge, the main contribution is from the resolved large eddies. This is consistent with the general understanding that eddies are larger in the far field but they are smaller near the trailing edge. The pattern that eddy sizes change from small to large as flow goes downstream can be easily seen on Fig. 1. In Fig. 6(d), the measured turbulent intensity $\overline{u'v'}/U^2$ is shown. Comparing Fig. 6(c) and Fig. 6(d), one can see that the shape is quite similar, mainly in the far wake region. But in the near wake region, the sharp peak right after the trailing edge as shown in Fig./,6(d) is lost in the simulation. Evidently a very thin shear layer after

640

the trailing edge produces the strong and fine turbulent eddies. Relatively poor agreement in the near field may be due to the three dimensionality of small scale and insufficient grid refinement.

attack is about 14°. And the Reynolds number of the simulation is 7.0×10^5. However, since the mesh size are not fine enough and the boundary layer on the foil surface is not resolved well in the

(a)

(b)

(c)

(d)
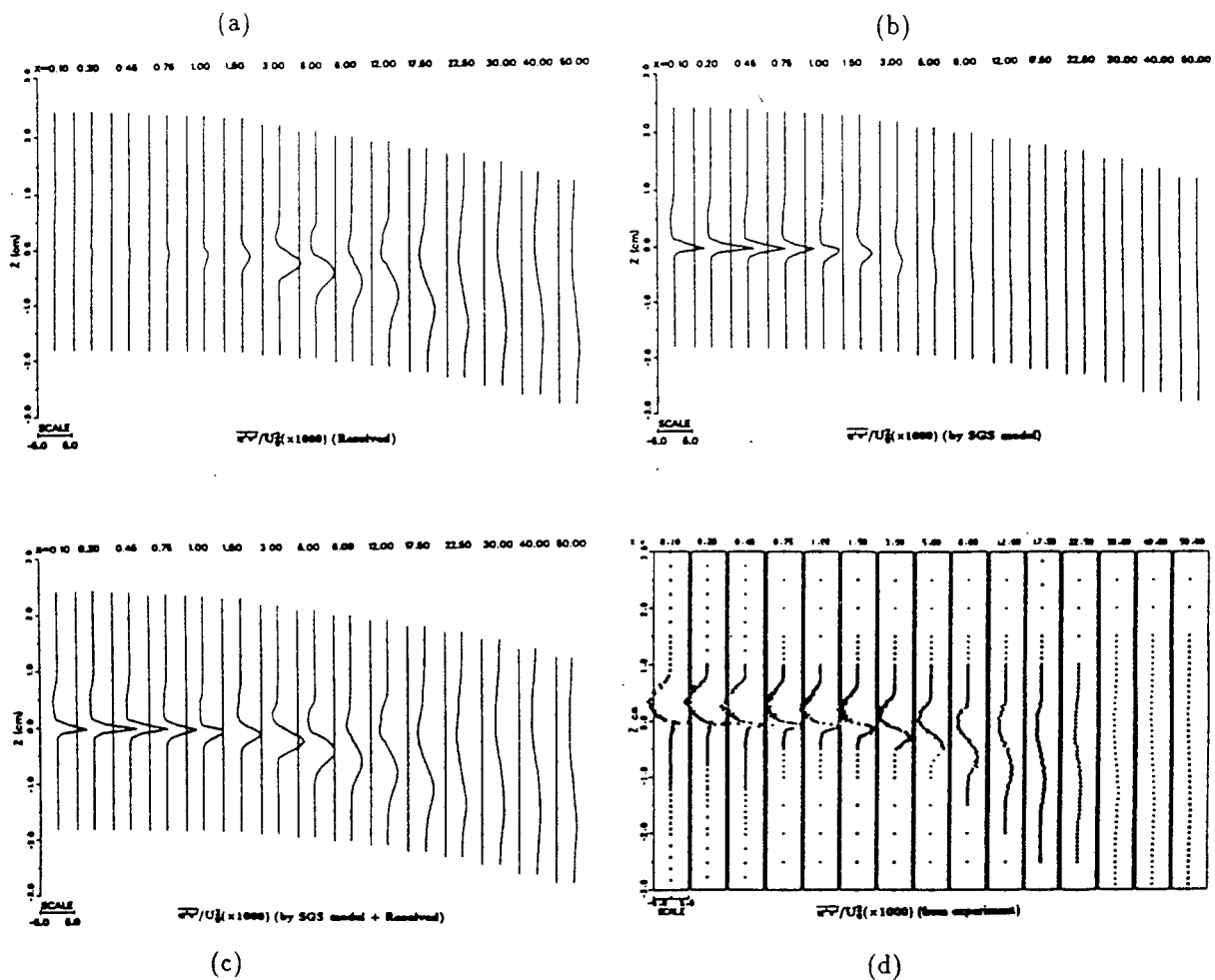
(a) Resolved Turbulent Intensity $\overline{u'v'}/U^2$ (b) Modeled Turbulent Intensity $\overline{u'v'}/U^2$
(c) Total Turbulent Intensity $\overline{u'v'}/U^2$ (d) Measured Turbulent Intensity $\overline{u'v'}/U^2$

Fig. 6 Comparison of Turbulent Intensity in the Wake

4.2. Tip Vortex Flow

A three dimensional foil with a modified NACA 4215 section and an elliptic planform has been studied. Extensive experimental research for tip vortex cavitation with this foil has been conducted [16, 17]. Tip vortex is the focus in the present numerical simulation. The coordinate axes are so chosen that x is along the main flow direction, y is normal to the plane of the foil, positive pointing from pressure side to suction side, and z is in the span-wise direction from the foil base to the tip of the foil. The effective angle of

current three dimensional simulation.

The lift coefficient is defined as $C_l = L/\frac{1}{2}\rho U^2 A_s$, where L is the total lift; A_s is the projected area of the foil. Calculated lift coefficient is 0.72, which is very close to the experimental result, $0.72 \sim 0.73$ [17].

Fig. 7 shows the velocity vectors projected on a cross-section normal to the flow direction. The swirl around the tip vortex is quite apparent. The interaction between wake and tip vortex can be observed by noting the sudden changing of flow direction below the swirl. The corresponding vorticity distribution (x-component) is

shown in Fig. 8. The vorticity contour lines form nearly concentric circles indicating the intensity

Fig. 9.

The simulated tip vortex trajectory is
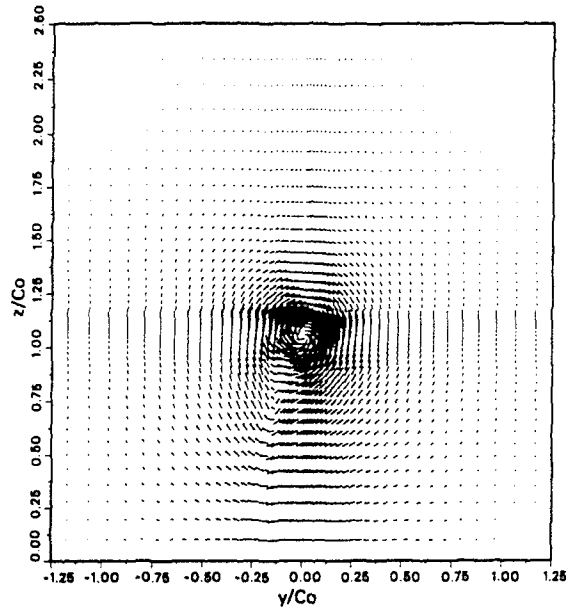
Fig. 7 Projected Velocity Vectors at $x/C_0 = 1.06$ Cross-Section
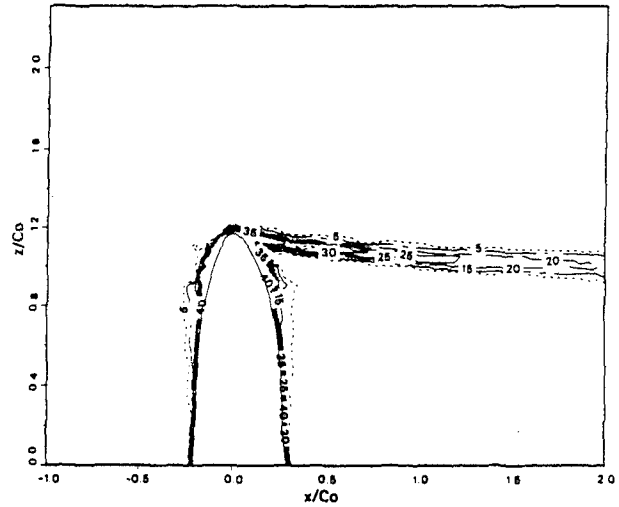
Fig. 9 Vorticity Magnitude at $y/C_0 = 0.0$ Cross-Section

Fig. 10 Tip Vortex Trajectory

Fig. 8 Vorticity Contours of x-Component at $x/C_0 = 1.06$ Cross-Section

increases towards the vortex core. Vorticity contours on a surface parallel to the x-z plane and through the axis of the tip vortex are shown in
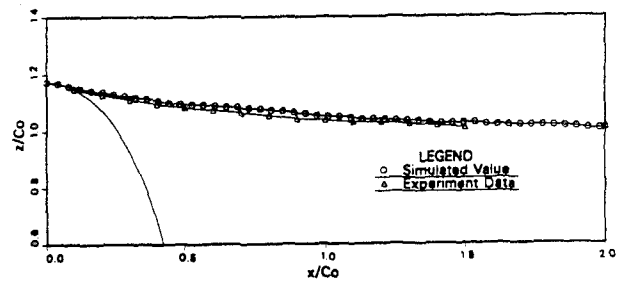
plotted and compared with the measurement in Fig. 10. The agreement is very good. It is worth pointing out that the current simulation has not tried to resolve the boundary layers on the foil surface. It is believed that the boundary layer on the foil surface germinates the tip vortex, but the above result seems to imply that the tip vortex trajectory is independent of the boundary layer. This result agrees with the measurement [16] that the tip vortex trajectory is insensitive to the Reynolds number and the angle of attack.

The pressure coefficient in the tip vortex core as a function of x is plotted in Fig. 11. It can be seen that the pressure reaches the lowest point at the tip where the tip vortex originates. The pressure increases in the downstream direction. This is understandable because the tip vortex core is very small at the beginning and grows in the downstream direction due to diffusion. Increasing core size means weakening vorticity and increasing pressure.
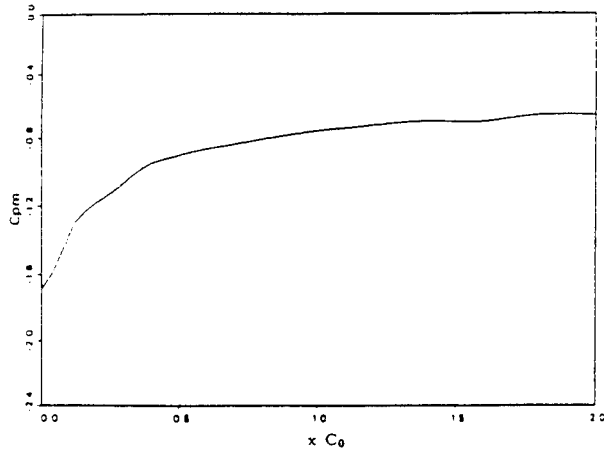
Fig. 11 Minimum Pressure Coefficient at Tip Vortex Core

Fig. 12 Nondimensional Circulation around Tip Vortex Core

It is a difficult task to measure the full details of the structure of tip vortex. On the other hand theoretical analysis of tip vortex has always required an assumption that the tip vortex is a Rankine vortex. The Rankine vortex model ignores two aspects of the real fluid flow phenomena. Firstly, according to the Rankine vortex model, the vorticity field should be axis symmetric about the vortex core. However, the wake behind the foil always disturbs this symmetry. The region affected by the wake becomes larger as the wake spreads wider along the streamwise direction. Measurements engaging the assumption of symmetric vorticity field could lead to errors in their data since the tangential velocity profiles around the tip vortex core are quite different depending on how the wake affects them. Secondly, the Rankine vortex model assumes that, the flow field around tip vortex is divided into rotational core region and irrotational outer region. And the vorticity is concentrated inside the core region. This cannot be true for the real flow situation because of the diffusivity of the fluid and turbulence. Again the wake plays an important role in distributing the vorticity in the flow field.

Numerical diffusion can distort the results of numerical simulations. But numerical simulations can provide at least a qualitative structure of the real tip vortex. Since the tip vortex is not symmetric and the vorticity is not just concentrated inside the core region, the traditional definition for core radius needs to be reconsidered. In the present study, the circulation Γ about the core is calculated first as following,

$$\Gamma = \oint \vec{u} \cdot d\vec{r}$$

The variations of Γ as function of radius from the core at several stations along streamwise direction have been plotted in Fig. 12. Note that Γ is nondimensionalized by taking theoretical value of $\frac{1}{2}C_l U^2 C_0$ as the reference value so that, in the ideal case, all curves in Fig. 12 would approach 1 asymptotically. The asymptotic values for the last four curves is about 1.05. This slight difference from 1 could be caused by the fact that the flow simulated here is bounded by the walls. By comparing the curves for different stations, one could see that the asymptotic value starts with about 0.75 at the tip and gradually increases to the maximum value of 1.05 at about $x/C_0 = 0.5$. This means that the vorticity in the z-direction is gradually changing the direction into the vorticity in the x-direction, i.e., the tip vortex. In other word, the circulation contributed to the lift is gradually converting into the circulation of tip vortex. This process finishes at about $x/C_0 = 0.5$ position. The steep gradient near the core shows that the vorticity is very strong near the core, and becomes weak as it goes far from the core.

The mean tangential velocity can be calculated based on the circulation calculated above. The mean tangential velocity at one of the x-station has been shown in Fig. 13. The corresponding tangential velocity profile of the Rankine vortex is compared in the same figure. As can be seen, in the core region, the two are quite close. But outside the core, they are very different. No-

643

tice that the former is rotational outside the core while the latter is irrotational. From this comparison, one could see that it is appropriate to define the tip vortex core radius as the distance from the core center to the maximum mean tangential velocity point.
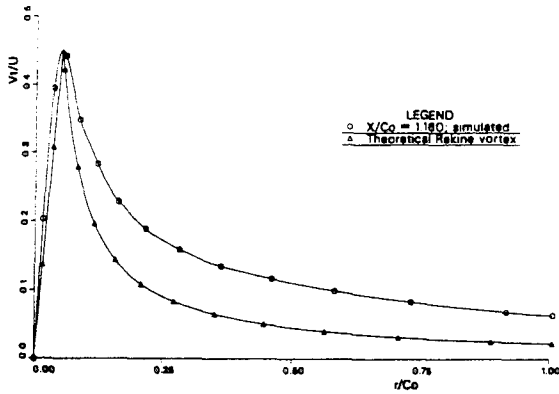
Fig. 13 Mean Tangential Velocity around Tip Vortex Core
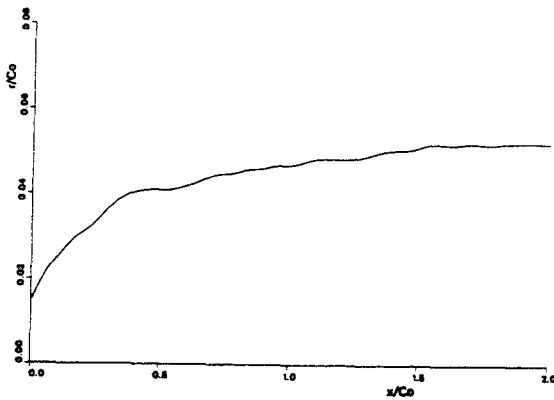
Fig. 14 Radius of Tip Vortex Core
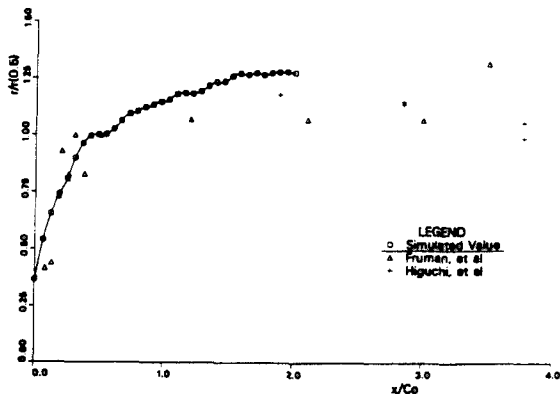
Fig. 15 Nondimensional Radius of Tip Vortex Core

The core radius calculated according to the above definition has been shown in Fig. 14. Obviously, the core radius increases in downstream direction. The diffusion of the vorticity in the core could be the reason for it. There have been some experimental measurements on the core radius of tip vortex [18], where the radius is nondimensionalized by the radius at half of the base chord position, namely, $r_c(0.5)$. In Fig. 15, the calculated core radius is compared with the experimental results based on the nondimensional
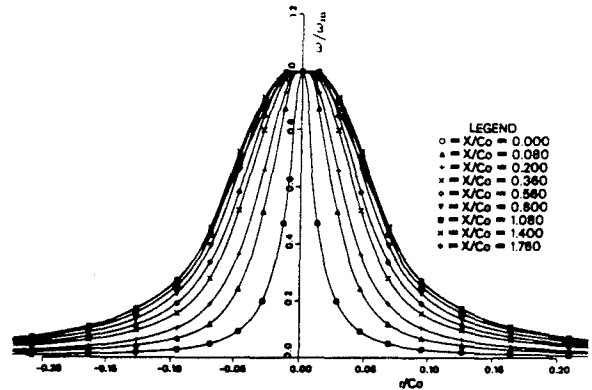
Fig. 16 Mean Vorticity around Tip Vortex Core
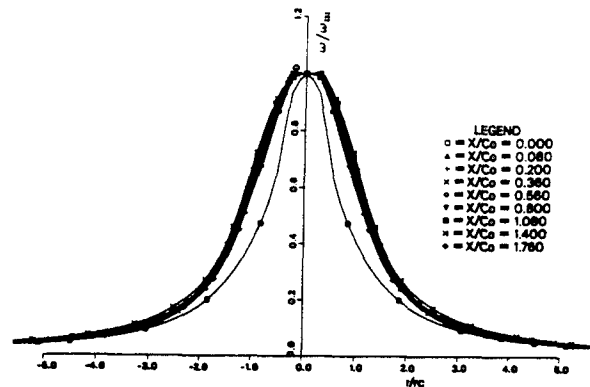
Fig. 17 Mean Vorticity around Tip Vortex Core

radius as described above. It can be seen that the agreement is fairly good.

In spite of the non-symmetric vorticity field around the tip vortex core, one could get a mean vorticity by means of the circulation, i.e.,

$$\omega = \frac{\Gamma}{2\pi r^2}$$

The profiles of mean vorticity calculated in this way have been nondimensionalized by its local maximum value and shown in Fig. 16. The

644

diffusion property of tip vortex core is quite obvious. When the radius is nondimensionalized by the local vortex core radius, one can obtain a very interesting result as shown in Fig. 17. All the mean vorticity curves have almost collapsed to one curve except the one at $x/C_0 = 0$. This could mean that the vorticity diffusion around the vortex core obeys a similarity rule.

5. SUMMARY

The numerical simulations of flows around the two dimensional foil and the three dimensional foil based on the compressible hydrodynamic equations have been studied. Compressible hydrodynamics has drawn more and more attention for solving various hydrodynamic flow problems. It has been proved that this set of equations has two major advantages over the incompressible equations. The parabolic property of the equations makes the numerical solution more convenient. And, by including the effect of compressibility enables the set of equations to correctly model the flows involving rapid accelerations, such as pressure waves generated by hydraulic transients and acoustics. It is very important to note that the incompressible flow equations does not retain such physical information. The large eddy simulation by utilizing the compressible hydrodynamic equations has the potential to treat various low Mach number flows and correctly simulate pressure fluctuations. In addition, multi-mesh system can serve as a useful tool to use the available computer resources effectively.

The simulation of two dimensional foil has shown that the mean flow field is quite accurately simulated by the present large eddy simulation method. The large eddies in the far downstream of the wake can be captured fairly accurately in terms of the turbulent intensity in that region, where large scale eddies contribute the most part to the turbulent intensity. However, in the near wake region, the small turbulent eddies are dominant, hence, the large eddy simulation method cannot resolve them well. The turbulence structure right after the trailing edge is so complicated that this simple strain rate model such as Smagorinsky SGS model cannot handle it well.

The numerical study of tip vortex flow has provided much knowledge on its structure. The independence of the tip vortex trajectory on the Reynolds number, boundary layer where the tip vortex originated, has been observed again from the numerical solution. The simulated tip vortex

shows that the ideal Rankine vortex assumption for such case is inapplicable. Two major effects have spoiled the assumption. One is the effect from the wake behind the foil, which destroys the symmetry of the vortex. The other is the effect of diffusivity because of which the vorticity does not exist only inside the core. The vorticity is strong inside the core, but there is no clear margin for the edge of the core. Instead, the vorticity is smoothly distributed by diffusion with the highest value at the core. The wake behind the foil also contributes to the re-distribution of the vorticity. Although the vortex is not symmetric, the core radius can be defined through the profile of the mean tangential velocity around the vortex core. By defining the maximum mean tangential velocity point as the edge of the vortex core, one could see that inside the core, the tangential velocity profile is quite close to the case of the Rankine vortex; while outside the core, it is very different from that of irrotational flow. By analyzing the circulation along the streamwise direction, one can see that the circulation contributed to the lift has completely converted into the circulation of the tip vortex up to the point of about half base chord length. The core radius as defined above has a similar trend as the experimental results. The mean vorticity profiles calculated from the circulation have suggested that the diffusion of the vorticity could follow the similarity rule when the radius is nondimensionalized with the core radius of the vortex.

REFERENCES

1. Chorin, A.J., "A Numerical Method for Solving Incompressible Viscous Flow Problem," Journal of Computational Physics, vol. 2, 1967, pp. 12-26.

2. Song, C.C.S., and Yuan, M., "A Weakly Compressible Flow Model and Rapid Convergence Methods," Journal of Fluids Engineering, vol. 110, 1988, pp. 441-445.

3. Song, C.C.S., and Yuan, M., "Simulation of Vortex-Shedding Flow about a Cylinder at High Reynolds Number," Journal of Fluids Engineering, vol. 112, 1990, pp. 155-163.

4. Song, C.C.S., He, J., Chen, C., and Chen, X., "Computation of Turbulent Flow for Hydraulic Machinery: Hydrofoil, Francis Turbine, and Draft Tube," International Research Center on Hydraulic Machinery (Beijing), Nov. 20-23., 1991

5. Deardorff, J.W., "A Numerical Study of Three-Dimensional Turbulent Channel Flow at Large Reynolds Number," Journal of Fluid Mechanics, vol. 41, 1970, pp. 452-480.

6. Schumann, U., "Sub-grid—Scale Model for Finite Difference Simulations of Turbulent Flows in Plane Channels and Annuli," Journal of Computational Physics, vol. 18, 1975, pp. 376-404.

7. Smagorinsky, J., "General Circulation Experiments with the Primitive Equations," Monthly Weather Review, vol. 91, No.3, 1963, pp. 99-164.

8. Bardina, J., Ferziger, J., and Reynolds, W.C., "Improved Sub-Grid Scale Models for Large Eddy Simulation," AIAA paper, 80-1357, 1980.

9. Lilly, D.K., "On the Application of the Eddy Viscosity Concept in the Inertial Subrange of Turbulence,", NCAR Manuscript, No.123, 1966.

10. Mason, P.J., and Callen, N.S., "On the Magnitude of the Subgrid-Scale Eddy Coefficient in Large-Eddy Simulations of Turbulent Channel Flow." Journal of Fluid Mechanics, vol. 162, 1986,p.439.

11. Piomelli, U., Moin, P., and Ferziger, J.H., "Model Consistency in Large Eddy Simulation of Turbulent Channel Flows," Physics of Fluids, Vol.31, 1988, p.1884.

12. Moin, P., and Kim, J., "Numerical Investigation of Turbulent Channel Flow," Journal of Fluid Mechanics, vol. 118, 1982, pp. 341-377.

13. Ghose, S., and Kline, S.J., "The Computation of Optimum Pressure Recovery in Two-Dimensional Diffuser," Journal of Fluids Engineering, vol. 100, 1987, pp. 419-426.

14. Cebeci, T., and Bradshaw, P., Momentum Transfer in Boundary Layers, Hemisphere Publishing Corporation, 1977.

15. Huang, J.L., "Personal Communications," 1991.

16. Arndt, R.E.A., Arakeri, V.H., and Higuchi, H., "Some Observations of Tip Vortex Cavitation," Journal of Fluid Mechanics, vol. 229, 1991, pp. 269-289.

17. Arndt, R.E.A., and Christian Dugue, "Recent Advances in Tip Vortex Cavitation Research," Proc. Intl. Symp. on Propulsors and Cavitation, Hamburg, Germany, June, 1992.

18. Maines, B.H., and Arndt, R.E.A., "Bubble Dynamics of Cavitation Inception in a Wing Tip Vortex," Cavitation and Multiphase Flow Forum, ASME Fluids Engineering Conference, Washington D.C., June 21-24, 1993.

DISCUSSION
by Professor Roger Arndt, University of Minnesota

The numerical results in this paper complement a companion experimental study of tip vortex cavitation (Maines and Arndt, 1993a, b). Although quantitative comparisons are not yet possible, there is a wealth of qualitative information that has provided guidance in our studies of cavitation inception. The authors have noted the lack of viscous effects on vortex trajectory which is in agreement with our experiments. They have also found that the minimum pressure in the vortex is very close to the tip in a region where the vortex structure is highly complex and cannot be modeled by axisymmetric analogs, such as the Rankine or Lamb vortex. Visual observations of cavitation as reported by many authors in the past gave the impression that the minimum pressure in the vortex is located about one-half chord length downstream where the vortex is fully rolled-up. However, careful observation of the inception process using high speed cinematography indicates that the minimum pressure is very close to the tip, $x/c_o \sim 0.15$. This is in agreement with detailed velocity measurements by Fruman et al. (1992).

As pointed out by the authors, numerical diffusion can distort the results of numerical simulations. The Reynolds number corresponding to the calculations in Figure 11 has not been stated. However, it is interesting to note that our experimental observations for a series of foils of identical planform, but with different cross sections and different boundary layer characteristics, indicate that an almost universal cavitation scaling law exists:

$$\sigma_1 = -C_{po} = k \, C_1^2 \, Re^{0.4}$$

where $0.045 < k < 0.073$ and Re is Reynolds number based on maximum chord length. Our initial thought was that the appropriate viscous scaling parameter is a Reynolds number based on circulation, Γ / ν, where the variation in k represents the dependence of the initial development of the vortex on the details of the boundary layer flow in the tip region. If one uses a value of k = 0.065 for the modified NACA 4215 hydrofoil studied in this paper, the equivalent Reynolds number for the calculation in Figure 11 would only be 18,000 which is well below the range of

our experimental data in which $600,000 < Re < 1,700,000$. This warrants further discussion.

In summary, this paper provides substantial insight into the vortex roll-up process. The interaction between the wake and the tip vortex is an important consideration which is fully substantiated by our experimental observations. Unfortunately, detailed comparisons between our cavitation experiments and the numerical results cannot be made until the flow at higher Reynolds number can be simulated.

References
Fruman, D.H., Dugue, C., Pauchet, A., Cerrutti, P. and Briancon-Marjolet, L. (1992), "Tip vortex roll-up and cavitation," Nineteenth Symposium on Naval Hydrodynamics, Seoul, Korea.
Maines, B.H. and Arndt, R.E.A. (1993a), "Bubble dynamics of cavitation inception in a wing tip vortex," Proceedings of the ASME Cavitation and Multiphase Flow Forum, FED Vol. 153, pp. 93-95.
Maines, B.H. and Arndt, R.E.A. (1993b), "Viscous effects on tip vortex cavitation," 4th International Symposium on Cavitation Inception, ASME Winter Annual Meeting, New Orleans.

Author's Reply: See common response for the above at the end of this section.

DISCUSSION
by Dr. Thomas T. Huang, David Taylor Model Basin

Could the authors provide the grid resolution requirements around the hydrofoil and tip vortex in order to reach grid-independent numerical solution. The discussor provided an estimate of grid resolution requirements as function of Reynolds number in their paper presented in this conference (paper 7.2). The solutions of C_p, C_τ, C_D, and C_L for wide range of grids must be presented. The computed C_p in the core of tip vortex must be compared with the measured cavitation inception number σ_i. We know for sure that the measured value of σ_i depends strongly on Reynolds number. The method presented by the authors will become much more useful if the requirements of grid-dependent solution are known a priori.

DISCUSSION
by Dr. P. M. Gresho, LLNL

I appreciate your concern re: difficulty of unsteady incompressible flow. But:

Q1. Do your presented computational results differ in any significant way from those of incompressible flows?

Q2: Have you done any simulations in which the compressibility ("noise" term in mass conservation equ) is significant/ important?

Author's Reply: See common response for the above at the end of this section.

Author's Reply to Drs. Arndt, Huang, and Gresho

The authors appreciate additional insights on the quantitative characteristics of tip vortex and tip vortex cavitation provides by Professor R. Arndt's experimental results. It appears that the primary structure of a tip vortex is not sensitive to the Reynolds number. Because our computation did not fully resolve the boundary layer, it is not possible to give the precise Reynolds number to the flow simulated. But it is quite clear the computation represents a very large Reynolds number case: certainly much greater than 18,000 quoted by Professor Arndt. The reason Figure 11 may appear to indicate relatively small Reynolds number is inadequate resolution of the core of the vortex where very sharp gradient exists. Indeed later calculation with finer grids in the core region results in lower pressure on the axis of the vortex while flow elsewhere is unaffected.

To answer Dr. P.M. Gresho's questions we would like to first point out that the effect of compressibility, no matter how small the compressibility may be, is significant when flow changes rapidly with time. For very small Mach number flow, the time averaged quantities simulated by this method are identical to that of incompressible flows. But even in a very small Mach number case, this method simulates flow noise directly while an incompressible flow model will not yield flow noise. Indeed we have simulated flow noise due to boundary layer separation and vortex shedding.

The main idea behind the Large Eddy Simulation (LES) method is to resolve only the large structure of the flow while the effect of small scale turbulence is modeled by a Subgrid Scale Turbulence Model. Therefore, it is not possible to attain a grid size independent condition unless the Direct Simulation method is used and all scale turbulence are resolved. Even in that case it will only be grid size independent in statistical sense. With LES method, the small the grid size the finer scale structure of the flow can be resolved. The grid size independence stated by Dr. T. T. Huang can be meaningful only when the long time averaged quantities are concerned. As it was stated previously, the flow near the core of the tip vortex for a very large Reynolds number case has very sharp gradient and we did not achieve the grid size independent condition. But the overall flow, except for a small region in the core and in the boundary layer, is fairly well simulated.

Numerical Calculations of Transitional Flow over Flat Plate in Turbulent Non-uniform Flows

S.H. Kang, M.R. Choi, and W.P. Jeon

(Seoul National University, Korea)

ABSTRACT

The behavior of the boundary layer over a flat plate in a non-uniform incoming flow was simulated using low Reynolds number k-ε models of Launder and Sharma and Chien and a transition model. Mean velocity profiles and skin-frictions on the flat plate were also measured in the wake generated by a circular cylinder at the upstream. The Computational Preston Method (CPM) proposed by Nitsche *et al.* was used to measure the skin-friction coefficients in the present study.

The Launder and Sharma model predicts earlier start and short transition length than the PTM model does and Chien's model shows also earlier start of transition and damped variation. These trends are generally the same with those of the uniform flow. The PTM transition model based on the low Reynolds number k-ε of Launder and Sharma does reasonably predict skin-frictions on a flat plate during transition. However more extensive calibrations of the PTM transition model is needed. The CPM method is verified as an useful tool to investigate skin-friction over the transitional boundary layer with reasonable accuracy. The simple construction and instrumentation for the technique are appreciated. Measured skin-friction coefficient gradually changes from the leading edge to the downstream. Transition length was considerably longer than in the uniform flow.

INTRODUCTION

Reliable and accurate prediction of turbulent flows over air and hydrofoils and through turbomachinery over wide range of flow condition is important for the design and performance prediction. A rotor of compressor or turbine rotates in the highly three-dimensional turbulent wake of stator, and a propeller operates in the stern wake. Therefore the incoming flow relative to a rotor as well as a propeller is unsteady. An efficient method is required that correctly simulates complex flows containing viscous effects; transition, leading edge separation, reattachment, non-equilibrium turbulent shear flow, boundary layer separation. Various numerical methods have been developed for the two or three dimensional, compressible or incompressible, steady or unsteady viscous passage flows. The CFD techniques for turbomachinery have reached a high level of maturity, however there is still need of more validation of the codes even for the two-dimensional steady turbulent flow over wing section.

Even without a recirculation or cavitation bubble on a blade, transition is a complex phenomena which has been studied but is still not well understood. A transition region usually extends over significant fraction of the blade. The importance of steady and unsteady transition in the flows of turbomachinery was summarized by Mayle[1]. Since the blade of turbomachinery operates in the highly turbulent and non-uniform flow field, many factors affect the boundary layer transition, i.e. the incoming flow condition, pressure gradient, curvature of blades, roughness and surface vibration, acoustic disturbances etc.. A model for the correct prediction of transition point on the blade does not yet available. The transition occurs under small disturbance circumstances by Tollmien-Schlichting process in a low-turbulence environment. Under high free stream turbulence conditions, non-linear bypass transition becomes dominant, which is poorly understood yet. Several researches were done to investigate the effects of free-stream turbulence intensity and length scale on the transition and heat transfer on a blade of turbomachinery as well as on a flat plate (cf. Abu-Ghanam and Shaw [2], Sohn and Reshotko[3], etc.).

In the transitional flow, the turbulence models have been less successful than in fully turbulent flow, mainly due to the intermittency and three-dimensionality of the flow. Techniques of DNS (direct numerical simulation), LES (large eddy simulation) or higher-order turbulence models can be used to simulate the transitional flow, however they still require too much computing time to be used for the practical engineering purposes. Two-equation

turbulence models, i.e. low Reynolds number k-ε model, as well as algebraic models, i.e. eddy viscosity model, have been widely used. The algebraic models of Cebeci-Smith and Baldwin-Lomax are difficult to be extended and modified for complex flow conditions. Low Reynolds number k-ε models were developed to treat the near wall damping effects and were applied to the calculation of flow in pipes, channels, and external boundary layers. Such a built-in function of the models makes them attractive as potential predictive tools for transitional boundary layers. Various efforts related to k-ε models were made to simulate transition during last two decades. Recent work by Schmidt and Patankar[4] was extensive and attractive. They evaluated the numerical characteristics of the Lam and Bremhorst[5] and Launder and Sharma[6] two-equation models. A modification was proposed that limits the production term in the turbulent kinetic energy eqaution and was based on a simple criterion and correlated to the free-stream turbulence level. This model was termed a production term modification model or PTM model. The model reasonably simulates skin-friction coefficient and Stanton number of zero-pressure and low accelerating flows on the flat plate. However the model is not fully confirmed for various conditions of flow.

Recently Stephens and Crawford [7] investigated the numerical prediction of boundary layer transition using the PTM model based on the model of Chien [8]. The model is one of the most widly used model for passage flow calculation of turbomachinery. They examined a new model for the case of Blair and Werle [9]. It was noted that the model does not reproduce the experimental Stanton number distribution as well as expected. The numerical predictions appeared to damp the transition of a boundary layer. They conducted a comparison between the transition results of the K.Y. Chien[8] and Launder and Sharma [6] and showed that the Chien's model predicts an earlier start of transition and damped distribution of skin-friction. The main reason of the problem was that the damping function f_μ of the model is a function of y^+ and for fully turbulent boundary layer. They concluded that the Chien model is not adequate for the transition study.

A numerical investigation[10] of the incompressible viscous flow through the controlled diffusion cascade blade of a compressor was carried out using the PTM model based on the low Reynolds number k-ε model of Launder and Sharma[6]. The development of the shear layer along the pressure and suction sides was generally well estimated. However, there was still a considerable discrepancy in the predicted profiles of mean velocity and turbulent kinetic energy. Taking into account the uncertainty in the measurement, the transport of turbulence in the shear layer, especially through the region of

transition, was reported to be one of reasons. For more detailed assessment of the numerical method, boundary layer measurements on the airfoil including the shear stress on the wall are needed not only with various free stream turbulent intensities but also in non-uniform incoming velocity profiles.

Noting that most of the transition model were studied using the measured data on the flat plate in a uniform flow with different level of turbulence intensity, their characteristics of predicting the transition shear layer of general profile were not investigated yet. More specifically, the behavior of the boundary layer over a flat plate in a non-uniform incoming flow is of practical interest, however there are not measured sets of data for the prediction method to be validated. When a flat plate is placed in a turbulent non-uniform shear layer, a new internal layer will be developed on the plate in the existing profiles of velocity, turbulent kinetic energy, and its rate of dissipation and production. The behavior of transition boundary layer was simulated using the low Reynolds number k-ε models of Launder and Sharma [6] and its PTM model and of Chien[8], and results were discussed in the present study .

Mean velocity profiles and skin-frictions on the flat plate were measured in the wake generated by the circular cylinder at the upstream. The data can be used to verify the various turbulence models of transition. Whether the flow over the leading edge is laminar-like or fully turbulent, skin-friction is sensitive parameter of importance and strongly related to heat transfer. Direct measurement of wall friction is not easy job, and almost all the methods need delicate instrumentations and advanced techniques. The simple preston tube method is known inadequate for such a developing layer. The Computational Preston Method (CPM) proposed by Nitsche et al.[11] was used to measure the skin-friction coefficients in the present study. An experimental study was performed to investigate the skin friction distributions on a flat plate with sudden change in roughness (from rough to smooth surface) under zero pressure gradient condition using the CPM method[12]. The growth of internal viscous layer was compared with measured data of Antonia and Luxton [13] as well as estimated ones using empirical correlations. The experience of CPM method is extended to transition flow in the present study.
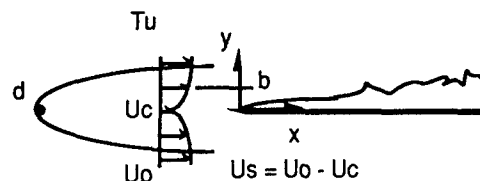

Fig. 1. Configuration of the flat plate and coordinate system.

NUMERICAL CALCULATION

Governing equations and turbulence models

For an incompressible steady turbulent flow, the continuity and Reynolds-averaged Navier-Stokes equations are the governing equations. The eddy viscosity μ_t is obtained by the low-Reynolds-number k–ε model. The transport equations for k and ε are written as

$$\mu_t = C_\mu f_\mu \rho \frac{k^2}{\varepsilon} \tag{1}$$

$$\frac{\partial}{\partial x}(\rho u k) + \frac{\partial}{\partial y}(\rho v k) = \frac{\partial}{\partial y}\left[\left(\mu + \frac{\mu_t}{\sigma_k}\right)\frac{\partial k}{\partial y}\right] + \mu_t\left(\frac{\partial u}{\partial y}\right)^2 \\ -(\rho\varepsilon + D) \tag{2}$$

$$\frac{\partial}{\partial x}(\rho u \varepsilon) + \frac{\partial}{\partial y}(\rho v \varepsilon) = \frac{\partial}{\partial y}\left[\left(\mu + \frac{\mu_t}{\sigma_\varepsilon}\right)\frac{\partial \varepsilon}{\partial y}\right] + C_1 f_1 \mu_t \frac{\varepsilon}{k}\left(\frac{\partial u}{\partial y}\right)^2 \\ -C_2 f_2 \frac{\rho\varepsilon^2}{k} + E \tag{3}$$

$\varepsilon + D$ actually denotes the nonisotropic dissipation rate, possessing a finite wall value; ε is the isotropic dissipation rate, that is zero at the wall; D is the low Reynolds number term. The functions and model constants are summarized as follows:

Launder and Sharma [6] Model

$$f_\mu = \exp\left[-\frac{3.4}{(1+R_t/50)^2}\right], \quad f_2 = 1 - 0.3\exp\left(-R_t^2\right) \tag{4}$$

$$C_\mu = 0.09, C_1 = 1.44, C_2 = 1.92, \quad \sigma_k = 1.0, \quad \sigma_\varepsilon = 1.3 \tag{5}$$

$$D = 2\mu\left(\frac{\partial k^{1/2}}{\partial y}\right)^2, \qquad E = 2\frac{\mu\mu_t}{\rho}\left(\frac{\partial^2 u}{\partial y^2}\right)^2 \tag{6}$$

Chien [8] Model

$$f_\mu = 1 - \exp\left[-0.0115 y^+\right], \quad f_2 = 1 - 0.22\exp\left(-(R_t/6)^2\right) \tag{7}$$

$$C_\mu = 0.09, C_1 = 1.35, \quad C_2 = 1.8, \quad \sigma_k = 1.0, \sigma_\varepsilon = 1.3 \tag{8}$$

$$D = 2\mu\frac{k}{y^2}, \qquad E = -2\mu\frac{\varepsilon}{y^2}\exp(-0.5 y^+) \tag{9}$$

where

$$R_t = \frac{\rho k^2}{\mu\varepsilon}, y^+ = \frac{\rho y u_\tau}{\mu} \tag{10}$$

Schmidt and Patankar [4] modified the value of function, f_μ, and limit the production rate of turbulent kinetic energy as follows:

$$f_\mu = min\{ f_{\mu o}, 1.0, 0.5 + 0.0025 R_t \} \tag{11}$$

$$P_k = 0 \text{, for } Re_\theta < Re_{\theta,C} \tag{12}$$

$$\left.\frac{dP_k}{dt}\right|_{max} = A \cdot P_k + B \text{, for } Re_\theta > Re_{\theta,C} \tag{13}$$

where Re_θ is Reynolds number based on momentum thickness. The coefficients A and B are functions of the free-stream turbulence intensity. These were calibrated considering the empirical correlations of the starting and ending locations of transition on a flat plate in uniform flow by Abu-Ghannam and Shaw [2]. The position of the free stream is not defined not only in the passage flow of blades but also over a flat plate in the wake. The actual free stream is the external flow of the wake, however turbulence of the free stream may not have direct affect on the boundary layer over the wall. As the wake flows over the plate, the internal layer will be developed from the leading edge. Therefore the value of turbulence intensity at the edge of the internal layer has strong affects on the shear layer over the surface, and the external flow has indirect influence upon growing and transition of the internal layer. Two cases were considered in the present study. The free stream value of turbulence intensity was used for PTM_e, and the value at the edge of internal layer δ_i for PTM_i csase. The location of δ_i was determined considering the slope of the wall layer and external wake profile.

Boundary conditions

The flow and equations are parabolic type and the calculation are carried out from the leading edge using marching procedure (Fig.1). At the inlet boundary $x = 0$, mean velocity profiles, kinetic energy and rate of dissipation profiles are estimated using the similarity solution of the plane wake described in the text [14].

$$\frac{U_o - u}{U_s} = \exp(-\xi^2/2) \tag{14}$$

$$\frac{k}{U_s^2} = 0.3\xi \exp(-\xi^2/2) \tag{15}$$

$$\varepsilon = \frac{U_s^3}{b R_T}\xi^2 \exp(-\xi^2) \tag{16}$$

where $R_T = \frac{U_s b}{v_t} = 12.5, \qquad \xi = \frac{y}{b}$

They are uniformly distributed from the centerline to the location of their maximum value. The dissipation rate along the free stream assumed very small for the specified value of k at the leading edge to remain to the downstream. On the plate, the no-slip condition is enforced. Since the low-Reynolds-number k–ε model is used, the boundary

651

conditions $k=0$ and $\varepsilon=0$ are imposed on the surfaces. The static pressure is assumed constant in the whole flow domain.

Numerical method

The discretized equations are obtained following a finite volume method. A staggered grid arrangement is used in which the scalar variables are located at the geometric center of a control volume, while the velocity components are located on the midpoints of the control faces. The unwind scheme is employed to evaluate the convection flux on the control surfaces. A pressure is constant and the integration of the continuity equation gives us the vertical component of velocity. A TDMA is used to obtain a numerical solution of the discretized equation.

EXPERIMENT AND DATA REDUCTION

Experimental apparatus and instrumentation

The experiments were performed in the 900mm x 900mm square section closed loop wind tunnel. The uniformity of mean flow is about 1% and the free-stream turbulence level is around 0.3% at the speed of 30 m/s. Boundary layer measurements were carried out on a smooth flat plate of 10mm thick and 1.6 m long flat plate, which was installed on a hinge at the center of the tunnel. The two-dimensionality and uniformity of the flow was adjusted by monitoring the static pressure on the plate. A circular cylinder of 5 mm diameter was mounted on the adjustable strut ahead of the plate. Mean velocity was measured using a total head tube of 0.6 mm diameter and kinetic energies were measured using a two components hot wire system of Kanomax Co..

Numerical Preston tube method (CPM)

The Preston tube method is one of the most widely used shear stress measuring techniques due to its simple construction. The correlation curve between the dynamic head of a wall Pitot tube, q and the corresponding wall shear stress, τ is usually represented by a calibration curve based on the law of the wall.

$$q^+ = F(\tau^+) \quad ; \quad q^+ = \frac{qd^2}{4\rho v^2} \quad ; \quad \tau^+ = \frac{\tau_w d^2}{4\rho v^2} \qquad (17)$$

where d is diameter of the Preston tube. If the effective distance from the wall corresponding to the tube diameter and the dynamic head is obtained from the law of the wall, the calibration curve can be obtained from direct calculation.

Nitsche et al. [11] reported an empirical curve of

displacement factor $K (= 2y_{eff} / d)$ as a function of $d^+ (= u_\tau d / v)$. Since the law of the wall is not generally known, he used the velocity profile of three parameters, as proposed by Szablewski [15].

$$u^+ = \int_0^{y^+} \frac{2(1+K_3 y^+) dy^+}{1+\left[1+4(K_1 y^+)^2 (1+K_3 y^+)\left(1-\exp\left(-y^+\sqrt{1+K_3 y^+}/K_2\right)\right)\right]^{0.5}} \qquad (18)$$

where K_1 formally corresponds to the von Karman constant, K_2 to Van Driest damping factor, and K_3 to the dimensionless pressure parameter. For $K=1.3$, $K_1 =0.4$, $K_2 =26$, $K_3 =0$, the empirical calibration curve according to Preston method is obtained and used for the fully developed turbulent boundary layer. The unknown parameters, K_1, K_2, K_3 (one of the parameters is fixed in some cases) and the value of wall shear stress are obtained analyzing the measured values of dynamic head using Preston tubes of different size. The procedure of the CPM is summarized as follows[11]:

(1) Measure dynamic heads using Preston tubes of different size.

(2) Assume the value of wall shear stress.

(3) Determine y_{eff} for each tube.

(4) Compare the calculated and measured dynamic heads.

(5) Go back to step (3), adjust shear stress and repeat step (4).

(6) Compare the converged wall shear stresses of each tube. If they are different each other, adjust parameters in the eq.(2). Go back to step (2) and repeat the same procedure until the converged stress is obtained.

The probe diameters should be small and not thicker than 20% of the boundary layer. The probe diameter ratio should be more than 1.5 to get significant differences in the basic shear stress[11].
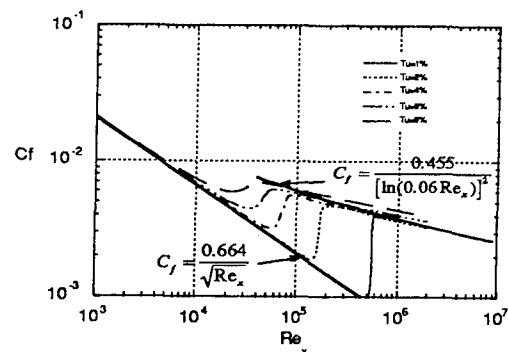

Fig.2 Skin-friction distributions on a flat plate in a uniform flow using LS model.

652

RESULTS AND DISCUSSION

Calculated results

The boundary layer on a flat plate in a uniform flow with free-stream turbulence intensity was simulated using Launder-Sharma(LS), Chien, and PTM models. Various grid spacing in the longitudinal and transverse directions and the initial profiles of turbulent kinetic energy and dissipation rate are tested for accurate and consistent prediction. Predicted distributions of skin-friction, $C_f (= 2\tau_w / \rho u_o^2)$ for various turbulence intensities are presented in Figs.2, 3, and 4. The LS natural transition model predicts earlier start and short transition length than the PTM model does. Chien's model shows also earlier start of transition and damped variation as discussed by Stephens and Crawford[7]. The PTM transition model successfully simulates the transition in Fig.5, since it was calibrated using measured data of Abu-Ghannam and Shaw [2]. The boundary layer over the leading edge is a laminar-like flow with high turbulence intensity, which is early diffused into the flow near the wall due to the turbulence in the external flow. These results confirm the discussed aspects in the previous studies of the uniform flow of high turbulence intensity [4, 7, 10].

Shear layer development on a flat plate in a turbulent wake was simulated using four turbulence model, i.e. Launder-Sharma (LS), Chien, PTM$_e$ and PTM$_i$ models. The values of free stream velocity, U_o, turbulence intensity, Tu, maximum velocity defect, U_s and half width of the wake, b are free parameters of the incoming flow. The values used in calculation are:

free stream velocity, U_o : 10, 20 m/s
maximum velocity defect U_s : 0.5,1, 2, 4 m/s
half width of the wake, b : 0.005, **0.01**, 0.02 , 0.04m
free stream turbulence intensity, Tu : 1, **2** %

The bold faced values are the standard values of each quantity when the others are changed. Kinetic viscosity, v is fixed as 1.25×10^{-5} m^2/s.

Before going into parametric study, the shear layer was simulated for the above standard values of wake. Simulated distributions of skin friction coefficient presented in Fig.6 shows that the LS natural transition models predicts earlier start and short transition length than the PTM model does. Chien's model shows also earlier start of transition and damped variation. These trends are generally the same with those of the uniform flow. PTM$_e$ and PTM$_i$ models show considerably different distributions from each other. PTM$_i$ model using the value of turbulence intensity at the edge of internal layer has stronger physical meaning, however there are not enough data to investigate their validity. Limited discussion will be given later in the present paper. The trend of C_f
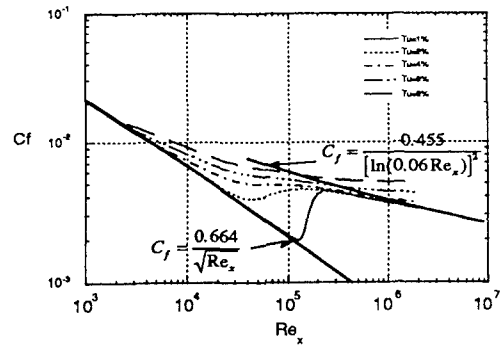
Fig.3 Skin-friction distributions on a flat plate in a uniform flow using Chien model.
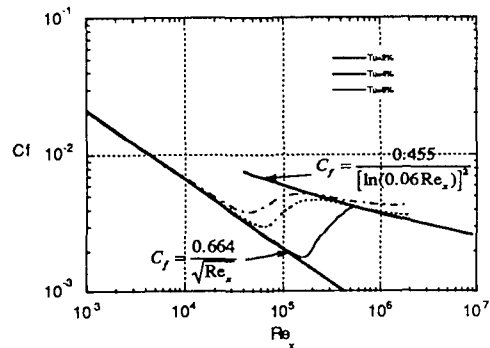
Fig.4 Skin-friction distributions on a flat plate in a uniform flow using PTM model.

distribution is not changed in Fig.7 for larger value of U_s = 2m/s.

The values of free stream velocity, U_o and maximum velocity defect, U_s may mainly contribute to development and transition of the internal layer. For the free stream velocity, U_o of 10 and 20 m/s, U_s was changed 1, 2, 4 m/s. The maximum value of turbulence intensity in the wake, which is dependent of only U_s / U_o, are 3.5, 7.0, 13.9 percent respectively at the leading edge. The variation of skin-friction distribution using the PTM$_i$ model are presented in Fig.8. The value of skin-friction coefficient along the plate is nearly the same for the same value of U_s / U_o, which means transition is strongly dependent upon turbulence intensity. The growth of internal layer is shown in Fig.9. The magnitude of δ_i were thicker than that in the uniform flow due to existing shear stress of the external flow, however growing rate is nearly same with the Blasius solution and increases more during transition. The effect of half width of the wake and free-stream
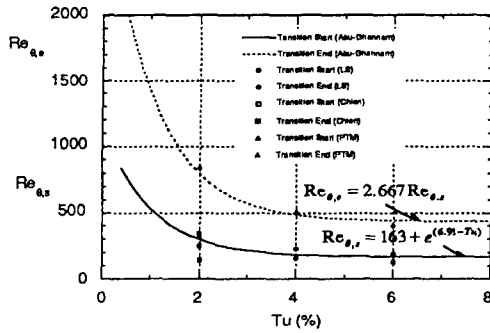
Fig. 5 Comparison of starting and ending locations of transition on a flat plate in a uniform flow.
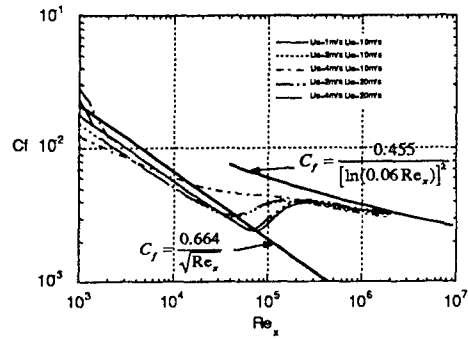
Fig.8 Skin-friction distributions on a flat plate in a wake using PTM_i model.
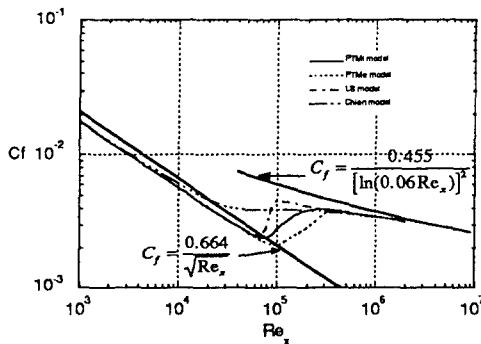
Fig.6 Skin-friction distributions on a flat plate in a wake for $U_s=1$ m/s and $U_o=10$ m/s.
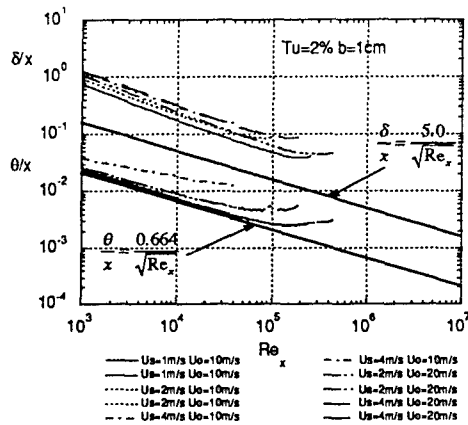
Fig.9 Predicted thickness of internal layer on a flat plate in a wake using PTM_i model.
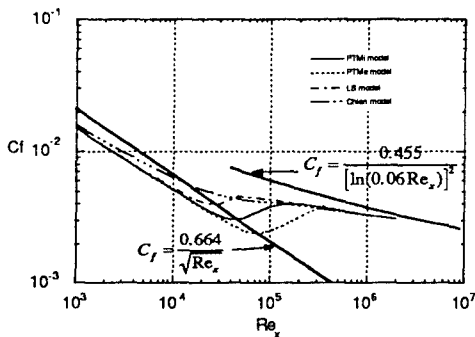
Fig.7 Skin-friction distributions on a flat plate in a wake for $U_s=2$ m/s and $U_o=10$ m/s.
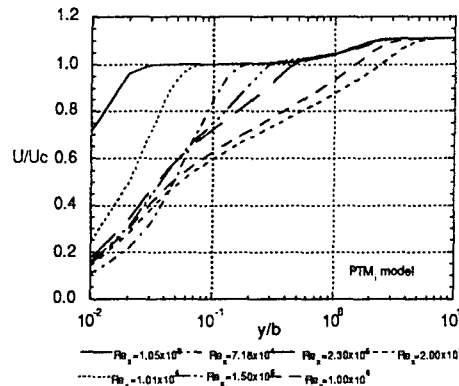
turbulence on the skin-friction distribution was very small, however the internal layer grows faster as the wake becomes thicker and free stream turbulence increases (not shown here). A wake profile in a strong turbulence intensity was not tried here, since the turbulence structure is not known yet.

Fig.10 Predicted profiles of velocity on a flat plate in a standard wake using PTM_i model.
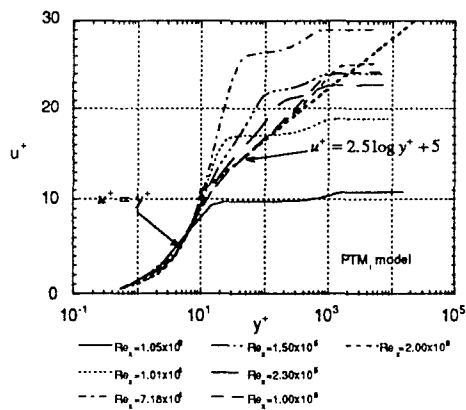
Fig.11 Predicted profiles of velocity on a flat plate in a standard wake using PTM_i model.

Fig.12 Predicted profiles of turbulent kinetic energy on a flat plate in a standard wake using PTM_i model.
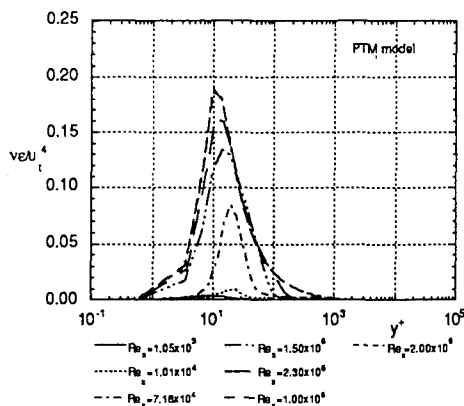
Fig.13 Predicted profiles of dissipation on a flat plate in a standard wake using PTM_i model.

Fig.14 Predicted profiles of kinetic energy production on a flat plate in a standard wake using PTM_i model

Simulated profiles of non-dimensionalized velocity presented in Figs.10 and 11. show how the internal layer develops from the Blasius to the logarithmic law profiles near the wall. The turbulent kinetic energy distributions are presented in Fig.12. The incoming turbulent kinetic energy in the wake rapidly decreases at the leading edge due to the zero boundary condition, however turbulence is self-generated and has its maximum value near the wall in the transition region. At the end of transition turbulent kinetic energy duffuses to the external flow and finally the profile approaches to the typical one of the equilibrium turbulent boundary layer. It is observed that the maximum value of kinetic energy during transition is larger than the peak value in the fully developed turbulent boundary layer at the downstream. The dissipation rate and production are presented in Figs.13 and 14 respectively. The rates rapidly increase near the wall ($y^+=10$ - 20) during the transition process, and show typical profiles of the equilibrium layer at the downstream, too. Turbulent kinetic energy production and its dissipation rate becomes nearly identical at the end of transition. The evolution of turbulence during transition seems to be reasonably simulated with the PTM_i model, however it should be confirmed by measurement.

The PTM transition model based on the low Reynolds number k-ε of Launder and Sharma does reasonably predict skin-frictions on a flat plate during transition. However need of extensive calibrations using various transition data is shown by the present numerical investigations.

655
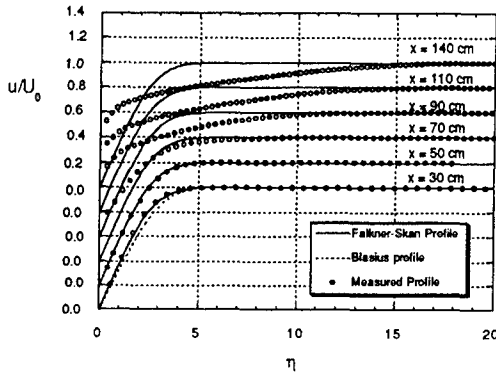
Fig. 15. Mean velocity profiles on the flat plate
in the uniform free stream.
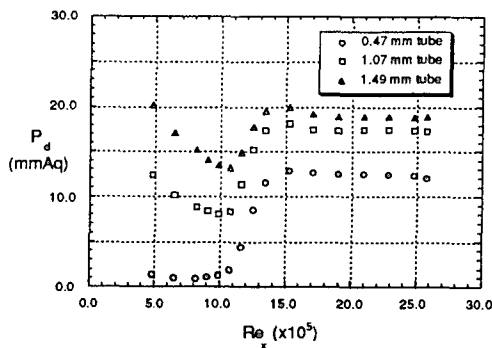
Fig. 17. Variation of skin-friction on the plate measured
by CPM technique in the uniform flow.

Fig. 16. Measured values of total pressure
by three Preston tubes of different size.
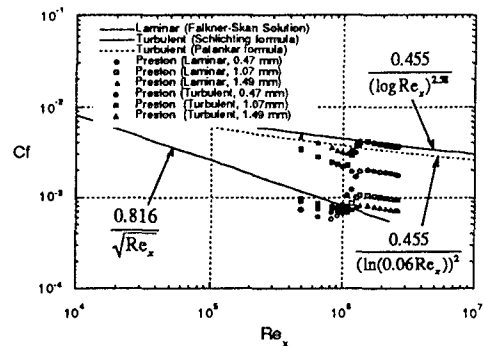
Fig. 18. Variation of skin-friction on the plate measured
by Preston tube method in the uniform flow.

Measurement of boundary layer in uniform flow

Measurement was carried out at the uniform speed of 25 m/s. Typical three regimes of flow, i.e. laminar, transitional, and turbulent, appear at this speed over the 1.5 m long flat plate in the present study. Mean velocity profiles at several stations of laminar, transitional and turbulent flows are shown in Fig.15. Since the plate was slightly inclined to keep parallel flow over the leading edge, the external flow was accelerated a little ($dU_o/dx = 0.096$ 1/s). The measured profiles over the leading edge nicely coincide with the Falkner-Skan flow with weak favorable pressure gradient. The flow changes near the wall and transfer to the external flow, then becomes fully turbulent boundary layer profile at the downstream. The transition starts at $Re_x = 8 \times 10^5$ (

$Re_\theta = 550$) and ends at $Re_x = 1.4 \times 10^6$ ($Re_\theta = 1400$). The value of shape factor slowly changes from 2.5 to 1.3. These results coincides with measured values of Sohn and Reshotko[3].

The measured values of total pressure by three Preston tubes of different diameter, i.e. 0.47, 1.07 and 1.49 mm, are presented in Fig.16. The total head decreases first along the plate with the boundary

layer thickness, then increases in the transition region, and decreases again over the turbulent region. The parameter K_1 was only adjusted to obtain skin-friction by CPM technique as was suggested in the previous study[7]. K_2 was fixed as 26 and K_3 as 0. Except the tube set of 1.07-1.49 mm (the diameter ratio is larger than 1.5), the estimated skin-friction coefficients show consistant values each other in Fig.17. They are in coincidence with values from turbulent empirical correlations, however smaller than the Falkner-Skan solution. This deviation may attribute to the inaccuracy of the effective distance in case of laminar flow in the CPM procedure. As expected, the conventional Preston tube method can not be used for the transitional boundary layer as shown in Fig.18. The variation of parameter K_1 is shown in Fig.19. It changes from 0.0 to 0.42 over the transition region. Due to the CPM profile adopted in the present study, the law of the wall in the limitted region of Preston tube diameter can be expressed as families of function of variable von-Karman constant. Non-dimensionalized velocity profiles using the measured shear velocity are plotted in Fig.20. The profile over the leading edge shows typical laminar flow characteristic (cf. however the turbulence level may be quite different from the laminar flow [3]) and

656

Fig.19. Variation of K_l along the plate in the uniform flow.
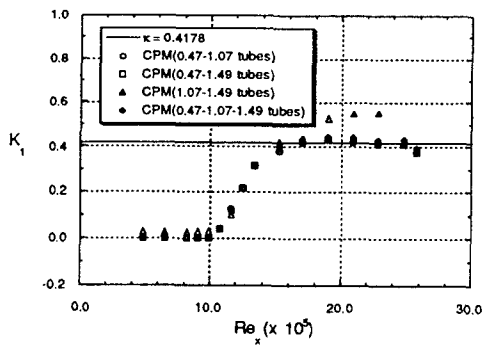
Fig. 20. Non-dimensional velocity profiles on the flat plate in the uniform flow.

becomes typical logarithmic profiles of the fully developed turbulent boundary layer at the far downstream location.

From this fundamental test in the uniform flow, the CPM technique is verified to be a useful tool to investigate the skin-friction of the transitional boundary layer with reasonable accuracy. The simple construction and instrumentation for the technique should be appreciated.

Measurement of boundary layer in the wake

The velocity distributions generated using a circular cylinder of 5 mm diameter ahead of the plate confirm the similarity solution[14] between $x/D=10$ and 30. When the wake center is adjusted to be located at the leading edge, the measured incoming velocity just ahead of the plate still coincides with the similarity profiles in Fig.21. The cylinder was located at 0.6 m upstream. The maximum value of velocity deficit U_s was 3.53 m/s and the half width of the wake, b was 0.0136 m at the position of the leading edge.

The thickness of the internal layer, which is estimated by comparing the velocity profile with the similarity profile of wake. The variation of thickness is compared with calculated values in Fig.22. Raw data of the dynamic pressure measured by Preston tubes are shown in Fig.23. The skin-friction coefficient gradually changes from the leading edge to the downstream in Fig.24. Transition length shows very long, i.e. it starts at $Re_x = 8 \times 10^4$ and ends at $Re_x = 2.0 \times 10^6$. This is partially due to the high level of turbulence intensity (5%) at the center of the incoming wake. However the length is longer than that of the uniform flow with the free stream intensity of 5%. Effects of the non-zero values of Reynolds stresses in the wake on the development of the internal layer are beyond the scope of the present study. The values of skin-friction using the conventional Preston tube method show that it is not
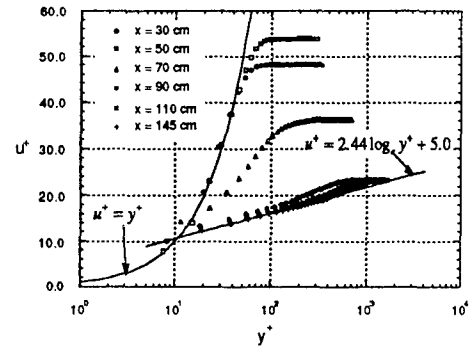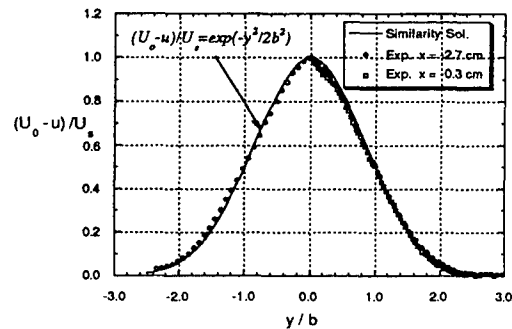
Fig. 21. Velocity profiles in the incoming wake ahead of the flat plate.
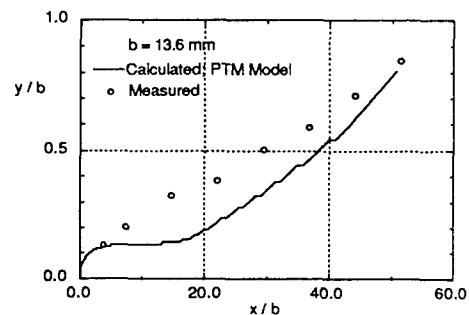
Fig. 22. Variation of the internal layer along the plate.

657
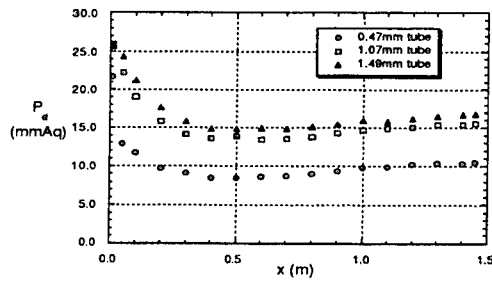
Fig. 23. Measured values of total pressure by Preston tubes of three different size.

Fig. 25. Variation of K_l along the plate in the uniform flow.
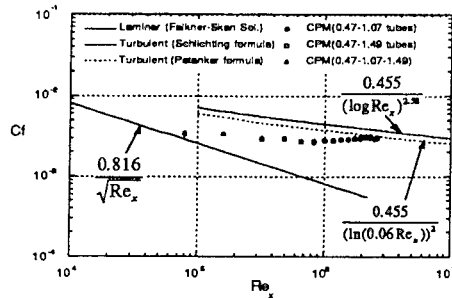
Fig. 24. Variation of skin-friction on the plate in the non-uniform incoming flow.

Fig.26. Non-dimensional velocity profiles on the plate in the wake.

valid for this case, too. The value of K_l at the first point is already large, i.e. 0.2, then monotonically increases to the von Karman constant, 0.42 in Fig.25. Considering these aspects of the flow, the boundary layer over the leading edge can be a laminar-like flow with high turbulence intensity, of which energy is diffused into the flow near the wall due to the natural turbulence production in the external flow. Further investigation is needed for turbulence characteristics here. Finally the non-dimensional velocity profiles are shown in Fig.26. Logarithmic region appears even at the first measuring point, however the profile considerably deviates from the fully developed profile.

Taking into account of small increases in the measured values over the plate due to the small acceleration of the free stream, the length of transition was shortly estimated in the both PTM_e and PTM_i calculations. Furthermore the transition is considerably delayed in the PTM_e calculation. The accuracy of CPM measurement should be further investigaed.

CONCLUSION

The results of the numerical and experimental study of the transitional boundary layer over the flat plate in a non-uniform flow are summarized as follows:

(1) The Launder and Sharma model predicts earlier start and short transition length than the PTM model does. Chien's model shows also earlier start of transition and damped variation. These trends are generally the same with those in the uniform flow. PTM_e and PTM_i models show considerably different distribution from each other.

(2) The value of skin-friction coefficient along the plate is nearly identical for the same value of U_s/U_o, which means transition is strongly dependent upon turbulence intensity within the internal layer.

(3) The PTM transition model based on the low Reynolds number k-ε of Launder and Sharma does reasonably predict skin-frictions on a flat plate during transition. However more extensive calibrations is needed.
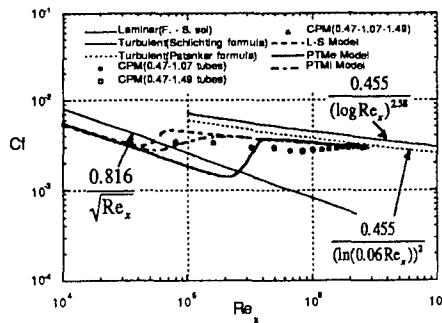
Fig. 27. Calculated and measured skin-friction coefficients on the flat plate in the non-uniform flow.

(4) The variation of skin-friction was obtained using the CPM technique. The method is verified as an useful tool to investigate skin-friction over the transitional boundary layer with reasonable accuracy. The simple construction and instrumentation for the technique are appreciated.

(5) The skin-friction coefficient gradually changes from the leading edge to the downstream. Transition length was considerably longer than in the uniform flow.

ACKNOWLEDGEMENT

REFERENCES

1. Mayle, R.E., "The Role of Laminar - Turbulent Transition in Gas Turbine Engines, The 1991 IGTI Scholar Lecture", J. of Turbomachinery, Trans. of ASME, Vol.113, pp. 509-537, 1991.

2. B.J. Abu-Ghannam and R. Shaw, "Natural Transition Boundary Layer - The Effects of Turbulence, Pressure Gradient, and Flow History", J. of Mech. Eng. Science, Vol.22, No.5, pp. 213-228, 1980.

3. K.H. Sohn and E. Reshotko, " Experimental Study of Boundary Layer Transition With Elevated Free stream Turbulence on a Heated Flat Plate," NASA CR 187068, 1991.

4. R.C Schmidt and S.V. Patankar, "Simulating Boundary Layer Transition With Low-Reynolds Number k-ε Turbulence Models: Part 2 - An Approach to Improving the Predictions," J. of Turbomachinery, Vol.113, 1991.

5. C.K.G. Lam and K. Bremhorst, "A Modified Form of the k-ε Model for Predicting Wall Turbulence," J. of Fluids Eng., Vol.103, pp.456-460, 1981.

6. B.E. Launder and B.I. Sharma, "Application of the Energy-Dissipation Model of Turbulence to the Calculation of Flow Near a Spinning Disc", Letters in Heat and Mass Transfer, Vol. 1, p. 131, 1974.

7. C.A. Stephens and M.E. Crawford, "An Investigation into the Numerical Prediction of Boundary Layer Transition Using the K.YChien Turbulence Model," NASA CR 185252, 1990.

8. K.Y. Chien ,"Predictions of Channel and Boundary Layer Flows with a Low Reynolds Number Turbulence Model," AIAA J., Vol.20, pp. 33-38, 1982.

9. W. Szablewski, "Turbulence Drenzschichten in Ablosenahe. Z.", Angrew. Math. Mech. 49, pp. 215, 1969.

10. S.H. Kang, J.S.Lee, Y.H. Kim and K.Y. Kim, " Numerical Calculations of the Turbulent Flow through a Controlled Diffusion Compressor Blade in Cascade", (submitted to J. of Turbomachinery), 1992.

11. W. Nitsche et al. ,"A Computational Preston tube Method," Turbulent Shear Flows, Vol. 4, 1983, pp. 261-276.

12. S.H. Kang, J.Y. Yoo, J.M. Lee, W.P. Jeon, " Characteristics of a Turbulent Boundary Layer on the Flat Plate with Sudden Change in Surface Roughness," Trans. of KSME, 16(12), 1992.

13. R.A. Antonia and R.E. Luxton, "The response of a turbulent boundary layer to a step change in surface roughness. Part2. Rough to smooth," J. of Fluid Mech., Vol. 53, 1972, pp. 737-757.

14. H.Tennekes and J.L Lumley, A First Course in Turbulence, The MIT Press, 1974.

15. M.F. Blair and M.J. Werle, " The Influence of Free Stream Turbulence on the Zero-Pressure Gradient Fully Turbulent Boundary Layer," United Technologies Research Center, Rept. R80-914388-12, 1980.

Computation of the Tip Vortex Flow on Three-Dimensional Foils with a Parabolized Navier-Stokes Solver

L.R.C. Eca and J.A.C. Falcao de Campos

(Instituto Superior Técnico, Portugal)

M. Hoekstra (MARIN, The Netherlands)

Abstract

A numerical method for the calculation of the incompressible viscous flow at the tip of wings is presented. The method is based on a finite-difference approximation of the Reynolds-averaged Parabolised Navier-Stokes equations for steady incompressible flow. An eddy viscosity algebraic turbulence model is used.

The method is applied to the calculation of the flow at the tip of wings with rectangular planform. The sensitivity of the numerical solution to the accuracy of the boundary conditions imposed at the viscous region boundaries is investigated by changing the location of the boundaries. The results show that the present method uses an efficient approach to the calculation of tip vortex flows. The specification of the inlet boundary conditions is also investigated and the use of Neumann boundary conditions is proposed to obtain a smoother solution close to the inlet boundary. A good agreement between the numerical predictions and experimental data is obtained. However, the size of the vortex core is overpredicted.

Nomenclature

$\vec{a}^i$ - Contravariant base vectors.

c - Wing chord.

C_p - Pressure coefficient, $\left(C_p = \frac{p - p_\infty}{\frac{1}{2}\rho U_\infty^2}\right)$.

g^{ij} - Contravariant metric tensor.

$\sqrt{g}$ - Jacobian of the coordinate transformation.

p - Pressure.

$\bar{p}$ - Pressure dependent variable, $\left(\bar{p} = \sqrt{g}p\right)$.

Re - Reynolds number, $\left(Re = \frac{U_\infty c}{\nu}\right)$.

U_∞ - Free-stream velocity.

U^i - Cartesian velocity components.

V^i - Contravariant velocity components.

$\overline{V}^i$ - Velocity dependent variables, $\left(\overline{V}^i = \sqrt{g}V^i\right)$.

x, y, z - Cartesian coordinates.

Γ^i_{jk} - Christoffel symbols of the second kind.

ξ, η, ζ - Curvilinear coordinates.

μ - Fluid effective viscosity.

ν - Fluid kinematic viscosity.

ρ - Fluid mass density.

τ^{ij} - Stress tensor.

1 Introduction

Several engineering problems are associated with the generation of trailing tip vortices on lifting surfaces of finite span. The dangers created by tip vortex wakes of aircraft to following aircraft and the noise and vibrations caused by rotor blade vortex interactions on helicopters are two examples of such problems in aeronautics. In marine applications, such as hydrofoils and marine propellers, tip vortex flows are often associated with cavitation. The rotational motion around the vortex center creates a low pressure region in the tip vortex core. If the pressure is sufficiently low cavitation will occur. Tip vortex cavitation is a major source of noise generated by the propeller and in some cases is the first type of cavitation to appear. The ability to predict the inception of tip vortex cavitation remains one of the present challenges of the propeller designer.

The objective of the present work was to initiate the development of a numerical method for the calculation of steady viscous flow on propeller blade tips. The flow at the tip of wings/hydrofoils is geometrically simpler than the flow on propeller

blade tips, but the main physical features of tip vortex flows are already present. Furthermore, the effect of the detailed shape of the tip on the tip vortex characteristics can already be investigated. Therefore, the subject of the present paper is the description of a numerical method for the calculation of steady incompressible viscous flow at the tip of wings/hydrofoils.

In incompressible flow, the first approaches to the calculation of tip vortex flows were reported by Govidan *et al.* in [1] and [2]. Govidan *et al.* used the parabolised Navier-Stokes equations to calculate tip vortex flows. In Govidan's approach, streamwise diffusion is neglected and the streamwise pressure gradient is obtained from inviscid flow calculations. This means that a full parabolisation of the Navier-Stokes equations is used. The numerical solution of the conservation equations is based on a formulation proposed by Briley and McDonald in [3], that uses a primary-secondary velocity decomposition. Govidan *et al.* applied the method to a rectangular wing with a rounded tip with promising results, [2].

Also in the present method we adopted the Parabolised Navier-Stokes[1] (PNS) equations, because tip vortex flows have a predominant flow direction. However, in the present method only streamwise diffusion is neglected. This means that only a partial parabolisation is obtained because the elliptic character is retained in the pressure field, the streamwise pressure gradient is obtained in the solution. These equations were proposed by Rubin, [5], for flows with a predominant flow direction. As shown by Rubin in [6], these equations contain all the important terms of the Navier-Stokes equations for high Reynolds number flows. The use of the Parabolised Navier-Stokes equations allows a more efficient solution procedure than the full Navier-Stokes equations.

In the recent literature there are some examples of the application of the PNS for incompressible viscous flow calculations. A method based on these equations has been developed in the last 10 years by Hoekstra and Raven for the calculation of ship stern flows, [7], [8], [9] and [10], and more recently Rosenfeld *et al.* in [11], presented a method for the calculation of the incompressible viscous flow over slender bodies. The method of Hoekstra and Raven is embodied in the computer code PARNASSOS, and was used as the starting point for the present method, which is described

in detail in [12].

The paper is organized in the following way : The mathematical formulation with the boundary conditions appropriate to this problem and the turbulence model are presented in section 2. The solution procedure is described in section 3. The results of the application of the method to the calculation of the flow at the tip of rectangular wings are presented and discussed in section 4. The conclusions of this paper are summarized in section 5.

2 Governing Equations

The Navier-Stokes equations can be written in several different forms. The strong conservation form of the equations in general boundary-fitted curvilinear coordinate systems has been derived by several authors, [13], [14], [15], and is generally accepted as the more suitable for numerical purposes, [14]. For steady incompressible flow these equations can be written as :

$$\frac{\partial}{\partial \xi^i} \left(\sqrt{g} V^i \right) = 0, \tag{1}$$

$$\frac{\partial}{\partial \xi^j} \left[\sqrt{g} \frac{\partial x^i}{\partial \xi^k} \left(\rho V^j V^k + g^{jk} p - \tau^{jk} \right) \right] = 0, \tag{2}$$

with

$$\tau^{jk} = \mu \left[g^{jm} \frac{\partial V^k}{\partial \xi^m} + g^{km} \frac{\partial V^j}{\partial \xi^m} - V^m \frac{\partial g^{jk}}{\partial \xi^m} \right]. \tag{3}$$

The tensorial summation convention applies; p is the pressure, ρ the fluid mass density, μ the fluid effective viscosity[2], V^i are the contravariant velocity components, $(x^1, x^2, x^3) = (x, y, z)$ are the coordinates of a cartesian coordinate system, $(\xi^1, \xi^2, \xi^3) = (\xi, \eta, \zeta)$ are the curvilinear coordinates, $\sqrt{g}$ is the Jacobian of the transformation between the two systems and g^{ij} is the contravariant metric tensor.

Equations (1) and (2) are written in divergence form and so a finite-volume discretization of these equations may satisfy a discrete analogue of the divergence theorem, [16], which means that a conservative discretization of the equations is possible. However, in the Parabolised Navier-Stokes[3] equations diffusion is neglected in the streamwise

---

[1]In [4] Rubin *et al.* refer to these equations as the Reduced Navier-Stokes equations when diffusion terms in the η momentum equation are neglected.

[2]The fluid effective viscosity, μ, is obtained with an isotropic eddy-viscosity algebraic turbulence model, see section 2.1

[3]The Parabolised Navier-Stokes equations will be denoted by PNS.

direction and the strong conservation form of the momentum equations, (2), expresses conservation of momentum in the coordinate directions of a cartesian coordinate system, (x, y, z), [16]. In general, the x, y, z directions of a cartesian coordinate system are not flow conforming and so the strong conservation form of the momentum equations may not be compatible with the physical approximations assumed in the PNS equations.

The contravariant form is a more attractive way to write these equations. This form of the equations expresses conservation of mass and momentum along the ξ, η, ζ directions of a boundary-fitted curvilinear grid, which may also be a flow conforming coordinate system. The Reynolds-averaged momentum equations in contravariant form on a boundary-fitted curvilinear grid (ξ, η, ζ) can be written in the following form for a stationary incompressible flow :

$$\rho V^j \frac{\partial V^i}{\partial \xi^j} + \rho V^j V^k \Gamma^i_{jk} + g^{ij} \frac{\partial p}{\partial \xi^j} - Dif = 0 \ , \ (4)$$

where

$$Dif = \frac{\partial \tau^{ij}}{\partial \xi^j} + \Gamma^i_{jk} \tau^{jk} + \Gamma^j_{jk} \tau^{ik} \ .$$

The tensorial summation convention applies, ξ is a streamwise coordinate, η a coordinate normal to the wall and ζ a transverse coordinate and Γ^i_{jk} are Christoffel symbols of the second kind. A partial parabolisation is obtained by neglecting the streamwise diffusion in the momentum equations, i. e. the terms with $j = 1$ in the viscous terms of equations (4). The elliptic character of the equations is retained in the pressure field.

Equations (4) are written in weak conservation form and so their numerical discretization may originate unphysical source terms in the discretized equations, [17]. Mynett et al., [18], used a different formulation of equations (4) to obtain an invariant finite-volume discretization of the equations. However, their formulation is also in weak conservation form. A finite-volume discretization of Mynett's formulation was applied by Segal et al. in 2-D calculations, [19]. One of the criteria proposed by Segal et al., [19], to evaluate the quality of the numerical discretization is that the discretized form of the conservation equations should be satisfied in a uniform flow. The discretization given by Segal et al., [19], satisfies this property in 2-D cases, but there is no proof that it will do so as well in 3-D, due to the presence of the Christoffel symbols of the second kind in the equations, [17].

An alternative way to write equations (1) and (4) is to use the cartesian velocity components, U^i, as the dependent variables. The contravariant velocity components, V^i, are related to the cartesian components, U^i, by the following equation :

$$V^i = \vec{a}^i \cdot \vec{U}, \tag{5}$$

where $\vec{U}$ is the velocity vector in cartesian components,

$$\vec{U} = (U^1, U^2, U^3),$$

and $\vec{a}^i$ are the contravariant base vectors,

$$\vec{a}^i = (\frac{\partial \xi^i}{\partial x}, \frac{\partial \xi^i}{\partial y}, \frac{\partial \xi^i}{\partial z}).$$

Substituting (5) in (1), (3) and (4) and with the help of the following metric relation, see for example [20],

$$\frac{\partial \vec{a}^i}{\partial \xi^k} = -\Gamma^i_{jk} \vec{a}^j, \tag{6}$$

the equations of conservation of mass and momentum along the ξ, η, ζ directions become :

$$\vec{a}^i \cdot \frac{\partial \vec{U}}{\partial \xi^i} = 0, \tag{7}$$

$$\rho \left(\vec{a}^j \cdot \vec{U} \right) \left(\vec{a}^i \cdot \frac{\partial \vec{U}}{\partial \xi^j} \right) + g^{ij} \frac{\partial p}{\partial \xi^j} - \left(\frac{\partial \tau^{ij}}{\partial \xi^j} \right)^\star = 0, \tag{8}$$

with

$$\tau^{ij} = \mu \left[g^{im} \left(\vec{a}^j \cdot \frac{\partial \vec{U}}{\partial \xi^m} \right) + g^{jm} \left(\vec{a}^i \cdot \frac{\partial \vec{U}}{\partial \xi^m} \right) \right], \tag{9}$$

and

$$\left(\frac{\partial \tau^{ij}}{\partial \xi^j} \right)^\star = g^{im} \left(\vec{a}^j \cdot \frac{\partial}{\partial \xi^j} \left(\mu \frac{\partial \vec{U}}{\partial \xi^m} \right) \right) + g^{jm} \left(\vec{a}^i \cdot \frac{\partial}{\partial \xi^j} \left(\mu \frac{\partial \vec{U}}{\partial \xi^m} \right) \right) + A, \tag{10}$$

$$A = \left(\vec{a}^i \cdot \frac{\partial \vec{a}^m}{\partial \xi^j} \right) \left(\vec{a}^j \cdot \mu \frac{\partial \vec{U}}{\partial \xi^m} \right) + \left(\vec{a}^j \cdot \frac{\partial \vec{a}^m}{\partial \xi^j} \right) \left(\vec{a}^i \cdot \mu \frac{\partial \vec{U}}{\partial \xi^m} \right). \tag{11}$$

Streamwise diffusion is neglected, i. e. the terms with $j = 1$ in the viscous terms of equation (8) are dropped.

In the PNS equations written with cartesian components, U^i, as dependent variables only the diffusion terms include derivatives of contravariant base vectors, term A of equation (10). Furthermore, there are no implicit geometrical identities in the equations. In the same equations

written with the contravariant velocity components, V^i, as the dependent variables, (4), the identity (6) is implicitly satisfied. This means that in a certain sense, equations (8) allow a more conservative discretization than equations (4), because the identity (6) has to be respected numerically in the discretization of equations (4) to avoid unphysical source terms in the discretized equations. A simple example is given by the calculation of a uniform flow with a discretized form of the PNS equations, [17]. In a uniform flow, the discretized momentum equations (8) are satisfied independently of the grid metric properties and of the discretization scheme because all the terms are identically zero. We note that equations (8) are not in divergence form and so the use of a finite-volume discretization technique, that would ensure the satisfaction of a discrete analogue of the divergence theorem, is not possible.

As mentioned before, the use of parabolised equations for the flow simulation implies that a physical meaning is attached to the grid, since diffusion is neglected in the streamwise direction. This means that if the ξ, η, ζ system is roughly flow conforming, the use of contravariant velocity components as dependent variables is much more attractive than the use of cartesian components, because it enables the possibility of using the physical characteristics of the flow in the solution procedure.

Taking into account these considerations, the PNS equations written with the cartesian components, U^i, as the dependent variables are used to obtain the discretized equations, but the dependent variables used in the calculation are the contravariant velocity components. This means that the relations between cartesian components and contravariant components,

$$U^i = \frac{\partial x^i}{\partial \xi} V^1 + \frac{\partial x^i}{\partial \eta} V^2 + \frac{\partial x^i}{\partial \zeta} V^3 , \qquad (12)$$

are used to obtain the final form of the discretized equations after the discretization of the equations (7) and (8). With this procedure, we exploit of the numerical advantages of discretizing the contravariant PNS equations with U^i as velocity dependent variables, and keep the flow-conforming contravariant velocity components as the dependent variables of the discretized equations. We note that substituting (12) in (7) and (8) we obtain the PNS equations written with V^i as dependent variables, equations (1) and (4). However, in the present formulation the substitution of (12) is made after the discretization of equations (7) is made after the discretization of equations (7)

and (8), which means that the discretization of the metric terms of the contravariant PNS equations with V^i as the dependent variables does not need to be dealt with explicitly.

Due to the existence of grid singularities the velocity variables chosen are not the contravariant velocity components, V^1, V^2 and V^3, [10], but these components multiplied by the Jacobian of the transformation, $\sqrt{g}$. At present, we also multiply the pressure by the Jacobian of the transformation to obtain the pressure dependent variable, for numerical reasons :

$$
\begin{aligned}
\overline{V}^i &= V^i \sqrt{g} \\
\overline{p} &= p\sqrt{g} \, .
\end{aligned}
\qquad (13)
$$

The flow solution is obtained by solving the continuity and momentum equations with the appropriate boundary conditions. The velocity component in the normal direction, V^2, is obtained by solving the continuity equation and the three momentum equations are used to obtain the remaining two components of the velocity and the pressure. The diffusion terms in the η momentum equation are dropped. As mentioned by Rubin et al. in [4] if the η coordinates are locally normal to ξ - at least near boundaries - all the diffusion terms in the momentum equation in the normal direction, η, may be dropped. This means that normal pressure variations, $\frac{\partial p}{\partial \eta}$, are essentially inviscid in origin and so the present set of equations represents an extension of interacting boundary layer theory.

2.1 Boundary Conditions

The flow around the tip of a wing has six boundaries. A schematic view of these boundaries in the physical and computational domain is given in figure 1. The six boundaries of the flow domain are denoted as follows : The inlet[4] $ABCD$ and the outlet $EFGH$. The external boundary $BFGC$, the wing surface and the inner[5] boundaries $ABFE$ and $CDHG$, which constitute the inlet and outlet of the cross-flow.

The inlet boundary is placed downstream of the stagnation region, because in the present method a downstream calculation procedure is used. Furthermore, a zonal approach is adopted in the present method and so the stagnation region may

---

[4] In figure 1 the inlet boundary is a spanwise section of the wing.

[5] In figure 1 the inner boundary is a chordwise section of the wing.

PHYSICAL DOMAIN

COMPUTATIONAL DOMAIN
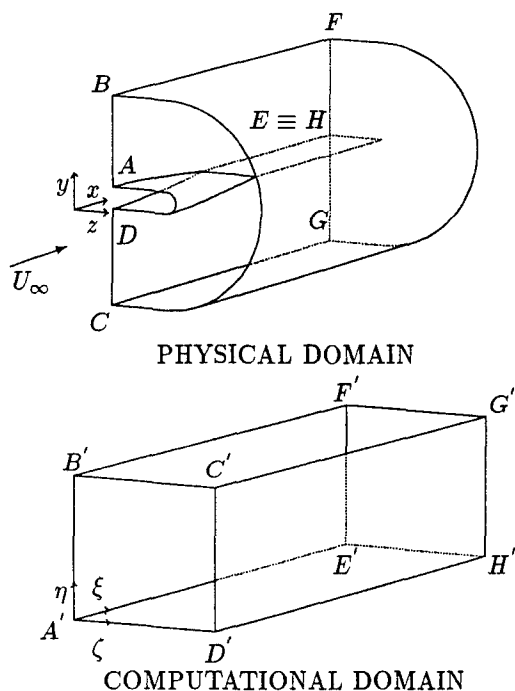
Figure 1: Illustration of the boundaries of the calculation of the flow at the tip of wings in the physical and computational domains.

be predicted with a boundary-layer method. The inlet boundary is not a natural boundary of the flow and so the choice between Dirichlet and Neumann boundary conditions is not clear, because in both cases some approximations will be required to specify the boundary conditions. From the implementation point of view, a straightforward option is to specify the three velocity components at the inlet boundary. However, it may be difficult to obtain a good estimate of the inlet velocity profiles and this may produce a non-smooth behaviour of the solution near the inlet boundary.

To improve the smoothness of the solution near the inlet boundary, Hoekstra in [10] suggests the use of a Neumann boundary condition for the normal velocity component, V^2. In the present work a different approach was tested. Neumann boundary conditions are applied to the three velocity components. A good estimate of the streamwise velocity gradient at the inlet boundary may be even more difficult than the estimate of the velocity profiles, but since the specification of streamwise velocity gradient is a weaker type of boundary condition, a less accurate prediction of its value should be less damaging to the solution than the use of a poor estimate of the velocity profiles.

In the present paper the two types of boundary conditions are compared, respectively the specification of velocity profiles and the specification of streamwise velocity gradient. In both cases the specified values are obtained with the help of a potential flow calculation, [21], and standard boundary layer profiles, [22].

At the outlet boundary a pressure boundary condition is required. The use of Dirichlet boundary conditions is not a good choice. A good approximation of the pressure field at the outlet boundary will be hard to obtain, due to the presence of the tip vortex and its influence on the pressure field. This leads us to choose a Neumann boundary condition. In the present calculations the streamwise pressure gradient was set equal to zero.

The typical cross-sections of the wing and of the wake in the physical space and in the computational domain are illustrated in figure 2.

WING   WAKE

PHYSICAL DOMAIN

COMPUTATIONAL DOMAIN
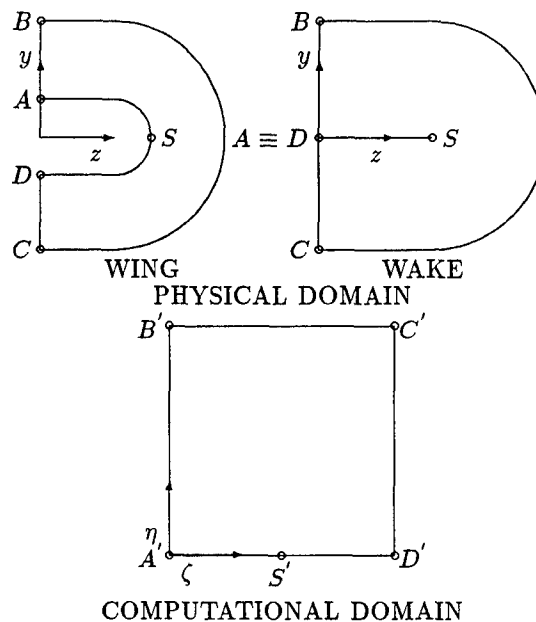
Figure 2: Illustration of the typical cross-section on the wing and wake and of the computational domain.

Boundary BC is the external boundary (surface $BFGC$ of figure 1), where the tangential components of the velocity and the pressure are prescribed by a potential flow calculation, [21]. Boundaries AB and DC are the inlet and outlet of the cross-flow (surfaces $ABFE$ & $CDHG$ of figure 1). Exact boundary conditions are available if the inner boundary is placed at the symmetry plane of the wing. For a given number of grid nodes, a finer discretization of the tip vortex region can be obtained if the inner boundary

665

is placed close to the tip. However, we will no longer have exact boundary conditions at the inner boundary and so approximate boundary conditions will have to be used. In the present applications the cross-stream derivatives $(\frac{\partial}{\partial \zeta})$ of the cartesian velocity components and of the pressure were set equal to zero. We note that it is not safe to impose zero cross-stream derivatives directly to the dependent variables, since they are a function of the grid properties.

Boundary AD has different properties in the cross-sections located on the wing and on the wake. On a cross-section of the wing it coincides with the wing surface, where the no-slip condition applies. The three velocity components are set equal to zero and the flow is calculated down to the wing, without wall functions. At the wake section, boundary AD is a fictitious boundary in the physical space. All the variables have to be calculated along this 'boundary', since the boundary nodes of the computational domain are field nodes in the physical space. A special treatment has to be included for point S where the transformation is singular, $\sqrt{g} = 0$.

2.2 Turbulence Model

There is a wide range of turbulence models available in the literature varying from the simple eddy-viscosity turbulence models, which can be algebraic or solve one or two transport equations, to the more complex second moment closures, which solve transport equations for each of the Reynolds stresses appearing in the momentum equations. The computer time required by the several models available is very different and according to Launder, [23], the use of a second moment closure can increase the computational time by 50 to 500% in comparison with an eddy-viscosity model. Although Launder suggests that the second moment closure is the more reliable for complex flows, [23], the time penalty is still very high compared with eddy-viscosity turbulence models. Bearing in mind that the more popular two-equation eddy-viscosity models have well known shortcomings, like for example the poor performance of the $k-\epsilon$ model in adverse pressure gradient, [24], we have adopted at this stage of the development the simple algebraic isotropic eddy-viscosity model of Cebeci & Smith, [25], which was already incorporated in PARNASSOS, [9].

The present implementation of the Cebeci & Smith turbulence model follows an approach sim-

ilar to the one given by Cebeci *et al.* in [26]. A detailed description can be found in [12].

3 Numerical Solution

3.1 Discretized Equations

The continuity and contravariant momentum equations written for the cartesian velocity components, (7) and (8), are discretized in a single block regular grid by a finite-difference approximation. The discretization procedure is similar to the one used in PARNASSOS. All the variables are defined on the grid nodes, (i, j, k)[6] since grid staggering is not used and Newton linearization is applied to the convective terms. The momentum equation in the ξ and ζ directions are discretized at the nodal points (i, j, k). The momentum equation in the normal direction, η, is discretized at $(i, j+\frac{1}{2}, k)$ and the continuity equation at $(i, j-\frac{1}{2}, k)$. A description of the different schemes used in the discretization process can be found in references [7] to [10] or [12]. With a careful discretization of the diffusion terms, [17], the present discretization technique only requires first derivatives of the grid coordinates.

The contribution to the discretized equations of the cartesian components of the velocity and pressure at the singularity is dealt with explicitly. The cartesian velocity components and pressure are taken from a previous iteration[7] and substituted in the discretized equations. This explicit treatment requires that the cartesian velocity components and pressure at the singularity have to be updated in the iterative procedure used to solve the discretized equations. The present approach is to obtain the cartesian velocity components and the pressure at the singularity in every iteration by the arithmetic mean of the surrounding nodes.

3.2 Solution Procedure

The solution procedure is based on the one used in the code PARNASSOS, [7], [8], [9] and [10]. Here we will only describe the major features of the procedure. A more detailed description can

---

[6]The indices refer to the ξ, η and ζ direction, respectively.

[7]The solution procedure has to be iterative due to the non-linearity of the equations.

be found in [12]. The solution is obtained iteratively by a space-marching process. Two iteration cycles can be distinguished : the local and the global iteration process.

The local iteration process refers to the solution of the flow at a streamwise station where all the grid nodes have the same main-stream coordinate, ξ. The solution is obtained simultaneously for all the variables with a Coupled Strongly Implicit Procedure (CSIP), [5]. Iteration is required by the non-linearity of the differential equations and by the incomplete factorization of the CSIP.

The discretization of the continuity equation at $(i, j - \frac{1}{2}, k)$ imposes that the normal velocity dependent variable, $\overline{V}^2$, has to be specified at the boundary $\eta = 0$ (Boundary AD of figure 2). On the wing surface $\overline{V}^2$ is known from the no-slip condition but in the wake its value has to be determined as part of the solution. The discretization of the η momentum equation at $(i, j + \frac{1}{2}, k)$ gives two algebraic equations per node for the determination of $\overline{p}$ at the 'boundary' $\eta = 0$, because each grid node of the physical domain is transformed into two in the computational domain[8]. One of the two equations can be used to obtain an equation for $\overline{V}^2$ along the fictitious boundary. However, it is not clear which equation should be used and large overshoots of $\overline{V}^2$ can be obtained at the fictitious boundary with this approach. In the present method $\overline{V}^2$ is calculated to ensure continuity of the pressure on the fictitious boundary for every iteration of the CSIP.

The discretized momentum equations at a streamwise station where all the grid nodes have the same main-stream coordinate, ξ, include the pressure field at the downstream station. This implies that in order to obtain the solution by a space-marching process in the main-stream direction, the pressure field at the downstream stations has to be taken from a previous sweep. The downstream marching process has to be repeated until the pressure field does not change between consecutive sweeps of the domain. This iterative procedure constitutes the global iteration process. To increase the convergence rate of this process each downstream sweep is followed by an upstream sweep to update the pressure field, [10]. The two sweeps form a predictor-corrector method for the pressure, which is constructed adding a quasi-time derivative of the pressure to the ξ momentum equation, [10]. Another improvement in the pressure field convergence can be obtained by using a multiple stepsize in the first sweeps to allow a rapid approach of the correct pressure level, [9]. This means that the grid is initially coarse in the main-stream direction and is subsequently refined in two or three stages.

4   Results and Discussion

A rectangular wing of aspect ratio 4 with a NACA 0015 airfoil section was used to investigate several numerical and physical aspects of the calculation of tip vortex flows with the present method. These aspects include the sensitivity to the extent of the computation domain. Namely, the location of the outlet boundary, inner boundary and external boundary. Numerical studies were also performed to evaluate the influence of the type of boundary conditions at the inlet. The latter studies were carried for two tip geometries. The different aspects investigated were analysed by comparing different numerical solutions with a reference case to be described below in section 4.1.

The calculations were all performed on a CRAY YMP. The code does not use parallelization, but the use of vectorization proved to be efficient in reducing the CPU time required. On the CRAY YMP the code runs typically at 70 MFlops with vectorization and at 8 MFlops without it.

In all the calculations, the global iteration process was stopped when the maximum pressure difference between consecutive sweeps, $(\Delta C_p)_{max}$, was less than 5.0×10^{-3}. The convergence criteria of the CSIP were differences between consecutive iterations of less than $1.0 \times 10^{-3} U_\infty$ in the physical components of the velocity and 2.0×10^{-4} in C_p.

4.1   Reference Test Case

The reference case in the present comparisons is a rectangular wing of aspect ratio 4 with a NACA 0015 airfoil section and a rounded tip, obtained by rotating the wing section at the tip around its chord. The angle of attack is 6.5 degrees and the Reynolds number based on the chord length is 8.5×10^5.

The boundaries of the viscous flow region for the reference case were placed at the following locations :

---

[8]The discretization of the ξ and ζ momentum equations is centered at (i, j, k) and so the two algebraic equations are equal.

- The inlet boundary is 10% of the chord downstream of the leading edge.

- The inner boundary, inlet and outlet of the cross-flow, is placed at a distance of 40% of the chord length inboard of the tip of the wing.

- The distance between the external boundary and the wing is 30% of the chord length at the station of maximum thickness of the wing.

- The outlet boundary is 1.82 chords downstream of the trailing edge.

The discretization of the viscous flow region was performed with 145 streamwise stations, including 81 on the wing and 64 in the wake. In the transverse sections of each streamwise station a 51×47 2-D grid was generated with an algebraic interpolation technique described in [12]. An illustration of the grid is given in figure 3. To obtain a clearer visualization of the grid the plots of the grid at the boundaries do not include all the grid lines.

WING SURFACE

EXTERNAL BOUNDARY

INNER BOUNDARY

WING STATIONS   WAKE STATIONS
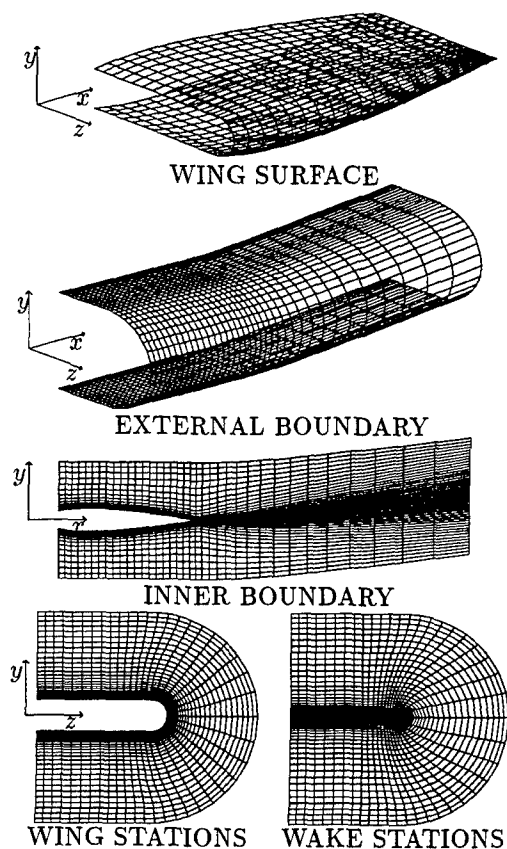
Figure 3: Illustration of the grid used in the reference case.

The convergence criteria were satisfied after 29 sweeps and the CPU time spent in this calculation was 38 minutes and 48 seconds.

4.2 Sensitivity to the Choice of the Size of the Computation Domain

In the present zonal approach to the calculation of tip vortex flows, some of the boundaries of the viscous region are artificial boundaries and so the specification of the boundary conditions will include approximations of the local flow. Examples of these boundaries are the inlet and outlet planes, the external boundary and the inner boundary. This excludes only the wing surface where we have a natural boundary of the flow. This section is dedicated to the evaluation of the sensitivity of the solution to the specification of the boundary conditions at the artificial boundaries of the viscous flow region, by changing their location. The inlet boundary is excluded from this investigation because the procedure used to estimate the inlet boundary conditions is based on simple approximations and so the comparison between solutions with inlet stations at different locations is not very conclusive.

The differences between the various calculations will be illustrated by comparing the solutions in two different streamwise stations. The two selected stations are located in the region of formation of the tip vortex, $\frac{x}{c} = 0.939$, and in the near wake, $\frac{x}{c} = 1.065$.

4.2.1 Outlet Boundary

At the outlet boundary a streamwise pressure boundary condition is required. In the present calculations the streamwise pressure gradient was set equal to zero, which is only true for an outlet station sufficiently far downstream of the wing. To evaluate the influence of this approximate boundary condition three different calculations were performed with outlet boundaries at $\frac{x}{c} = 1.741$, $\frac{x}{c} = 2.819$ (reference case), and $\frac{x}{c} = 4.000$. The three grids differ only in the location of the outlet boundary.

The differences between the dimensionless pressure and cartesian velocity components[9] calculated with outlet boundaries at $\frac{x}{c} = 2.819$ and $\frac{x}{c} = 4.000$ are smaller than 1.0×10^{-3} for all the streamwise stations, with the exception of the station at $\frac{x}{c} = 2.819$, where a maximum C_p difference of 5.0×10^{-3} occurs. This means that

---

[9]The cartesian velocity components are divided by the undisturbed velocity, U_∞, to obtain dimensionless components.

the imposition of zero streamwise pressure gradient at $\frac{x}{c} = 2.819$, has a neglible effect on the solution.

The differences between the solutions with outlet stations at $\frac{x}{c} = 1.741$ and $\frac{x}{c} = 2.819$ are larger than in the previous comparison. Downstream of $\frac{x}{c} \simeq 1.6$ the C_p differences between the two solutions become larger than 5.0×10^{-3} and at $\frac{x}{c} = 1.741$ the maximum C_p difference is 0.01. Upstream of the outlet boundary the differences decrease rapidly and at $\frac{x}{c} \simeq 1.3$ the maximum differences are smaller than 5.0×10^{-3}.

4.2.2 Inner Boundary

A simple approach was adopted for the specification of the boundary conditions at the inner boundary. The cross-stream derivatives of the pressure and of the cartesian velocity components are set equal to zero. The influence of these approximate boundary conditions was investigated by comparing the solutions of two calculations with inner boundaries at different locations.

One of the calculations is the reference case, where the inner boundary is located at 80% of the half-span, $\frac{z}{c} = 1.600$. The other calculation was performed on a grid with the inner boundary located at approximately 70% of the half-span, $\frac{z}{c} = 1.413$. This grid was constructed by adding extra grid lines at the inner boundary on each streamwise station of the grid used in the reference case. This is illustrated in figure 4 for a wing station.

Boundary at $\frac{z}{c} = 1.600,$ $W_{max} = 0.70 U_\infty$

Boundary at $\frac{z}{c} = 1.413,$ $W_{max} = 0.73 U_\infty$

$\longrightarrow = \vec{U}_\infty$

Figure 5: Comparison of the transverse velocity fields at $\frac{x}{c} = 0.939$ for solutions obtained with different locations of the inner boundary.

—— Reference Case   - - - Extra grid lines
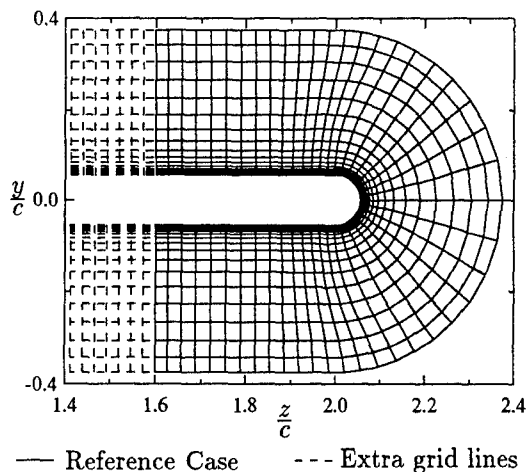
Figure 4: Comparison between the grid of the reference case and the grid with the inner boundary moved 20% of the chord inboard of the tip.

The comparison of the two solutions in their common region is presented in figures 5 and 6, where W_{max} stands for maximum transverse velocity component. In the wing station at $\frac{x}{c} = 0.939$ the imposition of zero cross-stream derivatives at $\frac{z}{c} = 1.600$ instead of 1.413 reduces the cross-flow velocity components. This reduction of cross-flow at $\frac{z}{c} = 1.600$, caused by the imposed boundary conditions, produces a non smooth behaviour of the transverse velocity field close to the external boundary on the upper surface. We recall that at the external boundary the tangential velocity components are imposed. A smooth so-

669

lution is obtained at the same location with the inner boundary moved inboard, which indicates that the perturbation in the transverse velocity field is caused by the imposition of zero cross-stream derivatives at the boundary and not by the imposed tangential velocity component at the external boundary. In the tip vortex region the two solutions are similar. However, the larger cross-flow velocities, obtained with the inner boundary moved inboard, produce a reduction in C_p minimum at the lower surface of the tip of 0.04. In the near-wake station, $\frac{x}{c} = 1.065$, the comparison between the cross-flow velocities of the two solutions is similar to the one described for the wing station.

The results obtained with the approximate boundary conditions suggest that the present approach is more efficient in the calculation of the tip vortex, than placing the inner boundary at the symmetry plane of the wing to obtain exact boundary conditions.

4.2.3 External Boundary

At the external boundary the tangential velocity components and the pressure are prescribed by a potential flow solution. The circulation imposed in the potential flow calculation to satisfy the Kutta condition at the wing's trailing edge does not include the viscous effects and so it is different from the circulation of the flow external to the viscous domain that would match the viscous solution. This means that the interaction between the viscous and inviscid solutions must be included in the solution procedure to obtain the exact boundary conditions at the external boundary. Since we do not perform viscous/inviscid interaction, the present boundary conditions are approximate boundary conditions. As a result of these approximate boundary conditions a pressure discontinuity is obtained at the trailing edge. We note that the circulation imposed in the potential flow calculation is independent of the location of the external boundary, but the tangential velocity components and pressure imposed at the external boundary are approximate values and so the location of the external boundary may influence the solution of the viscous region of the flow. To investigate the effect of the specification of the boundary conditions at the external boundary the solutions of two calculations with external boundaries at different locations are compared.

The two calculations were performed on grids with the external boundary located at a distance

— Boundary at $\frac{z}{c} = 1.600$

$\frac{x}{c} = 0.939$ --- Boundary at $\frac{z}{c} = 1.413$

C_p lines $\Rightarrow -0.35 \leq C_p \leq 0.05, \Delta C_p = 0.05$

— $-0.37 \leq C_p \leq 0.10$ --- $-0.41 \leq C_p \leq 0.10$

$\frac{x}{c} = 1.065$

C_p lines $\Rightarrow -0.30 \leq C_p \leq 0.10, \Delta C_p = 0.05$

— $-0.35 \leq C_p \leq 0.14$ --- $-0.38 \leq C_p \leq 0.15$
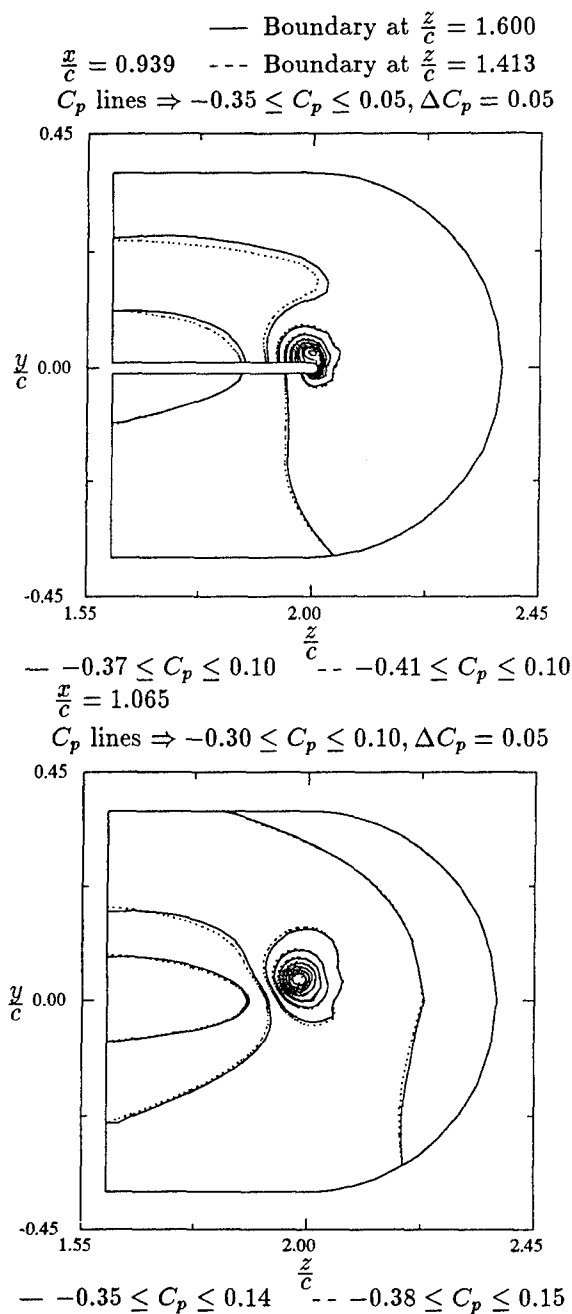
Figure 6: Comparison of the pressure fields at two different stations for solutions obtained with different locations of the inner boundary.

of 30% (reference case) and 42.5% of the chord length at the station of maximum thickness of the wing. The calculation performed with the external boundary closer to the wing is the reference case. The grid of the other calculation was constructed by adding extra grid lines[10] at the external boundary in each streamwise station of

---

[10]The procedure is equivalent to the one illustrated in figure 4.

Boundary moved outwards 12.5% c

$W_{max} = 0.69U_\infty$, $\frac{z}{c}$, $\longrightarrow = \vec{U}_\infty$
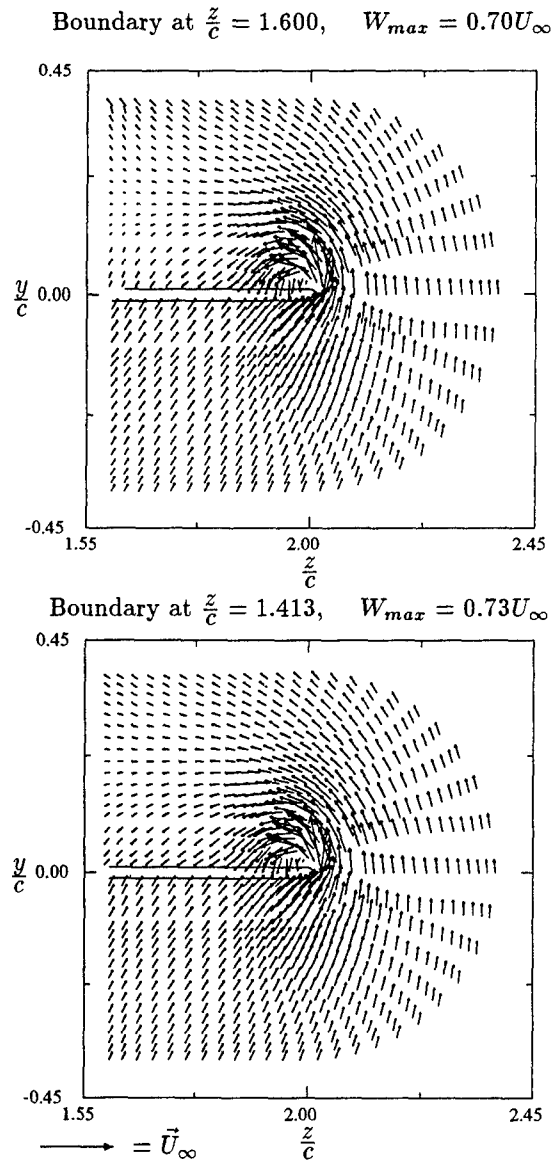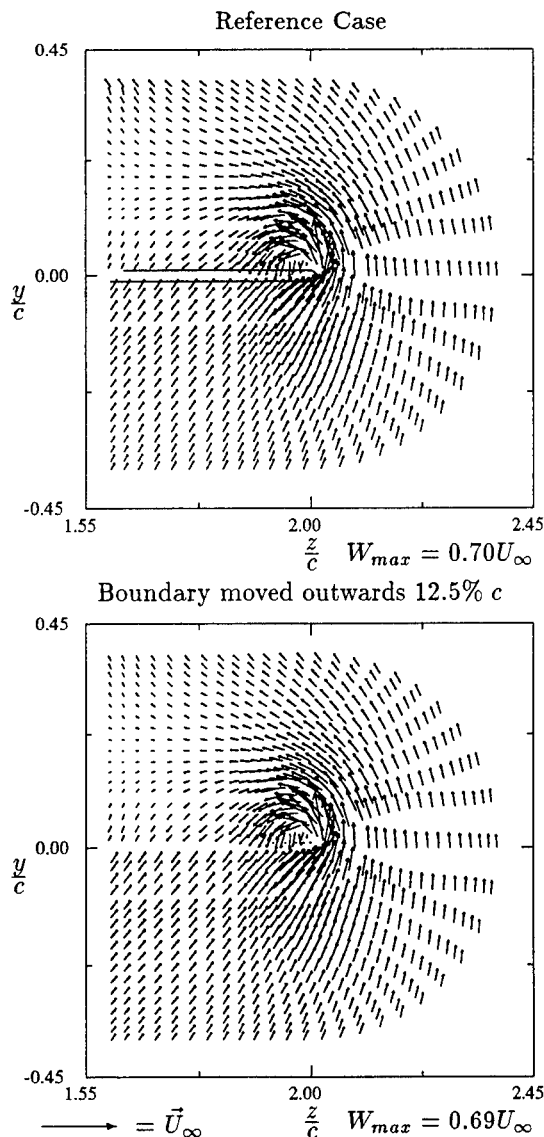
Figure 7: Comparison of the transverse velocity fields at $\frac{x}{c} = 0.939$ for solutions obtained with different locations of the external boundary.

the grid used in the reference case.

The comparison of the two solutions in their common region is presented in figures 7 and 8.

In the wing station at $\frac{x}{c} = 0.939$ there are no significant differences between the transverse velocity fields of the two calculations. The non-smooth behaviour of the transverse velocity field close to the external boundary on the upper surface is not present in the solution obtained with the external boundary moved outwards, because in the wider computation domain the local cross-flow components are determined by the boundary condition at the inner boundary without a conflict with the conditions imposed on the ex-

—— Reference Case

--- Boundary moved outwards 12.5% c

$\frac{x}{c} = 0.939$

C_p lines $\Rightarrow -0.35 \le C_p \le 0.05, \Delta C_p = 0.05$

—— $-0.37 \le C_p \le 0.10$ --- $-0.41 \le C_p \le 0.10$

$\frac{x}{c} = 1.065$

C_p lines $\Rightarrow -0.30 \le C_p \le 0.10, \Delta C_p = 0.05$

—— $-0.35 \le C_p \le 0.14$ --- $-0.38 \le C_p \le 0.15$
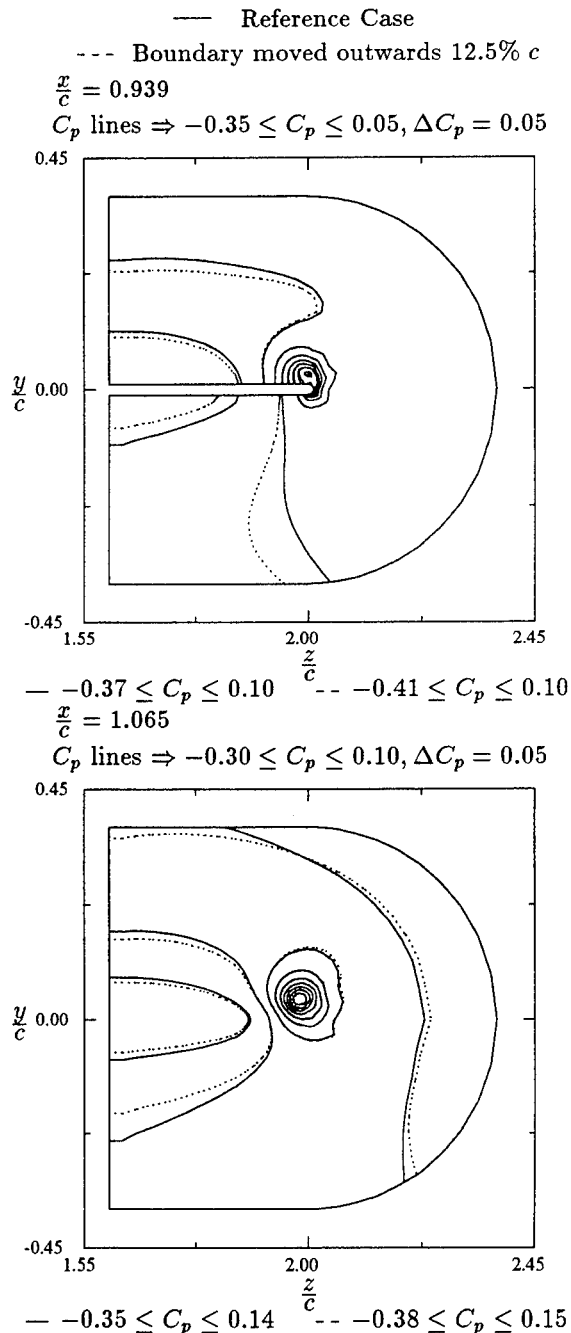
Figure 8: Comparison of the pressure fields at two different stations for solutions obtained with different locations of the external boundary.

ternal boundary (compare the earlier discussion in section 4.2.2). The pressure fields of the two solutions have clear differences close to the external boundary of the reference case, which in the lower surface also affect the surface pressure distribution. However, in the tip vortex region the effect of moving the external boundary outwards is not significant.

In the near wake station, $\frac{x}{c} = 1.065$, the comparison between the cross-flow velocities of the two solutions is similar to the one described for the wing station. The differences of the two solutions close to the external boundary of the reference case are larger than in the wing station, but the effect in the tip vortex region is still very small.

Reference Case

Boundary moved outwards 12.5 % c
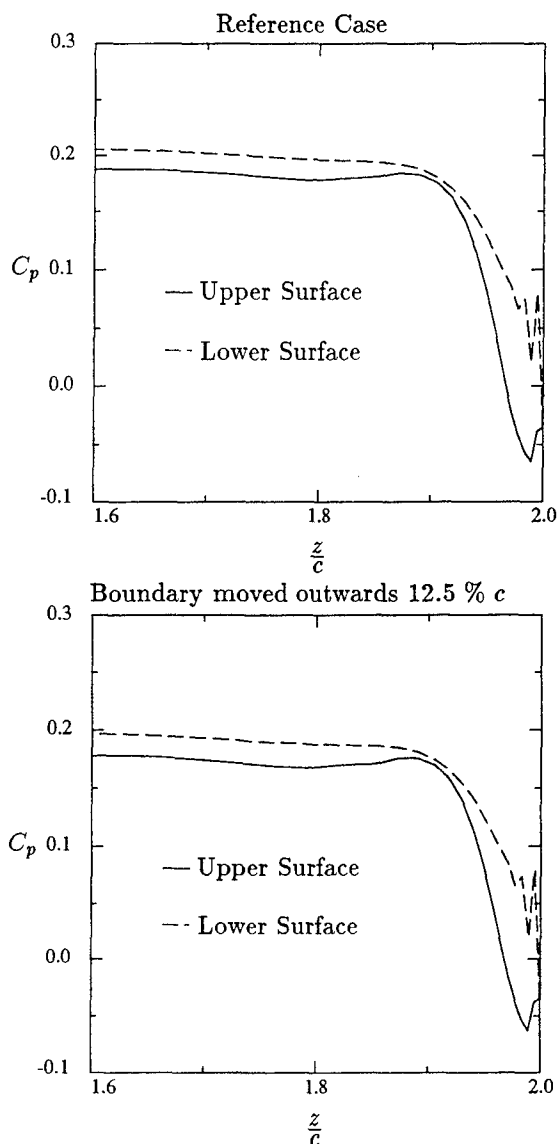
Figure 9: Pressure distribution at the trailing edge computed from the upper and lower surfaces of the wing for solutions obtained with different locations of the external boundary.

The pressure discontinuity at the trailing edge is illustrated in figure 9 for the calculations with the two different locations of the external boundary. The larger pressure discontinuities are obtained in the tip vortex region, where a small

pressure oscillation is obtained on the lower surface for both solutions. A small difference between the pressure level of the two solutions is obtained, but the pressure discontinuity is the same in the two calculations. These results indicate that the pressure discontinuity is mainly determined by the difference in circulation of the outer flow in the potential and viscous flow calculations, which is not affected by the change in the location of the external boundary.

The comparison of the results of the calculations performed with different locations of the external boundary showed that the influence of the approximate boundary conditions imposed at the external boundary on the solution in the tip vortex region are small. These results suggest that the present zonal approach is acceptable for tip vortex calculations, because it reduces substantially the size of the region to be discretized, compared with an alternative external boundary at a location where undisturbed flow conditions could be imposed. Further investigations will be required to address the influence of the viscous/inviscid interaction.

4.3 Specification of the initial velocity profiles

At the inlet station two types of boundary conditions were tested : prescribed velocity profiles and prescribed streamwise velocity gradients. It should be mentioned the the Neumann condition was applied as a Dirichlet condition, updated in the course of the solution process. So in the case of prescribed streamwise velocity gradient the velocity profiles at the inlet boundary are obtained iteratively. This makes the convergence usually slower than in the case of prescribed velocity profiles. However, the specification of velocity profiles at the inlet station may be difficult and a poor approximation of the initial velocity profiles can cause divergence of the solution close to the inlet station.

Our approach to the specification of the initial velocity profiles is based on simple assumptions. The velocity profiles are derived from standard boundary layer profiles, [22], defined by the local momentum thickness, θ, and skin friction coefficient, C_f. The values of θ and C_f at the inner boundary are obtained from a 2-D calculation, [27], and the spanwise variation of θ and C_f is obtained by a Hermite interpolation of the predicted 2-D values on the upper and lower sur-

faces at the inner boundary. In the potential flow region the velocity profiles are obtained from a potential flow solution, [21]. Due to numerical difficulties with the source-based panel method, it is not possible to calculate the potential flow solution at very small distances to the wing surface and so we have calculated the velocity components along a line $\eta = constant$ at a sufficient distance from the wing surface. In the region between this line and the viscous region thickness, determined by the specified θ and C_f, we assume that the potential flow velocity components do not change in the η direction.

The streamwise velocity gradient is specified applying the procedure described above to the first two stations of the grid and using a first order approximation to the derivatives. With this weaker boundary condition of the Neumann type, the velocity profiles at the inlet boundary are allowed to adjust to the local flow characteristics. As mentioned before, the streamwise velocity gradient is not specified implicitly in the calculation. The velocity profiles at the inlet boundary are updated in the course of the iteration process to obtain the specified streamwise velocity gradient. This makes the convergence rate of the solution lower and highly time consuming because the initial profiles change between consecutive sweeps. In the present solution the inlet velocity profiles were updated only when the maximum pressure difference between consecutive sweeps at the second streamwise station was $\Delta C_p > 2.0 \times 10^{-2}$.

The flow of the reference case was calculated with both types of inlet conditions. The results obtained with specified velocity profiles at the inlet boundary exhibit a rapid change of the pressure field in the initial streamwise stations. A clear visualization of the disturbances caused by the specification of the inlet velocity profiles is presented in figure 10, where the pressure field at the first calculated station, $\frac{x}{c} = 0.110$, of the two solutions is compared. The pressure field obtained with specified inlet velocity profiles is clearly disturbed by the specification of the initial velocity profiles. With specified streamwise velocity gradient a smooth pressure field is obtained at $\frac{x}{c} = 0.110$.

We found that the disturbances in the solution obtained with specified velocity profiles are restricted to the three initial stations and so it is important to know the effect of the inlet boundary conditions in the generation and development of the tip vortex. The calculated pressure fields of the two solutions are compared in figure 11,

Velocity Profiles

C_p lines $\Rightarrow -0.85 \leq C_p \leq 0.15, \Delta C_p = 0.05$

$-0.93 \leq C_p \leq 0.19$

Streamwise Velocity Gradient

C_p lines $\Rightarrow -0.80 \leq C_p \leq 0.10, \Delta C_p = 0.05$

$-0.80 \leq C_p \leq 0.10$

Figure 10: Comparison of the pressure fields at the first streamwise station for solutions obtained with different inlet boundary conditions.

for the streamwise stations at $\frac{x}{c} = 0.939$ and $\frac{x}{c} = 1.065$.

In the wing station, $\frac{x}{c} = 0.939$, the minimum pressure coefficient is 0.05 lower in the solution obtained with Neumann boundary conditions at the inlet station. The differences are smaller than the ones obtained at the inlet stations, but the effect of the different inlet boundary conditions is still visible in this region. However, the vortex location is virtually the same in the two calculations. In the wake stations, $\frac{x}{c} = 1.065$ in figure

673

—— Velocity Profiles

- - - Streamwise Velocity Gradient

$\frac{x}{c} = 0.939$

C_p lines $\Rightarrow -0.35 \le C_p \le 0.05, \Delta C_p = 0.05$

—— $-0.37 \le C_p \le 0.10$ - - - $-0.42 \le C_p \le 0.13$

$\frac{x}{c} = 1.065$

C_p lines $\Rightarrow -0.30 \le C_p \le 0.10, \Delta C_p = 0.05$

—— $-0.35 \le C_p \le 0.14$ - - - $-0.38 \le C_p \le 0.18$

Figure 11: Comparison of the pressure fields at two different streamwise stations for solutions obtained with different inlet boundary conditions.

11, the comparison of the two solutions is similar to the one described above for the wing station. The differences between the two solutions have become smaller than in the wing station; the tip vortex location is again hardly affected.

4.3.1 Effect of the Tip Geometry

It is interesting to know whether the behaviour of the solution process for the two types of inlet boundary conditions is the same for other tip geometries. Therefore the flow at the tip of a rectangular wing with a squared tip was also calculated. The wing aspect ratio (4) and airfoil section (NACA 0015) are the same as in the reference case. The same angle of attack and Reynolds number were used, respectively 6.5 degrees and 8.5×10^5. In the previous test cases the tip geometry is smooth. In a wing with a squared tip the geometry has two discontinuities in the tangential derivatives. The local features of the flow close to the geometry discontinuities make the specification of the inlet velocity profiles more difficult in this case. In the present specification of inlet velocity profiles no special treatment was included to account for the geometry discontinuities, the simple procedure described before was applied without any modifications and so the inlet conditions will locally be highly inaccurate. The grid used in these calculations is similar to the grid of the reference case illustrated in figure 3. The location of the boundaries and the streamwise stepsize are equal to the ones used in the reference case.

In the calculation performed with specified velocity profiles at the inlet boundary the pressure field did not converge in the initial stations of the grid. The pressure field showed a non-smooth behaviour in these initial stations and several jumps in $(\Delta C_p)_{max}$ are obtained in the first streamwise station downstream of the inlet plane. Nevertheless in the last sweeps performed, the pressure differences between consecutive sweeps downstream of the initial streamwise stations are three orders of magnitude smaller than the pressure differences close to the inlet boundary.

The same flow was calculated with specified streamwise velocity gradient at the inlet boundary. In this solution the inlet velocity profiles were updated only when the maximum pressure difference between consecutive sweeps at the second streamwise station was $\Delta C_p > 2.0 \times 10^{-2}$. With this type of boundary conditions it is possible to obtain a converged pressure field in the whole computation domain. The imposition of a weaker boundary condition at the inlet boundary removed the jumps of $(\Delta C_p)_{max}$ at the inlet boundary obtained with specified velocity profiles.

The pressure field at the first calculated sta-

C_p lines $\Rightarrow -0.85 \leq C_p \leq 0.10, \Delta C_p = 0.05$

$-0.92 \leq C_p \leq 0.11$

Streamwise Velocity Gradient

C_p lines $\Rightarrow -0.75 \leq C_p \leq 0.10, \Delta C_p = 0.05$

$-0.75 \leq C_p \leq 0.11$

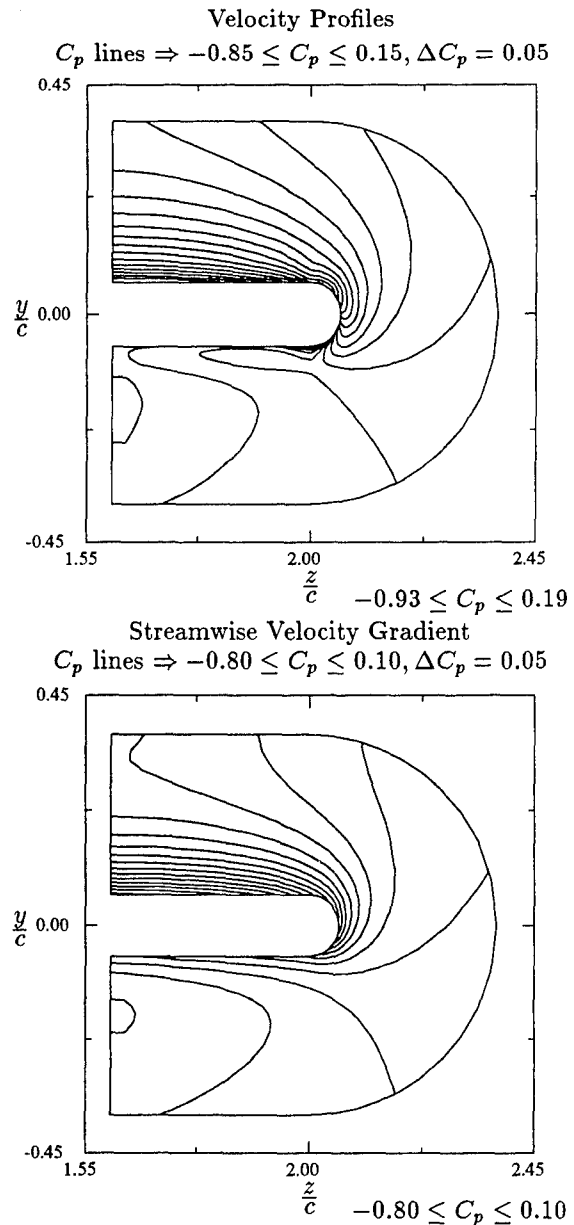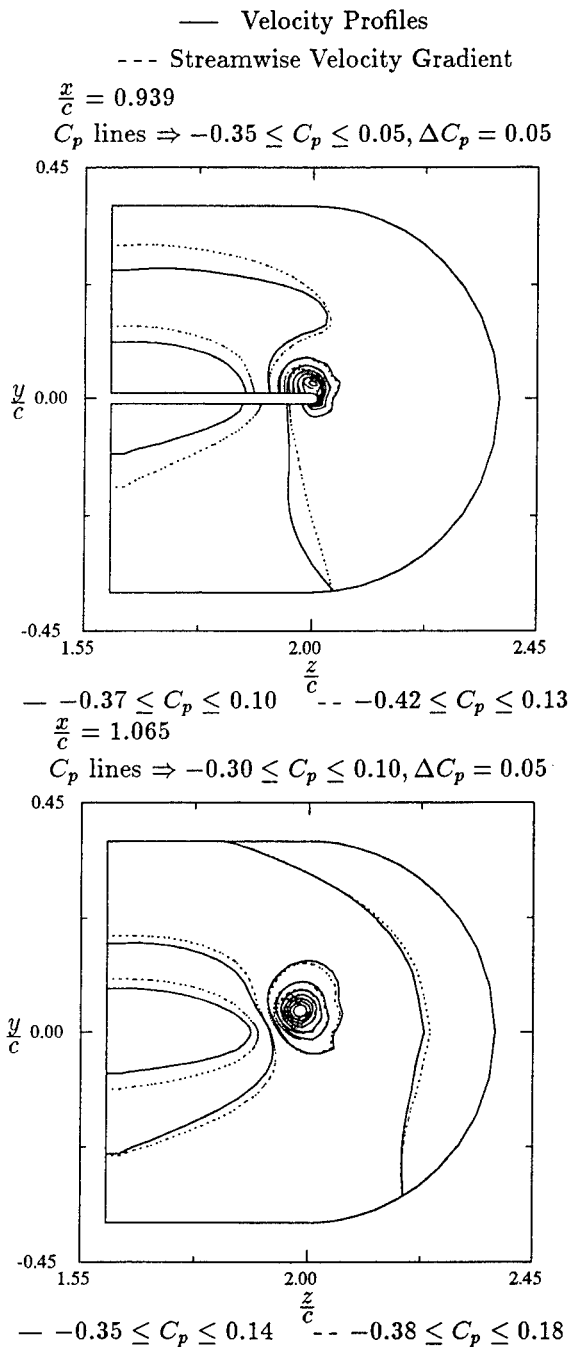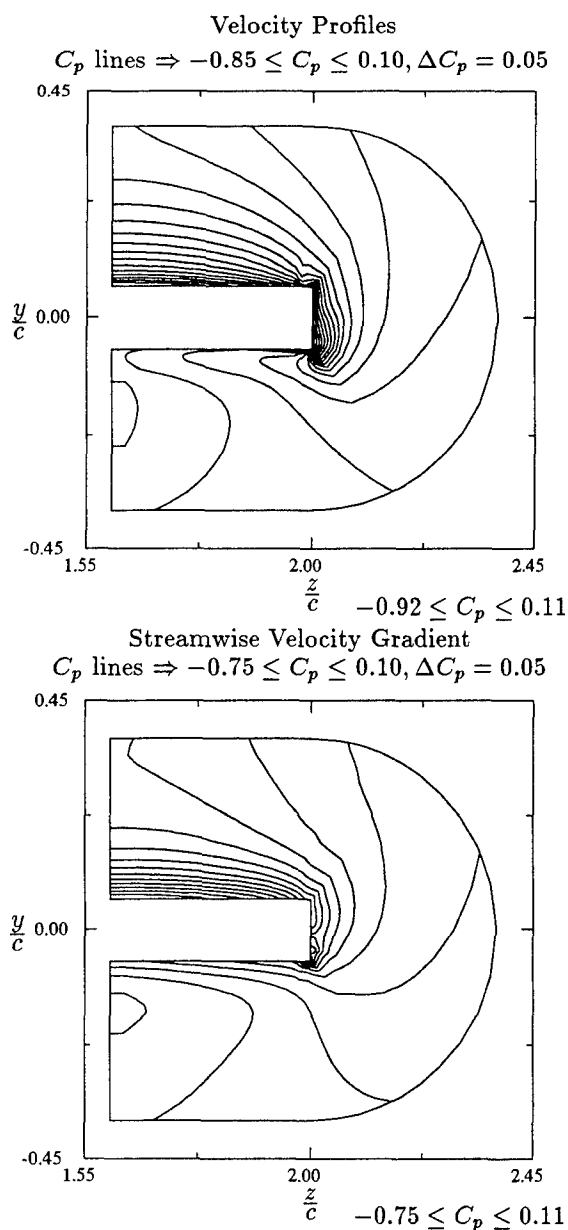Figure 12: Comparison of the pressure fields at the first streamwise station for solutions obtained with different inlet boundary conditions.

tion, $\frac{x}{c} = 0.110$, of the two solutions is compared in figure 12. The disturbances in the pressure field close to the inlet boundary are evident and a particularly non-smooth solution is obtained close to the geometry discontinuities. A smoother solution is obtained at $\frac{x}{c} = 0.110$ with specified streamwise velocity gradient.

The effect of the different inlet boundary conditions on the tip vortex generation and development is similar to the one obtained on a wing with a rounded tip.

These results show that the specification of inaccurate velocity profiles at the inlet boundary can deteriorate the convergence of the method close to the inlet boundary. The results obtained with streamwise velocity gradient at the inlet boundaries did not reveal any convergence difficulties of the method and the use of weaker boundary conditions enabled the adjustment of the solution to the local flow characteristics. This suggests that innaccuracies in the specification of the streamwise velocity gradient are less damaging to the solution process than inaccuracies in the specification of inlet velocity profiles. However, with Neumann boundary conditions at the inlet boundary the method becomes more time consuming than with specified velocity profiles.

4.4 Comparison with Experimental Results

The results obtained with the present method are compared with experimental results available in the literature, and with the results of the method of Govidan et al., [2], to evaluate its performance. The test cases include two wings of rectangular planform with a squared and a rounded tip.

4.4.1 Wing with Rounded Tip

The first test case is a rectangular wing of aspect ratio 6 with a NACA 0012 airfoil section and a rounded tip. The purpose of this test case is to compare the results of the present method with the results of the method of Govidan et al., [2]. The latter also uses a space-marching process to obtain the solution, but with a single sweep through the computational domain in the streamwise direction, because a full parabolisation of the Navier-Stokes equations is used, the streamwise pressure gradient is obtained from an inviscid flow solution. Although a different solution method is adopted by Govidan et al., the physical approximations assumed in the governing equations are the same as the ones used in the present method with the exception of the streamwise pressure gradient. The comparison of the results of the two methods enables the evaluation of the streamwise pressure gradient influence on tip vortex calculations. The calculations were performed for the conditions given in [2] : Angle of attack of 6.18 degrees and Reynolds number based on the chord length of 7.52×10^5.

$--- \quad -0.48 \leq C_p \leq -0.06, \Delta C_p = 0.06$

-0.48 -0.36 -0.24 -0.12 0.0
Govidan et. al., [2]

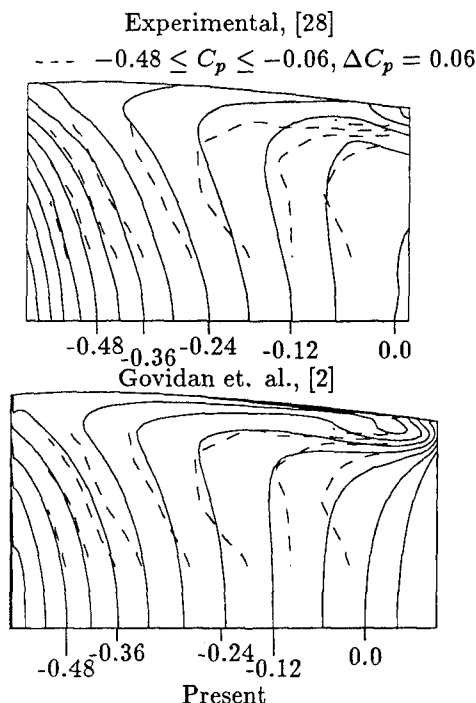
-0.48 -0.36 -0.24 -0.12 0.0
Present

Figure 13: Comparison between the predicted pressure distribution on the wing surface and experimental results for the flow at the tip of a rectangular wing, with an angle of attack of 6.18 degrees and a Reynolds number of 7.52×10^5.

The location of the boundaries of the computation domain were identical to the ones used by Govidan et al. in [2], with the exception of the outlet boundary. The results presented in [2] include only the wing region, the outlet station is 6% of the chord upstream of the trailing edge. In the method of Govidan et al., the flow solution at a transverse plane depends only on upstream occurrences and so there are no streamwise boundary conditions required at the outlet plane. In the present method, the elliptic character of the equations is retained in the pressure field and so a downstream pressure boundary condition is required at the outlet station. Close to the trailing edge of the wing, it is not possible to impose a physically acceptable boundary condition and so the outlet station has to be moved into the far wake. In the present grid, the outlet station is located three chords downstream of the trailing edge. The inlet boundary is 15% of the chord downstream of the leading edge. Like in the calculations of Govidan et al., the inlet boundary conditions of the present calculations consist of specified velocity profiles. The inner boundary, inlet and outlet of the cross-flow, is placed at a distance of 40% of the chord length inboard of the

tip of the wing. The distance between the external boundary and the wing is 30% of the chord length at the station of maximum thickness of the wing.

A number of 161 streamwise stations was used, including 81 on the wing and 80 on the wake. A 40×47 2-D grid was generated on each streamwise station[11].

In figure 13 the calculated pressure distribution on the wing surface is compared with the predictions of Govidan et al., [2], and the experimental results of Gray et al. [28], given in [2]. The present results show better agreement with the experimental results than the predictions of Govidan et al. Notice the mismatch of predicted and experimental isobars close to the leading edge in the results of Govidan et al. A significant improvement is obtained in the prediction of the pressure distribution close to the tip. We note that Govidan et al., [2], used a $120 \times 40 \times 47$ grid to discretize the viscous region between 15% and 94% of the chord, while the present results were obtained with an equal number of nodes in the transverse sections but with only 81 stations between 15% of the chord and the trailing edge.

4.5 Wing with Squared Tip

Experimental results including mean velocity LDV measurements have been reported recently by Falcão de Campos et al., [29], for a rectangular wing of aspect ratio 4 with a NACA 0015 airfoil section and a squared tip. The experimental investigations included flows at three different angles of attack, 4.5, 6.5 and 8.5 degrees at a Reynolds number of 8.5×10^5. These flows have been numerically simulated with the present method.

The boundaries of the viscous flow region were placed in the same locations as in the reference case of section 4. The grid has 145 streamwise stations, including 81 on the wing and 64 on the wake. In the transverse sections of each streamwise station a 51×47 2-D grid was generated. The calculations were performed with Neumann boundary conditions at the inlet station, i.e. the streamwise velocity gradient is specified.

The experimental measurements were performed on planes perpendicular to the undisturbed flow and the measuring plane does not coincide with a grid plane. To compare the present

---

[11]The grid is similar to the one used in the reference test case illustrated in figure 3.

676

Predicted   Experimental, [29]
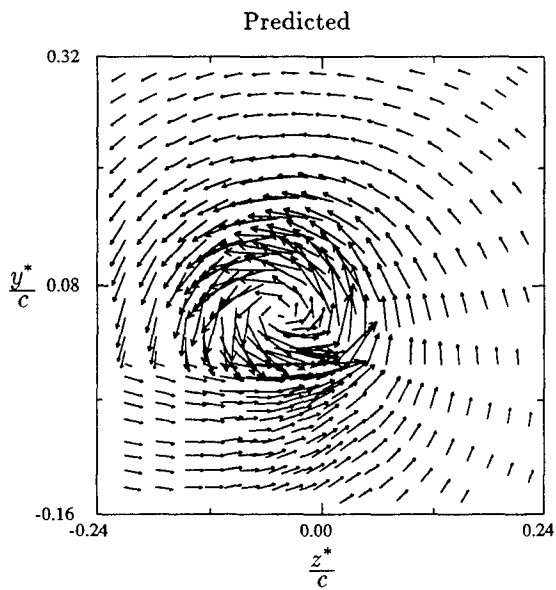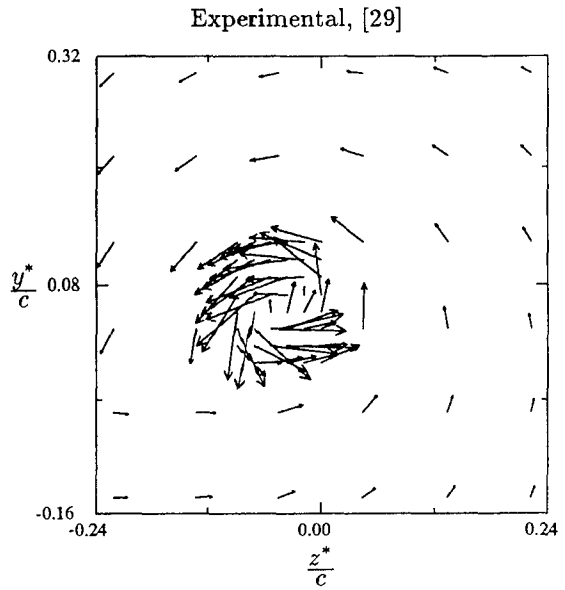
$\frac{x^*}{c} = 0.016$ $W^*_{max} = 0.41U_\infty$ $\frac{x^*}{c} = 0.016$ $W^*_{max} = 0.52U_\infty$
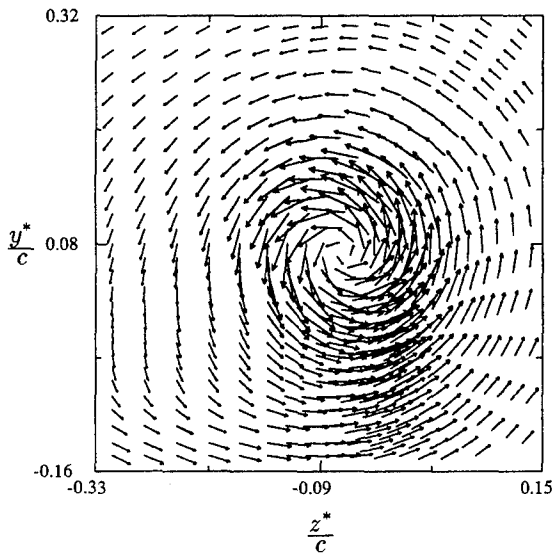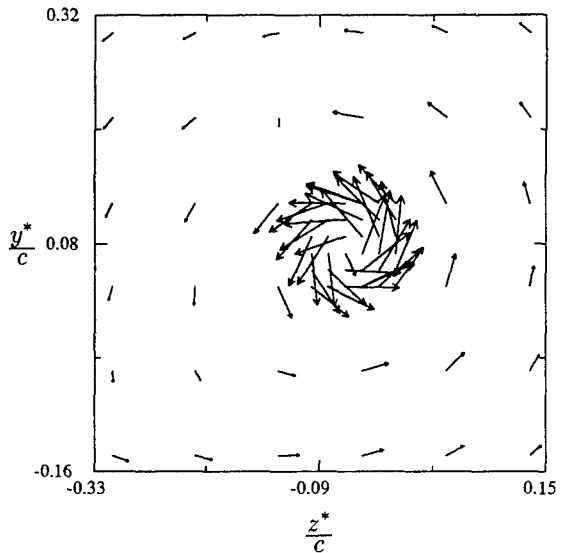
$\frac{x^*}{c} = 1.145$ $W^*_{max} = 0.33U_\infty$ $\frac{x^*}{c} = 1.145$ $W^*_{max} = 0.43U_\infty$

$\longrightarrow = 0.5\vec{U}_\infty$ $\longrightarrow = 0.5\vec{U}_\infty$

Figure 14: Comparison between the present pre-   Figure 14: (Cont.) Comparison between the
dictions and the experimental results for the flow   present predictions and the experimental results
at the tip of a rectangular wing with a squared   for the flow at the tip of a rectangular wing with
tip. Angle of attack 6.5 degrees and Reynolds   a squared tip. Angle of attack 6.5 degrees and
number of 8.5×10^5.   Reynolds number of 8.5×10^5.

results with the experimental data the velocity   investigations, which has the x^* direction aligned
components at the experimental measuring plane   with the undisturbed flow, U_∞. In the present
are obtained from the values at the grid nodes   comparisons the origin of the coordinate system
using linear interpolation along the ξ lines. Fur- (x^*, y^*, z^*), is placed at the tip of the trailing
thermore, the comparisons are performed in the   edge, $(x^* = 0, y^* = 0, z^* = 0) \equiv (x = 1.0, y =$
cartesian coordinate system of the experimental $0.0, z = 2.0)$.

677

The numerical predictions of the transverse velocity fields at $\frac{x^*}{c} = 0.016$ and $\frac{x^*}{c} = 1.145$ are compared with the experimental results in figure 14, for the flow with an angle of attack of 6.5 degrees. An excellent correlation of the tip vortex location is obtained in both planes, but in both cases the maximum transverse velocities are underpredicted in the calculations. Upon inspection it may be seen that a more diffused vortex is obtained in the calculations. This is particularly evident at the plane $\frac{x^*}{c} = 1.145$, where a nearly axisymmetric flowfield is obtained in the vicinity of the vortex core. However, the asymmetry of the vortex close to the trailing edge is well predicted and the flowfield away from the vortex center shows a very good correlation with the experimental results. The location of the vortical wake in the station close to the trailing edge, $\frac{x^*}{c} = 0.016$, is also well predicted. Furthermore, although the maximum values of the tranverse velocity components are larger in the experimental results, the downstream decrease of W^*_{max} in the predictions is very close to the experimental one.

The turbulence model used in this method does not account for streamline curvature effects. It is well documented in the literature that in the vortex core the turbulent diffusion should be negligible, see for example [30]. In the present turbulence model the eddy viscosity is related to the displacement thickness, which is determined along the grid η lines. The streamwise velocity defect in the tip vortex region causes an increase of the local displacement thickness and consequently of the eddy viscosity. This means that with the present model the eddy viscosity exhibits a maximum at the tip vortex region, which is in total contradiction with the physical characteristics of the flow. It is thought that the large values of the eddy viscosity in the vortex core may be reponsible for the overprediction of the vortex core size in the present calculations.

The overprediction of the vortex core size has a large effect on the calculated pressure in the vortex core. The minimum pressure coefficient in the vortex core is approximately proportional to the square of the inverse of the core size, which means that an accurate prediction of the core size is essential for a good prediction of the pressure field.

The comparison between predictions and experimental results for the flows with angles of attack of 4.5 and 8.5 degrees is similar to the one obtained with an angle of attack of 6.5 degrees, [12]. The correlation between the vortex location

of the predictions and experimental results is still excellent, but the vortex core size is again overpredicted. The location of the vortical wake close to the trailing edge is in good agreement with the experimental results for both angles of attack and the flowfield away from the vortex center is in excellent agreement with the experimental results.

5 Conclusions

A numerical method for the calculation of the steady, incompressible, viscous flow at the tip of wings was developed. The effect of the choice of the extent of the computation domain on the solution of tip vortex flows has been investigated by changing the location of the boundaries. The results showed that the present zonal approach to the calculation of tip vortex flows is efficient, because a large part of the flow field does not need to be discretized and a finer discretization can be obtained in the tip vortex region for a given number of grid nodes. However, the imposition of potential flow conditions at the external boundary implies that the viscous/inviscid interaction has to be incorporated in the solution procedure to account for the difference in the external flow circulation associated with the viscous and inviscid solutions respectively. In the present calculations the viscous/inviscid interaction is neglected and so a pressure discontinuity is obtained at the trailing edge.

The specification of appropriate inlet boundary conditions may be difficult. When initial velocity profiles are specified convergence problems in the initial stations may result if a poor estimate of the initial velocity profiles is used. An improved solution can be obtained by specifying the streamwise velocity gradient at the inlet boundary. However, this type of boundary condition reduces the convergence rate of the method, making it more time consuming. The comparison between the solutions obtained with the two types of boundary conditions suggests that the influence of small inaccuracies in the inlet velocity profiles is restricted to a small region close to the inlet boundary.

The present calculations showed that the streamwise pressure gradient of the inviscid flow solution is not a good approximation to the streamwise pressure gradient of the viscous flow in the tip vortex region. This was revealed in the comparison with experimental results, [28], of the present method and the method of Govidan et al.,

678

[2], which imposes the streamwise pressure gradient from inviscid flow calculations.

A good correlation between numerical predictions and experimental results was obtained for the calculation of the flow at the tip of a rectangular wing with a squared tip. However, the size of the tip vortex core is overpredicted in the present calculations. The turbulence model is likely to be responsible for the excess of diffusion in the tip vortex core, because the physical characteristics of the local flow are not well reproduced in the present model. The overprediction of the vortex core size still precludes an accurate prediction of the suction peak in the vortex core.

Acknowledgement

References

[1] Govidan T.R., Levy R., Shamroth S.J. - *Computation of The Tip Vortex Generation Process for Ship Propeller Blades* - 4th International Conference on Ship Hydrodynamics, Washington D.C., 1985.

[2] Govidan T.R., Jong F.J., Levy R., Shamroth S.J. - *Validation of a Forward Marching Procedure to Compute The Tip Vortex Generation for Ship Propeller Blades* - 17th Symposium on Naval Hydrodynamics, August-September 1988, The Hague, The Netherlands.

[3] Briley W.R., McDonald H. - *Three-Dimensional Viscous Flow with Large Secondary Velocity.* - Journal of Fluid Mechanics, Vol. 144, 1984, pp. 47-77.

[4] Rubin S.G., Tannehill J.C. - *Parabolized/Reduced Navier-Stokes Computational Techniques.* - Annual Review of Fluid Mechanics, Vol. 24, 1992, pp. 117-144.

[5] Rubin S.G. - *Incompressible Navier-Stokes and Parabolised Navier-Stokes Formulations and Computational Techniques.* - Computational Methods in Viscous Flows, Vol. 3 in the series Recent Advances in Numerical Methods in Fluids (ed. Habashi) Pineridge Press, 1984.

[6] Rubin S.G. - *Global Relaxation Procedure for a Reduced Form of the Navier-Stokes Equations.* - Proceedings of the 9th International Conference on Numerical Methods in Fluid Dynamics, Lecture Notes in Physics, Vol. 218, Springer-Verlag, 1985, pp. 62-71.

[7] Raven H.C., Hoekstra M. - *A Parabolised Navier-Stokes Solution Method for Ship Stern Flow Calculations.* - 2th International Symposium on Ship Viscous Resistance, Goteborg Sweden, March 1985.

[8] Hoekstra M., Raven H.C. - *Application of a Parabolised Navier-Stokes Solution System to Ship Stern Flow Computation.* - Osaka International Colloquium on Ship Viscous Flow, Osaka Japan, October 1985.

[9] Hoekstra M., Raven H.C. - *Ship Boundary Layer and Wake Calculation with a Parabolised Navier-Stokes Solution System.* - 4th International Conference on Numerical Ship Hydrodynamics", Washington D.C., 1985.

[10] Hoekstra M. -*Recent Developments in a Ship Stern Flow Prediction Code.* - 5th International Conference on Numerical Ship Hydrodynamics, Hiroshima, September 1989.

[11] Rosenfeld M., Israeli M., Wolfshtein M. - *A Method for Solving Three-Dimensional Viscous Incompressible Flows over Slender Bodies* - Journal of Computational Physics, Vol. 88, 1990, pp. 255-283.

[12] Eça L. - *Numerical Solution of the Parabolised Navier-Stokes Equations for Incompressible Tip Vortex Flows* - PhD Thesis, Instituto Superior Técnico, Lisbon, March 1993.

[13] Vinokur M. - *Conservation Equations of Gasdynamics in Curvilinear Coordinate Systems.* - Journal of Computational Physics, Vol. 14, 1974, pp 105-125.

[14] Warsi Z.U.A. - *Conservation Form of the Navier-Stokes Equations in General Nonsteady Coordinates.* - AIAA Journal, Vol. 19, February 1981, pp 240-242.

[15] Zhang H., Camarero R., Kahawita R. - *Conservation Form of the Equations of Fluid Dynamics in General Nonsteady Coordinates.* - AIAA Journal, Vol. 23, November 1985, pp 1819-1820.

[16] Hoekstra M. - *Some Fundamental Aspects of the Computation of Incompressible Flows.* - Second Osaka International Colloquium on Ship Viscous Flow, September 1991, Osaka Japan.

[17] Eça L., Hoekstra M. - *Discretization of the Parabolised Navier-Stokes Equations.* - First European Computational Fluid Dynamics Conference, Brussels, September 1992.

[18] Mynett A.E., Wesseling P., Segal A., Kassels C.G.M. - *The ISNaS Incompressible Navier-Stokes Solver: Invariant Discretization.* - Applied Scientific Research, Vol. 48, 1991, pp. 175-191.

[19] Segal A., Wesseling P., Van Kan J., Oosterlee C.W., Kassels K. - *Invariant Discretization of the Incompressible Navier-Stokes Equations in Boundary-Fitted Coordinates.* - International Journal of Numerical Methods in Fluids, Vol. 15, 1992, pp. 411-426.

[20] Sokolnikoff I. S. - *Tensor Analysis.* - John Wiley & Sons Inc., 1951.

[21] Raven H.C. - *Berekening van de potentiaalstroming rond draagvlakken met het programma DAWSON,* (in Dutch) *"Calculation of Potential Flow on Lifting Surfaces with the Program Dawson,* (Engl. Transl.) - MARIN Report $N^{\underline{o}}$ 50501-1-RD, May 1985.

[22] Hoekstra M. - *Generation of Initial Velocity Profiles for Boundary Layer Calculations.* - Marin Report $N^{\underline{o}}$ 50028-1-SR, March 1980.

[23] Launder B. - *On the Modelling of Turbulent Industrial Flows.* - First European Computational Fluid Dynamics Conference, Brussels, September 1992.

[24] Rodi W., Scheuerer G. - *Scrutinizing the $k - \epsilon$ Model Under Adverse Pressure Gradient Conditions.* - Journal of Fluids Engineering, Transactions of the ASME, Vol. 108, June 1986, pp. 174-179.

[25] Cebeci T., Smith A.M.O. - *Analysis of Turbulent Boundary Layers.* - Academic Press, November 1984.

[26] Cebeci T., Clark R.W., Chang K.C., Halsey N.D., Lee K. - *Airfoils with Separations and the Resulting Wakes.* - Journal of Fluid Mechanics, Vol. 163, 1986, pp. 323-347.

[27] Eça L.R.C., Falcão de Campos J.A.C. - *Analysis of Two-Dimensional Foils Using a Viscous-Inviscid Interaction Method.* - International Shipbuilding Progress, (accepted for publication).

[28] Gray R.B., McMahon H.M., Shenoy K.R., Hammer M.L. - *Surface Pressure Measurements at Two Tips of a Model Helicopter Rotor in Hover* - NASA CR-3281, 1980.

[29] Falcão de Campos J.A.C., George M.F., Mackay M. - *Velocity Measurements of the Tip Vortex Flow in the Near-Wake of Hydrofoils.* - 1993, Submitted for publication to the Journal of Fluids Engineering.

[30] Bradshaw P. - *Effects of Streamline Curvature on Turbulent Flow* - AGARDograph 169, AD - 768316, 1973.

DISCUSSION
by Dr. Spyros A. Kinnas
MIT

The authors presented a very interesting approach in solving the tip vortex simulation problem. I would like to ask two questions:

(a) They match a potential flow solution in the inner part of the span to a viscous representation of the outer part. How sensitive are the results on the cut-off location?

(b) In the case of a rectangular planform wing with round geometry in the spanwise direction, were they able to capture a similar vortex roll-up structure along the chord to that of a body of revolution at an angle?

Author's Reply

Our reply to the questions asked by Dr. Kinnas is:

(a) In our present approach, see section 2.1, the boundary conditions in the inner part of the span imply that cross-stream derivatives, $\dfrac{\partial}{\partial \varsigma}$, of the cartesian velocity components and of the pressure are set equal to zero. A potential flow solution is used to specify boundary conditions at the external boundary, without viscous-inviscid interaction. This means that approximate boundary conditions are used on both boundaries. The comparisons between results obtained with different locations of the inner and external boundaries presented in sections 4.2.3 and 4.2.4 show a small influence of the boundaries location on the solution in the tip vortex region.

(b) In this study we did not make any visualization of the limiting streamlines and so we have not yet performed a detailed analysis of the separation pattern at the tip of the wing. The vortex roll-up structure in the case of a round-nosed body of revolution at an angle of attack is strongly dependent on the angle of attack and can be rather complex, as shown for instance in Tobak and Peak, [1]. However, from the analysis of the cross-flow velocities close to the tip, [2], there may be some similarity between the rounded tip wing and the body of revolution at an intermediate angle of attack, where a single dominant vortical structure exists. Such structure has been captured with a similar method in the calculations of Rosenfeld et al., [3], for a prolate spheroid at 10° of incidence.

[1] Tobak, M. and Peake, D.J. *Topology of Three-Dimensional Separated Flows -* Annual Review of Fluid Mechanics, 1982, Vol. 15, pp. 61-85.

[2] Eca, L. *Numerical Solution of the Parabolized Navier-Stokes Equations for Incompressible Tip Vortex Flows*, PhD Thesis, Instituto Superior Técnico, Lisbon, March 1993.

[3] Rosenfeld, M., Israeli, M. and Wolfshtein, M. *A Method for Solving Three-Dimensional Viscous Incompressible Flows Over Slender Bodies*, Journal of Computational Physics, 1990, Vol. 88, pp. 255-283.

SESSION 13

LIFTING-SURFACE FLOW: UNSTEADY VISCOUS METHODS

Direct Numerical Simulation of Unsteady Propulsor Blade Section Forces on a Parallel Processor

W.B. Coney,[1] S.R. Breit,[2] and J.R. Webb[1]
([1]BBN Systems and Technologies, USA, [2]Kendall Square Research, USA)

ABSTRACT

This paper describes a numerical method, which has been implemented on a parallel processor, for the direct simulation of inviscid unsteady blade section forces, and its application to several two-dimensional blade-gust interaction problems.

The parallel implementation is discussed in some detail. Timing results obtained on a parallel computer are presented and nearly linear parallel speed-ups are demonstrated.

The application of the present method to three model problems is discussed and results are compared to theoretical, experimental and numerical solutions.

INTRODUCTION

The time-harmonic (blade-rate and its harmonics) and stochastic unsteady forces produced by interaction with non-uniform inflow are the dominant components of the low-frequency acoustic signature of a non-cavitating marine propulsor. Much research has been devoted to analytical and approximate numerical methods for predicting these forces and there has been considerable success with these approaches. However, with the recent dramatic increases in the speed of computers and the advent of parallel computers, direct numerical simulations of unsteady flows through marine propulsors are becoming increasing feasible. The ultimate benefit of such direct simulations will be the ability to deal with arbitrarily complex propulsor geometries and to include possible interaction between the blade-rate and turbulence ingestion mechanisms which are presently treated separately.

The prediction of the response of a two-dimensional blade section to an unsteady gust can be regarded as a preliminary step toward the fully three-dimensional model of the propulsor subject to an unsteady inflow. The force developed in response to harmonic gusts of varying nature has further been the subject of much analysis, leading to both analytical, Sears [1], Naumann and Yeh [2], Atassi [3], etc., and linearized numerical, Atassi and Akai [4], Chiang and Fleeter [5], Hsin [6], etc., approaches. Unsteady blade-gust interaction problems therefore provide a natural test bed for the exploratory development of a numerical simulation of unsteady propulsor forces.

This paper describes a numerical method, which has been implemented on a parallel processor, for the direct simulation of inviscid unsteady blade section forces, and its application to several two-dimensional blade-gust interaction problems. The results selected for presentation highlight circumstances for which "classical" unsteady airfoil theories, such as that of Sears [1], and numerical procedures based on a linearizing assumption of potential flow, for example those of Hsin [6] and of Chiang and Fleeter [5], appear to adequately predict the unsteady force, and circumstances for which they cannot. Three model problems are investigated:

1) transverse gust interacting with a foil

2) pitching foils upstream of a stationery foil

3) distributed vortex interacting with a foil.

The first problem is well modeled by an analytic solution, the second could at least potentially by modeled by an unsteady potential flow simulation, the third, however, requires use of a method which preserves detail of the vortical flow.

NUMERICAL APPROACH

In choosing a numerical method for direct simulations, it should be recognized that the unsteady flow through a typical marine propulsor is characterized by:

- very low Mach number (below 0.01),

- high Reynolds number (above 10^6),

- complex geometry, and

- small unsteady pressure (compared to the mean pressure),
  or small unsteady thrust (compared to the mean thrust).

With these issues in mind, we chose to implement the time-accurate pseudo-compressibility (TAP) method with upwind-biased spatial differencing, as described by Rogers & Kwak [7] for our simulations. In the limit where the pseudo-time step size is infinite, this method is nearly the same as the Newton iteration scheme of Athavale & Merkle [8]. The TAP method provides an incompressible flow solution which is a very good approximation of a low Mach number flow. In contrast, methods which account for compressible effects break down at very low Mach number. Our initial experience in applying this method to a two-dimensional model problem, with focus upon one aspect of the blade-vortex interaction, is described in Breit, et. al. [9].

The time integration scheme is second-order accurate and fully implicit, including the boundary conditions. Viscous terms are, for the present, neglected. A sparse, block-tridiagonal, linear system must be solved at each pseudo-time iteration. Unlike Rogers & Kwak [7], who use a line relaxation scheme to solve the linear system, we use the approximate LU factorization scheme recommended by Merkle and Athavale [8].

PARALLEL IMPLEMENTATION

Implementing the approximate LU factorization scheme on a massively parallel computer is a programming challenge because the degree of parallelism varies greatly during the course of the factorization procedure. The parallelization was accomplished on a BBN TC2000™ parallel computer. The implementation relied to a large extent on the high complete-exchange bandwidth and high random-access bandwidth of the TC2000 computer.

In theory, the highest parallel efficiency can be achieved if the smallest computational task that can be done in parallel involves the computations for a single grid point. We refer to this as a *point parallel* approach as opposed to a *domain decomposition* ap-

proach, where the smallest task involves computations for a sub domain of the grid. The domain decomposition approach requires less interprocessor communication than the point parallel approach, but at the cost of reducing the maximum achievable parallel efficiency. The choice of which approach to implement on a particular massively parallel computer depends on the characteristics of its interprocessor communication network. The interprocessor communication is fast enough on the TC2000 to enable a point parallel implementation of the LU algorithm.

The parallelization process was simplified by exploiting the memory management extensions and parallel directives provided by TC2000 FORTRAN. Some data are shared using an interleaving mechanism, with data declarations of the form

```
common, shared, interleaved /foo/ a(100),..
```

In this example, the set of 16-byte cache lines that contain array a are dynamically interleaved among the memories of the processors. Thus interprocessor communication is effected through shared memory instead of explicitly passing messages or packets between processors. Automatic load balancing is achieved by dynamically allocating computational tasks to processors. This approach avoids special mapping strategies where tasks and data are preallocated to specific processors. One benefit of this approach is that the number of lines of code that are associated with the parallel implementation is small compared to the total size of the program.

The LU method involves a forward elimination sweep over the grid and then a back substitution sweep in the opposite direction. Consider only the forward elimination sweep and denote a point in a structured 3D grid by the indices (i,j,k). The elimination for a point (i,j,k) can not be done until the points $(i-1,j,k)$, $(i,j-1,k)$ and $(i,j,k-1)$ have been completed. Thus the elimination must start at the point $(1,1,1)$, then proceed to the points $(2,1,1)$, $(1,2,1)$, $(1,1,2)$, and so on. Obviously the degree of parallelism varies widely during the course of the forward elimination sweep and there is a corresponding variation in the degree of parallelism during the back substitution sweep. It is therefore impossible to achieve linear speed-up of this algorithm. The maximum speed-up depends on the problem size and the number of processors.

In order to parallelize the approximate LU factorization we define a set of grid points in some plane n which satisfy

$$i + j + k = n + 2. \tag{1}$$

For example, on an $NxNxN$ grid, there are $3N$-2 such planes and the number of grid points in each plane is given by

$$q_n = \frac{1}{2} \begin{cases} (n+1)n, \\ \qquad \text{for } 1 \leq n \leq N; \\ (n=1)n - 3(n-N)(n-N+1), \\ \qquad N+1 \leq n \leq 2N-2; \\ (3N-1-n)(3N-n), \\ \qquad 2N-1 \leq n \leq 3N-2. \end{cases} \tag{2}$$

Such a plane is illustrated in figure 1 for a 16x16x50 grid (used in the investigation [10] of a three dimensional vortex convecting through a converging/diverging channel). In the forward elimination step of the LU algorithm, we loop sequentially over n in ascending order. In our $NxNxN$ example, from 1 to $3N$-2, but the operations can be done in parallel on points which lie on the same plane as defined above.
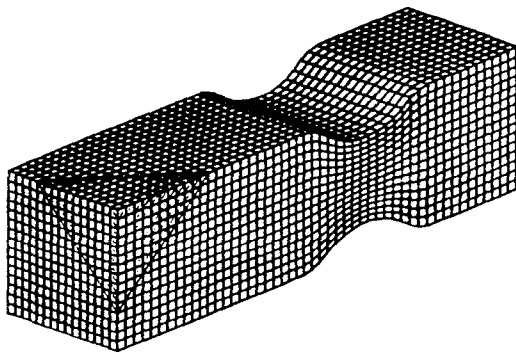

Figure 1. Planes of grid points available for point parallel calculations in the elimination/substitution sweeps of approximate LU factorization algorithm.

The parallelization is effected by means of the TC2000 FORTRAN spread do command, with the do statement acting over the number of grid points, n, on the current plane. The spread do potentially executes each loop iteration on a separate processor.

```
spread do
    do m = 1, n
    ...
    end do
end spread
```

It will be noted from Eq. 2 that for the cubic grid the number of points on the planes range between 1 and

$\frac{3}{4}N^2$, thus the degree of parallelism varies during the course of the forward elimination sweep. The back substitution sweep is similar except that we loop sequentially over n in descending order. Due to the variation in the degree of parallelism during the course of the forward and backward sweeps, the maximum achievable parallel efficiency decreases as the number of processors increases. The present approach is by no means the optimal one, but it does produce good results on a moderate number of processors and was easy to implement.

Parallel Timing Results

Figure 2 shows the parallel speed-up obtained with different numbers of processors for an implementation of an approximate LU factorization, similar to that discussed here. These particular results are for the parallelization, performed by a BBN team [11,12], of a parallel benchmark released by NAS. This benchmark is part of a suite of such benchmarks which are intended to, as a whole, "mimic the computation and data movement characteristics of large scale computational fluid dynamic (CFD) applications [13]." The grid size for this calculation was 64^3.
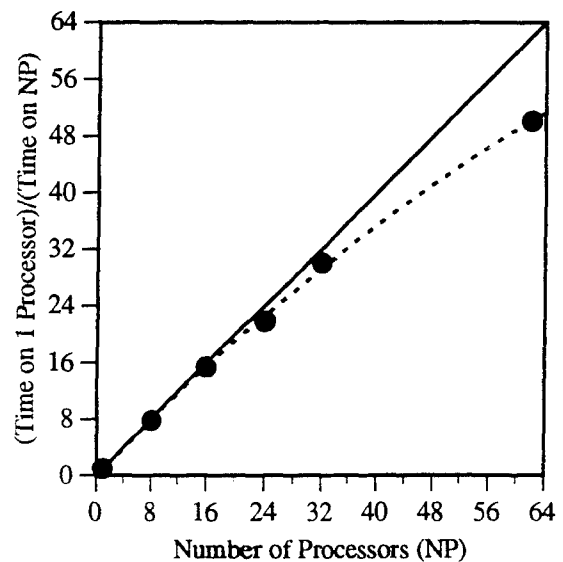

Figure 2. Parallel speed-up achieved for approximate LU factorization on a BBN TC2000 parallel computer.

The solid line in Fig. 2 represents the speed-up for a computation of ideal parallel efficiency, η,

$$\eta = \frac{\text{Time(1 processor)}}{\text{Time}(P \text{ processors}) \times P}. \tag{2}$$

687

Note in Fig. 2 that nearly ideal speed-ups are achieved for as many as $P=32$ processors, with quite good speed-up ($\eta=91\%$) obtained for the maximum number of processors, $P=55$, utilized in this study.

The fall-off in parallel efficiency with number of processors can, in part, be attributed to the previously discussed decrease in the maximum achievable efficiency for the present algorithm due to the varying degree of parallelism throughout the approximate factorization process. An additional drop-off in efficiency is due to the use of the relatively large number of synchronization barriers which are needed to achieve the parallelization as presently implemented. It should be noted that both sources of parallel efficiency loss would play a smaller role as the problem size is increased.
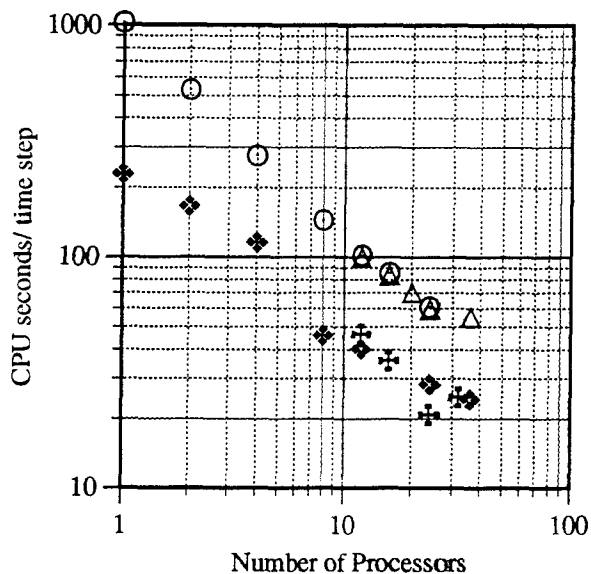

Figure 3. Parallel timing results achieved for present implementation on a time-shared, multiuser system. The various symbols denote runs with differing grids or boundary conditions.

Figure 3 shows some parallel timing results obtained with the present code. Results are for various unsteady simulations performed on the 2-D grids of Fig. 4, Fig. 6 and Fig. 7. Elapsed time per computational time step is plotted against the number of processors used for the computation. The Fig. 3 results are particularly noteworthy in that they are obtained for unsteady calculations using real geometries on a time-shared, multi-user computer, simultaneously in use by other users. This is in contrast with the more usual benchmark timing results, typically obtained under ideal operating conditions, on a "clean" computer. The present results reflect practical speed-ups obtained by performing the computations in

parallel. The speed-up is noted to be very nearly linear with the number of processors, up to the largest number of processors utilized in this study.

Even though the BBN TC2000 is no longer in production, we believe that these results illustrate the potential of parallel computing for the practical solution of computational fluid dynamics problems.

RESULTS

Foil in Steady Flow

Figure 4 shows a grid used in the present study. The section shown in Fig. 4 is here denoted "Foil 1". Foil 1 is a NACA 16 section with a thickness/chord ratio of 11.56% and camber to chord of 3.36%, and an $a=0.8$ mean camber line. The angle of attack was set to 0.8 degrees. The grid shown in Fig. 4 is a C-grid with 281x71 grid lines.
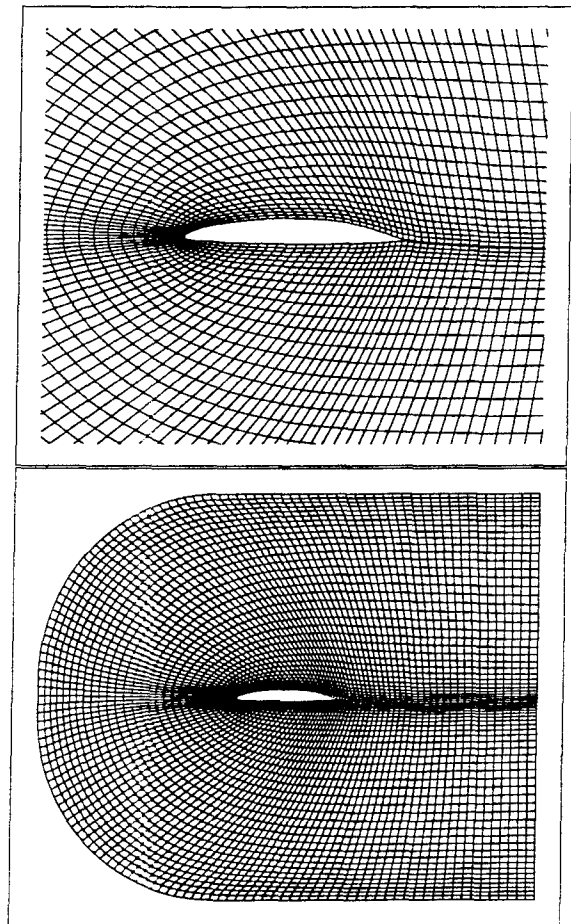

Figure 4. Grid used for Foil 1 transverse gust calculations, a C-grid with 281x71 grid points. For clarity of illustration only every second grid line is shown.

Figure 5 gives the steady-state pressure distribution on the surface of Foil 1 obtained by the present method and with a boundary element method [6]. We note that the differences are small, occurring mostly in the vicinity of the trailing edge. The lift coefficients, $C_L = L/(1/2 \rho V^2 c)$, obtained with the two methods are nearly identical, $C_L = 0.570$ from the present method, vs. $C_L = 0.576$ from the boundary element method.
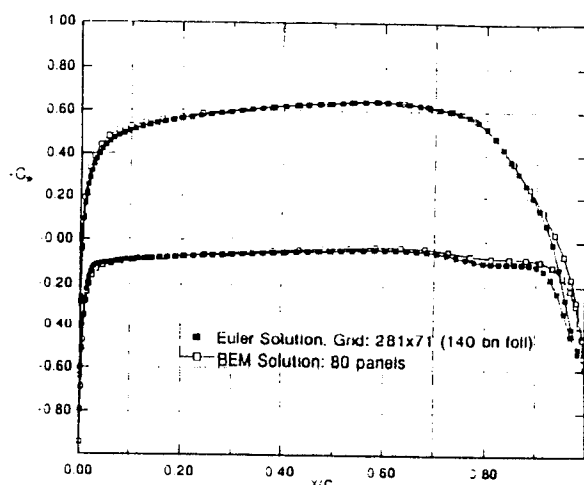

Figure 5. Steady pressure distributions computed for Foil 1 by present method and by a boundary element method [6].

$$C_p = \frac{p - p_\infty}{\frac{1}{2} \rho V^2}.$$

Transverse Gust

Transverse gusts interacting with three foil geometries were investigated. These geometries were:

- Foil 1: NACA 16 thickness form, $a=0.8$ mean camber line, $t/c=0.1156$, $f/c=0.0336$, $\alpha=0.8$ degrees.

- Foil 2: thickness form identical to that of Foil 1 without camber or angle of attack (see Fig. 6), $t/c=0.1156$, $f/c=0$, $\alpha=0$.

- Foil 3: one-half the thickness of Foil 2 (see Fig. 7), $t/c=0.0578$, $f/c=0$, $\alpha=0$.

The grids used in the transverse gust computations are shown in Fig. 4, Fig. 6 and Fig. 7. In each case a C-grid with 281x71 grid lines was utilized. The grids were generated with the aid of the INMESH [14] grid generation software.

Transverse sinusoidal gusts were modeled by imposing vertical velocity perturbations on the inflow boundary, the grid line which defines the outermost "C" in the grids of Fig. 4, Fig. 6 and Fig. 7. The imposed vertical perturbation velocity on the boundary was given by:

$$v_p(x,t) = \bar{v}_p e^{i(\omega t + kx)} \qquad (3)$$

Here k is the reduced frequency, $k = \omega c/2V$. A gust amplitude, $\bar{v}_p$, of 4 percent of the steady inflow velocity, V, was employed in the present study. Reduced frequencies of 0.5, 1.0, 2.0 and 5.0 were investigated. A time step size of $\Delta t V/c = 0.025$ was used in all of the presented results.
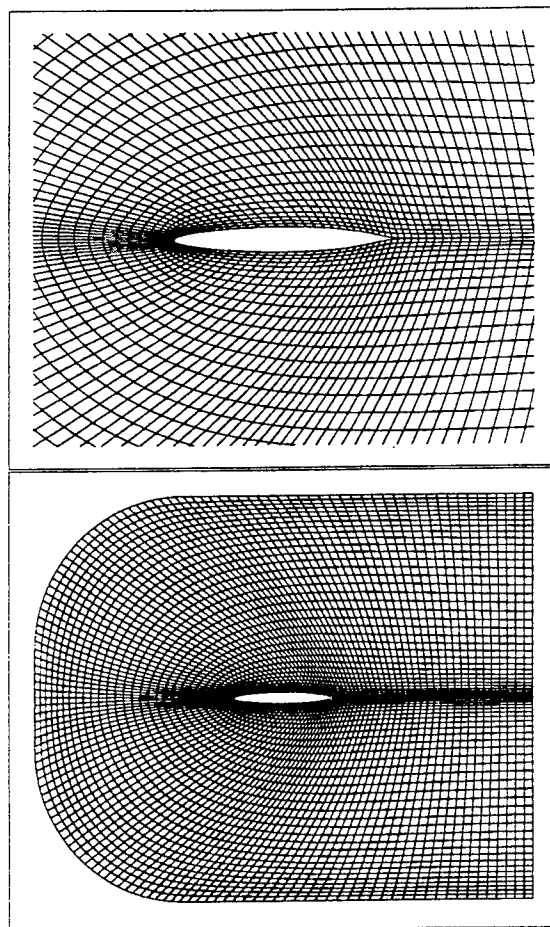

Figure 6. Grid used for Foil 2 transverse gust calculations, a C-grid with 281x71 grid points. For clarity of illustration only every second grid line is shown.

689

Figure 7. Grid used for Foil 3 transverse gust calculations, a C-grid with 281x71 grid points. For clarity of illustration only every second grid line is shown.
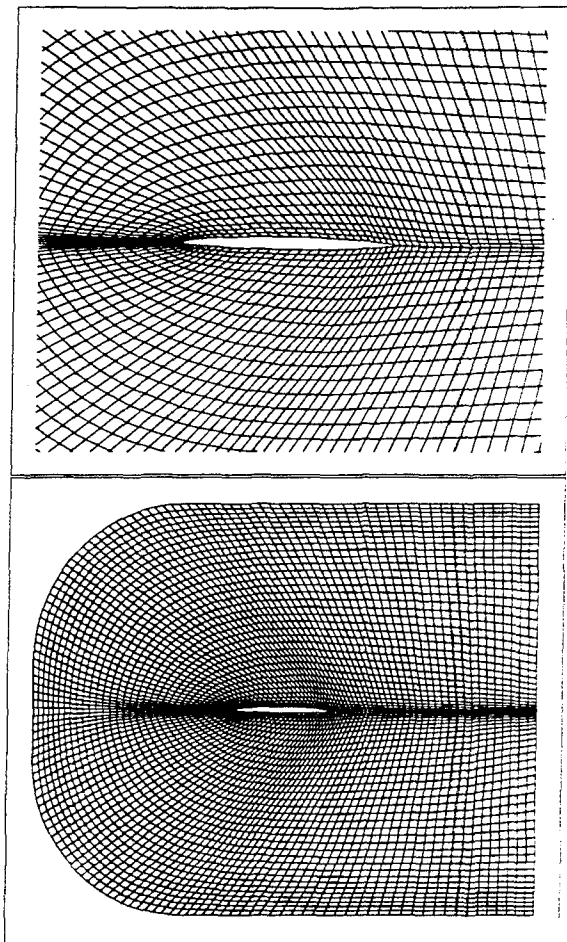
Figure 8 shows the resulting amplitude of the lift response to the transverse gust as a function of the reduced frequency, k. The unsteady lift amplitude in Fig. 8 is normalized by the quantity $\pi \rho V \overline{v}_p c$, the expected quasi-steady value. Also shown in Fig. 8 is the classical solution due to Sears [1] for an airfoil of zero thickness. We note that agreement between the present method and the Sears solution is relatively good. The value of the phase was also checked against the theoretical value for several of the investigated cases, and was similarly found to be in good agreement.

Flapping Foil

Detailed measurements of the flowfield about a foil experiencing unsteady time harmonic gusts have recently been performed at the Marine Hydrodynamics Laboratory at MIT [15,16,], and have been the subject of an ONR sponsored work-

shop at which comparisons between the experimental results and numerical simulations were presented [17]. The gusts were created by placing two small "flapping" foils in the water tunnel upstream of a larger stationery foil about which the measurements were made. This arrangement is shown schematically in Fig. 9
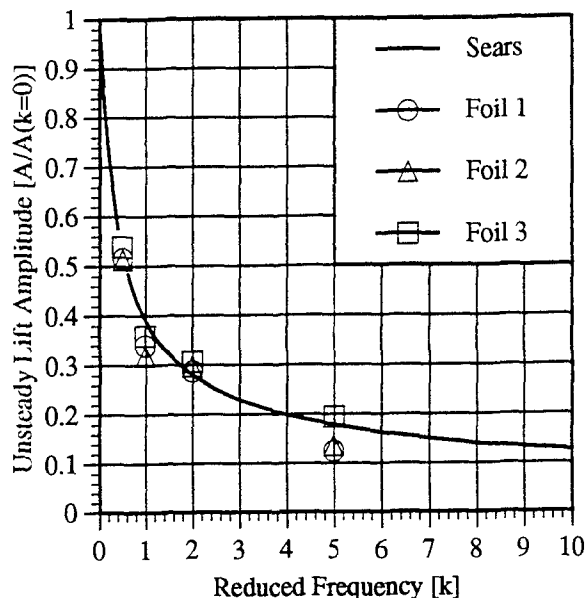
Figure 8. Unsteady lift amplitude due to a transverse gust. Results are shown at several reduced frequencies for the three foil geometries investigated with the present method. The classical solution due to Sears [1] is also shown.
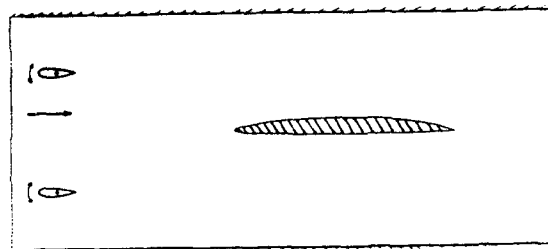
Figure 9. Schematic representation of the flapping foil experiment installed in the MIT water tunnel.

The MIT experiment focused upon measurement of the unsteady velocities in the boundary layer of the stationery foil, with particular emphasis on the trailing edge flows. While the present code is inviscid, and therefore cannot capture the character of such flows, the MIT data still provides a challenging simulation problem for which at least some comparisons with experimental results can be made.

690

Figure 10. Grid used for flapping foil simulation, a C-grid with 251x51 grid points.

what different foil geometry was actually tested by MIT in an attempt to make up for tunnel wall effects. The angle of attack and maximum camber used in the simulation were reduced somewhat so that the predicted lift matched the experimental value. This reduction in lift is attributed to viscous effects which are not modeled by the present method. Fig. 10 shows the grid used for the numerical simulation. We note that the inflow boundary of this grid is quite close to the leading edge of the stationery foil, in order to keep the flapping foils outside of the computational domain.
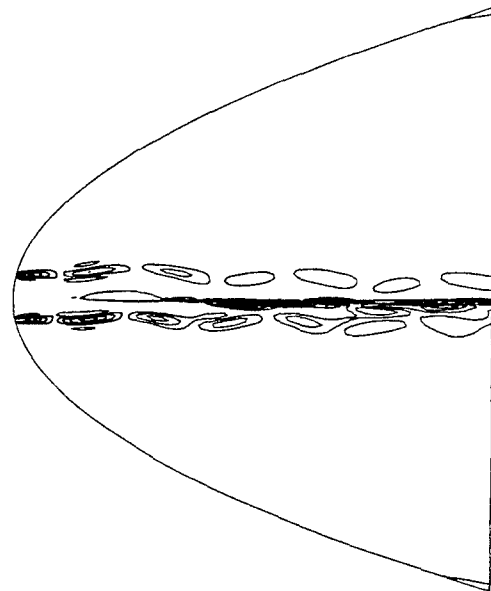
Figure 11. Predicted contours of vorticity induced by the flapping foils.

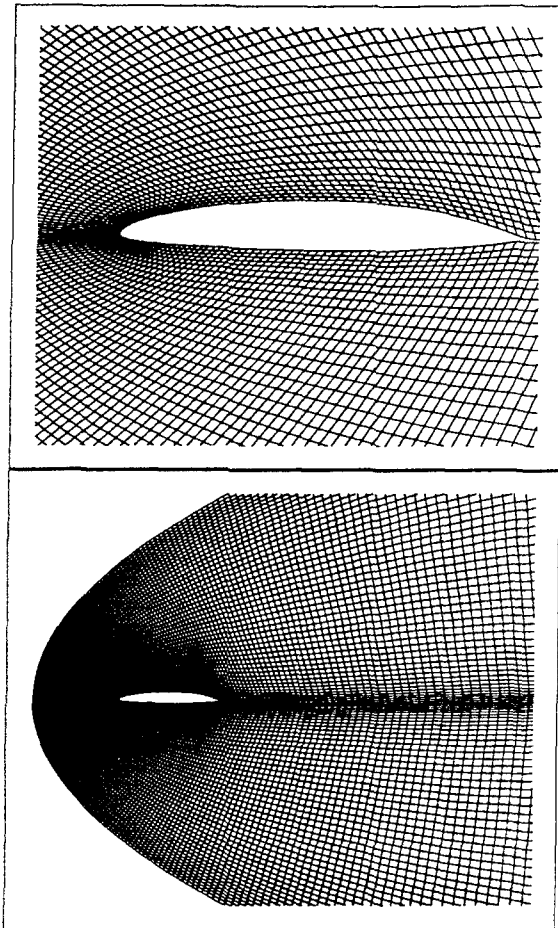The MIT researchers measured both steady and unsteady velocities at points defining a box surrounding the stationery foil. It was originally our intent to simply extrapolate this data to provide an inflow boundary condition for the numerical simulation. However, there proved to be insufficient data to so proceed. Therefore, a far field boundary condition model was constructed with potential flow singularities to model the effects of the primary elements of the flapping foil experiment. This model is described in the Appendix. Parameters in the model were estimated using a non-linear least squared error approximation to unsteady data and a direct calculation of the steady circulation.

The foil geometry used for the flapping foil simulation is similar to that of the previously described Foil 1, and corresponds to the "unbounded" foil shape which the MIT researchers were attempting to experimentally model in the water tunnel. A some-
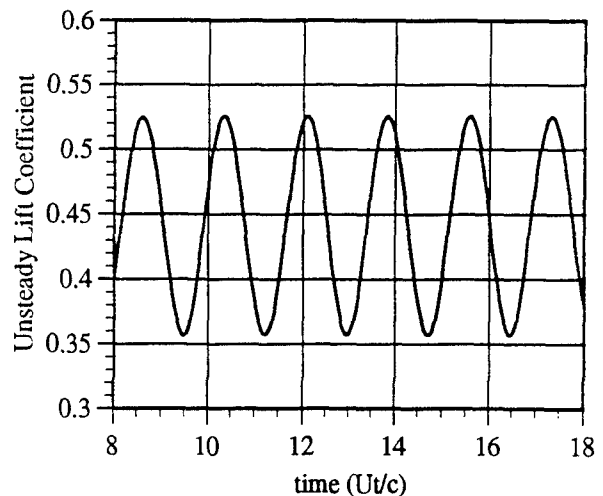

Figure 12. Unsteady lift, $C_L(t) = L(t) / \frac{1}{2}\rho V^2 c$, induced on the stationery foil.

691

Figure 11 is a contour plot of the predicted levels of vorticity after the simulation had been running for approximately 900 time steps. We note the presence of both the vorticity injected into the grid by the boundary condition representing the flapping foils and the induced vorticity shed by the stationery foil. The reduced frequency of the unsteady disturbance (in terms of the chord of the stationery foil) is 3.6, corresponding to a disturbance wavelength of somewhat less than twice the chord.

Figure 12 presents the resulting prediction of the unsteady lift. We note that the amplitude of the unsteady lift force is quite large relative to that which one would predict from classical theory, when only the nominal magnitude $(\bar{v}_p / V \approx 0.04)$ of the unsteady vertical velocity component (a purely transverse gust) is considered. We observe, however, that the unsteady velocity field introduced by the flapping foils differs substantially from that of such a transverse gust. This is made apparent in Fig. 13 which shows a vector field describing the unsteady component of velocity at the same time step as the vorticity contours of Fig. 11. The vector field was formed by subtracting the steady solution for the velocity field from the total unsteady solution. Contrast this with Fig. 14 which gives a similar vector field for a transverse gust of $k=2$.
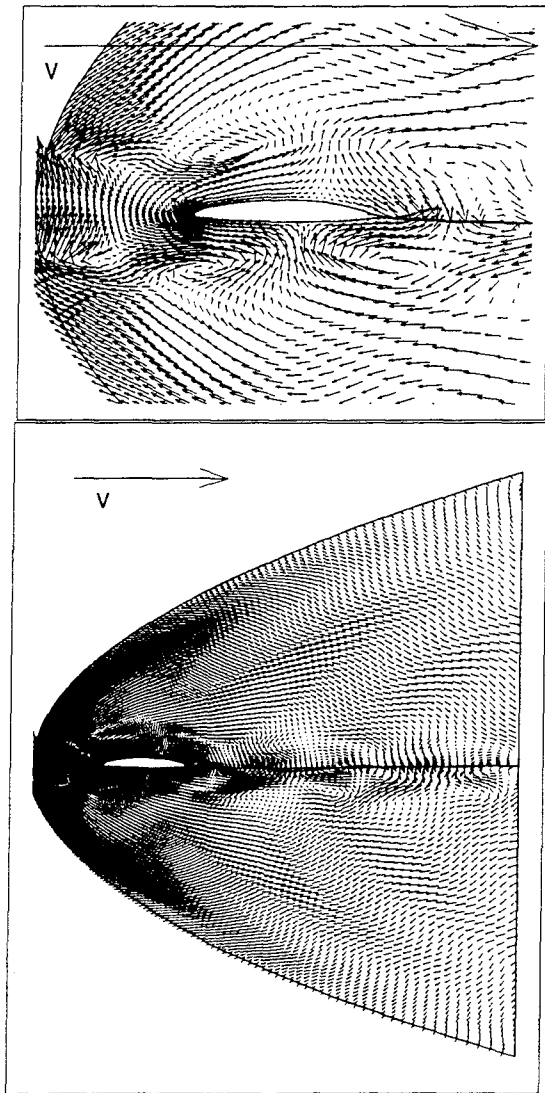

Figure 13. Vector representation of the unsteady velocity field. $(\vec{U} - \vec{U}_{steady})$ induced by the flapping foils. The large arrows represent the unit (freestream) velocity vectors.
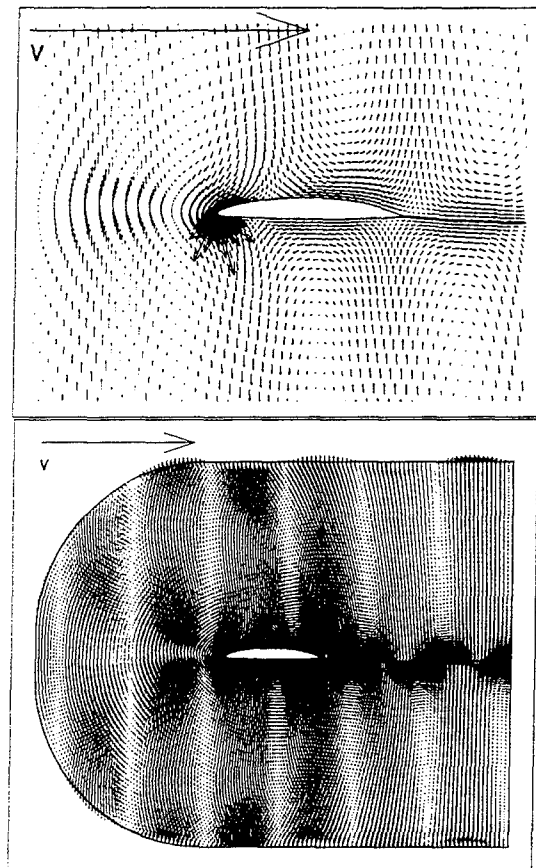
Figure 14. Vector representation of the unsteady velocity field. $(\vec{U} - \vec{U}_{steady})$ of a foil interacting with a transverse gust of $k=2$.

Vortex Chopping

Figure 15 presents a time history of predicted contours of vorticity as a distributed vortex interacts with a foil. Here the foil is a NACA 0012 thickness form without camber and with angle of attack set to zero. A C-grid with 99x33 grid lines was used for this calculation.

The vortex was generated by perturbing the inflow boundary in a manner similar to that employed for the flapping foil study. We specified an initial vorticity distribution of the form:

$$\omega(\mathbf{x}, t = 0) = \frac{\Gamma e^{-r^2/\delta^2}}{\pi \delta^2}, \quad r = \left| \mathbf{x} - \mathbf{x}_0 \right| \tag{3}$$

where Γ is the total circulation, δ is the core radius, and $\mathbf{x}_0 = (x_0, y_0)$ is the initial position of the vortex center.

The boundary velocities were perturbed consistent with the potential flow about such a vortex in the absence of the foil, and the nominal position of the vortex was convected, at each time step, with the uniform freestream.

For the results presented in Fig. 15, Γ=0.4, δ=0.1 and $x_0 = 0$. The vortex is seen to intersect with and be split by the foil. The distortion of the vortex is associated with the velocity induced by the foil, which is experiencing lift due to the presence of the velocity field of the vortex.

The results obtained with the present method are seen to agree well with numerical results obtained by Lee and Smith [18], who employed a discrete vortex method to investigate this model problem.

Figure 15. Vorticity contours depicting time history of a distributed vortex interacting with a foil.

CONCLUSIONS

A numerical method for the direct simulation of inviscid unsteady blade section forces has been implemented on a parallel processor. Timing results on the parallel computer showed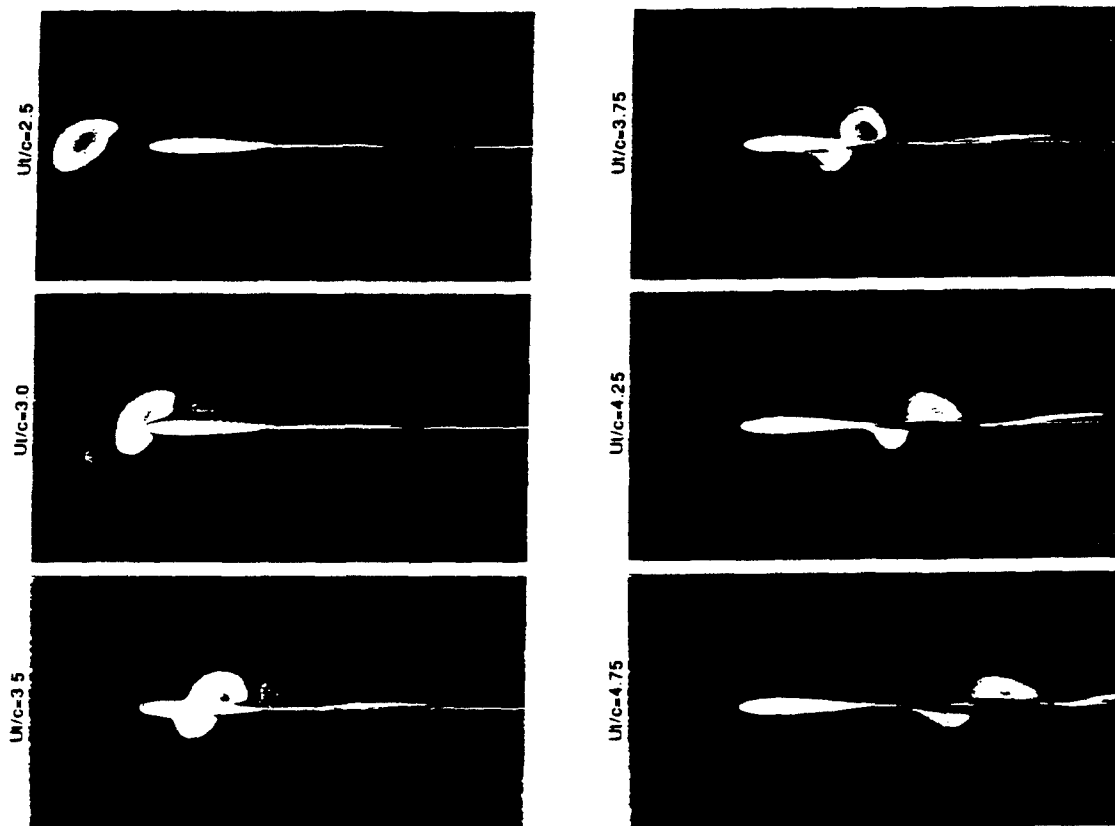 nearly linear speedups with the number of processors employed. The method was applied to three model problems and the results compared favorably with available solutions.

Even though the BBN TC2000 is no longer in production, we believe that these results illustrate the potential of parallel computing for the practical solution of computational fluid dynamics problems.

ACKNOWLEDGMENTS

REFERENCES

1. W. Sears, "Some Aspects of Non-Stationary Airfoil Theory and its Practical Application," Journal of the Aeronautical Sciences, 8(3), 104-108, 1941.

2. H. Naumann & H. Yeh, "Lift and Pressure Fluctuations of a Cambered Airfoil Under Periodic Gusts and Applications in Turbomachinery," Journal of Engineering for Power, 1-10, January, 1973.

3. H. Atassi, "The Sears Problem for a Lifting Airfoil Revisted -- New Results," Journal of Fluid Mechanics, 141, 109-122, 1984.

4. H. Atassi & T. Akai, "Aerodynamic and Aeroelastic Characteristics of Oscillating Loaded Cascades at Low Mach Number," Journal of Engineering for Power, 102, 344-351, 1980.

5. H.-W. Chiang & S. Fleeter, "Cascade Aeroacoustics Including Steady Loading Effects," Noise Control and Engineering Journal, 34(2), 61-72, 1990.

6. C.-Y. Hsin, "Development and Analysis of Panel Methods for Propellers in Unsteady Flow," Ph.D. Thesis, MIT Department of Ocean Engineering, 1990.

7. S. Rogers & D. Kwak, "Upwind Differencing Scheme for the Time-Accurate Incompressible Navier-Stokes Equations," AIAA Journal, 28, 253-262, 1990.

8. M. Athavale & C. Merkle, "An Upwind Differencing Scheme for Time-Accurate Solutions of Unsteady Incompressible Flow," AIAA Paper 88-3650, 1988.

9. S. Breit, W. Coney, A. Dickinson & J. Webb, "Computing Boundary Forces Due to Unsteady, Inviscid Incompressible Flow," AIAA Journal, 30(3), 592-600, 1992.

10. S. Breit, W. Coney, J. Webb, "Vortex Chopping Noise in Turbomachinery: Numerical Simulation on a Parallel Processor," presented at the ONR/DTRC Workshop on Quiet Turbomachinery Design, Annapolis, MD, November, 1991.

11. S. Breit, W. Celmaster, W. Coney, et. al. "The role of Architectural Balance in the Implementation of the NAS Parallel Benchmarks on the BBN TC2000 Computer," FED-Vol. 156, CFD Algorithms and Applications for Parallel Processors, ASME, 1993.

12. S. Breit, "Implementing the Incomplete LU Factorization Method on the BBN TC2000 Parallel Computer," Proceedings of the Conference on "Parallel Computational Fluid Dynamics," K.G. Reinsch, et. al., ed., Stuttgart, Germany, June 1991.

13. D. Bailey, J. Barton, T. Lasinski and H. Simon, The NAS Parallel Benchmarks, NAS White Paper, 1991.

14. R. Coleman, INMESH: An Interactive Program for Numerical Grid Generation, David W. Taylor Naval Ship Research and Development Center Report DTNSRDC-85/054, August 1985.

15. J. Rice, Investigation of a Two-Dimensional Hydrofoil in Steady and Unsteady Flows, SM thesis, Massachusetts Institute of Technology, Department of Ocean Engineering, June 1991.

16. P. Delpero, Investigation of Flows around a Two Dimensional Hydrofoil Subject to a High Reduced Frequency Gust Loading, SM thesis, Massachusetts Institute of Technology, Department of Ocean Engineering, February 1992.

17. "MIT/ONR Flapping Foil Workshop", Carderock Divison/NSWC, Bethesda, MD, March 29-30, 1993.

18. D. Lee and C. Smith, "Distortion of the Vortex Core During Blade/Vortex Interactions," AIAA 19th Fluid Dynamics, Plasma Physics and Lasers Conference, AIAA-87-1243, 1987.

APPENDIX:

Flapping Foil Boundary Condition

A far field boundary condition model is constructed with potential flow singularities to model the primary elements of the flapping foil experiment. Parameters in the model are estimated using a non-linear, least squared error approximation to unsteady data and a direct calculation of the steady circulation. All elements of the model are assumed to be two dimensional. The principal elements of the model are:

• A single, steady vortex representing the steady lift component on the fixed foil. The strength of the vortex is computed from the measured steady velocity field.

• Three unsteady vortices, each representing one of the two moving foils or the unsteady lift component on the fixed foil. Each vortex has a sinusoidally varying circulation distribution in time as in Eq. A-1. The magnitude, frequency and phase of the time variation are estimated from the experimental data.

• A straight, semi-infinite vortex wake attached to each of the unsteady point vortices. Vorticity is assumed to convect along the length of the wake at a constant rate which is estimated from the experimental data. The local strength of the wake is coupled to the time history of the associated point vortex and the convection velocity and consequantly is sinusoidal in both time and space. Eq. A-3 defines the dependence between the point vortex strength and the wake strength. The induced velocity is given by an integral over the length of the wake as shown in Eq. A-4.

• In order to ensure the velocity is defined at all locations where a computational boundary is likely to be positioned, the unsteady wakes are assumed to have finite, non-zero thickness. If a boundary point falls inside this region, the velocity due to the wake is computed to be the average of the velocity induced at the top and bottom of the region defined by the wake thickness.

• Effects due to free vorticity outside of the unsteady wakes and thickness effects of the various airfoils are not included.

The software implementing the boundary condition is provided in two parts. One is a subroutine called by the flow solver. The other is a program used to generate estimates of the parameters in the model from experimental data.

Induced Velocity Formulation

The basic element of the boundary condition model is a point vortex with time varying circulation and an attached wake. The circulation of the point vortex is assumed to be of the form:

$$\Gamma_v(t) = \Gamma_0 \sin(\omega t + \alpha) \qquad (A\text{-}1)$$

and the associated wake will be:

$$\Gamma_w(x,t) = \Gamma' \sin(kx + \beta) \qquad (A\text{-}2)$$

where we expect β to be time dependent. The strength of the wake will be related to the strength of the point vortex in the following way. Assume a constant convection velocity for the vorticity in the wake, U. For an infinitesimal change in the strength of the point vortex, $d\Gamma_v$, there is also, at some position Udt away, a filament of strength $-d\Gamma_v$. Since U is constant, we can say:

$$\Gamma_w(x,t) = \frac{d\Gamma_v(t - x/U)}{dt} \qquad (A\text{-}3)$$

We will be interested in the induced velocity at a particular point in time so we can treat Γ_w as a function of the distance along the wake. From these assumptions we can see:

$$\Gamma_w(x,t) = -\Gamma_0 \omega \sin\left(\omega(t - x/U) + \alpha + \frac{\pi}{2}\right)$$

From Eq. A-2 we can see:

$$\Gamma' = \Gamma_0 \omega$$

$$k = -\frac{\omega}{U}$$

and

$$\beta = \omega t + \alpha + \frac{\pi}{2}$$

The induced velocity from a point vortex is computed from:

$$V_x = -\frac{\Gamma_0 P_y}{2\pi r}$$

$$V_x = \frac{\Gamma_0 P_x}{2\pi r}$$

for the coordinate system defined Fig. A-1. The vortex is assumed to be located at the origin of the coordinate system and the velocity is computed at point P.
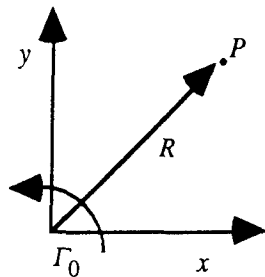

Figure A-1. Point vortex coordinates

For the wake, the situation is considerably more complicated. For a circulation distribution defined by Eq. A-2 and the coordinate system of Fig. A-2, the induced velocity is given by:

$$\vec{V}_w(x,y) = -\frac{\Gamma'}{2\pi}\int_0^\infty \sin(kx'+\beta)\left(\frac{y\vec{i}-(x-x')\vec{j}}{(x-x')^2+y^2}\right)dx'$$

(A-4)

where $\vec{i}$ and $\vec{j}$ are the unit vectors in the x and y coordinate directions. (The above epression is obtained by integrating the velocity due to a planar vortex sheet once in the direction parallel to the vortex filament we are representing with a point vortex.)
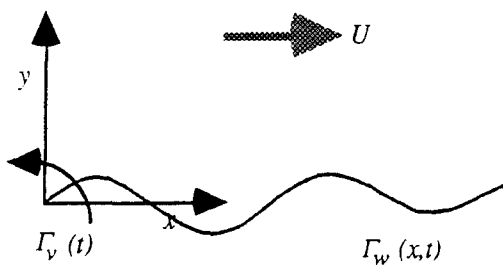
Figure 2. Wake Coordinates

In cases where $kx>0$ and $ky\approx0$, it is assumed the computation point is inside the viscous region of the wake. For these cases, the velocity is computed at the locations where $y=\pm1/2$ (wake thickness) and averaged. The wake thickness is a specified parameter.

Computing the Wake Induced Velocity

Eq. A-4 is evaluated numerically over a finite extent of the wake. In order for this approach to be valid, the influence of a semi-infinite wake must approach zero as the point of interest moves far upstream of the start of the wake. With this assumption, we can rewrite Eq. A-4 as:

$$\vec{V}_w(x,y) = -\frac{\Gamma'}{2\pi}\int_0^\infty \sin(kx'+\beta)\frac{-(x-x')\vec{j}}{(x-x')^2}dx'$$

(A-5)

where we have assumed $kx \gg ky$. We can rewrite this as:

$$\vec{V}_w(x,y) = \frac{\Gamma'}{2\pi}\int_0^\infty \frac{\cos\beta\sin kx' + \sin\beta\cos kx'}{kx-kx'}dkx'$$

(A-6)

and since we also require $x<0$, the singularity associated with $\frac{\cos x}{x}$ is not a difficulty.

We can say:

$$\int_0^\infty \frac{\sin(ax)}{\beta-x}dx = \sin(\beta a)\,\mathrm{ci}(\beta a)$$
$$-\cos(\beta a)(\mathrm{si}(\beta a)+\pi)$$

(A-7)

$$\int_0^\infty \frac{\cos(ax)}{\beta-x}dx = \cos(\beta a)\,\mathrm{ci}(\beta a)$$
$$+\sin(\beta a)(\mathrm{si}(\beta a)+\pi)$$

(A-8)

for $a>0$. The sine and cosine integral functions have been used here where:

$$\mathrm{si}(x) = -\int_x^\infty \frac{\sin t}{t}dt$$

$$\mathrm{ci}(x) = -\int_x^\infty \frac{\cos t}{t}dt$$

We are interested in the case where x approaches negative infinity. The integral functions evaluate to:

$$\lim_{x\to-\infty}\mathrm{si}(x) = -\pi$$

(A-9)

$$\lim_{x\to-\infty}\mathrm{ci}(x) = \pm\pi i$$

(A-10)

696

where we will take the real part of Eq. A-10. Substituting these into Eq. A-6 results in:

$$\lim_{x \to -\infty} \vec{V}_w = 0 \qquad \text{(A-11)}$$

This argument suggests using a finite portion of the wake will eventually converge as longer extents are integrated. No rigorous assesment of the convergence properties of the sequence generated by this process has been performed. Simple numerical experiments suggest it may be necessary to take 1000 or more periods of the wake to obtain accuracy in the range of 1 part in 10^4.

Computation of Unsteady Viscous Flow with Application to the MIT Flapping Foil Experiment

E. Paterson and F. Stern

(University of Iowa, USA)

ABSTRACT

A time-accurate unsteady viscous-flow method is validated through calculations and comparisons with the Massachusetts Institute of Technology flapping-foil experiment. Solutions are obtained using a small domain surrounding the foil, a tunnel domain that included the foil and the tunnel walls, and a complete domain that included the foil and both the tunnel walls and the upstream flappers. In the latter case, the CHIMERA overlaid-grid method was used. The solutions give similar overall agreement with the data for both steady and unsteady flow, which demonstrates that such problems can be handled with a variety of formulations, although the boundary data, cpu time, and storage requirements are different. The physics are complex with analogy to Stokes layers and explicated through analysis of the axial pressure gradient, which exhibits upstream and downstream traveling waves over the foil and in the near wake and in the intermediate wake, respectively, due to nonlinearities induced by the convective acceleration and steady/unsteady interactions. The nature of the unsteady displacement thickness suggests viscous-inviscid interaction as a possible mechanism for the axial pressure-gradient response.

NOMENCLATURE

c	= wave speed ($= \lambda/T$)
C_p	= pressure coefficient
L	= characteristic (foil) length
p	= pressure
Re	= Reynolds number ($= U_o L/v$)
t	= time
U_i	= ensemble averaged velocity components in Cartesian coordinates ($= U, V, W$)
$\overline{u_i u_j}$	= Reynolds stress tensor
x^i	= Cartesian coordinates ($= x,y,z$)
y^+	= wall coordinate ($= U_\tau y/v$)
δ	= boundary-layer thickness
γ	= phase angle
v	= kinematic viscosity
v_t	= eddy viscosity
ξ	= frequency parameter ($= \omega L/U_0$)
ξ^i	= curvilinear coordinates ($= \xi,\eta,\zeta$)
τ_w	= wall-shear stress
ϕ	= transport quantities (U,V,W)
ω	= circular frequency ($= 2\pi f$)

INTRODUCTION

Although most practical engineering flows are inherently unsteady and viscous, the physical understanding is in its infancy in comparison to steady flow, due to the complexity of performing experiments and computations even for simplified configurations, as evidenced by the sparse number of studies documented in the literature for unsteady vs. steady flow (e.g., the proceedings of this conference). Unsteady flows can be conveniently grouped into three categories: (1) natural, (2) forced, and (3) interacting. For all three, the predominant number of studies are experimental vs. computational, as indicated by the example references given.

Naturally unsteady flow refers to conditions under which the unsteadiness arises from flow separation and associated vortex wakes or jet and shear-layer instabilities. Most information is for two-dimensional flows, which includes the Reynolds number (Re) dependence of the separation points, vortex-shedding frequencies [i.e., Strouhal number(St)], and wake-patterns for a variety of bluff bodies both with sharp (e.g., flat plates at incidence) and smooth (e.g., circular cylinders) edges [1,2,3]. The situation is similar for three-dimensional flows, but the number of studies is drastically reduced [4,5].

Forced unsteady flow refers to conditions under which the unsteadiness arises from body motions or moving boundaries (e.g., rotor-type flows and control surfaces) or oscillating streams (e.g., boundary layers with oscillating external flows) such that there is an identifiable predominant forcing frequency. With respect to the former, relatively few studies have been conducted for realistic geometries, due to the complexity of such configurations and the geometric dependence of the resulting data. However, a number of studies have examined the idealized geometry of a pitching foil where the interest has ranged from inviscid flutter analysis [6] to dynamic stall [7-9]. The situation is similar for oscillating external flows where model problems such as flat-plate boundary layers (i.e., Stokes-layer overshoots, phase angles, and streaming) both for laminar and turbulent flow [10] and foils embedded in transverse gusts [11] have been studied.

Interacting unsteady flow refers to conditions under which both natural and forced unsteadiness are present and interact. Obviously, in this case, the least information is available, although this may, in fact, be the most important category with regard to engineering design improvement. The few studies that have been conducted were concerned with wake and separation control [12,13] and blade/vortex [14,15] and rotor/stator [16] interactions. In the former cases, it has been demonstrated that wakes with harmonic disturbances behave like nonlinear oscillators and are characterized by synchronization (i.e., lock-in) vs. non lock-in conditions depending on the ratio of the frequency of the disturbance f_e to St (i.e., state-selection diagram or resonant horns of amplitude vs. f_e/St), which has been further explicated through stability analysis [17], and similarly the ability to control separation through disturbances at certain f_e. In the latter cases, the studies are somewhat preliminary in that, thus far, the blade and stator flows, respectively, are usually steady.

The present work is part of a larger project at the Iowa Institute of Hydraulic Research (IIHR) specifically concerning the development of computational fluid dynamics (cfd) methods with application to marine propulsors. Marine propulsors are unique in comparison to related applications (e.g., turbomachinery, turboprops, and rotors) in that they operate in the thick hull boundary layer and/or appendage wakes such that complex naturally (hull flow) and forced (propulsor flow) unsteady interactions occur. Initially, cfd methods were applied to propeller/hull interaction utilizing an interactive approach, i.e., a body-force propeller representation in the viscous-flow method obtained interactively using a vortex-lattice propeller-performance method for specified inflow [18]. Subsequently, cfd methods were applied directly to calculating the propeller-blade and wake flows both for idealized [19] and practical turboprop and marine propulsors [20]. Currently, efforts are being directed towards extending the latter methods for unsteady flow with consideration to issues of efficient large-scale time-accurate computations for fixed- and moving-boundary problems [21, 22].

The present paper describes the initial efforts in extensions for unsteady-flow calculations and validation through calculations and comparisons with the Massachusetts Institute of Technology (MIT) Marine Hydrodynamics Laboratory flapping-foil experiment (ffx). ffx represents a two-dimensional simulation of propeller-blade and wake flow, i.e., a blade section (foil) embedded in vertical and horizontal gusts generated by upstream pitching foils (flappers) (figure 1). ffx was conducted such that calculations could be performed either for a small domain with given boundary data (sd), for the tunnel domain with a specified inflow (td), or for the complete domain, including the upstream flappers (cd). Associated with ffx was the 29-30 March 1993 Office of Naval Research (ONR)/MIT Unsteady-Flow Workshop in which various groups of researchers submitted blind computations (i.e., with only the experimental conditions and boundary data) for either sd, td, or cd and met at the workshop for the comparisons with the data and discussion. At the workshop, IIHR submitted blind computations for sd. Herein, these results will be presented along with more recent results for sd, td, and cd. In the latter case, the CHIMERA overlaid-grid method was used, which has also been under investigation for other fixed- and moving-boundary problems [22]. The recent results were presented at the 13 September 1993 post workshop meeting.

In the following, the computational method and ffx are described and the computational conditions, grids, and uncertainty are given. Then, the results are discussed for both steady and unsteady flow, including comparisons with the data, discussion of the ONR/MIT workshop and post workshop meetings, and analysis and analogy to Stokes layers. Lastly, some concluding remarks are made, including future work.

COMPUTATIONAL METHOD

The computational method is based on extensions of [19] for time-accurate unsteady-

flow calculations. Although the basic viscous-flow method [23] utilized in [19,20] was developed with the capability of unsteady-flow calculations, only very limited such calculations had previously been performed. In the following, an overview is given of the equations and coordinate system, turbulence model, discretization and velocity-pressure coupling, solution domains and boundary conditions, and grid generation. The modifications required for time-accurate computations are also discussed. The method is applicable to unsteady three-dimensional flow; however, the current presentation is for unsteady two-dimensional flow in view of ffx. Further details concerning the basic viscous-flow method are provided in [23] and associated references.

Equations and Coordinate System

The continuity and Reynolds-averaged Navier Stokes (RaNS) equations for unsteady incompressible flow are written in the physical domain using Cartesian coordinates and tensor notation with x positive downstream, y normal to x, and the origin at the foil leading edge (figure 1). In nondimensional form the equations are

$$\frac{\partial U_i}{\partial x^i} = 0 \tag{1}$$

$$\frac{\partial U_i}{\partial t} + U_j \frac{\partial U_i}{\partial x^j} + \frac{\partial \overline{u_i u_j}}{\partial x^j} + \frac{\partial p}{\partial x^i} - \frac{1}{Re} \nabla^2 U_i = 0 \tag{2}$$

with $\nabla^2 = \dfrac{\partial^2}{\partial x^j \partial x^j}$ and $U_i = (U,V,W)$ and $u_i = (u,v,w)$ are the components of the ensemble-averaged velocity and turbulent fluctuations, respectively, and p is the pressure. All variables are nondimensionalized using U_o, L, and ρ.

The Reynolds stress is related to the mean rate of strain by an isotropic eddy viscosity v_t

$$\overline{u_i u_j} = v_t \left(\frac{\partial U_i}{\partial x^j} + \frac{\partial U_j}{\partial x^i} \right) - \frac{2}{3} \delta_{ij} k \tag{3}$$

upon which (2) becomes

$$\frac{\partial U_i}{\partial t} + \left(U_j - \frac{\partial v_t}{\partial x^j} \right) \frac{\partial U_i}{\partial x^j} - \frac{\partial v_t}{\partial x^j} \frac{\partial U_j}{\partial x^i} + \frac{\partial}{\partial x^i} \left(p + \frac{2}{3} k \right) - \frac{1}{R_\phi} \nabla^2 U_i = 0 \tag{4}$$

where $\dfrac{1}{R_\phi} = \dfrac{1}{Re} + v_t$. \hfill (5)

Transformation of (1-5) into nonorthogonal curvilinear coordinates is such that the computational domain forms a simple rectangular parallelepiped with equal grid spacing. The transformation is a partial one since it involves the coordinates only and not the velocity components. The transformation is accomplished through the use of the expression for the divergence and "chain-rule" definitions of the gradient and Laplacian operators, which relate the orthogonal curvilinear coordinates $x^i = (x,y,z)$ to the nonorthogonal curvilinear coordinates $\xi^i = (\xi,\eta,\zeta)$. In this manner, (1-5) can be rewritten as follows

$$\frac{\partial}{\partial \xi^i} \left(b_i^j U_j \right) = \frac{\partial U^i}{\partial \xi^i} = 0 \tag{6}$$

$$g^{ij} \frac{\partial^2 \phi}{\partial \xi^i \partial \xi^j} - 2 a_\phi^j \frac{\partial \phi}{\partial \xi^j} = R_\phi \frac{\partial \phi}{\partial t} + S_\phi \tag{7}$$

with

$$2 a_\phi^j = \frac{R_\phi}{J} b_n^j \left(U_n - \frac{\partial x^n}{\partial t} - \frac{1}{J} b_n^m \frac{\partial v_t}{\partial \xi^m} \right) - f^j \tag{8}$$

and where $\dfrac{\partial x^n}{\partial t}$ is nonzero only for moving-grid applications.

Turbulence Model

Closure is attained through a quasi-steady application of the Baldwin-Lomax turbulence model with modifications to account both for the effects of wake asymmetry [24,25] and axial pressure gradients [26]. The former was used to obtain the solutions for all three domains (sd, td, and cd), whereas the latter was only used for td (denoted $td_{dp/dx}$).

For the standard Baldwin-Lomax model, in the near-wall layer

$$v_{t,i} = \ell_m^2 |\omega| \tag{9}$$

where the length scale is based on the mixing length

$$\ell_m = \kappa y \left(1 - \exp\left(-\frac{y^+}{A^+} \right) \right) \tag{10}$$

701

and the vorticity ω is used to determine the velocity scale. In the outer-layer

$$v_{t,o} = k C_{cp} F_{wk} F_{Kleb} \tag{11}$$

where

$$F_{Kleb} = \left(1 + 5.5 \left(C_{Kleb} \frac{y}{y_{max}}\right)^6\right)^{-1} \tag{12}$$

$$F_{wk} = \min\left(y_{max} F_{max}; C_{wk} y_{max} \frac{U_{diff}^2}{F_{max}}\right) \tag{13}$$

$$F(y) = y|\omega|\left(1 - \exp\left(-\frac{y^+}{A^+}\right)\right) \tag{14}$$

$$U_{diff} = \sqrt{\left(U^2 + V^2\right)_{max}} - \sqrt{\left(U^2 + V^2\right)_{min}} \tag{15}$$

F_{Kleb} is the Klebanoff intermittency function. In F_{wk}, the first and second expressions are effective in attached and separated boundary layers (and wakes), respectively. The velocity scale F_{max}, is determined from (14) and y_{max} is the corresponding y-coordinate. The empirical constants are: $\kappa = 0.4$, $k = 0.0168$, $C_{cp} = 1.6$, $C_{Kleb} = 0.3$, $C_{wk} = 0.25$, and $A^+ = 26$.

The standard Baldwin-Lomax model is not suitable for asymmetric wakes where two different values for y_{max} and F_{max} result from the merging of the suction- and pressure-side boundary layers. Therefore, the eddy viscosity on the far-wake centerline is rendered single-valued by taking the maximum value from both sides of the wake.

$$v_{t,fwk} = k C_{cp} F_{Kleb} \max\left(F_{wk,top}, F_{wk,bottom}\right) \tag{16}$$

The eddy-viscosity distribution is asymmetric due to the evaluation of F_{kleb} on each side of the wake. For both F_{Kleb} and F_{wk}, y is measured from the point of maximum wake deficit. Finally, since (11) is only valid in the far wake, a blending function is used to provide a smooth transition from the boundary layer to the far wake

$$v_{t,wk} = v_{t,fwk} + \left(v_{t,te} - v_{t,fwk}\right) \exp\left(-\frac{x - x_{te}}{20 \delta_{te}}\right) \tag{17}$$

where $v_{t,te}$ is the distribution at the trailing edge of the foil.

The effects of axial pressure gradient were investigated through the use of Granville's modified coefficients C_{cp} and C_{Kleb} such that they are functions of a Clauser-type pressure-gradient parameter $\bar{\beta}$

$$C_{kleb} = \frac{2}{3} - \frac{0.0132}{0.1724 + \bar{\beta}}$$

$$C_{cp} = \frac{3 - 4 C_{kleb}}{2 C_{kleb}(2 - 3 C_{kleb} + C_{kleb}^3)}$$

$$\bar{\beta} = -\frac{y_{max}}{u_\tau} \frac{dU}{dx^1}$$

Note that the zero gradient values $C_{cp} = 1.2$ and $C_{kleb} = 0.646$ are significantly different from standard Baldwin-Lomax values.

Discretization and Velocity-Pressure Coupling

The finite-analytic method is used to reduce (7) to algebraic form. Each local rectangular numerical element is linearized by evaluating the coefficients and source functions at the interior node P and transformed again into a normalized form by a simple coordinate stretching. In addition, the temporal derivative is expressed as a second-order backward finite difference. An analytical solution is obtained by separation of variables with specified boundary functions. As a result, a 9-point finite-analytic formula is obtained

$$\phi_P^n = \frac{1}{1 + \frac{3}{2} C_p \frac{R_\phi}{\tau}}$$
$$\times \left[\sum_1^8 C_{nb} \phi_{nb}^n + C_p \frac{R_\phi}{\tau}\left(2\phi_P^{n-1} - \frac{1}{2}\phi_P^{n-2}\right) - S_\phi \right] \tag{18}$$

The resulting computational stencil includes all eight neighboring nodal values and the values at the two previous time-steps. Since (18) is implicit, both in space and time, its assembly for all elements results in a set of simultaneous algebraic equations that is solved using a line-ADI approach with under-relaxation.

The coupling of the velocity and pressure fields in an efficient time-accurate fashion required changing from a SIMPLER algorithm, which requires global iterations for time accuracy, to a split-operator approach based on the PISO algorithm. The first step is to implicitly solve the momentum equations given the pressure field from the previous time step using (18). Next, the implicit pressure equation and the explicit velocity correction are solved iteratively until continuity is satisfied. In both steps, the finite-analytic coefficients C_{nb} are updated in each iteration, thus retaining the nonlinear nature of the RaNS equations.

Solution Domains and Boundary Conditions

In terms of the notation of figure 1, the boundary conditions are as follows.

For sd: on the top and bottom surfaces S_sd1,

$$U = U_e, \quad \frac{\partial V}{\partial y} = -\frac{\partial U_e}{\partial x}$$

$$p = -\int \left(\frac{\partial U_e}{\partial t} + U_e \frac{\partial U_e}{\partial x} + V_e \frac{\partial U_e}{\partial y} \right) dx \tag{19}$$

where irrotationality has been assumed so that the velocity derivatives in the evaluation of the pressure can be prescribed by the data and the upstream lower corner of the sd boundary (see figure 1) is fixed at an instantaneous reference pressure defined as the volume average over the computational domain [27]

$$p_{ref} = \frac{\int p d V}{V} \tag{20}$$

on the inlet S_sd2,

$$U = U_e, \quad V = V_e$$

$$-\frac{\partial p}{\partial x} = \frac{\partial U_e}{\partial t} + U_e \frac{\partial U_e}{\partial x} + V_e \frac{\partial U_e}{\partial y} \tag{21}$$

and on the exit plane S_sd3,

$$\frac{\partial^2 U}{\partial x^2} = 0, \quad \frac{\partial^2 V}{\partial x^2} = 0$$

$$p \rightarrow extrapoloted \tag{22}$$

where U_e and V_e are specified from the data.

For td: on the tunnel walls S_td1,

$$\frac{\partial U}{\partial y} = 0, \quad V = 0, \quad \frac{\partial p}{\partial y} = 0 \tag{23}$$

on the inlet, S_td2,

$$U = U_e, \quad V = V_e$$

$$-\frac{\partial p}{\partial x} = \frac{\partial U_e}{\partial t} + U_e \frac{\partial U_e}{\partial x} + V_e \frac{\partial U_e}{\partial y} \tag{24}$$

where U_e and V_e are a combination of the data (figure 3) and an inviscid model of an internal progressive wave (Appendix A), and on the exit plane S_td3,

$$\frac{\partial^2 U}{\partial x^2} = 0, \quad \frac{\partial^2 V}{\partial x^2} = 0 \tag{25}$$

$$p \rightarrow extrapoloted$$

For cd: on the tunnel walls S_cd1 and on the exit plane S_cd3, (23) and (25) are applied, respectively, on the inlet, S_cd2,

$$U = 1, \quad V = 0, \quad \frac{\partial p}{\partial x} = 0 \tag{26}$$

i.e., uniform flow is assumed, and on the flapper surfaces S_cdf,

$$U = -\alpha_1 \xi \cos(\xi \tau)(y - y_r)$$

$$V = \alpha_1 \xi \cos(\xi \tau)(x - x_r) \tag{27}$$

$$\frac{\partial p}{\partial n} = 0$$

where $\alpha = \alpha_1 \sin(\xi \tau)$ is the flapper angle, (x_r, y_r) is the center of rotation, τ is the nondimensional time, and ξ (= $\omega L / U_o$) is the frequency parameter (or St), which is twice the reduced frequency k (= $1/2\xi$).

Grid Generation

Three grid-generation techniques were used depending on the domain and grid topology. EAGLE [28] was used to generate c-grids for both the foil in sd (figure 2) and the flappers in cd (figure 4). Algebraic h-grids were used for td and cd (figures 3 and 4) with hyperbolic tangent stretching functions and transfinite interpolation such that the grid spacing was controlled along the foil surface, leading and trailing edges, and the flapper wakes. CHIMERA domain decomposition [29,30] was used for cd to resolve the oscillating flappers by decomposing cd into three separate, but coupled domains. Grid-to-grid communication was facilitated through bi-linear interpolation of the flow variables (U,V,p) from the foil grid to the flapper outer boundaries and from the flapper grids to the foil hole boundaries. Holes in the foil grid are created by excluding points that lay within specified boundaries on the flapper grids. Typically, these boundaries are specified such that a three or four point overlap region exists. The interpolation coefficients and holes and hole boundaries were determined a priori for each time step. Figure 4 shows global and detailed views of the overlaid grid system.

The use of oscillating, overlaid grids required modifications of the tridiagonal solver

to incorporate the hole boundary conditions and to solve across hole regions

$$a_i = a_i \bullet IBLANK_i$$
$$b_i = b_i \bullet IBLANK_i + (1 - IBLANK_i)$$
$$c_i = c_i \bullet IBLANK_i \qquad (28)$$
$$d_i = d_i \bullet IBLANK_i + (1 - IBLANK_i) \bullet \varphi_i$$

where $IBLANK$ is 0 for a hole point and 1 for a field point, a_i, b_i, c_i, and d_i correspond to the lower, center, upper diagonals, and right hand side of the tridiagonal matrix, respectively, and φ_i corresponds to the flow variable value inside or on the hole boundary.

MIT FLAPPING-FOIL EXPERIMENT

ffx represents a two-dimensional simulation of propeller-blade and wake flow, i.e., a foil embedded in vertical and horizontal gusts. The gust (i.e., traveling-wave) models the flow experienced by a propeller-blade section as it rotates through the nonuniform hull and/or appendage wake. The purpose of the experiment was to provide detailed measurements for validation of unsteady cfd methods and to provide data for the determination of appropriate Kutta conditions for unsteady potential-flow methods. Details of the experimental objectives, apparatus and procedures are documented in [31-33].

Experimental Geometry , Information, and Uncertainty

The experiments were performed in the closed-loop MIT Variable-Pressure Water Tunnel. The test section is 53 inches long and 20 inches square with a freestream turbulence level of about 1%. The foil is a modified NACA 66 with a chord and span length of 18 and 20 inches, respectively, and was fixed at an angle of attack of 1.18-1.34°. Transition was set at $x = 0.105$ on both sides using 0.050 inch diameter epoxy disks 0.008 inch high separated by 0.050 inch. The flappers are NACA 0025 with a chord and span length of 3 and 19.5 inches, respectively, and are driven by a variable-speed motor, which was designed to operate at reduced frequencies of up to 10. The flappers oscillated with an amplitude of 6° and a frequency of 16 Hz. The corresponding Re based on the foil chord length and reference velocity 20.94 ft/sec is 3.78×10^6 and the reduced frequency is $k = 3.6$

Velocity and surface-pressure measurements were made using a two-component laser Doppler velocimeter and miniature pressure transducers, respectively. For the unsteady measurements, the value at each time step is the ensemble, or phase, average over 250 periods and had a temporal discretization of 180 points over the period.

Prior to the workshop, steady and unsteady (U,V) data was provided on sd boundaries (figure 2) and a large portion of td inlet (figure 3) along with steady boundary-layer profiles. After the workshop, unsteady boundary-layer profiles and pressure data was provided at the locations shown in figure 1.

Experimental uncertainty is due to instrument accuracy, geometric uncertainty, and data processing. The velocity data on sd boundaries has a standard deviation of 0.029 in the streamwise direction and 0.016 in the vertical direction. Standard deviations for the boundary-layer profiles vary from about 0.15 close to the foil surface to about 0.025 at the edge of the boundary layer. The unsteady pressure measurements had a standard deviation of 0.02 based upon absolute pressure. There was some uncertainty in the foil angle of attack due to the difficulty of determining the precise location of the foil in the tunnel. The data was normalized by the velocity at the exit of the contraction measured without the flappers and foil, i.e., 20.94 ft/sec. This presents no problems for sd and td comparisons since they use the data for boundary conditions; however, cd was normalized based on a unit reference inlet value such that the presence of the flappers and foil are included, which results in a 3% lower velocity on S_{td2} in comparison to the data. A similar difference was confirmed by MIT through inviscid-flow predictions.

COMPUTATIONAL GRIDS, CONDITIONS, AND UNCERTAINTY

The grids for sd, td, and cd are shown in figures 2-4, respectively. sd and td grids have 181 x 80 (14,480) and 180 x 179 (32,330) points, respectively. cd has 240 x 179 (42,960) points and 71 x 40 (2840) points for the foil and flappers, respectively, for a total of 48,640. For each domain, approximately 40 points span the boundary-layer and the near-wall grid spacing was set such that the first grid point was located at $y^+ \approx 0.1$.

The experimental values of Re and ξ were used in the calculations. The calculations were made at an angle of attack of 1.34°. An additional td calculation was made for angle of attack 1.18°, which indicated a 2% change in the steady lift. The unsteady solution was unchanged. The solution submitted for the workshop (denoted sd_{orig}) used the data, which was smoothed using a cubic spline and

interpolated both in time and space along sd boundaries using a bi-quadratic polynomial, to evaluate the pressure from (19). However, the coarseness of the data introduced errors in the evaluation of (19) and lead to erroneous results, especially for pressure. Subsequently, a revised sd (denoted sd) used td to provide finer resolution data for the boundary conditions. For td inlet boundary S_{td2}, smoothed and interpolated data provided approximately 60% of the tunnel inflow area and, as previously mentioned, the remaining 40% was specified using a potential-flow approximation. For cd, the boundary-conditions were well-posed and required no special treatment. However, no turbulence model was used in the flapper domains. Lastly, for each domain, transition was fixed by forcing the eddy viscosity upstream of the boundary-layer trip to zero.

Time-step sensitivity studies were conducted for sd which showed that approximately 50 time steps/period provided a time-step independent solution. For sd and td, the time step was 1/50 of a period ($\Delta t = 0.01745$) and for cd, the time step was 1/64 of the period ($\Delta t = 0.01364$). Grid sensitivity studies were conducted for steady flow from which the boundary-layer and near-wall grid spacing described earlier was determined. Resolution of the point distribution in the wake of the flappers for both td and cd was not studied.

The steady-flow solution was used as the starting point for each calculation and typically 2 periods for sd and 4 periods for td and cd were required to attain a periodic solution. Cpu time per period on a CRAY YMP was 15 minutes, 45 minutes, and 2 hours for sd, td, and cd, respectively, and storage requirements ranged from 4 MW for sd to 8 MW for cd. Typically, 25 and 50 iterations were required for the implicit momentum and the pressure-velocity correction steps, respectively, to satisfy the convergence criterion of R < 0.0001, where the residual was defined as

$$R = \max\left\{\sum_{i=1}^{imax}\frac{|U(i,it)-U(i,it-1)|}{imax},\right.$$

$$\left.\sum_{i=1}^{imax}\frac{|V(i,it)-V(i,it-1)|}{imax}\right\}$$

(29)

and i, it, and $imax$ are the grid-point and iteration indices and total number of grid points, respectively.

Uncertainty in the solutions is due to the boundary conditions and truncation errors. For sd and td, the process of using data for boundary conditions introduces errors from smoothing and interpolating, experimental uncertainties, and insufficient spatial resolution. The numerical method is second-order in time and approximately first order in space. Therefore, given $\Delta t \approx 0.01$, the temporal truncation errors are $O(10^{-4})$.

COMPARISON OF SOLUTIONS AND DATA

sd, sd_{orig}, td, $td_{dp/dx}$, and cd results are compared with each other and the data. Comments are made concerning the overall results at the ONR/MIT Unsteady-Flow Workshop and post workshop meetings. The velocity, pressure, shear-stress, and force harmonic amplitude and phase are Fourier analyzed

$$U(x,y,t) = U_o(x,y) + \sum_{n=1}^{20} U_n(x,y)\sin[n\xi t + \gamma_n(x,y)]$$

$$U_n(x,y) = \sqrt{a_n^2 + b_n^2}$$

$$\gamma_n(x,y) = \tan^{-1}\left(a_n\big/b_n\right) \qquad (30)$$

$$a_n = \frac{2}{T}\int_{\tau=0}^{T} U(x,y,\tau)\cos(n\xi\tau)d\tau$$

$$b_n = \frac{2}{T}\int_{\tau=0}^{T} U(x,y,\tau)\sin(n\xi\tau)d\tau$$

where γ_n is with respect to the flapper angle.

Steady Flow (Zeroth Harmonic)

Figure 5 shows td and cd (U_0,V_0) on S_{td2} and S_{sd1} top and bottom, including data. On S_{td2}, cd U_0 shows smaller magnitude and flapper wakes with larger width and deficit than the data and V_0 in agreement. On S_{sd1}, td and data U_0 agree, whereas cd agrees in shape, but under predicts the magnitude. td and cd V_0 are similar, but show an axial decay in comparison to the data.

The surface pressure is shown in figure 6. sd and td are close to the data on the pressure side, but over predict on the suction side. cd is similar on the pressure side and closer to the data on the suction side. The latter is consistent with the lower inlet velocity. Over the adverse pressure-gradient region on the suction side, $td_{dp/dx}$ shows improvement (i.e., closer agreement with the data). The corresponding lift for sd, td, cd, sd_{orig}, and $td_{dp/dx}$ are 0.65, 0.65, 0.60, 0.54, and 0.63.

705

The wall-shear stress is shown in figure 7. The fixed transition along with a small region of separation on the last 5% on the suction side are displayed. sd and td agree, but cd shows lower values.

The steady velocity profiles are shown in figure 8. The solutions agree with the data, except near the trailing edge, where $td_{dp/dx}$ shows improvement, especially on the suction side. The change in the zero-gradient values of C_{kleb} and C_{cp} had a larger influence than the $\bar{\beta}$ corrections. cd shows a consistent 3% under prediction outside the boundary layer Wall-coordinate profiles of the data [34] indicate extensive regions of transitional flow on both the pressure (x < 0.76) and suction (x < 0.61) sides, (i.e., unexpected departures for the data from the logarithmic-overlap law) and boundary effects on the near-wall data, which may partly explain the differences between the solutions and data. However, the level of agreement for the solutions without and with the pressure-gradient modifications appears to be a general assessment of the current capabilities of isotropic turbulence models since it is consistent with the overall results reported in the literature.

Unsteady Flow

Figure 5 includes td and cd first-harmonic amplitude (U_1, V_1) and phase $(\gamma_{U1}, \gamma_{V1})$. On S_{td2}, cd agrees in amplitude shape and phase, but under predicts the former magnitude. Also shown are td second-harmonic amplitudes (U_2, V_2), which are large, particularly near the flapper wakes. On S_{sd1} top, td U_1 agrees in magnitude, but lacks the spatial oscillations in the data. cd U_1 is under predicted, but displays similar spatial oscillations as the data. td V_1 agrees in magnitude and shape and cd V_1 in magnitude with the data. On S_{sd1} bottom, both td and cd U_1 show agreement in magnitude, but under predict the spatial oscillations. td and cd V_1 show an axial decay in comparison to the data. The phases are in agreement with the data and show a downstream traveling wave [in the Fourier analysis, the argument of the trigonometric functions $(\xi t + \gamma)$ is equivalent to characteristic lines $\xi(t \pm x/c)$, which corresponds to downstream$(\gamma = -\xi x/c)$ or upstream$(\gamma = +\xi x/c)$ traveling waves].

Figures 9 and 10 show the lift and drag time histories. The magnitudes are similar; however, sd, td, and $td_{dp/dx}$ indicate a second harmonic, whereas cd is primarily first harmonic, and sd_{orig} shows large oscillations. There are larger differences for ΔC_D than ΔC_l

Figure 11 shows the surface-pressure first- and second-harmonic amplitude and phase. In comparison to the data, sd, td, and $td_{dp/dx}$ show amplitudes of similar magnitude. The shapes and zero values at certain x/L are different and unconfirmed by the limited data. $td_{dp/dx}$ shows improvement. The large second harmonic is consistent with the lift and drag and was attributed by MIT to an excited mode of tunnel vibration [33]. Recall the large td second-harmonic amplitudes on S_{td2}. cd first-harmonic amplitude is larger than the others and cd second-harmonic amplitude, the latter of which is similar to the others. This trend is consistent with the lift and drag. On both sides, cd and $td_{dp/dx}$ indicate increasing phase (i.e., upstream traveling wave), whereas sd and td indicate nearly constant values with 180° changes at the zero-value locations. The limited data indicate constant phase with no particular agreement with the solutions.

Figure 12 shows the wall-shear stress first- and second-harmonic amplitude and phase. The solutions show amplitudes of similar magnitude for both harmonics. The first-harmonic phases indicate: on the pressure side, decreasing values (i.e., downstream traveling wave) on the forebody and upstream traveling wave on the afterbody for sd, td, and $td_{dp/dx}$ and vice versa for cd; and on the suction side, downstream traveling wave for sd and td, cd similar to the pressure side, and upstream traveling wave for $td_{dp/dx}$. The second-harmonic phases indicate: on the pressure side, nearly constant values with 180° changes at the zero-value locations for sd, td, and cd and upstream traveling wave for $td_{dp/dx}$; and on the suction side, nearly constant values with 180° changes at the zero-value locations for sd, td, and $td_{dp/dx}$ and upstream taveling wave for cd.

The velocity first-harmonic amplitude and phase (U_1, γ_{U_1}) profiles are also shown in figure 8. Both the solutions and data indicate, for $x \leq 0.784$ (pressure side) and $\leq .9$ (suction side), amplitudes with small overshoots and phases with increasing lags with x and smooth transition across the boundary layer, whereas for x greater than these values, amplitudes and phases with a two-layer structure: relatively constant values of different magnitude for the inner and outer flows with a zero amplitude and 180° phase shift at the inner/outer boundary (i.e., boundary-layer thickness). The magnitudes are close to the data and $td_{dp/dx}$ shows improvement, especially near the trailing edge. In the wake, the solutions show large differences, especially near the wake centerline. sd, sd_{orig}, and td have a smaller amplitude near the centerline and a larger amplitude outside the boundary layer in

706

comparison to cd and and $td_{dp/dx}$, which show large overshoots. Initially, the phase shows a continuation of the boundary-layer response and then by $x = 1.1$, leads for sd, td, and $td_{dp/dx}$ and lags for cd and sd_{orig} on the pressure side and leads on the suction side.

Figure 13 shows axial-velocity contours for sd, td, and cd at $t = 0$. The difference in the domain size, consistency between the solutions, and wavy nature of the flow are evident. cd shows continuity across the overlaid-grid region and flapper wakes that are wider than td, which indicates almost zero width.

The solutions are similar in showing overall good agreement with the data, except for sd_{orig} unsteady lift and drag; however, detailed differences are evident between the solutions and the data. Since $td_{dp/dx}$ showed improvement, it alone will be used for further discussion.

Figure 14 shows the perturbation-velocity (i.e., difference between steady and unsteady) time-history contours, which vividly exhibit the features described with regard to the first-harmonic velocity profiles and data. $td_{dp/dx}$ trends are smoother, due to the coarseness of the data (13 points across the boundary layer).

Figure 15 shows the perturbation velocity vectors and particle traces at various time steps. The interaction between the flapper-induced vortices and foil is complex: distortion and increased speed on the suction ($c = 1.26$) vs. the pressure ($c = 1.05$) side such that 5 vs. 4 vortices are observed; and secondary counter-rotating vortices near the trailing edge and in the wake. The latter directly correlate with and explicate the region where the first-harmonic velocity profiles displayed the two-layer structure.

At the ONR/MIT Unsteady-Flow Workshop [35] and post workshop meetings, ten groups from naval laboratories (DTMB & NRL) and universities (Iowa, Cincinnati, Minnesota, Mississippi State, Penn State, VPI) submitted solutions using a variety of methods (inviscid, boundary-layer, and RaNS) and domains (sd, td, and cd). There were differences/difficulties between/with the solutions for both steady and unsteady flow: the groups using sd had similar problems; the steady lift ranged from 0.54 to 0.70; inability to predict the details of the steady separation; and the unsteady-flow trends varied considerably. However, three groups, Iowa, MSU [36], and PSU [37] had the best results of a similar encouraging level of agreement with the data.

ANALYSIS AND ANALOGY TO STOKES LAYERS

The results are further analyzed through discussion of the relationship between the flow pattern and axial pressure gradient. The analogy between the present flow and Stokes layers for other idealized geometries is discussed.

Figure 16 shows the perturbation axial pressure-gradient contours at the same time steps as figure 15. Comparison of the figures indicates the direct correspondence between the flow pattern and axial pressure gradient, i.e., the flow directions are consistent with the regions of favorable and adverse gradients. The complexity of the wake is evident, including higher harmonics and upstream and downstream traveling waves over the foil and in the near wake and in the intermediate wake, respectively. The upstream traveling waves are consistent with the surface-pressure first-harmonic phase.

The nature of this correspondence can be explicated by solving the axial Euler equation [i.e., (2) without the viscous and Reynolds-stress terms] for the axial pressure gradient and evaluating the relative importance of the various terms using Fourier analysis

$$U(x,y,t) = U_0(x,y)$$
$$+U_1(x,y)\sin(\xi t + \gamma_{U,1}(x,y))$$
$$+U_2(x,y)\sin(2\xi t + \gamma_{U,2}(x,y))$$
$$V(x,y,t) = V_0(x,y) \qquad (31)$$
$$+V_1(x,y)\sin(\xi t + \gamma_{V,1}(x,y))$$
$$+V_2(x,y)\sin(2\xi t + \gamma_{V,2}(x,y))$$

and $td_{dp/dx}$. Corresponding to orders U_o, U_1, and U_2, $2 + 11 + 19 = 32$ terms arise, respectively, which were evaluated along lines $j = 40$ and 185 outside the boundary layer at $y^+ \approx 10^4$ (figure 17a). In the latter cases, three terms are dominant, one from the temporal and two from the convective acceleration, such that

$$-\frac{\partial P}{\partial x} = P_{x,0} + \sum_{n=1}^{2} P_{x,n} \sin(n\xi t + \gamma_{U,n} + \hat{\gamma}_{px,n}) \quad (32)$$

where

$$P_{x,n} = \sqrt{\left(nU_n\xi + U_0U_n\frac{\partial\gamma_{U,n}}{\partial x}\right)^2 + \left(U_0\frac{\partial U_n}{\partial x}\right)^2}$$

$$\hat{\gamma}_{P_{x,n}} = \tan^{-1}\left(\frac{nU_n\xi + U_0U_n\frac{\partial\gamma_{U,n}}{\partial x}}{U_0\frac{\partial U_n}{\partial x}}\right) = \tan^{-1}(A) \quad (33)$$

and $\hat{\gamma}_{p_{x,n}}$ is with respect to $\gamma_{U,n} \approx -n\xi x/c$. Three cases are of particular interest: (1) $U_n \neq U_n(x)$ (i.e., $U_{x,n} = 0$) such that $A = \pm \infty$ and $\hat{\gamma}_{p_{x,n}} = \pm \pi/2$, where $+$ corresponds to a lead (i.e., temporal wave with $c \to \infty$) and $-$ to a lag (i.e., spatial wave with $c \to 0$); and (2) $U_n \approx ax$ (i.e., $U_{x,n} = a$) such that A and $\hat{\gamma}_{p_{x,n}} = 0$; and (3) $U_n \approx \sin(n\xi xB/c)$ (i.e., $U_{x,n} \approx \cos(n\xi xB/c)$) such that $A \approx \tan(n\xi xB/c)$ and $\hat{\gamma}_{p_{x,n}} \approx n\xi xB/c$, where $B = 1$ (i.e., U_n primarily first harmonic) corresponds to a temporal wave and $B \approx 2$ (i.e., U_n primarily second harmonic) an upstream traveling wave.

Figure 17b shows the velocity first- and second-harmonic amplitudes along j=40 and 185. The former is primarily second harmonic on the foil (i.e., case 3) and linearly decreasing in the wake (i.e., case 2), which is consistent with figure 5. Figure 17c indicates $B = 1.2$ and 1.8 on the pressure and suction sides, respectively, i.e., upstream traveling waves, which is consistent with figures 11 and 16. The latter is primarily third and second harmonic on the pressure and suction sides, respectively, on the foil and nearly zero in the wake.

Figure 17d shows the displacement-thickness first-harmonic amplitude. Similar spatial oscillations as U_1 are observed, but with relatively larger values in the near wake. The maximum value coincides with the location where $\hat{\gamma}_{p_{x,1}}$ changes from upstream vs. zero phase, which suggests viscous-inviscid interaction as the mechanism for the pressure-gradient response.

Figure 18 shows the velocity, pressure, and pressure-gradient first-harmonic phase for the outer ($y^+ \approx 10^4$), overlap ($y^+ \approx 200$), and sub-layer ($y^+ \approx 0.1$) regions. The pressure-gradient phase was obtained by differentiation of the pressure and, additionally, the outer region also includes the Euler-equation solution (33). The pressure and pressure gradient indicate upstream traveling waves. At the outer region, close agreement is shown between the two pressure gradients, which validates the Euler-equation analysis. On the foil in the outer and overlap regions, the velocity shows a downstream traveling wave, whereas in the sub-layer region it follows the pressure gradient, which is consistent with the wall-shear stress. In the wake, the velocity shows a downstream traveling wave.

Figure 19 shows the velocity first harmonic amplitude and phase in wall-coordinates. The largest overshoots occur near $y^+ \approx 1000$, where the phase abruptly changes from the outer to inner

values. The amplitudes display a double-peak across the boundary layer and the phase is constant in the sub-layer. The large change in phase shown in the overlap region ($10 < y^+ < 1000$) correspond to the lags shown in the velocity profiles. The role of the turbulence model vs. physics for the sub-layer region is unknown, as no data is available.

In conclusion, ffx physics are complex with analogy to Stokes layers (i.e., overshoots and phase shifts) for temporal, spatial, and traveling horizontal-wave external flows [10,38,39]. The latter study has shown the differences/similarities between these flows and that the response for the latter two is extreme due to nonlinearities induced by the convective acceleration such that further study is required, especially to document the nature of the interaction between the mean and turbulent motions. The present work supports this conclusion and, moreover, displays the additional complexity for combined vertical and horizontal waves.

CONCLUDING REMARKS

A time-accurate unsteady viscous-flow method has been validated through calculations and comparisons with the Massachusetts Institute of Technology flapping-foil experiment. Solutions were obtained using a small domain surrounding the foil, a tunnel domain that included the foil and the tunnel walls, and a complete domain that included the foil and both the tunnel walls and the upstream flappers. The latter case involved the use of the CHIMERA overlaid-grid method. The three solutions gave similar overall agreement for both steady and unsteady flow, which demonstrates that such problems can be handled with a variety of formulations, although the boundary data, CPU time, and storage requirements are quite different. The physics are complex with analogy to Stokes layers and are explicated through analysis of the axial pressure gradient, which exhibits upstream and downstream traveling waves over the foil and in the near wake and in the intermediate wake, respectively, due to nonlinearities induced by the convective acceleration and steady/unsteady interactions. The nature of the unsteady displacement thickness suggests viscous-inviscid interaction as a possible mechanism for the axial pressure-gradient response.

Future work involves a parametric study for the ffx geometry for combined- and vertical-wave inflows (Appendix A) to determine the effects of frequency and extensions for realistic unsteady propeller/hull/appendage flows.

REFERENCES

1. Fage, A. and Johansen, F.C., "On the Flow of Air Behind an Inclined Flat Plate of Infinite Span," Proc. Royal Society A, Vol. 116, 1927, pp. 170-197.

2. Tyler, E., "Vortex Formation Behind Obstacles of Various Sections," Philosophical Magazine, Vol. 11, No. 7, 1931, pp. 849-891.

3. Bearman, P.W. and Graham, J.M.R., "Vortex Shedding from Bluff Bodies in Oscillatory Flow: a Report on Euromech 119," J. Fluid Mech., Vol. 99, pp. 225-245.

4. Shirayama, S., "Flow Past a Sphere: Topological Transitions of the Vorticity Field," AIAA J., Vol. 30, No. 2, 1992, pp. 349-366.

5. Perry, A.E. and Watmuff, J.H., "The Phase-Averaged Large-Scale Structures in Three-Dimensional Turbulent Wakes," J. Fluid Mech., Vol. 103, pp. 38-51.

6. Theodorsen, T, "General Theory of Aerodynamic Instability and the Mechanism of Flutter," NACA Report No. 496, 1934.

7. McCroskey, W.J., "Unsteady Airfoils," Ann. Rev. Fluid Mech., Vol. 14, 1982, pp. 285-311.

8. Ghia, K.N., Yang, J., Ghia, U. and Osswald, G., "Analysis of Dynamic Stall Phenomenon through Simulation of Forced Oscillatory Flows," Proc. 5th Symp. on Numerical and Physical Aspects of Aerodynamic Flows, Long Beach, CA, 1992.

9. Ohmi, K., Coutanceau, M., Loc, T.P., and Dulieu, A., "Vortex Formation around an Oscillating and Translating Airfoil at Large Incidences," J. Fluid Mech., Vol. 211, 1990, pp.37-60.

10. Telionis, D.P., Unsteady Viscous Flow, New York, Springer-Verlag, 1981.

11. Commerford, G.L. and Carta, F.O., "Unsteady Response of a Two-Dimensional Airfoil at High Reduced Frequency," AIAA J., Vol. 12, No. 1, 1974, pp. 43-48.

12. Griffin, O.M. and Hall, M.S., "Review-Vortex Shedding Lock-on and Flow Control in Bluff Body Wakes," ASME J. Fluids Engineering, vol. 113, no. 4, 1991, pp. 526-537.

13. Katz, Y., Nishri, B., and Wygnanski, I., "The Delay of Turbulent Boundary Layer Separation by Oscillatory Active Control," AIAA 2nd Shear Flow Conference (AIAA 89-0975), Tempe, AZ, 1989.

14. Favier, D., Maresca, Ch., and Castex, A., "Experimental Study of 2D/3D Interactions Between a Vortical Flow and a Lifting Surface," Eur. J. Mech., B/Fluids, Vol. 8, No. 5, 1989, pp. 397-430.

15. Srinivasan, G.R., McCroskey, W.J. and Baeder, J.D., "Aerodynamics of Two-Dimensional Blade-Vortex Interaction," AIAA J., Vol. 24, No. 10, 1986, pp-1569-1576.

16. Rai, M.M., "Three-Dimensional Navier-Stokes Simulations of Turbine Rotor-Stator Interaction; Part II-Results," J. Propulsion, Vol. 5, No. 3, 1989, pp. 312-319.

17. Huerre, P. and Monkewitz, P.A., "Local and Global Instabilities in Spatially Developing Flows," Ann. Rev. Fluid Mech., Vol. 22, 1990, pp. 473-537.

18. Stern, F., Kim, H.T., Zhang, D.H., Toda, Y., Kerwin, J., and Jessup, S., "Computation of Viscous Flow around Propeller-Body Configurations: Series 60 C_B = .6 Ship Model," to appear, J. Ship Research.

19. Kim, H.T. and Stern, F., "Viscous Flow around a Propeller-Shaft Configuration with Infinite-Pitch Rectangular Blades," J. Propulsion Vol. 6, No. 4, 1990, pp. 434-444.

20. Stern, F., Zhang, D.H., Chen, B., Kim, H.T., and S.D. Jessup, "Computation of Viscous Flow around Propeller-Shaft Configurations," to appear, Proc. 20th ONR Symposium on Naval Hydrodynamics, Santa Barbara, CA, August 1994.

21. Kim, W.J., Chen, B. and Stern, F., "Efficient Unsteady Three-Dimensional Viscous-Flow Method with Application to Marine Propulsors," to appear, Proc. 20th ONR Symposium on Naval Hydrodynamics, Santa Barbara, CA, August 1994.

22. Paterson, E.G., "Computation of Natural and Forced Unsteady Viscous Flow," Ph.D. thesis, The Univerity of Iowa, expected May 1994.

23. Chen, H.C. and Patel, V.C., "Calculation of Trailing-Edge, Stern and Wake Flows by a Time-Marching Solution of the Partially-

Parabolic Equations," IIHR Report No. 285, Iowa Institute of Hydraulic Research, 1985.

24. Rodi, W. and Srinivas, K., "Computation of Flow and Losses in Transonic Turbine Cascades," Z. Flugwiss. Weltraumforsch, vol. 13, 1989, pp. 101-119.

25. Cebeci, T., Clark, R.W., Chang, K.C., and Halsey, N.B., "Airfoils with Separation and the Resulting Wakes," Proc. 3rd Symp. on Numerical and Physical Aspects of Aerodynamic Flows, Long Beach, CA, 1985.

26. Granville, P.S., "Baldwin-Lomax Factors for Turbulent Boundary-Layers in Pressure Gradients," AIAA J., Vol. 25, No. 12, 1987, pp. 1624-1627.

27. Roache, P.J., Computational fluid dynamics, Albuquerque, Hermosa publishers, 1972, pp. 184-185.

28. Thompson, J.F., "A Composite Grid Generation Code for General 3-D Regions," AIAA 25th Aerospace Sciences Meeting, Reno, NV, 1987.

29. Benek, J.A., "Extended Chimera Grid Embedding Scheme with Applications to Viscous Flows," AIAA 8th Computational Fluid Dynamics Conference, 1987, Honolulu.

30. Suhs, N.E., and Tramel, R.W., "PEGSUS 4.0 User's Manual," Arnold Engineering Development Center, AEDC-TR-91-8, 1991.

31. Rice, J.Q., "Investigation of a Two-Dimensional Hydrofoil in Steady and Unsteady Flows," M.S. Thesis, Massachusetts Institute of Technology, 1991.

32. Delpero, P.M., "Investigation of Flows around a Two-Dimensional Hydrofoil Subject to a High Reduced Frequency Gust Loading," M.S. Thesis, Massachusetts Institute of Technology, 1992.

33. Horwich Lurie, B. "Unsteady Response of a Two-Dimensional Hydrofoil Subject to High Reduced Rrequency Gust Loading," M.S. Thesis, Massachusetts Institute of Technology, 1993.

34. Chung, K.N., "Applications of a Zonal Approach and Turbulence Models to Foils and Marine Propellers," Ph.D Thesis, The University of Iowa, December 1993.

35. Fuhs, D., "Comparisons of Two-Dimensional Unsteady RaNS Calculations and Measurements," Carderock Divsison, Naval Surface Warfare Center report (in preparation).

36. Taylor, L.K., Busby, J.A., Jiang, M.Y., Arabshahi, A., Sreenivas, K., Whitfield, D.L., "Time-Accurate Incompressible Navier-Stokes Simulation of the Flapping Foil Experiment," Sixth International Conference on Numerical Ship Hydrodynamics, Iowa City, Iowa, Augst 1993.

37. Fan, S., Lakshminarayana, B., Barnett, M., "Low-Reynolds-Number k-ε Model for

Unsteady Turbulent Boundary-Layer Flows," AIAA J., Vol. 31, No. 10, 1993, pp. 1777-1784.

38. Patel, M.H., "On Laminar Boundary Layers in Oscillatory Flow," Proc. R. Soc. Lon. A, Vol. 347, 1975, pp. 99-123.

39. Choi, J.E., "Role of Free-Surface Boundary Conditions and Nonlinearities in Wave Boundary Layer and Wake Interaction," Ph.D Thesis, The University of Iowa, December 1993.

Appendix: A: Tunnel domain inflow, potential flow model

The inflow is divided into three regions: (1) between the bottom tunnel wall and the bottom flapper wake; (2) between the flapper wakes; and (3) between the top flapper wake and the top tunnel wall. For (1) and (3) an analogy can be made between the sinuous wake sheet of the oscillating flappers passing over the tunnel walls and a shallow-water wave. The potential flow describing these regions is:

$$U(x,y,t) = 1 \pm U_1 \frac{\cosh\left(\frac{\xi}{c}(2h \mp y)\right)}{\cosh\left(\frac{\xi h}{c}\right)} \cos\left(\xi\left[\frac{x}{c} - t\right]\right)$$

$$V(x,y,t) = -V_1 \frac{\sinh\left(\frac{\xi}{c}(2h \mp y)\right)}{\cosh\left(\frac{\xi h}{c}\right)} \sin\left(\xi\left[\frac{x}{c} - t\right]\right)$$

The region between the flappers (although not used in this paper) is

$$U(x,y,t) = 1 - U_1 \frac{\sinh\left(\frac{\xi y}{c}\right)}{\cosh\left(\frac{\xi h}{c}\right)} \cos\left(\xi\left[\frac{x}{c} - t\right]\right)$$

$$V(x,y,t) = -V_1 \frac{\cosh\left(\frac{\xi y}{c}\right)}{\cosh\left(\frac{\xi h}{c}\right)} \sin\left(\xi\left[\frac{x}{c} - t\right]\right)$$

A study was conducted to compare this model to two other models, one using unsteady, sinusoidal vortex sheets, and one using discrete Oseen vortices convecting at the freestream velocity. The chosen model was easiest to apply and gave the best correlation to the inlet data.
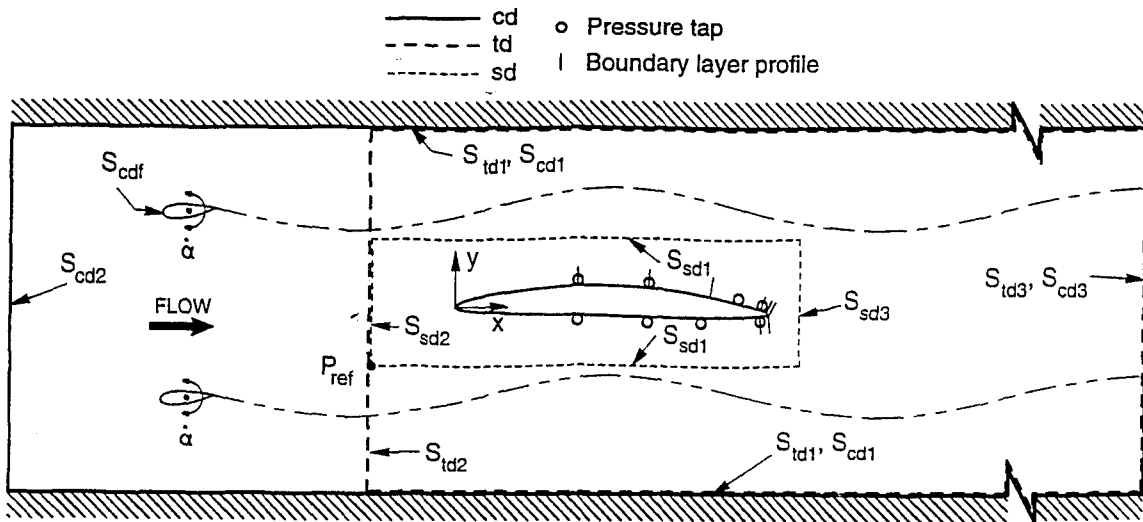
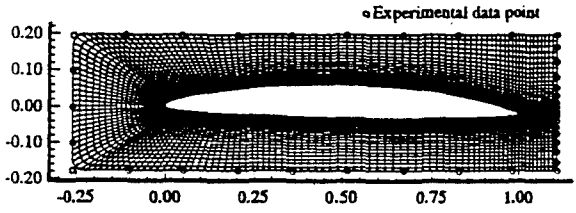Figure 1. Flapping-foil experiment geometry and solution domain boundaries.

Figure 2. Small-domain grid with data locations.
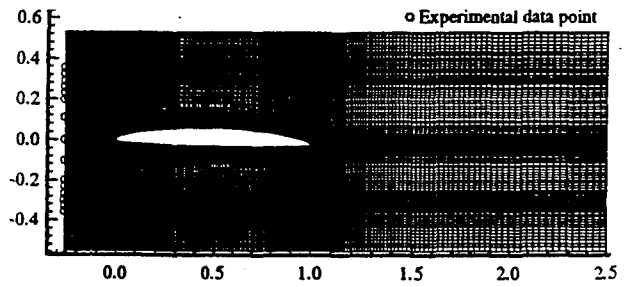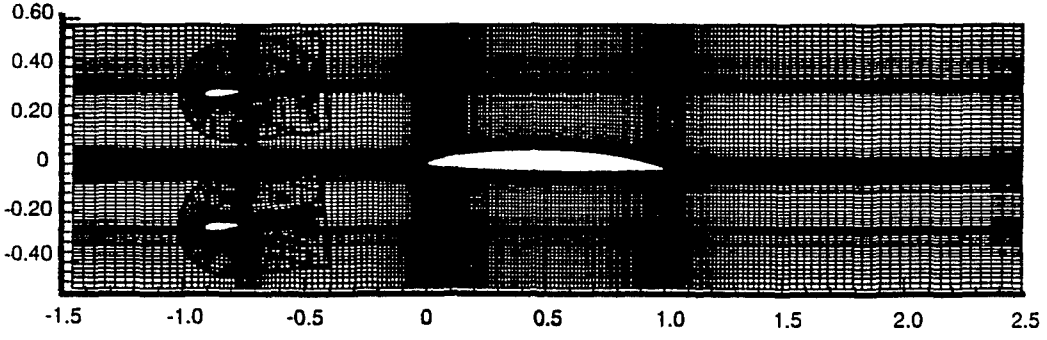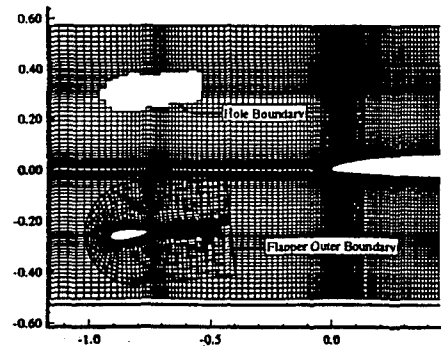

Figure 3. Tunnel-domain grid with data locations.

(a) complete domain

(b) detailed view

Figure 4. Complete-domain grids.

711

○ data ——— cd ---- td

(a) tunnel-domain inlet boundaries

(b) small-domain top boundary

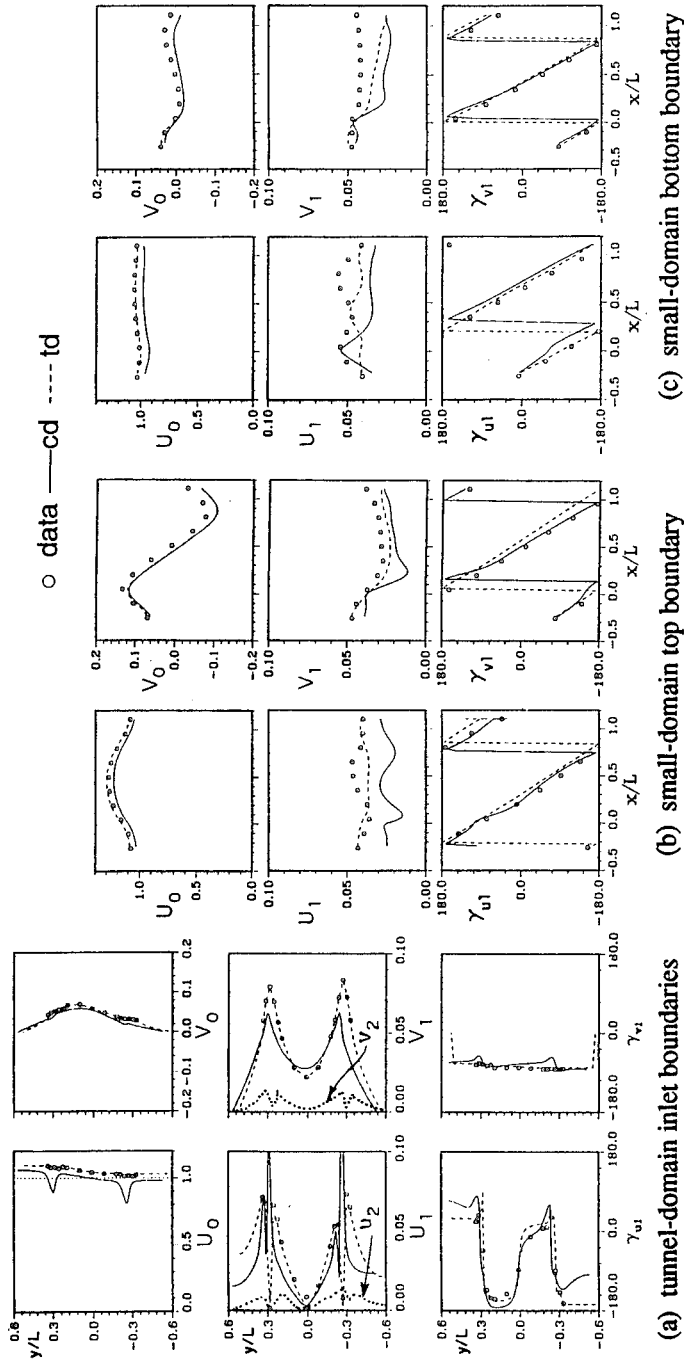**(c) small-domain bottom boundary**

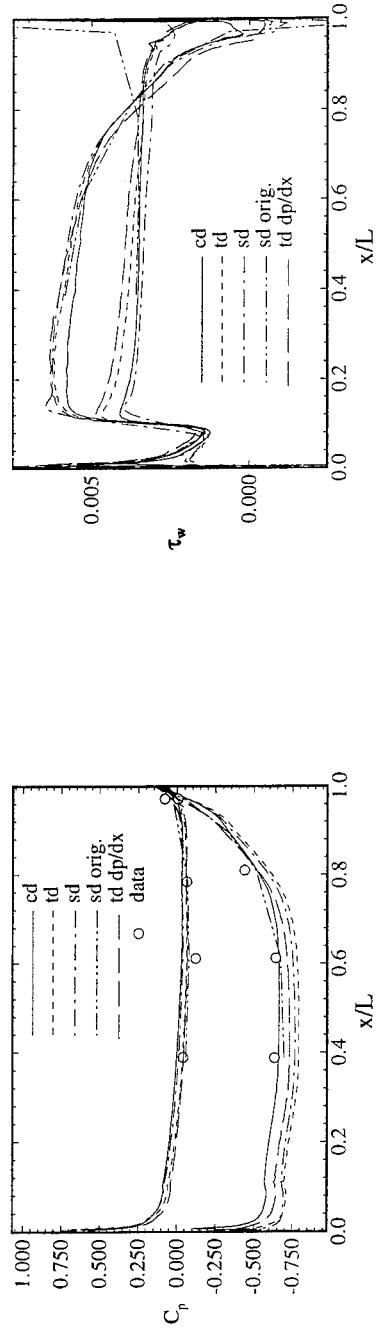Figure 5. Comparison of boundary data and tunnel- and complete-domain solutions.

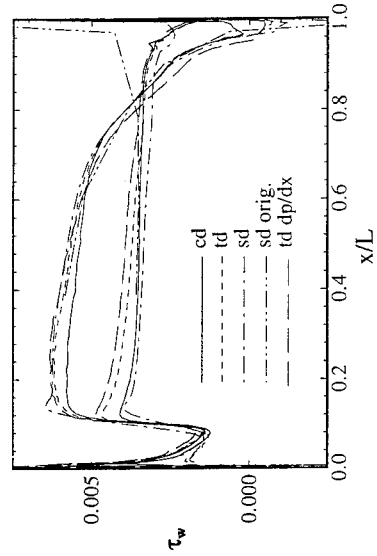Figure 6. Steady surface-pressure distribution: zeroth harmonic.

Figure 7. Steady wall-shear stress distribution: zeroth harmonic.

(a) suction side

(b) pressure side

(c) wake
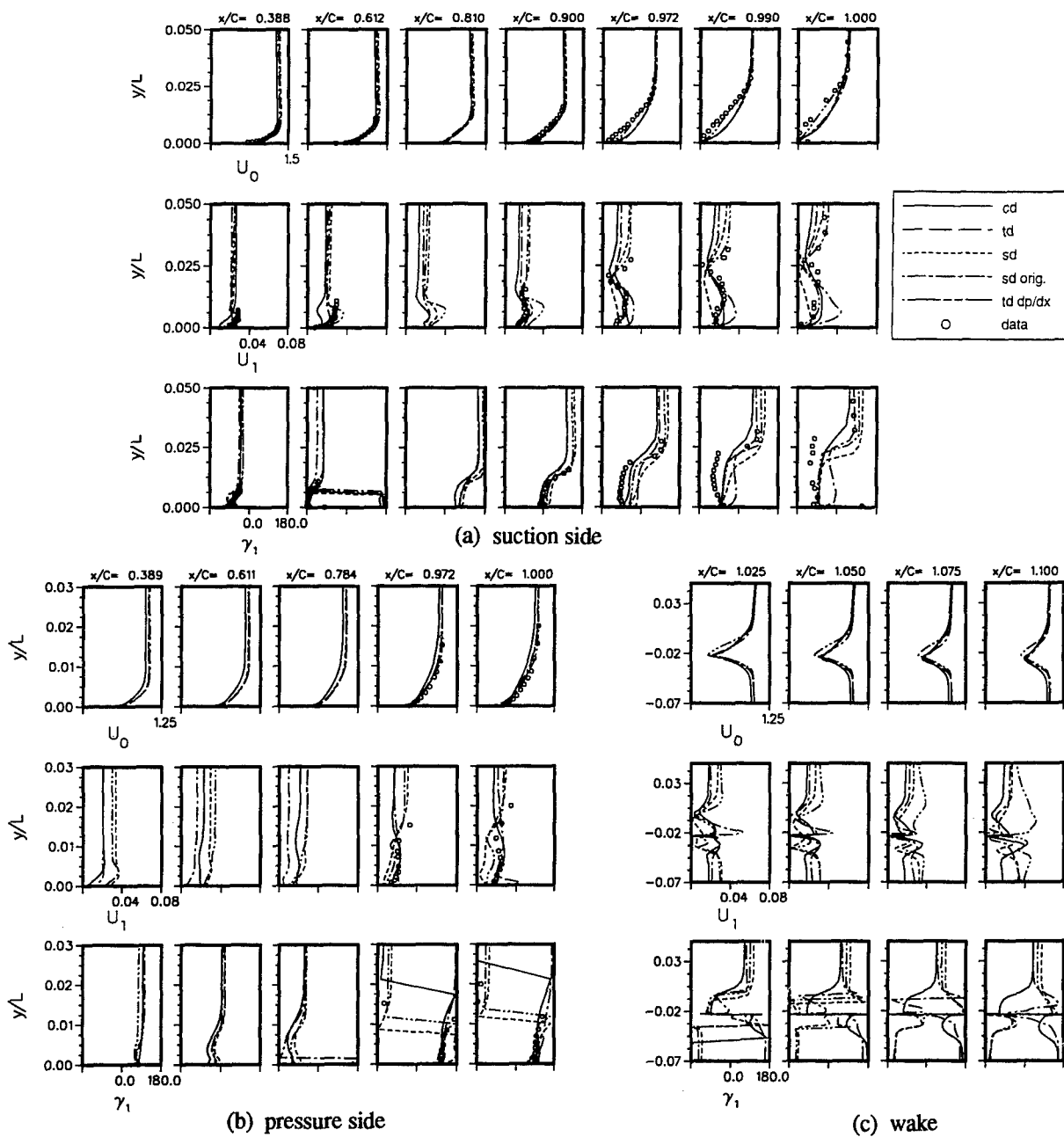
Figure 8. Velocity profiles.

Figure 9. Lift histories.

Figure 10. Drag histories
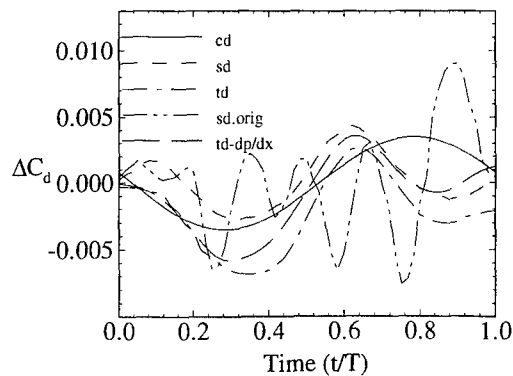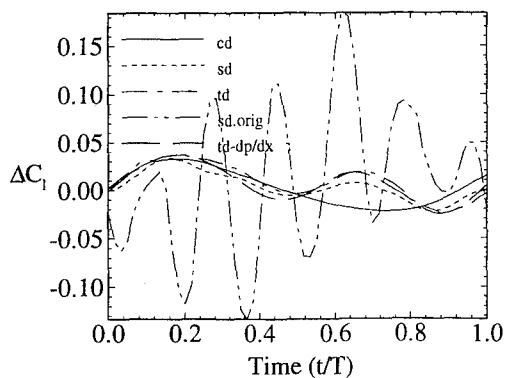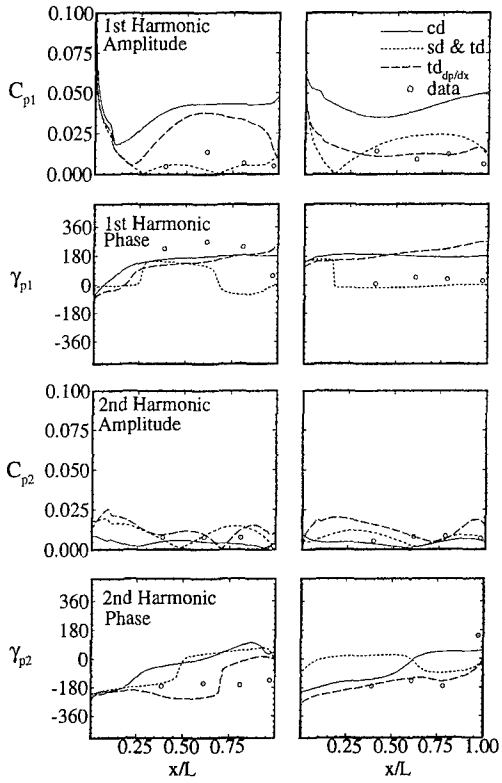
(a) suction side   (b) pressure side

Figure 11. Unsteady surface-pressure distribution: first and second harmonics.
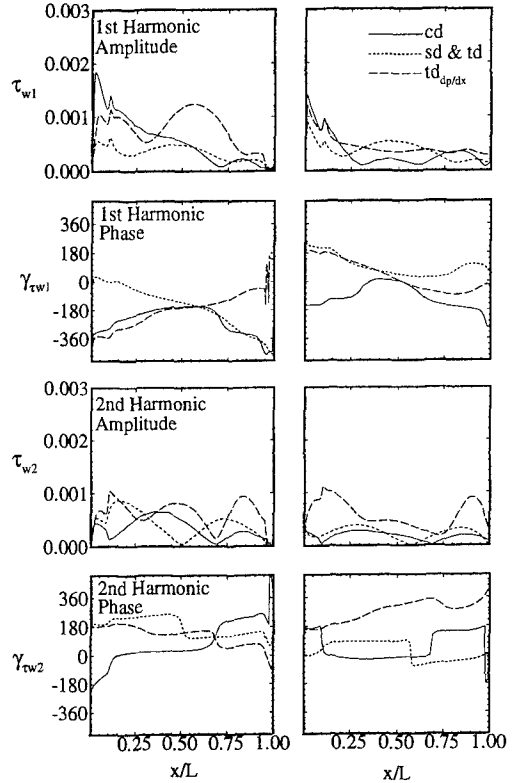
(a) suction side   (b) pressure side

Figure 12. Unsteady wall-shear stress distribution: first and second harmonics.
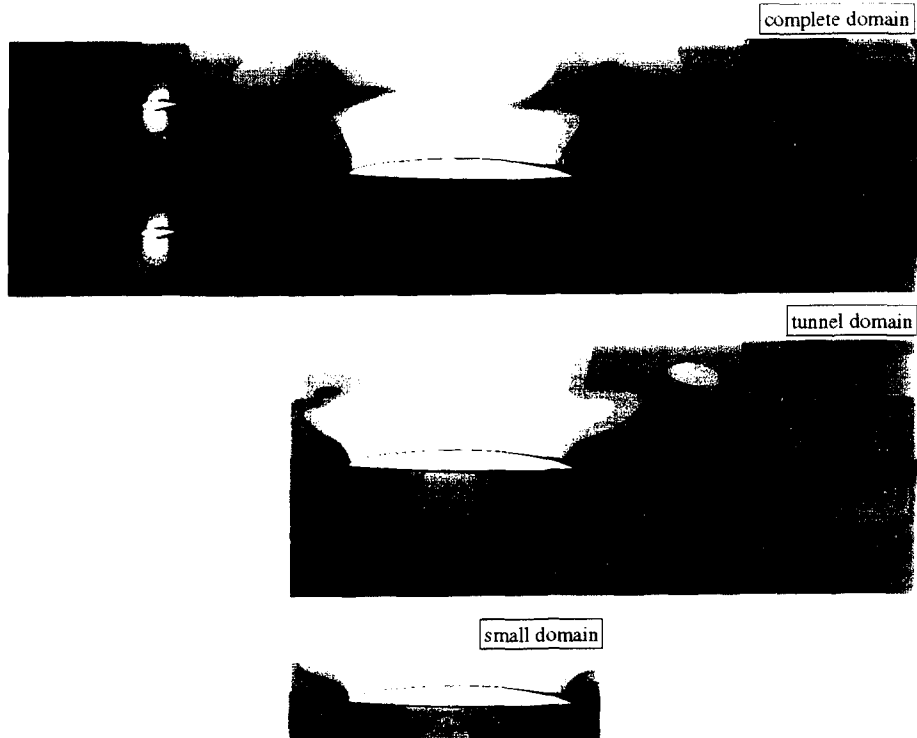
Figure 13. Axial velocity contours: time = 0.0.
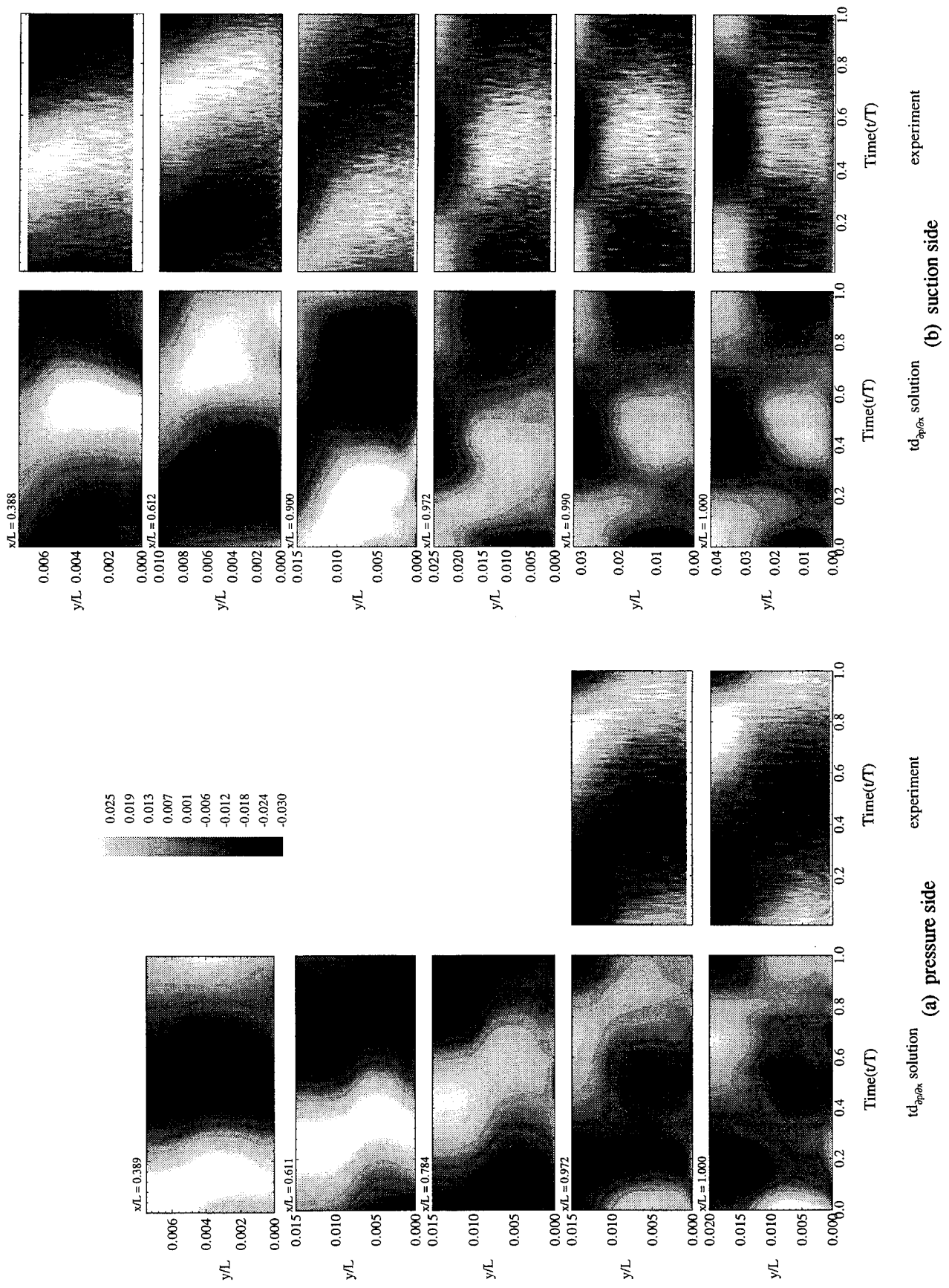
Figure 14. Perturbation-velocity time-history contours.

715

time = 0T

time = 1/5T

time = 2/5T

time = 3/5T

time = 4/5T

(a) overall view

(b) trailing-edge and wake details
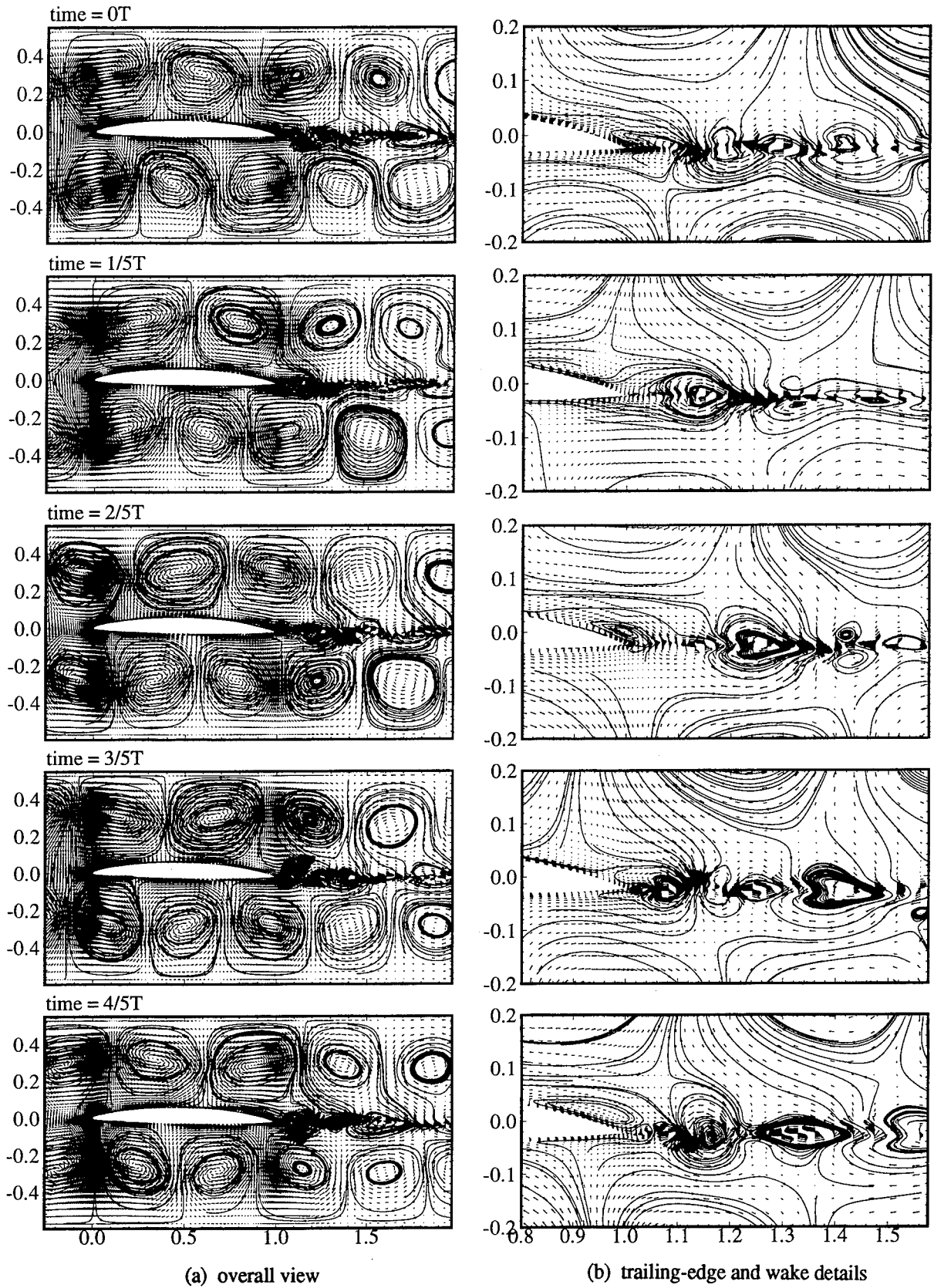
Figure 15. Perturbation-velocity vectors and particle traces: $td_{\partial p/\partial x}$ solution.

716

time = 0T

time = 1/5T

time = 2/5T

time = 3/5T

time = 4/5T
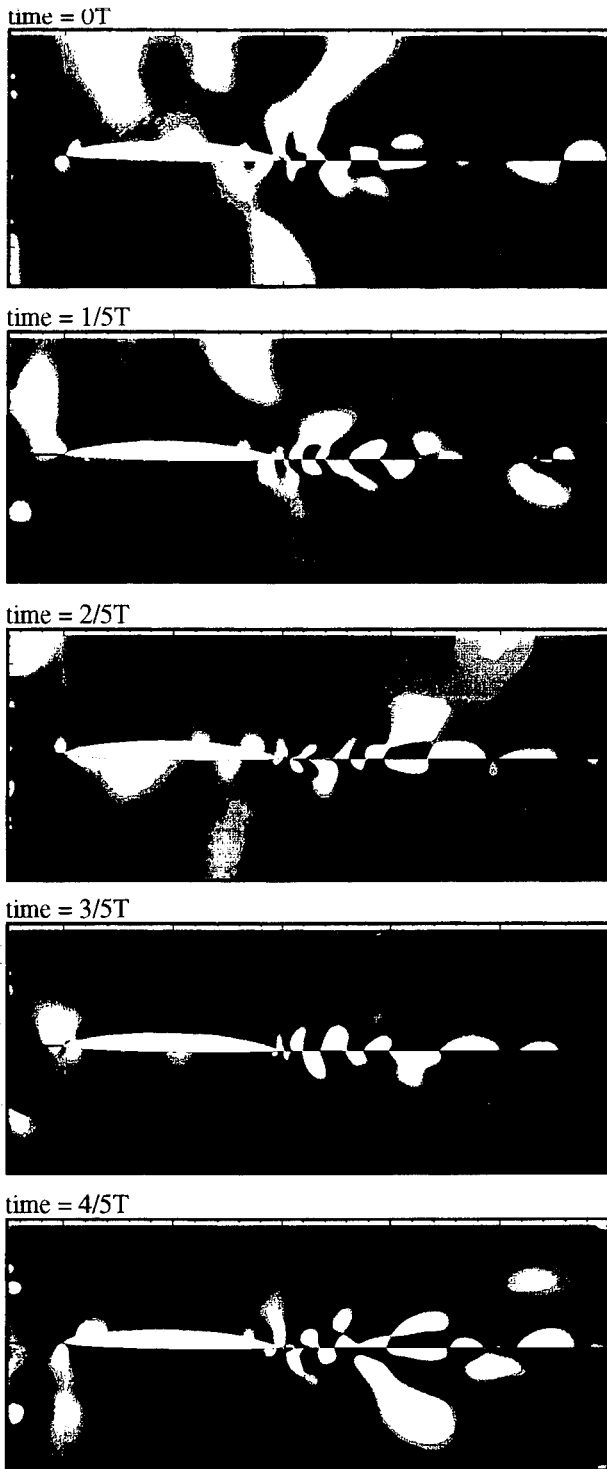
Figure 16. Perturbation axial pressure-gradient contours: $td_{dp/dx}$ solution.

(a) locations

(b) U_1 and U_2

(c) $\tan\left(\hat{\gamma}_{P_{x,1}}\right)$

(d) δ^* first-harmonic amplitude
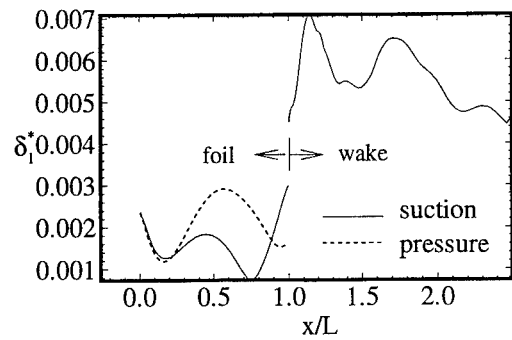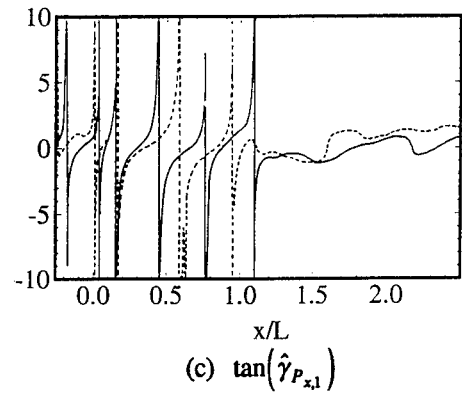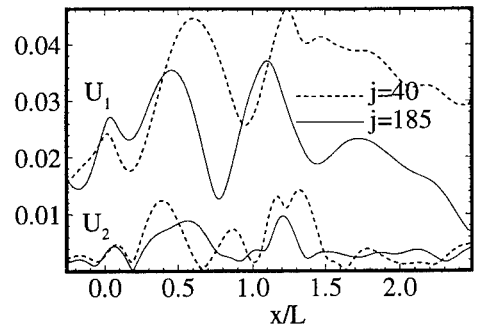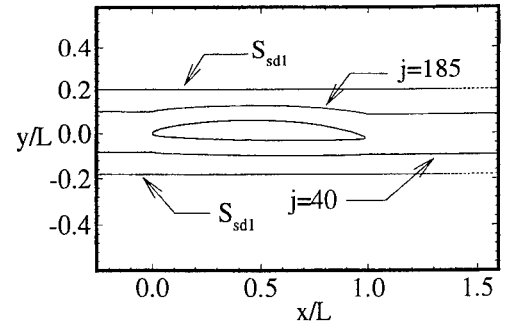
Figure 17. Euler equation analysis

717

Figure 18. Velocity, pressure and pressure-gradient first-harmonic phase
for outer, overlap and sub-layer regions: $td_{dp/dx}$ solution.
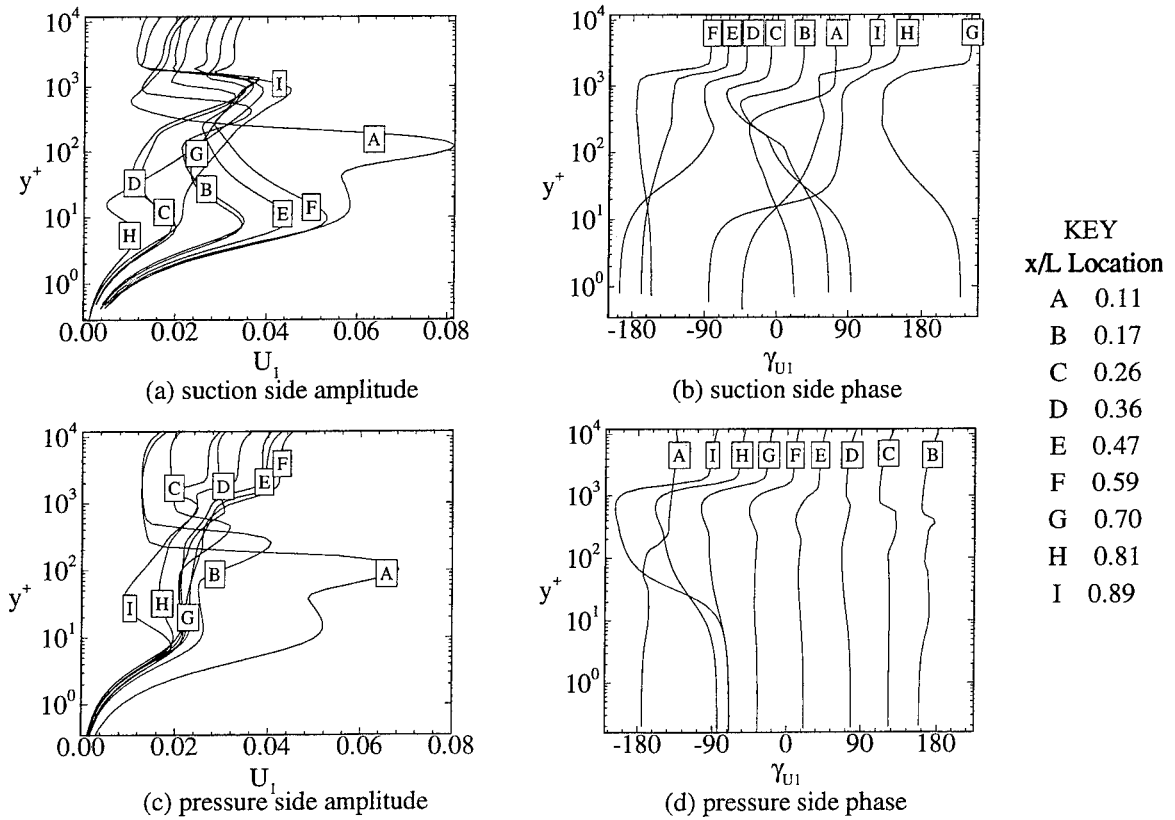
Figure 19. Velocity first-harmonic profiles in wall coordinates: $td_{dp/dx}$ solution.

718

DISCUSSION
by Dr. Ming Zhu, University of Tokyo

First, I would like to congratulate your nice work on the unsteady NS simulation. Please show your Fourier analyses results of field data about the vortex-foil interaction. I would like to know that with your formulation, how much the unsteadiness can be caught.

Authors' Reply

The first twenty harmonics where calculated for the boundary-layer profiles which showed that the frequency content was dominated by the first harmonic. However, the wake of foil showed a much richer frequency content. As far as the temporal resolution of the method is concerned, it is only limited by the time step used in the simulation. Since the method is implicit, fairly large time steps are used, thus making the resolution of higher harmonics difficult. However, if a broadband or higher frequency response was expected, the time step could be reduced such that the frequencies of interest were sufficiently resolved.

DISCUSSION
by Dr. D. H. Choi, Korea Advanced Institute of Science and Technology

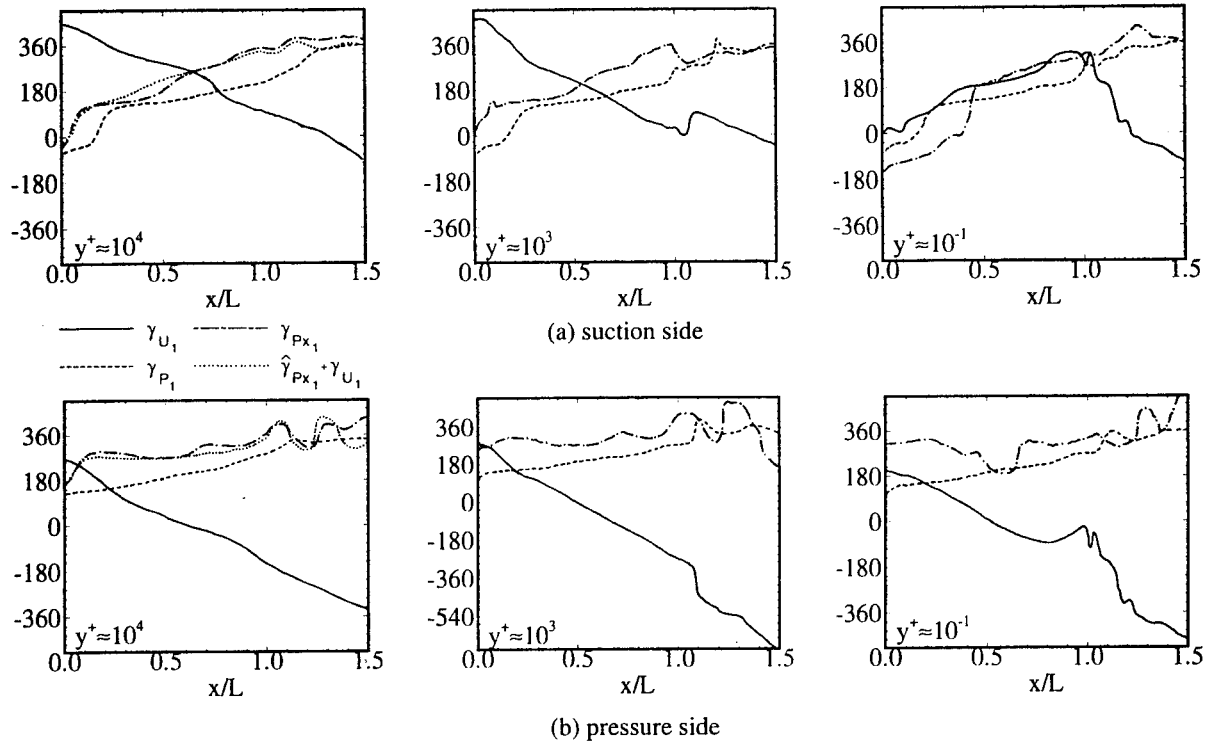The calculations have been performed with three different computational domains. In principle, if the boundary conditions are correct, the small domain solution should be most accurate as it eliminates any uncertainty or inaccuracy associated with outer regions. However, since available experimental data are sparsely distributed, the boundary conditions for the small domain calculation are supplemented by using the tunnel domain calculation. This essentially makes these two calculations identical as the small domain is a sub-domain of the tunnel domain. Therefore, the comparison of the two appears moot.

Authors' Reply

This is exactly the point that we wanted to make. At the ffx workshop, the participants who used the small domain had similarly poor solutions, i.e., erroneous higher harmonics in the pressure field. It was not clear that the small domain could be used for simulation of the ffx.

Therefore, to demonstrate the validity of the small-domain boundary-conditions, the tunnel domain solution was used in place of the data with the intention of making this moot comparison the proof that the formulation was correct.

DISCUSSION
by Dr. Charles C. Song, University of Minnesota

Did you compare the calculated unsteady pressure with experimental value? One should expect large differences between numerical results based on incompressible flow theory and the experiment, especially for higher frequency components.

Authors' Reply

Yes. The differences were large, but were most likely due to difficulties in obtaining accurate unsteady pressure data, not compressibility effects.

Time Accurate Incompressible Navier-Stokes Simulation of the Flapping Foil Experiment

L.K. Taylor, J.A. Busby, M.Y. Jiang, A. Arabshahi, K. Sreenivas, and D.L. Whitfield (CFD Laboratory, USA)

ABSTRACT

A numerical simulation of an experiment conducted in the Marine Hydrodynamics Laboratory at Massachusetts Institute of Technology (MIT) has been performed. The experiment was designed to study the flow about a two-dimensional hydrofoil undergoing high reduced frequency gust loading. The gust was created by two NACA 0025 hydrofoils oscillating sinusoidally in phase upstream of the stationary foil. Experimental data was taken in the flowfield near the stationary foil as well as on the foil itself. The numerical computations were performed on the entire experimental domain, including the flapping foils, through the use of a two-dimensional multiblock unsteady incompressible Navier-Stokes algorithm based on artificial compressibility. A comparison of the pressures and velocities on the bounding box and surface of the stationary foil are presented for the steady case, as well as time histories and an harmonic analysis at the same locations for the unsteady case.

NOMENCLATURE

A, B, $\overline{K}$	Flux Jacobians
$\overline{A}$	Roe Matrix
c_p	Pressure coefficient
E, F, K	Computational space flux vectors
$\hat{e}$, $\hat{f}$	Numerical flux vectors
J	Metric Jacobian
m	Newton iteration parameter
n	Time level index
p	Pressure
Q	Computational space dependent variable vector
q	Physical space dependent variable vector
Re_L	Reynolds number based on reference length
T, T^{-1}	Eigenmatrices
t	Time
u, v	Cartesian velocity components
U, V, θ_k	Contravariant velocities
x, y	Cartesian coordinates
β	Artificial compressibility parameter
∂	Partial differentiation
δ	Central difference operator
μ	Viscosity
ϱ	Density
τ	Time in computational space; fluid stress vector
ξ, η, k	Curvilinear coordinates

* Research Engineer
** Graduate Student
+ Professor

INTRODUCTION

Steady and unsteady computations were made of the MIT/ONR Flapping Foil Experiment [1,2] using the Mississippi State University incompressible Navier-Stokes code [3]. This code is three-dimensional; however, a two-dimensional version was developed for these computations. The artificial compressibility form of the equations is solved on a time-dependent curvilinear coordinate system. The equations are discretized in finite volume form and the numerical flux formulation at cell faces is based on Roe's approximate Riemann solver [4]. The equations are formulated for numerical solution as a formal Newton method where the time derivative of the dependent variable vector, except for the time derivative of pressure in the continuity equation, is included in the residual term. This system is then solved at each time step using what is referred to as discretized Newton-relaxation [5]. Relaxation is carried out at each time step using three symmetric Gauss-Seidel passes. The computations are second-order accurate in time. For steady state solutions, local time stepping is used and the Jacobian matrix is

Figure 1. Experimental Setup
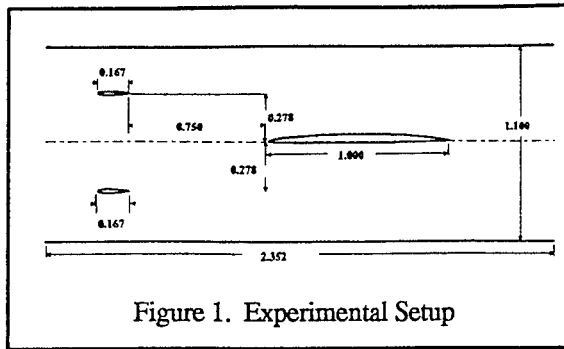
updated every 20 cycles. A Baldwin-Lomax turbulence model is used for all the computations.

The Navier-Stokes code is a multiblock dynamic grid code and the computations are performed using the rather complete configuration consisting of the water tunnel walls, flapping foils, and stationary foil (Figs. 1 and 2). No slip boundary conditions are used on the tunnel walls, flapping foils and stationary foil. A steady state solution is first obtained and then motion of the flapping foils is initiated by boundary conforming dynamic grids that move in pitch with the flapping foils at a reduced frequency of 3.62 based on the half-chord of the stationary foil. The grid extends approximately two stationary foil chord lengths upstream of the leading edge of the stationary foil and five stationary chord lengths downstream of the trailing edge of the stationary foil. (Note that the entire grid is not presented in Fig. 2.) Characteristic variable boundary

Figure 2. Computational Grid
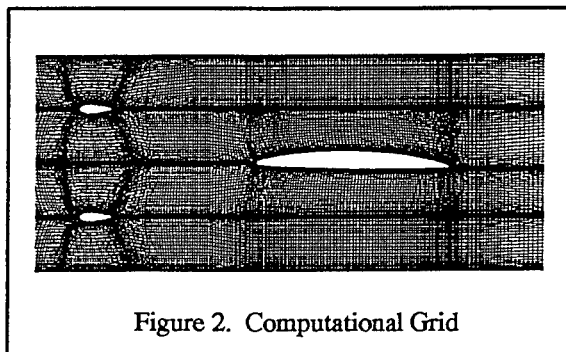
conditions are used at both the upstream inflow boundary and downstream outflow boundary. Velocities are specified at the inflow while static pressure is set at the outflow.

For these multiblock computations, four blocks are used. Block one extends from the lower tunnel wall to the centerline of the lower flapping foil. Block two extends from the top of block one to the centerline of the stationary foil. Block three extends from the

top of block two to the centerline of the upper flapping foil. Block four extends from the top of block three to the upper tunnel wall. All grids are H-type grids. This blocking arrangement allows the multiblock solutions to correspond exactly to a single block solution, even for unsteady flow. That is, there are no approximations at block boundary interfaces.

A presentation of the equations and numerical discretization will be given first, followed by a discussion of the numerical flux formulation and numerical solution method. Then a section containing a description of the stationary and dynamic grids that are used followed by an explanation of the post processing procedures that are necessary to examine the results. Finally, results for both the steady and unsteady cases along with conclusions are presented.

EQUATIONS AND NUMERICAL DISCRETIZATION

Governing Equations

The unsteady two-dimensional incompressible Navier-Stokes equations without body forces are written in Cartesian coordinates and in conservative form. The quantities used to nondimensionalize these equations are, a characteristic length, and freestream values of velocity, density, and viscosity. Pressure is normalized using the following relationship $(p - p_\infty)/\varrho_\infty V_\infty^2$, where the subscript denotes a freestream or reference value (3). The resulting set of nondimensional equations are then transformed to a general time-dependent body-conforming curvilinear coordinate system given by

$$\xi = \xi(x, y, t)$$
$$\eta = \eta(x, y, t) \qquad (1)$$
$$\tau = t.$$

The time-dependent nature of this transformation will allow all computations to be carried out on a fixed uniform computational domain even though components of the physical domain may be in motion.

Artificial compressibility is introduced after the transformation to insure that the continuity equation is satisfied for dynamic grid applications (6). The resulting set of equations may be written as

$$\frac{\partial Q}{\partial \tau} + \frac{\partial (E - E_v)}{\partial \xi} + \frac{\partial (F - F_v)}{\partial \eta} = 0 \qquad (2)$$

where

$$Q = J \begin{bmatrix} p \\ u \\ v \end{bmatrix}$$

$$E = J \begin{bmatrix} \beta(U - \xi_t) \\ uU + \xi_x p \\ vU + \xi_y p \end{bmatrix}, \qquad F = J \begin{bmatrix} \beta(V - \eta_t) \\ uV + \eta_x p \\ vV + \eta_y p \end{bmatrix}$$

$$E_v = J \begin{bmatrix} 0 \\ \tilde{T}_{\xi x} \\ \tilde{T}_{\xi y} \end{bmatrix}, \qquad F_v = J \begin{bmatrix} 0 \\ \tilde{T}_{\eta x} \\ \tilde{T}_{\eta y} \end{bmatrix}$$

and

$$U = \xi_t + \xi_x u + \xi_y v$$

$$V = \eta_t + \eta_x u + \eta_y v$$

$$\tilde{T}_{\xi x} = \xi_x \tau_{xx} + \xi_y \tau_{xy}$$

$$\tilde{T}_{\xi y} = \xi_x \tau_{yx} + \xi_y \tau_{yy}$$

$$\tilde{T}_{\eta x} = \eta_x \tau_{xx} + \eta_y \tau_{xy}$$

$$\tilde{T}_{\eta y} = \eta_x \tau_{yx} + \eta_y \tau_{yy}$$

with

$$\tau_{xx} = \frac{2\mu}{Re_L} \left[\left(\xi_x \frac{\partial u}{\partial \xi} + \eta_x \frac{\partial u}{\partial \eta} \right) \right]$$

$$\tau_{yy} = \frac{2\mu}{Re_L} \left[\left(\xi_y \frac{\partial v}{\partial \xi} + \eta_y \frac{\partial v}{\partial \eta} \right) \right]$$

$$\tau_{xy} = \tau_{yx} = \frac{\mu}{Re_L} \left[\left(\xi_y \frac{\partial u}{\partial \xi} + \eta_y \frac{\partial u}{\partial \eta} \right) + \left(\xi_x \frac{\partial v}{\partial \xi} + \eta_x \frac{\partial v}{\partial \eta} \right) \right]$$

where Re_L is the Reynolds number based on the characteristic length. J is the Jacobian of the inverse transformation $\frac{\partial(x, y, t)}{\partial(\xi, \eta, \tau)}$, given by

$$J = x_\xi y_\eta - y_\xi x_\eta$$

and the metric quantities are

$$\xi_x = J^{-1}(y_\eta)$$

$$\xi_y = J^{-1}(-x_\eta)$$

$$\xi_t = -x_\tau \xi_x - y_\tau \xi_y$$

$$\eta_x = J^{-1}(-y_\xi)$$

$$\eta_y = J^{-1}(x_\xi)$$

$$\eta_t = -x_\tau \eta_x - y_\tau \eta_y.$$

Numerical Discretization

A finite–volume discretization of Eq. (2) in two–dimensional computational space may be written as

$$\frac{\partial Q}{\partial \tau} + \frac{\delta_i(E - E_v)}{\Delta \xi} + \frac{\delta_j(F - F_v)}{\Delta \eta} = 0 \qquad (3)$$

where the indices i, j correspond to a cell center and the central difference operator δ is given by

$$\delta \bullet (\ ) = (\ )_{\bullet + \frac{1}{2}} - (\ )_{\bullet - \frac{1}{2}}. \qquad (4)$$

The increments $\Delta \xi$ and $\Delta \eta$ are set equal to one for simplicity and Eq. (3) becomes

$$\frac{\partial Q}{\partial \tau} + \delta_i(E - E_v) + \delta_j(F - F_v) = 0. \qquad (5)$$

In this expression, the dependent variable vector Q is considered to be constant throughout cell i, j, while the inviscid and viscous fluxes are assumed to be uniform over each of the four surfaces of the cell.

Temporal Discretization

The time derivative appearing in Eq. (5) is approximated with a general difference expression (7), which has been written for computational space, and is given by

$$\Delta Q^n = \frac{\theta_1 \Delta \tau}{1 + \theta_2} \frac{\partial}{\partial \tau}(\Delta Q^n) + \frac{\Delta \tau}{1 + \theta_2} \frac{\partial}{\partial \tau}(Q^n)$$

$$+ \frac{\theta_2}{1 + \theta_2} \Delta Q^{n-1} \qquad (6)$$

where

$$\Delta Q^n = Q^{n+1} - Q^n.$$

The two choices for θ_1 and θ_2 that were used exclusively in this work are $\theta_1 = 1$, $\theta_2 = 0$ and $\theta_1 = 1$, $\theta_2 = 0.5$, which correspond respectively to the backward Euler implicit scheme (first–order accurate in time) and the three point backward implicit

scheme (second-order accurate in time). Using Eq. (5) in Eq. (6) yields

$$\frac{\Delta Q^n - \frac{\theta_2}{1+\theta_2}\Delta Q^{n-1}}{\Delta \tau} + \frac{\theta_1}{1+\theta_2}R^{n+1} \qquad (7)$$

$$-\frac{(\theta_1 - 1)}{1 + \theta_2}R^n = 0$$

where

$$R^* = \left[\delta_i(E - E_v) + \delta_j(F - F_v)\right]^*.$$

In this particular application, the movement of the flapping foils dictate that a new grid must be generated at each time step. This implies that the Jacobian of the inverse transformation will be a function of the nondimensional time τ. The approach suggested by Janus (8) will be used to account for this dependence. First of all, the following two identities are needed:

$$\Delta Q^n = \Delta (Jq)^n \equiv J^{n+1}\Delta q^n + q^n\Delta J^n \qquad (8)$$

$$\Delta Q^{n-1} = \Delta (Jq)^{n-1} \equiv J^{n-1}\Delta q^{n-1} + q^n\Delta J^{n-1}.$$

Inserting Eq. (8) into Eq. (7) and simplifying leads to

$$\frac{\Delta q^n}{\overline{\Delta\tau}^{n+1}} - \frac{\theta_2}{1+\theta_2}\frac{\Delta q^{n-1}}{\overline{\Delta\tau}^{n-1}} + \left[\frac{\Delta J^n - \frac{\theta_2}{1+\theta_2}\Delta J^{n-1}}{\Delta\tau}\right]q^n$$

$$+\frac{\theta_1}{1+\theta_2}R^{n+1} - \frac{(\theta_1 - 1)}{1+\theta_2}R^n = 0 \qquad (9)$$

where

$$\overline{\Delta\tau}^* = \frac{\Delta\tau}{J^*}.$$

According to Janus (8), the evaluation of the bracketed term in Eq. (9) must be done with the same numerical scheme that is used to advance the Navier-Stokes equations in time in order to satisfy the geometric conservation law (9). Toward this end, consider the two-dimensional discretized geometric conservation law,

$$\frac{\partial J}{\partial \tau} + \delta_i(J\xi_t) + \delta_j(J\eta_t) = 0. \qquad (10)$$

Using the temporal discretization given by Eq. (6) yields

$$\frac{\Delta J^n - \frac{\theta_2}{1+\theta_2}\Delta J^{n-1}}{\Delta\tau} \qquad (11a)$$

$$= -\frac{\theta_1}{1 + \theta_2}R_J^{n+1} + \frac{(\theta_1 - 1)}{1+\theta_2}R_J^n$$

where

$$R_J^* = \left[\delta_i(J\xi_t) + \delta_j(J\eta_t)\right]^*. \qquad (11b)$$

Now, the left hand side of Eq. (11a) is identically the bracketed term of Eq. (9), thus Eq. (9) can be written as

$$\frac{\Delta q^n}{\overline{\Delta\tau}^{n+1}} - \frac{\theta_2}{1+\theta_2}\frac{\Delta q^{n-1}}{\overline{\Delta\tau}^{n-1}} \qquad (12)$$

$$+\left[-\frac{\theta_1}{1+\theta_2}R_J^{n+1} + \frac{(\theta_1 - 1)}{1+\theta_2}R_J^n\right]q^n$$

$$+\frac{\theta_1}{1+\theta_2}R^{n+1} - \frac{(\theta_1 - 1)}{1+\theta_2}R^n = 0.$$

The evaluation of both the convective and diffusive flux vectors contained in R will be discussed in the next section.

NUMERICAL FLUX FORMULATION

Convective Flux Evaluation

Flux-Difference Splitting

In this cell-centered finite-volume scheme, the convective numerical flux at cell faces is calculated using the Roe approximate Riemann solver (4). Although originally developed for compressible flow, this approximate Riemann solver can also be implemented in artificial compressibility formulations for incompressible flow (additional details may be found in Reference (10)). An essential ingredient of Roe's solver is the construction of a matrix $\overline{A}$ (q_L, q_R), which is representative of the local interface conditions. Roe (4) required this matrix to satisfy certain specific properties, two of which are

As $q_L \to q_R$, $\overline{A}$ $(q_L, q_R) \to A(q)$, where $A = \frac{\partial f}{\partial q}$

For any q_L, q_R, $\overline{A}$ $(q_L, q_R) \cdot (q_L - q_R) = f_L - f_R$.

The satisfaction of all these properties in compressible flow is guaranteed by uniquely averaging (11) the dependent variables and then using them in the evaluation of the matrix $\overline{A}$. These specially averaged variables are commonly referred to as Roe variables. An analogous set of Roe variables can be defined for incompressible flow (6, 12, 13) and are given by

Once these variables have been defined, the mechanics involved in computing the numerical fluxes are the same as those used for compressible flow.

A formulation of the numerical flux at cell face $i + 1/2$ which uses all Roe variables and metrics

724

$$u = \tfrac{1}{2}(u_L + u_R)$$

$$v = \tfrac{1}{2}(v_L + v_R).$$

corresponding to cell face $i + 1/2$ can be found in Reference (14). This higher-order numerical flux without limiters is

$$\hat{e}_{i+\frac{1}{2}} = [e(q_i)]_{i+\frac{1}{2}} + \sum_{j=1}^{3} \sigma^-_{j,i+\frac{1}{2}} r^{(j)}_{i+\frac{1}{2}} \tag{13}$$

$$+ \sum_{j=1}^{3} \left\{ \frac{1-\psi}{4} \left[\sigma^+_{j,i-\frac{1}{2}} - \sigma^-_{j,i+\frac{3}{2}} \right] \right.$$

$$\left. + \frac{1+\psi}{4} \left[\sigma^+_{j,i+\frac{1}{2}} - \sigma^-_{j,i+\frac{1}{2}} \right] \right\} r^{(j)}_{i+\frac{1}{2}}$$

where

$$\sigma^{\pm}_{j,i+p/2} = \lambda^{\pm(j)}_{i+1/2} \alpha_{j,i+p/2}$$

and

$$\alpha_{j,i-1/2} = \ell^{(j)}_{i+1/2} \cdot (q_i - q_{i-1})$$

$$\alpha_{j,i+1/2} = \ell^{(j)}_{i+1/2} \cdot (q_{i+1} - q_i)$$

$$\alpha_{j,i+3/2} = \ell^{(j)}_{i+1/2} \cdot (q_{i+2} - q_{i+1})$$

$\lambda^{\pm}$ corresponds to the positive and negative eigenvalues of the Roe matrix and $r^{(j)}$ and $\ell^{(j)}$ are the right and left eigenvectors, respectively. The subscript $i + 1/2$ in the above equations indicate that the metrics used are evaluated at cell face $i + 1/2$. The dependent variables in the eigenvalues and eigenvectors are the aforementioned Roe variables. The flux vector $e(q_j)$, however, is evaluated using the dependent variables. All of the results reported herein were obtained using this numerical flux vector with $\psi = 1/3$, which is third-order accurate in space.

Eigensystem of the Transformed Flux Jacobian Matrices

It is apparent from Eq. (13) that the eigenvalues and left and right eigenvectors of the Roe matrix must be known in order to perform the numerical flux calculation. The eigensystem for the Roe matrix can be obtained from the eigensystem of the transformed flux Jacobian by simply using the Roe variables in the latter.

The first step in deriving this eigensystem is the determination of the transformed flux Jacobian matrices. These matrices are defined as

$$A = \frac{\partial E}{\partial q}, \quad B = \frac{\partial F}{\partial q} \tag{14}$$

where E and F are given in Eq. (2) and the vector q is

$$q = \begin{bmatrix} p \\ u \\ v \end{bmatrix}. \tag{15}$$

The inviscid flux vectors E and F can be written compactly as

$$K = J \begin{bmatrix} \beta(k_x u + k_y v) \\ u\theta_k + k_x p \\ v\theta_k + k_y p \end{bmatrix} \tag{16}$$

where

$$\theta_k = k_t + k_x u + k_y v$$

and

$$K = E, \quad \theta_k = U \quad \text{for } k = \xi$$

$$K = F, \quad \theta_k = V \quad \text{for } k = \eta.$$

Expressing K in terms of the elements of q and performing the indicated differentiation as defined in Eq. (14) yields the transformed flux Jacobian matrices,

$$\overline{K} = \begin{bmatrix} 0 & \beta\hat{k}_x & \beta\hat{k}_y \\ \hat{k}_x & \hat{\theta}_k + u\hat{k}_x & u\hat{k}_y \\ \hat{k}_y & v\hat{k}_x & \hat{\theta}_k + v\hat{k}_y \end{bmatrix} \tag{17}$$

where

$$\hat{k}_m = Jk_m \quad \text{for } m = x, \ y, \ \text{and } t$$

$$\hat{\theta}_k = \hat{k}_t + \hat{k}_x u + \hat{k}_y v$$

and

$$\overline{K} = A, \quad \hat{\theta}_k = \hat{U} \quad \text{for } k = \xi$$

$$\overline{K} = B, \quad \hat{\theta}_k = \hat{V} \quad \text{for } k = \eta.$$

To facilitate the determination of the eigenvalues of the matrix $\overline{K}$, a similarity transformation will be introduced, which will operate on $\overline{K}$ and produce the matrix $\varkappa$. Since $\overline{K}$ and $\varkappa$ are similar matrices, they will have the same characteristic polynomial (15) and hence the same eigenvalues. However, the matrix $\varkappa$ will contain fewer nonzero elements than matrix $\overline{K}$,

and thus the computation of its eigenvalues will be far easier.

Consider the matrices M and M^{-1}

$$M = \begin{bmatrix} 1 & 0 & 0 \\ \dfrac{u}{\beta} & 1 & 0 \\ \dfrac{v}{\beta} & 0 & 1 \end{bmatrix}, \quad M^{-1} = \begin{bmatrix} 1 & 0 & 0 \\ -\dfrac{u}{\beta} & 1 & 0 \\ -\dfrac{v}{\beta} & 0 & 1 \end{bmatrix}. \quad (18)$$

Let $\varkappa = M^{-1}\overline{K}M$, then

$$\varkappa = \begin{bmatrix} \hat{\theta}_k - \hat{k}_t & \beta\hat{k}_x & \beta\hat{k}_y \\ \hat{k}_x + \dfrac{u\hat{\theta}_k}{\beta} & \hat{\theta}_k & 0 \\ \hat{k}_y + \dfrac{v\hat{\theta}_k}{\beta} & 0 & \hat{\theta}_k \end{bmatrix} \quad (19)$$

where

$$\varkappa = a, \ \hat{\theta}_k = \hat{U} \ \text{for} \ k = \xi$$
$$\varkappa = b, \ \hat{\theta}_k = \hat{V} \ \text{for} \ k = \eta.$$

The eigenvalues of $\varkappa$ can be calculated by using the first row to expand the determinant, which yields

$$\lambda_k^1 = \hat{\theta}_k$$
$$\lambda_k^2 = \hat{\theta}_k - \dfrac{\hat{k}_t}{2} + \hat{c} \quad (20)$$
$$\lambda_k^3 = \hat{\theta}_k - \dfrac{\hat{k}_t}{2} - \hat{c}$$

where

$$\hat{c} = \sqrt{\left(\hat{\theta}_k - \dfrac{\hat{k}_t}{2}\right)^2 + \beta\left(\hat{k}_x^2 + \hat{k}_y^2\right)}$$

and λ_k^i, $i = 1, 2, 3$ are the eigenvalues of A for $k = \xi$ and of B for $k = \eta$.

The right eigenvectors of $\varkappa$ are solutions corresponding to the respective eigenvalues of the equation

$$(\varkappa - \lambda_k^s D)\underset{\sim}{r}^s = 0, \quad s = 1, 2, 3. \quad (21)$$

The matrix P_k, whose columns are the right eigenvectors of $\varkappa$, can be written as

$$P_k = \begin{bmatrix} 0 & -c^- & -c^+ \\ -\hat{k}_y & \phi_1 & \phi_1 \\ \hat{k}_x & \phi_2 & \phi_2 \end{bmatrix} \quad (22)$$

where

$$c^+ = \dfrac{\hat{k}_t}{2} + \hat{c}, \quad c^- = \dfrac{\hat{k}_t}{2} - \hat{c},$$
$$\phi_1 = \hat{k}_x + \dfrac{u\hat{\theta}_k}{\beta}, \quad \phi_2 = \hat{k}_y + \dfrac{v\hat{\theta}_k}{\beta}.$$

Having developed a linearly independent set of right eigenvectors, the left eigenvectors will be constructed in such a way that the right and left eigenvectors will be orthonormal. One way to accomplish this task is to simply invert the matrix P_k, which yields

$$P_k^{-1} = \begin{bmatrix} 0 & \dfrac{\beta\phi_2}{c^+c^-} & \dfrac{-\beta\phi_1}{c^+c^-} \\ \dfrac{1}{2\hat{c}} & \dfrac{-\beta c^+\hat{k}_x}{2\hat{c}c^+c^-} & \dfrac{-\beta c^+\hat{k}_y}{2\hat{c}c^+c^-} \\ -\dfrac{1}{2\hat{c}} & \dfrac{\beta c^-\hat{k}_x}{2\hat{c}c^+c^-} & \dfrac{\beta c^-\hat{k}_y}{2\hat{c}c^+c^-} \end{bmatrix}. \quad (23)$$

The columns of P_k and the rows of P_k^{-1} are, respectively, the right and left eigenvectors of $\varkappa$ corresponding to the particular eigenvalues. In fact $\varkappa$ can be written as

$$\varkappa = P_k \Lambda_k P_k^{-1} \quad (24)$$

where Λ_k is a diagonal matrix whose elements are the eigenvalues λ_k. Recall that the original intent was to develop the eigensystem of the flux Jacobian matrices A and B. Having generated the eigensystem of $\varkappa$, the eigensystem of the flux Jacobians can be obtained as follows. Using Eq. (19), $\overline{K}$ can be expressed as

$$\overline{K} = M\varkappa M^{-1}. \quad (25)$$

Substituting the expression for $\varkappa$ in Eq. (24) into Eq. (25) yields

$$\overline{K} = MP_k \Lambda_k P_k^{-1}M^{-1} \quad (26)$$

or

$$\overline{K} = T_k \Lambda_k T_k^{-1} \quad (27)$$

726

where

$$T_k = MP_k \quad \text{and} \quad T_k^{-1} = P_k^{-1}M^{-1}.$$

Performing the indicated multiplication and simplifying, results in the following expressions for T_k and T_k^{-1}

$$T_k = \begin{bmatrix} 0 & -c^- & -c^+ \\ -\hat{k}_y & \hat{k}_x + \dfrac{u\lambda_k^2}{\beta} & \hat{k}_x + \dfrac{u\lambda_k^3}{\beta} \\ \hat{k}_x & \hat{k}_y + \dfrac{v\lambda_k^2}{\beta} & \hat{k}_y + \dfrac{v\lambda_k^3}{\beta} \end{bmatrix} \quad (28)$$

$$T_k^{-1} = \frac{-\beta}{2\hat{c}c^+c^-}\begin{bmatrix} \dfrac{2\hat{c}}{\beta}\left(u\hat{k}_y - v\hat{k}_x\right) & -2\hat{c}\phi_2 & 2\hat{c}\phi_1 \\ \dfrac{-c^+\lambda_k^3}{\beta} & c^+\hat{k}_x & c^+\hat{k}_y \\ \dfrac{c^-\lambda_k^2}{\beta} & -c^-\hat{k}_x & -c^-\hat{k}_y \end{bmatrix}.$$

Viscous Flux Evaluation

In this work, all velocity derivatives needed in the evaluation of the viscous flux vectors E_v and F_v are approximated using central differences. Cross derivative terms are calculated by simply averaging the appropriate metric quantities and dependent variables from surrounding cells. Gatlin [16] has given a detailed account of the evaluation of the remaining terms and it will not be repeated here.

NUMERICAL SOLUTION METHOD

The numerical solution of the nonlinear system of equations given by Eq. (12) is obtained by using Newton's method. This formulation is used for both steady state and unsteady solutions. The iterative nature of Newton's method will insure the compatibility of the computed pressure field and the divergence-free velocity field for unsteady calculations. The Jacobian matrix used in this solution procedure is computed by numerically differentiating the first-order Roe flux vector. This discretized Jacobian is then used in a Newton-relaxation scheme where Newton is the primary iteration and relaxation is the secondary iteration. Formally, Ortega and Rheinboldt [5] refer to this particular solution methodology as a discretized Newton-relaxation method, or DNR [17].

Reference [18] contains the basic derivation of the aforementioned scheme, while Reference [10] describes the implementation for incompressible flow. The remainder of this section will therefore only touch upon some of the fundamental concepts, while providing the details of its implementation for this particular application.

Newton Formulation and Jacobian Evaluation

Consider a system of nonlinear equations given by

$$N_1 (x_1, x_2, \cdots , x_n) = 0$$

$$N_2 (x_1, x_2, \cdots , x_n) = 0$$

$$\vdots$$

$$N_n (x_1, x_2, \cdots , x_n) = 0$$

(29)

or more concisely

$$N(x) = 0. \quad (30)$$

Newton's method for the vector-valued function $N(x)$ can be expressed as

$$N'(x^m)(x^{m+1} - x^m) = -N(x^m) \quad (31)$$

where $m = 1, 2, 3, \ldots$ and $N'(x^m)$ is the Jacobian matrix of $N(x^m)$ given by

$$N'(x^m) = \begin{bmatrix} a_{11}(x^m) & a_{12}(x^m) & \cdots & a_{1n}(x^m) \\ a_{21}(x^m) & a_{22}(x^m) & \cdots & a_{2n}(x^m) \\ & & \cdot & \\ & & \cdot & \\ & & \cdot & \\ a_{n1}(x^m) & a_{n2}(x^m) & \cdots & a_{nn}(x^m) \end{bmatrix} \quad (32)$$

where $a_{ij}(x^m) = \dfrac{\partial N_i(x^m)}{\partial x_j^m}$. The approach used to solve Eq. (31) is to replace the analytical Jacobian with a numerically approximated Jacobian. Ortega and Rheinboldt [5] refer to such a method as a discretized Newton iteration. Various finite-difference approximations have been suggested in the numerical analysis literature. A simple and straightforward approximation of the elements of the Jacobian is to replace the analytical Jacobian $a_{ij}(x^m) = \dfrac{\partial N_i(x^m)}{\partial x_j^m}$ with

$$a_{ij}(x^m) = \frac{N_i (x^m + he_j) + N_i (x^m)}{h}$$

where e_j is the jth unit vector. Dennis and Schnabel (19) point out that this is the same as approximating the jth column of the Jacobian by

$$j^{th} \text{ Column of } N'(x^m) = \frac{N(x^m + he_j) + N(x^m)}{h}$$

where a constant value of

$$h \cong \sqrt{\text{machine epsilon}}$$

was used for this work.

Equation (12) is nothing more than Eq. (30), since the only unknown appearing in this equation is q^{n+1}, that is, in Eq. (31) $x = q^{n+1}$. Thus, Eq. (31) becomes

$$N'(q^{n+1,m})(q^{n+1,m+1} - q^{n+1,m}) = - N(q^m) \qquad (33)$$

where now the a_{ij} in Eq. (32) are given by

$$a_{ij}(q^{n+1,m}) = \frac{\partial N_i(q^{n+1,m})}{\partial q_j^{n+1,m}}. \qquad (34)$$

It should be noted that the only terms in Eq. (12) that are functions of q^{n+1} are Δq^n and R^{n+1}. Recall that R^{n+1} is defined as

$$R^{n+1} = \left[\delta_i(E - E_v) + \delta_j(F - F_v)\right]^{n+1} \qquad (35)$$

or

$$R^{n+1} = \left[\delta_i(E(Q^{n+1}) - E_v(Q^{n+1})) + \delta_j(F(Q^{n+1}) - F_v(Q^{n+1}))\right].$$

As mentioned previously, the elements of the Jacobian matrix are calculated by using a finite difference approximation for the derivative. The first two terms of Eq. (13) are the first-order contribution to the higher-order Roe flux vector. It can be seen that the numerical flux at a cell face, say $i + 1/2$, will be a function of the metrics at $i + 1/2$ and the dependent variables on either side of the cell face. The same statement applies to the viscous flux vector if the cross-derivative terms are not included in its evaluation. Mathematically, for cell face $i + 1/2$, j one has

$$\hat{e}_{i+1/2,j} = \hat{e}_{i+1/2,j}\left(q_{i,j}^{n+1}, q_{i+1,j}^{n+1}\right)$$
$$\hat{e}_{v_{i+1/2,j}} = \hat{e}_{v_{i+1/2,j}}\left(q_{i,j}^{n+1}, q_{i+1,j}^{n+1}\right) \qquad (36)$$

and similarly for cell face i, $j + 1/2$

$$\hat{f}_{i,j+1/2} = \hat{f}_{i,j+1/2}\left(q_{i,j}^{n+1}, q_{i,j+1}^{n+1}\right)$$
$$\hat{f}_{v_{i,j+1/2}} = \hat{f}_{v_{i,j+1/2}}\left(q_{i,j}^{n+1}, q_{i,j+1}^{n+1}\right). \qquad (37)$$

Now, using the relationships in Eqs. (36) and (37), the left-hand side of Eq. (33) is

$$N'(q^{n+1,m})(q^{n+1,m+1} - q^{n+1,m}) = \qquad (38)$$

$$I_b\left[D\hat{e}_{v_{i-1/2,i-1}} - D\hat{e}_{i-1/2,i-1}\right]\Delta q_{i-1,j}^{n+1,m}$$

$$+ I_b\left[D\hat{f}_{v_{j-1/2,j-1}} - D\hat{f}_{j-1/2,j-1}\right]q_{i,j-1}^{n+1,m}$$

$$+ \left[\frac{I}{\Delta\tau^{n+1}} + I_b\left(D\hat{e}_{i+1/2,i} - D\hat{e}_{i-1/2,i}\right.\right.$$

$$- D\hat{e}_{v_{i+1/2,i}} + D\hat{e}_{v_{i-1/2,i}} + D\hat{f}_{j+1/2,j} - D\hat{f}_{j-1/2,j}$$

$$\left.\left. - D\hat{f}_{v_{j+1/2,j}} + D\hat{f}_{v_{j-1/2,j}}\right)\right]\Delta q_{i,j}^{n+1,m}$$

$$+ I_b\left[D\hat{e}_{i+1/2,i+1} - D\hat{e}_{v_{i+1/2,i+1}}\right]\Delta q_{i+1,j}^{n+1,m}$$

$$+ I_b\left[D\hat{f}_{j+1/2,j+1} - D\hat{f}_{v_{j+1/2,j+1}}\right]\Delta q_{i,j+1}^{n+1,m}$$

where

$$D\hat{e}_{i+1/2,j} = \left.\frac{\partial \hat{e}_{i+1/2,j}}{\partial q_{i,j}}\right)_m, \qquad D\hat{e}_{v_{i+1/2,i}} = \left.\frac{\partial \hat{e}_{v_{i+1/2,j}}}{\partial q_{i,j}}\right)_m,$$

$$D\hat{f}_{j+1/2,j} = \left.\frac{\partial \hat{f}_{i,j+1/2}}{\partial q_{i,j}}\right)_m, \qquad D\hat{f}_{v_{j+1/2,j}} = \left.\frac{\partial \hat{f}_{v_{i,j+1/2}}}{\partial q_{i,j}}\right)_m$$

and

$$I_b = diag\left(1, \frac{\theta_1}{1 + \theta_2}, \frac{\theta_1}{1 + \theta_2}\right)$$

$$\Delta q^{n+1,m} = q^{n+1,m+1} - q^{n+1,m}.$$

Note that the first subscript of the Dg ($g=e, e_v, f$ or f_v) term corresponds to the location of the cell face, and the second subscript corresponds to the location of the dependent variable vector that the numerical flux vector is differentiated with respect to. Also, the right-hand side of Eq. (33) is

$$- N(q^{n+1,m}) = \qquad (39)$$

$$- \left\{ I_a \left[\frac{q_{i,j}^{n+1,m} - q_{i,j}^{n}}{\Delta t^{n+1}} - \frac{\theta_2}{1 + \theta_2} \frac{\Delta q_{i,j}^{n-1}}{\Delta t^{n-1}} \right] \right.$$

$$+ I_a \left[\left(\frac{(\theta_1 - 1)}{1 + \theta_2} R_J^n - \frac{\theta_1}{1 + \theta_2} R_J^{n+1,m} \right) q_{i,j}^n \right]$$

$$\left. + I_b R_{i,j}^{n+1} - I_c R_{i,j}^n \right\}$$

where

$$I_a = diag(0, \ 1, \ 1)$$

$$I_c = diag\left(1, \ \frac{(\theta_1 - 1)}{1 + \theta_2}, \ \frac{(\theta_1 - 1)}{1 + \theta_2}\right).$$

Two items must be addressed pertaining to Eq. (39). First of all, the multiplication of a portion of the equation by the diagonal matrix I_a insures that a divergence free velocity field will be obtained when the iteration in m converges (6). Consequently, the temporal discretization of the continuity equation is taken to be first-order accurate, which leads to the definition of the matrices I_b and I_c in Eqs. (38) and (39). The second item deals with the evaluation of the term $R_J^{n+1,m}$, specifically Eq. (11b) must be evaluated as follows to insure that the conservation property at block interfaces is satisfied for blocks in motion (8).

$$R_J^{n+1,m} = \begin{cases} R_J^n, \text{ for } m = 1 \\ \\ R_J^{n+1}, \text{ for } m > 1. \end{cases} \qquad (40)$$

Solution of Linear Systems

A direct solution of the linear system of equations given by Eqs. (38) and (39) is in general not feasible. One way to circumvent this difficulty is to use a relaxation scheme to solve the linear system at each iteration of Newton's method. Using the notation of Reference (18), Eqs. (38) and (39) can be written as

$$(L + U + B)z = b \qquad (41)$$

where L is a lower block triangular matrix with zeroes on the diagonal, B is a block diagonal matrix, and U is an upper block triangular matrix with zeroes on the diagonal. In Reference (18), the solution of Eq. (41) was computed using the symmetric Gauss-Seidel

method. A forward pass solution for the change in dependent variable vector z was written as

$$(L + B)z^{(1)} + Uz^{(0)} = b \qquad (42)$$

where $z^{(0)} \equiv 0$. Without using $z^{(1)}$ to update b, a backward pass was made using

$$Lz^{(1)} + (B + U)z^{(2)} = b. \qquad (43)$$

Using Eq. (42), Eq. (43) can be written as

$$(B + U)z^{(2)} = Bz^{(1)} \qquad (44)$$

or

$$B\Delta z = - Uz^{(2)}$$

where $\qquad \Delta z = z^{(2)} - z^{(1)}.$

In this work, this procedure has been slightly modified. The forward pass is given by

$$(L + B)z^{(1)} + Uz^{(0)} = b \qquad (45)$$

where now $z^{(0)} \neq 0$ but is the solution from the previous time step. Once again, $z^{(1)}$ is not used to update b and the backward pass is given by

$$Lz^{(1)} + (B + U)z^{(2)} = b$$
$$\qquad (46)$$
$$\text{or} \qquad Bz^{(2)} = b - Lz^{(1)} - Uz^{(2)}.$$

All of the solutions contained herein were obtained with three of these symmetric Gauss-Seidel sweeps per Newton iteration.

Turbulence Modeling

The algebraic turbulence model of Baldwin-Lomax (20), which was used in Reference (3) for three-dimensional incompressible flow has been modified for two-dimensional flow. The turbulent wake model used is that of Renze, Buning and Rajagopalan (21). Multiple peaks in the F_{max} function are avoided by restricting the search to a specified distance away from vorticity generating surfaces. Also, the method introduced by Chen (22) to calculate wall shear stress and normal distances for nonorthogonal three-dimensional grids has been incorporated into a two-dimensional framework.

Multiblock Approach

An important aspect of computing the flowfield about complex geometries having disparate components with different topologies is grid generation. In this work a domain decomposition technique is used. Once the computation region is decomposed into distinct subregions, each of which

729

is gridded independently, the grid topology for each subregion is locally consistent with each component of the geometry. The mechanism by which the subregions are connected leads to a variety of approaches, such as the Chimera grid technique (23), the patch grid technique (24), and block-structured grid technique (25). All three approaches have their relative strengths and weaknesses. A common difficulty to Chimera and patched grid technique is constructing a proper scheme for transferring information between interface boundaries. Nevertheless, both Chimera and patched grid have been successful in modeling flows around multiple bodies in relative motion. One approach to overcome this difficulty (i.e. transfer of information between regions) is the use of block-structured grid techniques. The blocked grid idea is not new. It has been applied to three-dimensional problems by Weatherill and Forsey (26), Belk (27), and Arabshahi (28). The basic idea behind blocked grids is that the whole flowfield between the surfaces of the configuration and some outer farfield boundary consists of a set of blocks. The union of these blocks fills the entire flowfield without either gaps or overlaps; moreover, the grid has complete continuity (including slope continuity if desired) of grid lines across the block-block boundaries. This feature provides a relatively simple means of communication between neighboring blocks with stationary interfaces in computational space even though the blocks may be in motion in physical space. The approach adopted here with regard to block-block interface communication is a direct extraction-injection procedure which was taken by Belk (27). This means the information (such as $q, \Delta q$) from within the domain of one block can be extracted and then injected as phantom data in an adjacent block, thereby eliminating any error due to approximations at block boundaries.

STATIONARY AND DYNAMIC GRIDS

The two major requirements for the grids used in this study are: 1) to simulate the entire experimental configuration, and 2) to mimic the dynamic motion of the flapping foils. The stationary grid (i.e., the flapping foils are fixed) is generated using the algebraic capabilities of EagleView (29). The entire physical domain is divided into four blocks. Each block consists of an H-type grid comprised of 326x65 grid points with a normalized (by the foil chord length) spacing of 1.0×10^{-5} off solid surfaces. Vertical grid lines are aligned with experimental measurement locations upstream and downstream of the stationary foil. Figure 3 is a

schematic representation of the experimental measurement locations near the stationary foil.
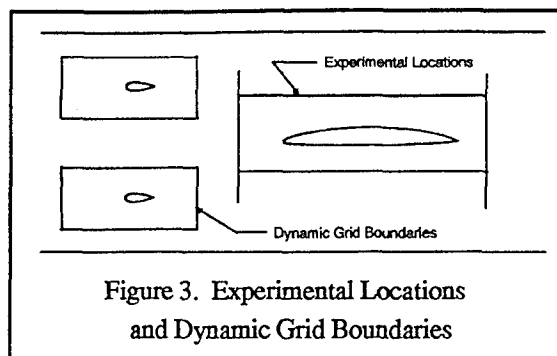

Figure 3. Experimental Locations and Dynamic Grid Boundaries

The efficiency of reconstructing a new grid at each time step to track the movement of the flapping foils is the primary concern for a dynamic grid. To minimize the number of grid points that had to be redistributed, each dynamic portion of the grid is restricted to approximately 101x33 grid points near the corresponding flapping foil. Figure 3 details the extent of this region. The movement of the foils is accomplished by keeping the outer boundary fixed and allowing the foil to oscillate within the confines of these fixed coordinate lines. Weight functions are used to provide a smooth grid distribution between the flapping foils and the outer boundary. These functions, denoted W_i and W_j, are based on an arc length distribution and assumed values from *zero* to *one* in each curvilinear direction. The value *zero* corresponds to no grid motion, while *one* implies full rotational motion. Thus, the surface of the foil will have a value of *one*, which decays to *zero* as the outer boundary is reached. The following combination of weight functions seemed to result in the smoothest grid distribution

$$W_{i,j} = W_i^2 \, W_j^2 \qquad (47)$$

The new position of each point is updated at each time step using the relation

$$X(new) = (1 - W_{i,j}) \, X(fix) + W_{i,j} \, L\cos(\alpha)$$

$$Y(new) = (1 - W_{i,j}) \, Y(fix) + W_{i,j} \, L\sin(\alpha), \qquad (48)$$

where *fix* denotes the original position at zero degrees angle of attack, L is the distance from the center of rotation, and α is the angle of attack. Since the grid reconstruction is restricted to a small region and an algebraic method is used to generate the new grid in this region, very little additional computational time is required to update the grid at each time step.

POST-PROCESSING

The computed results had to go through an elaborate post-processing procedure in order to be analyzed in an accurate and meaningful manner. In

particular the computed results had to be re-referenced to match MIT's reference conditions, and a harmonic analysis procedure had to be used to reduce the large quantity of data obtained from unsteady flows to a manageable set of data that could be easily understood.

The measured and computed data are both referenced to "freestream conditions". However, evaluation of the measured total pressure coefficient indicates that the reference velocity $\hat{u}_{ref}$ and pressure $\hat{p}_{ref}$, used by MIT, are not measured at the same location in the tunnel. As a result, $\hat{u}_{ref}$ and $\hat{p}_{ref}$ are not interchangeable with $\hat{V}_\infty$ and $\hat{p}_\infty$, the reference conditions used in the computations. Thus, to compare "apples with apples", it is necessary to re-reference the computed data to MIT's reference conditions.

The Fourier transform has proven to be an efficient tool for analyzing unsteady data. It works under the premise that any physical process can be described either in the time domain or the frequency domain. The current implementation uses a modified version of a discrete Fourier transform (30) in order to reduce the computing time required to perform the transform. The transform used can be defined as follows

$$h(t_j) = \overline{h} + \sum_{k=1}^{kmax} a_k \cos\left[k(j-1)\frac{2\pi}{N}\right] \qquad (49)$$
$$+ b_k \sin\left[k(j-1)\frac{2\pi}{N}\right]$$
$$j = 1, 2, ..., N$$

where

$$a_k = \frac{2}{N} \sum_{j=1}^{N} h(t_j) \cos\left[k(j-1)\frac{2\pi}{N}\right]$$

$$b_k = \frac{2}{N} \sum_{j=1}^{N} h(t_j) \sin\left[k(j-1)\frac{2\pi}{N}\right]$$

$$\overline{h} = \frac{1}{N} \sum_{j=1}^{N} h(t_j)$$

and

$$kmax = \begin{cases} \dfrac{N}{2} - 1 & \text{for } N \text{ even} \\[2mm] \dfrac{(N-1)}{2} & \text{for } N \text{ odd} \end{cases}$$

$$k = 1, 2, ..., kmax.$$
$$N = \text{\# of time steps per period}.$$

In terms of amplitude and phase, Eq. (49) can be written as

$$h(t_j) = \overline{h} + \sum_{k=1}^{kmax} C_k \sin(k\omega t_j + Q_k) \qquad (50)$$

where

$$C_k = \sqrt{(a_k^2 + b_k^2)}$$

$$Q_k = \tan^{-1}\left(\frac{a_k}{b_k}\right)$$

$$\omega t_j = \frac{2\pi}{N}(j-1).$$

RESULTS

As stated earlier, the computations are being compared with experimental data obtained by MIT (31). Both the steady-state and unsteady computations were carried out using the complete experimental configuration consisting of the water tunnel walls, flapping foils and stationary foil (Fig. 2). The location of the stationary foil coincides with the latest experimental information, specifically, the trailing edge is one centimeter below the centerline of the tunnel and the geometric angle of attack is 1.18 degrees. No slip boundary conditions were used on all solid surfaces, while characteristic variable boundary conditions were used at both the upstream inflow and downstream outflow boundary. Velocities were specified at the inflow while static pressure was set at the outflow. The artificial compressibility factor β was set to 10 for all calculations. All computations were for a Reynolds number of 3.78 million based on the stationary foil chord. The boundary layer on the stationary foil (both the suction and pressure sides) was tripped at a distance of 0.105 chord length from the leading edge, while the boundary layer on the flapping foils and tunnel walls was treated as completely turbulent. A nondimensional grid spacing of 1.0×10^{-5} off solid surfaces resulted in y^+ values of approximately 1.

Steady Results

For the steady-state computations, the flapping foils were held fixed. Since a steady state solution

731

was sought, local time stepping was used and the Jacobian matrices were updated every 20 cycles. One Newton iteration was used at each time step as well as three Gauss-Seidel sweeps.

Bounding Box Data

Computed velocities and static pressures were compared with measured data obtained for the bounding box shown in Fig. 3. Data for three "boxes" was available, but since the boxes were so close together, the data were nearly identical for each box. As a result, the computed results were compared with the data from the middle box. The location of each face relative to the trailing edge of the stationary foil and nondimensionalized with the foil chord is as follows: upstream face, 1.259; downstream face, -0.163; top face, 0.219; and bottom face, -0.153. The static pressures were measured at different locations than the velocities. The upstream static pressures were measured at 0.266 chord length in front of the leading edge of the stationary foil, while the downstream static pressures were measured at 0.156 chord length behind the trailing edge of the stationary foil.

Figure 4 compares the u-component of velocity. The agreement with measured data is good for both the upstream and downstream locations. Figure 5 compares the measured and computed static pressure coefficient at the upstream and downstream faces defined above. The largest discrepancy occurs as one moves from the position of the stationary foil to the upper and lower tunnel walls.
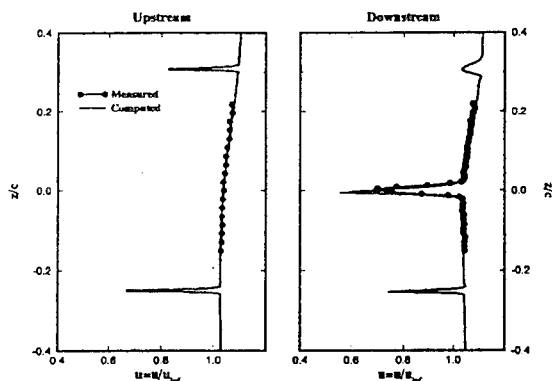

Figure 5. Static Pressure Coefficient

computed profiles on the pressure side, as well as on the suction side upstream of the x/c=0.900 location is good. However, it clearly deteriorates after this station. An argument could be made that this lack of agreement could entirely be attributed to the use of the Baldwin-Lomax turbulence model. However, the inability to match the experimental surface pressure distribution suggests that there may be additional factors. Assuming that the location of the foil in the tunnel and the angle of attack are correct, perhaps there is some slight natural flow angularity in the test section. Another plausible explanation might be that the actual machined geometry differs somewhat from the coordinates given in the experimental reports.

Figure 6. Steady State c_p Distribution

Figure 4. u-Velocity Component

Surface Data

Measured data was available at various locations on the surface of the stationary foil. A comparison of measured and computed surface pressure distributions is shown in Fig. 6. Two representative u-velocity profiles for both the suction and pressure side of the stationary foil are given in Fig. 7. The agreement between experimental and
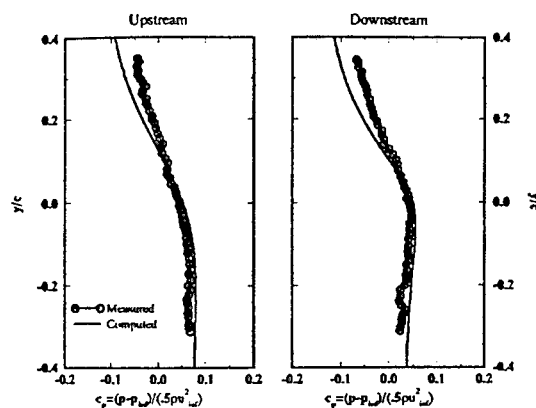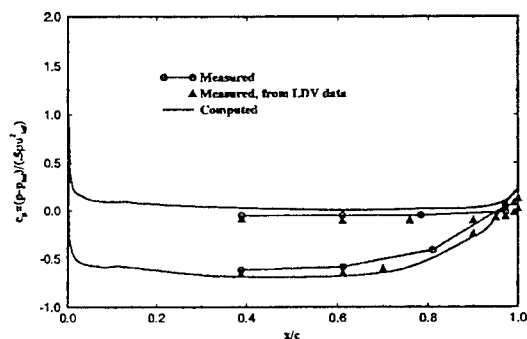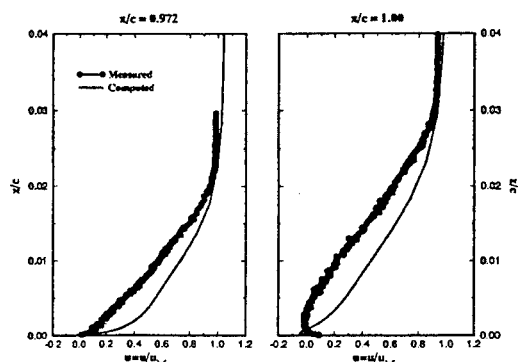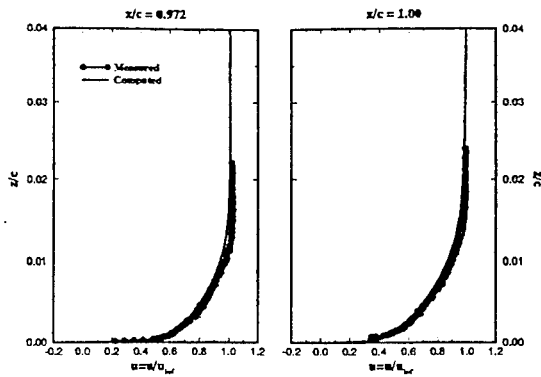

Figure 7(a). Suction Side

732

Figure 7(b). Pressure Side

Figure 7. Steady State Velocity Profiles

Unsteady Results

The unsteady solution used the steady state solution as an initial condition and the motion of the flapping foils was initiated by boundary conforming dynamic grids that moved in pitch with the flapping foils at a reduced frequency of 3.62 based on semi-chord of the stationary foil. A minimum nondimensional time step of 8.7×10^{-4} was used, which corresponds to 1000 time steps per period of motion for the flapping foils. The Jacobian matrix was updated every cycle and three Newton iterations were performed at each time step.

It should be noted that during the course of this work, several different time steps, both larger and smaller, were tried as well as different numbers of Newton iterations. It was found that nearly identical results were obtained for time steps both larger and smaller than the one reported here. However, different numbers of Newton iterations did affect the solution. Newton iterations of one, three and six were used for each time step. Little or no difference in the bounding box results could be seen for any of the different numbers of Newton iterations used. However, a distinct improvement in the viscous (surface) results could be seen between the three Newton iteration solution and the one Newton iteration solution. No significant improvement could be seen between the six and the three Newton iteration solution for either the bounding box or the viscous results.

Although no results were presented here, a grid with nearly twice the resolution in the direction normal to the flappers and foil was also used. The difference in solutions between those obtained from this grid and those presented here was virtually indistinguishable.

Bounding Box Data

The locations for the bounding box used in the steady state analysis are the same for the unsteady analysis, except for the downstream face. The downstream face is located at -0.108 chord length relative to the trailing edge of the stationary foil. For the unsteady case, the upstream and downstream faces of the box were extended into the wake regions. This provided very valuable experimental wake data for comparison with computations.

A comparison of the measured and computed results for the amplitude and phase of the first harmonic of the u-velocity are shown in Fig. 8 for all the faces of the bounding box. The agreement is good, especially on the upstream and downstream faces. It appears that the disturbances generated by the flapping foils are being convected downstream and are arriving at the upstream face with the correct amplitude and phase. Although the agreement at the downstream face does not appear to be quite as good, one can consider the phase at -180 degrees to be +180 degrees and the agreement is quite good .
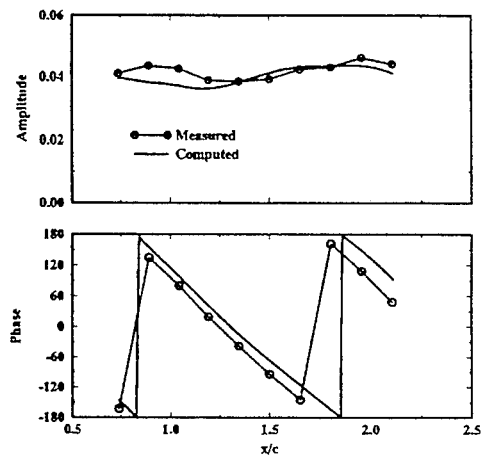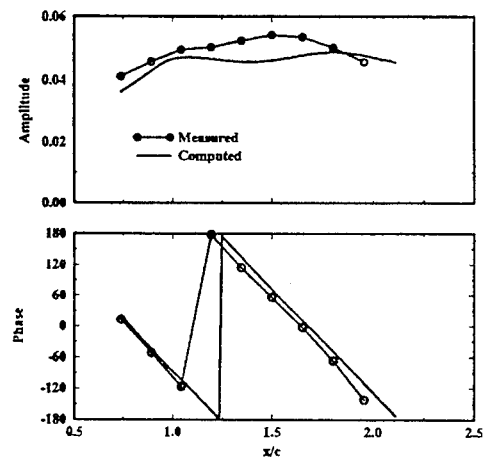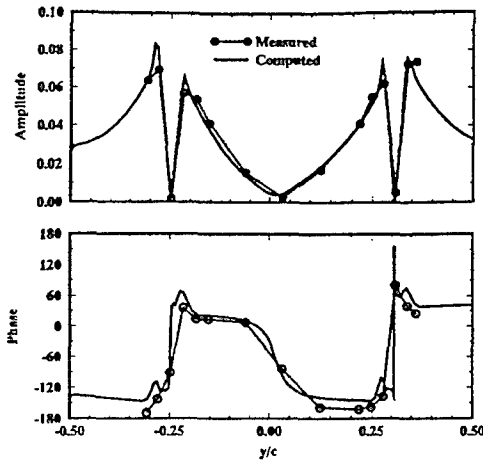

Figure 8(a). Top Face

Figure 8(b). Bottom Face
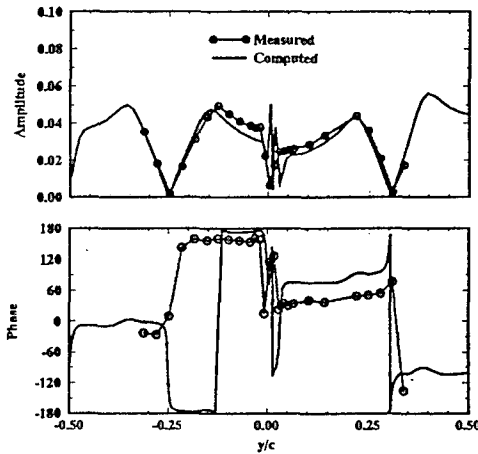
733

Figure 8(c). Upstream Face

Figure 8(d). Downstream Face

Figure 8. Unsteady Velocity on Bounding Box–
First Harmonic

Surface Data

The mean surface pressure distribution is plotted in Fig. 9, while the amplitude and phase of the unsteady surface pressure distribution is shown in Fig. 10. The discrepancy between the measured and computed mean surface pressure distribution is approximately the same magnitude as the steady state case. The amplitudes of the unsteady surface pressure distribution compare favorably for both the suction and pressure side, while the overall trend of the phase is captured.

Figure 11 contains mean velocity profiles from the suction and pressure side. Once again, the difference between the computed and measured values is about the same as in the steady state case. The amplitude and phase of the first harmonic of the unsteady u-velocity profiles appear in Fig. 12. The

computed amplitudes compare favorably with the measured data, while the phase for the pressure side agrees better than that of the suction side. Overall, the comparison of the mean unsteady results showed the same type of discrepancies as the steady results. Figure 13 shows a snapshot of the unsteady velocity distribution.

Figure 9. Mean c_p Distribution
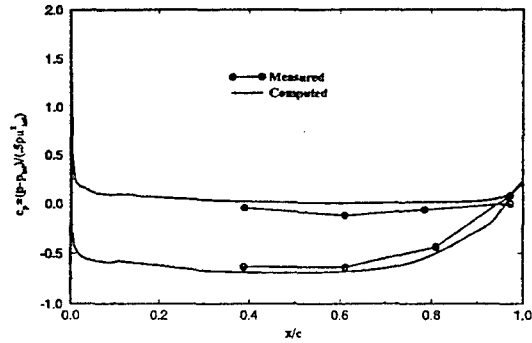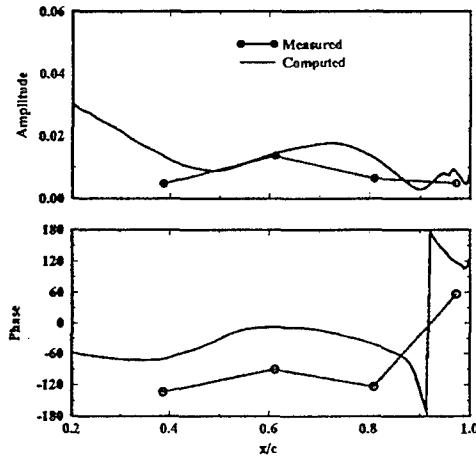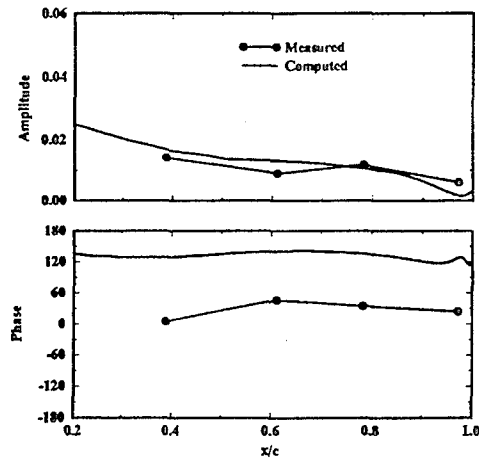

Figure 10(a). Suction Side

Figure 10(b). Pressure Side

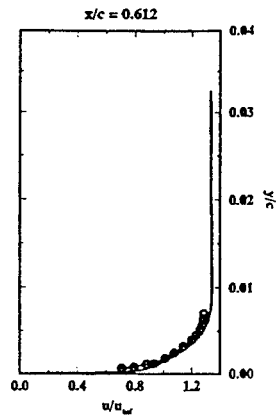Figure 10. Unsteady c_p Distribution –
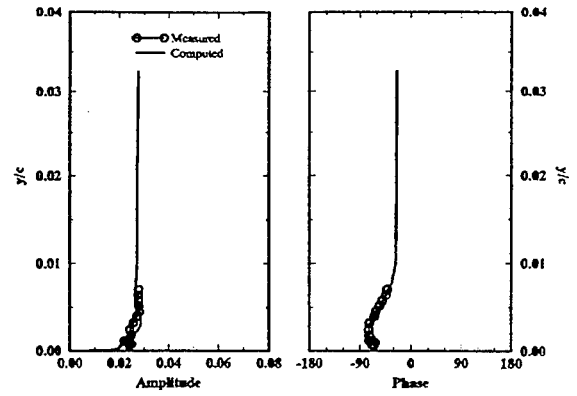First Harmonic

734

Figure 11(a). Suction Side
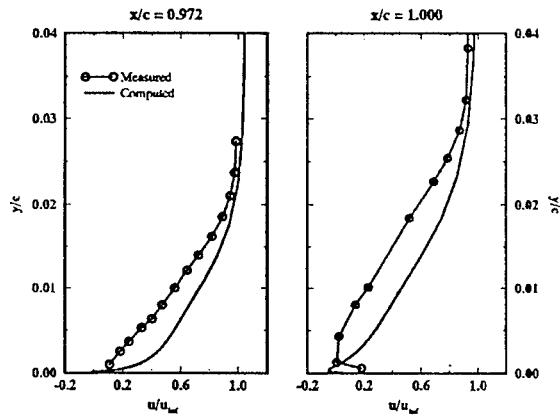

Figure 12(a). Suction Side, x/c = 0.612

Figure 11(b). Suction Side
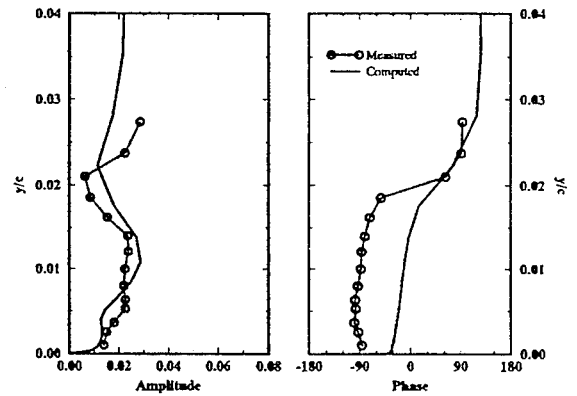
Figure 12(b). Suction Side, x/c = 0.972
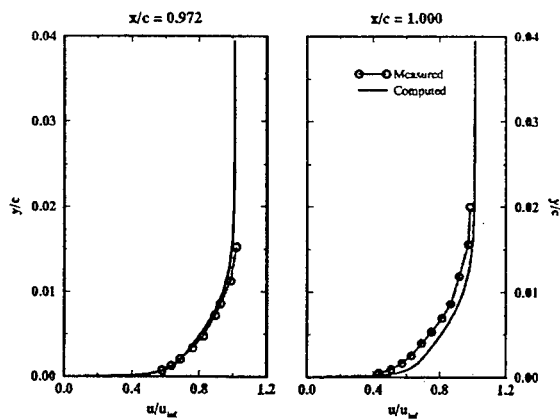
Figure 11(c). Pressure Side

Figure 11. Mean Velocity Profiles
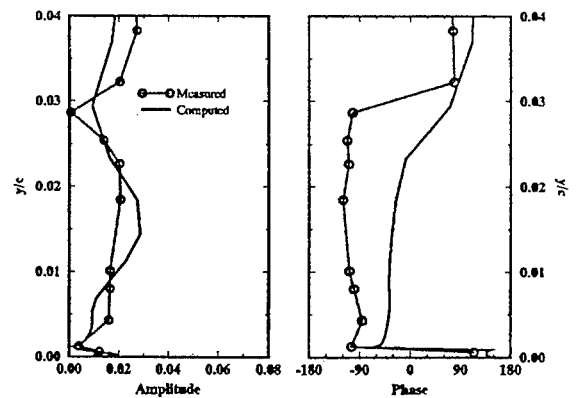
Figure 12(c). Suction Side, x/c = 1.00

735
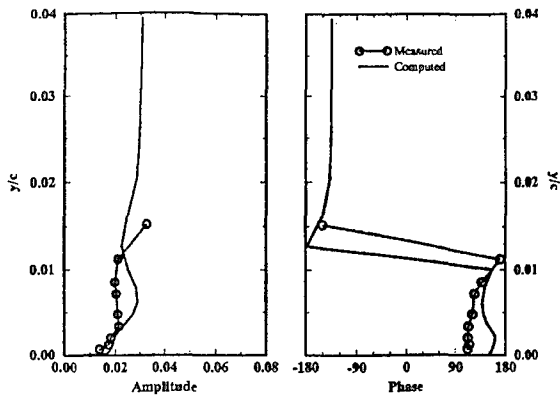
Figure 12(d). Pressure Side, x/c = 0.972
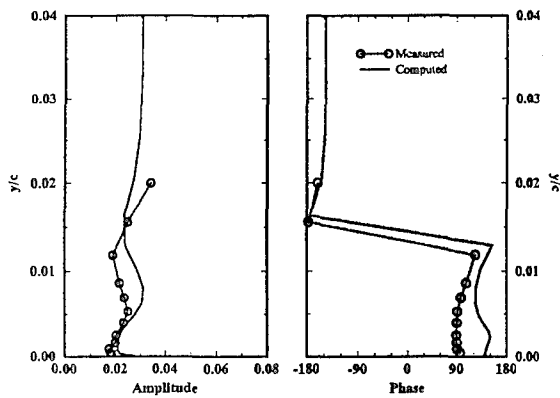
Figure 12(e). Pressure Side, x/c = 1.00

Figure 12. Unsteady Velocity Profiles–
First Harmonic

CONCLUSIONS

A two-dimensional multiblock unsteady incompressible Navier–Stokes algorithm based on artificial compressibility has been presented. The unsteady solution was obtained using a dynamic grid that was regenerated at each time step in order to mimic the motion of the flapping foils. For both the steady and unsteady cases, the computed results matched fairly well with the measured bounding box data. However, the computed results for the surface data (in particular, the suction side data) did not match the measured data to the same extent.

Since the solution appears to be grid independent, it seems as though at least two possibilities exist. Either the numerical simulation is not being conducted at precisely the same conditions as the experiment or, this is the best that can be expected from the technology in the current algorithm. As to the former, assuming that the angle of attack and location of the foil in the tunnel are accurate, possibilities could include; flow angularity in the test section, alterations in the geometry of the manufactured foil, and the type of flow over the flappers. From a numerical standpoint, the differences could be attributed to the turbulence model used.

Currently, work is being done to adapt the grid to the unsteady wake of the flapping foils in order to minimize the number of grid points required. Future work involves examining alternate turbulence models to see if the discrepancy in the results obtained on the surface can be resolved.

ACKNOWLEDGEMENTS
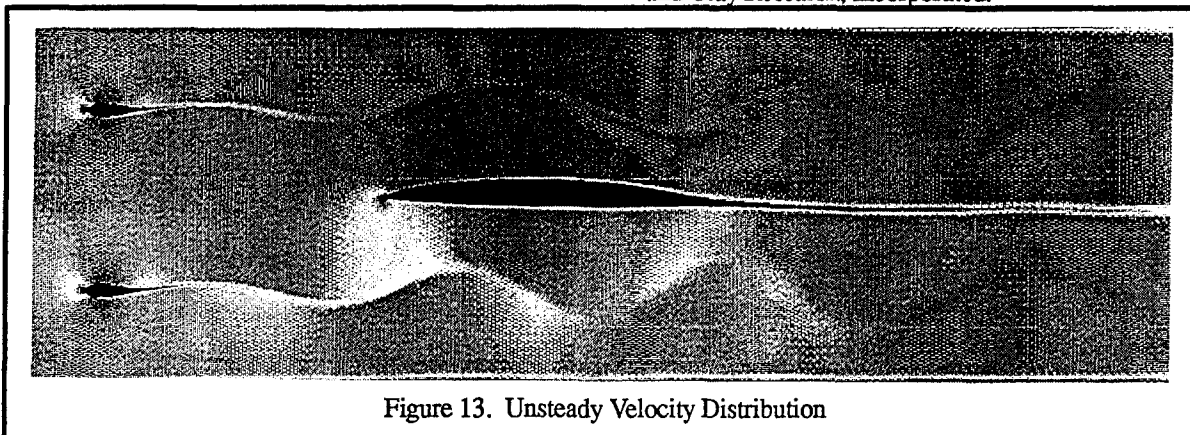
Figure 13. Unsteady Velocity Distribution

736

BIBLIOGRAPHIC REFERENCES

1. Rice, J.Q., "Investigation of A Two Dimensional Hydrofoil in Steady and Unsteady Flows," M.S. Thesis, Massachusetts Institute of Technology, June 1991.

2. Delpero, P.M., "Investigation of Flows around a Two Dimensional Hydrofoil Subject to A High Reduced Frequency Gust Loading," M.S. Thesis, Massachusetts Institute of Technology, February 1992.

3. Taylor, L.K. and Whitfield, D.L., "Unsteady Three-Dimensional Incompressible Euler and Navier-Stokes Solver for Stationary and Dynamic Grids," AIAA-91-1650, June 1991.

4. Roe, P.L., "Approximate Riemann Solvers, Parameter Vectors, and Difference Schemes," Journal of Computational Physics, Vol. 43, pp. 357-372, May 1981.

5. Ortega, J.M. and Rheinboldt, W.C., Iterative Solution of Nonlinear Equations in Several Variables, Academic Press, New York, 1970.

6. Pan, D. and Chakravarthy S., "Unified Formulation for Incompressible Flows," AIAA-89-0122, January 1989.

7. Beam, R.M., and Warming, R.F., "An Implicit Factored Scheme for the Compressible Navier-Stokes Equations," AIAA Journal, Vol. 16, No. 4, pp. 393-402, April 1978.

8. Janus, J.M., "Advanced 3-D CFD Algorithm for Turbomachinery," PhD Dissertation, Mississippi State University, May 1989.

9. Thomas, P.D., and Lombard, C.K., "Geometric Conservation Law and Its Application to Flow Computations on Moving Grids," AIAA Journal, Vol. 17, No. 10, 1979.

10. Taylor, L.K., "Unsteady Three-Dimensional Incompressible Algorithm Based on Artificial Compressibility," PhD Dissertation, Mississippi State University, May 1991.

11. Roe, P.L. and Pike, J., "Efficient Construction and Utilization of Approximate Riemann Solutions," in Computing Methods in Applied Sciences and Engineering, ed. R. Glowinski and J.L. Lions, 6:499-518, Amsterdam: North Holland, 1984.

12. Hsu, C.H., Hartwich, P.M. and Liu, C.H., "Incompressible Navier-Stokes Solutions for a Sharp-Edged Double-Delta Wing," AIAA -87-0206, January 1987.

13. Rogers, S.E. and Kwak, D., "Upwind Differencing for the Time-Accurate Incompressible Navi-er-Stokes Equations," AIAA Journal, Vol. 28, No. 2, PP.253-262, 1990.

14. Whitfield, D.L., Janus, J.M. and Simpson, L.B., "Implicit Finite Volume High Resolution Wave-Split Scheme for Solving the Unsteady Three-Dimensional Euler and Navier-Stokes Equations on Stationary or Dynamic Grids," Engineering and Industrial Research Station Report, MSSU-EIRS-ASE-88-3, Mississippi State University, Mississippi State, February 1988.

15. Sokolnikoff, I.S. and Redheffer, R.M., Mathematics of Physics and Modern Engineering, McGraw-Hill, Inc., New York, NY, 1966.

16. Gatlin, B., "An Implicit, Upwind Method for Obtaining Symbiotic Solutions to the Thin-Layer Navier-Stokes Equations," PhD Dissertation, Mississippi State University, August 1987.

17. Vanden, K.J., "Direct and Iterative Algorithms for the Three-Dimensional Euler Equations," PhD Dissertation, Mississippi State University, December 1992.

18. Whitfield, D.L., and Taylor, L.K., "Discretized Newton-Relaxation Solution of High Resolution Flux-Difference Split Schemes," AIAA-91-1539, June 1991.

19. Dennis, J.E., Jr. and Schnabel, R.B., Numerical Methods for Unconstrained Optimization and Nonlinear Equations, Prentice-Hall, Inc., Englewood Cliffs, New Jersey, 1983.

20. Baldwin, B.S. and Lomax, H., "Thin-Layer Approximation and Algebraic Model for Separated Turbulent Flows," AIAA-78-257, January 1978.

21. Renze, K.J., Buning, P.G. and Rajagopalan, R.G.," A Comparative Study of Turbulence Models for Overset Grids," AIAA-92-0437, January 1992.

22. Chen, J.P., "Unsteady Three-Dimensional Thin-Layer Navier-Stokes Solutions for Turbomachinery In Transonic Flow," PhD Dissertation, Mississippi State University, December 1991.

23. Benek, J.A., Steger, J.L. and Dougherty, F.C., "A Flexible Grid Embedding Technique with Application to the Euler Equations," Proceedings of the 6th AIAA Computational Fluid Dynamics Conference, Danvers, MA, 1983.

24. Rai, M.M., "A Conservative Treatment of Zonal Boundaries for Euler Equation Calculation," AIAA-84-0164, AIAA 22nd Aerospaces Sciences Meeting, Reno, NV, January 1984.

25. Thompson, J.F., "A Composite Grid Generation Code for General Three-Dimensional Regions," AIAA-87-0275, AIAA 25th Aerospace

Sciences Meeting, Reno, NV, January 1987. AIAA Journal, Vol. 26, No. 3, p. 271, March 1988.

26. Weatherill, N.P. and Forsey, C.R., "Grid Generation and Flow Calculations for Complex Aircraft Geometries Using a Multiblock Scheme," AIAA-84-1665, June 1984.

27. Belk, D.M., "Three-Dimensional Euler Equations Solutions on Dynamic Blocked Grids," PhD Dissertation, Mississippi State University, August 1986.

28. Arabshahi, A., "A Dynamic Multiblock Approach to Solving the Unsteady Euler Equations About Complex Configurations," PhD Dissertation, Mississippi State University, May 1989.

29. Remotique, M.G., Hart, E.T. and Stokes, M.L., "EAGLEView: A Surface and Grid Generation Program and Its Data Management," Software Systems for Surface Modeling and Grid Generation, ed. Robert E. Smith, NASA Conference Publiation 3143, Hampton, VA, April 1992.

30. Singleton, R.C., "An Algorithm for Computing the Mixed Radix Fast Fourier Transform," IEEE Transactions on Audio and Electroacoustics, Vol. AU-17, pp. 93-103, June 1969.

31. Kerwin, J., Keenan, D., Mazel, C., Horwich, and E., Knapp, M., "MIT/ONR Flapping Foil Experiment, Unsteady Phase," unpublished data.

DISCUSSION
by Dr. V. C. Patel, The University of Iowa
Institute of Hydraulic Research

This question is addressed to this as well as the previous paper. I am very surprised by the rather poor agreement in the velocity profiles with the Baldwin-Lomax model, even in steady flow, especially because this model was optimized for such airfoil flows! Why is that so?

Authors' Reply

Discussions of the tunnel domain with and without Granville's pressure-gradient modifications of the Baldwin-Lomax turbulence model have been included in the paper. It is important to emphasize that Granville's change in the zero-gradient values of C_{kleb} and C_{cp} had larger influence in improving the solution than the pressure-gradient corrections to these coefficients.

SESSION 14

LIFTING-SURFACE FLOW:
PROPELLER-RUDDER INTERACTIONS, AND OTHERS

Computation of Viscous Flow Around a Rudder Behind a Propeller: Laminar Flow Around a Flat Plate Rudder in Propeller Slipstream

H. Suzuki, (NKK Corporation, Japan)
Y. Toda (University of Mercantile Marine, Japan)
T. Suzuki (Osaka University, Japan)

ABSTRACT

The viscous flow computation of propeller–rudder interaction is presented through comparisons with experimental data including flow visualization and mean–flow measurements. The steady flow field is calculated by a viscous flow code coupled with a body–force distribution which represents the propeller. The transport equations are discretized using a staggered grid and the exponential scheme. The velocity–pressure coupling is accomplished based on the SIMPLER algorithm. Qualitative agreement is obtained between the calculations and the mean–flow data. Although the details of the flow field is different because of the laminar flow computation and numerical treatment, the computational results show the essential feature such as upward movement of propeller slipstream in port side vise versa in starboard side. The streaklines from one blade position are traced and compared with the flow visualization using dye and air bubbles. The results show very similar trends. Those comparisons show the conclusion that the present approach can simulate qualitatively the steady part of the flow field around a rudder in propeller slipstream.

NOMENCLATURE

C_T = thrust coefficient $(=2T/\rho V_A^2 \pi R_P^2)$

D_P = propeller diameter

fb_x = x wise body force per unit volume

fb_y = y wise body force per unit volume

fb_z = z wise body force per unit volume

fb_θ = θ wise body force per unit volume

J = advance coefficient $(= V_A/nD_P)$

K_T = thrust coefficient $(= T/\rho n^2 D_P^4)$

K_Q = torque coefficient $(= Q/\rho n^2 D_P^5)$

p = pressure

Q = propeller torque

R_n = Reynolds number $(= V_A D_P/\nu)$

R_h = hub radius

R_p = propeller radius $(= D_P/2)$

T = propeller thrust

u,v,w = velocity components in cartesian coordinates

x,y,z = cartesian coordinates

x,r,θ = cylindolical coordinates

n = number of propeller revolution

V_A = propeller advance speed

Greek symbols

Γ = circulation distribution

ν = kinematic viscosity

ρ = fluid density

1. INTRODUCTION

The interaction between a propeller and a rudder is one of the major problems from the viewpoints of not only maneuverability but also propulsive performance, so numerous studies have been performed for flow field around rudder behind a propeller without rudder angle. (Nakatake's review of this topic[1]) Among those studies, the flow field is calculated mainly by invicid–flow method under the assumption that the interaction is invicid, and in theoretical works the shapes of trailing vortex are assumed comparatively simple such as only consideration of propeller-slipstream contraction (Tamashima et al.[2], Ishida et al.[3]) . On the contrary, in experimental studies, it is reported that propeller slipstream is dramatically deformed by the rudder effect from the data of mean–flow measurement by Baba et al.[4] and Ishida et al.[3] and from the result of flow visualization of the propeller tip–vortex by Tanaka et al.[5] and Tamashima et al.[2].

Recently, a lot of fin type energy–saving devices which is installed on a rudder are proposed

and put to practical use. (for example, NKK-SURF[6], IHI A.T.Fin[7]) . For the better understanding and improvement of the performance of such devices, it is advisable to develop the calculation model which can express the phenomena which is observed in experiments.

On the other hand, with respect to the time–averaged flow of the propeller slipstream, it is reported that the computed propeller–hull interaction flow field by the method that propeller effect is represented by the body force distribution in the computation code of Navier–Stokes equation shows good agreement with the experimental result in propeller slipstream[8,9].

In this paper, the flow field with a flat plate rudder is computed by the Navier–Stokes solver coupled with analytical prescribed body–force distribution as the simplest model of propeller–rudder interaction problem. And the result are compared with experimental data for similar condition carried out in circulating water channel. Although the details of the flow field is different because of the laminar flow computation and numerical treatment, it is appeared that the method can express phenomenon which appeared in experimental data with respect to time–averaged flow. A simulation of the streakline from a rotating point on the propeller plane is similar to the flow visualization result. Moreover half domain computation and full domain computation are carried out and compared. These results are almost same for present laminar and steady flow computation.

In the presentation of the results and the discussion to follow, a Cartesian coordinate system is adopted in which $x-$, $y-$ and $z-$ axes are in the direction of the uniform flow, starboard side of the rudder and upward respectively. The origin is at the intersection of the shaft center line and the propeller plane. The mean velocity components in the direction of the coordinate axes are denoted by u, v, w. Unless otherwise indicated, all variables are nondimensionalized using the propeller diameter D_P, propeller advance speed V_A and fluid density ρ. In some part, the cylindolical (x, r, θ) coordinates in which $x=x$, $y=r\cos\theta$ and $z=r\sin\theta$ are used.

2. EXPERIMENTS

Mean–flow measurements and flow visualization were carried out in NKK Tsu Ship Model Basin, circulating water channel to compare with computational results. Experimental results are shown first to explain the phenomena of propeller–rudder interaction.

2.1 Model Rudder, Propeller and Their Arrangements

The principal dimensions of the propeller and the flat plate rudder are given in table 1. The leading edge and trailing edge of the 8mm flat plate rudder are tapered as shown in Fig.1.

The arrangement of the flat plate rudder and propeller open boat with the propeller is shown in Fig.2. The propeller open boat was attached front–side back so that the propeller shaft did not pass through the rudder. But this arrangement had a point that wake of the open boat was generated. So an extension shaft was attached to the propeller open boat so that the open boat did not have a large disturbance on the flow field. Length between propeller plane and the rudder leading edge was $0.30D_P$ (66mm) and the propeller shaft center depth from the free surface is $1.50D_P$ (330 mm) in order to minimize the free surface effect.

2.2 Mean–Flow Measurement

The device for measuring the propeller slipstream, which is unsteady flow field, should be preferably be carried out by a non-contact type Laser Doppler velocimetory or the equivalent; however, instruments of this type cannot be widely used now. Therefore, two spherical–type 5 hole pitot probes, one for the port and the other for starboard side of the center plane, were used in mean–flow measurements because it is easy to handle and able to measure time averaged velocities. Velocities were measured for the with and without rudder condition. The number of propeller revolution and the corresponding thrust and torque coefficients for both conditions are shown in table 2. Note that the thrust and torque for the with rudder condition are 4% larger and 2% smaller than those for the without rudder condition, respectively. It is similar as the other experimental data and might be due to the displacement effect of the rudder and the distortion of the trailing vortex geometry by rudder discussed later.

The mean–velocity field measurements were performed for both conditions and for three axial stations shown in Fig.3. These locations were just behind propeller plane $(x=0.125, 0.125D_P$ downstream of propeller plane) , $x=1.23$ (in case of with rudder, the trailing edge of the flat plate rudder) and the position at $x=2.0$ ($2D_P$ downstream of the propeller plane.

The results of the mean–flow measurement of the propeller slipstream are shown in Fig.4 and Fig.5 for the with and without rudder condition, respectively. The mean–velocity field without

propeller and rudder at first measurement station is shown in Fig.6 in order to check the effect of the open boat. Although a small region where the velocity defect is observed and it is asymmetric, the flow field is seems to be almost uniform in the present experimental region. In Fig.4, the time averaged propeller slipstream similar to a swirling jet is observed for the without rudder condition. From the cross-plane vectors, the swirl velocity is maximum just downstream of the propeller and decays gradually with downstream distance. The crossplane vectors outside the propeller slipstream at $x=0.125$ show the flow direction towards the shaft center. It shows the flow contraction by the propeller. The axial velocity is increased from $x=0.125$ to $x=1.23$ and decay very gradually. The concentration of the axial velocity contours near the propeller tip is the trace of the tip vortices and its associated vortex sheet, which diffuses with downstream distance.

For the with rudder condition shown in Fig. 5, very similar velocity distribution as that for the without rudder condition is observed at $x=0.125$. The diffusion of tip vortex sheet and so on are similar. However, the slipstream is clearly altered due to the rudder effect at the latter two stations. The slipstream moves upward (toward the free surface) in the port side and moves downward in the starboard side. The outer shape of the slipstream in one side altered from the half circle at $x=1.23$. It shows that the movement seems to be larger near the rudder surface. Tanaka et al.[10] explained the phenomena by the mirror image vortex due to the rudder. The propeller slipstream shows complicated shape at $x=2.0$ and the outer shape is enlonged in vertical direction and almost same in horizontal direction as compared with that for the without rudder condition. The cross plane velocity is smaller and the axial velocity is a little bit larger for the with rudder condition. The overall results of mean-flow measurement show similar results of Baba et al[4]. and Ishida[3] although the one measurement was carried out behind the hull.

2.3 Flow Visualization

Flow visualization was carried out for both with and without rudder condition. Streakline from one blade position was visualized by dye method according to Nagamatsu et al.[11]. The device is the tank which is attached on the boss part of the propeller and dye in the tank. When the propeller is rotating, water enters from boss part inlet and colored water go out from the small diameter tube which attached propeller trailing edge by their head difference. But this method can not be used for fast flow because dye defuses immediately. So, the number of propeller revolution n was selected as 7.16 $(r.p.s.)$ and propeller advance speed V_A was 0.63 (m/s) to keep the advance coefficient J same as in mean flow measurements.

The results are shown in Fig.7 for both conditions. The streaklines from $r=0.5R_P$ and $r=0.9$ R_P are shown in figure; where R_P is the propeller radius. For the without rudder condition (a) and c)), the helical streaklines are seen as usual and the streaklines are deformed drastically for the with rudder condition. It moves upward in port side and downward in starboard side. Note the transparent rudder enables to see streaklines in both side. The movement of streaklines is very similar to the tip vortex visualization by Tanaka et al[5]. shown in Fig.8. In this figure, the air bubble method was used for visualization. The results for similar condition are shown in figure. The deformation of those streaklines is corresponding to the enlargement of slipstream in vertical direction.

In the experiment, the phenomena observed in the previous studies is reproduced for the flat plate rudder. It is explained by Tanaka et al.[10] by images. So, if the nonlinear trailing vortex geometry including rudder effect is used for the calculation using iterative procedure, it can be expressed by invicid method. But, it seems difficult to treat the induced velocity at the vortex segment near the rudder. So, in this paper, the computation of Navier-Stokes equations for the time averaged flow field has been investigated if it can express the before mentioned phenomena or not.

3   COMPUTATION

3.1   Governing Equations and Computational Method

In this paper, the computation was carried out for the zero thickness flat plate rudder which had same profile as the rudder used in experiment and the time averaged flow using time averaged body force distribution following Stern et al.[9]. The computation was carried out for steady laminar flow case because the turbulence model in the slipstream was not clear, the present approach can not treat the complicated unsteady phenomena in the slipstream such as blade wake and so on and the grid number was limited due to the memory size of the computer. So, three-dimensional steady Navier-Stokes equations and the continuity equation are used for the governing equations. The equations are written in cartesian coordinates discussed in section 1 in the physical domain as follows;

$$u\frac{\partial u}{\partial x}+v\frac{\partial u}{\partial y}+w\frac{\partial u}{\partial z}=-\frac{\partial p}{\partial x}$$
$$+\frac{1}{Rn}(\frac{\partial^2 u}{\partial x^2}+\frac{\partial^2 u}{\partial y^2}+\frac{\partial^2 u}{\partial z^2})+fb_x \qquad (1)$$

$$u\frac{\partial v}{\partial x}+v\frac{\partial v}{\partial y}+w\frac{\partial v}{\partial z}=-\frac{\partial p}{\partial y}$$
$$+\frac{1}{Rn}(\frac{\partial^2 v}{\partial x^2}+\frac{\partial^2 v}{\partial y^2}+\frac{\partial^2 v}{\partial z^2})+fb_y \qquad (2)$$

$$u\frac{\partial w}{\partial x}+v\frac{\partial w}{\partial y}+w\frac{\partial w}{\partial z}=-\frac{\partial p}{\partial z}$$
$$+\frac{1}{Rn}(\frac{\partial^2 w}{\partial x^2}+\frac{\partial^2 w}{\partial y^2}+\frac{\partial^2 w}{\partial z^2})+fb_z \qquad (3)$$

$$\frac{\partial u}{\partial x}+\frac{\partial v}{\partial y}+\frac{\partial w}{\partial z}=0 \qquad (4)$$

where p is the pressure normalized by ρV_A^2, $Rn=V_A D_P/\nu$ is the Reynolds number defined in terms of V_A, D_P and molecular kinematic viscosity ν. The terms fb_x, fb_y and fb_z in the momentum equations are the components of the body force, normalized by $\rho V_A^2/D_P$ and represent the influence of the propeller. These will be discussed subsequently.

The equations are transformed into irregular orthogonal coordinates shown in Fig.9. The transformed equations are discretized by exponential scheme[12] using the staggered grid in which pressure is defined at the grid point and the velocity components are defined at half grid shifted points in x, y and z direction for u, v and w, respectively. The pressure–velocity coupling is accomplished based on the SIMPLER algorithm. The matrix is solved using tri–diagonal matrix solver and line–by–line iteration method. The steady converged solution was obtained by iterative procedure from the guessed initial condition (uniform flow except for the plate surface). After about 500 iterations, the converged solution was obtained.

10^3 was used for Reynolds number in the computation from the grid size discussed later. Note that the Reynolds numbers in the experiment are 2.4×10^5 and 1.2×10^5 for the mean–flow measurements and flow visualization, respectively.

3.2 Analytically–prescribed body force distribution

To represent the propeller effect in the numerical method, the body force fb_x in axial direction and fb_θ in circumferential direction are used corresponding to thrust and torque. Following the Stern et al.[9], the body force fb_x and fb_θ are prescribed using the loading condition in the experiment shown in table 2. Although the computation was carried out for both with and without rudder condition and the loading conditions were a little bit different in experiment, the loading condition for without–rudder condition was used for both condition because the zero thickness plate rudder which had a small displacement effect was used in the computation. Of course, the interactive method using a invicid propeller theory is preferred and the body force should be the function of θ for the with rudder condition. But, because the computer program which can treat the nonlinear training vortex geometry for with rudder condition like the program of Ishii[13] for the without propeller condition was not available, the same distribution as for the without rudder condition was used.

Following the noniterative calculation of Stern et al.[9], the circulation distribution on the propeller blade of Hough and Ordway[14] was used to determine body force.

The body force fb_x and fb_θ are written using the loading coefficient C_T $(=2T/\rho V_A^2 R_P^2)$, torque coefficient K_Q $(=Q/\rho n^2 D_P^5)$ and advance coefficient J $(=V_A/nD_P)$ as follows;

$$fb_x=A_x\sqrt{1-r^*} \qquad (5)$$

$$fb_\theta=A_\theta\frac{r^*\sqrt{1-r^*}}{(1-Y_h)r^*+Y_h} \qquad (6)$$

$$A_x=\frac{C_T}{\Delta x}\frac{105}{16(4+3Y_h)(1-Y_h)} \qquad (7)$$

$$A_\theta=\frac{K_Q}{\Delta xJ^2}\frac{105}{\pi(4+3Y_h)(1-Y_h)} \qquad (8)$$

where $r^*=(Y-Y_h)/(1-Y_h)$, $Y_h=R_h/R_P$ and $Y=r/R_P$; R_h is boss radius; R_P is propeller radius; T is thrust; Q is torque, Δx means x direction grid size at propeller plane. And C_T is easily calculated from K_T.

Body force distributions from K_T, K_Q and

744

J for without propeller condition in table 2 are shown in Fig.10. In the present computation, propeller is assumed without boss. fb_θ is non-zero from the equation (6) at $r=0$. But fb_θ is thought to be zero at the shaft center as shown in figure. fb_y and fb_z are decomposed from fb_θ as follows.

$$fb_y = -fb_\theta \sin\theta, \quad fb_z = fb_\theta \cos\theta \qquad (9)$$

In the computation, the fb_x, fb_y and fb_z are given at the points where u, v and w are defined, respectively, corresponding to the pressure points at the propeller plane. So, r and θ are calculated from y and z at those points and fb_x and fb_θ are calculated from eq.(5) through (8).

3.3 Solution domain and Computational Grid

In the computation, the detail propeller geometry, the thickness of rudder and the rudder stock were ignored. The arrangements of the propeller and the rudder is defined as follows; The propeller plane is $x=0$ and the propeller disk in which the body forces are non-zero is the circle whose radius is 0.5. With respect to the flat plate rudder, leading edge is $x=0.3$; trailing edge is $x=1.23$; upper edge is $z=0.65$; lower is $z=-0.65$, and it exists on $y=0$ in $z-x$ plane. Those arrangement is same as that in experiment.

Two Solution domains are used for the computation. One is the half (starboard side) domain using symmetric condition with respect to the shaft center line for the present geometry written as follows;

$$u(x,y,z)=u(x,-y,-z)$$
$$v(x,y,z)=-v(x,-y,-z)$$
$$w(x,y,z)=-w(x,-y,-z) \qquad (10)$$
$$p(x,y,z)=p(x,-y,-z)$$

This computation was carried out first to save the memory size. In this case, The solution domain is $[-3, 3.63]$, $[-0.05, 3.0]$ and $[-3.0, 3.0]$ in x, y and z directions, respectively. The other is the full (port and starboard sides) domain. The solution domain is $[-3.0, 3.0]$ in y direction and the same for the other direction as the half domain. Computational grid of the former case is shown in Fig.9. The grid system of latter case extended to negative y direction as same as positive y direction. The grid numbers are (63 , 32 , 61) in (x , y , z) direction, respectively for half domain computation and (63 , 61 , 61) for full domain

computation. The minimum grid spacing is 0.01 at propeller plane, rudder leading edge and trailing edge in x directions, and 0.05 in y and z directions in the region where y or z is less than 0.7. This uniform grid size near the propeller circle in cross plane is chosen from experimental results. Axial body force (fb_x) is embedded at $x=0.005$ and y and z direction body force (fb_y, fb_z) at $x=0$ in x direction due to the staggered grid system. Note fb_y is given at v point and fb_z at w point at $x=0.0$.

3.4 Boundary Conditions

The boundary conditions are as follows;

(1) on inlet plane $x=-3.0$, uniform flow condition is given. $u=1.0$, $v=w=p=0$

(2) on exit plane $x=3.63$, zero-normal(axial)-gradient condition is applied.

(3) on the outer boundary in y direction

$$y=\pm 3.0, \quad \partial(u,w,p)/\partial y=0, \quad v=0$$

(4) on the outer boundary in z direction

$$z=\pm 3.0, \quad \partial(u,v,p)/\partial z=0, \quad w=0$$

(5) on the rudder surface, no slip condition and zero-normal-pressure-gradient condition are imposed. $u=v=w=0.0$ and $\partial u/\partial y=0$

For the half domain computation, above symmetric condition eq(10) is used for u, w, p at $y=-0.05$ and v at $y=-0.025$ by using u, w, p at $y=0.05$ and v at $y=0.025$ of previous iteration except for on the flat plate rudder.

4. COMPUTATIONAL RESULTS AND DISCUSSION

Axial velocity contours and cross flow vectors of half domain computation for the with and without rudder conditions are shown in Fig.11 and Fig.12, respectively. The results of full domain computation are shown in Fig. 13 and Fig.14 for the with and without rudder conditions, respectively. The velocity distributions are drawn at three axial stations; a) at $x=0.01$ (just downstream of the propeller plane), b) $x=1.23$ (at rudder trailing edge), and c) $x=2.13$ (grid point near the station of experiment). From those figures, two computations show almost same results although the full domain computation show a little bit asymmetry with respect to the center line. So, for the present steady laminar flow computation, half domain computation can be used to get the very similar results by small computer as those of full domain computation. In the following, the results of full domain computation are discussed.

For the without rudder condition shown in

745

Fig.13 a), b), c), the computational results show general feature of the propeller slipstream. The axial velocity is accelerated and the swirl velocity is produced by the propeller at $x=0.01$. The swirl velocity is maximum just downstream of the propeller and decays with downstream distance. At $x=0.01$, the flow toward the shaft center exists outside the propeller slipstream corresponding to the contraction. The axial velocity is increased from $x=0.01$ to $x=1.23$ and decay very gradually. The axial velocity contours also show the diffusion of the tip vortex sheet. So, the computation can capture the flow field qualitatively. In comparison with experimental results shown in Fig.4, the acceleration of the axial velocity and swirl velocity are both underpredicted at just behind the propeller. It might be due to the coarse grid size at propeller plane and the effect of the boss. The body force distribution applied for this computation which is made based on the force measurement and Hough and Ordway circulation distribution also might be different from load distribution of mean–flow measurement condition. The acceleration and decay of the axial velocity is predicted fairly well if the underprediction at $x=0.01$ is considered. But the diffusion of the concentration of axial velocity contours near the propeller radius is faster than experiment. The reason is considered as the low Reynolds number computation and the numerical diffusion due to coarse grid in cross plane. The decay of the swirl velocity is much faster than that in experiment especially near the shaft center line. In experiment, the swirl velocity is larger as the position is closer to the shaft center line at all three stations. It suggests that the strong hub vortex exists, the diameter of its core is very small and its decay is slow. But in the computation, The large core of the hub vortex is observed at $x=0.01$ and decays very fast. It is due to the difference of Reynolds number and the coarse grid.

For the with rudder condition shown in Fig.15 a), b), c), the computation also show the general qualitative feature of flow field. At $x=0.01$, the velocity distribution is almost same as that for the without rudder condition. The high velocity region moves upward in the port side and downward in the starboard side at the latter two stations. The cross plane vectors are smaller than those for the without propeller condition. In comparison with experimental results shown in Fig.5, both axial velocity acceleration and swirl velocity are underpredicted similar as for the without rudder condition. At the rudder trailing edge, $x=1.23$, high velocity region has similar shape as the experimental high velocity region except near the flat plate. Near the flat plate, the

cross plane velocity is small due to the laminar boundary layer and the present computation resolution. It might be the reason why the upper edge of the slipstream has different shape from the experimental results. The difference of the decay of the axial velocity contour concentration and the cross plane velocity between in experiment and in computation is almost same as for the without rudder condition. The change of the direction of cross plane vector from the without rudder condition to the with rudder condition is predicted fairly well, although the difference is observed in detail due to the thickness effect and so on. At $x=2.13$, comparing with the experimental results at $x=2.0$, the position of high velocity region is predicted fairly well, but the outer shape of the slipstream is different. The movement of the slipstream near the center plane is small due to the laminar boundary layer and wake and small cross plane velocity. So, the gap between port side and starboard looks small, but the gap of the high velocity region show similar trend. Note that the vortices whose turning direction is anti–clockwise are observed in the upper part of the port side and in the lower part of the starboard side. It is also observed in experimental result of Tanaka et al.[10]. It is also noted that the lower velocity region near the center plane at $x=1.23$ is observed in lower part of the port side and upper side of the starboard side in experiment. It might be the movement of divided hub vortex. This phenomena is also seen in the computational results, but the movement is small and not clear due to the laminar boundary layer and the diffusion of hub vortex.

To compare the computation and experiment more precisely, the velocity profiles at nine heights at $x=1.23$ are shown in Fig.15 and Fig.16 for the without and the with rudder conditions, respectively. For the without rudder condition, the axial velocity and cross flow velocity are both underpredicted as discussed previously. For the axial velocity, the shape of the acceleration is well predicted. For v and w, overall shapes are predicted, but the w for $z=0$ show clearly the much larger diffusion of the hub vortex. For the with rudder condition, the three velocity components are also underpredicted. The velocity outside the boundary layer at $z=0.545$ is not affected by propeller in the computation although the influence of the propeller is observed in experiment. It might be due to the underprediction of the cross flow velocity. At $z=0.409$, the high axial velocity in the port side is predicted although the extent and the magnitude are underpredicted. At $z=0.273$ and 0.136, the larger region of high axial velocity and higher

746

axial velocity in the port side than in the starboard side observed in experiment are predicted similar fairly well. Horizontal velocity is smaller for the with rudder condition compared with for the without rudder condition. It is similar with experiment. The profiles of the axial velocity are very similar with experiment. At $z=0.0$, the velocity defect due to flat plate rudder is over-predicted because of the laminar flow computation and the coarse grid. The velocity distribution of both experiment and computation has the symmetric feature written in eq.(10).

From Fig.11 through Fig.16, the present computation show the large diffusion and the underprediction of velocity. It might be improved by turbulence model for at least plate boundary layer and wake and the finer grid. It also might be effective to use the Euler code.

Fig.17 and Fig.18 show the result of streakline tracing from the rotating point at propeller plane which is rotating at the same speed as the propeller blade. It has been conducted to investigate the model of training vortices in invicid theory for the with rudder condition. The procedure is as follows; (1) from the 72 points at every 5 degree θ at prescribed r, the streamlines are traced with time step $J/72$ ($n=1/J$, where n is the number of propeller revolution in the computation $D_P=1.0$, $V_A=1.0$). (2) The points at propeller plane were numbered in the unti-clockwise (positive θ) direction from 0 to M from $\theta=0$ and the 72nd point is same as the 0-th point. (3) For the streakline from 0-th point, the point at K-th time step on the streamline from K-th point ($K=0,M$) were drawn. Although the flow field is steady, the present streakline show the helical streaklines which are observed usually. In comparison with the flow visualization, the pitch of the helical streaklines is similar for both $r=0.5R_P$ and $r=0.9R_P$ for without rudder condition. It shows the pitch of the helical streakline is larger at $r=0.5R_P$ than $r=0.9R_P$. For the with rudder condition shown in Fig.18, the distortion of the helical streaklines are clear. It shows the helical streakline moves upward in the port side and downward in the starboard side. It also shows the low velocity region where the simulated air bubbles do not go further compared with outer part of the boundary layer. These streaklines show very similar phenomena as experimental results shown in Fig.7 and Fig.8. The streaklines which is observed from downstream show the enlargement of the slipstream in the vertical direction clearly.

Limiting streamlines on the flat plate rudder surface at the port side are shown in Fig.19. The uniform flow direction is from left to right in this figure. Although computational grid is so coarse, it is suggestive that upward flow exists on the rudder surface at the port side. The direction of limiting streamlines is similar as the direction of tufts on the surface of flow visualization by Tanaka et al.[10].

5. CONCLUDING REMARKS

This work presents mean flow measurement data and flow visualization of the flow field around the rudder in the propeller slipstream. The numerical method and the computational results for the flat plate rudder behind the propeller which represented by body force distribution are also presented. Although the Reynolds number of the computation is small and the number of grid is limited, the salient feature of the flow field for the time-averaged flow field has been predicted by present approach. In detail, there is some discrepancy due to the laminar flow computation and the numerical treatment. The present approach can be extended easily for the flat plate rudder with angle of attack in propeller slipstream and the rudder with zero thickness fins.

Finally, some of the issues that must be addressed while further developing the present approach are as follows: improvement of accuracy in calculating the propeller flow field ; introduction of appropriate turbulence model for at least the rudder boundary layer ; including the rudder shape (thickness and so on) effects by using body-fitted coordinate system ; using finer and appropriate grid for propeller flow field. Also of interest is to use present approach for the improvement of the invicid theory which treat the propeller-rudder interaction.

REFERENCES

1. Nakatake,K.: "On Ship Hull-Propeller-Rudder Interactions", 3rd JSPC Symposium on Flows and Forces of Ships, 1989, pp231-259 (in Japanese)

2. Tamashima,M., and Yang,C.J.,Yamazaki,R.: "A Study of the Flow around a Rudder with Rudder Angle behind Propeller", Transactions of the West-Japan Society of Naval Architects, No.83, 1992 (in Japanese)

3. Ishida,S.: "The Recovery of Rotational Energy in Propeller Slipstream by Fins installed after Propellers", Journal of the Society of Naval Architects Japan, Vol.159, 1986 (in Japanese)

4. Baba,E.,and Ikeda,T.: "Flow Measurements in the Slipstream of a Self-Propelling Ship with and without Rudder", Transactions of the West-Japan Society of Naval Architects, No.59, 1979 (in Japanese)

5. Tanaka,I., Suzuki,T., Toda,Y., and Kawashima,T.: "Flow visualization of propeller tip vorticties using air bubbles", 8th Symposium on Flow Visualization, 1980 (in Japanese)

6. Okamoto,Y., Kasahara,Y., Fukuda,M., and Shiraki,A.: "Development of a Energy-saving Device NKK-SURF (Swept-back up-thrusting Rudder Fin) ", NKK TECHNICAL REPORT, No.132, 1990 (in Japanese)

7. Mori,M.,Yamasaki,Y.,Fujino,R.,Ohtagaki,Y.: "IHI A.T.Fin -1st Report: Its Principle and Development-", Ishikawajima-Harima Engineering Review, Vol.23, No.3, 1983 (in Japanese)

8. Stern,F., Toda,Y.,and Kim,H.T.: "Computation of Viscous Flow Around Propeller-Body Configurations: Iowa Axisymmetric Body", Journal of Ship Research, Vol.35, No.2 June 1991

9. Stern,F.,Kim,H.T.,Patel,V.C.,and Chen,H.C.: "A Viscous Flow Approach to the Computation of Propeller-Hull Interaction", Journal of Ship Research, Vol.32, No.4, Dec.1988

10. Tanaka,I., Kawashima,T., and Toda,Y.,"On Flow Field Stracture Near Free Surface At the Stern Of Ship Models", Journal of the Kansai Society of Naval Architects, Japan, No.180, 1981 (in Japanese)

11. Nagamatsu,N., and Shimizu,H.: "Study on Propeller Slipstream", Journal of the Kansai Society of Naval Architects, Japan, No.197, 1985 (in Japanese)

12. Patanker,S.V.: "Numerical Heat Transfer and Fluid Flow", McGraw-Hill, New York, 1980

13. Ishii,N.: "The Influence of Tip Vortex on Propeller Performance", Journal of the Society of Naval Architects Japan, Vol.168, 1991 (in Japanese)

14. Hough,G.R., and Ordway,D.E.: "The Generalized Actuator Disk", Developments in Theoretical and Applied Mechanics, Vol.2, Pergamon Ga., 1965, pp 317-336

15. Suzuki,H., Toda,Y., and Suzuki,T.: "Numerical Simulation of a Flow Field Around a Flat Plate Rudder in Propeller Slipstream", Journal of the Kansai Society of Naval Architects, Japan, No.219, 1993 (in Japanese)

Table 1. Principal dimensions propeller and rudder

Propeller		
Number of Blades		5
Diameter	(mm)	220.0
Pitch Ratio		0.700
E.A.R.		0.600
Boss Ratio		0.170
Blade section		MAU-M
Direction of Rotation		Right
Rudder		
Thickness	(mm)	8.0
Chord	(mm)	205.0
Span	(mm)	286.0

Table 2. Propeller condition

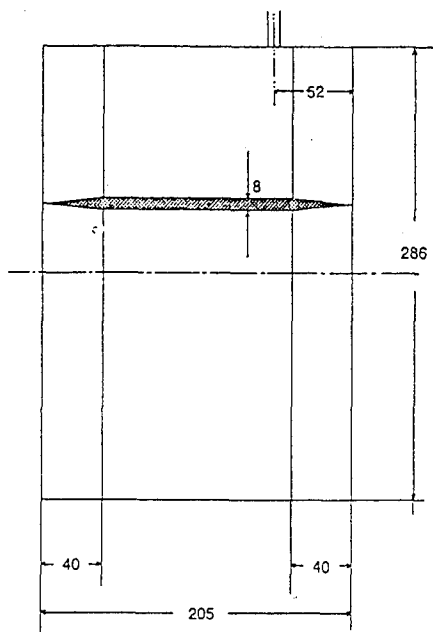| Propeller condition	
V_A (m/s)	1.26
n (r.p.s.)	14.32
J	0.40
WITHOUT RUDDER	
K_T	1.91×10^{-1}
K_Q	2.54×10^{-2}
WITH RUDDER	
K_T	1.98×10^{-1}
K_Q	2.50×10^{-2}

Fig.1　Profile of the rudder
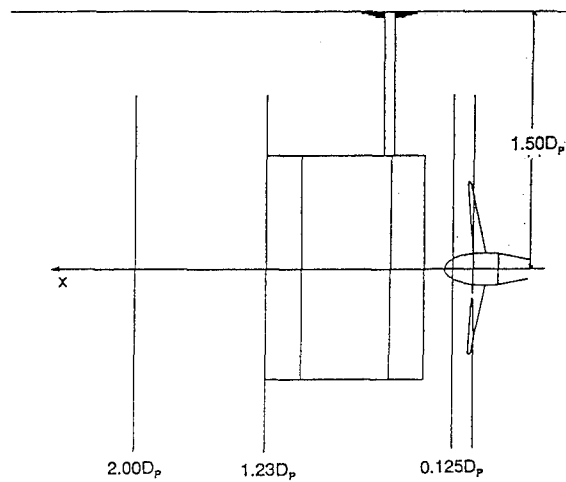
Fig.3　Measuring sections

Fig.2　Experimental set

749

a) $0.125D_P$ behind propeller

b) $1.23D_P$ behind propeller

c) $2.00D_P$ behind propeller

Fig.4   Measured axial and cross flow velocity distribution
(without rudder)

a) $0.125D_p$ behind propeller

b) $1.23D_p$ behind propeller

c) $2.00D_p$ behind propeller
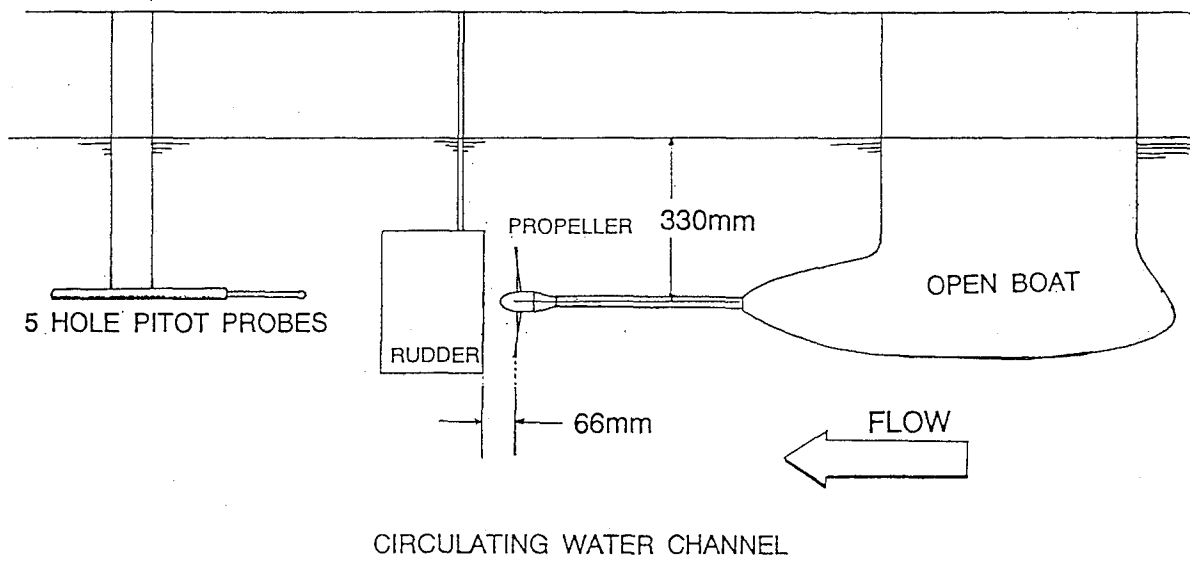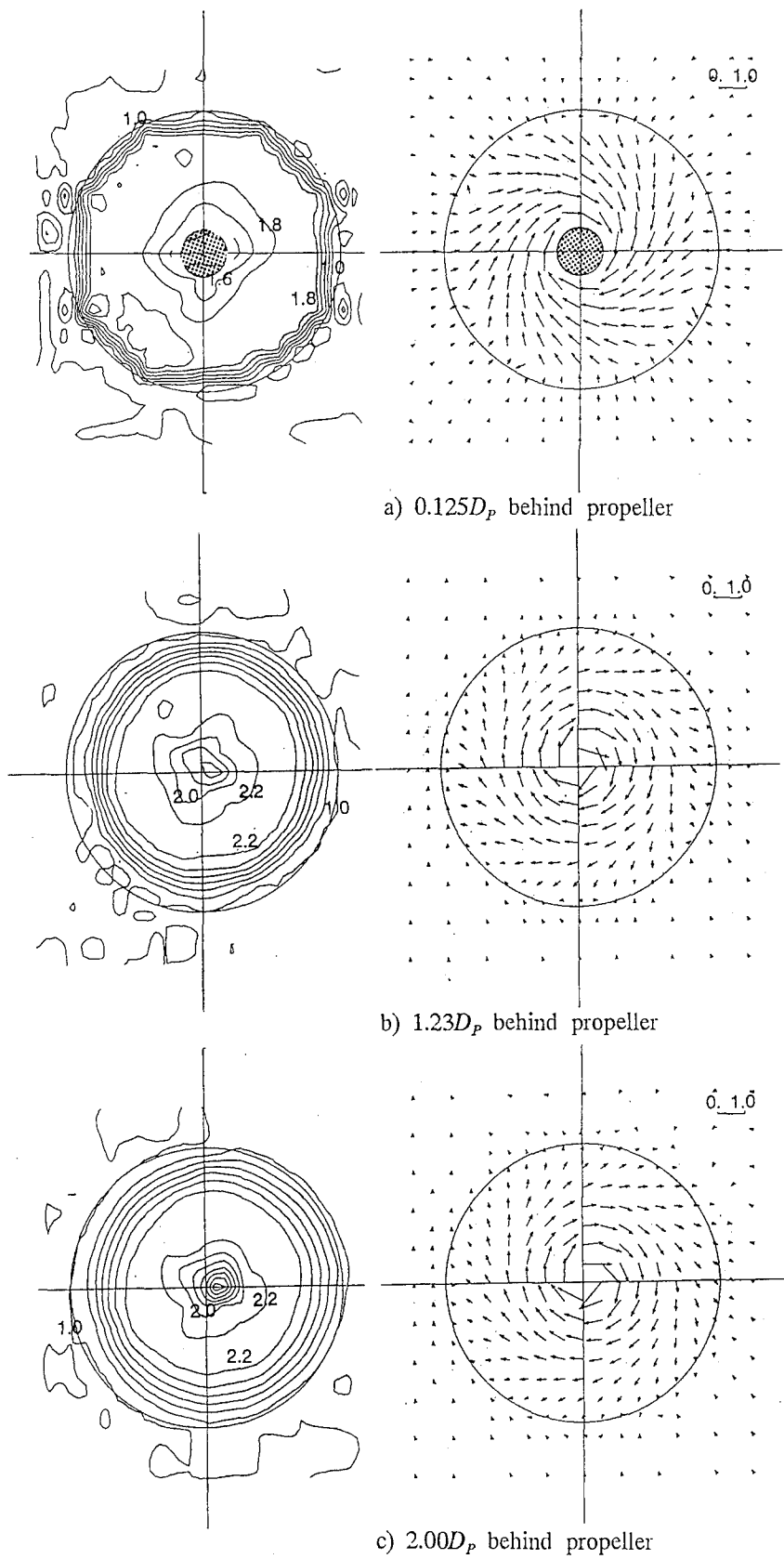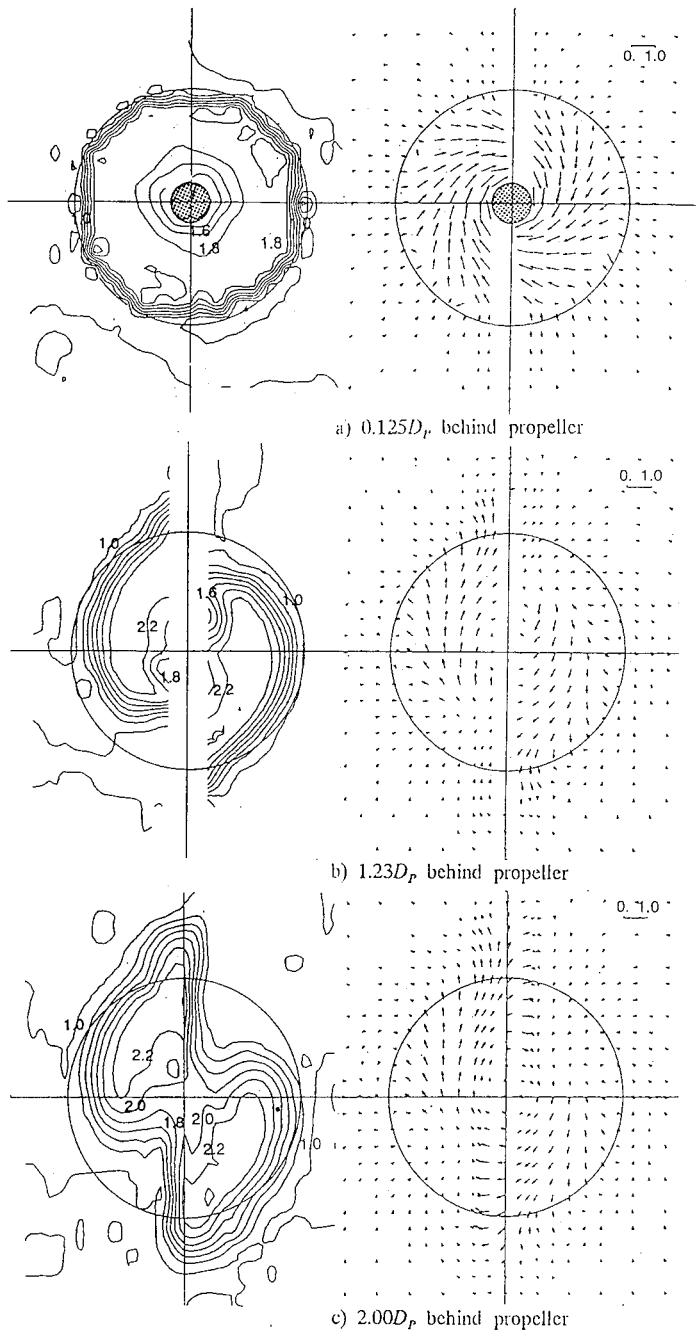
Fig.5 Measured axial and cross flow velocity distribution
(with rudder)
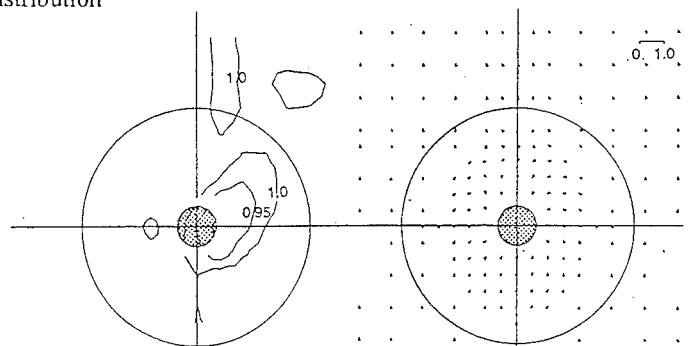
Fig.6 Axial and cross flow velocity distribution at $x=0.125$
(without propeller and rudder)
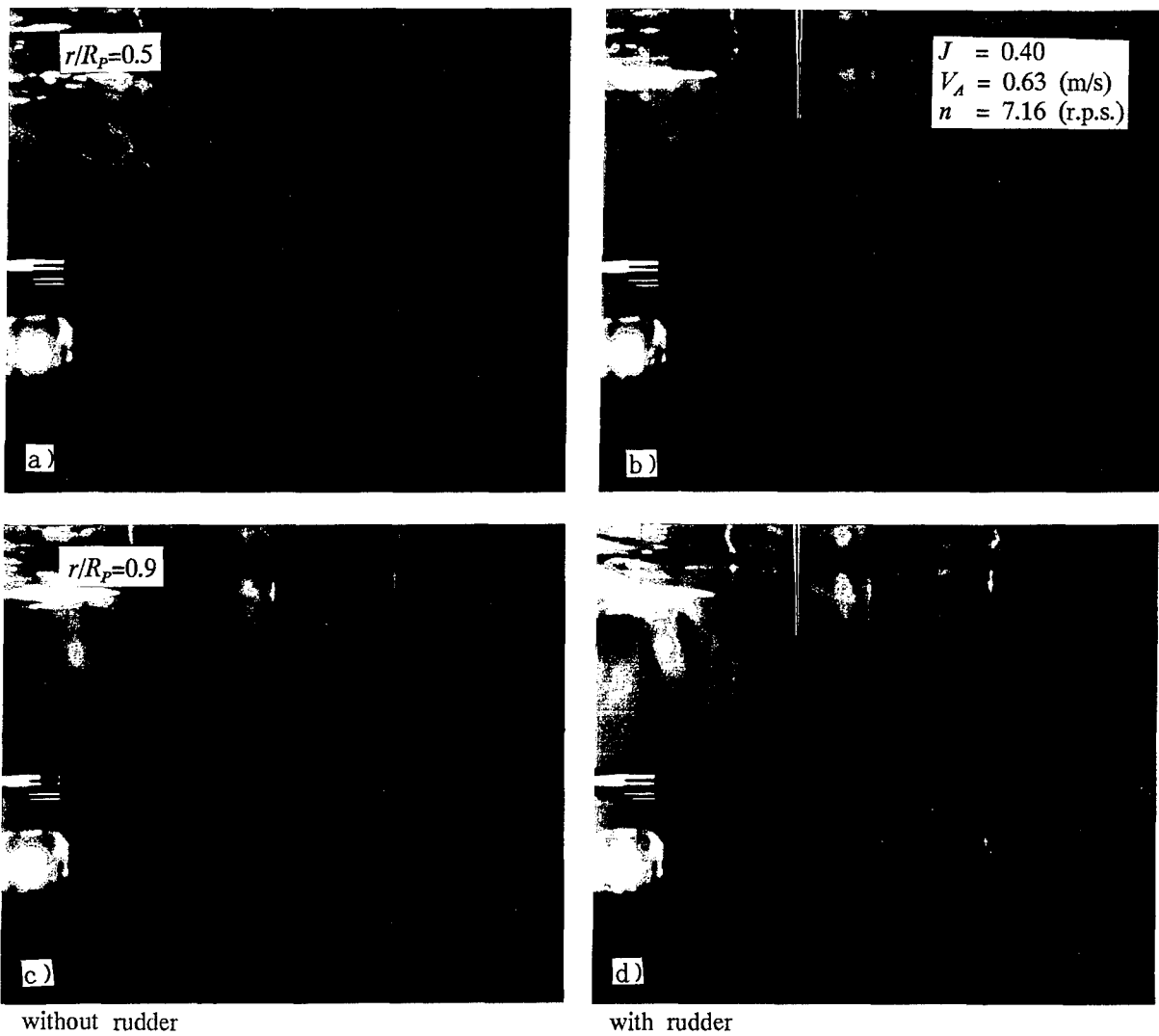
Fig.7   Flow visualization of the propeller slipstream using dye

In the figure the upper-left panel is labelled $r/R_P{=}0.5$ and marked a), the upper-right panel is marked b) with the box:

$$J = 0.40$$
$$V_A = 0.63 \ (m/s)$$
$$n = 7.16 \ (r.p.s.)$$

The lower-left panel is labelled $r/R_P{=}0.9$ and marked c); the lower-right panel is marked d).

without rudder   with rudder
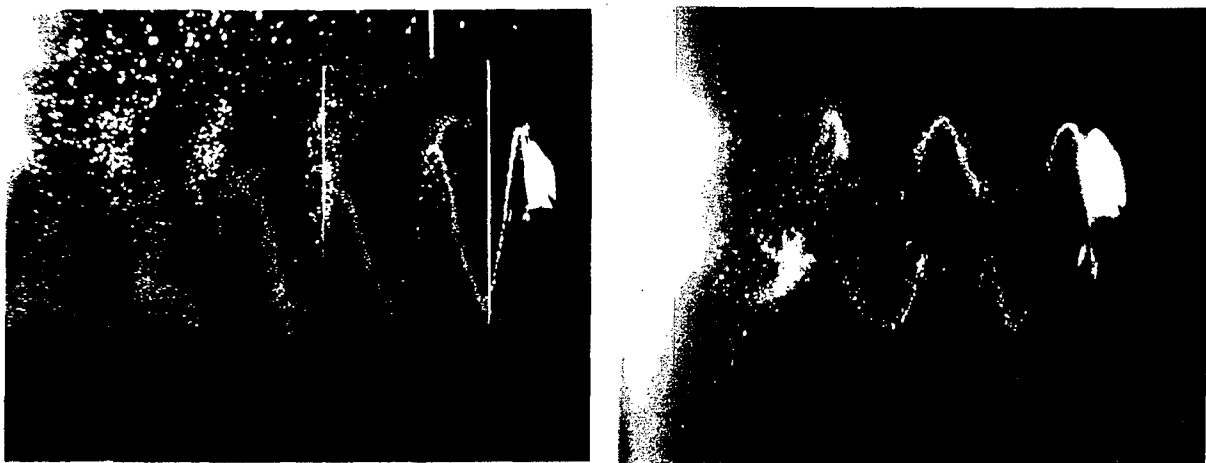
Fig.8   Flow visualization of the propeller tip vorticities using air bubbles[5]

752
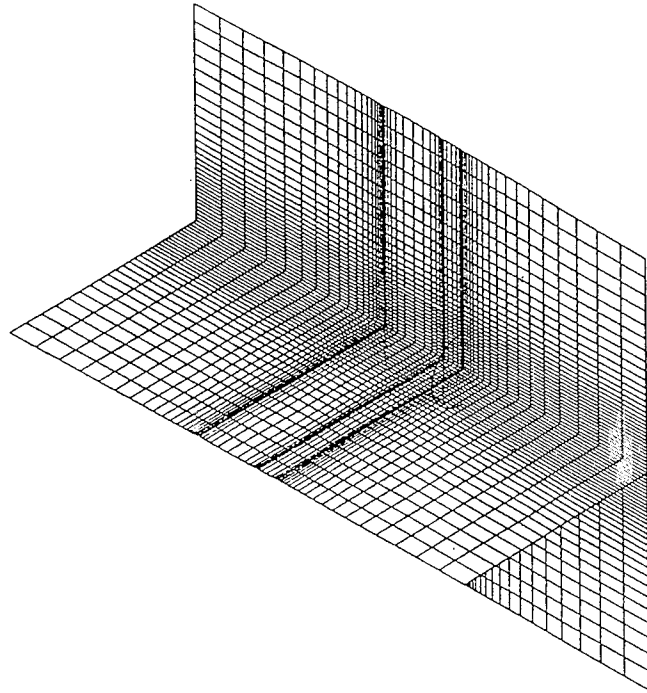
Fig.9   Computational Grid
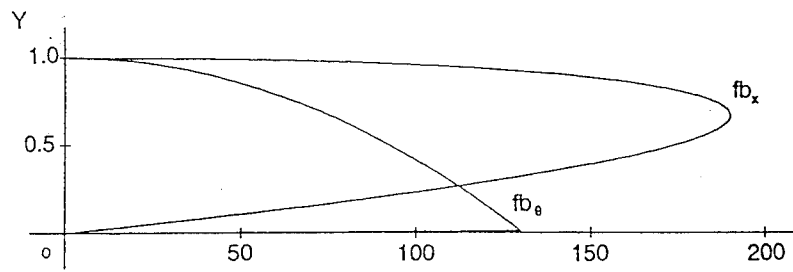
Fig.10   Body force distribution
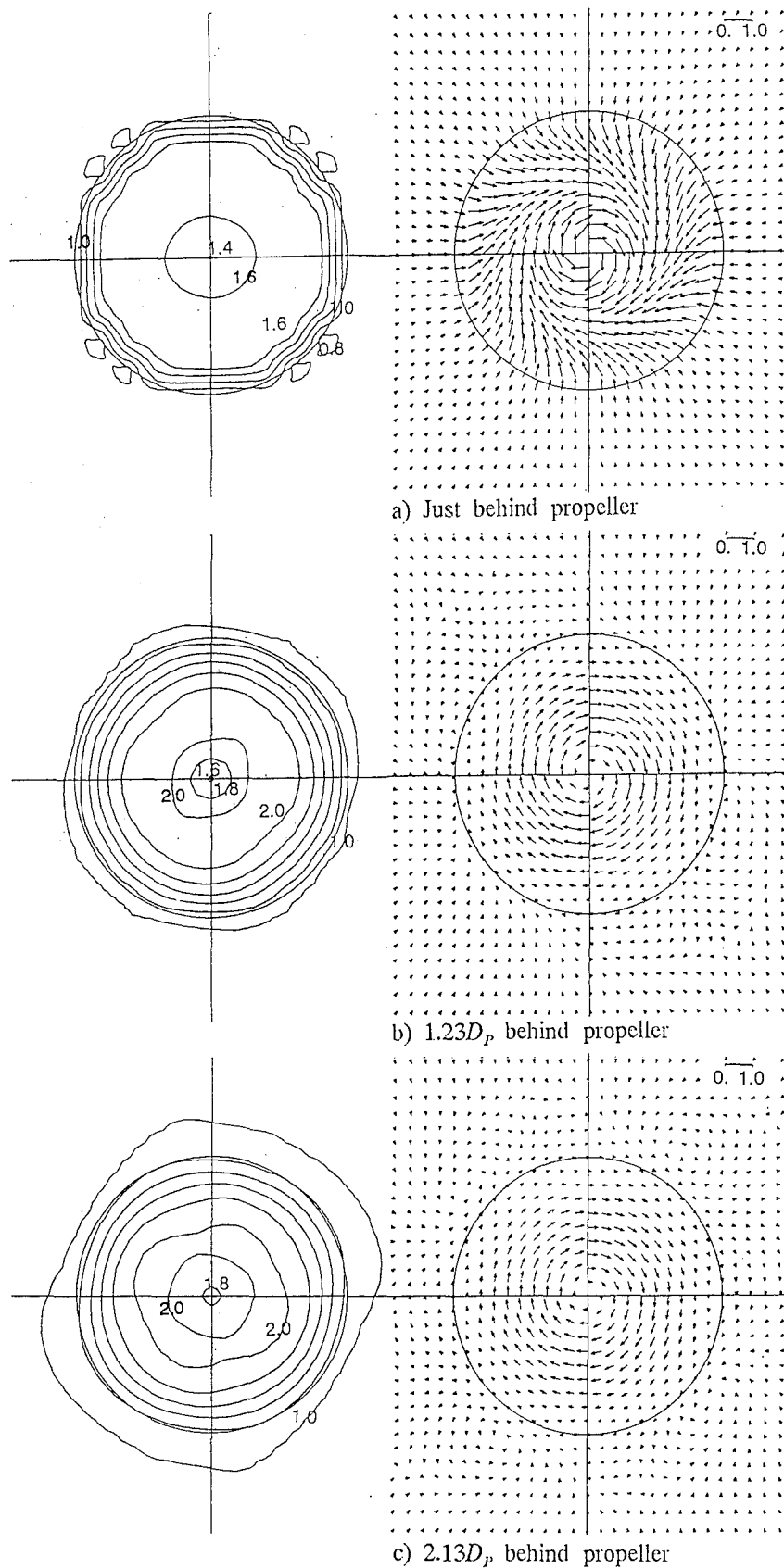
a) Just behind propeller

b) $1.23D_P$ behind propeller

c) $2.13D_P$ behind propeller

Fig.11 Computed axial and cross flow velocity distribution
(Half domain computation; without rudder)

a) Just behind propeller

b) $1.23D_P$ behind propeller

c) $2.13D_P$ behind propeller
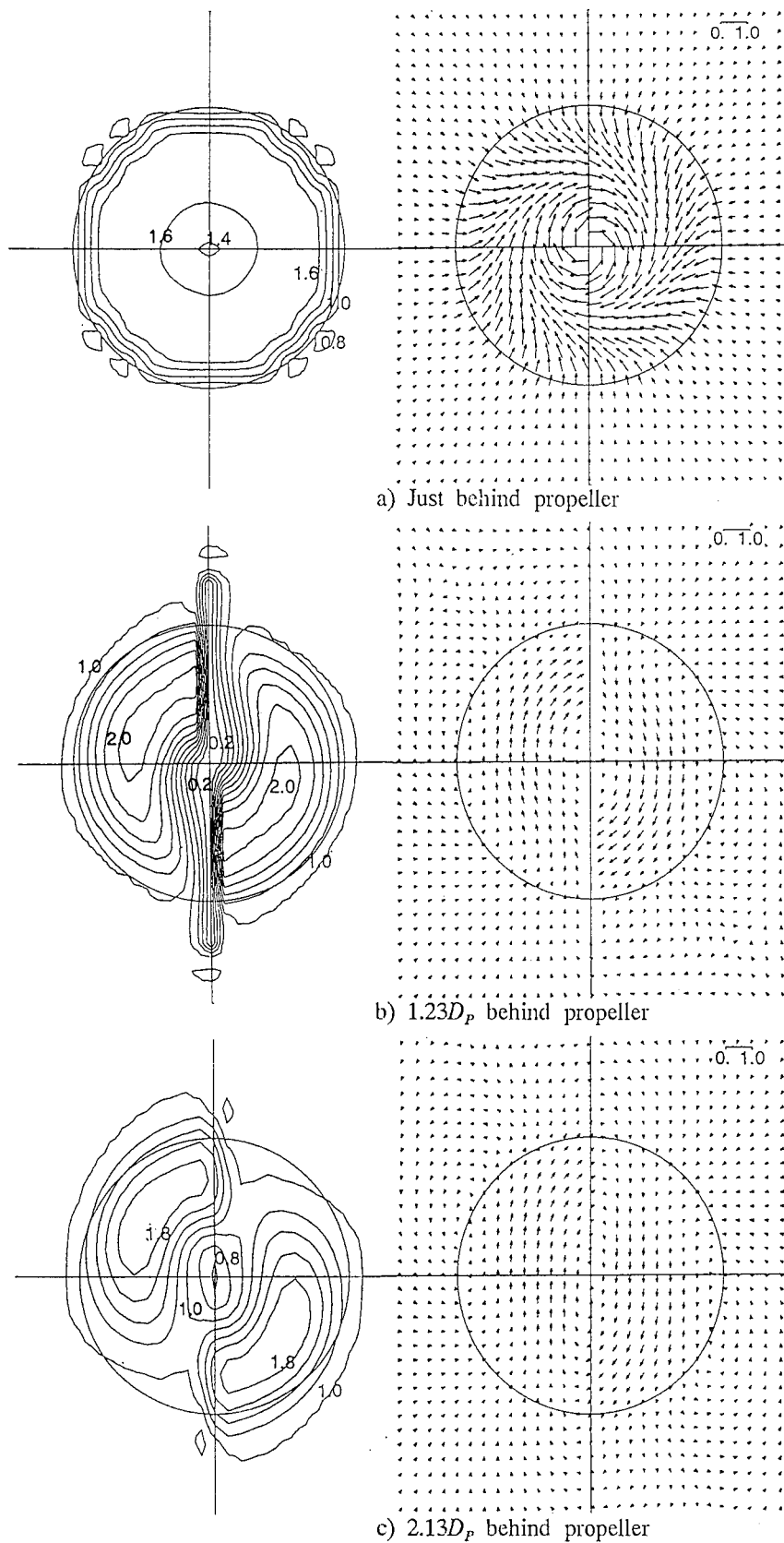
Fig.12 Computed axial and cross flow velocity distribution
(Half domain computation; with rudder)

755

a) Just behind propeller

b) 1.23D_P behind propeller

c) 2.13D_P behind propeller

Fig.13　Computed axial and cross flow velocity distribution
(Full domain computation; without rudder)

a) Just behind propeller

b) 1.23D_P behind propeller
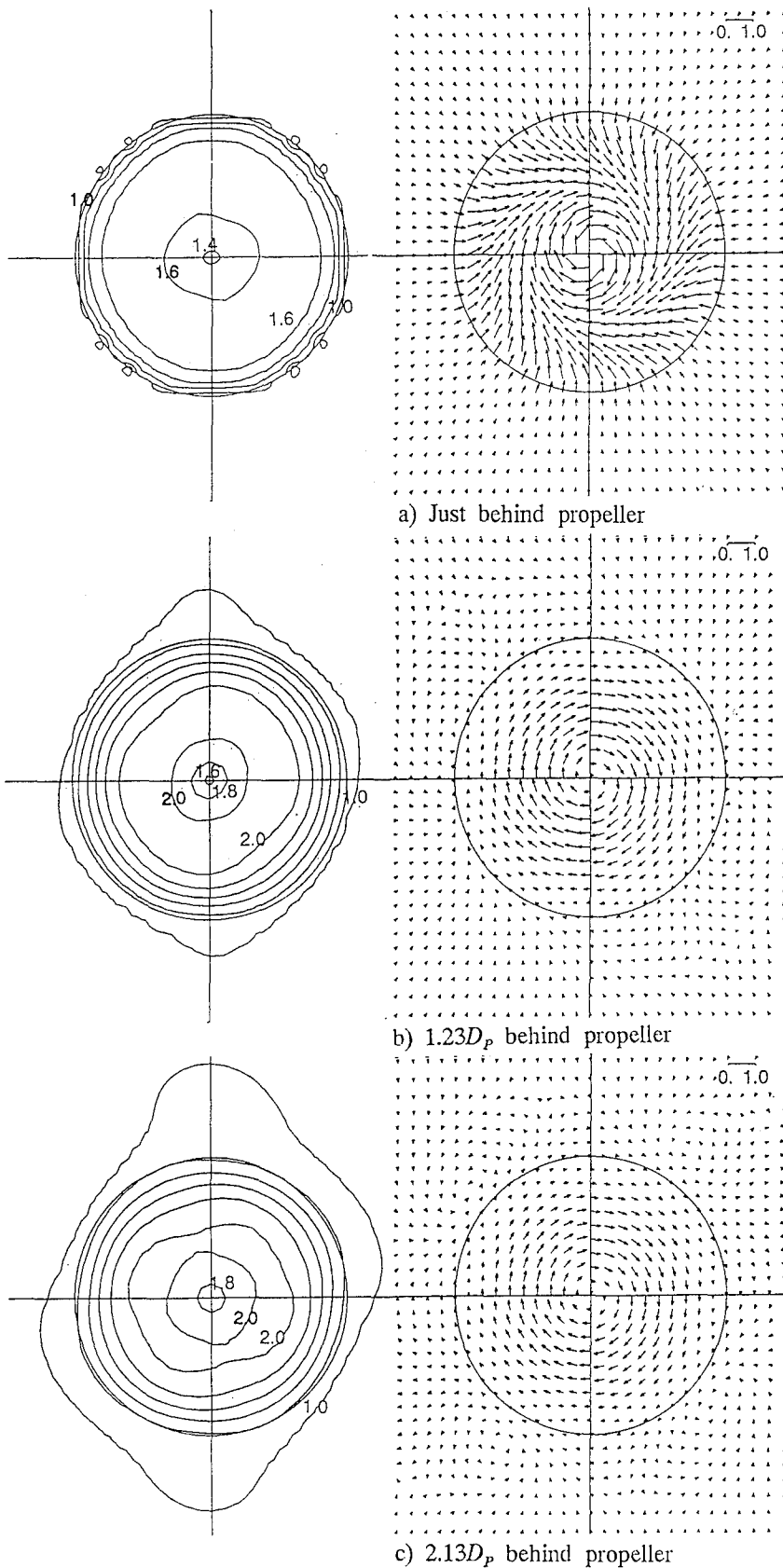
c) 2.13D_P behind propeller
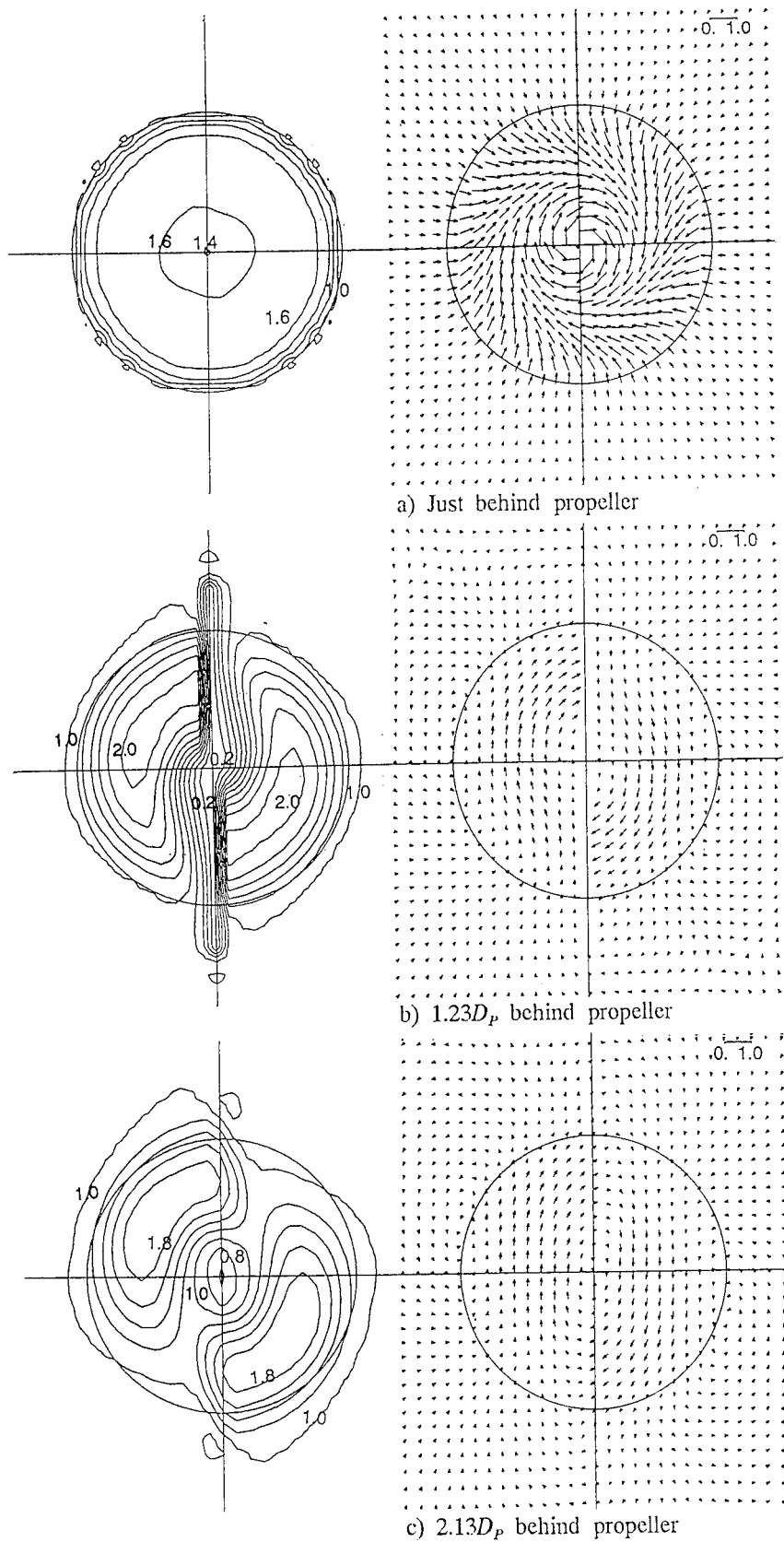
Fig.14 Computed axial and cross flow velocity distribution
(Full domain computation; with rudder)

757
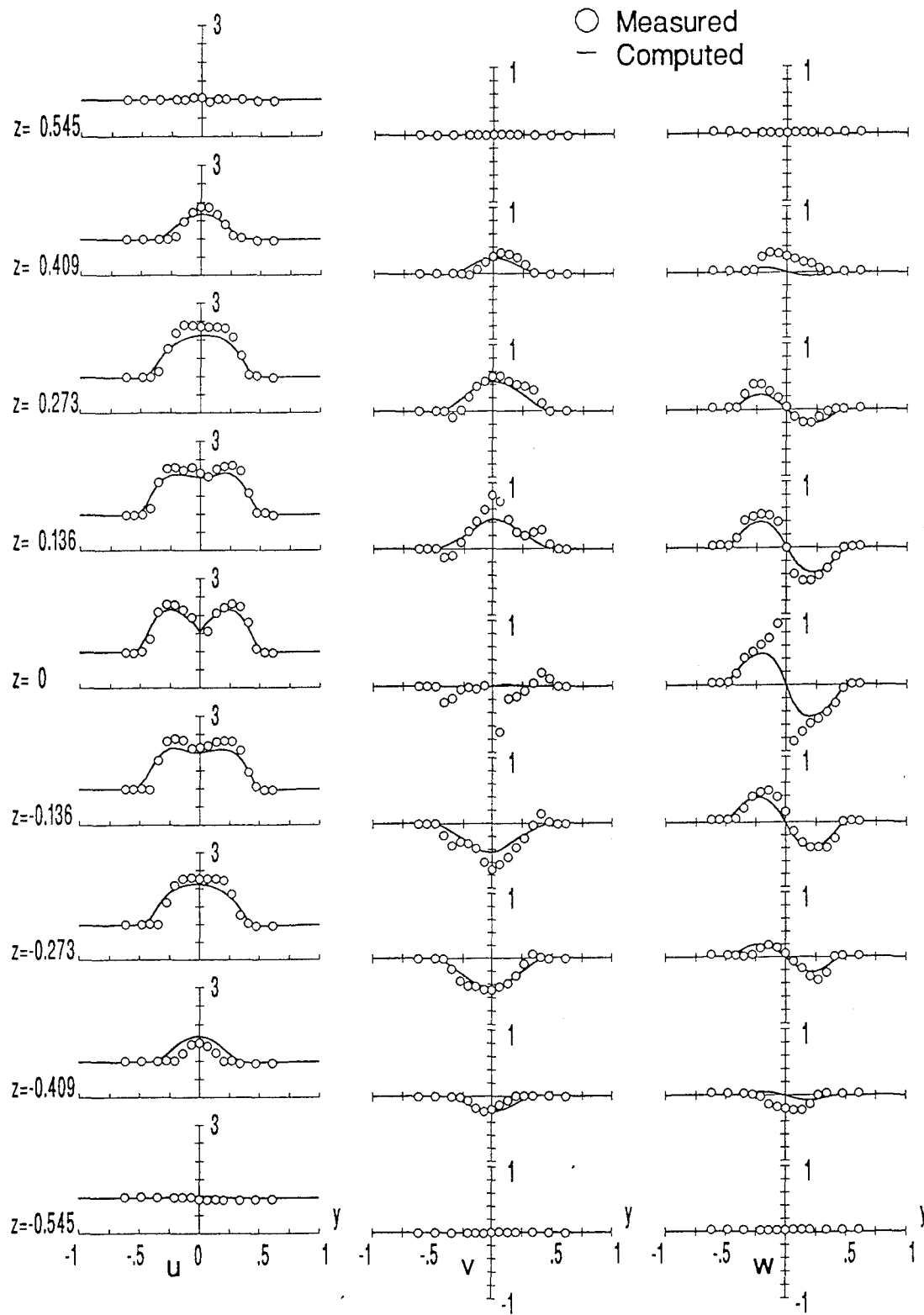
Fig.15 Comparison between measured and computed velocity profile at $x/D_P=1.23$ (without rudder)
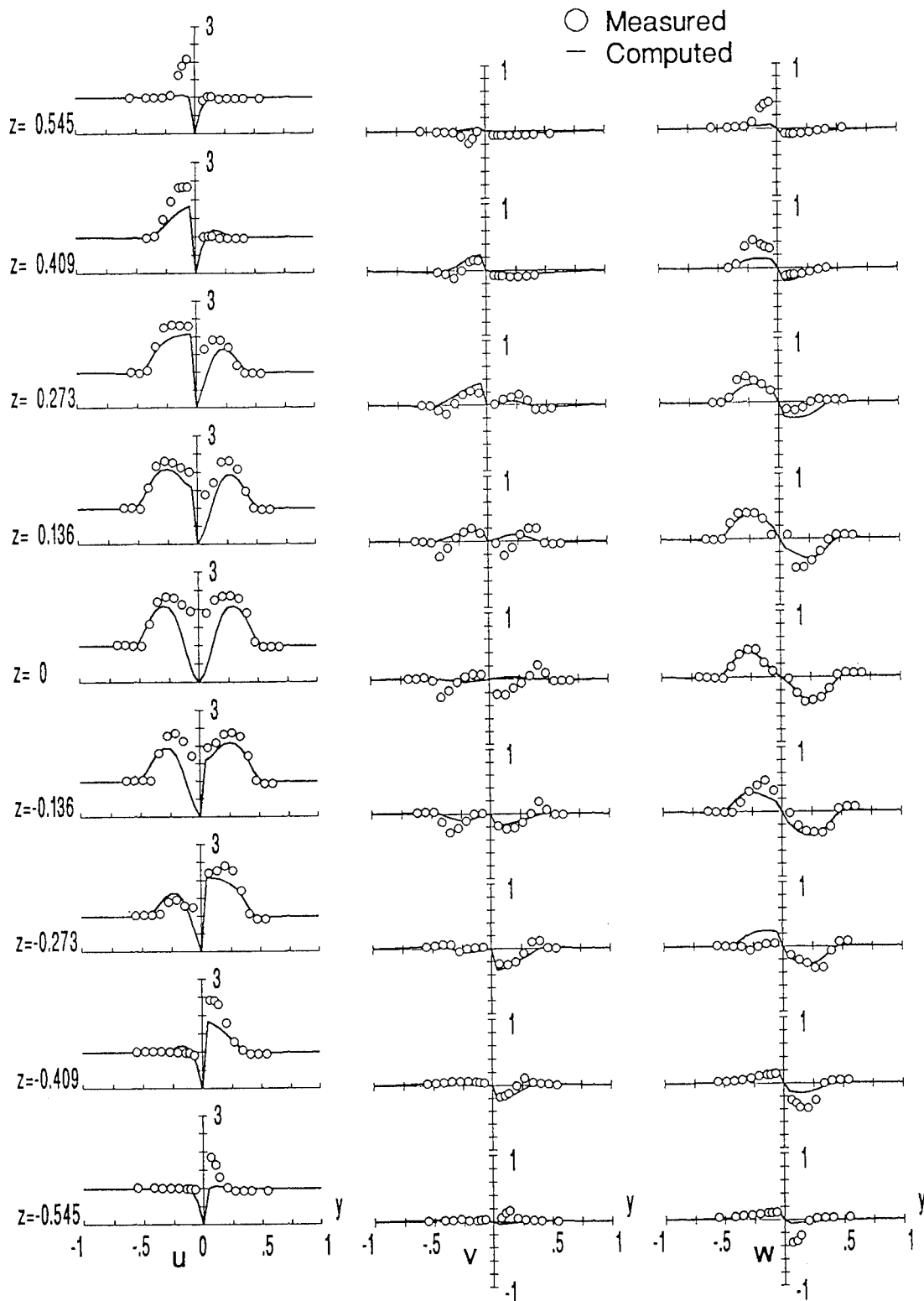
Fig.16 Comparison between measured and computed velocity profile at x/D_P=1.23
(with rudder)

Looking starboard side

Looking upward

Looking upstream

a) $r/R_P=0.5$

Looking starboard side

Looking upward

Looking upstream

b) $r/R_P=0.9$
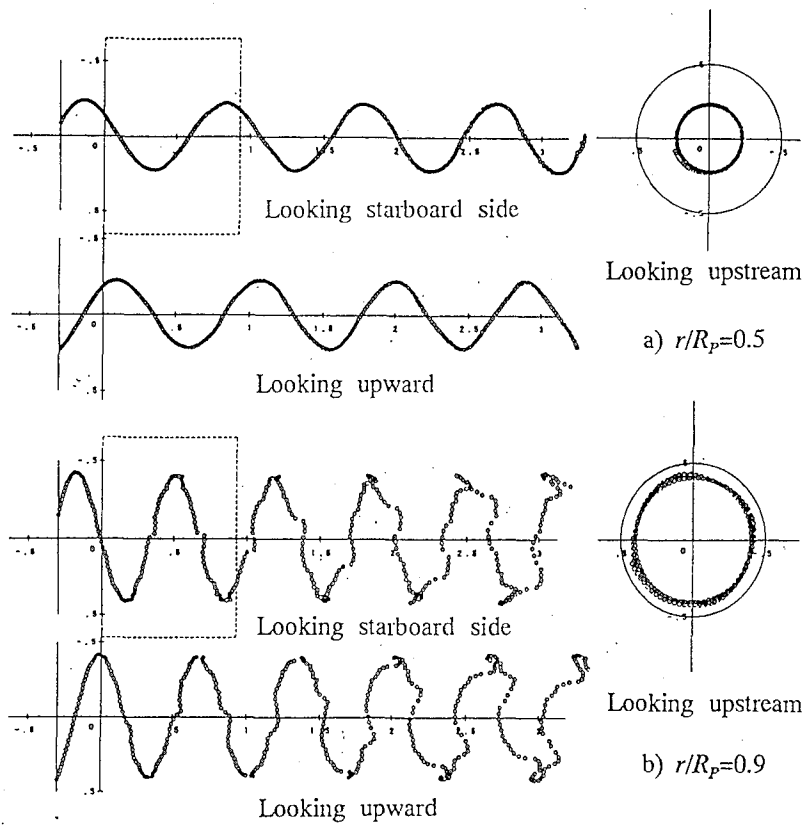
Fig.17 Computed streakline of a propeller slipstream (without rudder)

Looking starboard side

Looking upward

Looking upstream

a) $r/R_P=0.5$

Looking starboard side

Looking upward

Looking upstream

b) $r/R_P=0.9$

Fig.18 Computed streakline of a propeller slipstream (with rudder)

Fig.19　Limiting　stream　line　on
the　rudder　surface

Determination of Load Distribution on a Rudder in Propeller Slipstream Using a Nonlinear Vortex Model

B. Kirsten and S.D. Sharma

(University of Duisburg, Germany)

ABSTRACT

The ship rudder is a lifting surface of rather low aspect ratio. The free shear layers departing from the top and bottom edges of a rudder at an angle of attack tend to roll up even in way of the rudder, as can be easily observed by flow visualization in a cavitation tunnel, for instance. This already leads to a deviation from the simple linear dependence of lift force on angle of attack. The situation becomes much more complex for a rudder operating in a propeller slipstream where the root and tip vortices of the propeller periodically hit the rudder. To calculate the influence of the propeller on the rudder, the propeller slipstream is modeled by a vortex-line system of root and tip vortices; the rudder including the free shearlayer, by vortex-rings. This leads to a vortex-lattice method for stationary problems.

NOMENCLATURE

Coordinate Systems
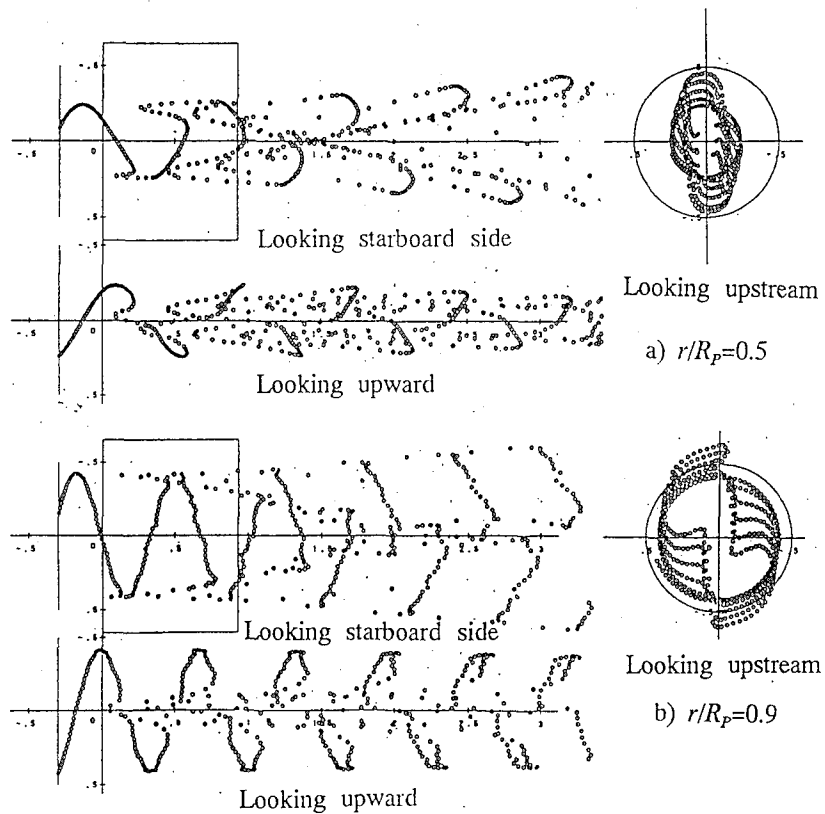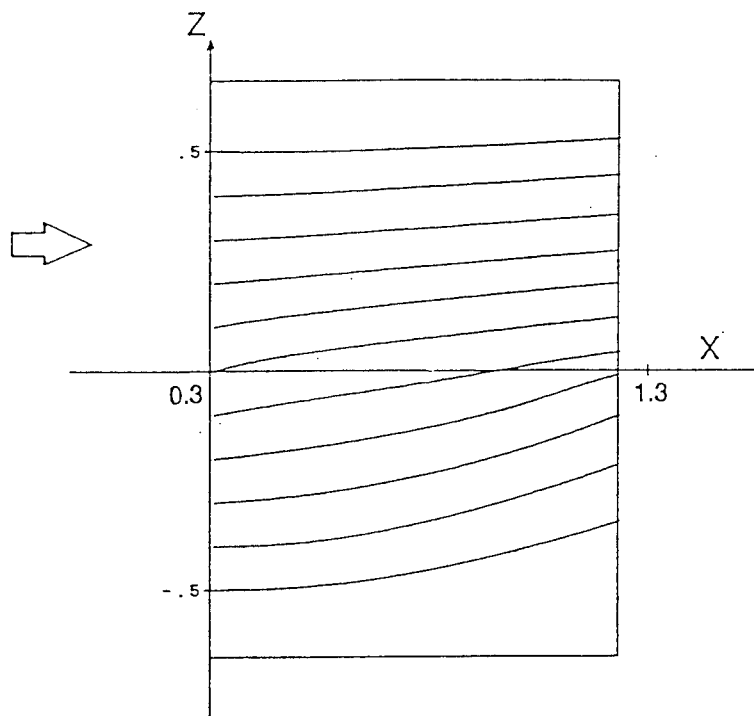
Two different coordinate systems are used alternatively depending on convenience.

The non-rotating system $Oxyz$ is righthanded, orthogonal, Cartesian, with origin O on (vertical) rudder axis at mid-height, x-axis in direction of uniform parallel (horizontal) inflow, and y-axis pointing upward. It is attached to the rudder but remains aligned to the inflow when the rudder is applied.

The rotating propeller-fixed system $Oxr\varphi$ is cylindrical, righthanded, with origin O at intersection of (horizontal) propeller axis and blade generatrix, x-axis in direction of uniform parallel (horizontal) inflow, and r-axis coincident with first blade generatrix.

Main Symbols

$\mathbf{A}$	Geometric influence coefficient matrix
$\vec{a}$	Radius vector $\vec{P}-\vec{S}$
$\vec{b}$	Panel boundary vector
c_L	Lift coefficient
c_{Th}	Thrust loading coefficient
D	Propeller diameter
J	Propeller advance coefficient
m	Number of control points
L	Rudder chord length
n	Propeller rate of turn
$\vec{P}$	Field point vector
R	Propeller radius
$\vec{S}$	Vortex point vector
$\vec{U}_\infty$	Velocity of uniform parallel inflow
$\vec{V}_{ind}$	Induced velocity
z	Number of propeller blades
β_i	Hydrodynamic induced pitch angle
Γ	Circulation
γ	Circulation density
Δc_p	Load distribution normalized by stagnation pressure of uniform inflow
$\Delta\vec{s}$	Vortex segment $\vec{S}_{i+1}-\vec{S}_i$
$\Delta\xi$	Axial separation of helical vortices
δ	Rudder angle of attack relative to $\vec{U}_\infty$
ϕ	Velocity potential
Λ	Aspect ratio
μ	Dipole moment density
ρ	Radius of asymptotic vortex cylinder
ρ	Mass density of fluid

1. INTRODUCTION

The steadily increasing concern for safety and environment necessitates continued improvement of the maneuverability of ships. Typically, the control force in maneuvering is generated through a rudder located at the stern in the slipstream of a screw propeller. In order to clarify the complex hydrodynamics of this configuration, several comparative model experiments with a rudder in open water and propeller slipstream have been conducted, notably by Baumgarten (1979) in a towing tank and by Kracht (1990) in a cavitation tunnel.

These experiments show that the combined free-vortex sheet shed from the rudder side edges and trailing edge begins to roll up already in way of the rudder and evolves further downstream into two tip vortex braids. In addition, the free-vortex sheets of the propeller blades, already rolled up into discrete tip and root vortices, impinge upon the rudder (see Fig. 1).

A complete theoretical description of this incompressible viscous flow problem would require a solution of unsteady Navier Stokes equations with appropriate boundary conditions. An analytical solution being out of question for this complex geometry, some numerical approximation would need to be found by means of finite difference equations with a very fine discretization to catch the real vortex structure. The computational effort would be formidable. However, if viscosity is neglected (except in so far it is implicitly responsible for generation and shedding of vorticity), the problem can be handled efficiently by a singularity method which if formulated as an integral equation constitutes a solution of the Laplace Equation for a velocity potential. This reasonable and almost standard simplification in lifting surface problems at high Reynolds numbers is adopted in the present paper. Moreover, it is assumed that the effect of the propeller slipstream on the rudder, which amounts to a slowly time-varying inflow in the rudder-fixed reference system, can be approximated by discrete quasi-steady steps.

For solving the potential equation, dipole singularities are distributed on the rudder center-plane and on the shear layer in the wake emanating from the side edges and the trailing edge; the propeller slipstream is idealized by discrete vortex lines. Boundary conditions necessarily imposed on the singular surfaces (no flux on the body and no force on the shed vortices) yield a nonlinear integral equation because the geometry of the shear layer is not known beforehand. Panelization of the singular surfaces reduces the integral equation to a system of (effectively nonlinear) algebraic equations which can be solved by iteration. A good overview of panel methods for vortex flows is given by Hoeijmakers (1989). Once the singularity strengths and locations are found, the velocity vector in the entire fluid domain including the boundary, i.e., the rudder surface can be calculated. Then also the pressure can be calculated everywhere by use of Bernoulli's equation.

Several singularity-based mathematical models for determining forces and moments on the propeller-rudder system as well as on the hull-propeller-rudder system have been formulated in the past, e.g., Brunnstein (1968), Tsakonas et al. (1970) and Klingbeil (1972). Due to the relatively low computer power available at that time these authors were forced to seek analytical solutions or estimates of the integrals involved as far as possible. An overview of the analytical approaches can be found in the books of Isay (1964, 1970). With present computing power a complex flow geometry can be better handled by a finer discretization of the flow boundary. Particularly suitable are panel methods which in case of simple singularities yield easily programmable algebraic equations, see, e.g., Belotserkovskii (1967).

The ship rudder is a classical lifting surface of small aspect ratio with a nonlinear lift characteristic arising from the influence of the separated secondary flow around the side edges. Such free-vortex sheets
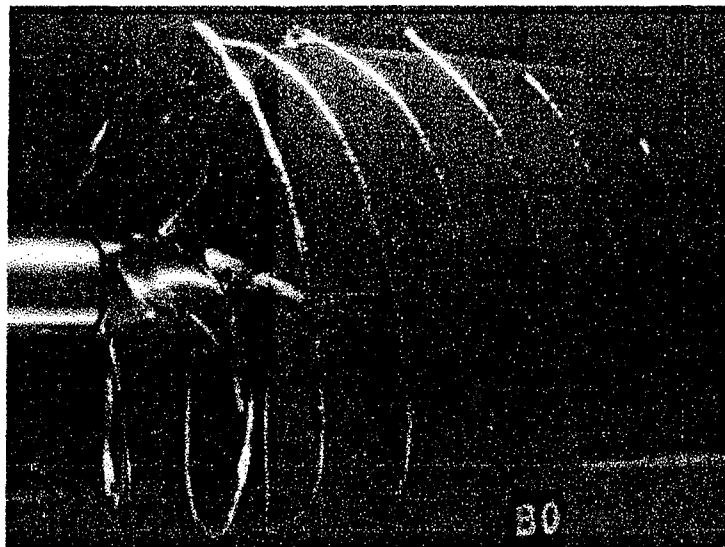

Figure 1. Rectangular streamline spade rudder at zero nominal incidence in the slipstream of a four-bladed propeller in a cavitation tunnel, reproduced from Kracht (1990).

shed from the side edges and subsequently rolling up have been computed by, among others, Schröder (1978) for low aspect-ratio wings and Wagner (1987), Wiemer (1987) and Haag (1988) for delta wings.

The problem becomes considerably more complex if the rudder is located in a propeller slipstream rather than in a uniform parallel inflow. The special case of a rudder in a nozzle was treated by Andrich (1989, 1990, 1991); however, the structure of free vortices shed by the propeller was prescribed on the basis of experimental observations (LDV measurements) rather than calculated as part of the complete solution.

The present work tries to compute the force-free configuration of the shear layers in the wake of
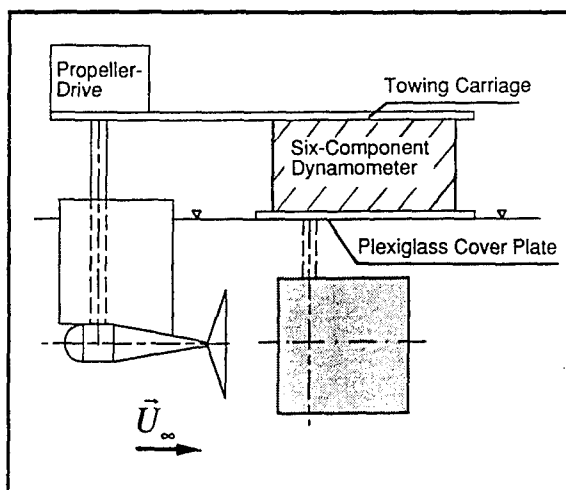

Figure 2. Schematic of reference model test in Duisburg Towing Tank (VBD): Rudder in slipstream, adapted from Baumgarten (1979).

Table 1. Propeller and rudder geometry and model test condition

Propeller: Wageningen B 4.55R			
Number of blades	4		
Diameter	180 mm	0.82	L
Pitch ratio		0.8	
E.A.R.		0.55	
Hub ratio		0.167	

Rudder: Rectangular, modified NACA 0018 profile			
Chord	220 mm	1.0	L
Span	213 mm	0.966	L
Thickness	40 mm	0.18	L

Test condition: Propeller-Rudder in towing tank			
Thrust coefficient (without rudder)		2.44	
Advance coefficient		0.444	
Rudder LE to rudder stock	70 mm	0.32	L
Rudder LE to propeller	95 mm	0.43	L
		(0.53	D)

the rudder as well as of the propeller, which necessitates solving a nonlinear integral equation. In distributing singularities on the shear layers of the rudder and the propeller particular attention must be paid to the vortex system of the propeller in way of the rudder.

A model test (see Fig. 2 and Table 1) conducted by Baumgarten (1979) in the Duisburg Ship Model Tank (VBD) was used as bench mark for validating the present study.

2. NONLINEAR VORTEX LATTICE METHOD

Choice of Singularity Method

The lift acting on a body at incidence in a stream can be explained by circulatory flow. In three-dimensional flows circulation may be generated by dipoles (oriented normal to the body surface). The other widely used type of singularity, namely, sources can only simulate the displacement effect of a body in a stream, but cannot satisfy the Kutta condition of smooth separation from the trailing edge which is the key to the generation of circulation. On the other hand, dipole distributions on the body surface can also simulate the displacement effect as long as the body has no sharp edges. For near a sharp edge the surface panels on opposite sides lie so close to each other that their induced velocities are almost self-canceling. The subdivision of a rudder surface, for example, in panels of constant dipole density would generate an almost singular system of algebraic equations with nearly zero elements on the side diagonals of the coefficient matrix.

Ship rudders typically have an aspect ratio from 1-2 and thickness ratio from 15-20 %. For such bodies the lift gain due to thickness effect is certainly not negligible, but presumably compensated for by an almost equal lift loss due to viscosity. By comparison, the nonlinear effect of separated flow around the side edges on the lift characteristic is much larger, as will be shown later. For this reason we simply place our dipoles on the rudder center-plane, ignoring not only viscosity but also thickness.

The model of flow around a rudder in slipstream is synthesized from two partial models: (i) rudder in uniform parallel inflow and (ii) propeller wake itself. Each partial model is separately validated by reference to available measurements. The ultimate criterion for the degree of detail to be simulated in each model is the adequate determination of pressure distribution on the rudder. This implies that the roll-up of the free-vortex sheets shed from the rudder side edges in way of the rudder itself must be simulated more precisely than the subsequent roll-up further downstream. For the same reason the bound vortices

of radially varying strength in the propeller blades and the associated wake vortex sheets with their immediate roll-up may be replaced by a simple horseshoe vortex for each blade.

In view of the rapid decay of the vortex-induced velocity with distance, each wake field is subdivided into a near field and a far field. In the near field the vortex is discretized and iteratively oriented to satisfy the no-force condition. In the far field (extending to infinity) an analytical truncation correction is applied rather than continuing the discrete vortex elements up to an arbitrary distance. Such far field approximation helps to reduce computing time and to prevent undue accumulation of numerical errors.

Definition of Boundary Value Problem

As explained in the Introduction, the Laplace Equation for the velocity potential

$$\Delta \Phi = 0 \qquad (2.1)$$

subject to the kinematic condition of no flux through all vortex sheets

$$\nabla \Phi \cdot \vec{n} = 0 \qquad (2.2)$$

and to the dynamic condition of no force on all free vortex sheets

$$\Delta c_p = 0 \qquad (2.3)$$

is solved by a singularity method. In steady flow, this dynamic condition is equivalent to requiring that the free vortex sheet is a stream surface. The singularity method is a collocation method with singularities, comprising basic solutions of the Laplace equation, suitably located outside the potential flow domain. The free parameters of the singularity distributions (strengths or locations) are determined by the boundary conditions. In the present lifting body problem dipoles are distributed on the shear layer representing the rudder and its wake, see, for instance, Schröder (1979) and Hoeijmakers (1989). The perturbation velocity generated by a surface distribution of dipoles is given by the potential

$$\phi_\mu = \frac{1}{4\pi} \iint_\sigma \mu \frac{\vec{a} \cdot \vec{n}}{|\vec{a}|^3} d\sigma \qquad (2.4)$$

Here μ is the dipole moment density on surface σ and $\vec{a} = \vec{P} - \vec{S}$ is the radius vector from dipole point $\vec{S}$ to field point $\vec{P}$.

The dipole layer induces at field point $\vec{P}$ the velocity

$$\vec{v}_\mu = \iint_\sigma (\vec{n} \times \nabla \mu) \times \frac{\vec{a}}{|\vec{a}|^3} d\sigma - \frac{1}{4\pi} \int_s \mu \frac{d\vec{s} \times \vec{a}}{|\vec{a}|^3} \qquad (2.5)$$

where s is the boundary of sigma.

The expression (2.4) for velocity potential is not directly involved in the determination of unknown dipole density μ. Rather, it is the total velocity which must satisfy the boundary condition (2.2) thereby yielding an integral equation

$$\left(\vec{v}_\mu + \vec{U}_\infty \right) \cdot \vec{n} = 0 \qquad (2.6)$$

to be solved. Here $\vec{U}_\infty = \left(U_x, 0, 0 \right)$ is the velocity vector representing the uniform parallel inflow.

Moreover, the dynamic boundary condition (2.3) must be satisfied, which means that for part of the singularity surface not only the dipole density but also its location is unknown beforehand. Hence, the integral equation to be solved is effectively nonlinear.

Numerical Solution

The nonlinear integral equation just derived is solved numerically by subdividing the bound and free vortex sheets into finite quadrilateral elements (panels) of constant dipole density. The approximation of constant density on each panel causes the surface integral in Equation (2.5) to disappear; the remaining line integral corresponds to the velocity field of a vortex line

$$\vec{v}_\Gamma = \int_s \frac{\Gamma}{4\pi} \frac{d\vec{s} \times \vec{a}}{|\vec{a}|^3} \qquad (2.7)$$

of constant circulation $\Gamma = -\mu$ on boundary s, see Martensen (1968). This is called a panel method of order zero or vortex-lattice method. In steady flow the circulation cannot change between successive panels on the free vortex sheet in the streamwise direction. Thus the free vortex surface is effectively modeled by vortex lines of constant strength which are at the same time also streamlines. Only the bound vortex surface comprises closed vortex rings, each of constant strength, whereby the side edge and trailing edge vortex rings extend to infinity, see Schröder (1979).

Since no general analytic solution exists for arbitrarily curved vortex lines, these are approximated by straight-line segments. Piecewise closed-form integration then reduces the integral equation to a summation equation.

Owing to the nonlinearity resulting from the unknown location of the free vortices, the above

equation has to be solved iteratively in a two-step procedure.

In preparation for the first step a stream surface is prescribed as location of the free vortex surface since this must be force-free. The kinematic boundary condition of no flux through the bound vortex surface then yields a linear system of algebraic equations for determining the unknown bound vortex strengths.

In the second step a new stream surface is calculated as next location for the free vortices. This is carried out as an Euler-Cauchy solution of an initial-value problem.

The above two-step procedure is repeated until the changes in bound vortex strengths and free vortex locations in two successive steps fall below prescribed error margins.

The propeller wake field is also calculated by the vortex lattice method. Instead of the vortex surface model used for the rudder, here each propeller blade including its wake is simply represented by a single horseshoe vortex of constant strength. The dynamic boundary condition of no force on the free vortices creates a nonlinearity also in this model which is handled by iteration as described above.

As stated previously, the velocities induced by the free vortices at any field point are computed by adding contributions from the near field and the far field. Discretization of the vortex lines is necessary only in the near field. Transition to the far field is so chosen that error in induced velocity at the field point of interest falls below a prescribed bound. In case of the rudder in open water the far-field free vortices are taken to be semi-infinite straight-lines. In case of the propeller alone the far-field free vortices are regular helices associated with blade tips and roots; for lack of an analytical expression for the velocity induced by a helical vortex line this field is idealized by two vortex cylinders, each of constant vortex density on its surface.

Induced Velocity Field of Vortex Line

Basis of a numerical solution in the vortex-lattice method is the discretization of curved vortex lines into straight vortices. Each vortex line is replaced by a finite number of straight-line segments so that the integral equation reduces to a summation equation.

According to Biot-Savart's Law a line element $d\vec{s}$ of an arbitrarily curved vortex line of constant circulation Γ induces at an arbitrary field point $\vec{P}$ the infinitesimal velocity:

$$d\vec{v} = \frac{\Gamma}{4\pi} \cdot \frac{d\vec{s} \times \vec{a}}{|\vec{a}|^3} \qquad (2.8)$$

where $\vec{a} = \vec{P} - \vec{S}$ is the radius vector from a point $\vec{S}$ on the vortex line to the field point $\vec{P}$.

This expression can be integrated in closed form only for a straight-line segment or for a closed circular ring, in the latter case only for a field point at the center.

A straight vortex line of constant circulation Γ, connecting points $\vec{S}_i$ and $\vec{S}_{i+1}$, (subsequently called vortex segment) induces at an arbitrary field point $\vec{P}$ in 3D space the velocity

$$\vec{v} = \frac{\Gamma}{4\pi} \cdot \int_{\vec{S}_i}^{\vec{S}_{i+1}} \frac{d\vec{s} \times \vec{a}}{|\vec{a}|^3} \qquad (2.9)$$

which can be expressed in closed form as

$$\vec{v} = \frac{\Gamma}{4\pi} \cdot \frac{\Delta\vec{s} \times \vec{a}_i}{|\Delta\vec{s} \times \vec{a}_i|} \cdot \left(\frac{\Delta\vec{s} \cdot \vec{a}_i}{|\vec{a}_i|} - \frac{\Delta\vec{s} \cdot \vec{a}_{i+1}}{|\vec{a}_{i+1}|} \right) \qquad (2.10)$$

where the vector $\Delta\vec{s} = \vec{S}_{i+1} - \vec{S}_i$ represents the vortex segment, and the vectors $\vec{a}_i = \vec{P} - \vec{S}_i$ and $\vec{a}_{i+1} = \vec{P} - \vec{S}_{i+1}$ are the radius vectors from its endpoints to the field point. In particular, for a semi-infinite straight vortex extending from $\vec{S}_i$ via $\vec{S}_{i+1}$ to infinity the expression reduces to

$$\vec{v} = \frac{\Gamma}{4\pi} \cdot \frac{\Delta\vec{s} \times \vec{a}_i}{|\Delta\vec{s} \times \vec{a}i|} \cdot \left(\frac{\Delta\vec{s} \cdot \vec{a}_i}{|\vec{a}_i|} + |\Delta\vec{s}| \right). \qquad (2.11)$$

Note that $\vec{S}_{i+1}$ here is not the endpoint but only a waypoint on the vortex segment.

If the field point lies on the vortex segment itself, the integral in (2.9) becomes singular; taking its Cauchy principal value, the induced velocity is found to be zero.

In numerically evaluating the summands of the induced velocity at any field point the following approximation is used to take advantage of the strong decay with distance from the vortex segment. If $|\vec{a}| \gg |\Delta\vec{s}|$, then the velocity induced by the vortex segment (VS) is taken to be

$$\vec{v}_{Far,VS} = \frac{\Gamma}{4\pi} \cdot \frac{\Delta\vec{s} \times \vec{a}_{Far,VS}}{|\vec{a}_{Far,VS}|^3} \qquad (2.12)$$

with the long-range field-point vector $\vec{a}_{Fern,WS} = (\vec{P} - \vec{S}_i)$.

The magnitude of the difference between the exact solution for the induced velocity (2.10) and its

approximation (2.12) normalized by the magnitude of inflow velocity $\vec{U}_\infty$ is defined as an error bound:

$$\varepsilon_{Far,VS} = \frac{\left|\vec{v}-\vec{v}_{Far,VS}\right|}{\left|\vec{U}_\infty\right|}. \qquad (2.13)$$

Estimated on the basis of this error bound, the minimum value for the distance beyond which the approximation may be used is found to be:

$$\left|\vec{a}_{Far,VS}\right| > 3\sqrt{\left|\frac{\Gamma/(4\pi)}{\vec{U}_\infty}\right|\frac{(\Delta\vec{s})^2}{2\varepsilon_{Far,VS}}}. \qquad (2.14)$$

3. RUDDER IN UNIFORM PARALLEL INFLOW

Bound and Free Vortex Sheets

The rudder skeleton surface is subdivided into quadrilateral panels, see Fig. 3. As the vortex segments are chosen to lie on the panel boundaries the geometrical grid is identical to the vortex grid. The control points lie at the intersections of the bisectors of opposite edges. The cross-product of these bisectors defines the panel plane; in case of warped panel, a surrogate plane.

Since the velocity field is explicitly required only at the location of the rudder, the roll-up of the side-edge vortices need not be fully simulated behind the trailing edge. Moreover, the free-vortex field is subdivided into a near field and a far field, the borderline lying downstream at the transition from finite vortex segments to the semi-infinite vortex.

For estimating the borderline between near field and far field the entire bound and free vortex sheet can be replaced by a horseshoe vortex since the free vortex sheet rolls up downstream into two tip vortices of equal but opposite circulation. For reasons of symmetry the two free vortex lines of the horseshoe vortex form at infinity a pair of straight-lines lying in a plane at an angle to the uniform parallel inflow which is less than the rudder angle of incidence.

The distance $\left|a_{Far,VH}\right|$ of the field point from the starting point of the semi-infinite vortex (VH) is determined by estimation so as to ensure that the magnitude of the velocity $\left|\vec{v}_{Far,VH}\right|$ induced by the semi-infinite vortex at the rudder trailing edge is less than a prescribed error bound $\varepsilon_{Far,VH}$. Only up to this point does the vortex line, as a chain of finite straight segments, need to be aligned to the flow. The error bound $\varepsilon_{Far,VH}$ is defined as the ratio of the magnitude of velocity $\left|\vec{v}_{Far,VH}\right|$ induced by the semi-
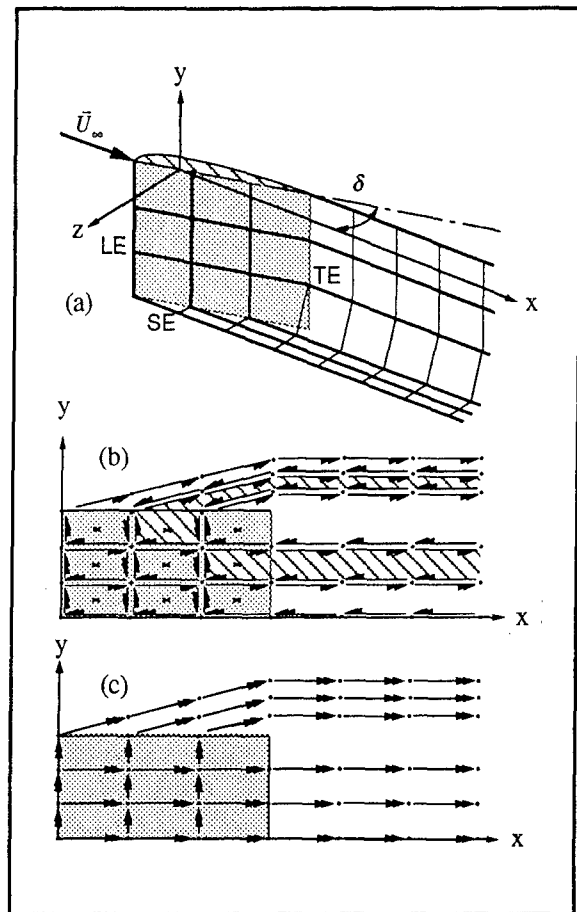

Figure 3. Vortex lattice model of rudder: (a) Initial configuration of discrete panels representing rudder and its vortex wake comprising trailing edge and side edge separation, (b) Configuration for computing circulation, (c) Configuration for computing velocity.

infinite vortex to the magnitude of velocity $\left|\vec{U}_\infty\right|$ of uniform parallel inflow.

$$\varepsilon_{Far,VH} = \frac{\left|\vec{v}_{Far,VH}\right|}{\left|\vec{U}_\infty\right|}. \qquad (3.1)$$

The minimum distance between the starting point of the semi-infinite vortex downstream from the rudder trailing edge is then given by:

$$\left|a_{Far,VH}\right| > \left|\frac{\Gamma/(4\pi)}{\vec{U}_\infty}\right|\left|\frac{1+\cos(\vartheta)}{\varepsilon_{Far,VH}\,\tan(\vartheta)}\right|. \qquad (3.2)$$

Here $\vartheta=\pi-52°$ is the angle between vortex axis and field-point vector at which the induced velocity of a semi-infinite vortex has a maximum. The circulation Γ of the rudder, considered as a flat

768

plate with a 2D lift coefficient gradient $c_L = 2\pi$, can be estimated to be

$$\Gamma = \pi L\, U_\infty \sin(\delta), \qquad (3.3)$$

where L is the chord length. Substitution of this value into Equation (3.2) yields the following minimum distance between a field point on the rudder trailing edge and starting point of the semi-infinite vortex:

$$\left| a_{Far,VH} \right| > \left| \frac{L \sin(\delta)}{4} \right| \left| \frac{1 + \cos(\vartheta)}{\varepsilon_{Far,VH} \tan(\vartheta)} \right|. \qquad (3.4)$$

According to this estimate, for a rudder angle $\delta = 15°$ and velocity error bound $\varepsilon_{Far,VH} = 1\%$, for instance, the minimum distance to far-field borderline becomes $\left| a_{Far,VH} \right| = 1{,}94\, L$.

Circulation of Bound Vortex

In principle we have to solve a nonlinear system of equations with two sets of unknowns, namely, circulations of the bound vortices and locations of the free vortices. As stated above, the locations of the free vortices have to be iteratively estimated. Then the no-flux condition on the rudder requires that at each control point the total velocity induced by all the vortices $\vec{V}_{ind}$ must yield together with the inflow velocity $\vec{U}_\infty$ a zero component along the normal $\vec{n}$ to the panel surface:

$$(\vec{V}_{ind} + \vec{U}_\infty) \cdot \vec{n} = 0. \qquad (3.5)$$

Thus the problem is reduced to the following system of algebraic equations:

$$\sum_{\mu=1}^{m} A_{\upsilon,\mu}\, \Gamma_\mu = -\vec{U}_\infty \cdot \vec{n}_\mu; \qquad \upsilon = 1, m \qquad (3.6)$$

where $A_{\upsilon,\mu}$ is the geometrical influence coefficient matrix, Γ_μ are the unknown circulations of the panel vortex rings, and m is the number of control points. This diagonally dominant set of equations is solved by a Gauß-Seidel algorithm.

Next, the previously estimated locations of the free vortex lines must be checked and, if necessary, corrected as explained in the next sub-section. After a necessary correction the circulations of the bound vortices must be recalculated. This iteration must be repeated until all prescribed error bounds are attained.

Elements of the coefficient matrix **A** are computed by adding the contributions of all vortices associated with a panel. Closed vortex rings on the bound vortex sheet comprise just four panel edge vortex segments, whereas the boundary panels comprise three bound vortex segments and two chains of free vortex segments extending downstream to infinity. In other words, boundary panels are represented by horseshoe vortices. Hence, there lie two counter-oriented vortices of, in general, unequal circulation on each common edge of neighboring panels on the bound vortex surface; on the free vortex surface this holds only for edges in the streamwise direction, see Fig. 3b. Once the circulations have been determined, for further computations the collinear edge vectors are added with the convention that positive sign points in the coordinate direction, see Fig. 3c.

Location of Free Vortices

There must be no pressure jump across the free vortex layer. It follows that the the free vortex surface coincides with a stream surface and that free vortex lines coincide with streamlines. The streamlines are calculated iteratively by an Euler-Cauchy algorithm. Starting from the rudder leading edge, each time an entire transverse row of free vortex segments (ending roughly in a plane normal to the inflow) is relocated; then all downstream nodal points of each free vortex line are displaced by the difference vector between the new and old locations of the last relocated vortex segment. When, marching downstream, this operation has been done for all transverse rows the whole free vortex lattice is realigned to the flow. Now, the bound vortex circulations are redetermined as described above. This two-step iterative procedure is truncated when the prescribed error bounds for the circulation of bound vortices and the location of free vortices have been reached.

The Euler-Cauchy single-step procedure was chosen here because the velocity field for computing new streamlines is reasonably available only at discrete points, namely, the nodes of the given vortex lines. Of course, in principle the induced velocity could be calculated at any arbitrary point, but physically meaningful results can be expected only either outside the shear layer or exactly on the vortex lines. Moreover, the continuously curved vortex lines have been approximated by straight segments whose ends only lie on the original lines.

The idealization of the free vortex field by vortex lines is adequately accurate as long as the separation between the various turns of the rolled-up vortex surface is larger than the neglected thickness of the shear layer. Furthermore, the transverse distance between vortex lines must be kept sufficiently small so that the planes connecting neighboring vortex segments do not intersect the rolled-up vortex sheet.
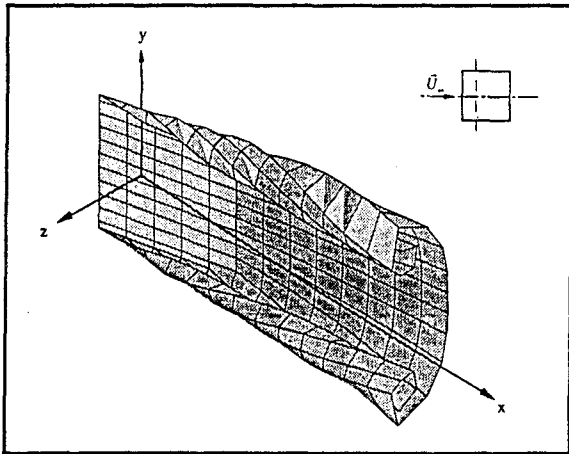
Figure 4. Computed bounded and free vortex sheets of a rectangular rudder in uniform parallel inflow ($\Lambda = 0.966$; $\delta = 15$ deg).

Finally, it is noted that the last downstream semi-infinite straight vortices are simply assumed to be aligned to the uniform parallel inflow.

Lift and Pressure Distribution

Once the strengths of bound vortices and the locations of free vortices are determined the induced velocity can be calculated at any field point of the flow by Biot-Savart's Law.

The force and moment on the rudder can be found by applying Kutta-Joukowski's Law. For this purpose, the effective velocity $\vec{V}_{eff}$ at the center of each bound vortex $\Gamma \cdot \vec{b}$ is determined as the sum of inflow velocity $\vec{U}_\infty$ and the induced velocity $\vec{V}_{ind}$; here $\vec{b}$ is any panel edge vector and Γ the sum of circulations of adjacent panel vortex rings on the rudder skeleton surface. The local lift force $\vec{F}_L$ on the vortex considered is proportional to the cross product of effective velocity vector and vortex vector:

$$\vec{F}_L = \rho \, \Gamma \, (\vec{V}_{eff} \times \vec{b}), \qquad (3.7)$$

where ρ is the mass density of the fluid. This local force can be resolved along any desired direction, for instance, normal to the rudder center-plane.

The local normal force divided by the panel area yields the pressure difference across the rudder assumed constant over any single panel; it is computed as follows. Each individual force according to Equation (3.7) is distributed as uniform pressure over two adjacent panels. For any single panel the sum of contributions from all edges yields the total pressure difference (between pressure side and suction side). The side edges and the trailing edge carry no vortices and, hence, do not contribute to the forces.

Each leading edge vortex bounds only one panel so its force is distributed over this one panel only.

An alternative approach would be to first calculate the velocity difference across the rudder at any control point and then via Bernoulli's Equation the corresponding pressure difference. It would require the conversion of edge vortices into a surface distribution of vorticity on the panel. This method is believed to be equivalent but awkward and, hence, is not used here.

Fig. 5 shows clearly the effect of the free vortex surface, which separates from the side edge and rolls up as seen in Fig. 4, on the load distribution over the rudder center plane. With increasing distance from the leading edge the spanwise variation of pressure difference deviates more and more from the classic elliptic distribution.

This load distribution was calculated using an equidistant grid of 40*20 elements in spanwise and chordwise directions on the rudder skeleton plane and 32 equidistant element rows behind the trailing edge up to a distance 1.6L downstream. This chosen near-field length follows from a velocity error bound $\varepsilon_{Far,VH} = 1$ % along with the measured lift coefficient gradient 0.7π. A closer estimate than in the example following Equation (3.4) was necessary since the computing time increases as the square of the number of elements of the free vortex surface.

Total force coefficients for the rudder in any direction (lift, drag and cross-force) are easily obtained by summing up the local forces on all bound vortices. Fig. 6 shows the thus calculated lift characteristic of the reference rudder as well as a linear approximation and two sets of measurements. Strikingly, the present calculation agrees better with measurements on a thin flat plate with sharp leading edge than with those on the reference streamline
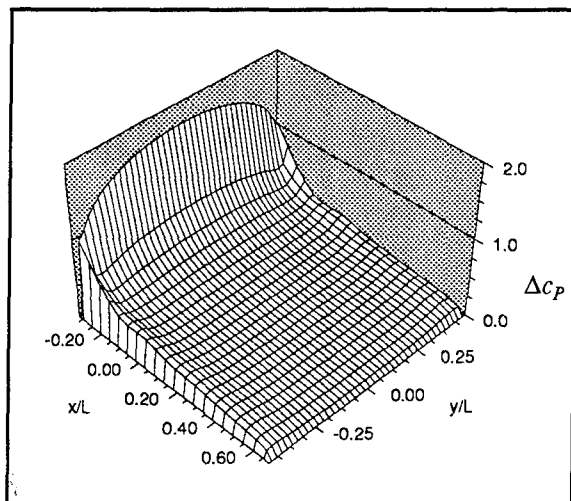

Figure 5. Computed normalized load distribution on the skeleton plane of a rectangular rudder in uniform parallel inflow ($\Lambda = 0.966$; $\delta = 15$ deg).
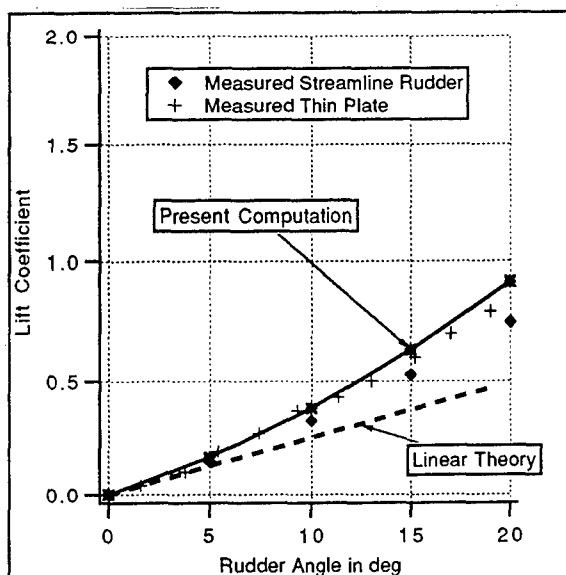
770

Figure 6. Lift characteristic of a rectangular rudder ($\Lambda = 0.966$) in uniform parallel inflow.

rudder of 0.18 thickness ratio. The measurements shown for the thin plate stem from Schlichting and Truckenbrodt (1969, p. 73). The lift coefficient gradient for a thin flat plate according to linear theory is $c'_L = \pi \Lambda / 2$ for aspect ratio $\Lambda < 1$ and, hence, $c'_L = 1.52$ for the present case.

4. PROPELLER SLIPSTREAM

Surrogate Horseshoe Vortex

Experiments reveal that the rudder is hit by already rolled-up propeller tip and root vortices, see Fig. 1. These vortices are, therefore, idealized as vortex lines in order to estimate the effect of propeller slipstream on the rudder. They are connected upstream by a bound vortex in each propeller blade and extend downstream to infinity. The bound vortex is located at the quarter-chord line of the blade skeleton surface. Although the root vortices seem to join into a single hub vortex, they are retained as individual vortex lines. This is necessary if induced velocities need to be determined within the streamtube formed by the root vortices, see Fig. 7.

According to measurements by Andrich (1989) the tip vortex is already fully developed within a quarter turn of the propeller. This is due to the steep drop of bound circulation near the tip. In any case, it happens well ahead of the rudder and, hence, we refrain from detailed modeling of the propeller flow and of the roll-up of its free vortex sheet. For consistency, the root vortices are assumed to be also fully rolled up into vortex lines before reaching the rudder.

As in the case of the flow around the rudder, the no-force condition on free vortex lines of *a priori* unknown location renders nonlinear the integral equation for determining propeller-blade bound circulation. Hence, a similar solution procedure is used here, of course, in the propeller-fixed coordinate system. However, for simplicity, two different vortex models are used for determining the circulations of bound vortices and the locations of free vortices within the horseshoe vortex system: For the former, a lifting surface model albeit with free vortices located on a fixed regular helical surface; for the latter, a lifting line model with free vortices iteratively aligned to the flow.

The propeller wake field is subdivided into a near field and a far field. In the near field discrete vortex lines are aligned to the resultant velocity field. For numerical reasons curved free vortex lines are approximated by straight vortex segments. The downstream continuation to infinity is modeled by a semi-infinite vortex cylinder (see Fig. 7) rather than by semi-infinite discrete lines as was the case for the rudder. Hence, in the far field discrete tip and root vortices are replaced by two semi-infinite circular vortex cylinders, each with a uniform vortex density on its surface. This far-field approximation is motivated by the fact that propeller tip and root vortices, for reasons of symmetry, ultimately lie on regular helical lines at downstream infinity, but no analytical solution is available for semi-infinite helical vortex lines as a convenient truncation correction.

The velocity field induced by a semi-infinite vortex cylinder can be expressed as a double integral, i.e., in axial and circumferential directions. At least the first integration can be done analytically, the second is performed by a Romberg quadrature.
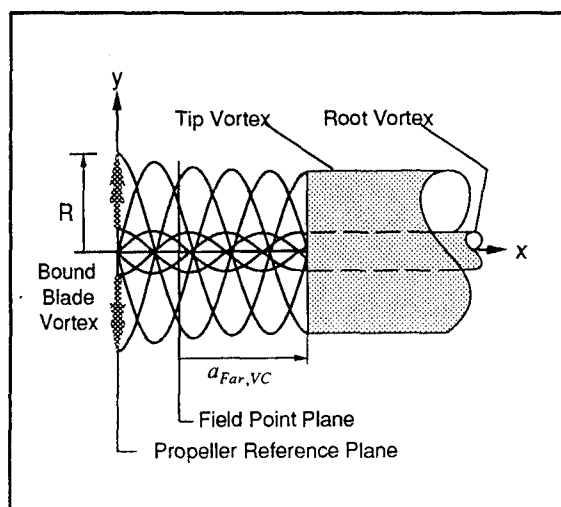

Figure 7. Vortex model of propeller slipstream comprising tip and root helical lines in the near field and cylindrical sheets in the far field.

771

The transition point from vortex segments to the vortex cylinder is determined such that the velocity error at any given field point resulting from the spreading of discrete line vortices on to the cylinder surface is less than a prescribed tolerance.

The velocity induced by a vortex cylinder at any arbitrary field point is according to Biot-Savart's Law given by:

$$\vec{v} = \frac{1}{4\pi} \int_0^{2\pi} \int_0^\infty \frac{d\vec{\omega} \times \vec{a}}{|\vec{a}|^3}. \tag{4.1}$$

Using a relative Cartesian coordinate system, whose x axis coincides with the cylinder axis and originates at the beginning of the cylinder, the components of the vortex element vector can be expressed as

$$d\vec{\omega} = \begin{pmatrix} (\gamma_x \rho\, d\varphi)\, d\xi \\ -(\gamma_u\, d\xi)\, \rho \sin(\varphi)\, d\varphi \\ (\gamma_u\, d\xi)\, \rho \cos(\varphi)\, d\varphi \end{pmatrix} \tag{4.2}$$

and those of the radius vector $\vec{a}=\vec{P}-\vec{S}$ from vortex element point $\vec{S}=(\xi,\rho\cos(\varphi),\rho\sin(\varphi))^T$ to field point $\vec{P}=(x,y,0)^T$ as

$$\vec{a} = \begin{pmatrix} x-\xi \\ y-\rho\cos(\varphi) \\ -\rho\sin(\varphi) \end{pmatrix}. \tag{4.3}$$

The uniform vortex density of the vortex cylinder has the components $\gamma_x = \dfrac{z\Gamma_z}{2\pi\rho}$ in the axial direction and $\gamma_u = \dfrac{z\Gamma_z}{2\pi\rho\tan(\beta_i)}$ in the circumferential direction, where z is the number of blades, Γ_z the circulation of a propeller blade tip/root vortex, $\rho\tan(\beta_i)$ the hydrodynamic induced pitch, and ρ the cylinder radius. The determination of hydrodynamic induced pitch will be explained in the next sub-section.

After analytical integration in the axial direction the velocity induced by the semi-infinite vortex cylinder is found to have the following components:

$$\vec{v} = \begin{pmatrix} \dfrac{\gamma_u}{2\pi}\left(C_x + \displaystyle\int_0^\pi \dfrac{\left(\rho^2 - y\rho\cos(\varphi)\right)x}{a_{yz}^2\ \sqrt{x^2+a_{yz}^2}}\, d\varphi \right) \\[3mm] \dfrac{\gamma_u}{2\pi}\displaystyle\int_0^\pi \dfrac{\rho\cos(\varphi)}{\sqrt{x^2+a_{yz}^2}}\, d\varphi \\[3mm] \dfrac{\gamma_x}{2\pi}\left(C_z + \displaystyle\int_0^\pi \dfrac{\left(y\rho - \rho^2\cos(\varphi)\right)x}{a_{yz}^2\ \sqrt{x^2+a_{yz}^2}}\, d\varphi \right) \end{pmatrix} \tag{4.4}$$

where $C_x = \begin{cases} \pi & \text{for } y<\rho \\ \dfrac{\pi}{2} & \text{for } y=\rho \\ 0 & \text{for } y>\rho \end{cases}$ $\quad C_z = \begin{cases} 0 & \text{for } y<\rho \\ \dfrac{\pi\rho}{2y} & \text{for } y=\rho \\ \dfrac{\pi\rho}{y} & \text{for } y>\rho \end{cases}$

and $a_{yz} = \sqrt{y^2 + \rho^2 - 2y\rho\cos(\varphi)}$ is the absolute value of the projection of vector $\vec{a}$ onto the yz-plane. For reasons of symmetry, the integration in the circumferential coordinate needs to cover only half the interval, that is, $0 < \varphi < \pi$.

The total far field of the propeller wake is the sum of the contributions of the two semi-infinite vortex cylinders (VC) representing the tip and the root vortices.

We now seek a minimum distance $|a_{Far,VC}|$ between the field point and the far field such that the normalized velocity induced by the far-field model is less than an error bound

$$\varepsilon_{Far,VC} = \left| \frac{v_\gamma}{\vec{U}_\infty} \right|. \tag{4.5}$$

Only within this range is it necessary to discretize the vortex lines of the propeller wake and to align them to the flow. Only the axial component of the induced velocity is considered for the purpose of this estimate since the radial and circumferential components are negligible by comparison. The estimate yields a minimum distance as the following function of propeller radius R, thrust loading coefficient c_{Th}, and normalized velocity error bound $\varepsilon_{Far,VC}$:

$$|a_{Far,VC}| = \frac{R}{2}\sqrt{\frac{c_{Th}}{\varepsilon_{Far,VC}\ \sqrt{c_{Th}+1}}}. \tag{4.6}$$

In the iterative no-force alignment of the free vortex segments of propeller wake a transition range $|a_{Trans,VC}|$ ahead of the vortex cylinders is specially considered. This is the distance between the last

772

aligned vortex segment of the near field and the beginning of the far field. In this transition range the discrete vortex segments are just located on regular helices of same radius as the far-field cylinder. The size of the transition range is determined such that the error resulting from substituting a uniform vortex cylinder for discrete helical vortices is less than a relative velocity error bound

$$\varepsilon_{Trans,VC} = \left| \frac{v_\Gamma - v_\gamma}{v_\Gamma} \right|. \qquad (4.7)$$

This estimate is obtained by comparing the velocities induced in the meridian plane of the vortex cylinder by a discrete vortex and and a vortex layer, both lying on the cylinder surface. Treating this as a 2D problem the following estimate is obtained:

$$a_{Trans,VC} > \frac{\Delta\xi}{2} \sqrt{\frac{1}{\varepsilon_{Trans,VC}} + 1}. \qquad (4.8)$$

This means that every individual vortex line must be continued as a chain of discrete vortex segments over an axial range $|a_{Trans,VC}|$ between the end of the near field and the beginning of the far field. The axial separation of the vortex lines corresponds to the width of the vortex layer $\Delta\xi$ and can be expressed as a function of induced hydrodynamic pitch $\rho \tan(\beta_i)$, cylinder radius ρ, and number of blades z:

$$\Delta\xi = \frac{2\pi}{z} \rho \tan(\beta_i). \qquad (4.9)$$

In the chosen reference case with a loading coefficient $c_{Th} = 2.44$ the distance from field point to far field must be at least $|a_{Far,VC}| > 5.7R$ for a normalized velocity error bound $\varepsilon_{Far,VC} = 0.01$. When aligning the free vortices, this distance must be increased by the transition range, which for a four-bladed propeller operating at advance coefficient $J = 0.444$ must be at least $|a_{Trans,VC}| > 2.1R$. For the latter estimate the hydrodynamic induced pitch far behind the propeller was taken, on the basis of momentum theory, to be $\rho \tan(\beta_i) = 0.262R$, see also next sub-section. This leads to an axial separation of vortices equal to $\Delta\xi = 0.412R$.

These values were used to compute the circumferentially averaged induced velocities due to the propeller at two axial locations $0.53D$ and $1.75D$ behind the propeller corresponding to rudder leading edge and trailing edge, respectively, in the reference case, see Fig. 8.

Circulation of Bound Blade Vortex

The circulation and the starting points of tip and root vortices of each propeller blade are determined by reducing the vortex lattice with radially varying circulation to a surrogate simple horseshoe vortex, see Schlichting (1969, p. 32). The location of each free vortex line depends
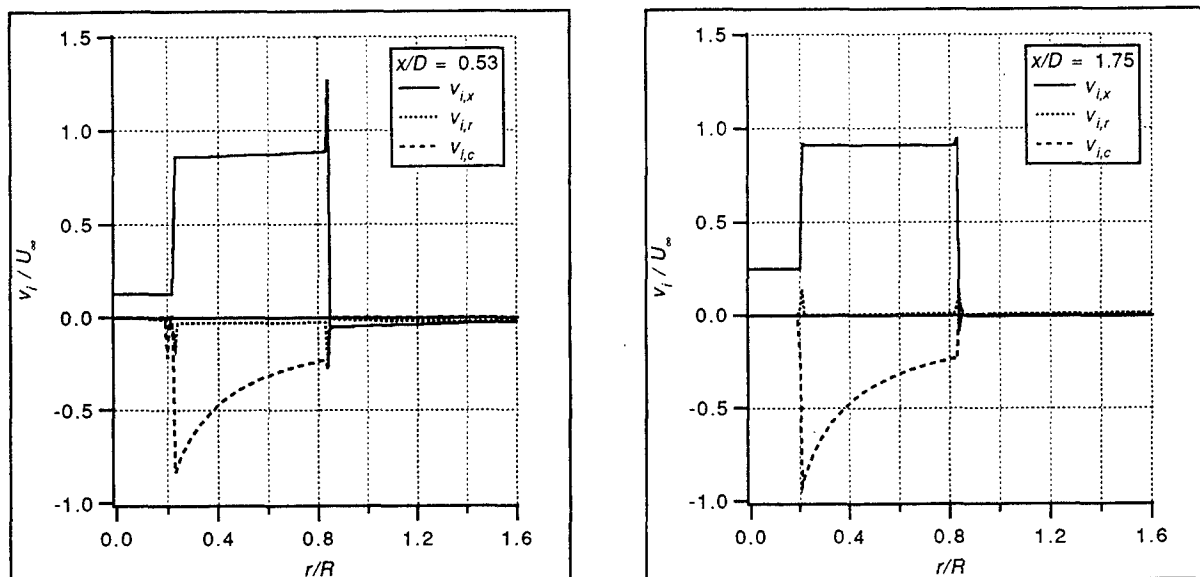

Figure 8. Computed propeller induced velocity components in the slipstream at rudder LE (left) and TE (right) (Wageningen B4.55R: $P/D = 0.8$; $c_{Th} = 2.44$).

773

on the starting point as well as on the circulation. Hence, the propeller thrust coefficient c_{Th} is also calculated from the vortex lattice in order to adjust the calculated circulation in proportion to the thrust measured on the propeller (in an open water model test). This simple adjustment is permissible since by Kutta-Joukowski's Law the lift is proportional to the circulation and, hence, also the thrust coefficient. Starting points of the tip and root vortices are not too sensitive to the circulation and are, therefore, not adjusted.

The constant circulation of the surrogate horseshoe vortex is taken equal to the peak value of the radially varying circulation in the vortex lattice. The width of the surrogate horseshoe vortex and, hence, the starting points of tip and root vortices are so chosen that the integrals under the curve of circulation as a function of radius between the peak value and the inner and outer endpoints, respectively, remain unchanged, see Fig. 9.

The radially varying bound circulation is determined as follows. The propeller blade is idealized by an array of radially neighboring horseshoe vortices, each with a bound part on the blade skeleton surface and a free part in the wake, see Fig. 10. The bound radial segment is located at quarter-chord from blade leading edge. The free segments start at the blade trailing edge and extend sufficiently far downstream on regular helices of pitch angle $\tan(\beta_i)$. The unknown circulations of this vortex lattice are determined by satisfying the no-flux condition on the blade skeleton surface at one control point at threequarter-chord from the leading edge within each horseshoe.
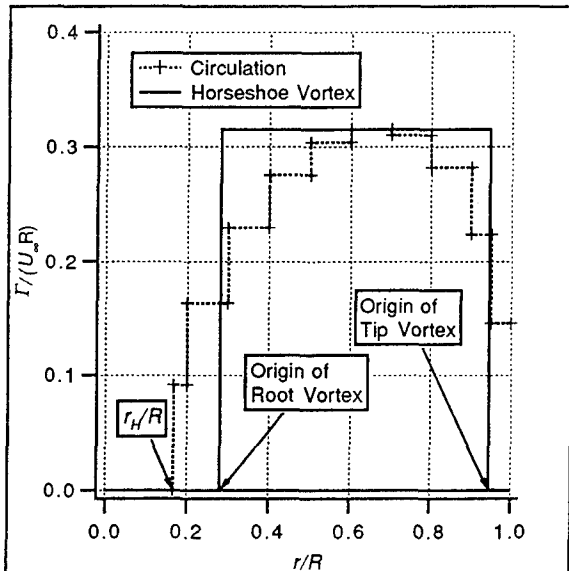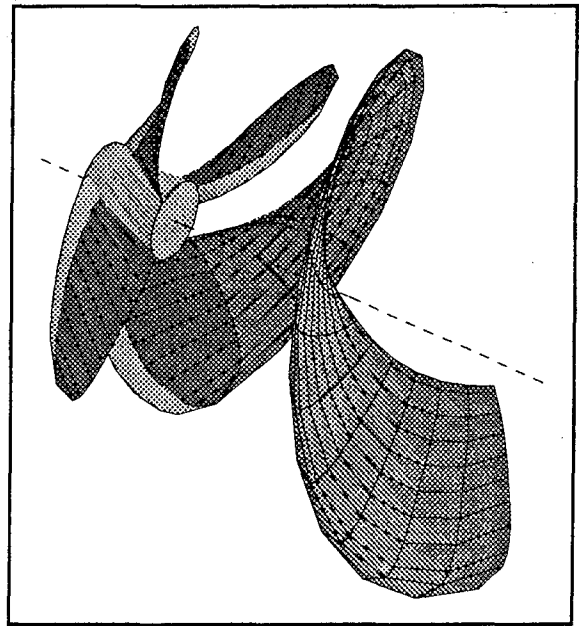

Figure 10. Vortex lattice model of propeller blades and their vortex wake sheets for computing radial variation of bound circulation.

The aforesaid pitch angle is found from an extension of Rankine's momentum theory to depend on local radius r/R, advance coefficient J, and thrust loading coefficient c_{Th}:

$$\beta_i = \arctan\left(\frac{J}{\pi} \frac{R}{r} \sqrt{c_{Th}+1}\right), \tag{4.11}$$

see Ulrich and Danckwardt (1956).

Location of Tip and Root Free Vortices

As in case of the rudder, propeller wake is subdivided into a near field and a far field. Unlike the rudder, here the flow is steady in a rotating propeller-fixed system only. The basic flow now includes an angular component so that during the iterative alignment of free vortices in the near field the displacement vector from old to new vortex location cannot simply be superimposed onto the remaining downstream vortex segments. The length of the vortex segment remains unchanged during all corrections in the near field. In the far field, as stated earlier, the helical vortex lines are smeared out on the surface of a semi-infinite circular cylinder. Their constant radius and pitch are found by iteration.

The iteratively corrected new location of the free vortices is calculated in the near field by the single-step Euler-Cauchy algorithm just as in case of the rudder. This is done in an iterative loop starting at the bound vortex in the blade and marching downstream one transverse array (comprising one tip and one root vortex segment per blade) at a time.

Figure 9. Radially stepped bound circulation on propeller blade and surrogate single horseshoe vortex.

Each free vortex segment is realigned to the flow found by averaging the velocities calculated at the last locations of its two endpoints. The remaining downstream vortex segments are provisionally displaced along helical surfaces of locally constant pitch as well as radially in proportion to the local radius so as to close the gaps created by the previous operation.

Final operation in the iterative loop is the adjustment of the semi-infinite vortex cylinders constituting the far field. The new radius (as well as pitch) is set equal to the average of its old value and the new value of the last realigned near-field segment. In the transition range between near field and far cylinder the radius and pitch of each vortex segment is found by linear interpolation to ensure continuous connection.

The above iteration is continued until the deviations in the vortex segment locations of the near field as well as of the far field between two successive steps become less than a prescribed error bound.

5. EFFECT OF PROPELLER ON RUDDER

In a slipstream the rudder is subject to a periodic flow at blade frequency (equal to propeller rate times number of blades). The periodic effect is reflected in the free vortex lines of the propeller wake hitting the rudder. Since the hydrodynamic pitch is quite low, successive propeller vortices lie close to each other compared to rudder size. Hence, the periodic variation of velocity on the rudder surface is relatively small and is felt only in a narrow zone.

The pressure field on the rudder is obtained essentially by superimposing the vortex models of the rudder and the propeller wake. In order to find the periodic effect of the free propeller vortices on the rudder to a first approximation, the pressure field is considered as a function of relative blade position. More precisely, it is calculated individually for a finite number of values of circumferential angle assuming quasi-steady flow in the non-rotating coordinate system $Oxyz$. The range to be covered equals one propeller turn divided by the number of blades, corresponding to a full period of inflow.

The rudder and its wake including side edge separation are modeled, as above, by vortex surfaces and subdivided into panels carrying transverse dipoles of constant surface density or, equivalently, vortex rings of constant circulation. Thanks to the assumption of quasi-steady flow, vortex rings on boundary panels reduce to horseshoe vortices extending downstream to infinity. Their free vortex lines are discretized as chains of straight vortex segments the last of which is semi-infinite.

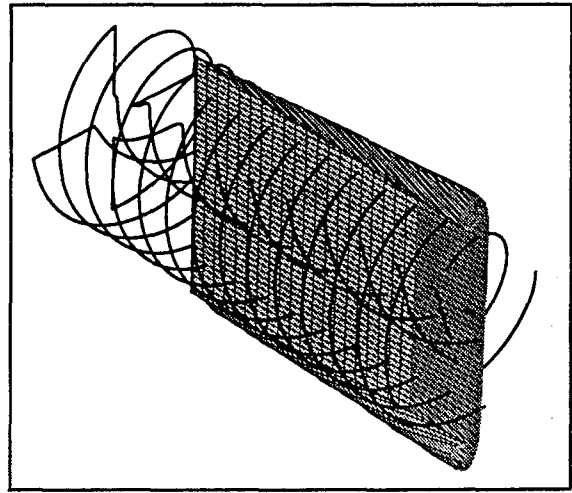The propeller wake is simulated by helical blade tip and root vortices ending in semi-infinite

Figure 11. Computed vortex lattice of the rudder ($\Lambda = 0.966$; $\delta = 5$ deg; $D/l = 0.82$; $\varphi = 0$ deg) with superimposed computed propeller vortices (Wageningen B4.55R: $P/D = 0.8$; $c_{Th} = 2.44$).

cylinders. Their circulations and locations are taken unchanged from the open-water computation. This means that the obstruction of the slipstream by the rudder is ignored.

Fig. 11 shows a computed vortex lattice of the propeller-rudder system.

Fig. 12 shows, for the two extreme relative positions of a four-bladed propeller, the computed normalized load distribution generated on the rudder by the propeller wake. Note that the rudder is at zero angle of attack. The pressure difference peaks in way of the propeller wake vortices arise from singularities in the velocity field when the field point approaches a potential-vortex axis. However, the spurious peaks largely cancel each other out so that the effect on integral values is much less serious as will be seen shortly.

Fig. 13 shows the computed normalized load distribution on the rudder at 15 deg angle of attack without and with propeller wake, the latter for a single relative position of the blades. The strong effect of propeller wake on the mean value of the load as well as on its chordwise and spanwise distribution is evident.

Fig. 14 shows the computed lift characteristic of the reference rudder in propeller slipstream, obtained by summing local lift forces over the rudder surface and averaging over one period. For comparison, two sets of model test measurements are also included. The expected increase in rudder load as a result of propeller wake is generally confirmed. However, with increasing incidence the discrepancy between computation and model test increases up to about 30 % at 20 deg rudder angle. Much of it seems to be the result of ignoring rudder thickness effects as already evident in Fig. 6.
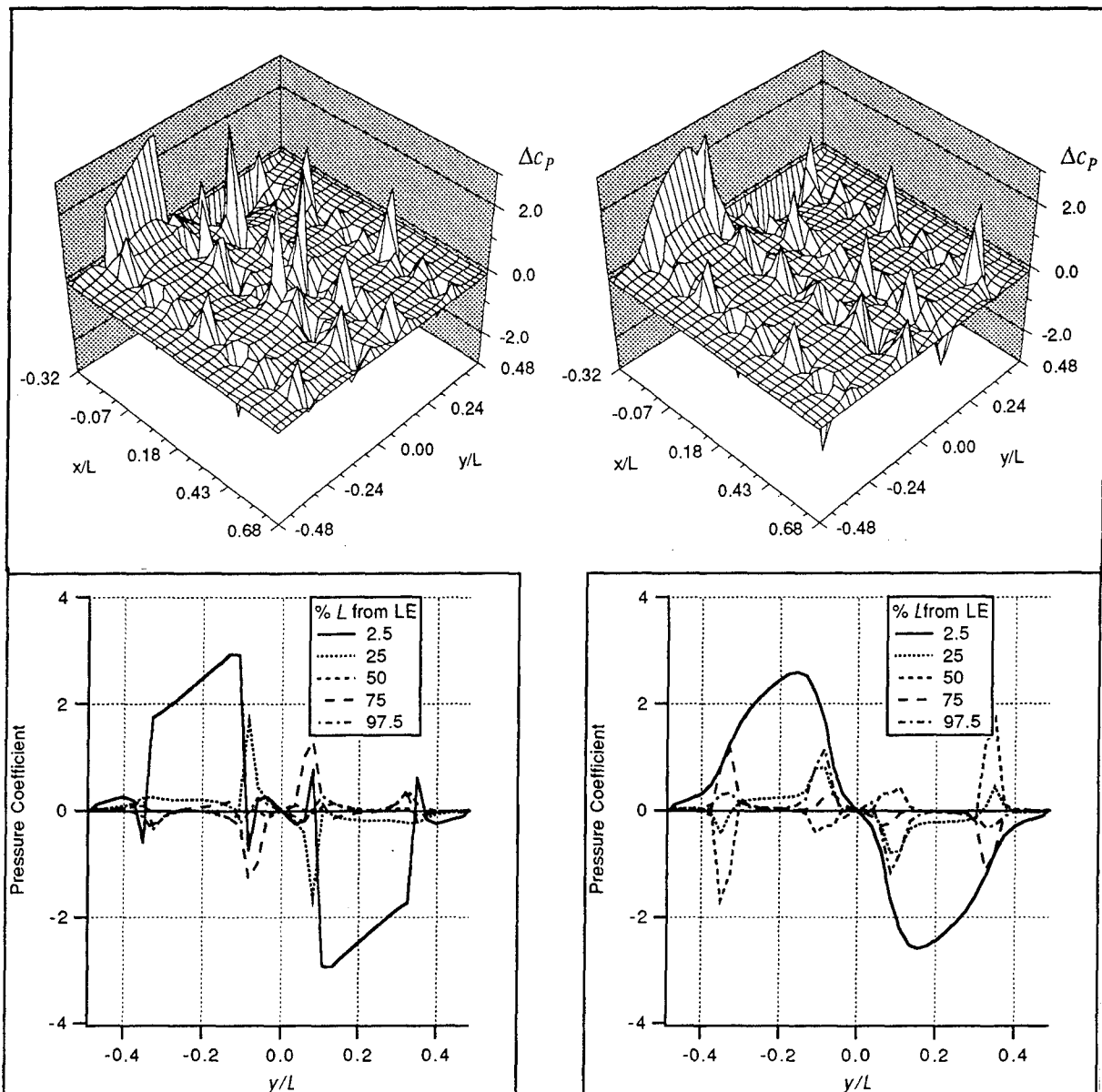
775

Figure 12. Computed normalized load distribution on the skeleton plane of a rectangular rudder in slipstream ($\Lambda = 0.966$; $\delta = 0$ deg;$D/l = 0.82$).

Top left: Perspective view, $\varphi = 0$ deg, Top right: Perspective view, $\varphi = 45$ deg

Bottom left: Cross sections, $\varphi = 0$ deg, Bottom right: Cross sections, $\varphi = 45$ deg

6. SUMMARY AND CONCLUSIONS

A computer code is developed to calculate the effect of propeller slipstream on the load distribution of a ship rudder. Quasi-steady potential flow is assumed. The resulting Laplace Equation for the velocity potential, under the boundary conditions of no flux across the body and no force on the wake shear layer, is solved numerically by a collocation (vortex lattice) method. In this integral method the rudder skeleton surface and the shear layer separating from the side edges as well as from the trailing edge are discretized in quadrilateral panels. Each panel carries a closed vortex ring of constant circulation. The propeller is idealized by one horseshoe vortex for each blade so that its wake comprises only tip and root vortices. Their circulation and starting points are derived from a vortex-lattice model similar to that for the rudder.

Despite steady flow the problem leads to a system of equations which, albeit linear in the unknown circulations of bound vortices, is nonlinear in the unknown locations of free vortices. It is solved by a two-step iteration by alternately
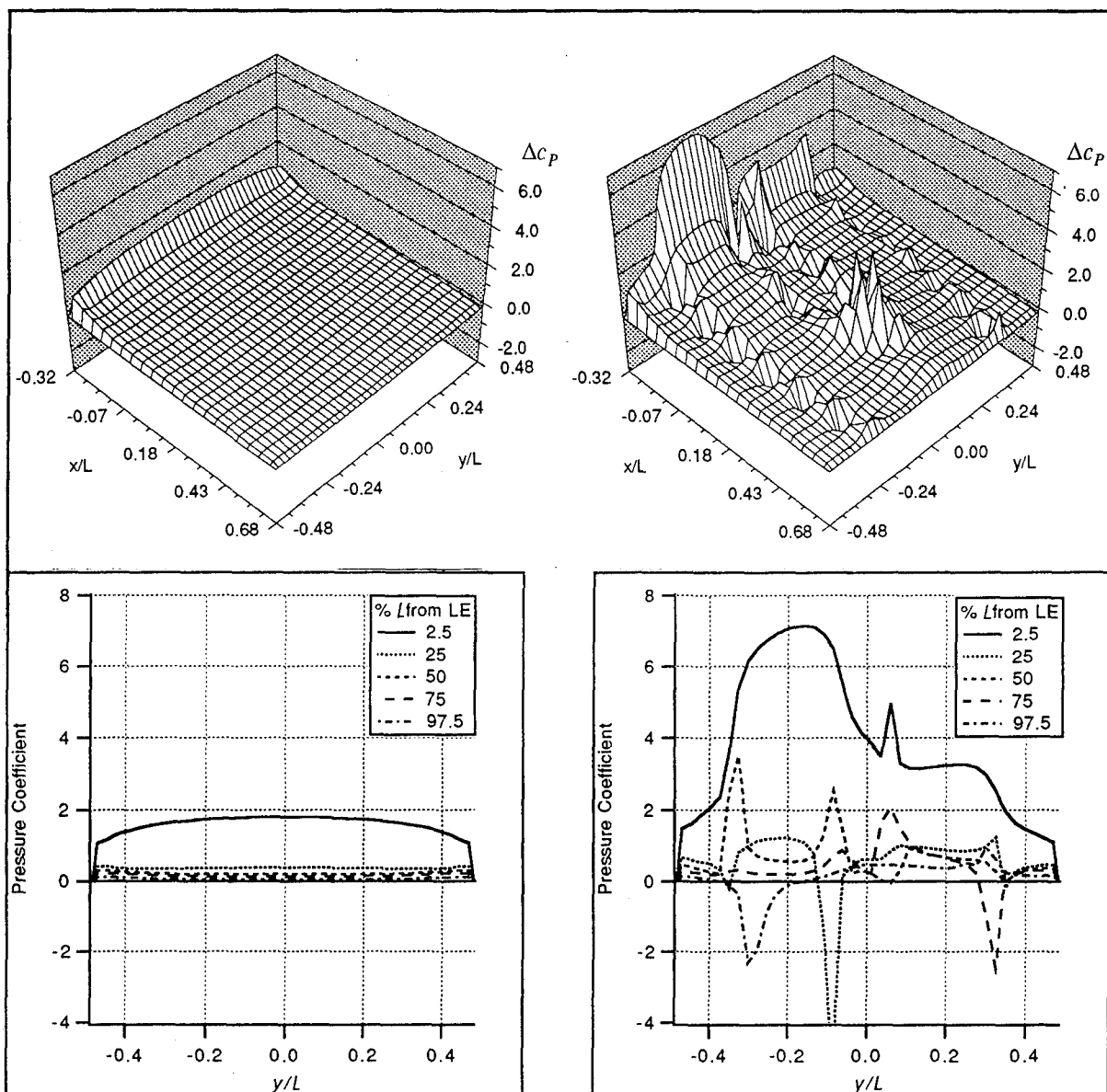
776

Figure 13. Computed normalized load distribution on the skeleton plane of a rectangular rudder in uniform parallel inflow (left) and in slipstream (right) shown in perspective view (top) and in cross sections (bottom) ($\Lambda = 0.966$; $\delta = 15$ deg;$D/l = 0.82$; Wageningen B4.55R: $P/D = 0.8$; $c_{Th} = 2.44$; $\varphi = 0$ deg)

determining the circulations for prescribed locations and aligning the locations to the updated circulations.

Despite neglect of viscosity and rudder thickness effects the computed lift characteristic of the rudder in uniform parallel inflow agrees well with measurements in the reference case up to about 20 deg incidence. Similarly, the computed propeller wake for the open-water condition at a thrust coefficient $c_{Th} = 2.5$ yields satisfactory agreement with measured velocities (not reproduced here) at the location of the rudder.

The effect of propeller slipstream on the rudder load distribution is found by superimposing the vortex models of the rudder and of the propeller wake. Since the flow is now periodic with blade frequency, discrete quasi-steady calculations are done for several different circumferential positions of the propeller. The computed period-averaged integrated lift characteristic of the rudder in slipstream generally follows the expected trend but differs from the time-averaged model test results by up to 30 % at 20 deg incidence. This is presumably due to rudder thickness effects and to perturbation of the propeller wake by the presence of the rudder. It requires further work.
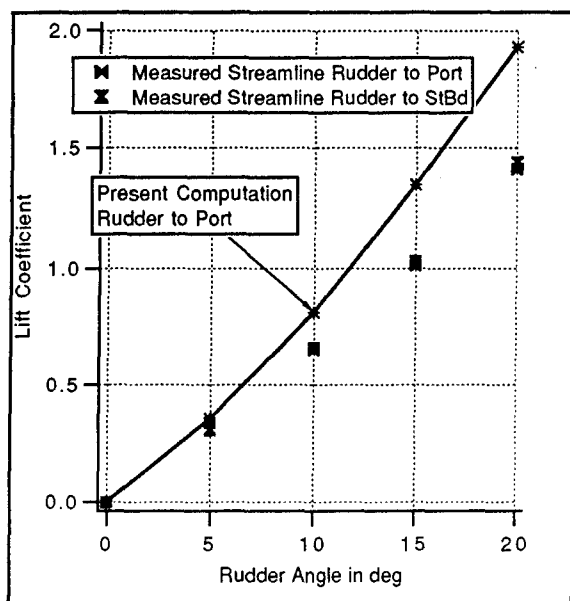
Figure 14. Lift characteristic of rectangular rudder ($\Lambda = 0.966$) in propeller slipstream (Wageningen B4.55R: $P/D = 0.8$; $c_{Th} = 2.44$).

REFERENCES

Andrich, D., "Hydrodynamische Wechselwirkungen in Propeller-Düse-Ruder-Systemen", Diss. Wilhelm-Pieck-Universität Rostock, 1989.

Andrich, D., "Theoretische und experimentelle Untersuchung der hydrodynamischen Wechselwirkung in Propeller-Düse-Ruder-Systemen", Teil I, Schiffbauforschung Vol. 29, No. 4, 1990, pp. 67-177.

Andrich, D., "Theoretische und experimentelle Untersuchung der hydrodynamischen Wechselwirkung in Propeller-Düse-Ruder-Systemen", Teil II, Schiffbauforschung Vol. 30, No. 1, 1991, pp. 3-13.

Baumgarten, B., "Analyse der Ruderkräfte durch Messung der Drücke am Ruder", No. 928, Versuchsanstalt für Binnenschiffbau Duisburg e. V. Duisburg, 1979.

Belotserkovskii, S.,M., The Theory of Thin Wings in Subsonic Flows, Translated from Russian: Holt, M., New York, Plenum Press, 1967.

Brunnstein, K., "Wechselwirkung zwischen Schiffsnachstrom, Schraubenpropeller und Schiffsruder", Diss. Universität Hamburg, 1968.

Haag, K., "Ein Panelverfahren zur Berechnung der Strömung um Flügel mit Vorkantenablösung - Zur stetigen Approximation von Wirbelschichten", Diss. RWTH Aachen, 1988.

Hoeijmakers, H.W.M., "Computational aerodynamics of ordered vortex flows", No. NLR TR 88088U, Amsterdam, The Netherlands, National Aerospace Laboratory NLR, 1989.

Isay, W.-H., Moderne Probleme der Propellertheorie, Ingenieurwissenschaftliche Bibliothek, István Szabó (Hrsg.), Berlin, Göttingen, Heidelberg, Springer-Verlag, 1970.

Isay, W.-H., Propellertheorie, Hydrodynamische Probleme, Ingenieurwissenschaftliche Bibliothek, István Szabó (Hrsg.), Berlin, Göttingen, Heidelberg, Springer-Verlag, 1964.

Klingbeil, K., "Der Einfluß von Nachlauf und Propellerstrahl auf die Querkraft am Ruder", Diss. Universität Rostock, 1972.

Kracht, A., "Ruder im Schraubenstrahl", No. 1178/1990, Versuchsanstalt für Wasserbau und Schiffbau, 1990.

Martensen, E., Potentialtheorie, Vol 12, Leitfäden der angewandten Mathematik und Mechanik, H. Görtler (Hrsg), Stuttgart, Verlag B. G. Teubner, 1968.

Schlichting, H., Truckenbrodt, E., Aerodynamik des Flugzeuges, 2. Band, Aerodynamik des Tragflügels (Teil II), des Rumpfes, der Flügel-Rumpf-Anordnung und der Leitwerke. 2. neubearbeitete Auflage, Berlin, Heidelberg, New York, Springer-Verlag, 1969.

Schröder, W., "Berechnung der nichtlinearen Beiwerte von Flügeln mit kleinem und mittlerem Seitennverhältnis nach dem Wirbelleiterverfahren in inkompressibler Strömung", Forschungsbericht No. 78-26, Deutsche Forschungs- und Versuchsanstalt für Luft- und Raumfahrt, 1978.

Tsakonas, S., Jacobs, W.R., Ali, A. R., "Application of the Unsteady-Lifting-Surface Theory to the Study of Propeller-Rudder Interaction", Journal of Ship Research, 1970, pp. 181-194.

Ulrich, E., Danckwardt, E., Konstruktionsgrundlagen für Schiffsschrauben und Berechnung eines Propellers nach der Wirbeltheorie, Fachbuchverlag Leipzig, 1956.

Wagner, S., Urban, Ch., Behr, R., "A Vortex-Lattice Method for the calculation of wing-vortex interaction in subsonic flow", Notes on Numerical Fluid Mechanics, Vol. 21, Panel Methods in Fluids with Emphasis on Aerodynamics, Ballmann, J., Eppler, R., Hackbusch, W. (Hrsg.), Braunschweig, Wiesbaden, Frieder. Vieweg & Sohn, 1987.

Wiemer, P., "Modellierung freier Wirbelschichten an Deltaflügeln mit einer wirbelangepaßten Panelmethode", Diss. RWTH Aachen, 1987.

Numerical Investigation of Flow and Thrust of an Oscillating 2D Hydrofoil

T.A. Videv, Y. Doi, and K.-H.Mori
(Hiroshima University, Japan)

ABSTRACT

Unsteady laminar viscous flow field around a 2D modified NACA 0012 foil is studied numerically. The foil is performing symmetric pitching, heaving and surging oscillations or their combinations. A parametric study is presented by changing the main governing parameters of the motion, although in a limited range of Reynolds numbers. Special attention is payed to the numerical validation and the propulsive abilities of such foil motions.

The viscous flow simulation is based on solving the 2D, laminar and incompressible Navier-Stokes equations in a mixed vorticity-stream function and vorticity-velocity formulation. An implicit factored finite difference numerical algorithm is used. Numerical tests indicate that the simulated flow is of sufficient accuracy to merit a physical analysis.

Principal results indicate strong unsteady viscous effects with massive flow separation and intensive vortical structures as a result of the leading and trailing edge separation and the further flow evolution. A dynamic stall may occur for some foil motions. From a propulsive point of view, a combined pitching and heaving motion with a shifted phase is the most effective one. Surging oscillations introduce additional dynamic effects. Governing parameters have complicated interrelated influence.

NOMENCLATURE

c - chord length

f - frequency of oscillation

h - heaving displacement

h_A - heaving amplitude

$\mathbf{J}$ - Jacobian; $\mathbf{J}\left(\frac{x,y}{r,\theta}\right) = x_r y_\theta - x_\theta y_r$

k - reduced frequency; $k = fc/2U_\infty$

r, θ - polar coordinates

r_p - distance to the pivot point location (axis of pitching)

Re - chord Reynolds number; $Re = U_\infty c/\nu$

s - surging displacement

s_A - surging amplitude

t - time variable

t^* - normalized time; $t^* = tU_\infty/c$

U_∞ - uniform flow velocity

α - angle of attack with respect to the free stream

$\vec{\omega}$ - vector of vorticity

Ψ - stream function

Ω - pitching angular velocity

INTRODUCTION

Investigations on the viscous flow phenomena around a pitching and/or heaving rigid or flexible airfoil and its dynamic performance have been one of the topics in the theoretical, computational and experimental unsteady fluid dynamics. It is stimulated not

only by the practical needs to prevent or to utilize the problems of dynamic stall and flutter phenomena, but also by the attempts to understand and to simulate high efficient flying and swimming propulsion. Some of the achievements in the area have been summarized in the review presented by McCroskey [1] and later by Carr [2] mainly concerning the first topics. Dedicated to the unsteady regimes, parts of the first and the second survey are pointing to the importance of unsteady separation, viscous-inviscid interaction, and validity of the Kutta condition leading to the conclusion that these effects may be far from negligible when certain periodic foil motions are studied. Despite the progress in these investigations during the last decade, involving sophisticated numerical approaches and recent experimental technologies, clear understanding of the complicated physical phenomenon and interrelated effects of all governing parameters seem to be still remote.

The topic of flying and swimming propulsion have been investigated, which involves the unsteady flow around oscillating lifting body. The continuous interest of many explorers such as Lighthill (1960) [3] and Wu (1961) [4] contributed to the present understanding of the hydrodynamical and biological aspects of swimming and flying. However, most of them have been studied theoretically (Lighthill[5], Karpouzian et al. [6]) and numerically mainly by means of ideal fluid model. Numerical models were limited to unsteady linear and nonlinear lifting line and lifting surface methods, incorporating distributed singularities (see Chopra [7], [8], [9]), vortex-lattice (for example Lan[10]) or panel approaches (Cheng[11]) concerning 2D and 3D rigid or/and flexible lifting bodies. Recently Kudo at al.[12] and Kubota et al.[13] have published their investigations based on a nonlinear, discrete vortex method.

This paper presents the results for the unsteady viscous flow simulation around 2D hydrofoil, performing pitching, heaving (plunging) and surging periodic oscillations

and some combinations of these motions. The main objectives are to analyze unsteady viscous flow phenomena and their contribution to the foil performance with respect to its propulsive abilities and efficiency. A method solving the full 2D, unsteady, incompressible, laminar Navier-Stockes equations was implemented. Although it is obvious that one needs 3D turbulent unsteady flow simulation combined with hydroelastic analysis for practical applications, the present study is limited to the 2D laminar cases. However, we are considering it as a necessary step for the further development.

The numerical algorithm proposed by Mehta (1977) [14] for dynamic stall study of a pitching 2D airfoil was adopted and extended for the objectives of the present study. The paper includes an analysis of the foil motion and phenomena with respect to the dynamic stall which is extended to the studies on swimming propulsion. The discussion on the theoretical formulation and numerical method used here is followed by the results for some pilot computations in order to ensure the validity of simulation. Main results are organized in a form of parametric study, performed separately for the studied types of foil oscillations.

The principal results are that strong unsteady viscous effects have been observed for the studied range of Reynolds numbers. These effects include leading edge separation initiated by the dynamic adverse pressure gradient, massive separation with a strong viscous-inviscid interaction, trailing edge separation and wake distortion. They could be hardly simulated properly by a inviscid model, whose affects on the foil performance might be remarkable. Either the applications of the boundary-layer theory or the thin-layer approximations are questionable.

Without forgetting that the present conference is held in honor of Professor Emeritus Louis Landweber, it is our pleasure to refer his contribution to these field. Although by means of potential model, he studied high frequency heaving oscillations of a

2D foil (Choi,Landweber[15]). A more accurate wake consideration is offered where the trailing edge vortex position is obtained as a part of the solution without any artificial hypothesis. One of the principal results of their paper concerns the crucial importance of accurate estimation of the position and the strength of the nascent vortex and we will be back to their opinion in the light of the results obtained during the present study.

FOIL MOTION AND PROBLEM DEFINITION

The main factors which may lay claims to any particular choice of theoretical formulation and its numerical implementation are connected with the physical phenomena to be investigated. For the present study these factors are the foil motions and some preliminary knowledge for the general flow features which have to be properly modeled.

Foil Motion

According to the stated objectives, the hydrofoil is allowed to perform all 2D transient motions; pitching, heaving (plunging) and surging or any combination of these three degrees of freedom. It will be realistic to limit the motion to harmonic sinusoidal oscillations characterized by frequency, amplitude and the uniform oncoming flow U_∞. The governing parameters in the case of heaving motion are the frequency of oscillation f_h and the heaving amplitude h_A as the mean transverse position may be always chosen as a reference axis. The periodic vertical displacement $h(t)$ is

$$h(t) = h_A \cos(f_h t) \qquad \text{(for t} \geq t_{0h}), \qquad (1)$$

where t_{0h} is the reference time when the oscillations have been initiated. The surging and pitching oscillations are defined in a similar manner as a periodic horizontal motion where $s(t)$ and inclination $\alpha(t)$ are given by

$$s(t) = s_A \cos(f_s t) \qquad \text{(for t} \geq t_{0s}), \qquad (2)$$
$$\alpha(t) = \alpha_A \cos(f_p t) \qquad \text{(for t} \geq t_{0p}), \qquad (3)$$

where t_{0s} and t_{0p} are the initial times of surging and pitching respectively. From a practical point of view, the cases are interesting when these motions are performed with the same frequency ($f = f_h = f_s = f_p$) but with or without a phase difference between them. Such motion is described by

$$
\begin{aligned}
h(t) &= h_A \cos(ft), \\
s(t) &= s_A \cos(ft + \phi_s), \qquad (4)\\
\alpha(t) &= \alpha_A \cos(ft + \phi_p),
\end{aligned}
$$

where ϕ_s and ϕ_p are phasings of surging and pitching with respect to the heaving oscillations. Additional parameters for the pitching stroke are the axis of pitching or the pivot point location r_p. In the present study, a generalization is made assuming that the pivot point may be located at an arbitrary distance from the foil. In the cases when the pivot point is located ahead of the leading edge or behind the trailing edge, the motion could be treated as a coupled pitching motion with heaving and surging oscillations whose pivot point is located on the chord. The idiosyncrasy of such motion is that the heaving and surging velocities and accelerations will depend on the pitching velocity and acceleration.

The foil motions with such parameters may be described introducing three coordinate systems: an inertial system (x_0, y_0), a translating non-inertial system fixed to the pivot point location (x_1, y_1), and a rotating system fixed on the foil (x, y) (Fig.1).

For the sake of convenience, normalized values of the main governing parameters are introduced; normalized pivot point location: $r_p^* = r_p/c$, and heaving and surging amplitudes: $(h_A^* = h_A/c)$ and $s_A^* = s_A/c$.

Hydrodynamical Model and General Flow Features

The 2D foil motion is taking place in a uniform oncoming flow U_∞. The fluid is assumed incompressible, viscous and unbounded. Although the present study is
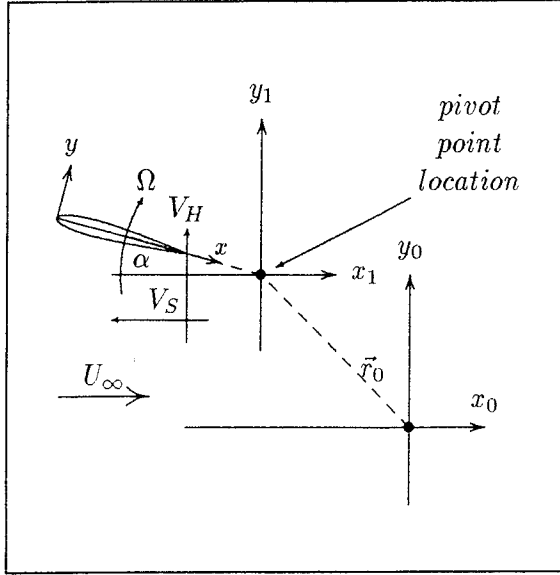
Fig. 1: Coordinate systems definition

limited to the laminar 2D flows, highly unsteadiness such as the dynamic changes of the effective incidence angle, strong separation and viscous-inviscid interaction may be expected. Flow separation and formation of intensive and stable vortical structures may have strong impact on the wake behavior. Such flow features have a claim on the abilities and accuracy of numerical scheme which have to be chosen.

Although the number of parameters for such a flow may be unlimited, a parametric study seems to be the only possibility for a systematic understanding of the flow. Variations of the parameters are chosen mainly from practical reasons. The study on the Reynolds number dependency has to be for a limited range according to the abilities of the algorithm.

GOVERNING EQUATIONS AND NUMERICAL ALGORITHM

With respect to the remarks made in the previous section, the flow is simulated by a finite difference approximation of unsteady, incompressible, 2D Navier-Stokes equations (NS eqs.), treated in a fixed and in a moving frame of reference.

Governing Equations

In a fixed coordinate system the vector form of the NS eqs. is

$$\left(\frac{D\vec{q_I}}{Dt}\right)_I = -\vec{\nabla}p + \frac{1}{Re}\nabla^2\vec{q_I}, \qquad (5)$$

where subscript I refers to the inertial frame of reference (x_0, y_0 - Fig.1). Eq.(5) is written in the rotating frame as

$$\frac{\partial \vec{q}}{\partial t} + \frac{1}{2}\vec{\nabla}(\vec{q}.\vec{q}) - \vec{q}\times(\vec{\nabla}\times\vec{q})$$
$$= -\vec{\nabla}p - \vec{In} + \frac{1}{Re}\nabla^2\vec{q}. \qquad (6)$$

The velocity vector $\vec{q}$ is relative to the rotating coordinate system fixed to the leading edge located by the vector $\vec{r}$ with respect to the origin of inertial frame of reference. The vector of inertial terms $\vec{In}$ reads as

$$\vec{In} = \frac{\partial \vec{V_T}}{\partial t} + \frac{\partial \vec{\Omega}}{\partial t}\times\vec{r} + 2\vec{\Omega}\times\vec{q} + \vec{\Omega}\times(\vec{\Omega}\times\vec{r}), \quad (7)$$

where the vector $\vec{V_T} = (V_S, V_H)$ represents the surging and heaving velocities.

The computational domain is defined in polar coordinates (r, θ), where the NS eqs. are rewritten in terms of the vorticity ω and the stream function Ψ as

$$\mathbf{J}\left(\frac{x,y}{r,\theta}\right)r^2\frac{Re}{L}\frac{\partial\omega}{\partial t} = r^2\frac{\partial^2\omega}{\partial r^2} + r\frac{\partial\omega}{\partial r} + \frac{\partial^2\omega}{\partial\theta^2}$$
$$-r\frac{Re}{L}\mathbf{J}\left(\frac{\omega,\Psi}{r,\theta}\right) - 2\frac{\partial\Omega}{\partial t}\mathbf{J}\left(\frac{x,y}{r,\theta}\right)r^2\frac{Re}{L}, \quad (8)$$

with a stream function defined by

$$r^2\frac{\partial^2\Psi}{\partial r^2} + r\frac{\partial\Psi}{\partial r} + \frac{\partial^2\Psi}{\partial\theta^2} = -\mathbf{J}\left(\frac{x,y}{r,\theta}\right)r^2\omega, \quad (9)$$

where $\mathbf{J}\left(\frac{x,y}{r,\theta}\right)$ and $\mathbf{J}\left(\frac{\omega,\Psi}{r,\theta}\right)$ are the Jacobians.

In order to generate the computational domain, the classical Joukowski transformation is used. Additional stretching near the the foil surface impoves the resolution at the boundary layer region. The O-grid in the physical domain is ilustrated in Fig.2. On
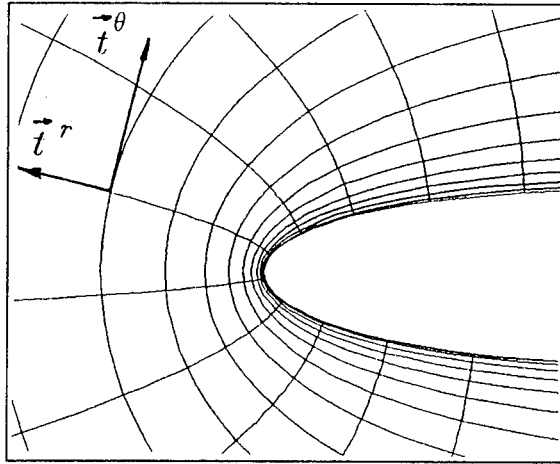
$$C_M = \frac{M}{0.5\rho U_\infty^2 c^2}, \qquad (10)$$

where, F_X and F_Y are the forces acting on the foil in x_0 and y_0 direction (Fig.1) and M is the moment with respect to the pivot point location.

The hydrodynamical efficiency of propulsion of the motion is defined as:

$$\eta = \frac{\text{work done by the propulsive force}}{\text{power required to create this force}}.$$

The path of the pivot point is described by the relations

$$S_X(t) = U_\infty (1 - V_S^*) t$$
$$S_Y(t) = U_\infty V_H^* t, \qquad (11)$$

where V_S^* and V_H^* are normalized surging and heaving velocities. Thrust force T and thrust coefficient C_T is defined as the force and the coefficient acting into the direction of propulsion (negative X axis in this case) and will coincide with the drag force F_X and drag coefficient C_X. In such case, the work W_T done by the thrust is

$$W_T = \frac{1}{\tau} \int_0^\tau F_X \frac{dS_X}{dt} dt$$
$$= -\frac{U_\infty}{\tau} \int_0^\tau (1 - V_S^*) F_X dt. \quad (12)$$

where τ is the time for a cycle of oscillation. The power consumed by the torque force $Q \equiv F_Y$ is

$$P_Q = \frac{1}{\tau} \int_0^\tau \left[F_Y \frac{dS_Y}{dt} + M \frac{d\alpha}{dt} \right] dt$$
$$= \frac{1}{\tau} \int_0^\tau (F_Y V_H^* + M\Omega) dt, \quad (13)$$

Then, the hydrodynamical efficiency of propulsion is :

$$\eta = \frac{W_T}{P_Q} = \frac{\frac{U_\infty}{\tau} \int_0^\tau (1 - V_S^*) F_X dt}{\frac{1}{\tau} \int_0^\tau (F_Y V_H + M\Omega) dt}$$
$$= \frac{\int_0^\tau (1 - V_S^*) C_X dt^*}{\int_0^\tau (V_H^* C_Y + C_M \Omega^*) dt^*}, \quad (14)$$

where Ω^* is normalized piching velocity and τ is at least one period of oscillation.

Fig. 2: O-grid system - physical domain

the surface , the constraint of no slip is applied to define the surface vorticity. At the downstream boundary, the flow is assumed to be governed with first order differential relations obtained from the tangential NS eqs. by dropping the viscous term. For the upstream condition, the uniform velocity is assumed. Both vorticity and stream function eqs. are subjected to periodicity in θ-direction.

The vorticity equations is solved by an implicit factored method. The truncation error has the order of $O[(\Delta r)^2 + (\Delta \theta)^4 + (\Delta t)^2]$, where Δr, $\Delta \theta$ and Δt are the space and time increments respectively. The Fourier transform method is used to solve the stream function equation by a direct approach. The vorticity and stream function equations are solved sequentially. The step is repeated until the convergence of surface vorticity is reached.

The surface pressure distribution is obtained by integrating the tangential component of NS eqs. For further details one may refer to the paper of Mehta [14] and [16].

Nondimensional coefficients are defined in the inertial frame as:

$$C_X = \frac{F_X}{0.5\rho U_\infty^2 c},$$
$$C_Y = \frac{F_Y}{0.5\rho U_\infty^2 c},$$

PILOT COMPUTATIONS

For the discussions on the real physical phenomena, it is necessary to examine the numerical accuracy. The following items should be studied; 1) time increment, 2) grid resolution and 3) parameters involved in the numerical procedure such as dissipative term, relaxation parameters, required accuracy for the surface vorticity convergence, minimum number of iterations for solving stream function-vorticity equations, etc. Although the quality of solution will depends on the flow complexity, we carry out this study through pilot computations.

Computational Parameters

(1) The effect of the time increment on the hydrodynamic loads was studied for several cases with different complexity[16]. Typical results are shown in Fig.3 where a), b) and c) are the results by Δt, $4\Delta t$ and $10\Delta t$ respectively. In a), the time increment is chosen properly corresponding to the flow complexity, but its refinement does not lead to any significant improvements of the quality of solution as seen in b). A further increase leads to an intensive oscillation around the mean value; c). Sometimes, it leads to a lack of convergence at all. During the present computations the time increment varies from case to case with respect to the physical parameters and flow complexity. The know-how obtained at the initial stages of the study results to a time adaptive procedure which is capable to increase (to the safe limit of $\Delta t^* \leq 0.01$) each 20 time steps or decrease the time increment automatically by factor of two if necessary.

(2) The grid resolution effects have been studied for the two grid systems; (66×42) and (130×84). An illustration of the influence of spatial resolution on flow pattern of a pitching foil is found in Fig.4. The simulated flows by the two grid systems are qualitatively identical, although qualitative discrepancies are observed around the leading and trailing edges. The coarse grid system
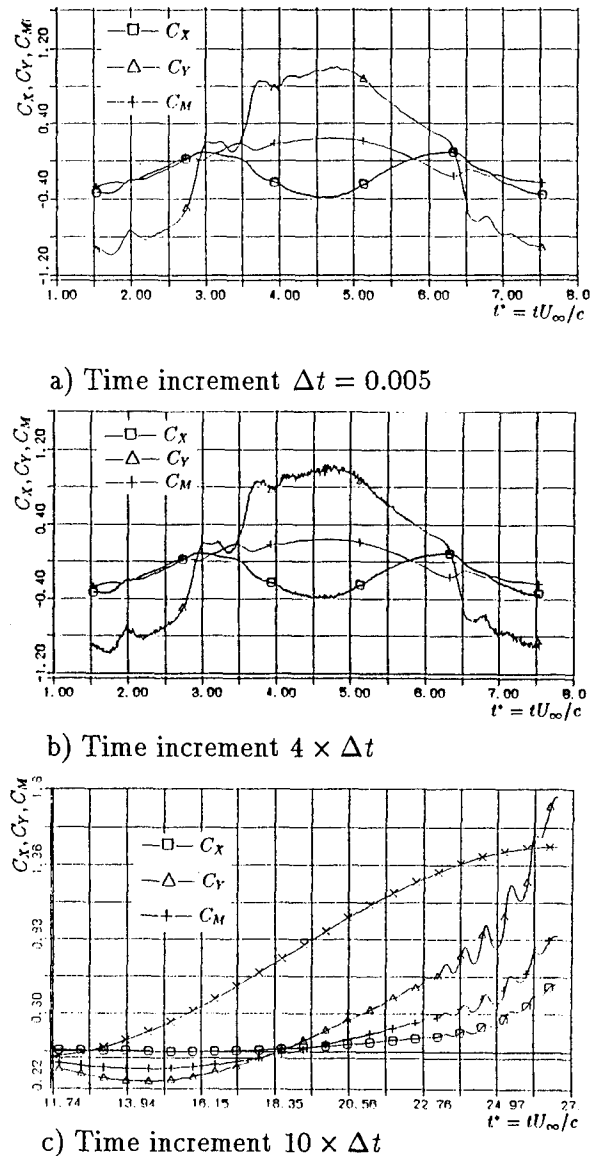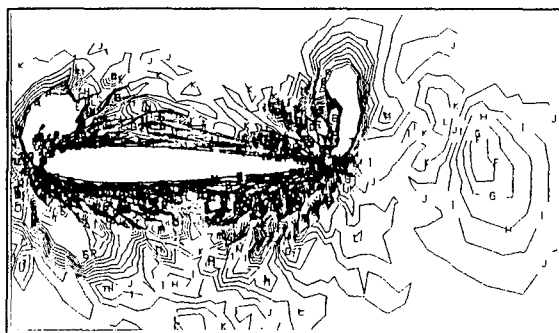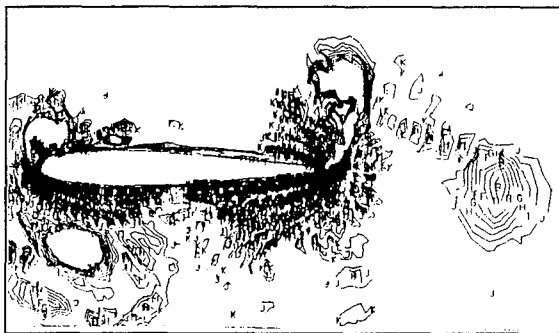

a) Time increment $\Delta t = 0.005$

b) Time increment $4 \times \Delta t$

c) Time increment $10 \times \Delta t$

Fig. 3: The effect of the time increment on the solution

784

a) Grid resolution (66 × 42)

b) Grid resolution (132 × 84)

Fig. 4: Vorticity contours by two grid resolution ($r_p^* = 5.0, k = 2.0$)

led to higher oscillations in force and slowed down the speed of convergence. Coarse grids cannot resolve small flow structures and gradients of the flow parameters with sufficient accuracy. It was seen that the grid resolution affects not only the pattern of the vorticity structures but also their intensity. Although further grid refinement is desirable, the second grid system of (130 × 84) can be concluded to be acceptable for the further discussions.

(3) The influence of other numerical parameters such as the number of iterations for the sequential solving of vorticity and stream function equations, the factors of the dissipative terms, and relaxation procedure, etc. have been studied. It was concluded that they are of secondary importance in comparison with the parameters already discussed. Special attention have to be payed to the criterion for convergence of the solution for the surface vorticity which is in direct connection

with the physical parameters, time increment and grid resolution. Their combined effects may lead to an undesirable oscillation of the solution. More detailed analysis and a study of the influence of round-off errors performed indirectly comparing single and double precision results may be found in the written discussions of [16].

Physical Parameters

As it has been pointed out, the validity of the numerical solution is dependent heavily on the main physical parameters governing the flow phenomena. The most primary parameter is the Reynolds number based on the chord length. For the present computations this limiting value was estimated to be about $Re \approx 1.0 \times 10^4$. In our case, however, it seems to be more proper to define an effective Reynolds number as

$$Re_{eff}(t) = \frac{U_\infty c \sqrt{(1 - V_x^*)^2 + \left(V_y^*\right)^2}}{\nu}, \quad (15)$$

where V_x^* and V_y^* are normalized velocities resulting from the foil motion. This parameter accounts to some extent for the flow complexity in combination with the effective incidence angle α_{eff}.

For high frequency and large amplitude oscillations (or very distant pivot point locations), it appears that we can not proceed with the computations regardless how fine the time step is. For a bit smaller values of parameters of the foil motion, high frequency oscillations in the vorticity field are observed around the leading and trailing edges of the foil. An example is presented in Fig.5 for the case with the reduced frequency of 1.0 and the pivot point located five chord lengths ahead the leading edge. The observed high frequency oscillations have rather numerical nature, although they are induced by physical reasons. Comments on similar results may be found in [14]. Our opinion is that the spectral method used combined with insufficient grid resolution can not handle with
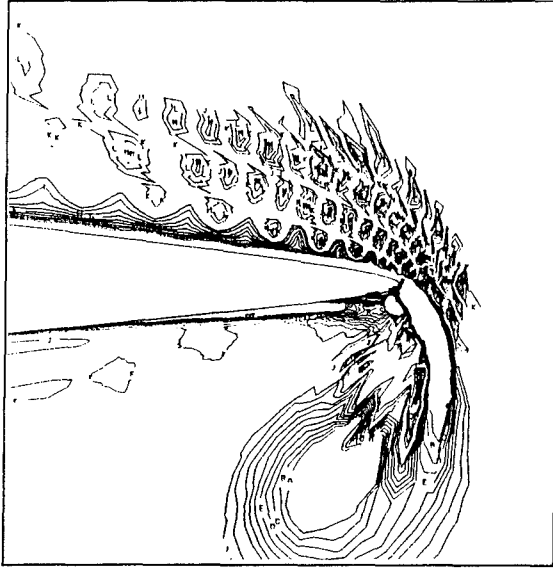
Fig. 5: Vorticity contours at the trailing edge $(r_p^* = -5.0, k = 1.0, \alpha = 12.8°)$

high gradients of the flow with sufficient accuracy. How this oscillation will evolve further depends mainly on the current stage of the foil motion. If their appearance is taking place relatively early in the cycle, they may destroy the solution.

Pilot Computations and Comparison with Experimental Flow Visualization

Accuracy evaluation may be performed by comparing the numerical results with other published results or available experimental data. Here a comparison is made with the experimental data obtained in the frames of the present study. Fig.6 shows one example of the comparisons; the particle path (for the time of exposition) and the contour lines of the stream function in the inertial frame of reference in which the experimental data were taken. The details about the experimental conditions may be found in [16]. The foil is pitching symmetrically with $k = 1.0, \alpha_A = 15°$ and $r_p^* = 5.0$. Reynolds number for the computations and experiment are both 0.5 $\times 10^4$. The experimental data were taken after the foil had performed several cycles of os-

cillations. The main flow structures observed in the experiment are well predicted numerically. Observed differences are in the range of uncertainty of experiments.

All the discussed results seem to indicate that the present numerical study is of sufficient accuracy to allow a physical interpretation of computational data.

HEAVING MOTION

Basic Flow Features

The flow evolution for a typical heaving motion is presented in Fig. 7, showing the streamlines in a frame attached to the foil at some selected stages during the two cycles of heaving motion. The foil is heaving according to eq.(1) with a reduced frequency k_h of 0.52 and normalized amplitude h_A^* of 0.6. All the results shown hereafter concern fully developed flows after the foil is accelerated to the required Reynolds number of 0.5 × 10^4. This stage serves as initial conditions for the consequent phase of harmonic oscillations with the prescribed governing parameters.

Initially, the flow is undisturbed and slightly separated at the trailing edge . At the next stage (in the present case the foil starts to move downward), the separation over the upper side of foil propagates upstream, while the front stagnation point rolls down (Fig.7 a)). Leading edge separation appears long after the effective incidence angle (α_{eff}) exceeded the static stall limits. This phase is illustrated in Fig.7 b). α_{eff} at this moment is about 30°. After the foil passed the zero level, the heaving velocity decelerates and the effective incidence angle also decreases. At this stage, the flow is fully separated. As the foil decelerates further, the leading edge vortices are convected faster (Fig.7 c), d)). In the second cycle, the vortices are shed into the wake and the flow differs in detail from the first cycle, although the general behavior shown in Fig.7 d) is similar to Fig.7 a). The formation of the leading edge vortex is postponed in the second cycle. This later formation leads to moderate intensity and faster convection
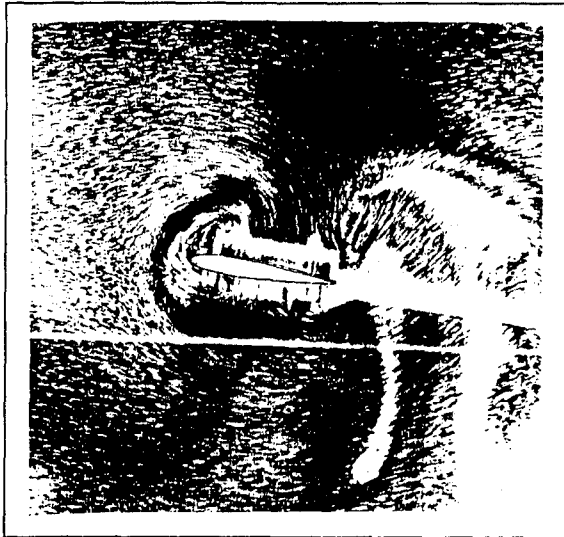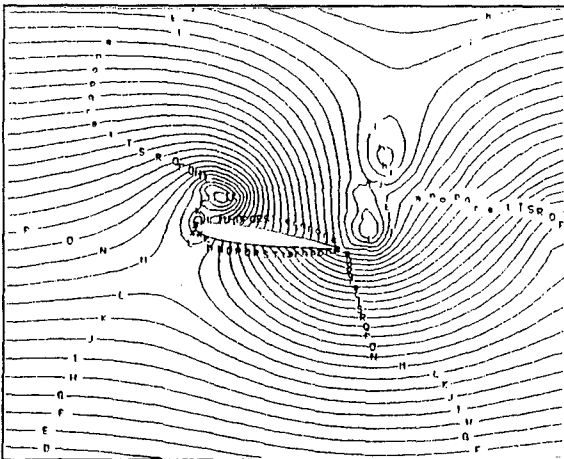
786

of vortices into downstream (Fig.7 e)). After two cycles, in Fig.7 f), the flow pattern is similar to that of c) with some differences caused by the wake influence.

Fig.8, the surface pressure distribution. As can be seen, the pressure is affected mainly by the leading edge vortex and its propagation over the foil surface and wake formation. A sharp suction peak observed at early stage is smoothened as the separation appear. The peak of the leading edge vortex travels along the chord into downstream. Its magnitude corresponds to the vortex intensity. The time history of the drag, lift and moment coefficients is presented in Fig.9. The dynamic changes in the induced forces follow the respective changes in the flow pattern and the pressure distribution. Negative drag means that a propulsive force is realized.

Parametric Study

In order to investigate the effect of acceleration, two cases are studied. They have the same effective incidence angle as a "standard" one, but the acceleration is twice larger or smaller; the first one has parameters $k = 0.26, h_A = 1.2$; for the second one $k = 1.04, h_A = 0.3$.

Flow patterns of these two cases are shown in Fig.10 and Fig.11. They may be compared with the results for the "standard heaving" case presented in Fig.7 b),c) and e). Small foil acceleration can not delay the leading edge separation. The stall vortex is well developed when for the case of large acceleration, the leading edge separation just starts with a short bubble (see Figs.10 a) and 11 a)). In the case of small k, it has much lower intensity than in the case of large frequences, but its diffusion covers a large area. Small inertial effects allow its detachment from the foil surface. The process of light stall in case of small k is illustrated in Fig.10 c). Strong flow separation at this stages leads to a large drag coefficient and low overall propulsive efficiency. Even at the same effective incidence, the flow is much smoother in case of large k

a) Experimental data

b) Streamlines- inertial frame

Fig. 6: Flow visualization and numerical data ($Re = 0.5 \times 10^4, r_p^* = 5.0, k = 1.0$)

a) $t^* = 1.10, h^* = 0.24, \alpha_{eff} = -30°$

b) $t^* = 1.93, h^* = -0.24, \alpha_{eff} = -30°$

c) $t^* = 3.32, h^* = -0.57, \alpha_{eff} = 10.5°$

d) $t^* = 4.10, h^* = -0.24, \alpha_{eff} = 30°$

e) $t^* = 5.25, h^* = 0.40, \alpha_{eff} = 24.6°$
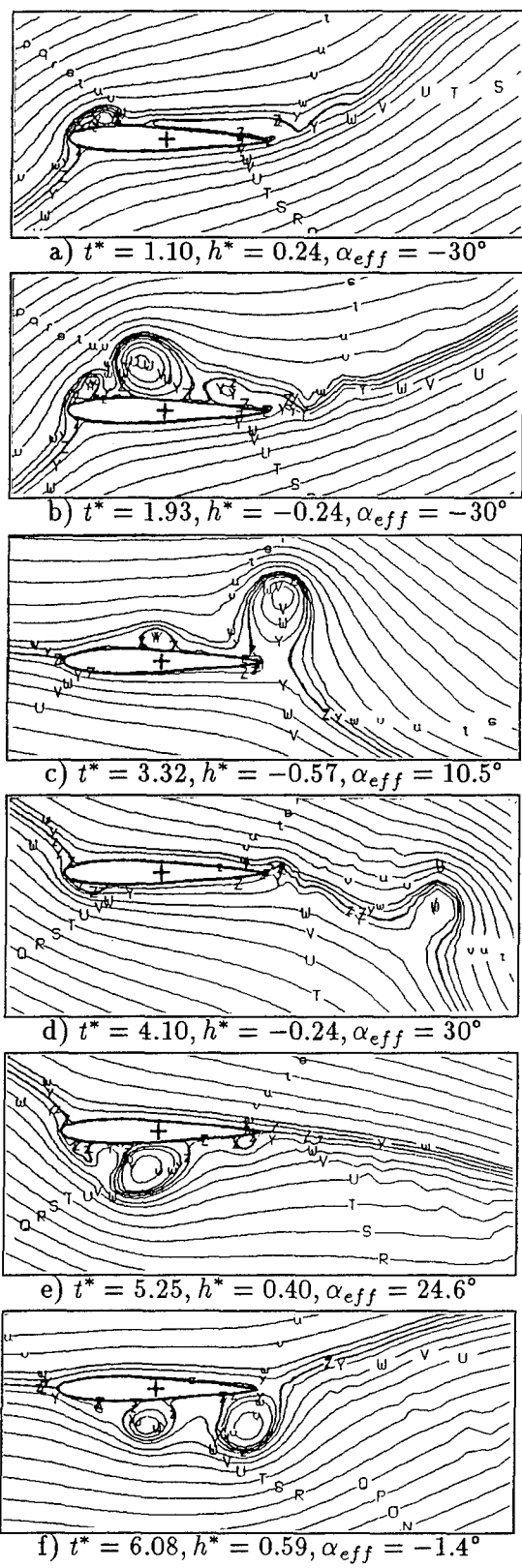
f) $t^* = 6.08, h^* = 0.59, \alpha_{eff} = -1.4°$

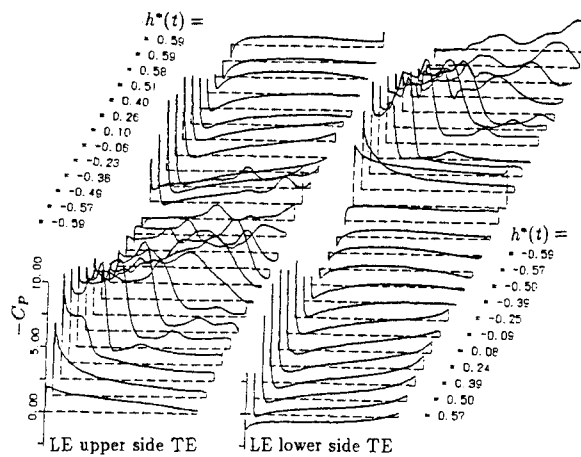Fig. 7: Streamlines in a moving frame ($h_A^* = 0.6, k = 0.52$)

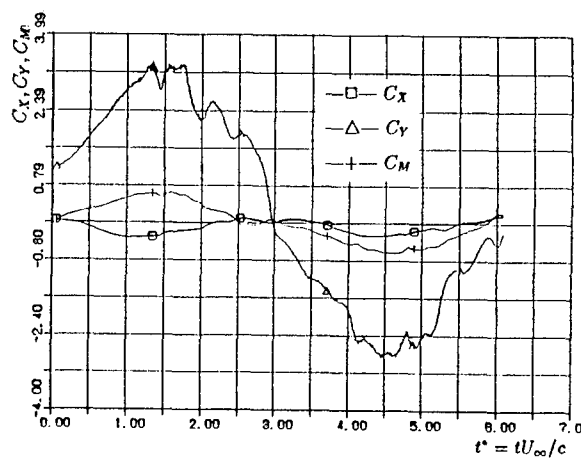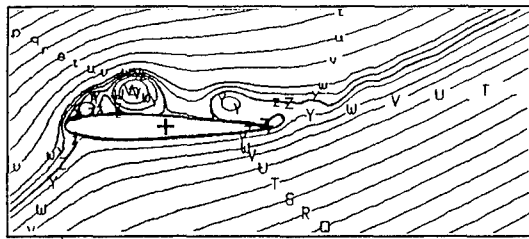Fig. 8: Surface pressure coefficient $-C_P$ ($h_A^* = 0.6, k = 0.52$)
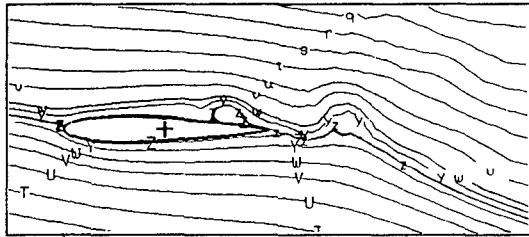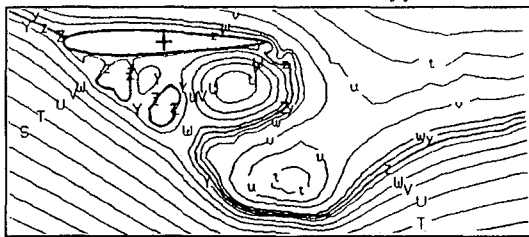

Fig. 9: Drag (C_X), lift (C_Y) and moment (C_M) coefficients ($h_A^* = 0.6, k = 0.52$)

a) $t^* = 2.21, h^* = 0.13, \alpha_{eff} = -30°$

b) $t^* = 6.63, h^* = -0.32, \alpha_{eff} = 10.5°$

c) $t^* = 11.05, h^* = 0.29, \alpha_{eff} = 18.0°$

Fig. 10: Streamlines in a moving frame ($h_A^* = 1.2, k = 0.26$; small acceleration)

a) $t^* = 0.55, h^* = 0.033, \alpha_{eff} = -30°$

b) $t^* = 1.66, h^* = -0.08, \alpha_{eff} = 10.5°$

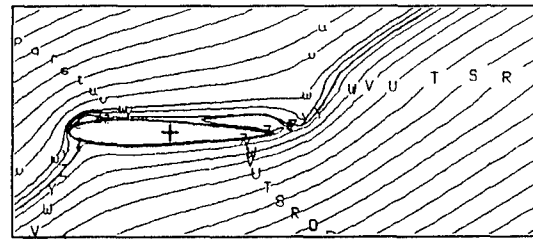c) $t^* = 2.76, h^* = 0.07, \alpha_{eff} = 18.0°$

Fig. 11: Streamlines in a moving frame ($h_A^* = 0.3, k = 1.04$; large acceleration)

(Fig.11 c)). The leading edge vortex formed during the downstroke is finally shed and improves the circulation around the foil to cause a better propulsion.
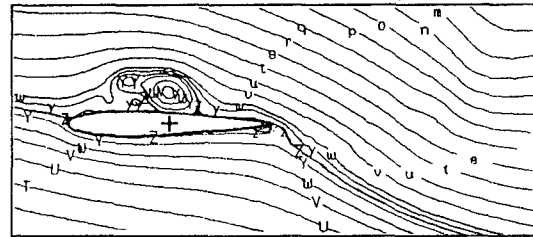
Performance

Fig.12 and Fig.13 present the drag, lift and moment coefficients for the discussed cases. The thrust force for the $k = 1.04$ (Fig.13) is larger than that of the $k = 0.26$ (Fig.12) and slightly larger than the "standard" one (Fig.9). The realized efficiency, $\eta = 0.16$, is comparable with that of the standard case ($\eta = 0.10$).
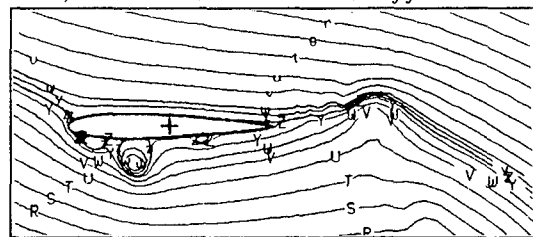
Small increase of the reduced frequency leads to slight improvement in the efficiency. In the cases of very high reduced frequency with small amplitude of oscillations, the efficiency drops rapidly as the thrust/lift ratio
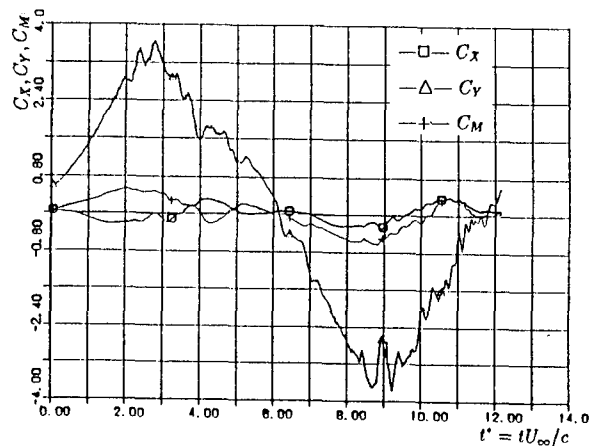

Fig. 12: History of drag (C_X), lift (C_Y) and moment (C_M) coefficient ($h_A^* = 1.2, k = 0.26$)

Fig. 13: Drag (C_X), lift (C_Y) and moment (C_M) coefficient $(h_A^* = 0.3, k = 1.04)$
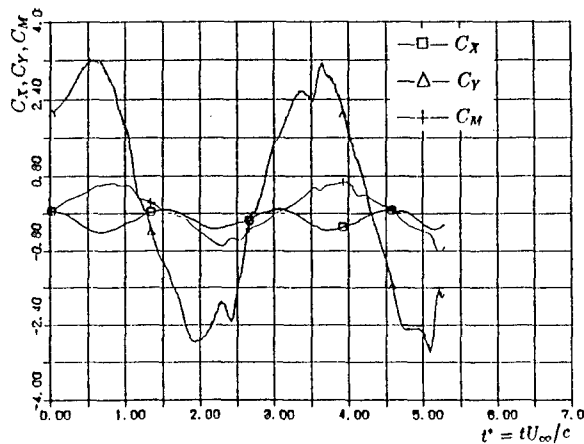

Fig. 14: Drag (C_X), lift (C_Y) and moment (C_M) coefficient $(h_A^* = 0.018, k = 7.78)$

decreases. The coefficients of the hydrodynamic loads for the case of $k = 7.78$ and $h_A^* = 0.018$ are presented in Fig.14. Because the inertial terms are large in this case, the viscous effect is reduced and there is no evidence of separation. The lift is completely out of phase which corresponds qualitatively to the result of Choi and Landweber [15]. However, the results differ quantitatively from those obtained by the potential flow methods. This is because the assumption of the Kutta condition is strongly violated.

Potential methods predict that the efficiency will decrease with the increase of reduced frequency (see for example Katz[17]). The results shown in Fig.12 and Fig.13 lead to the just opposite conclusion. The main reason is that the higher frequency decrease leading edge separation which is not included in potential schemes. When the reduced frequency is low and amplitude large, the flow is characterized by a strong leading edge separation at the early stages of heaving. Such result is caused by weak unsteady effects. This separation has strong impact on the wake and the resulted circulation. It leads to a large drag and low efficiency.
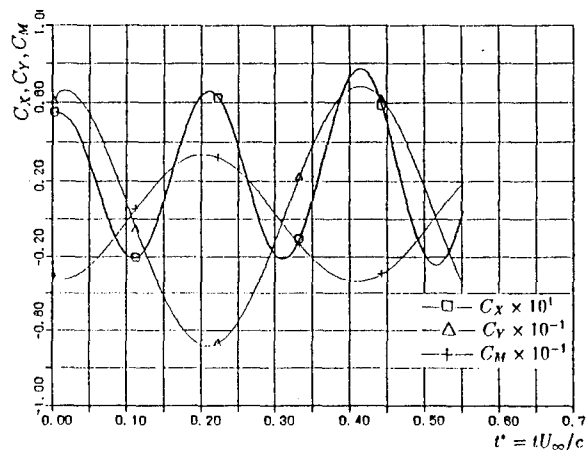
The principal result is that pure having

motion may produce a propulsive force but the efficiency is low.

PITCHING MOTION

The pitching motion is performed symmetrically according to the eq.3. The reduced frequency k, angular amplitude α_A and normalized pivot point location r_p^* can be the parameters of motion.

Cases when the pivot point is located far ahead or far behind the foil were studied in [16]. In these cases, the foil produces thrust but small in mean value. Fig.15 shows a typical example of the time history of the force coefficients; the pivot point is located between the leading edge and the middle of the foil chord. When the foil is pitching around an axis located near the middle of the chord, it can not produce a propulsive force.

Fig.16 shows one of the flow patterns, when the pivot point is located at the leading edge of the foil. In this case, leading edge separation is prevented almost completely. However, large trailing edge separation is generated which induces an increase of the drag.

Comparing with the heaving motion, it is revealed that acceleration of the foil is responsible for the unsteady effects. In the
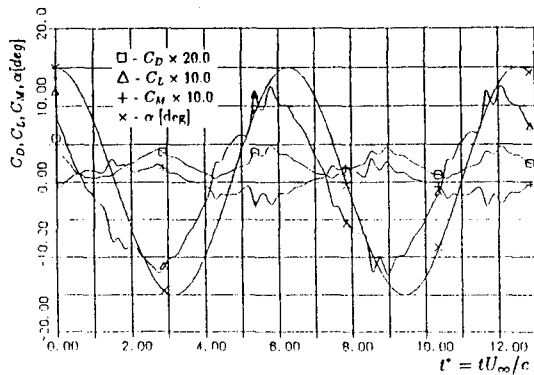
790

Fig. 15: Drag (C_L), lift (C_D) and moment (C_M) coefficients ($r_p^* = 0.1, k = 0.5, \alpha_A = 15°$)

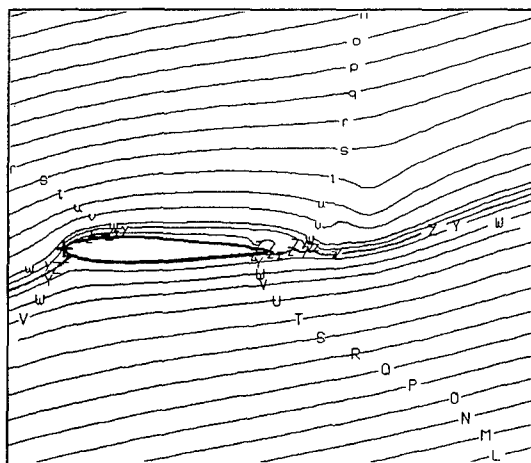

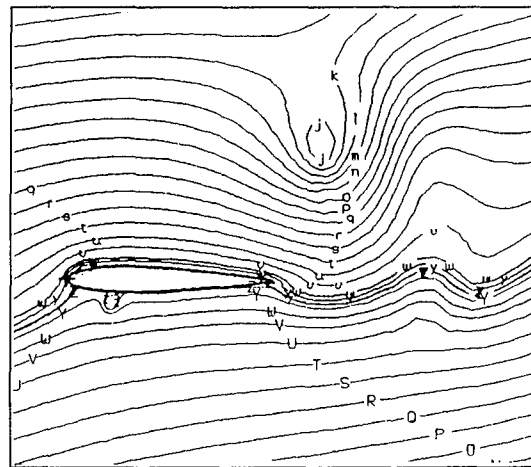Fig. 16: Streamlines in a moving frame ($r_p^* = 0.0, k = 1.5, \alpha_A = 15°, t^* = 1.05$)

Fig. 17: Streamlines in a moving frame ($r_p^* = 0.0, k = 3.0, \alpha_A = 15°, t^* = 1.05$)

pitching case, the acceleration is expressed by $k^2 r_p^* \alpha_A$, so that the flow near the trailing edge is highly dependent on the reduced frequency and the distance to the pivot point location. It is found out that the flow changes dramatically when the pivot point is located relatively near and ahead of the leading edge.

When the oscillations are of relatively low frequency, the trailing edge separation is large to lead to a large drag force. As the frequency of oscillations increases, the inertial terms play a more significant role. Trailing edge separation decreases rapidly when the leading edge separation is negligible (Fig.17). Wake development assists production of a propulsive force and relatively large forward thrust may be obtained. Time variations of the coefficients for this case are presented in Fig.18. The shift in phase of the lift improves additionally the efficiency ($\eta = 0.23$).

Further improvement of propulsive abilities was reached when the pivot point location was moved ahead to the leading edge by a half chord. The flow pattern is illustrated in Fig.19. Although small but intensified separation vortices are observed around the leading edge, quite high efficiency of 0.62 is realized for this case. The coefficients of
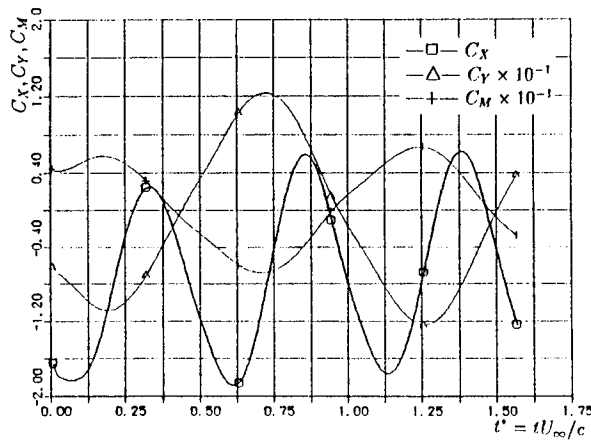
791

Fig. 18: Drag (C_X), lift (C_Y) and moment (C_M) coefficients $(r_p^* = 0.0, k = 3.0, \alpha_A = 15°)$

induced forces are shown in Fig.20. The combined effects of lift phasing, large suction at the leading edge, wake interaction and energy extraction from the near wake results in such higher efficiency. The present result may suggest how the pure pitching motion could be efficiently propulsive.

COMBINED MOTION

The case of combined motion is that heaving, pitching and surging motions are combined.

The "standard case" has the same reduced frequency and heaving amplitude as the standard heaving case $(k = 0.52, h_A = 0.6)$. Pitching is performed around a pivot point located at 0.25c from leading edge with the amplitude of 20°. The effective incidence angle at the pivot point location is ranging in $[-15°, 15°]$ during one cycle. Such motion may lead to an efficient propulsive force as strong separation can not be expected.

Fig.21 shows the flow pattern at the selected stages, visualized by the stream function contours in a moving frame fixed to the foil. Soon after the motion has begun, very small separation bubble formed earlier near the leading edge and a weak trailing edge sep-
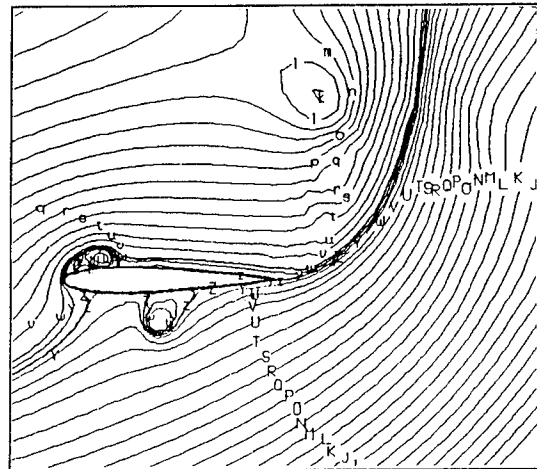

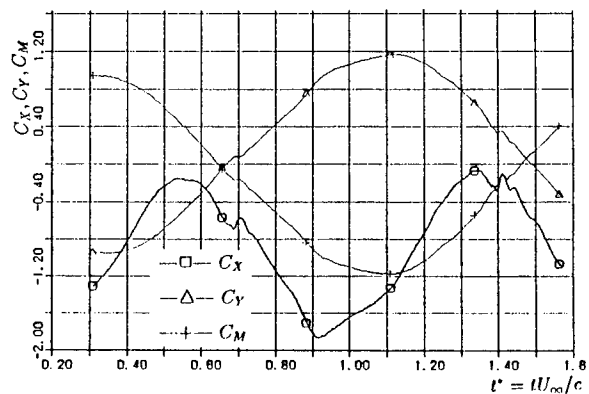Fig. 19: Streamlines in a moving frame $(r_p^* = -0.5, k = 3.0, \alpha_A = 15°, t^* = 1.45)$

Fig. 20: Drag (C_X), lift (C_Y) and moment (C_M) coefficients $(r_p^* = -0.5, k = 3.0, \alpha_A = 15°)$

aration are observed (Fig.21 a)). Stronger separations have been prevented by the foil acceleration at the initial stage. At the moment shown in Fig.21 a) the foil already decelerates and separation of the boundary layer grows. The trailing edge vortex is shed when the bubble separates in two smaller structures which travel into downstream over the foil. Fig.21 b) illustrates the flow, when the foil is at the maximum amplitude and starts its motion downward. Separation is stronger on the lower side. At the following stage, the separation vortices are washed into downstream (Fig.21 c)). A developed wake leads to delay of the flow evolution in comparison with the initial stage (Fig.21 a)) but does not prevent the flow separation when the foil is altering the direction of the heaving motion again (Fig.21 d)).

Such flow behavior is common and is repeated in the following cycles. Comparing with the result for the pure heaving and the pure pitching cases, the unsteady effects and wake interaction are less.

Fig.22 shows the pressure distribution on the foil. The wavy peak of pressure is caused by the leading edge vortex and its propagation in time. Fig.23 shows the time histories of drag, lift and moment coefficients. Qualitatively and in average, the behavior of the induced forces is comparable with the predictions made by the potential model (see for example [17]).

However, they differ in details. Separation of the boundary layer at the stages when the foil is about turning position is causing larger drag and loss of efficiency. It seems that viscous effects are considerable for the flows whose Reynolds number is around 0.5×10^4.

Parametric Study and Performance

Parametric studies are carried out by changing the frequency k, the amplitude heaving and pitching h_A, α_A, and the position of pitching axis r_p^* (Table1). **C0** is the standard case.

a) $t^* = 1.79, h^* = 0.05, \alpha_{eff} = 12°$

b) $t^* = 3.02, h^* = 0.60, \alpha_{eff} = 0.0°$

c) $t^* = 4.53, h^* = 0.00, \alpha_{eff} = -12°$

d) $t^* = 6.04, h^* = -0.60, \alpha_{eff} = 0.0°$

e) $t^* = 7.55, h^* = 0.00, \alpha_{eff} = 12°$
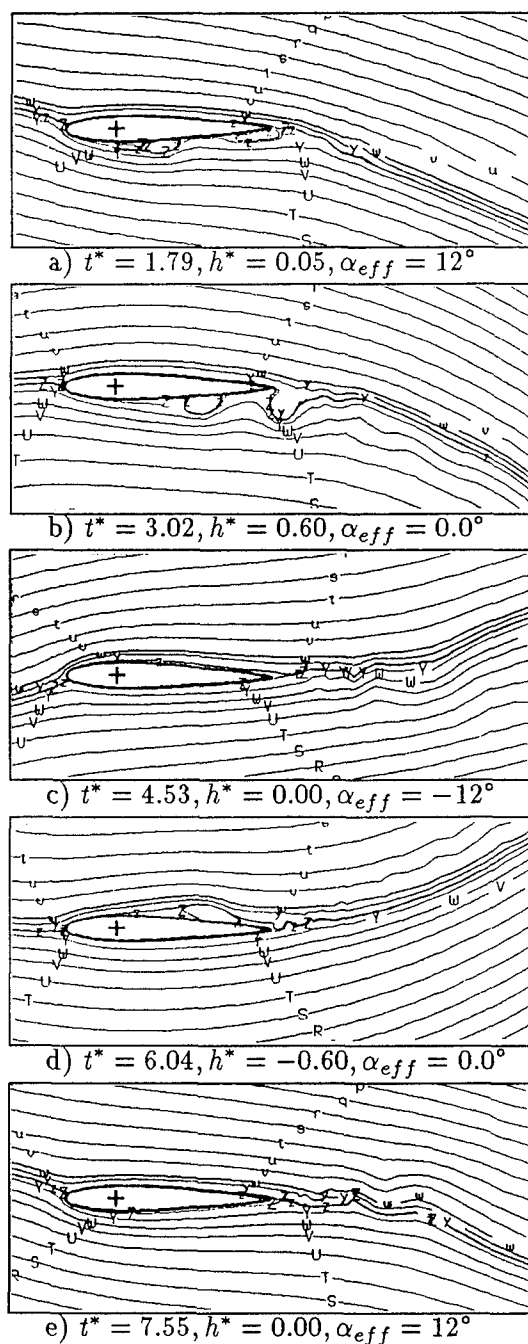
Fig. 21: Streamlines in a moving frame ($h_A^* = 0.6, k = 0.52, \alpha_A = 20°$)

Fig. 22: Surface pressure coefficient $-C_P$ ($h_A^* = 0.6, k = 0.52, \alpha_A = 20°$)

Table 1: Cases for the parametric studies of combined motion.

Case	k	h_A	α_A	r_p^*	η
C0	0.52	0.6	20°	0.25	0.47
C1	0.26	1.2	20°	0.25	0.51
C2	1.04	0.3	20°	0.25	0.41
C3	0.52	0.6	20°	0.00	0.55
C4	0.52	0.6	20°	0.50	0.48
C5	0.52	1.2	40°	0.25	0.61
C6	0.52	2.4	60°	0.25	0.55

The effects of the reduced frequency and the heaving amplitude are studied by the cases **C1** and **C2**. The effective incidence angle for these two cases is the same as the standard case. In case **C1**, the leading edge separation appears earlier due to the smaller dynamic effects. It covers a larger domain (Fig.24 a)) comparing with the standard case. The magnitude of induced forces is bigger as no stall effect is observed. When the foil is altering its direction of heaving, the energy of the shedding vortices is partially extracted back as shown in Fig.24 a). All these facts result in an improvement of efficiency (refer Table.1).

In the case **C2** where the acceleration and deceleration is high, the dynamic effects are stronger. The phase of acceleration delays leading edge separation much longer Fig.24 b). At the same time the trailing edge separation is more intensive to cause a worse performance.

The dependency on the pivot point location is investigated by the cases **C3** and **C4**. In the case **C3** where the pivot point is at the leading edge, the leading edge separation is prevented (Fig.24 c)). In the case **C4** an opposite tendency is observed as shown in Fig.24 d). The leading edge separation appears earlier due to the larger angular deceleration of the leading edge. Its reattachment leads to a trailing edge vortex. When the foil approaches the position of the maximum amplitude, the case of **C4** has a worse efficiency.

Fig. 23: Drag (C_X), lift (C_Y) and moment (C_M) coefficient ($h_A^* = 0.6, k = 0.52, \alpha_A = 20°$)

After the turn, the flow near the leading edge is accelerated, so that the disturbances are washed easier and the foil starts to produce thrust earlier than the other cases. Such a compensation results in a similar efficiency compared with the standard case.

The effect of pitching and heaving amplitude is studied in the case **C5**. Larger amplitude of heaving combined with larger pitching amplitude may be more efficient. The main reason is that the foil inclination compensates the increase of the effective incidence angle to make the thrust component of the reaction force larger. If the energy losses are not so large during the turn, a better efficiency could be obtained. Leading edge separation appears earlier and forms a series of vortices (Fig.24 e)). The mean value of the ratio C_X/C_Y is very high. When the foil approaches its heaving amplitude, the separation grows considerably. The shedding of the edge vortices leads to an energy extraction. However, much larger amplitude fails to increase the efficiency as seen in the case **C6**. The separation is much more intensive and remain longer after the foil is altering the direction of heaving. It causes a large drag force. This fact leads to a worse efficiency.

GENERAL DISCUSSION

Parametric studies described in the previous sections indicate that flow phenomena depend much more on the parameters of the motion than on the type of motion itself such as heaving, pitching and surging. Driving parameters have a complicated and interrelated influence on the flow pattern and induced forces. In the light of obtained results, conclusions like "as the reduced frequency increases, the mean thrust increases while the efficiency decreases." seem to be ambiguous. It could be true or could not be as it depends on the other parameters and all complexity of dynamic effects. For example, the resultant effective angle of attack, strong trailing and leading edge separation and stall depend much on the parameters. When driv-
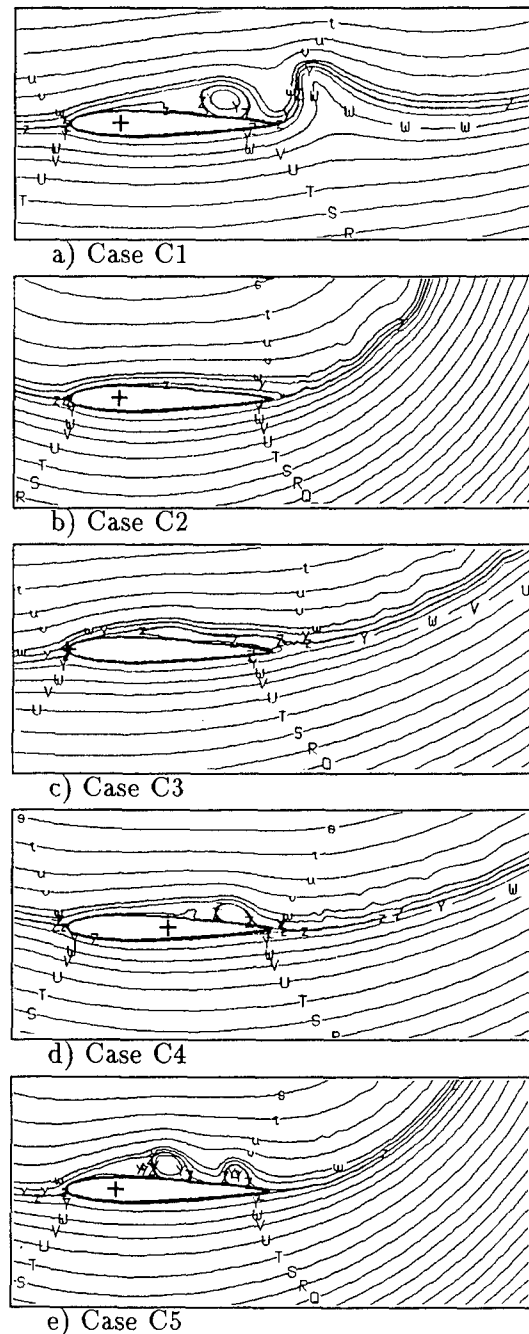

a) Case C1

b) Case C2

c) Case C3

d) Case C4

e) Case C5

Fig. 24: Parametric study of combined motion. Streamlines for the middle of the second cycle

795

ing parameters postulate a foil motion with significant foil acceleration and deceleration, strong unsteady dynamic effects govern the flow evolution. When the foil is accelerating, leading edge separation is prevented or postponed. If a separation appears at this stage, it produces intensive vortical structures which evolve rather by diffusion than by convection. On the other hand, the deceleration assists separation process. Quite different flow phenomena are observed for the cases characterized by small amplitude oscillations with extremely high reduced frequency Strong inertial forces govern the flow pattern overwhelming viscous effects. They will dump transition and turbulent effects as well.

From this point of view, the results obtained by a potential method may be questioned even qualitatively. Obviously, such methods will provide unrealistic results and misleading conclusions for strong unsteady viscous effects as studied.

The Reynolds number may affect the results not only quantitatively but qualitatively as well. Its effect is studied for the combined motion (case C0). Computations were carried out for $Re = 1.0 \times 10^3$ and $Re = 1.0 \times 10^4$, including $Re = 0.5 \times 10^4$ for the case C0. Its influence on the flow pattern is illustrated in Fig.25 as in Fig.21 d) for the standard case. It is well seen that the effect is not negligible even within this small variation. In the case of $Re = 1.0 \times 10^3$, the leading edge separation vanishes but the trailing edge separation is much stronger. For $Re = 1.0 \times 10^4$ the leading edge separation is stronger, but the scale is smaller and more intensive. The flow reattaches faster. Such qualitative differences are valid all the way during the motion. As a result a better efficiency ($\eta = 0.54$) is realized at higher Reynolds number. In the case of low Reynolds number the efficiency dropped to $\eta = 0.30$.

The time histories of force coefficients are shown in Fig.26 a) and b) for $Re = 1.0 \times 10^3$ and $Re = 1.0 \times 10^4$. the low and high Re respectively. Comparing efficiency

a) $Re = 1.0 \times 10^3$

b) $Re = 1.0 \times 10^4$
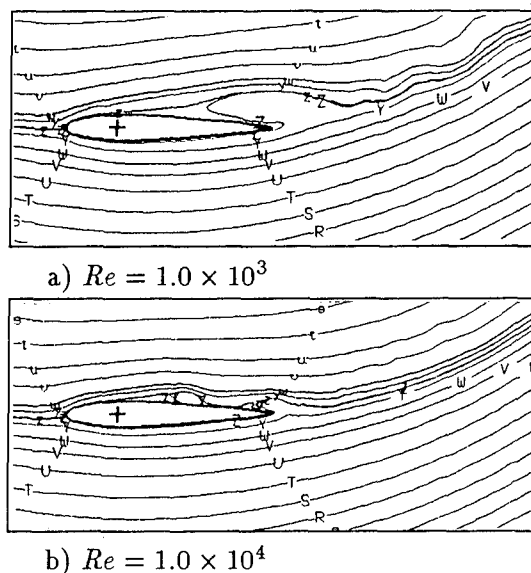
Fig. 25: Effect of Reynolds number on the flow pattern ($h_A^* = 0.6, k = 0.52, \alpha_A = 20°$)

coefficients for the three Reynolds numbers we may suggest that at really high Reynolds numbers the propulsion may be of considerable for the practice efficiency.

Except the cases of pitching with high frequency around a pivot point in front of the leading edge, the only motion with considerable high efficiency is the combined one. The efficiency is very sensitive to the variations of parameters. An extensive research is needed to specify in details the best combination of parameters for a more efficient propulsion system.

CONCLUSION

Numerical simulation of viscous unsteady flow around an oscillating 2D hydrofoil is performed. An implicit finite difference method is implemented. Main flow features and its dependency to the foil motion are investigated. Obtained results lead to the following main conclusions:

- Pilot computations and comparison of the numerical results with available experimental data concluded that the ba-

a) $Re = 1.0 \times 10^3$
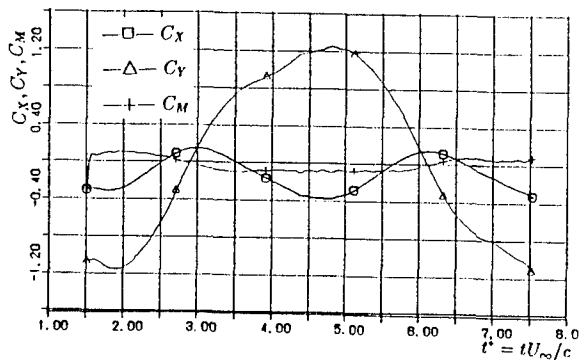
b) $Re = 1.0 \times 10^4$

Fig. 26: Effect of the Reynolds number on the indiced forces ($h_A^* = 0.6, k = 0.52, \alpha_A = 20°$)

sic flow features are modeled with sufficient accuracy to merit physical analysis. However, the accuracy simulations may be limited with respect to the used grid resolution.

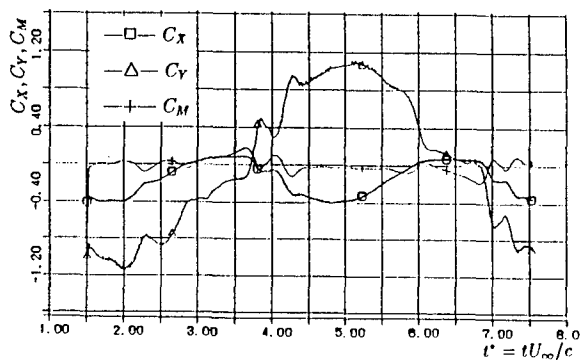- Basic flow features depend strongly on the main parameters governing the foil motion. The parametric study indicated their interrelated influence. The foil acceleration is revealed as a major physical parameter for the unsteady and viscous effects.

- The ability of an oscillating foil to produce forward thrust is in direct connection with the foil motion and resulted flow. Pure heaving motion can produce thrust but of limited efficiency. This conclusion is valid for the pitching motion, except the cases of very high frequency and the pivot point located slightly ahead of the leading edge of the foil.

- Combined foil motion can produce thrust force with high efficiency. Simulated results show the complicated nature of thrust production and the heavy dependence of the efficiency on the parameters of the motion. Further investigations may be needed for tuning these parameters if efficiency has to be improved.

- Complicated flow phenomena lead to the conclusion that 3D effects as well as turbulent effects may play an important role.

References

[1] McCroskey,W.J., "Unsteady Airfoils," Annual Review of Fluid Mechanics, 1982, pp. 285-311.

[2] Carr,L.W., "Dynamic Stall Progress in Analysies and Prediction," AIAA Paper 85-1769CP, 1985.

797

[3] Lighthill,M.J., "Note on the swimming of slender fish," Journal Fluid Mechanics, Vol. 9, 1960, pp. 305-317.

[4] Wu,T.Y., "Swimming of waving plate," Journal Fluid Mechanics, Vol. 10, 1961, pp. 321-344.

[5] Lighthill,M.J., "Biofluiddynamics of balistiform and gymnotiform locomotion. Part 2. The pressure distribution arising in two-dimensional irrotational flow from a general symmetrical motion of a flexible flat plate normal to itself," Journal Fluid Mechanics, Vol. 213, 1990, pp. 1-10.

[6] Karpouzian,G., Spedding,G. and Cheng,H.K., "Lunate - tail swimming propulsion. Part 2. Performance analysis," Journal Fluid Mechanics, Vol. 210, 1990, pp. 329-351.

[7] Chopra,M.G., "Hydromechanics of lunate - tail swimming propulsion," Journal Fluid Mechanics, Vol. 64, 1974, pp. 375-391.

[8] Chopra,M.G., "Large amplitude lunate - tail theory of fish locomotion," Journal Fluid Mechanics, Vol. 74, 1976, pp. 161-182.

[9] Chopra,M.G., "Hydromechanics of lunate - tail swimming propulsion. Part 2," Journal Fluid Mechanics, Vol. 79, 1977, pp. 49-69.

[10] Lan,C.E., "The unsteady quasi - vortex - lattice method with applications to animal propulsion," Journal Fluid Mechanics, Vol. 93, Part 4, 1979, pp. 749-765.

[11] Cheng,J.Y., Zhuang,L.X., Tong,B.G., "Analysis of swimming three - dimensional waving plates," Journal Fluid Mechanics, Vol. 232, 1991, pp. 341-355.

[12] Kudo,T., Kubota,A., Kato,H., Yamaguchi,H., "Study on Propulsion by Partially Elastic Oscillatinf Foil. 1st Report.

Analysis by Linearized Theory," J. Soc. Naval Arch. of Japan, Vol. 156, Nov. 1984, pp. 82-91. (in Japanese).

[13] Kubota,A., Kudo,T., Kato,H., Yamaguchi,H., "Study on Propulsion by Partially Elastic Oscillatinf Foil. 2nd Report. Numerical simulation by singularity distribution method and evaluation of scope for application to ship propulsion," J. Soc. Naval Arch. of Japan, Vol. 156, Nov. 1984, pp. 82-91. (in Japanese)

[14] Mehta,U.B., "Dynamic Stall of an Oscillating Airfoil," AGARD Paper 23, Unsteady Aerodynamics, AGARD CP-227, Sept. 1977.

[15] Choi,D.H., Landweber,L., "Inviscid Analysis of Two - Dimensional Airfoils in Unsteady Motion Using Conformal Mapping," AIAA Journal, Vol. 28, No. 12, Dec.1990, pp. 2025-2033.

[16] Videv,T.A. and Doi,Y., "Numerical Study of the Flow and Thrust Produced by a Pitching 2D Hydrofoil," J. Soc. Naval Arch. of Japan, Vol. 172, Nov. 1992, pp. 165-174.

[17] Katz,J. and Weihs,D., "Hydrodynamic propulsion by large amplitude oscillation of an airfoil with chordwise flexibility," Journal Fluid Mechanics, Vol. 88, Part 3, 1978, pp. 485-497.

APPENDIX

LIST OF PARTICIPANTS

LIST OF PARTICIPANTS

Alaez, Jose A.	El Pardo Model Basin	Spain
Alfievi, Alejandro	University of British Columbia	Canada
Ando, Jun	Kyushu University	Japan
Baba, Eiichi	Mitsubishi Heavy Industries, Ltd.	Japan
Bai, Kwang-Jun	Seoul National University	Korea
Bardisa, Enrique	Ingenieria de Sistemas de Informacion, S.L.	Spain
Beale, James	General Dynamics	USA
Beck, Robert	University of Michigan	USA
Bingham, Harry B.	Massachusetts Institute of Technology	USA
Boudreaux, James	General Dynamics Electric Boat Division	USA
Bruzzone, Dario	University of Genova	Italy
Busby,Judy	Mississippi State University	USA
Campana, Emilio	INSEAN-Italian Ship Model Basin	Italy
Campos, Jose A.C.F.	Instituto Superior Tecnico	Portugal
Chakrabarti, Subrata K.	Chicago Bridge & Iron	USA
Chen, Bin	The University of Iowa	USA
Chen, Changsi	St. Anthony Falls Hydraulics Laboratory	USA
Chen, Hamn-Ching	Texas A&M University	USA
Chen, Lea-Der	The University of Iowa	USA
Choi, Do H	Korea Advanced Institute of Science	Korea
Choi, Jung-Eun	The University of Iowa	USA
Chuang, Jim	Technical University of Nova Scotia	Canada
Coakley, Scott	University of California Berkeley	USA
Coney, William B.	BBN Systems and Technologies	USA
Dagan, Arie	The University of Iowa	USA
Deshpande, Manish	The Pennsylvania State University	USA
DiMascio, Andrea	INSEAN	Italy
Doi, Yasuaki	Hiroshima University	Japan
Dommermuth, Douglas G.	Science Applications International	USA
Eca, Luis	Instituto Superior Tecnico	Portugal
Ettema, Robert	The University of Iowa	USA
Farmer, James	Princeton University	USA
Feng, Jinzhang	The Pennsylvania State University	USA
Fine, Neal E.	Engineering Technology Center	USA
Gresho, Philip M.	L-262 Lawrence Livermore National Laboratory	USA
HaUy, David	DREA	Canada
Haussling, Henry J.	Carderock Div Naval Surface Warfare Center	USA
Hendrix, Dane M.	David Taylor Model Basin, NSWC	USA
Hering, Robert	The University of Iowa	USA
Hino, Takanori	Ship Research Institute, JAPAN	Japan
Hong, Sa-Young	KRISO	Korea
Hsin, Ching-Yeh	Massachusetts Institute of Technology	USA
Hsiung, Chi-Chao	Technical University of Nova Scotia	Canada
Huang, Hanping	The University of Iowa	USA
Huang, Thomas T.	David Taylor Model Basin	USA
Huang, Yifeng	Massachusetts Institute of Technology	USA
Hubbard, Bryan J.	Texas A&M University	USA
Hubbard, Phil	The University of Iowa	USA
Jameson, Antony	Princeton University	USA
Janssen, Marlene	The University of Iowa	USA

Johnson, Timothy A.	The University of Iowa	USA
Ju, Sangseon	Daewoo Shipbuilding and Heavy Machinery	Korea
Kang, Shin-Hyoung	Seoul National University	Korea
Kataoka, Katsumi	Kyushu University	Japan
Kim, Keunjae	Daewoo Shipbuilding & Heavy Machinery Ltd.	Korea
Kim, Wu Joan	The University of Iowa	USA
Kinnas, Spyros A.	Massachusetts Institute of Technology	USA
Korsmeyer, F. Thomas	Massachusetts Institute of Technology	USA
Kring, Dave	Massachusetts Institute of Technology	USA
Kux, Jurgen H.	Institute of Schiffbau, Hamburg	Germany
Kwag, Seung Hyun	Hyundai Maritime Research Institute	Korea
Kwak, Young Ki	Hyundai Maritime Research Institute	Korea
Landweber, Louis	The University of Iowa	USA
Larsson, Lars	FlowTech Intemafional AB	Sweden
Lee, Ho Young	Hyundai Maritime Research Institute	Korea
Lee, Young Woo	Hyundai Maritime Research Institute	Korea
Lee, Yu-Tai	David Taylor Model Basin	USA
Lenoir, Marc	CNRS/ENSTA Centre de l'Yvette	France
Lew, Jae-Moon	Chung-Nam National University	Korea
Li, Ding	China Ship Scientific Research Center	PR China
Lin, Woei-Nfin	Science Applications International Corporation	USA
Longo,Joe	The University of Iowa	USA
Martinelli, Luigi	Princeton University	USA
Maskew, Brian	Analytical Methods, Inc.	USA
Miller, Richard	The University of Iowa	USA
Nhyata, Hideaki	University of Tokyo	Japan
Morgan, William B.	David Taylor Model Basin	USA
Mori, Kazu-hiro	Hiroshima University	Japan
Nakos, Dimitrios E.	InTec Software & Consulting	USA
Newman, J. Nicholas	Massachusetts Institute of Technology	USA
Noblesse, Francis	David Taylor Model Basin	USA
Odabasi, A. Yucel	Istanbul Technical University	Turkey
Parthasarathy, Ramkumar N.	The University of Iowa	USA
Patel, V.C.	Iowa Institute of Hydraulic Research	USA
Paterson, Eric G.	The University of Iowa	USA
Perez-Rojas, Luis	Escuela Tecnica Superior de Ingenieros Navales	Spain
Pettersen, Bjomar	University of Trondheim	Norway
Purtell, Patrick	Office of Naval Research	USA
Pyo, Sangwoo	Massachusetts Institute of Technology	USA
Raven, Hoyte C.	MARIN	Netherlands
Reed, Arthur M.	David Taylor Model Basin	USA
Rhee, Shin Hyung	The University of Iowa	USA
Rood, Edwin P.	Office of Naval Research	USA
Saisto, Ilkka A.	Helsinki University of Technology	Finland
Salvesen, Nils	Science Applications International Corporation	USA
Sclavounos, Paul D.	Massachusetts Institute of Technology	USA
Scolan, Yves-Marie	Principia RD	France
Shahshahan, Ali	Loras College	USA
Shan-na, Som D.	University of Duisburg	Germany
Sirviente, Ana I.	The University of Iowa	USA
Song, Charles C.S.	St. Anthony Falls Hydraulics Laboratory	USA
Sotiropoulos, Fofis	The University of Iowa	USA
Stem, Fred	Iowa Institute of Hydraulic Research	USA
Suzuki, Hiroyoshi	Osaka University	Japan

Tahara, Yusuke	The University of Iowa	USA
Tanaka, Ichiro	Osaka University Dept of Naval Architecture	Japan
Taylor, Lafe K.	Mississippi State University	USA
Telste, John	Naval Surface Warfare Center	USA
Toda, Yasuyuki	Kobe University of Mercantile Marine	Japan
Tuck, Ernest 0.	University of Adelaide	Australia
Tulin, Marshall	University of California Santa Barbara	USA
Videv, Todor A.	Hiroshima University	Japan
Visonneau, Michael	Ecole Centrale de Nantes	France
Walter, Joel	The University of Iowa	USA
Wang, Henry T.	Naval Research Laboratory	USA
Watson, Stephen J.P.	Defence Research Agency	UK
Weber, Larry J.	The University of Iowa	USA
Westlake, Paul C.	University of Southampton	UK
Whitfield, David L.	Mississippi State University	USA
Wooden, Bruce J.	Specialized Systems, Inc.	USA
Wu, Jin	University of Delaware	USA
Yang, Cheng-I	David Taylor Model Basin	USA
Yao, Yitao	University of California, Santa Barbara	USA
Yu,Xuewen	Technical University of Nova Scotia	Canada
Zhang, Daohua	The University of Iowa	USA
Zhu, Ming	University of Tokyo	Japan